REPORT DOCUMENTATION PAGE
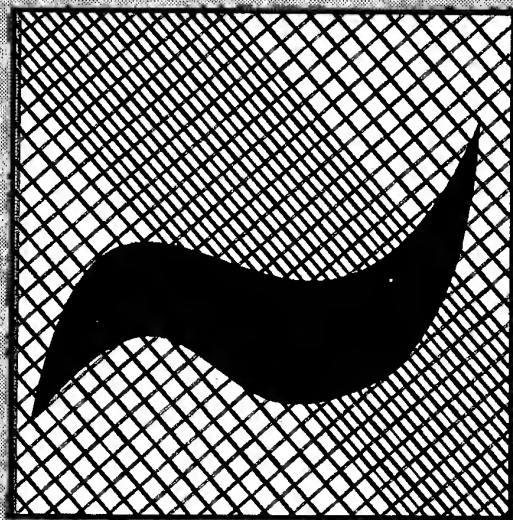
Form Approved OMB No. 0704-0188

1. AGENCY USE ONLY (Leave blank)	2. REPORT DATE July 1996	3. REPORT TYPE AND DATES COVERED Conference Proceedings

4. TITLE AND SUBTITLE 1st International Conference on Composite Science and Technology	5. FUNDING NUMBERS F6170896W0072

6. AUTHOR(S)

Conference Committee

7. PERFORMING ORGANIZATION NAME(S) AND ADDRESS(ES) University of Natal Private Bag X10 Dalbridge 4014 South Africa	8. PERFORMING ORGANIZATION REPORT NUMBER N/A

9. SPONSORING/MONITORING AGENCY NAME(S) AND ADDRESS(ES) EOARD PSC 802 BOX 14 FPO 09499-0200	10. SPONSORING/MONITORING AGENCY REPORT NUMBER CSP 96-1005

11. SUPPLEMENTARY NOTES

12a. DISTRIBUTION/AVAILABILITY STATEMENT Approved for public release; distribution is unlimited.	12b. DISTRIBUTION CODE A

13. ABSTRACT (Maximum 200 words)

The Final Proceedings for First International Conference on Composite Science and Technology (ICCST/1), 18 June 1996 - 20 June 1996

The Topics covered include: Infrastructural use of composites Numerical Modeling Composites design Processing of composites and Experimental studies

14. SUBJECT TERMS			15. NUMBER OF PAGES 672
			16. PRICE CODE N/A

17. SECURITY CLASSIFICATION OF REPORT UNCLASSIFIED	18. SECURITY CLASSIFICATION OF THIS PAGE UNCLASSIFIED	19. SECURITY CLASSIFICATION OF ABSTRACT UNCLASSIFIED	20. LIMITATION OF ABSTRACT UL

ICCST/1

Composite Science and Technology

19970113 014

Edited by
S. Adali and V. E. Verijenko

18 - 20 June, 1996
Durban, South Africa

DISCLAIMER NOTICE

UNCLASSIFIED

Technical Report
distributed by

DEFENSE
TECHNICAL
INFORMATION
CENTER

UNCLASSIFIED
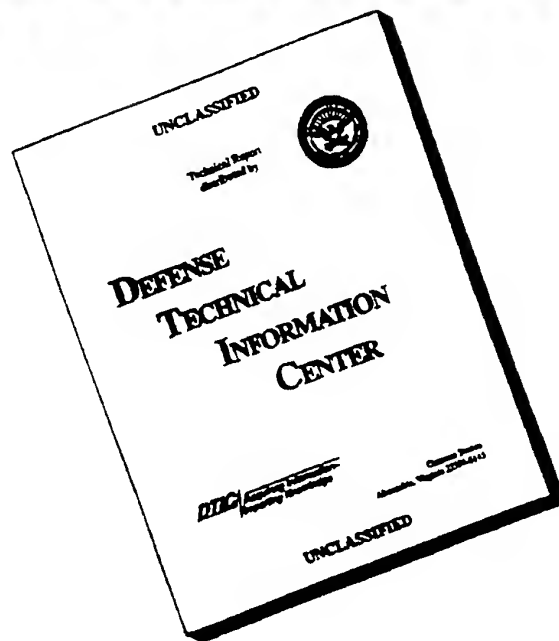
**THIS DOCUMENT IS BEST
QUALITY AVAILABLE. THE
COPY FURNISHED TO DTIC
CONTAINED A SIGNIFICANT
NUMBER OF PAGES WHICH DO
NOT REPRODUCE LEGIBLY.**

Proceedings of the First International Conference on Composite Science and Technology

18 - 20 June 1996
Durban
South Africa

Edited by: S. Adali and V.E. Verijenko
Department of Mechanical Engineering,
University of Natal, Durban,
South Africa.

PREFACE

The topics covered at ICCST/1 include a broad spectrum of subjects involving mechanics and technology of the composite materials and reflect the diverse nature of engineering applications using composites. The advances made in the material science, structural and production aspects of composites led the way to stronger and versatile materials, to tailor-made structures and superior manufacturing processes. The wide choice of design possibilities in composite structures involving not only material, but also manufacturing aspects, provides a challenging field for researchers and at the same time makes composites undoubtedly the material of the future.

It is in this spirit that the First International Conference on Composite Science and Technology has been launched. It is hoped that it will serve its intended objectives by expanding the frontiers of knowledge in composites, bringing scientists, engineers and technologists together for lively discussions and establishing friendship among the practitioners of composites engineering.

Composites is an ever growing field and many research issues of basic, applied and product-related natures are waiting to be studied. It is hoped that ICCST/1 contributes to this endeavour by providing a forum for the dissemination and discussion of knowledge.

The response to the call for papers has resulted in well over 100 papers from 26 countries. However, due to the time constraints, in order to keep the quality of papers at a high level and to provide a relatively small forum for the delegates to meet each other, the technical committee limited the number of papers to 100. For this reason all the papers were subjected to a careful screening before being accepted.

We thank the keynote speakers, plenary session speakers, authors and session chairpersons for their contributions to the conference and look forward to welcoming our delegates to ICCST/1.

Sarp Adali
Viktor E Verijenko

Durban
May 1996

Acknowledgements

CONTENTS

(i)

OPTIMIZATION OF SHEAR–DEFORMABLE LAMINATED PLATES UNDER BUCKLING LOAD

S. ADALI   A. RICHTER   V. E. VERIJENKO

Department of Mechanical Engineering, University of Natal, Durban 4001, South Africa

1. INTRODUCTION

In the present study the optimal buckling design of composite plates is investigated using the general buckling analysis given in [1]. Generally laminated plates under in–plane loading are studied. The specific optimization problem chosen to illustrate the general approach involves a symmetrically laminated angle–ply plate as this is a commonly used configuration in various engineering applications. The optimal ply angle is determined so as to yield the maximum critical buckling load. The effects of various assumptions and problem parameters on the optimal design are discussed.

General aspects of the design of composite laminated thin plates are discussed in [1] where a number of models are developed. The survey of theoretical and experimental results on the buckling and postbuckling behaviour of flat and cylindrical composite panels is given in [2] for various stacking sequences and boundary conditions with the effects of anisotropy and transverse shear deformation included. The optimum designs of laminated plates subject to constraints on strength, stiffness, buckling loads, and fundamental natural frequencies are examined in [3]. The stiffness invariant formulation is used in [4] and [5] for buckling optimization of laminated composite plates with symmetric lay–up.

2. BUCKLING ANALYSIS

Consider a simply supported laminated plate of length a, width b and thickness h under axial compressive loads in x–direction, $\overline{T}_x$, and in y–direction, $\overline{T}_y$. The laminate consists of k plies of thickness t_i and fiber orientations θ_i, where $i = 1, \ldots, k$, so that $\sum_{i=1}^{k} t_i = h$.

Coordinate system $Oxyz$ is introduced with z axis in the transverse direction. The origin of the coordinate system is located at the middle surface of the laminate. The coordinates of the plate are given by $0 \leq x \leq a$, $0 \leq y \leq b$, and $-h/2 \leq z \leq h/2$. The displacements in the directions x, y, and z are denoted by u, v, and w, respectively, while θ_x and θ_y denote the rotation angles of the cross–section normal in the x and y planes, respectively.

The general engineering theory of laminated plates described in [1] is employed to compute the buckling load $\overline{T}_{cr}$ with the loading parameter $\mu = \overline{T}_y/\overline{T}_x$ specified

as an input parameter. The theory takes account of transverse shear deformations and the nonsymmetry of the stacking sequence. The governing equations have the following form in terms of the displacement w, rotation angles and the Airy stress function $F(x, y)$:

$$c_y \frac{\partial^4 F}{\partial x^4} + (c - 2c_{xy})\frac{\partial^4 F}{\partial x^2 \partial y^2} + c_x \frac{\partial^4 F}{\partial y^4} =$$

$$B_{yx}\frac{\partial^3 \theta_x}{\partial x^3} + (B_x + C)\frac{\partial^3 \theta_x}{\partial x \partial y^2} + (B_y + C)\frac{\partial^3 \theta_y}{\partial x^2 \partial y} + B_{xy}\frac{\partial^3 \theta_y}{\partial y^3},$$

$$\frac{\partial w}{\partial x} = -\theta_x + \frac{1}{K_x}\left[D_x \frac{\partial^2 \theta_x}{\partial x^2} + (D + D_{xy})\frac{\partial^2 \theta_y}{\partial x \partial y} + D\frac{\partial^2 \theta_x}{\partial y^2} + C_{xy}\frac{\partial^3 F}{\partial x^3} + \right.$$

$$\left. (C_x - C)\frac{\partial^3 F}{\partial x \partial y^2}\right],$$

$$\frac{\partial w}{\partial y} = -\theta_y + \frac{1}{K_y}\left[D_y \frac{\partial^2 \theta_y}{\partial y^2} + (D + D_{yx})\frac{\partial^2 \theta_x}{\partial x \partial y} + D\frac{\partial^2 \theta_y}{\partial x^2} + C_{yx}\frac{\partial^3 F}{\partial y^3} + \right.$$

$$\left. (C_y - C)\frac{\partial^3 F}{\partial x^2 \partial y}\right], \tag{1}$$

$$D_x \frac{\partial^3 \theta_x}{\partial x^3} + (2D + D_{yx})\frac{\partial^3 \theta_x}{\partial x \partial y^2} + (2D + D_{xy})\frac{\partial^3 \theta_y}{\partial x^2 \partial y} + D_y \frac{\partial^3 \theta_y}{\partial y^3}$$

$$+ C_{xy}\frac{\partial^4 F}{\partial x^4} + (C_x + C_y - 2C)\frac{\partial^4 F}{\partial x^2 \partial y^2} + C_{yx}\frac{\partial^4 F}{\partial y^4} + \overline{p} = 0,$$

where $\overline{p}$ is the nominal load and stiffnesses in geometrical directions are

$$
\begin{array}{ll}
B_x = (B_{22}C_{11} - B_{12}C_{12})/B, & B_{xy} = (B_{22}C_{12} - B_{12}C_{22})/B, \\
B_{yx} = (B_{11}C_{12} - B_{12}C_{11})/B, & B_y = (B_{11}C_{22} - B_{12}C_{12})/B, \\
B = B_{11}B_{22} - B_{12}^2, & C = C_{33}/B_{33}, \\
c_x = B_{22}/B, & c_{xy} = c_{yx} = B_{12}/B, \\
c_y = B_{11}/B, & c = 1/B_{33}, \\
C_x = c_x(C_{11} - C_{12}c_{yx}/c_x), & C_{xy} = c_y(C_{12} - C_{11}c_{xy}/c_y), \\
C_{yx} = c_x(C_{12} - C_{22}c_{yx}/c_x), & C_y = c_y(C_{22} - C_{12}c_{xy}/c_y), \\
D_x = D_{11} - C_{11}B_x - C_{12}B_{yx}, & D_{xy} = D_{12} - C_{11}B_{xy} - C_{12}b_y, \\
D_{yx} = D_{12} - C_{22}B_{yx} - C_{12}B_x, & D_y = D_{22} - C_{22}B_y - C_{12}B_{xy}, \\
D = (D_{33}B_{33} - C_{33}^2)/B_{33}, &
\end{array} \tag{2}
$$

matrices $\{B\}_{i,j=1}^3$, $\{C\}_{i,j=1}^3$, $\{D\}_{i,j=1}^3$ are stiffnesses in material directions, and K_x and K_y are shear stress stiffnesses.

The buckling equations can be obtained from the governing equations by formal specification of the nominal load $\overline{p}$ in (1) as described in [1], viz.

$$\overline{p} = -\overline{T}_x \left(\frac{\partial^2 w}{\partial x^2} + \mu \frac{\partial^2 w}{\partial y^2} \right) \tag{3}$$

The first term in the above equation accounts for the formation of axial waves during buckling when the deflection w changes in x direction, while the second

term arises due to the formation of transverse waves when the deflection w changes in y direction.

The analysis of laminated plates described by equations (1) can be simplified by neglecting the contribution of various effects. If the transverse shear strains are neglected, then

$$K_x \to \infty, \qquad K_y \to \infty \tag{4}$$

In this case the expressions in (1) containing $1/K_x$ and $1/K_y$ are eliminated.

The assumptions (4) are approximately valid for thin plates. However, its effect cannot be neglected for thick plates as shown in the present study. The effects of various simplifications on the optimal designs are studied further in Section 5.

3. METHOD OF SOLUTION

Displacement $w(x,y)$ and rotating angles $\theta_x(x,y)$, $\theta_y(x,y)$ of a simply supported plate can be expressed in terms of double trigonometric series

$$\theta_x = \sum_{m=1}^{\infty} \sum_{n=0}^{\infty} \theta_x^{mn} \cos(\lambda_m x) \sin(\lambda_n y),$$

$$\theta_y = \sum_{m=1}^{\infty} \sum_{n=0}^{\infty} \theta_y^{mn} \sin(\lambda_m x) \cos(\lambda_n y), \tag{5}$$

$$w = \sum_{m=1}^{\infty} \sum_{n=0}^{\infty} w_{mn} \sin(\lambda_m x) \sin(\lambda_n y),$$

and the Airy stress function and the nominal load as

$$F = \sum_{m=1}^{\infty} \sum_{n=0}^{\infty} F_{mn} \sin(\lambda_m x) \sin(\lambda_n y), \qquad \overline{p} = \sum_{m=1}^{\infty} \sum_{n=0}^{\infty} p_{mn} \sin(\lambda_m x) \sin(\lambda_n y), \tag{6}$$

where $\lambda_m = \pi m/a$, $\lambda_n = \pi n/b$, and θ_x^{mn}, θ_y^{mn}, w_{mn}, F_{mn}, and p_{mn} are the unknown Fourier coefficients.

Substituting (5) and (6) into the governing equations (1), the following system of algebraic equations is obtained:

$$\begin{aligned}
F_{mn} b_{11} + \theta_x^{mn} b_{12} + \theta_y^{mn} b_{13} + w_{mn} b_{14} &= 0 \\
F_{mn} b_{21} + \theta_x^{mn} b_{22} + \theta_y^{mn} b_{23} + w_{mn} b_{24} &= 0 \\
F_{mn} b_{31} + \theta_x^{mn} b_{32} + \theta_y^{mn} b_{33} + w_{mn} b_{34} &= 0 \\
F_{mn} b_{41} + \theta_x^{mn} b_{42} + \theta_y^{mn} b_{43} + p_{mn} &= 0
\end{aligned} \tag{7}$$

where the coefficients $\{b_{ij}\}_{i,j=1}^{4}$ are given in [1].

The solution of these equations in terms of w_{mn} is given by

$$w_{mn} = -\frac{p_{mn}}{A} \left[b_{11}(b_{22}b_{33} - b_{23}b_{32}) - b_{12}(b_{21}b_{33} - b_{23}b_{31}) + b_{13}(b_{21}b_{32} - b_{22}b_{31}) \right] \tag{8}$$

3

where

$$A = b_{24}[b_{11}(b_{32}b_{43} - b_{33}b_{42}) - b_{12}(b_{31}b_{43} - b_{33}b_{41}) + b_{13}(b_{31}b_{42} - b_{32}b_{41})]$$
$$- b_{34}[b_{11}(b_{22}b_{43} - b_{23}b_{42}) - b_{12}(b_{21}b_{43} - b_{41}b_{23}) + b_{13}(b_{21}b_{42} - b_{22}b_{41})] \quad (9)$$

The axial buckling load for the mode (m, n) can be calculated from (3) using solution (8):

$$\overline{T}_b(m, n; \theta) = \frac{A}{\lambda_m^2 + \mu\lambda_n^2}\Big[b_{11}(b_{22}b_{33} - b_{23}b_{32}) - b_{12}(b_{21}b33 - b_{23}b_{31})$$
$$+ b_{13}(b_{21}b_{32} - b_{22}b_{31})\Big]^{-1} \quad (10)$$

The critical buckling load $\overline{T}_{cr}$ is determined by minimizing (1) over the integer values of $m = 1, 2, 3, \ldots$ and $n = 0, 1, 2, \ldots$ so that

$$\overline{T}_{cr}(\theta_i) = \min_{m,n} \overline{T}_b(m, n; \theta_i) \quad (11)$$

The dimensionless buckling load is defined as

$$T_b = \frac{\overline{T}_b}{bE_2}, \qquad T_{cr} = \frac{\overline{T}_{cr}}{bE_2} \quad (12)$$

where E_2 is the Young's modulus of a ply in the transverse direction.

The buckling operator (10) corresponds to the most general analysis of the laminated plate, i.e. model 2, as described in Section 2.

4. OPTIMIZATION PROBLEM

The optimal design problem involves the computation of the maximum critical buckling load of the laminated plate for a given thickness ratio h/b and aspect ratio a/b. The general theory presented in the previous sections is applied to a symmetric angle–ply laminate. The optimization is carried out with respect to the ply angle θ for a given loading parameter μ with the ply angles given by $\theta_i = (-1)^{i+1}\theta$ for $1 \leq i \leq k/2$ and $\theta_i = (-1)^i\theta$ for $k/2 < i \leq k$, where k is an even number.

The optimal design problem can be stated as follows

Determine T_{max} and the optimal ply angle θ_{opt} so as to maximize T_{cr}, viz.

$$T_{max} = \max_\theta \min_{m,n} T_b(m, n; \theta) \quad (13)$$

The optimization procedure involves the stages of evaluating the buckling load $T_{cr}(\theta)$ for a given θ and improving the fiber orientation to maximize $T_{cr}(\theta)$.

5. NUMERICAL RESULTS

Numerical results are given for a laminate with a stacking sequence $((+\theta/-\theta)_2)_{sym}$ made of a graphite–epoxy composite $T300/5208$ with the following properties

$$E_1 = 135\,GPa, \quad E_2 = 10.97\,GPa, \quad G_{12} = G_{13} = 5.77\,GPa,$$
$$G_{23} = 3.45\,GPa, \quad \nu_{12} = \nu_{13} = 0.24, \quad \nu_{23} = 0.49 \quad (14)$$

4

These values are taken from [6] where elastic and strength properties of composite laminates are discussed in detail.
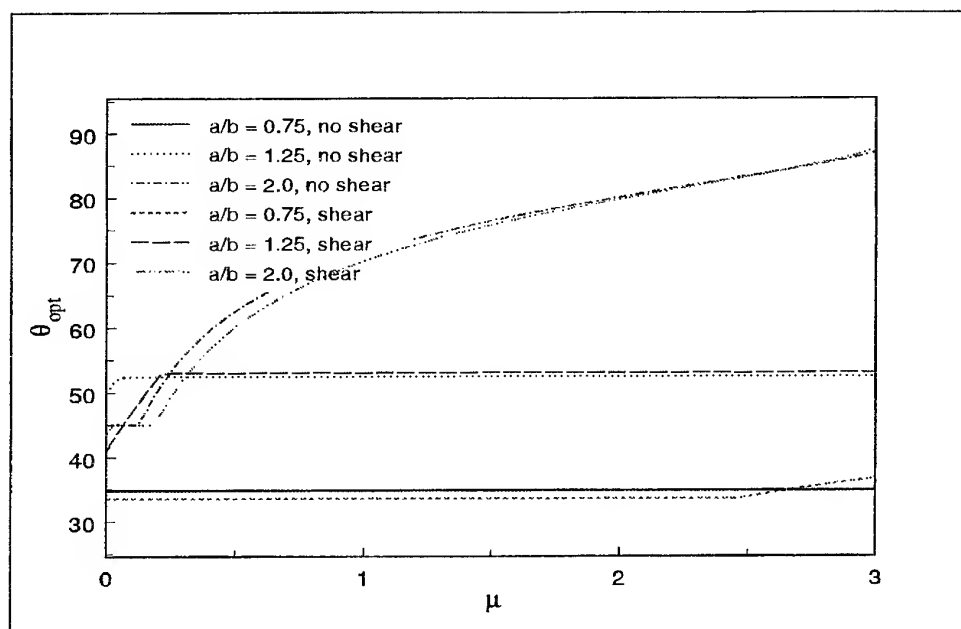
Figure 1: Optimal ply angle vs loading parameter.

Optimization results for thick plates with a thickness ratio $h/b = 0.1$ are given in Figs. 1 and 2 with and without the effect of shear deformation. The optimal ply angles versus the loading parameter are shown in Fig. 1 for aspect ratios $a/b = 0.75$, 1.25, and 2. This result illustrates the need to take the shear deformation into account in the optimal design of thick laminated plates. The corresponding values of the maximum buckling load are shown in Fig. 2. Again the buckling load is overestimated if the effect of shear is neglected.

6. CONCLUSIONS

Optimal design of laminated plates under combined in–plane loads is given with the objective of maximizing critical buckling load over ply angles. General theory of laminated plates is employed for the buckling analysis and various effects were discussed.

Numerical results demonstrate the effect of shear deformations on the optimal design of laminated plates. The effect of shear deformation is assessed for thick plates. The optimal designs are presented for plates with different geometry and under different loading conditions. It is observed that optimal ply angle exhibits jump discontinuities with respect to problem parameters which is a common occurrence in the optimal design of composite structures under buckling loads.

REFERENCES

1. V. Vasiliev, *Mechanics of Composite Structures*, Taylor & Fransis, London, 1993.

2. A. W. Leissa, 'Buckling of laminated composite plates and shell panels', *AFWAL-TR-85-3065*, Air Force Wright Aeronautical Laboratories, Wright-Patterson AFB, 1985.

3. S. Adali, 'Lay-up optimization of laminated plates under buckling loads', in *Buckling and Postbuckling of Composite Plates*, Ed. by G. G. Turvey and L. H. Marshall, Chapman and Hall, London, 1995, 329-365.

4. H. Fukunaga, 'Netting theory and its application to optimum design of laminated composite plates and shells', in *Proc. 29th Structures, Structural Dynamics and Materials Conf.*, Williamsburg, VA, 18-20 April 1988, Part 2, 983-991.

5. H. Fukunaga and G. N. Vanderplaats, 'Stiffness optimization of orthotropic laminated composites using lamination parameters', *AIAA J.* **29** (4), 641-646 (1991).

6. J. N. Reddy and A. K. Pandey, 'A first-ply failure analysis of composite laminates,' *Computers & Structures* **25** (3), 371-393 (1987).
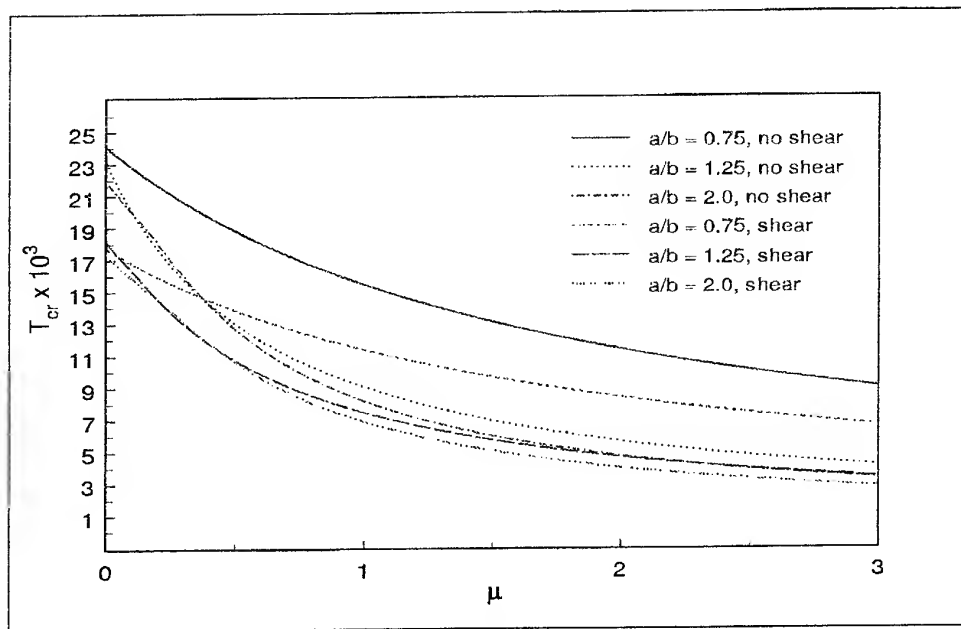
Figure 2: Maximum buckling load vs loading parameter.

PREDICTION OF FAILURE MECHANISMS AND MECHANICAL PROPERTIES OF FASTENED GRP UNDER BENDING USING ARTIFICIAL NEURAL NETWORKS

S. M. Al-Alawi, A. C. Seibi, S. K. Al-Oraimi

SULTAN QABOOS UNIVERSITY
College of Engineering
P.O. Box 33, Al Khod 123
Sultanate of Oman

ABSTRACT

This paper presents a novel approach in predicting the stiffness, strength, failure modes, and locations of bolted joints in glass fibre reinforced polyester mat laminates under bending. Parameters that affect the flexural properties of GRP as well as failure modes and locations were used to develop an Artificial Neural Network (ANN) model. The contribution of these variables on the distressing mechanisms is then found. Results indicate that the ANN model can accurately predict these variables and, therefore, can be considered as a reliable tool for assessing the design parameters of GRP bolted joints under flexural loadings. ANN can also be used to perform sensitivity analysis on the model's input variables once this model is properly developed and tested.

INTRODUCTION

Composite structures such as fibre reinforced plastics (FRP), pultruded fibre reinforced plastics (PFRP), and glass fibre reinforced plastics (GRP) have been widely used in automotive and aeronautical industries. Such composites are favoured over conventional materials since they are light in weight, provide higher strength, resist corrosion, and could possess electromagnetic transparency [1]. The integration of these composite materials into most current structures requires a joining process. This process is carried out through the use of adhesives or by using rivets or bolts. The bolted connections are more common in industry since they are cheaper, easier to fabricate, and provide easy interchangeability [1].

Even though from the economics point of view bolted connections might offer a cheaper solution, structure safety should not be overlooked or ignored. The presence of joints in any structure made of several connected parts always introduces a particular challenge to engineers and raises many important safety questions and considerations that must be answered. Understanding the stiffness and strength behaviour of connections is crucial to understanding the effect on the overall structure and to designing safe and economical structures.

Experimental studies have demonstrated that the mechanical properties of bolted joints can be affected by many variables such as temperature and moisture, joint geometry, clamping conditions, and many other variables [2]. Most of these studies, however, examined the strength behaviour of bolted joints under uniaxial tension and reported the effects of joints geometry on the tensile strength and stiffness of GRP materials and did not consider their flexural behaviour. The effects of joint geometry on the flexural behaviour of GRP are described in [3]. Based on the experimental results of this study, the failure modes of single bolt under bending joints can be categorized as shown in Figure 1.

This paper, therefore, utilizes the experimental results obtained in [3] to develop an artificial intelligence-based model that is capable of predicting stiffness, strength, failure modes, and locations. This artificial neural network model was also used to perform sensitivity analysis and to study the behaviour of the specimen geometry without having to resort to costly and time-consuming experiments, hence, providing both cost and time savings.

bending net-tension bearing net-tension & bearing
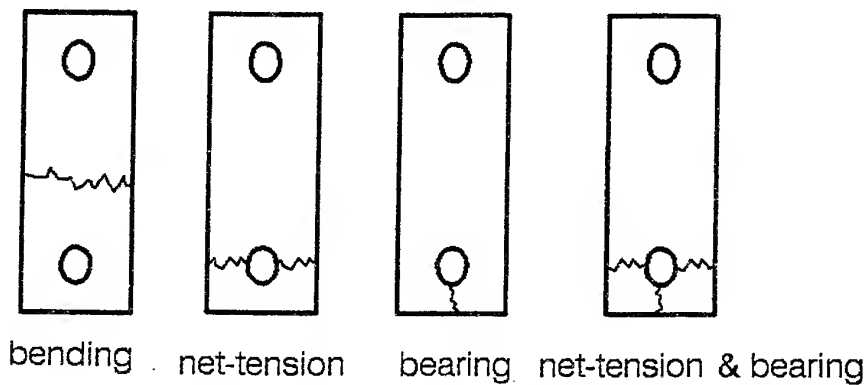
Figure 1. Schematic diagram of failure modes of bolted joints

DESIGN OF THE ANN MODEL

Artificial Neural Networks are network models that are designed based on the neural structure of the human brain [4]. The ability of ANN systems to spontaneously learn from examples, reason over inexact and fuzzy data, and to provide adequate and quick responses to new information not previously stored in memory has generated increasing acceptance for this technology in the different engineering fields. As a result of numerous applications in engineering, this new tool has demonstrated remarkable success.

ANN Architectural Design

As illustrated by Figure 2, the network architecture is composed of many simple processing elements that are organized into a sequence of layers. These are the input layer, the hidden layer, and the output layer. The neurons in the input layer receive three input signals representing the specimen length (SL), specimen width (SW), and specimen pitch (SP); hence, three neurons were used for input in the ANN architecture. The output layer, on the other hand, consists of three output neurons representing the failure strength (FSG), stiffness (ST), and failure location in that specimen (FL).
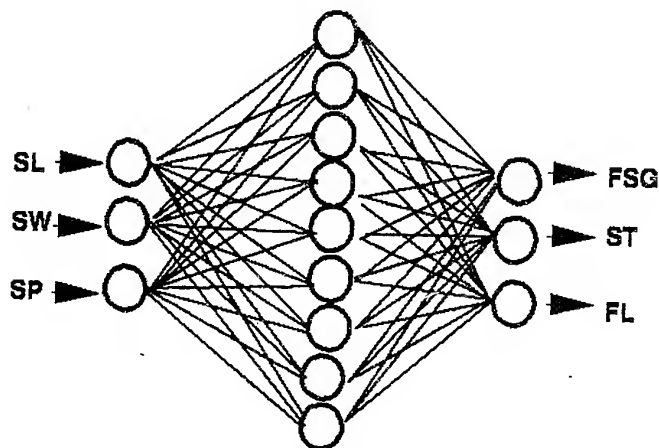
Figure 2. The proposed ANN model's architecture

Between the input and output layers, generally, there is one or more hidden layers. Determining the number of hidden layers to use and the appropriate number of neurons to include in each hidden layer is not an exact science. Research in this area [5, 6] proved that one or two hidden layers with an adequate number of neurons is sufficient to model any solution surface of practical interest. As a result of evaluating a number of hidden node configurations and computing the root mean square error for both the design points and the test points, it was determined that a network with 7 to 10 nodes

8

in the hidden layer would be a good choice. The network containing 9 hidden nodes, however, yielded the smallest error over the region of interest. Based on these results, one hidden layer containing 9 neurons was used to develop the ANN architecture.

Data Preparation
Before the ANN model can be used to provide the desired output, the model should be trained. To do that, a set of input-output patterns are first prepared. The set is developed through experimental work where the effects of changing input parameters such as the specimen length (SL), specimen width (SW), and specimen pitch (SP), etc. on the failure strength (FSG), stiffness (ST), and failure location in that specimen (FL) are examined. The input and output parameter ranges used in this study are shown in Table 1. Patterns within these ranges are evenly distributed so that the training can cover all possible typical values. If this is not the case, training will tend to focus on regions where training patterns are densely clustered and neglect those that are sparsely populated, hence, producing inaccurate gains.

Network Training
The multilayer feedforward network used in this work is trained using the backpropagation (BP) paradigm developed in reference [7]. The BP algorithm uses the supervised training technique. In this technique, the interlayer connection weights and the processing element thresholds are first initialized to small random values. The network is then presented with a set of training patterns, each consisting of an example of the problem to be solved (the input) and the desired solution to this problem (the output). These training patterns are presented repeatedly to the ANN model, and weights are adjusted by small amounts that are dictated by the general delta rule [7]. This adjustment is performed after each iteration when the network's computed output is different from the desired output. This process continues until weights converge to the desired error level or the output reaches an acceptable level. The system of equations that provides a generalized description of how the learning process is performed by the BP algorithm is described by Simpson [8].

Table 1. Examples of training patterns used in developing the ANN model

Parameter	Input	Input	Input	Output	Output	Output
Case Number	SL (mm)	SW (mm)	SP (mm)	FSG (KN)	FST (KN/mm)	Failure Location *
45	130	14	8	0.500	0.090	1.0
18	70	18	10	0.933	0.267	3.0
50	130	16	6	0.510	0.133	2.0
68	160	16	12	0.920	0.144	4.0

* Where Failure Location is 1=bending, 2=net-tension, 3=bearing, and 4=net-tension & bearing

For the present work, the training process was performed using the NeuroShell® simulator. After several adjustments to the network parameters, the network converged to a threshold of 0.0001. The trained model prediction was in good agreement with the actual test results, hence, producing an R^2 value of 0.896 for the specimen failure strength (FSG), 0.838 for the stiffness (FST), and 0.991 for the failure location. These results show that approximately 91% of the variation in the dependent variables (output parameters) can be explained by the independent variables (input parameters) selected and the data set used. Having trained the network successfully, the next step is to test the trained network, using the test data, in order to judge its performance.

Network Testing and Validation

The generalization capability of the model was also tested by presenting 10 test sets that were excluded from the experimental data prior to network training. Figures 3 and 4 provide the results and illustrate the relationship between actual and predicted values.

To validate these results, four of the more common statistical indices, generally used to determine model accuracy and performance, were used. These parameters were mean absolute deviation (MAD), mean squared error (MSE), mean absolute percentage error (MAPE), and coefficient of
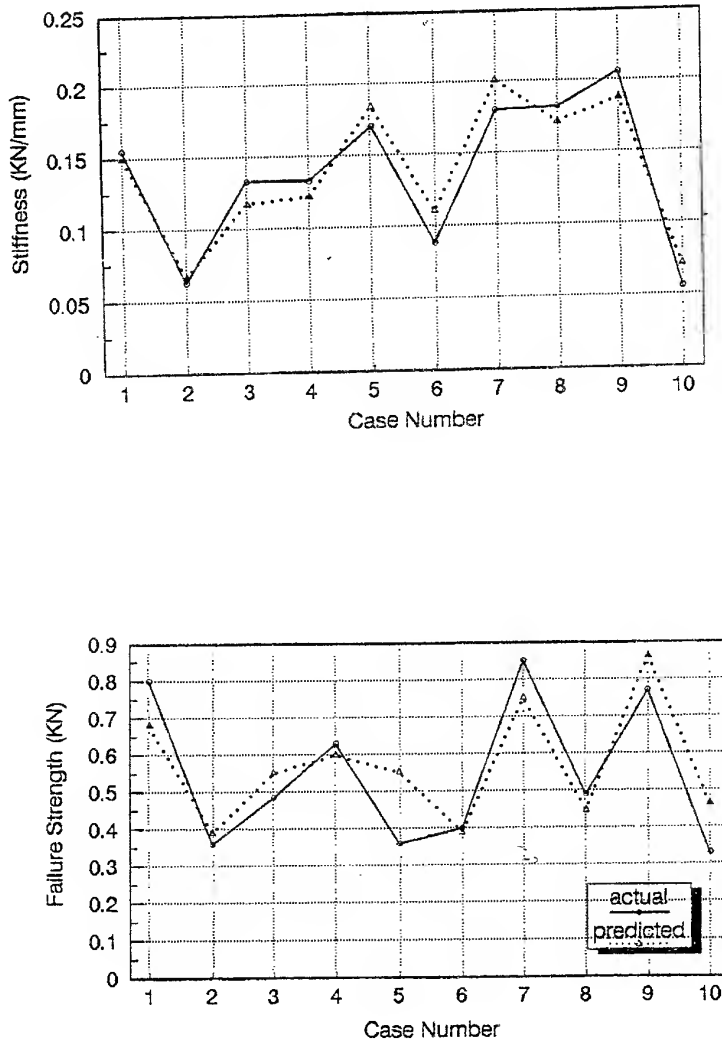
Figure 3. ANN prediction vs. actual experimental values for (a) stiffness and (b) strength

determination (R^2). Statistical analysis of the results shown in Table 2 indicates that the R^2 value for the testing set was 0.752 for the specimen strength, 0.911 for the specimen stiffness, and 0.975 for the identification of the specimen failure location. The MAPE was 14.01, 10.71, and 3.26. These results demonstrate that the ANN-based model can predict the specimen strength, stiffness, and failure location with an accuracy of approximately 86, 89, and 97 percent, respectively.

10

Table 2. Statistical analyses of the ANN model results

Statistical Parameter	Strength	Stiffness	Location
Mean Absolute Deviation (MAD)	0.0819	0.0137	0.0863
Mean Squared Error (MSE)	0.0095	0.0002	0.0211
Mean Absolute Percentage Error (MAPE)	14.014	10.707	3.263
Coefficient of Determination (R^2)	0.7517	0.9119	0.9752
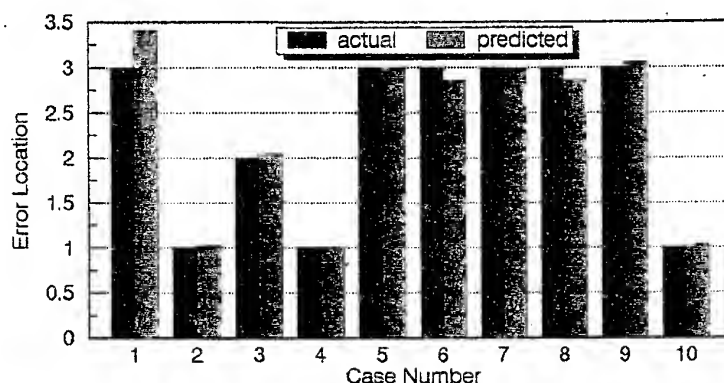
Figure 4. Actual vs. predicted specimen failure location for the test cases given

It is clear from this figure that the ANN predicted the failure location accurately in 9 of the 10 cases. In the first case, the ANN prediction was not entirely incorrect since the ANN predicted the failure to be net-tension and bearing when, in reality, the failure was bearing.

ANN AS AN ANALYTICAL TOOL IN DESIGN
An artificial neural network can also be a useful analytical tool. It can be used to determine the contribution of input variables to the variations in the output variable(s).

Once the model is developed and it produces accurate results, contribution of the different independent variables to the variation of the dependent variable values can be obtained from the model using the NeuroShell® utility. Examination of the input variables' contribution revealed that the specimen width (SW) had a substantial influence (51%) on the variation in strength, stiffness, and the identification of the failure location. This result is followed by the effect of the specimen length (SL) of approximately 32%. On the other hand, the contribution of the specimen pitch was 17.0%. These contributions are shown in Table 3.

Table 3. The contribution of the input parameters to the output results

Input Parameter	Specimen Length (mm)	Specimen Width (mm)	Specimen Pitch (mm)
Contribution %	32.0	51.0	17.0

An artificial neural network-based model can also be used to perform sensitivity analysis in order to see the effect of a specific input variable(s) such as length, width, pitch, etc. on the model's output. For example, Figure 5 shows the variation of strength and stiffness with respect to changes in the pending span and specimen width. It is important to mention that the strength represents the failure load of the specimen. It can be seen from the graph that both properties are unaffected by the change in length. However, the effects of the specimen's width change are apparent. The graph also shows that the strength and stiffness reach maximum values at a specimen's width of 17 mm. after which a decrease in values of both properties is observed.
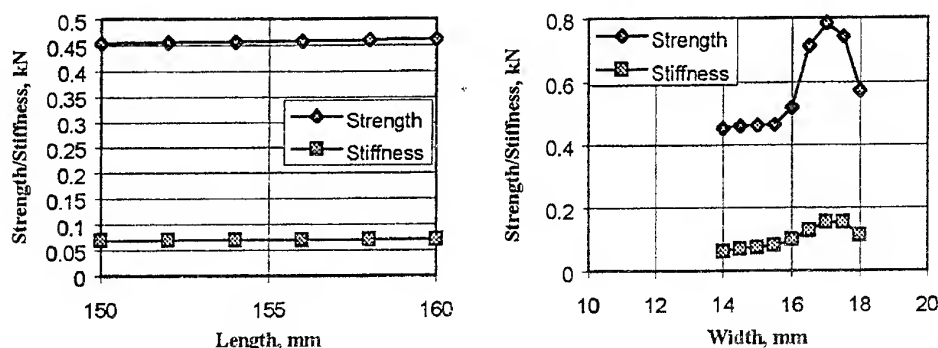
Figure 5. Effects of varying specimens' length and width on the stiffness and strength values

CONCLUSIONS

Model results indicate that the specimens' strength, stiffness, and failure location values are mostly influenced by the specimen width and length and, therefore, should be of prime consideration in GRP design decisions. ANN provides mechanical engineers with a promising tool that can be used in assessing the effect on the model output parameters without having to rely on expensive and time-consuming experiment. The use of this advanced modelling tool can result in extensive time and cost savings for the user.

REFERENCES

[1]   S. Ramakrishna, H. Hamada & M. Nishiwaki "Bolted joints of pultruded sandwich composite laminates", Composite Structures, Vol. 32, pp. 227-235, 1995.

[2]   C. Cooper & G. J. Turvey "Effect of joint and bolt torque on the structural performance of single bolt tension joints in pultruded GRP sheet material", Composite Structures, Vol. 32, pp. 217-226, 1995.

[3]   A. C. Seibi, S. K. Al Oraimi, S. M. Al-Alawi "Effects of joint geometry on the flexural behaviour of glass reinforced plastics", Proceedings of the First International Conference on Composite Science and Technology, Durban, South Africa, June 18-20, 1996.

[4]   R. P. Lippmann, "An Introduction to Computing with Neural Nets," IEEE ASSP Magazine, Vol. 4, No. 2, April 1987, pp. 4-21.

[5]   R. Hecht-Nielsen, "Theory of the Backpropagation Neural Network," Proc., Int. Joint Conf. on Neural Networks, IEEE, Washington, D. C., Vol. 1, pp. 593-605, 1989.

[6]   A. Lapedes and R. Farber, "How Neural Network Works," Neural Information Processing Systems, American Institute of Physics, pp. 442-456, 1988.

[7]   David E. Rumelhart and James L. McClelland, Parallel Distributed Processing: Exploration in the Microstructure of Cognition, Vol. 1, Foundations, Massachusetts, MIT Press, 1986.

[8]   Patrick K. Simpson, Artificial Neural Systems: Foundations, Paradigms, Applications, and Implementations, First Edition, Elmsford, New York: Pergamon Press, Inc., 1990.

PRODUCTION OF NiAl MATRIX COMPOSITES

Richard J. Arsenault[1] and Ralph F. Krause Jr.[2]

[1] Metallurgical Materials Laboratory, Dept. of Materials & Nuclear Engineering
University of Maryland, College Park, MD 20742-2115
[2] Ceramics Division, National Institute of Standards and Technology
Gaithersburg, MD 20899

INTRODUCTION

Future aerospace power systems will require materials which are less dense, possess greater strength and stiffness, and can be used at higher temperatures than current state-of-the-art monolithic materials. Intermetallic matrix composites, especially those with aluminide matrices have been identified as possible candidates [1,2]. Methods of fabricating various reinforced matrix composites need to be developed. Of the numerous intermetallics under consideration, NiAl is especially attractive because of its combination of low density (5.9 g/cm^3), high melting temperature (1910K), high thermal conductivity, and excellent oxidation resistance [3]. Although the prospect of NiAl is intriguing, its viability is in doubt because of its low strength at elevated temperatures and poor fracture toughness. An approach for increasing both strength and damage tolerance is through the use of composite reinforcements.

Two classes of NiAl matrix composites were produced, and their strength as a function of temperature was determined. One class consisted of discontinuous composites containing either whisker Al_2O_3 or particulates of Al_2O_3 or TiB_2. The other class was a continuous filament composite, using single crystal Al_2O_3 (Saphikon). The room temperature strengths of the discontinuous composites were greater than that of the pure NiAl, but their strengths regressed with an increase in temperature becoming only slightly stronger above 900 K. The continuous filament composites were only slightly stronger at room temperature and less strong at higher temperatures than pure NiAl.

MATERIALS AND PROCESSING

NiAl powder, which was obtained in varying purity from several sources, was used to form matrices for both the continuous and discontinuous composites. The matrix powder size was varied from 5 to 150 μm for the discontinuous composites and from 140 to 200 μm for the continuous filament composites.

The size of the Al_2O_3 and TiB_2 particulate reinforcements which were

equiaxial powders, also varied from 5 μm to 150 μm. The whiskers were ~ 10 μm in diameter by 100 μm in length. The continuous filaments were uncoated (no protective sizing), 125 μm diameter, c-axis orientated, single crystal Al_2O_3 purchased from Saphikon, Inc., Milford, CT.

Individual compact disc billets of sintered NiAl and composites of selected discontinuous particulates and whiskers in NiAl matrix were successfully obtained by hot pressing (Table 1). Dry mixed powders of the components were carefully leveled in graphite sleeves (150 mm OD 130 mm H) of various inside diameters (Table 1), which were lined with graphite foil (130 μm thickness) as a release agent. Graphite punches which ends were also lined with graphite foil confined the powders in the sleeve. A graphite fiber-wound die (200 mm OD x 130 mm H) contained the sleeve to restrain hoop stresses during pressing. The assembly was supported between graphite rams (90 mm dia) which were loaded hydraulically in a vacuum hot press apparatus. The die assembly was surrounded by a graphite furnace in a vacuum chamber. The graphite rams were connected to water-cooled steel rams which could move through sealed ports at the top and bottom of the vacuum chamber. Initially the compact was loaded to 9 kN. After the chamber was evacuated to 10^{-4} torr, the die assembly was heated at a rate of 1000K/hr. The temperature was controlled led by a two color optical pyrometer focused on the outside surface of the die assembly. The final load was applied when the test temperature was reached. Following 1 h at the test temperature, the die assembly was cooled to 600K, after which the loading was discontinued. The billet was removed from the die assembly using a hand-operated press, < 4 kN.

Table 1 Hot Pressed Samples

Volume Fraction (%) and Whisker/Particle Size (μm)	Mass (g)	Diam. (mm)	Stress (MPa)	Temp. (K)
20% TiB_2(150)/NiAl(150)	100	25	90	1673
20% TiB_2(150)/NiAl(150)	105	25	90	1673
20% TiB_2(5)/NiAl(5)	426	50	56	1673
20% Al_2O_3(wh)/NiAl(5)	224	50	56	1673
NiAl(75)	326	50	56	1673
NiAl(5)	415	50	56	1673
20% Al_2O_3(75)/NiAl(75)	357	50	56	1673
20% Al_2O_3(5)/NiAl(5)	352	50	56	1673
20% Al_2O_3(75)/NiAl(75)	285	100	50	1723
20% Al_2O_3(wh)/NiAl(75)	285	100	50	1723
NiAl (0.5μm)	297	100	50	1723
20% Al_2O_3(0.5μm)/NiAl(0.5μm)	279	100	50	1723

Both the particulate and matrix powders used to produce a specific composite were approximately the same size, for example, 5 μm Al_2O_3 and 5 μm NiAl. Attempts to

extrude compact discs at 1473K with a 8:1 extrusion ratio resulted in low yields of useful composite. Optical and scanning electron microscopy indicated that the discontinuous composites had negligible porosity and that the reinforcement was randomly distributed.

The "powder cloth" process [4] for fabrication of continuous filament-reinforced composites is shown schematically in Fig.1. The matrix phase is initially processed into a flexible, cloth-like sheet by combining the matrix powder with a fugitive organic binder such as poly tetrafluoroethylene (PTFE) (Teflon®). The mixture is blended with the aid of a volatile organic wetting agent (high purity kerosene [stoddard]) to produce a pliable "dough" with a putty-like consistency. This dough is finally rolled into sheets of powder cloth and cut to size to fit in the hot pressing die. The powder in the cloth ultimately becomes the matrix phase of the composite once binder removal and consolidation has occurred.

POWDER CLOTH METHOD OF COMPOSITE FABRICATION

MML 428
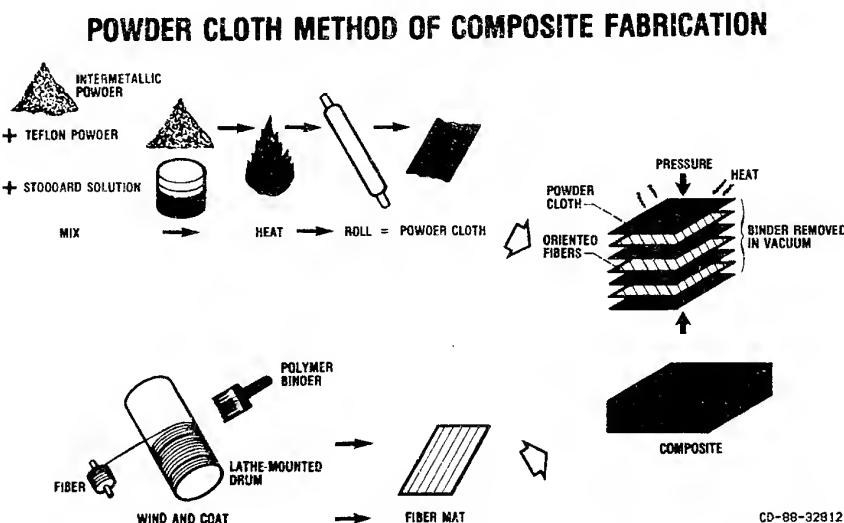
Fig.1   Powder cloth method of composite fabrication [Ref.4].

The reinforcing filament mat is prepared by wrapping a continuous length of reinforcing filament around a lathe-mounted drum. Uniform filament spacing is maintained by use of a translating wire guide assembly. The filaments are then coated with a solution of organic binder dissolved in an organic solvent. Once the solvent evaporates, the filament mat is removed from the drum and cut to the desired size and orientation to be used in assembly of the composite panel.

The composite panel is assembled by stacking alternating layers of matrix cloth and fiber mat in a combination which achieves the desired panel thickness and filament

orientation. Filament volume fraction is controlled by the thickness of the powder cloth, the volume fraction of matrix powder in the powder cloth, and the spacing and diameter of the filaments in the reinforcing mat.

The powder cloth/filament mat stack is consolidated by vacuum hot pressing (VHP). Initially, the composite assembly is heated while under vacuum to an intermediate temperature range in which binder "burn-off" (volatilization of the polymers) is accomplished. After the binder removal portion of the hot pressing cycle, the matrix powder and filaments are subjected to increased temperature and pressure in order to consolidate the composite panel. The time/temperature/ pressure parameters were varied. External equipment limitations (e.g. strength of the die materials, recovery of the vacuum, etc.) set the limits for establishing the hot pressing cycle. In practice, the hot pressing parameters are selected, through trial and error, to obtain a fully dense matrix, to minimize filament/matrix reaction, to avoid mechanical damage to the filaments, to remove completely all organic binders (minimizing contamination), and to reduce process cycle time for efficient use of equipment. Figure 2 is shows various typical temperature-time-pressure relationships what were investigated, with this technique a volume fraction of 25% could easily be obtained.
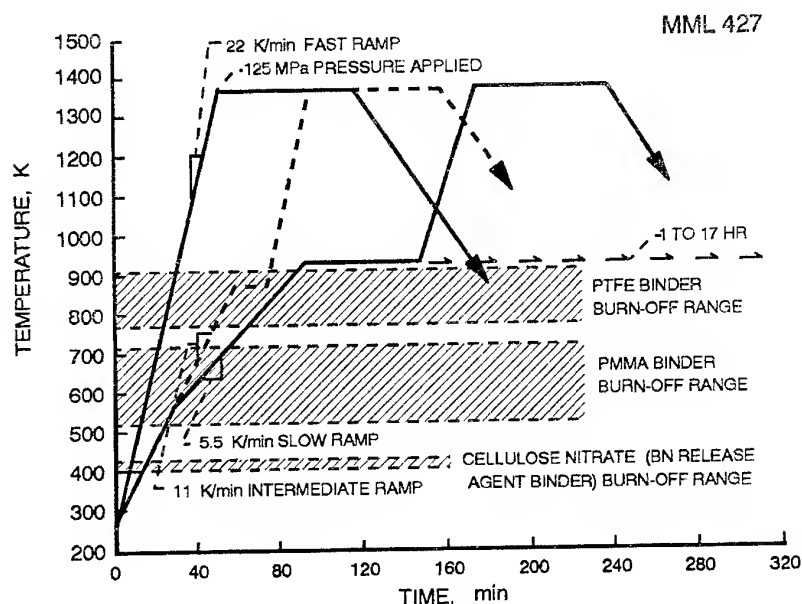
Fig.2

Typical time-temperature profiles evaluated for hot pressing intermetallic based composites [Ref.4].

Following the VHP, the sample was encapsulated in an evacuated Mo container and subjected to hot isostatic pressing (HIPing) to ensure complete densification of the composite. After HIPing at 1533 K at 138 MPa for 4 hours, Mo cladding was removed by chemical etching in a bath of 45% nitric acid, 45% water, and 10% sulfuric acid. The resulting composite plates measured 15 cm long by 5 cm wide and 0.3 cm thick with 6 plys of filaments comprising a total of about 25 volume fraction (V_f) of the composite. As an alternative to the powder-cloth process, composite plates were fabricated without the use of fugitive binders by directly hot-

pressing filaments in a die of matrix powders, followed by the same process as above. HIPing. A disadvantage of the binderless technique is that it is more labor intensive and the maximum filament volume fraction possible is only about 10%. Since filaments are manually placed in the powder die the filament distribution is less uniform and filament alignment is poorer than is achieved by winding [5].

MECHANICAL PROPERTIES

The continuous filament powder cloth (binder) composites were slightly stronger at room temperature but weaker at 1200 K than a monolithic NiAl hot pressed and HIPed from matrix sheets [5]. Strength degradation appears to be the result of the binder decomposing to form graphite islands at the filament-matrix interface during hot pressing, and also the degradation of the Al_2O_3 filaments by NiAl. Filament push-out tests indicated that the binderless composite had twice the bond strength than the binder composite, but large through-section cracks which occurred upon machining the former precluded any tensile strength tests.

The particulate and whisker reinforced composites in the NiAl matrix were much stronger than the pure NiAl composites at 300 K, as shown in Fig.3, but their strengths regressed with rise in temperature such that above 900 K, there was hardly any distinction among the different composites and the pure NiAl composites [6].
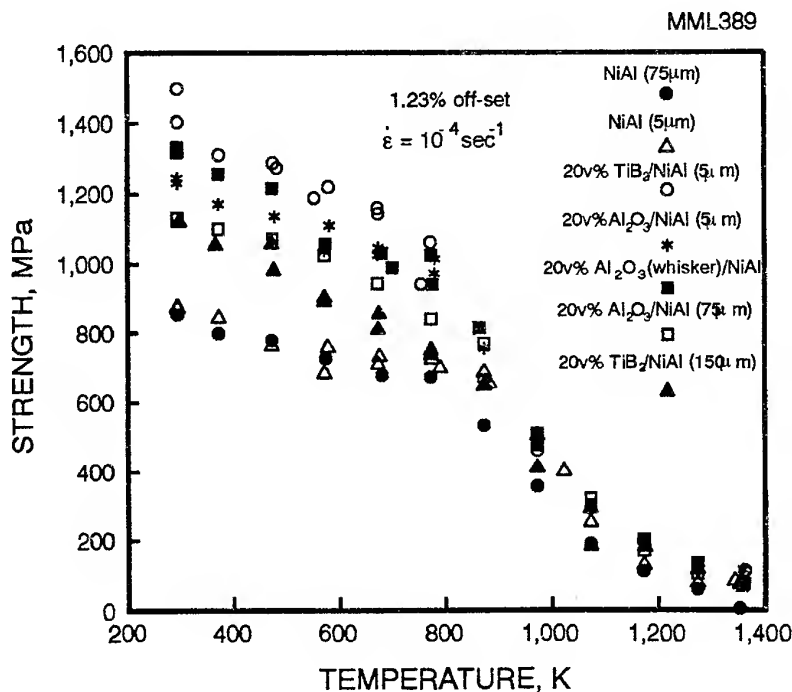
Fig.3

The yield stress of the discontinuous whisker and particulate reinforced NiAl [Ref.6].

CONCLUSIONS

From a consideration of the data the following conclusions can be obtained:

17

- Both discontinuous whisker and particulate and continuous filament NiAl matrix composites have been successfully produced.

- Primarily because of the filament strength degradation, the properties of the continuous filament Al_2O_3/NiAl composites fall well below expectations and, therefore, the composite is unsuitable for structural applications.

- The whisker and particulate reinforced NiAl composites are stronger than the pure NiAl compact at room temperature. Their strengths regress with increase in temperature such that any difference in strength at high temperatures is not significant.

ACKNOWLEDGEMENTS

REFERENCES

[1]   D.L. McDanels and J.R. Stephens, "High Temperature Engine Materials Technology - Intermetallic and Metal Matrix Composites," NASA TM 100844 (1988).

[2]   J.R. Stephens, "High Temperature Metal Matrix Composites for Future Aerospace Systems," NASA TM 100212 (1986).

[3]   R.D. Noebe, R.R. Bowman, and M..V. Nathal: "Physical and Mechanical Properties of the B2 compound NiAl", Inter.Met.Rev., vol.338, pp. 193-232 (1993).

[4]   J.W. Pickens, R.D. Noebe, G.K. Watson, P.K. Brindley and S.L. Draper, "Fabrication of Intermetallic Matrix Composites by the Powder Cloth Process", NASA Tech. Meno. 102060 (1989).

[5]   R.R. Bowman, A.K. Misra and S.M. Arnold, "Processing and Mechanical Properties of Al_2O_3 Fiber-Reinforced NiAl Composites", submitted for publication.

[6]   J. Liu, K. Xu and R.J. Arsenault, "Effect of Particle Type and Shape on the Strengthening of NiAl Matrix Composites", ICCM 10, ed. by K. Street, A. Poursantip, 1995, Vol II, pp.785-792.

A 5-AXES FILAMENT WINDER WITH SOFTWARE CONTROL

J. Atangana Ateba

Département du Génie Mécanique,
Ecole Normale Supérieure d'Enseignement Technique,
Université de Douala,
B.P. 1872 Douala, Cameroun

INTRODUCTION

This paper presents a filament winding system including, : - a numerical control unit, - a five axes filament winding machine with heating device for thermoplastic prepregs, - a micro-computer with a special software, AutoWind 5.0. That software was firstly developed as PC-FIL 2.0 to control a 8-axis filament winder insuring the same functions [1, 2, 3]. This study shows the simplifications realised to reduce from eight to five, the number of axes to be controlled.

DESIGN OF MACHNE

The machine allows to wind revolution structures in glass fibres preimpregnated with thermoplastic resin, and to heat these structures at the deposit point of the fibre on the mandrel during the winding process. A numerical control unit synchronizes the movements of the main components such as : - the mandrel, - the feed-eye, - the ultrasound heating head (Fig. 1). The specificity of this machine dwells on coupling some movements of both the feed-eye and the heating head, the case in which we have the longitudinal and the transversal movements and the rotation around (A, y). Further more, the feed-eye has to rotate around the heating head axis for controlling the winding angle. The five axes are controlled by servomotoreducers.

The numerical control unit "CYBER 3000" is an industrial modular unit, which can control more axes. It uses its own low-level programming language. It can be programmed directly from its keybord or can be loaded with externally prepared data and programmes through a RS-232 interface. For complex sequences, direct programmation reveals too complicated and external preparation of control programmes is necessary.

The micro-computer is used to prepare data and programmes for the numerical control unit. A software has been developed, "AutoWind 5.0", for the 5-axis machine, it generates the data used to load the numerical control unit. It also produces a graphical simulation of the process on the colour video display of the micro-computer.

The whole chain has not been represented. Different axes of movements are shown (Fig. 1), without the servomotoreducers.
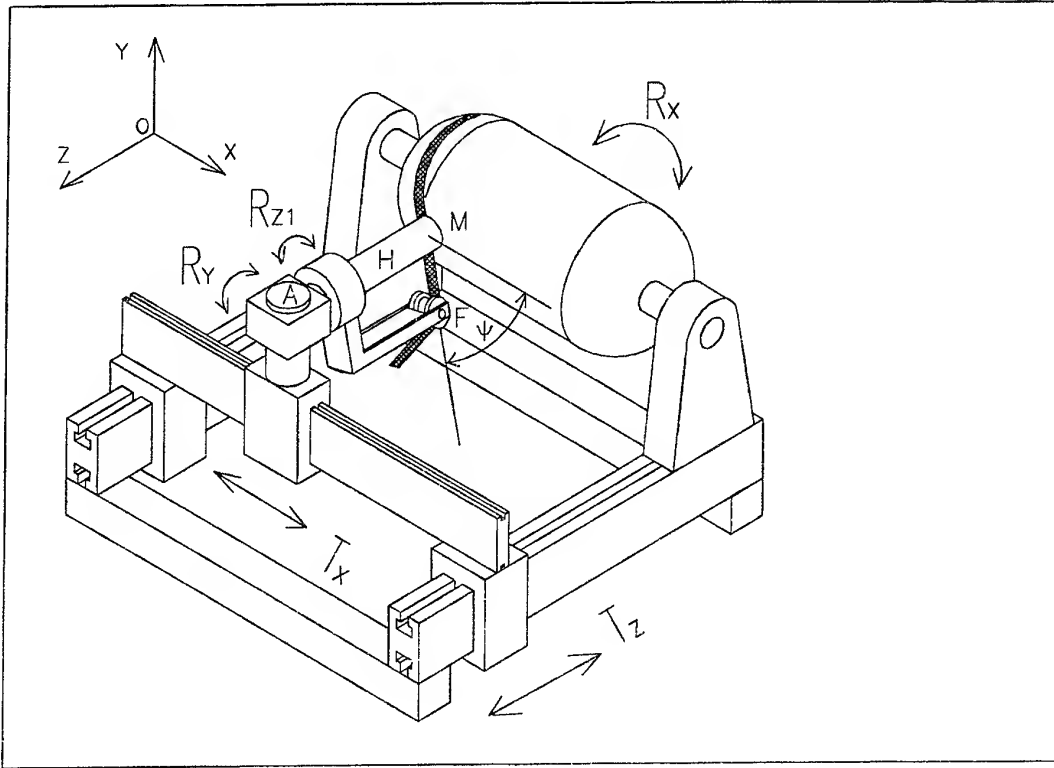
Figure 1 : 5-axis thermoplastic filament winding machine.

where M - deposit point, H - ultrasound heating head, F - feed-eye, R_x - rotation of the mandrel around (o, x) axis, R_y - rotation of the system composed of the heating head H and the feed-eye F around the vertical axis (A, y), R_{z1} - the rotation of the feed-eye around the heating head H.

MATHEMATICAL ANALYSIS

The control of the machine necessitates to know the location of the deposit point M, the feed-eye F and the heating head H.

The heating head, articulated at point A, maintained at a constant distance d perpendicularly to the deposit point M, lies in the horizontal plane $Y_A = 0$ (Fig. 2) ; then we also have Y_M. Completed coordinates of point M are defined by :

$$
\begin{aligned}
X_M &= x \\
Y_M &= 0 \\
Z_M &= R
\end{aligned}
\tag{1}
$$

where R - radius of the mandrel at point M, x - location of the cross-section of the vessel on (o, x) axis.

The control of the heating head takes into acount the coordinates of its articulation A determined by :

$$X_A = x + d\sin(\beta)$$
$$Y_A = 0$$
$$Z_A = R + d\cos(\beta) \qquad\qquad (2)$$
$$\beta = Arctn\left(\frac{dR}{dx}\right)$$

where d - constant distance from M to A ; $\dfrac{dR}{dx}$ - derivative of the radius R on (o, x) axis.

The feed-eye F, articulated on the heating head H, describes a circle centred on M, for the controlling of the winding angle. Its coordinates are determined by :

$$X_F = x + r\cos(\psi)\cos(\beta)$$
$$Y_F = -r\sin(\psi) \qquad\qquad (3)$$
$$Z_F = R - r\cos(\psi)\sin(\beta)$$

where r - distance from M to F ; ψ - the winding angle defined by Clairaut [4].

$$R\sin(\psi) = constant \qquad\qquad (4)$$

Figure 2–b : The winding angle

Figure 2–c : The rotation of the heating head

Figure 2–a : Geometrical parameters
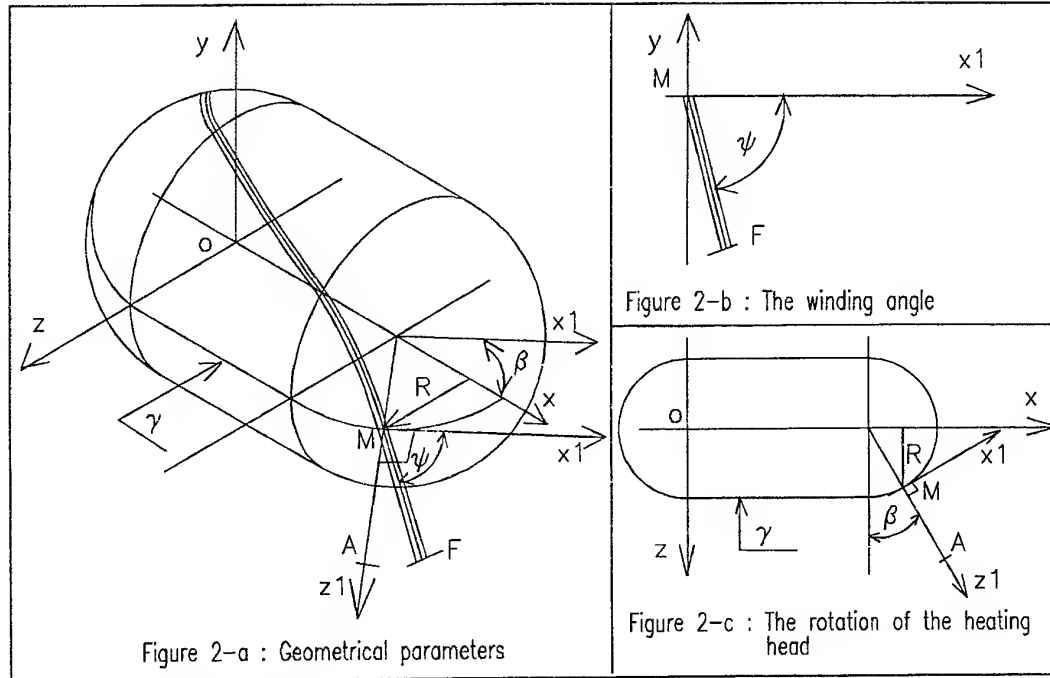
Figure 2 : A cylindrical mandrel ended by two spherical domes.

where γ - curve described by the deposit point M on the (o, z, x) plane ; β - rotation of both the feed-eye and the heating head around the (A, y) axis ; (M, z1) - both the heating head head and the feed-eye axis ; (M, x1) - perpendicular to (M, z1) at point M. The other parameters are defined above.

PROGRAMMING

The software was developed for an IBM/PC compatible micro-computer. The programmme allows control of the following parameters (Fig. 1 and 2) :

R_x : the rotation of the mandrel

T_x : the longitudinal movement of both the feed-eyeand the heating head

T_z : the transversal movement of both the feed-eye and the heating head

R_{z1} : the rotation of the feed-eye around its own axis

R_y : the rotation of both the heating head and the feed-eye around the vertical axis (A, y)

The programme is written in Turbo-BASIC. It generates a file in which the parameters necessary to the numerical control unit are stored. When operating the machine, this file has to be loaded in the control unit through the RS-232 interface.

SIMULATION

The simulation example presented (Fig. 3) shows two curves :

(A) the mandrel pattern : 1, 2, 3, 4, 5, 6, 7 indicate the successive positions of the deposit point M on the mandrel for a round trip.

(B) the heating head articulation, A path : 1, 2, 3, 4, 5, 6, 7 indicate the successive positions of that articulation for a round trip.

The process is simulated in a cartesian coordinates system (Fig. 3) : the mandrel pattern is given in the horizontal plane (o, x, R) ; the articulation of both the heating head and the feed-eye trajectory is described under the mandrel pattern, in the horizontal plane (o, z, x) by its coordinates (X_A, Z_A).
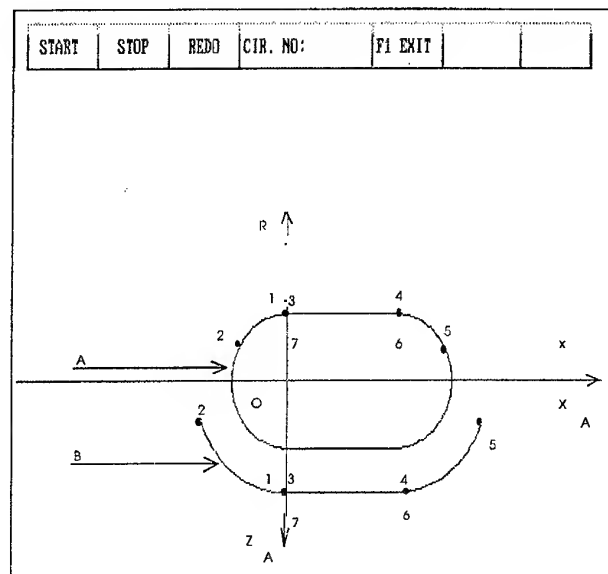
Figure 3 : The screen configuration before the winding simulation

(Fig. 4) shows the screen configuration after simulation of the winding process. The view (A) shown at left of the main view (B), appears during the simulation and gives an idea of the winding on domes; we can see a hole in its centre corresponding to the end closure.
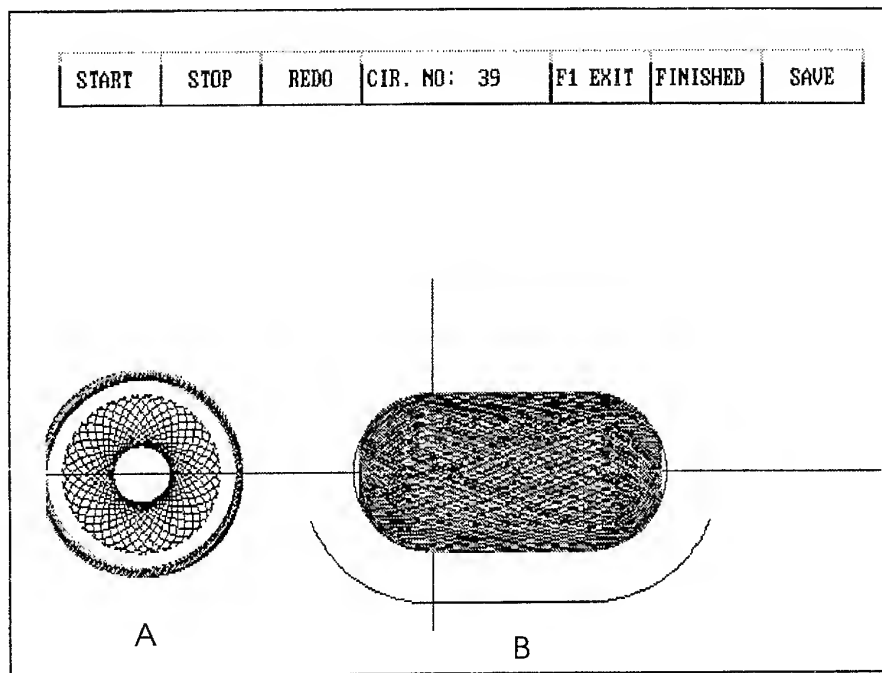
Figure 4 : Screen configuration after the winding process

23

CONCLUSION

In this paper we presented a computer aided software for thermoplastic filament winding and the type of machine to be controlled. The software controls the feed-eye and the heating head positions. In addition to its simplicity in entering data and its rapidity in computation, the software has proved its efficiency in winding different combined revolution geometries. The graphical representation of the mandrel, heating head and feed-eye movement facilitates the operating control of the process.

REFERENCES

[1] Atangana Ateba, J., Aivazzadeh, S., Verchery, G. "Simulation and control of a filament winding machine with heating device for thermoplastic prepregs." *Composites Modelling and Processing Science* **5**, pp. 423-429 (1993).

[2] Atangana Ateba, J., Aivazzadeh, S., Verchery, G. "Software for simulation of thermoplastic filament winding of axi-symetric structures." *Materials and Technologies* **1**, pp.307-318 (1994).

[3] Atangana Ateba, J., Aivazzadeh, S., Verchery, G., Hearn, D. "PC-FIL 2.0 : un logiciel pour l'enroulement filamentaire des structures composites." *Composites /Plastiques Renforcés Fibres de Verre Textile* **11**, pp. 9-13 (1995).

[4] Shibley A. M., "Filament winding." *Handboook of Fiber-glass and Advanced Plastics Composites, (1971)*.

MODELLING METAL MATRIX COMPOSITES BEHAVIOUR: FROM PROCESSING TO IN-SERVICE LOADING

L. BAROUMES [1], A. BENALLAL [1], R. BILLARDON [1], I. VINÇON [1]
and B. DAMBRINE [2]

[1] Laboratoire de Mécanique et Technologie, ENS de Cachan / CNRS / Université Paris 6,
61 avenue du Président Wilson, 94235 Cachan Cedex, France
[2] SNECMA, Corbeil, France

1. INTRODUCTION:

This work deals with the modelling of the thermo-mechanical behaviour of a unidirectional Metal Matrix Composite made of a titanium-based matrix (Ti 6-2-4-2, 6% Al, 2% Sn, 4% Zr, 2% Mo) reinforced by SM1140 SiC fibres. The MMC sheets which are produced by SNECMA, have a periodical hexagonal fibre configuration. Compared to metallic superalloys, this MMC presents a combination of low density and good strength at high temperature. In particular, first experimental tests have revealed good properties under creep and fatigue loadings. Since these final mechanical properties strongly depend on the residual stresses induced by the elaboration process of the material, the aim of this study is to use finite element analyses in order to optimise this process.

The forming process consists of a hot transversal pressing applied to a set of 12 alternate matrix foils and unidirectional fibres tapes. During cooling from T_m to 20 °C at constant $\dot{T}$, the pressure P is released from P_m to zero at a given temperature T_p (see *Fig.1*). The thermal residual stresses induced by this forming process are due to the mismatch of the matrix and fibres thermal expansion coefficients and are strongly dependent on both the cooling rate and the value of the temperature at which the pressure is released [1-2].
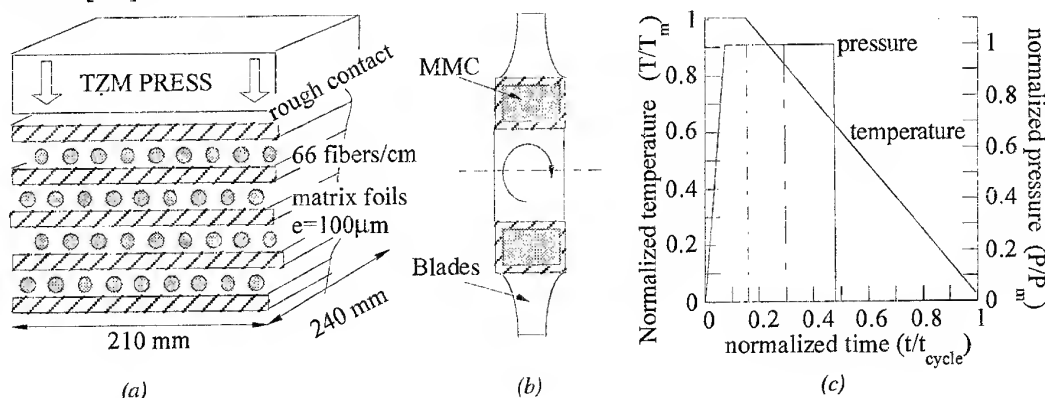
Fig. 1: (a) principle of hot pressing; (b) example of application in a turbine disk; (c) basic thermomechanical loading during elaboration processing.

To model the forming process, a Finite Element model is used. It consists of a basic unit cell associated to boundary conditions which take advantage of both the periodical morphology of the MMC microstructure and the symmetry of the thermo-mechanical loadings applied during the loading process.

Most closed form analyses which have already been used to model this kind of problem [3-6] are elastic or elasto-plastic. Since the prediction of the residual stress field within the composite is the aim of this study, it is essential to take account of the rate dependent inelastic behaviour of the matrix [7]. The FE model used herein includes visco-plastic constitutive equations with isotropic and kinematic hardenings for the matrix whereas the fibres are assumed to be isotropic elastic.

The behaviour of such composite materials is known to be influenced by the thermo-mechanical properties of the fibre/matrix interface (carbon-coating or interface layers) [3-4, 8]. For instance several analyses have been made with values of the thermal expansion coefficient and elastic moduli of the interface layer intermediate between the values of the same properties for the fibres and the matrix. It has

25

been shown for different cooling histories that in this case radial and hoop stresses in the matrix are reduced compared with what is predicted if perfect interface is assumed. For the MMC considered herein, the fibres have a 2μm thick carbon-rich coating. At elevated temperatures during the first part of consolidation, a titanium-carbide interphase is produced by a diffusion reaction between the matrix and the coating. However, since the thickness of this interphase has been observed by SNECMA to be very small (<1μm), this layer has not been taken into account in the FE model contrary to the coating itself.

2. MODELLING OF THE BEHAVIOUR OF THE CONSTITUENTS:

The constitutive equations used to model the thermo-elasto-visco-plastic behaviour of the Ti 6-2-4-2 matrix are based on the thermodynamic approach of irreversible processes [9]. A partition of the total strain ε between elastic and visco-plastic strains is assumed :

$$\varepsilon = \varepsilon_e + \varepsilon_{vp} \tag{1}$$

Two internal variables denoted by p and α respectively describe the isotropic (R) and kinematic (X) hardenings. The complete model corresponds to the following equations:

Thermo-elasticity: $\qquad \varepsilon = \frac{1+\nu(T)}{E(T)}\sigma - \frac{\nu(T)}{E(T)}\,\mathrm{tr}(\sigma)1 + \alpha(T)(T-T_0)1 \qquad (2)$

Von Mises criterion: $\qquad f = J_2(\sigma-X) - R - \sigma_y \quad$ with $\quad J_2(\sigma-X) = \sqrt{\frac{2}{3}(\sigma-X):(s-X)} \qquad (3)$

Flow rule: $\qquad \dot{\varepsilon}_{vp} = \frac{3}{2}\left(\frac{f}{K(T)}\right)^{n(T)}\frac{s-X}{J_2(s-X)} \quad$ with $\quad s = \sigma - \frac{1}{3}\,\mathrm{tr}(\sigma)1 \qquad (4)$

Equivalent viscoplastic strain: $\quad \dot{p} = \sqrt{\frac{2}{3}\,\dot{\varepsilon}_{vp}:\dot{\varepsilon}_{vp}} \qquad\qquad\qquad\qquad\qquad\qquad (5)$

Isotropic hardening rule: $\qquad R = Q(T)(1 - \exp(-bp)) \qquad\qquad\qquad\qquad\qquad (6)$

Kinematic hardening rule: $\qquad \dot{X} = \frac{2}{3}C(T)\dot{\varepsilon}_{vp} - \gamma(p)X\dot{p} \quad$ with $\quad \gamma(p) = \gamma_\infty + (\gamma_0 - \gamma_\infty)\exp(-\omega p) \quad (7)$

where T denotes temperature. The values of the temperature dependent material parameters have been identified from isothermal mechanical tests performed at temperatures between 20 and 950°C [10]. To implement these constitutive equations in the general purpose code ABAQUS, a user-defined material routine has been developped through a programming environment called VISCOENDO using an implicit Newton algorithm [11].

The detailed microstructure of SM 1140 fibres is shown in *Fig. 2 (a)*. Their elastic properties are identical to those of SCS-6 fibres and differ only by the failure stress level. The core is modelled as an isotropic thermo-elastic material and the values of the material parameters are assumed to vary linearly between 20 and 1100°C (see *Table 1*).
Two different types of coatings have been considered viz. a C+SiC coating and a C coating. The C+SiC coating is modelled as a transversely isotropic material with values of the thermal expansion coefficient and elastic moduli intermediate between the values of the same properties for the fibres and the matrix. The C coating is a softer material which is assumed to be isotropic with properties closer to those of the real SM1140 carbon-rich coating (see *Table 1*).

Table 1: fibre properties [6,12-13].

Constituent	Property	Temperature (°C)	Young's modulus (GPa)	Poisson's ratio	Shear modulus (GPa)	Coefficient of thermal expansion $10^{-6}/°C$
SM 1140 core	isotropic	20	E=393	ν=0.25	—	α = 3.93
		1100	E=354	ν=0.25		α = 4.56
Coating C+SiC	transversely isotropic	—	E_{rr}=150 $E_{\theta\theta}=E_{zz}$=163	$\nu_{r\theta}$=0.72 $\nu_{\theta z}$ =-0.01	$G_{r\theta}=G_{rz}$=62	$\alpha_{zz}=\alpha_{\theta\theta}$=4.1 α_{rr}=18.7
Coating C	isotropic	—	E=34.48	ν=0.2	—	α=3.3

3. NUMERICAL MODELLING OF THE FORMING PROCESS:

The FE model developped is a basic triangular unit cell with a fibre volumetric fraction V_f equal to 35%. The in-plane boundary conditions taking account of the symmetries of the problem are given in **Fig. 2 (b)**. In the fibre direction a so-called generalized plane strain state is assumed. To model such a situation with ABAQUS special triangular and quadrangular elements are used together with two extra nodes which are common to all the elements of the mesh. The degrees of freedom of these extra nodes enable to impose generalized plane strain conditions, viz. a uniform variation of the model thickness (i.e. a uniform ε_{zz} strain) in the fibre direction. The whole mesh is given in **Fig. 3**. The refined zone consists in four layers of quadrangular elements of uniform size, the mid-two layers corresponding to the coating. Perfect bondings between the three phases are assumed.

The point load applied at point A is controlled in order to induce on line BC a distributed load equivalent to the imposed pressure loading. Since the studied cooling rates are known to be sufficiently low, an uncoupled thermomechanical analysis is performed with a uniform temperature across the whole mesh [7]. Starting point of the analysis corresponds to a stress-free solid state at a temperature denoted by T_m.
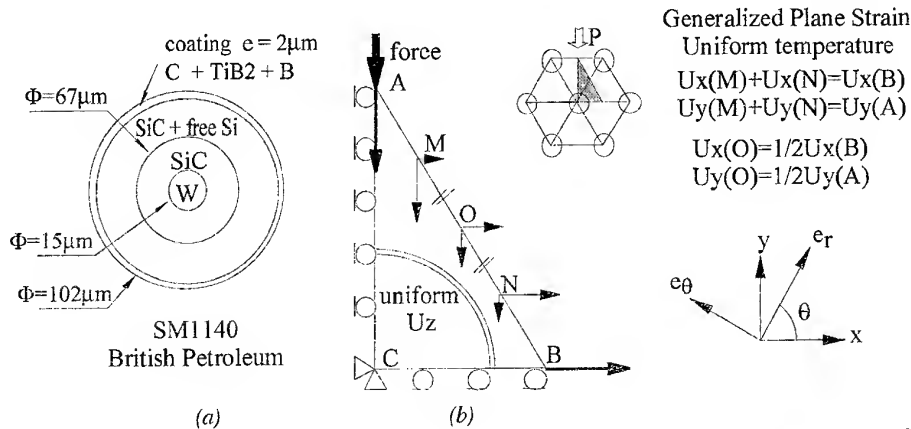
Fig. 2: (a) microstructure of SM1140 fibres; (b) periodic hexagonal array, basic unit cell and boundary conditions.

The precise loading history is described in details in the following:

As long as the applied pressure P is non negligible a perfect no-sliding contact is assumed between the press tools and the surface of the formed composite. Since the sheet is assumed to be infinitely large in the (x, z) plane, at constant temperature T_m, this situation corresponds to zero macroscopic displacements in x and z directions. These boundary conditions are obtained by imposing plane strain and no-displacement at point B. Then, when cooling starts, the imposed boundary conditions take account of a global thermal contraction in x and z directions evaluated as a mean value of the theoretical free thermal contractions of matrix and press tools. After complete release of the pressure, completely free cooling is assumed with generalized plane strain conditions, free x-displacement at point B and free y-displacement at point A.

725 nodes 255 elements 1404 DOF
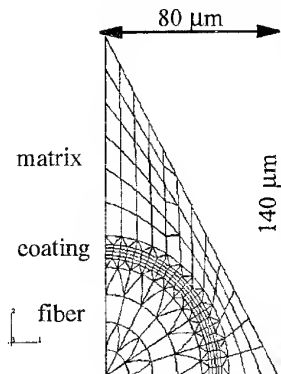
Fig. 3: mesh

The above-described FE model has also been used to simulate subsequent thermo-mechanical tests on the composite, viz. uniaxial tests in the fibre direction. Again, the generalised plane strain scheme has been used to impose various uniaxial loadings to study the stress-strain response of the MMC at room and in-service temperatures.

4. APPLICATION:

In this section all the stresses are normalized by the same value σ_m.

27

4.1. Influence of cooling rates:

This sub-section is devoted to the analysis of the influence of different cooling rates $\dot{T}$ on the residual stresses, the pressure $P=P_m$ being always released at $T_p = 0.6{*}T_m$. The effect of the cooling rate within the range $(0.2\ \dot{T}_p,\ 6\ \dot{T}_p)$ on the stresses induced in the matrix along the interface is illustrated in *Fig. 4*: the magnitude of the radial and hoop stresses at the Gauss point closest to the interface and at $\theta = 0°$ varies by about 20% and 15 % respectively, whereas the axial stress remains almost constant. The evolution of these residual stresses with respect to the radial distance to the center of the fiber and with respect to angle θ are given in *Fig. 5* and *Fig. 6* respectively: they are maximum along the interface where they are independent of the orientation. *Fig. 7* shows the Von Mises stress history during cooling and illustrates the influence of the cooling rate on the final level of the residual stresses. A more detailed analysis of the results of the simulations shows that the rate dependence of the matrix plays a role up to $0.7{*}T_m$ and is without any influence when cooling continues below this temperature since the matrix response is then thermo-elastic.
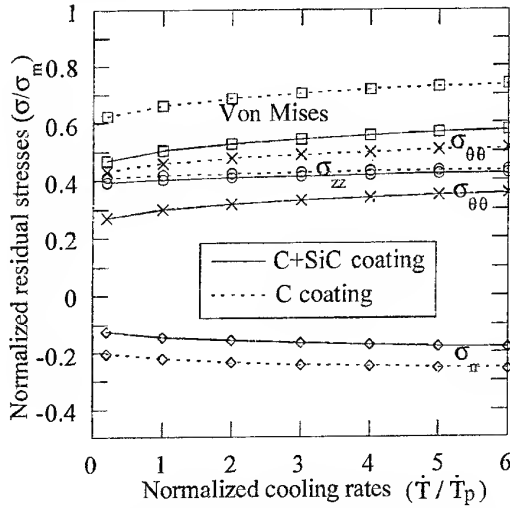
Fig. 4: effects of cooling rates and various coatings on the interfacial residual stresses in the matrix (P_m released at $0.6{*}T_m$)

Fig. 5: residual stresses distribution at $q=0°$ for C coating, $\dot{T}_p$ cooling rate and release of the pressure P at $0.6T_m$.

Fig. 6: residual stresses in the matrix along the interface. $\dot{T}_p$ cooling rate and release of the pressure P at $0.6T_m$.
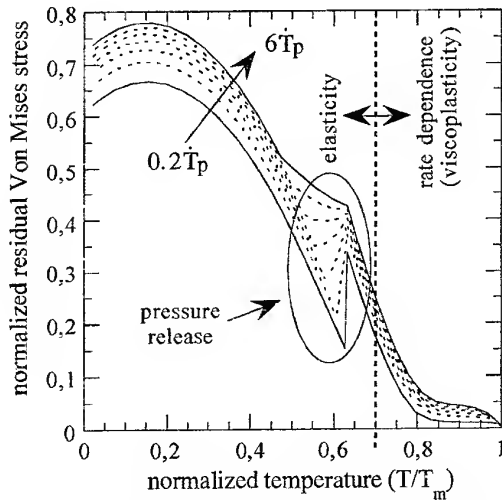
Fig. 7: Von Mises stress within the matrix versus cooling history for C coating, various cooling rates and release of the pressure P at $0.6T_m$.

28

4.2. Influence of the temperature at which pressure is released:

This sub-section is devoted to the analysis of the influence of the temperature T_p at which pressure is released on the residual stresses, the cooling rate $\dot{T}_p$ being always constant. The corresponding results are shown in *Fig. 8* and the main conclusion is the following: the lower the temperature T_p, the lower the absolute magnitude of the residual stresses is; however it is worth noting that this effect is negligible first, at very high temperatures T_p for which the matrix is perfectly viscous and second, for low temperatures $T_p < 0.8*T_m$ below which the matrix remains elastic. The maximum effect of this parameter on the magnitude of radial, hoop and axial stresses in the matrix at the interface is 40%, 35% and 25% respectively. *Fig. 9* illustrates that higher residual stresses induces lower longitudinal stress-strain properties at room temperature. The experimental data plotted in that figure show that, compared to the values obtained if the pressure is released at $0.6*T_m$, the failure strain and the yield stress are decreased by 28 and 19% respectively if the pressure is released at temperatures higher than $0.9*T_m$.
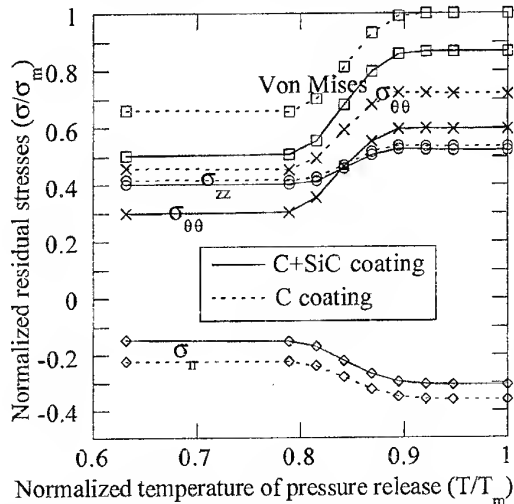
Fig. 8: effects on the residual stresses of the temperature at which the pressure is released for various coatings at constant cooling rate $\dot{T}_p$.
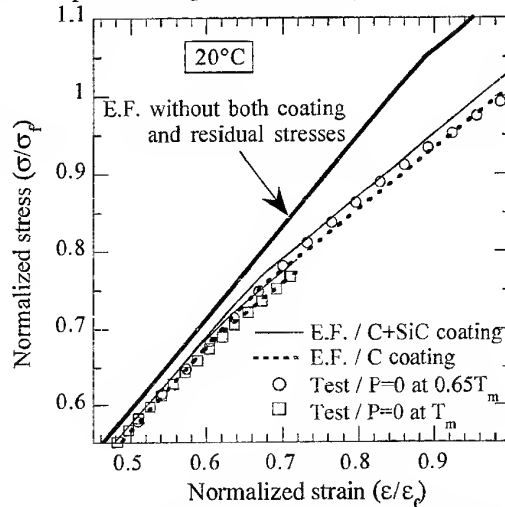
Fig. 9: longitudinal stress-strain response of MMC sheets at 20°C. Experimental data vs simulations for various coatings without or with residual stresses corresponding to a pressure release at $0.6*T_m$ or T_m.

This result is rather well predicted by the numerical simulations which can also be compared to the prediction of the behaviour of a composite with nill residual stresses at both room and in-service 550°C temperatures *(Fig. 9, 10)*.

4.3 Influence of the coating:

All the simulations have been performed with both C+SiC and C coatings. Radial and hoop residual stresses in the matrix are about 20 and 30% respectively smaller for C+SiC coating than for C coating whereas longitudinal σ_{zz} stresses are not affected (see *Fig. 4, 6, 8*). It can be a posteriori verified that the assumption of perfect bonding between the phases is valid since radial stresses are always compressive during the forming process. Since the residual stress state in the matrix is higher for this case, the yield stress is lower at both room and in-service temperatures for C coating whereas the longitudinal stiffness is hardly affected *(Fig. 9-10)*. It is worth noting

Fig. 10,: longitudinal stress-strain response of MMC sheets at 550°C. Experimental data vs simulations for various coatings without or with residual stresses corresponding to a pressure release at $0.6*T_m$.

that these coating effects on the longitudinal behaviour are nearly negligible in comparison with the transverse behaviour which is strongly dependent on matrix damage and debonding phenomena [14].

29

5.CONCLUSIONS:

Processing residual stresses in unidirectional MMC sheets have been estimated using a FE model with rate dependent viscoplastic constitutive equations for the Ti 6-2-4-2 matrix. The sensibility of processing parameters (various cooling rates and temperatures at which pressure is released) and coating properties have been investigated. The main results are the following:

1) During the beginning of the cooling, i-e till the matrix is anelastic, both pressure and low cooling rate decrease the values of the final residual stresses. The processing cycle can be optimized if the temperature at which the pressure is released is chosen as being equal to about $0.8*T_m$ and if high cooling rates are considered after pressure release.

2) The numerical simulations of subsequent unidirectional mechanical tests at 20°C and 550°C in the fibre direction on MMC sheets with residual stresses are in good agreement with the experimental data.

3) The residual stresses are of higher absolute magnitudes when considering a C coating instead of a C+SiC coating. However, both the stiffness and the yield stress of the MMC in the fibre direction are hardly influenced by the thermo-mechanical properties of the coatings.

REFERENCES:

[1] Bahei-el-din, Y.A., Dvorak, G.J., "Mechanics of hot isostatic pressing of a densified unidirectional SiC/Ti composite", *Acta Metallurgica and Materialia* Vol 43, No 7, pp 2531-2359 (1995)

[2] Durodola, J.F., Derby, B., "An analysis of thermal residual stresses in Ti-6-4 alloy reinforced with SiC and Al_2O_3 fibres", *Acta Metallurgica and Materialia* Vol 42, No 5, pp1525-1534 (1994)

[3] Pindera, M.J., Freed, A.D., Arnold, S.M., "Effects of fiber and interfacial layer morphologies on the thermoplastic response of metal matrix composites", *International Journal of Solids and Structures*, Vol 30, No 9, pp 1213-1238 (1993)

[4] Doghri, I., Jansson, S., Leckie, F.A., Lemaitre, J. "Optimisation of coating layers in the design of ceramic fiber reinforced metal matrix composites", *Journal of Composite Materials*, Vol 28, No 2, pp 167-187 (1994)

[5] Dvorak, G.J., Chen, T., Teply, J. "Thermomechanical stress fields in high-temperature fibrous composites. 1: Unidirectionnal laminates", *Composites Science and Technology* 43, pp 347-358 (1992)

[6] Doghri, I., Leckie, F.A. "Elasto-plastic analysis of interface layers for fiber-reinforced metal-matrix composites", *Composites Science and Technology* 51, pp 63-74 (1994)

[7] Jeong, G.S., Allen, D.H., Lagoudas, D.C. "Residual stresss evolution due to cool down in viscoplastic metal matrix composites", *International Journal of Solids and Structures*, Vol 31, No 19, pp 2653-2677 (1994)

[8] Swain, R.E., Reifsnider, K.L., Jayaraman, El-Zein, M. "Interface/Interphase concepts in composite material systems.", *Proceeding of American Society for Composites*, fourth technical conference, American Society for Composites pp 377-386 (1989)

[9] Lemaitre, J., Chaboche, J.-L. "Mechanics of solid materials", *Cambridge University Press* (1990)

[10] Baroumes, L., Vinçon, I., "Identification du comportement thermo-elasto-visco-plastique de l'alliage Ti 6-2-4-2", *Internal Report*, LMT-Cachan (1995)

[11] Florez, J, Billardon, R, Hakem, N, "Viscoendo users' guide", *Internal Report*, LMT-Cachan (1992)

[12] Sherwood, J.A., Quimby, H.M., "Micromechanical modeling of damage growth in titanium based Metal matrix composites", *Proceeding of first international conference on composites engineering*, pp 483-484 (1994)

[13] Li, D.S., Wisnom, R., "Finite element micromechanical modelling of unidirectional fibre-reinforced Metal-Matrix Composites", *Composites Science and Technology* 51, pp 545-563 (1994)

[14] Liu, S., Zhu, J.,"Effective moduli of unidirectional fiber composites containing radial cracking and interfacial debonding", *International Journal of Damage Mechanics* Vol 4, pp 380-401 (1995)

STATISTICAL FRACTURE BEHAVIOR OF PLANAR COMPOSITES WITH WEIBULL FIBER

I. J. BEYERLEIN and S. L. PHOENIX

Theoretical and Applied Mechanics, Cornell University,
Ithaca, NY 14853, USA

INTRODUCTION

Under an increasing tensile load, failure of a composite, consisting of parallel, elastic fibers well bonded to an elastic matrix and perhaps containing a central notch of size $N \geq 0$ breaks progresses by random fiber fractures in the form of crack extension or microcracking (Fig. 1). Where and when fibers break is governed by a combination of material variability and stress concentrations due to previous fiber breaks. Consequently composite strength, toughness, and critical crack size will be statistical, requiring statistical models for crack growth and fracture resistance. Failure depends on the development of a crack or cracks in statistically weaker or less tough regions in the material, and modelling precisely how a failure cluster or 'crack' grows involves a complex interaction of the statistically distributed flaws, subsequent fiber breakage, and the micromechanics of stress transfer. This work continues a series on the statistical aspects of the fracture of composites by coupling new computational tools, such as the break (BIS) or quadratic (QIS) influence superposition techniques [1-2] for micromechanical analysis to Monte Carlo (MC) simulation. MC results guide in developing scaling laws and analytical approximations for composite strength, fracture resistance, and microcracking useful for much larger composites. The MC simulations (see [3]) use BIS, and all probability models incorporate asymptotic expressions for the Hedgepeth [4] load redistribution constants derived in [5].

As in [3,6], we use the common Weibull distribution for fiber strength, with shape parameter $2 \leq \gamma \leq 30$ (from high to low variability) and scale parameter x_0. Comparisons between the MC results and previously developed models confirm that an important transition emerges at $\gamma = 2$, where damage at the crack tip becomes more diffuse. Here we present MC results for $\gamma = 2$ and discuss why some earlier simplifications [6] will not work for $\gamma \leq 2$. We consider fiber strengths which do not vary along the fiber length, forcing fibers to fail in the notch plane, eliminating the possibility of staggered breaks, debonding, and fiber pullout. Nevertheless, we show that increased variability leads to substantial apparent toughening, and interesting statistical effects without resorting to matrix yielding, and fiber debonding and pullout.

STATISTICAL FEATURES OF MONTE CARLO SIMULATIONS

Figure 2 shows a plot of the mean lamina fracture stress μ_c normalized by the mean fiber strength $\mu_f = x_0 \, \Gamma(1+1/\gamma)$ versus N and compares this MC data with the simple unique fiber strength ($\gamma = \infty$, $\mu_f = x_0$) version. As shown in Fig. 2, the latter leads to non-conservative estimates for small N and extremely conservative

31

estimates for large N, especially when there is significant scatter in the fiber strengths, $\gamma \leq 10$. In the short N regime, composite failure is dominated by microcrack formation distributed over the whole specimen with one emerging as dominant. However for N greater than some critical value $N_t(\gamma)$, the fracture strength decreases with N. For smaller γ, the reduction in strength with increasing notch length appears to be milder than the inverse-square-root law in N, and we reason that R-curve behavior is associated with stronger fibers which pin crack extension unless the applied stress is further increased. As γ decreases, the number of relatively stronger fibers a stable, growing crack may encounter increases, contributing to the growing macroscopic toughness. Thus there exists a trade-off between toughness and strength when reinforcing composites with low γ fibers and when expecting notch type 'flaws' on the order of a few fiber diameters. Naturally, fracture strength variability is strongly affected by the heterogeneity of the material. For smaller γ and short notch lengths $N < N_t(\gamma)$, the composite coefficient of variation (CV) increases with N due to the variability in failure sequences and modes between the upper and lower tail specimens. But for larger N, the CV begins to decrease with increasing N due to less variation in the basic failure modes and the tendency for stable crack growth prior to instability.

Figures 3a to 3b plot the MC simulation data for various values of notch length N and for $\gamma = 5$ and 2, respectively, along with the limiting case $\gamma = \infty$. Weibull coordinates are used so that a Weibull distribution would plot as a straight line. These failure load distributions are clearly non-Weibull in shape, and their variability has been reduced relative to that of the fibers. The stress scale is normalized by K_N, the stress concentration factor for an N-sized notch, yet there is still a relative increase in composite strength as N is increased. Especially for large N and $\gamma = 2$. The composite becomes substantially stronger than in the $\gamma = \infty$ case as N increases, as seen earlier in Fig. 2. These results demonstrate the significant influences of statistical fiber strength and the resulting random, cumulative failure processes on the composite strength, and thus, motivate the need for better probabilistic failure analysis. In particular, from the more subtle details of the simulation results, we develop in [6] scaling laws, statistical models, and analytical expressions which explain the apparent toughening and R-curve effects for long N, despite the lack of any obvious dissipative, crack-tip mechanisms, such as frictional fiber pull-out.

PROBABILITY MODELS FOR CRACK GROWTH

First we present several probability models for composite strength and crack growth when N is very small; details appear in [6]. First we quote the asymptotic expression $K_{N+j} \approx (\sqrt{\pi}/2) \sqrt{N+j+1}$, where K_{N+j} is the maximum stress concentration in the first intact fiber ahead of a crack of $N + j$ broken fibers [5]. Fundamental to the composite probability failure model is what we call the *weakest-end-model*, in which the crack extends according to the failure of the weakest of the two fibers at each tip of a growing crack. Applying this idea at each stage of extension, we obtain for $W_{N,2}(x)$, the probability that the notch of size N grows indefinitely and becomes catastrophic,

$$W_{N,m}(x) = \prod_{j=0}^{\infty}\{1 - \exp(-m(K_{N+j}x/x_0)^{\gamma})\} \approx \prod_{j=0}^{M^*(x)}(1 - \exp(-m(K_{N+j}x/x_0)^{\gamma}) \qquad (1)$$

where $m = 2$ and $M^* = M^*(x)$ is the upper limit in which the product converges. $M^*(x)$ physically represents the amount of crack growth prior to catastrophic failure at stress x. Considering its importance, we derive an expression for $M^*(x)$ in [6]. Taking $m = 1$ in (1) corresponds to the mode of extension from only one side of a notch of length N (other end pinned). In the short N regime, we observe many spatially distributed, small fiber break clusters that develop under the initial stages of loading. We model their growth by contiguous extension from this isolated break and easily obtain

$$W^*_m(x) \approx (1 - exp(-(x/x_0)^{\gamma}) \prod_{j=1}^{M^*(x)}(1 - exp(-m(K_j x/x_0)^{\gamma}), \qquad (2)$$

where $m = 1$ for one-sided and 2 for weakest-end extension respectively. Let $P_{N,m}(x)$ be the composite failure probability by notch N extension or by naturally occurring clusters, one developing into a propagating crack. This is

$$P_{N,m}(x) \approx 1 - [1 - 1_{[N>0]}W_{N,m}(x)][1 - W^*_m(x)]^{N_p^*}, \qquad (3)$$

where N_p^* is the number of fibers in the composite minus those cut by the notch and the two notch root fibers. As shown in Fig. 4, the significant deviations in the upper tails and median ranges between $W_{N,2}(x)$ and $P_{N,2}(x)$ further illustrate the transition in failure mode from failure largely due to naturally developing clusters in the upper tail to failure from the notch in the lower tail. Thus a composite failure criterion based on notch extension alone would greatly overestimate the median failure strength. All the above models neglect previous stress concentrations experienced by the surviving adjacent and subadjacent fibers ahead of the crack tip, an important consideration as N increases and γ decreases. At present, we consider the worst case, thus generating a lower bound on the failure stress by calculating the probability that at least one fiber in the crack-tip vicinity fails due to an overload. In [6], we develop this subadjacent failure model (superscript '(s)') in more detail.

As shown in Fig. 2, R-curve behavior (relative increase in notch strength) seems to persist for N greater than the critical notch size $N_t(\gamma)$ especially for small γ, which is a notch region in which failure is predominantly by initial notch extension. In [6], we also develop the statistical failure distributions associated with R-curve behavior in increasing notch length N. In the models, fiber break sequences leading to instability at stress x occur as follows: In stable notch extension, the crack may grow on both sides until it arrests at a relatively strong 'blocking' fiber and then grow strictly on the opposite side until this blocking fiber is overcome, but then it may encounter another blocking fiber and then switch over and grow on the opposite side again, and so on, back and forth until the critical $M^*(x)$ is reached. The distribution for fracture resistance with the inclusion of up to b blockers, denoted $R^b_N(x)$ is the sum of all failure probabilities $R_{N,b}(x)$ that include

33

fracture sequences containing only b blocking fibers, $0 \le b \le M^*$. We extend the model and define $R^{(s),b}{}_N(x)$ as that including the probability of naturally growing crack and subsequent fiber fracture. In this case, the fracture resistance can be viewed as the effort required for the initiation and growth of the crack to instability and ultimate failure. Figure 5 compares $P_{N,1}(x)$ and $P_{N,2}(x)$ and $R^{(s),1}{}_N(x)$, $R^{(s),2}{}_N(x)$, $R^{(s),3}{}_N(x)$ with the MC data for composite strength for $N = 51$ and $\gamma = 5$. Clearly $P_{N,1}(x)$ and $P_{N,2}(x)$ representing one sided and weakest-end schemes, respectively, provide relatively loose lower and upper apparent bounds, and the blocker models provide dramatic improvements with the 3-blocker case working extremely well, especially in the lower tail where more blockers are required. In the upper tail, $M^*(x)$ is generally less than 10 or 20, so the likelihood of encountering several blocking fibers diminishes and hence, the reason for the convergence of $R_{N,b}(x)$, for $b = 1, 2, 3, \ldots$ in the upper tail. However, in the lower tail (weaker specimens), the combined effect of high $M^*(x)$ and low γ increases the opportunities for crack growth to encounter many blocking fibers and forcing it to alternate from the left to right sides of the crack until failure, thus increasing fracture resistance.

As noted earlier in Fig. 2, composite strength scales inversely with N, though milder than $N^{-1/2}$, especially for $\gamma \le 5$. For $\gamma \le 10$ and large N, we derive an approximation for $W_{N,1}(x)$ in [6], calculating a lower (upper) bound on the failure probability (failure stress). For very large N, we find that the asymptotic behavior of the notched strength of the composite at probability level P will eventually scale in proportion to $\{(2/\sqrt{\pi})/\sqrt{N+1}\}\{C^*\log_e(N+1)\}^{1/\gamma}$ as $N \to \infty$ for some constant C^* which depends on P and is between 1/2 and 1. Also in [6], we determined an asymptotic expression for $P_{N,1}(x)$, $P_{N,2}(x)$, $R_{N,0}(x)$, $R^1{}_N(x)$, and $R^{(s),1}{}_N(x)$ for large N, (i.e. $N \ge 7$). In Fig. 6, we demonstrate the excellent agreement between the product forms of $R_{N,0}(x)$, $R^1{}_N(x)$, and $R^{(s),1}{}_N(x)$ with their corresponding asymptotic expression.

DISCUSSION AND CONCLUSIONS

Probability models for crack growth and fracture strength, and analytical approximations successfully capture the effects of variability in fiber strength $2 \le \gamma \le 30$ on the statistics of the fracture process and fracture resistance of a composite lamina with a transverse notch of N contiguous broken fibers ($0 \le N \le 51$). When introducing variability in fiber strength, we observed flaw tolerance but lower strengths for short N and higher apparent toughness, postponement of catastrophic failure, and higher strengths for long N, relative to the unique fiber strength composite. Our analytical results suggest that for $N >> 100$, $\gamma \ge 3$ composites gradually become notch sensitive, such that strength scales inversely in proportion to $\{N^{-1/2}\}\{\log_e N\}^{1/\gamma}$ which is milder than $N^{-1/2}$. Based on these MC results, we plan to further study differences in statistical fracture response for cases where $0 < \gamma < 2$.

Theory developed in [6] shows that increasing composite size (volume) by orders of magnitude will enhance many of the effects observed in Figs 2, 3 for longer

notches, and composite loads at high reliability, all inaccessible by Monte Carlo simulation alone. Both the MC simulation and analytical results show that the extreme lower tail also characterizes how sensitive the material is to flaws, defects, or cracks. Using statistical models developed in this work, we can predict the behavior of the lower tail at these probability levels, which would otherwise require a prohibitive number of about 10^7 replications.

REFERENCES

[1] Sastry, A. M., Phoenix, S. L. "Load redistribution near non-aligned fibre breaks in a two-dimensional unidirectional composite using break-influence superposition." *J Mat Sci Lett* **12**, pp. 1596-1599 (1993).

[2] Beyerlein, I. J., Phoenix, S. L. "Stress concentrations around multiple fiber breaks in an elastic matrix with local yielding or debonding using quadratic influence superposition." *J. Mech. Phys. Solids* (1996) to appear.

[3] Beyerlein, I. J., Phoenix, S. L. "Statistics of fracture for an elastic notched composite lamina containing Weibull fibers-Part I: Features from Monte-Carlo simulation." *Engng Fract Mech* (1996).

[4] Hedgepeth, J. M. "Stress concentrations in filamentary structures." NASA TN D-882, (1961).

[5] Beyerlein, I. J., S. L. Phoenix, Sastry, A. M. "Comparison of shear-lag theory and continuum fracture mechanics for modeling fiber and matrix stresses in an elastic cracked composite lamina." *Int. J. Solids Structures* In press (1996).

[6] Beyerlein, I. J., Phoenix, S. L. "Statistics of fracture for an elastic notched composite lamina containing Weibull fibers-Part II: Probability models of crack growth." *Engng Fract Mech* (1996).
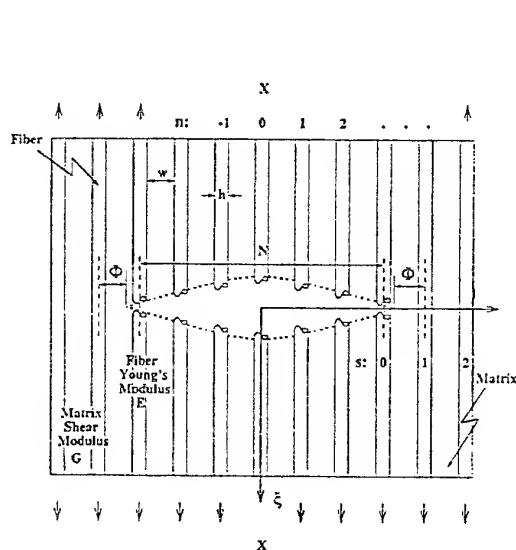
Fig. 1 2-D fiber composite lamina with central group of *N* fiber breaks.
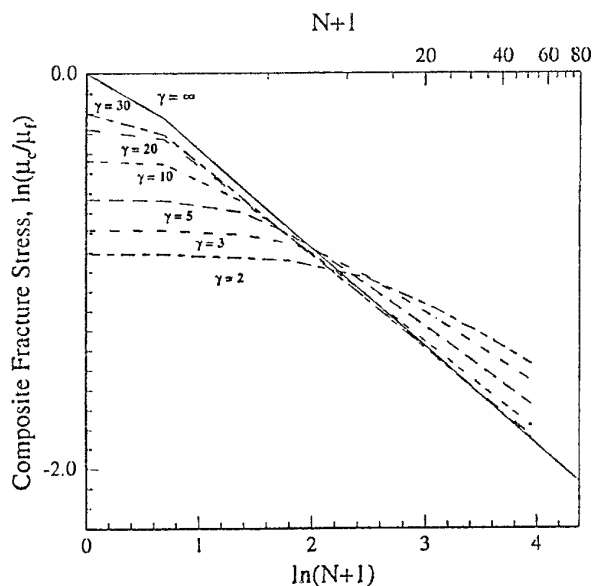
Fig. 2 Log-log plot of the mean composite fracture stress versus *N*.
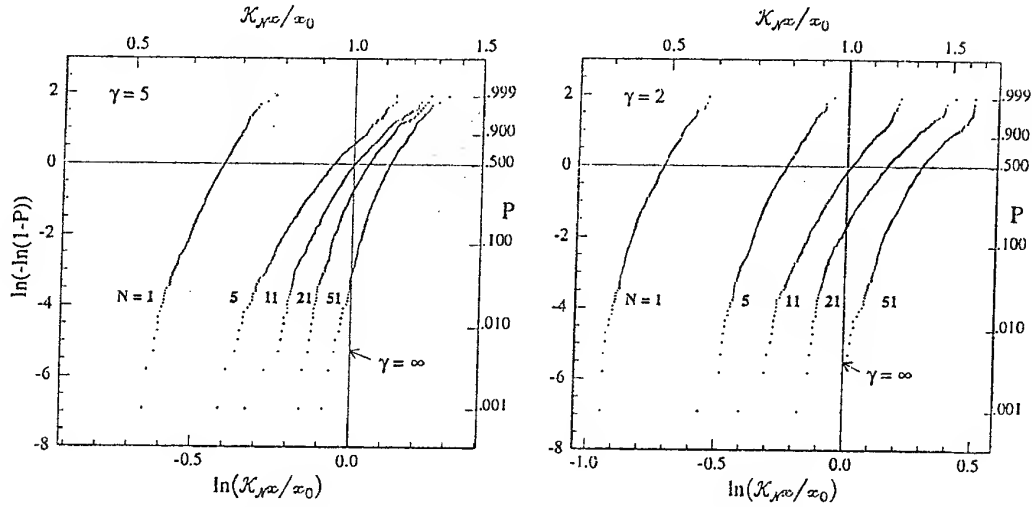
Fig. 3   Composite fracture strength distributions for various N and $\gamma = 5$ and $\gamma = 2$.
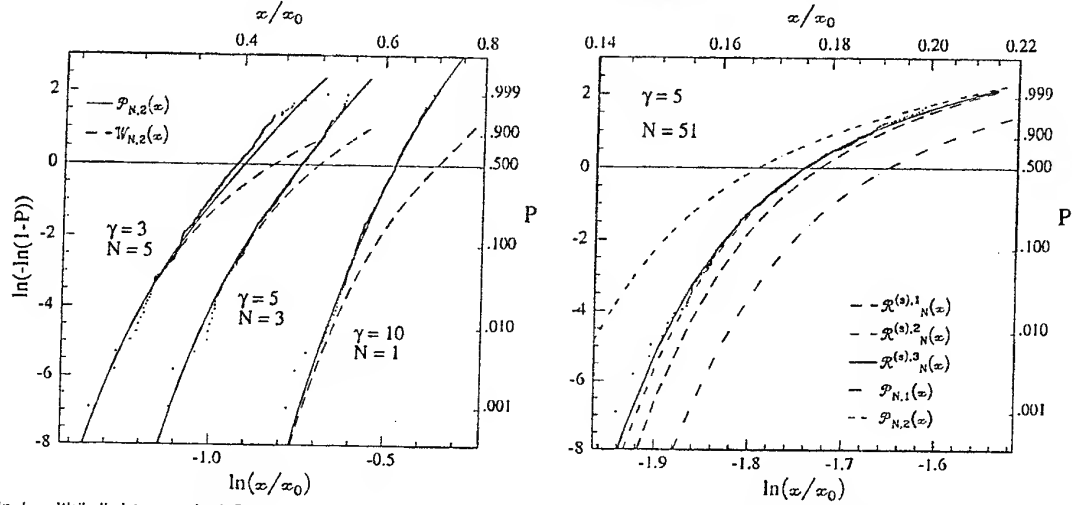
Fig. 4   Weibull plot comparing MC data with $P_{N,2}(x)$ (solid) and $W_{N,2}(x)$ (dashed).

Fig. 5   Weibull plot comparing MC data with $P_{N,2}(x)$, $P_{N,1}(x)$, and $R^{(s),b}{}_N(x)$.
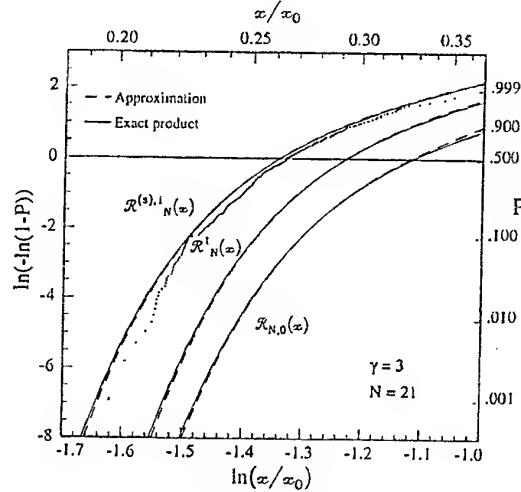
Fig. 6   Weibull plot comparing MC data with product and analytical forms of $R^{(s),b}{}_N(x)$.

MECHANICS OF LONG CYLINDRICAL COMPOSITE SHELLS WITH

SHAPE MEMORY RING STIFFENERS

VICTOR BIRMAN
University of Missouri-Rolla
Engineering Education Center
8001 Natural Bridge Road
St. Louis, Missouri 63121, USA

INTRODUCTION

The paper presents an exact solution of the problem of mechanics of long cylindrical composite shells with shape memory alloy (SMA) ring stiffeners. The reverse transformation in these stiffeners is employed to control deformations and stresses in the shells subjected to an internal pressure. The solution employs Tanaka's one-dimensional constitutive relation to characterize the response of a SMA stiffener and the Timoshenko solution for isotropic shells reinforced by elastic rings generalized for the case of a composite shell material. The proposed approach may present an attractive alternative to previously suggested shells with SMA layers [1].

ANALYSIS

Consider a cylindrical shell with outer or inner ring stiffeners. The stiffeners are bonded to the surface of the shell so that they experience the same deformations as the corresponding cross section. Relatively small temperature variations necessary to trigger a phase transformation do not cause a noticeable change of the shell temperature. This assumption is based on the fact that the SMA transformation temperatures can be "tailored" so that the material austenite start temperature is very close to the operating temperature (for example, the austenite start temperature of nitinol $Ni_{55}Ti$ is $34.5^{0}C$). Such tailoring can be achieved with a relative ease, as was shown in the monograph of Funakubo [2].

When the shell is subject to an internal pressure, it experiences an expansion resulting in failure of the composite material. This expansion can be limited by the ring stiffeners. Typically, these stiffeners should have a large cross sectional area to significantly reduce the shell expansion. However, in the case of SMA stiffeners this requirement can be relaxed because their resistance is enhanced by the reverse transformation from martensite to austenite. In the process of this transformation, the modulus of elasticity of SMA increases, resulting in a higher resistance to expansion. However, even more important is the fact that the material tends to contract in the process of reverse transformation. The contraction being restrained, a compressive pressure is applied by SMA rings to the shell. The result of both

an increase of the modulus of elasticity of SMA and the compressive pressure applied by SMA rings is a decrease of the radial deformation and the corresponding reduction of the stresses in the shell.

1. Mechanics of a SMA ring

The constitutive relation employed in the present work was developed by Tanaka and Sato [3]. This one-dimensional equation can be used here by assumption that the rings are thin so that circumferential stresses are dominant. According to the Tanaka theory, the rate constitutive relation can be integrated by assumption that material constants are independent of the state variable. However, following the approach of Brinson [4], it is possible to show that the same result is obtained in the case where the material constants are linear functions of the martensitic fraction. This assumption accepted in the SMA theories of Tanaka-Sato [3], Liang-Rogers, Brinson, and Boyd-Lagoudas is justified in numerous applications. Therefore, the constitutive equation describing the reverse transformation is taken in the form:

$$\sigma - \sigma_0 = D(\xi)\epsilon - D(\xi_0)\epsilon_0 + \Omega(\xi)\xi - \Omega(\xi_0)\xi_0 + \Theta(T - T_0) \tag{1}$$

where the subscript zero identifies the initial state, σ and ϵ are the circumferential stress and strain, D and Θ are the elastic and thermoelastic moduli of the material, respectively, Ω is the material function, and ξ is a martensitic fraction. Note that following Brinson [4] the thermoelastic modulus was assumed constant.

Eqn. (1) usually overestimates the magnitude of constrained recovery stresses. The modified semi-empirical law proposed by Birman [5] can address this problem. This law can be reduced to the form (1) where the modulus of elasticity and the material function are multiplied by a coefficient obtained from an experimental constitutive curve.

The elastic modulus and the material function in eqn. (1) are given by

$$D(\xi) = D_a + (D_m - D_a)\xi$$

$$\Omega(\xi) = -\epsilon_L D(\xi) \tag{2}$$

where D_a and D_m are the elastic moduli corresponding to the austenitic and martensitic phases, respectively, and ϵ_L is the recovery strain limit.

The martensitic fraction in the process of the reverse

transformation (transformation kinetics) is [3]:

$$\xi = \exp[a_A(A_s-T)+b_A\sigma] \qquad (3)$$

where a_A and b_A are constants that depend on the transformation temperatures of the material, and A_s is the austenite start temperature. The stress interval where the reverse transformation is possible (nucleation criterion) taken as in [3] is omitted here for brevity.

Note that it is impractical to expect that the operational temperature will always coincide with the austenite start temperature. Therefore, at relatively low activation temperatures the rings will remain in the martensitic phase. In this case, the constitutive equation for the rings can be simplified accordingly. The value of the activation temperature corresponding to the start of the reverse transformation can be specified from the nucleation criterion.

The strain in the constitutive equation can be related to the axisymmetric deformation of the ring, w, by

$$\epsilon = w/R \qquad (4)$$

R being the radius of the ring.

Finally, the relationship between the stress in the ring and the pressure q applied by the ring to the shell of the thickness h is

$$\sigma = qR/h \qquad (5)$$

2. Deformations of a long cylindrical shell with closely spaced SMA rings

Consider an axisymmetric equilibrium of a multilayered symmetrically laminated cylindrical shell. The theory of geometrically linear elastic shells is employed in the present paper. The approach of Timoshenko to the axisymmetric analysis of a shell with ring stiffeners is employed [6]. This results in the following equation for the radial deflection of the shell (w_s):

$$w_{s,xxxx}+4\beta^4 w_s = p/D_{11} \qquad (6)$$

where D_{11} is the bending stiffness of the composite material, and

$$4\beta^4 = A/(D_{11}a^2), \qquad A = (A_{12}^2/A_{11}-A_{22}) \qquad (7)$$

a being the shell middle surface radius, and A_{ij} its extensional stiffnesses.

The axial deformation of the shell can be found from the boundary condition related to free axial deformations:

$$u_{,x} = (A_{12}/A_{11})w_s/a \qquad (8)$$

In the case of an axial restraint, the corresponding solution can be superimposed on the results generated using the present solution. Once the displacements u and w_s have been found, the stresses in each layer of the shell can be evaluated using standard stress-strain relationships.

Integration of eqn. (6) yields the result similar to that previously obtained by Timoshenko for isotropic shells [6]:

$$w_s = p/(4\beta^4 D_{11}) + C_1 \sin\beta x \sinh\beta x + C_2 \sin\beta x \cosh\beta x +$$

$$C_3 \cos\beta x \sinh\beta x + C_4 \cos\beta x \cosh\beta x \qquad (9)$$

The constants of integration C_i are obtained from the boundary conditions for the cross sections of the shell supported by SMA rings experiencing radial deflections w. The corresponding boundary conditions are:

$$w_{s,x} = 0, \qquad w_s = \delta - w \qquad \text{at } x = 0, s \qquad (10)$$

where x is the axial coordinate, s is the spacing of SMA rings, and

$$\delta = pa^2/A \qquad (11)$$

is a radial deflection of the shell without the rings.

Transformations similar to those presented by Timoshenko [6] yield the relationship between the internal pressure p, the pressure applied by the rings to the shell, and the deflection w:

$$qb\beta[\chi_1(2\alpha) - \chi_2^2(2\alpha)/2\chi_3(2\alpha)] = p - qba^2/FD(\xi) \qquad (12)$$

where F is the cross section of a ring, and $\chi_i(2\alpha)$ are the functions of $\alpha = \beta s/2$.

Now the exact solution can be obtained as follows. First, the allowable value of the deflection w is specified for a prescribed internal pressure based on the strength requirements. Then the value of the martensitic fraction is assumed and the corresponding stress and temperature are evaluated from eqns. (1,3). This enables us to find the value of q and to use eqn. (12) to specify the pressure p. Detailed numerical studies omitted here due to space limitations will be presented in the extended journal version. However, an illustration of the potential of SMA rings is

shown in Fig. 1 using data for $Ni_{55}Ti$.

The results presented in Fig. 1 were obtained for a ring that experienced a complete reverse transformation from martensite to austenite. As follows from Fig. 1, an increase of temperature results in higher circumferential stresses corresponding to the complete transformation. These stresses can generate a very significant pressure on the shell reducing its radial expansion and stresses. Negative stresses correspond to temperatures below the austenite finish level in the unloaded material ($A_f = 49^0C$). This is due to the fact that a compressive stress has to be applied to SMA to cause its complete reverse transformation at temperatures below A_f.
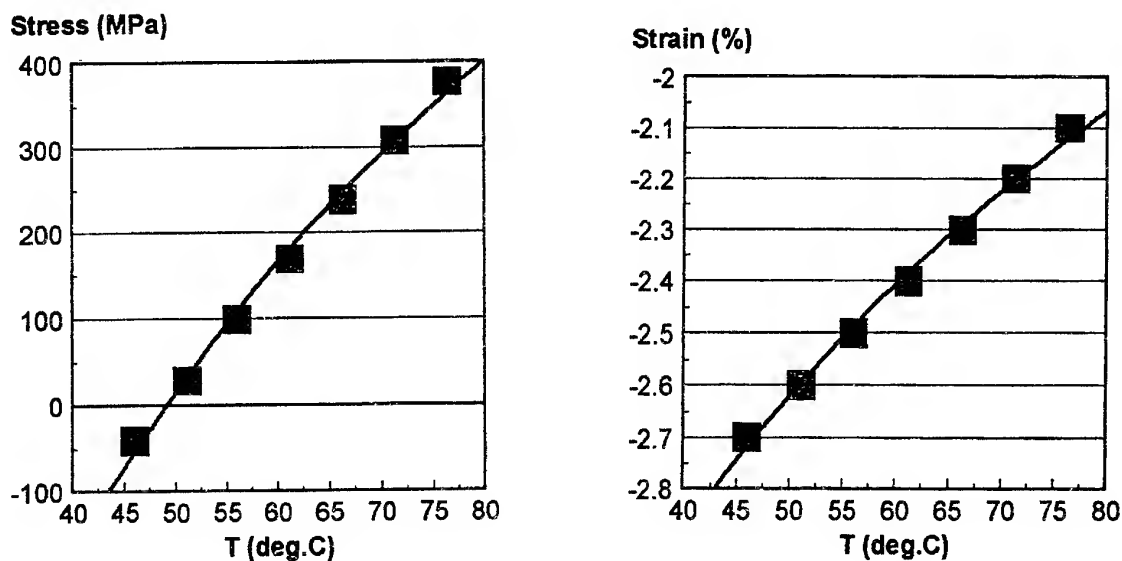
Fig. 1
Stresses and strains corresponding to a complete reverse
transformation of a SMA ($Ni_{55}Ti$) ring

The results in Fig. 1 were obtained using eqn. (1) without the coefficient proposed in Ref. 5. This is due to the lack of experimental data for SMA rings. However, the presence of a coefficient would result in quantitative changes without altering the character of the curves and conclusions.

The solution presented here is valid for pipelines or long cylindrical pressure vessels. This is because bending is affected only by the rings, while the boundary conditions at the

ends of the shell are disregarded. This implies that global bending is negligible in the central part of the shell.

CONCLUSIONS

The exact solution of the problem of bending of a symmetrically laminated long cylindrical shell reinforced by SMA rings and subjected to internal hydrostatic pressure was developed. SMA rings are in the martensitic phase prior to loading. When the shell is loaded, the rings experience constrained recovery and apply compressive pressure to the shell. An increase of the ring modulus of elasticity associated with the reverse transformation also contributes to the effectiveness of the approach proposed in the paper.

ACKNOWLEDGEMENT

REFERENCES

[1] Paine, J.S.N., Rogers, C.A. and Smith, R.A. "Adaptive composite materials with shape memory alloy actuators for cylinders and pressure vessels." *Journal of Intelligent Material Systems and Structures,* **6**, pp. 210-219 (1995).

[2] Funakubo, H. Shape Memory Alloys. Gordon and Breach, New York (1984).

[3] Sato, Y. and Tanaka, K. "Estimation of energy dissipation in alloys due to stress-induced martensitic transformation." *Res Mechanica,* **23**, pp. 381-393 (1988).

[4] Brinson, L.C. "One-dimensional constitutive behavior of shape memory alloys: thermomechanical derivation with non-constant material functions and redefined martensite internal variable." *Journal of Intelligent Material Systems and Structures,* **4**, pp. 229-242 (1993).

[5] Birman, V. "Review of constitutive equations for shape memory alloys." *Proceedings of the 11-th ASCE Engineering Mechanics Conference* (in press). ASCE, New York (1996).

[6] Timoshenko, S. Theory of Plates and Shells. McGraw Hill, New York (1940).

ON THE USE OF DIFFERENT POLYNOMIAL SERIES WITH THE RAYLEIGH-RITZ METHOD

R.E. BROWN and M.A. STONE

Dept of Aeronautical Engineering, University of the Witwatersrand, P.O. WITS, 2050

Extensive literature emphasising the use of special sets of polynomials for Rayleigh-Ritz solutions to plate problems exists. This paper uses mathematical analysis and numerical results to show that the perception created that convergence can be improved by the use of special sets of polynomials is erroneous and that the only effect of the choice of set (for given polynomial degree) is on the numerical stability of the solution.

INTRODUCTION

The Rayleigh-Ritz method has been widely used for the analysis of laminated plates. In this method, solutions are obtained by minimising the total potential energy with respect to the coefficients of an approximating series representing the displacement. The only restrictions on the series chosen is that it satisfies the geometric boundary conditions [1], is complete [1] and does not inherently violate the natural boundary conditions [2]. When these conditions are met, solutions converge to the exact solution as more terms in the series are retained. Different series types (e.g. trigonometric, hyperbolic, polynomial) yield different results for the same number of terms in the series and the efficiency of the solution will depend to some extent on the type of series chosen.

In the case of isotropic or specially orthotropic plate problems, trigonometric series yield simple solutions since the stiffness and mass matrices are diagonal. Difficulties arise, however, when trigonometric series are applied to problems involving boundary conditions other than simple support or to generally orthotropic laminates. In these cases other types of series have been applied. Polynomial series, which allow straightforward algebraic manipulation, have recently been extensively used. Prior to the mid-1980's their use was limited because of the perceived difficulty in setting up series inherently satisfying the geometric boundary conditions. A means to overcome this difficulty by recursively generating higher terms of the series, based on starting polynomials specific to the boundary conditions under consideration, was presented by Bhat [3]. Bhat used the Gram-Schmit process to generate orthogonal sets of polynomials but reasons for selection of orthogonal rather than non-orthogonal polynomials were not given. Bhat compared his results for isotropic plates to those generated using the beam characteristic functions [4] and the simply supported plate functions [5]. Both of these types of functions consist of combinations of trigonometric and hyperbolic terms. It was shown that the orthogonal polynomials offered improved convergence.

Although Bhat did not suggest that the improved convergence was a direct result of the use of orthogonal functions, this would appear to be the interpretation of many researchers who have applied Bhat's orthogonal polynomials to other problems. It would appear that, in most instances where Bhat's approach has been used, emphasis is placed on construction of the orthogonal polynomials rather than on the ease by which starting polynomials can be generated for different boundary conditions [6–12]. Moreover, some recent results [13] suggest that the actual set of polynomials used plays a direct role in the convergence of the method. The objective of the present work is to show that the particular polynomial series used does not affect convergence directly. It will be shown that the results obtained for a given problem are strictly independent of the polynomial series chosen and will depend only on the degree of the polynomial represented by the series. The only practical difference between series representing the same degree polynomial will be shown to be the numerical stability (with respect to inversion and the extraction of

43

eigenvalues) of the resulting stiffness and mass matrices. These assertions will be justified by presenting numerical results, obtained using a number of different sets of polynomials, for bending and vibration of laminated plates having different boundary conditions.

POLYNOMIAL BASES

Define a polynomial over $\mathbb{R}^2$ of degree n as any map

$$
\begin{aligned}
P \quad &: \quad \mathbb{R}^2 \to \mathbb{R} \\
&: \quad (x, y) \mapsto \sum_{q=0}^{n} \sum_{i=0}^{q} c'_{iq} x^i y^{q-i}
\end{aligned}
\tag{1}
$$

where the $c'_{iq} \in \mathbb{R}$. For convenience this polynomial can be written in matrix form. Define

$$
\begin{aligned}
t_{j(i,q)} \quad &: \quad (x, y) \mapsto x^i y^{q-i} \\
c_{j(i,q)} \quad &= \quad c'_{iq}
\end{aligned}
\tag{2}
$$

where $0 \le q < n$ and $0 \le i < q$, using the renumbering transform

$$
j : (i, q) \mapsto q(q+1)/2 + 1 + i
\tag{3}
$$

Define the column matrices

$$
\begin{aligned}
\mathsf{C} \quad &= \quad [c_i] \\
\mathsf{T}(x, y) \quad &= \quad [t_i(x, y)]
\end{aligned}
\tag{4}
$$

where $i = 1, \ldots, k(n)$ and the matrix rank $k(n) = (n+1)(n+2)/2$. Then

$$
\begin{aligned}
P \quad &: \quad \mathbb{R}^2 \to \mathbb{R} \\
&: \quad (x, y) \mapsto \mathsf{C}^T \mathsf{T}(x, y)
\end{aligned}
\tag{5}
$$

Let $[\mathbb{R}\,]_m$ be the set of all real column matrices of rank m. The set of all polynomials over $\mathbb{R}^2$ of degree n is

$$
\mathcal{P}^n = \{ \mathsf{P} = (\mathsf{C}')^T \mathsf{T} : \mathsf{C}' \in [\mathbb{R}\,]_{k(n)} \}
\tag{6}
$$

A *complete basis* for $\mathcal{P}^n$ is a column vector $\mathcal{B} = [\mathsf{B}_1, \ldots, \mathsf{B}_m]$, where each $\mathsf{B}_i \in \mathcal{P}^n$, such that there exists $\mathsf{A}_i \in [\mathbb{R}\,]_m$ such that

$$
(\mathsf{A}_i)^T \mathcal{B} = \mathsf{P}_i
\tag{7}
$$

for every $\mathsf{P}_i \in \mathcal{P}^n$, subject to the linear independence condition that no real matrix A' besides the identity matrix exists such that

$$
\mathsf{A}' \mathcal{B} = \mathcal{B}
\tag{8}
$$

If there are two complete bases $\mathcal{B}$ and $\overline{\mathcal{B}}$ for $\mathcal{P}^n$, then since $\mathcal{B} \subset \mathcal{P}^n$ it follows from (7) that there exists a real matrix A such that

$$
\mathsf{A} \overline{\mathcal{B}} = \mathcal{B}
\tag{9}
$$

Hence one complete basis for $\mathcal{P}^n$ can always be written in terms of any other.

Note too that it is obvious that $\hat{\mathcal{B}} = \mathsf{T}$ is a complete basis for $\mathcal{P}^n$ since in this case the various A_i are just the coefficients C' of the polynomials. Term this basis the *trivial basis* for $\mathcal{P}^n$.

Given any complete basis $\mathcal{B}$ for $\mathcal{P}^n$, from (9) there exist real matrices A and A' such that

$$
\begin{aligned}
\mathsf{A} \mathcal{B} \quad &= \quad \hat{\mathcal{B}} \\
\mathcal{B} \quad &= \quad \mathsf{A}' \hat{\mathcal{B}}
\end{aligned}
\tag{10}
$$

44

implying that $A' = A^{-1}$ and hence that A and A' are both square. Hence all complete bases for $\mathcal{P}^n$ have the same number of elements. Consequently, since all polynomial series descriptions of the displacement must be complete bases no gains in efficiency can be expected by changing from one series to another.

For plates the total potential energy can be expressed as

$$\Pi = \frac{1}{2}Q^T K Q - Q^T L \quad \text{and} \quad \Pi = \frac{1}{2}Q^T K Q - \frac{1}{2}\lambda Q^T M Q \tag{11}$$

for the load-deformation and eigenvalue problems respectively. $Q^T \mathcal{B}$ is the transverse deflection, K is the stiffness matrix, L is the loading matrix, M is the mass or geometric stiffness matrix and λ is an eigenvalue. Minimisation of Π with respect to Q yields

$$KQ = L \quad \text{and} \quad KQ = \lambda M Q \tag{12}$$

for the two problems respectively. A change of basis from $\mathcal{B}$ to $\bar{\mathcal{B}}$, where $A\bar{\mathcal{B}} = \mathcal{B}$, allows (11) to be written as

$$\Pi = \frac{1}{2}\bar{Q}^T A^T K A \bar{Q} - \bar{Q}^T A^T L \quad \text{and} \quad \Pi = \frac{1}{2}\bar{Q}^T A^T K A \bar{Q} - \frac{1}{2}\lambda \bar{Q}^T A^T M A \bar{Q} \tag{13}$$

Minimisation of this expression with respect to $\bar{Q}$ yields equations of the same form as (12):

$$\bar{K}\bar{Q} = \bar{L} \quad \text{and} \quad \bar{K}\bar{Q} = \lambda \bar{M}\bar{Q} \tag{14}$$

but with transformed matrices $\bar{K} = A^T K A$, $\bar{L} = A^T L$ and $\bar{M} = A^T M A$. Hence a change of basis has no effect on the form of the problem but results in a new set of matrices which in general will have different conditioning to the set of matrices obtained using the original basis.

NUMERICAL RESULTS

Perhaps the most widely used polynomials in the Rayleigh-Ritz method are the orthogonal series originally developed by Bhat [3], see for example [6-12]. An alternative approach to the generation of orthogonal polynomials was developed by Chow et al [14]. Several authors have proposed the use of simple polynomial series with no requirement for orthogonality. Barharlou and Leissa [15] proposed that the trivial basis be used in conjunction with constraint matrices. Qatu [16] also used non-orthogonal polynomial series but imposed boundary conditions using starting polynomials similar to those of Bhat. Recently Al-Obeid and Cooper [13] presented results using a similar approach to that of Qatu, differing only in the choice of dimensionless co-ordinates.

Results are presented here for symmetrically laminated plates with two different sets of boundary conditions: all edges simply supported and all edges clamped. Two laminate constructions are considered: $[0]_s$ and $[+45]_s$. The $[0]_s$ laminate is specially orthotropic and gives rapid convergence. Convergence for the $[+45]_s$ laminate is slower. The case of bending under a uniform transverse pressure is chosen for the load-deformation problem and the free vibration case is chosen for the eigenvalue problem.

The plates treated here have aspect ratio of unity and are constructed using a unidirectional CFRP with elastic properties [17] $E_1 = 138\,\text{GPa}$, $E_2 = 8.96\,\text{GPa}$, $G_{12} = 7.1\,\text{GPa}$ and $\nu_{12} = 0.3$. Through thickness shear deformation and rotary inertia are ignored.

To allow identification of possible differences in the convergence of the various approaches, results were generated for increasing polynomial degree. For the simply supported plates, series having 64, 81 and 100 terms are used while for the clamped plates series having 100, 121 and 144 terms are used. Higher degree series are used for the clamped plates since the additional geometric boundary conditions reduce the number of independent coefficients in a series of given degree.

45

Values obtained using polynomial approaches given in [13–16] are compared to those obtained using Bhat's polynomials. Numerical calculations were all performed using Matlab Version 3.5*l* on a 486-DX50 PC.

The dimensionless parameters

$$w = \frac{\delta E_1 h^3}{12\left(1 - \nu_{12}\nu_{21}\right) a^4 q} \quad \text{and} \quad \Omega = \frac{\omega a^2}{h} \sqrt{\frac{12\left(1 - \nu_{12}\nu_{21}\right)\rho}{E_1}} \tag{15}$$

are used for deflection and frequency respectively. (δ is the deflection, E_1 is the lamina longitudinal Young's modulus, h is the plate thickness, ν_{12} and ν_{21} are the lamina major and minor Poisson's ratios, a is the plate length, q is the transverse pressure, ρ is the material density and ω is the natural frequency.)

Tables 1 and 2 show the results obtained using Bhat's polynomials for the simply supported and clamped plates. w_c is the deflection parameter at the plate centre and w_q is the same parameter at the quarter point (i.e. x and y both one quarter of length). Subscripts to Ω indicate the mode of vibration.

Table 1: Results for simply supported plates (Bhat's polynomials)

	$[0]_s$ Plate			$[+45]_s$ Plate		
	Number of terms			Number of terms		
	64	81	100	64	81	100
$w_c \times 10^2$	1.2059626	1.2070669	1.2070669	1.2135995	1.2196759	1.2250114
$w_q \times 10^3$	6.6916837	6.6831290	6.6831290	7.5121783	7.5598976	7.5978179
$\Omega_1 \times 10^1$	1.1289718	1.1289717	1.1289717	1.1395732	1.1361367	1.1336117
$\Omega_2 \times 10^1$	1.7131899	1.7131898	1.7131782	2.1404317	2.1402123	2.1401400
$\Omega_3 \times 10^1$	2.9020899	2.8696301	2.8696301	3.2970263	3.2849201	3.2779470
$\Omega_4 \times 10^1$	4.0740931	4.0740931	4.0740231	3.4095957	3.3910196	3.3889365

Table 2: Results for clamped plates (Bhat's polynomials)

	$[0]_s$ Plate			$[+45]_s$ Plate		
	Number of terms			Number of terms		
	100	121	144	100	121	144
$w_c \times 10^3$	2.6739550	2.6753911	2.6753911	4.0571042	4.0550969	4.0548935
$w_q \times 10^3$	1.1584915	1.1583236	1.1583236	1.9592352	1.9609077	1.9604310
$\Omega_1 \times 10^1$	2.3853209	2.3853129	2.3853129	1.9954321	1.9950523	1.9948913
$\Omega_2 \times 10^1$	2.9719569	2.9719569	2.9719446	3.3363208	3.3363100	3.3362941
$\Omega_3 \times 10^1$	4.1768453	4.1728281	4.1728281	4.6542808	4.6505962	4.6491284
$\Omega_4 \times 10^1$	6.0235888	6.0235884	5.9975638	4.8477398	4.8450916	4.8447945

Table 3 shows the minimum and maximum number of significant digits to which agreement with the above results is obtained when using various other sets of polynomials. The good agreement between the results of [14–16] and those obtained using Bhat's polynomials provides strong evidence that the results are strictly a function of the degree of the polynomial basis and are independent of how the basis is constructed. Small discrepancies that exist result from numerical error in matrix inversion and eigenvalue extraction. A reasonable indicator of numerical stability is the Linpack condition estimator which gives the reciprocal of the condition of a matrix in the 1-norm. Condition numbers close to one indicate good stability while numbers close to zero indicate poor stability and the possibility of larger errors in the matrix inversion and eigenvalue extraction operations. Considering the stiffness and mass matrices arrived at using the approaches of [3] and [14–16] the condition numbers are mostly within one order of magnitude and all tend to decrease

46

as the number of terms in the series increases. Of these approaches, the smallest condition numbers occur with the method of [15] when applied to the $[+45]_s$ clamped plates where the minimum condition of the stiffness matrix is found to be of order 10^{-12} and of the mass matrix of order 10^{-14}. The corresponding smallest condition numbers for the three remaining approaches are only of the order 10^{-9} and 10^{-12} respectively. This suggests that the poorer agreement of the results of [15] for the $[+45]_s$ clamped plate is a consequence of numerical instability.

Table 3: Number of significant digits in agreement

		Polynomial set							
		Ref. 14		Ref. 15		Ref. 16		Ref. 13	
		min	max	min	max	min	max	min	max
$[0]_s$ Plate	w_c	15	16	13	14	15	16	4	8
simply	w_q	15	15	12	14	15	15	5	7
supported	Ω_{1-4}	13	16	12	15	13	16	6	14
$[+45]_s$ Plate	w_c	13	14	10	11	14	15	2	3
simply	w_q	13	14	10	11	13	14	2	3
supported	Ω_{1-4}	13	16	11	14	14	16	3	7
$[0]_s$ Plate	w_c	14	16	11	12	14	15	3	4
clamped	w_q	14	14	10	11	14	14	3	3
	Ω_{1-4}	14	16	12	15	14	16	3	6
$[+45]_s$ Plate	w_c	11	14	8	11	11	13	2	2
clamped	w_q	11	13	7	10	11	13	2	3
	Ω_{1-4}	11	15	8	11	11	14	2	5

Ill-conditioning of the stiffness and mass matrices explains why the results of the method of [13] do not agree well with those of the other approaches. Here the matrices tend to have poor condition numbers for all of the plates analysed, with the minimum values for both the stiffness and mass matrices being of order 10^{-16}. The results are thus likely to be heavily dependent on the eigenvalue extraction algorithm and the type of computer used. This could explain why the values presented in [13] are, for similar polynomial degree, quite different to those of [14] (and indeed to those generated by the present authors using the method of [13]). The conclusion that the polynomials developed in [13] yield superior convergence compared to polynomials developed by other authors is thus most likely based on unreliable numerical data.

CONCLUDING REMARKS

It has been shown that the particular set of polynomials used does not strictly affect results obtained by the Rayleigh-Ritz method. Different sets of polynomials of the same degree are observed to have no effect the form of the problem but may be expected to influence the conditioning of the stiffness, mass and geometric stiffness matrices. Thus the argument that convergence can be improved by the selection of special sets of polynomials is erroneous. In particular, the emphasis placed on the generation of orthogonal polynomials should be questioned in light of the present work.

The results clearly show that, from a designer's point of view, all of the polynomials considered offer adequate performance. The only real need for the use of special polynomials might be to ensure numerical stability for cases where higher degree polynomials are necessary. Studies focussing on the relationship between polynomial series construction and matrix stability could thus be justified. It is worth noting that orthogonal polynomials will probably not be best in this regard for plates since, for numerical stability of the relevant matrices obtained by the Rayleigh-Ritz method, one would be seeking orthogonality on the level of the second derivatives of the functions and not of the functions themselves.

REFERENCES

[1] Langhaar H.L., *Energy Methods in Applied Mechanics*, John Wiley, New York (1962).

[2] Stone M.A. and Chandler H.D., 'Errors in double sine series solutions for simply supported symmetrically laminated plates', *Int. J. Mech. Sci.*, Vol 38, pp 517-26 (1996).

[3] Bhat R.B., 'Natural frequencies of rectangular plates using characteristic orthogonal polynomials in Rayleigh-Ritz method', *J. Sound Vib.*, Vol. 102, pp 493-9 (1985).

[4] Leissa A.W., 'The free vibration of rectangular plates', *J. Sound Vib.*, Vol 31, pp 257-93 (1973).

[5] Dickenson S.M. and Li E.K.H., 'On the use of simply supported plate functions in the Rayleigh-Ritz method applied to the flexural vibration of rectangular plates', *J. Sound Vib.*, Vol 80, pp 292-7 (1982).

[6] Kim C.S., 'Comment on "Natural frequencies of rectangular plates using characteristic orthogonal polynomials in Rayleigh-Ritz method"', *J. Sound Vib.*, Vol 108, pp 166-8 (1986).

[7] Dickenson S.M. and Di Blasio A., 'On the use of orthogonal polynomials in the Rayleigh-Ritz method for the study of the flexural vibration and buckling of isotropic and orthotropic rectangular plates', *J. Sound Vib.*, Vol. 108, pp 51-62 (1986).

[8] Pandey M.D. and Sherborne A. N., 'Buckling of anisotropic composite plates under stress gradient', *J. Engng. Mech.*, ASCE, Vol 117 pp 260-75 (1991).

[9] Liew K.M. and Lam. K.Y., 'Application of two-dimensional orthogonal plate function to vibration of skew plates', *J. Sound Vib.*, Vol 139, pp 241-52 (1990).

[10] Liew K.M. and Lam. K.Y., 'A Rayleigh-Ritz approach to transverse vibration of isotropic and anisotropic trapezoidal plates using orthogonal plate functions', *Int. J. Solids Structures*, Vol 27, pp 189-203 (1991).

[11] Liew K.M., Hung K.C. and Lim K.M., 'Method of domain decomposition in vibrations of mixed edge anisotropic plates', *Int. J. Solids Structures*, pp 3281-301 (1993).

[12] Hung K.C., Liew K.M., Lim M.K. and Leong S.L., 'Boundary beam characteristics orthonormal polynomials in energy approach for vibration of symmetric laminates-I:Classical boundary conditions', *Compos. Struct.*, Vol 26 pp 167-84 (1993).

[13] Al-Obeid A. and Cooper J.E., 'A Rayleigh-Ritz approach for the estimation of the dynamic properties of symmetric composite plates with general boundary conditions' *Compos. Sci. Tech.*, Vol 52, pp 289-99 (1995).

[14] Chow S.T., Liew K.M., Lam K.Y., 'Transverse vibration of symmetrically laminated rectangular composite plates', *Compos. Struct.*, Vol. 20, 1993, pp 213-26 (1993).

[15] Barharlou B. and Leissa A.W., 'Vibration and buckling of generally laminated composite plates with arbitrary edge conditions', *Int. J. Mech. Sci.*, Vol. 29, pp 545-55 (1987).

[16] Qatu M.S., 'Free vibration of laminated composite rectangular plates', *Int. J. Solids Structures*, Vol 28, pp 941-54 (1991).

[17] Leissa A.W. and Narita Y., 'Vibration studies for simply supported symmetrically laminated rectangular plates', *Compos. Struct.*, Vol 12, pp 113-32 (1989).

MACROSCOPIC CHARACTERISATION OF THE INTERACTION REGION (INTERFACE-INTERPHASE) BETWEEN CONSTITUENT MATERIALS IN A POLYMER RELATED COMPOSITE SYSTEM

A.H. CARDON
COSARGUB - Free University Brussels(VUB)
VUB (TW-KB)
Pleinlaan, 2
B-1050 Brussels - Belgium

INTRODUCTION

In a composite system the interaction level between the different basic phases, continua or materials, is a key element for the global stiffness and strength properties of the system. The interactions of any type : mechanical, electrical and physico-chemical, are developed in a thin region between the basic bulk constituants. The general concept of this interaction region was first described as the mesophase by P.S. Theocaris, [1].

If one of the phases has a viscoelastic behaviour, the interaction with the elastic phase occur under relaxation conditions and stress transfer takes place between the viscoelastic and the elastic regions.
Such stress transfers occur not only between matrix and fibres in a lamina but also between lamina, function of the angle between the fibres, and function of the stacking sequence in a general laminate.

Exact relaxation conditions are only realised if perfect interface conditions exist along the separation surface between the phases. In general a spatial region of interaction is developed within the two basic components along the original, or theoretical, interface with changing material properties from the bulk properties of one of the layers to the bulk properties of the other layer.

We can introduce some "degree" of adhesion, or interaction, in between the perfect interface and the "no interaction", controlled by the stiffness properties of the interaction region. The transverse dimension of this interaction region is very small and that region cannot be obtained under bulk form. As consequence the properties of the interphase cannot be measured by any classical direct experimental method. A thin layer treatment of the interphase, similar to plate or shell theories, can introduce some global moduli of this interaction region integrated over the thickness. The introduction of those moduli in micromechanical models or in the computation of some composite characteristic to be compared with some experimental result, by the procedure of the mixed numerical-experimental techniques can give access to the macroscopic properties of the interaction region.

CONTINUUM MODEL OF THE INTERACTION REGION

One of the phases of the composite system is generally present under solid form, fibres in composite materials or the adherend in a bonded joint.
The original surface, S_0, is treated, or prepared, by some special techniques, from plasma treatment for fibers to some abrasive methods for adherends. As result we obtain a surface $S^* > S_0$ with a specific surface state $\phi(S^*) \neq \phi(S_0)$.
The second phase is introduced in an uncured state and after a curing process, under controlled temperature and pressure variations, the composite system is obtained.

As consequence of the surface treatment we have a boundary layer along the original interface over a certain thickness, t_1, in the first phase. The presence of the first phase with his boundary layer changes the conditions of molecular development in the polymer phase within a boundary region along the original interface over a thickness t_2.

Finally we obtain around S_0 an interaction region composed of the boundary layer of the first solid phase and a border region of the resin phase. Those two regions, with properties different from the bulk properties of the original constituants form the interphase or interaction region between the basic continua with thickness $t = t_1 + t_2$.
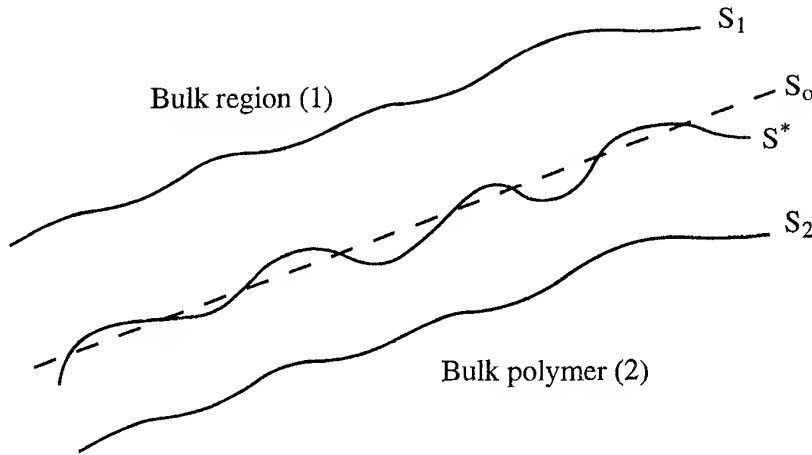
S_1 is the surface between the boundary layer of region (1) and the bulk region (1)
S_2 is the surface between the border region of (2) and the bulk polymer (2).

The interphase region from S_1 to S_2 is a continuum with changing properties over his thickness. This real situation can be modelled by the introduction of a surface S_1' in the bulk region (1), tangent to S_1, and parallel to S_0, and a surface S_2' in the bulk polymer (2), tangent to S_2 and parallel to S_0.

By this model we have :
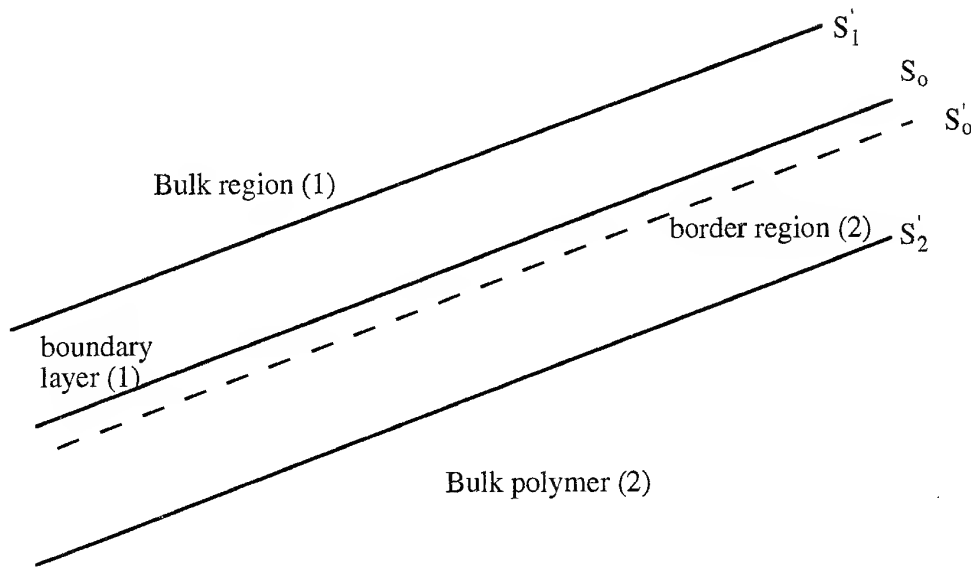
S_o' is the mid surface between S_1' and S_2' considered as the reference surface, $z = 0$, for the analysis of the properties of the interaction region.

PERFECT INTERFACE CONDITIONS

In most of the theories of composites perfect interface conditions are used by assuming the continuity of displacement and stress vector along the interface $z = 0$, or :

$$\bar{u}_{(1)} = \bar{u}_{(2)}$$

$$\bar{T}_{(1)}^{(z)} = \bar{T}_{(2)}^{(z)} \qquad \text{along } z = 0.$$

For the stress components we have along $z = 0$ for a perfect interface :

$$\sigma_{zz}^{(1)} = \sigma_{zz}^{(2)} \quad , \quad \tau_{zx}^{(1)} = \tau_{zx}^{(2)} \quad , \quad \tau_{zy}^{(1)} = \tau_{zy}^{(2)}$$

IMPERFECT INTERFACE CONDITIONS

In order to have a model closer to the physical reality imperfect interface conditions were proposed by J. Achenbach and H. Zhu (1989), [2], further developed and applied by Z. Hashin (1991), [3] and [4].

Such imperfect interface conditions are defined, along $z = 0$, as :

$$\sigma_{zz}^{(1)} = \sigma_{zz}^{(2)} = D_z \, [u_z]$$

$$\tau_{zx}^{(1)} = \tau_{zx}^{(2)} = D_x \, [u_x]$$

$$\tau_{zy}^{(1)} = \tau_{zy}^{(2)} = D_y \, [u_y] \quad ,$$

where $[u_i]$ are the jumps $u_i^{(1)} - u_i^{(2)}$.

(D_x, D_y, D_z) are the control parameters of the imperfect interface.

If $D_i \rightarrow \infty$ we obtain the perfect interface conditions.

If $D_i = 0$, $T_i^{(1)} = T_i^{(2)} = 0$ and we have the situation of disbond between the two regions.

The value of the control parameters D_i between 0 and ∞ give us the possibility to define the degree of interaction. This can be done by the introduction of D_i in a micromechanics model as was showed by Z. Hashin, [3] and [4], or by Josiuk and Kouider, [5], for an inhomogeneous interphase.

INTERPHASE CONDITIONS

For simplicity we consider the two basic materials as isotropic linear elastic or linear viscoelastic so that the correspondence principle can be applied.

The constitutive equations of the bulk continua are :

$$\overset{+}{\sigma}_{ij} = \overset{+}{\lambda}_{(1),(2)} \; \overset{+}{\varepsilon}_{kk} \; \delta_{ij} + 2 \overset{+}{\mu}_{(1),(2)} \; \overset{+}{\varepsilon}_{ij}$$

where $\overset{+}{f}$ is the Carson transformation of f, defined as

$$\overset{+}{f} = p \, \pounds(f) = p \int_{0}^{\infty} e^{-pt} \, f(t) \, dt \quad ,$$

with the interesting property that $(cte)^+ = cte$.

Along the surfaces S_1' ($z = +t/2$) and S_2' ($z = -t/2$) we have perfect interface conditions between the two original bulk continua and the interaction region.

In the transition between a linear elastic and a linear viscoelastic continuum, it is reasonable to assume that the interaction region is a linear viscoelastic graded continuum with constitutive equations :

$$\overset{+}{\sigma}_{ij} = \overset{+}{\lambda}(z) \; \overset{+}{\varepsilon}_{kk} \; \delta_{ij} + 2\overset{+}{\mu}(z) \; \overset{+}{\varepsilon}_{ij} \; .$$

Following this assumption and the perfect interface conditions along S_1' and S_2' we can describe the behaviour of the interaction region starting from a plate or shell type method as suggested by the very small dimension of t in comparison with the surface dimensions of S_i'.

This type of approach was presented and discussed by A.H. Cardon, [6], and A.H. Cardon et al., [7].

Introducing the serie developments of the displacement components and the Lamé functions of the interaction continuum, we obtain the control parameters of this interphase as coefficients between the stress and the displacement jumps in between S_1' and S_2' .

In those expressions : $\left(\dfrac{d\overset{+}{\lambda}^{*}}{dz}\right)_{z=0}$ and $\left(\dfrac{d\overset{+}{\mu}^{*}}{dz}\right)_{z=0}$ are the control elements of the interface parameters.

MIXTED NUMERICAL-EXPERIMENTAL TECHNIQUES

The last decades, consequence of the difficulty, and sometimes impossibility, to obtain uniform stress and strain states, in multiphase or composite continua, necessary for the application of classical experimental methods for the thermomechanical characteristics of those continua, a large number of mixed numerical-experimental techniques were developed. An excellent overview can be found in the doctoral thesis of Hua Hongxing (1993), [8], and in the invited lecture by A.H. Cardon et al. at the 10th International Conference on Experimental Mechanics (1994), [9].

The general basis of the MNET is the comparison of some global characteristic of the system obtained by numerical computation based on a model and some estimated parameters, with a direct accurate measurement of the same global characteristic.

By changing the estimated parameters, till the difference between the computed and measured values of the global characteristic is lower than an imposed limit, we have a "measurement" of those parameters.

This mixed numerical-experimental technique can be applied for the characterisation of the interphase region between bulk adhesive and bulk adherend in a bonded joint. For fiber reinforced polymer matrix composites the control parameters of the interaction region fibre-matrix are obtained by mixed numerical-experimental techniques applied on micromechanical models of the transverse properties.

CONCLUSIONS

Mixed numerical-experimental techniques can give access to the characteristic data of the interaction region between basic materials in a composite system assumed to be a gradient elastic, or viscoelastic, linear continuum. The slopes of the variable material moduli of the interaction region, along the mid surface of this region, are the control parameters of the stiffness properties of the interphase.

REFERENCES

[1]   Theocaris, P.S. "The Mesophase Concept in Composites", Springer Verlag, 1987.

[2]   Achenbach, J.D. and Zhu, H. "Effect of interfacial zone on mechanical behaviour and fracture of fibre reinforced composites"., J. Mech. and Phys. of Solids 37 (1989), pp. 381-393.

[3]   Hashin, Z. "Composite materials with interphase : thermoelastic and inelastic effects" in Inelastic Deformation of Composite Materials (ed. G.Dvorak), Springer Verlag, (1991), pp. 3-34.

[4]   Hashin, Z. "Composite Materials with viscoelastic interphase : creep and relaxation". Mechanics of Materials, 11-2 (1991), pp. 135-148.

[5]   Josiuk, J., Kouider, M.W. "The effect of an inhomogenous interphase on the elastic constants of transversely isotropic composites". Mechanics of Materials 15 (1993), pp. 53-63.

[6]   Cardon, A.H. "From micro- to macroproperties of polymer based composite systems by integration of the characteristics of the interphase regions". Composite Structures, 24, (1993), pp. 213-217.

[7]   Cardon, A.H., De Wilde, W.P., Van Hemelrijck, D., Van Vinckenroy, G., Sol, H., De Visscher, J. "Experimental characterisation of the interface-interphase properties in composite systems by mixed numerical-experimental techniques" in "Recent Advances in Experimental Mechanics" (Eds. J.F. Silva Gomes et al.), Balkema, (1994), pp. 35-38.

[8]   Hongxing Hua, "Identification of plate rigidities of anisotropic rectangular plates, sandwich panels and circular orthotropic disks using vibration data". PhD-thesis in Applied Sciences, 1993, Free University Brussels (VUB).

[9]   Cardon, A.H., Sol, H., De Wilde, W.P., Vantomme, J., Hongxing, H. and De Visscher, J. "Mixed Numerical-Experimental Techniques : Recent Developments and Potentials for the Future of Experimental Mechanics". Invited Lecture at the 10th Int. Conference on Experimental Mechanics, July 1994.

LAMINATED PLATE THEORIES FOR ANGLE-PLY PLATES

V. Carvelli[1], K. Rohwer[2] and M. Savoia[1]

[1] University of Bologna, Faculty of Engineering, Istituto di Tecnica delle Costruzioni
Viale Risorgimento 2, 40136 Bologna, Italy.
[2] DLR, Institute of Structural Mechanics, Lilienthalplatz 7, D-38108 Braunschweig, Germany.

INTRODUCTION

Angle-ply lamination schemes are often used for composite plates in engineering applications; in fact, the possibility of changing the lamination angle allows for a very flexible design, and the plate stiffness can be increased significantly with respect to cross-ply laminations by varying the angle of laminae reinforcement. Nevertheless, in spite of their importance for technical applications, analytical theories and numerical methods are rarely adapted to cover the case of angle-ply plates.

In the present paper, laminated plate theories are applied to angle-ply plates with the aim of obtaining some information about their ranges of applicability. In particular, Classical, First-Order and Third-Order Shear Deformation Theories [1], and the two-dimensional theory recently proposed in [2] are considered. Comparison between the various theories is performed for antisymmetrically laminated angle-ply plates, concerning vertical deflection, displacement and stress distributions over the thickness for different plate slendernesses, stacking sequences and material properties. To this purpose, laminated plate theories are compared with the exact 3-D elasticity solution [3].

The analysis performed here is very useful to assess the accuracy of various theories and to remedy the lack of information about their behaviour for angle-ply plates [4,5].

PLATE THEORIES

Fig. 1 shows a simply-supported rectangular ($A \times B$) laminated plate, constituted by N layers according to an antisymmetric angle-ply lamination scheme. The reference mid-plane, the top face, bottom face and layer interfaces are denoted by Ω, Ω_t, Ω_b, Ω_i ($i=1,..,N-1$), respectively. Moreover u_1, u_2, u_3 are the displacements components.
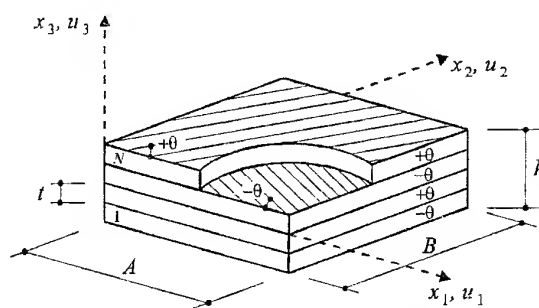
Fig. 1. Antisymmetric angle-ply plate.

a) Three-Dimensional Elasticity Solution

Equilibrium equations for each layer, and stress balance at the top, bottom faces and layer interfaces can be written in terms of displacements as [3] ($\alpha,\beta,...=1,2$):

$$C_{\alpha\beta\gamma\delta}u_{\gamma,\delta\beta} + C_{\alpha\beta33}u_{3,3\beta} + C_{\alpha3\gamma3}\left(u_{\gamma,33} + u_{3,\gamma3}\right) = 0$$

$$C_{33\gamma\delta}u_{\gamma,\delta3} + C_{3333}u_{3,33} + C_{\alpha3\gamma3}\left(u_{\gamma,3\alpha} + u_{3,\gamma\alpha}\right) = 0 \tag{1a}$$

$$C_{\alpha3\gamma3}\left(u_{\gamma,3} + u_{3,\gamma}\right) = 0, \quad C_{33\gamma\delta}u_{\gamma,\delta} + C_{3333}u_{3,3} = q_3/2 \; \{-q_3/2\} \quad \text{at } \Omega_t \; \{\text{at } \Omega_b\} \tag{1b}$$

$$\left[C_{\alpha3\gamma3}\left(u_{\gamma,3}+u_{3,\gamma}\right)\right]=0, \quad \left[C_{33\gamma\delta}u_{\gamma,\delta}+C_{3333}u_{3,3}\right]=0 \qquad \text{at } \Omega_i \qquad (1c)$$

where C_{ijhk} is the constitutive tensor, q_3 is transverse load, the bracket [•] denotes the jump between adjacent layers of the enclosed argument and the summation convention for repeated indices is used.

Transverse load varying according to a sinusoidal law is considered. Hence, the following displacement field and load distribution, are adopted ($\alpha\neq\beta$):

$$u_\alpha = U_\alpha^1(x_3)\ \cos\vartheta_\alpha x_\alpha\ \sin\vartheta_\beta x_\beta + U_\alpha^2(x_3)\ \sin\vartheta_\alpha x_\alpha\ \cos\vartheta_\beta x_\beta \qquad (2a)$$

$$u_3 = U_3^1(x_3)\ \cos\vartheta_1 x_1\ \cos\vartheta_2 x_2 + U_3^2(x_3)\ \sin\vartheta_1 x_1\ \sin\vartheta_2 x_2 \qquad (2b)$$

$$q_3 = q_3^o\ \sin\vartheta_1 x_1\ \sin\vartheta_2 x_2 \qquad (3)$$

where $U_i^1(x_3)$, $U_i^2(x_3)$ (i=1,2,3) are unknown functions and $\vartheta_1=\pi x_1/A$, $\vartheta_2=\pi x_2/B$. Substituting eqns (2) in (1a) and collecting terms depending by the same trigonometric law, the following system of differential equations is obtained, for each layer:

$$-A_{1\alpha}U_\alpha^1 + A_{2\alpha}U_{\alpha,33}^1 - A_{3\alpha}U_\beta^1 + A_{4\alpha}U_{3,3}^2 - A_{5\alpha}U_\alpha^2 - A_{6\alpha}U_\beta^2 + A_{7\alpha}U_{\beta,33}^2 - A_{8\alpha}U_{3,3}^1 = 0$$
$$-A_{1\alpha}U_\alpha^2 + A_{2\alpha}U_{\alpha,33}^2 - A_{3\alpha}U_\beta^2 - A_{4\alpha}U_{3,3}^1 - A_{5\alpha}U_\alpha^1 - A_{6\alpha}U_\beta^1 + A_{7\alpha}U_{\beta,33}^1 + A_{8\alpha}U_{3,3}^2 = 0$$
$$-A_{4\gamma}U_{\gamma,3}^1 - A_{8\gamma}U_{\gamma,3}^2 - A_9 U_3^2 - A_{10}U_3^1 + A_{11}U_{2,33}^2 = 0 \qquad (4)$$
$$A_{4\gamma}U_{\gamma,3}^2 + A_{8\gamma}U_{\gamma,3}^1 - A_9 U_3^1 - A_{10}U_3^2 + A_{11}U_{3,33}^1 = 0$$

where

$$A_{1\alpha} = \left(C_{\alpha\alpha\alpha\alpha}\vartheta_\alpha^2 + C_{\alpha\beta\alpha\beta}\vartheta_\beta^2\right), \quad A_{2\alpha} = C_{\alpha3\alpha3}, \quad A_{3\alpha} = \left(C_{\alpha\alpha\beta\beta} + C_{\alpha\beta\alpha\beta}\right)\vartheta_\alpha\vartheta_\beta,$$
$$A_{4\alpha} = \left(C_{\alpha\alpha33} + C_{\alpha3\alpha3}\right)\vartheta_\alpha, \quad A_{5\alpha} = 2C_{\alpha\alpha\alpha\beta}\vartheta_\alpha\vartheta_\beta, \quad A_{6\alpha} = \left(C_{\alpha\alpha\alpha\beta}\vartheta_\alpha^2 + C_{\alpha\beta\beta\beta}\vartheta_\beta^2\right), \qquad (5)$$
$$A_{7\alpha} = C_{\alpha3\beta3}, \quad A_{8\alpha} = \left(C_{\alpha\beta33} + C_{\alpha3\beta3}\right)\vartheta_\beta, \quad A_9 = C_{\gamma3\gamma3}\vartheta_\gamma^2, \quad A_{10} = C_{\gamma3\delta3}\vartheta_\gamma\vartheta_\delta, \quad A_{11} = C_{3333}$$

The solution of (4) can be obtained as a linear combination of 12 eigensolutions:

$$U_\alpha(x_3) = c_\alpha e^{\lambda x_3}, \quad U_3(x_3) = c_3 e^{\lambda x_3} \qquad (6)$$

where λ and (c_α, c_3) are eigenvalues and eigenvectors of the homogeneous system obtained by substituting eqns (6) in the top, bottom and interface conditions (1b,c).

b) Savoia, Laudiero and Tralli's two-dimensional theory

This theory is based on the only kinematic constraint of transverse inextensibility ($\varepsilon_{33}=u_{3,3}=0$). Virtual work principle gives the following equilibrium equations [2]:

$$Q_{\alpha\beta\gamma\delta}u_{\gamma,\delta\beta} + Q_{\alpha3\gamma3}u_{\gamma,33} = 0 \qquad (7a)$$

$$\int_h Q_{\alpha3\gamma3}\left(u_{\gamma,3\alpha} + u_{3,\gamma\alpha}\right)dx_3 = -q_3 \qquad \text{at } \Omega \qquad (7b)$$

where Q's are the reduced elastic coefficients based on plane stress conditions. Eqns (7) are solved by adopting eqns (2a) for u_α and, for the transverse displacement,

$$u_3 = W\sin\vartheta_1 x_1\ \sin\vartheta_2 x_2 \qquad (8)$$

where W is an unknown quantity. Making use of eqns (2a,3,8), eqns (7) become:

$$-A_{1\alpha}^{r}U_{\alpha}^{1}+A_{2\alpha}^{r}U_{\alpha,33}^{1}-A_{3\alpha}^{r}U_{\beta}^{1}-A_{5\alpha}^{r}U_{\alpha}^{2}-A_{6\alpha}^{r}U_{\beta}^{2}+A_{7\alpha}^{r}U_{\beta,33}^{2}=0$$

$$-A_{1\alpha}^{r}U_{\alpha}^{2}+A_{2\alpha}^{r}U_{\alpha,33}^{2}-A_{3\alpha}^{r}U_{\beta}^{2}-A_{5\alpha}^{r}U_{\alpha}^{1}-A_{6\alpha}^{r}U_{\beta}^{1}+A_{7\alpha}^{r}U_{\beta,33}^{1}=0 \tag{9a}$$

$$\int_{h}\left(A_{7\gamma}^{r}\vartheta_{\delta}U_{\gamma,3}^{1}+A_{2\gamma}^{r}\vartheta_{\gamma}U_{\gamma,3}^{2}+A_{10}^{r}W\right)dx_{3}=0$$

$$\int_{h}\left(-A_{2\gamma}^{r}\vartheta_{\gamma}U_{\gamma,3}^{1}-A_{7\gamma}^{r}\vartheta_{\delta}U_{\gamma,3}^{2}-A_{2\gamma}^{r}\vartheta_{\gamma}^{2}W\right)dx_{3}=-q_{3}^{o} \tag{9b}$$

where coefficients A^{r}'s are analogous to those reported in eqns (5) but are evaluated with reduced elastic coefficients Q's.

c) Classical, First-Order and Third-Order (Reddy) Theories

Classical Lamination Plate Theory (CLT) is the extension of Kirchhoff-Love theory to laminated plates [1]. It is based on the following displacement field:

$$u_{\alpha}=u_{\alpha}^{0}-w_{0,\alpha}, \quad u_{3}=w_{0} \tag{10}$$

where, for angle-ply plates, in-plane and transverse displacements are written as ($\alpha\neq\beta$):

$$u_{\alpha}^{0}=U_{\alpha}\sin\vartheta_{\alpha}x_{\alpha}\cos\vartheta_{\beta}x_{\beta}, \quad w_{0}=W\sin\vartheta_{1}x_{1}\sin\vartheta_{2}x_{2} \tag{11}$$

First-Order Shear Deformation Lamination Theory (FSDLT) extends Mindlin's theory to laminated plates [1] and allows shear deformations to be taken into account in the simplest way. Linear variation of in-plane displacements in x_3-direction is adopted:

$$u_{\alpha}=u_{\alpha}^{0}+x_{3}\psi_{\alpha}, \quad u_{3}=w_{0} \tag{12}$$

where u_{α}^{0} and w_{0} are analogous to eqns (11), and

$$\psi_{\alpha}=\Psi_{\alpha}\cos\vartheta_{\alpha}x_{\alpha}\sin\vartheta_{\beta}x_{\beta} \tag{13}$$

Finally, Third-Order Shear Deformation Lamination Theory (HSDLT) proposed by Reddy [1] is based on the following simple displacement field:

$$u_{\alpha}=u_{\alpha}^{0}+x_{3}\psi_{\alpha}-x_{3}^{3}\left(4/3h^{2}\right)\left(w_{0,\alpha}+\psi_{\alpha}\right), \quad u_{3}=w_{0} \tag{14}$$

obtained by imposing the condition of vanishing transverse shear stresses $\sigma_{\alpha3}$ on the top and bottom surface of the laminated plate.

NUMERICAL RESULTS

The results are presented according to the following non-dimensional forms:

$$\left\{\overline{\sigma}_{\alpha\alpha},\overline{\sigma}_{\alpha\beta}\right\}=\left\{\sigma_{\alpha\alpha},\sigma_{\alpha\beta}\right\}\left(h^{2}/A^{2}q_{3}\right), \quad \overline{\sigma}_{\alpha3}=\sigma_{\alpha3}\left(h/Aq_{3}\right) \tag{16}$$

Transverse shear stresses for CLT, FSDLT and HSDLT are obtained by equilibrium equations. Material constants for the two plates analysed are reported in Table 1.

Plate I. Stress distributions for $(A=B)/h=5$ are reported in *Figs. 2a-d.* The 2-D theory [2] is very accurate when compared with 3-D results, whereas this is not the case for FSDLT and CLT. HSDLT gives slightly better results then classical theories. *Figs. 2e,f* show the plate center deflection vs. plate slenderness ratio and degree of orthotropy of layers. In the last case, material properties are selected as $E_2=8$ *GPa,* $E_1/E_2=1$ to 30, $G_{13}=E_1/25$. Theories which take shear deformations into account (FSDLT and HSDLT)

give sufficiently accurate results, whereas CLT strongly underestimates the center deflection for moderately thick plates or strongly orthotropic layers. On the contrary, 2-D theory always gives very accurate results, the error in the evaluation of plate deflection being <2% for $A/h>5$ and for the whole range of layer orthotropy considered.

Plate II. This plate is made of a soft core with two stiff external layers. Stress distributions are reported in *Figs. 3a-d* for $(A=B)/h=10$. Even though the plate is thin, due to the mismatch of material properties between core and external layers CLT, FSDLT, HSDLT give erroneous results, e.g., maximum normal and shear in-plane stresses approximately half of exact 3-D values. On the contrary, 2-D theory provides for very accurate results, being able to accurately describe in-plane displacements through the thickness. The plate center deflection is depicted in *Fig.3e,f*. It is worth noting that, for $A/h<20$, the error of CLT, FSDLT and HSDLT is greater than 35%; the results are even worse for strongly orthotropic layers (*Fig.3f*), whereas 2-D theory is very accurate (error<2%) over the whole range of slendernesses and orthotropies considered.

CONCLUSIONS

This comparative study gives useful information on the efficiency of laminated theories for angle-ply plates. It reveals that CLT gives satisfying results only for slender plates $(A/h \geq 25)$. FSDLT and Reddy's HSDLT usually give similar results. They are sufficiently accurate for moderately thick plates when the layers are made of the same material, whereas they give erroneous results for plates with soft core. The best results are given by 2-D theory proposed in [2], both in terms of stresses and displacement.

REFERENCES

[1] Reddy, J. N. "Energy and variational methods in applied mechanics." John Wiley & Sons, New York (1984).

[2] Savoia, M., Laudiero, F., Tralli, A. "A two-dimensional theory for the analysis of laminated plates." *Computat. Mechanics* **14**, pp. 38-51 (1994).

[3] Savoia, M., Reddy, J. N. "A variational approach to three-dimensional elasticity solutions of laminated composite plates." *J. Appl. Mech.* **59**, pp. 166-175 (1992).

[4] Rohwer, K. "Application of higher order theories to the bending analysis of layered composite plates." *Int. J. Solids Struct.* **29**, pp. 105-119 (1992).

[5] Carvelli, V. "Comparison of some lamination theories applied to antisymmetric angle-ply plates in bending." DLR IB 131-95/22, Braunschweig (1995).

Plate I

layer	E_1 (GPa)	E_2 (GPa)	E_3 (GPa)	G_{12} (GPa)	G_{13} (GPa)	G_{23} (GPa)	ν_{12}	ν_{13}	ν_{23}	$\theta°$	t/h
1 to 4	200	8	8	5	5	2.2	0.25	0.25	0.25	30	0.25

Plate II

layer	E_1 (GPa)	E_2 (GPa)	E_3 (GPa)	G_{12} (GPa)	G_{13} (GPa)	G_{23} (GPa)	ν_{12}	ν_{13}	ν_{23}	$\theta°$	t/h
1 and 4	200	8	8	5	5	2.2	0.25	0.25	0.25	45	0.1
2 and 3	10	0.8	0.5	0.7	0.6	0.07	0.35	0.35	0.3	45	0.4

Table 1: Material constants for the plates considered in the numerical examples.
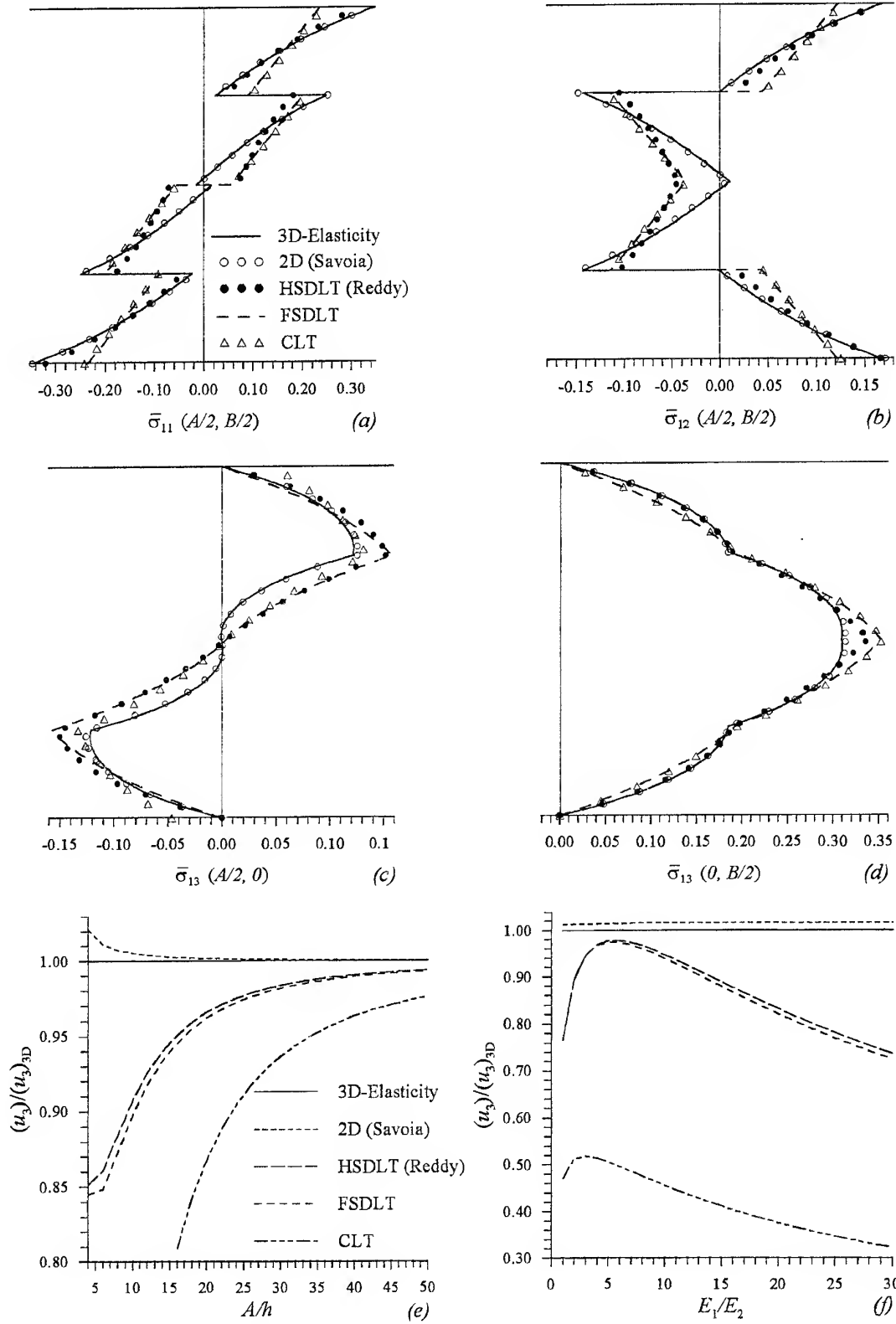
Fig. 2. Plate I: (a-d) stress distributions over the thickness; (e-f) plate center deflection vs. plate slenderness and layer degree of orthotropy.
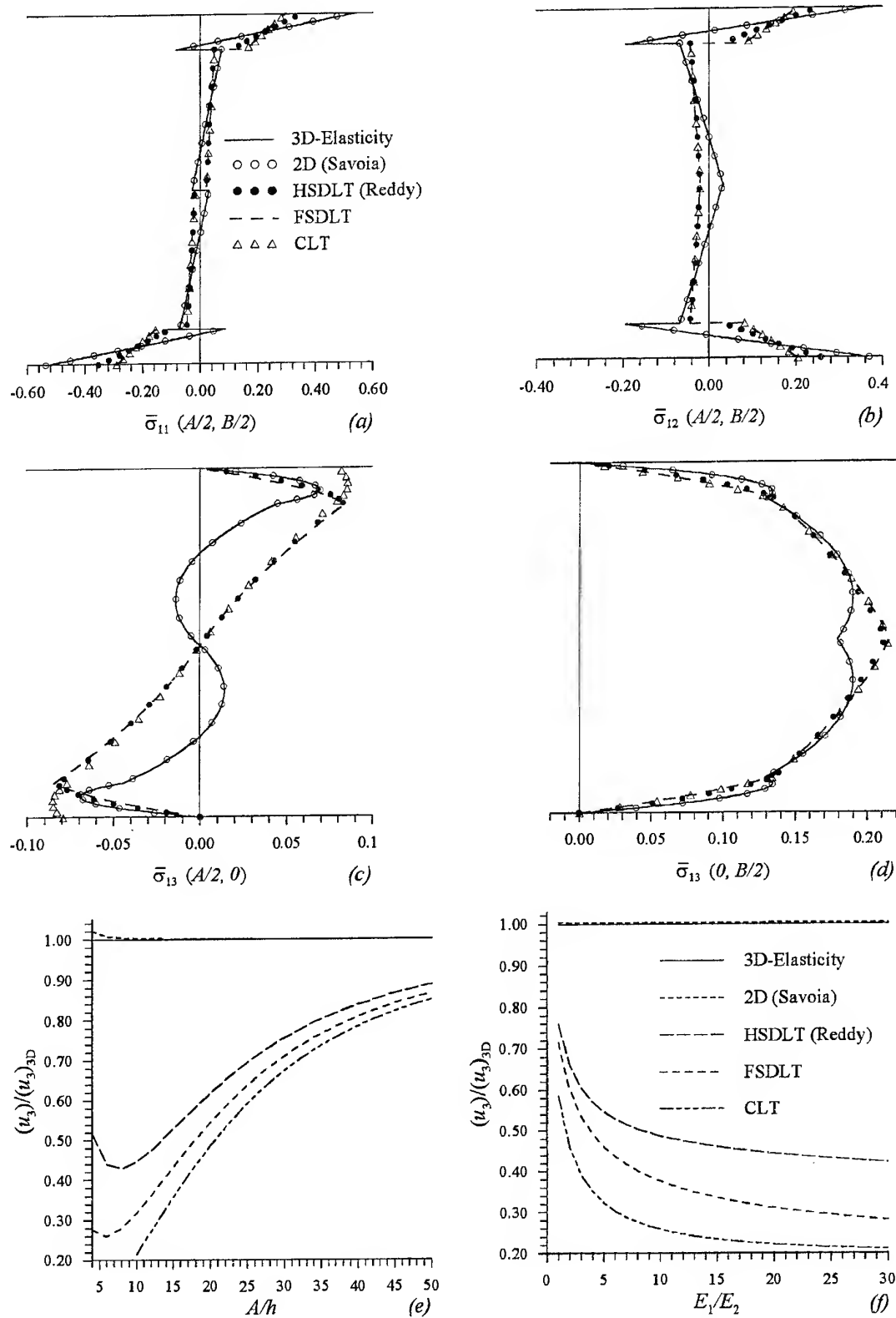
Fig. 3. Plate II: (a-d) stress distributions over the thickness; (e-f) plate center deflection
vs. plate slenderness and degree of orthotropy of external layers.

60

APPLICATION OF TAGUCHI'S METHOD ON THE OPTIMAL PROCESS DESIGN OF AN INJECTION MOLDED PC/PBT AUTOMOBILE BUMPER

R. S. Chen, H. H. Lee, and C. Y. Yu

Department of Engineering Science
National Cheng-Kung University
No. 1 University Road, Tainan, Taiwan, 70101

INTRODUCTION

The case studied in this paper concerns the quality of an injection molded PC/PBT automobile bumper. The mold was constructed and mold trials was proceeded by a group of senior workers. The process conditions selected at their best efforts underwent serious manufacturing problems: there were silver streaks on almost every product's surface, in addition to filling difficulties. We decided to conducted a research on solving the manufacturing problems.

After brain storming in several group discussions we made a conjecture (which may be confirmed in physical experiments) that if the magnitudes and the variations over the product surface of the bulk temperature gradients and the mold-wall shear stresses [3] of the polymer during the injection process can be minimized, the silver streaks developed on the products' surface might also be minimized. Therefore these two characteristics are chosen as performance criteria.

The experiment was divided into two stages: a preliminary experiment and a principal experiment. These experiments were carried out using a flow simulation program, namely C-MOLD [4]. Whenever necessary, confirmation experiments were conducted physically on an injection machine. The purpose of the preliminary experiment is to choose the factors that affect the performance most and to verify the additivity of the performance measures, i.e., the validity of the data fitting model [6]

$$\text{response} = \text{mean response} + \sum_{\text{all factor}} \text{factor effect}$$

THE PRELIMINARY EXPERIMENT

In the preliminary experiment there were 10 factors chosen and the two levels of each factor studied in the experiment are given in Table 1. Taguchi's L_{12} orthogonal array [1, 2] was used as shown in Table 2, note that column 8 is not assigned any factor and used

as an error estimate [6]. The signal to noise ratios, for the underlying case (the smaller the better), are calculated using the formula [1, 2, 7]

$$SN_1 = -10\log\left(\sum_{j=1}^{N} T_j \Big/ N\right), \quad SN_2 = -10\log\left(\sum_{j=1}^{N} S_j \Big/ N\right)$$

where T_j and S_j are respectively the bulk temperature gradient and the mold-wall shear stresses on product's surface position j. For the case studied a total of $N = 84$ positions were taken into survey. Each quantity (T_j or S_j) was evaluated over the time spanned the entire injection process, i.e. [5]

$$T_j = \sum_{i=1}^{n}\left(\frac{\Delta T_{ji}}{\Delta t_i}\right)^2 \Big/ n, \quad S_j = \sum_{j=1}^{N} S_{ji} \Big/ n$$

where T_{ji} and S_{ji} represent respectively the bulk temperature difference and the mold-wall shear stresses on product's surface position j at time t_i [5].

Table 1. Factors and Their Levels Studied in the Preliminary Experiment

Factor	Description	Level 1	Level 2
A	Fill time (sec)	10	15
B	Fill/postfill switch (%)	93	97
C	Injection speed (%)	1 (Slower)	II (Faster)
D	Coolant flow rate (liter/min)	10	130
E	Postfill time (sec)	100	120
F	Hot runner temperature (° C)	15	35
G	Holding pressure (%)	100	85
1	Injection temperature (° C)	275	245
J	Mold temperature (° C)	90	70
K	Holding pressure time (sec)	10	4

Table 2. The L₁₂ Array Used in the Preliminary Experiment and the SN Responses

Trial no.	1	2	3	4	5	6	7	8	9	10	11	SN1	SN2	SN1+SN2
	A	B	C	D	E	F	G		I	J	K			
1	1	1	1	1	1	1	1	1	1	1	1	-62.84	-86.33	-149.2
2	1	1	1	1	1	2	2	2	2	2	2	-61.26	-91.94	-153.2
3	1	1	2	2	2	1	1	1	2	2	2	-60.96	-92.30	-153.3
4	1	2	1	2	2	1	2	2	1	1	2	-63.30	-86.33	-149.6
5	1	2	2	1	2	2	1	2	1	2	1	-63.31	-89.62	-152.9
6	1	2	2	2	1	2	2	1	2	1	1	-57.71	-92.81	-150.5
7	2	1	2	2	1	1	2	2	1	2	1	-65.27	-88.93	-154.2
8	2	1	2	1	2	2	2	1	1	1	2	-63.42	-88.69	-152.1
9	2	1	1	2	2	2	1	2	2	1	1	-60.64	-91.07	-151.7
10	2	2	2	1	1	1	1	2	2	1	2	-58.92	-95.18	-154.1
11	2	2	1	2	1	2	1	1	1	2	2	-66.13	-88.08	-154.2
12	2	2	1	1	2	1	2	1	2	2	1	-62.48	-92.16	-154.6

Table 3. ANOVA Summary for SN_1 in the Preliminary Experiment

Source	Level 1	Level 2	SS	dof	V	F	P(%)
A	-61.57	-62.81	4.66	1	4.66	20.0	6.80
B	-62.40	-61.98	0.54	1	0.54		
C	-62.78	-61.60	4.16	1	4.16	17.9	6.03
D	-62.04	-62.34	0.26	1	0.26		
E	-62.03	-62.36	0.33	1	0.33		
F	-62.30	-62.08	0.14	1	0.14		
G	-62.14	-62.24	0.03	1	0.03		
I	-64.05	-60.33	41.5	1	41.5	179	63.4
J	-61.14	-63.24	13.2	1	13.2	56.8	19.9
K	-62.05	-62.34	0.25	1	0.25		
Error(pooled)			1.62	7	0.23		3.92
Total			65.0	11			100

Table 4. ANOVA Summary for SN_2 in the Preliminary Experiment

Source	Level 1	Level 2	SS	dof	·V	F	P(%)
A	-89.89	-90.69	1.90	1	1.90	3.20	1.59
B	-89.88	-90.70	2.02	1	2.02	3.43	1.74
C	-89.32	-91.26	11.3	1	11.30	19.1	13.0
D	-90.66	-89.92	1.61	1	1.61		
E	-90.55	-90.03	0.80	1	0.80		
F	-90.21	-90.37	0.08	1	0.08		
G	-90.44	-90.15	0.25	1	0.25		
I	-88.00	-92.58	62.9	1	62.9	107	75.8
J	-90.07	-90.51	0.57	1	0.57		
K	-90.16	-90.42	0.21	1	0.21		
Error(pooled)			4.13	7	0.59		7.89
Total			81.7	11			100

Table 5. ANOVA Summary for SN_1+SN_2 in the Preliminary Experiment

Source	Level 1	Level 2	SS	dof	V	F	P(%)
A	-151.46	-153.50	12.5	1	12.5	48.8	32.07
B	-152.28	-152.68	0.47	1	0.47		
C	-152.10	-152.86	1.75	1	1.75	6.80	3.91
D	-152.70	-152.26	0.57	1	0.57		
E	-152.57	-152.39	0.10	1	0.10		
F	-152.51	-152.46	0.01	1	0.01		
G	-152.57	-152.39	0.10	1	0.10		
I	-152.05	-152.91	2.23	1	2.23	8.71	5.17
J	-151.22	-153.75	19.2	1	19.2	75.1	49.7
K	-152.20	-152.76	0.93	1	0.93	3.63	1.76
Error(pooled)			1.54	6	0.26		7.37
Total			37.9	11			100

Results of the analysis of variance [6] are shown in Tables 3, 4, and 5. From Table 3, the factors that affect the performance most are injection pressure (I), mold temperature (J), fill time (A), and injection speed (C), . For minimal bulk temperature gradient, the predicted process condition is at $A_1C_2I_2J_1$ for which the predicted signal to noise ratio is

$$SN_{1,opt} = M + (-61.57 - M) + (-61.60 - M) + (-60.33 - M) + (-61.14 - M) = -58.07$$

where $M = -62.19$ is the mean values of SN_1 in Table 3. A value of -57.57 was obtained from a confirmation experiment. The difference $|(-58.07)-(-57.57)| = 0.50$ is well below the 95% confidence interval [1, 7]

$$\sqrt{F_{0.05:1:v_e} V_e \left(\frac{1}{n_{eff}} + \frac{1}{r} \right)} = \sqrt{5.59 \times 0.23 \times \left(\frac{1}{12(1+4)} + \frac{1}{1} \right)} = 1.35$$

Thus the additivity of the model can be assumed. Similar results can be deduced by analyzing SN_2 and SN_1+SN_2, and are summarized as follows

Response	Significant Factors	Optimal Conditions	Predicted Response	Response in Confirmation	Confidence Interval	Additivity
SN_1	I, J, A, C	$A_1C_2I_2J_1$	-58.07	-57.57	1.35	OK
SN_2	I, C, B, A	$A_1B_1C_1I_1$	-86.22	-86.33	2.83	OK
SN_1+SN_2	J, A, I, C, K	$A_1C_1I_1J_1K_1$	-149.11	-149.27	1.77	OK

THE PRINCIPAL EXPERIMENT

From the results of the preliminary experiment, 8 significant factors were chosen and the levels of each factor studied in the experiment are given in Table 6. Taguchi's L_{18} orthogonal array [1, 2, 7] used in the experiment and the signal to noise response are shown in Table 7. Results of the analysis of variance are shown in Tables 8, 9, and 10; the significant factors and optimal conditions are summarized as follows

	Significant Factors	Optimal Conditions
Based on SN_1	D, E, C, A	$A_1C_1D_1E_3$
Based on SN_2	D, C, G, E	$C_2D_3E_3G_2$
Based on SN_1+SN_2	E, A, C, G	$A_1C_1E_3G_1$

According to the information revealed above and the economics considerations, four sets of process conditions were selected for physical mold trials: (a) $A_1B_2C_1D_1E_3F_2G_3H_3$, (b) $A_1B_1C_3D_3E_3F_1G_2H_2$, (c) $A_1B_2C_1D_3E_3F_1G_1H_2$, and (d) $A_1B_2C_1D_2E_3F_1G_2H_2$. All the four sets of process conditions appeared to have much better performance comparing to the original process conditions and the condition (d) was found to be the most stable one in terms of filling and surface quality, in particular, the silver streaks problem.

CONCLUSIONS

This paper presents a case study on the design of manufacturing process to improve the quality of an injection molded polycarbonate/poly(butylene terephthalate) automobile bumper. The bumper, by the original process condition, was undergoing serious manufacturing problems: there were silver streaks on almost every product's surface, in

addition to filling difficulties. The predicted process condition was tested on an 2500-ton injection molding machine to confirm the results. The injection molded bumpers were examined and, as expected, the silver streaks did not occur any more. Analysis of the experimental results reveals that the main factors that directly relate to the generation of silver streaks are the mold temperature, the fill time, the fill/postfill switch over control, and the injection rate.

Table 6. Factors and Their Levels Studied in the Principal Experiment

Factor	Description	Level 1	Level 2	Level 3
A	Fill time (sec)	12	15	-
B	Hot runner temperature (∘ C)	D - 10	D - 25	D - 40
C	Fill/postfill switch (%)	91	95	99
D	Injection temperature (∘ C)	245	260	275
E	Mold temperature (∘ C)	70	80	90
F	Holding pressure time (sec)	6	9	12
G	Injection speed (%)	I (Slow)	II (Moderate)	III (Fast)
H	Holding pressure (%)	85	90	95

Table 7. The L_{18} Array Used in the Principal Experiment and the SN Responses

Trial	1	2	3	4	5	6	7	8	Response		
no.	A	B	C	D	E	F	G	H	SN1	SN2	SN1+SN2
1	1	1	1	1	1	1	1	1	-59.17	-90.62	-149.8
2	1	1	2	2	2	2	2	2	-60.17	-88.76	-148.9
3	1	1	3	3	3	3	3	3	-61.72	-86.23	-147.9
4	1	2	1	1	2	2	3	3	-56.58	-91.51	-148.1
5	1	2	2	2	3	3	1	1	-57.50	-89.33	-146.8
6	1	2	3	3	1	1	2	2	-64.85	-85.12	-149.9
7	1	3	1	2	1	3	2	3	-61.15	-89.01	-150.1
8	1	3	2	3	2	1	3	1	-61.67	-87.67	-149.3
9	1	3	3	1	3	2	1	2	-57.31	-89.50	-148.8
10	2	1	1	3	3	2	2	1	-61.54	-85.82	-147.4
11	2	1	2	1	1	3	3	2	-59.97	-92.49	-152.5
12	2	1	3	2	2	1	1	3	-61.77	-88.24	-150.0
13	2	2	1	2	3	1	3	2	-58.75	-88.80	-147.6
14	2	2	2	3	1	2	1	3	-63.40	-88.14	-151.5
15	2	2	3	1	2	3	2	1	-60.08	-89.96	-150.0
16	2	3	1	3	2	3	1	2	-62.80	·-86.23	-149.0
17	2	3	2	1	3	1	2	3	-57.32	-91.07	-148.4
18	2	3	3	2	1	2	3	1	-62.87	-90.65	-153.5

Table 8. ANOVA Summary for SN_1 in the Principal Experiment

Source	Level 1	Level 2	Level 3	SS	dof	V	F ·	P(%)
A	-60.01	-60.95	-	3.903	1	3.903	14.0	3.85
B	-60.72	-60.20	-60.52	0.847	2	0.423		
C	-60.00	-60.01	-61.43	8.188	2	4.094	14.7	8.10
D	-58.41	-60.37	-62.67	54.49	2	27.25	98.0	57.2
E	-61.90	-60.51	-59.02	24.88	2	12.44	44.7	25.8
F	-60.60	-60.31	-60.54	0.259	2	0.125		
G	-60.33	-60.85	-60.26	1.266	2	0.633		
H	-60.47	-60.64	-60.32	0.308	2	0.154		
Error(pooled)				2.780	10	0.278		5.02
Total				94.24	17			100

Table 9. ANOVA Summary for SN₂ in the Principal Experiment

Source	Level 1	Level 2	Level 3	SS	dof	V	F	P(%)
A	-88.64	-89.04	-	0.749	1	0.749		
B	-88.69	-88.81	-89.02	0.330	2	0.165		
C	-88.66	-89.58	-88.28	5.299	2	2.649	7.90	6.37
D	-90.86	-89.13	-86.53	56.80	2	28.40	84.7	77.3
E	-89.34	-88.73	-88.46	2.440	2	1.220	3.60	2.44
F	-88.59	-89.07	-88.87	0.698	2	0.349		
G	-88.68	-88.29	-89.56	5.077	2	2.538	7.60	6.07
H	-89.01	-88.48	-89.03	1.165	2	0.582		
Error(pooled)				3.019	9	0.335		7.85
Total				72.64	17			100

Table 10. ANOVA Summary for SN1+SN2 in the Principal Experiment

Source	Level 1	Level 2	Level 3	SS	dof	V	F	P(%)
A	-148.6	-149.4	-	8.070	1	8.079	40.1	13.4
B	-149.4	-149.0	-149.5	0.939	2	0.469		
C	-148.7	-149.6	-149.7	3.934	2	1.967	9.80	6.01
D	-149.3	-149.5	-149.2	0.296	2	0.148		
E	-151.2	-149.2	-147.5	42.45	2	21.23	105.4	71.6
F	-149.2	-147.4	-149.4	0.191	2	0.095		
G	-149.0	-149.1	-149.8	2.295	2	1.147	5.70	3.22
H	-149.5	-149.1	-149.4	0.393	2	0.196		
Error(pooled)				2.013	10	0.201		5.82
Total				58.76	17			100

REFERENCES

[1] Taguchi, G. "Introduction to Off-line Quality Control", Central Japan Quality Control Association, Nogoya, Japan, 1980.

[2] Kackar, R. N., "Off-Line Quality Control, Parameter Design, and the Taguchi Method", *Journal of Quality Technology*, Vol. 17, pp. 176-209, 1985.

[3] Isayev, A. I., ed., *Injection and Compression Molding Fundamentals*, Marcel Dekker, Inc., 1987.

[4] *C-MOLD Reference Manual*, AC Technology Inc., Ithaca, NY, 1992.

[5] *C-FLOW User's Guidel*, AC Technology Inc., Ithaca, NY, 1992.

[6] Box, G. E. P, Hunter, W. G., and Hunter J. S., *Statistics for Experimenters*, John Wiley & Sons, Inc., 1978.

[7] Ross, P. J., *Taguchi Techniques for Quality Engineering*, McGraw-Hill Book Co., 1989.

AN INVESTIGATION OF THE STRESS DISTRIBUTION IN MULTI-FASTENED COMPOSITE JOINTS USING THREE-DIMENSIONAL MODELLING

S. CHUTIMA[1] and A.P. BLACKIE[2]

[1] Department of Mechanical Engineering, King Mongkut's Institute of Technology Thonburi, Bangkok 10140, Thailand
[2] Department of Mechanical Engineering, University College London, London WC1E 7JE, UK

INTRODUCTION

The demand to utilize glass fibre reinforced plastic (GFRP) has increased recently in many engineering applications due to their high strength to weight ratio and relatively high specific stiffness. For components that require dismantling for routine inspection and repair mechanical fasteners are commonly employed. However, this method of fabrication does lead to regions of high stress concentration in the vicinity of the fastening when the laminates are subject to in-service loading[1]. Determination of the stress distribution at the bolt-laminate interface would assist in the optimization of joint design, particularly for the more often used multi-fastened joint configuration.

Considerable experimental work has been done to investigate the behaviour of mechanical fastened composite laminates[2-15] when subject to in-plane loading. Matthews et al.[2] investigated riveted joints and found that a 90°/±45° lay-up provided significantly lower bearing strengths than a 0°/±45° lay-up. Quinn and Matthews[3] examined GFRP 0°, ±45° and 90° laminates and showed that the stacking sequence having a 90° ply at, or, near the surface exhibited higher strength. Collings[4] concluded that for 0°/±45° CFRP laminates, joined by a single bolt, the bearing strength was significantly lower for stacking sequences having 0° plies grouped together. This study proposed that the optimum bearing tensile strength may be achieved using a ratio of 0° to 45° piles equal to 2:1, while an equal percentage of both piles provided optimum shear strength. Ramkumar and Tossavainen[5] have shown that the bearing strength drops when the percentage of adjacent plies having the same fibre orientation is increased. For glass fibre/epoxy laminates Kretsis and Matthews[6] showed that 0°/±45° laminates gave better bearing strengths than other lay-ups investigated. Marshall et al.[7] considered the cross ply GRP's and concluded that laminates having a fibre orientation of 90° in the outer layer failed at higher applied stresses. Recently, Hamada et al.[8] demonstrated that for quasi-isotropic carbon-epoxy laminate having plies of 0° orientation on the outer surfaces and alternate 90° and ±45° plies in the centre of laminate provided the highest bearing strength.

In an attempt to address the practical problems associated with mechanically fastening composite laminates a number of studies, both experimental and analytical, have been undertaken on multi-fastened joints. Oplinger[9] reported a remarkable increase in the gross section strength for glass/epoxy laminates of ±45° lay-ups, fastened using three pins in a single row compared with a single pin joint. A similar comparison for 0°/90° showed only slightly higher strengths in the multi-fastened configuration. Tests undertaken on multi-bolted GRP joints by Godwin et al.[10] showed that two bolts in parallel (perpendicular to the loading direction) resulted in higher failure strengths than

two bolts in series (aligned with the loading direction). A pitch value (p) of $2.5d$ and an e/d ratio of 5 was proposed for a single row of bolts to achieve optimum joint strength; in this particular case a tensile failure mode predominated.

The significance of bolt pre-load in conferring improved joint performance is well recognised, however, suitable analysis of this condition requires the evaluation of the interlaminar shear and through thickness stresses. Matthews et al.[11] used a modified three-dimensional element to model layers of CFRP laminates. Results obtained in this study, which considered a rigid frictionless bolt with the clamping on laminate area under washer, showed good agreement with experimental results[12]. Smith et al.[13] modelled clamp-up effects on composite laminates utilizing a simple three-dimensional analysis. However, this approach was limited by the requirement to obtain reliable experimental data for the constants included in the solution. Marshall et al.[7] considered a cross ply GRP and employed twenty-noded iso-parametric brick element to model a composite plate connected to a rigid frictionless pin. The stress profiles at the pin-hole interface were shown to be improved by the clamping pressure. Sherbian[14] studied the nonlinear interlaminar behaviour on fibreglass epoxy $[(0/90)_3,0]_s$ laminates using twenty-two-noded elements, equivalent to half the laminate thickness, to accommodate gap interface elements in the model. It is found that, for a laminate having high axial stiffness, pin elasticity produced a through-thickness variation in the net, bearing and shear-out stresses. Chen[15] developed a three-dimensional finite element technique for bolted joint composite laminates based on an incremental restricted variation principle. It was claimed that these results were in general agreement with experimental work.

In this current study a general finite element code[16], I-DEAS MS1.3c, was used to conduct the finite element analysis. The model of a double-lap joint between GRP outer lap laminates joined to a perfectly rigid fixture inner-lap, using aluminium alloy bolts, is described. Contact friction at the joint interfaces have been modelled using gap elements. The effects of the laminate stacking sequence, joint geometry and clamping pressure and the stress distribution in the laminate were evaluated. Details of these variables are given in the Finite Element Models section. The joint strength and failure mode were also evaluated using the Azzi-Tsai theory[17] to compute a ply failure index and strength criterion, and the onset of delamination was determined by the method proposed by Hashin-Rotem[18].

DESCRIPTION OF PROBLEM

A typical double lap multi-bolted joint consisting of plates having infinite width, as used in this investigation, is shown in *Figure 1*. The planes of symmetry may be identified as coincident with the line of centres, parallel to the loading direction. The inner lap was considered to be joined to the outer lap by a series of perfect fit aluminium bolts and clamped at the end furthest from the bolts. The in-plane tensile loads were applied at the end of the composite plates furthest from the bolts. The lateral constraint was applied to the laminate in the form of a clamping pressure exerted by the washer.

FINITE ELEMENT MODELS

The inner-lap of the joint was modelled as a perfectly rigid plate and a corresponding model of one of the GRP laminate outer laps was also constructed. The symmetry plane was taken as coincident with the line along the mid-plane of the inner lap. Eight-noded solid elements were used having material properties given in *Table 1* and a thickness

equal to the lamina thickness. Thus, the eight ply laminate was represented by eight layers of elements aligned so that the specified material properties were consistent with the ply orientation. The perfect fit aluminium bolts were modelled using six-noded solid elements having the material properties given in *Table 1*. The bolts were fixed at one end to the rigid inner lap, thereby providing zero relative displacement between the bolt and hole centre at this location. Adjacent nodes along the hole boundary subtended an angle of 15° at the centre of the hole. Node to node gap elements were used to model the contact between coincident nodes of the laminate plate and the bolts. For the interface between coincident nodes of the inner lap and the outer lap, node to ground elements were employed.

To evaluate the effect of stacking sequence on the stress distribution in the laminate a model having an overall length (*l*) of 50.8 mm, pitch distance (*p*) 38.1 mm, row spacing (*s*) 38.1 mm, edge distance (*e*) 38.1 mm and hole diameter (*d*) 6.35 mm was used. Eight ply laminates having a total thickness (*t*) of 6 mm and stacking sequences of $(0/45/-45/90)_s$, $(45/90/0/-45)_s$, $(0/90/45/-45)_s$, $(0_2/90_2)_s$, $(90_2/0_2)_s$ and $(90/0/90/0)_s$ were adopted. *Figure 2* shows the ply designation of the laminate in this study. An in-plane force of magnitude 10 kN was applied to the laminate, as described. Analysis was undertaken, in the first instance, without considering any lateral constraint and friction at the contact interfaces.

The quasi-isotropic laminate, $(0/45/-45/90)_s$, was then utilized to evaluate the influence of joint geometry on various parameters. A constant hole diameter, *d*, of 6.35 mm was used, while the pitch distance was varied between $4d$ and $8d$, the row spacing between $2d$ and $6d$ and the edge distance between $2d$ and $6d$. Interfacial friction between the composite outer lap and the bolts was considered only in the circumferential direction, while friction between the inner and outer lap contact surface was confined to the loading direction. A coefficient of friction equal to 0.2 was adopted.

The effect of bolt tightening was examined using elements similar to those used in the previous analysis and a model having the following joint geometry: pitch diameter $6d$, row spacing $4d$ and edge distance $6d$. The bolt tightening torque was varied from 0 to 8 Nm and was represented by a uniform clamping pressure applied directly on an annulus representing the washer contact area on the outer surface of the laminate. Loading was applied to the model in two steps: firstly, the clamping pressure was applied and the stiffness matrix and deformed nodal displacements computed. These values were subsequently used in the second step, the application of a 10 kN tensile in-plane load at the end of the laminate furthest from the joint. A coefficient of friction of 0.2 was also applied to the contact surfaces between the bolt and laminate and the inner and outer laps of the joint. In the analysis the fixed boundary condition in the y- and z- directions were specified for nodes on the loaded edge, permitting displacement only in the x-direction.

RESULTS AND DISCUSSION

The following definitions were used to normalize the stresses for comparative assessment. The radial contact stress, through thickness and interlaminar shear stress were normalized by the average bearing stress, $\overline{\sigma}_B$, where,

$$\overline{\sigma}_B = \frac{Tensile\ load}{d \times t} \tag{1}$$

In order to obtain the ply-by-ply failure index, the Azzi-Tsai[17] expression was used.

The effect of the stacking sequence on the radial contact stress distribution and the maximum inter-laminar shear stress on the hole boundary at the laminate/plate interface, is shown in *Figure 3a* and *Figure 3b*, respectively. In almost all of the lay-ups investigated, with the exception of the (0/90/45/-45)$_s$ laminate, the radial contact stress increases in magnitude as the angular position is increased, with respect to the bearing plane, attaining a maximum value at an angular position of 30° for the orthotropic, (0$_2$/90$_2$)$_s$ and quasi-isotropic (0/90/45/-45)$_s$, laminates and 45° for most of the other laminates considered. In contrast the results for the (45/90/0/-45)$_s$ laminate exhibit a maximum value on the bearing plane which decreases continuously around the contact interface until, at an angular position of approximately 45° the contact stress increases, peaking at an angular position of about 80°, before deminishing at larger angular positions. These results indicate that the peak radial contact stress only occurs on the bearing plane when the laminar orientation at the outer surface is inclined at 45° to loading direction.

In *Figure 3b* it may be observed that for all the laminates investigated the maximum inter-lamina shear stress was recorded at the interface between the two innermost plies, designated as 7 an 8 in this study, (ply 8 is at the surface of the laminate adjacent to the rigid inner lap plate). This is to be expected since the maximum bending moment in the fastener will occur at the laminate-plate interface. The variation in the inter-lamina shear stress at this position is similar for all the laminates studied, peaking at approximately 45°, although the magnitude of the stress variation for the (45/90/0/-45)$_s$ and (0/45/-45/90)$_s$ laminates is somewhat different. In the case of the (45/90/0/-45)$_s$ laminate the stress is lower compared with the others for intermediate and high angular positions (>60°), whereas the (0/45/-45/90)$_s$ laminate exhibits significantly lower values at low to intermediate angular positions, (<60°). It was for this reason, given the marginal differences exhibited in the radial contact stress, that the quasi-isotropic laminate (0/45/-45/90)$_s$ was chosen for the second phase of this study: to investigate the effects of friction and bolt pre-load on the stress distribution and failure of the composite laminate. The location of the peak radial and interlaminar stresses is considered to be a function of several parameters including ply orientation and bolt distortion and this is subject to further investigation.

The effect of varying the joint geometry on the maximum normalised radial contact stress, recorded by the application of an in-plane load to a quasi-isotropic inner lap laminate with interfacial friction at the contact surfaces, is shown in *Figure 4*. The effect of varying the edge distance, as a function of hole diameter (*d*) between 2*d* and 4*d*, as shown in *Figure 4a*, was to cause a reduction in the maximum radial contact stress for all pitch distances examined. However, a further increase in edge distance to 6*d* showed no significant effect. In contrast, increasing the row spacing, as a function of bolt diameter, for the same range in pitch distances (*Figure 4b*) caused a continuous increase in the maximum radial contact stress. This result clearly indicates that a minimum row spacing is preferred, however, this parameter should not be considered in isolation since the net tensile stress must also be considered for optimum joint design.

The effect of bolt tightening on the stress distribution in the laminate for intermediate values of pitch distance, 6*d*, and row spacing, 4*d*, was examined. A lateral pressure equivalent to a tightening torque of 4 Nm was applied to the model. The normalised stress distribution on the laminate surface and at each ply interface on the contact surface, for the inboard row only, is given in *Figure 5*. As observed in *Figure 3*, the

maximum radial contact stress occurs either on the bearing plane or at angular positions corresponding to 45° or 80° to the loading or positive x-direction, depending on the ply orientation. These results also show that the highest radial contact stress was recorded at an angular position of 45° on the laminate surface, adjacent to the rigid inner lap.

Although not presented here the stress distribution for the outboard row was similar to that observed for the inboard row, however, the magnitude of the stresses was significantly reduced. This is to be expected from previous work showing the effect of load transfer to the inboard row in comparison to the outboard row for double row multi fastened joints[19,20].

The results obtained for the stress variation along the hole boundary at the inner and outer lap interface as a consequence of changing the clamping pressure in a range corresponding to bolt tightening torques of 0.5 to 8Nm, are given in *Figure 6*. The characteristic curve showing the variation in the normalised radial contact stress does not change significantly with clamping pressure, although increasing the bolt torque marginally reduces the peak value of the stress recorded at angular positions of 45°. A similar response is shown in *Figure 6b* for the variation in the interlaminar shear stress. However, the variation in the normalised through thickness stress, as shown in *Figure 7*, is somewhat different exhibiting an increase in magnitude with increasing angular position and clamping pressure. The change in through thickness stress is indicative of peeling of the laminate about a transverse axis through the inboard hole.

A qualitative evaluation of the deformation produced as a consequence of bolt clamping and in-plane loading of the composite outer-lap is shown in the displacement contour plots given in *Figure 8*. Applying only a lateral constraint to the laminate, equivalent to a bolt tightening torque of 8 Nm, resulted in the deformation shown in *Figure 8a* and *8b*, and caused a maximum displacement of 0.05 mm compared with the unloaded condition. In both cases considerable deformation was recorded in the vicinity of the washer as well as lateral twisting and longitudinal bending of the laminate. The deformation produced by the application of a tensile load without bolt clamping is illustrated in the contour plot shown in *Figure 8c*. This may be compared with *Figures 8d, e,* and *f* in which tightening torques of 0.5, 4 and 8 Nm have been applied, respectively. Clearly, increasing the clamping pressure reduces the maximum deflection of the laminate whilst increasing the relative displacement, in the loading direction, between the inner and the outer surface

The ply failure and delamination indices were investigated using the stress resultant obtained in conjunction with the failure criterion[17,18] described earlier. The average combined stresses for each element were calculated from the stress components at all Gaussian points in any specific element. The failure indices were then calculated based on the uniaxial strength of the GRP lamina, as shown in *Table 2*. The failure indices for elements on the hole boundary, representing the ply in contact with the rigid plate, are shown in *Figure 9*. This surface was selected since stress analysis indicated that this was the critical lamina in the joint. The effect of a clamping torque of 4 Nm, for both inboard and outboard holes, is also shown in this figure. These results indicate that the application of a 10 kN in-plane load almost caused ply failure on the inboard row at an element on the hole boundary corresponding to an angular position of approximately 40° with respect to the bearing plane. The effect of bolt pre-load was to lower the failure indices at all the recorded elements on the hole boundary. In terms of joint performance, this confirms the benifit afforded by preloading the fasteners. The relative magnitude of

71

both indices indicate that ply failure, as opposed to delamination, is the predominant failure mechanism for this paticular double lap configuration.

The effect of row spacing and edge distance on the ply failure index for the same joint configuration is shown in *Figure 10*. Increasing the bolt row spacing from 2d to 6d increases the peak index value by 20%, whereas, increasing the edge distance from 2d to 4d lowered the index by a similar amount. A further increase in edge distance from 4d to 6d appeared to produce an insignificant change in the value of the failure index. These observation are consistent with the findings given earlier concerning the effect of joint geometry on the radial contact stress at the hole boundary and demonstrates the overriding influence of this stress component in determining ply failure in this particular case.

CONCLUSIONS

Three dimensional stress analysis for a range of different laminates forming the outer lap of the mechanically fastened joint, connected by a double row of fasteners to a rigid fixture, has shown that the maximum radial contact and interlaminar shear stresses occur on the hole boundary of the inboard row at the laminate-plate interface. This is attributed to the effect of bending of the fastener and interfacial friction. The location of the peak stress on the hole boundary is dependent on ply lay-up and varied from 30° to 45° with respect to the bearing plane for most the laminates investigated. The magnitude of the peak interlaminar shear stress for the quasi-isotropic laminate was found to be 50% lower than the other laminates considered in this investigation.

For the quasi-isotropic laminate the effect of increasing the bolt tightening torque, up to a maximum value of 8 Nm, on the radial contact and interlaminar stresses was to lower the peak stress at the laminate-plate interface with the exception of the through thickness stress, which naturally shows the converse effect.

Preloading the fasteners was shown to cause small transverse and longitudinal deflections in the laminate which were significantly increased with the application of an in-plane load. However, increasing the tightening torque reduced the magnitude of these out of plane displacements.

Edge distance and row spacing was shown to influence the ply and delamination failure indices and the results suggest that the row spacing for this double lap configuration should be minimized, consistent with an appraisal of the net tension stress; whereas, the optimum edge distance was considered to be equivalent to four times the bolt diameter. Comparison of the ply and interlaminar indices indicated that ply failure was the predominant failure mode for the quasi-isotropic laminate and that first ply failure would occur at an angular position close to 40° on the hole boundary, with respect to the loading direction.

ACKNOWLEDGEMENT

REFERENCES

1. Crews, J. H., Hong, C. S. and Raju, I. S. "Stress-concentration factors for finite orthotropic laminates with a pin-loaded hole" *NASA Technical paper 1862*, May 1981.

2. Matthews, F. L., Nixon, A. and Want, G. R. "Bolting and riveting in fibre reinforced plastics" *Proceedings of Reinforced Plastics Congress*, British Plastic Federation, Brighton, November, 1976.

3. Quinn, W. J. and Matthews, F. L. "The effect of stacking sequence on the pin-bearing strength in glass fibre reinforced plastic" *Journal of Composite Materials* **11**, pp.139-145 (1977).

4. Collings, T. A. "The strength of bolted joints in multi-directional CFRP laminates" *Composites* **8**, pp.43-55 (1977).

5. Ramkumar, R. L. and Tossavainen, E. W. "Bolted joint in composite structures: Design, analysis and verification task I test result- single fastener joints" *AFWAL-TR-84-3047*, 1984.

6. Kretsis, G. and Matthews, F. L. "The strength of bolted joints in glass fibre/epoxy laminates" *Composites* **16**, pp.92-102 (1985).

7. Marshall, I. H., Arnold, W. S., Wood, J. and Mousley, R. F. "Observation on bolted connections in composite structures" *Composite Structures* **13**, pp.133-151 (1989).

8. Hamada, H., Haruna, K. and Maekawa, Z.-I. "Effect of stacking sequences on mechanically fastened joint strength in quasi-isotropic carbon-epoxy laminates" *Journal of Composites Technology & Research* **17**, pp. 249-259 (1995).

9. Oplinger, D. W. "On the structural behavior of mechanically fastened joints in composite structures" *Proceedings of a Conference on Fibrous Composites in Structure Design*, San Diago, California, Nov. 14 - 17, pp.575-602 (1978).

10. Godwin, E.W., Matthews, F.L. and Kilty, P.F., Strength of multi-bolt joints in GRP, *Composite* **13**, pp.268-272 (1977).

11. Matthews, F. L., Wong, C. M. and Chryssafitis, S. "Stress distribution around a single bolt in fibre-reinforced plastic" *Composites* **13**, pp.316-322 (1982).

12. Stockdale, J. H. and Matthews, F. L. "The effect of clamping pressure on bolt bearing loads in glass fibre reinforced plastics" *Composites* **7**, pp.34-38 (1976).

13. Smith, P. A., Ashby, M. F. and Pascoe, K. S., "Modelling clamp-up effects in composite bolted joints" *Journal of Composite Materials* **21**, pp.878-897 (1987).

14. Sherbian, S. M. "The effects of nonlinear interlaminar shear behavior on the modeling accuracy of $[(0/90_3,0]_s$ and $[(+45/-45)]_{3s}$ pin-loaded laminates." *Journal of Composites Technology & Research* **13**, pp.236-248 (1991). ·

15. Chen, W.-H., Lee, S.-S. and Yeh, J.-T. "Three-dimensonal contact stress analysis of a composite laminate with bolted joint." *Composite Structures* **30**, pp.287-297 (1995).

16. I-DEAS Master Series 1.3c., 2000 Eastman Drive, Milford, OH 45150, USA, 1993.

17. Azzi, V. D. and Tsai, S. W. "Anisotropic strength of composites." *Experimential Mechanics* **5**, pp.283-288 (1965)

18. Hashin, Z. and Rotem, A. "A fatigue failure criterion for fibre reinforced materials" *Journal of Composite Material* **7**, pp.448 (1974)

19. Blackie, A.P. and Chutima, S. "Stress distribution in multi-fastened composite plates" *Composite Structures*, manuscript in preparation.

20. Chutima, S., and Blackie, A.P "Effect of pitch distance, row spacing, end distance and bolt diameter on multi-fastened composite joints" *Composites Part A* **27A**, pp.105-110 (1996)

21. Starr, T. F. "Glass-Fibre Databook" Chapman & Hall, London, 1993.

Table 1. Material properties of GRP lamina and aluminium bolts

Material	E_1 GPa	E_2 GPa	E_3 GPa	$G_{12}, G_{23},$ and G_{31} GPa	v_{12}	v_{23}	v_{31}
GRP[7]	31.85	10.20	7.14	2.14	0.328	0.199	0.045
Al 6061-T6	68.3	68.3	68.3	25.7	0.33	0.33	0.33

Table 2. Material strengths of the uniaxial GRP ply[21].

Properties	X (MPa)	Y (MPa)	S (MPa)	R (MPa)
Estimated	60	60	60	60
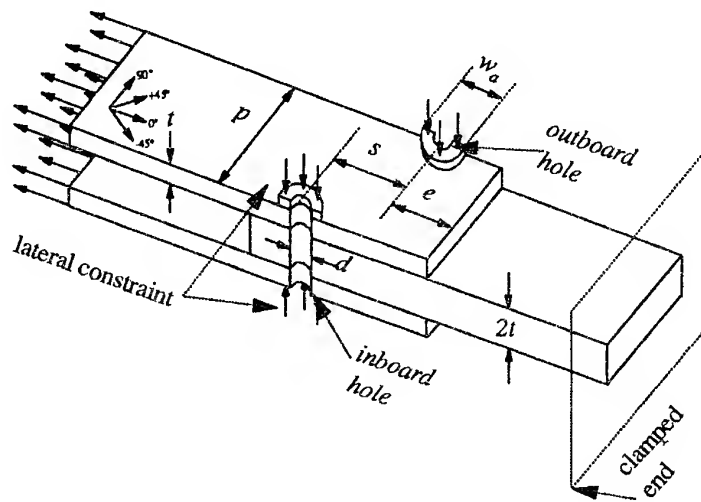
Figure 1. Physical model of multi-fastened composite joint.
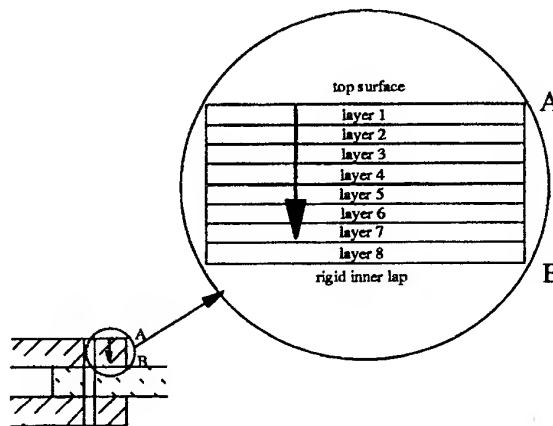
Figure 2. Lay-up designation of composite laminate.

a) normalized radial contact stress
b) normalized interlamina shear stress
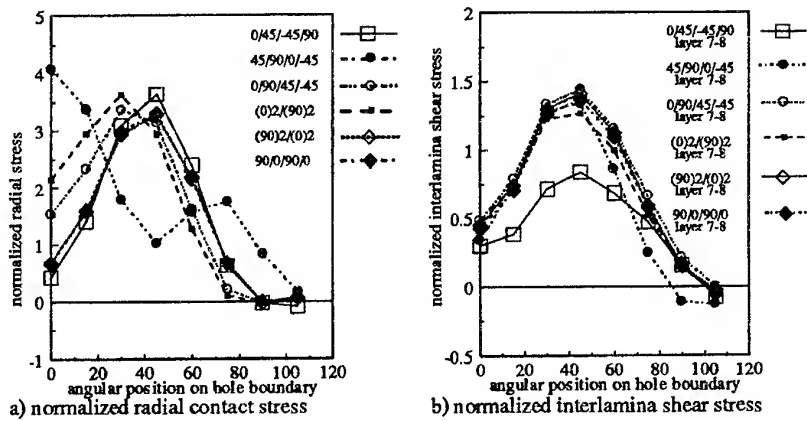
Figure 3. Comparison of (a) normalized radial contact stress and (b) normalized interlaminar shear stress at the laminate-plate interface for different stacking sequences.

a) effect of edge distance (s=6d)
b) effect of row spacing (e=6d)
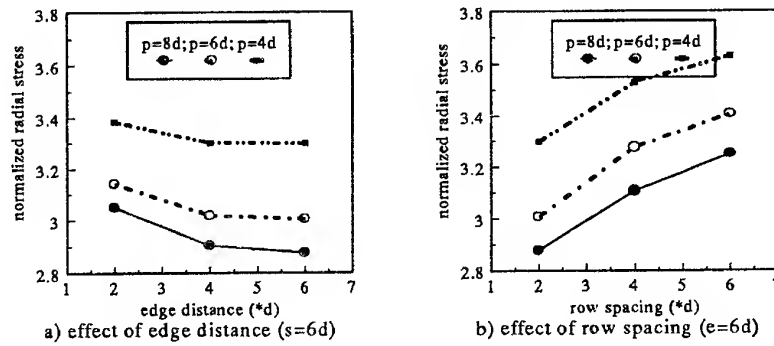
Figure 4. Effect of geometric variables on the maximum radial contact stress for the quasi-isotropic laminate.
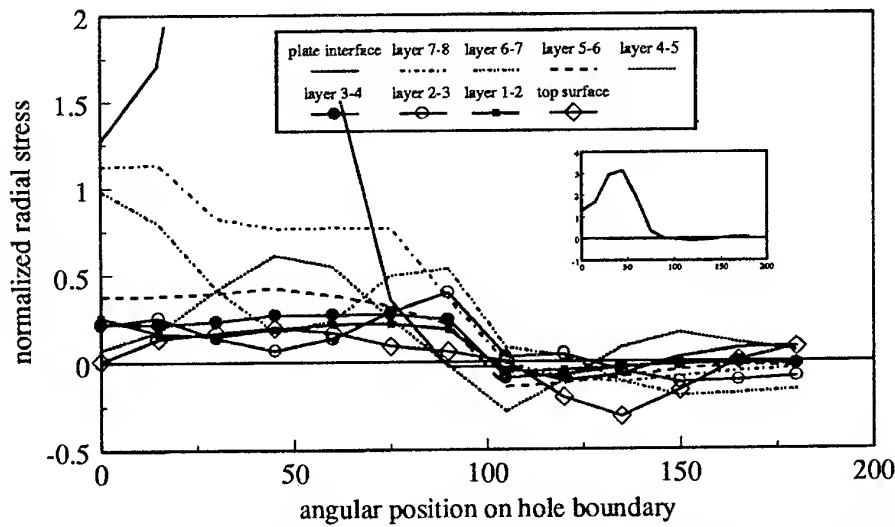
Figure 5. Typical stress distribution for interface nodes on the hole boundary of the inboard row.

a) normalized radial contact stress   b) normalized interlaminar shear stress
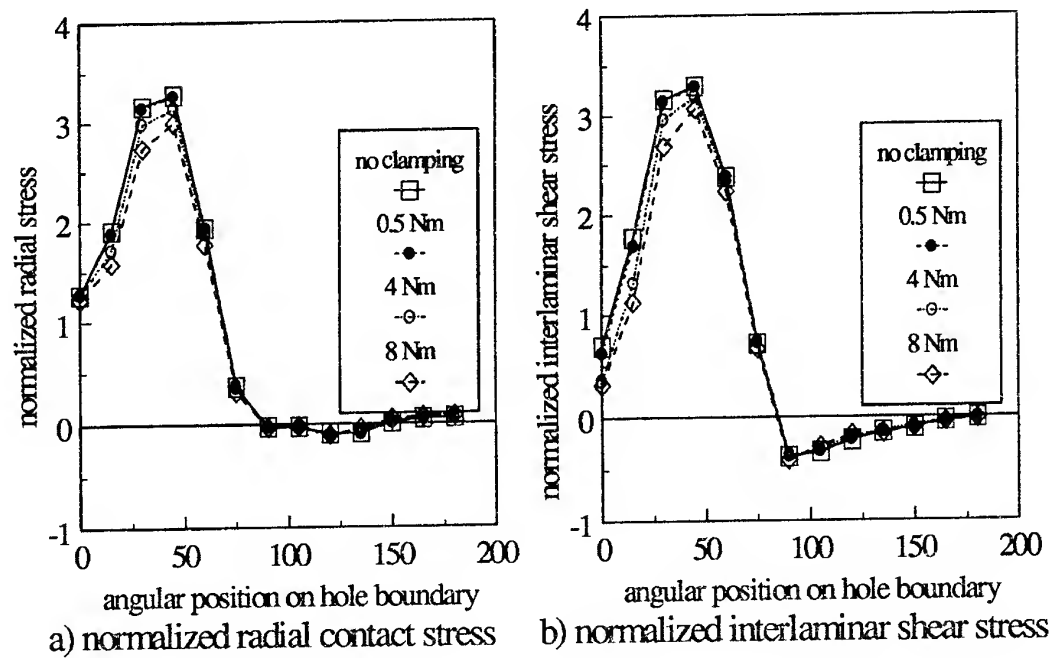
Figure 6. Effect of bolt tightening torque on (a) normalized radial contact stress and (b) normalized interlamina shear stress of nodes along the hole boundary at the laminate-plate interface.
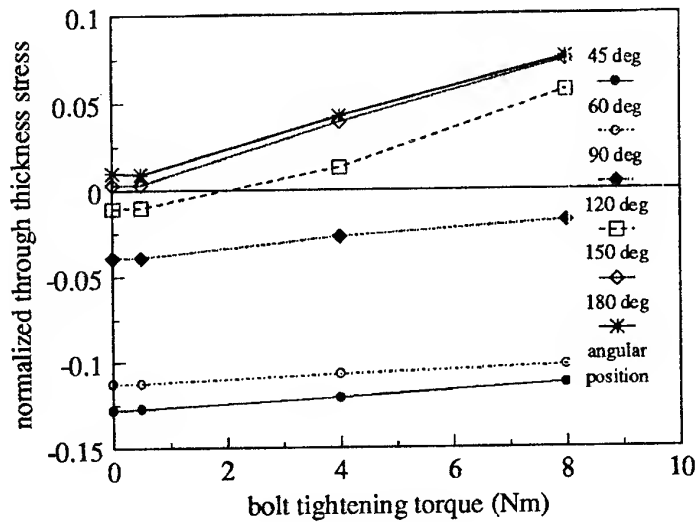
Figure 7. Normalized through thickness stress as a function of tightening torque for a range of angular positions along hole boundary.
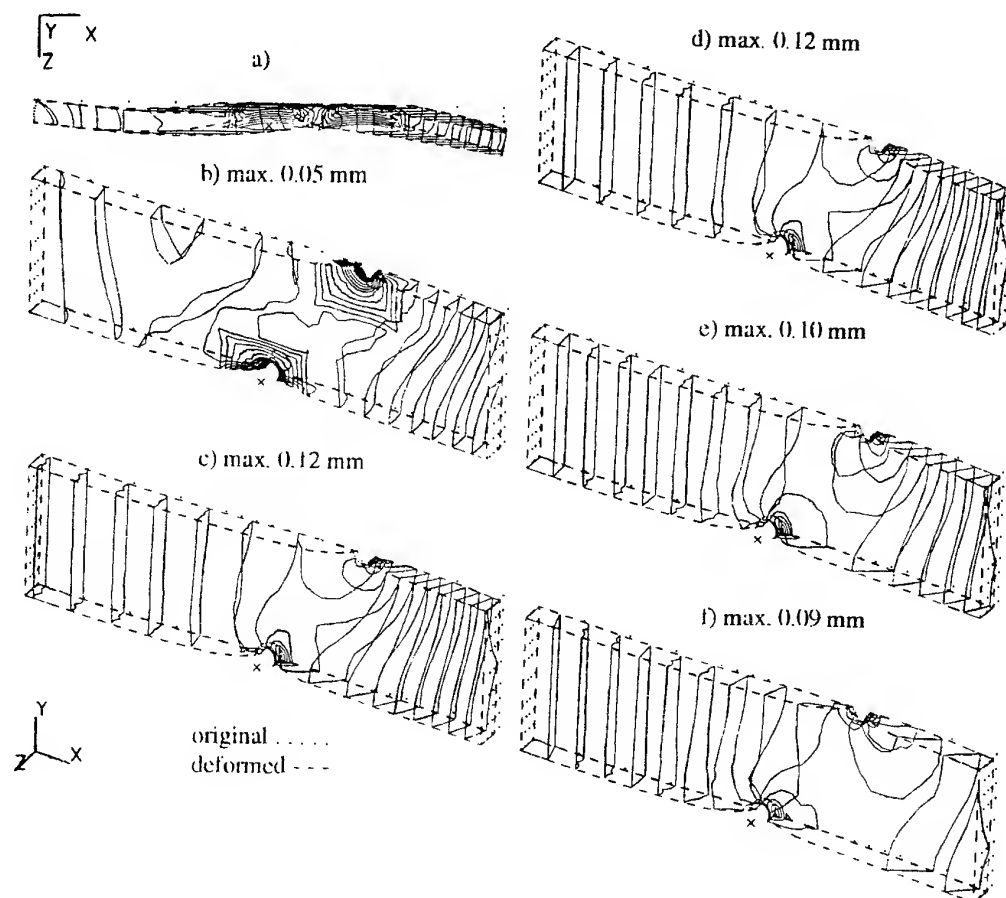
Figure 8. Contour plots showing the deformation of a multi-fastened composite laminate as a result of the following loading conditions: (a) and (b) a lateral constraint equivalent to a bolt tightening torque of 8 Nm; (c), (d), (e) and (f) a 10 kN tensile load in addition to bolt tightening torques of 0, 0.5, 4 and 8 Nm, respectively. The maximum displacements for each load case, compared with the unloaded condition, are given adjacent to each figure.

77
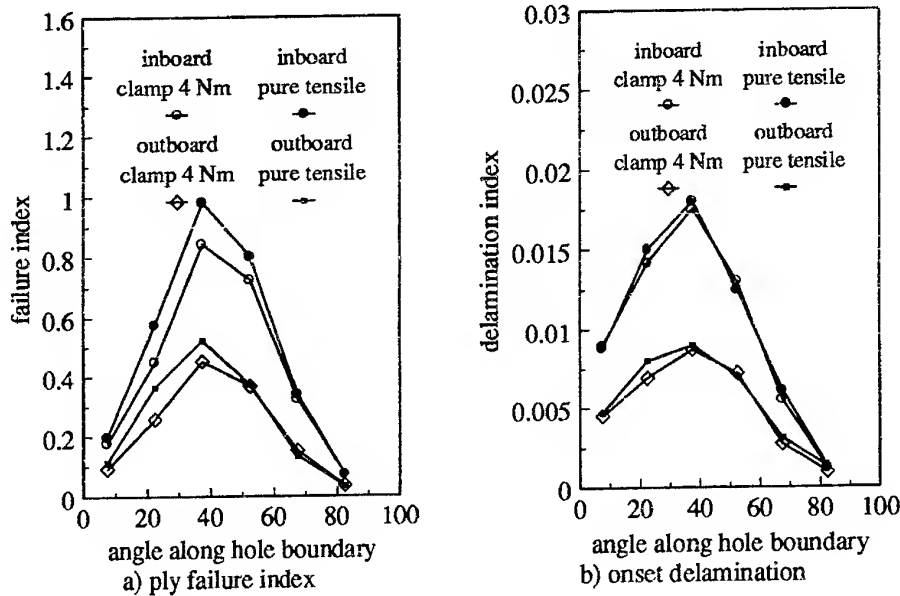
Figure 9. Comparison of the ply failure index and the onset of delamination index for a double lap joint (i) without bolt tightening and (ii) with a tightening torque of 4 Nm.
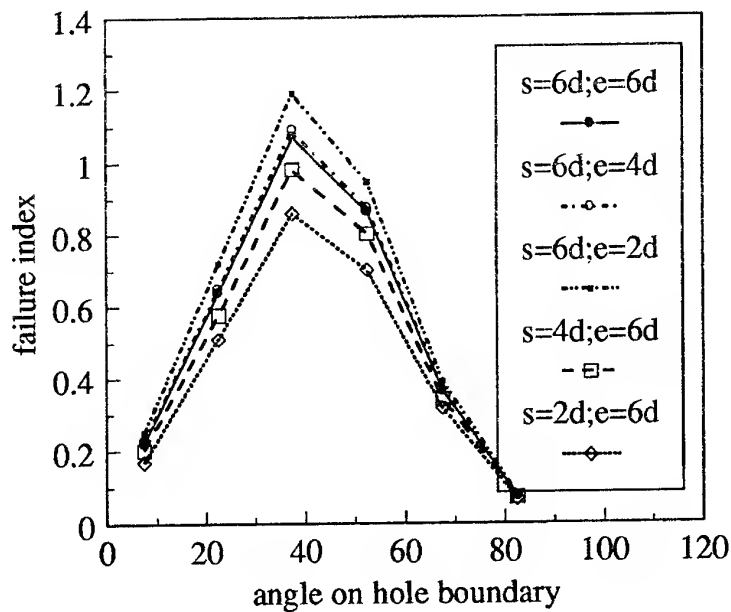
Figure 10. Effect of row spacing and edge distance on failure index (constant pitch distance = 6d).

TOUGHNESS OF GLASS-FIBRE MARINE COMPOSITES: IMPACT RESISTANCE CHARACTERISATION

P. Compston[1], P.-Y.B. Jar[1], P. Davies[2] and J.H. Hodgkin[3]

1. Department of Engineering, Faculty of Engineering and Information Technology,
The Australian National University, Canberra ACT 0200, Australia
2. Marine Materials Laboratory, Institut Francais pour la Recherche sur L'Exploitation
de la Mer (IFREMER), France
3. Commonwealth Scientific and Industrial Research Organisation (CSIRO),
Division of Chemicals and Polymers, Australia

INTRODUCTION

This paper presents a study of the damage tolerance of four glass-fibre marine composites under low speed impact loading. Glass-fibre composites are currently used in marine environments and one of those used in this study, glass-fibre reinforced orthophthalic polyester (glass/PO), has been used by the pleasure boat industry for many years. However as the range of applications in marine environments expands [1-4], composites with improved mechanical properties are required. For economic reasons, it is desirable to use glass fibres as the reinforcement. Therefore, using matrix resins with improved mechanical properties and ageing resistance is the most cost effective way of improving marine composites.

Damage within marine structures made from fibre composite materials is commonly in the form of delamination [3,5], which can reduce strength and stiffness and have an adverse affect on performance. In response to this problem, the composites in this study have been made using stitched fibres. The stitching of fibres has been shown to enhance delamination resistance [6]. While impact during service may not cause catastrophic failure, it can cause damage in the form of delamination. This impact induced delamination will be Mode II dominated [7], which is a shearing mode of failure. Therefore, this study will focus on Mode II delamination resistance under impact loading, which will be applied at low speed in order to simulate a practical situation.

Since the fibre type and the size are the same for each composite, the strength of the interface bond is likely to vary with the matrix. Our previous study on the delamination resistance of these composites, under Mode I & II static loading, has shown that an improved interface bond will improve delamination resistance for crack initiation [8]. Variations in the level of fibre-matrix adhesion between the composites produced results that were not always consistent with the order of matrix toughness. This interface effect has also been reported in static delamination testing of carbon fibre composites [9-12]. Hibbs et al. [12] in particular stressed that the translation of resin toughness to delamination resistance is highly dependent on fibre-matrix adhesion at the interface. However, Mode II delamination of carbon fibre composites under impact loading has been shown to increase with matrix ductility [13]. It is important, therefore, to determine whether the delamination resistance of these marine composites, under impact loading, is dominated by matrix toughness or by the interface.

This paper will focus on a low speed penetration impact study, which induces Mode II delamination in the test specimen. It will also give a brief outline of a low speed Central Notch Impact (CNI) study. As the penetration study supplements the CNI study, results from both studies will be presented then discussed in relation to results from the earlier static delamination study.

EXPERIMENTAL

The four composites used in this study are reinforced with E-glass fibres which have a multi-compatible size. The polymer matrix however is different for each composite. The matrices used are DGEBA epoxy (EP), vinyl ester (VE), isophthalic polyester (PI) and orthophthalic polyester (PO). The vinyl ester resin is of particular interest due to its resistance to ageing in a marine environment [14]. The mechanical properties of the resins are given in Table 1. From the data for tensile strength and failure strain, the toughness of the resins is estimated to be in the order of; EP > VE > PI > PO.

Table 1: Matrix Resin Properties

Matrix Resin	Modulus (GPa)	Failure Strength (MPa)	Failure Strain (%)
DGEBA Epoxy (EP)	3.1	70	7.1
Vinyl ester (VE)	3.5	83	4.2
Iso Polyester (PI)	2.4	75	3.8
Ortho Polyester (PO)	3.4	62	1.7

The composites for the penetration impact study were made by hand lay-up at IFREMER in France. They consisted of 8 stitched layers of fibres in a $[0/90_4]_s$ lay-up, with a fibre volume fraction of 35%. The specimens were 5mm thick and machined to a length and width of 70mm using a water cooled diamond saw. The panels with the epoxy and vinyl ester matrices were postcured at 90°C for 6 hours, while the panels with the polyester matrices were stabilised at room temperature for 1 month.

For penetration, the specimens were placed over a 50mm diameter hole in the base plate of a Radmana (ITR 2000) Instrumented impact tester. They were held in position with an air clamp and penetrated by a pneumatically driven steel probe, of 12.7mm diameter. The pressure to drive the probe was set at 600 kPa for each test, giving an initial impact speed of 3.5 m/s. A total of 3 specimens from each composite were tested under this condition. A displacement transducer and a force sensor were attached to the probe. The displacement transducer was activated for the duration of the test and the force sensor recorded force data when the probe was in contact with the specimen. This data produced a load versus displacement curve. The maximum load point on this curve is taken as the point at which penetration occurs. The area under the curve up to this point gives the energy absorbed in resisting penetration, E_{max}. To outline the fracture pattern, each specimen was photographed post-impact in front of a strong light. The light contrasted the damaged and undamaged regions. To determine the delamination fracture area, specimens were sectioned along the fibre direction and radially (ie. at 45° to the direction of the stitched fibres). The end of the section from which the delamination crack propagated was dipped in black ink. Capillary action forced the ink to flow up through the delamination cracks, enabling them to be clearly identified and measured.

Delamination resistance of the composites was characterised using dynamic strain energy release rate in Mode II, G_{II}^D, that was measured in a CNI test using central notch flexure (CNF) specimens. Details of the measurement were reported in a previous paper [15]. Here, it is assumed that the G_{II}^D for the CNF specimens can be used directly to estimate the total energy consumption for delamination crack growth during the penetration impact. The total energy for delamination, E_D, is determined as follows,

$$E_D = D_A \cdot G_{II}^D \qquad (1)$$

where D_A is the total delamination fracture area in the specimen. The energy for fibre fracture, E_F, at the maximum load point can also be estimated,

$$E_F = F_N \cdot (E_{FFP} \cdot F_{PN}) \qquad (2)$$

where F_N is the number of fibres intersecting the volume of material penetrated by the probe, E_{FFP} is the energy required to create a single fracture point on a fibre, and F_{PN} is the

number of fracture points for each fibre. In this study, F_{PN} was found to be one. The energy required for matrix deformation and fracture, E_M, is then simply,

$$E_M = E_{max} - (E_D + E_F) \qquad (3)$$

All the electron micrographs presented in this paper were taken using a Cambridge S360 Scanning Electron Microscope (SEM).

RESULTS AND DISCUSSION

The results from the penetration impact tests are summarised in Table 2. The co-efficient of variation (CV) is given for E_{max} and D_A, while values for E_D and E_M are also given as percentages of E_{max}. The results from the CNI tests, $G_{II}{}^D$ are also presented in Table 2. A load-displacement curve from a penetration impact test on a glass/EP specimen is given in Fig.1(a). The shape of the curve is typical for all specimens tested. The energy required for penetration, E_{max} was calculated from the maximum load point. The force reading after this point is attributed to the friction between the probe and the specimen that was observed during testing. Although E_{max} is highest for the glass/EP composite, there is little variation in this result.

Table 2: Results of Penetration Impact Tests

Composite	E_{max} (J) (CV %)	$G_{II}{}^D$ (KJ/m^2)	D_A (10^{-3} m^2) (CV %)	E_D (J) (% of E_{max})	E_F (J)	E_M (J) (% of E_{max})
Glass/EP	80.0 (16)	2.04	7.6 (16)	15.5 (19.4)	4.1	60.4 (75.5)
Glass/VE	72.1 (22)	1.77	9.8 (10)	17.2 (23.9)	4.1	50.8 (70.5)
Glass/PI	75.9 (33)	1.54	13.7 (9)	21.0 (27.7)	4.1	50.7 (66.8)
Glass/PO	75.7 (18)	1.41	15.3 (18)	21.6 (28.5)	4.1	50.0 (66.1)

Fig.1(b) shows a glass/VE specimen after a penetration impact test. Before penetration each specimen was observed to undergo a significant deflection. It was suspected that at some stage during the deflection, the specimen was only supported at 4 points, that is, at the four corners of the specimen. This resulted in the diamond-shaped fracture pattern seen in Fig.1(b), with the two major axes parallel to the fibre directions. In the case of extensive damage, the diamond-shaped damage can be extended furthest to the edge of the specimen in the direction of the fibres, as is also evident in Fig.1(b). When this happens, a larger specimen is needed to retain the complete fracture pattern within the specimen.

(a)   **(b)**
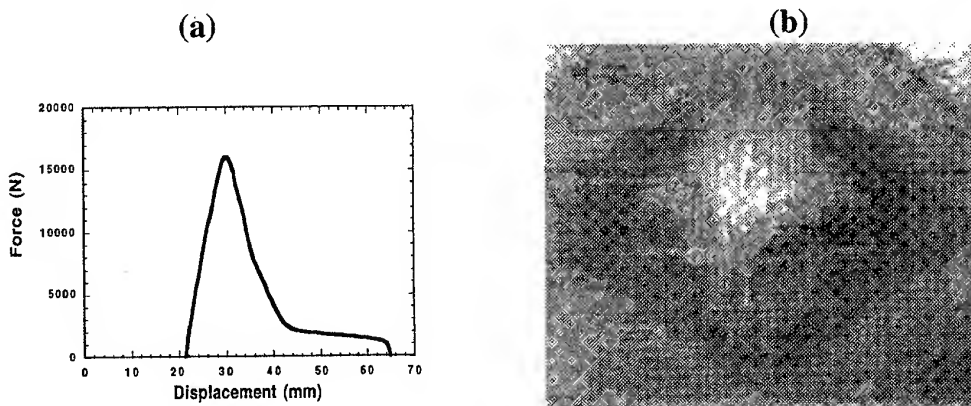
Fig. 1 (a) Load-Displacement plot from Glass/EP specimen, and (b) Fracture pattern in Glass/VE specimen after penetration impact.

The fracture behaviour in the penetration impact specimens is illustrated by the micrograph in Fig.2(a). It is from one section of the glass/PI composite and is representative of the

fracture behaviour for each composite. The dark line running through the centre the $[0/90_4]_s$ layers illustrates that damage is in the form of delamination, and that the crack runs through the intraply region. The number of delaminations was consistent with the number of layers in the laminate. However, the distribution of the delamination lengths varied within the specimen. Longer delaminations were measured in the centre of the specimens compared to the delaminations at the edges. This is expected since the shear force applied during the test would be at a maximum in the centre of the specimen. The average fracture area due to delamination, D_A for each composite is illustrated in Fig.2(b). The glass/EP composite, which has the toughest matrix resin, has the least delamination fracture area, and the glass/PO composite with the most brittle matrix has the highest delamination fracture area. In fact, the results correspond directly to matrix toughness, with delamination fracture area increasing as matrix toughness decreases. In view of the fracture behaviour illustrated in Fig.2(a), this result suggests that while crack propagation tends to the interface region the extent of delamination damage is determined by the matrix.

(a)   **(b)**
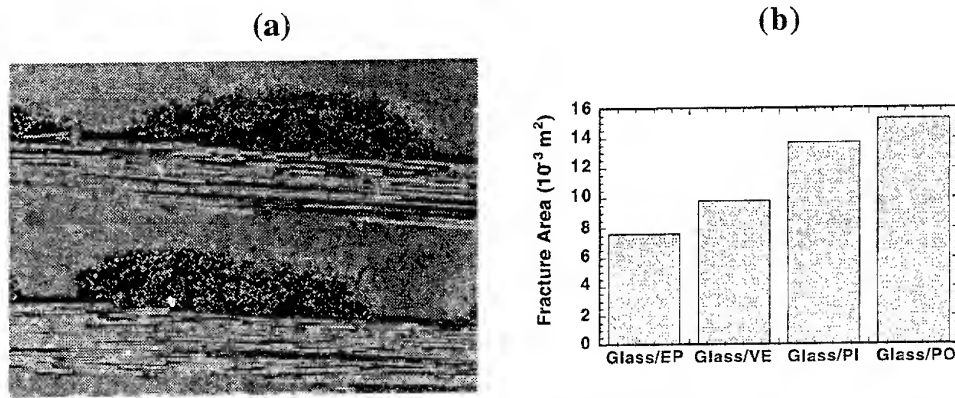
Fig.2 (a) Delamination crack path in glass/PI specimen, and (b) Delamination fracture area, after penetration impact.

The bending of the specimens during the test penetration impact specimens indicates that delamination would be Mode II dominated. The $G_{II}{}^D$ results from the CNI tests show that Mode II delamination is matrix dominated, as do the results for D_A in the penetration impact test. Therefore, the $G_{II}{}^D$ results have been used to estimate the energy consumed by delamination, E_D, in the penetration impact specimens (equation (1)). The absolute values of E_D, and E_D as a percentage of penetration energy E_{max}, show that a smaller proportion of the penetration energy is consumed for delamination in the composites with a tougher matrix. As only one fibre fracture point was observed in the specimens after impact, the energy consumed by fibre fracture, E_F, in each composite was only 4.1 J (equation (2)). The remainder must therefore be the energy consumed by matrix deformation and fracture, E_M (equation (3)). The absolute values show energy consumption increasing with matrix toughness. In particular, E_M given as percentage of E_{max} shows that the matrix is the largest energy absorbing component of the composites, and the percentage value increases with matrix toughness.

While the results so far indicate that damage tolerance in terms of delamination resistance is dominated by matrix toughness, the values for E_{max} show little variation. In fact the values for the glass/PI and glass/PO composites which have the two most brittle resins, are slightly higher than value for the glass/VE composite which has a tougher matrix resin. The explanation for this lies in the figures for delamination fracture area D_A. The creation of the delaminations would dissipate energy. As shown by the values for E_D, this was quite a large amount for the glass/PI and glass/PO. The dissipation of this energy has acted as a toughening mechanism, thus increasing the E_{max} value.

The results of these two impact studies show that Mode II delamination resistance of these marine composites under impact loading is dominated by the toughness of the matrix resin. In the penetration impact study the results for delamination fracture area support this conclusion, especially as the loading conditions for each composite were identical. In the

case of the G_{II}^D results from the CNI tests, this conclusion is supported by the fracture surface characteristics of the CNF specimens, shown in Fig.3. The micrographs of the glass/EP and glass/VE composites show a high density of hackle marks in the areas of pure matrix resin between the fibres. This extensive deformation illustrates how the tough resins have absorbed the impact energy. The lower density of hackle marks and evidence of brittle fracture features in the micrographs of the glass/PI and glass/PO composites indicate less matrix deformation and energy absorption during impact. However, the matrix domination of delamination resistance under impact loading was not reflected in all the results of an earlier static delamination study. Mode I and Mode II critical strain energy release rates for crack initiation in the glass/PI composite were only slightly lower than the results for the glass/EP composite, despite a large difference in matrix toughness. In both cases the glass/PI composite gave higher values than the glass/VE composite. Examination of the fracture surface of the static test specimens revealed more matrix still attached to the fibres in the glass/PI composite than the glass/EP or the glass/VE composites. This higher level of fibre-matrix adhesion in the glass/PI composite had been more effective at involving the matrix resin in the fracture process, and was reflected in the results for crack initiation. However, the impact study results are consistent with matrix toughness and not the level of fibre-matrix adhesion, indicating the role of the interface in resisting delamination is insignificant compared to the role of the matrix. It should be noted however that at the maximum load in the static Mode II delamination test, when fast fracture occurs, the results do correspond directly to the order of matrix toughness.
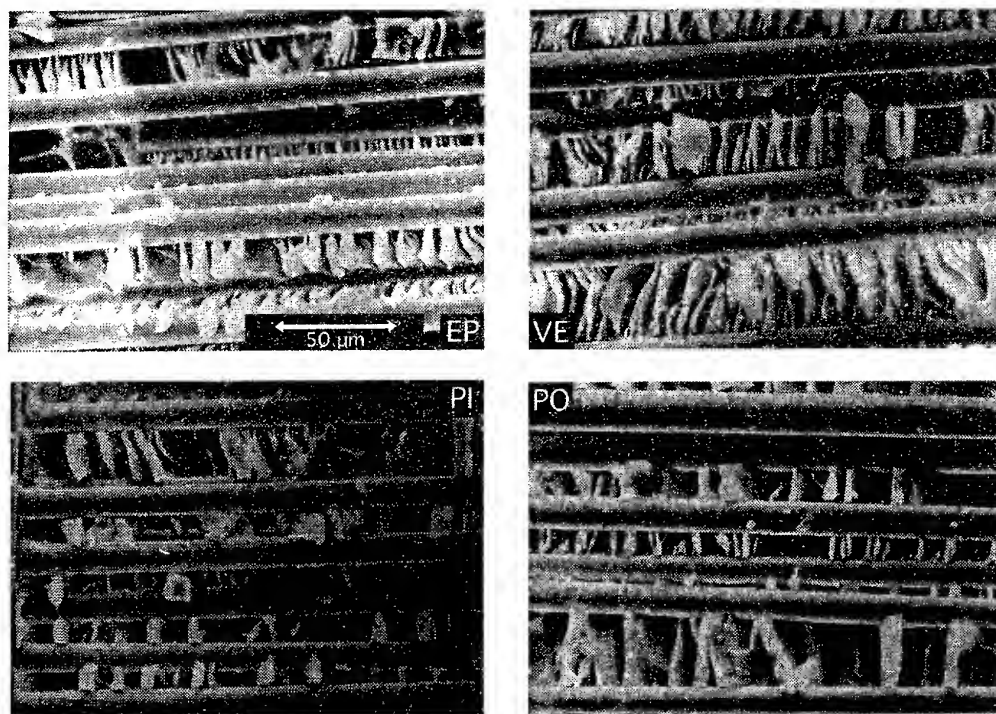
Fig.3 Micrographs, of the same scale, showing fracture surfaces from the CNI study.

CONCLUSIONS

The Mode II delamination resistance of glass-fibre marine composites, under low speed impact loading, has been investigated. The study consisted of a penetration impact test and a Central Notch Impact Test. The conclusions are as follows:

1) The resistance to Mode II delamination is dominated by matrix toughness. Under identical loading conditions, the delamination fracture area in the composites from the penetration impact tests was seen to decrease as matrix toughness increased. The results

from the CNI tests show strain energy release rate, G_{II}^D, increasing with matrix toughness.

2) The varying level of fibre-matrix adhesion in these composites, which influenced results from static delamination tests, is not reflected in the results of this impact study.

3) While use of the toughest resin will minimise delamination damage, it will not necessarily lead to an increase in the energy required for penetration of the composite. The results suggest that the dissipation of energy in composites with low matrix toughness, by way of delamination, will serve to increase the energy required for penetration.

4) From a practical point of view, the glass/EP composite will experience less delamination damage when subjected to a low speed impact.

Future work will involve the use of very low impact energies to characterise the barely visible impact damage tolerance of these marine composites.

ACKNOWLEDGMENTS

REFERENCES

[1] Maccari A. et al. "..Applications of Composite Materials on Large Passenger Vessels and Merchant Ships". *Proc.Int.Conf., Nautical Construction With Comp. Mat.*, P.Davies & L.Lemoine eds. IFREMER, Paris, pp.39-47 (1992).

[2] Lemiere Y. "The Evolution of Composite Materials in Submarine Structures." *Proc.Int.Conf., Nautical Construction With Comp. Mat.*, P.Davies & L.Lemoine eds. IFREMER, Paris, pp.441-449 (1992).

[3] Leslie J.C. "Development of a Composite Submarine Radome." The Tenth International Conference on Composite Materials, Whistler, Canada, pp.669-676 (1995)

[4] Hihara et al. "Marine Applications for Advanced Composites." *Int. Conf. on Advanced Composites*, T. Chandra & A.K. Dhingra eds. Wollongong, Australia, pp.95-100 (1993).

[5] Barnouin B. et al. "Damage Observed During Inspection of Composite Pleasure Boats." *Proc.Int.Conf., Nautical Construction With Comp. Mat.*, P.Davies & L.Lemoine eds. IFREMER, Paris, pp.389-393 (1992).

[6] Dransfield K., Baillie C. & Mai Y.-W. "Improving the Delamination Resistance of CFRP by Stitching - A Review." *Composites Science and Technology* **50**, pp.305-317 (1994).

[7] Wang H. & Vu-Khanh T. "Fracture Mechanics and Mechanisms of Impact-Induced Delamination in Laminated Composites." *Journal of Composite Materials* **29** (2), pp.156-178 (1995).

[8] Compston P., Jar P.-Y.B. & Davies P. "Matrix Effect on the Interlaminar Fracture Toughness of Glass-Fibre Marine Composites." *Composites Science and Technology,* submitted.

[9] Madhukar M.S. & Drzal L.T. "Fiber-Matrix Adhesion and its Effects on Composite Mechanical Properties: IV. Mode I and Mode II Fracture Toughness of Graphite/Epoxy Composites." *Journal of Composite Materials* **27** (7), pp.936-968 (1992).

[10] Jar P.-Y.B., Mulone R., Davies P. & Kausch H.-H. "A Study of the Effect of Forming Temperature on the Mechanical Behaviour of Carbon-Fibre/PEEK Composites." *Composites Science and Technology* **46**, pp.7-19 (1993).

[11] Albertsen H., Ivens J., Peters P., Wevers M. & Verpoest I. "Interlaminar Fracture Toughness of CFRP Influenced by Fibre Surface Treatment: Part 1. Experimental Results." *Composites Science and Technology* **54**, pp.133-145 (1995).

[12] Hibbs M.F., Tse M.K. & Bradley W.L. "Interlaminar Fracture Toughness of some Toughened Graphite/Epoxy Composites." Toughened Composites ASTM STP 937. N.J. Johnson ed. American Society for Testing and Materials, Philadelphia, pp.115-130 (1987).

[13] Maikuma et al. "Mode II Interlaminar Fracture of the Center Notch Flexural Specimen under Impact Loading." *Journal of Composite Materials* **24**, pp.124-147 (1990).

[14] Gutierrez et al. "A Study of the Ageing of Glass-Fibre Resin Composites in a Marine Environment." *Proc.Int.Conf., Nautical Construction With Comp. Mat.*, P.Davies & L.Lemoine eds. IFREMER, Paris, pp. 338-346 (1992).

[15] Jar P.-Y.B., Compston P., Davies P. & Takahashi K. "Delamination Toughness of Glass Fibre Reinforced Composites under Impact Loading". *Conference on Marine Applications for Composite Materials*, Florida. (1996).

METHOD OF FORECASTING THE DURABILITY OF CONVEYOR BELTS AND EVALUATION OF PHYSICAL - MECHANICAL PROPERTIES OF ELEMENTARY LAYERS ON THIS DURABILITY

Krystyna Czaplicka
Główny Instytut Górnictwa
Pl. Gwarków 1,
40-166 Katowice,
Poland

INTRODUCTION

Conveyor belts used in mining industry can be treated as flat multilayer composites consisting of several interlayers of properly impregnated fabric or bonded cloth and lining. The fabrics are made entirely of polyamide, polyester or aramid fibres, most often woven crosswise. The linings are made either of rubber or PVC. All interlayers together constitute the core of the belt transmitting longitudinal and transversel forces.

The physical - mechanical properties of the composite layers as well as their number influence, to a great extent, the elastic and viscoelastic properties of the composite. Knowing the behaviour of the composite material one can forecast its durability at the assumed criterion of failure.

The aim of the paper is to answer the question: to what extent the durability of the belt changes as a result of changes of physical - mechanical properties of its elementary layers.

1. STIFFNESS OF ELEMENTARY LAYERS OF LAYER COMPOSITES AND AN ANALYSIS OF POSIBILITIES TO DESIGN THE COMPOSITE STIFFNESS

The stiffness of composite layers, just as in the case of traditional materials, is described by the relationships between the stress and strain of the material. The material constants appearing in these equations can constitute a set of engineering constants (moduli of elasticity or deformability) of component layers of the composite. The relationships are similar to those for traditional materials except the number of independent constants. In the case of conventional materials their number is equal two, and for anisotropic layers - four.

The stress as a measure of internal forces and the strain resulting in consequence of their action constitute two variables, the functions of which are the stiffness and strength of

the material. The mechanisms of deformation and failure are also interpreted as derivatives of the states of stress and strain.

The dependence between the stress and strain is a function either of material deformability (S) or its stiffness (Q). The material properties of the composite layer can equally be described by a set of material constants of either the stiffnes (Q) or deformability (S) types.

Knowledge of the stiffness of the component material - composite layer is necessary when calculating the mutual relationships between the stress and strain. It is also the basis to calculate the engineering constants. However, it is not necessary in calculations of the stiffness of multilayer composites [1].

1.1. Exemplary calculations of the stiffness of layer materials of conveyor belts

Three - interlayer PVC belts and rubber belts with polyamide fabric interlayers have been taken for testing. In the presented example the interlayer reinforcing the belt has obviously an anisotropic structure while the PVC or rubber interlayers are isotropic. Table 1 shows the initial data of elementary layers, necessary for further calculations.

Table 1. Engineering data of various types of multi-interlayer belts

interlayer of the polyamide PAT M350		PVC		rubber
E_x [KN/m]	1900	E_x [KN/m]	25.22	46
E_y	503	$E_y = E_x$	25.22	46
v_{xy}	0.463	v_{xy}	0.24	0.22
v_{yx}	0.135	$v_{yx} = v_{xy}$	0.24	0.22
G_s	238	G_s	10.17	15
stiffness (Q)				
$m=(1-v_x v_y)^{-1}$	1.066672	$m=(1-v)^{-1}$	1.315789	1.282
$Q_{xx}=mE_x$	2026.677	$Q_{xx}=mE$	33.184	58.974
$Q_{yy}=mE_y$	536.536			
$Q_{xy}=mv_y E_x$	273.602	$Q_{xy}=mvE$	7.964	12.974
$Q_{yx}=mv_x E_y$	248.416			
$Q_{ss}=G_s$	238	$Q_{ss}=G_s$	10.17	15
deformability (S)				
$S_{xx}=1/E_x$	0.000526	$S_{xx}=1/E_x$	0.03965	0.02174
$S_{yy}=1/E_y$	0.001988			
$S_{xy}=-v_y/E_y$	-0.00027	$S_{xy}=-v/E$	-0.00952	-000478
$S_{yx}=-v_x/E_x$	-0.00024			
$S_{ss}=1/G_s$	0.0042	$S_{ss}=1/G$	0.0983	0.0666

where: E_x, E_y - Young moduli in x and y directions,

ν_x, ν_y - Poisson ratios,

G_s - shearing modulus.

Having at one's disposal the calculated above components of the tensor of deformability or stiffness of material, it is possible to calculate the strain components at the defined loading conditions of the material.

1.2. Analysis of the possibilities to design the stiffness of layer composites

The stiffness of multilayer composites is strictly related with the orientation of layers. Modulus of stiffness of such composites is a sum of moduli of individual layers, taking into account their thickness. Strength properties of multilayer composites depend, in general , on their array and thickness of the layers and, of course, on their mechanical - physical properties. The properly made composite, liable to plane state of stress, should be symmetrical in the transverse section in relation to the plane of the layers. If not, the plane state of stress in the plane of layers would cause non - dilatational strain of the whole layer composite, in the plane of transverse section in relation to the plane of layer array. At the same time the adjacent layers should be chosen in such a way that the difference of the non-dilatational strain between them, as a result of occurring of the defined state of stress, should be the smallest one. In the course of applying the load on the material, the smaller inter-layer internal strain will then be generated, for which the materials of the layers are extremely susceptible.Thus, the knowledge of geometry of the composite and known representations of deformability tensors for particular layers are the initial condition to calculate the matrix of the representation of deformability tensor [2]. If the composite is loaded with the set of external corces (N_1, N_2, N_3) causing the plane state of stress (s_1, s_2, s_6),

where: $N_1 = h \cdot s_1$, $N_2 = h \cdot s_2$, $N_3 = h \cdot s_3$, h - composite thickness then the relationship between the stress state and strain of the composite can be presented by means of formulae of the type as follows:

$$N_1 = A_{11} \cdot \varepsilon_1 + A_{12} \cdot \varepsilon_2 + A_{13} \cdot \varepsilon_3 \text{ etc.}$$

or inversely:

$$\varepsilon_1 = N_1 \cdot \sigma_{11} + N_2 \cdot \sigma_{12} + N_3 \cdot \sigma_{13} \text{ etc.}$$

In both formula types, the strain is related to the central layer (the assumption of invariability of the strain along the composite thickness). The matrix A_{ij} or its inverse matrix a_{ij} are the matrices of stiffness and deformability of the composite, respectively. Their elements are calculsted from the relationship:

$$A_{11} = \int Q_{11} \cdot dz \text{ ,etc.}$$

where: z – integration variable along the composite thicknesss from 0 to h.

Here, the same interrelationships between the components (symmetry, zeoring) hold as for the examples of anisotropic composite layers. Based on the knowledge of the materices of stiffness or deformability of the composite, it is possible to calculate the engineering constants of the material, in the moduli of stiffness and Poisson`s ratios. The engineering constants of the composite can be calculated from the relationship:

$$E_1 = \frac{1}{A_{11}h} \quad ; \quad E_2 = \frac{1}{A_{22}h} \quad ; \quad E_3 = \frac{1}{A_{33}h}$$

$$V_{21} = -\frac{a_{21}}{a_{11}} \quad ; \quad V_{31} = \frac{a_{31}}{a_{11}} \quad ; \quad V_{13} = \frac{a_{13}}{a_{33}}$$

Fig. 1. shows calculated this way the moduli E_1, E_2, E_6 of the belt vs. the moduli of the interlayer. Similarly, Fig. 2 presents the variability of Poisson`s ratios.

According to the above - presented procedure, one can calculate the longitudinal stiffness (Q_{11p}), transverse (Q_{22p}) and shearing stiffness (Q_{12p}) of the interlayers and of the belt $(A_{11}, A_{22}, A_{12},$ respectively). Assuming the experimental data to be the basic ones, the concept of the coefficients of variability of stiffness has been introduced. The calculated coefficient of the variability of stiffness, multiplied by 100%, shows by what percentage the stiffness has changed in relation to the stiffness of the initial material (i.e. that either of the belt or interlayers with the material constants cited in Table 1).

The specification of variability of the coefficients of stiffness of a belt vs. the value of direct modulus of elasticity has been presented in Fig. 3.

Figures 4 and 5 testify the fact how insignificant is the influence of Young`s modulus of isotropic belt lining (made either of PVC or rubber) on the strength properties of the belt.

2. CALCULATIONS OF THEORETICAL DURABILITY OF LAYER MATERIAL OF THE CONVEYOR BELT

The failure can be considered as termination of the preceeding process od straining. Then, investigation of the final strain can be used to make a rough evaluation of the moment of failure of the material, assuming an extrapolation of the obtained solution up to the failure of course, a criterion should be selected, defining the moment of failure.

As an example of the criterion, a certain boundary strain can be assumed.

With the term „constant strength" one defines the maximum value of the stress tolerated by a sample for the „infinite time period", without breaking.The time up to the failure at creeping is the time after which a sample loaded with a constant force undergoes a failure. Failure is the process proceeding in time, with the durability being an unambiguous function of the stress and temperature. Thus, the definition „constant strength" is conventional. Basing on the Maxwell`s [3] equation and the derived from it the creep equation one can give an equation defining the time up to the failure vs. the value of the constant stress. Attainment of a specified critical value ε_{max} has been assumed to be the criterion of the long term striength.

On the basis of the creep curves $\varepsilon_x = f(\lg t)$ one can easily find that the limit creep value will be $\sigma = E_\infty^* \cdot \varepsilon_{max}$

In the discussed case, the maximum strain at the static tension test has been assumed to be the maximumm strain. Entering the specified above conditions into the creep equation, the approximate expression for the durability is obtained as follows:

$$ t_{max} = \frac{\eta_0^*}{\sigma_x}\left(\varepsilon_{max} - \varepsilon_{x,0}\right)\exp\left[\frac{\left|f_x^*\right|}{m^*}\right] $$

where:

$$ f_x^* = \left(1 + \frac{E_\infty}{E}\right)\sigma_x - E_\infty \varepsilon_{max} $$

E - Young`s modulus
E_∞ - high-elasticity modulus
m - coefficient of the rate of high - elasticity strain,
σ_x - working stress
η_0^* - coefficient of viscosity.

According to the three - parameter model both creeping and stress relaxation are the processes characterized by an asymptotoc course up to the defined constant limit values. In the case of the belts investigated, this assumption can be accepted with a minor error. However, the process of unloading, i.e. that of strain relaxation would have to last up to an end, i.e. zero. Testing the belts after a certain period of operation, it has been found that this simplication leads to considerable errors.

Since, the durability calculated on the basis of the above equation is not accurate, as all the above - presented considerations do not take into account the occurrence of the final strain in the material. If the Maxwell`s model is substituted by the Burger`s one, then with application of an additional damper, this will allow to introduce to the equation an additional strain. In the case of conveyor belts it is diffucult to imagine that , after a long period of operation at a constant stress, i.e. in creep condition, and after subsequent unloading, the strain would relaxate to zero. Shown in Fig. 6 is the influence of the elasticity modulus of the interlayer of the belt under testing on the variability of Young`s modulus and high- elasticcity modulus.

Fig.7 presents the durability of the belt calculated on the basis of the above - cited fiormula vs. the modulus of elasticcity.

Fig. 8 presents, for the working stress of the belt (10% of the rated strength), the relationship between its durability and the coefficient of direct elasticity of the belt and interlayers.

Investigations of the influence of elastic properties of the lining on belt durability have revelaed no important dependance.

3. SUMMARY

- There is the possibility to design the elastic and high - elasticity properties of a multilayer conveyor belt depending on the elastic properties of its components.

- Using the Maxwell`s equation and taking also into account the final strain, it is possible to calculate the durability of of the material at the assumed criterion.

- The elasticity and high - elasticity properties of the belts have an important influence on their durability.

Detailed statements

- The most important influence of the modulus of direct elasticity of the interlayers is observed in the case of the modulus E_1 of direct elasticity of the belt. The lowest influence takes place in the case of the shearing modulus E_6 of the belt. The similar variability of the Poisson`s ratios is negligible.

- The variability of the elastic properties of the lining has no important effect on the elastic properties of the belt.

- The degree of increasing of the individual types of belt stiffness (longitudinal, transverse and shearing) vs. the modulus of direct elasticity of the interlayers is the same and should be considered as important.

- An increment of the modulus of elasticity of the interlayers should always be strongly

- balanced, not to lower too much the material elasticity (Fig. 6).

- An excessive increase of the Young`s modulus results in lowering of its durability (Fig. 7).

4. REFERENCES

[1]   Tsai S.W., Hahn H.T. - „Introduction to composite materials", Lancaster-Basel, 1990.

[2]   Goldman A.J. - „Prediction of deformation properties of polymeric and composite materials", American Chemical Society, 1994.

[3]   Czaplicka K. - „Analisis of stress relaxation processes in conveyor belts", Mechanics of Composite Materials, vol. 30, no 4, 1994.
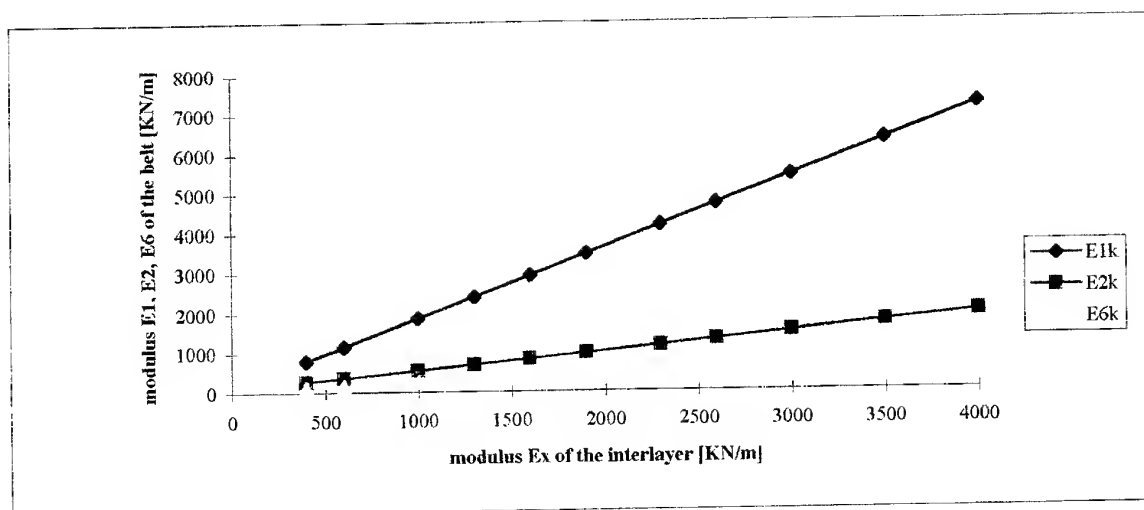
Fig.1. Modulus E_1, E_2, E_6 of the belt vs the modulus of the interlayer.
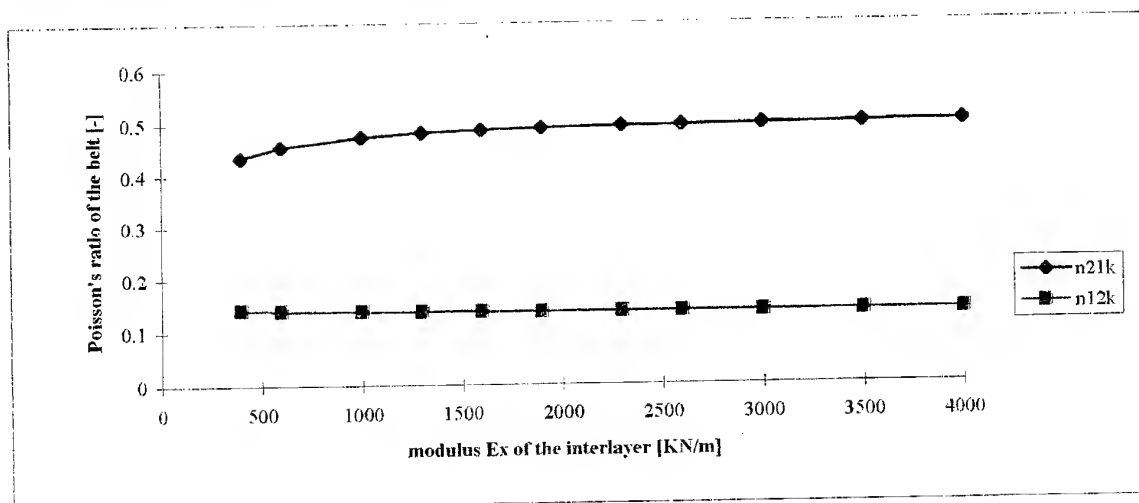
Fig.2. Poisson's ratios of the belt vs the modulus of the interlayer.
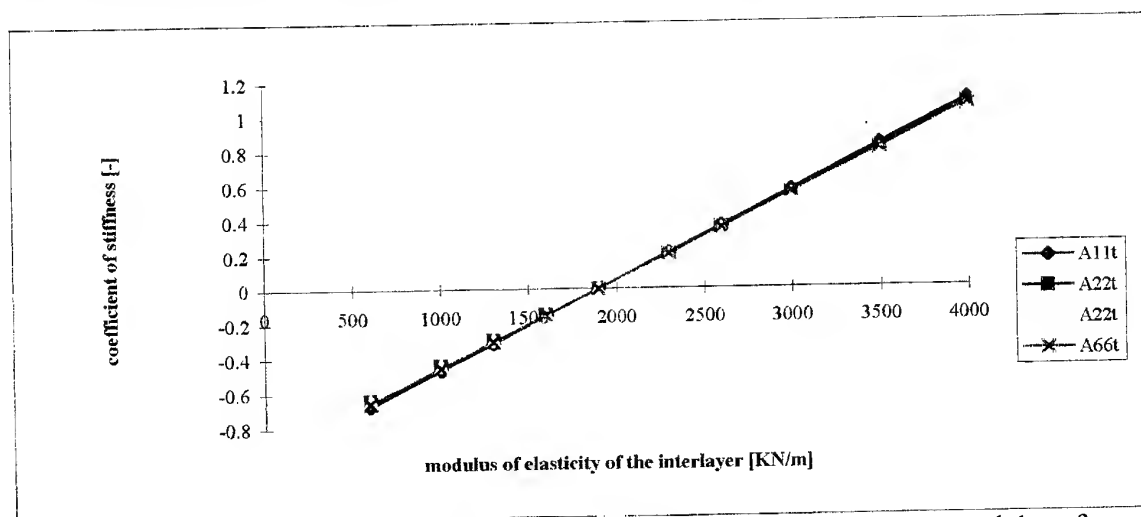
Fig.3. Variability of the coefficients of stiffness of a belt vs the value of direct modulus of elasticity of the interlayer.
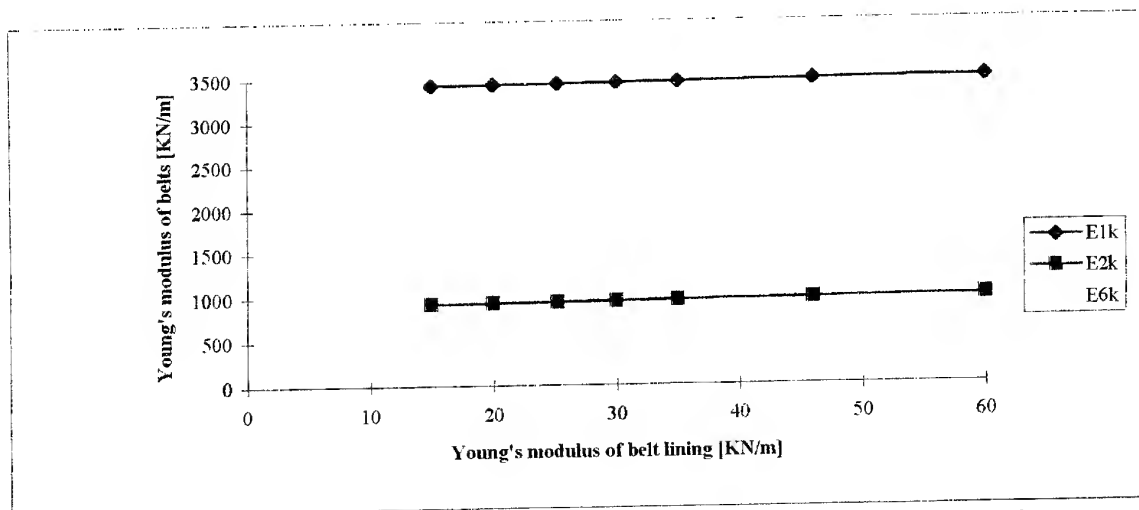
Fig.4. Variability of Young's modulus of the belt in a function of Young modulus of isotropic belt lining.
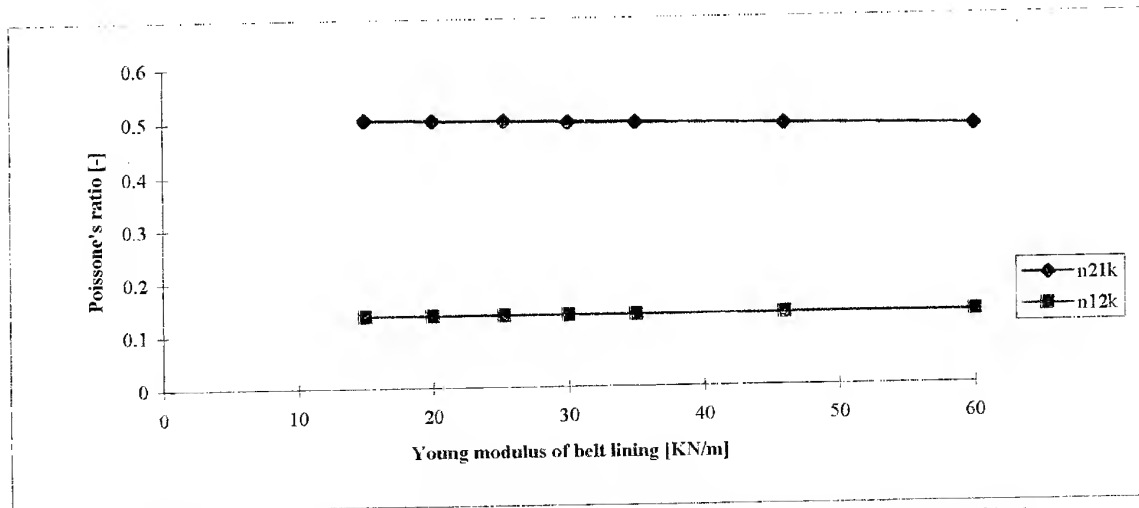
Fig.5. Variability of Poisson's ratio of the belt in a function of Young modulus of belt lining.
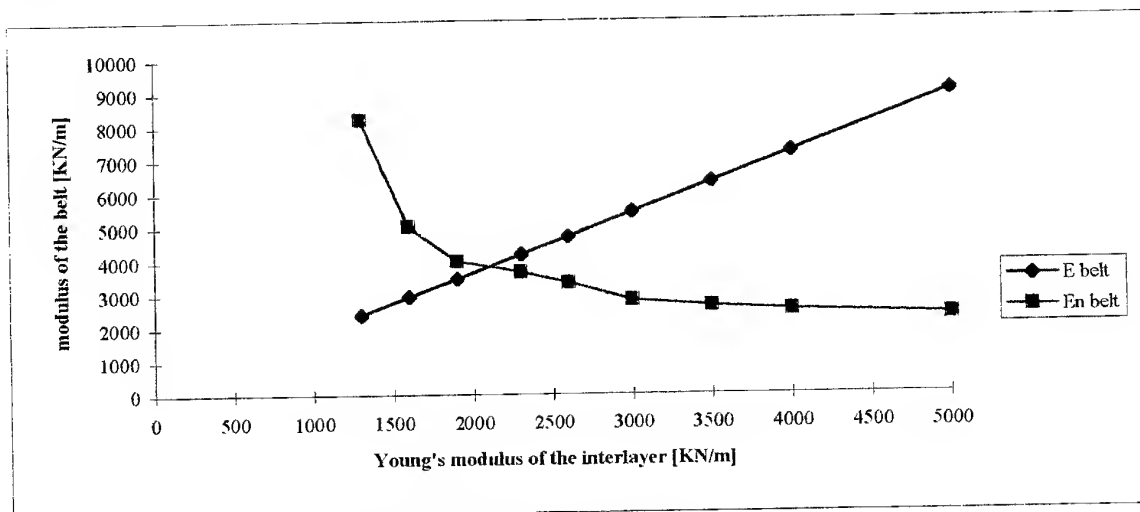
Fig.6. Influence of the elasticity modulus of the interlayer of the belt in a function of Young's modulus and high-elasticity modulus.
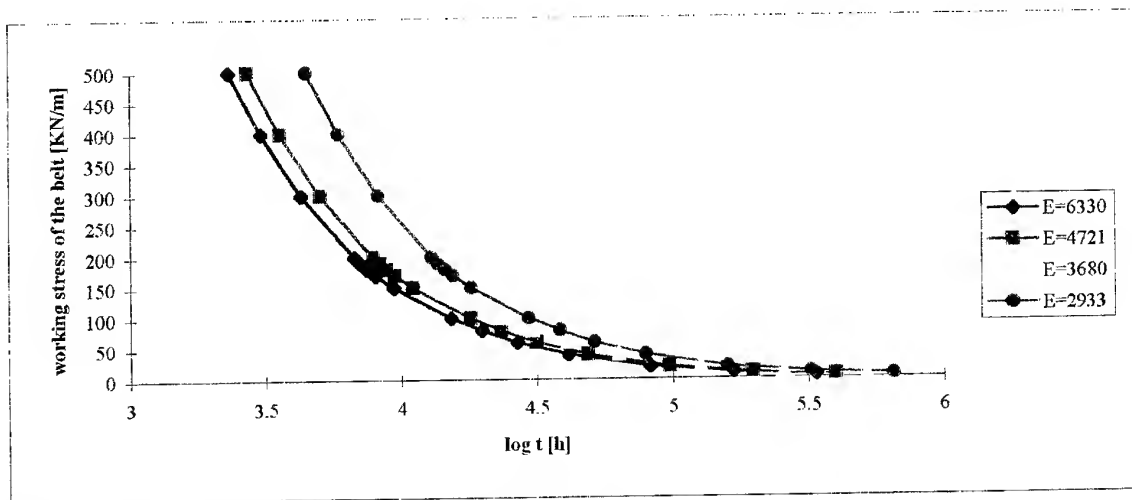
Fig.7. Durability of the belt vs. the modulus of elasticity.
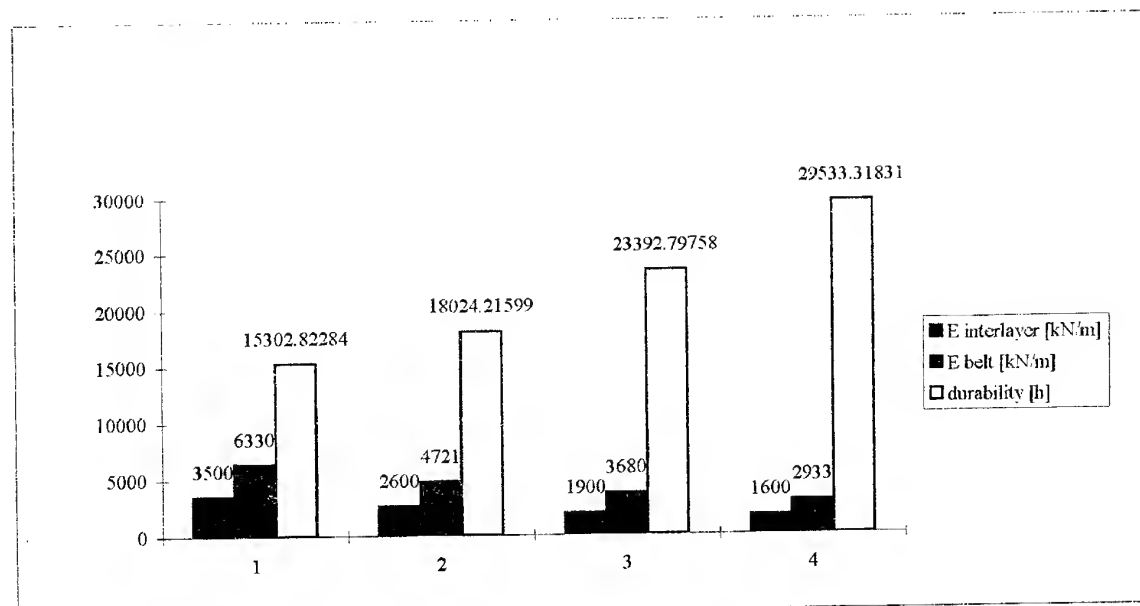
Fig.8. Durability in a function of Young's modulus of belts and interlayer.

93

NUMERICAL MODELING OF ENERGY ABSORPTION IN WOVEN COMPOSITE STRUCTURES.

* Louis DAGBA & Christian WIELGOSZ
Laboratoire de Mécanique et Matériaux
Ecole Centrale de Nantes
1 Rue de la Noë 44072 Nantes cedex 03- FRANCE

e-mail: dagba@ecn02.ec-nantes.fr

INTRODUCTION

The use of composite materials in crashworthy structures offers significant weight and cost reduction relative to metal structures.
In the last decade, several authors [7-8-12-14] have shown by crushing tests on circular tube specimens the ability of composite materials to absorb energy. In spite of the considerable work done in experimental studies, reliable numerical models are not yet available to predict the energy absorption behaviour of composite structures.
The objective of this study effort is to simulate energy absorption behaviour of composite plate by using LS-DYNA3D [10] software. Based upon experimental studies, woven composites characteristics were described completely. Chang [2-3-4] degradation rules which are based on experimentals results, were used to understand failure progression in structures. The well known knee behaviour, which is the First Ply Failure *(FPF)* in the famous paper of Reifsnider [11] was clearly identified and load carried capacity of structure is in agreement with experimental results.
At present, there are insufficient experimental data on progression of damage in such loading cases where inertial effects play an important role - then, only numerical simulations of damage progression will give correct comprehension answer of this phenomenon.

NOMENCLATURE

Q_{ij}	Reduced Stiffness Matrix
σ_{11}, σ_{22}, τ_{12}	Longitudinal, Transverse, and in-plane stresses
σ_{11}^r, ε_{11}^r	Failure stress and strain in direction 1
E_{11}, E_{22}	Lamina elastic moduli in the longitudinal and transverse directons
G_{12}	In-plane shear modulus
ν_{12}, ν_{21}	Lamina major and minor Poisson's ratios
1, 2, 3	Coordinates in lamina system
α	Nonlinear shear stress parameter
V^m	Velocity of shell midsurface
θ	Angular velocity vector
V	Velocity of any point of midsurface

(*) To whom correspondence should be sent.

I - EXPERIMENTAL PROCEDURE

I-A - MATERIAL DATA

The material used in this investigation is Glass-Polyester. A glass woven was impregned by Polyester resine. The tested structure is formed by 8 ply of twill weave: figure 1.
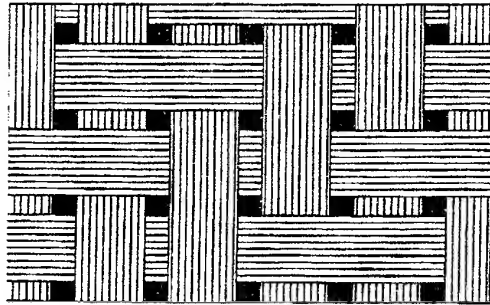
Fig.1: Twill weave.

The specimens (fig.2) were cut from twill panel and subjected to quasi-static tensile load to derive In-plane elastic charateristics : Zeitouni [16]. Table 1 sumarizes fiber volume fraction and elastic properties of studied structure.
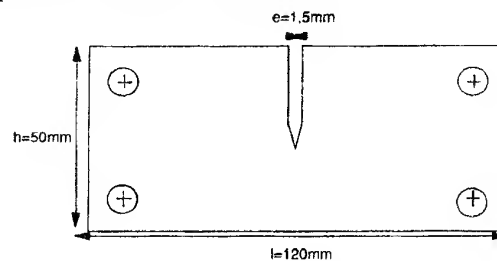
Fig. 2 : geometry of studied fabric.

E_{11}	σ_{11}^r	ε_{11}^r	ν_{12}	G_{12}
13400 MPa	156 MPa	1.16 %	0.20	2040 MPa

Table 1

I - B - DYNAMIC TENSILE TEST

The test fixture as shown schematically in figure 3 was conducted by Zeitouni [16] at Materials Laboratory of Ecole Centrale de Nantes.
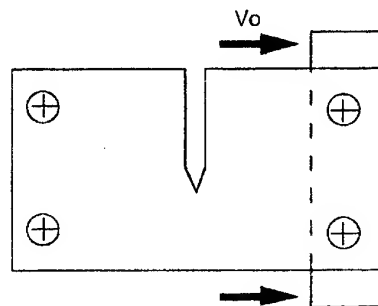
Fig.3: Schematic view of testing machine.

96

A rigid bar is subjected to axial velocity V_0 which impacts one extremity of specimen fixture. An elastic wave propagates through the specimen and causes deformation and the final rupture appears at approximatively 5.5mm. Different values of V_0 = 10.5, 15, 25 m/s were applied to a rigid bar. Here, we have only deal with the case of V_0 =10.5m/s.

I - C - EXPERIMENTAL RESULTS

Displacement is recorded at one end of specimen whereas load carried by structure is at another end.
The pattern of failed specimen and the load displacement curve are shown in figures 4a and 4b. The scheme of figure 4a shows that damage occurs only in a localised zone behind initial cutting.
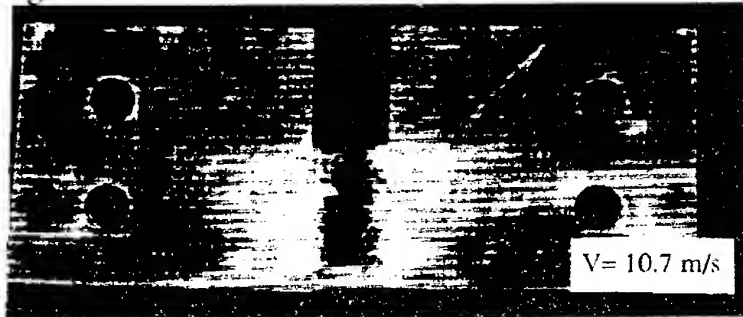
Fig. 4.a : failed specimen with localised damage zone.
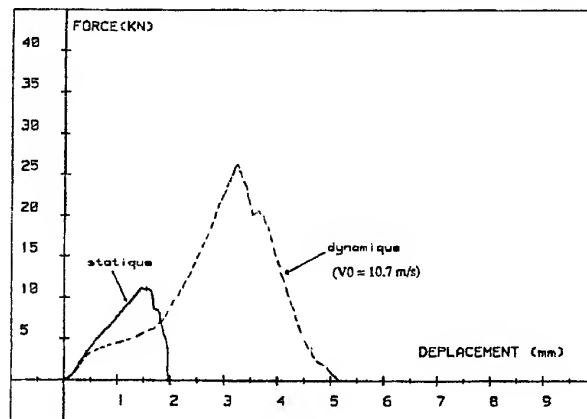
Fig.: 4.b: Load - displacement curves
for static and dynamic.

II - NUMERICAL RESULTS
    II-A   CONSTITUTIVE RELATIONS OF LAMINATES

The woven structure is considered to have an inelastic behaviour. As described by [9-13-14-15], the nonlinearities between shear stresses and shear strains are more important than nonlinearities between normal stresses and normal strains. This behaviour is taken into account by the following relation suggested by Tsai :

$$2\varepsilon_{12} = \frac{\tau_{12}}{G_{12}} + \alpha.\tau_{12}^3 \tag{1}$$

where α is material constant.
We assume plane stress state in this study and use classical laminated theory to derive constitutive equations of laminate which is given by :

97

$$\begin{Bmatrix} \varepsilon_{11} \\ \varepsilon_{22} \\ \gamma_{12} \end{Bmatrix} = \begin{bmatrix} S_{11} & S_{12} & 0 \\ S_{21} & S_{22} & 0 \\ 0 & 0 & S_{66} \end{bmatrix} \begin{Bmatrix} \sigma_{11} \\ \sigma_{22} \\ \tau_{12} \end{Bmatrix} \qquad (2)$$

or : $\quad \{\varepsilon\} = [S]\{\sigma\}, \qquad (3)$

$$\{\sigma\} = [S]^{-1}\{\varepsilon\} = [Q]\{\varepsilon\} \qquad (4)$$

with,

$$Q_{11} = \frac{E_1}{1 - \nu_{12} \cdot \nu_{21}} \qquad Q_{22} = \frac{E_2}{1 - \nu_{12} \cdot \nu_{21}}$$

$$Q_{12} = \frac{E_1 \cdot \nu_{21}}{1 - \nu_{12} \cdot \nu_{21}} = \frac{E_2 \cdot \nu_{12}}{1 - \nu_{12} \cdot \nu_{21}} = Q_{21} \qquad (5)$$

$$Q_{66} = G_6$$

thus :

$$\begin{Bmatrix} \sigma_1 \\ \sigma_2 \\ \sigma_6 \end{Bmatrix} = \begin{bmatrix} Q_{11} & Q_{12} & 0 \\ Q_{21} & Q_{22} & 0 \\ 0 & 0 & Q_{66} \end{bmatrix} \begin{Bmatrix} \varepsilon_1 \\ \varepsilon_2 \\ \varepsilon_6 \end{Bmatrix} \qquad (6)$$

Chang's degradation rules are used to model progressive failure in composites .

II-B   FINITE ELEMENT MODEL
The model uses Belytschko-Lin-Tsai [1] shell elements. These elements are based on co-rotational and velocity strain formulation. The velocity at any point of the shell is given by:

$$V = V^m - \hat{z}e_3 \times \theta \qquad (7)$$

The structure is discretised on 240 and 480 shells. The effects of meshing size are less pronounced for the large mesh.

II-C   RESULTS AND COMMENTS
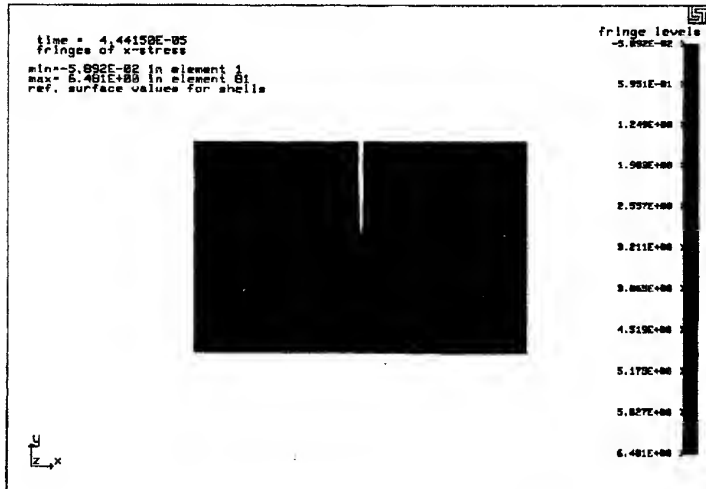
Fig. 5 : localised damage zone

98
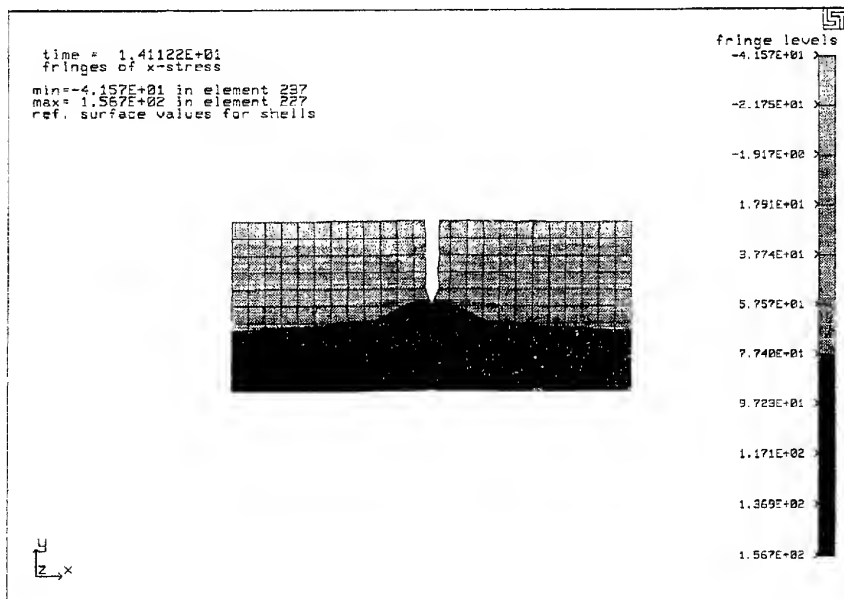
Fig.6 : Evolution of normal stresses

Favorable comparaisons are noted about extended damage zone (figures 5 and 6). The load curve versus time shows a pic value which is nearly the same of experimental results: (fig.-7). When the elastic stress limit is reached, the macroscopic properties of fabric are reduced according to degradation rules as shown in figure 7.
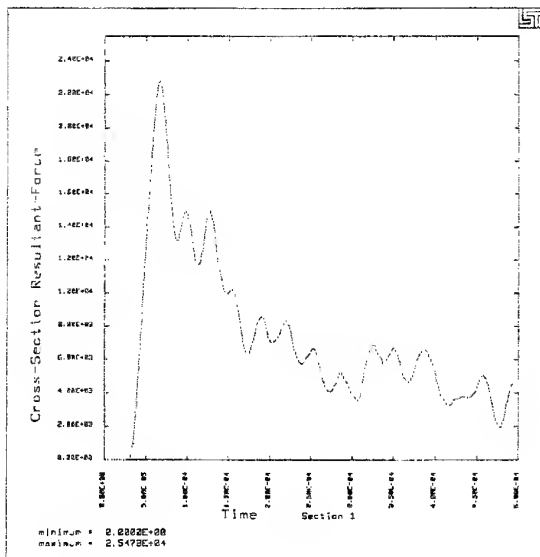
Fig.7 : Carried load versus time (N/sec)

III- CONCLUSION

Behaviour up to failure in fabric composites subjected to high dynamic tensile, can be well modeled by Chang's progressive damage theory. A modified material characteristics coupled with description of damage parameters - which are based on macroscopic damage theory - makes crash response simulation of woven structures possible.

99

We have shown in [6] that Shear stresses are also important in fabric composites. Further works concerning hybrid woven composites(Glass- Kevlar - Epoxy) where energy absorption is more pronounced, is currently studied with modified Chang degradation rules.

REFERENCES:

[1]   Belytschko, T. W., Chiang, H. Y., Improvements in Low-order Shell Elements for Explicit Transient Analysis, *Analytical and Computational Models of Shells*, A. K. Noor and Belytschko, T. W., ASME - CED, **3** , pp. 383-398 (1989).

[2]   Chang, F. K., K.Y.Chang, A Progressive Damage Model for Laminated composites Containing Stress Concentrations, *J. of Comp. Mater.*, **2 1**, (1987), pp. 834-855.

[3]   Chang, F. K., R. A. Scott, G. S. Springer, Failure Strength of Nonlinearly Elastic Composite Containing a Pin Loaded Hole, *J. of Comp. Mater.*, **1 8** , (1984), pp. 464-477.

[4]   Chang, F. K., Post-Failure Analysis of Bolted Composite Joints in Tension or Shear-out Mode Failure, *J. of Comp. Mater.*, **2 1** , (1987), pp. 809-833.

[5]   Christensen, R. M, Mechanics of Composite Materials, Lawrence National Laboratory, University of California, ed. Wiley, (1979).

[6]   Dagba, L., C. Wielgosz, Modélisation Numérique d'une plaque Composite sollicitée par Traction Dynamique, *Deuxième Colloque National en Calcul des Structures*, 1, Hermes ed. (1995), pp. 415-420.

[7]   Farley, G. L., The effects of Crushing Speed on the Energy-Absorption capability of Composite Tubes, *J. of Comp. Mater.*, **2 6** , (1992), pp. 1314-1329.

[8]   Farley, G. L., Relationship between Mehanical - Property and Energy Absorption Trends for Composite Tubes, *NASA Report* , **L- 17087**, (1992).

[9]   Hahn, H. T., Nonlinear Behavior of Laminated Composites, *J. of Comp.Mater.*, **7** , (1973), pp. 257-271.

[10] Hallquist, J. O., DYNA3D User's Manual (Non Linear Dynamic Analysis of Structures in three Dimensions), Lawrence National Laboratory, 1992.

[11] Highsmith, A. L., K. L. Reifsnider, Stiffness Reduction Mechanisms in Composite Laminates, *Damage in Composite Materials*, ASTM STP **775**, Philadelphia PA, (1982), pp.103-117.

[12] Kindervater, G. L., Composite Strength and Energy Absorption as an Aspect of Structural Crash Resistance , In *Structural Crashworthiness and Failure*, ed. N. Jones, T. Wierzbicki, Elsevier, (1993), pp. 189-235.

[13] Sims, F. D., Nonlinear Elastic Behavior of Unidirectional Composite Laminae , *J. of Comp. Mater.*, **7** , (1973), pp. 103-108.

[14] Tsai, S. W., Hahn, T. H., Nonlinear Elastic Behavior of Unidirectional Composites Laminated, *J. of Comp. Mater.*, **7** , (1973), pp. 102-118.

[15] Yamada, S. E., Analysis of Laminate Strength and its Distribution , *J. of Comp. Mater.*, **1 2** , (1978), pp. 275-284.

[16] Zeitouni, R., Contribution à l'étude de l'Absorption d'énergie par Mécanisme de Déchirure des Matériaux Composites , *Ecole Centrale de Nantes*, **Thesis**, (1992).

Commercial Implications of Using Composite Materials

A Desport, W M Banks & A S McDonald
Centre for Advanced Structural Materials, University of Strathclyde,
Glasgow, G1 1XJ, UK.

Abstract

Often commercial impracticalities, rather than technical drawbacks, are cited as a reason for avoiding the implementation of composite materials. This paper addresses these issues. Financial implications of the application of composites and the costs associated with R&D programmes are discussed. Models that offer a framework for marketing and strategic planning are presented within the context of the composites industry.

1. Introduction

The use of composites is on an exponential increase. They are being applied across a wide field of technology. Fibre-reinforced composites, play an essential role in the aerospace industry. Their properties have earned huge savings by reducing mass and providing the possibility for better aerodynamics, leading to huge fuel savings (one of the biggest costs in the industry). In the automotive industry, which is generally concerned with very cost sensitive mass production of components, the up-take of the technology has been less enthusiastic. There are new materials being developed which are reducing the costs of changing to and using composites with new production procedures making mass production more viable.

It is necessary to consider the potential benefits, potential profits, etc., which can be gained from the use of these new materials before plunging into extensive development programmes. In this context, the need for new design thinking, and new design capability cannot be stressed too highly. This applies to both the academic institutions and industrial concerns who are beginning to implement composite materials into their product range. There is a common misconception that it is possible, when developing an existing product with composite materials; to merely replace the existing material without changing the design. This leads to results that do not illustrate the underlying benefits of composites. They have to be developed as a part of the design procedure.

The designer of products using composite materials must remember that their properties are often very different from more conventional materials. Even when incorporating components in new materials into an older product, it is often necessary to go back to the drawing board and take account of these differences in behaviour. This is not always an economically attractive prospect for industry.

2. Financial Implications

From the very early days of assessing the use of a new material, it is necessary to consider the financial aspects. Such factors as reduced weight, corrosion resistance, etc., need to be considered, so that the technical benefits and drawbacks can be thoroughly evaluated. When an evaluation of the potential performance benefits has been made, it is then necessary to undertake an assessment of

the financial implications of the use of the new material. This can be achieved by constructing a list of potential income and savings benefits against potential costs.

Commonly, it is found that the initial use of the new material appears to increase the cost of production rather than decrease it. This is often due to the initial small-scale production. It is therefore necessary to do forward projections of output quantities and raw material volume needs, in order to see how the price of the incoming raw material would fall with increased production.

Potential cost benefits from the use of composite materials include:

- *Reduced cost of materials in the product:* in the implementation of a composite material, the increased structural efficiency can lead to the reduction in the amount of the material used. Thus a direct cost-of-material saving is obtained.
- *Reduced cost of manufacture:* the concept of parts consolidation on an existing product from the introduction of a new material can lead to a more effective product and a more efficient manufacturing procedure. This may have to arise from the complete redesign of a component, which can be a substantial cost.
- *Reduced tooling costs:* tooling costs are of great concern when a new process is implemented. Composites can provide a significant reduction in tooling costs, especially for lower volume production
- *Improved product performance:* the performance of a product can undoubtedly be improved by incorporating new materials. In such cases, it may be possible to charge a higher price for a premium product or alternatively, maintain the old price and increase market share.
- *Reduced warranty claims:* the good corrosion resistance, fatigue performance, etc. of composite materials means that manufactures who incorporate composites into their products will see the life span and durability of their products increase. This can result in the reduction of warranty claims for products that degrade or fail under guaranteed warranty. This will undoubtedly lead to reduced product replacement costs and redevelopment costs, with the added benefit of improving reputations for producing quality products that can lead to increased sales.

3. The Costs of Development

In the development of the use of composites there will often be an initial potential loss due to the costs of re-equipping, R&D, etc. These costs can be recognised as *immediate costs* and *recurring costs*.

In order to develop the use of new materials a significant R&D programme will often be needed. Regularly, the properties of new materials in certain applications will be unknown and new manufacturing procedures will have to be developed to produce new products. The prototyping time-scale from concept to actual product has been substantially reduced with the use of rapid prototyping and the development of finite element analysis. This has helped reduce the scale of the experimental testing that needs to be undertaken.

All the departments within a company that will be involved with the product life cycle should also be involved at the development stage. From design and manufacturing to purchasing, marketing, sales and servicing, there will have to be interdepartmental collaboration in order to iron out any problems that may not be foreseen by an individual department. The costs of recruiting and training in the new skills needed to carry through the R&D exercise and later in the manufacturing process need to be taken into account at an early stage.

The initial stages in the product evaluation will incorporate a market research assessment, to determine potential sales for the product. For a new concept, as is often the case for composites, the marketing department will need to assess the customers' understanding of the new product. The customer may have had little experience with composite components and may not have confidence in them. Hence, the customer may have to be educated in the benefits that composites can have for them or their company. The market research would be designed to assess the impact of the improved or new product in the matter of selling price acceptability, volume-sales potential, etc. Obviously, the impact of the margin between the selling price and ex-factory costs on the one hand, and potential volume on the other hand, will be two major factors in the business plan.

The manufacturing costs need to be considered as early as possible in the project. It may be cost effective to out-source the prototyping to companies who are specialists in the manufacture of composite components. This would enable rapid prototyping and early identification of problems. Once a final prototype has been developed, the possibility of manufacturing in-house can be assessed.

A cost benefit analysis can be used to evaluate new plant requirements; including such aspects as installation and maintenance. This can also be used to assess if new plant would be more profitable than the old plant (not strictly applicable if the new plant is for a new product).

The material costs are probably one of the initial hurdles to overcome as composites are generally more expensive than the traditional materials but as production volumes increase this will decrease. Discussions can be held with the material suppliers at the initial stages of the project to ascertain the discounts available on larger volume production (as these can be substantial).

The cost of potential new test procedures and test facilities should also be taken into account. Often there is a higher cost initially with new materials than with the older materials as frequency of testing is usually higher, especially in the early years.

From the above considerations the immediate and recurring costs can be estimated and combined to give an overall estimate of the costs.

4. Overall Financial Appraisal

Once the final prototype has been developed and is ready for manufacture, an accurate financial picture of the process involved can be developed. The completion of the product design will allow a fully defined list of materials to be drawn up along with the determination of the precise manufacturing process. Investment in plant and equipment can then be determined.

The financial appraisal should provide accurate values for the following:
- material costs,
- labour costs,
- overheads.

Following this a value for the cost per unit as a function of the output volume can be determined.

5. Marketing & Strategic Planing

A material change in a product may not necessarily alter the product but in the case of replacement of metals with composite materials will undoubtedly change the design in one aspect or another. Therefore a new product is formed even though it may merely replace an existing component and will need market research to determine the potential for sales of the new product.

It would be beneficial to carry out market research on the following topics:
- current usage of composites in the specific industry,
- the opinion of the industry regarding the use of composites; to assess the level of understanding there is of composite materials,
- what would the market like to see being developed?

In the case of a major re-design of the product, there could be relatively long development times. However, with the use of rapid prototyping techniques and perhaps supply-chain co-operation projects this time should be greatly reduced. This can help minimise development costs and enable the company to more accurately control and predict the release of the product on to the market. Figure 1 illustrates a strategic model for industrial technological innovation that incorporates the concepts of co-operation and communication between producers, suppliers and even competitors[1].
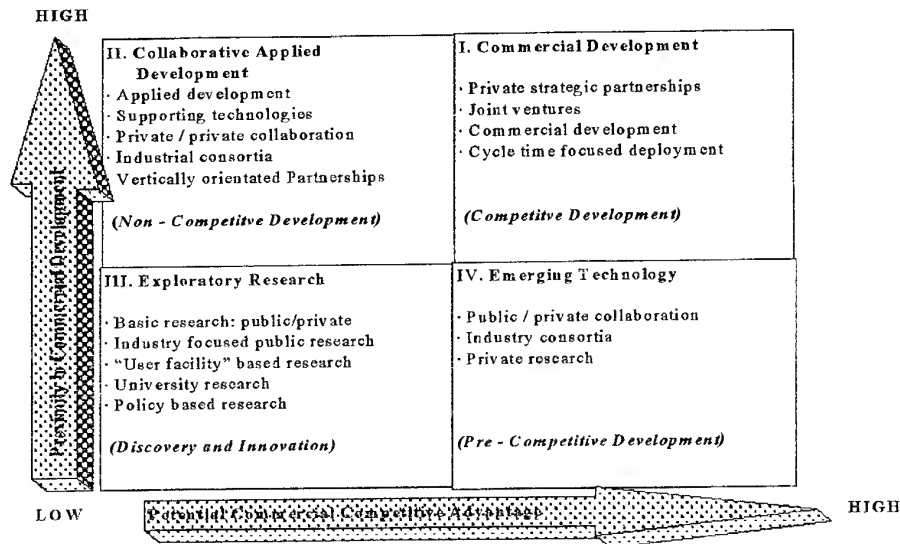
Figure 1: *A Strategic Model for Industrial Technological innovation*

From the market research and other considerations a business plan can be drawn up, determining the basis upon which the project would get the go-ahead or not. A project plan can then be drawn up from the business plan which could clarify and diagramatically demonstrate the project time-table.

The significance of new versus existing products, and new versus existing markets is the way to initialise the formation of a strategy. This categorising gives rise to four types of strategy illustrated by Figure 2.

PRODUCTS

MARKETS		Existing	New
	Existing	Market Penetration	Product Development
	New	Market Development	Diversification

Figure 2: *A categorisation of marketing Strategy*

Market penetration is when a firm attacks existing or current markets with existing products and is not generally an area for improvements in marketing or manufacturing techniques. Taking a current product into a new market for that product is known as *market development* a strategy that centres on market selection and targeting. *Product development* is when a firm launches a new product into an existing market (often this would be a composite replacement of a metallic component). Launching new products into new markets is termed *diversification*. Generally this is the most attractive area for composite materials as there is unlikely to be the design restrictions (often imposed for traditional materials) which can be encountered during product development.

Another approach to determining a marketing strategy is based upon the work done by Morris[2]. His view is that all strategies fall within one of three generic categories: overall cost leadership; differentiation and focus. This is illustrated by Figure 3 below:

STRATEGIC ADVANTAGE

	Uniqueness	Low Cost Position
Industry wide	**Differentiation**	**Overall Cost Leadership**
Particular Segment Only	**Focus/Niche Marketing**	

(with "STRATEGIC TARGET" labelling the left-side rows)
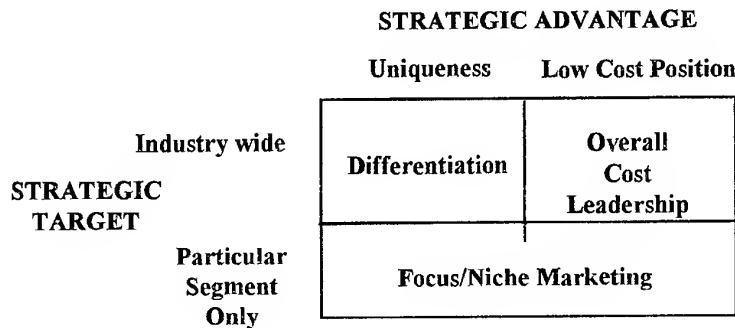
Figure 3: *Generic Cost Strategies*

Overall cost leadership is an attempt by the company to have the lowest cost position in the industry, with the aim of being a price leader in the market. This strategy is often concerned with economies of scale with the firm trying to maximise market share and size with high volume production. This is not often a strategy implemented by companies involved in composite manufacturing due to the generally high unit costs involved compared with metallic components and lower production rates.

Differentiation relies on the company's distinguishing features of its products such as quality, warranties, service and distribution. With these features the company aims to attack the whole market place. This strategy often depends upon how its customers perceive the image of the company compared with the image of the competitors. This approach is often used by companies in the composites field as they stress performance benefits and the high-tech image of composite materials. Such a strategy tends to have a direct effect on a company's cost position.

Focus (or niche marketing) directs a company's efforts toward a specific area of the market place, offering specialised products. Such is the position of many of the smaller companies involved in composites manufacture. Due to economic low volume production possibilities they can often offer products in a range that can be tailor made to suit their customer's requirements.

The strategies described are not independent of each other. Indeed a company can pursue market penetration, focus and market development at the same time.

Day[3] provides six criteria to identify flaws or areas for improvement in marketing strategy.
- *Suitability:* Which is the proposed strategy consistent with the foreseeable environmental threats and opportunities? Does the strategy exploit or enhance a current competitive advantage, or create a new source of advantage?
- *Validity:* Are the key assumptions about the environmental trends and the outcomes of the strategy realistic? Are the assumptions based on reliable and valid information?

- *Consistency:* Are the basic elements of the strategy consistent with each other and with the objectives being pursued?
- *Feasibility:* Is the strategy appropriate to the available resources? Are the basic elements and premises of the strategy understandable and acceptable to the operating managers who will have the responsibility of implementation?
- *Vulnerability:* To what extent are the projected outcomes dependent on data or assumptions of dubious quality and origin? Are the risks of failure acceptable? Are there adequate contingency plans for coping with these risks? Can the decision be reversed in the future? How long will it take? What are the consequences?
- *Potential rewards:* Are the projected outcomes satisfactory in light of the objectives for the business? Are the adjustments to the objectives acceptable to the stake holders?

Taking the above questions into consideration, the implications of developing composite components in a difficult market place where change and innovation are scarce such as in today's global economic climate.

6. Conclusions

Often in technology led companies, such as may of those in the composites industry, it can be easy to place too much emphasis on technical perfection to the detriment of other commercial considerations. Full and accurate assessments of production and development costs are essential for both the general financial planning within a company and the evaluation of particular products. Similarly without thorough market interrogation it is extremely difficult to produce sellable products or a sustainable long-term position within the market. It is essential that companies involved in the manufacture of products in composite materials be aware of these considerations. Indeed, it would be very useful for them to establish their own frameworks within which to assess these considerations.

References

[1] McConnell, D.P., 'Managing R&D in Competitve times -Helping R&D Managers and Providers Develop a Strategy for Success', Materials Technology, Volume 10, No.s 1/2, January/February 1995.

[2] Morris, M. H., 'Industrial & Organisational Marketing', 1992.

[3] Day, G.S., 'Strategic Market Planning: The Pursuit of Competitive Advantage', St Paul, MN: West Publishing Co., pp 152, 1984.

Solution Using the Higher-Order Shear Deformation Theory for Laminated Composite Surface Structures

Shenglin Di   and   Heinrich Rothert
Institute for Structural Analysis, University Hannover, Germany

- Introduction

- Fundamental field variables

- Governing equations

- Continuity of the transverse shear stresses and strains

- Solution of a cylindrical shell under inner pressure

- Numerical examples

- Summary and conclusions

• Introduction

- Single layer theories
  - **adequate** — for the estimation of global characteristics (deflections, fundamental frequencies, buckling load, etc.)
  - **inadequate** — for the estimation of higher-order frequencies, mode-shapes and distribution of stresses, etc.

- Layer-wised theories
  - complicated in formulation and difficult in finding the solution
  - If using zero shear condition to reduce the number of unknowns, a C^1 continuity for displacement field is required

- Three dimensional theories — high accuracy but most difficult

- Single layer theories with warping function — overcome the disadvantages of single layer theories but the formulation remains to be simple and easier to implement

• Fundamental field variables
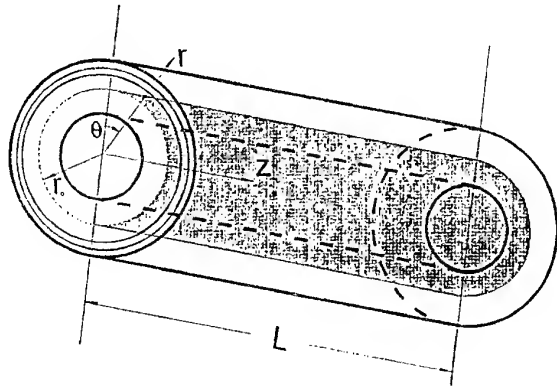
Coordinate system of cylindrical shell
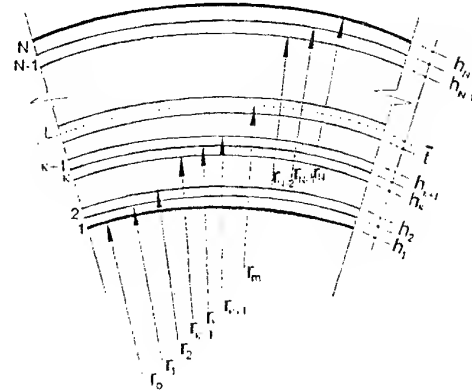
Nomenclature for the stacking sequence

Displacement field

$$
\left.\begin{aligned}
u^{\kappa} &= u_0 + t\vartheta_1 + t^2\psi_1 + t^3\phi_1 + \hat{t}\varphi_1, \\
v^{\kappa} &= v_0 + t\vartheta_2 + t^2\psi_2 + t^3\phi_2 + \hat{t}\varphi_2, \\
w^{\kappa} &= w_0,
\end{aligned}\right\} \qquad t = r - r_m \in \left[-\frac{h}{2}, \frac{h}{2}\right]
$$

piecewise linear term(zigzag function):

$$
\hat{t} = t_c^{\kappa} + \delta^{\kappa} t,
$$

$$
t_c^{\kappa} = \sum_{i=1}^{\kappa-1} \delta^i h_i - \left(\sum_{i=1}^{L-1} \delta^i h_i + \delta^L \bar{t}\right) - \delta^{\kappa} t_{\kappa-1}, \qquad \delta^i = (-1)^i
$$

108

Kinematics relations

$$\varepsilon_z^\kappa = \frac{\partial u^\kappa}{\partial z} = u_{0,z} + t\,\vartheta_{1,z} + t^2\psi_{1,z} + t^3\phi_{1,z} + \hat{t}\,\varphi_{1,z},$$

$$\varepsilon_\theta^\kappa = \frac{\partial v^\kappa}{r\partial\theta} + \frac{1}{r}w^\kappa = \frac{1}{r}(v_{0,0} + t\,\vartheta_{2,0} + t^2\psi_{2,0} + t^3\phi_{2,0} + \hat{t}\,\varphi_{2,0} + w_0),$$

$$\varepsilon_r^\kappa = \frac{\partial w^\kappa}{\partial r} = 0,$$

$$\gamma_{\theta r}^\kappa = \frac{1}{r}\frac{\partial w^\kappa}{\partial\theta} + \frac{\partial v^\kappa}{\partial r} - \frac{v}{r}$$

$$= \frac{1}{r}w_{0,0} + \vartheta_2 + 2t\psi_2 + 3t^2\phi_2 + \delta^\kappa\varphi_2 - \frac{1}{r}\left(v_0 + t\,\vartheta_2 + t^2\psi_2 + t^3\phi_2 + \hat{t}\,\varphi_2\right)$$

$$= \left[r_m\vartheta_2 + \left(r\delta^\kappa - \hat{t}\right)\varphi_2 + \left(2rt - t^2\right)\psi_2 + \left(3rt^2 - t^3\right)\phi_2 + w_{0,0} - v_0\right]\frac{1}{r},$$

$$\gamma_{rz}^\kappa = \frac{\partial u^\kappa}{\partial r} + \frac{\partial w^\kappa}{\partial z} = \vartheta_1 + 2t\psi_1 + 3t^2\phi_1 + \delta^\kappa\varphi_1 + w_{0,z},$$

$$\gamma_{z\theta}^\kappa = \frac{\partial v^\kappa}{\partial z} + \frac{1}{r}\frac{\partial u^\kappa}{\partial\theta}$$

$$= v_{0,z} + t\,\vartheta_{2,z} + t^2\psi_{2,z} + t^3\phi_{2,z} + \hat{t}\,\varphi_{2,z} + \frac{1}{r}\left(u_{0,0} + t\,\vartheta_{1,0} + t^2\psi_{1,0} + t^3\phi_{1,0} + \hat{t}\,\varphi_{1,0}\right).$$

Stresses and strains relations

$$\begin{Bmatrix}\sigma_z\\\sigma_\theta\\\tau_\theta\\\tau_{rz}\\\tau_{z\theta}\end{Bmatrix}^\kappa = \begin{bmatrix}Q_{11}&Q_{12}&0&0&Q_{16}\\Q_{21}&Q_{22}&0&0&Q_{26}\\0&0&Q_{44}&Q_{45}&0\\0&0&Q_{54}&Q_{55}&0\\Q_{61}&Q_{62}&0&0&Q_{66}\end{bmatrix}^\kappa \begin{Bmatrix}\varepsilon_z\\\varepsilon_\theta\\\gamma_\theta\\\gamma_{rz}\\\gamma_{z\theta}\end{Bmatrix}^\kappa,$$

- ## Continuity of the transverse shear stresses and strains (in Cardician system)

	Inter-element Surface	Inter-layer Surface
Displacements u_i	Continuous	Continuous
Strains ε_{xx}, ε_{yy}, ε_{xy}, ε_{zz}	Continuous	Continuous
Strains ε_{xz}, ε_{yz}	Continuous	Discontinuous

Layer $\kappa+1$

Layer κ

$$\varepsilon_{xz} = \theta_x + 3z^2\phi_x + (-1)^\kappa\psi_x + \frac{\partial w}{\partial x}$$

$$\varepsilon_{xz}^+ = \cdots\cdots + \psi_x + \cdots$$

$$\varepsilon_{xz}^- = \cdots\cdots - \psi_x + \cdots$$

• Governing equations

the theorem of minimum potential energy

$$\int \left(\sigma_z \delta\varepsilon_z + \sigma_\theta \delta\varepsilon_\theta + \tau_{z\theta}\delta\gamma_{z\theta} + \tau_{zr}\delta\gamma_{zr} + \tau_{\theta r}\delta\gamma_{\theta r} \right)\left(1 + \frac{t}{r_m} \right) dt dA - \int q \delta w dA = 0.$$

variation equations

$$\delta u_o = 0, \quad N_{z,z} + N_{\alpha,\theta}/r_m = 0,$$

$$\delta v_o = 0, \quad N_{z\theta,z} + (N_{\theta,\theta} + N'_{\alpha})/r_m = 0,$$

$$\cdots \quad \cdots \quad \cdots \quad \cdots \quad \cdots \quad \cdots \quad \cdots$$

$$\delta\varphi_1 = 0, \quad S_{z,z} + S_{\alpha,\theta}/r_m - S_{zr} = 0,$$

$$\delta\varphi_2 = 0, \quad S_{z\theta,z} + (S_{\theta,\theta} - S_\alpha)/r_m = 0.$$

final governing equation

$$Ku = q$$

$$q = \begin{bmatrix} 0 & 0 & -q & 0 & 0 & 0 & 0 & 0 & 0 & 0 & 0 \end{bmatrix}^T.$$

$$u = \begin{bmatrix} u_o & v_o & w_o & \vartheta_1 & \vartheta_2 & \psi & \psi_2 & \phi_1 & \phi_2 & \varphi_1 & \varphi_2 \end{bmatrix}^T.$$

Solution Procedure:

i) chose the solution for the generalised variables **u**, with it the whole displacements should satisfy the boundary condition;

ii) calculate the strains using geometrical equations and then the stresses using Hook's low;

iii) obtain the stress resultants by straightforward integration of stresses through the thickness;

iv) solve the equilibrium equation to obtain the generalised variable vector **u**;

v) calculate all the physical quantities, i.e. the displacements, the strains and the stresses, etc.

- Solution of a cylindrical shell under inner pressure both ends simply supported by shear diaphragms

material constants

$$Q_{16} = Q_{26} = Q_{45} = 0,$$

boundary conditions

$$z = 0, l: \quad N_z = M_z = P_z = F_z = S_z = \vartheta_2 = \psi_2 = \phi_2 = \varphi_2 = w_o = 0.$$

assume the transverse surface load

$$q_{inner} = q_o \sin \frac{m\pi z}{l} \cos n\theta \quad \text{and} \quad q_{outer} = 0,$$

the Navier type solution can be introduced as

$$
\begin{aligned}
(u_o, \vartheta_1, \psi_1, \phi_1, \varphi_1) &= (C_{uo}, C_{\vartheta 1}, C_{\psi 1}, C_{\phi 1}, C_{\varphi 1}) \cos \frac{m\pi z}{l} \cos n\theta, \\
(v_o, \vartheta_2, \psi_2, \phi_2, \varphi_2) &= (C_{vo}, C_{\vartheta 2}, C_{\psi 2}, C_{\phi 2}, C_{\varphi 2}) \sin \frac{m\pi z}{l} \sin n\theta, \\
w_o &= C_{wo} \sin \frac{m\pi z}{l} \cos n\theta.
\end{aligned}
$$

Natural boundary conditions

- for the innermost layer (the 1st layer)

    using the zero shear condition at the inner surface of the laminated shell:

    $$\tau_{zr}^1 = \frac{1}{r}\left[C_1^1(r) - C_1^1(r_m) \right],$$

    $$\tau_{\theta r}^1 = \frac{1}{r^2}\left[C_2^1(r) - C_2^1(r_m) \right];$$

- for the kth layer

    using the continuous condition at the interface between the $(k-1)$th and the kth layers:

    $$\tau_{zr}^\kappa = \frac{1}{r}\left[C_1^\kappa(r) + r_{\kappa-1}\tau_{zr}^{\kappa-1}(r_{\kappa-1}) - C_1^\kappa(r_{\kappa-1}) \right],$$

    $$\tau_{\theta r}^\kappa = \frac{1}{r^2}\left[C_2^\kappa(r) + r_{\kappa-1}^2 \tau_{\theta r}^{\kappa-1}(r_{\kappa-1}) - C_2^\kappa(r_{\kappa-1}) \right]$$

• Numerical examples

i) Comparison for a 3 layers shell (*90°/0°/90°, S=2,4,10,50,100,500*);

ii) The through thickness distribution of stresses and displacements for the three layers shell (*90°/0°/90°, S=4,10,100*);

iii) Comparison of the influence of different terms in the displacement field for three layers symmetric ply-up and four layers unsymmetric ply-up shells (*90°/0°/90°, 0°/90°/0°/90°* and *90°/0°/90°/0°, S=10*);

iv) Distribution of the in-plane displacement *v* for a ten layers shell (*90°/0° /90°/0°/90°*)symm. in case of *S=4*;

v) Discussion on the influence caused from the different layer thicknesses for a five layers shell (*90°/0°/90°/0°/90°, S=4*);

vi) Analysis of a sandwich cylindrical shell with soft kernel.

Through thickness distribution of transverse shear stress $\overline{\tau}_{rz}$
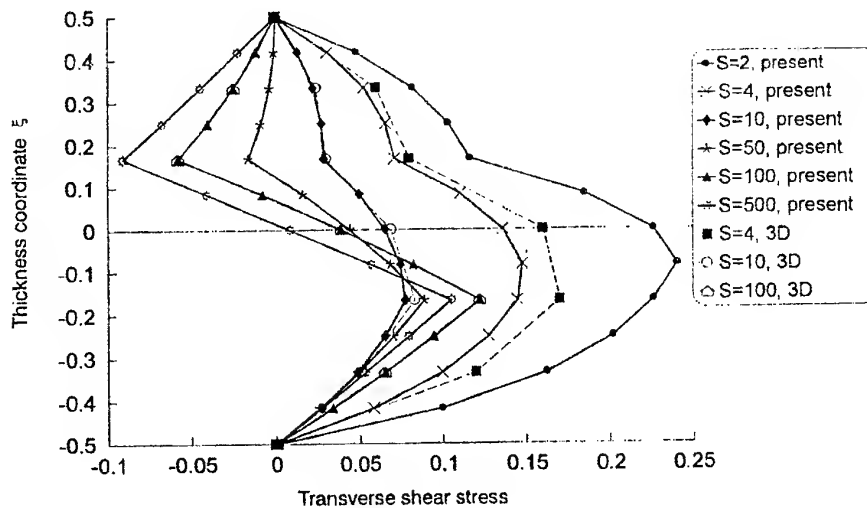
Example 1: Comparison for a 3 layers shell (*90°/0°/90°, S=2, 4, 10, 50, 100, 500*);

112

Distribution of inplane displacement v for ten layers cylindrical shell
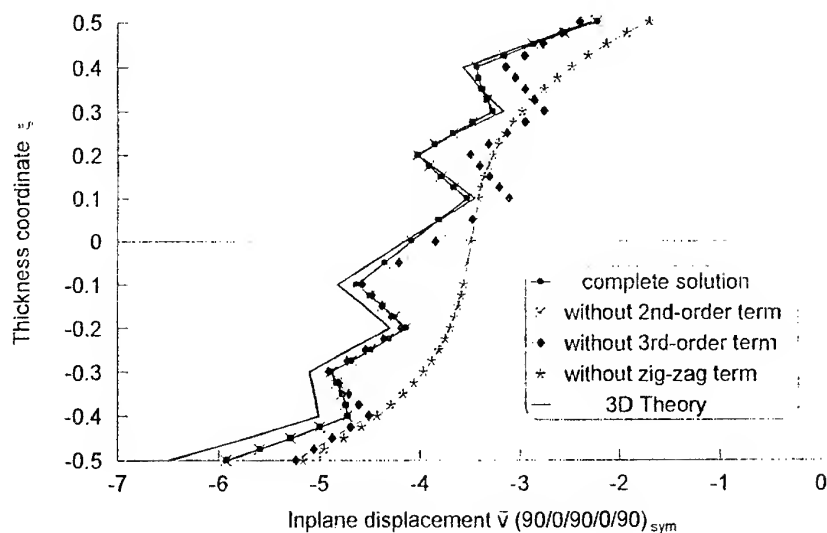
Example 4: Distribution of the in-plane displacement v for a ten layers shell $(90°/0°/90°/0°/90°)$symm. in case of $S=4$;

Influence of thickness ratio on the displacement distribution
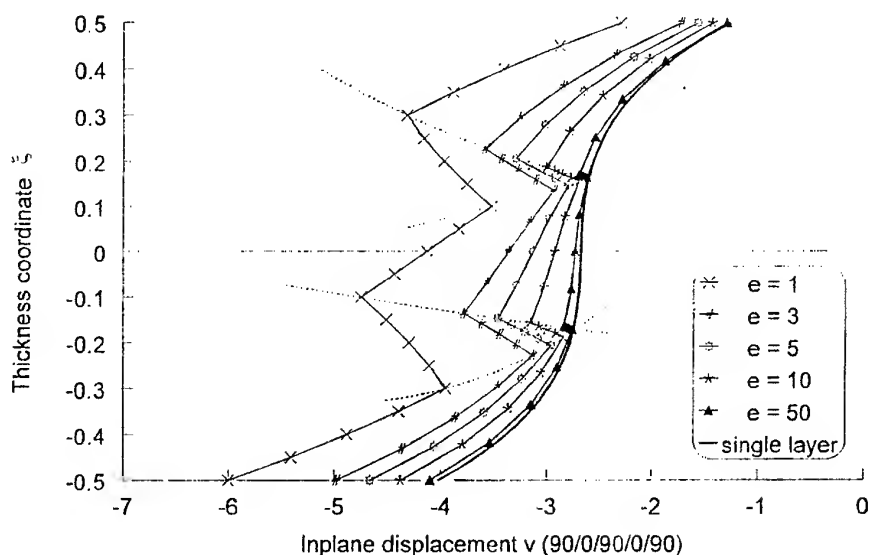
Example 5: Five layers shell $(90°/0°/90°/0°/90°, S=4)$;

Distribution of inplane displacement v for a sandwich cylindrical shell
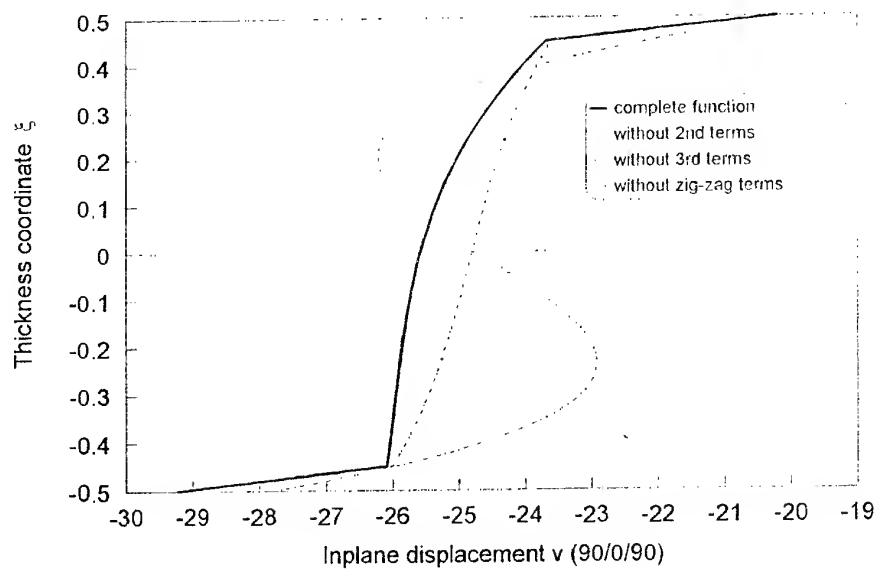
Example 6: Sandwich cylindrical shell with soft kernel.

Influence of Young's moduli on the normalised displacement distribution for a sandwich cylinder
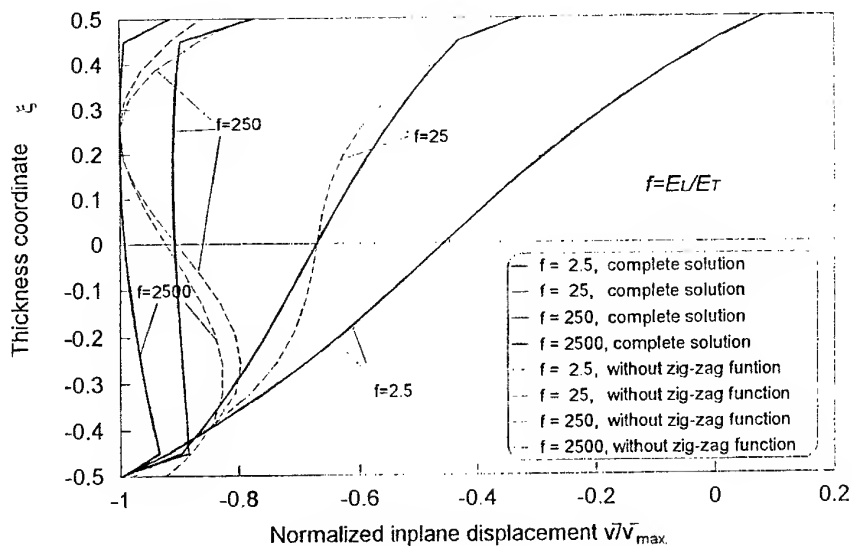
Example 6: Sandwich cylindrical shell with soft kernel.

Distribution of inplane displacement v for a sandwich cylindrical shell
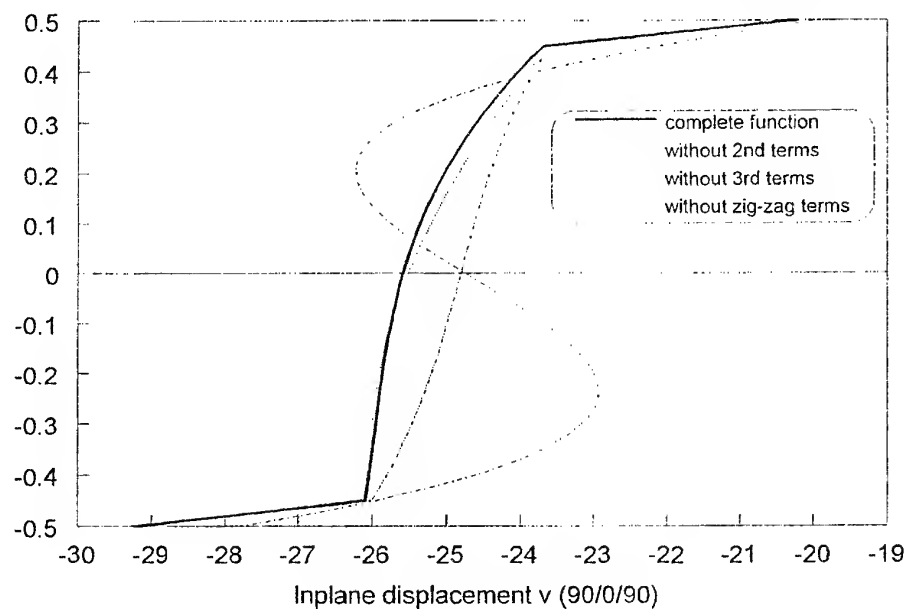
Example 6: Sandwich cylindrical shell with soft kernel.

Influence of Young's moduli on the normalised displacement distribution for a sandwich cylinder
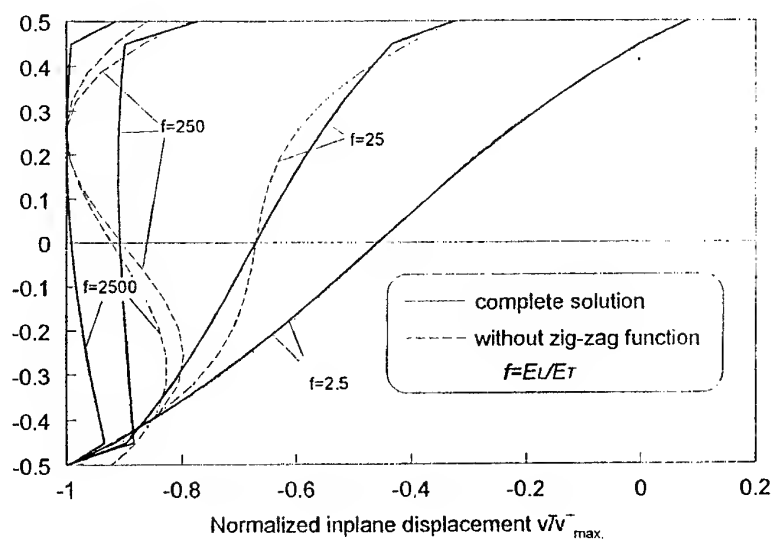
Example 6: Sandwich cylindrical shell with soft kernel.

Summary and conclusions

- Analytical formulations for the orthotropic and anisotropic cylindrical shells have been proposed using a higher-order shear deformation theory.

- By supplementing this with a very effective piece-wise linear function, the whole profiles of the displacements are very close to the results of a three-dimensional elasticity theory.

- This theory demands only a C^0 continuity for the assumed displacements, therefore is very suitable for the implement of the finite element formulation.

- The solutions presented here for the bending of both ends simply supported, cross-ply cylindrical shells give very accurate results for both the displacements and the transverse shear stresses.

- The piece-wise linear function plays a very important role in most cases. its effects are usually more obvious than the 2nd and 3rd terms.

- For unsymmetric ply-up laminates, errors caused from dropping the second-order terms and the third-order terms are of the same quantitative level.

THE USE OF COMPOSITES FOR RAILWAY ELECTRIFICATION STRUCTURES

S.D.W DU PLESSIS

IRENCO (PTY) LTD, PO BOX 520, IRENE, 1675, SOUTH AFRICA

INTRODUCTION

The severity of the corrosion experienced on steel structures around the Southern African coastline and the cost of preventative maintenance on these structures has prompted Irenco to develop alternative structures. The excellent corrosion and strength properties of composite materials were used to develop a system of overhead electrification structures.

STRUCTURAL REQUIREMENTS

The composite structure has to support a set of overhead conductors subject to operational and environmental loads such as wind within a prescribed position relative to the rail. To achieve this objective the structures need to have similar load bearing and deflection characteristics as the steel structures traditionally used.

The following table gives an indication of the load requirements for these structures.

MAXIMUM ALLOWABLE
WIDTH OF MAST = 560mm
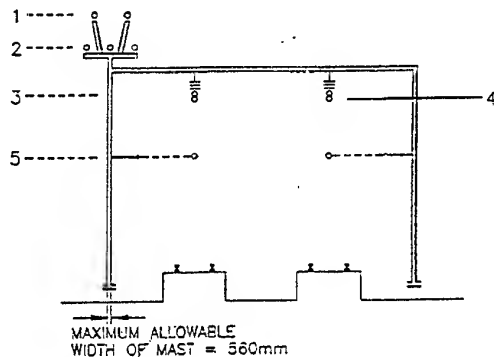
WIRE PARAMETERS	SIZE mm^2	DIAMETER STRAND/mm	MASS kg/km	MAX TENSION N @-5°C	MAX HEIGHT m
5) CONTACT WIRE Cu	161	15	1429	22000	6.000
4) CATENARY WIRE Cu	100	19/2.65	943	7500	8.000
3) FEEDER WIRE Al	800	61/4.25	2402	11300	8.125
2) PHASE WIRES ACSR	50	6/1/3.35	214	3400	9.000
1) EARTH WIRE ACSR	50	6/1/3.35	214	3400	9.800

STRUCTURAL DESIGN

It was decided to use glass reinforced polyester because of its excellent insulating properties and the good strength to cost ratio. The stiffness of GRP is much lower than that of steel and therefore the cross section of the composite mast had to increase to allow a higher moment of inertia.

A lattice type structure was used as it gave the maximum stiffness for the amount of material used. Material properties had to be determined for design purposes and especially the buckling behaviour as two of the longitudinals of a square lattice mast will always be in compression. The material testing will be discussed in more detail in the following section covering testing.

A finite element model was developed to predict the stresses and deflections in the structure. It was found that the FEM models predicted much lower deflections than that measured in practice. This variation between FEM models and the experimental lattice model was also recorded by Hollaway and Ishakian [1]. A possible explanation for this is the fact that the intersection between the diagonals and the longitudinal is modelled as a single point while this is not true in practice.

TESTING

A whole range of tests have been done including material tests, environmental tests, conductivity tests and strength and deflection tests on completed structures.

MATERIAL TESTS

The composite matrix was tested to determine the material characteristics such as flexural stiffness, compressive strength, glass to resin ratio etc. These values were used for the initial design model and typical results of buckling tests are shown in figure 1.
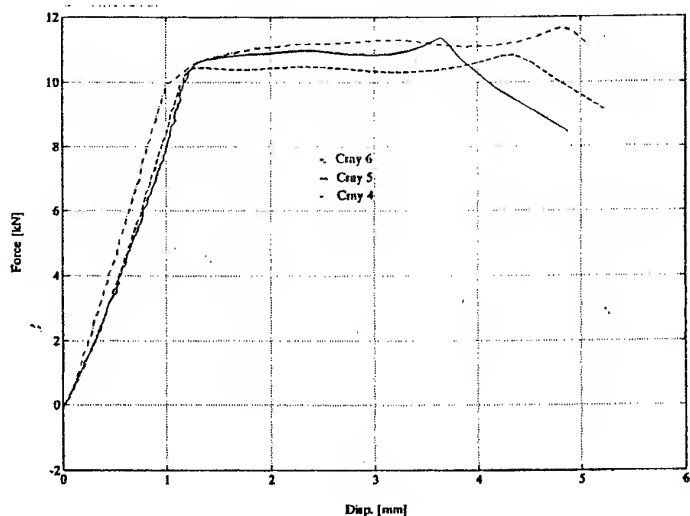
FIGURE 1:   Typical buckling test results

PRODUCT TESTS

A 10m long test bed was built for testing a complete mast section in bending to determine the deflection, creep and ultimate breaking strengths. The deflection is measured by means of a laser designator bolted to the base of the mast to eliminate errors due to the deflection of the test bed under load. A typical acceptance test consists of the following:

LOAD	MEASUREMENT
66% of operational load	Measure deflection and creep after 24 hours
100% of operational load	Measure deflection
Ultimate design load	Verify design strength
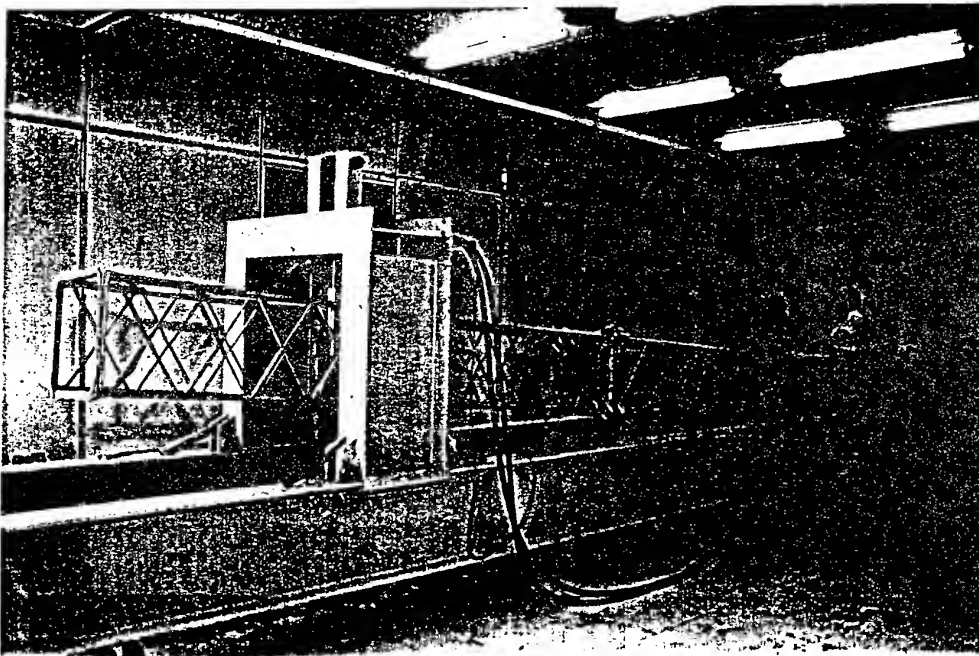
ENVIRONMENTAL TESTS

A beam section of a mast was tested in an accelerated environmental test chamber to determine the extend of infra red radiation, ultra violet radiation, salt water and temperature on the load bearing capability of the structures. The beams were rotated by 90 degrees every six hours. After spending six hours at each station the beams were considered to have undergone an effective six hours of accelerated environmental testing.
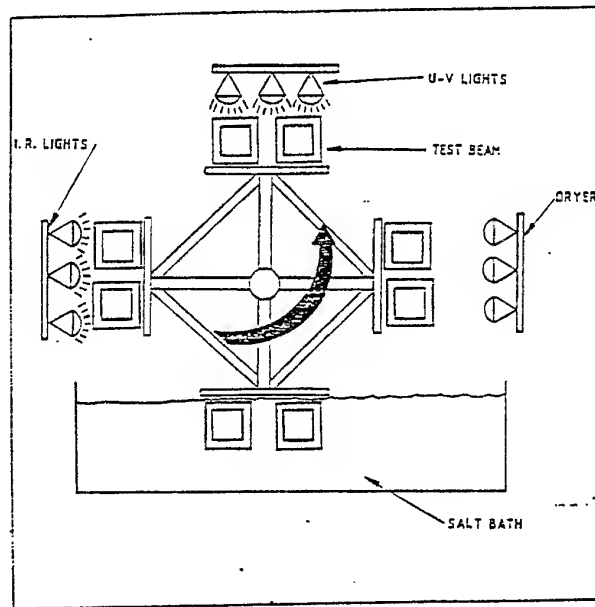
FIGURE 2: Environmental test machine

After each period of six hours of effective exposure, at least one sample is cut from each of the beams in the testing machine. The cut fibres of the test beams are then sealed against water penetration. This process continued until the last batch of samples has been cut from the test beams after 180 hours of effective exposure.
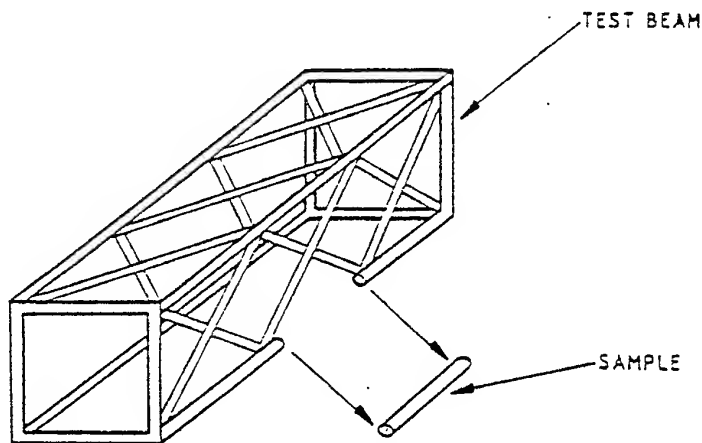
FIGURE 3:   Removal of samples for testing purposes

It was found that the average loss of strength over a period of 180 hours of accelerated exposure is **2.7%** and is acceptable.

STATIC FATIGUE TESTS

GRP material tends to deteriorate with time depending on the magnitude and duration of the load that is applied. The International Electrotechnical Commission found that the loss of strength was linearly proportional to the log of the time duration of the applied load. It was also found that the applied load on the insulator followed a similar pattern and that the slope of the load vs log-time line was 9%. Since the insulators are connected to the structure it can be assumed that the loading on the structure is the same as that on the insulators. Thus it must be proved that the slope of the strength time line is less than that of the load time line and that the two lines do not intersect.

To prove that the two lines do not intersect it is postulated that the slope of the strength time line is 8% or less. The samples are tested in order to validate this assumption. To plot the strength time line two samples have to be tested at 0.1 minute strength and at 96 hours strength. If the 96 hour sample does not fail under a load of 62% of the 0.1 minute test the slope of the strength log-time line is less than 8%. The results is shown in figure 4.
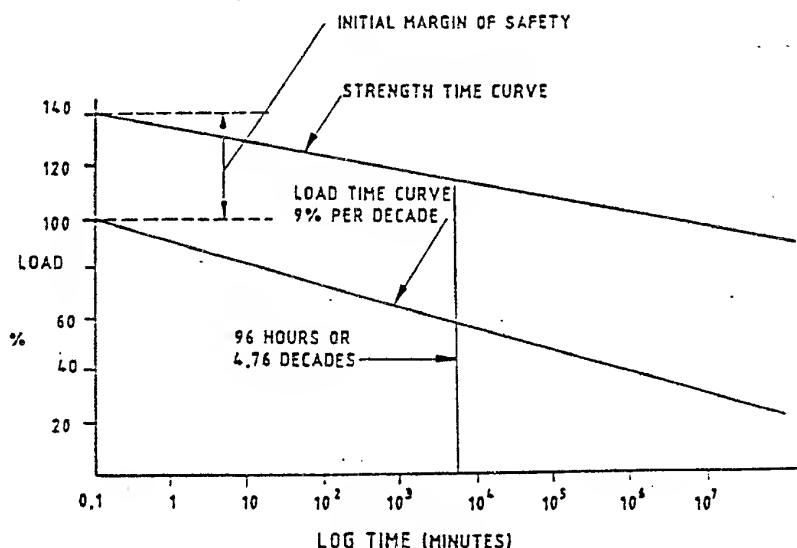
FIGURE 4:   Sustained load-time and strength time curves for the structure and the material respectively

MANUFACTURING PROCESS

The beam sections are manufactured by pulling E-glass roving through a resin bath and by laying the wetted glass roving onto a steel jig in a predetermined pattern. The resin is cured by lowering an oven over the rotating jig for approximately 45 minutes. After curing the jig is collapsed inside the fibreglass beam and the beam is removed for finishing and post curing. The whole process is schematically illustrated in figure 5.

THE FIBRESTRUC PROCESS
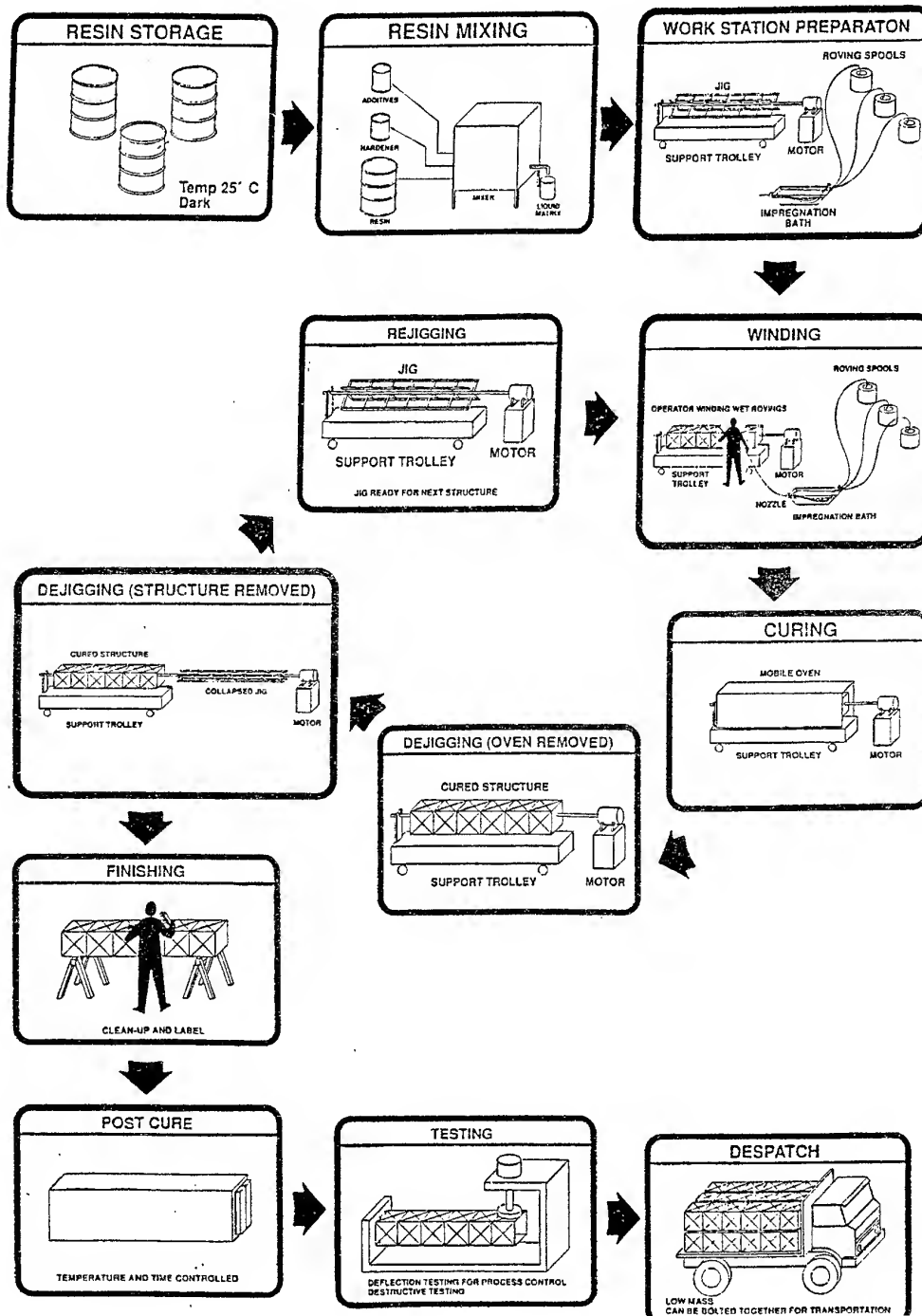
FIGURE 5:   The Fibrestruc manufacturing process

Quality checks is done by means of barcoll hardness tests and weighing of the beam sections to verify the amount of material used.

THE FINAL PRODUCT

The mast sections are built up using beams that vary between 2.7 and 3.1 meter in length. The individual beams are sized according to the bending moment expected at its base position in the mast. The boom of the gantry structure is connected to the masts by means of stainless steel brackets.

The foundations are made by placing a 2 meter long fibreglass beam into the foundation hole. The beam is levelled and secured in place while concrete is poured into the foundation hole. After the concrete sets the fibreglass mast is bolted to the foundation stub using stainless steel fittings. No reinforcing steel or cast in bolts are required as in the case of the traditional foundations.

A complete gantry structure weighs 600 kg compared to the 3000 kg of a traditional steel gantry manufactured from I-beam sections. The insulation properties of GRP allowed Spoornet to suspend the 3kV conductors without insulators. Tests on a beam section at 25kV was done for a year in a high pollution area (salt spray) with positive results.

CONCLUSION

GRP was successfully used to manufacture structures for overhead electrification in a highly corrosive environment although the cost of GRP material is still the biggest obstacle in replacing steel and concrete as a construction material.

REFERENCES

[1] I Mech E CONFERENCE PUBLICATIONS, Designing with Fibre Reinforced Materials, pp. 63 - 66, 1977

EXPLICIT FINITE DIFFERENCE METHOD
IN THE DYNAMIC ANALYSIS OF
LAMINATED COMPOSITE STRUCTURES

E.G.Evseev[1] and E.V.Morozov[2]

[1] Department of Computational Mechanics, Moscow State University of Aviation Technology
27, Petrovka str., Moscow, 103767 Russia

[2] Department of Mechanical Engineering, University of Natal, Private Bag X10, Dalbridge
4014, Durban, South Africa

INTRODUCTION

Design and analysis of the composite pressure vessels and tanks under static loading is quite well developed area. However in some cases the dynamic analysis of mechanical behavior for that kind of structures is the essential part of design process. This work presents an approach for dynamic analysis of the composite thin-walled shells based on the explicit scheme of the grid–characteristic finite difference method.

PROBLEM STATEMENT

The method of analysis discussed is based on the general equations of mechanics of thin-walled composite structures. These equations take into account the orthotropy, laminated structure, and low interlaminar shear stiffness of the composite material.

Let us consider the axisymmetric deformation of the shell of spherical shape. Helical filament winding manufacturing process provides the orthotropic structure of composite material. The angle of reinforcement orientation φ is changed along the meridian of the shell. The constitutive relationships have the following form:

$$N_\alpha = C_{11}\varepsilon_\alpha + C_{12}\varepsilon_\beta; \qquad N_\beta = C_{12}\varepsilon_\alpha + C_{22}\varepsilon_\beta;$$

$$M_\alpha = D_{11}\kappa_\alpha + D_{12}\kappa_\beta; \qquad M_\beta = D_{12}\kappa_\alpha + D_{22}\kappa_\beta; \tag{1}$$

$$Q_\alpha = K_1\psi_\alpha,$$

where wall stiffness coefficients are determined by the formulas:

$$C_{mn} = \int_{-h/2}^{h/2} B_{mn} d\gamma; \qquad D_{mn} = \int_{-h/2}^{h/2} B_{mn} \gamma^2 d\gamma;$$

$$K_1 = h^2 \left(\int_{-h/2}^{h/2} \frac{d\gamma}{G_{\alpha\gamma}} \right)^{-1}.$$

Here h is the wall thickness. We use the spherical coordinates (α, β, γ), where α and β are the meridian and hoop lines respectively and γ is the normal coordinate, which is orthogonal to the tangent plane.

The coefficients $B_{mn}(m, n = 1, 2)$ are the stiffness coefficients for the elementary layer oriented under the angle φ to meridian of the shell. They contain all the information on the wall structure and mechanical properties of the components, and can be calculated using the known equations of mechanics of composite materials [1–2]); $G_{\alpha\gamma}$ is the shear modulus of elementary layer. It is supposed that thin layered wall of the shell has symmetrical allocation of the layers with respect to the middle surface.

The geometric equations have the form:

$$\varepsilon_\alpha = \frac{1}{R} \left(\frac{\partial u}{\partial \alpha} + w \right); \qquad \varepsilon_\beta = \frac{1}{R} \left(u \cot \alpha + w \right);$$

$$\kappa_\alpha = \frac{1}{R} \frac{\partial \theta_\alpha}{\partial \alpha}; \qquad \kappa_\beta = \frac{\theta_\alpha}{R} \cot \alpha; \qquad \psi_\alpha = \frac{1}{R} \frac{\partial w}{\partial \alpha} - \frac{u}{R} + \theta_\alpha,$$

(2)

where R is the radius of sphere, u and w are tangent (meridional) and normal displacements, and θ_α is the rotation angle of normal element to the sphere surface.

Effective elastic moduli E_α and E_β and Poisson's ratios $\nu_{\alpha\beta}$ and $\nu_{\beta\alpha}$ can be presented in terms of wall stiffnesses as

$$E_\alpha = \frac{1}{h} \left(C_{11} - \frac{C_{12}^2}{C_{22}} \right); \qquad E_\beta = \frac{1}{h} \left(C_{22} - \frac{C_{12}^2}{C_{11}} \right);$$

$$\nu_{\alpha\beta} = \frac{C_{12}}{C_{11}}; \qquad \nu_{\beta\alpha} = \frac{C_{12}}{C_{22}}.$$

(3)

Substituting the geometric equations (2) into constitutive relationships (1) and taking into account equations (3), we obtain

$$N_\alpha = \frac{E_\alpha h}{(1 - \nu_{\alpha\beta}\nu_{\beta\alpha}) R} \left(\left(\frac{\partial u}{\partial \alpha} + w \right) + \nu_{\alpha\beta} \left(u \cot \alpha + w \right) \right);$$

$$N_\beta = \frac{E_\beta h}{(1 - \nu_{\alpha\beta}\nu_{\beta\alpha})\,R}\left(\nu_{\beta\alpha}\left(\frac{\partial u}{\partial \alpha} + w\right) + u\cot\alpha + w\right);$$

$$M_\alpha = \frac{E_\alpha h^3}{12\,(1 - \nu_{\alpha\beta}\nu_{\beta\alpha})\,R}\left(\frac{\partial\theta_\alpha}{\partial\alpha} + \nu_{\alpha\beta}\theta_\alpha\cot\alpha\right);$$

$$M_\beta = \frac{E_\beta h^3}{12\,(1 - \nu_{\alpha\beta}\nu_{\beta\alpha})\,R}\left(\nu_{\beta\alpha}\frac{\partial\theta_\alpha}{\partial\alpha} + \theta_\alpha\cot\alpha\right);$$

$$Q_\alpha = hG_{\alpha\gamma}\left(\frac{1}{R}\frac{\partial w}{\partial\alpha} - \frac{u}{R} + \theta_\alpha\right).$$

(4)

The equations of motion can be obtained from the equilibrium equations by adding the inertia terms and have the following form:

$$\frac{\partial N_\alpha}{\partial\alpha} + (N_\alpha - N_\beta)\cdot\cot\alpha + Q_\alpha = \rho h R\frac{\partial^2 u}{\partial t^2} - R\,p_\alpha(t,\alpha);$$

$$\frac{\partial Q_\alpha}{\partial\alpha} + Q_\alpha\cdot\cot\alpha - (N_\alpha - N_\beta) = \rho h R\frac{\partial^2 w}{\partial t^2} - R\,q(t,\alpha);$$

(5)

$$\frac{\partial M_\alpha}{\partial\alpha} + (M_\alpha - M_\beta)\cdot\cot\alpha - RQ_\alpha = \frac{1}{12}\rho h^3 R\frac{\partial^2\theta_\alpha}{\partial t^2},$$

where $p_\alpha(t,\alpha)$ and $q(t,\alpha)$ are tangent and normal components of load.

Substituting the relations (4) into equations (5), we obtain the system of equations of motion in terms of displacements

$$\frac{\partial^2 u}{\partial t^2} - \frac{\partial^2 u}{\partial\alpha^2} = \left(1 + \nu_\alpha - \frac{E_\beta}{E_\alpha}\nu_\beta\right)\cot\alpha\cdot\frac{\partial u}{\partial\alpha} + \left(1 + \nu_{\alpha\beta} + \eta^2\right)\frac{\partial w}{\partial\alpha}$$

$$+ \left(\nu_{\alpha\beta} + \frac{E_\beta}{E_\alpha} - \cot^2\alpha - \eta^2\right)u$$

$$+ \left(1 + \nu_{\alpha\beta} - (1 + \nu_{\beta\alpha})\frac{E_\beta}{E_\alpha}\right)w - \eta^2\theta_\alpha + p_\alpha(t,\alpha);$$

$$\frac{\partial^2 w}{\partial t^2} - \eta^2\frac{\partial^2 w}{\partial\alpha^2} = -\left(-1 + \frac{E_\beta}{E_\alpha}\nu_{\beta\alpha} + \eta^2\right)\frac{\partial u}{\partial\alpha} + \eta^2\cdot\cot\alpha\cdot\frac{\partial w}{\partial\alpha}$$

$$-\eta^2\frac{\partial\theta_\alpha}{\partial\alpha} + \left(\frac{E_\beta}{E_\alpha} - \nu_{\alpha\beta}\right)\cot\alpha\cdot u + \left(\frac{E_\beta}{E_\alpha} - \nu_{\alpha\beta}\right)w$$

$$-\eta^2\cdot\cot\alpha\cdot\theta_\alpha + q(t,\alpha);$$

$$\frac{\partial^2 \theta_\alpha}{\partial t^2} - \frac{\partial^2 \theta_\alpha}{\partial \alpha^2} = -\frac{R^2}{h^2} \cdot 12\eta^2 \cdot \frac{\partial w}{\partial \alpha} + \left(1 + \nu_{\alpha\beta} - \frac{E_\beta}{E_\alpha} \nu_{\beta\alpha}\right) \frac{\partial \theta_\alpha}{\partial \alpha}$$

$$\tag{6}$$

$$-\frac{R^2}{h^2} \cdot 12\eta^2 \cdot u - \left(\nu_{\alpha\beta} + \frac{E_\beta}{E_\alpha} \cdot \cot^2 \alpha - \frac{R^2}{h^2} \cdot 12\eta^2\right) \theta_\alpha \,,$$

where

$$\eta^2 = \frac{1 - \nu_{\alpha\beta}\nu_{\beta\alpha}}{2(1 + \nu_{\alpha\beta})}.$$

The system (6) consists of three partial differential equations of the second order with respect to time variable t and coordinate α. We can rewrite this system as follows

$$\frac{\partial^2 u}{\partial t^2} - \frac{\partial^2 u}{\partial \alpha^2} = F_1 \left(\frac{\partial u}{\partial \alpha}, \frac{\partial w}{\partial \alpha}, u, w, \theta_\alpha, p_\alpha(t, \alpha)\right);$$

$$\frac{\partial^2 w}{\partial t^2} - \eta^2 \frac{\partial^2 w}{\partial \alpha^2} = F_2 \left(\frac{\partial u}{\partial \alpha}, \frac{\partial w}{\partial \alpha}, \frac{\partial \theta_\alpha}{\partial \alpha}, u, w, \theta_\alpha, q(t, \alpha)\right); \tag{7}$$

$$\frac{\partial^2 \theta_\alpha}{\partial t^2} - \frac{\partial^2 \theta_\alpha}{\partial \alpha^2} = F_3 \left(\frac{\partial w}{\partial \alpha}, \frac{\partial \theta_\alpha}{\partial \alpha}, u, \theta_\alpha\right).$$

This is the system of hyperbolic type which is appropriate for dynamic analysis of structure. In this case we can use a numerical method based on extracting procedure of rapidly oscillating components [3].This technicue has been effectively used for analysis of dynamic responce of cylindrical shells and thin–walled curvilinear composite bars [4–5].

Let us introduce new vector-column of unknown variables

$$\vec{U} = \left\| \frac{\partial u}{\partial t}, \frac{\partial w}{\partial t}, \frac{\partial \theta_\alpha}{\partial t}, \frac{\partial u}{\partial \alpha}, \frac{\partial w}{\partial \alpha}, \frac{\partial \theta_\alpha}{\partial \alpha}, u, w, \theta_\alpha \right\|^T \tag{8}$$

and the right-hand side vector-column

$$\vec{F} = \left\| F_1, F_2, F_3, 0, 0, 0, \frac{\partial u}{\partial t}, \frac{\partial w}{\partial t}, \frac{\partial \theta_\alpha}{\partial \alpha} \right\|^T, \tag{9}$$

As a result, we obtain the first order hyperbolic system of equations in the form

$$\frac{\partial \vec{U}}{\partial t} + A \frac{\partial \vec{U}}{\partial \alpha} = \vec{F} \left(t, \alpha, \vec{U}\right). \tag{10}$$

In this equation, A is the hyperbolic matrix consisting of nine rows and nine columns

$$
A = \begin{bmatrix}
0 & 0 & 0 & -1 & 0 & 0 & 0 & 0 & 0 \\
0 & 0 & 0 & 0 & -\eta^2 & 0 & 0 & 0 & 0 \\
0 & 0 & 0 & 0 & 0 & -1 & 0 & 0 & 0 \\
-1 & 0 & 0 & 0 & 0 & 0 & 0 & 0 & 0 \\
0 & -1 & 0 & 0 & 0 & 0 & 0 & 0 & 0 \\
0 & 0 & -1 & 0 & 0 & 0 & 0 & 0 & 0 \\
0 & 0 & 0 & 0 & 0 & 0 & 0 & 0 & 0 \\
0 & 0 & 0 & 0 & 0 & 0 & 0 & 0 & 0 \\
0 & 0 & 0 & 0 & 0 & 0 & 0 & 0 & 0
\end{bmatrix}. \tag{11}
$$

The components of the right-hand side vector of the system (10) are presented by the following equations

$$
F_1 = \left(\left(1 + \nu_{\alpha\beta} - \frac{E_\beta}{E_\alpha} \nu_{\beta\alpha} \right) \cot \alpha \right) U_4 + \left(1 + \nu_{\alpha\beta} + \eta^2 \right) U_5
$$

$$
- \left(-\nu_{\alpha\beta} - \frac{E_\beta}{E_\alpha} \cot^2 \alpha + \eta^2 \right) U_7 + \left(1 + \nu_{\alpha\beta} - (1 + \nu_{\beta\alpha}) \frac{E_\beta}{E_\alpha} \right) U_8
$$

$$
- \eta^2 U_9 + p_\alpha(t, \alpha);
$$

$$
F_2 = -(1 + \nu_{\beta\alpha}) \frac{E_\beta}{E_\alpha} + \eta^2 U_4 + \eta^2 \cdot \cot \alpha \cdot U_5
$$

$$
\eta^2 U_6 + \left(\frac{E_\beta}{E_\alpha} - \nu_{\alpha\beta} \right) \cot \alpha \cdot U_7 + \left(\frac{E_\beta}{E_\alpha} - \nu_{\alpha\beta} \right) U_8 \tag{12}
$$

$$
- \eta^2 \cdot \cot \alpha \cdot U_9 + q(t, \alpha);
$$

$$
F_3 = -\frac{R^2}{h_2} \cdot 12\eta^2 \cdot U_5 + \left(1 - \nu_{\alpha\beta} - \frac{E_\beta}{E_\alpha} \nu_{\beta\alpha} \right) U_6
$$

$$
- \frac{R^2}{h^2} \cdot 12\eta^2 \cdot U_7 - \left(\nu_{\alpha\beta} + \frac{E_\beta}{E_\alpha} \cdot \cot^2 \alpha - \frac{R^2}{h^2} \cdot 12\eta^2 \right) U_9;
$$

$$
F_4 = F_5 = F_6 = 0; \quad F_7 = U_1; \quad F_8 = U_2; \quad F_9 = U_3.
$$

This form of equations gives the possibility for implementation of an explicit and stable homogeneous method for the numerical integration. The system (7)

is converted to the first order hyperbolic system (10) using new vectors (8) and (9). The new system contains the matrix (11) and right– hand side vector (12).

One of the main difficulty which takes place in this case is the presence of the terms like $R^2 h^{-2}$ with large coefficients in the right–hand side of the system. In order to overcome this obstacle we can split an explicit finite difference method in order to extract the strongly oscillating components of solution. The method of splitting consists of two main steps. At the first step the analytical solution of the Cauchy problem for the system of ordinary differential equations is obtained. The right–hand side vector of this system contains the terms with the large parameters. At the second step, the first order hyperbolic system of equations is numerically integrated and the large parameters are removed from the right–hand side vector. The solution obtained for the first step is used as initial data at the second stage. The method provides the stable numerical process of calculations for wide range of values of parameters.

CONCLUSIONS

Thus, the system of equation and numerical method suggested in this work give the possibility for dynamic analysis of composite thin–walled shells. It can also be used as a direct analysis technique for optimum design procedures.

REFERENCES

[1]Vasiliev,V.V. "Mechanics of Composite Structures." Taylor & Francis,(1993).

[2]Vorobey,V.V., Morozov, E.V., and Tatarnikov, O.V."Analysis of Thermoloaded Composite Structures." Moscow, Mashinostroenie (1992).

[3]Evseev,E.G., and Semenov,A.Yu."A Method for Numerical Solution of the Equations for the Dynamics of Thin Shells, Based on Separating out Rapidly Oscillating Components." *Soviet Math. Dokl.*Vol.41,1, pp. 118–121 (1990).

[4]Evseev,E.G., and Morozov,E.V. "Nonplanar Deformation of a Circular Thin-Walled Composite Bar under Dynamical Loading."*Mechanics of Solids*,Vol. 29,5, pp.159-169 (1994).

[5]Evseev,E.G., and Morozov,E.V. "The Finite-Difference Techniques for Static and Dynamic Problems in Mechanics of Composite Structures." *Advances in Structured and Heterogeneous Continua*,pp.390-399, N.Y., Allerton Press (1994).

STATIC INDENTATION AND IMPACT BEHAVIOUR OF GRP PULTRUDED SECTIONS

M. S. Found, G. J. Holden* and R. N. Swamy
SIRIUS, Department of Mechanical and Process Engineering
University of Sheffield, Mappin Street, Sheffield S1 3JD, UK.

INTRODUCTION

Composite structures may be subjected to impact damage during assembly, service or maintenance. Such damage may comprise of indentation, matrix cracking, debonding, delamination or fibre fractures. Visible damage usually occurs if an impact is above a threshold impact energy, which depends on laminate stiffness, and causes strength degradation of the laminate. The mechanical response of laminates is an essentially global response mainly by flexural distortion and locally by indentation [1]. Since inspection of damage is often only possible from one surface an assessment of structural integrity of laminates in terms of frontface damage associated with indentation would be particularly useful. Therefore an understanding of the relationship between indentation and impact behaviour of composite materials is of importance.

The overall aim of a programme of work at Sheffield on the impact behaviour of FRP composites is to study the effect of static indentation and single and repeated impacts on plain and stiffened laminates and to assess their damage tolerance. This paper reports the findings on static indentation and single impacts on three plain GRP pultruded sections.

EXPERIMENTAL

The materials were E-glass fibres impregnated with an isophthalic polyester resin to produce three pultruded sections comprising of random continuous filament mat (CFM) and unidirectional rovings, with a resin-rich surface veil and are designated materials A, B and C (see Fig. 1). Material A was removed from the web of an I-beam supplied by Creative Pultrusions Inc, and had a thickness of 6.35 mm and a fibre volume fraction of 38%. Materials B and C were flat sheets supplied by Fibreforce Composites Ltd, with thicknesses of 6.35 and 4.75 mm respectively and fibre volume fractions of 34%.

An instrumented dropweight impact rig, briefly described in reference [2], was used for both static indentation tests and single impact tests. Static indentation tests were undertaken by clamping the laminate between two annular rings of 100 mm internal diameter and incrementally driving the instrumented indentor, of 12 mm diameter with a hemispherical nose, into the laminate. The laminate surface displacements (their

*Present address: BAe Defence Ltd, Warton, Preston, UK.

difference equals the indentation) and force in terms of strain were recorded with respect to the indentor displacements. Indentation was continued until an audible sound was heard from the laminate which indicated the initiation or propagation of damage. The permanent indentation was recorded after the test at two different time intervals to ensure that relaxation of the material was complete.

Dropweight impact tests were conducted from a height of 0.5 m for which the impact velocity of the impactor was measured at approximately 3 m/s. The impact energy was varied by using masses in the range of 0.6538 to 2.4731 kg to produce kinetic energies of 3-11 J. During impact the impact and rebound velocity, acceleration, force and central deflection with respect to time were recorded and stored in a computer and the data processed using compatible software.

Damage was assessed after both indentation and impact tests using x-radiography, sectioning and microscopy and photographic techniques. The structural integrity of the damaged samples was assessed via residual compressive strength tests. For these tests 30 mm wide coupons were cut parallel to the unidirectional roving (i.e. the 0° fibres or pultruded direction) ensuring that the damage site was in the middle of the specimen width. The tests were conducted using an antibuckling guide in a Mayes universal testing machine at a crosshead rate of 1 mm/min. For comparison purposes compressive strength tests were also conducted on specimens containing a drilled hole of 12 mm diameter, similar to the size of the indentor/impactor. Further details on experimental techniques and material properties are given in Holden [3].

RESULTS

The force-deflection curves for the three materials were linear for small deflections. Initiation of damage in the form of matrix cracking occurred when the slopes became non-linear and the audible cracking which occurred after significant non-linear behaviour was identified as backface cracking. The force-indentation behaviour presented in Fig. 2 is almost linear for small indentations and then follows a modified contact law [4] given by:

$$F = k\alpha^{3/2} \tag{1}$$

where F is the contact force, α is the indentation and k is the stiffness parameter which depends on the properties of the indentor and the laminate. Materials B and C, which have similar properties, deviate from equation (1) at loads corresponding to initiation of damage identified from the load-deflection curve. However, for the stiffer material A deviation from the contact law did not occur until the onset of more significant damage in the form of backface cracking.

With further increase in the indentation force damage on both surfaces occurred and there appears to be a similar relationship for all of the materials as indicated in Fig. 3. At lower loads the relationship between permanent indentation on the upper surface and

132

cracking on the lower surface is linear. The rate of increase slows down as the force increases towards a level to cause full penetration of the indentor. For material C the damage occurred approximately simultaneously whilst for materials A and B there was some permanent indentation prior to backface cracking.

The behaviour of each of the materials under impact loading is compared in Fig. 4 for the load-deflection response at an incident kinetic energy of 6.9 J. For materials A and B the curves are very similar in terms of peak load, deflection at peak load and total deflection. In comparison material C has a much lower peak load and this occurs at about twice the deflection of the other materials although its total deflection is similar. The damage produced with increasing impact energies in terms of permanent indentation and backface cracking is shown in Fig. 5. Although there is considerable scatter in the test data, especially for material B, the relationship between frontface and backface damage is linear with material C sustaining considerable damage and material A limited backface cracking. Neither non-destructive evaluation nor destructive sectioning techniques revealed any internal damage in the form of matrix cracking or delamination as a result of loading by static indentation or impact.

The effect of increasing backface crack length on residual compression strength for both static indentation and impact loading is presented in Fig. 6. The lines represent best fits through the data for each of the materials and show limited scatter. The behaviour is linear with a crack produced during static indentation giving rise to a greater reduction in strength especially for small cracks, i.e. at smaller loads.

DISCUSSION

Static indentation may be predicted using a modified contact law [4, 5] until the onset of damage. The law is based on the through-thickness laminate properties (E_3) and using the assumption $E_2 = E_3$ gives an underestimation of indentation for the thicker materials. This suggests that the longitudinal fibres, which take much of the strain during this type of loading configuration, produce an increase in the apparent out-of-plane modulus. Once damage occurs permanent indentation is dependent on the flexural stiffness with materials having the higher values of E_1 and E_3 giving greater resistance to indentation. With increasing damage the indentor moves quickly into the material producing large permanent indentation. Similarly for backface cracking the materials with the higher flexural stiffness give the better resistance to cracking.

The force-deflection curves (Fig. 4) do not show any fall in load up to the peak load, which is often caused by damage, and when the maximum load is reached there is a rapid increase in deflection producing a large area under the curve indicative that the materials are absorbing most of the impact energy. Furthermore the damage produced did not significantly change the force-deflection behaviour of the materials.

For the same range of permanent indentation the relationship between backface crack length and frontface indentation is linear for both static indentation and impact behaviour (see Figs. 3 and 5). Oxley [6] observed a similar relationship for the impact behaviour of a woven CFRP laminate at low impact energies. However to produce the same

133

backface crack size induces a higher force and greater permanent indentation with impact loading compared with static loading for the GRP results reported. Furthermore, the damage relationship is independent of flexural stiffness for static loading but dependent upon it for the impact case. This suggests that the type of loading governs the behaviour of the damage and that the damage is not just dependent on the force. More significantly, it appears that backface damage may be predicted from the measurement of frontface damage for both static and impact loading.

From knowledge of the backface crack size the structural integrity may be assessed in terms of the residual compressive strength (see Fig. 6). Whilst in terms of static indentation and impact behaviour the stiffer material A appears to offer most resistance, once backface damage occurs the percentage reduction in compressive strength is similar for all materials with a slightly higher reduction for the static case.

CONCLUSIONS

The type of loading appears to determine the damage behaviour of circularly clamped GRP pultruded sections. The stiffer material A appears to offer the greater resistance to damage for both static indentation and impact loading. For both loading conditions backface cracking may be predicted from permanent indentation of the frontface. The residual compressive strength of the materials may be determined from the size of the backface crack. The relationship between permanent indentation and crack length is independent of flexural stiffness for static loading but dependent upon it for impact loading.

REFERENCES

1. Lagace, P. A., Ryan, K. F. and Graves, M. J. Effect of damage on the impact response of composite laminates. AIAA Paper 91-1079-C pp. 1137-1143 (1991).
2. Kumar, M., Found, M. S. and Howard, I. C. A drop-weight instrumented impact test to compare the effect of single and multiple impacts. Proceedings of 2nd International Seminar on Experimental Techniques and Design in Composite Materials, ed. M. S. Found, Sheffield Academic Press, pp. 84-101 (1995).
3. Holden, G. J. Static indentation and impact behaviour of glass reinforced plastic pultruded sections. M.Phil. thesis, University of Sheffield (1995).
4. Sun, C. T. An analytical method for evaluation of impact damage energy of laminated composites. Composite Materials : Testing and Design (4th Conference) ASTM STP 617, pp. 427-440 (1977).
5. Yang, S. H. and Sun, C. T. Indentation law for composite laminates. Composite Materials : Testing and Design (6th Conference) ASTM STP 787, pp. 425-449 (1982).
6. Oxley, M. The effect of low velocity impact damage on the performance of a woven CFRP. Ph.D. thesis, University of Sheffield (1991).

MSF/PAPER17/LAC
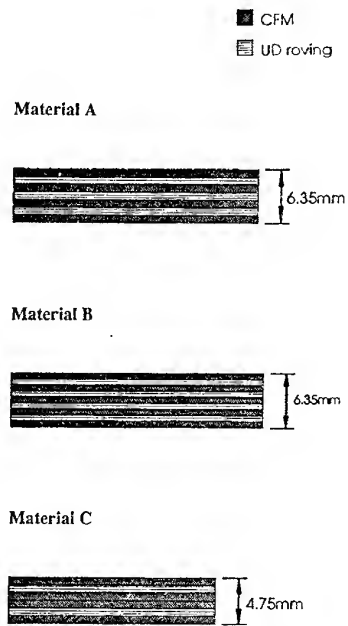
Fig. 1. Lay-up and thickness of pultruded sections.

Material A

6.35mm

Material B

6.35mm

Material C

4.75mm
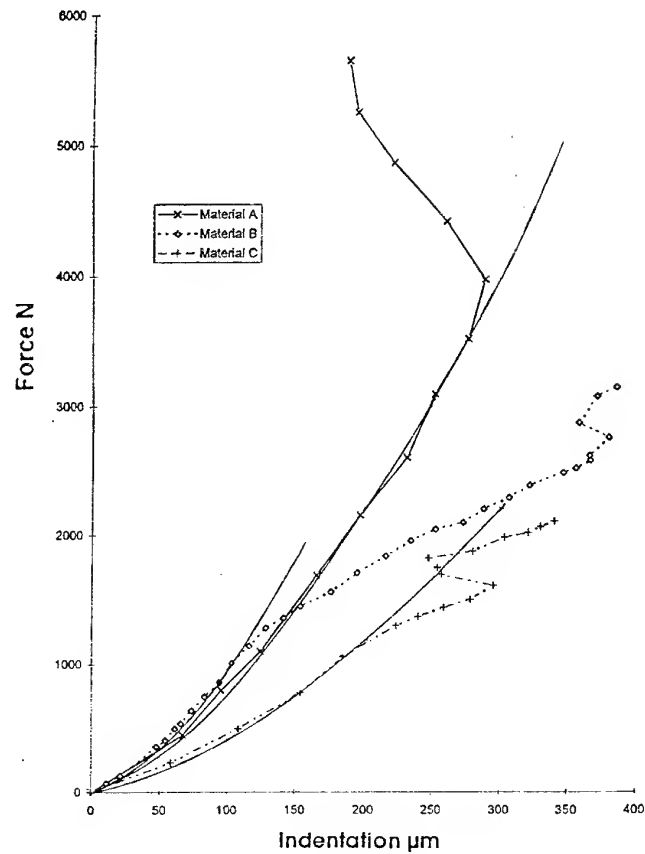
Fig. 2. Force-indentation behaviour compared with modified contact law.
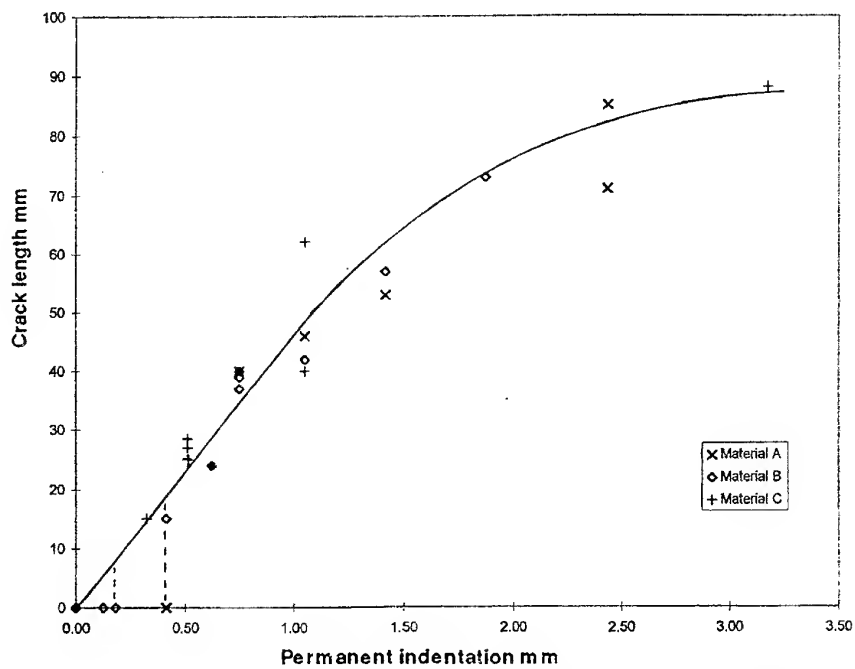
Fig. 3. Relationship between frontface permanent indentation and backface crack length for static indentation tests.

135
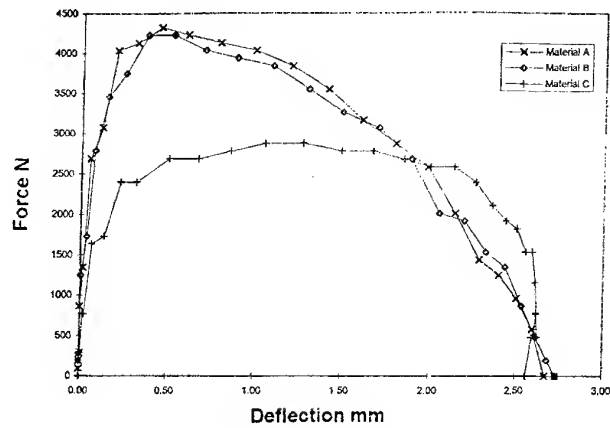
Fig. 4. Force-deflection response during impact loading.
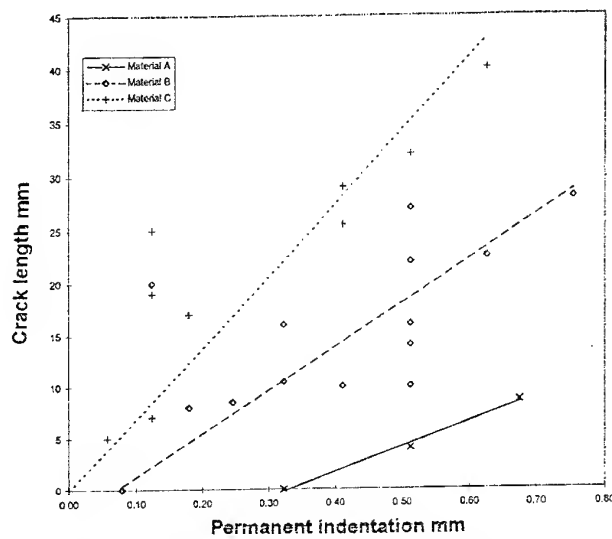
Fig. 5. Relationship between frontface permanent indentation and backface crack length for impact tests.
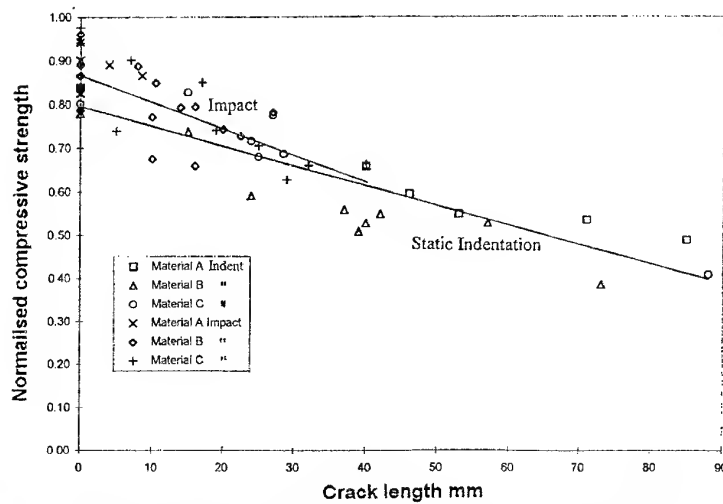
Fig. 6. Assessment of structural integrity in terms of compressive strength for both static indentation and impact tests.

136

BEHAVIOUR OF STIFFENED CFRP SECTIONS

M. S. Found, I. C. Howard and A. P. Paran
SIRIUS, Department of Mechanical and Process Engineering,
University of Sheffield, Mappin Street, Sheffield S1 3JD, U.K.

INTRODUCTION

It is difficult to predict the damage tolerance of complex composite structures based on the evaluation of plain test coupons. Furthermore, many present designs tend to be conservative such that the potential weight-saving is not fully achieved. Increasing the laminate section thickness as a means of reducing impact damage is not cost effective for many aerospace applications. Significant improvements in resistance to impact damage may best be achieved with the use of a thin membrane to absorb the energy with the structural stiffness being provided by careful design and positioning of local stiffeners. The presence of localised stiffeners increases the available elastic energy which can be absorbed before fracture starts [1]. This principle has been used in aerospace applications such as the development of CFRP wing boxes [2, 3].

The overall aim of a programme of work at Sheffield on impact behaviour of FRP composites is to study the effect of static indentation and single and repeated impacts on plain and stiffened laminates and to assess their damage tolerance. This paper reports the preliminary findings on single impacts on CFRP panels stiffened with T-type stiffeners and compares their performance with that of unstiffened panels.

EXPERIMENTAL

Stiffened CFRP panels nominally 220 mm wide x 1 m long were supplied by Hurel-Dubois UK to the configuration shown in Fig. 1. In additional plain panels of the same 3-ply lay-up were supplied for comparison. The material was a five-harness satin weave CFRP, supplied in prepreg sheets by Ciba-Geigy, designated Fibredux 914C-713-40. The panels were laid up in three plies as (0/90, ±45, 0/90) and 0/90 stiffeners added, each panel being moulded in one shot by Hurel-Dubois to produce a panel thickness of 0.8 mm and a nominal 58% fibre volume fraction.

An instrumented dropweight impact rig was used for the tests. The rig can be adapted to also conduct static indentation tests [4]. Impact tests were undertaken by clamping the panels between two annular rings of 100 mm internal diameter, the lower ring having slots to accept the stiffeners. The instrumented hemispherical indentor of 12 mm diameter was released by an electromagnetic switch from a height of 0.5 m for which the impact velocity was measured at approximately 3 m/s. The impact energy was varied by using masses in the range 0.1412 to 0.1913 kg to produce kinetic energies of 0.56-

0.83 J. During impact the impact and rebound velocity, acceleration, force and central deflection with respect to time were recorded and stored in a computer and the data processed using compatible software. Damage was assessed after the impact tests using x-radiography, ultrasonic c-scan and sectioning and microscopy techniques. For the preliminary results reported here the impacts were in the middle of the bay between the stiffeners. Subsequent tests will take place adjacent to the toe of the stiffeners and directly over the stiffeners.

RESULTS

The force-time and displacement-time responses for plain panels and panels with T-stiffeners spaced 63 and 53 mm apart are presented in Figs. 2-4 respectively. The forces are obtained from filtered accelerometer data. With increasing mass i.e. increasing incident energy change in behaviour is determined by the amount of damage sustained. For both the plain panel and the stiffened panel with the stiffeners spaced 63 mm apart a change in structural response is observed, identified by an increase in impact duration. However, for the same incident energy the time response reduces with increasing panel stiffness. Examination of the displacement-time histories for each of the panels shows the influence of transverse vibrations which appear to be significant for the plain panel but reduce in amplitude and decay time with increasing panel stiffness.

Figs. 5 and 6 compare the force-displacement behaviour for the three different panel geometries at the minimum energy and at the higher energy respectively. At minimum energy the peak force is similar and the deflection is controlled by panel stiffness. At the higher test energy the peak load is significantly higher in the stiffest panel since it suffered little damage. The diagrams also show an instantaneous force, i.e. without displacement, at the onset of impact. The magnitude of this force increases with increasing mass and panel stiffness and is associated with the inertia of the panel and the mechanical properties at the contact interface. Inspection of the backface of each of the panels revealed damage predominantly in the form of cracking in the 90° fibre direction i.e. parallel to the stiffeners for the stiffened panels. The increase in crack length appeared to increase linearly with impact energy, with reduced cracking observed with increasing section stiffness. For the range of impact energies evaluated there was no visually observable permanent indentation on the frontface of any of the panels.

DISCUSSION

One of the problems in the interpretation of impact test data is in the analysis of the force-time history obtained from accelerometers. By careful interpretation of the signals prior to filtering it is possible to ascertain the separate responses of the impactor, rig constraint and test panel. The use of simple models involving appropriate spring-mass combinations allow separation of these effects and also allow comparisons between predicted and actual vibrations. Careful selection of low-pass filter parameters must be employed to ensure that significant events are not removed by filtering and thus prevent misleading interpretation of the impact event. Analysis of the vibrational response of a

simple model showed that the panel displacement commences at a short duration of time after contact by the impactor which can be clearly seen when comparing (a) the force-time histories with (b) the displacement-time histories for each of the panels as shown in Figs. 2-4. This behaviour also confirms the response in terms of instantaneous force shown in Figs. 5 and 6.

The linear increase in backface crack length with impact energy for this material has previously been identified [5]. However at energies approaching those to cause penetration the behaviour is non-linear. Since the inspection of damage in many structures is often only possible from one surface the interpretation of backface damage alone is of little value. It is therefore proposed to continue these preliminary investigations at higher impact energies, at least sufficient to cause permanent frontface damage in the form of indentation and cracking. A means of interpretation of indentation has been proposed for a wing box section subjected to impact damage [3]. Whilst the increase in panel stiffness due to local stiffening suppresses backface cracking it appears that once the fracture processes are initiated that significantly more damage may occur in the form of delaminations identified in terms of damage area from ultrasonic or x-ray measurements [1].

The importance of damage with increasing panel stiffness will also be evident from the next stage of the test programme when impacts will be performed adjacent to the toe of the stiffeners and directly in-line with the stiffeners. The work on impact testing will be repeated under identical constraints for static loading to ascertain correlations with a method for which analysis is much simpler. Since geometric effects are significant for low velocity impacts care must be taken in translating the behaviour of laboratory tests to predicting the likely response of real structures, especially where the failure mechanisms are observed to be quite different. Ultimately, of major concern is the structural integrity of various stiffened sections. Kolax [2] has shown that the percentage residual compressive strain of stiffened sections subjected to 50 J impact was similar to the effect of a flat panel containing a 25 mm drilled hole.

CONCLUSIONS

When CFRP panels are subjected to impact loading the effect of damage on structural response may be identified by an increase in impact duration. At the higher incident impact energy the peak force is greater in the stiffest panel since it sustained the least damage. Damage in the form of backface cracking in the 90° fibre direction increases linearly with incident impact energy but at a reducing rate with increasing section stiffness. A vibrational analysis of the whole system based on simple models enables a correct interpretation of the response of accelerometer data and a means of monitoring the effectiveness of filtering.

REFERENCES

1. Davies, G. A. O. and Zhang, X. Impact damage prediction in carbon composite structures. International Journal of Impact Engineering, 16(1) pp. 149-170 (1995).

2. Kolax, M. W. Composite wing : results of Deutsche Airbus Technology Program. 37th International SAMPE Symposium, pp. 1146-1159 (1992).

3. Tropis, A., Thomas, M., Bounie, J. L. and Lafon, P. Certification of the composite outer wing of the ATR72. Proceedings of Institution of Mechanical Engineers, 209, Part G : Journal of Aerospace Engineering, (4), pp. 327-339, (1995).

4. Kumar, M., Found, M. S. and Howard, I. C. A drop-weight instrumented impact test to compare the effect of single and multiple impacts. Proceedings of 2nd International Seminar on Experimental Techniques and Design in Composite Materials, ed. M. S. Found, Sheffield Academic Press, pp. 84-101 (1995).

5. Oxley, M. The effect of low velocity impact damage on the performance of a woven CFRP. Ph.D. thesis, University of Sheffield (1991).
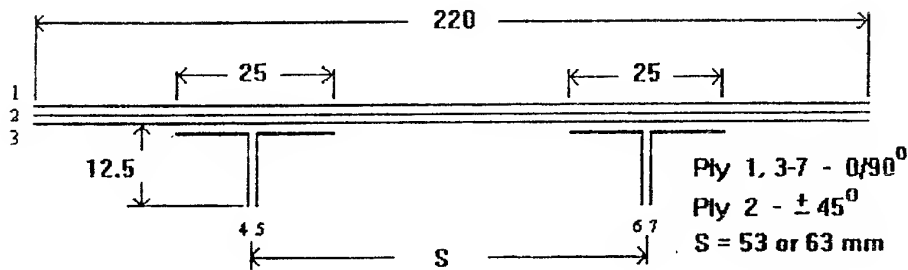
Fig. 1.   Panel geometry and ply lay-up.
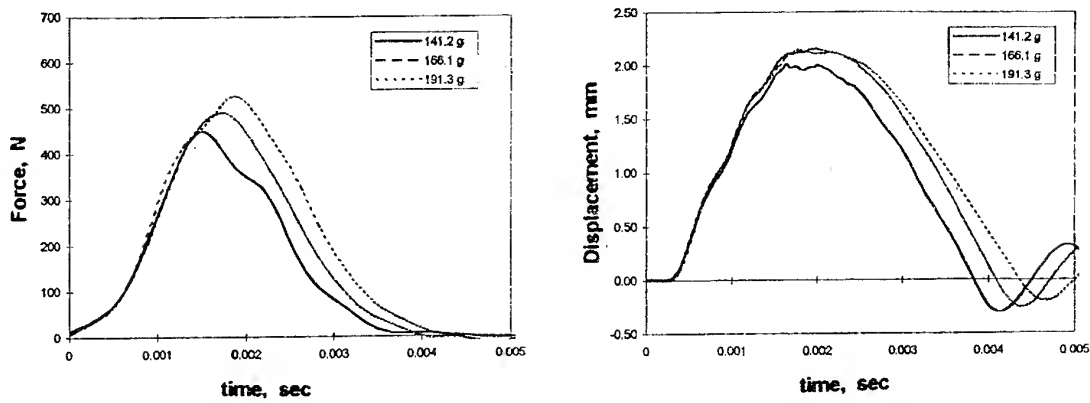
Fig.2   (a) Force-time and (b) displacement-time histories for plain panels.
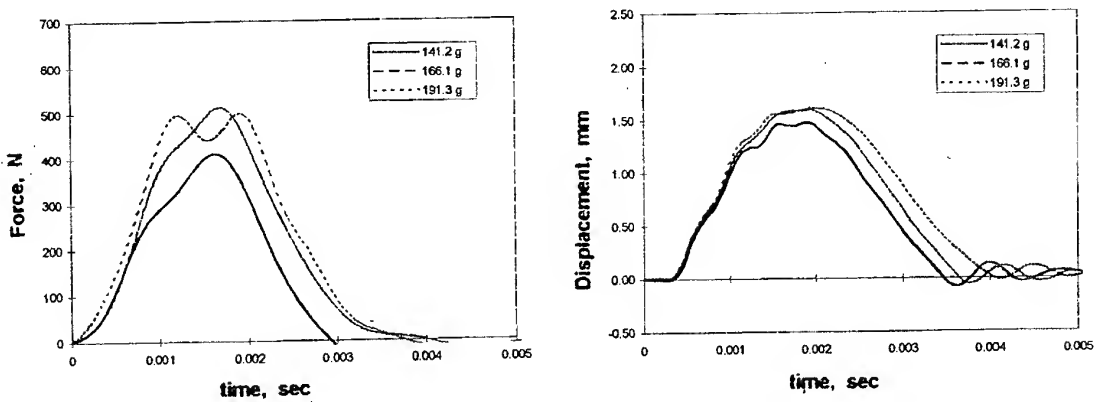
Fig. 3   (a) Force-time and (b) displacement-time histories for panels with stiffener spacing of 63 mm.
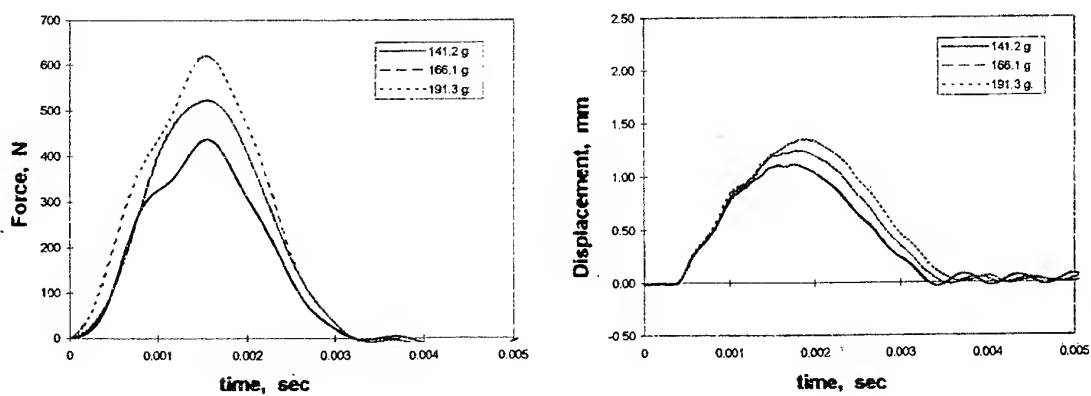
Fig. 4   (a) Force-time and (b) displacement-time histories for panels with stiffener spacing of 53 mm.

141
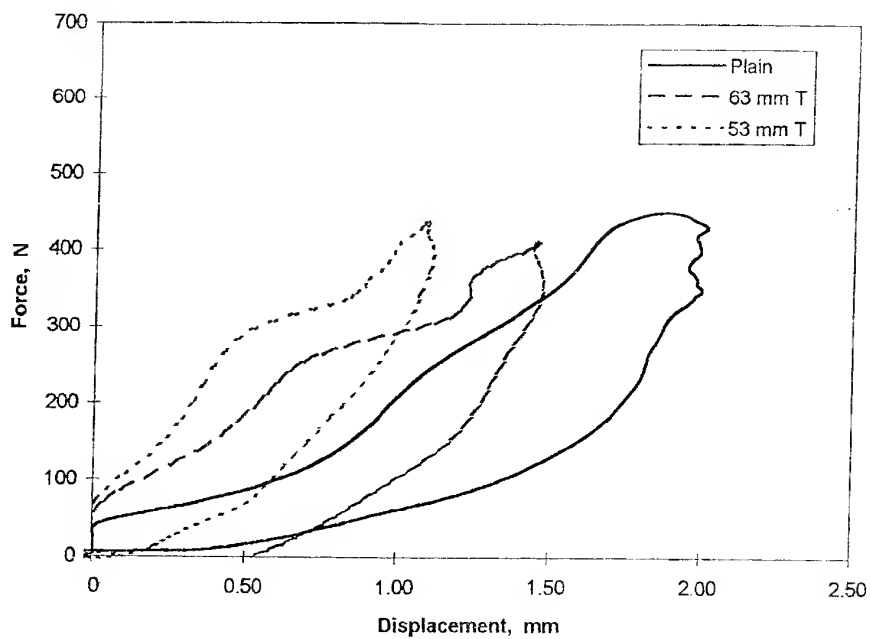
Fig. 5   Comparison of force-displacement of each panel at minimum incident impact energy of 0.56 J.
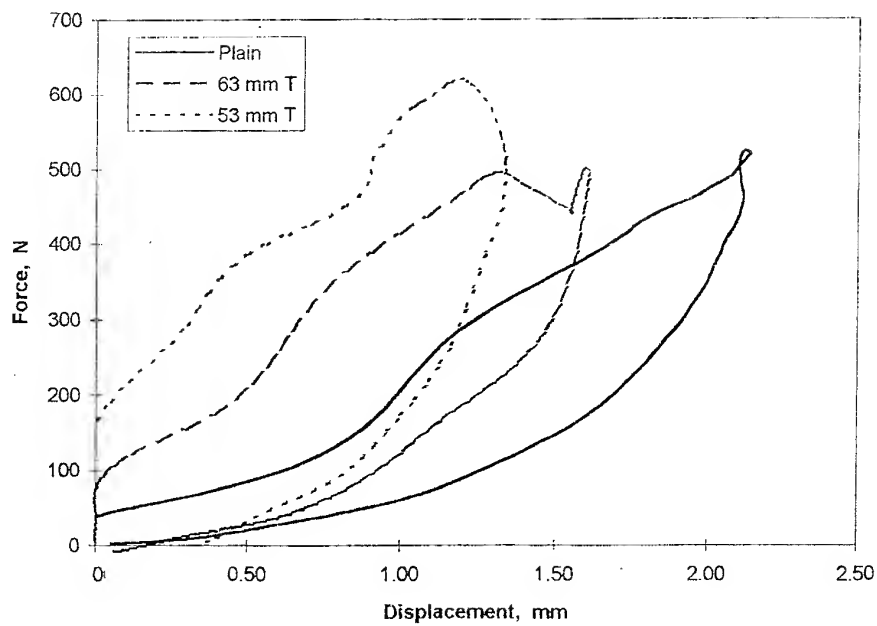
Fig. 6.   Comparison of force-displacement of each panel at an incident impact energy of 0.83 J.

142

ADVANCED TECHNIQUES FOR THE IDENTIFICATION OF MATERIAL PARAMETERS OF THICK COMPOSITE PLATES

PER S. FREDERIKSEN

Department of Solid Mechanics
Technical University of Denmark, DK–2800 Lyngby, Denmark

INTRODUCTION

This paper deals with an inverse technique for the identification of orthotropic elastic constants of composite plates. The method is a numerical/experimental approach in which the free parameters (elastic constants) of a numerical model of the plate vibration are adjusted to fit a range of measured natural frequencies the best. The method constitutes a reliable, non-destructive and fast alternative to conventional static test methods. The approach is well established and described in the case of thin plates modelled by the classical plate theory, e.g. [1]. Related approaches employing thin plates can be found in e.g. [2-3]. Here, focus is on recent developments of the method employing thick plates. The use of such plates in conjunction with frequencies of higher modes assures a significant transverse shear effect. This enables the identification of the two transverse shear moduli along with the four in-plane elastic constants. Previous work has described the experimental techniques [4] and the mathematical aspects [5] for solving the inverse problem. In a recent study also the problem of designing the experiment to optimize the reliability of the parameter estimates has been considered [6].

The accuracy of the numerical model is decisive for the accuracy of the identified parameters. In the present paper, the experience with an improved model compared to that used in [4-5] is described. Theoretically, the more advanced model is employed to asses the systematic errors in the identification associated with the use of the previous model. Such investigations show that the improved model has increased accuracy of the estimates of the transverse shear moduli significantly.

Previous work has considered only the flexural vibration of the plate. However, for thick plates of a certain size, it is possible also to measure natural frequencies of in-plane modes of vibration. Hereby, a method similar but independent of that using the flexural natural frequencies has been established, but only the in-plane parameters can be identified in this case.

The performance of the identification approach is illustrated by experimental results of a thick composite plate employing both in-plane and flexural natural frequencies. The results of the two tests show good agreement. Also, results of conventional static tests were found to agree well with those of the dynamic tests.

IDENTIFICATION APPROACH

A rectangular plate of constant thickness h, length a and width b is considered (Fig. 1). The plate is composed of an orthotropic material with principal material directions 1-2-3
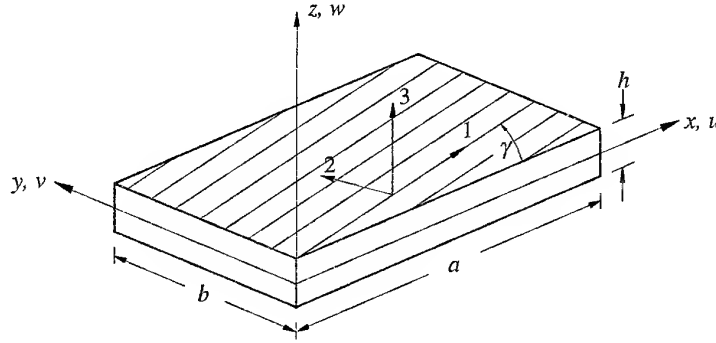
Fig. 1. Definition of plate and material co-ordinate systems.

oriented at an angle γ from the plate coordinate system x-y-z.

In the parameter estimation problem, a non-linear least squares approach is employed in which the free parameters (elastic constants) contained in the parameter vector θ are adjusted to minimize the deviations between measured and calculated frequencies:

$$\underset{\theta}{\text{Minimize}} \quad \Phi(\theta) = \sum_{i=1}^{I} \left(\frac{f_i^e - f_i(\theta)}{f_i^e} \right)^2 \tag{1}$$

Here, f_i^e is the measured value of the i'th natural frequency, $f_i(\theta)$ is the corresponding predicted frequency, which is a nonlinear function of the elastic constants, and I is the number of frequencies. Details of the minimization of Φ are given in [5].

THICK PLATE VIBRATION MODELS

Thick plates with all edges free are considered. Since no exact solutions for the vibration of such plates exist, approximate displacement based theories are employed.

The analysis for predicting the natural frequencies of the thick plate vibration is linear and limited to plates which are symmetric about the midplane. Hence, the analysis of the out-of-plane (flexural) and in-plane vibration can be performed separately. Two different higher-order plate theories are considered for the analysis of the flexural vibration.

Theory I

This is the shear deformation theory of Reddy [7] previously used in [4-5]. Omitting the in-plane components, the displacement field is function of three variables, w_0, ψ_x, and ψ_y:

$$u(x,y,z) = z\psi_x(x,y) - z^3 \frac{4}{3h^2} \left(\frac{\partial w_0(x,y)}{\partial x} + \psi_x(x,y) \right)$$

$$v(x,y,z) = z\psi_y(x,y) - z^3 \frac{4}{3h^2} \left(\frac{\partial w_0(x,y)}{\partial y} + \psi_y(x,y) \right)$$

$$w(x,y,z) = w_0(x,y) \tag{2}$$

144

The displacement field (2) neglects the transverse normal strain. Therefore, plane-stress reduced constitutive equations are employed in this theory, involving six elastic constants: $\theta_I = \{E_1, E_2, G_{12}, v_{12}, G_{13}, G_{23}\}^T$. Here, E_1 and E_2 are the two in-plane Young's moduli in the primary and secondary direction of orthotropy, respectively, G_{12} is the in-plane shear modulus, v_{12} is the in-plane major Poisson's ratio and G_{13} and G_{23} are the transverse shear moduli.

Theory II

The second and more advanced theory is described by six displacement functions [8]:

$$u(x,y,z) = z\psi_x(x,y) + z^3\phi_x(x,y), \quad v(x,y,z) = z\psi_y(x,y) + z^3\phi_y(x,y),$$
$$w(x,y,z) = w_0(x,y) + z^2\zeta_z(x,y) \tag{3}$$

This theory employs three-dimensional constitutive equations involving all nine orthotropic elastic constants. For the purpose of identification, reliable estimates of the transverse Young's modulus E_3 and Poisson's ratios v_{13} and v_{23} cannot be obtained due to the small significance on the vibration frequencies of these parameters. Therefore, the free parameters to be identified using this model are as for model I: $\theta_{II} = \{E_1, E_2, G_{12}, v_{12}, G_{13}, G_{23}\}^T$. The remaining parameters, E_3, v_{13} and v_{23} are constrained, either individually or by relating them to the free parameters.

Theory III

For the in-plane vibration, a simple displacement field is chosen which neglects the transverse normal strain:

$$u(x,y,z) = u_0(x,y), \quad v(x,y,z) = v_0(x,y), \quad w(x,y,z) = 0 \tag{4}$$

Assuming plane stress, the parameter vector is defined by the four in-plane constants only, $\theta_{III} = \{E_1, E_2, G_{12}, v_{12}\}^T$.

Approximate solutions of these theories for the free vibration are obtained using the Ritz method. The corresponding models are termed I, II and III, respectively. Details and performance of the numerical models I and II can be found in [9].

THEORETICAL RESULTS

Model errors inevitable affect the identification by introducing systematic errors in the parameter estimates. None of the models produce exact solutions, but previous comparisons with computationally very intensive 3-D finite element calculations have shown that model II yields very accurate frequency results for single layer plates that are considered here [9]. It seems reasonable to assume that the systematic errors associated with model II is negligible for such plates. Therefore, the more advanced model II may be used as a reference against which the performance of the previous used model I can

be compared. This is done by generating a set of natural frequencies with model II. The following test values (units omitted) are used for the orthotropic elastic constants: $E_1 = 100$, $E_2 = 10$, $\nu_{12} = 0.3$, $G_{12} = G_{13} = 5$, $G_{23} = 3.5$, $E_3 = 10$, $\nu_{13} = 0.3$, $\nu_{23} = E_2/2G_{23} - 1 = 3/7$. Then, based on the calculated frequencies, model I is used to identify the first six parameters. The results are shown in Table 1 for discrete values of a/h ranging from 40 to 8. The corresponding per cent differences between the estimates and the above prescribed values are shown in parentheses. The in-plane parameters are practically unaffected by using the less accurate model I. The error of G_{13} is slightly higher but still acceptable. In contrast, the estimates of G_{23} are significantly too high, about 5%. It is important to note that this error is nearly insensitive to the length-to-thickness ratio, despite the fact that the model errors increase for increasing a/h. This is because the sensitivities of the frequencies with respect to the transverse shear moduli also increase for increasing a/h, yielding in general a higher reliability of the estimates.

TABLE 1

Values of elastic constants estimated with model I from frequencies calculated with model II; $a/b = 1.8$, $\gamma = 0°$, $I = 12$

a/h	E_1	E_2	G_{12}	ν_{12}	G_{13}	G_{23}
∞	100	10	5	0.3	5	3.5
40	99.99 (-0.01%)	10.001 (0.01%)	4.997 (-0.06%)	0.2999 (-0.03%)	5.039 (0.77%)	3.677 (5.05%)
30	99.98 (-0.02%)	10.001 (0.01%)	4.996 (-0.08%)	0.2999 (-0.04%)	5.038 (0.76%)	3.686 (5.31%)
20	99.97 (-0.03%)	10.000 (0.00%)	4.994 (-0.12%)	0.2999 (-0.03%)	5.035 (0.70%)	3.697 (5.64%)
15	99.96 (-0.04%)	9.998 (-0.02%)	4.992 (-0.16%)	0.3001 (0.00%)	5.030 (0.59%)	3.704 (5.82%)
10	99.99 (-0.01%)	9.996 (-0.04%)	4.990 (-0.21%)	0.3006 (0.20%)	5.011 (0.22%)	3.708 (5.93%)
8	100.11 (0.11%)	9.998 (-0.02%)	4.990 (-0.20%)	0.3016 (0.52%)	4.988 (-0.24%)	3.703 (5.80%)

EXPERIMENTAL RESULTS

Identification results for a unidirectional glass/epoxy composite with fibres aligned along the plate axis ($\gamma = 0°$) are presented in the following. The plate dimensions were: $a = 180$mm, $b = 120$mm, $h = 10.1$mm, giving a length-to-thickness ratio of $a/h = 17.8$.

Following the technique described in [4], twelve flexural and nine in-plane natural frequencies were measured (Table 2). Six material parameters were identified from the flexural frequencies employing models I and II, respectively, and four in-plane

parameters were identified independently by using the in-plane natural frequencies and model III. The relative differences between measured and calculated frequencies obtained at the solutions are also given in Table 2. It is observed that the residuals are all very small. Note in particular that the residuals does not reveal that model I is less accurate than model II. Comparing the estimated parameters (Table 3), however, shows the trend found in the previous section and illustrates the effect of using the improved model II. For example, G_{23} is estimated 5.4% higher with model I than with model II.

As seen in Table 2, the in-plane vibration modes have significantly higher frequencies than the flexural vibration modes. Even though it is recognized that the epoxy material is viscoelastic, hence the material properties are frequency dependent, the agreement between the flexural and in-plane dynamic test results is very close. Also, a reasonable agreement with static tensile test results was found.

TABLE 2

Experimental frequencies and final residuals

i	f_i^e (Hz) flexural, [4]	e_i^* (%) [a] model I	e_i^* (%) [a] model II	f_i^e (Hz) in-plane	e_i^* (%) [a] model III
1	748.32	−0.158	−0.167	7069.6	0.117
2	1482.7	0.067	0.062	7277.1	0.119
3	1787.3	0.031	0.036	9361.2	0.008
4	2095.5	0.079	0.091	10293	0.193
5	2271.0	0.049	0.052	11089	−0.172
6	3678.0	0.149	0.156	12174	−0.129
7	3956.3	−0.151	−0.161	12606	−0.143
8	4411.3	−0.020	−0.011	13672	0.047
9	4649.1	−0.073	−0.073	14319	−0.038
10	5093.0	−0.040	−0.045	–	–
11	5915.8	0.077	0.076	–	–
12	6300.2	−0.008	−0.015	–	–

[a] Final residuals defined by: $e_i^* = 100 \times \left(f_i^e - f_i(\theta^*) \right) / f_i^e$ where "*" denotes solution.

TABLE 3

Elastic constants of unidirectional glass/epoxy composite

Method	E_1 (GPa)	E_2 (GPa)	G_{12} (GPa)	v_{12}	G_{13} (GPa)	G_{23} (GPa)
Identification						
Flexural, model I, [4]	42.7	11.5	4.61	0.296	4.74	4.26
Flexural, model II [a]	42.7	11.5	4.62	0.297	4.68	4.04
In-plane, model III	43.2	11.6	4.72	0.287	–	–
Static tensile tests, [4]	43.4	10.2	–	0.320	–	–

[a] With constraints: $E_3 = E_2$, $v_{13} = v_{12}$, $v_{23} = E_2/2G_{23} - 1$.

CONCLUSION

An advanced higher-order plate theory has been implemented in a procedure for identifying material constants of thick composite plates. The theory employs three-dimensional constitutive relations involving all nine orthotropic elastic constants. Since only the four in-plane constants and the two transverse shear moduli are considered as free parameters some constraints must be prescribed for the remaining three constants. The improved model has resulted in more accurate estimates of the transverse shear moduli. A less accurate model previously used in the identification method was shown to overpredict the transverse shear moduli whereas the in-plane parameters were practically unaffected by the model errors.

For specimens of a certain size, in-plane natural frequencies can be measured with a similar accuracy and ease as the flexural frequencies. In this way, an independent dynamic characterization of the in-plane elastic constants has been established. Experimental results obtained by the flexural and in-plane dynamic test methods have shown good agreement.

REFERENCES

1. Pedersen, P., Frederiksen, P. S. "Identification of orthotropic material moduli by a combined experimental/numerical approach." *Measurement* **10**, pp. 113-118 (1992).
2. Ayorinde, E. O., Gibson, R. F. "Elastic constants of orthotropic composite materials using plate resonance frequencies, classical lamination theory and an optimized three-mode Rayleigh formulation." *Composite Engineering* **3**, pp. 395-407 (1993).
3. Moussu, F., Nivoit, M. "Determination of elastic constants of orthotropic plates by a modal analysis/method of superposition." *Journal of Sound and Vibration* **165**, pp. 149-163 (1993).
4. Frederiksen, P. S. "Experimental procedure and results for the identification of elastic constants of thick orthotropic plates." *DCAMM report no. 506*, Technical university of Denmark, 18 p. (1995).
5. Frederiksen, P. S. "Identification of elastic constants including transverse shear moduli of thick orthotropic plates." *DCAMM report no. 500*, Technical university of Denmark, 25 p. (1995).
6. Frederiksen, P. S. "Design of optimal experiment for the estimation of elastic constants from plate natural frequencies." *Proceedings of the 2nd International Conference on Inverse Problems in Engineering: Theory and Practice, Le Croisic, France* (1996).
7. Reddy, J. N. "A simple higher-order theory for laminated composite plates." *Journal of Applied Mechanics* **51**, pp. 745-752 (1984).
8. Lo, K. H., Christensen, R. M. and Wu, E. M. "A high-order theory of plate deformation." *Journal of Applied Mechanics* **44**, 663-676 (1977).
9. Frederiksen, P. S. "Single-layer plate theories applied to the flexural vibration of completely free thick laminates." *Journal of Sound and Vibration* **186**, pp. 743-759 (1995).

STABLE ALGORITHMS OF THE METHOD OF INITIAL FUNCTIONS IN THE ANALYSIS OF THICK LAMINATED COMPOSITE STRUCTURES

S. M. GALILEEV[1], A. V. MATROSOV[2]

[1] Department of Mechanical Engineering, University for Water Communications, 5/7 Dvinskaya Street, S. Petersburg, 198035, Russia

[2] Department of Hydraulic Engineering, University for Water Communications, S. Petersburg, Russia

INTRODUCTION

The method of initial functions (MIF) enables a number of static and dynamic problems of homogeneous and layered anisotropic plates to be solved without employing any hypotheses about the character of the stress and strain state of the structure. Its computational implementation using trigonometric series for an approximation of the initial functions allows to find exact solutions which comply with specific boundary conditions on the crossing surface of the plate. These boundary conditions depend on a kind of trigonometric functions in the expansions of the initial functions.

On a computational realization of MIF using trigonometric series the algorithm of the method has a computational instability which shows itself in an ill-conditioned matrix of linear algebraic equations for finding coefficients in trigonometric expansions of unknown initial functions under higher harmonics.

This fact restrains an application of the MIF for analysis of plates under local and distributed loads.

In the present paper, two computationally stable algorithms of the MIF are presented. The developed algorithms ensure that the new static and dynamic problems of multi-layered plates can be solved applying the method of initial functions.

TRADITIONAL ALGORITHM OF THE METHOD OF INITIAL FUNCTIONS

Consider a linearly-elastic anisotropic thick plate with 21 elastic constants A_{ij} in the rectangular coordinate system XYZ of dimensions $a \times b$ in the coordinate plane XY and thickness $z = h$. Basic equations of the MIF may be expressed as [1]

$$U = LU^0, \qquad (1)$$

where $U = \{u, v, w, \sigma_z, \tau_{yz}, \tau_{xz}, \sigma_x, \sigma_y, \tau_{xy}\}$ is a vector of displacements and stresses the entries of which are functions of variables x, y, z; $U^0 = \left\{\tau_{xz}^0, \tau_{yz}^0, \sigma_z^0, w^0, v^0, u^0\right\}$ is

a vector of initial functions of variables x, y determined on the initial surface $z = 0$; $L = [L_{ij}], i = 1, ..., 9; j = 1, ..., 6$ is a matrix of differential operator functions of the MIF.

Usually not all of the initial functions are known. They can be found satisfying the boundary conditions on the bottom surface $z = h$.

Assume that the loading on the top surface $z = 0$ and bottom one $z = h$ are given and characterized by the vectors $U_\sigma^0 = \left\{ \tau_{xz}^0, \tau_{yz}^0, \sigma_z^0 \right\}$ and $U_\sigma^+ = \left\{ \tau_{xz}^+, \tau_{yz}^+, \sigma_z^+ \right\}$ correspondingly. Using the standard procedure of the method [2] and satisfying the conditions on the surface $z = h$, the system of differential equations for finding unknown initial displacements $U_W^0 = \{w^0, u^0, v^0\}$ may be obtained as

$$L_W^+ U_W^0 = U_\sigma^+ - L_\sigma^+ U_\sigma^0, \tag{2}$$

where $L_W^+ = [L_{ij}]_h, i, j = 4, 5, 6$; $L_\sigma^+ = [L_{ij}]_h, i = 4, 5, 6; j = 1, 2, 3$ are the matrices of operator functions L_{ij} determined when $z = h$.

Expanding the initial functions U_W^0, U_σ^0 and the functions on the bottom surface U_σ^+ into the trigonometric series and denoting one term as

$$\begin{aligned} U_\sigma^0 &= T_\sigma \tilde{U}_\sigma^0 \\ U_W^0 &= T_W \tilde{U}_W^0 \\ U_\sigma^+ &= T_\sigma \tilde{U}_\sigma^+, \end{aligned} \tag{3}$$

where $T_\sigma = \lceil s_m c_n, c_m s_n, s_m s_n \rfloor$, $T_W = \lceil s_m c_n, c_m s_n, s_m s_n \rfloor$ are the diagonal matrices, $\tilde{U}_\sigma^0 = \left\{ \tau_{1mn}^0, \tau_{2mn}^0, \sigma_{mn}^0 \right\}$, $\tilde{U}_W^0 = \left\{ w_{mn}^0, v_{mn}^0, u_{mn}^0 \right\}$, $\tilde{U}_\sigma^+ = \left\{ \tau_{1mn}^+, \tau_{2mn}^+, \sigma_{mn}^+ \right\}$ are the numerical vectors, $s_m = \sin \alpha_m x$, $c_m = \cos \alpha_m x$, $s_n = \sin \alpha_n y$, $c_n = \cos \alpha_n y$, $\alpha_m = \pi m / a$, $\beta_n = \pi n / b$, the equations (1) become algebraic and the governing differential equations (2) go into linear algebraic equations for finding coefficients of the unknown initial functions $\tilde{U}_W^0$ in the expansion (3)

$$\tilde{L}_W^+ \tilde{U}_W^0 = \tilde{U}_\sigma^+ - \tilde{L}_\sigma^+ \tilde{U}_\sigma^0, \tag{4}$$

where $\tilde{L}_W^+$, $\tilde{L}_\sigma^+$ are the numerical matrices received as a result of utilizing the operator functions in the matrices L_W^+, L_σ^+ on the initial functions (3) when formally substituting $\partial_1^2 = -\alpha_m^2$ and $\partial_2^2 = -\beta_n^2$ where $\partial_1 = \partial / \partial x$, $\partial_2 = \partial / \partial y$ are differential operators in the entries of the matrices L_W^+, L_σ^+.

When m and n increase the matrix $\tilde{L}_W^+$ in the equations (4) becomes ill-conditioned and this algorithm of the MIF becomes unstable.

FIRST STABLE ALGORITHM

The computationally stable algorithms are based on the fact of a computer stability of the traditional algorithm of the MIF within a small neighborhood of the initial surface $z = 0$.

The plate is partitioned into an essential number of layers to maintain the stable computation in the first layer. Then the unknown entries in the vector U^0 are found using the traditional algorithm of the method while satisfying the boundary conditions on the bottom surface $z = h$. After this the displacements and stresses into the first layer can be computed and these computed values of the stresses on the bottom surface of the first layer are used as the boundary (initial) stresses for the plate which thickness is a sum of the thicknesses of second, third etc. layers, i.e. the layers from 2 to n make up this new plate. Then the coefficients of the unknown initial functions on the top surface of second layer of the given plate (it's the top one of the new plate) are found satisfying the boundary conditions on the bottom surface using again the traditional algorithm of the MIF for the new plate. The thickness of second layer (it's the first layer for the new plate) should make the computer stability for the calculation of the entries of the vector U. Such a procedure is repeated to the next layers.

This technique ensures the stable calculation along the thickness of the plate.

SECOND STABLE ALGORITHM

This algorithm is based on the Godunov's idea of improving the method of initial parameters for solving a system of linear differential equations [3].

Let us divide the plate into p-th layers. The thickness of each one is h_k, $k = 1, ..., p$; $h_1 + h_2 + \cdots + h_p = h$.

The stress and strain state of the first layer may be found using the equations (1). When the load on the initial surface is as (3) one can write the vector of displacements and stresses on the first layer in the form

$$U^1 = T\overline{L}\,C^0 \qquad (5)$$

where $\overline{L} = \left[\tilde{L}_1, \tilde{L}_2, \tilde{L}_3, \tilde{L}_0\right]$, $\tilde{L}_0 = \left[\tilde{L}_4, \tilde{L}_5, \tilde{L}_6\right]\tilde{U}^0_\sigma$, $C^0 = \{w^0_{mn}, v^0_{mn}, u^0_{mn}, 1\}$, $T = \left\lceil s_m c_n, c_m s_n, s_m s_n, s_m s_n, c_m s_n, s_m c_n, c_m c_n, c_m c_n, s_m s_n \right\rfloor$. Here $\tilde{L}_i$, $i = 1, ..., 6$ are the columns of the numerical matrix $\tilde{L}$ received after the substitution $\partial_1^2 = -\alpha_m^2$, $\partial_2^2 = -\beta_n^2$ in the matrix L from the equations (1).

Then the entries of the vector U^1 on the bottom surface $z = h_1$ of the first layer are calculated

$$U^1_{h_1} = T\overline{L}_{h_1}C^0$$

and the columns of the numerical matrix $\overline{L}_{h_1}$ are orthogonalized. By this procedure a (4×4) upper triangle matrix W_1 is produced such as

$$\overline{L}_{h_1} = \overline{L}^1 W_1, \qquad (6)$$

where $\overline{L}^1 = \left[\overline{L}^1_1, \overline{L}^1_2, \overline{L}^1_3, \overline{L}^1_0\right]$ is a (9×4) matrix with the orthogonal columns moreover the first three ones $\overline{L}^1_1, \overline{L}^1_2, \overline{L}^1_3$ are ortho-normalized.

151

To calculate the vector of displacements and stresses into the second layer the initial functions are taken as

$$U_0^1 = T^0 \overline{L}_+^1 C^1, \tag{7}$$

where $C^1 = \{w_{mn}^1, v_{mn}^1, u_{mn}^1, 1\}$ and $T^0 = [T_\sigma, T_W]$ is a diagonal matrix, $\overline{L}_+^1$ is the upper (6×4) block of the matrix $\overline{L}^1$ and the vectors C^0, C^1 are connected as

$$W_1 C^0 = C^1. \tag{8}$$

Then the vector of displacements and stresses on the bottom surface of the second layer $z = h_2$ may be derived as

$$U_{h_2}^2 = T \overline{L}_{h_2} U_0^1 = T \left(\overline{L}_{h_2} \overline{L}_+^1 \right) C^1. \tag{9}$$

Orthogonolizing the matrix $\left(\overline{L}_{h_2} \overline{L}_+^1 \right)$ we can find the matrices $\overline{L}^2, W_2$ and then the procedure (7)–(8) is repeated for the third layer and so on.

For the last p-th layer the vector U^p will be calculated as

$$\begin{aligned} U^p &= T \overline{L} \, \overline{L}_+^{p-1} C^{p-1}, \\ W_{p-1} C^{p-2} &= C^{p-1}. \end{aligned} \tag{10}$$

The entries of vector C^{p-1} are found by satisfying the boundary conditions on the bottom surface of the p-th layer of the plate $z = h_p$.

The entries of the vector of displacements and stresses for the k-th layer can be found as

$$U^k = T \left(\overline{L}_0^k + w_{mn}^{k-1} \overline{L}_1^k + v_{mn}^{k-1} \overline{L}_2^k + u_{mn}^{k-1} \overline{L}_3^k \right), \tag{11}$$

where the coefficients $w_{mn}^{k-1}, v_{mn}^{k-1}, u_{mn}^{k-1}$ are calculated using the recurrent relations

$$W_k C^{k-1} = C^k, k = p - 1, ..., 1 \tag{12}$$

from the solution of the linear algebraic equations (12) with the upper triangular matrix W_k.

Thus the equations (6)–(12) are the principal scheme of the stable algorithm of the MIF. The procedure of the orthogonalisation (6) is very important because the matrix $\left(\overline{L}_{h_p} \overline{L}_+^{p-1} \right)$ in the last layer is well-conditioned.

In this paper the equations of the algorithm are derived for the initial functions in the form (3) which are only one term in the expansion of the initial functions in trigonometric series. Applying this algorithm to every term of series the stable algorithm of the MIF will be obtained.

NUMERICAL EXAMPLES

In the application of the new algorithms of MIF we consider a ten-layered square plate $a \times a$ leaned at corners against square columns $b \times b$ under concentrated load
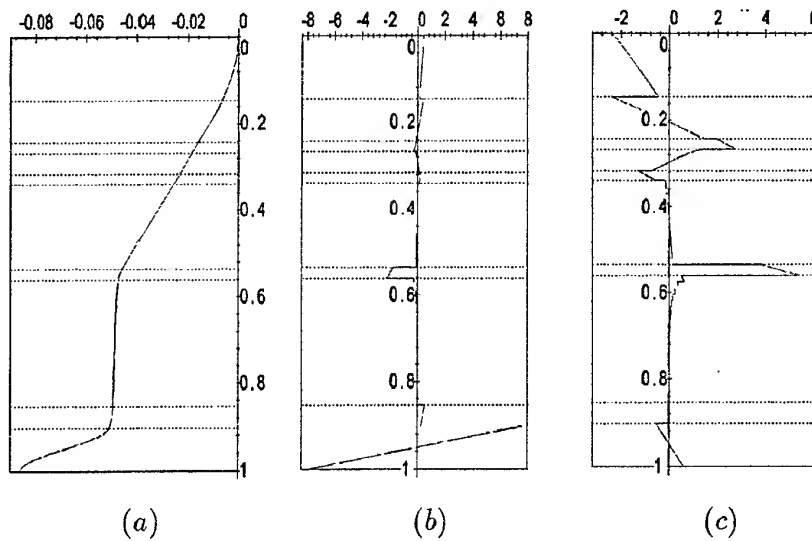
Figure 1: Dimensionless stresses of a ten-layered square plate in terms of the dimensionless thickness of the plate in various cross-sections: $(a) - \sigma_z/q$, $(b) - \sigma_x/q$ in the section $x = y = 0$ above a support, $(c) - \sigma_x/q$ in the centre of the plate $x = y = a/2$ under a concentrated load.

on the centre of the top surface. Such a load is modeled as uniformly distributed load q on a square rectangle $c \times c$. Geometry and loads of the plate are as follows: $a/h = 5$, $a/b = 6$, $a/c = 10$, $h_1 : h_2 : h_3 : h_4 : h_5 : h_6 : h_7 : h_8 : h_9 : h_{10} = 6 : 4 : 1 : 2 : 8 : 1 : 12 : 2 : 4$, where h, h_i – thicknesses of plate and layers. Physical and mechanical characteristics of layers are: *layer 1*, isotropic, $E = 0.315 \times 10^5$, $\nu = 0.2$, $\rho = 2500$; *layer 2*, transversally isotropic, $E = 10^5$, $E/E' = 5$, $E/G' = 20$, $\nu = \nu' = 0.1$, $\rho = 2000$; *layer 3*, isotropic, $E = 0.72 \times 10^5$, $\nu = 0.33$, $\rho = 2800$; *layer 4*, orthotropic, $E_x = 0.46 \times 10^5$, $E_y = 0.16 \times 10^5$, $E_z = 0.112 \times 10^5$, $G_{xy} = 0.045 \times 10^5$, $G_{yz} = 0.043 \times 10^5$, $G_{xz} = 0.033 \times 10^5$, $\nu_{xy} = 0.27$, $\nu_{xz} = 0.07$, $\nu_{yz} = 0.3$, $\rho = 1600$; *layer 5*, isotropic, $E = 0.72 \times 10^5$, $\nu = 0.33$, $\rho = 2800$; *layer 6*, transversally isotropic, $E = 10^4$, $E/E' = 3$, $E/G' = 5$, $\nu = \nu' = 0.1$, $\rho = 2000$; *layer 7*, isotropic, $E = 2.1 \times 10^5$, $\nu = 0.3$, $\rho = 7800$; *layer 8*, continuously inhomogeneous, $E = E_0 \exp(0.5z)$, $\rho = \rho_0 \exp(0.05z)$, $\nu = 0.2$, $E_0 = 10^4$, $\rho_0 = 2000$, $z \in [0, h_8]$; *layer 9*, isotropic, $E = 0.008 \times 10^5$, $\nu = 0.47$, $\rho = 1200$; *layer 10*, isotropic, $E = 0.315 \times 10^5$, $\nu = 0.2$, $\rho = 2500$. Units of elastic constants are MPa, unit of density – kg/m^3. Initial functions are expanded in trigonometric series using a cosine system. In this case boundary conditions on the cross surface could be treated as clamped edges. Number of terms in series is mn when $m = n = 30$. Inhomogeneous eighth layer is divided in 26 sub-layers to approximate variation of elastic constants. Some results are presented in Fig. 1. It can be seen that in the section above the corner support lower layers are compressed in z and x directions more significantly and that this part of structure is the most dangerous one for damage. In the centre of the plate under concentrated load the greatest compressed stresses are in the first and second layers and the great stretch stress is

153

Table 1: Dimensionless natural frequencies ω_i^* for ten-layered plate.

m, n	1,1	1,2	2,1	2,2	5,5	15,15	30,30
ω_1^*	0.939	1.939	1.899	2.732	10.304	58.104	121.052
ω_2^*	17.324	12.665	12.800	14.954	17.591	61.052	175.196
ω_3^*	45.192	17.450	17.357	18.274	36.459	93.788	178.832
ω_4^*	63.194	45.224	45.256	45.384	38.969	106.993	189.550

in the seventh layer where elasticity modulus are the greatest.

Also four sequential natural dimensionless frequencies $\omega^* = \omega a / \sqrt{E_1/2\rho_1(1+\nu_1)}$ for each form of vibration m, n are calculated. The results are in Table 1.

CONCLUSION

The developed algorithms extend the range of applicability of the method of initial functions. Plates and shells under distributed and locally concentrated loads can be solved using this exact analytical method. which allows to find exact solutions without making any assumptions about the stress and strain state of multi-layered plates and shells with an arbitrary number and sequence of layers which can significantly differ in their physical and mechanical properties. Such solutions can be used for estimating accuracy of various numerical methods. Also solutions for stable vibration of plates and shells under higher frequency loads can be found when these stable algorithms of the MIF are used.

REFERENCES

[1] Galileev S. M., Matrosov A. V. "Method of initial functions for three-dimensional analysis of anisotropic elastic structures." *Analysis of complicated structures*, LICI, Leningrad, pp.114-119 (1988) (in Russian)

[2] Adali S., Verijenko V. E., Galileev S. M., Matrosov A. V. "Method of initial function in the three-dimensional analysis of laminated composite structures." *Composites Modelling and Processing Science. Proc. of Ninth. Int. Conf. on Composite Materials(ICCM/9). Madrid, 12-16 July*, pp.23-30 (1993)

[3] Godunov S. G. "On numerical solution of boundary problem for linear system of differential equations." *Success of mathematics* **16**, #3, pp.171-174 (1961) (in Russian)

THREE DIMENSIONAL SOLUTIONS OF THE THEORY OF ELASTICITY IN MECHANICS OF COMPOSITE MATERIALS

S. M. GALILEEV[1], A. V. MATROSOV[2], V. E. VERIJENKO[3]

[1] Department of Mechanical Engineering, University for Water Communications, 5/7 Dvinskaya Street, S.Petersburg, 198035, Russia
[2] Department of Hydraulic Engineering, University for Water Communications, S.Petersburg, Russia
[3] Department of Mechanical Engineering, University of Natal, Durban, South Africa

INTRODUCTION

Practical requirements of composite mechanics call for drawing such mathematical methods which enable analytical solutions to be found for relatively simple elements of structures and investigate all details of stress-strain state (SSS). Thanks to these solutions we could reach necessary level of knowledge which is necessary to an understanding of the character of SSS in more complicated structures. Using this techniques we should be implied that such the solutions allow to receive complete information about the character of SSS of structures. This fact is a basis for designing of many technological decisions which determine an outlook of using new materials and structures from them. Completeness of the character of SSS for thick-walled structures is especially actual. Imperfections of technology could be seen exactly in these structures. Exact solutions of the theory of elasticity enable to find such information which allows us to estimate strength, stiffness, stability and reliability of designed structures.

Many problems which appear with connection with mentioned above tasks can be solved using the method of initial functions (MIF). This method allow to find three-dimensional solution of static and dynamic problems of the composite mechanics. In addition one of the main problem concerned with estimating of accuracy and reliability of approximate methods for analysis of composite structures is solved.

BASIC EQUATIONS OF THE METHOD OF INITIAL FUNCTIONS

In the theory of elasticity, the general solution of the problem of linearly-elastic anisotropic body with 21 elastic constants A_{ij} in the rectangular coordinate system XYZ may be expressed in terms of the arbitrary functions $F_i(x, y, z, t)$

$(i = 1, 2, 3)$ as

$$U = \begin{bmatrix} B \\ S \end{bmatrix} F \tag{1}$$

where $U = \{u, v, w, \sigma_z, \tau_{yz}, \tau_{xz}, \sigma_x, \sigma_y, \tau_{xy}\}$ is a vector of displacements and stresses; $F = \{F_1, F_2, F_3\}$ is a vector of arbitrary functions each of them satisfies the differential equation [1]

$$(D_0\partial_3^6 + D_1\partial_3^5 + D_2\partial_3^4 + D_3\partial_3^3 + D_4\partial_3^2 + D_5\partial_3 + D_6) F_i = 0; \ i = 1, 2, 3;$$
$$B = [B_{ij}], i, j = 1, 2, 3; \ S = [S_{ij}], i = 1, ..., 6, j = 1, 2, 3, \tag{2}$$

where $\partial_3 = \partial/\partial_z$; B_{ij}, S_{ij}, D_i –operators depending on the elastic constants A_{ij} , density ρ and the differential operators $\partial_1 = \partial/\partial x, \partial_2 = \partial/\partial y, \partial_t = \partial/\partial t$. From the equation (1), it is possible to derive the general solutions of the problem in the theory of elasticity such as those of Bussinesk-Galerkin, Papkovich-Neiber and of some others.

The functions $F_i(x, y, z, t)$ of displacements and stresses may be expressed in terms of initial functions which are the entries of the vector of stress and strain state, determined on the surface $z = 0$. After this the representation (1) allow to obtain the basic equations of MIF [2]

$$U = LU^0, \tag{3}$$

where $U^0 = \{\tau_{xz}^0, \tau_{yz}^0, \sigma_z^0, w^0, v^0, u^0\}$, $L = [L_{ij}], i = 1, ..., 9; j = 1, ..., 6$ is a matrix of operator functions of MIF.

Basic equations of the method for circular cylindrical shells may be expressed in the form (3) with $U = \{u, v, w, \sigma_r, \tau_{rz}, \tau_{r\theta}, \sigma_z, \sigma_\theta, \ \tau_{z\theta}\}$, $U^0 = \{u^0, v^0, w^0, \sigma_r^0, \tau_{rz}^0, \tau_{r\theta}^0\}$ and L_{ij} are operator exponent series in terms of the coordinate r ; the entries of the vector U are functions in terms of $r, \theta, \ z, \ t$ and the entries of the vector of initial functions U^0 are functions in terms of $\theta, \ z, \ t$. Similar equations are derived for spherical shells and unclosed shells [3].

A consideration of bound problems for plates and shells including layered ones allow to state and solve the problems from a common position and, it is extremely important, to estimate for sure the accuracy of solutions. For a large class of problems the MIF enables exact solutions to be derived without employing any hypotheses about the character of the stress and strain state of the structures.

Exact governing differential equations of the bending problem of an anisotropic plate subjected to the load on the top surface $U_\sigma^0 = \{\tau_{xz}^0, \tau_{yz}^0, \sigma_z^0\}$ and on the bottom one $U^+ = \{\sigma_z^+, \tau_{yz}^+, \tau_{xz}^+\}$ may be found in the form [4]

$$L_W^+ U_W^0 = U^+ - L_\sigma^+ U_\sigma^0, \tag{4}$$

$$(a) \qquad\qquad (b) \qquad\qquad (c)$$
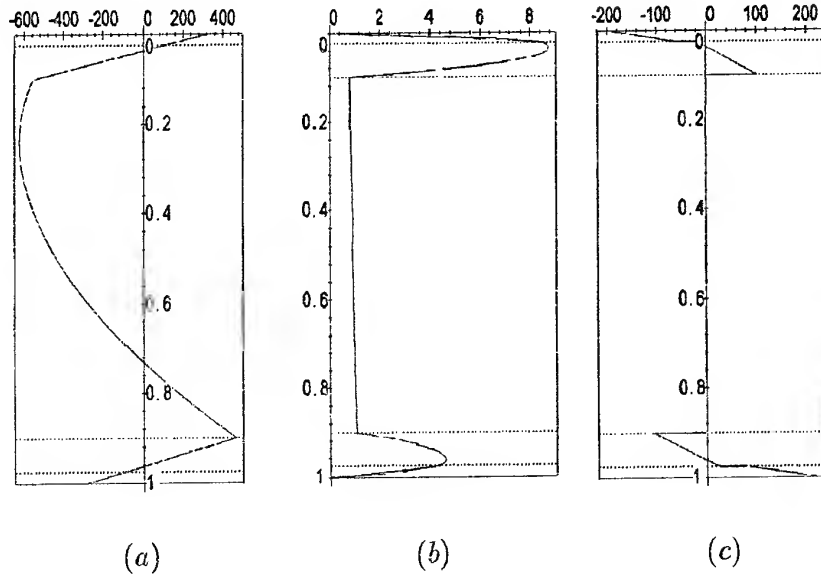
Figure 1: Graphs of the dimensionless displacement (a) in the x direction uE_1/q_0h and the dimensionless stress (b) τ_{xz}/q_0 in the section $x = 0$, $y = a/2$, and the dimensionless stress σ_x/q_0 in the section $x = y = a/2$ in terms of dimensionless thickness of plate z/h. Dot lines are boundaries of layers.

where $U_W^0 = \{w^0, v^0, u^0\}$, $L_W^+ = [L_{ij}]_h$, $i, j = 4, 5, 6$, $L_\sigma^+ = [L_{ij}]_h$, $i = 4, 5, 6, j = 1, 2, 3$ are the matrices of operator functions L_{ij} determined when $z = h$.

When the initial functions U^0, the functions U^+ are expanded in trigonometric series the system of differential equations (4) transforms to the system of three linear algebraic equations in terms of the unknown coefficients in expanding of the functions U_W^0 in trigonometric series.

Using (3), main equations of the MIF for the analysis of laminated composite plates may be derived. The layers are assumed to be perfectly bonded such that the interface conditions at any surface are expressed as

$$\left\{\tau_{xz}^k, \tau_{yz}^k, \sigma_z^k, w^k, v^k, u^k\right\} = \left\{\tau_{xz}^{k+1}, \tau_{yz}^{k+1}, \sigma_z^{k+1}, w^{k+1}, v^{k+1}, u^{k+1}\right\},$$

where the superscript k refers to the k-th layer. No restrictions on the thicknesses of layers, the number and sequence of layers, elastic constants and densities of layers are imposed [5].

The stresses and displacements of the k-th layer may be expressed in terms of the initial functions as

$$U^k = L^k L_0^{k-1} \cdots L_0^2 L_0^1 U^0, \tag{5}$$

157
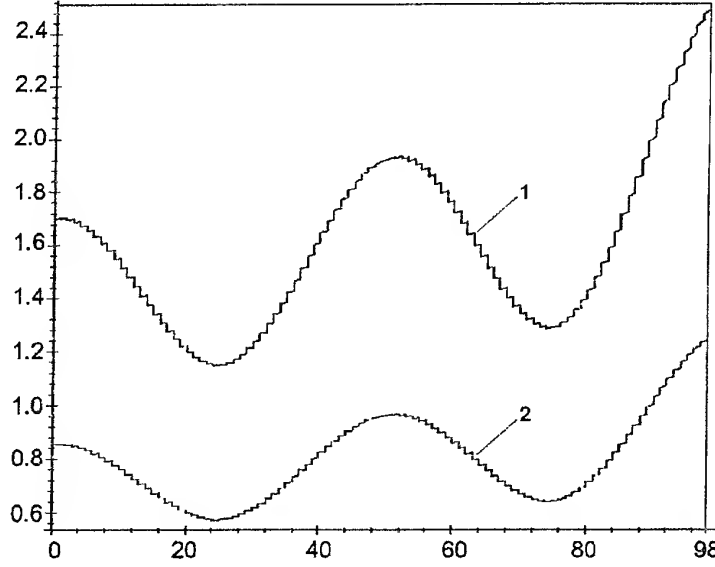
Figure 2: Variations of dimensionless circumferential stress σ_θ/q along different sections of the shell: $1 - z = 0$, $2 - z/l = 0.5$.

where the operator functions L_{ij}^k in the matrix L^k are determined for $z \in [0, h_k]$, the elastic constants A_{ij}^k and the density ρ_k of the k-th layer (for static problems $\partial_t \equiv 0$ or $\rho_k \equiv 0$); $L_0^n = \left[L_{ij}^n\right]$, $n = (k-1), ..., 1; i, j = 1, ..., 6$ are the matrices of operator functions determined when $z = h_n$.

We should note the MIF allows to take into account another types of contact between layers than mentioned above. In this case using displacements and stresses in going from one layer to another, one can model slipping of the layers, presence of friction forces, thin glue and another plies and also another details of later contact.

NUMERICAL EXAMPLES

As the first example let us find the displacements and stresses for a five–layered symmetrical simply supported square plate $(a \times a)$ under the uniformly distributed normal load $\sigma_z^0 = q$, $\tau_{xz}^0 = 0, \tau_{yz}^0 = 0$ on the top surface with the following layer characteristics (the subscripts refer to the layer number): $a/y = 5$, $h_1/h = h_5/h = 0.025$, $h_2/h = h_4/h = 0.075$, $h_3/h = 0.8$; $E_1 = E_5 = 7 \times 10^4 MPa$, $\nu_1 = \nu_5 = 0.3$ (aluminum); $E_2 = E_4 = 2.6 \times 10^4 MPa$, $E_2' = E_4' = 8.4 \times 10^3 MPa$, $G_2' = G_4' = 3 \times 10^3 MPa$, $\nu_2 = \nu_4 = 0.13$ (glass fiber and epoxy matrix);

$E_3 = 19.6 MPa$, $\nu_3 = 0.4$ (polystyrene). Notice that the layers number 2 and 3 have significantly different physical and mechanical characteristics. Calculations are made expanding initial functions in trigonometric series using sinus system. Some results are given in Fig. 1. It can be seen that the displacement in the x direction through the filler layer has nonlinear character and the bearing layers resist the full load.

Second example is concerned with the analysis of circular cylindrical laminated shell with the length $2l$ subject to uniformly distributed band load q on a part of the outer surface of the shell. The section $z = 0$ divides the shell on two equal parts. The shell consists of 100 layers, first 98 ones are transversely isotropic and 2 inner ones are isotropic. The load is symmetrical relative to a cross-section $z = 0$ with the width $2b$. The geometry of the shell is: $R/R_0 = 2$, $l/R_0 = 10$, $b/R_0 = 5$, $h_k/R_0 = 0.01$, where R, R_0 – outer and inner radius, h_k – a thickness of k-th layer. The layer characteristics: $E_k = (0.6 \times \sin(\pi(2k + 23)/50) + 2) \times 10^4 MPa$, $E'_k = (2.15 \times \sin(\pi(2k - 27)/50) + 3.55) \times 10^4 MPa$, $G'_k = (0.035 \times \sin(\pi(2k - 27)/50) + 0.535) \times 10^4 MPa$, $\nu_k = 0.015 \times \sin(\pi(2k - 27)/50) + 0.415$, $\nu'_k = 0.01 \times \sin(\pi(2k + 23)/50) + 0.078$, $k = 1, ..., 98$ (such a regularity in variation of physical and mechanical properties can be found in composite hardware); $E_{99} = 2 \times 10^5 MPa$, $\nu_{99} = 0.3$ (steel), $E_{100} = 2.4 \times 10^5 MPa$, $\nu_{100} = 0.3$ (steel). Here the cosine system of trigonometric functions are used. Some results[1] are presented in Fig. 2. Breaks in the stresses σ_θ can be seen in going from a layer to a layer. The stresses in two steel layers are not presented on Fig.2 because they have big values and graphs of stresses in composite material would be as a straight line. The values are as those: $\sigma_\theta^{99}/q = (19.45, 19.64)$, $\sigma_\theta^{100}/q = (23.54, 23.78)$ along the section $z = 0$ and $\sigma_\theta^{99}/q = (9.77, 9.86)$, $\sigma_\theta^{100}/q = (11.82, 11.94)$ along the section $z/l = 0.5$, where first and second numbers correspond to the top and bottom layer surfaces. This results show that the MIF is rather powerfully analytical method for analysis of composite structures on the micro-layered level.

CONCLUSION

The method of initial functions allows to find exact solutions without making any assumptions about the stress and strain state of multi-layered plates and shells with an arbitrary number and sequence of layers which can significantly differ in their physical and mechanical properties. Since the order of the governing linear system of equations is independent of the number of layers, thus enabling a combined macro- and micromechanical analysis to be undertaken. Presented results are exact solutions of bending problems for the plate and circular cylindrical shell under the given boundary conditions.

---

[1]They were calculated by Miroshnichenko I.N.

REFERENCES

[1] Galileev S.M., Matrosov A.V. "Operators and functionals of displacements and stresses in the theory of elasticity for an anisotropic body." *Analysis of space structures*, LICI, Leningrad, pp.154–161 (1986) (in Russian)

[2] Galileev S.M., Matrosov A.V. "Method of initial functions for three-dimensional analysis of anisotropic elastic structures." *Analysis of complicated structures*, LICI, Leningrad, pp.114-119 (1988) (in Russian)

[3] Galileev S.M., Miroshnichenko I.N. "Method of initial functions for analysis of anisotropic composite circular cylindrical shells.", *Shipbuilding industry:composite materials* **17**, pp.29-39 (1991) (in Russian)

[4] Adali S., Verijenko V.E., Galileev S.M., Matrosov A.V. "Method of initial function in the three-dimensional analysis of laminated composite structures." *Composites Modelling and Processing Science.Proc.of Ninth.Int.Conf.onComposite Materials(ICCM/9). Madrid, 12-16 July*, pp.23-30 (1993)

[5] Galileev S.M., Matrosov A.V., Verijenko V.E. "Method of initial functions for layered and continuously nonuniform plates and shells." *Mechanics of composite materials* **30**, #4, pp.531-539 (1994) (in Russian)

NON–CLASSICAL PROBLEMS OF COMPOSITE FAILURE

A.N.Guz'

Institute of Mechanics, Kiev, Ukraine

INTRODUCTION

The present article presents a quite brief description (as an annotation) results on investigation of non–classical problems and fracture mechanisms, obtained by the author and his co–authors in the Institute of Mechanics, Ukrainian Academy of Sciences, beginning with 1967. Three following problems and fracture mechanisms relative sequentially are considered: 1) fracture in compression along reinforcing elements in composite materials; 2) fracture in the form of bearing strain of ends in compression of composite materials; 3) fracture in the form of "separating into fibers" in compression or tension along reinforcing elements in composite materials.

Two following features are typical for the mentioned investigation of the author and his co–authors (in comparison with investigations of other authors).

The first – are investigations have been carried out with application of the most strict and accurate formulations within the framework of deformable bodies mechanics; so, in case of investigation of the phenomenon of stability loss the three-dimensional linearized theory of stability of deformable bodies was applied and in case of investigation of the stress–strain state three–dimensional equations of static of deformable bodies were applied.

The second – is the analysis of problems 1–3 of fracture mechanics, considered in the present article and related to composite materials has been carried out within the framework of the continual approximation (a homogeneous orthotropic body model with averaged constants – three–dimensional formulation) and within the framework of a piece-wise homogeneous medium model (three–dimensional equations for the filler and the binder, . conditions of continuousness at the boundary of interface).

We note, that the mentioned piecewise–homogeneous medium model (in three– dimensional formulation) is the most strict and accurate within the framework of deformable bodies mechanics as applied to composite materials; some refinements (specification of results) are possible at the expense of consideration of other boundary conditions on surfaces of interface and other determining equations for the filler and the binder.

It is typical the application of quite approximate calculating schemes for scientists, investigating nonclassical problems and fracture mechanics mechanisms; in case of composite materials such approximate schemes and models are used for an analysis of fracture

in microstructure of composite. The application of approximate schemes and models leads to significant qualitative errors and, in many cases to quantitative distinctions; therefore, it is complecated to carry out the analysis of the mentioned problems and mechanisms of fracture mechanics in case of using approximate schemes and models. The noted position determines the significance of results on investigation of nonclassical problems and mechanisms of fracture, which are obtained with sufficiently strict calculating schemes and models.

It should be noted, that the foregoing nonclassical problems and fracture mechanisms have not been adequately elucidated in the generalized monographic literature. They were not sufficiently considered in the nineth volume of the collective monographs [1,2] of encyclopedic character and they did not even mentioned in the recently published fourth volume manual [3] on fracture mechanics. Additional information on these and other results or nonclassical problems of fracture mechanics, obtained in the Institute of Mechanics (Kiev) may be obtained from the list of literature, presented in monographs [4-7].

1. FRACTURE OF COMPOSITES IN COMPRESSION ALONG REINFORCING ELEMENTS.

Fracture mechanism under consideration is realized in "the most clean" form in unidirectional fibrous and laminated composites in compression along reinforcing elements; it is also realized in orthogonal-reinforced composites and in composites with slight bending in a structure. In these cases the beginning of fracture process is identified with stability loss in a structure of a material, when the value of critical load (strength limit for this fracture mechanism) is determined not by dimensions and the shape of a specimen or a structural element, but by parameters characterizing the structure of composite (concentration of the filler and the binder etc.). A simple criterion of realisation of fracture mechanism under consideration exists – critical load, corresponding to stability loss in the structure of material, must be less then critical load, corresponding to stability loss of the whole specimen or a structural element.

In investigation (by virtue of internal character of instability) "an infinite" composite is considered and as a result of solving of a corresponding problem on eigenvalues the dependence of load on the parameter of wave formation is determined.

For investigation of the mentioned fracture mechanism many authors used various approximate models, based on applied two- and single-dimensional theories of plates and rods. Results, obtained using one of such very approximate approaches are placed in the nineth-volume monographs [1] and, in subsequent years in other monographs; the analysis of these results is presented in a monograph [4]. By virtue of complexity of the phenomenon under consideration, approximate models and approaches lead to essential qualitative errors and, in many cases, to quantitative differences; in this connection it is complecated to carry out the analysis of the mentioned fracture mechanism using approximate models.

For the first time in author's studies the analysis of the mentioned fracture mechanism has been carried out with application of the three-dimensional linearized theory of stability of deformable bodies for elastic (brittle fracture) and plastic (fracture of composites with a metal matrix) models. Such an approach eliminates the occurance of errors,

162

typical for various approximate models; main results, obtained by the author and his co-authors are presented in a monograph [4]. Two approaches with application on the three dimensional linearized theory of stability of deformable bodies are developed. The first approach is based on application of a homogeneous anisotropic body model with averaged constants; in this case, parameters, characterizing the structure of composite, are included in values of averaged constants. The second approach is based on application of a piecewise–homogeneous medium model, when, separately for the filler and the binder, equations of the three–dimensional linearized theory of stability of deformable bodies are used and conditions of continuousness of stress vectors and displacements on the boundary of interface of the filler and the binder are satisfied.

The continual theory under consideration, constructed within the framework of the mentioned first approach, along with determination of theoretical strength limits also provides a way of explanation of the nature of fracture for the case under consideration. For determination of the nature of fracture (fracture mechanism) within the framework of the mentioned theory the character of propagation of small perturbations, caused by the initial stage of fracture is considered.

In keeping with [4] the continual theory of internal and surface fracture, under consideration, in compression, the fracture process is represented in the following manner. Initially near–the–surface fracture occurs with quantities of external load slightly less quantities of a minimal over averaged shear modulus, which is determined as for a homogeneous anisotropic body. On further increasing of load (up to quantities slightly less over the value of a minimal averaged shear modulus) near defects internal fracture occurs. On reaching by external load the value of a minimal averaged shear modulus internal fracture occurs, which propagates avalanche–like (instantly) over planes, almost perpendicular to direction of external load.

Analogous results are also obtained for plastic fracture; in this case a tangent averaged shear modulus, calculated in the moment of stability loss, serve as an averaged shear modulus. On such approach (within the framework of the continual theory) long–term fracture of composites was also considered. Main results on the continual theory under consideration, corresponding to the mentioned at the beginning of this section the first approach, are presented in a monograph [4].

Within the framework of the second approach (a piecewise–homogeneous medium model) mechanisms of internal and near–the–surface fracture for fibrous and laminated composites with a polymer and metal matrix in unidirectional compression are investigated. For fibrous composites cases of one fiber (composite with a small concetration of the filler), for two fibers, infinite periodic series of fibers and a doubly–periodic system of fibers as applied to cases of internal and near–the–surface fracture are investigated. Main results are presented in a monograph [4] and are also partially incorporated into doctors thesis of I.Yu.Babich, Vic.N.Chekhov and Yu.N.Lapusta.

2. FRACTURE IN THE FORM OF BEARING STRAINS OF ENDS IN COMPRESSION.

Mechanisms with fracture in bearing strains of ends are sufficiently wide spread among various mechanisms, realized in fracture of composites. It lies in the fact, that, for in-

stance, in uniaxial compression of speciments and structural elements from composites local fracture of a material near ends occurs, and the mentioned fracture, therewith, does not propagate far from ends decreases in moving from them.

We note, that in experimental investigations of fracture mechanisms, considered in the previous section, design and technological techniques, excluding occurence of fracture mechanism bearing strains of ends, were utilized. As it was noted in the previous section, in particular, the development of bearing strains is eliminated by winding of specimens ends over lateral surfaces near ends and encapsulating them into casings from more rigid material, via expansion of a square of transverse section near ends etc. We also note, that experimental investigation of fracture phenomenon in bearing strains of ends is rather complex and not always leads to single valid results. It is associated with obtaining the result usually during experimental investigations (a photograph of a fractured near an end specimen or the quantity of strength limit), corresponding to already completed fracture process with bearing strains of ends. For investigation or description of the phenomenon under consideration it is necessary to obtain an information on initial stage of fracture (in an effort to find out reasons and a mechanism of a corresponding phenomenon); but a complex illustration of a destroyed near an end specimen (corresponding to the final stage of fracture) does not permit to identify process on the initial stage of fracture.

A mechanism of stability loss in the structure of composite, which has a character of near-the-surface stability loss near a loaded end with forms of stability loss, which attenuate in moving of the end, is the most probable on the initial stage of fracture in bearing strains of ends (for unidirectional composites or orthogonal-reinforced composites in loading along axes of symmetry). Using such interpretation of the phenomenon a series of results with application of various approximate calculating models, based on single- and two-dimensional models of plates and rods are obtained.

In the studies of the author, for the first time, the analysis of the mentioned fracture mechanism was carried out with application of the three-dimensional linearized theory of stability of deformable bodies. Within the framework of such an approach results for the continual theory and a piecewise-homogeneous medium model are obtained. The continual theory for elastic (brittle fracture) and plastic (fracture of a composite with a metal matrix) models is developed; theoretical strength limits, corresponding to fracture in bearing strains of ends, therewith, are determined. In conformity with the continual theory the fracture process in bearing strains of ends begins slightly earlier, than internal fracture, corresponding to fracture of the whole specimen. This conclusion is in complete agreement with experimental results and explaines the necessity to take additional design and technological techniques, partially described above, in order to obtain in experimental investigations results for a total (internal) fracture of the whole specimen. Results on the continual theory are presented in a monograph [4].

Using the mentioned approach a series of results for a piecewise-homogeneous medium models as applied to the simplest problems for laminated composites are obtained; these results were included into a doctoral thesis of Yu.V.Kohanenko.

3. FRACTURE IN THE FORM OF "SEPARATION OF FIBERS".

Fracture mechanism under consideration is not observed for homogeneous materials

(metals and alloys) and is specific to composites with a distinct direction of primary reinforcement. This mechanism consists in separation of a material into separate parts along direction of action of compressive load under condition, that compressive load is directed along the direction of reinforcing in unidirectional composites and in one of directions of reinforcing in composites with obviously expressed direction of primary reinforcement. Fracture mechanism, considered in this section, following [4], arbitrary we will call "separation into the fibers". We note, that the mentioned fracture mechanism was repeatedly observed in fracture of wood.

It is of interest to note, that similar phenomena are also observed in tension of a composite along the direction of primary reinforcement; references on sources, when cases of fracture "separation into fibers" type in tension, are presented in a monograph [4]. This note has sufficient importance in connection with association of some authors the occurance of "separation into fibers" in compression with a transverse elongation (at the expense of Poisson ratio) reaching limited quantities. The mentioned approach, therewith, in no way, can't explain the occurance of "separation into fibers" in tension, in the context of the transverse compression taking place in this case, and the material fracture along the direction of action of tensile load (perpendicular to transverse shortening). In this connection we come to conclusion, that in case of fracture ("separation into fibers") under consideration, a rather complex fracture mechanism in the structure takes place. We also note, that even in case, of one would think, successful application of a concept of limited transverse elongation in case of compression of unidirectional composites it remains an unclarified a mechanism of fracture in the structure, since the concept of limited transverse elongation operates with integral characteristic and the force does not act in this direction.

Fracture under consideration is a total fracture over planes and surfaces, which are located along reinforcing elements. Therefore, it is quite logical to anticipate (apparently, it is beyond doubts) that the mentioned type of fracture occurs as a result of action of forces, directed perpendicular to reinforcing elements. Origin of this fracture mechanism as well as in compression along reinforcing elements, as in a series of cases in tension also along reinforcing elements allow to exclude from the fracture mechanism under consideration, of various type phenomena, associated with stability loss. Nevertheless, in uniaxial compression–tension along reinforcing elements external load is applied only along reinforcing elements; therefore, the fracture type under consideration may originate only at the expense of internal forces (stresses) *which act perpendicular to the direction of external load and originate as a result of the influence of the microstructure of composite.* This, it is necessary to determine a mechanism of origin of the mentioned stresses in the microstructure of a composite and find out the possibility reaching of these stresses (in microstructure) limited quantities, corresponding to the mentioned fracture type, on condition, that stresses along the direction of reinforcement (along the direction of applied external loads) do not reach limited quantities.

It is know from experimental investigations on micromechanics, that in the structure of a composite owing to different reasons of technology, curvings of reinforcing elements originate; a series of photographs, illustrating the mentioned phenomenon are presented in a monograph [4] and other publications, partially mentioned in [4]. On this basis in studies of the author mentioned in [4] for the first time it was proposed the explanation of fracture mechanism, by "separation into fibers" *at the expense of internal stress, which originate due to curvings in microstructure and act on surface elements the normal to*

165

which coincides with the normal to curve interface of media.

We note, that in solving the mentioned problem in case of application of the continual theory it is necessary to construct such a theory, which would allow to determine selfbalanced (within curvatures) stresses; usually, continual theory provides determination of a stress on elements, dimensions of which essentially exceed dimensions of curvatures.

The above formulated problem has been positively solved within the framework of the three–dimensional continual theory; main results concerning this problem are presented in a monograph [4].

Within the framework of the strict three–dimensional piecewise–homogeneous medium model for laminated and fibrous composites the above formulated problem has been also positively solved in studies of the author and S.D.Akbarov. Results on this trend are presented in a monograph [6] and in the Special Issue [7], and are also included into S.D.Akbarov doctoral thesis.

It should be noted. that the above considered problem was for a periodic curvature. Analogous results are obtained as applied to local curvatures also, partially these results are reflected in a monograph [6] and in the Special Issue [7].

It should be noted, that investigations on non–classical problems of fracture mechanics in parallel with the Institute of Mechanics of Ukrainian Academy of Sciences are also carried in other scientific centers.

REFERENCES

1. *Composite materials*, V.1–8 / Broutman L.I. and Krock R.H., Chief Editors /, New York and London, Academic Press (1973–1976).

2. *Fracture. An Advanced Treatise*, V.1–7 / Liebowitz H., Chief Editor/, New York and London, Academic Press, (1968–1972).

3. *Fracture mechanics and strength of materials*, V.1–4 / Panasyuk V.V., Chief Editor /, Handbook, Kiev, Naukova Dumka, (1988–1990), (in Russian).

4. Guz' A.N. *Mechanics of fracture of composite materials in compression*, Kiev, Naukova Dumka, (1990), 632 pp. (in Russian).

5. *Mechanics of composite materials and structures elements*, V.1–3 / Guz' A.N., Chief Editor /, Kiev, Naukova Dumka, (1980–1983), (in Russian).

6. *Non–classical problems of fracture mechanics*, V.1–4 / Guz' A.N., Chief Editor /, Kiev, Naukova Dumka, (1990–1994), (in Russian).

7 Micromechanics of composite materials: Focus on Ukrainian research. *Special Issue. Applied Mechanics Reviews*, V.45, N 2 (1992), pp.13–101.

COMPOSITE STRUCTURES IN COMPRESSION ALONG PARALLEL INTERFACIAL CRACKS

IGOR A. GUZ

ICA, University of Stuttgart, Pfaffenwaldring 27, 70569 Stuttgart. Germany

INTRODUCTION

At the present time there is a large amount of studies devoted to the stability problems of composites and in the most of them it is assumed that structural elements of the material are rigidly attached. However, in real composites the usual concept of ideal contact between structural elements does not always correspond to reality. Various cases of delaminations in composites (such as cracks, non-adhesion, exfoliations,slippage zones and similar imperfections) can arise due to the manufacturing technology or operating conditions. Investigations of stability of laminated composites with intercomponent delaminations are fulfilled mostly within the scope of various approximative theories (such as continual theory) or applied schemes (bar, shell and others). But the most accurate results can be obtained only within the scope of TLTDBS [2]. Application of the model of piecewise-homogeneous medium and fundamental equations of TLTDBS, which are used in this paper, allows to eliminate the restrictions imposed on using the approximative theories and schemes as well as inaccuracies they involve. The present study is devoted to investigation of the internal instability [1] of composites with various interface defects.

PROBLEM STATEMENT

The general problem statement for a composite of an arbitrary laminated structure, which may consist of an arbitrary combination of layers and half-spaces, was considered in [4,6,7]. It was supposed there that the composite has interlaminar cracks and is situated in conditions of the plane strain state in compression along layers by "dead" loads applied at infinity in such a manner that equal shortenings along all layers are provided in direction of loading. (This is the uniform precritical state.) Cracks were simulated by mathematical sections regadless of reasons of their occurance. Layers of the investigated structure were assumed to have various mechanical characteristics and thicknesses. They were simulated by compressible or incompressible, elastic or elastic-plastic, isotropic or orthotropic (with elasto-equivalent directions which are parallel and perpendicular to interfaces) bodies. In the case of elastic-plastic layers the generalized conception of the continuous loading, which allows to neglect the changings of loading and offloading zones during the stability loss, was utilized. All investigations were fulfilled with the Lagrangian coordinate system (which is Cartesian one in the non-deformed state) using the
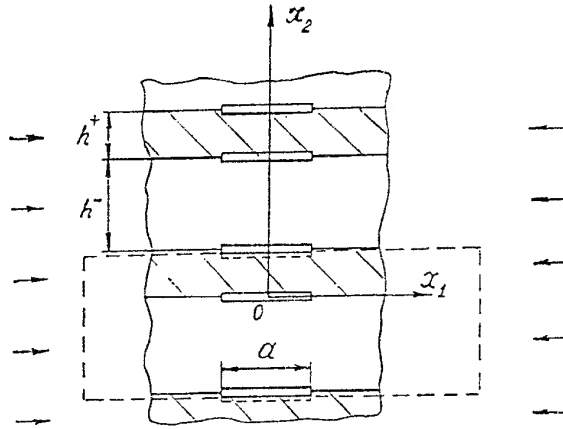
Figure 1: Periodical system of parallel interfacial cracks.

static method of investigation of static problems of TLTDBS [2]. Besides that, the classification of cracks was introduced in [4]. It was based on certain indiscrepant simplifications, connected not with the changing of equations, but only with geometrical characteristics of the composite and the cracks. Macrocracks, structural cracks and microcracks were discerned in this classification. Problems of internal and local instability for such structures had been solved for the case of absence of cracks (perfectly rigid-connected or sliding without friction layers [3]) and for the case of interlaminar microcracks [4-8] and structural cracks [6] within the scope of the above-mentioned exact approach.

Now let us consider a composite consisting of alternating compressible layers with thicknesses h^+ and h^-. Further all the values correspond to these layers will be marked with "+" and "−" indexes, respectively. Let parallel cracks (each of a length a, where a is of the same order as layer thicknesses) exist in the material, namely, one crack on each interface boundary (Fig. 1). Due to the classification of cracks [4] they are macrocracks. The material with cracks may be treated as a periodical structure with a period $T = h^+ + h^-$ along the $0x_2$ axis. Therefore, the stability equations [2,4] for perturbations of displacements (u_i) and stresses (t_{ij}) will be as follows $(n = 0, \pm 1, \pm 2, \ldots)$

$$\omega^+_{ij\alpha\beta}\frac{\partial^2 u^+_\alpha}{\partial x_i \partial x_\beta} = 0 \quad for \quad x_2 \in [nT, h^+ + nT];$$

$$\omega^-_{ij\alpha\beta}\frac{\partial^2 u^-_\alpha}{\partial x_i \partial x_\beta} = 0 \quad for \quad x_2 \in [-h^- + nT, nT] \tag{1}$$

As the material structure and applied loads are periodical along the $0x_2$ axis, it is obvious that forms of stability loss with a period along $0x_2$ axis, which is multiple to that of material structure, are to be considered $(k = 1, 2, \ldots; \quad i, j = 1, 2)$:

$$u_i(x_1, x_2) = u_i(x_1, x_2 + kT), \quad t_{ij}(x_1, x_2) = t_{ij}(x_1, x_2 + kT) \tag{2}$$

Let us specify the problem statement for $k = 1$, e.g. the form of stability loss with the period equal to that of material structure. In this case the equations (1)
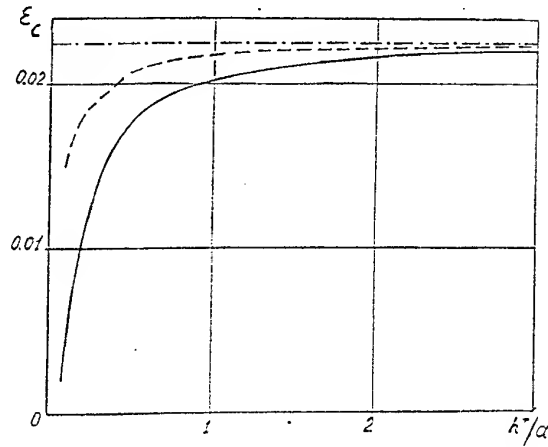
Figure 2: Critical strains for the case of $h^-/a = 1$, $c_f = 50\%$.

(when $n = 0$) with the following uniform boundary conditions and conditions of the attenuation for perturbations in moving from the cracks are to be solved ($i = 1, 2$):

$$u_i^+(x_1, 0) = u_i^-(x_1, 0), \quad t_{2i}^+(x_1, 0) = t_{2i}^-(x_1, 0) \quad for \quad x_1 \notin [-a/2, a/2]$$

$$t_{2i}^+(x_1, 0) = 0, \quad t_{2i}^-(x_1, 0) = 0 \quad for \quad x_1 \in [-a/2, a/2]$$

$$u_i^+(x_1, h^+) = u_i^-(x_1, -h^-), \quad t_{2i}^+(x_1, h^+) = t_{2i}^-(x_1, -h^-) \quad for \quad x_1 \notin [-a/2, a/2] \quad (3)$$

$$t_{2i}^+(x_1, h^+) = 0, \quad t_{2i}^-(x_1, -h^-) = 0 \quad for \quad x_1 \in [-a/2, a/2]$$

$$u^+(x_1, x_2)\,|_{x_1 \to \pm \infty} \longrightarrow 0; \quad u^-(x_1, x_2)\,|_{x_1 \to \pm \infty} \longrightarrow 0$$

The last condition in (3) follows from (2) when $k = 1$. (1),(3) are the eigenvalue problem with respect to the loading parameter which is included in components of the tensors ω^+ and ω^-. These tensors depend also on the governing equation for corresponding layer and are determined from [2].

The problems for the other forms of stability loss with a period equal to two, three, etc. periods of structure may be formulated similarly. It should be underlined, however, that for all the materials which were numerically investigated, realization of the form of stability loss with a period equal to that of structure, has been observed.

NUMERICAL RESULTS

Let us consider a composite with linear-elastic layers. The solving of the above-formulated problem will be carried out utilizing the method of finite differences. For this purpose the difference scheme having the first order of approximation is proposed. The difference eigenvalue problem is formulated in accordance with the differential problem of stability (1),(3) by the variational-difference method. This problem is a generalized completely determined eigenvalue problem, because a uniform precritical state is realised in a composite. The convergence of the mentioned difference scheme was proved earlier in [11] where the gradient iterative process was used for the finding of the least eigenvalue of the difference eigenvalue problem.
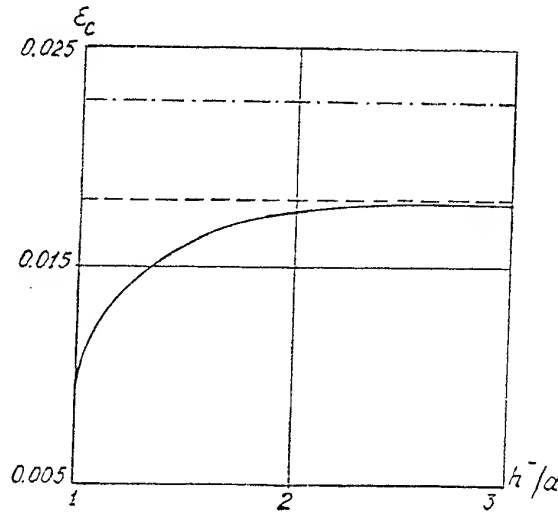
Figure 3: Critical strains for the case of $h^+/a = 0.2$, $c_f = 50\%$.

This iterative process is also applied in the present paper. Numerical results, which had been obtained by the above method for isotropic and orthotropic layers with one or several microcracks and with two parallel structural cracks, are presented, for instance, in [4-8].

Assume that each layer of the composite consists of a matrix reinforced by continuous parallel fibers. Therewith, directions of the reinforcement are mutually perpendicular in adjacent layers. The layers with thicknesses h^- are reinforced in the perpendicular to the plane $x_1 O x_2$ direction, the layers with thicknesses h^+ – in the direction of axis $O x_1$ (Fig. 1). This is so called composite of the lateral-torsional stacking. Let us suppose also that geometrical dimensions of structural elements inside of each layer are such that these layers are orthotropic homogeneous in continual approximation. Values of Young moduli and Poisson ratios for fibers (E_f, ν_f) and matrix (E_m, ν_m) are presented, for instance, in [9] for many constructional materials of a similar structure. Effective constants for each layer can be calculated according to well-known formulae if E_f, ν_f, E_m, ν_m and the volume concentration of fibers in layers (c_f) are known. These effective constants are used in defining of critical strains of the problem under consideration.

Numerical investigation has been carried out for the forms of stability loss with a period equal to one, two or three periods of structure $(k = 1, 2, 3$ in (2)). Critical strain for $k = 1$ has proved to be less than for other k for all considered values of elastic constants and layer thicknesses. In this connection, critical strain corresponding to the form of stability loss with $k = 1$ will be further refered to simply as critical strain in compression along periodical system of cracks. Values of critical strains are presented in Fig. 2,3 for the concerned problem of compression along periodical system of parallel macrocracks (continuous curves) in comparison with critical strains for the problem of compression along microcracks (hatched-dotted curves) and two parallel cracks (hatched curves). Calculations were fulfilled for

carbon fibers Tornel-300 ($E_f = 239GPa$, $\nu_f = 0.2$) in epoxy matrix ($E_m = 2GPa$, $\nu_m = 0.4$). As we see, values of critical strains are nearly the same, when thickness of one of the layers is rather large ($h^+ > 2$). In this case all three types of cracks may be treated as microcracks, e.g. the appropriate value of critical strain is determined by the properties of adjacent layers only. When $h^-/a > 2$ (Fig. 3), the values of critical strains for the cases of macrocracks and structural cracks almost coinside. In other words, when thickness of rigid layer is small and thickness of soft one is rather large, stability of periodical system of parallel crack is determined by stability of the pair of parallel cracks (structural cracks, using the classification [4]). The above-maid conclusions correspond to the obvious physical considerations on which the classification of cracks (dividing them into macrocracks, structural cracks and microcracks) is based.

It should be underlined that as against to stability loss in compression along microcracks and structural cracks (when local failure in crack vicinity may occur but the failure of the whole material may not happen at the same time), stability loss in compression along periodical system of cracks can cause failure of material as a whole. In the last case a phenomenon which is similar to the plastic hinge is observed.

CONCLUSIONS

The problem on instability of laminated composites in compression along periodical system of parallel interfacial cracks has been solved in this paper within the scope of the exact statement — the most exact results may be obtained only using the model of piecewise-homogeneous medium and equations of TLTDBS [2]. The eigenvalue problem with respect to the loading parameters has been formulated for cases of compressible, elastic and elastic-plastic, orthotropic and isotropic layers. Numerical results have been obtained for various sorts of orthotropic layers with the particular interface cracks utilizing the method of finite differences. In so doing, the difference scheme having the first order of approximation has been proposed. It has been concluded after the analysis of these results that the interaction of the cracks in the periodical system of parallel interlaminar macrocracks may cause the decrease of critical strains in several times to compare with the case of two parallel interlaminar cracks. This interaction has no influance when the layer thicknesses are two times greater than the crack lengths.

REFERENCES

[1] Biot, M.A. "Mechanics of incremental deformations." Willey, New York, USA (1965).

[2] Guz, A.N. "Foundations of three-dimensional theory of deformable bodies stability." Vyshcha Shkola, Kiev, Ukraine (1986) (In Russian).

[3] Guz, I.A. "Estimation of critical loading parameters for composites with imperfect layer contact." *International Applied Mechanics* **28**, pp. 291-296 (1992).

[4] Guz, I.A. "Computational schemes in three-dimensional stability theory (the piecewise-homogeneous model of a medium) for composites with cracks between layers." *International Applied Mechanics* **29**, pp. 274-280 (1993).

[5] Guz, I.A. "The strength of a composite formed by longitudinal-transverse stacking of orthotropic layers with a crack at the boundary." *International Applied Mechanics* **29**, pp. 921-923 (1993).

[6] Guz, I.A. "Stability and failure of layered composites with interface cracks." *Computational Mechanics '95. Vol. 2. Theory and Applications. (Edited by S.N. Atluri, G. Yagawa, T.A. Cruse).* Springer-Verlag, pp. 2317-2322 (1995).

[7] Guz, I.A. "Composite materials with delaminations: Numerical investigations of stability in compression." *Short Papers of Eighth Nordic Seminar on Computational Mechanics, Göteborg, November 17-18, 1995. (Edited by R. Larsson, N-E. Wiberg).* Deptartment of Structural Mechanics, Chalmers University of Technology, Sweden (1995).

[8] Guz, I.A., Kokhanenko, Yu.V. "Stability of the laminated composite material in compression along the microcrack." *International Applied Mechanics* **29**, pp. 702-708 (1993).

[9] "Handbook of fillers and reinforcements for plastics." (Edited by H.S. Katz and V. Milevski). Van Nostrand Reinhold Company, New York, USA (1978).

ANALYSIS OF GROWTH OF IRREGULAR (EUTECTIC) COMPOSITES *IN SITU*

E. Guzik[1] and J.W. Wyrzykowski[2]

[1] Faculty of Foundry Engineering, University of Mining and Metallurgy, Reymonta 23, 30-059 Kraków, Poland

[2] Faculty of Materials Science and Engineering, Warsaw University of Technology, Narbutta 85, 02-524, Warszawa, Poland

INTRODUCTION

Unidirectionally solidified eutectics (also known as *in situ* composites) are playing an increasingly important role in the development of new materials of the group „High technology". Among many different kinds of eutectics microstructures: regular (non - faceted / non - faceted) and irregular (non - faceted / faceted). The first is typical of metal - metal systems (a low melting entropy of the two phases) and the second is characteristic of the two important casting alloys, Fe - C and Al - Si (the one phase with a high melting entropy; graphite and silicon).Many researches have studied eutectic stable growth both theoretically and experimentally.

Hunt and Jackson [1] have explained the growth behaviour of the regular eutectic (an isothermal solid - liquid interface) by the following unique relationship between the total interface undercooling (ΔT), the growth rate (v) and the interlamellar or interfibre spacing (λ_1):

$$\Delta T = K_1 v \lambda_1 + K_2 / \lambda_1 \qquad (1)$$

In addition, applying the condition of growth at minimum undercooling [2] („operating point");

$$\{d(\Delta T) / d\lambda\}_{v=const} = 0 \qquad (2)$$

to equation (1) gives

$$\lambda_1^2 v = K_2 / K_1 = const \qquad (3)$$

where K_1 and K_2 can be evaluated from phase diagram and thermodynamic data

$$K_1 = \frac{\overline{m} C_0 P}{f_\alpha f_\beta} D \qquad \text{and} \qquad K_2 = 2\overline{m}\left(\frac{\Gamma_\alpha \sin \Theta_\alpha}{f_\alpha |m_\alpha|} + \frac{\Gamma_\beta \sin \Theta_\beta}{f_\beta m_\beta} \right) \qquad \text{(4 a \& b)}$$

$$\text{with} \quad \overline{m} = \frac{|m_\alpha| \cdot m_\beta}{|m_\alpha| + m_\beta},$$

$$\Gamma_i = \sigma_i / \Delta S^i,$$

where m_α and m_β liquid slopes, C_0 concentration difference („length") of eutectic tie - line, Γ Gibbs - Thomson coefficient, Θ wetting angle, f volume fraction, m liquidus slope, P function of volume fraction (see [1]), D diffusion coefficient in liquid, σ surface energy, ΔS volumetric entropy of fusion, i index for α or β phase

The equation (1) describe rather well the growth of regular eutectic, e.g. Al - Cu and Sn - Pb. For irregular eutectic systems, the experimental average values of λ obtained at a given growth rate v are significantly higher than predicted by equation (1). Irregular eutectics (e.g. Fe - C, Al - Si) characterized by the presence of a faceted phase, whose growth kinetics are strongly affected by planar defect mechanisms („stiffness" of growth) and therefore they are very anisotropic. A average spacing ($<\lambda> = (\lambda_1 + \lambda_2)\,0,5$ - shown Fig. 1) will then be determined by the ability of graphite or Si to branch (λ_2) or to produce a new flake to fill the gap. Growth of irregular eutectic has been studied theoretically by several authors [3 - 15].

A recent treatment of Magnin and Kurz [4] uses an averaged non - isothermal coupling condition over the whole solid - liquid interface. The growth parameters are related by the equation:

$$<\lambda>^2 v = \phi^2 K_2 / K_1 \qquad (5)$$

where

$\phi\,(= <\lambda>/\lambda_1)$ is a constant for a given system, e.g. Fe- C, $\phi = 5.4$ and Al- Si, $\phi = 2.3$ [7].

a)   b)
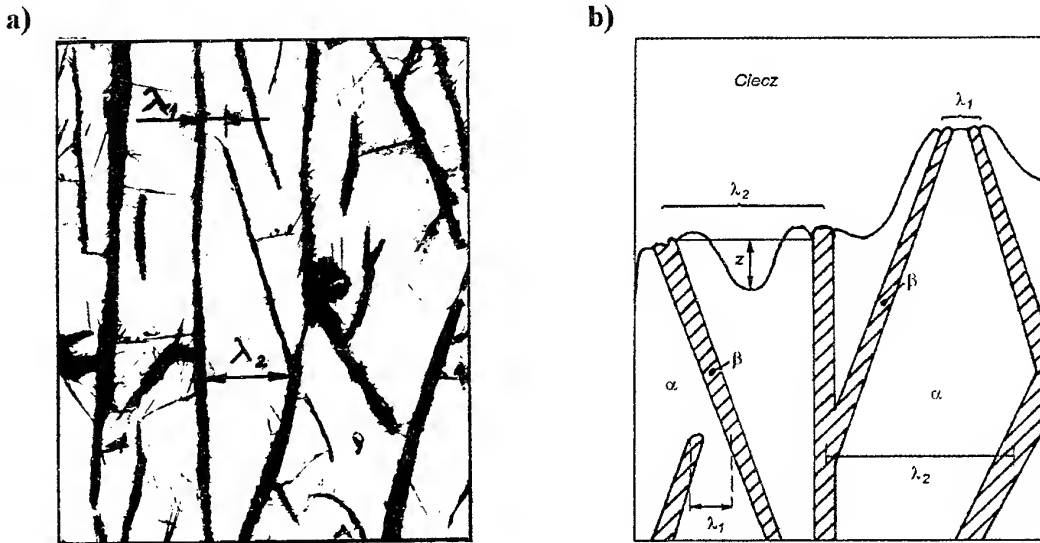
Fig. 1. Structure of graphite eutectic; γ(Fe) - graphite (a) [3] and schematic of irregular eutectic growth (b) [4]

In the paper theoretical (analytical) model of irregular composites *in situ* (oriented eutectic) are presented. The model takes into consideration the essential role of the faceted phase as the leading phase in the crystallization of such eutectic kind.

MATHEMATICAL MODEL

The lamellar growth irregular eutectic (non - faceted / faceted type; nf - f) will be cooperative, and the supposed solid - liquid (s/l) interface profile is schematically shown in Fig. 2; where z is the depth of the depression in the nonfaceted phase α and l is the protrusion of the leading faceted phase β.

If the imposed temperature gradient in the liquid (G), is constant over the s/l interface, the non - isothermal coupling condition can be expressed as [4]

$$\frac{1}{S_\beta}\int_{-S_\beta}^{0}\left[\Delta T_c(x)+\Delta T_r(x)+Gf_1(x)\right]dx = \frac{1}{S_\alpha}\int_{0}^{S_\alpha}\left[\Delta T_c(x)+\Delta T_r(x)+Gf_2(x)\right]dx = \overline{\Delta T} \quad (6)$$

where
$\Delta T_c(x)$ is the interface undercooling for solute diffusion [1];

$$\Delta T_c(x) = m_i\left[C_e - C(x,y = 0)\right], \quad (7)$$

and $\Delta T_r(x)$ is the undercooling due to interface curvature [1].

$$\Delta T_r(x) = -\Gamma_i \frac{d^2 f/dx^2}{\left[1+\left(df/dx\right)^2\right]^{3/2}}, \quad (8)$$

The shape of solid - liquid interface (parameters z and l) in the two - dimensional model are written as:

$$f_1(x) = \left[\frac{16l}{\lambda^4 f_\beta^4} - \frac{4\tan\Theta_\beta}{\lambda^3 f_\beta^3}\right]\cdot\left(x+S_\beta\right)^4 + \left(\frac{\tan\Theta_\beta}{\lambda f_\beta} - \frac{8l}{\lambda^2 f_\beta^2}\right)\left(x+S_\beta\right)^2 + l \quad (9a)$$

$$f_2(x) = \left(\frac{4\tan\Theta_\alpha}{\lambda^3 f_\alpha^3} - \frac{16z}{\lambda^4 f_\alpha^4}\right)\cdot\left(x-S_\alpha\right)^4 + \left(\frac{8z}{\lambda^2 f_\alpha^2} - \frac{3\tan\Theta_\alpha}{\lambda f_\alpha}\right)\left(x-S_\alpha\right)^2 - z \quad (9b)$$

where
parameters z and l shown in Fig. 2; C_e - eutectic concentration,
$f_1(x), f_2(x)$ is the biquadratic even function

Solutions equation (6) leads to [3]

$$\overline{\Delta T} = K_1 v\lambda + K_2/\lambda + GE'\lambda + G^2E''\lambda^3 + GE'''\lambda^3 v \quad (10)$$

where (for $G\lambda^2 f^2/240\,\Gamma < 1$):
E' and $E'' = f(f, \Gamma, \Theta, m, \overline{m})$,

$$E''' = f(\,C_o, D, P, f, \Pi\,\overline{m}\,),$$

$$\Pi_i^{'} = \sum_{n=1}^{\infty} \frac{1}{(n\Pi)^2} \sin(n\Pi f_i), \qquad [4]$$
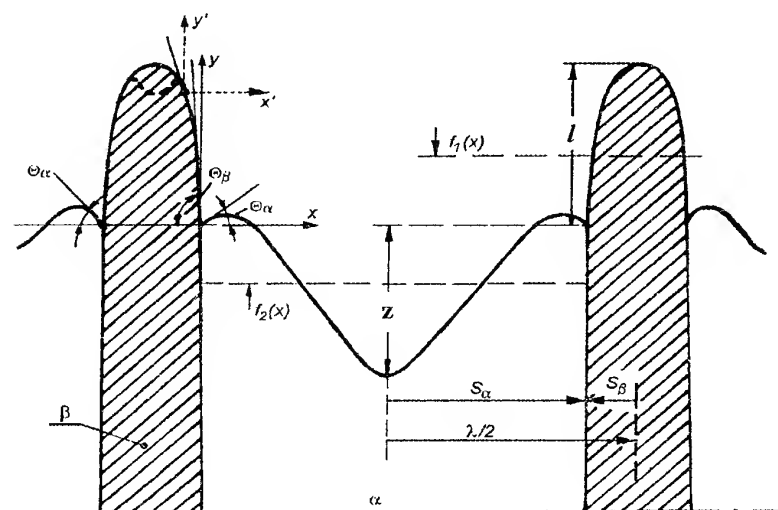
Fig. 2. The schematic solid - liquid interface of lamellar eutectic growth: $\lambda = 2(S_\alpha + S_\beta)$, Θ_β and Θ_α are the contacting angles of phases at the conjunction point

a)   b)

Fig. 3. Structures and shape of solid-liquid interface obtained in graphite eutectic, $v = 1,38 \cdot 10^{-5}$ (a) and $v = 5,56 \cdot 10^{-5}$ (b), cm/s

176

The operative points („operating range"[4]) on the growth curve is defined using a morphological criterion to characterize the branching (between λ_1 and λ_2, see. Fig. 1.) behaviour of the faceted phase. Differentiation of equation (10) leads to basic relationship on which the growth of the irregular eutectic depends
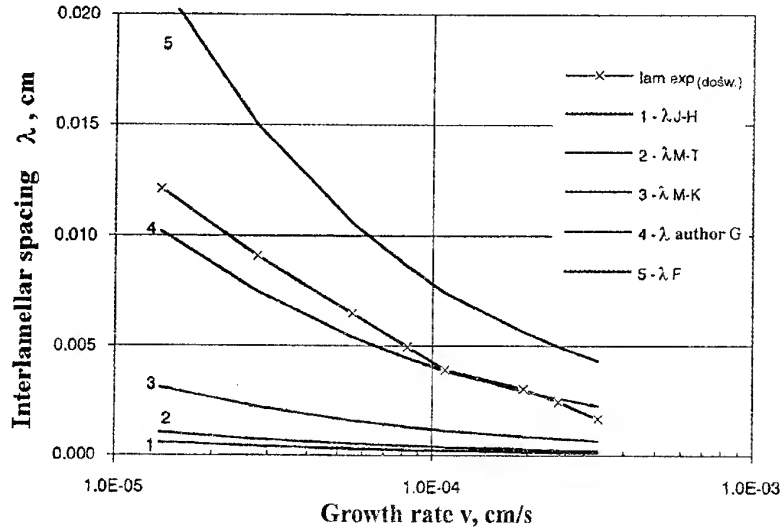
Fig. 4. Relationship of interlamellar spacing λ of graphite eutectic and growth rate v and comparison with theoretical models: 1 [1], 2 [7], 3 [4], 4 [equation 11], 5 [6]

$$3\langle\lambda\rangle^4\left(G^2E''+GE'''v\right)+\phi'^2\langle\lambda\rangle^2\left(K_1 v+GE'\right)=K_2\phi'^4 \tag{11}$$

where

$$\phi'=0,5+\frac{e}{2}\frac{\lambda'}{\lambda_1} \tag{12}$$

$$e=f\left(\Theta_\beta,f_\beta,G,m_\beta,C_0,v,D,P,\Pi_\beta\right);$$

$$\lambda'=f\left(\Gamma_\beta,\Theta,f_\beta,v,C_o,m_\beta,D,G,\Theta_\beta,\Pi_\beta,P\right);$$

$$\lambda_1=f\left(\Gamma_\alpha,\Gamma_\beta,f_\alpha,f_\beta,D,C_o,P,v,m_\alpha,m_\beta\right).$$

A new interpretation of the irregular eutectic growth theory (equation 11) is proposed. For the experimental verification of the elaborated model the results of the unidirectional crystallization of the eutectic under question as well as observations of the „freezed" solid - liquid interface of the graphite eutectic in the γ(Fe) - 4,28 %C alloys were utilized [3]. Figure 3 shows microstructure of quenched growing interface morphology of γ(Fe) - C graphite eutectic under stable growth condition. The experimental results of parameters λ are compared in Fig. 4 to the theoretical relationships (equation. 11). It was proved that the elaborated analytic model of the growth of the irregular eutectic, as compared with models described up to now in the literature [1, 4, 6, 7], allows to determine more precisely the interlamellar spacing λ in the eutectic. Good agreement has been obtained between theory (new model of irregular eutectic growth) and spacing λ measured in pure Fe - C eutectic alloys with lamellar structure.

CONCLUSIONS

An new analytical (equation 11) which describes irregular eutectic (irregular composite *in situ*) growth is presented. It is based upon Jackson and Hunt's and Magnin and Kurtz treatments. The proposed shape of the solidification front of irregular eutectic, characterized by a suitable function as well as applying the non-isothermal solid - liquid interface for modeling purposes allows calculation of the characteristic depression in the nonfaced phase (e.g. austenite) and the protrusion of the leading phase (e.g. graphite). Application of the model to the e.g. unidirectional graphite eutectic yields values for interlamellar spacing λ which are in good agreement with experiment.

REFERENCES

[1] Jackson K. A., Hunt J. D. „Lamellar and rod eutectic growth." Trans. Metall. Soc. AIME **236**, pp. 1129 - 1142 (1966).

[2] Tiller W. A. „Liquid metals and solidification." ADM, Ohio Cleveland (1958).

[3] Guzik E. „A model of irregular eutectic growth taking as an example the graphite eutectic in Fe - C alloys." Monograph **15**, AGH Kraków, pp. 1 - 87 (1994).

[4] Magnin P., Kurz W. „An analytical model of irregular eutectic growth and its application to Fe - C." Acta Metall. **35**, pp. 1119 - 1127 (1987).

[5] Fisher D. J., Kurz W. „A theory of branching limited growth of irregular eutectics." Acta Metall. **28**, pp. 777 - 792 (1980).

[6] Fraś E. „Theoretical basis of the grain growth of irregular eutectics."Arch. Hutn. **29**, pp. 79 - 93 (1984).

[7] Magnin P., Trivedi R. „Eutectic growth: a modification of the Jackson and Hunt theory." Acta Metall. Mater. **39**, pp. 453 - 467 (1991).

[8] Magnin P., Mason J. T., Trivedi R. „Growth of irregular eutectics and the Al - Si system." Acta Metall. Mater. **39**, pp. 469 - 480 (1991).

[9] Khan S., Ourdjini A., Elliott R. „Interflake spacing - growth velocity relationship in Al - Si and Al - CuAl$_2$." Mat. Science Technol. **8**, pp. 516 - 522 (1992).

[10] Khan S., Elliott R. „Solidification kinetics of the unmodified aluminium - silicon flake structure." Acta Metall. Mater. **41**, pp. 2433 - 2439 (1993).

[11] Liu J., Zhou Y., Shang B. „Lamellar eutectic stable growth - I. Modeling." Acta Metall. Mater. **38**, pp. 1625 - 1630 (1990).

[12] Liu J., Zhou Y., Shang B. „Lamellar eutectic stable growth - II. Experiment on Al - Si eutectic." Acta Metall. Mater. **38**, pp. 1631 - 1634 (1990).

[13] Li Y. X., Liu B. C. „Study of the solid - liquid interface during unidirectional solidification of cast iron." Trans. Am. Fundrym. Soc. **98,** pp. 483 - 488 (1990).

[14] Liu J., Elliott R. „Irregular eutectic solidification." Mat. Science and Engineering. **A173,** pp.129 - 132 (1993).

[15] Sens H., Eustathopoulos N., Camel D., Favier J.J. „Solidification of binary and Sr-modified Al-Si eutectic alloys: theoretical analysis of solute fields." Acta Metall. Mater. **40**, pp. 1783 - 1789 (1992).

STRUCTURAL ANALYSIS OF A COMPOSITE MULTI-RING FLYWHEEL FOR ENERGY STORAGE SYSTEM

Sung K. Ha[1] and Stephen W. Tsai[2]

[1] Dept. of Mech. Eng. Hanyang University, HaengDang-Dong, Sungdong-Ku, Seoul, 133-791, Korea (Fax: 82-2-281-4021)
[2] Dept. of Aero. and Astro. Stanford University

INTRODUCTION

The purpose of an energy storage system is to save energy when energy is plentiful, then return the energy when the energy source is not available. The conventional electrochemical energy storage has, however, the drawbacks of short life and low specific energy density. A kinetic energy storage system of high energy density and longer life has, thus, been being developed for many applications[1,2].

A flywheel energy storage system consists of a rotating rotor, a supporting device, and an energy charge/discharge device. The flywheel stores the electric energy as the inertial energy and converts the stored inertial energy into the electric energy whenever needed[2-4]. The total energy stored in the flywheel is defined as the multiplication of the mass moment of inertia of the rotor about the spin axis and the square of the angular velocity of the rotor[2,5]. In order to maximize the stored energy, the rotor has to be designed to rotate as high as possible without any material failure in the rotor. A composite material of high specific strength has thus been used for the rotor which is assembled with the multi-ring interference[4-6]. By using the multi-ring interference assembled composite ring, the prestress developed due to the interference can reduce the net stresses in the rotating rotor, and give the higher rotating speed and capability of storing the higher energy[5].

In this study, a structural analysis has been performed considering interferences, ply-by-ply variation of material properties and fiber orientations. The thick cylinder is assumed to be in the state of plane strain so that all the displacements and stresses are independent of the axial and circumferential directions. A general analytical solution for each ring has been obtained and expressed in terms of a symmetric 2 by 2 stiffness matrix where the displacement vector consists of radial displacements at inner and outer surfaces, and the force vector of radial directional normal stresses at inner and outer surfaces. The force vector, the normal stress was multiplied by its radius, which results in the symmetric stiffness matrix. For a rotor of N rings, there would be 2N unknown coefficients. The 2N equations are thus expressed using the conditions of the radial directional displacement and stress continuity at (N-1) interfaces and the boundary conditions at the inner and outer surface. Using the stiffness matrix the continuity conditions are easily considered and a system of symmetric N+1 equations is obtained. The stiffness matrix derived by other investigators are, however, unsymmetric and need the more expensive way of solving[7]. The radial distribution of the stresses and displacements are dependent upon the variation of the amount of interferences and ply

angle in each ply. An optimum design is thus performed maximizing the total stored energy. For that purpose the sensitivity of the strength ratio in each ring with respect to the interferences and the lay-up angles is derived by using the global stiffness matrix.

STRESS ANALYSIS AND OPTIMAL DESIGN

The composite flywheel rotor considered in this study is made of thick-layered multiple rings with different lay-up angle in each ring and different interference at each interface as shown in Figure 1. The flywheel rotor is assumed to be cylindrically orthotropic and the rotor is subject to the axisymmetric centrifugal force due to rotation and the internal and external pressures. The problem is thus treated as a plain strain problem ignoring the axial and circumferential displacements. Governing equations are solved and expressed in terms of the global matrix with the radial displacements to solve. Once the displacements are obtained, the stresses and strength ratios are calculated for all the rings. The optimization is then formulated maximizing the energy stored in the flywheel rotor. The sensitivities of the strength ratios and the radial displacements with respect to the interferences and lay-up angles are thus derived using the results of the stress analysis. The procedure of structural analysis and optimum design in this study is explained and shown in Figure 2.

Stress Analysis

The stress distribution in each ring is governed by the radial equilibrium equation, which is written in cylindrical coordinates as[8]

$$\frac{\partial \sigma}{\partial r} + \frac{\sigma_r - \sigma_\vartheta}{r} + \rho r \omega^2 = 0 \tag{1}$$

where σ_r and σ_θ are the radial and circumferential stresses, respectively, and ρ denotes a density, ω the rotational angular velocity. The nonzero stress-strain relation in the cylindrical coordinate system is written as

$$\begin{pmatrix} \sigma_\theta \\ \sigma_z \\ \sigma_r \\ \sigma_{\theta z} \end{pmatrix} = \begin{bmatrix} Q_{11} & Q_{12} & Q_{13} & Q_{16} \\ Q_{21} & Q_{22} & Q_{23} & Q_{26} \\ Q_{31} & Q_{32} & Q_{33} & Q_{36} \\ Q_{61} & Q_{62} & Q_{63} & Q_{66} \end{bmatrix} \begin{pmatrix} \varepsilon_\theta \\ \varepsilon_z \\ \varepsilon_r \\ \varepsilon_{\theta z} \end{pmatrix} \tag{2}$$

where σ, ε and $\mathbf{Q}$ are the stresses, strains and moduli in the cylindrical coordinate. In the axisymmetric case, the strains are defined by the r-directional displacement u_r.

$$\varepsilon_\theta = \frac{u_r}{r} \quad , \quad \varepsilon_z = 0$$

$$\varepsilon_r = \frac{\partial u_r}{\partial r} \quad , \quad \varepsilon_{\theta z} = 0 \tag{3}$$

After substituting Equations (2) and (3) into Equation (1), the r-directional displacement u_r and normal stress σ_r can be solved, i.e.,

$$U_r = -\rho\,\omega^2\,\varphi_0\,r^3 + C_1\,\varphi_1\,r^\kappa + C_2\,\varphi_2\,r^{-\kappa} \tag{4}$$

$$\sigma_r = -\rho\omega^2\,\varphi_3\,r^2 + C_1\,r^{\kappa-1} + C_2\,r^{-\kappa-1} \tag{5}$$

where

$$\kappa = \sqrt{\frac{Q_{11}}{Q_{33}}} \tag{6}$$

The parameters used in Equations (4) and (5) are defined as

$$\varphi_0 = \frac{1}{(9 - \kappa^2)\,Q_{33}} \tag{7}$$

$$\varphi_1 = \frac{1}{Q_{13} + \kappa Q_{33}} \tag{8}$$

$$\varphi_2 = \frac{1}{Q_{13} - \kappa Q_{33}} \tag{9}$$

$$\varphi_3 = \frac{3\,Q_{33} + Q_{13}}{(9 - \kappa^2)\,Q_{33}} \tag{10}$$

C_1 and C_2 in Equations (4) and (5) are unknown coefficients to be determined from the boundary conditions. In order to derive the stiffness matrix, the radial displacements at inner and outer surface are written in a displacement vector,

$$\mathbf{u} = \mathbf{f_u} + \mathbf{G}\,\mathbf{\Phi}\,\mathbf{C} \tag{11}$$

where

$$\mathbf{u} = \begin{pmatrix} U_{r_1} \\ U_{r_2} \end{pmatrix}, \qquad \mathbf{f_u} = -\rho\,\omega^2\,\varphi_0 \begin{pmatrix} r_1^3 \\ r_2^3 \end{pmatrix},$$

$$\mathbf{G} = \begin{bmatrix} r_1^\kappa & r_1^{-\kappa} \\ r_2^\kappa & r_2^{-\kappa} \end{bmatrix}, \quad \mathbf{\Phi} = \begin{bmatrix} \varphi_1 & 0 \\ 0 & \varphi_2 \end{bmatrix} \quad \text{and} \quad \mathbf{C} = \begin{pmatrix} C_1 \\ C_2 \end{pmatrix} \tag{12}$$

In Equation (12), r_1 and r_2 denote the radial coordinates at inner and outer surfaces of a ring. The radial normal stresses at those two surfaces can be also written in a force vector,

$$\mathbf{f_b} = \mathbf{f_\sigma} + \mathbf{\Gamma}\,\mathbf{G}\,\mathbf{C} \tag{13}$$

181

where

$$\mathbf{f_b} = \begin{pmatrix} -r_1\,\sigma_{r_1} \\ r_2\,\sigma_{r_2} \end{pmatrix}, \quad \mathbf{f_\sigma} = -\rho\,\omega^2\,\varphi_3 \begin{pmatrix} -r_1^3 \\ r_2^3 \end{pmatrix} \quad \text{and} \quad \mathbf{I}^* = \begin{bmatrix} -1 & 0 \\ 0 & 1 \end{bmatrix} \qquad (14)$$

A relation of stresses and displacements at inner and outer surface of each ring is derived by eliminating C_1 and C_2 in Equations (11) and (13). The derived equation can be expressed as

$$\mathbf{k\,u} = \mathbf{f_b} + \mathbf{f_\omega} \qquad (15)$$

The ring stiffness matrix $\mathbf{k}$ is

$$\mathbf{k} = \mathbf{I}^*\,\mathbf{G}\,\boldsymbol{\Phi}^{-1}\,\mathbf{G}^{-1}$$

$$= \frac{1}{\zeta_2} \begin{bmatrix} \kappa\,\zeta_1\,Q_{33} - \zeta_2\,Q_{13} & -2\,\kappa\,Q_{33} \\ -2\,\kappa\,Q_{33} & \kappa\,\zeta_1\,Q_{33} + \zeta_2\,Q_{13} \end{bmatrix} \qquad (16)$$

where

$$\zeta_1 = \zeta^{-\kappa} + \zeta^{\kappa}, \quad \zeta_2 = \zeta^{-\kappa} - \zeta^{\kappa}$$

$$\zeta = \frac{r_1}{r_2} \qquad (17)$$

Notice that, in defining the force term $\mathbf{f_b}$ of Equation (14), the stress component was multiplied by its radius, and the stiffness matrix $\mathbf{k}$ becomes symmetric. In Equation (15) $\mathbf{f_\omega}$ is related to the inertial force and defined as

$$\mathbf{f_\omega} = -\mathbf{f_\sigma} + \mathbf{k}\,\mathbf{f_u} = \begin{pmatrix} f_{\omega_1} \\ f_{\omega_2} \end{pmatrix} \qquad (18)$$

Equations (1)~(18) apply to any arbitrary ring. At each interface between two adjacent rings (e.g., i and $i+1$), the continuous radial traction and continuous radial displacement considering the interference δ should be satisfied;

$$\sigma_{r_1}^{(I+1)} = \sigma_{r_2}^{(I)} \qquad (19)$$

$$u_{r_1}^{(I+1)} = u_{r_2}^{(I)} + \delta^{(I)} \qquad (20)$$

Combining all the ring stiffness matrix equations by using the continuity equations yields the global stiffness matrix equation;

$$\mathbf{K\,U} = \mathbf{F}_b + \mathbf{F}_\omega + \mathbf{F}_\delta \qquad (21)$$

where

$$K = \sum_{i=1}^{N} k^{(i)} = \begin{bmatrix} K_{11}^{(1)} & \cdots & 0 & 0 & \cdots & 0 \\ \vdots & \ddots & \vdots & \vdots & \ddots & \vdots \\ 0 & \cdots & K_{22}^{(l-1)} + K_{11}^{(l)} & K_{12}^{(l)} & \cdots & 0 \\ 0 & \cdots & K_{21}^{(l)} & K_{22}^{(l)} + K_{11}^{(l+1)} & \cdots & 0 \\ \vdots & \ddots & \vdots & \vdots & \ddots & \vdots \\ 0 & \cdots & 0 & 0 & \cdots & K_{22}^{(N)} \end{bmatrix} \quad (22)$$

The global displacement vector **U** and the global force vectors are as followings;

$$U = \begin{pmatrix} u_{r_1}^{(1)} \\ \vdots \\ u_{r_1}^{(l-1)} \\ u_{r_1}^{(l)} \\ \vdots \\ u_{r_2}^{(N)} \end{pmatrix}, \qquad F_b = \sum_{i=1}^{N} f_r^{(i)} = \begin{pmatrix} -r_1 \sigma_{r_1}^{(1)} \\ 0 \\ \vdots \\ \vdots \\ 0 \\ r_{N+1} \sigma_{r_2}^{(N)} \end{pmatrix} \quad (23)$$

$$F_\omega = \sum_{i=1}^{N} f_\omega^{(i)} = \begin{pmatrix} f_{\omega_1}^{(1)} \\ \vdots \\ f_{\omega_2}^{(l-1)} + f_{\omega_1}^{(l)} \\ f_{\omega_2}^{(l)} + f_{\omega_1}^{(l+1)} \\ \vdots \\ f_{\omega_2}^{(N)} \end{pmatrix}, \qquad F_\delta = \sum_{i=1}^{N} f_\delta^{(i)} = \begin{pmatrix} f_{\delta_1}^{(1)} \\ \vdots \\ f_{\delta_2}^{(l-1)} + f_{\delta_1}^{(l)} \\ f_{\delta_2}^{(l)} + f_{\delta_1}^{(l+1)} \\ \vdots \\ f_{\delta_2}^{(N)} \end{pmatrix} \quad (24)$$

The force term f_δ in Equation results from the interferences between the adjacent rings satisfying the displacement continuity condition (Equation 20),

$$f_\delta^{(i)} = k^{(i)} \begin{pmatrix} 0 \\ \delta^{(i)} \end{pmatrix} = \begin{pmatrix} f_{\delta_1}^{(i)} \\ f_{\delta_2}^{(i)} \end{pmatrix} \quad (25)$$

where $\delta^{(i)}$ is the outer interference of i-th ring. Notice that the global stiffness matrix is symmetric, F_b has only the boundary pressures given at the inner and outer surfaces since the internal stresses were canceled out due to the stress continuity equation. F_ω are the internal inertial forces due to the rotation.

Now we can solve the system of N+1 equations and obtain the displacements $u^{(i)}$ at each interface. The strains and stresses are then calculated using the relationship in Equations (2) and (3). Once the stresses in the cylindrical coordinates are calculated, the on-axis strains and stresses can be calculated by transformation;

$$\sigma_{on} = Q_{on} \, \varepsilon_{on} = Q_{on} T \varepsilon \quad (26)$$

where **T** is a transformation matrix defined as

183

$$
T = \begin{bmatrix} \cos^2\theta & \sin^2\theta & 0 & \cos\theta\sin\theta \\ \sin^2\theta & \cos^2\theta & 0 & -\cos\theta\sin\theta \\ 0 & 0 & 1 & 0 \\ -2\cos\theta\sin\theta & 2\cos\theta\sin\theta & 0 & \cos^2\theta-\sin^2\theta \end{bmatrix} \tag{27}
$$

The failure of the material can then be accessed by using Failure Criterion; 3-dimensional Tsai-Wu quadratic failure criterion has been used[9],

$$
\sigma_{on}^{(l)\mathrm{T}}\,\widetilde{F}^{(l)}\,\sigma_{on}^{(l)} + \overline{F}\,\sigma_{on}^{(l)}\,R^{(l)} - R^{(l)2} = 0 \tag{28}
$$

Solving Equation (28) yields a strength ratio $R^{(i)}$ indicating the material failure with a value greater than 1. The strength parameters $\widetilde{F}$ and $\overline{F}$ are defined in terms of the material strengths;

$$
\widetilde{F} = \begin{bmatrix} \dfrac{1}{XX'} & -\dfrac{1}{2}\sqrt{\dfrac{1}{XX'}\dfrac{1}{YY'}} & -\dfrac{1}{2}\sqrt{\dfrac{1}{XX'}\dfrac{1}{YY'}} & 0 \\[2ex] -\dfrac{1}{2}\sqrt{\dfrac{1}{XX'}\dfrac{1}{YY'}} & \dfrac{1}{YY'} & -\dfrac{1}{2YY'} & 0 \\[2ex] -\dfrac{1}{2}\sqrt{\dfrac{1}{XX'}\dfrac{1}{YY'}} & -\dfrac{1}{2YY'} & \dfrac{1}{YY'} & 0 \\[2ex] 0 & 0 & 0 & \dfrac{1}{S^2} \end{bmatrix} \tag{29}
$$

$$
\overline{F} = \begin{bmatrix} \dfrac{1}{X} - \dfrac{1}{X'} & \dfrac{1}{Y} - \dfrac{1}{Y'} & \dfrac{1}{Y} - \dfrac{1}{Y'} & 0 \end{bmatrix} \tag{30}
$$

where X and X' are the tensile and compressive strengths in the fiber direction, Y and Y' in the matrix direction, and S the shear strength.

Optimization

The objective of this study is to design a flywheel rotor of composite materials which can have a maximum storage energy. In order to achieve the goal with the given inner and outer radii, interferences at each interface and ply angles in each ring are used as the design variables with constraints that each ring should not fail. Since, in the flywheel, motor/generator is usually installed inside of the rotor, the gap growth, i.e., the radial displacement of the inner surface should not exceed a given value u_o. The optimization is thus formulated as

Maximize ω^2

Subjected to $R^{(i)} < 1$ and $u_{r_1}^{(1)} < u_o$ \hfill (31)

Find ω^2, $\theta^{(i)}$, and $\delta^{(i)}$

where the superscript i is ranging from 1 to N.

The sensitivity analysis is performed on the strength ratio R and the displacements with respect to the design variables denoted by x_j, i.e., the angular velocity ω^2, the ply angles $\theta^{(i)}$, and the interferences $\delta^{(i)}$. Since the strength ratio R of each ring is a function of on-axis stresses, the sensitivity of the strength ratio R is calculated using the chain rule,

$$\frac{\partial R}{\partial x_j} = \frac{\partial R}{\partial \sigma_{on}} \frac{\partial \sigma_{on}}{\partial x_j} \tag{32}$$

where $\partial R / \partial \sigma_{on}$ is obtained using Equation (28),

$$\frac{\partial R}{\partial \sigma_{on}} = \frac{2\sigma_{on}^T \widetilde{F}^T + \overline{F}R}{2R - \overline{F}\sigma_{on}} \tag{33}$$

In Equation (32), $\partial \sigma_{on} / \partial x_j$ is now calculated using Equation (26);

$$\frac{\partial \sigma_{on}}{\partial x_j} = Q_{on} \frac{\partial T}{\partial x_j} \varepsilon + Q_{on} T \frac{\partial \varepsilon}{\partial x_j} \tag{34}$$

The derivatives of the transformation matrix T with respect to the ply angle $\theta^{(i)}$ can be calculated using Equation (27). The derivatives of the strains with respect to the design variables x_j are derived using the strain-displacement relations of Equation (3),

$$\frac{\partial \varepsilon}{\partial x_j} = \left[\frac{1}{r} \frac{\partial u_r}{\partial x_j} \quad 0 \quad \frac{\partial}{\partial x_j}\left(\frac{\partial u_r}{\partial r}\right) \quad 0 \right]^T \tag{35}$$

The derivatives of the radial displacement in Equation (35) can be now calculated using the global stiffness matrix Equation (21);

$$K\frac{\partial U}{\partial x_j} = \frac{\partial F_b}{\partial x_j} + \frac{\partial F_\omega}{\partial x_j} + \frac{\partial F_\delta}{\partial x_j} - \frac{\partial K}{\partial x_j}U \tag{36}$$

Since F_b is expressed by external pressures given at the inner and outer surfaces, its sensitivity vanishes. The other terms in the right hand side of Equation (36) are calculated using Equations (22) and (24),

$$\frac{\partial F_\omega}{\partial x_j} = \sum_{i=1}^{N}(-\frac{\partial f_\sigma^{(i)}}{\partial x_j} + \frac{\partial k^{(i)}}{\partial x_j}f_u^{(i)} + k^{(i)}\frac{\partial f_u^{(i)}}{\partial x_j}) \tag{37}$$

$$\frac{\partial F_\delta}{\partial x_j} = \sum_{i=1}^{N}(\frac{\partial k^{(i)}}{\partial x_j}\delta^{(i)} + k^{(i)}\frac{\partial \delta^{(i)}}{\partial x_j}) \tag{38}$$

185

$$\frac{\partial K}{\partial x_j} U = \sum_{i=1}^{N} \frac{\partial k^{(i)}}{\partial x_j} u_r^{(i)} \tag{39}$$

Equations (37)~(39) can be evaluated using the definitions in Equations (14), (16), (18) and (25). Hence, the derivatives of the radial displacement in Equation (36) can be now calculated using the right hand side term expressed in Equations (37)~(39) and the global stiffness matrix K which were LU decomposed in solving Equation (21). The second component in Equation (35) can be similarly obtained using Equations (2), (15) and (36).

For the calculation of optimization, the algorithms of the sequential linear programming(SPL) and modified feasible direction have been adopted with a golden section method and polynomial equation for a line search.

RESULTS AND DISCUSSION

The optimal design has been obtained using the stress and sensitivity analysis. All the parameters have been normalized so that they have the same order of magnitude; the stresses by the tensile strength X in the fiber direction and the length by the inner radius. The geometry of the rotor and the initial values are shown in Table 1. A composite material of T300/5208 (Graphite/Epoxy) has been used and its material properties are listed in Table 2[10]. The value of the gap growth u_o inside the ring is taken as 0.2mm. Four cases of different sets of design variables are considered; in the first case, only rotating speed ω is a design variable, in the second case, the rotating speed ω and ply angles $\theta^{(i)}$, in the third case, the rotating speed ω and the interferences $\delta^{(i)}$, the fourth case, ω, $\theta^{(i)}$ and $\delta^{(i)}$.

For each case, the maximum rotating speed and the corresponding SED are calculated and shown in Table 3; the maximum rotating speed is defined as the highest speed at which all the materials are safe. The effect of the interferences on the maximum rotating speed is much greater than that of the ply angles as shown in Table 3. The distribution of the ply angle calculated for cases 2 and 4 is shown in Figure 3 and the distribution of the interferences for cases 3 and 4 is also shown in Figure 4. The distribution of the stresses σ_θ, σ_z and σ_r for all the cases are calculated and shown in Figure 5. Notice that, in case 4, the radial stress is reduced while the circumferential stress increases. As a result, compared to the other cases, the strength ratios of more rings in the fourth case have reached the limit value 1 at the maximum rotating speed as shown in Figure 6. That implies that the radial stress is more critical than the other components of stresses. The distribution of the radial displacement is shown in Figure 7 where the inside radial displacement satisfy the optimal constraint as in Equation (31).

CONCLUSION

The ring stiffness matrix for the analysis of a multi-ring composite flywheel is derived and assembled into a symmetric global matrix so that the size of total equations is reduced and the continuity equations at each interface can be easily incorporated. The sensitivity analysis is also performed using the local and global matrices. It is found that

186

the more energy can be stored in the composite flywheel rotor using the multiple rings where the interferences and ply angles can vary in the radial direction. The optimal design has attained 2.4 times of total energy compared to the case of 0 degree layer and no interference. It is also noticed that the interferences are much more important than the ply angles in increasing the total energy without material failure.

It is expected that the more energy could be attained by varying the thickness of each ring as well. A state of generalized plane strain could be also incorporated by extending the dimension of the symmetric stiffness matrix to N+2.

REFERENCES

[1] Rodriguez, G. E., Studer, P. A. and Baer, D. A. "Assessment of Flywheel Energy Storage for Space Craft Power System." *NASA Technical Memorandum 85061* (1983)

[2] Khan, A. A. "Maximization of Flywheel Performance." M.S. Thesis, University of Maryland (1984)

[3] Mitchell Olszewski, Eisenhaure, D. B., Norman Beachley and Kirk, J. A. "Advenced Energy Systems-On the Fly or Under Pressure." *Mechanical Engineering,* June (1988)

[4] Kulkarri, S. "Energy and Technology Review." *Lawrence Livermore National Laboratory, UCRL-52000-82-3,* March (1982)

[5] Ries, D. M. "Manufacturing Analysis for a Composites Multi-Ring Flywheel." M.S. Thesis, University of Maryland (1991)

[6] Portnov, G.G. Composite Flywheels, *Structure and Design* (Edited by Herakovich C. T. and Tarnopollskii Y. M.), Vo. 2, Elseviser Science Publishing Company Inc., New York, U.S.A., pp. 531-582 (1989)

[7] Larry S. Chien and T. Tzeng "A Thermal Viscoelastic Analysis for Thick-walled Composites Cylinders." *Composite Material,* Vol. 29, No. 4, pp. 525-548 (1995)

[8] Lekhenitskii, S. G. *Anisotropic Plates* (Translated by Tsai, S. W. and Cheron, T.), Gordon and Breach Science Publishers Inc., New York, U.S.A., pp. 1-5, 106-116, 150-155 (1986)

[9] Tsai, S. W. *Composites Design,* Think Composites, Dayton, U.S.A. (1988)

[10] Tsai, S. W. and Hahn, H. T. *Introduction to Composite Materials,* Techonomic Co., Wesport, U.S.A., pp. 1-24 (1980)
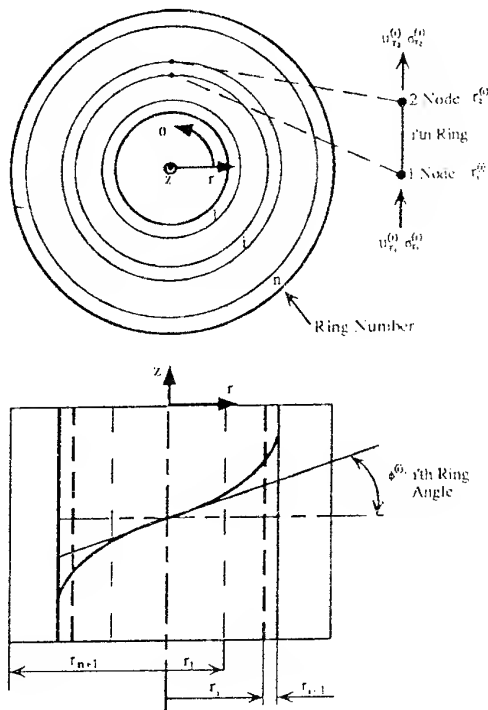
Fig. 1 Model of flywheel rotor and definition of I'th ring components
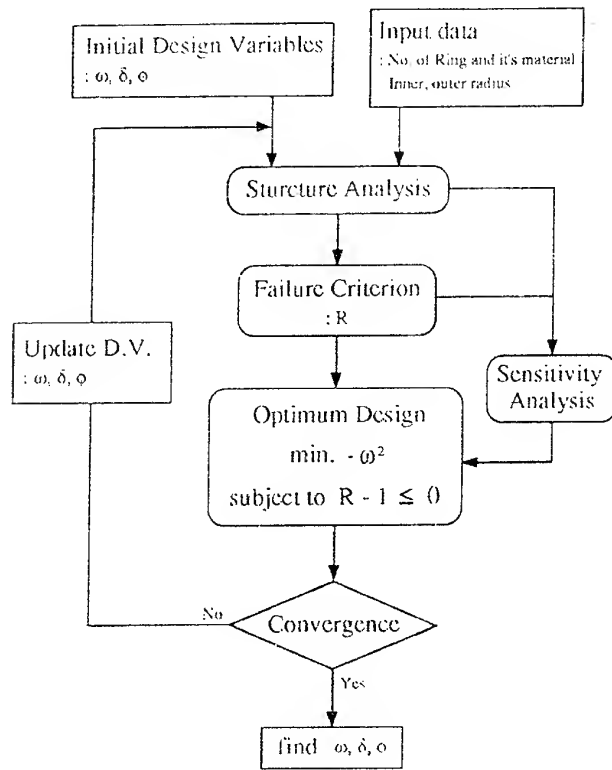
Fig. 2 Design procedure of composite multi-ring flywheel rotor

Table 1 Geometric input data and initial design variables of flywheel rotor

Input Data	value	[unit]
Inner radius	0.05	[m]
Outer radius	0.1	[m]
No. of Ring	10	[number]
Initial angle ($\phi^{(i)}$)	20	[degree]
Initial interference ($\delta^{(i)}$)	0.000005	[m]
Length	0.1	[m]

Table 2 Material properties of Graphite/Epoxy(T300/5208)

Material Property	value	unit
$E_{\theta\theta}$	181	GPa
$E_{zz}=E_{rr}$	10.3	GPa
$G_{\theta z}=G_{\theta r}$	7.17	GPa
G_{rz}	7.17	GPa
$v_{\theta r}=v_{\theta z}$	0.28	
v_{rz}	0.28	
X	1500	MPa
X'	1500	MPa
Y	40	MPa
Y'	246	MPa
S	68	MPa
ρ	1600	kg/m³

Table 3 Cases of optimum design flywheel rotor and their results

CASE	D. V.	Max. ω [rpm]	SED [Wh/kg]
1	ω ($\phi = 0, \delta = 0$)	55900	29.75
2	ω, ϕ ($\delta = 0$)	56400	30.28
3	ω, δ ($\phi = 0$)	86900	71.88
4	ω, ϕ, δ	87000	72.05
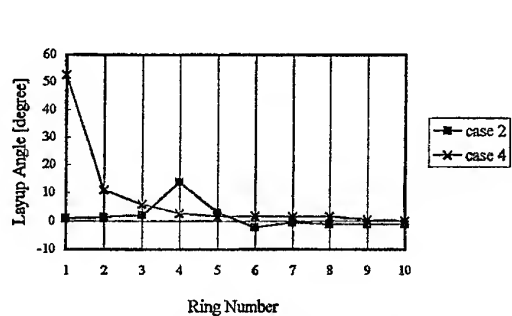
Fig. 3 Distribution of optimum layup angle
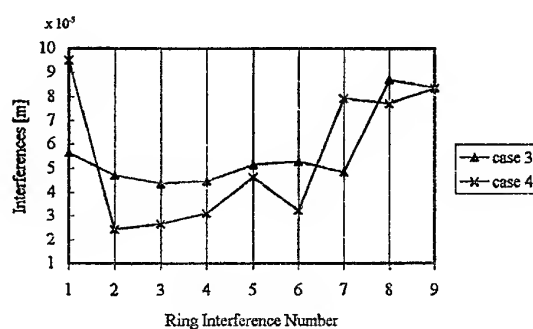
Fig. 4 Distribution of optimum interferences
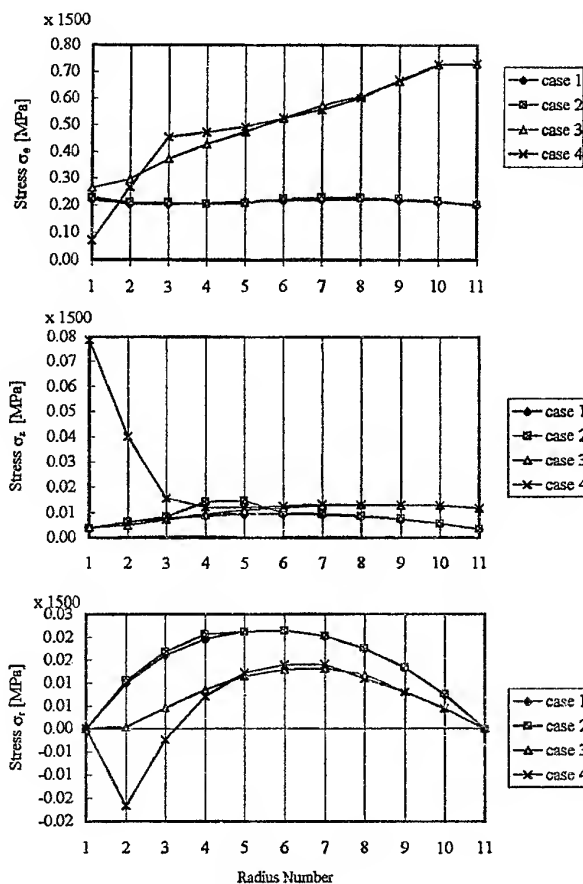
Fig. 5 Comparison of stresses in each case
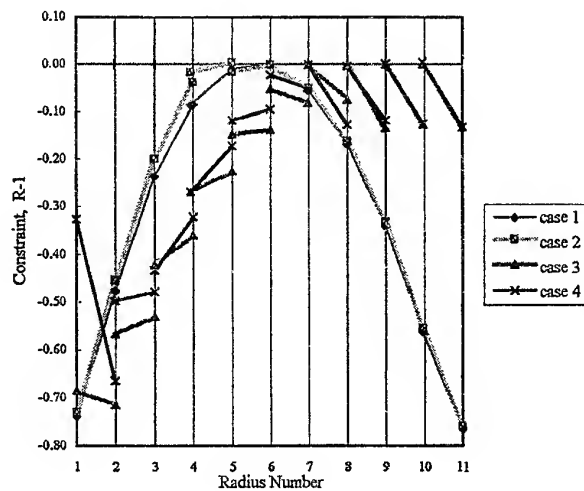
Fig. 6 Comparison of constraints in each case
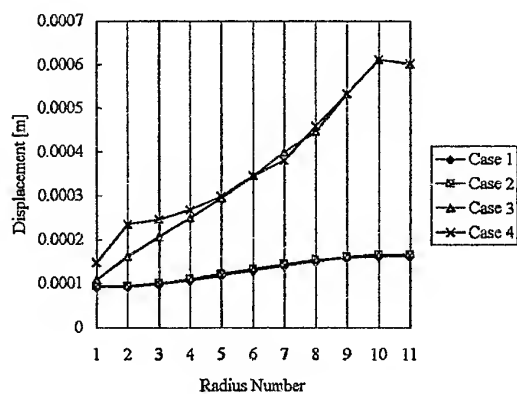
Fig. 7 Distribution of radial displacements along the radial coordinate for each case

189

PREDICTIVE MODELS FOR THE EDGE EFFECT IN LIQUID COMPOSITE MOLDING

A. Hammami, F. Trochu, R. Gauvin[*] and P.Y. Bakalemian
Center for Applied Research on Polymers
Mechanical Engineering Department

ECOLE POLYTECHNIQUE DE MONTREAL
C.P. 6079, SUCC. CENTRE-VILLE, MONTREAL (QUEBEC)
CANADA, H3C-3A7

INTRODUCTION

In Liquid Composite Molding (LCM) processes such as RTM or SRIM, preformed fabrics are preplaced in the mold cavity. The mold is then closed and a liquid thermoset resin is injected. Since it is difficult to precisely cut the fiber preform to the exact shape of the mold, sometimes a gap exists between the preform and the mold edge. This gap, even small (1 or 2 mm), can create a preferential flow path for the resin which disrupts the filling of the mold cavity. Such flow perturbation is called the edge effect. With existing numerical simulations models it is possible to simulate an edge effect by locally changing the permeability. However, this is not satisfactory. The ideal case will be a model to predict the edge effect from the geometry of the gap and the porosity of the surrounding material. To respond to this need, this paper presents two models for the edge effect. The first model is derived from the analysis of the flow between two fractured porous soil layers. In the second model, the flow is assumed to take place in a cylindrical channel as in Poiseuille flow. Since these models cannot cover all cases, an empirical parameter, which evaluates the importance of the transverse flow is also presented. Experimental as well as simulation results are presented.

EDGE EFFECT ANALYSIS

Let us consider a clearance "d" between the edge of the reinforcement and the mold edge as shown in figure 1. The edge effect occurs when the flow velocity u_f in the channel between the porous medium and the mold edge is larger than the flow velocity u_m inside the porous reinforcement. The velocity u_f in the channel is defined as a function of the physical parameters governing the flow : d (channel width), k (permeability tensor of the porous medium), μ (viscosity of the fluid). If one uses Navier-Stokes equation in the open channel and based on assumptions proposed by Beavers-Joseph [1] and further studied by others [2,3,4,5,6,7] an equivalent permeability for the edge channel could be defined as follows :

$$k_{c_1} = \frac{d^2}{12} \qquad (1)$$

This correspond to the equivalent permeability of an infinite planar crack of width "d" in a porous medium [8].

(*) To whom correspondance should be adressed.
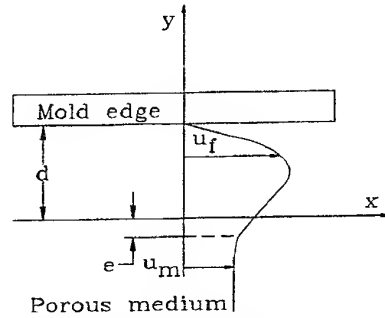
Figure 1. Schematics of the edge effect on the fluid velocity.

Lee and Fong [9] present a more complex expression for the equivalent permeability. However, for channel sizes between 1 and 3 mm which represent most practical cases, there is no significant difference in the values of k_c obtained by their expression and equation (1) which turnsout to be much simpler. As a matter of conclusion with this model, when the transverse flow is neglected, the equivalent permeability of the channel is only function of its width. However, when compared to experiments previously performed [7,10] it was found that this model is not always valid. Obviously, the reinforcement permeability has a strong effect but the geometry of the channel could also be a factor.

In order to integrate the cavity thickness, a second model is proposed. This model assumes that the flow is taking place in a cylinder, having the same cross section as the channel. The radius R of the equivalent cylinder is given by :

$$R = \left(\frac{dh}{\pi}\right)^{1/2} \qquad (2)$$

The flow inside an impermeable cylinder is governed by Navier-Stokes equation. If x is the axis of the principal channel path, the flow equations can be written as follows :

$$\frac{\partial P}{\partial x} - \mu\left(\frac{\partial^2 u}{\partial y^2} + \frac{\partial^2 u}{\partial z^2}\right) = 0 \qquad (3)$$

$$\frac{\partial P}{\partial y} = \frac{\partial P}{\partial z} = 0 \qquad (4)$$

The pressure gradient is constant in the plane and depends only on x. We assume that the fluid velocity has only one component along the x direction which depends solely on the radius r, the position of a fluid particle. Following this, the continuity equation will be satisfied and in cylindrical coordinates, equation (3) will be expressed as follows :

$$\frac{1}{r}\frac{d}{dr}\left(r\frac{du}{dr}\right) = \frac{1}{\mu}\frac{dP}{dx} \qquad (5)$$

When integrating in equation (5) the fluid velocity inside the cylinder with the following boundary conditions, i.e., $u = 0$ at $r = R$ and $u = $ constant at $r = 0$, equation (5) can be written as follows :

$$u = \frac{dP}{dx}\frac{1}{4\mu}\left(R^2 - r^2\right) \qquad (6)$$

When integrating equation (6) from 0 to R, the flow rate through the cross section of the cylinder is

$$q_v = \frac{\pi}{8\mu}\frac{dP}{dx}R^4 \qquad (7)$$

192

The relation obtained in equation (7) is called Poiseuille Formula. So the average fluid velocity inside the cylinder is given by :

$$u = \frac{R^2}{8\mu} \frac{dP}{dx} \qquad (8)$$

By integrating over the cross sectional area of the cylinder as in Darcy's law, an equivalent permeability which depends on both the cavity thickness and channel size is obtained :

$$k_{c_2} = \frac{R^2}{8} = \frac{h.d}{8\pi} \qquad (9)$$

Equivalent permability values obtained with the two models for different channel sizes and a cavity thickness of 2.35 mm have been compared to the permeability values obtained by iterative simulation with the software RTMFLOT [11]. The results are given in table 1.

Table 1: Equivalent permeability values obtained for various channel sizes with the two models and by simulation for a 2.35 mm cavity.

d (mm)	k_c from simulation $(.10^{-8} m^2)$	$k_c = d^2/12$ $(.10^{-8}\ m^2)$	$k_c = hd/8\pi$ $(.10^{-8}\ m^2)$
1	2.0	8.3	9.35
2	5.1	33.3	18.7
3	7.1	75	28

Even if the model of equation (9) is closer to the k_c obtained from iterative simulation, in fact, in this case neither of the two models gives acceptable results when compared with experiments. In other cases, not reported here, even for the same dimension but for a different reinforcement or a different volume fraction, the geometric model gives good results. This is due to the transverse flow as shown in figure 3b.

TRANSVERSE FLOW ANALYSIS

Numerical simulations of the edge effect show clearly the existence of a pressure gradient in the direction transverse to the channel. This pressure gradient yields a transverse flow which can be observed experimentally [7]. Here, an empirical approach is suggested to describe the perturbation caused by the transverse flow. This approach is formulated after a series of experiments performed with various reinforcements. A new parameter is defined to indicate when it is appropriate to consider the transverse flow. Since the transverse flow is affected by the channel size d, the transverse permeability k_y and the anisotropy m of the reinforcement, the following *transverse flow factor* is introduced :

$$\eta = \frac{12\,k_y}{d^2}.m \qquad (10)$$

where n is defined as :

$$m = \sqrt{\frac{k_y}{k_x}} \qquad (11)$$

Then, the following expression for η becomes :

$$\eta = \frac{12\,k_y^{3/2}}{d^2\,k_x^{1/2}} \qquad (12)$$

193

Now that a *transverse flow factor* is defined, a threshold value should be set to determine when the transverse flow can be neglected or not.

MATERIALS AND EXPERIMENTAL PROCEDURE

Flow experiments were conducted with two types of fabrics. The first one is a non stitched fabric, J.B. Martin 82675. It is a balanced fabric having two plies at 90°. These plies are connected by polyester yarns. This fabric has a surface density of 320 g/m^2 . The second fabric is a Brochier EB 315, which has a surface density of 315 g/m^2. It is an Injectex fabric having a larger permeability along the weft than the warp direction. For example, for a fibre fraction of 27 %, the permeability along the weft is 4 times that of the warp. The permeability of the two fabrics was measured using the unidirectional flow method [12]. For each fibre volume fraction, 4 runs were performed, 2 along the weft direction and 2 along the warp direction. The permeability values for each fabric are reported in table 2. The fluid used in the experiment is corn syrup with an average viscosity ranging from 98 to 110 cp. The corn syrup offers the advantage of being a Newtonian fluid, which can be cleaned easily from the mold cavity. Two hardened rectangular glass plates with an aluminium picture frame form a cavity of 120 mm in width by 930 mm in lentgh. A pressure transducer is mounted near the inlet port and a hyraulic cylinder mounted on a traction-compression machine is used as a pumping unit. To ensure a straight flow front at the beginning of the reinforcement impregnation, the reinforcement is positioned about 6 cm away from the injection port.

Table 2 : Permeability values obtained for the J.B. Martin and the Brochier fabrics.

	Permeability in the weft direction (m^2)	Permeability in the warp direction (m^2)	Fiber volume fraction V_f(%)
82675, 5 plies	$1.15.10^{-9}$	$1.15.10^{-9}$	26.6
82675, 7 plies	$0.29.10^{-9}$	$0.29.10^{-9}$	37.23
EB-315-01-120, 6 plies	$1.21.10^{-9}$	$0.281.10^{-9}$	31.41

RESULTS AND DISCUSSION

Table 3 gives the values of the *transverse flow factor* η for various channel sizes in a 2.35 mm thick cavity for the three fabrics considered. Based on this table, several experiments were conducted to establish the limit value of the *transverse flow factor* η. These experiments are identified by an asterix in the table. From the analysis of all these experiments, the limit value was selected at $\eta=0.5$, meaning that if $\eta < 0.5$, the transverse flow is negligeable. If $\eta > 0.5$ then, the transverse flow should be taken into account

Table3 : Values of parameter η for various channel sizes and reinforcements.

d (mm)	η JB M. 82675, 5 plies $k_y=1.15.10^{-9}m^2$	η JB M. 82675, 7 plies $k_y = 0.29.10^{-9}m^2$	η (EB-315-01-120, 6 plies), warp $k_y = 1.219.10^{-9} m^2$	η (EB-315-01-120, 6 plies), weft $k_y = 0.28.10^{-9} m^2$	η JB M. 81011, 3 plies $k_y = 0.03.10^{-9}m^2$
1	13.8	3.48(*)	30.51(*)	1.612(*)	0.235
2	3.45(*)	0.87(*)	7.628	0.403	0.058(*)
3	1.533(*)	0.386(*)	5.953	0.179	0.026(*)
4	0.862(*)	0.217	1.906	0.100(*)	0.014
5	0.552	0.139	1.220	0.064	0.009
6	0.383	0.096	0.406(*)	0.044	0.006

(*) The asterix identify the cases tested.

Figure 3 shows the results for two experiments. Figure 3a gives an example for the JBM 82675 with a channel of 6 mm and η=0.383, where the transverse flow is negligeable. Figure 3b is for the same fabric with a channel size of 2 mm, η=3.45 and where the transverse flow is significant.
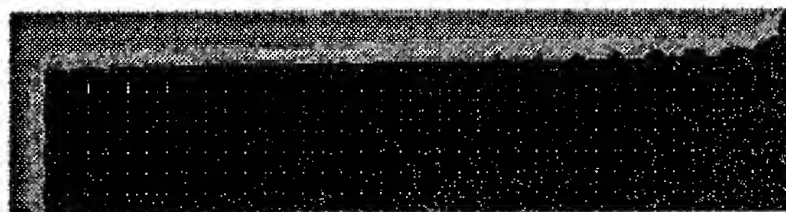
(a)

(b)

Figure 3 Edge effect with (a) negligeable transverse flow, η=0.383, and (b) significant transverse flow, η=3.45 for JBM 82675, 5 plies.

The procedure in the simulation to include the transverse flow effect cannot be demonstrated here because the lack of space. However we would like to briefly present it. To achieve this, the first row of elements in the simulation as shown in figure 4 is chosen in such a way that the frontier between the channel and the reinforcement lies in that element. The permeability of that first row of elements k_r is then defined taking into account either one of the two geometric models (k_c) and the transverse permeability of the reinforcement k_y with the following equation :

$$k_r = k_c \frac{d}{l} + k_y \frac{(l-d)}{l} \qquad (13)$$
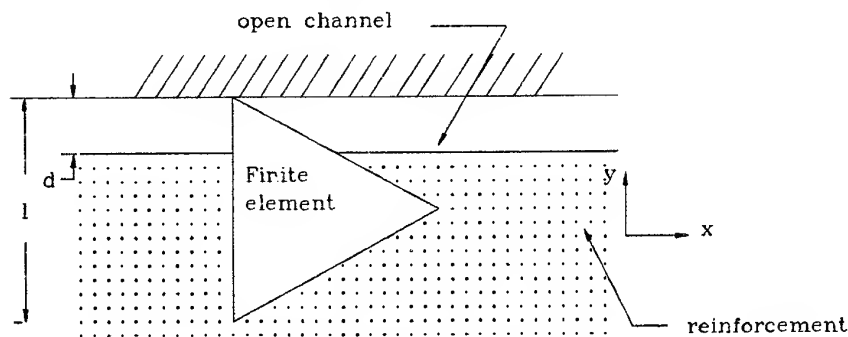
Figure 4 The boundary element.

CONCLUSION

In this work, two theoritical models were presented to evaluate and predict the edge effect in liquid composite molding. The first model assimilates the channel to an infinite planar opening of width d in a porous medium. In the second model, the flow is assumed to take place in a cylindrical channel as in Poiseuille flow. The results show that in several cases, these models predict the edge effect quite well. However, in some cases, the perturbation caused by the transverse flow from the channel to the preform cannot be neglected. A *transverse flow factor* η was defined to determine when the transverse flow should be taken into account. In that case, a model to calculate the equivalent permeability of the channel was presented for flow simulation with an edge effect.

REFERENCES

1. Beavers, G. S. and Joseph, D.D, Boundary Conditions at a Naturally Permeable Wall. *J. Fluid Mechanics. 30, 197-207*(1967).
2. Beavers, G.S., Sparrow, E.M. and Magnuson, R.A, Experiment on Coupled Parallel Flows in a Channel and a Bounding Porous Medium. *Journal of Basic Engineering, 843-848*(1970).
3. Beavers, G.S., Sparrow, E.M. and Masha, B.A., Boundary Condition at a Porous Surface Which Bounds a Fluid Flow, *AIChE Journal, 20,596-597*(1974).
4. Vafai, K. and Thiyagaraja, R., Analysis of Flow and Heat Transfer at the Interface Region of a Porous Medium. *Int. J. Heat and Mass Transfer, 30, 1391-1405*(1987).
5. Vafai, K. and Tien, L.C., Boundary and Inertia Effects on Flow and Heat Transfert in Porous Media. *Int. J. Heat and Mass Transfer, 24, 195-203*(1981).
6. Beavers, G.S., Sparrow, E.M, Non-Darcy Flow Trough Fibrous Porous Media. *J. Applied Mechanics, 711-714*(1969)
7. Hammami, A., Gauvin, R., Trochu, F., Touret, O. and Ferland, P., Analysis of the edge effect on flow patterns in liquid composites molding. *Proceedings of ICCM-10, III, 277-284* (1995).
8. Schneebeli, G., Hydraulique Souterraine. *Collection de la direction des Etudes et Recherches d' Electricité de France* (1978).
9. FONG, L. and Lee, J. L, Performing Analysis of Thermoformable Fiber Mats-Preforming Effects on Mold filling. *J. Reinf. Plast. Comp. 13, 637-663*(1994).
10. Hammami, A. Étude des perturbations de l'écoulement lors du moulage par transfert de résine, *PhD Thesis, Mechanical engineering Departement, Ecole Polytechnique de Montreal* (1996).
11. Trochu, F., Gauvin, R., Gao, D.M. and Boudreault, J.F., RTMFLOT: An Integrated Software Environment for the Computer Simulation of the Resin Transfer Molding Processs. *48th Annual Conference, Composites Institute, The Society of the Plastics Industry, Inc., February 8-11, 1993*.
12. Ferland, P., Guittard, D. and Trochu, F., Concurrent Methods for Permeability Measurement in the Resin Transfer Molding Process. *accepted in Polymer Composites, 1995*.

SINGLE TOW IMPREGNATION AND CONSOLIDATION EXPERIMENTS OF THERMOPLASTIC COMPOSITE PREFORMS

F. Haupert and K. Friedrich

Institute for Composite Materials Ltd., University of Kaiserslautern,
Erwin Schroedingerstraße 58, 67663 Kaiserslautern, Germany

ABSTRACT

Processing of composite materials with thermoplastic matrices is very complicated due to the high viscosity of the matrix material. Therefore, the impregnation parameters have to be investigated in order to achieve both a good impregnation of the fibers and a high consolidation quality of the different layers. The aim of the present study was to consolidate tows consisting of polymer powder between glass fiber bundles with a surrounding polymer sheath. Since impregnation was meant to occur under nearly the same conditions as in continuous processes such as thermoplastic filament winding or pultrusion, only one or two tows were impregnated during the experiments under defined processing parameters such as impregnation temperature, pressure, and time.

INTRODUCTION

Polymeric composites are predestinated for low weight and high stiffness constructions. New developments have also focussed on the use of thermoplastic matrices, because of their advantageous mechanical properties, especially the higher toughness when compared to traditional thermosets. Another advantage of these thermoplastic matrices is that no final curing process in an oven or autoclave is necessary. Therefore, these materials are especially suitable for continuous manufacturing processes such as thermoplastic filament winding [1,2] or pultrusion [3]. Impregnation, consolidation and cooling are performed continuously during the manufacturing process. However, still a major problem in processing of thermoplastic composites is the high viscosity of the matrix material. As a result, impregnation parameters like temperature, pressure and time have to be optimized properly in order to achieve both, a good fiber distribution and a strong bonding between fibers and matrix [4]. For improved thermoplastic composite preforms, the impregnation and consolidation times are very short. Furthermore, during a continuous process such as filament winding only one or just a few raw material tows are processed at the same time. These processing conditions therefore determine how to carry out comparable impregnation experiments: They have to be performed with a small number of raw material tows under a wide range of pressures with a well defined impregnation temperature and time. These were the requirements for the design of the impregnation equipment built up during this study. Impregnation temperature, pressure, and time were varied in a wide range. In order to characterize the impregnation and consolidation quality of consolidated tows, a special shear test had to be developed. Furthermore microscopic investigations of impregnated cross sections were performed.

EQUIPMENT AND EXPERIMENTS

Within the frame of the present study a special impregnation device was designed enabling the investigation of the impregnation and consolidation behaviour of single tows at very short times of pressure. The mold of the impregnation tool had a groove with a width depending on the thickness of the tow (Figure 1) and a length of 70mm. The temperature of the mold was measured by a thermocouple and controlled via a PID-controller. In order to achieve defined consolidation pressure profiles, the impregnation facility was integrated in a universal testing machine. The parameters influencing the impregnation and consolidation quality were temperature, pressure, and time (Figure 2). In order to determine the optimum processing window, each parameter was varied in a wide range while keeping the others constant.
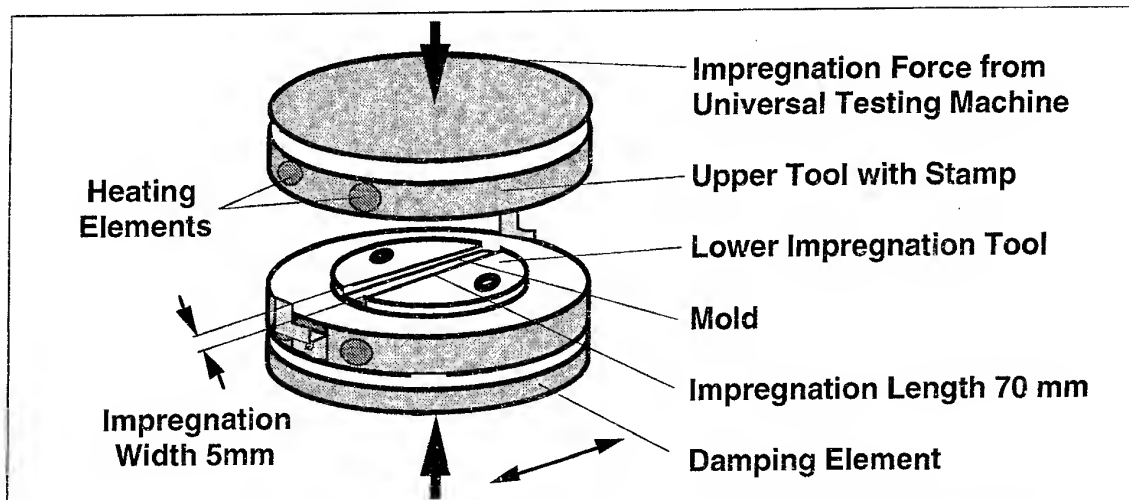
Figure 1: Single tow impregnation tool (Impregnation area = Impregnation width 5mm x Impregnation length 70 mm)
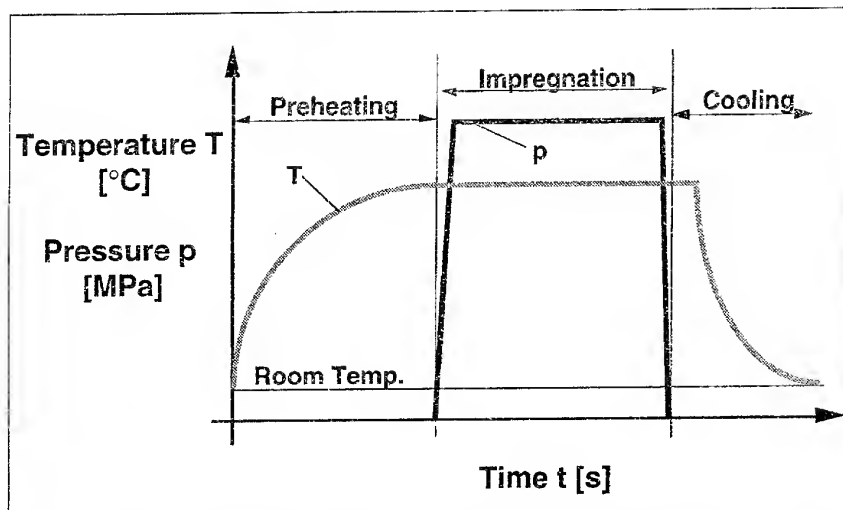
Figure 2: Temperature and pressure profile during an impregnation experiment

The impregnation experiments were performed as follows: First the prepared sample (Figure 3b) was put into the heated mold. Then, the also heated stamp was moved down until it just reached the sample surface without applying pressure. Under this condition, the sample was heated up for one minute (i.e. preheating period in Figure 2). Preliminary experiments with an embedded thermocouple showed that this time was sufficient for the sample to reach the temperature of the heated tool components (+/-1°C). After the preheating phase the impregnation program was started. The testing machine closed the mold thus generating the impregnation pressure. After the predetermined impregnation time the machine opened the mold and the sample was taken out of the mold. Figure 2 shows the temperature and pressure profiles during the experiment.

MATERIALS INVESTIGATED AND SAMPLE PREPARATION

The material investigated was a polymer powder impregnated and with a thin polymer sheath surrounded flexible fiber bundle (Figure 3a). This tow offers a high degree of flexibility in comparison to stiffer tapes, but is more difficult to process by filament winding or pultrusion. The particular components consisted of glass fibers and a polybutyleneterephtalate matrix material (GF-PBT-2400tex).
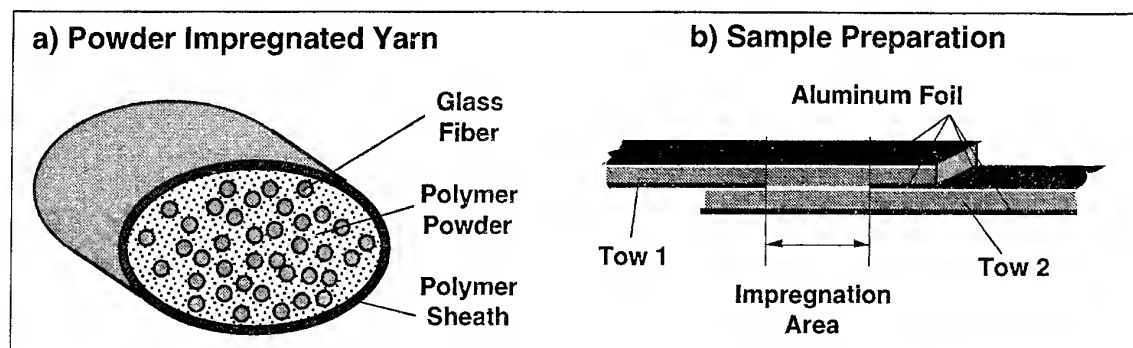
Figure 3: Raw materials for impregnation and consolidation experiments

In order to perform short time impregnation experiments a special sample preparation was necessary. The main problem was to avoid sample sticking to the mold. For this reason the two tows were partly wrapped in an aluminium foil, as shown in Figure 3b. This also helped to define quite precisely the actual impregnation area.

EXPERIMENTAL METHODS

In order to process this intermediate material, both the surrounding polymer sheath and the powder have to be heated up to an optimum impregnation temperature. Higher temperatures result in a degradation of the matrix material and poor interfacial bonding between fibers and matrix. Lower temperatures lead to higher matrix viscosity and hence to low impregnation quality, and therefore to voids. Another important processing parameter is the impregnation pressure, which is responsible for the matrix flow between the fibers. If this pressure is to high, the fibers are compressed and so, the permeability of the fibers is reduced. A further increase of pressure can even destroy the fibers. The third parameter varied during these investigations is the impregnation time.

Two different impregnation experiments were performed. The first one was the impregnation of one single tow. Impregnation parameters such as temperature, pressure, and time were varied systematically. The impregnation of the fibers was investigated just qualitatively by using scanning electron microscopy. During the second type of experiments, two tows were impregnated and consolidated next to each other over a well defined length. In this case, the consolidation quality was determined more quantitatively by the use of a special shear test. The ends of the tows were clamped into a tow tensioning device, so that a shear load could be applied to the consolidated tow surfaces (Figure 3). By knowing the consolidation area, and the ultimate shear force, the shear strength could be calculated. In the frame of this work, it was demonstrated, that this shear strength is a very sensitive parameter for characterizing the impregnation and consolidation quality of the two tows welded together.

RESULTS

Figure 4 shows the correlation between the shear strength of the impregnated area and the consolidation time. For this parameter combination, i.e. $T_c = 250°C$ impregnation temperature and $p_c = 1MPa$ impregnation pressure, even very short impregnation times of less than three seconds resulted in very good shear strength values of about 35 MPa. A further increase of impregnation time up to 60 s did not improve the shear strength values furthermore. For the longest impregnation times, a beginning degradation of the matrix material, resulting in a decrease of shear strength was even observed. The next parameter varied was the impregnation temperature. These experiments were performed for impregnation times of both one second as well as two and a half seconds. The impregnation pressure amounted to 1MPa for both experiments. In addition, the impregnation temperature was altered between 210°C and 320°C, i.e. from below and above the crystallite melting temperature of PBT ($T_{cm}=223°C$). Figure 5 illustrates the correlation between the consolidation temperature and the resulting shear strength for the one second impregnation time experiments.
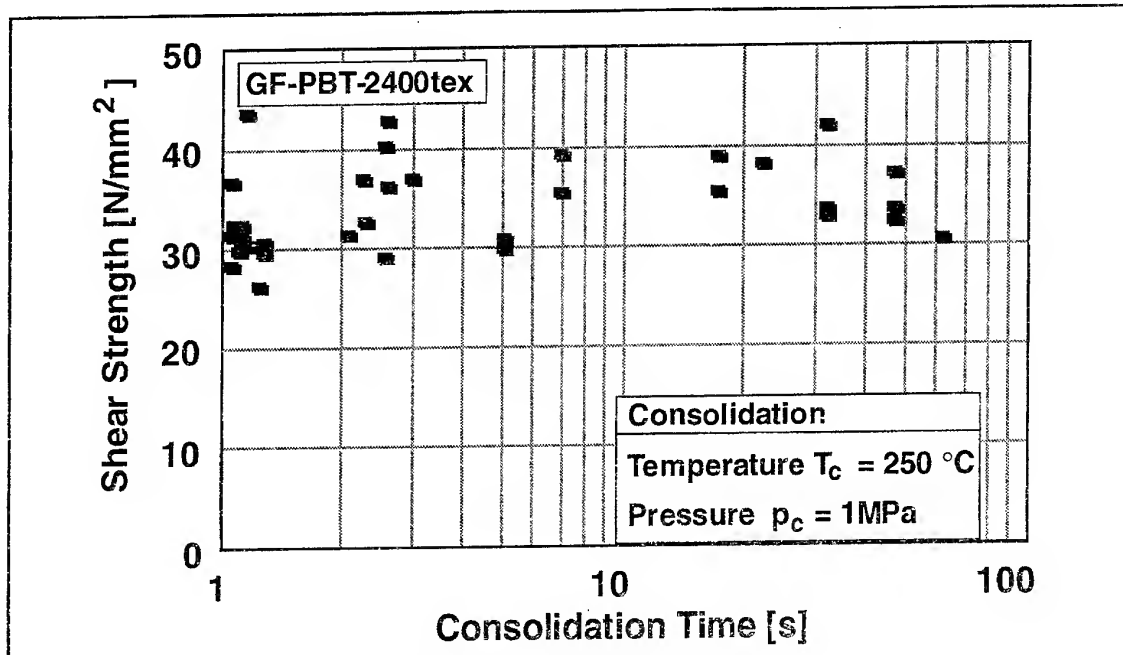
Figure 4: Shear strength as a function of consolidation time
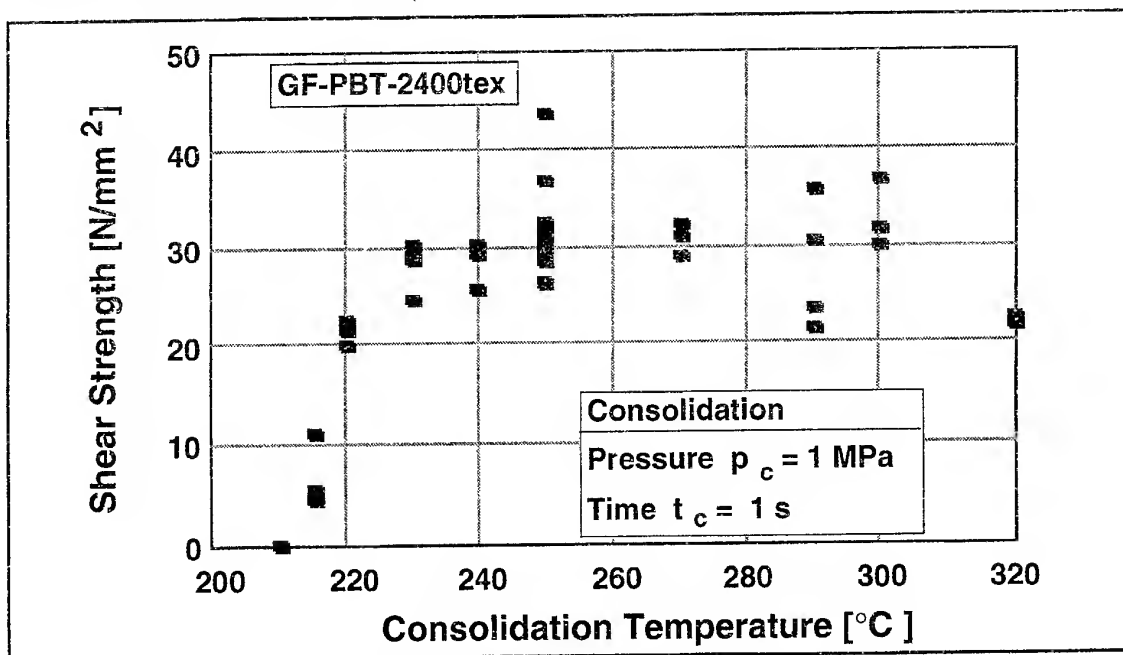
Figure 5: Shear strength as a function of consolidation temperature (Time 1 s)

As expected, impregnation temperatures lower than 220°C resulted in very poor consolidation qualities. For this parameter combination, the optimum consolidation temperature was 250°C. Here, shear strength values of about 33 N/mm² were reached. A further increase of temperature resulted in a decrease of shear strength due to beginning degradation of the matrix material. The same tendency of the results was observed for the impregnation experiments with the 2,5 seconds impregnation time (Figure 6). In this case, the best impregnation temperature was between 240°C and 250°C. As expected, for the 2,5 s im-

200

pregnation time, the corresponding average shear strength values were higher as for the one second experiments.

The correlation between consolidation pressure applied and the resulting interlaminar shear strength is given in Figure 7. It can be seen that even very low impregnation pressures of less than 1MPa resulted in shear values of 32 MPa. A further increase of pressure of 3 MPa raised the average shear strength values up to 40 MPa.
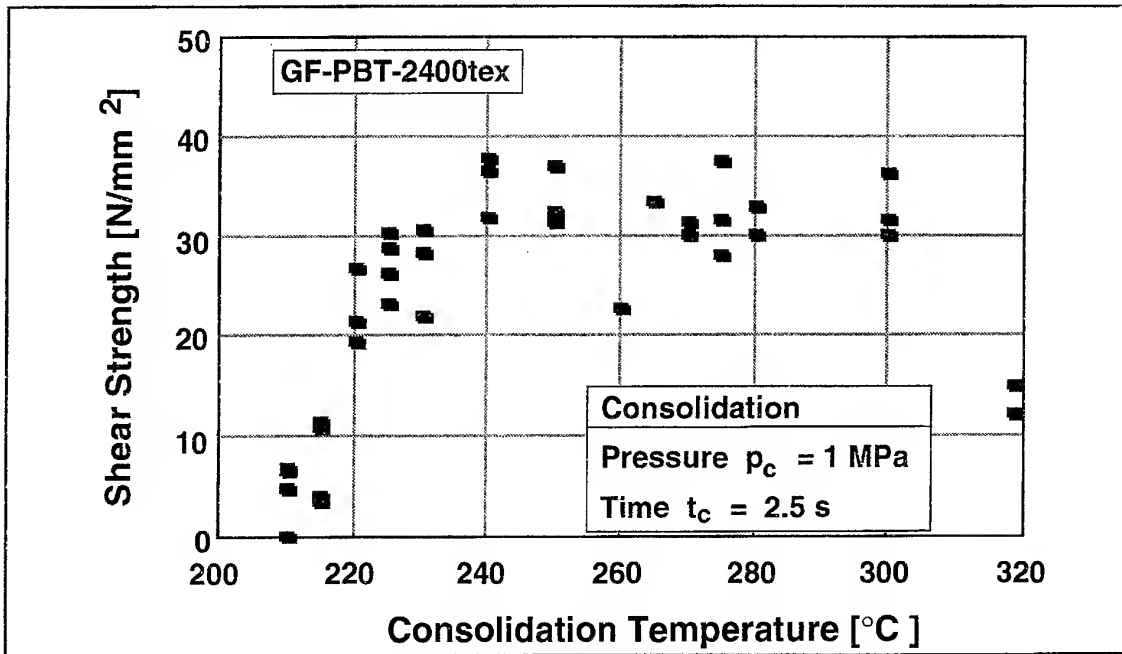
Figure 6: Shear strength as a function of consolidation temperature (Time 2,5 s)
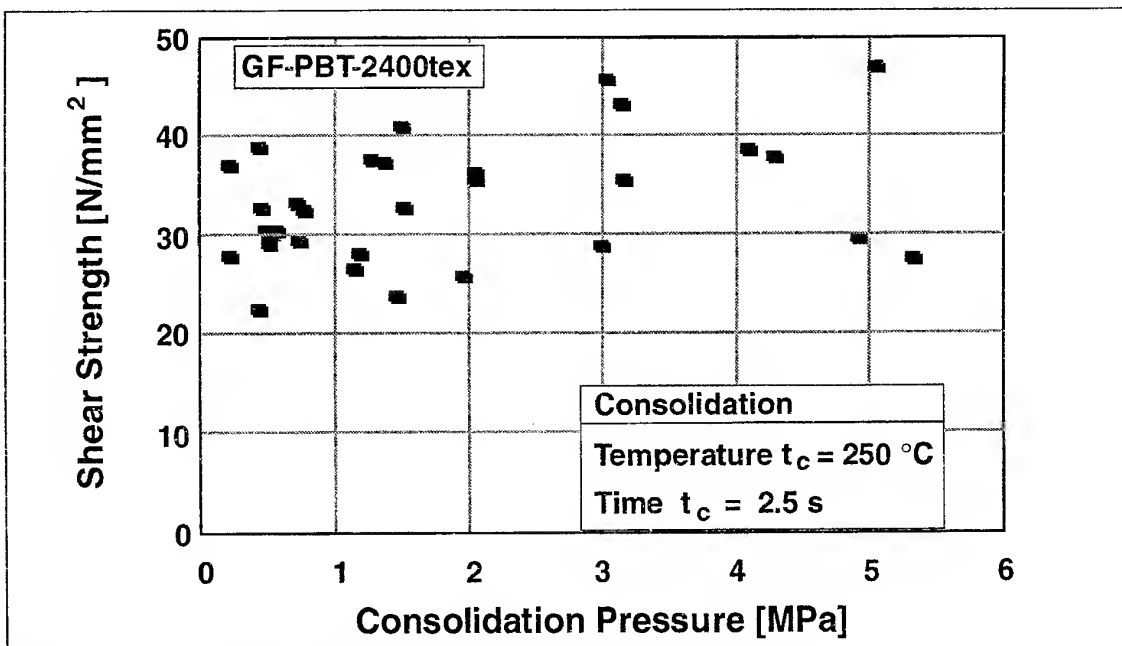
Figure 7: Shear strength as a function of consolidation pressure

A further very important criterion for the impregnation and consolidation quality of the powder impregnated tows is the fiber and matrix distribution. Figure 8 demonstrates microscopic cross sections of impregnated samples after different impregnation temperatures. The void content could be reduced remarcably, due to the lower viscosity at the higher temperature level.
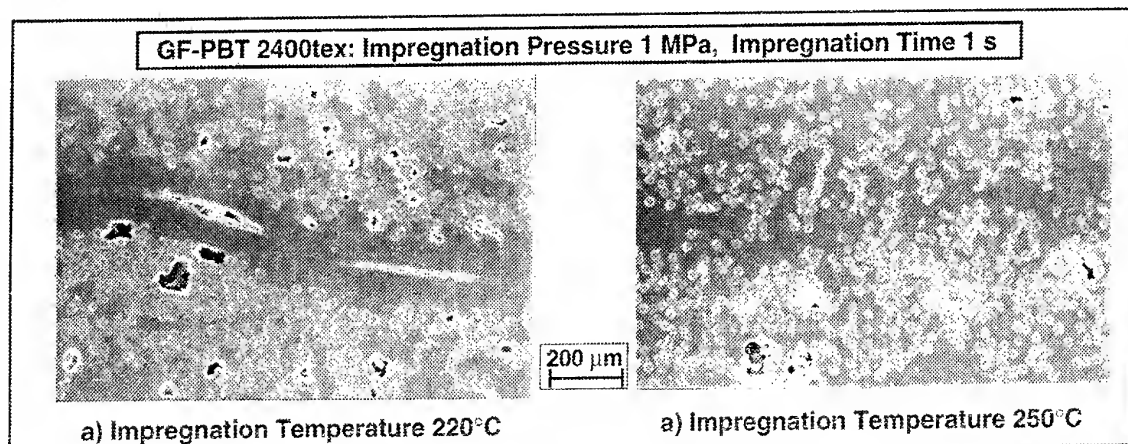
Figure 8: Fiber and matrix distributions at different impregnation temperatures(GF-PBT 2400tex, pressure 1MPa, time 1s)

CONCLUSIONS

In the frame of the present study, the impregnation and consolidation behaviour of a particular polymer powder impregnated and sheath surrounded intermediate fiber composite preform was investigated. The impregnation parameters time, temperature, and pressure were systematically varied, and their influence on the impregnation quality was determined using a specially developed shear test. The results of these investigations represent a basis for a further modelling of the impregnation behaviour of this material preform.

ACKNOWELEDGEMENTS

REFERENCES

[1] F. Haupert, K. Friedrich: "On Processing and Properties of Rings Wound from Thermoplastic Powder Impregnated Continuous Fiber Composites", Proc. "Advancing with Composites '94", Milano. Italy, May 2-7, pp. 237-249, (1994)

[2] F. Haupert, K. Friedrich: "Processing Related Consolidation of High Speed Filament Wound Continuous Fiber / Thermoplastic Composite Rings", Proc. "Flow Processes in Composite Materials '94", Galeway, Ireland, July 7-9, pp. 279-289, (1994)

[3] V. Klinkmüller, K. Friedrich: "Pultrusion of Flexible, Continuous Glass Fibre / Thermoplastic Powder Impregnated Bundles", High Technology Composites in Modern Applications. Eds. S.A. Paipetis and A.G. Youtsos, University of Patras, Applied Mechanics Laboratory, pp. 214-221, (1995)

[4] V. Klinkmüller, M.K. Um. M. Steffens, K. Friedrich, B.S. Kim: "A New Model for Impregnation Mechanisms in Different GF/PP Commingled Yarns", Applied Composite Materials 1, pp. 351-371, (1995)

ON THE MECHANICAL BEHAVIOR OF FIBER-REINFORCED COMPOSITES

F. Hild, A. Burr and P. Feillard

LMT, 61 avenue du Président Wilson, F-94235 Cachan Cedex, France.

INTRODUCTION

A Continuum Mechanics formulation applied to unidirectionally reinforced Composites is written within the framework of the Thermodynamics of Irreversible Processes [1]. The first step in establishing such a model is to identify the internal variables which define the state of the material. The second step is to derive the expression of the state potential $\overline{\psi}$ in terms of the state variables and the third one is to determine the evolution laws of the internal variables.

The state potential $\overline{\psi}$ is made up of the sum of two terms: viz. the elastic energy density $\overline{\psi}_e$ and the stored energy density $\overline{\psi}_s$. The elastic part is directly related to the applied load. The stored energy density is concerned with residual stress fields giving rise to macroscopic strains with no applied load. When the local behavior is elastic, the stored energy density is expressed as the total energy density associated with the residual stress field. Therefore by considering two elastic steps, the total free energy density can be evaluated following a so-called 'cut and paste' technique introduced by Volterra [2]. This approach will be used to model the behavior of unidirectional fiber-reinforced composites.

Loading a composite consisting of a brittle matrix supported by stronger fibers, usually causes multiple matrix cracking which is accompanied by interfacial debonding and sliding. In the following, we assume that the whole matrix-cracking process occurs at load levels lower than the fiber breakage mechanism, and therefore only the former mechanism will be analyzed. The aim of this paper is to derive a state potential and to introduce the relevant internal variables to model matrix cracking, debonding and sliding. It is worth noting that the same formalism can be used to analyze fragmentation tests on single filaments for which the only relevant mechanisms to consider are fiber breakage and subsequent debonding and pull-out. Similarly, the study of fatigue enters the same framework.

MICROSCOPIC DESCRIPTION OF THE DEGRADATION MECHANISMS

The matrix cracks, which are assumed to be perpendicular to the fiber direction, cause a stiffness reduction when the stress is tensile. Furthermore it is the closure

of the cracks which indicates the onset of increased stiffness when the specimen is subsequently loaded in compression. In the following, we will use elementary cells of length L, characterizing the crack spacing, and consisting of two different materials (m) and (f) as shown in Fig. 1, where E is the Young's modulus of the unbroken composite, E_m that of part (m), and E_f that of part (f). There is a matrix crack at the center of the cell. Because the matrix contains initial flaws of random strength, there is a distribution of matrix cracks characterized by a probability density function $F(L)$ depending on the applied stress $\bar{\sigma}$. The presence of matrix cracks implies a potential energy density change $\Delta\bar{\varphi}_c$

$$\Delta\bar{\varphi}_c = \frac{1}{\bar{L}} \int_0^{+\infty} \Delta\varphi_c(L)LF(L)dL \quad \text{with} \quad \bar{L} = \int_0^{+\infty} LF(L)dL \qquad (1)$$

where $\Delta\varphi_c(L)$ is the average potential energy density change due to the presence of a crack in a cell of length L, and $\bar{L}$ the average crack spacing. In the framework of Linear Elastic Fracture Mechanics, it is shown that the potential energy change $\Delta\varphi_c(L)$ is equal to $\bar{\sigma}^2\omega_c/E$, where ω_c is dependent on the crack density (i.e. a/L, see Fig. 1) as well as on the fact that cracks interact or not. This first basic mechanism is purely dissipative and therefore only influences $\bar{\psi}_e$.
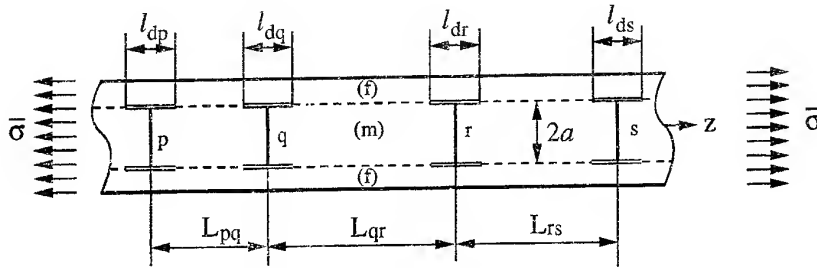
Fig. 1. Distribution of crack spacing L and debond length l_d.

Debonding followed by sliding gives rise to inelastic strains and hysteresis loops. To describe these phenomena, different models have been proposed [3,4]. They all consider a friction length l_F here assumed to be equal to the debond length l_d (Fig. 1). Similarly to cracking, which is a mode I mechanism, debonding *per se* is a purely dissipative mechanism as well. When debonding and slip occur simultaneously, a self-balanced microscopic stress field is involved. The corresponding strains in the matrix and in the fiber are denoted by $\Delta\epsilon_m(z, L)$ and $\Delta\epsilon_f(z, L)$, respectively, where z is the current coordinate. These strain differences result from the 'cut and paste' procedure described previously. By application of the principle of virtual work [5], the overall inelastic strain $\bar{\epsilon}_{in}$ is expressed as

$$\bar{\epsilon}_{in} = \frac{1}{\bar{L}} \int_0^{+\infty} \left[\int_0^L \Delta\epsilon_f(z, L)dz \right] F(L)dL \qquad (2)$$

Since the additional stress field is self-balanced the debonding and sliding processes are able to store energy. This result shows that to fully characterize both mecha-

nisms the knowledge of the stored energy density $\overline{\psi}_s$ is crucial. It is expressed as the total elastic energy density associated with the residual stress field

$$\overline{\psi}_s = \frac{1}{\overline{L}} \int_0^{+\infty} \left[\int_0^L \left\{ f E_f \Delta \epsilon_f^2(z, L) + (1 - f) E_m \Delta \epsilon_m^2(z, L) \right\} dz \right] F(L) dL \quad (3)$$

where f is the volume fraction of part (f).

MACROSCOPIC DESCRIPTION OF THE DEGRADATION MECHANISMS

The matrix cracking process described by an internal damage variable complies with the requirement of a fully dissipative mechanism. In a Continuum Mechanics framework, the presence of a crack results in a stiffness reduction defined by an internal damage variable D [6]. In the framework of Continuum Damage Mechanics, the potential energy density change can be written as follows

$$\Delta \overline{\varphi}_e = \frac{\overline{\sigma}^2}{2E} \frac{D}{1 - D} \quad (4)$$

so that the Gibbs' elastic energy density of a damaged material is written as $\overline{\varphi}_e = \overline{\sigma}^2 / 2E(1 - D)$. Eqn. (4) shows that the correct internal variable modeling cracking is the damage variable D whereas the corresponding potential energy density change depends upon the damage variable D as well as the applied stress level, and therefore is not an acceptable measure of the degradation due to matrix cracking. Eqns. (1) and (4) show that the damage variable D is a function of all the statistical moments of the crack spacing distribution. A 3D formulation requires an anisotropic damage description. In the case of cracking perpendicular to the fiber direction, the generalization is straight forward since the only compliance change is given in the fiber direction, and therefore only one scalar damage variable is needed and the previous 1D analysis is relevant. To fully characterize the debonding and sliding mechanisms two variables are needed. The first one is the inelastic strain $\overline{\epsilon}_{in}$, and the second one denoted by d is introduced to define the stored energy density level

$$\overline{\psi}_s = \frac{E}{2} \frac{\overline{\epsilon}_{in}^2}{d} \quad (5)$$

This expression can be found in [7] to model concrete and rocks for which there is no conjunction between matrix-cracking and debonding, and sliding. However, in the study of ceramic-matrix composites there is a non-uniform stress field along the debond crack, thus Eqn. (5) does not allow to relate, *a priori*, the variable d to a debond crack density. In a 3D formulation, a second order tensor is needed to model the inelastic strains due to debonding and slip. Since each operative slip system can be integrated separately in terms of energetic contributions, the internal damage variables can be defined separately for each inelastic strain component. Therefore there are as many debond damage variables as non-vanishing inelastic strain components [5]. In the case of cracking perpendicular to the fiber direction,

205

only one inelastic strain component is different from zero, viz. the normal component along the fiber direction. Similarly, only one scalar debond damage variable is needed.

In addition to the total strain $\overline{\epsilon}$, the total free energy density $\overline{\psi}$ is dependent on three internal variables: one damage variable D modeling matrix cracking and related to the crack spacing distribution, two variables $\overline{\epsilon}_{in}$ and d describing debonding and sliding, and related to the debond length distribution and to the crack opening distribution

$$\overline{\psi} = \frac{E(1-D)}{2}\left(\overline{\epsilon} - \overline{\epsilon}_{in}\right)^2 + \frac{E}{2}\frac{\overline{\epsilon}_{in}^2}{d} \tag{6}$$

The associated forces are defined as follows

$$\overline{\sigma} = \frac{\partial\overline{\psi}}{\partial\overline{\epsilon}} \quad , \quad Y = -\frac{\partial\overline{\psi}}{\partial D} \quad , \quad y = -\frac{\partial\overline{\psi}}{\partial d} \quad , \quad \overline{X} = \frac{\partial\overline{\psi}}{\partial\overline{\epsilon}_{in}} \tag{7}$$

Eqn. (7.1) defines the macroscopic stress $\overline{\sigma}$. Eqn. (7.2) defines the energy release rate density Y playing a similar role as the energy release rate $\mathcal{G}$ in Linear Elastic Fracture Mechanics. Combining Eqns. (7.1) and (7.2), one shows that the energy release rate density Y is proportional to the square of the 'effective stress' $\overline{\sigma}/(1-D)$. Similarly, Eqn. (7.3) defines the stored energy density y released during debonding and sliding. Since the variable d depends upon the details of the interfacial behavior, the definition of its associated force is also dependent upon the interfacial behavior. Lastly, Eqn. (7.4) defines the back stress $\overline{X}$ related to debonding and sliding. Again its exact value depends upon the interfacial behavior. To determine the evolution laws of the internal variables, two ways can be followed. The first one is using simulations of the complete micromechanical model along the lines developed for instance in [8] to get the distributions of crack spacing L and debond length l_d, and then the state potential. The second one is by performing experiments. The damage variable D is obtained by measuring the initial unloading modulus and the corresponding inelastic strain is $\overline{\epsilon}_{in}$ (Fig. 2). To measure the variable d, the stored energy $\overline{\psi}_s$ has to be evaluated, for instance by using methods developed in [9] or [10].

EXAMPLES

In this section, expressions of the three internal variables D, $\overline{\epsilon}_{in}$ and d are derived in some particular cases. Eqn. (1) can be written in terms of an equivalent cracking length $\overline{L}_c$ defined by

$$\overline{L}\Delta\overline{\varphi}_c = \overline{L}_c\Delta\varphi_c(\overline{L}_c) \tag{8}$$

It is worth noting that when $\Delta\varphi_c(\overline{L}_c)$ is inversely proportional to $\overline{L}_c$, then $\Delta\varphi_c(L)$ is inversely proportional to L for any value of L and any distribution F. The relevant length to consider is the average crack spacing $\overline{L}$. In that case a local damage theory is applicable since the matrix cracks are not interacting with each other. Otherwise, choosing the equivalent cracking length equal to the average
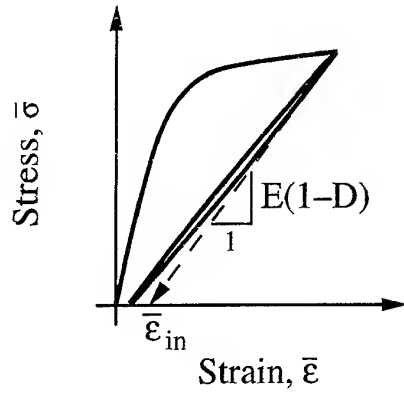
Fig. 2. Schematic stress / strain curve.

crack spacing is *a priori* only a crude approximation. The damage variable then depends upon the higher order moments of the crack spacing distribution and a non-local damage description seems more appropriate. Using a shear lag analysis [11], the damage variable D is linked to crack spacings $\overline{L}_c$ and $\overline{L}$ by

$$\frac{D}{1-D} = \frac{(1-f)E_m}{fE_f}\frac{\tanh(\beta\overline{L}_c)}{\beta\overline{L}} \tag{9}$$

where the constant β is a function of the elastic and geometric properties of the fiber and the matrix. When $\beta\overline{L}_c > 3$ (i.e., $\tanh(\beta\overline{L}_c) \cong 1$), $D/(1-D)$ is inversely proportional to $\beta\overline{L}$. This last result can also be found in the framework of Linear Elastic Fracture Mechanics for non interacting cracks. The strain distribution $\Delta\epsilon_f(z,L)$ in the friction zone in the part (f) is assumed to be linear and characterized by a constant interfacial sliding strength τ [12]. If the debond strength is negligible so that there is no longitudinal stress jump at the crack tip [4], the inelastic strain $\overline{\epsilon}_{in}$ is given by [5]

$$\overline{\epsilon}_{in} = \frac{\tau\overline{l}_d^2}{4E_fR\overline{L}_c} \tag{10}$$

where R is the fiber radius, and $\overline{l}_d$ is the equivalent debond length defined the same way as the equivalent cracking length $\overline{L}_c$. Eqns. (2) and (10) show that the inelastic strain is a function of the crack spacing distribution as well as the debond length distribution. If the crack spacing distribution is such that the smallest spacing is greater than the debond length, there is a *unique* debond length value. The definition of the variable d is directly obtained from the evolution of the debond length $\overline{l}_d$ as well as its definition in the expression of the stored energy $\overline{\psi}_s$ given in Eqn. (3)

$$d = \frac{4(1-f)E_m}{3fE_f}\frac{\overline{l}_d}{\overline{L}_c} \tag{11}$$

207

The damage variable d defines the size of the slip zone related to the crack spacing length $\bar{l}_d/\bar{L}_c$. If the stress redistribution is more complex [8], the previous results do not apply: the damage variable d is proportional to the ratio $\bar{l}_d/\bar{L}_c$ only if the stress field ahead of the debond crack tip is assumed to be unaltered by the presence of sliding and cracking.

REFERENCES

[1] D. B. Coleman and M. E. Gurtin, Thermodynamics with Internal Variables. *J. Chem. Phys.* **47**, pp. 597-613 (1967).

[2] V. Volterra, Sur l'équilibre des corps élastiques multiplement connexes. *Annales Scientifiques de l'Ecole Normale Supérieure, Paris* **24**, pp. 401-518 (1907).

[3] J. Aveston, G. A. Cooper and A. Kelly, Single and Multiple Fracture. *Proceedings National Physical Laboratory : Properties of Fiber Composites*, IPC Science and Technology Press, Surrey, England, pp. 15-26, (1971).

[4] J. W. Hutchinson and H. M. Jensen, Models for Fiber Debonding and Fiber Pull-Out in Brittle Composites with Friction. *Mech. Mat.* **9**, pp. 139-163 (1990).

[5] A. Burr, F. Hild and F. A. Leckie, Micro-Mechanics and Continuum Damage Mechanics. *Arch. Appl. Mech.* **65**, pp. 437-456 (1995).

[6] J. Lemaitre and J. Dufailly, Modélisation et identification de l'endommagement plastique des métaux. *Proceedings 3ème congrès français de mécanique*, Grenoble (France), (1977).

[7] S. Andrieux, Un modèle de matériau microfissuré avec frottement. *C. R. Acad. Sci. Paris* **Série II**, pp. 329-332 (1981).

[8] P. Feillard, G. Désarmot and J. P. Favre, Theoretical Aspects of the Fragmentation Test. *Comp. Sci. Tech.* **50**, pp. 265-279 (1994).

[9] A. Chrysochoos, O. Maisonneuve, G. Martin and H. Caumon, Plastic and Dissipated Work and Stored Energy. *Nucl. Eng. Des.* **114**, pp. 323-333 (1989).

[10] C. Cho, J. W. Holmes and J. R. Barber, Estimation of Interfacial Shear in Ceramic Composites from Frictional Heating Measurements. *J. Am. Ceram. Soc.* **74**, pp. 2802-2808 (1991).

[11] H. L. Cox, The Elasticity and the Strength of Paper and other Fibrous Materials. *Br. J. Appl. Phys.* **3**, pp. 72-79 (1952).

[12] A. Kelly and W. R. Tyson, Tensile Properties of Fibre-Reinforced Metals : Copper/Tungsten and Copper/Molybdenum. *J. Mech. Phys. Solids* **13**, pp. 329-350 (1965).

HAIL IMPACT TESTING OF THIN-SKINNED CARBON FIBRE COMPOSITE PANELS

K.J. JACKSON and M.L. SCOTT

Department of Aerospace Engineering, Royal Melbourne Institute of Technology

and

Cooperative Research Centre for Aerospace Structures Limited
506 Lorimer Street, Fishermens Bend, Victoria, 3207, Australia

INTRODUCTION

Thin-skinned carbon fibre composite structures have many characteristics which make them attractive to the aerospace industry. Such components are, however, particularly susceptible to impact damage. Such damage may be difficult to detect and can result in significant reductions in the stiffness and strength of the damaged component [1].

Hail impacts are an important source of in-service damage for composite components used in aerospace applications [2]. This paper is a report on an investigation of the response of thin-skinned carbon fibre/epoxy composite panels to hail impact. The development of an hail impact facility is described, followed by the results of hail impact tests on both flat and stiffened composite panels.

EXPERIMENTAL FACILITY

A system has been developed to conduct hail impact tests on thin-skinned fibre composite panels. The hail impact facility is shown in Figures 1a and 1b and is capable of launching hailstones of up to 51 mm in diameter at velocities between 0 and 50 m/s. The elements of this facility include equipment to manufacture synthetic hailstones, a gas gun to launch the hailstones, velocity measurement equipment and a rig to support the specimens to be tested.
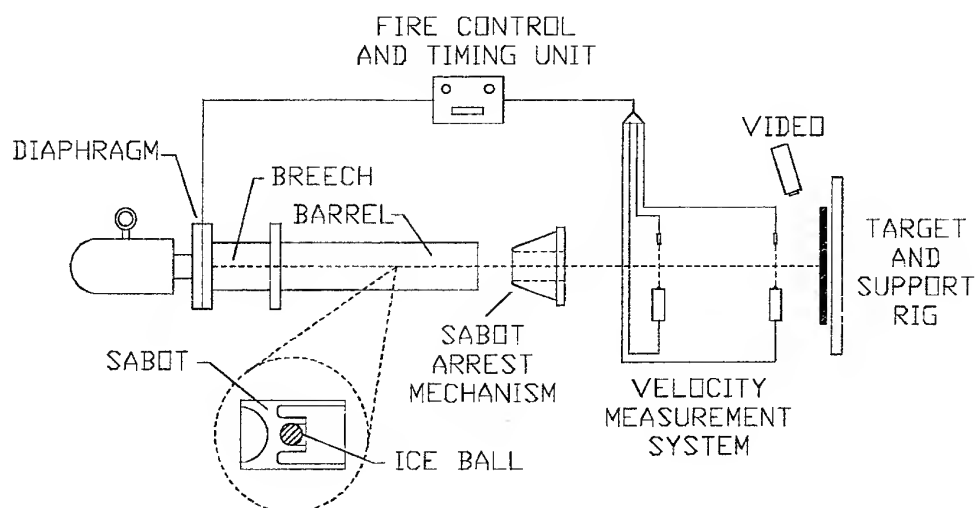
Figure 1a. Schematic of Hail Impact Facility
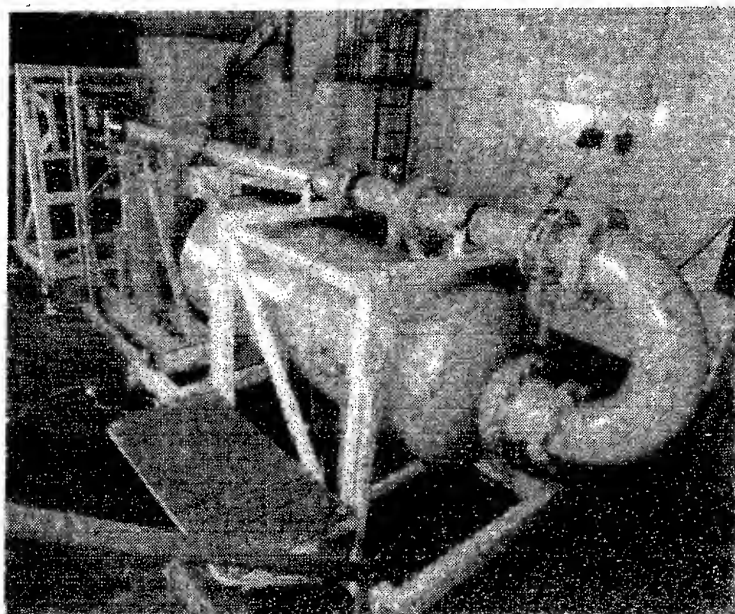
Figure 1b. Hail Impact Facility

Synthetic Hailstones

Ice balls provide a close approximation to natural hail and are commonly used as synthetic hailstones in hail impact tests. The method used to manufacture the ice balls is similar to that described in Reference 3. Silicone rubber split moulds are used to produce ice balls of 12.7, 25.4, 38.1 and 50.8 mm in diameter. The moulds are filled with distilled water and frozen at -18°C. Freezing is done in stages to help prevent air from being trapped in the ice ball. A 51 mm diameter ice ball and mould is shown in Figure 2.
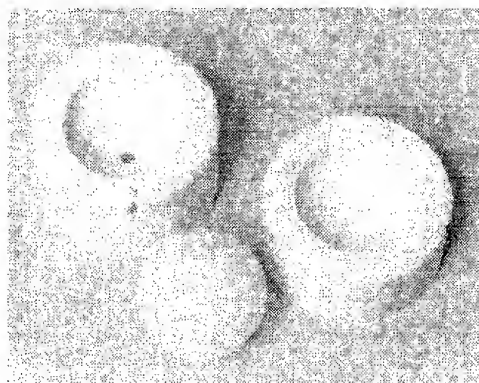
Figure 2. 51 mm Diameter Ice Ball and Mould

Hail Launcher

The hail impact facility employs a gas gun to launch ice balls at test specimens. The ice balls are supported during launch by a reusable container, or sabot, which is separated from the ice ball by a mechanical device when the sabot leaves the gas gun barrel. The air gun consists of a receiver of high pressure air coupled to a breech and barrel by a frangible diaphragm. Ice balls are placed in a sabot which is then loaded into the breech of the gun. The receiver is pressurised using a supply of high pressure air. Bursting the

210

diaphragm vents the high pressure air from the receiver into the barrel of the gun which causes the sabot to accelerate down the gas gun barrel.

Examples of ice ball sabots are shown in Figure 3a. The sabot was designed to create a pressure seal in the barrel of the gun to prevent the uncontrolled escape of air between the sabot and the barrel; this improves the consistency of the air gun velocity-pressure relationship. The sabot is cast from a poly-urethane elastomer. The front of the sabot is an open ended cylinder with a cup at its base to support the ice ball and was designed in conjunction with the sabot arrest mechanism. Sabots for different diameter ice balls are produced by changing the size of the supporting cup. The sabot was designed to be stiff enough to retain its shape during launch and is also able to withstand the significant stretching and deformation associated with its arrest.
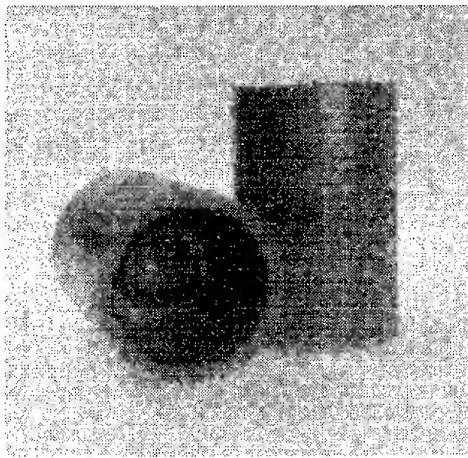
Figure 3a. Ice Ball Sabots   Figure 3b. Sabot-Ice Ball Separation
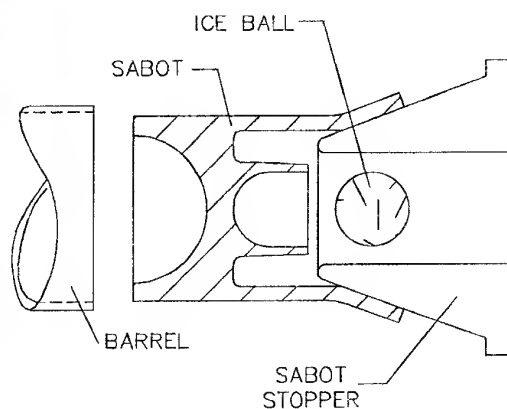
The sabot arrest mechanism has been designed to separate the ice ball from the sabot upon exit from the gas gun barrel. This mechanism consists of a steel cone mounted on a lever which is attached to supporting structure by tension springs. The method by which the ice ball is separated from the sabot is illustrated in Figure 3b. As the sabot leaves the barrel of the gun it strikes the cone and is brought to rest. The ice ball leaves the supporting cup in the sabot and passes through the hole in the center of the cone and on to the target.

Velocity Measurement and High Speed Photography

The ice ball velocity is recorded immediately after the ice ball has separated from the sabot. The velocity measurement system consists of two photo-detectors, illuminated by lasers, connected to an electronic timer. The ice ball interrupts the two beams of light in quick succession, generating start and stop pulses for the timer, and recording the ice ball transit time. The distance between the light beams is known and therefore the velocity of the ice ball can be determined.

High speed video equipment operating at 4000 frames per second was used to record the impact of the ice ball on the test specimens. A 51 mm diameter ice ball both in flight and impacting a flat test specimen at 31.6 m/s is shown in Figure 4. Video footage is also used to determine if the ice ball is whole or fragmented prior to impact.

| (a) $t = -0.5\ ms$ | (b) $t = 0.5\ ms$ | (c) $t = 1.5\ ms$ |
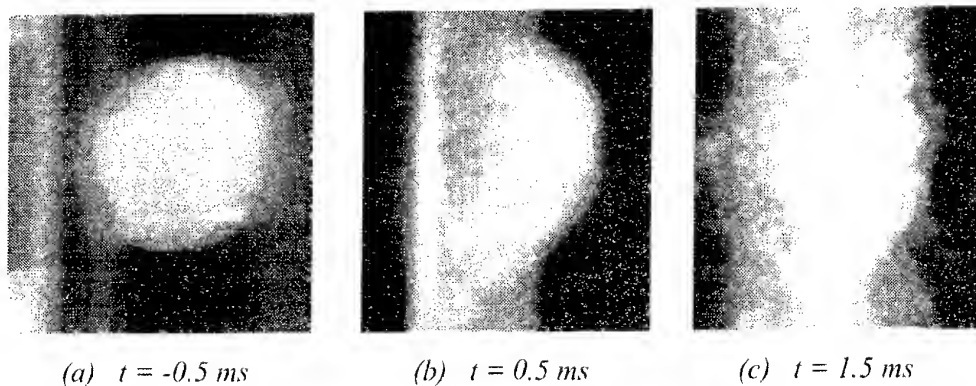
Figure 4. High Speed Photography of Ice Ball Impact
(Impact occurs at t = 0.0 ms)

Target Support Rig

As shown in Figures 1a and 1b, a rig has been designed to support the test specimens. Panels are clamped into steel frames and are then bolted into a free standing rig supported on leveling jacks and castor wheels. The rig is designed so that both large and small test specimens may be impacted at any point on the "working area" of each panel and also to allow for oblique impact tests.

IMPACT TESTING

Preliminary impact tests were conducted to evaluate the damage resulting from hailstones, falling at terminal velocity, impacting thin-skinned carbon fibre/epoxy composite components. Testing was restricted to ice balls of 51 mm in diameter and all impacts were normal to the specimen surface. Hail impact damage was characterised by visual and by ultra-sonic (C-scan) inspection.

Impact Velocity and Energy

Assuming the hailstone to be a sphere of solid ice (Specific Gravity = 0.92), its terminal velocity in a standard atmosphere can be determined by the empirical formula [4]:

$$V_t = 4.43\sqrt{d}$$

with V_t in m/s and d in mm. For ice balls with a diameter of 51 mm and mass of 62 g, the above expression gives a terminal velocity of 31.6 m/s and a kinetic energy of 31 J.

Test Specimens

Flat and blade-stiffened test specimens were manufactured from unidirectional T300/914C pre-impregnated carbon/epoxy tape. Panels were vacuum bagged and cured in an autoclave at a temperature and pressure of 175°C and 690 kPa respectively. Panel dimensions were 330 mm square with a working area of 250 x 250 mm and were chosen to be typical for panels used for control surfaces (ailerons etc.) on mid-size transport aircraft. The flat panel specimens were made with an eight ply quasi-isotropic lay-up $[+45/-45/90/0]_s$ and were approximately 1 mm thick. Blade-stiffened panels, as shown in Figures 5a and 5b, consist of eight plies in the test working area, built up to 14 plies in the clamped region. These panels have three 25 mm high stiffeners with a run-out angle of 45°. Two ±45° plies are extended from the stiffener into the skin to improve the skin-stiffener interface. All panels were C-scanned prior to testing.
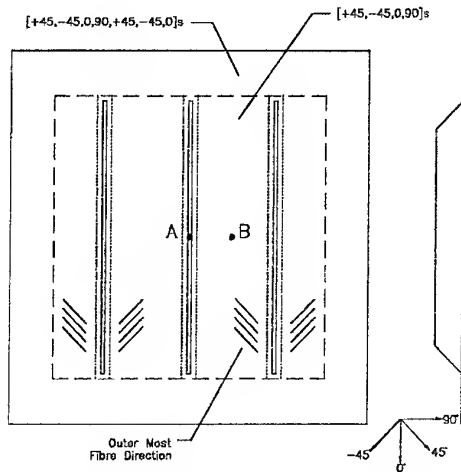
Figure 5a. Stiffened Panel Lay-up   Figure 5b. Stiffener Lay-up
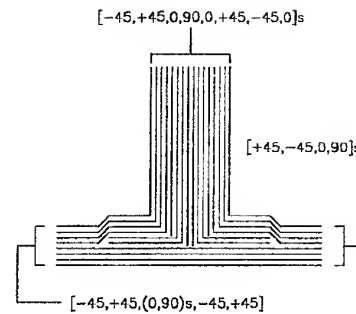
Results and Discussion

Flat panel specimens were impacted with ice balls at velocities ranging between 25.0 and 42.5 m/s. This resulted in hailstone impact energies of up to 56 J. Panels were impacted both in the centre and in the corners. Visual inspection showed no surface damage and C-scan data showed no ply delamination.

Table 1. Stiffened Panel Impact Tests

Panel No.	Impact Location (Refer Figure 5a)		Ice Ball Mass (g)	Impact Velocity (m/s)	Impact Energy (J)
SBS001	Stiffener	A	62	39.2	48
SBS002	"	A	62	33.9	36
SBS003	"	A	62	35.9	40
SBS004	"	A	62	29.8	28
SBS005	Mid-bay	B	62	36.5	41
SBS006	"	B	62	36.8	42
SBS007	"	B	62	36.7	42

The impact tests conducted on the stiffened panels are summarised in Table 1. The typical delamination patterns for hailstone impacts on the stiffener and mid-bay of the panels are shown in Figures 6a and 6b respectively (delaminated regions are surrounded by borders). All stiffened panels show delamination damage in the stiffener run-out region, however this damage is not visible on the impact side of the panel. The extent of this damage and its distribution is influenced both by the impact velocity and by the location of the impact. Hail impacts caused no localised damage (delamination or indention) around the impact site for either mid-bay or stiffener impacts.

The failure of the hail impacts to cause localised damage in either the flat or stiffened panels is attributed to the crushing and failure of the ice ball upon impact. This reduces the peak impact load on the specimen and distributes this load over a relatively large area. Delamination damage in the stiffener run-out regions is attributed to impact induced bending of the stiffener peeling the stiffener away from the skin. This remote type of damage in the stiffener run-out region of the panel was also observed after tool drop type impact tests employing a steel impactor [5].

213
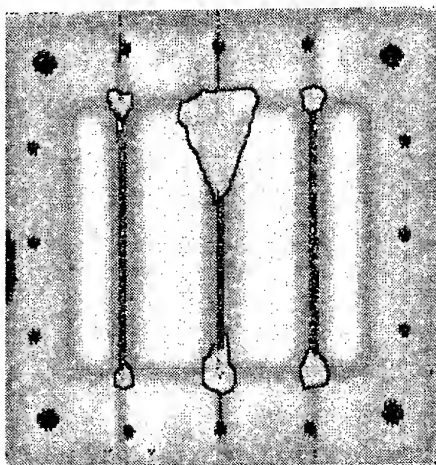
(a) Impact on Stiffener (SBS001)   (b) Impact Mid-bay (SBS006)
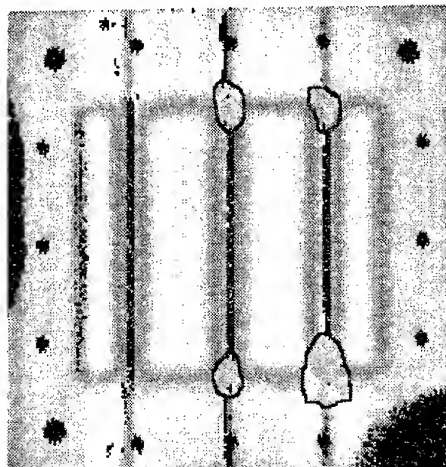
Figure 6. C-Scan Images of Damaged Stiffened Panels

CONCLUSIONS

An experimental facility developed to conduct hail impact tests with synthetic hailstones of up to 51 mm in diameter at velocities of up 50 m/s has been described and the behaviour of thin-skinned carbon fibre/epoxy composite panels when subjected to hail impact has been investigated.

Impact tests on both flat and stiffened panels show that, for the impact energies considered, hail impact caused no localised damage to flat or stiffened panels. Stiffened panel specimens did however exhibit substantial damage in the stiffener run-out regions, remote from the impact location. Transverse tension stresses in the skin-stiffener interface due to bending are considered to be the primary cause of this delamination. To eliminate this problem, a design which provides a more gradual transfer of load from the stiffener to the skin is required.

REFERENCES

[1] Stolfa, A.N. and Scott, M.L., "Certification Issues for New Structural Concepts in Composite Airframes", *Proceedings Fifth Australian Aeronautical Conference*, Melbourne, Victoria, pp 107-114, September 13-15, 1993.

[2] Anon., "Hail Smashes AMR's Fleet", *Aviation Week and Space Technology*, pp 30, May 8, 1995.

[3] Jenkins, D.R. and Mathey, R.G., "Hail Impact Testing Procedure for Solar Collector Covers", *National Bureau of Standards Report NBSIR-82-2487*, Washington D.C. National Engineering Lab., 1982.

[4] Kensche, Ch.W., "Environmental Effects on Gl-Ep Rotor Blades", *Proceedings 1993 European Community Wind Energy Conference*, Lübeck-Travemünde, Germany, March 8-12, 1993.

[5] Cheung, A.K.H. and Scott, M.L.,"Low Velocity Impact and Static Indentation of Thin Stiffened Composite Panels", *Proceedings Second Pacific International Conference on Aerospace Science and Technology-Sixth Australian Aeronautical Conference*, Melbourne, Victoria, pp 631-638, March 20-23, 1995.

DESIGN OPTIMISATION OF COMPOSITE STRUCTURES USING THE FINITE ELEMENT METHOD AND MATHEMATICAL PROGRAMMING TECHNIQUES

D. Jonson[1] and V.E. Verijenko[2]

[1]Center for Engineering Research, Technikon Natal, Durban, South Africa
[2] Department of Mechanical Engineering, University of Natal, Durban, South Africa

INTRODUCTION

The use of composite materials in the manufacture of primary components in high performance structural systems has demonstrated the potential of this new class of materials. The design flexibility offered by fibre reinforced matrices and their high strength and stiffness to weight ratios provides the structural engineer with a material that may, in principle, be tailored to deal with a complex operating specification very efficiently. However the flexibility offered by composites is also largely responsible for the difficulty experienced in the design of complicated high performance structures. The orthotropic nature of the individual layers in the laminate and the discontinuous nature of the composite introduces a large number of design parameters to the design process. This situation results in large and complex design problems that require a considerable amount of effort when compared against the traditional techniques used for the design of structures in isotropic materials. The following study discusses the foundations for a rationalised redesign process based on design variable sensitivity analysis which has been implemented by integrating reliable optimisation strategies with a finite element analysis code.

OPTIMISATION STRATEGY

The solution strategy used requires the generation of a high quality explicit approximate problem statement. The approximate problem is expressed in terms of design variable sensitivity data which is generated by finite element analysis. An optimisation algorithm is then employed to seek the optimum of the approximate problem within a specified move limit envelope. In this case the modified feasible directions algorithm developed by Vanderplaats [1] has been used. The approximate optimum should, depending on the quality of the approximation, lie relatively close to the real optimum. The convergence is checked between iterations by executing a full finite element analysis. If it is found that the convergence criterion has been satisfied then the process is terminated otherwise a new approximate problem is constructed and the process is repeated. The computational effort is therefore reduced by eliminating the need to execute a computationally expensive finite element analysis whenever response data is required.

APPROXIMATION TECHNIQUES

Several techniques are employed in the generation of the approximate problem such as the reduction of the number of design variables by linking, the temporary deletion of non-critical constraints and the construction of high quality approximations for the retained constraints. Design variable linking effectively reduces the number of independent design variables that need to be considered during the design cycle by eliminating those variables that may be expressed in terms of another variable. Constraint deletion reduces the size of the approximate sub-problem further, this is achieved by examining the value of each of the constraints, if the value falls below some threshold criterion then the constraint is temporarily eliminated from consideration during the design cycle. The approximate functions that are to be representative of the original constraints are generated from Taylor series expansions of the constraints about the present design variable vector, ie.

$$g_j(\mathbf{X}) = g_j^0 + \sum_{i=1}^{n} \frac{\partial g_j}{\partial X_i^0}(X_i - X_i^0) \qquad j = 1, \ldots, m_R \tag{1}$$

where m_R is the set of retained constraints.

Design variable sensitivity analysis

From equation (1) it is evident that the gradients or sensitivities of the structural responses contained in the constraint approximations are required. This data is obtained by design variable sensitivity analysis which is closely associated with the finite element analysis. The gradient information is acquired through the direct differentiation of the finite element system equation, this effectively yields the nodal displacement gradients that may be used to calculate the gradients of other quantities via constitutive relationships.

Displacement Sensitivities

The global stiffness equation is given by:

$$K\mathbf{u} = \mathbf{P} \tag{2}$$

where K is the reduced global stiffness matrix, $\mathbf{P}$ the reduced load vector and u the nodal displacement vector. The stiffness matrix, load and displacement vectors are in general expressed in terms of the design variables $\mathbf{X}$. Differentiation of the system equation with respect to the design variables results in the following equation for the displacement sensitivities:

$$\frac{\partial \mathbf{u}}{\partial X_i} = K^{-1}\left(\frac{\partial \mathbf{P}}{\partial X_i} - \frac{\partial K}{\partial X_i}\mathbf{u}\right) \tag{3}$$

The decomposed stiffness matrix is available as a by-product of the displacement solution and therefore the displacement sensitivities may be solved for once the derivative of the reduced global stiffness matrix has been assembled.

Approximation of the Tsai-Hill Failure Criterion

The optimisation of composite structures is considered here in terms of weight minimisation subject to failure conditions in each ply of the laminate. The failure criterion employed is the well known Tsai-Hill approach which states that a ply in a composite laminate is considered to have failed if the magnitude of the failure index exceeds one, ie.

$$T_i \leq 1.0 \qquad i = 1, N \tag{4}$$

where N refers to the number of layers in the laminate. The Tsai-Hill failure criterion is expressed in terms of the layer stresses as follows:

$$T_t = [(\frac{\sigma_1}{F_1})^2 + (\frac{\sigma_2}{F_2})^2 - (\frac{\sigma_1 \sigma_2}{F_1^2}) + (\frac{\sigma_1 2}{F_1 2})^2]^{\frac{1}{2}} \tag{5}$$

where σ_1, σ_2 and σ_{12} are the ply stresses in the principle material directions and F_1, F_2 and F_{12} are the strengths of the ply again referred to the material directions. The constraint based on the Tsai-Hill failure criterion is then given as

$$G_j = 1 - T_t \geq 0 \tag{6}$$

Using a linear expansion about the present design vector, the approximation of the Tsai-Hill failure criterion is then given in terms of the sensitivity data as follows,

$$G_j = 1 - \sum_{i=1}^{N} \frac{\partial T_i}{\partial X_i} X_i \tag{7}$$

where

$$\frac{\partial T_t}{\partial X_i} = \frac{1}{2T_t} \frac{2\sigma_1 - \sigma_2}{(F_1)^2} \frac{\partial \sigma_1}{\partial X_i} \frac{1}{2T_t} [\frac{2\sigma_2}{(F_2)^2} - \frac{\sigma_1}{(F_1)^2}] \frac{\partial \sigma_2}{\partial X_i} \frac{1}{T_t} \frac{\sigma_{12}}{(F_{12})^2} \frac{\partial \sigma_{12}}{\partial X_i} \tag{8}$$

Calculation of stress gradients

From the above formulation for the gradients of the Tsai-Hill failure indices it is noted that the gradients of the stresses in the material directions are also required. These are given by the derivative of the stress-strain constitutive equation as follows,

$$\{\frac{\partial \sigma}{\partial X_i}\} = \frac{\partial [\overline{Q}]}{\partial X_i} \{\epsilon\} + [\overline{Q}]\{\frac{\partial \epsilon}{\partial X_i}\} \tag{9}$$

The strain sensitivity is given by

$$\frac{\partial \epsilon}{\partial X_i}\} = \{\frac{\partial \epsilon^0}{\partial X_i}\} + \frac{\partial z}{\partial X_i} + z\{\frac{\partial \kappa}{\partial X_i}\}$$

where $[\overline{Q}]$ is the transformed reduced stiffness matrix for the layer, ϵ is the total strain for the laminate, ϵ^0 refers to the mid-plane strain and z refers to the distance from the mid-plane.

APPLICATION EXAMPLE

The following example demonstrates the application of theory described above for the optimisation of a composite structure. Figure 1 shows a composite rectangular plate with a central hole which is simply supported at both the shorter sides allowing rotational displacements at these edges. The loading consists of a normal uniform pressure applied to the edges of the hole resulting in the bending of the plate.
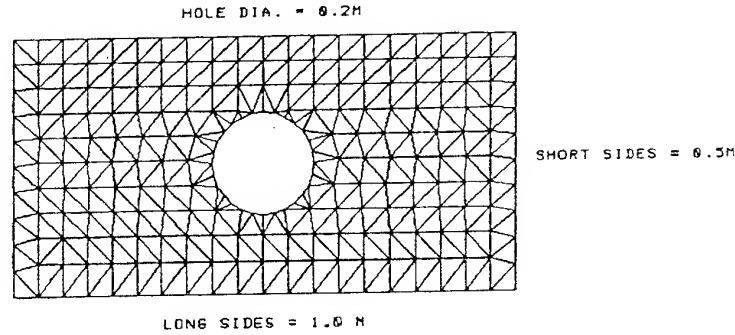
Figure 1 Composite Rectangular Plate with Central Hole

The laminate is composed of a four layers which are symmetric about the mid-plane. The first and fourth layers have an orientation angle of ninety degrees while the second and third layers were orientated at zero degrees. All the layers in the laminate are Kevlar in an epoxy matrix. Typical material properties are given in Table 1. The objective of the optimisation study was to reduce the weight of the structure using the thicknesses of the layers as design variables. Due to the symmetry of the layup there were therefore two design variables, h_1 and h_2. The constraints placed on the optimisation presses were stress related in the form of the Tsai-Hill Criterion. Move limits of 50 percent were imposed on the design variables and a convergence criteria of 0.01 was specified for the objective function and design variables.

E_x	76.00 GPa
E_y	5.50 GPa
G_xy	2.30 GPa
ν	0.34
ρ	1460 kg/m^3

Table 1: Propertiesof Kevlar reinforced epoxy

Iteration	Weight [kg]
1	11.68
2	8.76
3	7.01
4	5.84
5	4.67
6	4.50
7	4.82
8	4.81

Table 2: Weight reduction iteration history

Layer	Initial Thickness	Final Thickness
1 & 4	2.000 mm	0.348 mm
2 & 3	2.000 mm	1.303 mm

Table 3: Initial and final values of layer thicknesses

Eight complete design iterations were required to reduce the weight of the composite laminate from 11.68 kg to 4.82 kg. The iteration history of the objective function is shown in Table 2. The design variable history is shown in Figure 2 and initial and final values of the layer thicknesses are shown in Table 3. The initial reduction in weight was rapid and was limited by the move limits placed on changes of the design variables. The reduction in the thicknesses of the layers was also restricted by the move limits in iterations one to five, this resulted in the layer thicknesses remaining equal. After the fifth iteration the Tsai-Hill constraint on the second layer dominated the optimisation process as this layer was most sensitive to changes in the design variables therefore causing the divergence of the layer thicknesses.
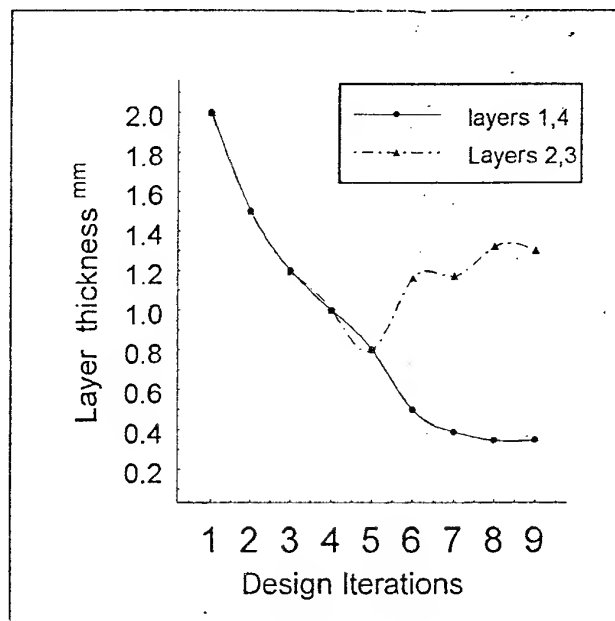
Figure 2: Design Variable Iteration History

CLOSURE

The foundation for the development of a structural design synthesis capability for composite structures has been presented in this work. The central goal of the methodology described here is the efficient representation of the optimisation problem in order that the optimisation process be reliable and efficient. In essence the

approach combines the most sophisticated methods that are available for the two phases of the optimisation process, ie. response prediction and optimisation. The versatility of finite element analysis allows response prediction to be carried out for a wide range of structural systems. The flexibility of the mathematical programming approach on the other hand describes the optimisation problem in a standard format and is therefore applicable to most design situations. The seamless integration of these powerful tools therefore represents an opportunity for the development of automated optimisation systems that are required for the design of modern high performance structures.

REFERENCES

[1] Vanderplaats G.N. An Efficient Feasible Directions Algorithm for Design Synthesis, *AIAA Journal*, Vol. 22, pp.1633-1640, 1984

[2] Santos J.L.T. , Godse M.M., Chaung K.H. and Stone T.A. An Interactive System for Structural Design Sensitivity Analysis and Optimisation, *Proceedings of the First International Conference*, Computational Mechanics Publications, June, 1989

[3] Shoup T.E. and Mistree F. Optimisation Methods with Applications for Personal Computers, Prentice Hall, 1987

[4] Brama T.,Applications of Structural Optimisation Software in the Design Process, *Proceedings of the First International Conference*, Computational Mechanics Publications, June, 1989

[5] COSMOS/M Users Guide (Volume 1) Version 1.7, Preprocessing, Analysis and Postprocessing Interface, Appendix , May 1993

[6]Ward P. and Cobb W.G.C. Application of I-DEAS Optimisation for the Static and Dynamic Optimisation of Engineering Structures, *Proceedings of the First International Conference*, Computational Mechanics Publications, June, 1989

[7] Reklaitis G.V., Ravindran A. and Ragsdell K.M., Engineering Optimisation: Methods and Applications, John Wiley and Sons, 1983

[8] Vanderplaats G.N., Muira H., Nagendra G. and Wallerstein D. Optimisation of Large Scale Structures Using MSC/Nastran, *Proceedings of the First International Conference*, Computational Mechanics Publications, June, 1989

EXPERIMENTAL INVESTIGATION OF CUMULATIVE DAMAGE AND FATIGUE LIFE DISTRIBUTION OF COMPOSITE LAMINATES

T. Y. Kam and K. H. Chu

Department of Mechanical Engineering

National Chiao Tung University

Hsin Chu 300, Taiwan

Republic of China

INTRODUCTION

Laminated composite materials have been used extensively in the construction of high performance structures such as automotive, marine and aerospace structures which are susceptibe to fatigue failure. Hoping that catastrophic failure can be avoided, fatigue of laminated composite materials has thus become an important topic of research and a vast amount of research work in this respect has been reported in the literature [1-8]. In particular, a review paper on fatigue damage models for laminated composite materials was given by Hwang and Han [9]. It was demonstrated that most of the models express fatigue damage in a functional form,

$$D = F\left(n,\ r,\ f,\ T,\ M, \cdots\right) \tag{1}$$

where n is number of fatigue cycles, r applied stress level, f frequency, T temperature, and M moisture content.

For a constant amplitude loading,

$$
\begin{array}{llll}
D=0 & \text{when} & n=0 & \\
D=1 & \text{when} & n=N & \tag{2}
\end{array}
$$

The above fatigue damage function was assumed to have a trend of either A, B, or C in Fig. 1. The properties of damage trends A, B and C are summarized as follows:

Damage trend	$\dfrac{dD}{dn}$	$\dfrac{d^2D}{dn^2}$
A	monotonic decreasing	negative
B	constant	0
C	monotonic increasing	positive

There is, however, no direct experimental evidence to support the correctness of the above damage trends for composite materials. In this paper, experimental investigation of fatigue damage of carbon/epoxy specimens is presented. Experimental results are used to

221

construct the damage trend and life distribution of the composite laminate subject to fatigue. Implications of the damage trend and life distribution are elaborated and discussed.

EXPERIMENTAL PROCEDURE

Fatigue tests of $[45°/-45°/45°/-45°]_s$ and $[45°/-45°_2/45°]_s$ carbon/epoxy specimens (see Fig. 2) made of prepreg tapes were performed using a computer controlled 10-ton Instron testing machine. The ultimate strengths of the laminates were determined via static tensile tests. A typical stress-strain relation is shown in Fig. 3. It is noted that material nonlinearity of the $[45°/-45°_2/45°]_s$ specimen is very obvious. During fatigue tests, maximum displacement of each specimen at each cycle was recorded by the computer via the stroke sensor of the testing machine. A set of fourteen to sixteen specimens was tested for each of the following stress levels: r=0.95, 0.9 and 0.85 with mean stress equal to half of the ultimate strength. Multi-stress fatigue tests of the specimens were also performed. The failure of the specimens was mainly due to fracture of matrix.

RESULTS AND DISCUSSIONS

The fatigue damage at any fatigue cycle n is defined as the ratio of strain at that cycle, $\varepsilon(n)$, to failure strain, ε_f.

$$D = \frac{\varepsilon(n) - \varepsilon_0}{\varepsilon_f - \varepsilon_0} \tag{3}$$

where ε_0 is the initial strain induced by mean stress.

Since both $\varepsilon(n)$ and ε_f have been determined from measured maximum displacement at the nth cycle and the end of fatigue life, respectively, the damage in the above equation can be estimated experimentally. Fig. 4 shows the experimentally determined damage functions of various stress ratios for the $[45°/-45°/45°/-45°]_s$ laminate. It is noted that based on the present results in Fig. 4 the damage trends do not look like those in Fig. 1 and in fact they can be divided into three stages, namely, early, stable and final stages, in which damage accumulated in the specimen increases drastically in the early stage, slows down in the stable stage and again bulids up till fracture in the final stage. The three stages can be illustrated in Fig. 5 using the damage trend of r=0.85 as an example. It worths pointing out that Hwang and Han [9] have used eqn (3) to construct a cumulative damage model. The damage trends predicted by their model for various stress levels are shown in Fig. 5 for comparison. It is noted that Hwang and Han's model predicts very different damage trends as comparing with the experimental ones. This finding has not been reported in the literature and thus should be valuable for fatigue study of composite laminates. Fatigue test results of $[45°/-45°_2/45°]_s$ specimens have shown that the fatigue life of the specimens can be well modeled by the Weibull distribution. For instance, Figs 6-8 show the experimental fatigue lives fitted by the Weibull distribution (α is shape

parameter and θ is characteristic life) for the specimens subjected to various stress sequences (n_i is number of cycles for stress ratio r_i). The results also show that the coefficient of variation can be as high as 70%. Therefore, an accurate fatigue damage model must be constructed and variation of fatigue life considered if more reliable prediction of fatigue behavior of composite materials is desired.

CONCLUSION

Experimental investigation of fatigue properties of composite laminates was performed. Test results on damage trends and life distributions of the laminates subjected to various stress conditions were presented. It has been shown that the commonly assumed damage trends are invalid for the composite material under consideration, Weibull distribution is appropriate for modelling fatigue life of the laminates and variation of fatigue life is very high. These properties are important for fatigue reliability study of composite laminates.

ACKNOWLEDGEMENT

REFERENCES

1. Yang, J. N. and Liu, M. D., "Fatigue and Residual Strength Degradiation for Graphite/Epoxy Composite under Tension-Compression Cyclic Loading.", J. Composite Material, Vol. 12, pp. 19-39 (1978).
2. Hashin, Z., "Cumulative Damage Theory for Composite Materials: Residual Life and Residual Strength Methods.", Composite Science and Technology, Vol. 23, pp. 1-19 (1985).
3. Chou, P. C. and Croman, R., "Residual Strength in Fatigue Based on the Strength-Life Equal Rank Assumption.", J. of Composite Materials, Vol. 12, pp. 177-194 (1978).
4. Wang, S. S. and Chim, E. S. M., "Fatigue Damage and Degradation in Random Short-Fiber SMC Composites.", J. of Composite Materials, Vol. 17, pp. 145-150 (1983).
5. Wang, S. S., Goetz, P. P. and Corten, H. T., "Shear Fatigue Degradation and Fracture of Random Short-Fiber SMC Composites.", J. of Composite Materials, Vol. 18, pp. 2-20(1984).
6. Han, K. S. and Hamadi, M., "Fatigue Life Scattering of RP/C.", 38th Annual RP/CI Conference, SPI (1983).
7. Radhakrishnan, K., "Fatigue and Reliability Evaluation of Unnotched Carbon Epoxy Laminates.", J. Composite Materials, Vol. 18, pp. 21-31 (1984).
8. Yang, J. N., Lee, L. J. and Sheu, D. Y., "Modulus Reduction and Fatigue Damage of Matrix Doiminated Composite Laminates.", J. Composite Structures, Vol. 21, pp. 91-100 (1992).
9. Hwang, W. and Han, K. S., "Cumulative Damage Models and Multi-Stress Fatigue Life Prediction.", J. of Composite Materials, Vol. 20, pp. 125-153 (1986).
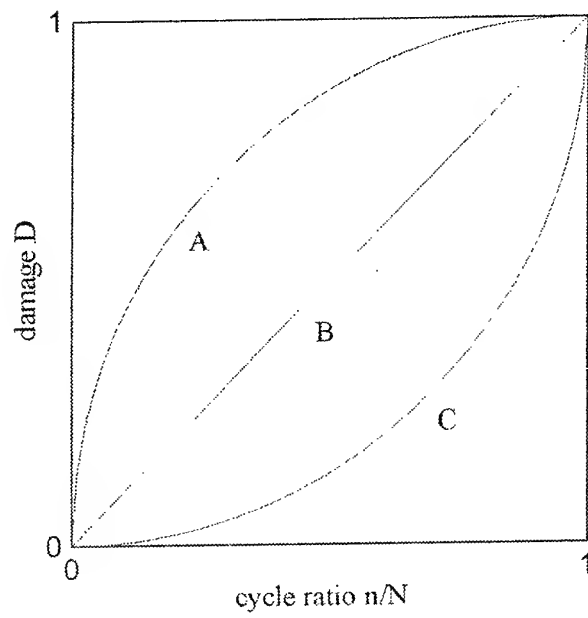
Fig. 1　Various types of damage trend
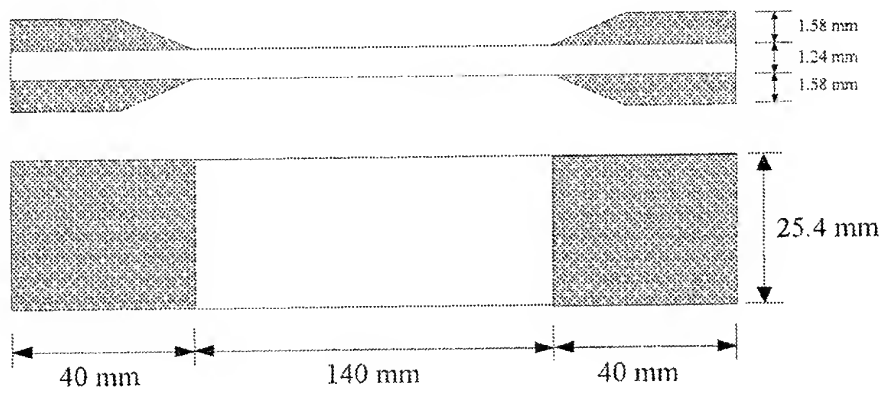
Fig. 2　Dimensions of specimen
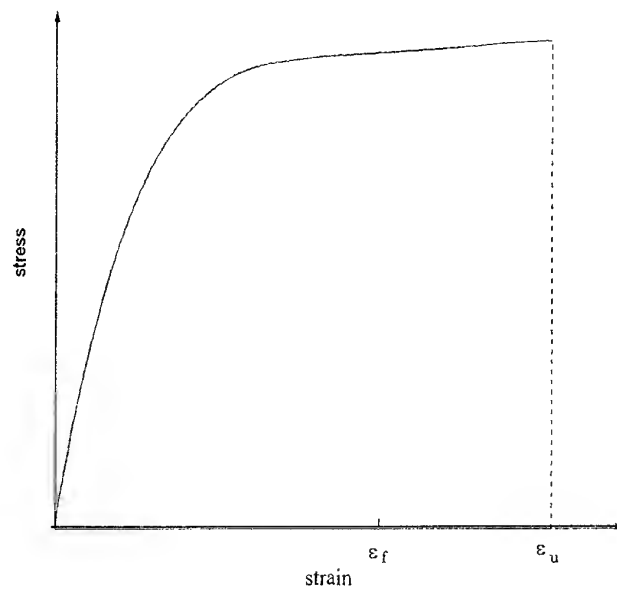
Fig. 3 Stress-strain curve of $[45°/-45°_2/45°]_S$ laminate
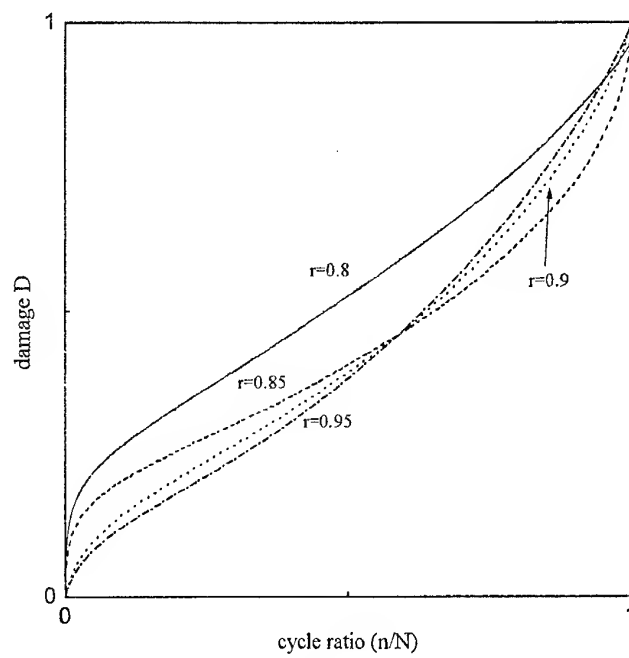
Fig. 4 Damage functions of various stress ratio for
$[45°/-45°/45°/-45°]_s$ laminate.

225
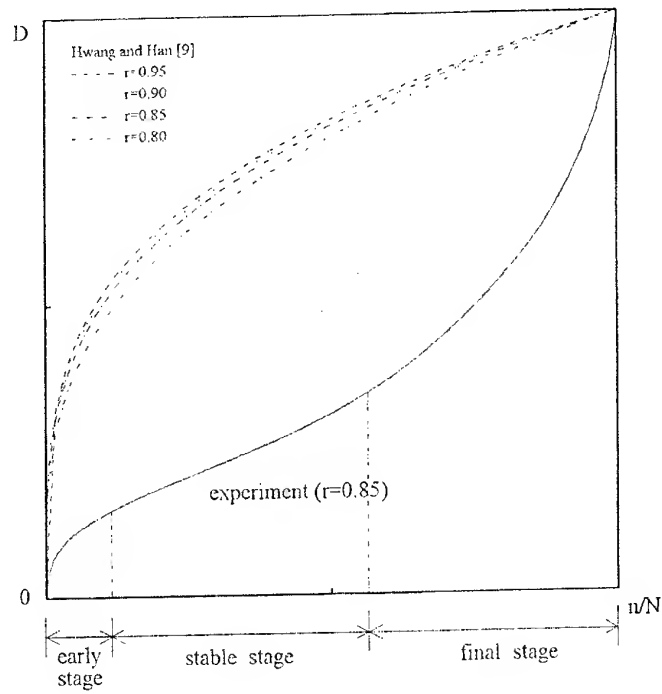
Fig. 5 Damage trends obtained by different methods
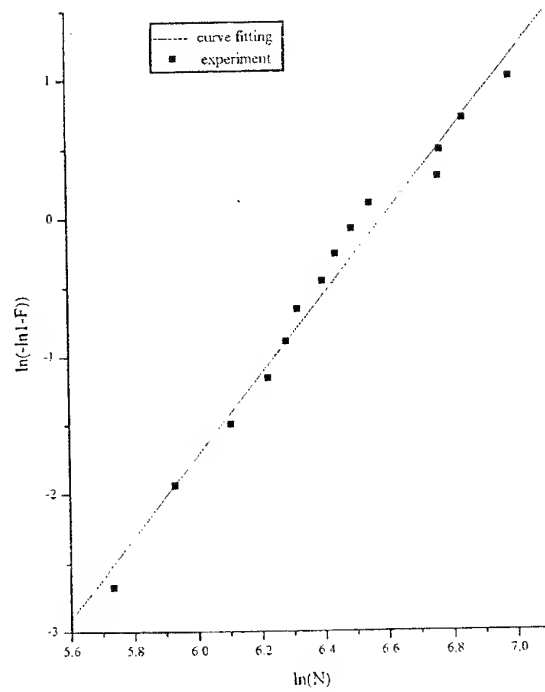
Fig. 6 Fatigue life data at r=0.9 fitted by Weibull
distribution (R=1-F(n); α=2.92501, Θ=729.77)

226
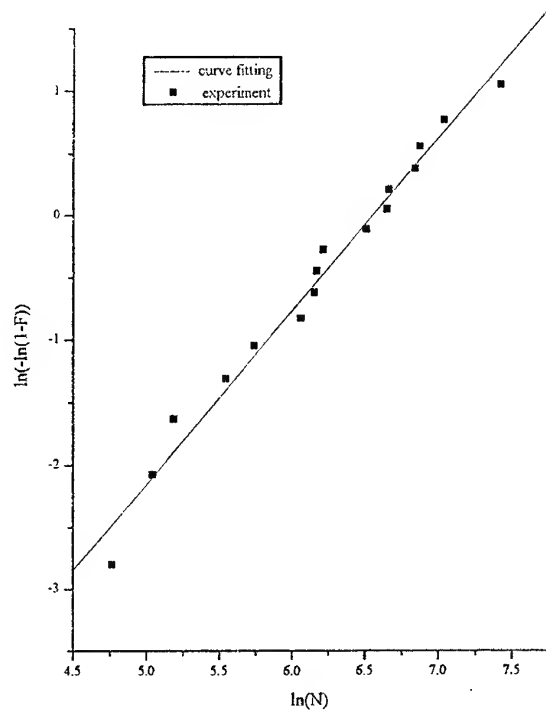
Fig. 7 Fatigue life data fitted by Weibull distribution
$(r_1=0.95, r_2=0.90, n_1=80)$
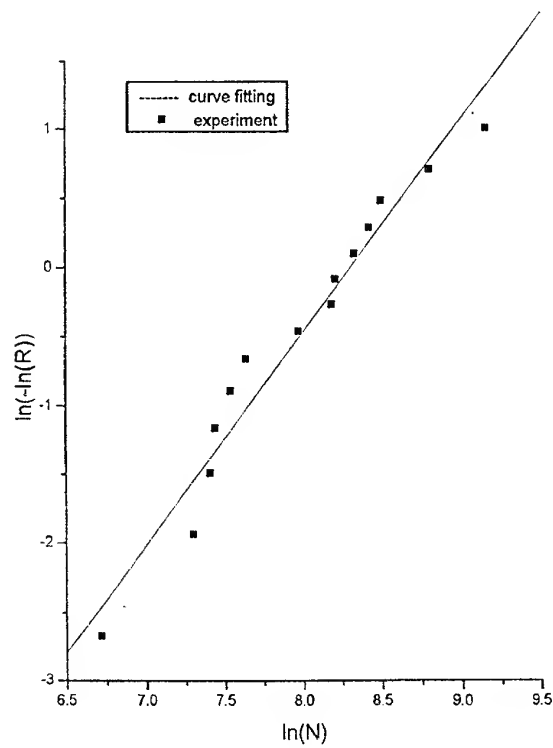
Fig. 8 Fatigue life data fitted by Weibull distribution
$(r_1=0.95, r_2=0.90, r_3=0.85, n_1=80, n_2=150)$

Flow characteristics and forming defects in SMC
- Relation between fibre orientation and defects-

T. Katayama[1], M. Shinohara[2], T. Inaho[1],
Y. Hayakawa[3], and M. Hakotani[3]

[1]Doshisha Univ., Tanabe-cho. Kyoto, Japan
[2]Maizuru College of Tech., Kyoto, Japan
[3]Takeda Chemical Industries, Ltd., Yodogawa-ku, Osaka, Japan

INTRODUCTION

Sheet Moulding Compound (SMC) products such as one piece panel , have always stiffening ribs. In this product, some defects are observed. They are sink mark, weld lines, warpage and heat cracks. These defects are greatly influenced by moulding condition of SMC, especially material flow. In the design of the mould, the material flow is an important factor. But the material flow of SMC is complex and unsteady. So, CAE system of SMC is needed to design moulding die. Therefore, we are constructing the data base to design the compression moulding process of SMC.

In this paper, we investigated flow characteristics and forming defects of SMC products. In flow characteristics, we paid attention to the branch of the material flow around the rib part. To obtain the relation between the flow characteristics and the defects, Moulding Processes for T-shaped products were carried out in varying the charge pattern and the shape of the rib. Then we measured the warpage and observed the heat crack. On the other hand, we took the fibre orientation in the cross section of moulding products.

Moreover, to Construct CAE system of SMC, we tried to calculate the thermal shrinkage in cooling down after the process, using the deformation model for the numerical analysis where SMC has the anisotropic homogeneity.

MOULDING CONDITION

We used SMC which thickness is about 2 mm, and determined the number of layers to be thickness of products, 5 mm. To make the layer flow clear, two colours of SMC were laminated in turn. The charge ratios are 30%, 60% and 100%, and they express in area, ratio between the die and materials.

In moulding, we used a 150t press machine and set closing speed at 0.15 mm/s, the moulding pressure at 10MPa, and the moulding temperature at 140°C. Regarding the rib shape, the width , B is 2, 5, 10, 20, 40, 60 and 80 mm, the height, H is 10, 20, 30 and 40 mm, the thickness of products is 5 mm and the radius of the rib corner, R is 0 and 5 mm.

In measuring the warpage, we measured three points and calculated the warpage of products. We defined that the concave shape warpage is positive value and the convex shape warpage is negative value.

229

FLOW CHARACTERISTICS

We investigated flow characteristics, especially the material branch around the rib. Experimental method is a short-shot method in moulding process in the rib height, 20mm, and we calculated incremental flow ratio between rib and plane from short-shot data at each incremental stage. As we thought that the flow ratio between rib and plane is varying unsteadily, we divided the filling state of rib into three stages, as stage I, stage II, and stage III. In dividing into three stages, the filling ratio between filling material and rib volume is $0 \sim 1/3$ as stage I, $1/3 \sim 2/3$ as stage II, and $2/3 \sim 1$ as stage III. And we defined that, in the case of the 100% flow ratio, all materials flow to plane, as opposed to 0% where all materials flow to rib. We used parameter, B/ts, which expresses the geometry of die, where B is rib width and ts is the material thickness at beginning to flow to rib, because, in the previous study[1]-[6], it well characterised the material flow during the compression moulding process. Fig.1 shows the relationship between flow ratio and B/ts. These graphs show generally the declivity to the right side, and the flow ratio is 0% over some B/ts values.

In stage I of the 30% charge, the flow ratio is about 100% at small B/ts. This means that the most of the materials flow to plane. But, for over 1.0 in B/ts, the flow ratio shows 0%. This shows that no materials flow to plane. In stage II, owing to the higher filling ratio to rib in comparison with the case of stage I, some of the materials flow to the plane at the bigger B/ts. In stage III, the larger part of the materials flow to the plane at the less than 3 in B/ts . But, over 3 in B/ts , we can find no material flow to plane till the end of filling up rib. In this case, the plane part begins to be filled after the rib is full.

a) stage I

b) stage II

c) stage III
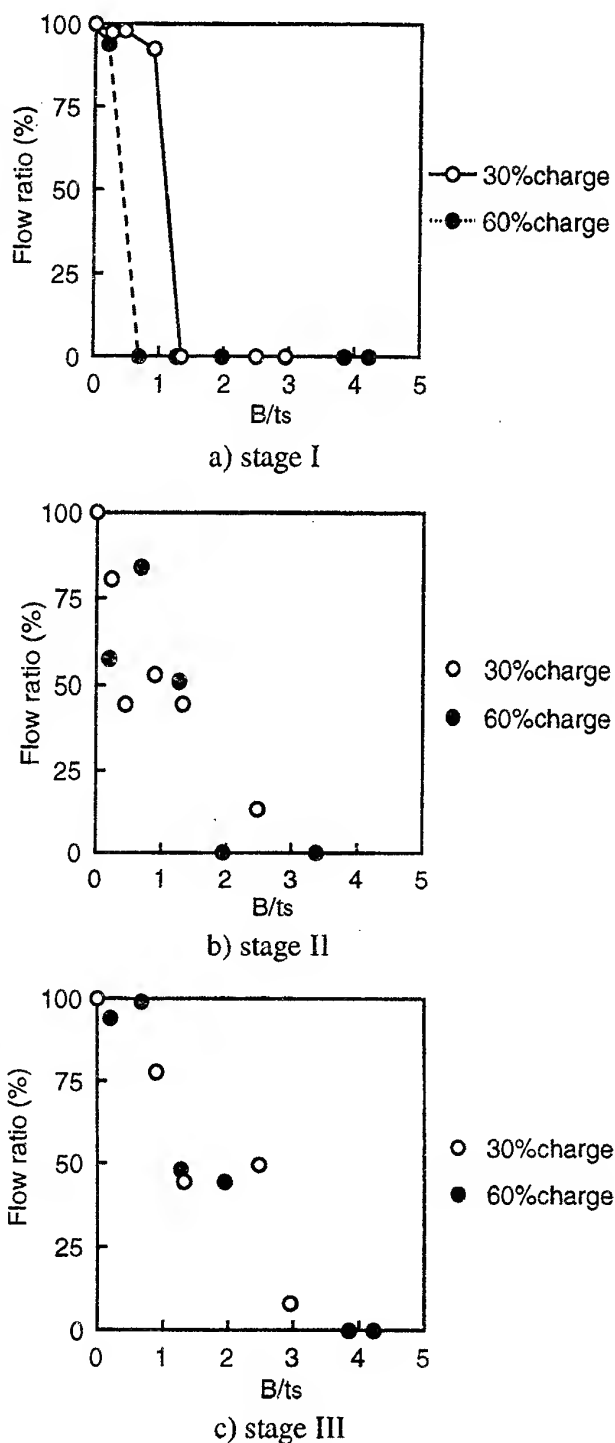
Fig.1 Relationship between Flow ratio and B/ts.

230

Regarding 60% charge, in stage I, the flow ratio becomes 0% at the smaller B/ts in comparison with the case of 30% charge, because the materials in 60% charge exist in some part of plane over the rib at the initial stage. As the process goes on, the relation between the flow ratio and B/ts is similar to the one in 30% charge.

FIBRE ORIENTATION AND DEFECTS
Effect of charge pattern on defects

Fig.2 shows the relationship between warpage and B/t where B is the rib width and t is the thickness of products. In 100% charge, the maximum warpage is obtained around 1.0 in B/t. Photo.1 shows the fibre orientation in the cross section of a product. The fibre orientation makes a long circuit at the upper part of the rib corner. We think that this is the reason for warpage. On the other hand, the warpage in 30 % and 60% charge is greatly reduced in comparison with one in 100% charge. The fibre orientation in the part charge does not make a long circuit at the upper part of the rib corner. That is why warpage is reduced.

As the fibre orientation depends mainly on the material flow during moulding process, we investigated the flow state of moulding. In 100 % charge, the materials flow only to rib, because there is no space at plane. As SMC has glass fibre in plane, the bending rigidity is high. So, the fibre layer in SMC makes a

Fig.2 Relationship between Warpage and B/t.
(H=10mm, R=0mm)

a) B=5mm, H=10mm, R=0mm

b) B=20mm, H=10mm, R=0mm

Photo.1 Cross section of product.

long circuit around the rib corner. While, in 30% and 60% charge, as there is space at plane, the materials have the ability to flow to both rib and plane at the same time. So, these processes need the lower forming force and the rounding of the fibre layer hardly formed around the rib corner.

However, there is still a little warpage where B/t is about 1.0. Because, in less than 3 in B/ts, the material flow to plane is obtained before filling up rib as the above. That

means the flow characteristics in the smaller B/ts are more similar to the ones in 100% charge.

Thermal shrinkage analysis

One of the aims of our study is to construct CAE system in SMC. Warpage was calculated by thermal shrinkage analysis in cooling down after the process. Table 1 shows material constants of SMC used in this analysis. SMC is modelled to have the anisotropic homogeneity in the numerical analysis. The fibre orientations in each element are obtained by measuring products.

Fig.3 shows warpage from this analysis. Comparing the numerical result with experiment, in the smaller height of rib, we had a good agreement in quality and we are agreeable to experiments. It is confirmed from this result that the warpage depends deeply on the fibre orientation. To obtain the better solution, we have to consider to take the exact fibre orientation by using smaller element.

Table 1 Material constant of SMC used in this analysis.

Longitudinal modulus	EL	12.0 GPa
Transverse modulus	ET	7.2 GPa
Shear modulus	Es	6.9 GPa
Poisson's ratio		0.29
Thermal expansion coefficient	α L	2.3×10^{-5} 1/K
	α T	7.5×10^{-5} 1/K
Moulding temperature		140℃
Room temperature		25℃
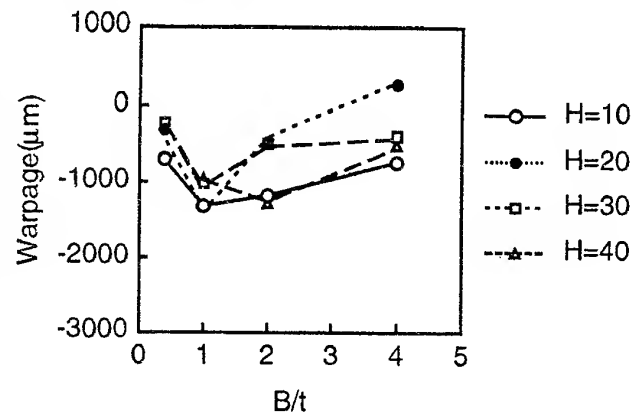
Fig. 3 Relationship between warpage and B/t.
(analysis, 100% Charge)

Effect of charge pattern on heat cracks

In 100% charge, heat cracks were observed at the opposite side against the rib (called " back face") and the side face of the rib. Fig.4 shows the presence of the heat cracks. However, in 30% and 60% charge, we could not find the heat cracks on any surface. Photo.2 shows the fibre orientation in the cross section of rib.

In 100% charge, the flow pattern shows a snaking flow and a buckling around the rib. As the result, there is a weld line or a resin rich part around rib. Around the rib corner near the back face, the meander becomes greater in the lower height of rib due to buckling. It is considered that the heat crack occurs when a weld line or a resin rich part exists at the stress concentrated part.

On the other hand, in 30% and 60% charge, the snaking and the buckling did not occur, because the materials have the ability to flow to both rib and plane as the above in the flow characteristics. Therefore, it is hard to find the heat crack in the low charge.
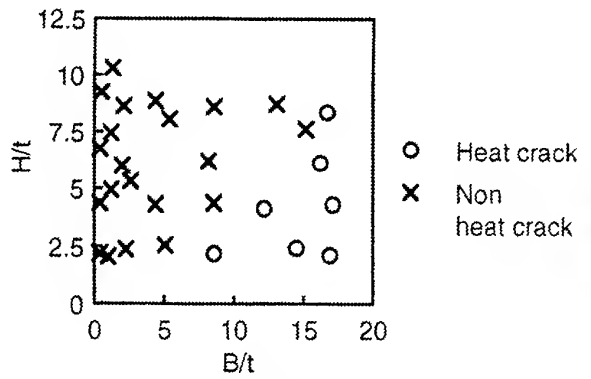
a) back face
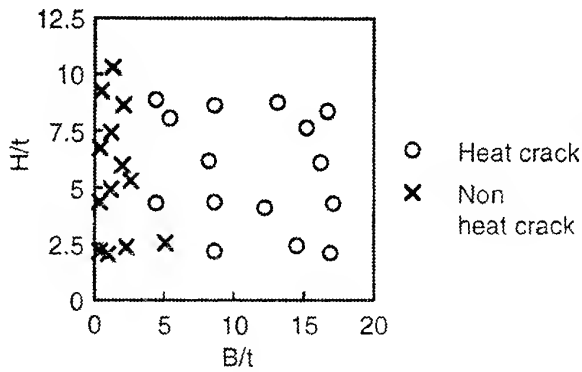
b) side face

Fig.4 Presence of heat crack.

a) 100% Charge

b) 60% Charge

c) 30% Charge

Photo.2 Cross section of product.
(B=40mm, H=10mm, R=0mm)

Residual stress analysis

As we considered that the fibre orientation and the residual stress seemed to influence on the heat cracks , we calculated the residual stress in consideration of the fibre orientation. This model is the same as the warpage analysis, but we used non-liner incremental method to consider the constraint condition.

Fig.5 shows the distribution of the equivalent stress. It is established that the stress concentration in 100% charge is nearly equal to the one in 30% and 60 % charge. The place, where the stress concentration occurs, agrees with the place where the heat crack occurs. We find the weak structure such as a weld line and a resin rich at this place, but, in 30% and 60% charge, there is no weak structure at this place.

a) B=40mm, H=40mm, 100%Charge

b) B=60mm, H=40mm, 100% Charge

Fig.5 Distribution of equivalent stress.

233

Fig.6 shows the relationship between the maximum equivalent stress and B/t. The maximum stress increases radically till B/t becomes about 3. This result has a good agreement with Fig.4. From this numerical result, the tendency, of the heat crack occurring, is able to be estimated, but the existence of the heat crack is not able to be decided.

We have to consider the use of the smaller element or to use the heterogeneous model in order to obtain the heat crack.
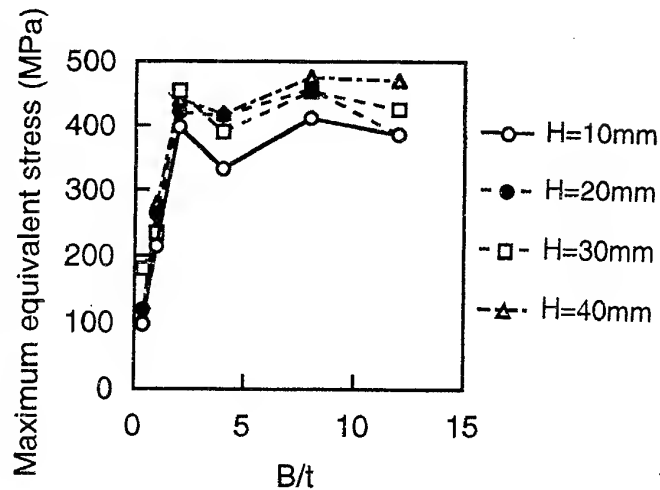
Fig. 6 Relationship between Maximum equivalent stress and B/t.

CONCLUSION

1. In the smaller B/ts , the flow characteristics of the part charge are similar to the ones of 100% charge.
2. The warpage and the heat crack can be reduced by the low charge process.
3. The warpage can be suppressed by the very small B/ts or the large B/ts during the low charge process.
4. The heat crack occurs by the interaction between the stress concentration and the weak structure such as a weld line and a resin rich.
5. The analysis using the anisotropic homogeneity model can predict the tendency of warpage and heat crack.

REFERENCES

[1] WALTER MICHAELI, " Simulation of moulding and part performance-An integrated CAE-approach." ,Composite institute, The Society of the Plastics Ind. (11-C)(1990)

[2] DUCK-KI KIM, "Experimental investigation and numerical simulation of SMC in compression moulding" , Journal of Materials Processing Technology, 49, pp.333-344 (1995)

[3]T.HIRAI and T. KATAYAMA, "Flow state of composite material in the forging die during the molding process" , Proc. of ICCM-II, p.1283(1978).

[4]M.YAMABE,T.FUJIWARA,T.HIRAI,T.KATAYAMA, " Rheological behavior of fiber reinforced composite material during compression molding" , Proc. of 31st International SAMPE Symposium,pp.1666(1986).

[5]T.HIRAI, T.KATAYAMA, M.YAMABE, K.WATANABE, " Effects of asymmetrical configuration of rib parts on defects of SMC products" ,Proc. of International Symposium on FRP/CM, pp.1(5-c)(1988).

[6]T.HIRAI, T.KATAYAMA, M.YAMABE, M.ISHIJIMA, " Experimental and numerical flow analysis in SMC compression moulding under low charge ratio" , Proc. of ICCM/VIIIpp.1(10-N) (1991).

HIGHER ORDER DISPLACEMENT DISCONTINUITY ELEMENTS FOR ANALYSIS OF STRESSES IN AN ELASTIC ANISOTROPIC MEDIUM WITH CRACKS

M.A. Kayupov[1], S. Sakurai[2] and M. Kuriyagawa[3]

[1] Institute of Mining, National Academy of Sciences , Kazakhstan
Currently: Geotechnology Department, National Institute for Resources and Environment, 16-3, Onogawa, Tsukuba City, Ibaraki Pref., 305, Japan; tel.: (+81)-(298)-58-8538; fax: (+81)-(298)-58-8508; E-mail: kayupov@nire.go.jp
[2] Department of Architecture and Civil Engineering, Kobe University, Japan
[3] Geotechnology Department, National Institute for Resources and Environment, Japan

INTRODUCTION

The Displacement Discontinuity Method (DDM) provides a very convenient representation of cracks in two-dimensional (2D) elastic media. The original version of the method, as presented by Crouch [4], is based on a solution for a 2D constant displacement discontinuity element. The constant elements have the advantage of simplicity, however, displacement discontinuity models with such elements can not accurately predict the stresses and displacements for field points in close vicinity of crack surfaces. To avoid this difficulty and to guarantee accurate results in these areas, higher order and crack tip elements were used in 2D isotropic analysis [1-3, 9].

In the paper, new analytical influence functions for higher order and crack tip displacement discontinuity elements are used in the Higher Order DDM for anisotropic analysis of crack problems. The integration method and analytical influence functions for similar stress discontinuity elements were reported in the paper [7]. The derivation of the influence functions was based on S.G.Lekhnitskii's [8] analytical solution for a single concentrated force applied at an arbitrary point of the continuous infinite anisotropic plane. Along with the analytical functions their Taylor series approximations are also provided. The last can be employed to calculate stresses and displacements at the points distant from the elements. The functions can be used to solve the generalized plane strain problems with 3D boundary conditions by the DDM computer codes, and an elastic homogeneous medium with arbitrary anisotropy may be considered. The accuracy of the computer code is demonstrated by example problems and the results are in a good agreement with the known analytical solutions.

DISPLACEMENT DISCONTINUITY ELEMENTS

Let us consider a displacement discontinuity element in a homogeneous, infinite, linear elastic, anisotropic medium without body forces. The element looks like an infinite flat band that is parallel to axis Oz (Figure 1 *a*). The displacement discontinuities D being distributed on the band do not depend on the coordinate z. Since for prearranged conditions any plane xy, perpendicular to axis Oz, is at the same state, it is possible to consider the plane Oxy only. The straight segment AB belongs to both the band and the plane Oxy. Further in the paper we will call the segment AB as an element, however, keeping in mind that the displacement discontinuities D (D_ξ, D_η, D_z) are distributed on the infinite band (Figure 1 *b*). Thus, the displacements u are continuous everywhere in the plane Oxy except over the line segment AB. Following the book [5] we can distinguish two surfaces of the element by saying that one surface is the positive one of $\eta=0$, denoted $\eta=0_+$, and the other is the negative one, denoted $\eta=0_-$. The displacement
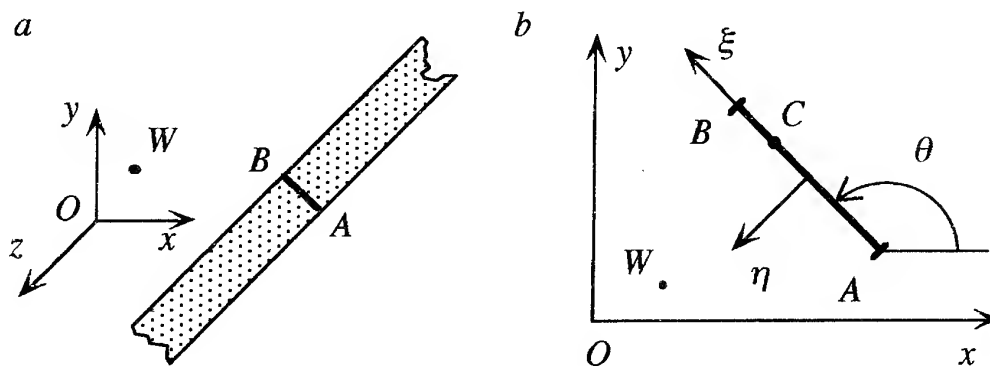
Figure 1. The infinite band (*a*) and the local coordinate system $\xi\eta$ (*b*).

discontinuity D_α ($\alpha = \xi$, η, z) is defined as the difference in displacement between the two surfaces of the element as follows

$$D_\alpha = u_\alpha(\xi, 0_-, z) - u_\alpha(\xi, 0_+, z) \qquad (\alpha = \xi, \eta, z).\tag{1}$$

Lekhnitskii's formulae [6, 8] can be used for determining stresses and displacements at an arbitrary point $W(x_W, y_W)$ of the anisotropic plane Oxy (Figure 1 *b*) due to the displacement discontinuities applied on the element AB.

$$\sigma_x = 2\mathrm{Re}[\mu_1^2\Sigma_1 + \mu_2^2\Sigma_2 + \mu_3^2\lambda_3\Sigma_3], \quad u_z = 2\mathrm{Re}\sum_{k=1}^{3} r_k\Pi_k, \text{ etc.}\tag{2}$$

Here Re[ ] means real part of the complex number between brackets; Π_j and Σ_j are complex variable functions.

CONSTANT, LINEAR, PARABOLIC AND HIGHER ORDER DISPLACEMENT DISCONTINUITY ELEMENTS

The displacement discontinuity D $\{D_\xi, D_\eta, D_z\}$ changes as polynomial function along the segment (element) AB and at point $C(x_C, y_C)$ on the segment AB (Figure 1 *b*),

$$D(t) = D_k(t / L_{AB})^k, \quad D_k \equiv D_k \{D_{\xi k}, D_{\eta k}, D_{zk}\} = \text{const}.\tag{3}$$

Here and in the remainder, t is the distance between point A and point C on the segment AB; constants $D_{\xi k}$, $D_{\eta k}$ and D_{zk} are independent displacement discontinuities in the directions ξ, η and z, respectively; L_{AB} is the length of the segment AB and parameters ω_{Wj}, ω_{Aj}, ω_{Bj}, Λ_j, Ω_j are defined as follows

$$\omega_{Wj} = x_W + \mu_j y_W, \quad \omega_{Aj} = x_A + \mu_j y_A, \quad \omega_{Bj} = x_B + \mu_j y_B,\tag{4}$$

$$\Lambda_j = \frac{\omega_{Wj} - \omega_{Bj}}{\omega_{Wj} - \omega_{Aj}}, \quad \Omega_j = \frac{\omega_{Wj} - \omega_{Aj}}{\omega_{Bj} - \omega_{Aj}}, \quad (j = 1, 2, 3),$$

where x_W, y_W, x_A, y_A and x_B, y_B are coordinates of the points W, A and B, respectively. If $k=0$ in the expression (3) then we have a Constant Element. If $k=1$ or

$k=2$ then we have Linear or Parabolic Elements, respectively. If $k>2$ then we will call such an element as k-order one.

For these elements, complex variable functions Π_j and Σ_j in the equations (2) are

$$\Pi_j = \Omega_j^k\left(\frac{\Omega_j^{-k-1}}{k+1} - \ln\Lambda_j - \sum_{l=1}^{k+1}\frac{\Omega_j^{-l}}{l}\right)\sum_{\alpha=\xi,\eta,z}\frac{L_{AB}(B_{\alpha j}\mu_j + C_{\alpha j})D_{\alpha k}}{\omega_{Bj} - \omega_{Aj}}, \qquad (5)$$

$$\Sigma_j = -\Omega_j^{k-2}\begin{bmatrix} k\Omega_j\ln\Lambda_j - \sum_{l=1}^{k+1}\left(1-\frac{k}{l+1}\right)\Omega_j^{-l} + \\ +\frac{1}{\Lambda_j} + k - 1 + \Omega_j^{-k}\sum_{l=1}^{2}\frac{l}{k+l}\cdot\Omega_j^{1-l} \end{bmatrix}\sum_{\alpha=\xi,\eta,z}\frac{L_{AB}(B_{\alpha j}\mu_j + C_{\alpha j})D_{\alpha k}}{(\omega_{Bj} - \omega_{Aj})^2}.$$

If $|\Omega_j| > 1$ then $\ln\Lambda_j = \ln\left(1 - \frac{1}{\Omega_j}\right) = -\sum_{l=1}^{\infty}\frac{1}{l\Omega_j^l};\quad \frac{1}{\Lambda_j} = \frac{1}{1-\frac{1}{\Omega_j}} = \sum_{l=1}^{\infty}\frac{1}{\Omega_j^{l-1}}$

and

$$\Pi_j = \frac{L_{AB}}{\omega_{Bj} - \omega_{Aj}}\sum_{\alpha=\xi,\eta,z}(B_{\alpha j}\mu_j + C_{\alpha j})\sum_{l=1}^{\infty}\frac{D_{\alpha k}}{(l+k)\Omega_j^l}, \qquad (6)$$

$$\Sigma_j = -\frac{L_{AB}}{(\omega_{Bj} - \omega_{Aj})^2}\sum_{\alpha=\xi,\eta,z}(B_{\alpha j}\mu_j + C_{\alpha j})\sum_{l=1}^{\infty}\frac{l}{l+k}\cdot\frac{D_{\alpha k}}{\Omega_j^{l+1}}.$$

LEFT ROOT DISPLACEMENT DISCONTINUITY ELEMENT

For the element, $D(t) = D_{lr}\sqrt{t/L_{AB}}$, $D_{lr} \equiv D_{lr}\{D_{\xi lr}, D_{\eta lr}, D_{zlr}\} = \text{const}$.

Complex variable functions Π_j and Σ_j in the equations (2) are

$$\Pi_j = -\frac{2L_{AB}}{\omega_{Bj} - \omega_{Aj}}\left(1 + \frac{1}{2}\sqrt{\Omega_j}\ln\frac{\sqrt{\Omega_j}-1}{\sqrt{\Omega_j}+1}\right)\sum_{\alpha=\xi,\eta,z}\left(B_{\alpha j}\mu_j + C_{\alpha j}\right)D_{\alpha lr}, \qquad (7)$$

$$\Sigma_j = -\frac{L_{AB}}{(\omega_{Bj} - \omega_{Aj})^2}\left[\frac{1}{2\sqrt{\Omega_j}}\ln\frac{\sqrt{\Omega_j}-1}{\sqrt{\Omega_j}+1} + \frac{1}{\Omega_j-1}\right]\sum_{\alpha=\xi,\eta,z}\left(B_{\alpha j}\mu_j + C_{\alpha j}\right)D_{\alpha lr}.$$

If $|\Omega_j| > 1$ then

$$\Pi_j = \frac{2L_{AB}}{\omega_{Bj} - \omega_{Aj}}\sum_{l=1}^{\infty}\frac{1}{2l+1}\cdot\frac{1}{\Omega_j^l}\sum_{\alpha=\xi,\eta,z}\left(B_{\alpha j}\mu_j + C_{\alpha j}\right)D_{\alpha lr}, \qquad (8)$$

$$\Sigma_j = \frac{L_{AB}}{(\omega_{Bj} - \omega_{Aj})^2}\left(\sum_{l=1}^{\infty}\frac{1}{2l-1}\cdot\frac{1}{\Omega_j^l} + \frac{1}{1-\Omega_j}\right)\sum_{\alpha=\xi,\eta,z}\left(B_{\alpha j}\mu_j + C_{\alpha j}\right)D_{\alpha lr}.$$

237

RIGHT ROOT DISPLACEMENT DISCONTINUITY ELEMENT

For the element, $D(t) = D_{rr}\sqrt{1 - t/L_{AB}}$, $\quad D_{rr} \equiv D_{rr}\{D_{\xi rr}, D_{\eta rr}, D_{zrr}\} = $ const.

Complex variable functions Π_j and Σ_j in the equations (2) are

$$\Pi_j = \frac{L_{AB}}{\omega_{Bj} - \omega_{Aj}}\left[2 + \sqrt{1 - \Omega_j}\ln\frac{\sqrt{1 - \Omega_j} - 1}{\sqrt{1 - \Omega_j} + 1}\right]\sum_{\alpha = \xi, \eta, z}\left(B_{\alpha j}\mu_j + C_{\alpha j}\right)D_{\alpha rr}, \qquad (9)$$

$$\Sigma_j = -\frac{L_{AB}}{\left(\omega_{Bj} - \omega_{Aj}\right)^2}\left[\frac{1}{2}\frac{1}{\sqrt{1 - \Omega_j}}\ln\frac{\sqrt{1 - \Omega_j} - 1}{\sqrt{1 - \Omega_j} + 1} - \frac{1}{\Omega_j}\right]\sum_{\alpha = \xi, \eta, z}\left(B_{\alpha j}\mu_j + C_{\alpha j}\right)D_{\alpha rr}.$$

If $|\Omega_j| > 1$ then

$$\Pi_j = -\frac{2L_{AB}}{\omega_{Bj} - \omega_{Aj}}\left[\sum_{l=1}^{\infty}\frac{1}{2l+1}\cdot\frac{1}{\left(1 - \Omega_j\right)^l}\right]\sum_{\alpha = \xi, \eta, z}\left(B_{\alpha j}\mu_j + C_{\alpha j}\right)D_{\alpha rr}, \qquad (10)$$

$$\Sigma_j = \frac{L_{AB}}{\left(\omega_{Bj} - \omega_{Aj}\right)^2}\left[\sum_{l=1}^{\infty}\frac{1}{2l-1}\cdot\frac{1}{\left(1 - \Omega_j\right)^l} + \frac{1}{\Omega_j}\right]\sum_{\alpha = \xi, \eta, z}\left(B_{\alpha j}\mu_j + C_{\alpha j}\right)D_{\alpha rr}.$$

In the equations (5) - (10), coefficients $B_{\alpha j}$ and $C_{\alpha j}$ ($\alpha = \xi$, η, z) depend on elastic properties of the medium and the angle θ (Figure 1 b). These coefficients can be found analytically.

NUMERICAL EXAMPLES

As an example, let us consider a straight crack (Figure 2 a). The center of the crack coincides with the center of the coordinate system Oxy. The length of the crack is equal to $2c$. Traditional approximation of the crack surfaces by displacement discontinuity elements is shown in Figure 2 b. According to this approach, the crack is approximated by the "chain" of boundary elements. Although the above analytical influence functions can be used in the general Higher Order Displacement Discontinuity Method [3, 9], an alternative technique seems to be more efficient and accurate one in this particular case. Unlike the usual DDM boundary approximation, we can use coinciding boundary elements to model the straight crack (Figure 2 c). Each such element has the same length as the crack. However, any element has its own influence function. Boundary conditions are satisfied at several nodal points. The nodes have the same positions for different elements. If the number of the nodes equals n then Constant, Linear, Parabolic, 3rd-order, ... , $(n-2)$-order elements, together with Left and Right Root ones, are used to solve the problem. In the numerical examples shown below, $n=11$ for any boundary element. This technique makes the results continuous in close vicinity of the crack.

Slit within an isotropic medium in triaxial stress field with remote stress components $\sigma_x^o = 0.347$, $\sigma_y^o = 0.913$, $\sigma_z^o = 0.740$, $\tau_{xy}^o = 0.150$, $\tau_{xz}^o = 0.250$, $\tau_{yz}^o = -0.200$ (generalized plane strain problem). Table 1 compares closed-form and numerical solutions for stresses along the ray r drawn from near the tip of the slit (Figure 2 a).
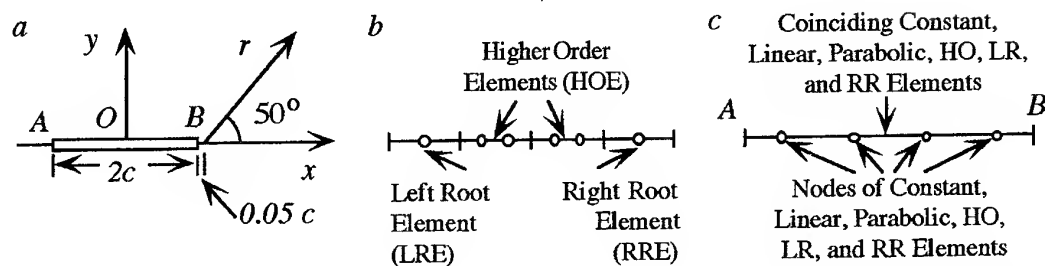
Figure 2. Crack (slit) and the ray r where stresses are calculated (a), traditional approximation scheme of the crack surfaces by displacement discontinuity elements (b), and the approximation scheme used in this work (c).

Table 1. Stresses along the ray r (Figure 2 a).

r/c *	Analytical solution [10]	Numerical solution [1]	This work	Analytical solution [10]	Numerical solution [1]	This work
		σ_x			σ_y	
0.0	2.428	2.452	2.406	2.994	3.021	2.982
0.4	0.258	0.263	0.254	1.465	1.465	1.467
1.0	0.241	0.241	0.242	1.128	1.132	1.128
		σ_z			τ_{xy}	
0.0	1.781	1.793	1.767	0.492	0.499	0.492
0.4	0.854	0.857	0.854	0.205	0.210	0.205
1.0	0.767	0.768	0.767	0.125	0.128	0.126
		τ_{xz}			τ_{yz}	
0.0	0.250	0.251	0.250	-0.656	-0.662	-0.653
0.4	0.310	0.309	0.310	-0.260	-0.261	-0.260
1.0	0.279	0.279	0.279	-0.217	-0.217	-0.217

* r is the distance along the ray between the point under consideration and the axis Ox.

Table 2. Stresses and displacements in the walls of the pressurized crack.

x/c	Analytical solution [8]			This work		
	σ_x	u_x/c	u_y/c	σ_x	u_x/c	u_y/c
		Upper crack wall ($y=0.00001c$)				
0.0	-1.077	-0.679	3.985	-1.077	-0.679	3.983
0.3	-0.971	-0.930	3.802	-0.971	-0.930	3.800
0.6	-0.824	-1.109	3.188	-0.824	-1.108	3.186
0.9	-0.382	-1.144	1.737	-0.380	-1.143	1.733
		Lower crack wall ($y=-0.00001c$)				
0.0	-1.077	0.679	-3.985	-1.077	0.679	-3.983
0.3	-1.183	0.365	-3.802	-1.183	0.365	-3.800
0.6	-1.330	-0.022	-3.188	-1.330	-0.023	-3.186
0.9	-1.772	-0.552	-1.737	-1.774	-0.553	-1.733

239

Pressurized crack (plane strain problem). Dimensionless internal pressure is equal to $p=-1.00$. Dimensionless coefficients in the matrix $\|a\|$ of the generalized Hooke's law [8] $\sigma=\|a\|\varepsilon$ are shown below.

$$
\|a\| = \begin{bmatrix}
2.137 & -1.145 & -0.335 & 0.000 & 0.000 & -1.534 \\
-1.145 & 2.627 & -0.235 & 0.000 & 0.000 & 0.684 \\
-0.335 & -0.235 & 0.931 & 0.000 & 0.000 & -0.172 \\
0.000 & 0.000 & 0.000 & 6.908 & -2.469 & 0.000 \\
0.000 & 0.000 & 0.000 & -2.469 & 4.057 & 0.000 \\
-1.534 & 0.684 & -0.172 & 0.000 & 0.000 & 4.492
\end{bmatrix}
$$

A comparison between the closed form solution [8] for stresses and displacements in the crack walls, and the numerical solution, is given in Table 2.

CONCLUSIONS

The new analytical influence functions for Root, Constant, Linear, Parabolic and k-order ($k>2$) displacement discontinuity elements have been used in the Higher Order DDM for analysis of crack problems. The accuracy of the computer code has been demonstrated by example problems and the results have been in a good agreement with the known analytical solutions.

ACKNOWLEDGMENT

REFERENCES

[1] Brady, B.H.G., Bray, J.W. "The boundary element method for elastic analysis of tabular orebody extraction, assuming complete plane strain." *Int. J. Rock Mech. Mining Sci. & Geomech. Abstr.* 1, vol. 15, pp. 29-37 (1978).
[2] Chan, H.C.M. "Analytical influence functions for displacement discontinuity and point force elements." *Int. J. for Numerical and Analytical Methods in Geomechanics* 16, pp. 669-682 (1992).
[3] Crawford, A.M., Curran, J.H. "Higher-order functional variation displacement discontinuity elements." *Int. J. Rock Mech. Mining Sci. & Geomech. Abstr.* 3, vol. 19, pp. 143-148 (1982).
[4] Crouch, S.L. "Solution of plane elasticity problems by the Displacement Discontinuity Method." *Int. J. for Numerical Methods in Engineering* 10, pp. 301-343 (1976).
[5] Crouch, S.L., Starfield, A.M. *Boundary Element Methods in Solid Mechanics.* London: George Allen & Unwin (1983).
[6] Erzhanov, Zh.S., Aitaliev, Sh.M., Masanov, Zh.K. *Stability of Horizontal Workings in Sloping Stratum* (in Russian). Alma-Ata: Nauka (1971).
[7] Kayupov, M.A., Sakurai, S., Akutagawa, S. "BEM based calculating schemes for tunnels." *Proceedings of the 8th International Congress on Rock Mechanics (Tokyo, Japan, 1995)*, Rotterdam: Balkema, vol. 2, pp. 601 - 605 (1995).
[8] Lekhnitskii, S.G. *Theory of Elasticity of an Anisotropic Elastic Body.* San Francisco: Holden-Day, Inc. (1963).
[9] Shou, K.J., Crouch, S.L. "A higher order Displacement Discontinuity Method for analysis of crack problems." *Int. J. Rock Mech. Mining Sci. & Geomech. Abstr.* 1, vol. 32, pp. 49-55 (1995).
[10] Sneddon, I.N., Lowengrub, M. *Crack Problems in the Classical Theory of Elasticity.* New York: John Wiley (1969).

240

STACKING SEQUENCE OPTIMIZATION OF LAMINATED PLATES

C. W. KIM, W. HWANG, H. C. PARK and K. S. HAN

Department of Mechanical Engineering
Pohang University of Science and Technology
Pohang 790-784, Korea

INTRODUCTION

Composite materials in mechanical, aerospace, and other branches of engineering are increasingly used due to their excellent weight saving and the ease of tailoring. In spite of tremendous progress in analytical capability to analyze the behavior of composite materials and structures, there is a lack of design models which may allow efficient tailoring of their properties to specific requirements for structural components. To improve this long-pending problem, the optimum design of composite materials has been a subject of research for many years. The usual object of optimum design is to design layer thickness or layer orientation which will give the minimum weight [1] or the maximum stiffness [2] under in-plane or transverse loadings. Strength was considered as constraints in many problems [1-3]. There are, however, a few studies which consider the strength criterion as an object function of optimum design. Quadratic failure criteria such as Tsai-Wu theory have been used widely for predicting failure of composite materials subject to combined stresses [4]. Recently, the quadratic failure criteria are applied to the optimal stacking sequence design of laminated plates having maximum strength [5].

The present paper treats the optimal stacking sequence design of symmetrically laminated plates under in-plane loadings for maximum strength. Tsai-Wu failure criterion is taken as objective function. Design variables are ply orientation angles. Adjoint variable method is used to formulate optimal design problem. To treat worst-case design, optimal design problem is formulated as min-max problem considering environmental parameters. Based on the adjoint variable method, accurate design sensitivities are calculated using state equation and its results are verified with finite difference method. Optimal stacking sequence design as well as worst stacking sequence design are presented. To compare optimum design with worst case, load carrying ability factor (F_{LC}) is defined by square root of the ratio of worst design result to the optimum design result. Numerical results are given for various loading conditions and aspect ratios.

ANALYSIS

The plate stresses are calculated using classical lamination theory (CLT). The constitutive equations for a symmetrically laminated composite plate are

$$
\begin{bmatrix} \sigma_x \\ \sigma_y \\ \tau_{xy} \end{bmatrix}^{(k)} = \begin{bmatrix} \overline{Q}_{11} & \overline{Q}_{12} & \overline{Q}_{16} \\ \overline{Q}_{12} & \overline{Q}_{22} & \overline{Q}_{26} \\ \overline{Q}_{16} & \overline{Q}_{26} & \overline{Q}_{66} \end{bmatrix}^{(k)} \begin{bmatrix} \varepsilon_x \\ \varepsilon_y \\ \gamma_{xy} \end{bmatrix}^{(k)} \tag{1}
$$

where $\overline{Q}_{ij}$ is transformed stiffness matrix and can be written as follows:

241

$$\overline{Q}_{11} = Q_{11}\cos^4\theta + Q_{22}\sin^4\theta + 2(Q_{12} + 2Q_{66})\sin^2\theta\cos^2\theta$$

$$\overline{Q}_{22} = Q_{11}\sin^4\theta + Q_{22}\cos^4\theta + 2(Q_{12} + 2Q_{66})\sin^2\theta\cos^2\theta$$

$$\overline{Q}_{12} = (Q_{11} + Q_{22} - 4Q_{66})\sin^2\theta\cos^2\theta + Q_{12}(\cos^4\theta + \sin^4\theta)$$

$$\overline{Q}_{16} = (Q_{11} - Q_{12} - 2Q_{66})\cos^3\theta\sin\theta - (Q_{22} - Q_{12} - 2Q_{66})\cos\theta\sin^3\theta$$

$$\overline{Q}_{26} = (Q_{11} - Q_{12} - 2Q_{66})\cos\theta\sin^3\theta - (Q_{22} - Q_{12} - 2Q_{66})\cos^3\theta\sin\theta$$

$$\overline{Q}_{66} = (Q_{11} + Q_{22} - 2Q_{12} - 2Q_{66})\sin^2\theta\cos^2\theta + Q_{66}(\cos^4\theta + \sin^4\theta) \qquad (2)$$

Hooke's law in conjunction with the strain-displacement relation and the stress and moment resultant definition yields following relations for a laminated composite plate:

$$
\begin{bmatrix} N_x \\ N_y \\ N_{xy} \\ M_x \\ M_y \\ M_{xy} \end{bmatrix} =
\begin{bmatrix}
A_{11} & A_{12} & A_{16} & B_{11} & B_{12} & B_{16} \\
A_{12} & A_{22} & A_{26} & B_{12} & B_{22} & B_{26} \\
A_{16} & A_{26} & A_{66} & B_{16} & B_{26} & B_{66} \\
B_{11} & B_{12} & B_{16} & D_{11} & D_{12} & D_{16} \\
B_{12} & B_{22} & B_{26} & D_{12} & D_{22} & D_{26} \\
B_{16} & B_{26} & B_{66} & D_{16} & D_{26} & D_{66}
\end{bmatrix}
\begin{bmatrix} \varepsilon_x^o \\ \varepsilon_y^o \\ \gamma_{xy}^o \\ \kappa_x \\ \kappa_y \\ \kappa_{xy} \end{bmatrix}
\qquad (3)
$$

where A_{ij}, B_{ij} and D_{ij} are extensional stiffness matrix, coupling matrix, and bending stiffness matrix, respectively. The matrices can be written as follows:

$$A_{ij} = \int_{-\frac{t}{2}}^{\frac{t}{2}} \overline{Q}_{ij}^{(k)} dz \qquad B_{ij} = \int_{-\frac{t}{2}}^{\frac{t}{2}} \overline{Q}_{ij}^{(k)} z\, dz \qquad D_{ij} = \int_{-\frac{t}{2}}^{\frac{t}{2}} \overline{Q}_{ij}^{(k)} z^2 dz \qquad (4)$$

PROBLEM FORMULATION

Sensitivity analysis

Every iterative algorithm for solving optimization problem requires gradient of functions. The accuracy of optimal solutions depends on the design sensitivity analysis. Most engineering optimization problems use finite difference method for its convenience in spite of its truncation error and round off error. To get more accurate design sensitivity, state space method [6] is adopted to formulate optimization problem and adjoint variable method is used. In the state space method, governing equation is defined as a state equation and state variables represent behavior of system. The analysis procedures of laminated plates are considered as a set of state equations. The transformed stiffness matrix $\overline{Q}$, extensional stiffness matrix A, bending stiffness matrix D, strain ε, and stress σ are state variables, z, while stacking sequence θ is design variables, b. The resulting state equations are,

$$h_1 = \{\overline{Q}\} - f(\theta) = 0 \qquad h_2 = \{A\} - f(\overline{Q}) = 0 \qquad h_3 = \{D\} - f(\overline{Q}) = 0$$

$$h_4 = \begin{Bmatrix} \varepsilon^o \\ \kappa \end{Bmatrix} - f(A, D) = 0 \qquad h_5 = \{\sigma\} - f(\overline{Q}, \varepsilon^o, \kappa) = 0 \qquad (5)$$

In adjoint variable method, the design sensitivity vector l^i of a function $\Psi_i(z,b)$ can be written [13]:

$$l^i = \frac{\partial \Psi_i^T}{\partial b} - \frac{\partial h^T}{\partial b} \lambda^i \qquad (6)$$

The adjoint variable vector l^i is calculated from the solution of following adjoint equation

$$J^T \lambda^i = \frac{\partial \Psi_i^T}{\partial z}$$ (7)

where J denotes the Jacobian matrix and $J = \frac{\partial h}{\partial z}[z^o, b^o]$. The design sensitivities can be calculated by the above eqs. (6) and (7).

Optimization procedure

The optimization problem that we consider here is to maximize the strength of composite laminates for given layer thickness. Each layer angle is taken as a design variable. To consider strength, Tsai-Wu quadratic failure criterion is used. State space method is used to formulate optimal design problem. To treat worst-case design, optimal design problem is formulated as min-max problem considering environmental parameter, α. In this problem, maximum failure index through thickness is treated as environmental parameter. The optimization problem can be expressed in mathematical form as follows:

$$\textit{Minimize} \quad \textit{Maximum} \quad F(\sigma_1, \sigma_2, \tau_{12})$$

$$t_{min} < \alpha < t_{max}$$

with the state equation $h(z, b, \alpha) = 0$ (8)

$$F = \left(\frac{1}{X} - \frac{1}{X'}\right)\sigma_1 + \left(\frac{1}{Y} - \frac{1}{Y'}\right)\sigma_2 + \frac{\sigma_1^2}{XX'} + \frac{\sigma_2^2}{YY'} + \frac{\tau_{12}^2}{S^2} - \frac{\sigma_1 \sigma_2}{2\sqrt{XX'YY'}}$$ (9)

where, $F(\sigma_1, \sigma_2, \tau_{12})$ is Tsai-Wu failure criterion and defined as failure index ($F.I.$). Min-max design formulation can be reduced to a parametric optimal design formulation using a dummy design variable $b(j+1)$ and a new constraints. The reduced parametric formulation can be written as follows [6]:

$$\textit{Minimize} \quad \Psi_0 = b(j+1)$$

$$\textit{subject to} \quad \Psi_1 = \textit{Maximum} \, F(\sigma_1, \sigma_2, \tau_{12}) - b(j+1) < 0$$

$$t_{min} < \alpha < t_{max}$$

with the state equation $h(z, b, \alpha) = 0$ (10)

In some cases, the above Tsai-Wu failure criterion is not applicable especially, when the unidirectional angle ply laminates are subjected to axial force or torsion [7]. For instance, minus failure index values occur near $20°$ to $30°$ when the unidirectional angle ply laminates are subjected to tensile loading N_x as shown in Fig. 1. As a result, the optimum angle, which gives minimum failure index, is found to be around $20°$. This result is not only far from reality but also meaningless in the view point of physical meaning. To avoid this inconsistency, it is assumed that transverse compressive strength is same as tensile strength i.e., $Y' = Y$.

NUMERICAL RESULTS AND DISCUSSION

Some examples are presented to demonstrate the effect of optimization of stacking sequence on the strength of composite plates. The optimization problem stated in eq. (10) is solved by gradient projection algorithm with the design sensitivity information. A conceptual flow chart for solving the process of optimal design problem is given in Fig. 2. In calculating numerical solutions, following material properties of T300/5208 graphite/epoxy are applied:

$E_{11} = 181$ GPa $\qquad E_{22} = 10.30$ Gpa $\qquad G_{12} = 7.17$ GPa $\qquad v_{12} = 0.28$
$X = X' = 1500$ MPa $\qquad Y = Y' = 43.8$ MPa $\qquad S = 86.9$ MPa

Sensitivity analysis

The design sensitivities of 2nd layer of $[0/45/90]_s$ laminated plate subjected to shear load N_{xy} = 100 MN/mm are calculated and the results are tabulated in Table 1. The sensitivities evaluated by F.D.M. with various step size are also compared with present design sensitivity in Fig. 3. The comparison results show that present design sensitivity calculated by adjoint variable method is very accurate. It can be seen that all the results evaluated by F.D.M. give reliable design sensitivities for a relatively wide range of step size from 10^{-7} to 10^{-3}. However, in certain ranges of step size the large amounts of numerical error are observed when the design sensitivities are evaluated by F.D.M.

Table 1 Accuracy of Design sensitivity ($[0/45/90]_s$ laminate, N_{xy}=100MN/mm)

i	b_i	l_i^I	$l_i^{(f)}$	$l_i^{(b)}$	$l_i^{(c)}$
1	0	4.6370	4.6371	4.6369	4.6370
2	45	2.5673e-8	7.2049e-5	-7.1998e-5	2.5781e-8
3	90	-4.6370	-4.6369	-4.6371	-4.6370
4		-1.0000	-1.0000	-1.0000	-1.0000

l_i^I: adjoint variable method $l_i^{(f)}$: forward finite difference scheme
$l_i^{(b)}$: backward finite difference scheme $l_i^{(c)}$: central finite difference scheme

Illustrative examples

To demonstrate the validity of the method developed, the worst solutions as well as optimal solutions are presented. The load carrying ability factor, F_{LC} is defined by the square root of the ratio of worst failure index to optimal failure index. The load carrying factor implies the ratio of loading capabilities between the worst designed laminate and optimum designed laminate under Tsai-Wu failure condition. It can be written as follows:

$$F_{LC} = \sqrt{\frac{\text{worst failure index}}{\text{optimum failure index}}} \qquad (11)$$

To verify present method, optimum solutions of $[\theta]_s$ and $[\theta_1/\theta_2]_s$ laminates subjected to uniaxial tensile loading are sought. It is obvious that the maximum strength of the laminates occurs when the all layer angles are $0°$ and the minimum strength of the laminates occurs when the all layer angles are $90°$. The same results are obtained in this study as shown in Fig. 4 and Table 2 (case 1). Fig. 4 shows three dimensional plot and contours of the objective function with respect to design variables under uniaxial loading.

It can be seen in the figure that minimum failure index is found in $[0]_{2s}$ laminate while $[90]_{2s}$ laminate has maximum failure index. As it is expected, F_{LC} is 37.5 which is exactly same as the ratio of transverse strength to longitudinal strength. Another calculations are carried out using in-plane biaxially loaded plates ($N_x{:}N_y$ = 1:2). This loading condition is the same as cylindrical pressure vessel under internal pressure. The worst and optimal stacking serquence are obtained and presented in Table 2 (case 2). It can be seen that the optimum solutions are close to the $[\pm54.7]_s$ laminate which is the optimum result from the netting analysis of cylindrical pressure vessel subjected to internal pressure. The comparison of the worst solutions to the optimum solutions gives that the optimally designed plate can carry the external loads as much as 13.3 times than the worst designed plate.

The worst and optimum solutions under various loading conditions [$(N_x, N_y, N_{xy}) = (0, 0, 1)$, $(1, 4, 0)$, and $(1, 2, 1)$] are evaluated and presented in Table 2. It is found that the optimized laminate can carry the external loads more than ten times greater than the worst designed laminate under a shear loading (case *3*). In cases *4* and *5*, the load carrying ability factors are found to be 21. 7 and 28.6, respectively. It is very interesting that optimum solutions vary with number of plies while worst solutions do not change.

Table 2 Optimum and worst results of symmetric laminated plates under in-plane loading

Case	No. of Layers	Loading Ratio (N_x, N_y, N_{xy})	Optimum Angle	Worst Angle	F_{LC}
1	2	(1, 0, 0)	[0]$_s$	[90]$_s$	37.5
	4		[0/0]$_s$	[90/90]$_s$	37.5
2	2	(1, 2, 0)	[90]$_s$	[0]$_s$	2.0
	4		[±53.7]$_s$	[0/0]$_s$	13.3
3	2	(0, 0, 1)	[0]$_s$ or [90]$_s$	[45]$_s$	1.7
	4		[±45]$_s$	[45/45]$_s$	10.5
4	2	(1, 4, 0)	[90]$_s$	[0]$_s$	4.2
	4		[±62.6]$_s$	[0/0]$_s$	21.7
5	2	(1, 2, 1)	[58.3]$_s$	[-31.7]$_s$	7.4
	4		[79.4/37.1]$_s$	[-31.7/-31.7]$_s$	28.6

CONCLUSIONS

An efficient approach for strength optimization of composite laminates subjected to in-plane loadings is presented. The layer angles could be regarded as design variables without difficulty by taking Tsai-Wu quadratic failure criterion as an objective function. The design sensitivity with respect to layer angle is analyzed based on the adjoint variable method. It is found that this method provides more precise design sensitivity than F.D.M. In conclusion, the numerical results show that the failure index is minimized successfully and the reasonable optimal stacking sequence design is sought.

REFERENCES

[1] Schmit, L. A., Jr. and Farshi, B., "Optimum Laminated Design for Strength and Stiffness," *Int. J. for Numerical Methods in Engineering* 7, pp. 519-536 (1977).
[2] Fukunaga, H. and Sekine, H., "Optimum Design of Composite Structures for Shape, Layer Angle and Layer Thickness Distributions," *Journal of Composite Materials* 27, pp. 1479-1492 (1993).
[3] Adali, S., Summers, E. B. and Verijenko, V. E., "Optimization of Laminated Cylindrical Pressure Vessels under Strength Criterion," *Composite Structures* 25 pp. 305-312 (1993).
[4] Rowlands, R. E., "Strength (Failure) Theories and their Experimental Correlation," Failure Mechanics of Composites, G. C. Sih and A. M. Sudra, eds., Elsevier Sci. Pub., B. V., (1985).
[5] Graesser, D. L., Zabinsky, Z. B., Tuttle, M. E. and Kim, G. I., "Optimal Design of a Composite Structure," *Composite Structures*, 24, pp. 273-281 (1993).
[6] Haug, E. J., and Arora, J. S., *Applied Optimal Design*, John Wiley (1979).
[7] Kim, C. W., Song, S. R., Hwang, W., Park, H.C., and Han, K.S., "On the Failure Indices of Quadratic Failure Criteria for Optimal Stacking Sequence Design of Laminated Plate," Applied Composite Materials 1, pp. 81-85 (1994).
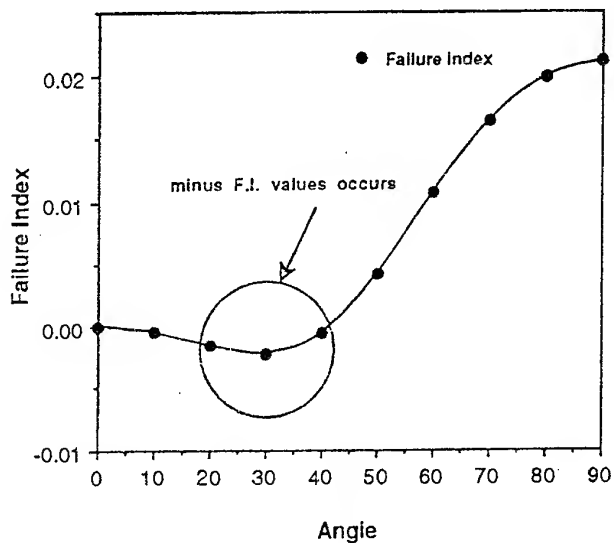
Fig. 1 Failure index of Tsai-Wu failure criterion ($Y \neq Y'$)
$[+\theta'-\theta]_S$ laminate, N_x=0.5 MN/mm
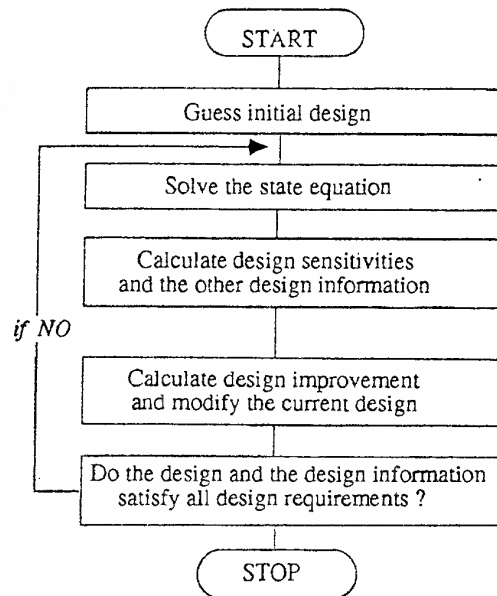
Fig. 2 Flow chart of optimization process
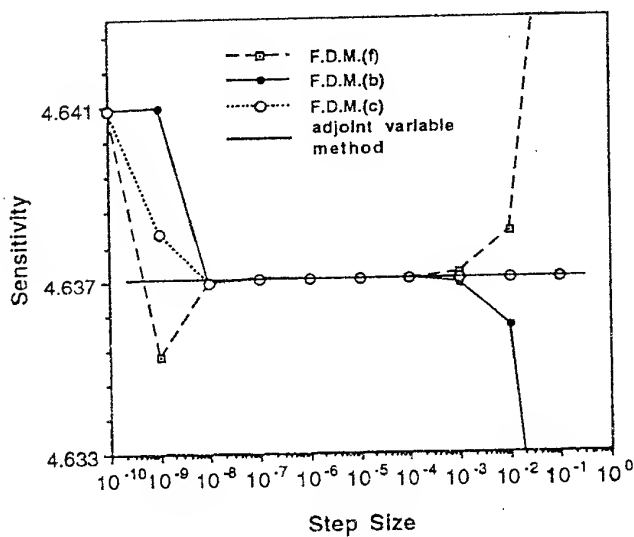
Fig. 3 Variation of design sensitivity using finite difference
method with step size change [0/45/90]$_S$ laminate,
N_{xy} = 100 MN/mm
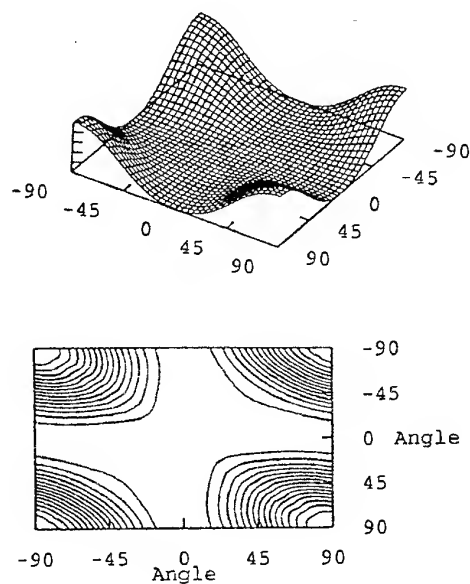
Fig. 4 Surface and contours of the object function
under uniaxial loading

246

ANALYSES OF CROSS-PLIED COMPOSITE CYLINDRICAL SHELLS UNDER AXISYMMETRICAL LOADING

H. Kim

Korea Institute of Nuclear Safety, Taejon, South Korea

F. G. Yuan

Department of Mechanical and Aerospace Engineering

North Carolina State University, Raleigh, NC 27695

INTRODUCTION

Shell structures are utilized in a wide spectrum of engineering fields due to their load-carrying attributes in various directions and geometric requirements. The laminated shells to match potential loading directions offers a considerable advantage in the design of various structural components. Yuan[1-2] recently obtained analytical solutions in composite shells for the quasi three-dimensional problems where the stresses are independent of the axial direction. Since it is critical to provide accurate stresses and deformation to evaluate initial failure criteria, the response of the shells under various loadings merits the use of analytical techniques. In this paper, response of composite cylindrical shells under axisymmetrical loading is investigated. Using Frobenius method, four eigenvalues are studied separately. The closed form solution based on Flügge shell theory are also used for comparison purposes.

MATHEMATICAL FORMULATION

Consider a cross-plied composite circular cylindrical shell under axisymmetric loading. The equilibrium equations in each lamina can be written in terms of cylindrical coordinates :

$$\frac{\partial \sigma_r}{\partial r} + \frac{\partial \tau_{rz}}{\partial z} + \frac{\sigma_r - \sigma_\theta}{r} = 0, \quad \frac{\partial \sigma_z}{\partial z} + \frac{\tau_{rz}}{r} = 0 \tag{1}$$

The engineering strain-displacement relations are written as:

$$\varepsilon_r = \frac{\partial u_r}{\partial r}, \quad \varepsilon_\theta = \frac{u_r}{r}, \quad \varepsilon_z = \frac{\partial w}{\partial z}, \quad \gamma_{rz} = \frac{\partial u_r}{\partial z} + \frac{\partial w}{\partial r} \tag{2}$$

The stress-strain relations are:

247

$$\begin{Bmatrix} \sigma_r \\ \sigma_\theta \\ \sigma_z \\ \tau_{rz} \end{Bmatrix} = \begin{bmatrix} C_{11} & C_{12} & C_{13} & 0 \\ C_{12} & C_{22} & C_{23} & 0 \\ C_{13} & C_{23} & C_{33} & 0 \\ 0 & 0 & 0 & C_{55} \end{bmatrix} \begin{Bmatrix} \varepsilon_r \\ \varepsilon_\theta \\ \varepsilon_z \\ \gamma_{rz} \end{Bmatrix} \tag{3}$$

A solution which is periodic in z with the period $2l$ is given for the displacements u_r and w in the following form

$$u_r = \sum_{n=1}^{\infty} U(r) \cos \frac{n\pi z}{l}, \quad w = \sum_{n=1}^{\infty} W(r) \sin \frac{n\pi z}{l} \tag{4}$$

Substitution of (2,3,4) into (1) leads to

$$\begin{bmatrix} L_{11} & L_{12} \\ L_{21} & L_{22} \end{bmatrix} \begin{Bmatrix} U \\ W \end{Bmatrix} = 0 \tag{5}$$

where

$$L_{11} = \frac{d^2}{dr^2} + \frac{1}{r}\frac{d}{dr} - \frac{\xi^2}{r^2} + \alpha_1, \quad L_{12} = \alpha_2 \frac{d}{dr} + \frac{\alpha_3}{r}$$

$$L_{21} = \alpha_4 \frac{d}{dr} + \frac{\alpha_5}{r}, \quad L_{22} = \frac{d^2}{dr^2} + \frac{1}{r}\frac{d}{dr} + \alpha_6$$

and

$$\alpha_1 = -\frac{C_{55}}{C_{11}} N^2, \quad \alpha_2 = \frac{C_{13}+C_{55}}{C_{11}} N, \quad \alpha_3 = \frac{C_{13}-C_{23}}{C_{11}} N,$$

$$\alpha_4 = -\frac{C_{13}+C_{55}}{C_{55}} N, \quad \alpha_5 = -\frac{C_{23}+C_{55}}{C_{55}} N, \quad \alpha_6 = -\frac{C_{33}}{C_{55}} N^2, \quad \xi^2 = \frac{C_{22}}{C_{11}}, \quad N = \frac{n\pi}{l}$$

The set of differential equations (5) is of the fourth-order and will be solved by the Frobenius method. The function W are assumed to be in the following form:

$$W(r) = \sum_{k=0}^{\infty} w_k \, r^{k+\lambda} \tag{6}$$

where the coefficients w_k and the index λ are as yet undetermined. Substituting (6) into the second equation of (5) and integrating results in

$$U(r) = -\sum_{k=0}^{\infty} \frac{(k+\lambda)^2 w_k}{\alpha_4 (k+\lambda+\alpha-1)} r^{k+\lambda-1} - \sum_{k=0}^{\infty} \frac{\alpha_6 w_k}{\alpha_4 (k+\lambda+\alpha+1)} r^{k+\lambda+1} \tag{7}$$

where $\alpha = \alpha_5/\alpha_4$. (6) and (7) are inserted into the first equation of (5). The roots for λ are

$$\lambda_{1,2} = 1 \pm \xi, \quad \lambda_3 = \lambda_4 = 0$$

(i) $\lambda_{1,2} = 1 \pm \xi$ case (real root case), w_0 = arbitrary constant

$$W_i(r) = \sum_{k=0}^{\infty} w_{2k} \, r^{2k+\lambda_i}$$

$$U_i(r) = -\sum_{k=0}^{\infty} \frac{(2k+\lambda_i)^2}{\alpha_4(2k+\lambda_i+\alpha-1)} w_{2k} r^{2k+\lambda_i-1} - \sum_{k=0}^{\infty} \frac{\alpha_6}{\alpha_4(2k+\lambda_i+\alpha+1)} w_{2k} r^{2k+\lambda_i+1} \quad (i=1,2) \quad (8)$$

where $\quad w_{2k} = -\dfrac{1}{p}[(\alpha_6 e_1 e_2 + e_4 e_5 - e_6)w_{2k-2} + \alpha_1 \alpha_6 e_5 w_{2k-4}]$

$$p = e_1 e_2 e_3^2, \quad e_1 = \frac{1}{\alpha_4(2k+\lambda_i+\alpha-1)}, \quad e_2 = (2k+\lambda_2-1)^2 - \xi^2, \quad e_3 = (2k+\lambda_i)$$

$$e_4 = \alpha_1(2k+\lambda_i-2)^2, \quad e_5 = \frac{1}{\alpha_4(2k+\lambda_i+\alpha-3)}, \quad e_6 = \alpha_2(2k+\lambda_i-2)+\alpha_5$$

(ii) $\lambda = \pm 0$ cases, w_0 = arbitrary constant for λ_3 and λ_4

For $\lambda_3 = 0$ case,

$$W_3(r) = \sum_{k=0}^{\infty} w_{2k} r^{2k}$$

$$U_3(r) = -\sum_{k=0}^{\infty} \frac{(2k)^2}{\alpha_4(2k+\alpha-1)} w_{2k} r^{2k-1} - \sum_{k=0}^{\infty} \frac{\alpha_6}{\alpha_4(2k+\alpha+1)} w_{2k} r^{2k+1} \tag{9}$$

For $\lambda_4 = 0$ case,

$$W_4(r) = \sum_{k=0}^{\infty} w_{2k}' r^{2k} + \sum_{k=0}^{\infty} w_{2k} r^{2k} \ln r$$

$$U_4(r) = -\sum_{k=0}^{\infty} \frac{4k}{\alpha_4(2k+\alpha-1)}\left(\frac{k+\alpha-1}{2k+\alpha-1} + k\ln r\right) w_{2k} r^{2k-1}$$

$$+ \sum_{k=0}^{\infty} \frac{\alpha_6}{\alpha_4(2k+\alpha+1)^2}\{1 - (2k+\alpha+1)\ln r\} w_{2k} r^{2k+1} \tag{10}$$

$$- \sum_{k=0}^{\infty} \frac{(2k)^2}{\alpha_4(2k+\alpha-1)} w_{2k}' r^{2k-1} - \sum_{k=0}^{\infty} \frac{a_6}{\alpha_4(2k+\alpha+1)} w_{2k}' r^{2k+1}$$

where

$$w_{2k}' = -\frac{1}{p}[E_1' w_{2k-2} + E_2' w_{2k-4} + E_1 w_{2k-2}' + E_2 w_{2k-4}' - P' w_{2k}]$$

$$E_1 = \alpha_3 e_1 e_2 + e_4 e_5 - e_6, \quad E_2 = \alpha_1 \alpha_3 e_5$$

$$E_1' = \alpha_3(e_1' e_2 + e_1 e_2') + e_4' e_5 + e_4 e_5' - e_6', \quad E_2' = \alpha_1 \alpha_3 e_5'$$

For a perfectly bonded composite shell with N layers there exist 4N unknowns. The interface continuity provides 4(N-1) equations. By incorporating the tractions at the inner and outer surfaces, all the unknowns, thus the solution for the shell, can be obtained.

RESULTS AND DISCUSSION

The method of approach has been implemented for studying composite laminated shells under axisymmetric loading. The Flügge shell theory is used as a reference for comparative purpose for the case of a simply supported composite shell under external sinusoidal pressure. Exact elasticity solutions are obtained for the long composite laminated shell under periodic band loads. The lamina material elastic constants for graphite/epoxy are: $E_L = 138$ GPa, $E_T = 8.9$ GPa, $E_Z = 9.3$ GPa, $G_{LT} = G_{LZ} = 5.17$ GPa, $G_{TZ} = 2.89$ GPa, $\upsilon_{LT} = \upsilon_{LZ} = 0.3$, $\upsilon_{TZ} = 0.54$. The normalized stress distributions for the graphite/epoxy with stacking sequences [0/90]$_s$ and [0/90/0/90] are shown in Figs. 1-4 and 5-8, respectively, for the case of a simply supported composite shell under the external sinusoidal pressure. The interlaminar normal stress σ_r in Fig. 1 and Fig. 5 shows that the boundary conditions for the inner ($\sigma_r/p = 0$) and outer surfaces ($\sigma_r/p = 1$) are satisfied. It is observed that the exact elasticity solution and Flügge shell solution are in good agreement as the S (mid radius R-to-thickness ratio) increases. The distributions of the in-plane stress σ_θ in Fig. 2 and Fig. 6 show discontinuities between the 0/90 interfaces. Maximum stress values occur on the inner surface for [0/90/0/90] case and in the lower half ply regions for [0/90]$_s$ case. In Fig. 3 and Fig. 7, σ_z mimics the behavior of σ_θ, with smaller stress magnitudes and also shows the discontinuity between the 0/90 interfaces. The interlaminar shear stress τ_{rz} distribution at Z/L= 0.25 is depicted in Fig. 4 and Fig. 8. Although τ_{rz} shows a close agreement between the exact elasticity solution and Flügge shell solution, there is a substantial inconsistency in the lower half ply regions for [0/90]$_s$ and in the midsurface for [0/90/0/90]. It is also expected that the discrepancy between exact elasticity and Flügge shell solutions vanishes as the S increases.

REFERENCES

1. F. G. Yuan, "Exact Solutions for Laminated Composite Cylindrical Shells in Cylindrical Bending", *Journal of Reinforced Plastics and Composites*, Vol. 11, No. 4, pp. 340-371, 1992.
2. F. G. Yuan, "Bending of Filament Wound Composite Laminated Cylindrical Shells", *Composite Engineering Journal*, Vol. 3, No. 9, pp. 835-849, 1993.
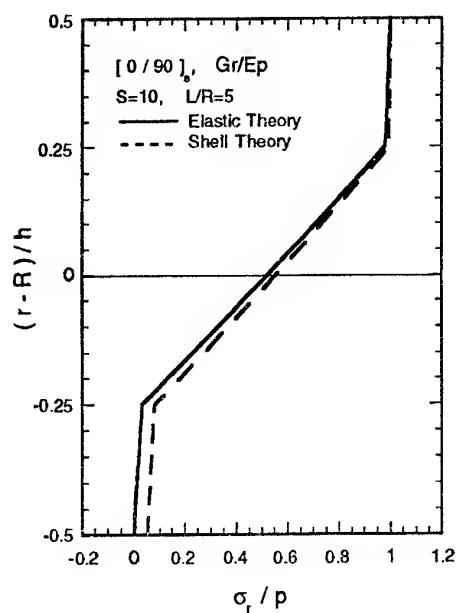
Fig. 1 Through-laminate-thickness of σ_r at $Z/L = 0$
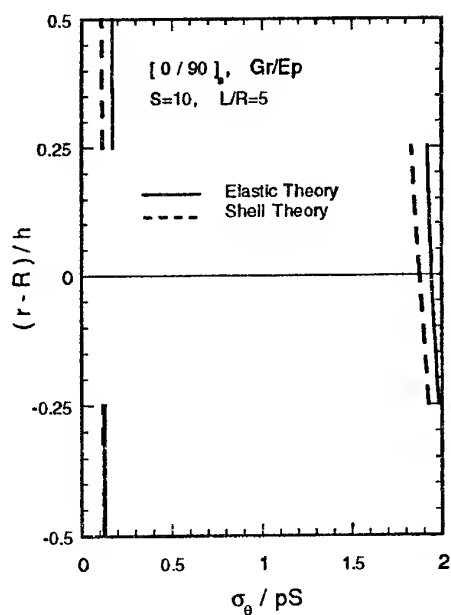
Fig. 2 Through-laminate-thickness of σ_θ at $Z/L = 0$
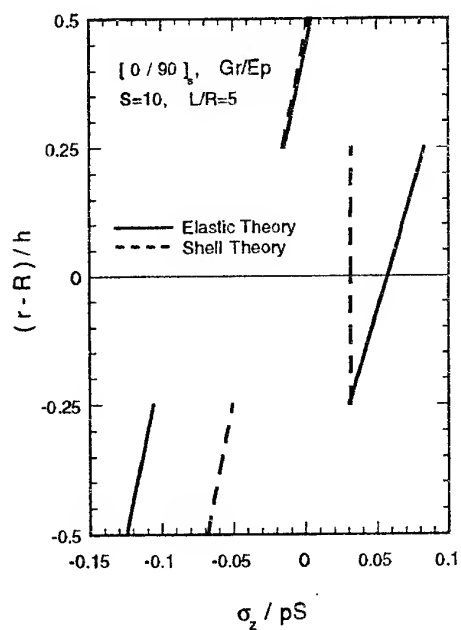
Fig. 3 Through-laminate-thickness of σ_z at $Z/L = 0$
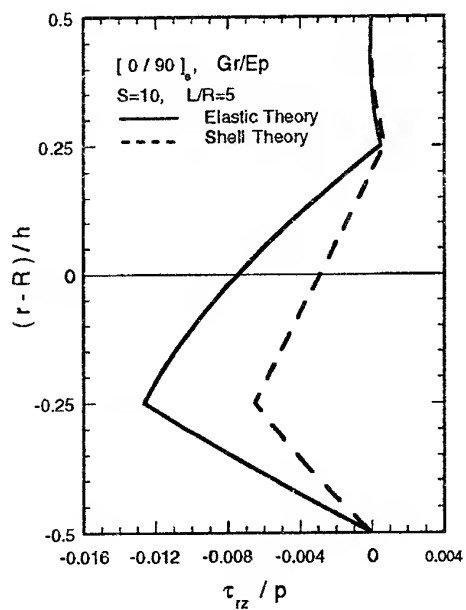
Fig. 4 Through-laminate-thickness of τ_{rz} at $Z/L = 0.25$

251
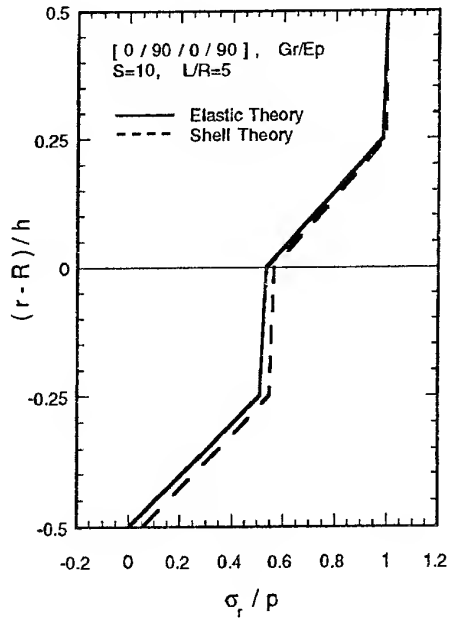
Fig. 5 Through-laminate-thickness of σ_r
at $Z/L = 0$
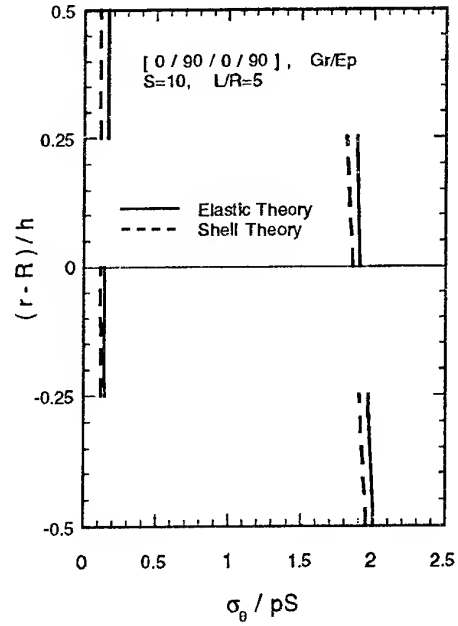
Fig. 6 Through-laminate-thickness of σ_θ
at $Z = L = 0$
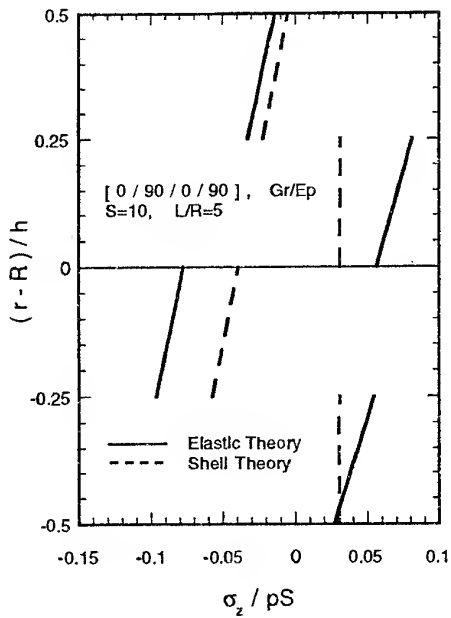
Fig. 7 Through-laminate-thickness of σ_z
at $Z/L = 0$
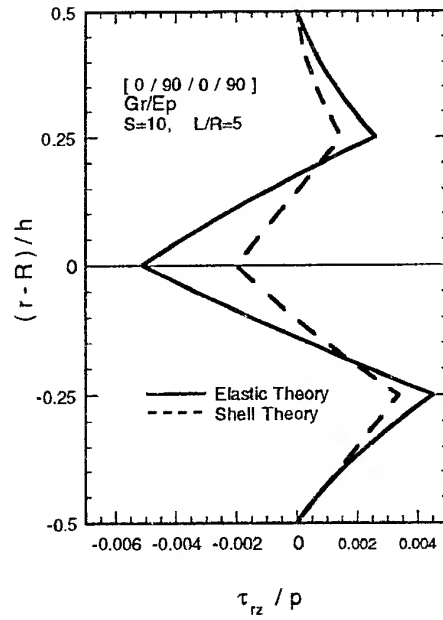
Fig. 8 Through-laminate-thickness of τ_{rz}
at $Z/L = 0.25$

252

THE DESIGN AND MANUFACTURE OF A
LOW THERMAL EXPANSION COMPOSITE MATERIAL
FOR HIGHWAY BRIDGE APPLICATIONS

E. Klang[1], Ph.D. and D. Richards[2], Ph.D., P.E.

[1] Associate Professor, North Carolina State University, Raleigh, NC, USA
[2] Consulting Engineer, Durham, North Carolina, USA

INTRODUCTION

Today infrastructures, particularly bridges, are receiving significant attention from local and national governments and from industry. The typical design of bridges creates many problems in both construction and maintenance. The design of a bridge has to allow for expansion due to the material expanding. This causes expansion joints to be incorporated into bridges. The thermal expansion forces created by the range of temperatures that a bridge experiences could be eliminated by changing to a material with a mechanical property of low thermal expansion, and therefore expansion joints in bridges could be eliminated from the design.

This paper is from research that focused on creating a composite material with a lower coefficient of thermal expansion, alpha, by using woven fibers. The title of the dissertation is *Woven Hybrid Fiber-Reinforced \ Multiphase-Matrix Composites For Low Thermal Expansion Applications* [1]. Creating low thermal expansion composites, in general, is nothing new. The aerospace industry has been studying this for years because of the extreme temperatures encountered by vehicles in space. There has been success in producing low thermal expansion materials by using straight fibers in manufacturing and using classical laminate theory to analyze the materials. The problem, however, has been that this type of material is very expensive and has not been used on a large scale by industry. The composite materials used in the aerospace industry are produced primarily by an autoclave type process, which is very labor intensive. To reduce the cost of producing the material, other methods of production were explored in connection with this research. Textile preforms were considered due to the recent developments in this area by the automobile industry and other industries
utilizing composite materials, such as those manufacturing sports and recreational products.

This paper contains a summary of the fibers, type of weave, matrix, manufacturing process, and primary method of evaluating the samples that were selected. It then focuses on problems with current bridge materials, the use of woven fiber reinforced composites in bridge applications, and the cost implications.

GENERAL DESCRIPTION OF THE MATERIALS AND THE MANUFACTURING PROCESS

The two fibers used in this research were Kevlar-49 and E-Glass. Many combinations of fibers could have been tried, but Kevlar-49 and E-Glass were good choices. The basic idea was to create a thermal expansion situation where one fiber with negative and one fiber with positive expansions could control the coefficient of thermal expansion (CTE), alpha.

To control the scope of the research and to avoid becoming over burdened with too many variables, the 8-HSW was determined to be the best choice. This was a good selection due to the mechanical idea of the fibers being straighter for a longer distance in this weave compared to the plain or five-harness satin weaves. The plain weave and Five Harness Satin Weave are very popular textile preforms, as is the 8-HSW.

The matrix, Atlac-580-05, is a modified Vinyl Ester Resin from Reichhold Chemical, Inc.[2]. The matrix is a premium urethane modified bisphenol vinyl ester with excellent corrosion resistance and high temperature performance.

The manufacturing process chosen for this research was Resin Transfer Molding (RTM). Given the limited budget and laboratory environment available for the research, RTM was the easiest process and provided good quality results. In the manufacturing process, 6 layers of the woven material were placed in the mold to get approximately 60 percent fiber versus the matrix.

The layers were arranged with 3 warp sides of the woven fabric pointing up from the bottom and 3 warp sides of the woven fabric pointing down. This gave a symmetric lay-up of the fibers and kept the finished product from curing with a curvature when removed from the mold.

The various parameters that were adjusted in obtaining a low alpha, coefficient of thermal expansion, composite material were:

1. Different Combinations of the fibers, Kevlar-49 and E-Glass, in the 8-HSW.

2. Different amounts of the filler, Fused-Silica, in the resin, combined with fibers.

3. Treating fibers to influence the mechanical behavior of fibers and resin bonding.

Parameters that were standard and not adjusted in the composite material:

1. Fiber content was maintained at 60 % in all samples.

2. RTM was the manufacturing method used in all samples. All samples were made from the same mold.

3. All 8-HSW samples were hand woven by the same individual and on the same loom.

4. All fibers, Kevlar-49 and E-Glass, were taken from the same spools, respectively.

5. All samples were of the same stacking sequence for symmetrical lay-ups of the composite material.

Final Design:

Fiber Content: 100 % Kevlar-49 in the Axial (Warp) Direction.
100 % E-Glass in the Transverse (Fill) Direction.

Resin Content: Neat matrix, Atlac-580, with no filler added.

Alpha Values: Measured from Room Temperature, 20° C, to 95° C:
alpha = +3.2 ppm / C at 26.5° C (80° F)
alpha = +5.9 ppm / C at 93.3° C (200° F)

Modulus of Elasticity:

E = 26.52 GPa (3.85 E+6 psi)

Many methods are used to evaluate composites, and in particular the CTE of composite materials. The author relied primarily on Finite Element Analysis(FEA) to evaluate and analyze the woven hybrid fiber reinforced composite samples produced as part of this research. Most FEA work to date in the area of fiber reinforced composites has related to obtaining the stress in the material and/or the stress at the matrix-fiber interface. In this research FEA was used to estimate the CTE. In building the model, a 3 dimensional element was used for the matrix and 2 dimensional rod elements were used for the fibers. Domination by the fiber structure is important, and this is accomplished by this method of modeling.

COST IN LARGE STRUCTURES WITH COMPOSITES

In large civil structures composites are being considered much more than in the past. There have been some situations where composite materials have been used for larger structures, but manufacturing problems have prevented composites from being used on a large scale. The aerospace and automobile industries have used composites more than other industries. For these applications either the cost was reduced by mass production or cost was not a controlling parameter if, for example, weight savings was a major factor in the design. In the aerospace industry a substitute material was often not available, due to the fast pace of new design concepts.

Just as mass production decreases cost in the aerospace and automobile industries, mass production of bridges would lower the cost of the structure and improve the manufacturing techniques. Producing standard sections of bridges off site and then transporting them to the location would be cost effective and cannot be done with steel or concrete due to their weight. Using a lighter weight material is a factor that could quickly move the design concepts of bridges into another era by lowering the dead loads.

The cost factor was an important consideration during this research, which considered the options available in creating low thermal expansion materials in composites. As discussed, a textile preform was chosen to allow manufacturing methods other than an autoclave to be used.

ADVANTAGES OF USING COMPOSITES IN BRIDGES

One acknowledged area of difficulty in designing bridges is in designing joints. Joints cause design and maintenance headaches for bridges. In the design of bridges, joints have to be included to allow the bridge to move due to the thermal expansion of the material used in the building of the structure. A North Carolina Department of Transportation (NCDOT) engineer who was interviewed made the interesting comment that no one makes a waterproof joint for bridges ! When the joint gets dirty and stops working, these problems can cause critical damage and sometimes failure to bridges.

The second problem with having joints in bridges is that after the bridge is built the joint must be maintained. From the NCDOT engineer's comment above, it is clear that this is no easy task. Maintenance in bridges has been, and is becoming even more so, very costly. The labor to inspect a bridge is very time consuming and costly.

Another problem with having joints in bridges along with stiff columns is the Seismic loads on bridges. Joints hurt the ability of bridges to deal with transverse loads created by seismic loading. Not having joints in bridges would help the design process.

As mentioned in the introduction, the use of composites in bridges would eliminate the need for expansion joints in bridges, and this would have a domino effect on designing the structure and on maintenance. No joints in bridges, from a structural analysis point of view, would be desirable and result in a stronger structure.

With a lighter material, new ways of putting together the structure would quickly arise. The design side would not have the huge dead loads that are present with concrete and steel.

Like any innovative engineering concept, at first it will be difficult to gain acceptance of this idea of changing from the standard bridge building materials like steel and concrete. What may accelerate the rate of acceptance is the fact that too many bridges in the United States are in need of repair. The Federal Highway Administration (FHWA) reported in 1988 that the United States had over 570,000 bridges and more than 238,000 were classified as deficient. The cost to eliminate the deficiencies, by replacing or rebuilding, was estimated at BILLION DOLLARS [3]. The FHWA reported in 1992 that, with 589,000 bridges in the United States, eliminating the deficiencies would cost 90 BILLION DOLLARS [4].

Other problems are contributing to the rising costs of bridges, and these should also be considered when selecting the material to be used in building bridges. One example is regulations from the Occupational Safety and Health Administration (OSHA). OSHA's regulations of volatile organic compounds has driven the cost of repainting a steel bridge from below $2 per square foot to sometimes $30 per square foot [5].
To illustrate the effect of these regulations, the cost of repainting New York City's bridges in 1989 was $5.4 million dollars, but after OSHA's regulation took effect in 1992 New York City spent $53.8 million dollars on repainting it's bridges [6]. Woven fiber reinforced composite bridges would not require painting and would add to the beauty in the landscape.

Corrosion is another big problem for concrete bridges and steel bridges. Salt, which is used on bridges to cause the ice and snow to melt, is very harsh to concrete and steel and over the years has created a significant amount of damage to bridges in the United States. Woven fiber reinforced composite bridges would have no problem with corrosion from salt.

Cost could be seen as a driver both for and against the use of woven fiber reinforced composite materials in bridges. There is a risk factor in building bridges with woven fiber reinforced composite materials before a sufficient database of proven properties has been developed. The database is needed to ensure a safe end result and to protect those who rely on composite materials. But it will be expensive to develop woven fiber reinforced composites.

Also woven fiber reinforced composite materials currently may be viewed as expensive compared to concrete and steel. However, the cost of the materials and of the actual production process is only one critical factor to consider. Life span of the structure is also very important and is being looked at more and more. Present day bridges are very expensive to build and maintain. If it can be shown that using woven fiber reinforced composite materials will reduce costs over the lifetime of a bridge and if sufficient data can be quickly produced, then woven fiber reinforced composite materials have a great chance of becoming the material of choice for infrastructure investment.

When large structures are viewed as reasonable items to be made out of woven fiber reinforced composite materials, then it is likely that improvements will come fast, hopefully followed by cost reductions. Manufacturing techniques are likely to improve exponentially when the popularity of fiber reinforced composites grows. Many options can spring out of using a lighter material like composites.

[1]   Richards, D.H., "Woven Hybrid Fiber-Reinforced \ Multiphase-Matrix Composites For Low Thermal Expansion Applications", dissertation, *North Carolina State University*, Raleigh, NC, USA, 1995.

[2]   Reichhold Chemical, Inc., Product Literature , Atlac-580 Matrix, RTP, North Carolina, 27709, USA, 1994.

[3]   Abed-Al-Rahim, I., "Analysis of Relationships Affecting Deterioration and Improvement of Bridges", dissertation, *North Carolina State University*, Raleigh, NC, USA, 1991.

[4]   Xanthakos, P.P., Theory and Design of Bridges, John Wiley & Sons, Inc., New York, NY, USA, 1994.

[5]   Robison, R., "Safeguarding Steel", *Civil Engineering*, April, pages 50-52, USA, 1992.

[6]   Freyermuth, C.L., "Building Better Bridges: Concrete vs. Steel", *Civil Engineering*, July, pages 66-69, USA, 1992.

LARGE DEFLECTION EFFECTS OF CRACKED ALUMINUM PLATES REPAIRED WITH BONDED COMPOSITE PATCHES

J. C. Klug and C. T. Sun

School of Aeronautics and Astronautics, Purdue University
West Lafayette, Indiana 47907, USA

INTRODUCTION

In order to extend the service life of an aging aircraft, the cracked components must be replaced or repaired. If the number of cracks is small and the crack size is small relative to the size of the component, it is often most economical to employ crack arrestment methods to regain the load carrying capacity of the component. A repair method using composite patches to reinforce the cracked structure has been shown to be very promising owing to the light weight, high stiffness and strength of the composite [1].

One of the most challenging aspects of bonded repair technology is stress analysis of the repaired structure. The difficulty arises from the fact that a plane stress metallic panel under in-plane loading would develop highly complicated 3-D stresses if composite patches are bonded to its surfaces either symmetrically (double-sided) or unsymmetrically (single-sided). Unsymmetric repairs present the greatest challenge in modeling due to the presence of out-of-plane bending. It is this out-of-plane bending that can lead to large deflection effects. The two side views in Figure 1 show the bending induced from thermal residual stresses due to the thermal mismatch and from the off axis loading.

The use of a full 3-D finite element model to perform stress analysis is computationally costly and can even cause ill conditioning when high aspect ratio elements are used for the thin patch and adhesive [2,3]. Other 2-D analysis [4] are only good for symmetric repairs. In this paper, a simple analysis using Mindlin plate theory is investigated to model the host and repair plate while spring elements model the connecting adhesive layer. The crack in aluminum is characterized by fracture mechanics using the stress intensity factor. Some different variables affecting the large deflection solution are investigated including the effects of host and repair plate thicknesses and thermal residual stresses.

MODEL DESCRIPTION

Figure 2 shows a typical single-sided patch configuration. A complete derivation of the finite element model is given in Reference [3]. The plate nodes are located on the mid-

259

planes of the aluminum plate and patch. The adhesive nodes lie along the patch-adhesive and adhesive-aluminum plate interfaces. Constraint equations are imposed on the patch-adhesive and adhesive-aluminum interfaces in order to enforce compatibility. The adhesive layer is modeled by three springs for the transverse shear stiffness in the xz and yz-planes and the axial stiffness in the z-direction.

The modified crack closure technique [5] is used to calculate the strain energy release rate. It is assumed that the strain energy released during crack extension is equal to the work needed to close the opened crack surfaces. It is also assumed that the adhesive cracks along the aluminum crack region. Generally, the nodal forces and relative displacements from the geometric nonlinearity are nonlinear, and the energy required to close the crack front is the summation of the work done for each increment. However, it has been found that the relation between the nodal forces and relative displacements are linear at the crack tip. Thus, the work done for each increment is linear and a single step closure approach can be taken.

The strain energy release rate is computed for Mode I fracture loading. The same procedure can be used for mixed mode loading. A 4-noded Mindlin plate element (S4R) is used to model the aluminum plate. Figure 3 shows a 2-D finite element model for the aluminum plate near the crack tip at point b. Assume the crack front extends from b to c. Since the extension, Δa, is very small, the crack opening displacements at b are taken to be the same as those at a. Thus, the strain energy release rate can be calculated as the work done by the nodal force (moment), F_y^b (M_x^b), in closing the crack opening displacement (rotation), u_y^a (ψ_y^a). The total strain energy release rate is obtained as

$$\overline{G}_{total} = \overline{G}_u + \overline{G}_\psi = \frac{1}{2\Delta a}\left\{F_y^b\left(u_y^a - u_y^{a'}\right)\right\} + \frac{1}{2\Delta a}\left\{M_x^b\left(\psi_y^a - \psi_y^{a'}\right)\right\} \qquad (1)$$

where $\overline{G}_u$, $\overline{G}_\psi$ and $\overline{G}_{total}$ are the transitional, rotational, and total strain energy release rates, respectively. Note that these strain energy release rates are the respective energies released (over the total plate thickness) per crack tip.

The fracture parameter for the aluminum crack is often given in terms of the stress intensity factor. The maximum stress intensity factor is located on the tension side of the plate and is composed of

$$K_I = K_u + K_\psi = \sqrt{\frac{\overline{G}_u E_s}{t_s}} + \sqrt{\frac{3\overline{G}_\psi E_s}{t_s}} \qquad (2)$$

where the subscript s denotes parameters associated with the aluminum plate. K_u is the plane stress relation of the stress intensity factor to the strain energy release rate and is the

value of K_I at the plate midplane. K_ψ is the stress intensity factor due to pure bending.

RESULTS

The material properties and plate dimensions are listed in Table 1. The thickness of the aluminum and repair are listed for four configurations in Table 2. The aluminum crack length, 2a, is 50 mm. The boron/epoxy 0° fiber is in the y-direction, perpendicular to the aluminum crack.

Table 1 Material Properties and Dimensions

Material	Material Properties	Dimensions (mm)	Thermal Expansion Coefficient
Aluminum	$E_s = 71.02$ GPa $\nu_s = 0.32$	$L_s = 180$ $W_s = 120$	$\alpha_s = 23.0 \times 10^{-6}/^\circ C$
Boron/Epoxy	$E_1 = 208$ GPa $E_2 = E_3 = 25.44$ GPa $G_{12} = G_{13} = 7.24$ GPa $G_{23} = 4.94$ GPa $\nu_{12} = \nu_{13} = 0.1677$ $\nu_{23} = 0.0350$	$L_r = 76$ $W_r = 38$ ply thickness = 0.127	$\alpha_1 = 4.5 \times 10^{-6}/^\circ C$ (fiber direction) $\alpha_2 = 23.0 \times 10^{-6}/^\circ C$ (transverse direction)
Adhesive	$G_a = 0.965$ GPa $\nu_a = 0.32$	$t_a = 0.1016$	

Table 2 Aluminum and Repair Plate Thicknesses

Case Number	Aluminum Plate Thickness, t_s (mm)	Repair Plate Thickness, t_r (mm)	$\dfrac{t_s}{t_r}$	$\dfrac{t_r}{t_a}$
1	2.29	0.762	3.0	7.5
2	11.14	0.762	15.0	7.5
3	22.29	0.762	30.0	7.5
4	2.29	0.127	18.0	1.2

The first case is for a mechanical loading. The aluminum plate is subjected to an in-plane, uniform loading up to 150 MPa. Quarter model symmetry is used for the plate. The outer boundary conditions are free.

Since the spring model contains many simplifying assumptions, comparisons are made to a 3-D adhesive element solution. The initial model consists of 8-noded plate elements connected by 20-noded reduced integration adhesive elements. Comparisons of the stress intensity factor of the 3-D adhesive to the spring adhesive are shown in Figure 4. The stress intensity factor is normalized by the infinitely wide panel solution, $K_{I\infty}$, and plotted

at two locations through the plate thickness, Kf at the free edge and Km at the midplane. The linear solution, labeled L, is constant over the applied stress due to the normalization. The 3-D and spring adhesive solutions using large deflection theory are labeled N for nonlinear and S for spring, respectively. It can be easily seen that the spring and 3-D adhesive models compare well. The plot shows that the stress intensity factor is largest at the free edge and can be over predicted by linear analysis.

Figures 5-7 show the results for cases 2-4. Figures 5 and 6 show that as the ratio of the aluminum-to-repair thickness is increased, the effect of the nonlinear deformation on the stress intensity factor decreases. In fact, Figure 6 shows that the linear and nonlinear solutions are nearly identical. For case 4 in Figure 7, the aluminum-to-repair thickness is close to that of case 2, but the repair-to-adhesive thickness ratio has decreased and there is much more difference between the nonlinear and linear solutions. Thus, the offset of the repair due to the adhesive layer is very important.

The second case considers the effect of the thermal residual stresses due to the thermal coefficient mismatch of the aluminum and repair as shown in Table 1. The effective thermal residual stress, ΔT, is the value which can be used to account for the residual stresses arising from the curing cycle. Ordinarily, the value of ΔT is taken as the difference in ambient temperature of the component and the cure temperature. For a typical adhesive like FM 73 this would be -100°C. However, it is felt that the value of ΔT may not be accurate, and the actual ΔT should be lower due to the manner in which the adhesive cures. The thermal residual stresses cause the repair to be in compression and the aluminum plate to be in tension resulting in a stress intensity factor.

The normalized stress intensity factor over the absolute value of ΔT is shown for cases 1 and 4 in Figure 8. The stress intensity factor is normalized by the plane strain critical stress intensity factor, $K_{Ic} = 34$ MPa$\sqrt{m}$, for aluminum 2024-T3. The maximum value of the stress intensity factor has shifted to the aluminum-adhesive interface and is labeled Ki. The crack tip displacement is larger at the adhesive-aluminum interface than at the free edge due to the curvature caused by the residual stresses. As ΔT increases, the linear solution under predicts the stress intensity factor. However, there is not a large difference in the maximum out-of-plane deflection between the linear and nonlinear solutions.

The final example uses the case 1 geometry to examine the effect of the initial thermal residual stresses followed by a mechanical loading on the stress intensity factor. Figure 9 shows the normalized stress intensity factor at the free edge. For low applied stress levels the maximum stress intensity factor will occur at the adhesive-aluminum interface. As the stress is increased, the maximum will switch to the free edge. The linear plot refers to the linear solution without residual stresses. The actual difference between the solution with and without thermal residual stresses is very small. This is because Kf is very small for residual stresses and using superposition, the mechanical load solution would be shifted

up by this very small value. The plot shows that there is a large difference between the linear and nonlinear solutions. As the initial thermal residual stress increases, Kf increases more for the nonlinear than the linear solution.

Figure 10 shows the curvature of the aluminum midplane of a slice taken along the y-axis from the center of the crack to the outer edge of the plate. The shaded area shows region of the aluminum which is covered by the repair. Two values of ΔT, -50°C and -100°C, are shown by the dashed and solid lines, respectively. The plot shows that as the mechanical load is applied, the curvature begins to shift as shown in Figure 1. This curvature change due to the thermal residual stresses followed by the mechanical loading has been experimentally noted by Belason [6].

CONCLUSIONS

Large deflection theory is important in cases where both the aluminum-to-repair plate and repair plate-to-adhesive thickness ratios are small. The effect is important for the mechanical loading, but may not be important for an initial thermal residual stress. When thermal residual stresses are taken into account before a mechanical load is applied, the change in geometry due to the residual stress can have a large effect on the resulting stress intensity factor. In this case, the linear solution will at first under predict and later overpredict the stress intensity factor as the applied load is increased. The stress intensity factor varies through the plate thickness. When the effect of thermal residual stresses are taken into account, the maximum value of the stress intensity factor is at the adhesive-aluminum interface. As a mechanical load is applied, the maximum stress intensity factor will switch to the free edge of the aluminum plate.

REFERENCES

[1] Baker, A. A. and Jones, R., *Bonded Repair of Aircraft Structure*, Martinus Nijhoff Publishers, Dordrecht, The Netherlands, (1988).

[2] Chue, C., Chang, L., and Tsai, J., "Bonded Repair of a Plate With Inclined Central Crack Under Biaxial Loading," *Composite Structures* 28, pp. 39-45, (1994).

[3] Sun, C., Klug, J., and Arendt, C., "Analysis of Cracked Aluminum Plates Repaired with Bonded Composite Patches," *AIAA Journal* 34, pp. 369-374, (1995).

[4] Young, A., Rooke, D. P., and Cartwright, D. J., "Analysis of Patched and Stiffened Cracked Panels Using the Boundary Element Method," International Journal of Solid Structures 29, pp. 2201-2216, 1992.

[5] Rybicki, E. and Kanninen, M., "A Finite Element Calculation of Stress Intensity Factors by a Modified Crack Closure Integral," *Engineering Fracture Mechanics* 9, pp. 931-938, (1977).

[6] Belason, E., "Fatigue and Static Ultimate Tests of Boron/Epoxy Doublers Bonded to 7075-6 Aluminum With a Simulated Crack," *18th Symposium of the International Conference on Aeronautical Fatigue*, Melbourne, Australia, May, 4, (1995).
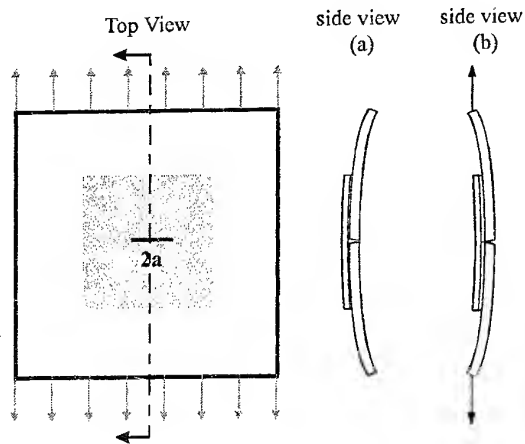
Figure 1 Curvature due to a) thermal residual stresses and b) mechanical load
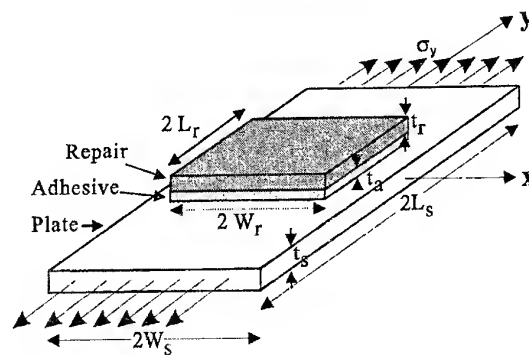
Figure 2 Sample bonded repair
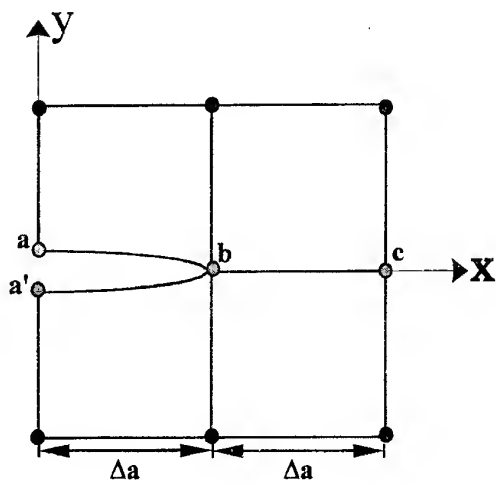
Figure 3 Aluminum plate crack tip elements (top view)
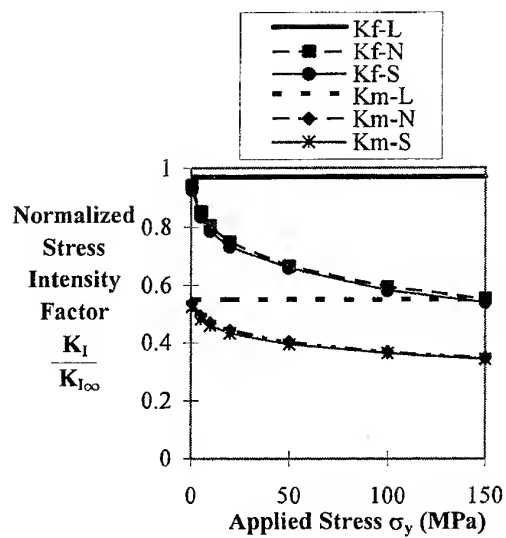
Figure 4 Comparison of adhesive models for Case 1

264
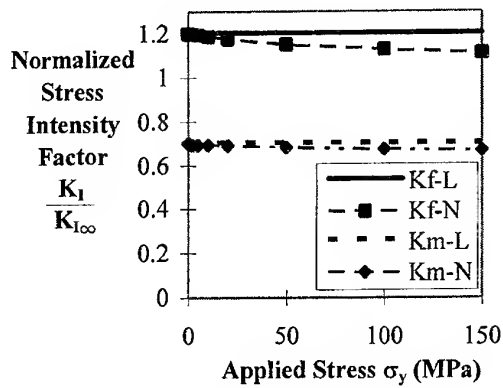
Figure 5 Normalized stress intensity factor for Case 2
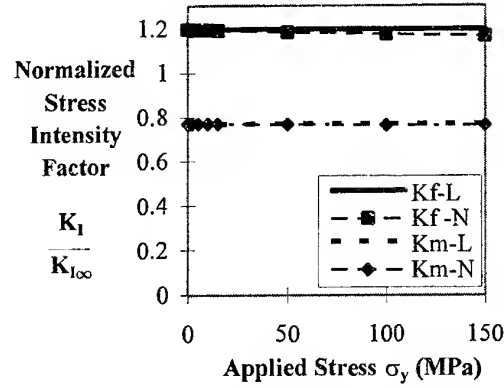
Figure 6 Normalized stress intensity factor for Case 3
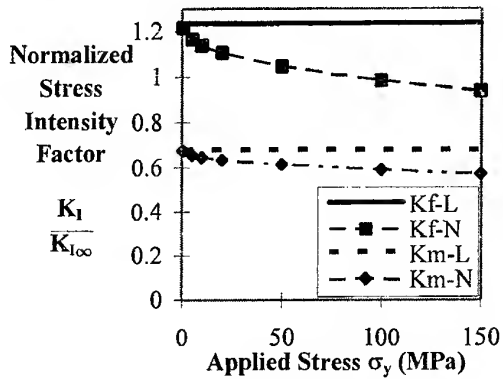
Figure 7 Normalized stress intensity factor for Case 4
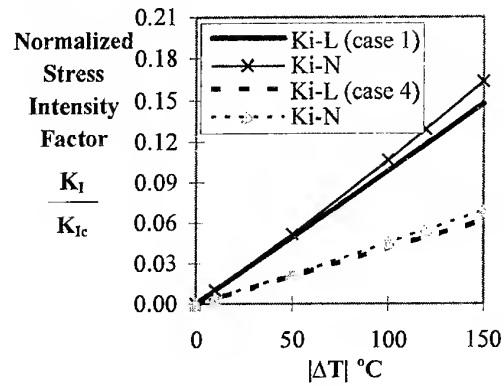
Figure 8 Normalized stress intensity factor with thermal residual stresses
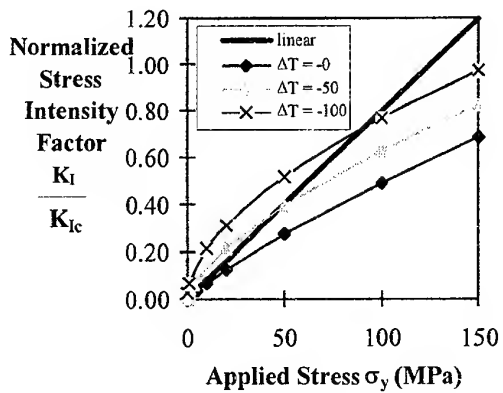
Figure 9 Normalized stress intensity factor with thermal residual stresses followed by mechanical load
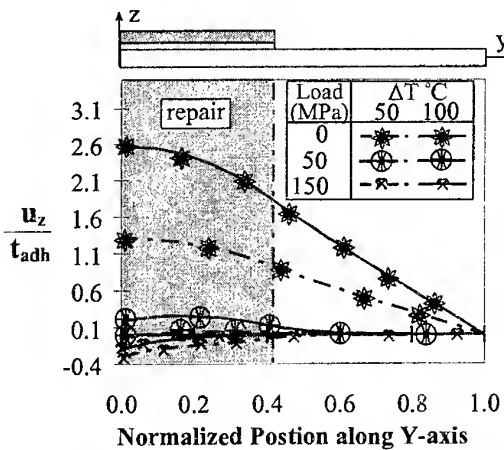
Figure 10 Curvature of aluminum plate midplane along the y-axis

265

FABRICATION OF SiCp-Al COMPOSITES
BY A MODIFIED EXTRUSION METHOD

S. KOHARA
Department of Materials Science and Technology
The Science University of Tokyo
Noda, Chiba 278, Japan

ABSTRACT

In the present study, the fabrication method and the properties of low cost metal matrix composites have been investigated.   SiC powder as a reinforcement, extrusion as a fabrication method and unsealed three-piece can as a container for powder were adopted.   The three-piece can is composed of a cylinder and two lids and formed by assembling the three pieces to make a can without sealing.   Mixtures of SiC and atomized aluminum powders with the compositions of 10-20 vol.% SiC were put into the cans and extruded at high temperatures.   The effects of die shape and extrusion temperature were investigated to determine the optimum extrusion conditions.   The hardness, the tensile strength and the wear resistance of fabricated composites were tested.   The SiCp-Al composites fabricated by this method are low cost and can be used as the wear resisting material.

INTRODUCTION

For the industrial applications of fiber or whisker reinforced metal matrix composites, the high cost of the composites is a problem.   Inexpensive fabrication methods as well as inexpensive reinforcement materials are required now.   Both fiber and whisker are good reinforcements for metals, however, their costs are too high for the industrial use.   Ceramic powders are inexpensive compared to fibers or whiskers and can be used as the reinforcement for metals.

The particulate shape of ceramic powders may have less strengthening effects on the metal matrix than fibers or whiskers.   In general, the hardness of ceramics is higher than that of metals.   Therefore, the properties other than the strength, such as hardness or wear resistance, should be considered for the use of the ceramic powder reinforced composites.

Silicon carbide is one of candidates as the reinforcement for metal matrix.   Powder of silicon carbide is manufactured on a industrial scale at present and the cost is not so high.

In general, silicon carbide particulate reinforced aluminum has been fabricated with the pressure infiltration, or the squeeze casting which are the liquid phase processing

[1] . The liquid phase processing is rather energy and time consuming processing compared to the solid phase processing.

Extrusion is an efficient manufacturing process using the plastic deformation and has been used for the fabrication of particulate materials in the field of powder metallurgy [2] [3] [4] [5] . Extrusion can be also applied for the fabrication of metal matrix composites from particulate raw materials as a solid phase processing.

In the extrusion of metal powder, powder is packed in a thin metal can and sealed after degassing or evacuation. However, this is hard and time consuming treatment. Unsealed can instead of sealed and evacuated can is possibly used for reducing the cost and saving the time.

In the present study, the fabrication method for SiCp-Al composites by extrusion with unsealed can and the properties of the fabricated composites have been investigated.

EXPERIMENTAL

Silicon carbide (β -SiC) powder and atomized aluminum powder were used as the raw materials in the present study. The powders were blended using a powder mixer with the compositions of 10, 12.5, 15, 17.5 and 20 vol.% SiC and packed into aluminum cans. The dimensions and the shape of a can are shown in Fig.1. The can is composed of three pieces, a cylinder and two lids, and assembled to form a can without sealing. The lids were made from a commercial aluminum rod and the cylinders, from a commercial aluminum pipe by machining. The lid was tightly fitted one end of the cylinder and the blended powder was poured into the can and then, another lid with a small hole to let escape gas was fitted the other end of the cylinder. The can including blended powders was set in a extruding machine and extruded with the speed of 0.6 mm/s. The extrusion temperatures are 450-635 ℃. Three types of dies with different semidie angles shown in Fig.2 were adopted in this study to determine the optimum die shape for the extrusion of composites.
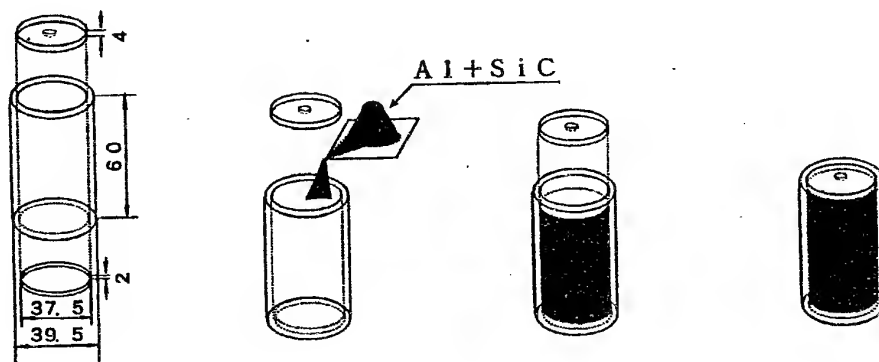
Fig. 1 Powder billet for extrusion, dimensions and preparing process.

The tensile strength of the extruded composites was measured with the specimens machined from the extruded bars. The hardness was measured at the cross-sections of the extruded bars. The wear resistance of the composites was tested with a pin on disc type wear tester.
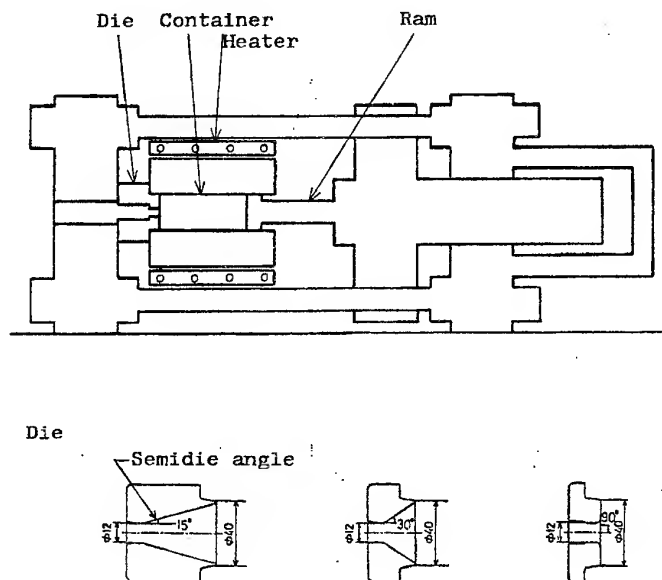
Fig. 2 Extruding machine and dies used in the present study.

RESULTS

The results of the extrusion experiments with three types of dies and extrusion temperatures from 450 to 600 °C are summarized in Table 1. The extruded bars were evaluated by the appearance. The surface of the good extruded bar was smooth, but cracks were observed on the surface of the badly extruded bar. The experimental results show that the lower the SiC content, the smaller the semidie angle and the higher the extrusion temperature, the better the extruded products.

From the results of the above mentioned experiments, the next extrusion experiments were carried out using only a die with semidie angle of 15 ° and at temperatures from 450 to 635 °C. The experimental results are summarized in Table 2. With these conditions, good extruded products were obtained in most cases except at low (450 °C) or high (635 °C) temperatures. The average hardness of the extruded composites is plotted against the SiC content in Fig.3. The average hardness of the composites increased with SiC content up to 20%. The tensile strength of the composites was measured with the specimens machined from the extruded bars. The change in tensile strength with the SiC content is shown in Fig.4. The tensile strength of the extruded composites increased with SiC content up to 15%, but did not increase at 20 %. The changes in the stress-strain curves of the extruded composites

269

Table 1　Results of extrusion experiments (1).

Semidie angle	15°				30°				90°			
SiC %	450	500	550	600	450	500	550	600	450	500	550	600 °C
10	O	O	O	O	Δ	Δ	O	O	×	×	Δ	O
15	Δ	⊙	O	O	Δ	Δ	Δ	O	×	×	×	Δ
20	×	Δ	O	O	×	×	×	Δ		×	×	×

Table 2　Results of extrusion experiments (2).

Semidie angle	15°					
SiC %	450	500	550	600	625	635 °C
10	O	O	O	O	O	Δ
12.5	Δ	O	O	O	O	Δ
15	Δ	Δ	O	O	O	×
17.5	×	Δ	O	O	O	×
20	×	Δ	O	O	O	×

O : Good　Δ: Not good　× : Bad
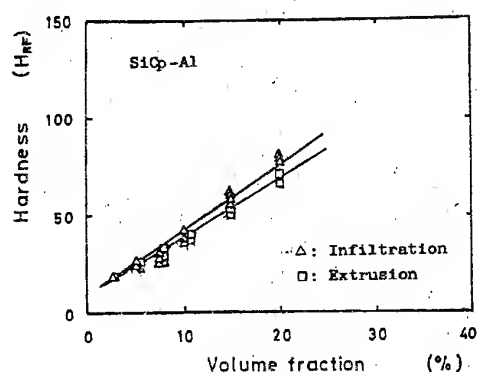
Fig. 3　Change in hardness with
SiC volume fraction.
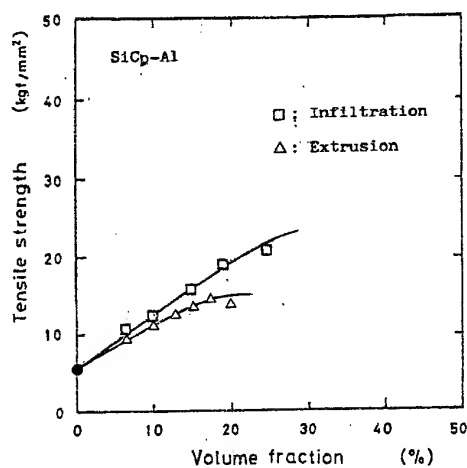
Fig. 4　Change in tensile strength
with SiC volume fraction.

270
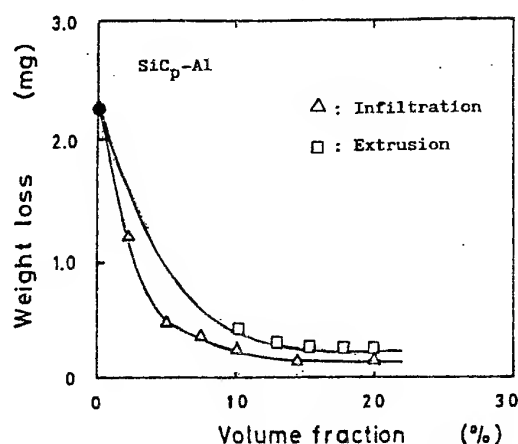
Fig. 5 Change in weight loss in wear test with SiC volume fraction.

were checked The tensile strength varied a little, but the elongation at fracture decreased very much by making the composite.

The results of the wear test is shown in Fig.5 and compared with the composites made by other method. The weight loss by wear of the composites decreased with increasing the SiC content. Though the wear resistance of the extruded SiCp-Al composites is a little inferior to the SiCp-Al composites made by the infiltration method, the difference between the two types of composites is not so large.

DISCUSSION

In the industrial application of the fiber or whisker reinforced metal matrix composites, the high cost of the composites is a big problem. If fiber or whisker is not used, the cost of the composites will be lowered, but the properties of the composites will also fall behind. Ceramic powders instead of fibers or whiskers can be used as the reinforcement for the metal matrix, however, the strengthening effects of the ceramic powder on the metal matrix will not be good as the fibers or whiskers because of the particulate shape of particles. The properties other than the strength should be considered for the application of the composites. Although the tensile strength of the SiC powder reinforced aluminum is not high, the special features of the ceramic powder reinforced metal are considered to be the hardness or wear resistance.

Usually particles of aluminum powder are covered by a thin aluminum oxide film and the adhesion between the film and matrix is so strong that the oxide film can not be removed easily. Even if aluminum powder packed into a can is evacuated, the oxide film still remains on the surface of particles. It is better to break the surface layer by the severe plastic deformation as extrusion and create the new surface for the

consolidation of metal powder. The lid and cylinder are welded by the severe plastic deformation during extrusion and form a closed can. Thus, unsealed cans can be used as the container for fabricating aluminum matrix composites

The strength of the SiCp-Al composites made by the infiltration method was higher than that of the SiCp-Al composites made by this method. It may be due to the difference of bonding between SiC particles and aluminum matrix. The infiltration method is a liquid phase processing, but extrusion is a solid phase processing. The interfacial bonding in the liquid phase processing is stronger than that in the solid phase processing.

The tensile strength of this composites rather falls with increasing the SiC content in the range higher than 20 vol% SiC. This fact may indicate the limit of this method, that is, the dispersion particulate particles strengthening by the solid phase processing. However, the SiCp-Al composites is useful as a wear resisting material when the cost is taken into consideration.

CONCLUSIONS

The fabrication method and the properties of SiC particulate reinforced aluminum as the low cost composite were investigated and the followings were concluded.

(1) The modified extrusion method with unsealed three-piece can is applicable for fabricating the SiCp-Al composites.

(2) The tensile strength of the fabricated composites increases with the SiC content up to about 15 vol.% SiC, but little increases for the higher SiC content.

(3) The wear resistance of the SiCp-Al composites is high enough and comparable with that of the composites made by the other method such as an infiltration method.

REFERENCES

[1]   S. Kohara; Materials and Manufacturing Processes, 5, p.51, (1990).

[2]   S.Krishnamurthy, I.Weiss and F.H.Froes; Proceedings of Powder Metallurgy and Related High Temperature Materials, p.135, (1987).

[3]   A.Murase and G. Abe; Proceedings of Powder Metallurgy World Congress Part 2, p.859, (1993).

[4]   Y.Ohashi, T.Fukuda, M.Nishiguchi, and J.Kikuchi; Proceedings of Powder Metallurgy World Congress Part 2, p.863, (1993).

[5]   H.Hoshino and S.Kohara ; Advances in Powder Metallurgy and Particulate Materials Vol.6, p.31, (1994).

DYNAMICS OF DELAMINATED COMPOSITE MATERIAL BEAMS AND PLATES

M. KRAWCZUK, W. OSTACHOWICZ and A. ŻAK

Institute of Fluid Flow Machinery, Polish Academy of Sciences, Poland

INTRODUCTION

The use of composite materials in various construction elements has substantially increased over the past few years. These materials are particularly widely used in situations where a large strength-to-weight ratios are required. Composite materials similarly to isotropic materials are subjected to various damages, mostly cracks and delaminations. They result in local changes of the stiffness of the element and consequently its dynamic characteristics are altered. Changes of natural frequencies and mode shapes, amplitudes of forced vibrations and also coupling of vibrations forms are observed. The dynamic characteristics of damaged elements can be correlated with the location and size of damages. These relations are frequently used in diagnosis of such constructional elements – for example [1–2].

This work presents the method of modelling delaminations in the composite beams and plates based on the finite element formulation [3–5]. Elaborated models enable the analysis of the influence of the delamination (i.e. its length and location) and also material properties on the dynamic characteristics of constructions made of composite materials. In the delaminated region additional boundary conditions are applied. It is assumed that the delamination extends to the full width of the element and remains open (i.e. contact forces between lower and upper parts are neglected in the model). Also an easy modification of these elements is possible, according to the analysis of the specific damage (i.e. multiple delaminations).

DELAMIANTED BEAM FINITE ELEMENT

GENERAL DESCRIPTION

A discrete model of a delaminated part of the beam is presented in the Fig.1. The delaminated region is modelled by three beam finite elements (I, II and III) which are connected at the tip of the delamination by additional boundary conditions.

The layers are located symmetrically with respect to the x–z plane. Each element has three nodes at $x = -L/2$, $x = 0$, $x = L/2$. At each node there are three degrees of freedom which are axial displacements q_1, q_4, q_7, transverse displacements q_3, q_6, q_9 and the independent rotations q_2, q_5, q_8. Additionally, it is assumed that the number of degrees of freedom is independent of the number of layers.
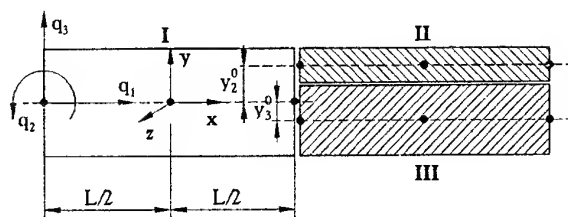
Fig.1. The delaminated region of a beam modelled by finite elements.

273

Neglecting warping, the displacements u and v of a point can be expressed as:

$$\begin{cases} u(x, y) = u^0(x) - y \cdot \phi(x) \\ v(x, y) = v^0(x) \end{cases} \tag{1}$$

where $u^0(x)$ denotes the axial displacement, $\phi(x)$ the independent rotation, and $v^0(x)$ the transverse displacement.

In the finite–element modelling, the bending displacement $v^0(x)$ is assumed to be cubic polynomial in x, while the axial displacement $u^0(x)$ and the rotation $\phi(x)$ are assumed to be quadratic. Additionally, it is assumed that the shear strain variation is linear, as proposed by Tessler and Dong [6]. Employing the above conditions, the displacements and rotation in the element may be written in the following form:

$$\begin{cases} u^0(x) = a_1 + a_2 x + a_3 x^2 \\ \phi(x) = a_4 + a_5 x + 3a_9 x^2 \\ v^0(x) = a_6 + a_7 x + a_8 x^2 + a_9 x^3 \end{cases} \tag{2}$$

The coefficients a_1–a_9 can be expressed in terms of the element degrees of freedom by using the nodal conditions and next the matrix of the shape functions for the single layer can be determined.

Employing the shape functions matrix for the single layer, the inertia matrix of the whole element may by calculated as a sum of all single layer inertia matrices. In the same way the stiffness matrix for the whole element can be obtained when the strain–displacement matrix for each layer is evaluated.

BOUNDARY CONDITIONS AT THE TIP OF THE DELAMINATION

In order to connect elements modelling the delaminated area of the beam (I, II and III) the following boundary conditions are applied at the tip of the delamination:

$$\begin{cases} u_1^0(x) = u_2^0(x) + y_2^0 \phi_2(x) & \phi_1(x) = \phi_2(x) = \phi_3(x) \\ u_1^0(x) = u_3^0(x) + y_3^0 \phi_3(x) & v_1^0(x) = v_2^0(x) = v_3^0(x) \end{cases} \tag{3}$$

where y_2^0 and y_3^0 denote distances between neutral axes of elements I-II and I-III, respectively (see Fig.1).

Using the relations for coefficients a_1–a_9 for a single element layer and taking into account relations (3), it can be found that coefficients a_1–a_9 for elements I, II and III must satisfy the following relations:

$$\begin{cases} a_1^{II} = a_1^I - y_2^0 a_4^I & a_1^{III} = a_1^I - y_3^0 a_4^I & a_4^I = a_4^{II} = a_4^{III} & a_7^I = a_7^{II} = a_7^{III} \\ a_2^{II} = a_2^I - y_2^0 a_5^I & a_2^{III} = a_2^I - y_3^0 a_5^I & a_5^I = a_5^{II} = a_5^{III} & a_8^I = a_8^{II} = a_8^{III} \\ a_3^{II} = a_3^I - 3y_2^0 a_9^I & a_3^{III} = a_3^I - 3y_3^0 a_9^I & a_6^I = a_6^{II} = a_6^{III} & a_9^I = a_9^{II} = a_9^{III} \end{cases} \tag{4}$$

where the superscripts I, II and III denote the number of the element in the region of the delamination.

The shape functions matrices, the inertia matrices and also the stiffness matrices of elements II and III can be obtained in the same way as it was described for the element I.

274

DELAMINATED PLATE FINITE ELEMENT

GENERAL DESCRIPTION

The same concept, as it was for the beam element, is used in case of modelling the delamination region in the composite plate (see Fig.2). The delamination is modelled by three plate finite elements which are connected in the delamination crack tip using the same type boundary conditions. Material layers in the element are located symmetrically with respect to x–y plane. Each element has eight nodes with five degrees of freedom.
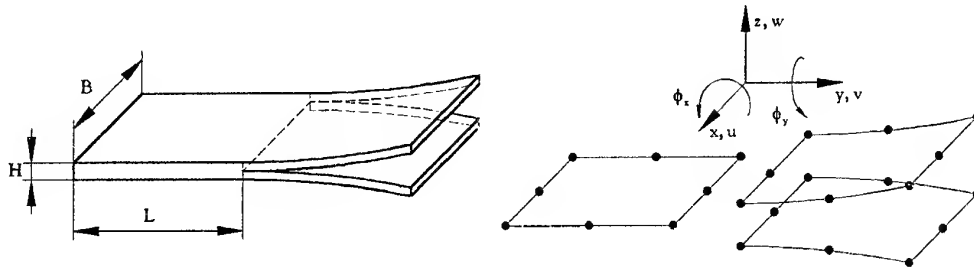
Fig.2. The delamination in a plate modelled by tree finite elements.

Axial displacements u, v and w in a single layer can be expressed as:

$$\begin{cases} u(x,y,z) = u^0(x,y) - z \cdot \phi_x(x,y) \\ v(x,y,z) = v^0(x,y) - z \cdot \phi_y(x,y) \\ w(x,y,z) = w^0(x,y) \end{cases} \tag{5}$$

where $u^0(x,y)$, $v^0(x,y)$, $w^0(x,y)$ denote mid–plane displacements, while $\phi_x(x,y)$ and $\phi_y(x,y)$ denote independent rotations. To approximate the axial mid–plane displacements and rotations biquadratic shape functions for eight–node isoparametric element have been used.

Using standard finite element formulae the inertia matrix of the whole element can be determined as a sum of single layer inertia matrices. Similarly, the stiffness matrix can be evaluated if the strain–displacement matrix for each single layer is previously calculated.

BOUNDARY CONDITIONS AT THE TIP OF THE DELAMINATION

To connect elements modelling the delamination area and to satisfy continuity of the displacements the following conditions must be fulfilled (see figure below):

$$z_2^0 = \frac{h_1 - h_2}{2} \quad z_3^0 = \frac{h_1 - h_3}{2}$$
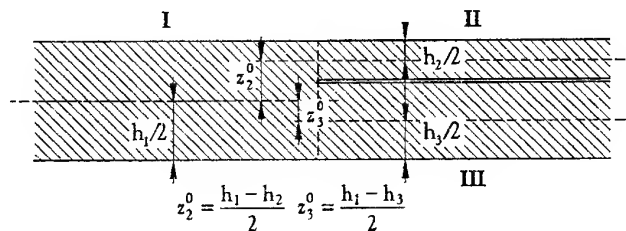
Fig.3. The cross–section of the plate in delamination crack tip.

$$\begin{cases} u_2^0 = u_1^0 - z_2^0 \cdot \phi_x & u_3^0 = u_1^0 - z_3^0 \cdot \phi_x \\ v_2^0 = v_1^0 - z_2^0 \cdot \phi_y & v_3^0 = v_1^0 - z_3^0 \cdot \phi_y \end{cases} \tag{6}$$

where z_2^0 and z_3^0 are the distances between neutral axes of elements I-II and I-III.

Applying relations (6) to (5), the displacement fields of elements II and III, which model the delamination region, may be evaluated. Analogously, the inertia and stiffness matrices of these elements can be found.

NUMERICAL EXAMPLES

NATURAL FREQUENCIES OF THE COMPOSITE BEAM

Numerical calculations have been carried out for the cantilever beam (see Fig.4.a) of the following dimensions: length 600 mm, height 25 mm and width 50 mm. The beam was made of graphite-epoxy composite (see Appendix). It was assumed that all layers of the beam have the same mechanical properties, i.e. the volume fraction of fibres and the angle of fibres in each layer are identical.
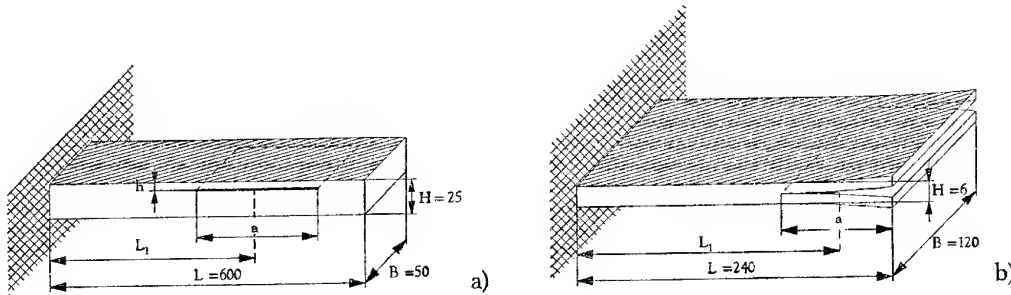
Fig.4. The geometry of the analysed: a) composite beam, b) composite plate, with the delamination.

The first example illustrates the influence of the delamination position along the beam height on the changes of the first bending natural frequency for four different volumes fraction of fibres. The length of delamination was 37.5 mm (a/L=0.0625) and the centre of the delamination was located 431.25 mm from the free end of the beam (L_1/L=0.71875). The angle of fibres (measured from x-axis of the beam in the x-z plane) was 45°, whereas the relative volume fraction of fibres was: 0.2, 0.4, 0.6 and 0.8. In this case the beam was modelled by 17 finite elements (2 elements in layers modelling delamination and 15 elements outside the delaminated region). The results of numerical calculations are given in Fig.5.a. It is clearly shown that the natural frequency is the most reduced when the delamination is located along the neutral axis of the beam. When the delamination is located near the upper or lower surface of the beam the changes of the natural frequency is negligible.

The next example shows the influence of the location of the delamination along the beam length on the changes of first bending natural frequency. The delamination was located along the neutral axis of the beam. The length of the delamination was 37.5 mm (a/L=0.0625). The same number of elements was used as in the first example. It is easy to find that the changes of natural frequency strongly depend on the location of delamination. For the analysed beam the largest reduction of natural frequency is observed if the centre of the delamination is located at the node of the mode shape associated with this frequency.
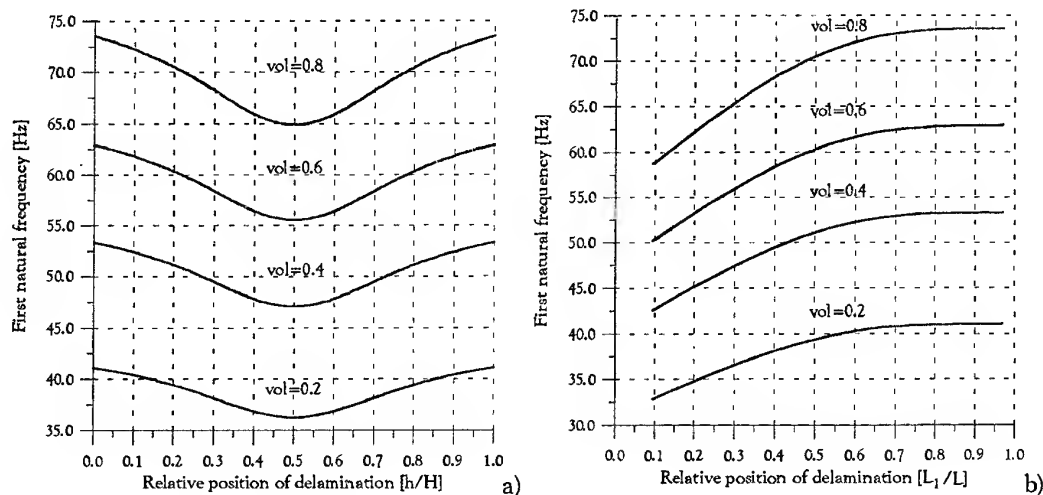
Fig.5. The effect of the delamination location along: a) the beam height, b) the beam length, on the first bending natural frequency.

NATURAL FREQUENCIES OF THE COMPOSITE PLATE

Numerical calculations for the cantilever composite plate have been carried out for the following plate dimensions: length 240 mm, width 120 mm and height 6 mm (see Fig.4.b). The plate was consisted of six layers of materials with changing angle of fibres $\pm 45°$. Each layer of the plate was made of graphite-epoxy composite (see Appendix). It was assumed that all mechanical properties except the angle of fibres are the same in each layer. The mechanical properties of the applied material are the same like in case of the beam.
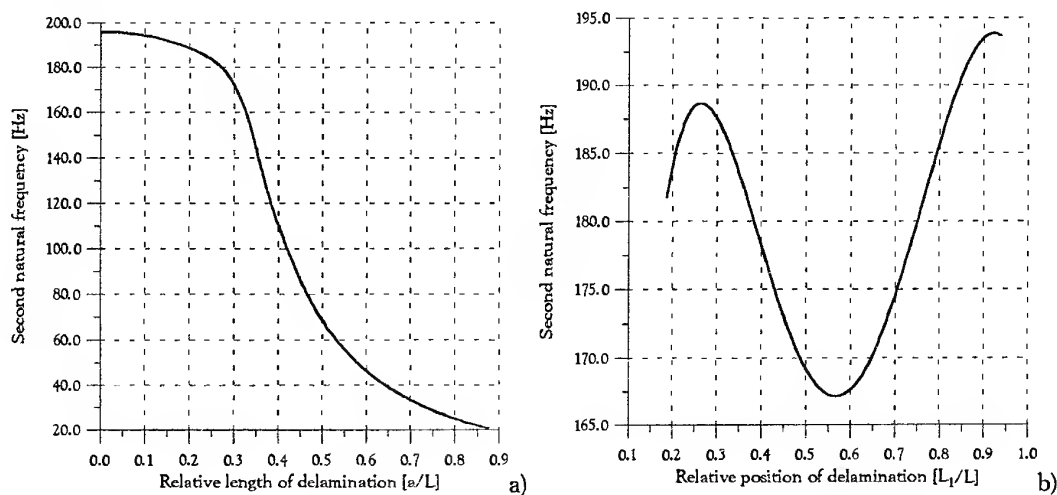
Fig.6. The influence of the delamination: a) length, b) position on the first natural frequency of the cantilever composite plate.

The first example presents the influence of the length of the delamination on the second bending natural frequency (Fig.6.a). It was assumed that the delamination expands from the free end of the plate. The delamination was located along the neutral axis of the plate. It is noted that when the length of the delamination increases the values of natural frequency is greatly reduced.

277

The last example shows how the location of the delamination along the plate length influences on the drop of the second bending natural frequency (Fig.6.b). The delamination was located along the neutral plane of the plate. The length of delamination was 30 mm (a/L=0.125). It is easy to find that the changes in natural frequency strongly depend on the location of delamination. For the analysed plate the largest decrease in natural frequency is observed when the centre of the delamination is located at the node of mode shape associated with this frequency.

CONCLUSIONS

As a result of this work models of the finite beam and plate elements have been elaborated. These elements enable the analysis of the influence of delaminations on the dynamic characteristics of the constructions made of composite materials.

The method of modelling the delamination in composite beams and plates is flexible and allows to analyse the influence of multiple delaminations and also material properties (i.e. position and volume fraction of fibres) on natural frequencies of beams and plates with various boundary conditions.

ACKNOWLEDGEMENTS

APPENDIX

The properties of the components of graphite-epoxy reinforced composite [7-8] analysed in the paper are as follows:
- epoxy resin – $E_m = 3.43$ GPa, $v_m = 0.35$, $\rho_m = 1250$ kg/m^3,
- graphite fibre – $E_f = 275.6$ GPa, $v_f = 0.2$, $\rho_f = 1900$ kg/m^3.

BIBLIOGRAPHY

[1]   Bently D.E., Muszyńska A., "Early detection of shaft cracks on fluid-handling machines". Proceedings of the International Symposium on Fluid Machinery Troubleshooting, 53-58, Anaheim, (1986).

[2]   Ju F.D., Mimovich M.E., "Experimental diagnosis of fracture damage in structures by the modal frequency method". ASME Journal of Vibration, Acoustics, Stress, and Reliability in Design. 110, 456-463, (1988).

[3]   Ostachowicz W., Krawczuk M.: "Dynamic analysis of delaminated composite beam". Machine Vibration (Springer-Verlag), No.3, pp.107-116, (1994).

[4]   Krawczuk M., Ostachowicz W., Żak A.: "Natural frequencies of delaminated composite beam". Proceedings of XII Polish Conference on Computer Methods in Mechanics, Warsaw-Zegrze, Poland, 9-13 May 1995, pp.171-172.

[5]   Krawczuk M., Żak A., Ostachowicz W.: "Analysis of natural frequencies of a layered composite plate delamination". Reports of The Fluid Flow Machinery Institute, No. 307/95, (1995).

[6]   Tessler, S.B. Dong, "On a hierarchy of conforming Timoshenko beam elements". Computer and Structures 38, 334-344, (1991).

[7]   Kalamkarov A.L., "Composite and reinforced elements of construction". John Willey and Sons, New York, 1992.

[8]   Vinson J.R., Sierakowski R.L., "Conduct of Structures Composed of Composite Materials". Martinus Nijhoff, Dorchester, 1989.

OPTIMIZATION OF PREPREG PARAMETERS FOR THERMOPLASTIC FILAMENT WINDING BY TESTING OF CURVED SAMPLES

Bernd Lauke, Wieland Beckert, Ralf Voigtländer

Institute for Polymer Research Dresden e. V. , Hohe Str. 6, 01069 Dresden

ABSTRACT

The filament winding of thermoplastic matrix composites is known as a common technology in the research area but is hardly used in industry mainly because of unsatisfactory knowledge about special properties of the used prepreg materials and its influence on the composite properties as well as the process itself. A special filament winding device has been developed that provides the opportunity to vary different process parameters to enable the optimization of the process of consolidation and the material properties of the composites. Efficient and reproducible experiments as well as the registration of process parameters are guaranteed by a computer aided control of the process.

Our paper provides results in processing commingled yarn consisting of glass fibres and polyamide (PA) fibres as matrix material to composite rings. To access the bonding quality of the manufactured ring samples the following experiments have been used: i) interlaminar shear strength measurement by a recently developed shear device, ii) fracture toughness determination by the curved double cantilever beam test (CDCB) and iii) ring tension testing.

For the testing of curved ring samples the theoretical background for data reduction has been derived and is provided in the paper.

INTRODUCTION

Compared with traditional epoxy matrix composites continuous-fibre-reinforced thermoplastics provide some advantages, such as higher toughness, and thus they are attractive for aerospace and automotive applications.

Among manufacturing methods the filament winding technique is of special interest, mainly due to its high production speed. In recent years this technology has been increasingly applied to fibre reinforced thermoplastics where in-situ consolidation is reached during processing (see, for example Ref. [1], [2], [3]).

Different combinations of matrix and fibres as basic materials for composite processing are now available on the market, as pre-impregnated tapes and tows, and commingled and powder-impregnated yarns.

The present paper is concerned with the manufacture of laminated rings from commingled yarns consisting of glass fibres and polyamide (PA 6) fibres as matrix with a filament winding laboratory device that allows the variation of several process parameters. The process parameters were previously varied to achieve the optimum processing window for our set-up, i. e. it was intended to maximize winding speed and to minimize energy consumption while obtaining composites of high quality.

To evaluate the consolidation quality between the layers of the rings, shear strength and crack resistance measurements of curved samples have been carried out. A method for measuring the shear strength of thin curved samples is proposed herein. The curved double cantilever beam (CDCB) test is a method to measure mode I delamination toughness of curved composite materials. A finite element model for this geometry is

presented, that takes into consideration nonlinear deformational effects, orthotropic material properties and local mixed mode load at crack-tip.

THERMOPLASTIC FILAMENT WINDING

Filament winding device

The filament winding device is shown schematically in Fig. 1. Its main components are the preheating chamber, the hot air gun at the consolidation point, the hot air heated mandrel, and the control unit.
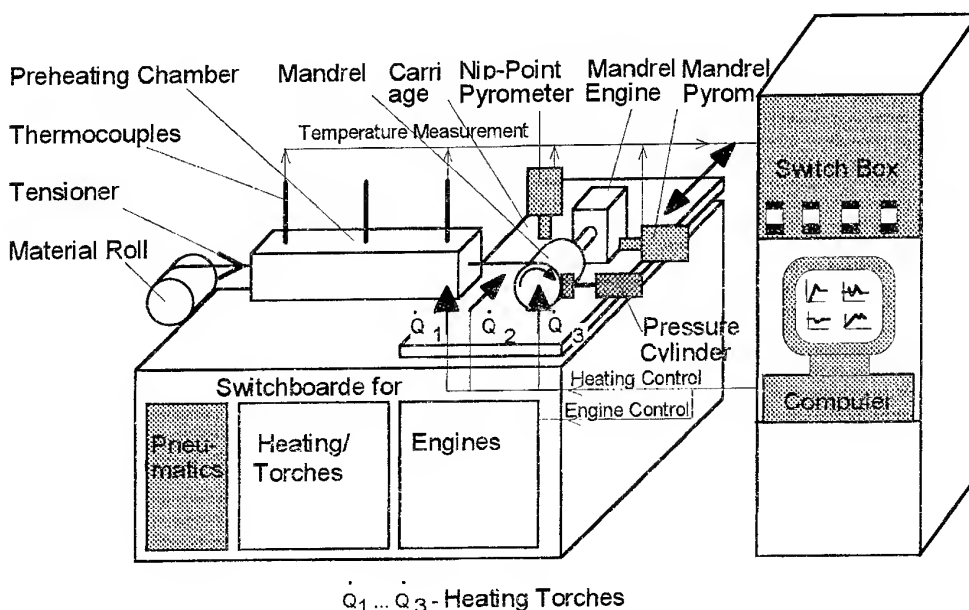
Fig. 1: Thermoplastic filament winding device

Optimum consolidation is necessary to achieve composite rings with high mechanical properties, especially with high bonding quality between successive layers. Thus the heating systems within the preheater, at the consolidation point and that of the mandrel are most important. An experimental and theoretical investigation of an infrared preheating process has recently been published [4]. The results show that high processing speeds can only be realized by using an effective convective preheating chamber. Thus the commingled yarn is heated in a hot-air-preheater (L=100 cm) and is than wound on a steel or aluminium mandrel. To obtain good consolidation, the bundle is further heated up at the consolidation point (also called nip-point) by a hot air while under pressure of a compaction roller. Additionally, a tension force is applied to the tow by a friction brake. The core component is the PC-control-unit that controls all the parameters of the process to obtain stable manufacturing conditions. The following winding parameters have been used: 1) winding speed, 5 cm/s; 2) mandrel carriage movement, 2mm per round; 3) temperature at the end of the preheater, 270 °C; 4) temperature of the mandrel, 240°C; nip-point temperature, 320 °C.

Material

The prepreg material was made by air texturing and consists of reinforcing glass fibres and PA-fibres as matrix forming a commingled yarn. The glass fibres as well as the polymer fibres were manufactured on our laboratory devices. Yarns with a fineness of 720 tex (1 tex =1g/1000m) have been made, however, this value was reached by the combination of yarns with different fineness, for example: 2x360 tex and 4x180 tex. Additionally, the fibre were coated with five chemically different sizings.

EXPERIMENTS AND THEORETICAL BASIS

The characterization of the delamination properties is a very important task for testing of composite materials. The interlaminar shear strength and the fracture toughness in mode I or II loading are the most sensitive quantities for evaluating the fabrication quality especially the consolidation of the composite rings.

The usually applied method in shear strength measurement is the short-beam test, however, with thermoplastics it is difficult to meet the requirements of the standard. Other test set-ups are single and double lap joint tests. A literature survey and discussions of the benefits and draw-backs of these tests is given, for example, by Kinloch [5]. However, all these tests are for plane samples only and that is the reason why we have developed a method for measuring the interlaminar shear strength of curved samples [6].

A standard test for characterizing mode I delamination toughness of straight laminate samples is the Double-Cantilever Beam (DCB)-Specimen. As an equivalent test method for curved structures produced by the filament winding technology the Curved Double Cantilever Beam (CDCB) geometry has been proposed in the literature [7], [8], [9] where some coarse schemes for reduction of experimental data's of the CDCB-test have been used. Though they allow an interpretation of test results in quality, some improvements in quantity have been obtained recently [10]. A finite element (FE) model provides the basis for the analysis of experimental results and can be used for a valuable data reduction scheme.

Experiments

After the application of the filament winding technique rings of unidirectional (circumferentially) reinforced composites are obtained with the diameter of the mandrel. Three different test have been carried out to get knowledge about the ring quality: the Ring Tension test, the Compression Shear test and the Curved Double Cantilever Beam test. The test configurations are shown in Fig. 2 and 3. The rings are prepared for testing by grinding and cutting them (with a diamond saw) into pieces; quarter rings for the CDCB-test and smaller pieces for the CS-test. These samples with an arc length L, width B and thickness D are now tested under compression load to obtain the interlaminar shear strength. The CDCB-Specimen consists of a composite material quarter ring with fibres oriented in circumferential direction, an artificial crack notch of length a_0 introduced in the thickness-midplane during processing by means of a PI-foil and two pierced aluminium loading blocks glued at the cantilever ends.
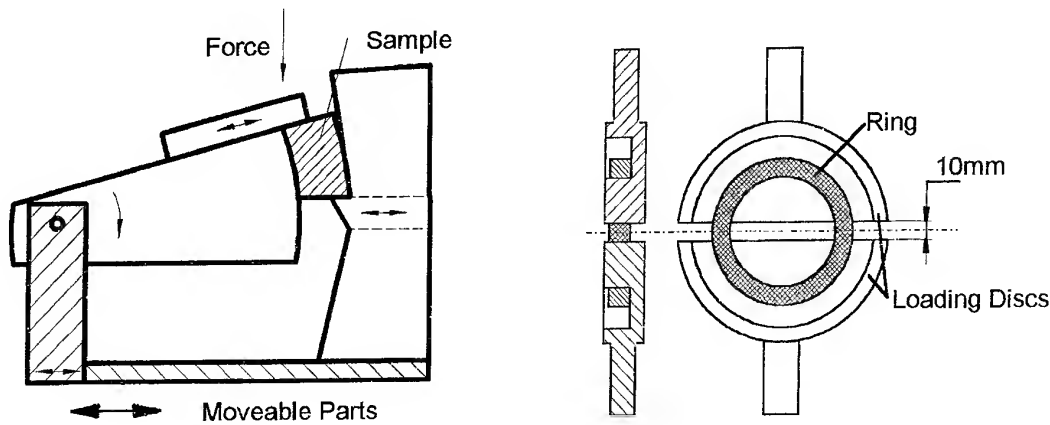
Fig. 2: Experimental test set-ups for the Compression Shear test (left) and Ring Tension test.
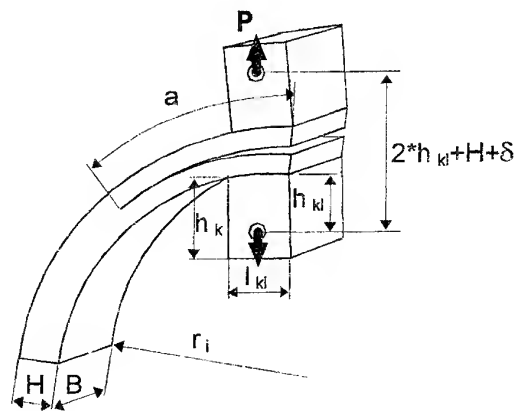
Fig. 3: Geometry of the CDCB-test and model

Shear strength and stress distribution

From the force measurement with the CS-test device the shear strength is obtained by the maximum force under consideration of loading geometry (angle and span ratio)

$\tau_{max} = F_{max}/A_0$, with $A_0 = B \times L$ as the sample area within which the force acts. The tests have shown that delamination starts in the same moment when the maximum load is reached.

A shear strength criterion is based on the inherent assumption that the sample fails simultaneously at all points within the delamination area. This would require a homogeneous stress distribution and a sample without defects. The latter will never be the case in practice, however, the former one depends on the test conditions and material properties. To examine the stress situation in the sample a FE-model with the commercial finite element software ANSYS has been established (see [11]).

Although the shear stress distribution along the curved compression shear sample is not uniform in general an optimum aspect ratio (dependent on the material properties) of $L/D \approx 2$ can be found where the test set-up is appropriate to determine the interlaminar shear strength of composites.

During the CDCB-test the loading force-displacement dependence $P(\delta)$ for stable crack-extension is monitored together with debonding crack length a. The FE-model (ANSYS) is built up from 8-node 2D-solid elements with orthotropic linear elastic material properties and utilizes nonlinear analysis in order to account for large deflection and rotational effects.

The debonding toughness is characterized by a critical value for the energy release rate G_c, that is defined by the change in total potential energy with crack length. To characterize the mixed mode state the stress intensity factors K_I and K_{II} were extrapolated to $r \rightarrow 0$ from the relative displacements of adjacent crack-face points in the vicinity of the FE-models crack-tip, for more details and the relevant equations see [10]. The investigation of the mixed mode state revealed, that in general the mode II part of the crack-tip loading is smaller than 5-10% of the K_I value as long as the crack propagates in the mid-plane, otherwise large Mode II contributions appear.

To simplify the data reduction, a simple empirical approximation is used alternatively, the so-called compliance method: $G(a,\delta) = \dfrac{P \cdot \delta}{2B} \left(\dfrac{1}{C_0(a)} \cdot \dfrac{\delta C_0(a)}{\delta a} \right)$. Usually the relation between the compliance C and the crack length a according to BERRY [12] is used: $C(a) = c_1 \cdot (a)^{c_2}$. If we compare our FE-results with the empirical one it can be concluded that this simple method is applicable with a discrepancy smaller than 10% for the rather complicated test configuration.

DISCUSSION

Composite rings with different fibre volume content and several coatings have been manufactured. The shear and tensile strength values are summarized in Fig. 4 and 5. It becomes clear that there exists an optimum in fibre content at about 55 vol.-%. At higher fibre contents the matrix material is not sufficient to impregnate the reinforcing fibres leading to fibre damage during processing. Fibre volume fractions lower than 40 % result in squeezing of the molten polymer out of the ring. If the engineer has certain demands on the material properties than we are able to provide the optimal prepreg and process parameters. Fig. 5 shows the strength values for different coating systems. Fibres without any coating provide the lowest values, corresponding to „a". The highest mechanical properties are obtained with the system „fr5", which consists of a cationic aminosilane. A typical crack resistance curve determined by the CDCB-test is shown in Fig. 6 for samples with a thickness of H= 4,8 mm. The dots are the experimental values and the curves are calculated with the FE-model on the basis of the empirical compliance method. The agreement between the values shows that the application of that simple data reduction scheme is reasonable also for the CDCB-test geometry. As further calculations have shown, a sample thickness of about 5mm is optimal. Thicker samples result in higher forces which are critical for the adhesion between the sample and the aluminium loading blocks; smaller samples show a higher scattering because of the stronger influence of the crack deviation from the sample mid-plane.
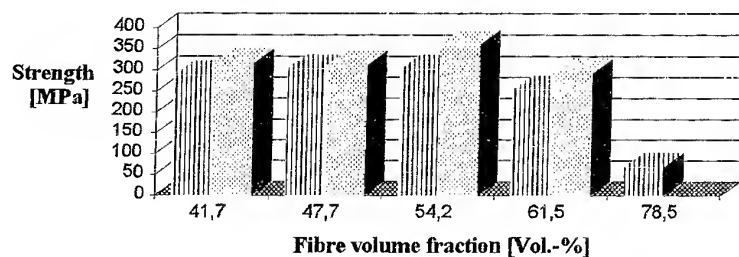
Fig. 4: Strength as a function of fibre volume fraction
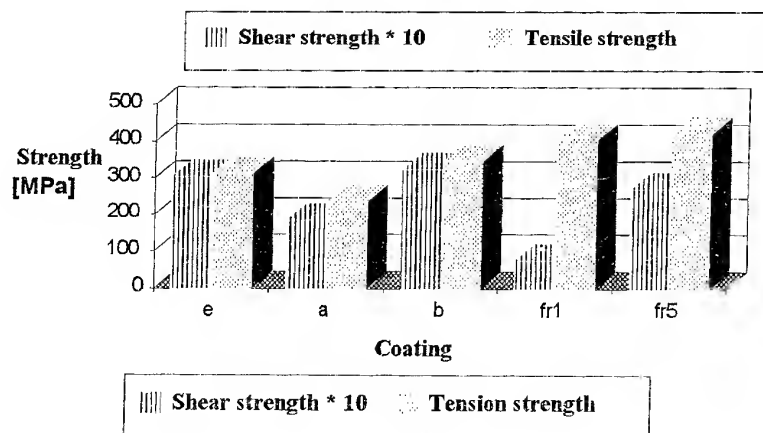
Fig. 5: Strength as a function of fibre coatings, fibre volume fraction, v=0.47
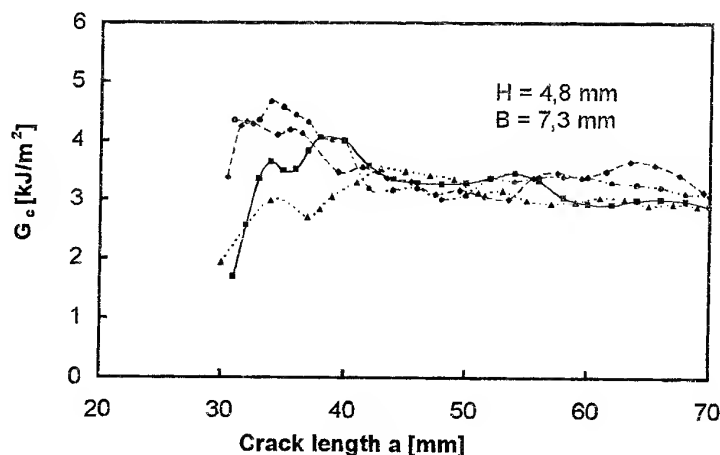
Fig. 6: Critical energy release rate as a function of crack length, dots:experiment, curves: theory

REFERENCES

[1]   Wittich, H., Friedrich, K., *Proc. 22nd AVK-Conference*, Mainz, Germany, May 1989.
[2]   Dickmann, O., Lindersson, K., and Svennson, L., *Plastics and Rubber Processing and Applications* **13**, pp 9-14 (1990).
[3]   Haupert, F., Friedrich, K., *Composite Manufacturing* **6**, pp. 201-204 (1995)
[4]   Lauke, B., Schöne, A., Schuster, J., Friedrich, K., Composite Engineering 4 (1994) 309-316
[5]   Kinloch, A.J., *Adhesion and Adhesives*, Chapman & Hall, 1994
[6]   Lauke, B., K. Schneider, Friedrich, K., ECCM-Conference, April, 1992, Bordeaux, Preprint p. 313-318.
[7]   Foral, R. F. *Key Engineering Materials* **37**, pp.137-148 (1989)
[8]   Wittich, H., *Ph Thesis*, TU Hamburg-Harburg, January 1993
[9]   Lauke, B., Friedrich, K., *Composites Manufacturing* **4**, pp. 93-101 (1993)
[10] Beckert, W., Lauke, B., Friedrich, K., Applied Composite Materials **1**, pp. 395-400 (1995)
[11] Lauke, B, Beckert, W., Schneider, K., Applied Composite Materials **1**, pp. 267-271, (1994)
[12] Berry, J. P., *J. Appl. Phys.* **34**, pp. 62-66 (1963)

MICROWAVE INTERACTION WITH CERAMICS AND ITS APPLICATION TO SOLID SOLUTIONS

J.B. Li[1], X.Y. Kong[1], Y. Huang[1], Z.P. Xie[1], N. Mahomed[2] AND B.H. Sun[2]

[1] Dept of Mat. Sci. & Eng., Tsinghua University, Being. 100084, P.R.China.
[2] Centre for Research in Applied Technology, Peninsula Tech, P.O. Box 1906, Bellville 7535, SA

Abstract

Microwave energy has been used in the heating and processing of foods and some soft materials for decades. Recently, microwaves have been used in the heating of high melting point materials such as ceramics and inorganic materials. This paper reviews the main factors that affect microwave heating of ceramic materials and reports on some experimental results concerning microwave processing of solid solutions of high melting point metal carbides.

Titanium and zirconium carbide are widely used as reinforcement for ceramic materials due to their high-hardness and high-melting points. Their hardness is greatly affected by the composition and their solid solutions have higher properties than pure elemental crystals. But synthesis of their solid solutions have been considered to be difficult.

A new convenient way to synthesize the (Ti, Zr)C carbide solutions were found by using fine co-precipitated $ZrTiO4$ powder as the raw material. By heating it with carbon black over 1800°C, the near pure solid solution powder of (TiZr)C was obtained. This solid solution powder was metastable and easily decomposed into two phases of TiC and ZrC by annealing it at 1000-1400°C, and the separated phases were found to form unique microstructures. Microwave processing caused the phase separation of the two elemental components of TiC and ZrC to be more effective than conventional annealing. The relationships of the separated two phases were different because of different heating facilities. The microstructure of the material processed by conventional annealing showed network-like patterns while the other processed by microwave processing showed striated or modulated patterns. These ex-solution phenomena and their unique structures are expected to provide new ways in designing stronger grain boundaries of ceramic materials and in preparing the nano-materials.

Keywords: *Microwave processing, Ceramic materials, Spinodal decomposition, Microstructure, Modulation, Network.*

1.   Introduction

A microwave is a type of electromagnetic wave with a wavelength of 1mm - 1m. It is traditionally used to heat soft materials such as rubber and wood, and commonly used in the heating and cooking of foods. Recently, research efforts on the application of microwave processing to hard materials such as inorganic and ceramic materials have become popular. The main applications of microwaves in materials processing are in the areas of sintering of ceramic materials, powder synthesis and metal/ceramic joining. In these applications, microwave processing has been shown to have many advantages compared to conventional heating.

Firstly, the application of microwaves to ceramic sintering is considered to have the following merits over conventional heating techniques[1] :

1) The internal heating may turn out to be more economical than conventional heating;

2) Reduced cracking and thermal stress - due to the heat in microwave processing being generated inside the component while in a conventional furnace the heat is provided from the outside;

3) Reduced contamination from walls of the containment vessel;

4) Leads to increased properties of strength and hardness due to a more rapid heating rate that minimizes the possibility of segregation and impurity concentration in the grain boundaries.

Secondly, the application of microwaves to the synthesis of inorganic powders is considered to have the following benefits:

1) Rapid heating and quick cooling makes it possible to maintain the stable phases and states between the elevated and ambient temperatures, thus obtaining some metastable phases;

2) Selective absorption of microwave energy by different phases makes internal localisation possible to obtain graded fine particles.

3) A soft substance absorbs the energy more quickly than the hard ceramic; it is therefore easy to coat a thin film on the particles and dry it so that it sticks on the surface strongly.

4) Enhanced diffusion causes impurities to be removed resulting in a purer crystal phase.

The application of microwave technology to the joining of ceramics and metals has the advantage of heating the ceramic side to a higher temperature than the metal side resulting in a shortened joining time.

Our focus will be on the heating selectivity of microwaves, and we expect to obtain some special metastable phases or structures by using microwave processing.

2. Some factors of microwave processing to materials

According to the transparent ratio of their energies throughout, most materials could be classified into one of the following three kinds [2]:

1. Good conductors such as most metals that deflect the microwaves back perfectly and can be used as guides and shields;

2. Insulators such as glass, mica and some polymers that allow the microwave rays to transmit through it without any loss of energy - these are also called microwave transparent materials.

3. Dielectric substances such as water and aliphatics through which most of the microwaves pass with a large amount of energy loss. The lost energy might be converted to thermal energy to cause a heating effect. The amount of lost energy depends on the dielectric constant and tan δ (loss tangent) of materials. Most ceramic materials belong to this group. Microwaves passed through these may be coupled with microwaves with a frequency of 10^{12} - 10^{15} Hz resulting in a polar molecular or polarized lattice with some charged ions and space charge. But the details of the heating and coupling mechanisms are not clear.

The heating efficiency of microwaves to inorganic materials would be affected by a lot of factors such as:

- Electrical conductivity of materials
- Dielectric constant and loss tangent and their dependence on temperature
- Kind of coupling species with microwave
- Moisture of materials
- Heat starting temperature
- Density of the materials
- Point defects in crystal grains and grain size
- Interface in materials
- Thermal conductivity and thermal capacity of materials.

If two kinds of particles with different microwave absorption efficiencies were to be neighboured side by side, a temperature difference would result between the two particles. We call this phenomenon *Selectivity of Microwave Interaction* in material, or selective heating of microwaves. This means that some crystal may be sensible to microwave coupling and others may be insensible. The different sensibilities of materials to microwave interaction is expected to be used to design the microstructure of ceramic materials.

TiC was considered to be more sensible than ZrC because TiC has a higher dielectric constant (ε) and a higher loss tangent (tan δ). The original object of this report was to investigate the difference of microwave interaction between the compounds of titanium and zirconium.

3.   Synthesis of (Ti, Zr)C solid solution and phase separation

3.1   Preparation of carbide solid solution

According to the current knowledge about the phase diagram of TiC and ZrC as shown in Figure 1[3], the TiC and ZrC would form a non-limited solid solution only over 2000°C. While cooling down to ambient temperature, this solid solution would separate into two limited solutions. This means that it is difficult to synthesize the

(Ti,Zr)C solid solution. We found a simple way to prepare a nearly perfect solid solution with composition of $(Ti_{0.5}Zr_{0.5})C$ by carbonisation of the oxides.

The synthesis method of the (TiZr)C carbide solution is to use the co-precipitated $ZrTiO_4$ oxide compound mixed with carbon black as start materials and heat the mixture powder to over 1800°C for a few hours. In order to obtain the solid solution of (TiZr)C, the fired powder must be cooled down quickly to room temperature. The product was identified by X-ray diffraction to be nearly a complete solid solution with composition of (Ti0.5Zr0.5)C as shown in Figure 2a.

3.2 Phase separation by annealing and their structures

The solid solution was thermal-treated by two heating facilities - a conventional furnace (graphite heating) and a microwave furnace - to compare the difference between the heat treatment effects.

Figure 3 depicts SEM photographs of microstructures in the specimen annealed in the conventional furnace at 1200°C. It shows two phases, one with a bright-white colour and another with a grey colour. The morphology of these two phases showed a net-work like relationship. The composition analysis by EDAX means showed that the two phases were primary solutions of TiC and ZrC. The grey phase was TiCss that contained 75 - 95 % of TiC and 25 - 5 % ZrC. And the bright phase was ZrCss that contained 75 - 95 % ZrC and 25 - 5 % TiC.

Figure 4 depicts the microwave annealed specimen with a unique microstructure. The morphology under SEM has striated and modulated patterns. This kind of pattern is similar to a typical pattern observed in spinodal decomposition materials[5][6]. The compositions of the two striated phases were tending more to elemental TiC and ZrC than that of conventional annealed specimens.

By comparing the X-ray diffraction peaks of Figures 2b and 2c with 2a, one can easily find the evidence of phase separation after annealing. These peaks also indicated that microwave annealing is more efficient than the conventional annealing to generate the spinodal decomposition because the distance between the peak positions of $(111)_{ZrC}$ and $(111)_{TiC}$ crystal faces becomes far greater than by conventional annealing.

The reason for the different microstructures could be the response to microwave coupling with materials and microwave enhancing effects due to ionic diffusion. Some non-thermal effects of microwaves should be taken into account. It is believed that by changing the conditions of material synthesis and microwave annealing, many unique patterns of the phases separated from (Ti, Zr)C solution might be generated as observed in other spinodal decomposition materials, such as perthite, stinglets, strings, rods, beads, fractured beads, interlocking, and interpenetrating, some of which may be useful in mechanical and electrical properties.

These network-like structures are considered to possibly increase the bonding strength of ceramic grain boundaries. And the modulated structures obtained by microwave processing have an advantage of decomposing micro-sized particles finer into nano-

sized particles. Figure 5 are HRTEM photographs of the interface structure between the two separated phases. From Figure 5a, the interface of TiC and ZrC shared the lattices of each other without a clear boundary. Figure 5b indicated the same twin character of diffraction pattern inside TiC.

4. Conclusions

1) The full solid solution of $(Ti_{0.5}Zr_{0.5})C$ was synthesized by the carbonisation of the co-precipitated compound $ZrTiO_4$ mixed in carbon black at over 1800°C .

2) The solid solutions decomposed into two elemental limited solid solution phases of TiCss and ZrCss after annealing it between 1200°C.

3) Microwave annealing separated the solid solution into two phases with striated and modulated pattern. But conventional annealing separated the solution into two phases with network-like patterns.

4) Microwave annealing separated the solution more completely in composition than conventional annealing. The reason for this was considered to be the enhancing mechanism of microwave to ionic diffusions and microwave coupling with the materials.

These experimental results have given a hint that micro-sized ceramic particles could be changed into nano-sized particles by spinodal decomposition in microwave annealing.

References

[1] Quian Fengsheng, Microwave Heating Technology and Their Application (Chinese), Eds, Heilongjiang Press, pp 49-69 (1985).

[2] Nakanishi and Banto, Inorganic Fine Materials Chemistry, Eds, Sankyo Press (Japanese) pp 95 (1986).

[3] H. Holeck, Material Selection for Hard coatings, *J. Vac. Sci. Technol.* A4 (6)2661 - 2669 (1986).

[4] M. A. Janney and H. D. Kimrey, Diffusion - controlled process in microwave fired oxide ceramics, *Microwave Processing of Materials*, Vol. 124, cds: W. H. Sutton, M, H, Brooks and I. J. Chabinsky, pp 215-227 (1988).

[5] M. Suel and D. Andelman, Domain shapes and pattern: The phenomenology of modulated phases, *Science*, 267(27), pp 476-483 (1995).

[6] T. Sakuma, Y. Yoshizawa and H. Sato, The modulated structures formed by isothermal aging in ZrO2 - 5.2mol% Y2O3 alloy, *J. Mater. Sci*, 20, 1085-1092 (1985).

List of figures (available from the authors):

FAILURE OF DELAMINATED CARBON/EPOXY COMPOSITE BEAMS UNDER CYCLIC COMPRESSION

J.M. Lifshitz and D. Gildin
Material Mechanics Laboratory
Faculty of Mechanical Engineering
Technion - Israel Institute of Technology
Haifa, 32000, ISRAEL

INTRODUCTION

Transverse impact loading of laminated fiber reinforced composites is an important issue that has been studied extensively [1]. The result of such an impact is often some damage in the form of delamination, matrix cracking and fiber fracture. The delamination may impair the load-carrying capacity of the laminate, mainly when it is loaded in compression [2-4]. Local buckling of sub-laminates may take place before global buckling, followed by a reduction in the buckling load of the remaining undamaged laminate.

Under compressive cyclic loading, the problem of predicting fatigue life is magnified by the presence of delaminations. In addition to the initial delamination, caused by impact, interlaminar stresses between adjacent layers at free edges lead to new delaminations [5-7], which are more likely to grow near the top and bottom surfaces than in the interior [8]. Our experimental results show that indeed, the process of failure starts at an early stage of the fatigue life, by buckling of sub-laminates at the external surface of the specimen.

The structure of such sub-laminates is unsymmetric and inplane load is coupled with transverse bending. As a result, out-of-plane deflections begin simultaneously with application of the compressive load and 'one wonders whether it is even possibly to have a classical, bifurcation buckling problem for such plates' [Leissa, 9]. The conditions required for the unsymmetric plate to remain flat are investigated in [9] and it is demonstrated that buckling can occur provided edge moments (or transverse forces) are present at the boundaries. Lagace et al [10] calculated 'pseudo' buckling loads of unsymmetric laminate using a Rayleigh-Ritz assumed modes energy methods and concluded that the mechanical couplings reduce the buckling load significantly.

The purpose of this presentation is to show two aspects of an experimental study, conducted with graphite/epoxy laminated beams under compressive cyclic loading. The first is the effect that an initial delamination crack has on the fatigue life of the composite beam. The second is to follow the sequence of events that lead to catastrophic failure of the beam.

EXPERIMENTAL SETUP

Compressive cyclic tests were conducted on composite beams made of AS4/3502 graphite/epoxy, with stacking sequence of $[(45/90/-45/0)_6]_s$. The beams, 100 mm long, 8 mm wide and 6.4 mm thick, were cut from panels, manufactured by IAI (Israel Aviation Industries, Ltd). About half of the specimens contained artificial delaminations, located at different distances from the free surface.

All the tests were photographed continuously by two video cameras; one was focused on the specimen's side and the other on the MTS counter. The specimen's side that faced the camera was painted white, so that any delamination that developed during the cyclic loading showed on the video. The gage length between the end tabs was 30 mm.

A total of 65 specimenst were tested in compression-compression using a 10-Hz sine

291

wave loading function with a load ratio R=10. The cyclic load levels of the virgin specimens were 70%, 75%, 80% and 85% of the static compressive strength (580 MPa). Those of the specimens that contained initial delamination were 70%, 75%, and 80% of the original static compressive strength.

To determine the effect of an initial delamination crack on the performance of laminated beams, a well defined 'realistic' delamination crack was generated, by subjecting virgin specimens to three point bending, with a span of 30 mm [4]. Using this method, the crack tip was sharp and the problem of a resin rich edge was eliminated. To obtain some distribution of delamination location, a sharp groove was marked along each specimen at different distances from the center line prior to bending. When the groove was more than 10 layers away from the external faces of the specimen, the delamination normally took place at the location of the groove and extended along half of the specimen's length. The locations of the initial delaminations in this study, measured by the ply number from the external surface of the laminate, is shown in Fig. 1.

BUCKLING OF AN UNSYMMETRIC LAMINATED BEAM

The initial delamination over half of the specimen's length turns the original symmetric specimen into two unsymmetric sections. Our purpose is to calculate the buckling load of a single unsymmetric laminated beam, as a function of the number of layers. Consider an unsymmetric beam of length ℓ and width b, composed of n plies, each of thickness t, with some boundary conditions. The plane of the plies is x,y where x is the longitudinal direction of the beam. The beam is subjected to axial compressive force (per unit width) N. When dealing with unsymmetric laminated plates, the inplane force and moment resultants are related to the midplane strains and curvatures in the usual form,

$$\begin{Bmatrix} N \\ M \end{Bmatrix} = \begin{bmatrix} A & B \\ B & D \end{bmatrix} \begin{Bmatrix} \varepsilon^0 \\ \kappa \end{Bmatrix} \tag{1}$$

For beams, the following simplifying assumptions can be made:

(a) the transverse displacement is a function only of x, $w=w(x)$.
(b) only N_x does not vanish, whereas $N_y=N_{xy}=0$.
(c) M_y and M_{xy} are small and therefore disregarded.

When these assumptions are used in eq. (1), one can write four equations,

$$N_x = A_{11}\varepsilon_x^0 + A_{12}\varepsilon_y^0 + A_{16}\gamma_{xy}^0 - B_{11}w'' \tag{2}$$

$$0 = A_{21}\varepsilon_x^0 + A_{22}\varepsilon_y^0 + A_{26}\gamma_{xy}^0 - B_{21}w'' \tag{3}$$

$$0 = A_{61}\varepsilon_x^0 + A_{62}\varepsilon_y^0 + A_{66}\gamma_{xy}^0 - B_{61}w'' \tag{4}$$

$$M_x = B_{11}\varepsilon_x^0 + B_{12}\varepsilon_y^0 + B_{16}\gamma_{xy}^0 - D_{11}w'' \tag{5}$$

Eqs. (3) (4) are used to express ε_y^0 and γ_{xy}^0 as functions of ε_x^0 and w" ($=d^2w/dx^2$). The results are substituted in eqs. (2) and (5). Finally, N_x and M_x are substituted in the equation of equilibrium (6),

$$M_x'' + N_x w'' = 0 \tag{6}$$

and the result is

$$Rw'''' + N_x w'' = 0 \qquad (7)$$

where R is a function of the laminate constants A_{ij}, B_{ij} and D_{11}. When the laminate is symmetric, $R=-D_{11}$ and eq. (7) is reduced to the simple expression

$$D_{11} w'''' + N w'' = 0 \qquad (8)$$

where N is the magnitude of the compression load ($N_x=-N$).

The buckling load is given by

$$N_{cr} = k\pi^2 R / \ell^2 \qquad (9)$$

where the value of k depends on the boundary conditions: k=1 for simple supports, and k=4 for fixed (movable) ends.

RESULTS AND DISCUSSION

Our interest is to determine the average stress ($\sigma_{xx}(1)$) acting on the sub-laminate of the test specimen when the sub-laminate buckles, and the total average stress (σ_{xx}) on the entire specimen at that time. It turns out that when the number of plies in a sub-laminate is a multiplication of four (the number of plies in the basic unit) with an integer, the two stresses are equal ($\sigma_{xx}(1)=\sigma_{xx}$). In all other cases the difference is very small. Results for $\sigma_{xx}(1)$, normalized with respect to the compressive strength (580 MPa), of 18 mm long sub-laminates, with simply supported ends, are shown in Fig. 2(a). We see that a sub-laminate of , say, 12 plies should buckle during the first loading cycle at a normalized load of 0.7. This, however , does not happen, since the actual boundary conditions are closer to fixed ends than to pinned. Sub-laminates at the surface that contain up to 7 plies, are expected to buckle at the first cycle. Unfortunately, we did not succeed in producing delaminations very close to the surface.When some plies are degraded by the cyclic load, their stiffness change and their contribution to resisting buckling diminishes. The result for a beam with degraded $\pm 45^0$ plies is shown in Fig. 2(b).
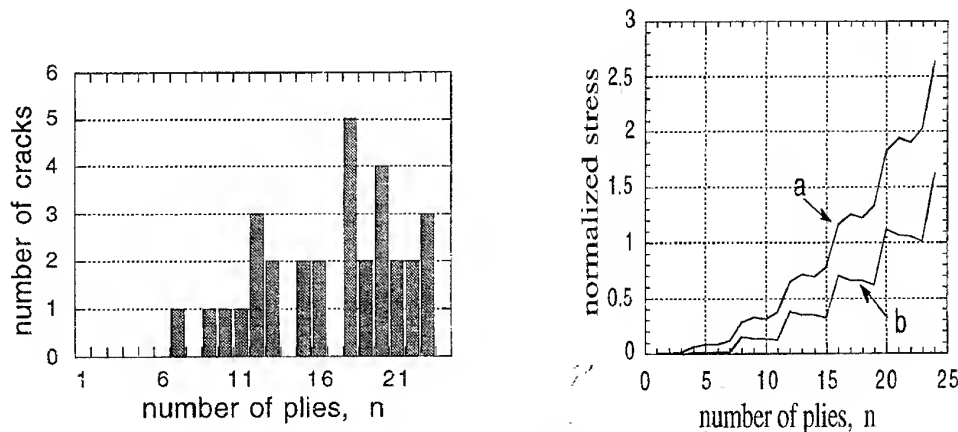
Fig.1 Distribution of initial delaminations.   Fig. 2 Normalized stress at (a) virgin and (b) degraded, sub-laminate buckling.

Some aspects of the failure process are shown in Fig. 3 for three specimens (#12, #34 and #32) with an initial delamination and in Fig. 4 for two virgin specimens (#69 and #55). Specimen #32, that was loaded to 80% of the static strength, had an initial delamination between layers 10 and 11. Up to 7082 cycles there was no visible damage in

#12
70%

295125   313122   313239   319663   319664   319712   319713

#34
75%

11100   11348   11578   16140   16142   17965   17966

19461   19462   19476   19477

#32
80%

7082   7083   7090   7091
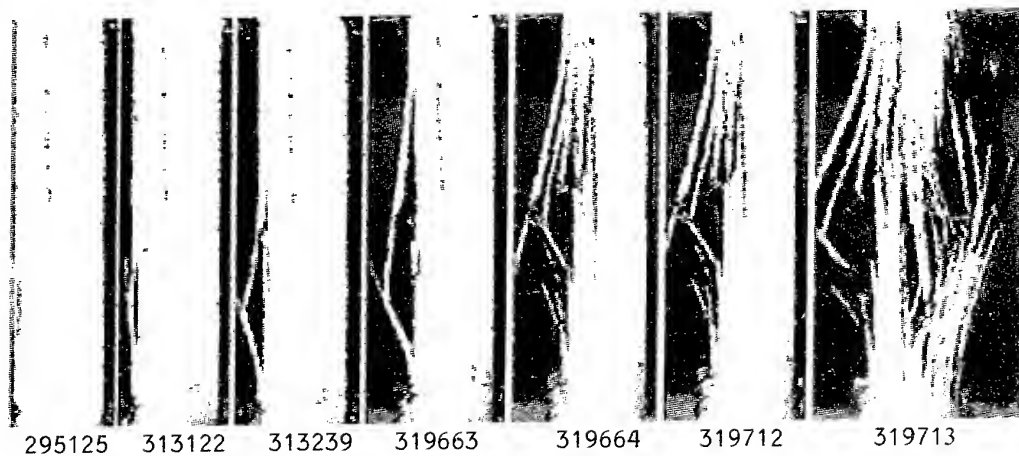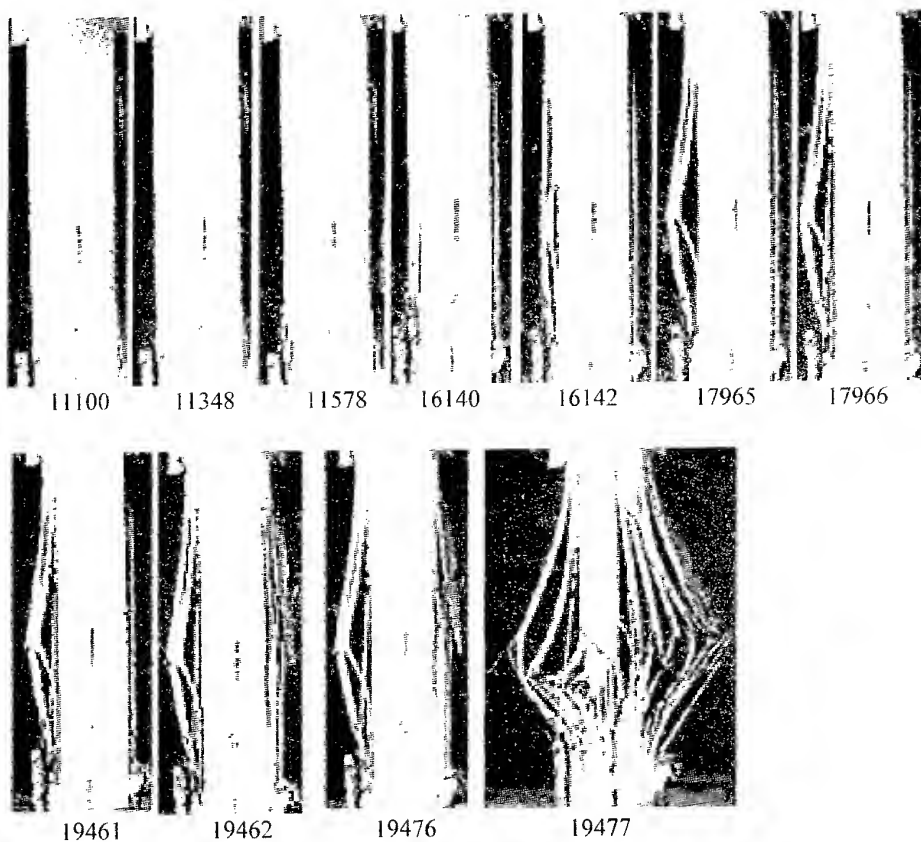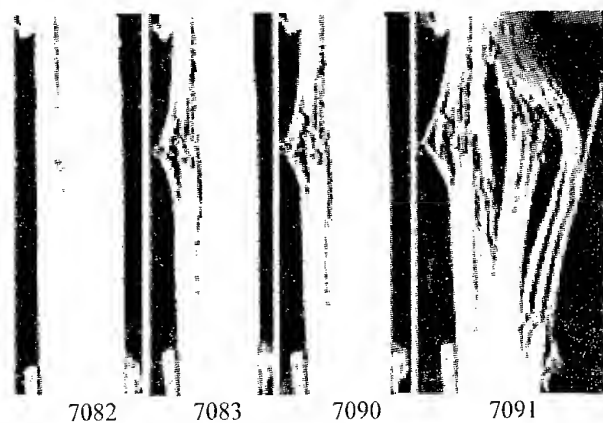
Fig. 3. Fracture process of 3 beams with initial delamination,
at 3 load levels (70%, 75%, 80% of strength)

294

#69
75%

11406 11407 15847 15848 15849 15850 15851 15853

19930 19931 19967 19968

#55
80%

9802 10513 11647 11710 11883 11884 16222 16223

16507 16508 16585 16586 16587
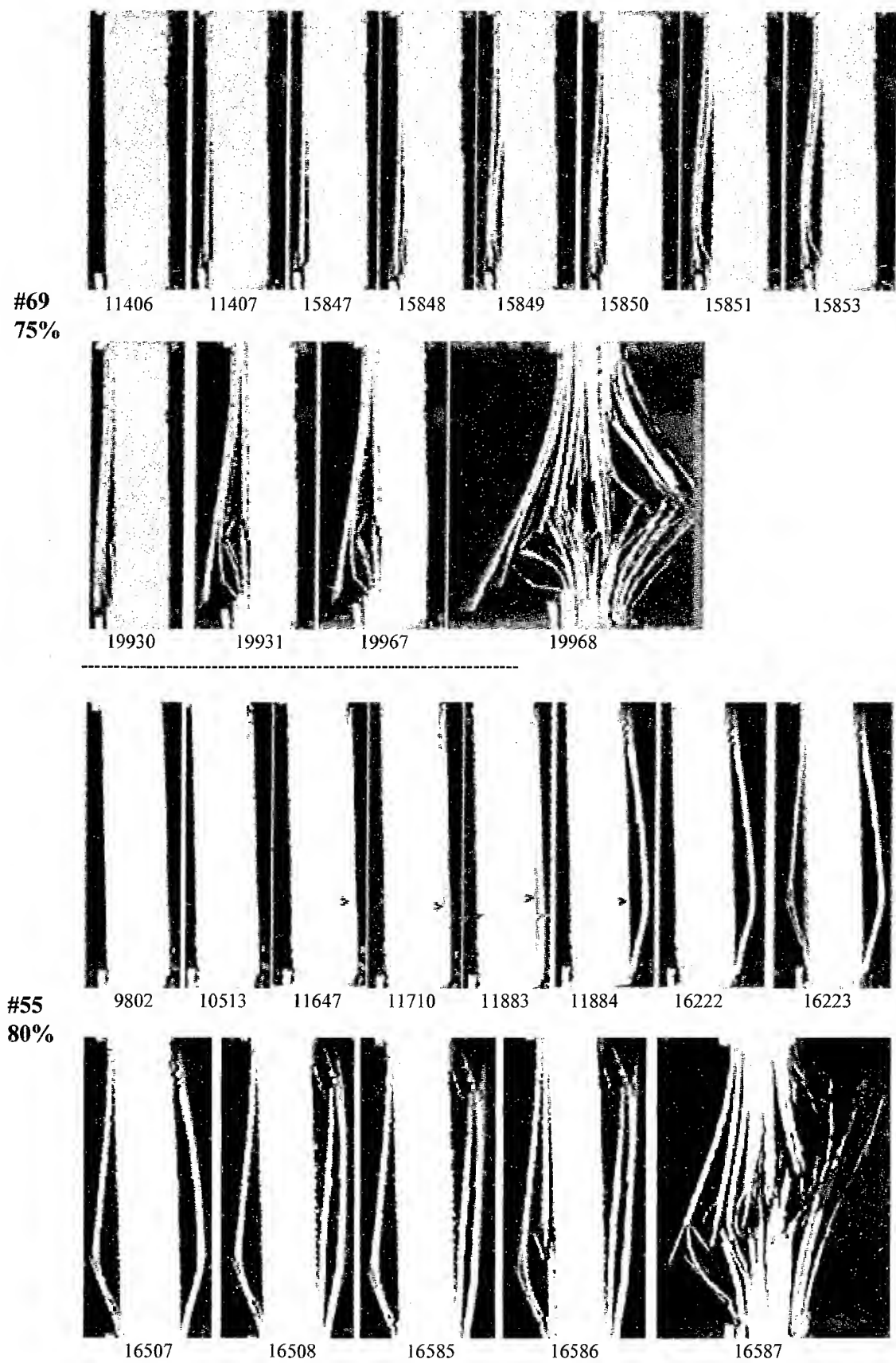
Fig. 4. Fracture process of 2 virgin beams at 2 load levels (75%, 80% of strength)

295

the specimen. The next cycle (7083) caused catastrophie damage to the entire sub-laminate, increasing the average stress on the remaining cross section to the static strength of the specimen, causing failure after a few more cycles. Similar sequence of events took place with specimen #12, that had a delamination between layers 16 and 17. When the sub-laminate fractured at 319664 cycles, the average stress in the remaining cross section reached the static strength and the specimen failed after a small number of additional cycles. The difference between #12 and the previous specimen is that the fracture of the 16 plies sub-laminate was preceded by a development and buckling of a thin sub-laminate, about 4 plies thick, beginning after 295125 cycles. This gradual crack propagation, seen in the first 4 pictures of #12, is not typical to most specimens in our study. More typical is a sudden burst of delamination crack, as seen in #34 (with the initial crack located between layers 21 and 22) between 16140 and 16142 cycles or 19461 and 19462 cycles. Here too the average stress on the remaining cross section was equal to the static strength and it took a couple of additional cycles to cause total fracture.

The pictures in Fig. 4 show the sequence of events leading to total failure of two virgin specimens. First visible fracture of a thin sub-laminate took place in cycle no. 11407. 4440 cycles later a second delamination was developed in jumps, followed by more 'peeling' of thin sub-laminates until total fracture. The next specimen (#55) also failed by generating thin sub-laminates, on both sides of the specimen, all of them in jumps.

S-N curves of the experimental results are difficult to draw, due to the large scattering of results. However, when average values are used for virgin and delaminated specimens separately, both curves show a 'normal' increase of life with decreasing load level. Moreover, the two curves practically coincide.

REFERENCES

1. Abrate, S., "Impact on Laminated Composite Materials",AMR 44, No. 4, pp. 155-190 (1991).
2. Marshal, R.D., Sandorff, D.E. and Lavraitis, K.N., "Buckling of a damaged sub-laminate in an impacted laminate"J. Composite Technology & Research, Vol 10, p.107-113 (1988).
3. Sjoblom, P. and Hwang, H.W., "Compression after impact, the $5000 data point. Paper presented at 34th Int. SAMPE Symposium, Reno, May 1989.
4. Ishai, O. and Shragai, A., "Effect of Impact Loading on Damage and Residual Compressive Strength of CFRP Laminated Beams", J. of Composite Structures, Vol. 14, pp. 319-337 (1990).
5. Rodini, B.T., Jr., and Eisenmann, J.R. in Fibrous Composites in Structural Design, Plenum Press, New York, pp. 441-457 (1980).
6. O'Brien, T.K., "Characterization of Delamination Onset and Growth in a Composite Laminate", in Damage in Composite Materials, ASTM STP 775, pp. 140-167 (1982).
7. Black, N.F. and Stinchcomb, W.W., "Compression Fatigue Damage in Thick, Notched Graphite/Epoxy Laminates", in Long-Term Behavior of Composites, ASTM STP 813, pp. 95-115 (1983).
8. Whitcomb, J.D. and Raju, I.S., "Analysis of Interlaminar Stresses in Thick Composite Laminates with and without Edge Delamination", Delamination and Debonding of Materials, ASTM STP 876, pp69-94 (1985).
9. Leissa, A.W., "Conditions for Laminated Plates to Remain Flat Under Inplane Loading", Composite Structures 6, pp. 261-270 (1986).
10. Lagace,P.A., Jensen, D.W. and Finch, D.C., "Buckling of Unsymmetric Composite Laminates", Composite Structures 5, pp. 101-123 (1986).

BUCKLING OF DELAMINATED PLATES WITH A REPAIRING FASTENER

Chien-Chang Lin and Shou-Hsiung Cheng

Department of Applied Mathematics
National Chung-Hsing University
Taichung, Taiwan 40227, R.O.C.

ABSTRACT

A two-dimensional model using continuous analysis procedures for predicting the buckling load of the delaminated rectangular plates with a repairing fastener is presented in this study. The plate is constructed by two indentical sub-plates to have higher stiffness and strength, but when this bonding plate structure is debonded in some region, its stiffness will be reduced and the plate is easier buckled under compressive load. In order to increase the compressive load-carrying capacity of the layer structure, a fastener or blind rivet is usually applied at the delaminated region. The method presented in the study is straight forward, simple and accurate to determine the buckling load of delaminated plates with a repairing fastener. For illustrative purpose, some numerical examples accounting for the effect of fastener locations on the the local buckling are presented, results show that the present method is effective and useful in engineering applications.

INTRODUCTION

Delamination is one of the most common failure modes in composite structures. For composite laminates during their service life, delaminations may occur due to many reasons such as manufacturing defects, external impact loading. Because delamination can signficantly reduce the compressive strength and stiffness of laminate, repairment of such damaged componets is necessary if replacement deems to be too costly or can be avoid. Although adhesive bonding of composite patches on the surface of the damaged componets is desirable, they are generally successful for thin metallic structures with transverse cracks. For composite structures with delamination flaws under in-plane compressive load, such patching repairment seemingly may not be effective. Since delaminated structure may occur local buckling predominatly in the delaminated region un-

der compressive load, an alternate method, the usage of inserting fasteners or rivets in the delmainated regions appears to be more effective.

Since Chai et al. [1] presented an analytic one-dimensional model for the analysis of delmaination buckling of beam-plate, several investigators have made studies related to this subject such as [2-4]. Bottega and Maewal [5] and Yin [6] studies circular delmaination of a laminate under compression. Chai and Babcock [7], Shivakumar and Witcomb [8], Yin and Jane [9], Jan and Yin [10], Kassapoglou [11], and Yeh and Tan [12] study a laminate with elliptic shape delmination under compressive load. Wang [13] presented a new continuous analysis concept for layered structure with debonds. Wang et al. [14] extend the continuous analyis concept to determine the local buckling load of beam-plates and plates with single and multiple delamination of arbitrary shapes. The method also have been used by Wang and Huang [15] for determining strain energy release rate of skin/stiffener interface delamination. Repair by adhesive bonded patches have been studied by several invetigators. Although fasteners are useful for repairing delaminated structures, analytic studies on this topic are very limited. An analytical study on the buckling of a circular delamination restrained by a fastener or rivet was presented by Huang [16] using the Rayleigh-Ritz method.

In this study, an analytical model for simulating the effect of the fastener on the local buckling load of the delaminated plates is investigated.

FORMULATION

The plate is constructed by two indentical sub-plates of composite laminate to have higher stiffness and strength, but when this bonding plate structure is debonded in some region, its stiffness will be reduced. We consider the embedded crack is located at the center interface of the plate and the debond region is completely seperated. The upper and lower parts are each applied by in-plane loads of the same magnitude. Under compressive load, the plate is easier occured local delamination buckling or thin-film delamination buckling. In order to increase the compressive load-carrying capcity of the layer structure, a fastener or blind rivet is usually applied at the delamination region. A representative compressed plate having an embedded delamination with a repairing fastener is shown in Figure 1 for illustration. The adhesive layer between the upper and lower part of the plate is similar to an elastic foundation and can

be modeled by an infinite set of parallel springs capable of providing normal reaction force $q(x, y)$. In the aspect of dealing with delaminated structure, our method of analysis is based on continuous analysis introduced in [13] analyzing structures with debonds, and used in [14] for buckling analysis of delmainted beams and plates. When the plate structure is debonded at a certain region, the upper part of the plate on this delaminated area is treated as a sub-plate on a continuously distributed support but with fictitiously added transverse forces q_i at a number of discrete points in the delaminated region so as to make the net transverse traction at each of these points to vanish during buckling. According to the model for the continuous analysis procedure mentioned above, we divide the debonded region into N subdivisions and require that the conditions $\int\int_{\Delta A_i} q(x, y)dxdy = q_i$ be satisfied at each subdivision in the delaminated region which lead to N equations for N unknown fictitious forces and the buckling load parameters. The results of the model by using such a continuous analysis method should converge to results of the original structure when the number of discrete points taken in the delaminated region increase to a sufficient number. On the other hand, the effect of a fastener or a rivet on the local buckling behavior of the delaminated plate is mathematically modeled as assuming the upper and lower part of the delaminated plate subjected to a transversely inward concentrated loading, respectively, at the fastener position. The unknown concentrated loading may be determined from the reaction force by the fastener owing to its elongating during local buckling of the delaminated plate. The model using continuous procedure for a compressed plate having a rectangular delamination region with a repairing fastener is shown in Figure 2.

The equilibrium equations governing the buckled state of the plate are as follows:

$$\frac{\partial^2 M_x}{\partial x^2} + 2\frac{\partial^2 M_{xy}}{\partial x\partial y} + \frac{\partial^2 M_y}{\partial y^2} + N_x\frac{\partial^2 w}{\partial x^2} + 2N_{xy}\frac{\partial^2 w}{\partial x\partial y} + N_y\frac{\partial^2 w}{\partial y^2} + q$$

$$+ [\sum_{i=1}^{N} q_i\delta(x - x_i)\delta(y - y_i)] - Q\delta(x - x^f)\delta(y - y^f) = 0 \qquad (1)$$

where (N_x, N_y, N_{xy}), and (M_x, M_y, M_{xy}) are stress resultants and stress couples respectively, $\delta(x - x_i)$, $\delta(y - y_i)$, $\delta(x - x^f)$, and $\delta(y - y^f)$ are the Dirac delta functions, x_i and y_i are the location of the unknown fictitious forces, Q is the transversely concentrated loading imopsed by the fastener during the plate buckling, and x^f and y^f are the locations of the fastener.

For homogeneous orthotropic plate, $B_{ij} = A_{16} = A_{26} = D_{16} = D_{26} = 0$, the constitutive equation are

$$
\left\{
\begin{array}{c}
N_x \\
N_y \\
N_{xy} \\
\hline
M_x \\
M_y \\
M_{xy}
\end{array}
\right\}
=
\left(
\begin{array}{ccc|ccc}
A_{11} & A_{12} & 0 & & & \\
A_{12} & A_{22} & 0 & & 0 & \\
0 & 0 & A_{66} & & & \\
\hline
& & & D_{11} & D_{12} & 0 \\
& 0 & & D_{12} & D_{22} & 0 \\
& & & 0 & 0 & D_{66}
\end{array}
\right)
\left\{
\begin{array}{c}
\epsilon_x \\
\epsilon_y \\
\epsilon_{xy} \\
\hline
\kappa_x \\
\kappa_y \\
\kappa_{xy}
\end{array}
\right\}
\tag{2}
$$

in which

$$
\epsilon_x = \frac{\partial u}{\partial x} \qquad \epsilon_y = \frac{\partial v}{\partial y} \qquad \epsilon_{xy} = \frac{\partial u}{\partial y} + \frac{\partial v}{\partial x}
$$

$$
\kappa_x = -\frac{\partial^2 w}{\partial x^2} \qquad \kappa_y = -\frac{\partial^2 w}{\partial y^2} \qquad \kappa_{xy} = -2\frac{\partial^2 w}{\partial x \partial y}
\tag{3}
$$

where u, v, and w are displacements of the middle-plane of the plate, respectively; A_{ij} is extensional stiffness, D_{ij} is bending stiffness, $(\epsilon_x, \epsilon_y, \epsilon_{xy})$ are inplane strain components, $(\kappa_x, \kappa_y, \kappa_{xy})$ are curvature components. By substituting equations (2) and (3) into equations (1.a)~(1.c), we obtain

$$
D_{11}\frac{\partial^4 w}{\partial x^4} + 2(D_{12} + 2D_{66})\frac{\partial^4 w}{\partial x^2 \partial y^2} + D_{22}\frac{\partial^4 w}{\partial y^4} - N_x\frac{\partial^2 w}{\partial x^2} - 2N_{xy}\frac{\partial^2 w}{\partial x \partial y} - N_y\frac{\partial^2 w}{\partial y^2}
$$

$$
- q - [\sum_{i=1}^{N} q_i \delta(x - x_i)\delta(y - y_i)] + Q\delta(x - x')\delta(y - y') = 0
\tag{4}
$$

We are only interested in the critical buckling loads of the plate under compressive loadings in the present study, i.e.,

$$
N_{xy} = 0, \qquad N_x = -P_x, \qquad N_y = -P_y,
$$

For the adhesive of the composite plate,

$$
q = q(x, y) = -k_f \cdot w, \qquad k_f = \frac{E_a}{h}
\tag{6}
$$

where E_a is Young's modulus and h is thickness of the adhesive.

By substituting equations (5), (6) into equation (4) , we may rewrite the governing equation as follows:

$$D_{11}\frac{\partial^4 w}{\partial x^4} + 2(D_{12} + 2D_{66})\frac{\partial^4 w}{\partial x^2 \partial y^2} + D_{22}\frac{\partial^4 w}{\partial y^4} + P_x\frac{\partial^2 w}{\partial x^2} + P_y\frac{\partial^2 w}{\partial y^2} + k_f w$$

$$+ Q\delta(x - x^J)\delta(y - y^J) = \sum_{i=1}^{N} q_i \delta(x - x_i)\delta(y - y_i) \qquad (7)$$

ANALYTICAL SOLUTION

The boundary conditions for an a by b rectangular plate are

$$at \quad x = 0 \quad and \quad a: \qquad w = 0, \qquad M_x = -D_{11}\frac{\partial^2 w}{\partial x^2} - D_{12}\frac{\partial^2 w}{\partial y^2} = 0 \qquad (8)$$

$$at \quad y = 0 \quad and \quad b: \qquad w = 0, \qquad M_y = -D_{12}\frac{\partial^2 w}{\partial x^2} - D_{22}\frac{\partial^2 w}{\partial y^2} = 0 \qquad (9)$$

We represent the transverse displacement w by double Fourier sine series,

$$w = \sum_{m=1}^{\infty} \sum_{n=1}^{\infty} W_{mn} \sin \alpha_m x \sin \beta_n y \qquad (10)$$

where $\alpha_m = m\pi/a$ and $\beta_n = n\pi/b$. The general solution (10) satisfies the simply supported boundary conditions listed in equations (8) and (9). We also expand the Dirac Delta functions into appropriate sine series,

$$\delta(x - x^J)\delta(y - y^J) = \sum_{m=1}^{\infty} \sum_{n=1}^{\infty} D_{mn} \sin \alpha_m x \sin \beta_n y \qquad (11)$$

$$\delta(x - x_i)\delta(y - y_i) = \sum_{m=1}^{\infty} \sum_{n=1}^{\infty} E_{mn} \sin \alpha_m x \sin \beta_n y \qquad (12)$$

where

$$D_{mn} = \frac{4}{ab} \sin \alpha_m x_r \sin \beta_n y_r$$

$$E_{mn} = \frac{4}{ab} \sin \alpha_m x_i \sin \beta_n y_i$$

Substituting equations (10), (11), and (12) into equation (7), the Fourier coefficients W_{mn} can then be obtained as follows:

$$W_{mn} = \frac{1}{\lambda_{mn}} \frac{4b^2}{D_{22}R} \left(\sum_{i=1}^{N} q_i \sin \alpha_m x_i \sin \beta_n y_i - Q \sin \alpha_m x^f \sin \beta_n y^f \right) \quad (13)$$

where

$$\lambda_{mn} = \frac{D_{11}}{D_{22}} m^4 \pi^4 R^4 + \frac{2(D_{12} + 2D_{66})}{D_{22}} m^2 n^2 \pi^4 \frac{1}{R^2} + n^4 \pi^4 - \bar{P}_x m^2 \pi^2 \frac{1}{R^2} - \bar{P}_y n^2 \pi^2 + \bar{k}_f$$

with

$$R = \frac{a}{b}, \qquad \bar{P}_x = \frac{P_x b^2}{D_{22}}, \qquad \bar{P}_y = \frac{P_y b^2}{D_{22}}, \qquad \bar{k}_f = \frac{k_f b^4}{D_{22}}$$

The fastener will be elongated w during local buckling of the delaminated plate. In the other words, if we assume the diameter of the fastener hole is small enough compared with the delamination size, the fastener will impose an transversely concentrated inward loading Q on the sub-plate in order to defend the deformation of the sub-plate during local buckling. The unknown concentrated load Q can be determined by considering the additional condition

$$at \quad x = x^f \quad and \quad y = y^f : \qquad w = \frac{QL^f}{2E^f A^f} \quad (14)$$

where L^f is the length, E^f is Young's modulus, and A^f is the cross section area of the fastener. By substituting equation (14) into equation (10), we obtain

$$Q = \frac{\displaystyle\sum_{i=1}^{N} \xi_i q_i}{\Delta} \quad (15)$$

where

$$\xi_i = \sum_{m=1}^{\infty} \sum_{n=1}^{\infty} \frac{1}{\lambda_{mn}} \sin \alpha_m x_i \sin \beta_n y_i \sin \alpha_m x_f \sin \beta_n y_f$$

$$\Delta = \frac{D_{22} L^f R}{8 E^f A^f b^2} - \sum_{m=1}^{\infty} \sum_{n=1}^{\infty} \frac{1}{\lambda_{mn}} \sin^2 \alpha_m x^f \sin^2 \beta_n y^f$$

By substituting equation (15) into equation (13), we obtain

302

$$W_{mn} = \frac{1}{\lambda_{mn}} \frac{4a^2 R}{D_{22}} \left[\sum_{i=1}^{N} (\sin \alpha_m x_i \sin \beta_n y_i - \frac{\xi_i}{\Delta} \sin \alpha_m x^J \sin \beta_n y^J) q_i \right] \quad (16)$$

and the alternate condition for maintaining net zero traction at the delaminated regions is

$$\int \int_{\Delta A_j} k_f w(x,y) dx dy = q_j \quad (17)$$

where ΔA_j is the area of the subdivision in the delaminated region. Equation (17) may be approximated for small enough ΔA_j by

$$k_f w(x_j, y_j) \Delta A_j = q_j \quad (18)$$

In order to satisfy the net zero traction condition at each subdivision over the delaminated region, we arrive at the following equation by substituting equation (10) in conjunction with equation (16) into equation (18):

$$\sum_{i=1}^{N} \{ \sum_{m=1}^{\infty} \sum_{n=1}^{\infty} \frac{\bar{K}}{\lambda_{mn}} [(\sin \alpha_m x_i \sin \beta_n y_i - \frac{\xi_i}{\Delta} \sin \alpha_m x^J \sin \beta_n y^J)$$

$$\sin \alpha_m x_j \sin \beta_n y_j] - \delta_{ij} \} q_i = 0, \quad \bar{K} = \frac{4k_f b^2 \Delta A_j}{D_{22} R}, \quad j = 1, \ldots, N \quad (19)$$

However, for the case without fastener, equation (19) becomes

$$\sum_{i=1}^{N} \left[\sum_{m=1}^{\infty} \sum_{n=1}^{\infty} \frac{\bar{K}}{\lambda_{mn}} (\sin \alpha_m x_i \sin \beta_n y_i \sin \alpha_m x_j \sin \beta_n y_j - \delta_{ij}) \right] q_i = 0 \quad (20)$$

Equation (19) can be represents in matrix form as follows:

$$[A]\{q\} = 0 \quad (21)$$

For non-trivial solution, the critical load can be determined by requiring the determinant of the coefficient matrix of equation (21) to vanish.

NUMERICAL RESULTS

303

The plate in all numerical examples are square homogeneous orthotropic composite laminate under uniform uniaxial compression, in which each laminae having material properties as follows:

$$D_{11}/D_{22} = 10 \quad and \quad (D_{12} + 2D_{66})/D_{22} = 1$$

While the computer program is prepared for any spring constant $\bar{k}_f$, results for $\bar{k}_f/\pi^4 = 10$ have been generated in all numerical examples. For checking the validation of the present method, we firstly consider a plate having a central square delamination repaired by a fastener at the center of delamination region as shown in Figure 3(for c=d=0). As expected, it can be seen from Table 1 that the buckling loads increase as the fastener regidity $E^f A^f/L^f$ increases and as the delamination size $(a_d = b_d)$ decreases. Obviously, the buckling loads not only decreases to a constant value(which corresponding to the case of plate without fastener) with fastener having very low rigidity but also increases to a constant value with fastener having high rigidity($\geq 10^2$). This fact shows that the present analysis is effective. Results show that the fastener with rigidity $E^f A^f/L^f = 10^2$ is reasonably considered to be rigid and to be used in the following examples. To explore the effect of fastener locations on the buckling loads, we consider two examples for illustration.

Example 1: Consider a square plate having a central square delamination with a fixed size delamination($a_d/a = b_d/b = 0.3$) as shown in Figure 3. Buckling loads corresponding various fastener locations are shown in Figure 4. Results reveal that the effect of fastener locations on the buckling loads is signficant and fastenering at the center of delamination region is the most signficant one.

Example 2: Consider a square plate having a central square delamination with various size(as shown in Figure 3). Buckling loads corresponding to the plates repaired with fastener varying along the line $y = b/2$(i.e., c=0) and the line $x = a/2$(i.e., d=0) are illustrated in Figure (5.a) and Figure (5.b), respectively. Results not only show that the effect of fastener locations on the delamination size is signficant but also exhibits that the effect on the buckling loads by fastener locations is more signficant with varying along $y = b/2$ than that with varying along $x = a/2$. Results given in Figure 5 reveal that the optimum locations of fastener are on the centerline $y = b/2$ ranging from d=-0.4 to 0.4. Moreover, it can be noted that the nondimensional buckling loads for the delaminated plate with a central location(c=0,d=0) fastener increase 95% (for $a_d/a = 0.1$), 104% (for $a_d/a = 0.2$), 118% (for $a_d/a = 0.3$), 134% (for

$a_d/a = 0.4$), 146% (for $a_d/a = 0.5$), respectively. This reflects the fact that the effect of repairing fastener is more signficant when the delamination size becomes larger.

CONCLUDING REMARKS

A two-dimensional model for determining the buckling load of a delaminated plates repaired by a fastener has been proposed. According to the results obtained in this study , we have following concluding remarks :

1. The method presented in the study is simple and effective.
2. The effect of fastener location on the delamination buckling loads is signficant and fastenering at the center of the delamination region is the most signficant one.
3. The effect of repairing fastener on the delamination buckling load is more signficant when the delamination size is larger.
4. The model should be useful in engineering application.

ACKNOWLEDGMENT

REFERENCES

1. Chai, H., Babcock, C.D., and Knauss, W.G., "One Dimensional Modeling of Failure in Laminated Plates by Delaminations Buckling," International Journal of Solids and Structures, Vol.17, pp.1069-1083 (1981).
2. Simitses, G.J., Sallam, S., and Yin, W.L., "Effect of Delamination of Axially Loaded Homogenuous Laminated Plates," AIAA Journal, Vol.23, No.9, pp.1437-1444 (1985).
3. Yin, W.L., Sallam, S., and Simitses, G.J., "Ultimate Axial Load Capacity of a Delaminated Beam-Plate," AIAA Journal, Vol.24, No.1,pp.123-128 (1986).
4. Kardomateas, G.A., and Schmueser, D.W., "Buckling and Postbuckling of Delaminated Composites under Compressive Loads Including Transverse Shear Effects," AIAA Journal, Vol.26, No.3, pp.337-342 (1988).
5. Bottega, W.J., and Maewal, A., "Delamination Buckling and Growth in Laminates," ASME Journal of Applied Mechanics, Vol.50, pp.184-189

(1983).

6. Yin, W.L., "Axisymmetric Buckling and Growth of a Circular Delamination in a Compressed Laminate," International Journal of Solids and Structures, Vol.21, pp.503-514 (1985).

7. Chai, H., and Babcock, C.D., "Two-Dimensional Modeling of Compressive Failure in Delaminated Laminates," Journal of Composite Materials, Vol.19, pp.67-98 (1985).

8. Shivakumar, K.N., and Whitcomb, J.D., "Buckling of a Sublaminate in a Quasi-Isotropic Composite Laminate," Journal of Composite Materials, Vol.19, pp.2-18 (1985).

9. Yin, W.L., and Jane, K.C., "Refined Buckling and Postbuckling Analysis of Two-Dimensional Delamination-I. Analysis and Validation, International Journal of Solids and Structures, Vol.29 No.5, pp.591-610 (1992).

10. Jane, K.C., and Yin, W.L., "Refined Buckling and Postbuckling Analysis of Two-Dimensional Delamination-II. Results for anisotropic laminates and conclusion", International Journal of Solids and Structures, Vol.29 No.5, pp.6111-639 (1992).

11. Kassapoglou, C., "Buckling, Post-Buckling and Failure of Elliptical Delaminations in Laminates under Compression," Composite Structures, Vol.9, pp.139-159 (1988).

12. Yen, M.K., and Tan, C.M., "Buckling of Elliptically Delaminated Composite Plates," Journal of Composite Materials, Vol.28, pp.36-52 (1994).

13. Wang, J.T.S., "Continuous Analysis of Layered Structures with Debonds," Chinese Journal of Mechanics, Vol.9, No.2, pp.81-90. (1993)

14. Wang, J.T.S., Cheng, S.H., and Lin, C.C., "Local Buckling of Delaminated Beams and Plates Using Continuous Analysis ," Journal of Composite Materials, Vol. 29, No. 10, pp.1374-1402 (1995).

15. Wang, J.T.S., and Huang, J.T., "Skin/stiffener Interface Delamination Using Continuous Analysis," Composites Structures. Vol. 30, pp.319-328 (1995).

16. Huang, J.Y., "Analysis of a Sublaminate in Compressively Load Laminate under a Transverse Loading at its center," Composite Structures, Vol. 28, pp. 315-322 (1994).

Table 1. Buckling loads for a square delaminated plate repaired by a fastener with various rigidity (for c=d=0)

$\dfrac{E^f A^f}{L^f}$	$\dfrac{P_x b^2}{D_{22} \pi^2}$		
	$a_d/a = 0.1$	$a_d/a = 0.2$	$a_d/a = 0.3$
10^3	43.99	43.82	43.18
10^2	43.99	43.82	43.18
5×10^1	43.99	43.82	43.02
2.5×10^1	37.20	36.51	35.28
10^1	29.74	28.81	27.33
1	23.41	22.30	20.66
10^{-1}	22.69	21.56	19.89
10^{-2}	22.61	21.48	19.81
10^{-3}	22.60	21.47	19.81
10^{-4}	22.60	21.47	19.81
without fastener	22.60	21.47	19.81
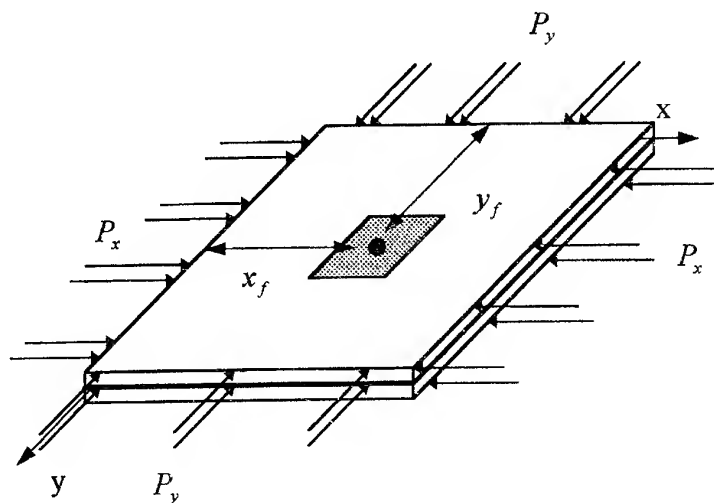
Figure 1. A representative compressed plate having an embedded delamination with a repairing fastener
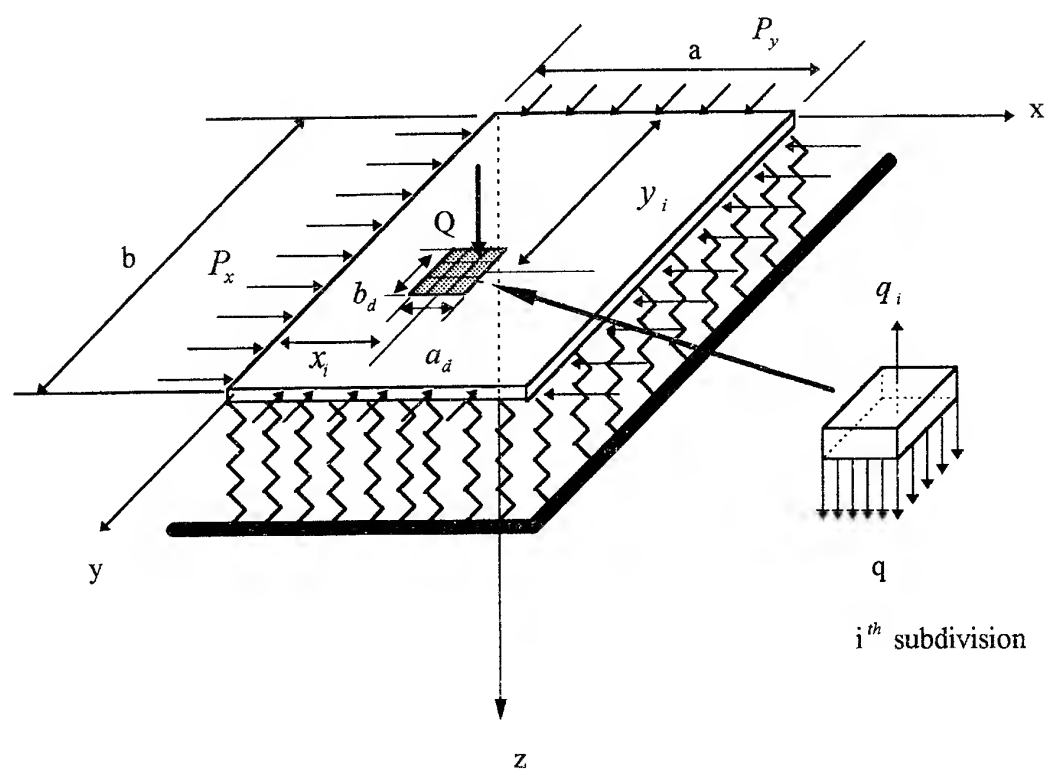
Figure 2. The model of delaminted plates with a repairing fastener for continuous analysis
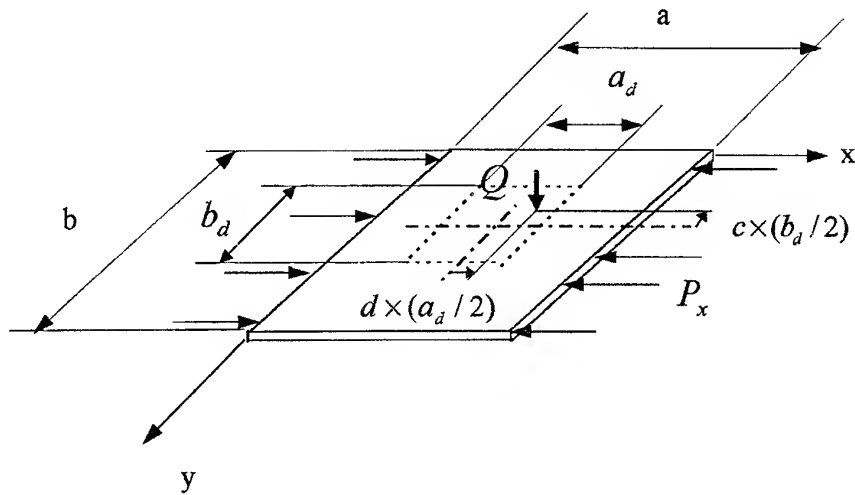
Figure 3. A simply-supported square plate having a central delamination with different locations of fastener under uniform uniaxial compression
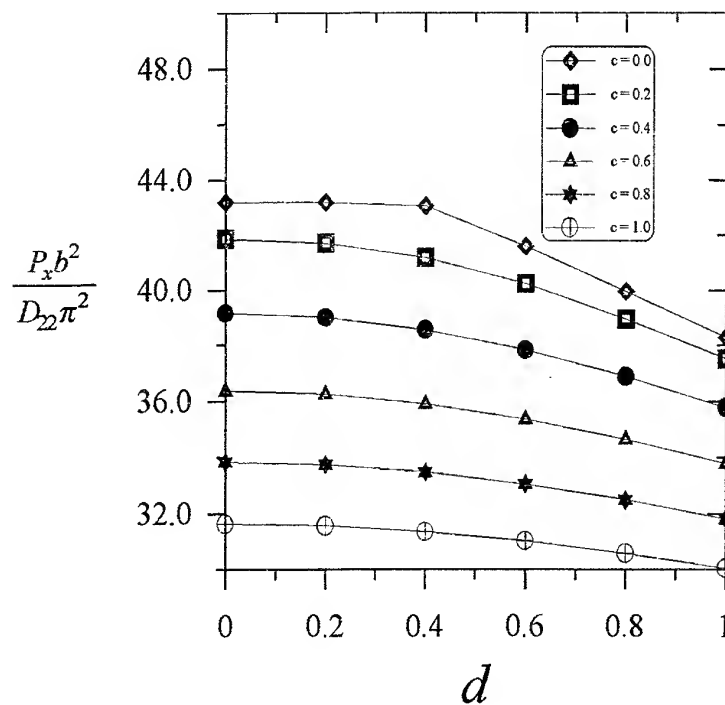
Figure 4. Effect on buckling loads by fastener locations for a square plate having a central delamination with fixed size
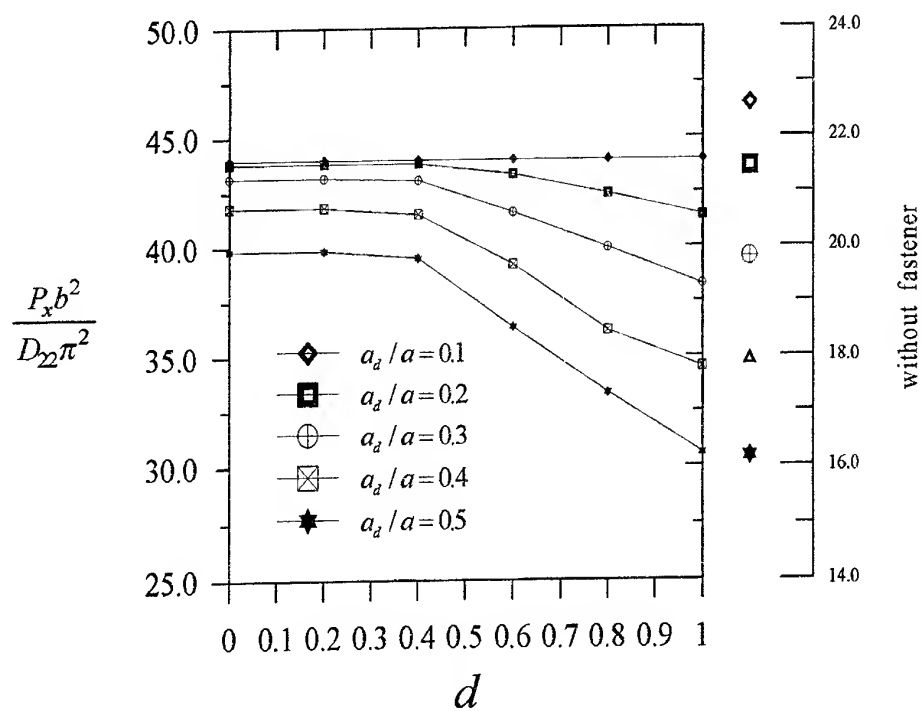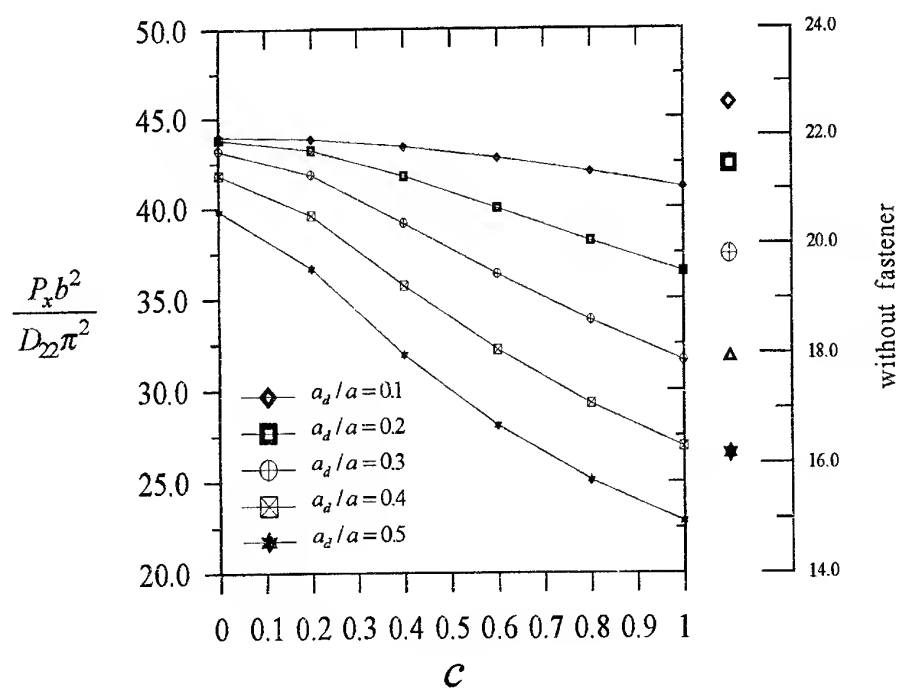
309

Figure 4. Effect on buckling loads by fastener locations for a square plate
having a central delamination with various size

NEAR TIP DAMAGE AND SUBCRITICAL CRACK GROWTH
IN A PARTICULATE COMPOSITE MATERIAL

C.T. Liu
Phillips Laboratory
OL-AC PL/RKS
10 E. Saturn Blvd.
Edwards AFB CA 93524-7680
USA

INTRODUCTION

Generally speaking, composite materials may be defined as a combination of two or more materials into a polyphase material wherein each of the constituents retains its separate properties. In recent years, structural analysis of composite materials has been dominated by fiber reinforced materials and their laminates. It is interesting to note, however, that enormous volumes of particulate composites are used annually. These composites may consist of soft particles in hard matrices, as with a number of metal alloys, or hard particles in soft matrices, as with gaskets, seals, solid propellant, etc. Particulate composite structures may also be subject to failure by fracturing but the processes involved may be complex.

In past years, a considerable amount of work has been done in studying crack growth behavior in highly filled polymeric materials[1-5]. These materials consist of hard particles contained in a soft binder. It is known that the material response of such material depends on the microstructure of the material. The presence of filler particles in the binder will increase the stiffness and the strength of the particulate composites. In addition, experimental data reveal that a material's microstructure at the crack tip can have a significant effect on the local damage near the crack tip and crack growth behavior in the particulate composites. Therefore, to properly understand and characterize fracture, damage characteristics near the crack tip must be determined.

In the present study, the development of microstructural damage and fracture process near the crack tip in a highly filled polymeric material was examined and its effects on crack growth behavior are discussed.

THE EXPERIMENTS

In this study, centrally cracked specimens (Fig. 1) were used to study local damage near the crack tip and crack growth behavior in a particulate composite under constant displacement rate (2.54 mm/min.) at room temperature. The specimens were made of a highly filled polymeric material, containing hard particle in a rubbery matrix. Prior to testing, the specimens were conditioned at the test temperature for an hour and were then tested at the constant displacement rate until the specimen fractured. During the test, photographs, taken at a given time interval, were used to determine local damage and fracture mechanisms near the crack tip as well as crack growth behavior in the material.

RESULTS AND DISCUSSION

It is well known that, on the microscopic scale, a highly filled polymeric material can be considered an inhomogeneous material. When these materials are stretched, the different sizes and distribution of filler particles, the different crosslink density of polymeric chains, and the variation on the bond strength between the particles and the binder can produce highly nonhomogeneous local stress and strength fields. Depending on the magnitude of the local stress and the local strength, damage can be developed in the material, especially near the crack tip region. The damage developed in the material may be in the form

of microvoids or microcracks in the binder or in the form of dewetting between the binder and the filler particle. The growth of the damage in the material may occur as material tearing or as successive nucleation and coalescence of the microcracks. These damage processes are time-dependent and are the main factor responsible for time-sensitivity of the strength degradation as well as the fracture behavior of the material. Therefore, to obtain a better understanding of crack growth behavior, a detailed knowledge of damage mechanisms in the crack tip region is required.

A typical set of photographs showing the crack surface profile during the opening and growth of a crack in the composite material specimen is shown in Figure 2 and a similar sequence for the polyurethane specimen is shown in Figure 3. It is seen in Figure 2 that crack tip blunting occurs both before and after crack growth. Due to the heterogeneous nature of the composite material, the degree of blunting varies with the position of the advancing crack tip. This suggest that the local microstructure near the crack tip plays a significant role in the blunting phenomenon. Since the magnitude of crack tip blunting is closely related to the microstructure of the material, it is expected that different materials' microstructure will produce different degrees of blunting. A comparison of Figures 2 and 3 reveals that the magnitude of blunting at the crack tip in the composite material is significantly larger than in the polyurethane specimen. Although the magnitudes of crack tip blunting are different for the two material, crack growth behavior in the two materials is similar. For the composite material (Fig. 2) during the blunting stage, voids were developed ahead of the crack tip. The crack advanced by coalescing with these voids. When this occurred, the crack tip resharpened temporarily. Thus, the process consisted of a blunt-growth-blunt phenomenon which is highly nonlinear. For the polyurethane specimen (Fig. 3), the near tip behavior was qualitatively the same as in the composite material, but on a much smaller scale. Thus the blunt-growth-blunt phenomenon observed in the composite material specimen may also occur in the polyurethane specimen, but in such small increments that crack growth appears smooth and continuous. Based on these experimental findings, it can be concluded that the most dominant local physical effect of adding particles to the matrix to form a particulate composite appears to be the development of severe blunting and a large damage zone ahead of the crack tip.

It is known that the presence of a crack in a stretched specimen will redistribute the stress in the neighborhood of the crack, especially near the crack tip region. The high stress or strain will undoubtedly lead to a high damage near the crack tip region. Insight into damage development in the neighborhood of the crack tip, especially inside the highly damaged zone or the failure process zone, can be obtained by studying Figure 2. As shown in Figure 2, the failure process zone is always developed ahead of the blunted crack tip. Prior to crack growth, the direction of the developed failure process zone with respect to the original crack plane varies from specimen to specimen. This is believed to be related to the size of the high strain region as well as the local microstructure of the material in that region. For a large magnitude of tip blunting, the size of the highly strained region is also large. Therefore, depending on the local microstructure, the direction of the failure process zone shows a relatively large variation. Experimental results reveal that before crack growth, the failure process zone has developed either above or below or along the crack plane. After crack growth, the successively developed failure process zones at the tip of the propagation crack undulate about the crack plane, resulting in the zig-zag shape of crack growth as shown in Figure 2. It is interesting to note that the crack has a tendency to grow in the average direction which is perpendicular to the applied loading direction. It should be pointed out that in addition to the effect of local microstructure, the change of the stress concentration location as a result of crack tip blunting is also a contributing factor to the variation of failure process zone direction. Experimental data shows that when the crack tip is extensively blunted, the stress concentration location changed from the tip of the sharp crack to the upper and lower corners of the blunted crack. Therefore, the probability of developing a failure process zone near the corners of the blunted crack is considerably increased.

Typical plot crack growth rate versus time is shown in Figure 4. The data in Figure 4 reveal that the crack does not grow in a continuous and smooth manner. It appears that crack growth rate undergoes

irregular fluctuation. In other words, the crack rate growth process consists of a slow-fast-slow phenomenon.

As mentioned earlier, the damage process zone is a time-dependent process and it requires some time to develop the failure process zone ahead of the crack tip. The crack advanced by coalescence of large voids with the main crack tip. As the crack advanced into the failure process zone, a complicated stress redistribution occurs near the crack tip region and the local stresses are transferred in the direction of the tip of the failure process zone. When the tip of the main crack and the tip of the failure process zone coincide, the main crack tip resharpens temporarily. Thus, the crack growth process consists of blunt-growth-blunt and slow-fast-slow phenomena as shown in Figure 4.

CONCLUSIONS

The local damage near the crack tip and the crack growth behavior in a highly filled polymeric material were investigated. Experimental results indicate that the basic mechanism of near tip crack opening and growth involves formation and growth of voids ahead of the crack tip which produce severe blunting. The process of blunt-growth-blunt is repeated and indicates a highly nonlinear process. Experimental data also indicate that the time-dependent damage process is a contributing factor to the time-dependent fracture behavior near the crack tip, and the crack-damage interaction is a contributing factor to the fluctuation of the crack growth behavior.

REFERENCES

1. Beckwith, S.W. and Wang, D.T., "Crack Propagation in Double-Base Propellants", AIAA Paper 78-170, 1978.

2. Liu, C.T., "Variability in Crack Growth in a Composite Material", AIAA Paper 83-1015, 1983.

3. Liu, C.T., "Crack Growth Behavior in a Composite Propellant with Strain Gradients", AIAA Paper 85-0615, 1985.

4. Liu, C.T., "Crack Growth Behavior in a Composite Propellant with Strain Gradients - Part II", *Journal of Spacecraft and Rockets* 27 6, pp. 647-652 (1990).

5. Liu, C.T., "Crack Propagation in a Composite Solid Propellant", *Proc. Society of Experimental, Spring Conf.* Pp. 614-620, 1990.
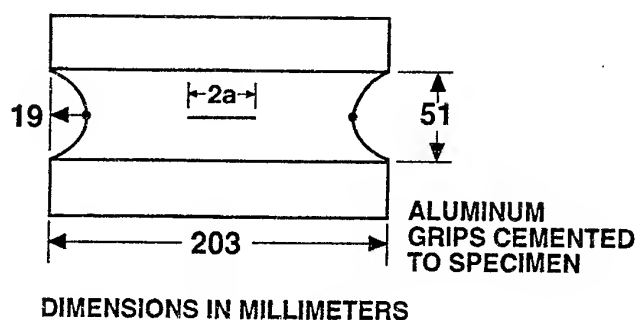
Fig. 1 Specimen geometry

313
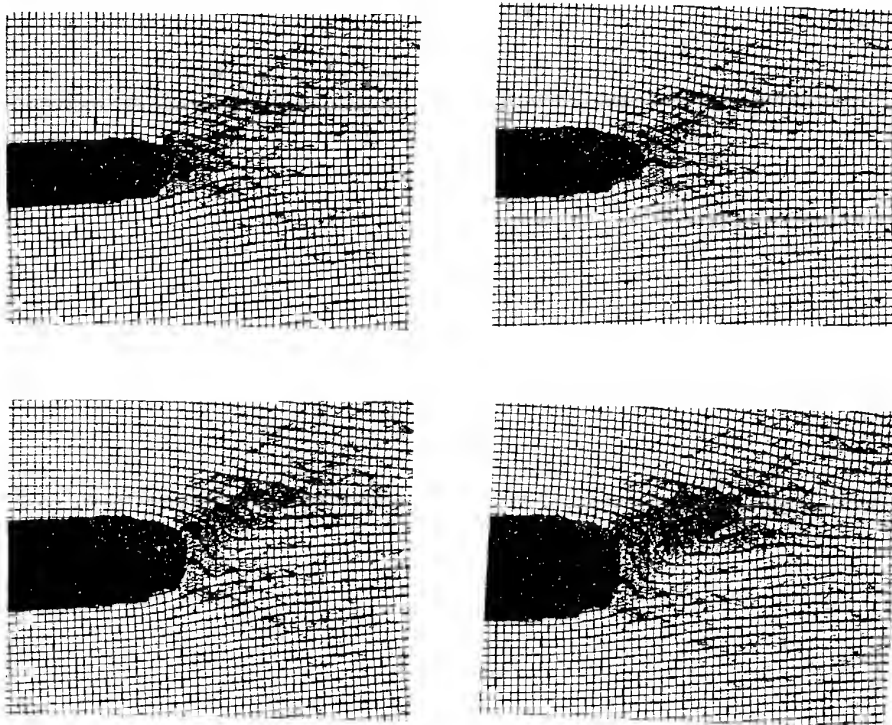
(a) During crack propagation
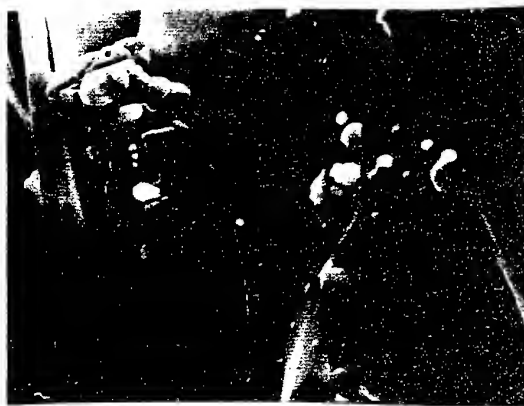
(b) Micrograph (2.25 KX) of the failure process zone

Fig. 2 Crack tip profiles for the particulate composite material.
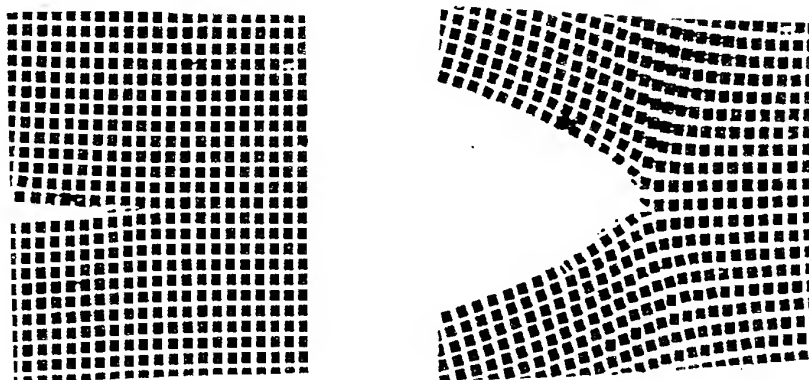
Fig. 3 Crack tip profiles for polyurethane.
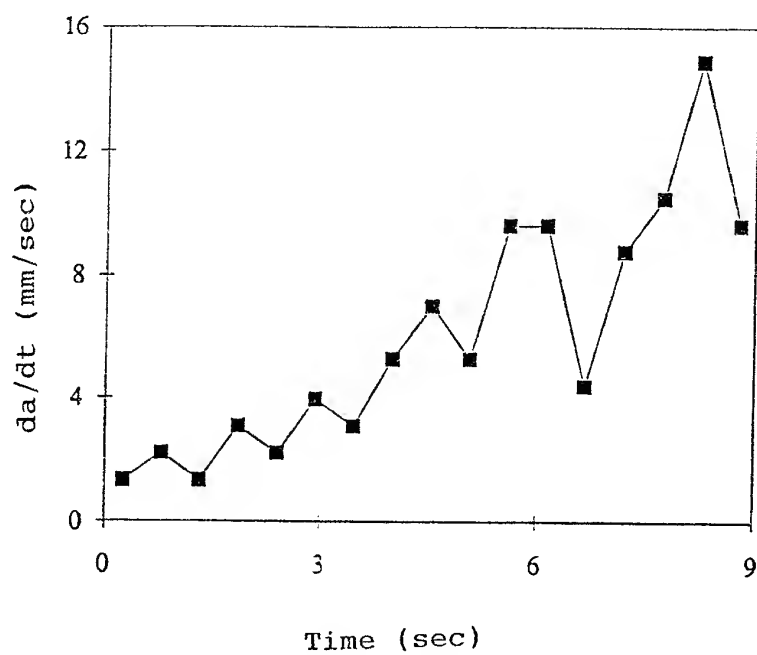
Fig. 4 Crack growth rate as a function of time.

315

A SOLUTION FOR PRODUCTION OF AN INTEGRATED COMPOSITE MULTICOMPONENT

Utimia Madaleno

Materials Technology Dept., Engineering Division

OGMA - Aeronautical Industry of Portugal, S.A.

2615 - ALVERCA - PORTUGAL

ABSTRACT

Over the last years developments within the AirBus program has received a great deal of attention by composites fabrication unit in OGMA-Portugal.

Phenolic carbon fibre prepreg is the base material due to the electrical characteristics, the low smoke and toxic gas generation, as well as low heat release.

Aluminium tools for single parts are originally proposed to be used in autoclave processing. Volume variation in each mould during cure cycle are the biggest limitations to successful production, particularly dimensional parameters and warping.

The aim of the study herein conducted, intended to point the benefits of manufacturing a total new conception of the shelf using a composite mould.

INTRODUCTION

For a number of years aluminium has been the material suitable for advanced applications and a strong candidate for use in tooling and moulds required by the plastics industry.

Fibre reinforced materials are being each time major elements in aerospace structures and still developments are being made, increasing knowledge of their behaviour. Probably less research has been made concerning moulds and manufacturing technology.

Curing of the graphite prepreg on a tool under vacuum and high pressure, requires durability, resistance and surface hardness of the mould.

The non-complexity of the parts being manufactured and the conventional principal associated to sheet metal structure assemble, immediately pointed aluminium as the ideal material to produce simple parts, simplifying the conception of the moulds.

The moulds still in production were conceived six years ago, when the knolowge and background was probably not adequate and yet nor sensible to the basic principle of composites conception - 'manufacture with composite materials is integration of multicomponents by using as less fabrication cycles as possible'.

Machined aluminium moulds were produced to get the shape of the four different parts, assembled by an adhesive [Fig.1]. Different size and volume of each mould, allied to the large thermal capacity of aluminium, created several difficulties to the management of the cure cycle. Nevertheless, the prototypes were obtained by autoclave curing. Each part seemed to be a success. But the problem showed-up during assembling. The tolerances were too tight in the zones adhesively bonded, for the volume expansion of aluminium mass was different for each case. Long parts became longer then expected, and the opposite happened to the larger ones. Rework the moulds showed to be the only way out.

adhesive joint
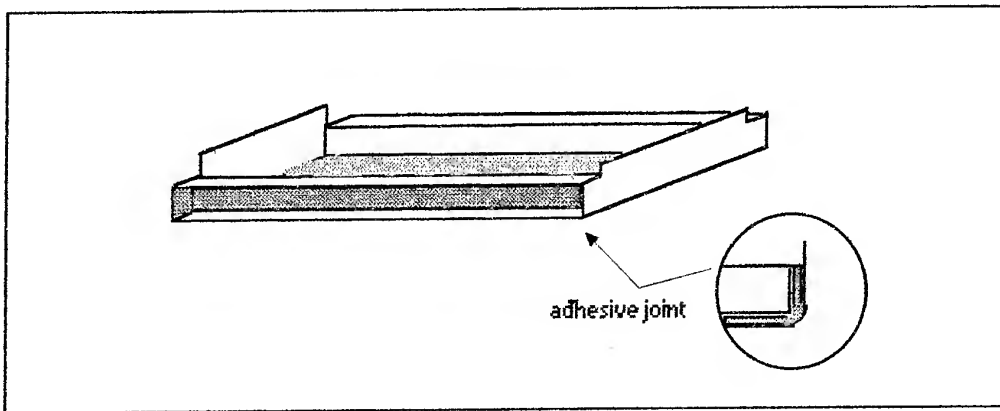
Fig. 1 - Shelf adhesively bonded

From the analysis of the final dimensions of simple parts and mould configuration, some conclusions were important for future industrialisation processes. These are, a) to avoid male and female in complicated shapes, b) different adjoined thickness will better produce a high-integrity composite if moulded on one-sided tooling [Fig.2], c) 90° angles, on thin parts cannot be obtained by using the same angle on the tool [Fig.3], d) large parts, not very thick, with the edges dropped in angles, cannot be moulded in a block of material.
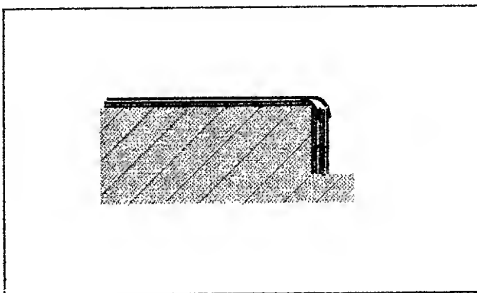
Fig. 2 - Different adjoined thickness
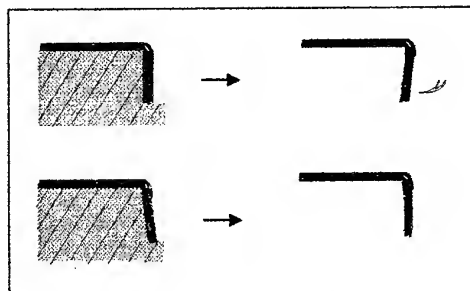
Fig. 3 - Variation of angles on the part

Fig. 4 - Volume reduction of the tool
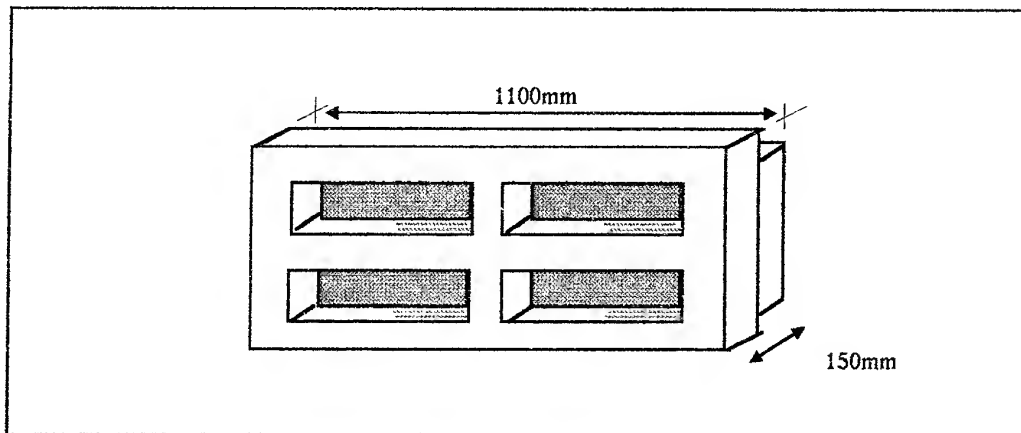
Large and thick aluminium blocks need a volume reduction, to allow thermal expansion of the piece as easily as possible [Fig.4]. This is also a better way to control the temperature on the part, and to reduce autoclave cycle costs.

After the time spent controlling all the parameters, it would be better to think over the reliability/profit of the project. Cure cycle was not 100% controllable; too much work over each part; too many hours to assure the quality of the assembly bonded. In fact, a long/costly production cycle has been put on.

ANALYSIS AND DISCUSSIONS

A NEW TOOL

The project of a new tool is based on the principle that a composite structure can be done directly in one cycle, as long as the parts to be cured are resin-rich.
Three of the parts are co-cured in a tool made by a reinforced carbon/epoxy structure, with the surface smoothly finished by an elastomer. The longerons are made over rubber tooling, with a soft elastomeric face [Fig.5].

These two parts are positioned on the graphite mould, and adjusted by a monolithic shape, to give a better finishing surface to the co-cured system.
Elastomeric tools work by slightly expanding with temperature, which creates pressure on the skin and stringer flanges, thus compacting the laminate. few

Compared with aluminium ones, these respond quicker to temperature changes because of their low thermal expansion(very close to the graphite components), being therefore, easier to control. Besides, the surface quality of the part are extremely good.
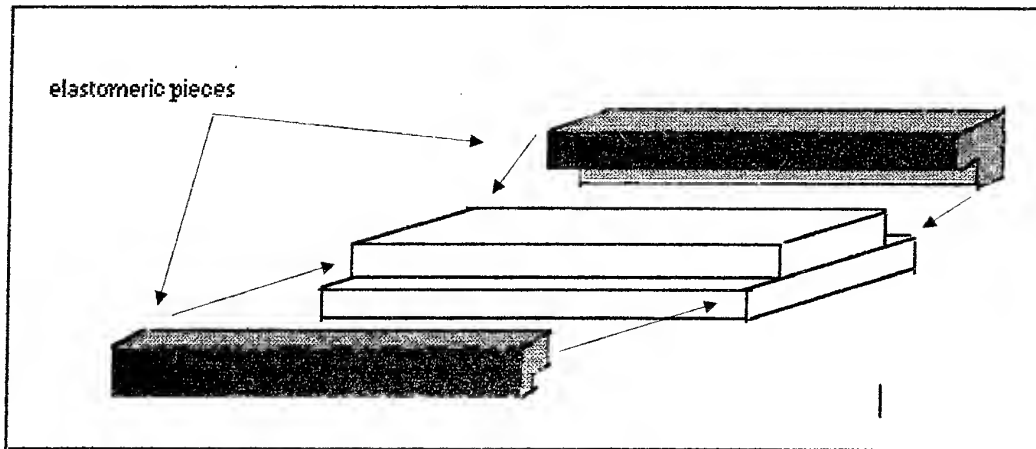
Fig. 5 - The new composite tooling

Some disadvantages also arise by using this type of mould. They are relatively expensive and easily damaged and deteriorated after a limited number of autoclave runs. Nevertheless, good handling and maintenance, as well as surface protection by an adhesive teflon, allows a number of cycles fairly high.

COMPARISON OF SYSTEMS

An attempt is made to compare separate and co-cured structure, in terms of autoclave-hours job, mechanical response, man-working-hours, and costs evaluation.
In general, a co-cured structure has advantages like, a) strength, b) stiffness and c) high dimensional stability and durability. On the contrary, bonds are best kept to a minimum. Additionally, one more production cycle, rises the chances of processing imperfection.
Table 1 summarises some of the disadvantages that represent a discontinuity created by a bonded joint.

Table 1

BONDED STRUCTURE	CO-CURED STRUCTURE
two shot process	one shot process
bigger number of tooling	less number of tooling
more man-hours work	(usually) less man-hours work
additional manufacturing fases	no-additional manufacturing fases
bigger energy costs	lower energy costs
possible high stress concentration	no stress concentration (for the same configuration)
less effective shear load transfer	effective shear load transfer
failures initiated by contamination or degradation	different origin for failures

Overall comparing the two systems, the composite mould has many advantages over the aluminium one. Results of the trial are presented on Chart1.
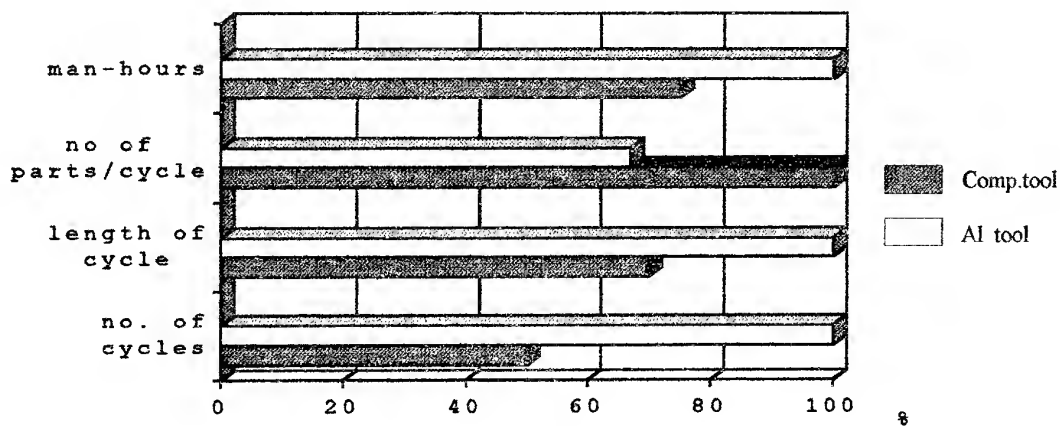
It is clearly concluded that there are no doubt about the benefits under taken with the composite mould. It is likely this choice in near future.

FINAL CONSIDERATIONS

The assumption that an aircraft structure has to be made from many small parts either bonded or mechanically fastened is less considered in newer projects. Nevertheless it is

important to produce reliable and safe flying structures, it is also necessary to profit from the economic and technical benefits that new technologies and materials can bring.

One of the principal advantages of fibrous composites is the consolidation of several parts into a single and larger component. Conception and certification of a composite structure is already costly itself. Prototyping is only a small jump over the industrialisation process, hence, directly associated with the tooling, production parameters and cost. This is the best way to avoid failures due to lack of attention given to the mould.

ACKNOWLOWGEMENTS

RESIN INFUSION CO-CURED PATCH REPAIR

Utimia Madaleno
Materials Technology Dept., Engineering Division
OGMA - Aeronautical Industry of Portugal, S.A.
2615 - ALVERCA - PORTUGAL

ABSTRACT

The increased use of composites in both military and commercial aircraft, causes some problems for the air forces and airlines. This requires development of the repair methods, standardisation of materials and processes. The basic goal is to restore a part's structural integrity with ease of repair, in the shortest time span, at the least cost.
The study herein conducted was to show a method of repair, by resin infusion, that should match the strength and stiffness of the original part, with a low degree of porosity, and high fibre volume content. Trials on processability and feasibility of the infusion technique have been made on laminates representative of typical repair thickness.

INTRODUCTION

Project engineers concerned with structures and materials easily understand that continued and expanded use of composites, critically interferes with development of both structurally adequate and economically practical repair technologies, which must be born in mind during the design phase.
The ability to control all the complex parameters when attempting to perform repairs on field, becomes very limited, and may well force it to have a strength response considerably different from the original fabrication.
The quickest repair method is probably to bolt a patch over the damaged area. This is not new, and it is borrow from conventional sheet metal repair. Bolted repairs bring some advantages over bonded ones, specially in what concerns facility limitations, but do require additional cut-outs structurally undesirable. These are, drilling and associated problems, geometric arrangement of fastener pattern, back-side access, thickness, shape and material of the patch. In general, bolt holes weaken structures and in most cases are not satisfactory.
Bonding a patch is usually more reliable because it produces no regions of increased stress and the only surface preparation required for the repaired part is solvent wipe, drying, sanding and cleaning out of damage. The patch can either be composite or metal, applied by a cure- in- place, with vacuum.

experience, the tendency is to abandon the hard patch bond, by using wet or prepreg lay-up. These are now common repair procedures, highly suitable for field repair. The material are easily storable, the repair performed with portable equipment, and is also the cheapest process. Eventhow, in most of the cases, it is applied only to cosmetic or non structural repairs because all wet techniques have at least de disadvantage of requiring some skill and being affected by high void content when compared with prepreg techniques. Also, these resin systems have low T_g , arising in poor hot/wet properties for the laminate.

Nevertheless, performances of modern resin systems may become a competitive challenge to prepreg materials if reliable simple methods can be successfully developed.

CRITERIA

The first objective of the study is that all the common criteria for repairs must be considered. Among these are a) static strength and stability, b) durability, c) weight and balance, d) aerodynamic smoothness, e) environment, f) operational temperature, g) cost.

The principle adopted for this trial is to keep to a minimum the variety of general repair materials requiring cold storage. Taking into account the limitations of repair activity field, efforts were concentrated on processability and physico-chemical tests, to demonstrate the feasibility of the technique. Here, to form a composite patch in place, instead of a resin film, an adhesive is selected. Whenever possible, the same adhesive can also be used to bond pre-cured composite or metallic plate on damaged structures.

This is related with a technique here-called *co-cured patch by resin infusion*, in which an adhesive film is interleaved between dry fabric plies. The impregnation occurs as the viscosity of the resin decreases along with cure temperature, under a vacuum pressure.

The criteria chosen to validate the process is, a) to adjust process parameters based on impregnation, curing and laminate properties, b) to perform mechanical tests and determine the basic mechanical properties. The results of the second step will be made available in a later stage of the study.

MATERIALS

The materials chosen for this study are, each one, well known on the aeronautical field, and normally considered as references, either for having already been qualified by many companies, or for being specifically applied in repairs of structural parts.

REINFORCEMENTS

The styles of high strength fabric here considered are a) plain weave, and b) semi-unidirectional, 3000 nominal filament count per tow carbon fibre.

The fabrics have commercial references from BROCHIER Textiles.
The plain weave - LIVERTEX G814 (193 g/m^2), and the semi-UD is LIVERTEX G827 (160 g/m^2, 98% carbon in one direction and 2% glass in the transverse one).

MATRIX

As matrix, unsupported adhesive films were selected, taking into account parameters like, low curing temperature (below 120 °C), flow properties for prefect impregnation of the dry fibre, simple and functional storage conditions, and a nominal weight compatible with the one of the fibre ($\cong$ 150 g/m^2).

The adhesives considered are - CIBA BSL 312, HYSOL EA 9682-6, and the American Cyanamid- CYTEC M 1146.

PROCESSING EVALUATION

It is essential that the resin systems evaluated show suitability for the proposed impregnation thecnique, specially when on uncontrolled environments.
The goal is to achieve an acceptable curing at low temperatures, i.e., around 100 °C. The adhesive material must not be too sensitive to extreme shop environment, and its degree of tack has to admit ease of handling in the repair procedure, in the widest range of temperatures as possible.
About the cured in place laminate, it should have good fibre wetting, a low void content, and its fibre volume content as close as possible to 50%, not very different form a typical manufactured laminate.

In the work performed, the first concern was the rheological analysis of each resin system for examination of the viscisity profile as a function of the temperature.
All the three resins showed to behave very close to each other, and even the minimum viscosity, is in any case located between 90 °C and 120 °C. The gel time was also determined by the multifrequency method. These two parameters lead to the conclusion that gelification occurs at the identified temperature level and after a period of time (between 15 to 40 min.) considered enough to allow perfect wettability for fully embedding of the reinforcement.

The viscosity profiles of the three resin systems are plotted in Graph. 1 [4].

To conclude the preliminary study, evaluation of curing and residual enthalpies of the adhesives has been done. Evaluation of the glass transition temperature was also done, for this is a very significant parameter on hot/wet properties of the laminates produced.
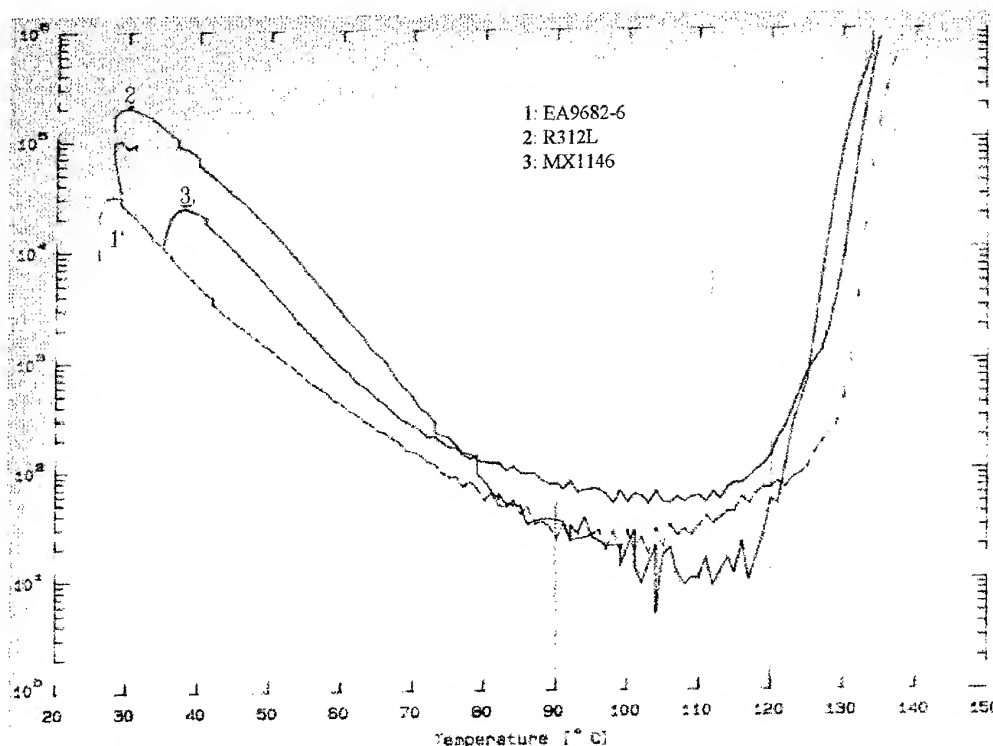
Graph 1 - Viscosity profiles of the resin systems

After some measurements around the minimum viscosity temperatures (see Graph 1), the conclusion was that the curing level for any of the adhesives could be between 95°C and 105°C, for 3 to 5 hours, with no sacrifice of the degree of curing and the corresponding residual properties.

FEASIBILITY

After the physico-chemical tests, shop trials had to be done to demonstrate the feasibility of the resin infusion technique. For that, different configurations were considered to validate the process, by adequate control of the laminates' fibre/resin ratio.

The two reinforcements considered intended to show the possibility of using heavier and lighter fabrics as long as the resin content could be kept from 35 to a maximum of 50%, very close to typical ratio values for tape and fabric prepregs.

For the plain weave, the sequence adopted was the 1:1 interleaving of fabric and adhesive [Fig. 1]. For the semi-UD, each adhesive ply was sided by the reinforcement, meaning the need for fibre to fibre contact [Fig. 2].
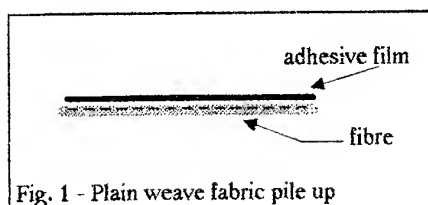
Fig. 1 - Plain weave fabric pile up

This made the manufacture more difficult to process than the one using plain weave. Nevertheless, with a well controlled manufacturing process, both configurations presented good laminates. Care must be taken on the choice of bagging materials, not to pump-out
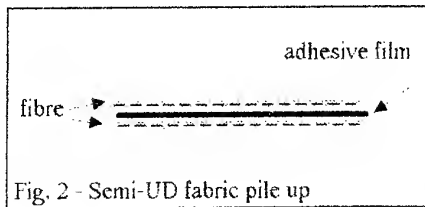
Fig. 2 - Semi-UD fabric pile up

too mush amount of resin, specially when using the UD fabric.

Observation of the samples by micrographic analysis, generally showed sound laminates, in spite of some defects like little porosity and lake of wetting.

Results are demonstrated by micrographic prints of samples related to the considered configurations. Different magnifications of some samples are presented on Fig. 3
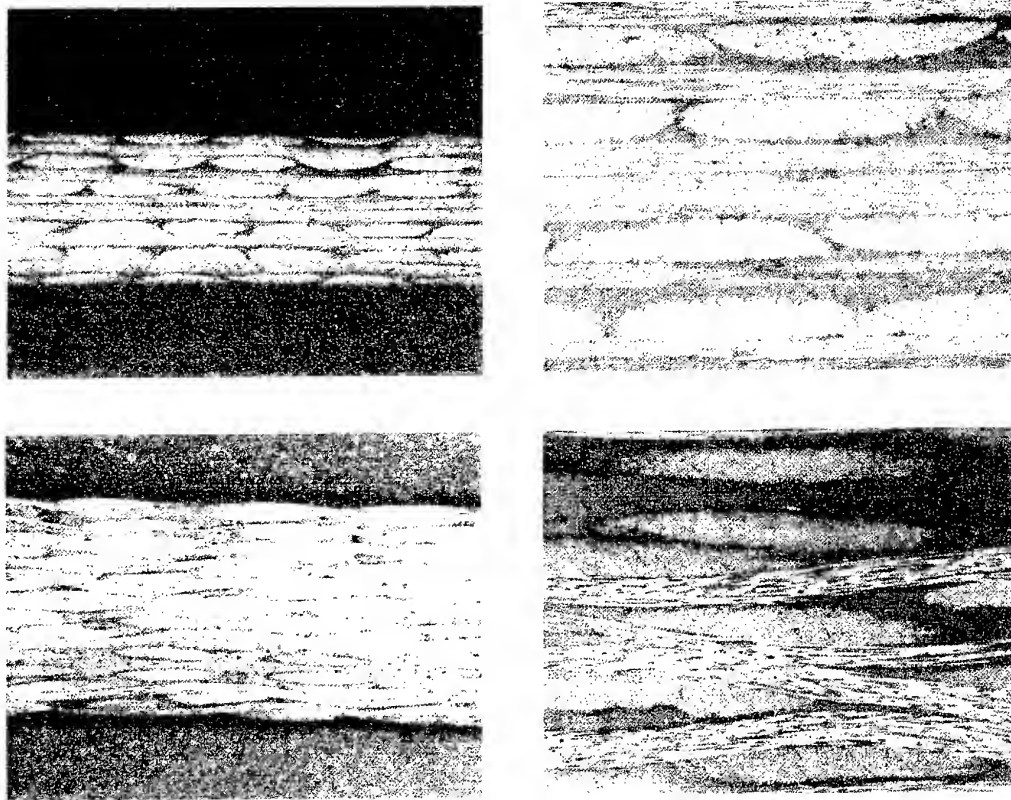
Fig. 3 - Micrographic samples using resin infusion technique

BUILD UP OF A REPAIR

The build up of the repair look about the same when performed on a monolithic structure, or a sandwich one since, apart of the specificity of eventually restoring or removing the core, the skin is usually recovered by bonding together two different materials. Therefore, the reactions at the interface are equally important.

The principle here used is that better advantages are taken from the resin infusion co-cured patch with a pyramidal pile up, i.e., the fibre orientation of repaired and original material, are parallel [Fig. 4].

Fig. 4 - Pyramidal pile up

Previous trials with this type of repair procedure demonstrated that the patch had good strain absorption. Introduction of weight is not critical, and the surface is aerodynamically smooth.

CONCLUSIONS

The results of this study show that in a preliminary analysis of the resin infusion technique, the selected materials and the configurations, where successfully chosen.

Efforts were concentrated on physic-chemical tests and processability. The physico-chemical behaviour of the adhesives evaluated showed to perform according with the requirements established for the infusion technique.

Validation was made using laminates with typical repair thickness, manufactured with two different carbon fibre weave. Visual and micrographic analysis demonstrated sound laminates with low void content and little surface wetting defects.

Previous approaches to this repair procedure confirmed that the general parameters to be considered on repair, are better achieved when infusion co-cured patch is used to restore the integrity of a composite surface. Cost evaluation was also a concern.

Complementary tests are now being performed, specially on mechanical behaviour of the laminates and on its influence over a repaired structure.

Acknolowgements

REFERENCES

[1]Pairaudeau & Simpson "Design Philosophy for Composite Materials"
[2]Graf, Svabonas & Gurtman "Analysis of Structural Composite Materials"(1979)
[3]Hart-Smith,J.L."Joining Fibre Reinforced Plastics"(1986)
[4]Aerospatiale documents(1995)
[5]Hatsu Ishida & J. Koening "Composite Interfaces" (1986)
[6]"Future of Metal Adhesive Bonding in Aircraft Industry and Fokker". EACMT,22nd Annual Meeting (1990)
[7]"Standardisation of Composite Repairs by Evaluation of Resin systems and Repair Techniques". EACMT Meeting (1989)

DAMPING AND WORK OF FRACTURE STUDIES ON TOUGHENED EPOXY COMPOSITES

S.K. Malhotra[1], M. Subramanian[2] and R. Krishnamurthy[3]

1, 2   FRP Research Centre, Indian Institute of Technology, Madras 600 036, India

3   Department of Mechanical Engineering, I.I.T. Madras 600 0 36, India

ABSTRACT

Epoxy matrix composites are increasingly being used for dynamic structural applications in aerospace, automotive and other engineering industry due to their high specific strength and modulus. For dynamic applications, the material should have good damping capacity. Conventional epoxies can be toughened using a synthetic elastomer such as Caboxyl Terminated Butadiene Acrylonitrile (CTBN). Unidirectional glass fibre composite specimens were made of varying fibre content (v_f) with unmodified and modified epoxy matrics. Results of Dynamic Mechanical Analysis (DMA) and Work of Fracture (WoF) tests conducted on these specimens are presented.

INTRODUCTION

Epoxy matrix composites are increasingly being used for dynamic structural applications in aerospace, automotive and other engineering industry. This is mainly due to their high specific strength and modulus. For dynamic applications, the material should have good damping capacity. Epoxy matrices can be toughened using a synthetic elastomer-carboxyl Terminated Butadiene Acrylonitrile (CTBN). The studies of various researchers (1-5) reveal that the tougher matrices promote various energy dissipation mechanisms such as crack tip plastic deformation, shear yielding, crazing, etc. The use of CTBN toughened epoxy for composites increases its damping significantly (6).

In the present paper, damping and toughness characteristics of glass fibre composites having varying fibre content (v_f) prepared using CTBN modified epoxy is studied.

EXPERIMENTAL WORK

a) Specimen Preparation:

The epoxy resin used was Hindustan Ciba-Geigy-LY556 with hardener Piperidine (a cyclo-aliphatic amine). The synthetic elastomer used for modifying epoxy was CTBN. First an adduct of epoxy/CTBN is prepared by mixing epoxy resin (62.5%), CTBN (37.25%) and triphenylphosphine (o.25%). The mixture is heated to 120 deg. C for 1/2 hour. The hardener (Piperidine) is added to preheated adduct and mixed thoroughly. Unidirectional glass fibre/epoxy composite specimens of varying V_f are prepared using this epoxy mix.

b) Dynamic Mechanical Analysis (DMA):

DMA tests are conducted using Rheovibron Dynamic Viscoelastometer. The samples 0.5 mm thick are tested in longitudinal flexural mode of vibration. A heating rate of 3 deg C/min and a frequency of 35 Hz is used. Loss factor (tan δ) is directly read.

c) Work of Fracture (WoF) measurement:

Work of fracture gives the total energy required to cause the complete failure of the sample. The rectangular bar specimen (as per ASTM-D790-86) are subjected to 3-point bending tests until the complete failure. The work of fracture is calculated by dividing the area under the load/displacement curve by the cross-sectional area of the sample.

RESULTS AND DISCUSSION

The glass fibre composite samples for DMA studies were made with epoxy LY556/9% piperidine hardener. Fig.1 shows the damping characteristics (tan δ Vs temperature) of unmodified matrix composites for varying V_f Similar curves for glass fibre composite samples prepared with modified matrix containing 15% CTBN are given in Fig.2.

330

It is observed that tanδ (in temperature range of 30-80 deg.C) reduces as v_f increases. This is due to reduction in the volume of matrix available for damping. But reduction in tan δ is not appreciable upto a v_f of 25%. This is due to the fact that interfaces between fibre and matrix contribute to damping by promoting slip between fibre and the matrix. At higher v_f (40-50%), reduction in tan δ is much higher. This is due to the fact that large number of interfaces contributing to damping cannot compensate for loss in damping due to reduction in volume of matrix.

It can be observed from the region corresponding to steep rise of damping close to Tg (glass transition temperature) that Tg increases with the addition of fibres. This increase in Tg is associated with a corresponding reduction in tan δ peak values. This is due to the fact that interface effect on damping is insignificant in this region.

Fig.3 gives the variation of tan δ (at a constant temperature of 50 deg.C) with the addition of elastomer for samples having varying v_f. It is observed that samples with high v_f give lower tanδ value and there is very little effect of addition of CTBN on tan δ. For all composites, maximum value of tan δ is obtained for about 15% CTBN content.

Fig.4 shows the % increase in WoF with CTBN content in the matrix for varying fibre content. It is observed that at lower v_f the addition of CTBN is more effective in increasing the WoF and its effect decreases with increase in v_f. This can be due to the suppression of toughening mechanisms such as matrix shear yielding, cracktip plastic deformation, etc., with the addition of glass fibres.

The addition of CTBN to the composites increases fibre pull-out (a composite toughening mechanism) by the formation of modified interfaces. The effectiveness of CTBN in improving toughness of composites decrease with the increase in v_f. The toughness characteristics of composites is matrix dominated at low v_f and fibre dominated at high v_f.

331

CONCLUSIONS

Following conclusions are derived from the present study:

a) Energy dissipation in long fibre composites, predominantly occurs at the fibre/matrix interface. The interfaces of the composites is modified to enhance the damping. These modified interface increase the friction between matrix and fibre, which results in higher damping. Damping of composite (tan δ) is improved by introducing a low modulus interface between the fibre and matrix.

b) The loss factor (tan δ) increases as long as rubber particles (CTBN) form a fine dispersion in the matrix. Once elastomeric particles form an inhomogeneous blend with epoxy, loss factor tends to decrease

Both tan δ and WoF are maximum for 15% CTBN content.

c) DMA study of composites suggests that addition of fibres increases Tg of the matrix and reduces tan δ peak value.

d) The composites with CTBN modified matrix show comparatively higher damping than the unmodified matrix. Modified matrix composites do not show appreciable reduction in tan δ with addition of fibres upto 25% v_f. The damping capacity of composites is very much reduced for v_f of 40-50%.

e) At high v_f, addition of CTBN results in very little increase in tan δ. High v_f causes considerable increase in Tg, which is due to higher stiffness of the composite and thermal lag effect.

REFERENCES

1) E.H.Rowe,etal, Modern Plastics, Aug. 1970, pp.110-117
2) S.C. Kunz,etal, Polymer, V-23,1982, pp.1897-1906
3) A.J. Kinlock,etal, J.Mater.Sci., V-21, 1986, pp.105-1056
4) S. Bandyopadhyay, Mater, Sci.Eng., A125, 1990, pp.157-184
5) R.A. Pearson and A.F.Yee, J.Mater, Sci. V-24, 1989m pp.2571-2580
6) Sudon Hong,eal, Tough Composite Materials-Recent developments, Noyes pubn., New Jersey, USA (1983), PP.262-269.

Fig. 1

Fig. 2

333
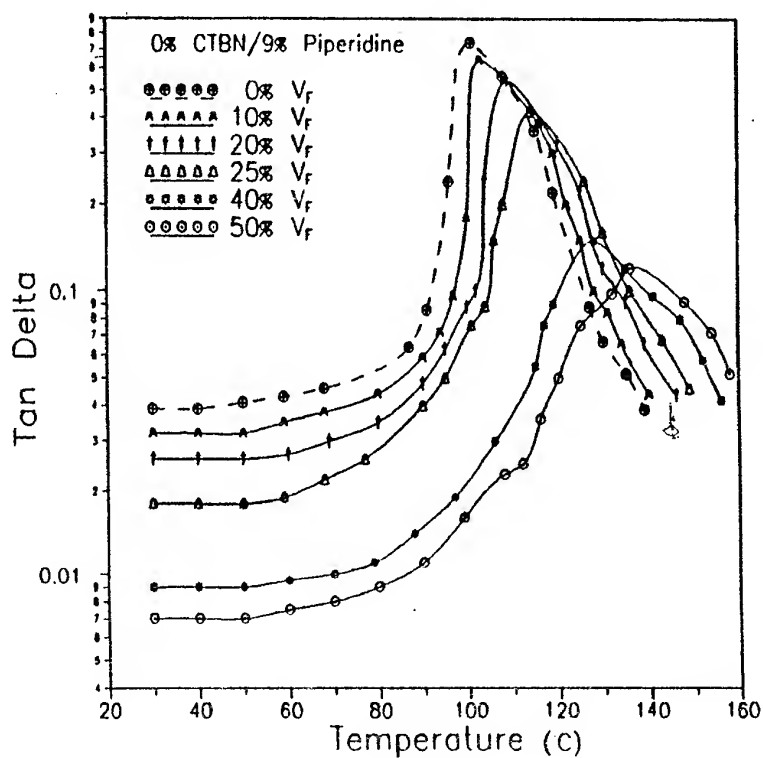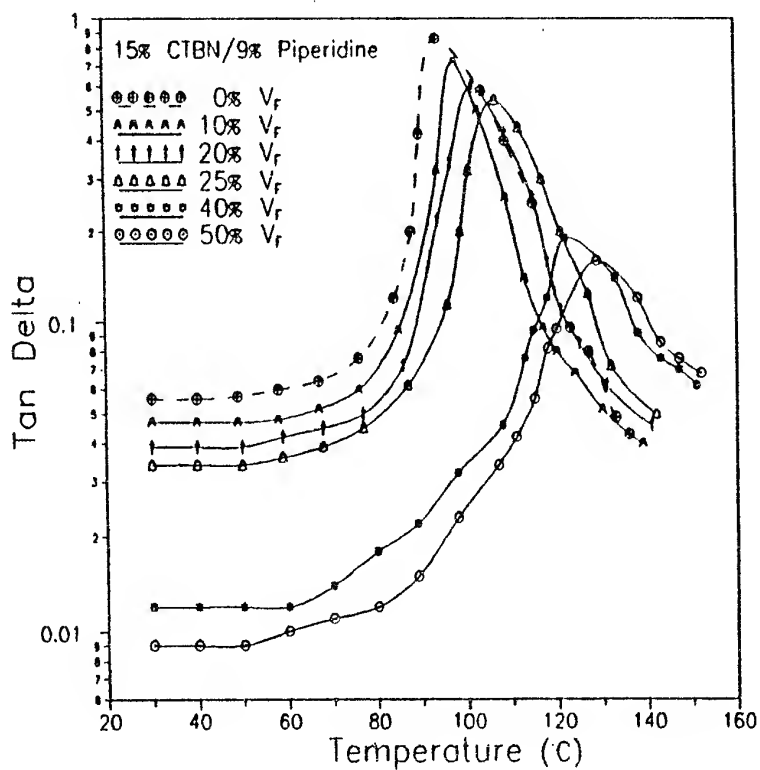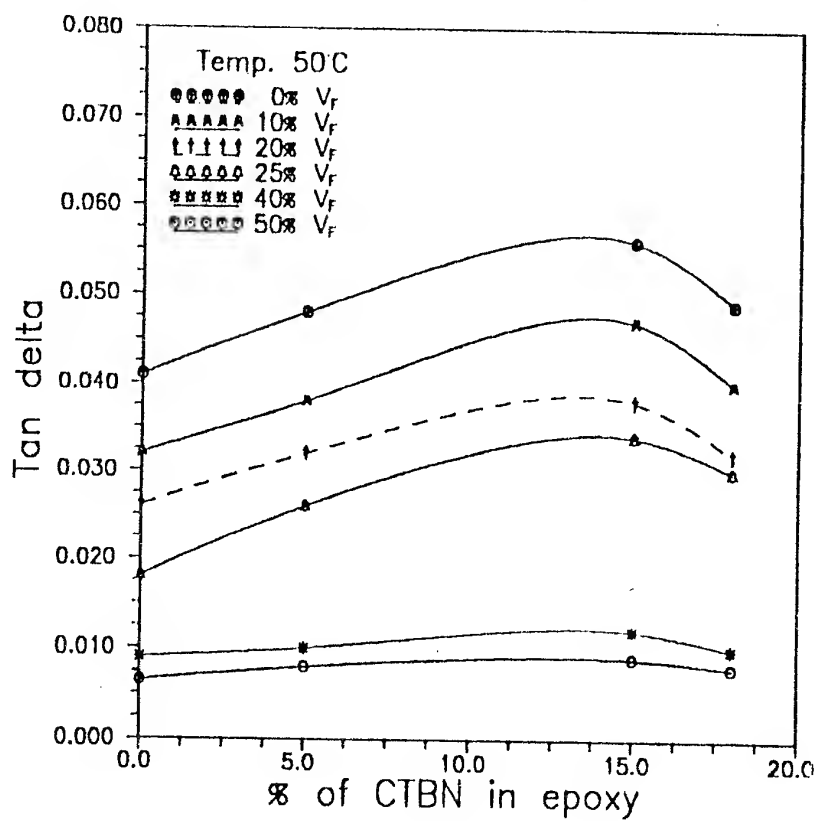
Fig. 3
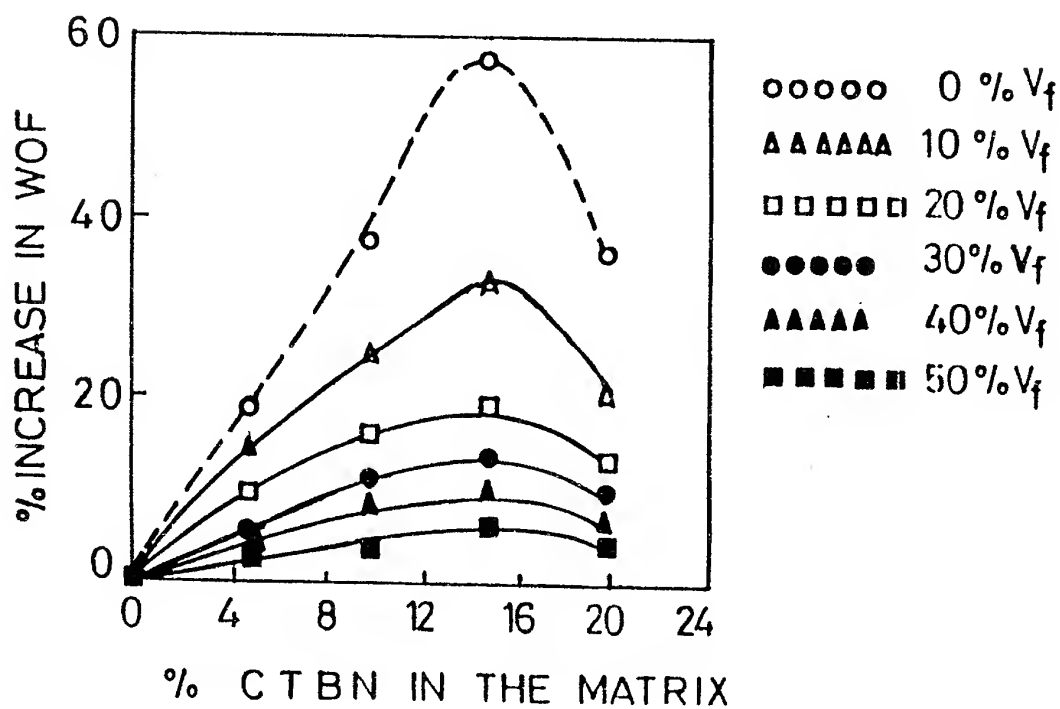
Fig. 4

334

HIGH LOADED POLYMERS BASED ON BIOGRADABLE MATERIALS

M. Mall, R. Schnabel, Sl. Marinow, J. Trempler, T. Fischer

Department of Materials Science, Mathin-Luther-University Halle-Wittenberg, Germany

INTRODUCTION

The chemical resistance and long-term stability of modern polymers often presents a problem at the time of disposial, which is characterized by high cost a lack of disposal facilities. For applications where no economical recycling methods are available, biogradable plastics should be the material of choise.

The objective of this work is the development of mixtures based on renewable raw materials (starch derivatives) for selected products with specific property goals, which can be processed using conventional plastic machines. In order to improve its properties, renewable modifiers (wood fiber, polyethylene glycol) were added to the plastics. To this end, investigations of the processability of mixtures and their morphology as well as final properties were to be carried out.

In processing of high loaded polymers following problems are encountered:

- with low shear rates, plastic behavior can arise with corresponding yield stresses which describe processing limits

- as opposed to impregnating resins, the investigated polymers have higher viscosities in processing range which cause an insufficient fiber wetting

MATERIALS AND METHODS

In order to reduce the number of experiments, mixtures were developed using the method of simplex grid plans and also mixture plans. This enabled a relatively wide range of concentrations to be investigated. These plans can always be used when the properties to be observed only depend on composition and not on the quantity of the mixture. Mixture plans are thus chiefly used to examine compound variables.

The objective of this method was to determine a function for a property of a compound depending on its composition. By creating mathematical models of this type, prior

computation can be used to predict the properties of any composition of the compound being investigated. Figure 1 shows the compositions for ten mixture points.
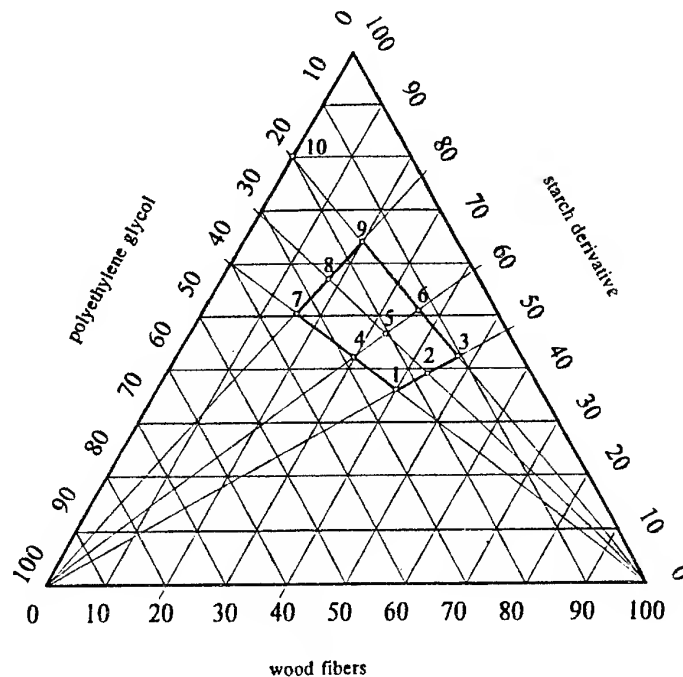
Figure 1: Simplex grid plan

Polymers and wood fibers were processed on a kneading machine to form a homogenious mixture. After grinding, samples were taken for measurement on a high pressure capillary rheometer. The ground material was pressed into boards from which samples were made for rheological, thermomechanical, thermodynamic, mechanical and light microscopy investigation.

In order to characterise flow behavior, tests were carried out using a rheometer with plate/plate instrument and a high-pressure capillary rheometer with a nozzle diameter of 1 mm and a capillary length of 30 mm. The measurements were conducted in a shear velocity range of 0,01 - 1.000 s^{-1} and were used to compare the mixtures with differing filler contents with respect to their processability on extruders and inject molding machines, the objektive being to investigate the impact of filler content on processability. Viscoelastic properties were investigated on a rheometer which offered the possibility of operating in the oscillation mode (Carri Med) to obtain the storage modulus G' and the loss modulus G", as the measure for the elastically stored energy and the viscous component. The same rheometer were used to characterize the relaxation behavior. This enabled stationary shear to be created, i.e. a constant speed

was set. After sudden braking, the course of shear stress was determined as a function of time. This produced a decay curve determined by the relaxation time. The residual stresses taken to be yield stresses.

Two different methods were used for thermodynamic tests (sessile drop method and depended drop method).

The tests of mechanical properties were carried out using the flexural impact test (DIN 53 453) and the tensile test (DIN 53 455).

Measuring the water intake of pressed panels was carried out in accordance with DIN 53 495, i.e. water absorption was measured compared to delivery state after water retention at a temperature of 23°C for 96 hours to obtain the diffusion coefficient.

The microscopy investigations were used to determine the structure and distribution of wood fibers in the matrix depending on filler content and the penetration and wetability of wood particles with polymer material.

RESULTS AND DISCUSSION

Tensile strength, elastic modulus and the impact strength were modeled within the simplex grid plan with the help of a special cubic regression polynom. The isolines of the impact strength are shown in the simplex lattice in figure 2.
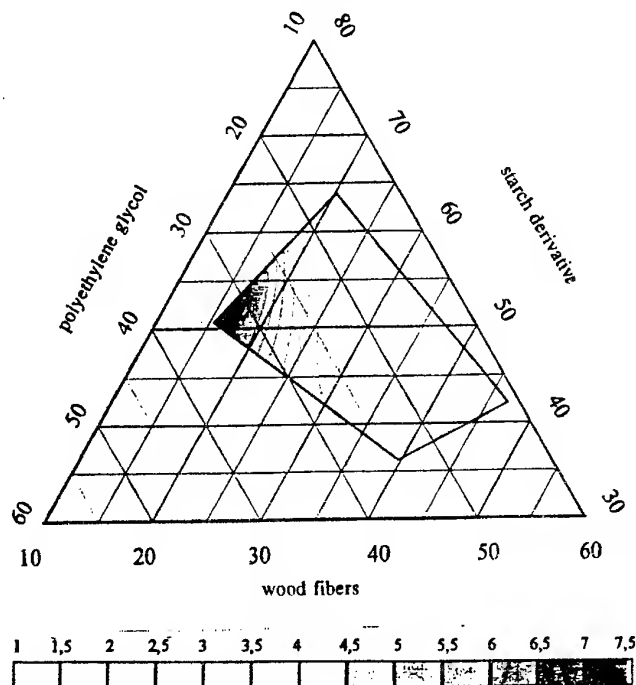
Figure 2: Isolines of the impact strength

337

$$y = b_s \cdot x_s + b_p \cdot x_p + b_H \cdot x_H + b_{SP} \cdot x_s \cdot x_p + b_{PH} \cdot x_p \cdot x_H + b_{SH} \cdot x_s \cdot x_H + b_{SPH} \cdot x_s \cdot x_p \cdot x_H$$

R^2 = 0,7793 $\bar{R}^2$ = 0,7392

	b_S	b_P	b_H	b_{SP}	b_{SH}	b_{PH}	b_{SPH}
Koeffizient	-2,5062	27,1852	0,0761	12,3561	11,7280	-20,5370	-136,8048
SE	2,7876	10,8830	2,2794	24,9566	11,1529	21,6761	58,4252

The standard errors of the regression coefficients are relativ high. The cause for these high values are the high standard errors of the test results.

Figure 3 shows a summary of important material characteristics including the used factors.

——— tensile strength

– – – elongation at tensile strength

✗✗✗✗ elastic modulus

······ impact strength

–·–·– density

–··–·· vicat softening temperature

factors:

tensile strength [N/mm²]	: 5
elastic modulus [N/mm²]	: 0,02
elongation [%]	: 2
impact strength [kJ/m²]	: 10
density [g/cm³]	: 20
vicat softening temperature [°C]	: 1
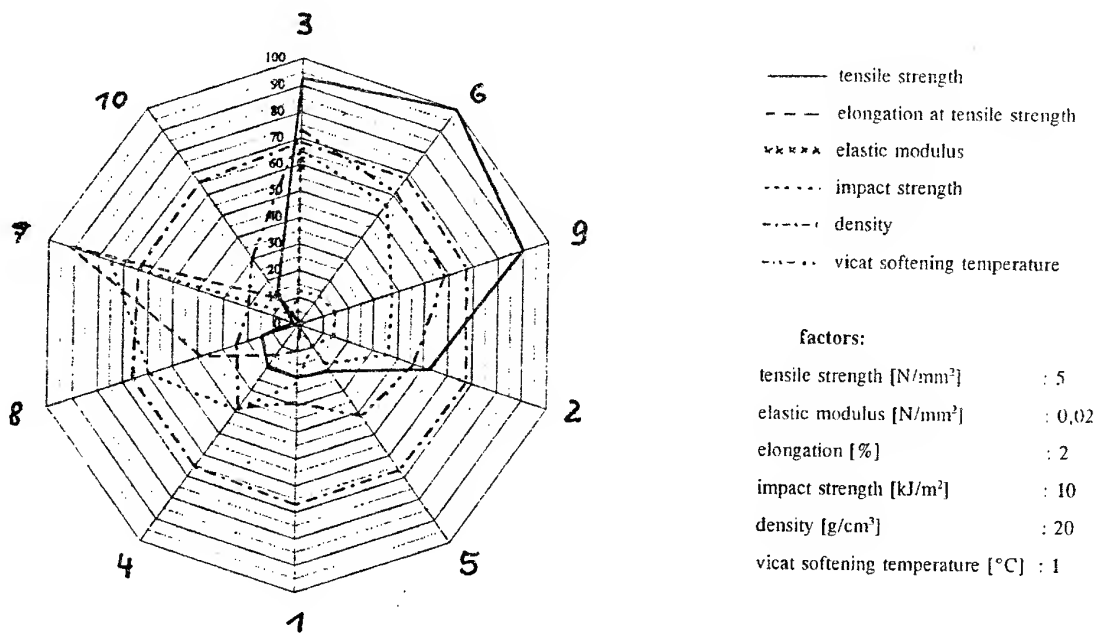
Figure 3: Material characteristics

The rheological investigations showed that the content limit of wood fiber with regard to the processing cabability is about 50%. Figure 4 shows a typical example of viscosity curves at temperatures of 140, 150 and 160°C for 4 different filler contents.

shear rate [s⁻¹]
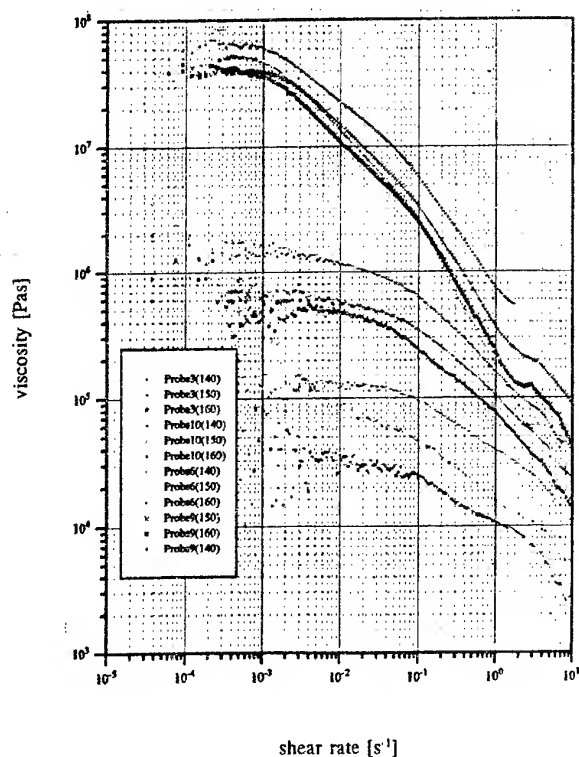
Figure 4: Viscosity functions

When varying concentration and temperature, its usefull to show viscosity functions as invariant characteristics using the Vinogradov/Malkin method. The best fit for the determination of the displacement factor a_T was obtained with the Arrhenius equation. The validity of well-known models for suspension rheology was evaluated. The best approximation was obtained using the Eilers equation. A theoretical maximum volume concentration of 0,4 is possible.

Oscillation measurements showed that at a constant concentration, the intercepts of the G' and G'' curves are shifted parallel to the x-axis to higher frequencies as temperature is increased, that is, the viscous component increases with increasing temperature.

The microscopy investigations showed that the wood fibres have been well moistened by the matrix - a finding which is also reflected by the mechanical and thermodynamic parameters.

By using the data of the surface tension and the OWEN-WENDT-RABEL equation polar and disperse parts of surface tension were calculated. Figure 5 showes the curves and the regressions equations.
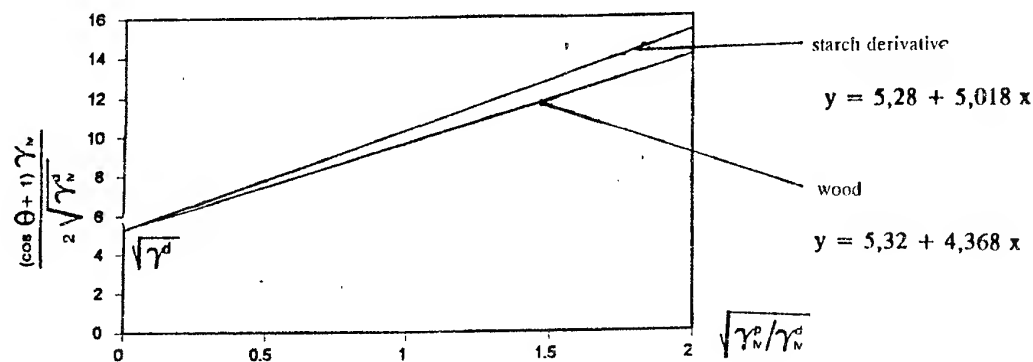
Figure : Polar and disperse parts of surface energy

The calculated interfacial tension between polymer and wood fibers is in the range of 0,42 - 0,84 mN/m.

The diffusion coefficient were calculated by using the data of water absorption, as shown in figure 6. As opposed to other plastics, which are in the range of 0,1 - 6,3% water absorption/24h the investigated mixtures are in the range of 3 - 20%.
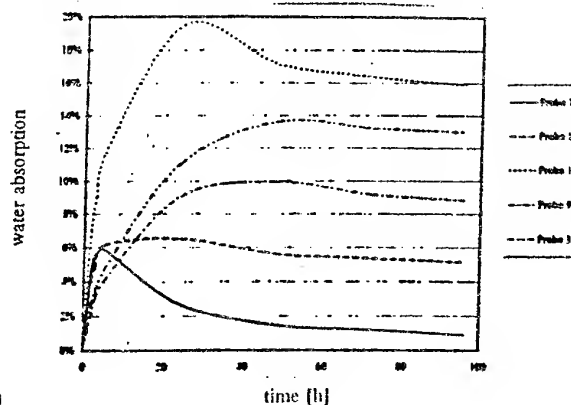
Figure 6: Water absorption

The water absorption is important for the biological degradation. For that reason the degradation can be rapidly (depending on the test piece wide and the moisture).

CONCLUSIONS

The investigated mixtures are processable on conventional plastic machines. The processability limitations when additional processing agents are not used occur with filler contents of 50% (that means about 40 vol-% depending on the processing technique and the flexibilizer content). Furthermore, without the addition of surface-active agents, by higher filler contents no complete wetting of the filler material is possible. Because of the low interfacial tension a good phase boundery was obtained, as shown in mechanical behavior.

METHOD OF INITIAL FUNCTIONS IN THE THEORY OF ANISOTROPIC PLATES WITH ARBITRARY BOUNDARY CONDITIONS

A. V. Matrosov

Department of Hydraulic Engineering, University for Water Communications,
5/7 Dvinskaya Street, S.Petersburg,198035,Russia

INTRODUCTION

One of the analitical methods for solving boundary problems for linearly-elastic solids with finite dimensions is the method of crosswise superposition, proposed by Lamé [1] and based on general solutions for infinitely long elastic domains (infinite layer, wedge, cylinder). These solutions may be called general because, having sufficient functional arbitrariness, they allow to find solutions satisfying boundary conditions on two equidistant surfaces bounding an elastic body with infinite dimension a long of one of coordinates and parallel to one coordinate surface.

For construction the general solution (in above sense) of a boundary problem for three-dimensional domain $x \in [0, a]$, $y \in [0, b]$, $z \in [0, h]$ it is necessary to sum three such solutions in three orthogonal directions. Using double Fourier series for each solution we may note that these series satisfy identically the governing equation inside the domain and have sufficient functional arbitrariness for fulfilling the three boundary conditions on each of the six sides. Because of the interdependence the expression for a coefficient of a term in one series will depend on all the coefficients of the other series and finally the solution involves solving the infinite system of linear algebraic equations giving the relation between the unknown coefficients and loading forces.

Such an approach for an elastic isotropic rectangle is developed for static and dynamic problems in [2],[3].

As noted in [2], one may construct infinite number of general solutions for an infinite layer. The solutions which simplifies receiving the coefficients of the linear algebraic equations is chosen for the specific boundary problem.

The solution for an anisotropic layer found with the method of initial functions (MIF) have sufficient functional arbitrariness for it to be used in the superposition method. This paper deals with using the MIF for finding solutions of boundary problems for a hexahedron in the Cartesian coordinates XYZ with sides which are not parallel to the coordinate surfaces.

341

MAIN EQUATIONS FOR ELASTIC ANISOTROPIC PARALLELEPIPED

Consider a linearly-elastic anisotropic parallelepiped $x \in [0, a], y \in [0, b], z \in [0, h]$ in the rectangular coordinate system XYZ. Basic equations of the MIF may be expressed as [4]

$$U = LU^0, \tag{1}$$

where $U = \{u, v, w, \sigma_z, \tau_{yz}, \tau_{xz}, \sigma_x, \sigma_y, \tau_{xy}\}$ is a vector of displacements and stresses the entries of which are functions of variables x, y, z; $U^0 = \{\tau_{xz}^0, \tau_{yz}^0, \sigma_z^0, w^0, v^0, u^0\}$ is a vector of initial functions of variables x, y determined on the initial surface $z = 0$; $L = [L_{ij}], i = 1, ..., 9; j = 1, ..., 6$ is a matrix of differential operator functions of the MIF in the form of power series of variable z

$$L = \sum_{k=0}^{\infty} L_k z^k, \tag{2}$$

and L_k are matrices with entries depending on differential operators $\partial_1 = \partial/\partial x$, $\partial_2 = \partial/\partial y$, $\partial_t = \partial/\partial t$, 21 elastic constants A_{ij} and density ρ.

Suppose the initial functions U^0 are expanded into double Fourier series on the complete systems of trigonometric functions in x and y coordinates

$$U^0 = \sum_{m=0}^{\infty} \sum_{n=0}^{\infty} \sum_{i=1}^{4} T_{mn}^{0i} U_{mn}^{0i}, \tag{3}$$

where U_{mn}^{0i} are vectors of coefficients of trigonometric series, T_{mn}^{0i} – diagonal matrices which are upper (6×6) blocs of trigonometrical functions matrices from the complete system

$$
\begin{aligned}
T_{mn}^1 &= \lceil c_m s_n, s_m c_n, s_m s_n, s_m s_n, s_m c_n, c_m s_n, s_m s_n, s_m s_n, c_m c_n \rfloor \\
T_{mn}^2 &= \lceil s_m c_n, c_m s_n, c_m c_n, c_m c_n, c_m s_n, s_m c_n, c_m c_n, c_m c_n, s_m s_n \rfloor \\
T_{mn}^3 &= \lceil c_m c_n, c_m s_n, s_m c_n, s_m c_n, c_m s_n, c_m c_n, s_m c_n, s_m c_n, c_m s_n \rfloor \\
T_{mn}^4 &= \lceil s_m s_n, c_m c_n, c_m s_n, c_m s_n, c_m c_n, s_m s_n, c_m s_n, c_m s_n, s_m c_n \rfloor
\end{aligned}
\tag{4}
$$

Here $s_m = \sin \alpha_m x$, $c_m = \cos \alpha_m x$, $s_n = \sin \beta_n y$, $c_n = \cos \beta_n y$, $\alpha_m = m\pi/a$, $\beta_n = n\pi/b$. Notice that indexes m, n with or without subscripts reffer to the trigonometrical functions of x and y correspondingly when p reffers to the trigonometrical functions of variable z with $\gamma_p = p\pi/h$ instead of α_m or β_n everywhere in this paper.

Acting the operator functions L_{ij} in (1) on U^0 (3), we obtain the representation of the vector of displacements and stresses U as

$$U = \sum_{m=0}^{\infty} \sum_{n=0}^{\infty} \sum_{i=1}^{4} T_{mn}^i L_{mn}^i U_{mn}^{0i}, \tag{5}$$

where L_{mn}^i are numerical matrices received as a result of formal substitutions $\partial_1^2 = -\alpha_m^2$ and $\partial_2^2 = -\beta_m^2$ in L from (1).

Taking into account the representation (2) finally the vector U can be obtained as a function of three variables x, y, z

$$U_z = \sum_{m=0}^{\infty} \sum_{n=0}^{\infty} \sum_{k=0}^{\infty} \sum_{i=1}^{4} z^k T_{mn}^i L_{mnk}^i U_{mn,z}^{0i}, \tag{6}$$

where L_{mnk}^i are numerical matrices after formal substitutions as in (5) in L_k from (2). When obtaining the solution (6), the MIF has been applied in the z direction. The subscript z in the vector U is used to indicate this fact. Also the solutions in two other coordinate directions can be obtained in the form

$$U_x = \sum_{n=0}^{\infty} \sum_{p=0}^{\infty} \sum_{k=0}^{\infty} \sum_{i=1}^{4} x^k T_{np}^i L_{npk}^i U_{np,x}^{0i} \tag{7}$$

$$U_y = \sum_{p=0}^{\infty} \sum_{m=0}^{\infty} \sum_{k=0}^{\infty} \sum_{i=1}^{4} y^k T_{pm}^i L_{pmk}^i U_{pm,y}^{0i}. \tag{8}$$

Here $U_{np,x}^{0i}$, $U_{pm,y}^{0i}$ are vectors of coefficients in trigonometrical series of the initial functions determined on the initial surfaces $x = 0$ and $y = 0$ correspondingly.

GOVERNING EQUATIONS FOR ANALYSIS OF ELASTIC HEXAHEDRON

Let us consider an elastic anisotropic hexahedron bounded by six planes $z = a_i^1 x + b_i^1 y + c_i^1$, $x = a_i^2 y + b_i^2 z + c_i^2$, $y = a_i^3 z + b_i^3 x + c_i^3$, $i = 1, 2$ and contained into a parallelepiped $x \in [0, a]$, $y \in [0, b]$, $z \in [0, h]$.

For definiteness, assume loads are given on its six sides by their rectangular components P_x^i, P_y^i, P_z^i, $i = 1, ..., 6$. Using three received solutions (6),(7),(8) on the assumption that initial functions on the surfaces $x = 0$, $y = 0$ and $z = 0$ are expanded into double Fourier series with unknown coefficients $U_{np,x}^{0i}$, $U_{pm,y}^{0i}$, $U_{mn,z}^{0i}$, we can find out values of stresses on inclined planes of the parallelepiped in terms of unknown coefficients. Then an infinite system of algebraic linear equations can be derived equating obtained coefficients to coefficients in Fourier series expanding of given loads on the same harmonics. Every coefficient in representation of stresses on every side of elastic hexahedron in the form of trigonometric series is a linear function of all unknown coefficients in trigonometrical expansions of the initial functions.

Let us demonstrate deriving a representation of the stresses and displacements on one side of the hexahedron $z = a_1^1 x + b_1^1 y + c_1^1$. The vectors of displacements and stresses on other sides can be found out along very similar lines.

Substitution $z = a_1^1 x + b_1^1 y + c_1^1$ in the functions (6)-(8) transforms these functions of x, y, z into the functions of two variables x, y which can be expanded into

trigonometric series. Every term in (6)-(8) can be presented as

$$\left(a_1^1 x + b_1^1 y + c_1^1\right)^k T_{mn}^i(x,y) = \sum_{m_1=0}^{\infty} \sum_{n_1=0}^{\infty} \sum_{j=1}^{4} T_{m_1 n_1}^j C_{m_1 n_1}^{j,mnki}$$

$$x^k T_{np}^i(y, a_1^1 x + b_1^1 y + c_1^1) = \sum_{m_1=0}^{\infty} \sum_{n_1=0}^{\infty} \sum_{j=1}^{4} T_{m_1 n_1}^j A_{m_1 n_1}^{j,npki} \tag{9}$$

$$y^k T_{pm}^i(a_1^1 x + b_1^1 y + c_1^1, x) = \sum_{m_1=0}^{\infty} \sum_{n_1=0}^{\infty} \sum_{j=1}^{4} T_{m_1 n_1}^j B_{m_1 n_1}^{j,pmki}$$

where $A_{m_1 n_1}^{j,npki}$, $B_{m_1 n_1}^{j,pmki}$, $C_{m_1 n_1}^{j,mnki}$ are diagonal matrices (9×9) of Fourier coefficients (remember that m_1, n_1 in $T_{m_1 n_1}^j$ correspond to the trigonometrical functions of x, y in (4)).

Substituting (9) in (6)-(8) and changing the order of summing, the vectors of displacements and stresses on this first inclined plane of the parallelepiped using three derived solutions can be obtained in the form

$$U_x^1 = \sum_{m_1,n_1=0}^{\infty} \sum_{j=1}^{4} T_{m_1 n_1}^j \left\{ \sum_{n,p=0}^{\infty} \sum_{i=1}^{4} \sum_{k=0}^{\infty} A_{m_1 n_1}^{j,npki} L_{npk}^i U_{np,x}^{0i} \right\}$$

$$U_y^1 = \sum_{m_1,n_1=0}^{\infty} \sum_{j=1}^{4} T_{m_1 n_1}^j \left\{ \sum_{p,m=0}^{\infty} \sum_{i=1}^{4} \sum_{k=0}^{\infty} B_{m_1 n_1}^{j,pmki} L_{pmk}^i U_{pm,y}^{0i} \right\} \tag{10}$$

$$U_z^1 = \sum_{m_1,n_1=0}^{\infty} \sum_{j=1}^{4} T_{m_1 n_1}^j \left\{ \sum_{m,n=0}^{\infty} \sum_{i=1}^{4} \sum_{k=0}^{\infty} C_{m_1 n_1}^{j,mnki} L_{mnk}^i U_{mn,z}^{0i} \right\}.$$

It can be seen that every term in the trigonometric expansions (10) is a linear function of the all unknown coefficients of the corresponding initial functions.

As the loads $P^1 = \left\{ P_x^1, P_y^1, P_z^1 \right\}$ are given only on the part of the inclined plane $z = a_1^1 x + b_1^1 y + c_1^1$ of the parallelepiped (our hexahedron is inside it), we determine their values on the remaining part of the inclined plane as zero and expand these functions into trigonometric series in x and y coordinates

$$P^1 = \sum_{m,n=0}^{\infty} \sum_{i=1}^{4} T_{mn,\sigma}^i P_{mn}^{i1}, \tag{11}$$

where $T_{mn,\sigma}^i$ – (3×3) upper blocks of the matrices (4), P_{mn}^{i1} – (3×1) vectors of Fourier coefficients. The components of the vector P^1 can be represented in terms of the components of the stress tensor as

$$P_x^1 = \sigma_x l + \tau_{xy} m + \tau_{xz} n$$

$$P_y^1 = \tau_{xy} l + \sigma_y m + \tau_{yz} n \tag{12}$$

$$P_z^1 = \tau_{xz} l + \tau_{yz} m + \sigma_y n,$$

344

where l, m, n are the direction-cosines of the outward normal to the first side of the hexahedron.

Substituting (10) in (12) and equating the coefficients on the same harmonics, the infinite system for satisfying boundary conditions on the first side of the hexahedron can be obtained in the form

$$\Phi_{mn}^{i1} + \Psi_{mn}^{i1} + \Theta_{mn}^{i1} = P_{mn}^{i1}$$
$$i = 1...4; m, n = 0, 1, 2, ...,$$

(13)

where Φ_{mn}^{i1}, Ψ_{mn}^{i1}, Θ_{mn}^{i1} are linear functions of the components of the vectors of unknown coefficients of the initial functions $U_{np}^{0,i}$, $U_{pm}^{0,i}$, $U_{mn}^{0,i}$ correspondingly.

A similar set of equations can be derived for satisfying boundary conditions on the other five sides of the hexahedron. Finally the governing infinite system of linear equations can be derived as

$$\Phi_{ij}^{lk} + \Psi_{ij}^{lk} + \Theta_{ij}^{lk} = P_{ij}^{lk}$$
$$l = 1...4; k = 1...6; m, n = 0, 1, 2, ...$$

(14)

Here the superscript k refers to the boundary surface of the hexahedron.

To write down the coefficients in (14) in explicit form is rather difficult because of the complicated structure of the matrices L_{mnk}^{i}, L_{npk}^{i}, L_{pmk}^{i} in (6)–(8), but represented technique is very algorithmic and all coefficients can be obtained with designed software.

After solving the infinite system (14) the dicplacements and stresses in the hexahedron can be calculated using (6)-(8). The sum of three vectors U_x, U_y, U_z will give the exact sokution of the formulated problem.

In practice, the number of terms in all expansions is restricted. Thus, the infinite algebraic system (14) becomes finite one the order of which depends on the required accuracy of calculations of the displacements and stresses.

In this paper the algorithm is proposed when the sides of the hexahedron are loaded by the given forces. One can define another conditions on the hexahedron sides such as: displacements or mixed conditions (normal stress and two tangent displacements or vice versa).

CONCLUSIONS

The proposed algorithm of the superposition method with the MIF for constructing the suitable solutions enables to receive rather easy the governing system of algebraic equations using the computational technique. This approach allows to find out solutions for various problems of mechanics of anisotropic linearly-elastic body with variable parameters of geometry.

REFERENCES

[1] Lamé G. "Leçons sur la théorie mathémathique de l'élasticité des corps solids." *Paris:Bachelier*, 335p. (1852)

[2] Grinchenko V.T., Ulitko A.F. "Three-dimensional problems in theory of elasticity and plasticity: Equilibrium of elastic bodies with cononical shapes." *Kiev:Naukova Dumka*, 280p. (1985) (in Russian)

[3] Grinchenko V.T., Meleshko V.V. "Steady vibrations and waves in elastic bodies." *Kiev:Naukova Dumka*, 283p. (1981) (in Russian)

[4] Galileev S.M., Matrosov A.V. "Method of initial functions for three-dimensional analysis of anysotropic elastic structures." *Analysis of complicated structures*, LICI, Leningrad, pp.114-119 (1988) (in Russian)

BOUNDARY VALUE PROBLEMS OF THE LINEAR THEORY OF TWO-COMPONENT ELASTIC COMPOSITES

D.Natroshvili, A.Djagmaidze

Georgian Technical University, Tbilisi, Republic of Georgia

Abstract

Boundary value problems for the system of differential equations of the generalized theory of two-component composites are investigated when the regular body under consideration is either homogeneous or piecewise homogeneous and contains interior cuts (or cuts on the interface) in the form of two-dimensional open manifolds of arbitrary shape. For these problems the potential method is developed in various function spaces and by means of the theory of pseudodifferential equations on manifolds with boundary the existence and uniqueness theorems are proved. The almost best regularity results (C^α–smoothness with $\alpha < 1/2$) are obtained for solutions. Two computational methods - boundary element method and method of regular sources - are treated.

The investigation deals with the three-dimensional boundary value problems (BVPs) of the linear theory of two-component elastic composites ("elastic mixtures"). In the last forty to fifty years there have been many important developments to this direction in the theory of elastic continua and nowadays there exist several mathematical models of such composites (see [1-15] and references therein).

Our aim is to unite mathematically all these models and construct a general theory of solvability of the BVPs involving the corresponding problems of each particular model. It should be noted that many problems are treated and solved for the first time.

The systems of differential equations appearing in these models can be combined and written in the following general form

$$a_1 \, \Delta u' + b_1 \, \text{grad div} \, u' + c \, \Delta u'' + d \, \text{grad div} \, u'' -$$
$$\alpha(u' - u'') - \nu(D_t u' - D_t u'') = \rho_{11} D_t^2 u'' - \rho_{12} D_t^2 u'' + F',$$

$$c \, \Delta u' + d \, \mathrm{grad \, div} \, u' + a_2 \, \Delta u'' + b_2 \, \mathrm{grad \, div} \, u'' +$$
$$\alpha(u' - u'') + \nu(D_t u' - D_t u'') = \rho_{12} D_t^2 u' + \rho_{22} D_t u'' + F''; \qquad (1)$$

here $u' = (u'_1, u'_2, u'_3)$ and $u'' = (u''_1, u''_2, u''_3)$ are the so-called partial displacements, a_p, b_p, c, d $(p = 1, 2)$ are real constants expressed in terms of the mechanical and physical characteristics of the two phase composite in question, ρ_{kj} are the partial densities, α is the coefficient of interacting between the two components. while ν is the diffusion coefficient; F' and F'' are given bulk forces; Δ is the Laplacian and $D_t = \partial/\partial t$.

For particular values of the above constants we have different models (e.g., $\alpha > 0$, $\nu > 0$, $\rho_{12} = 0$ or $\alpha > 0$, $\nu = 0$, $\rho \neq 0$ correspond to the shift models; $\alpha = 0$, $\nu \geq 0$, $\rho_{12} = 0$ or $\alpha = 0$, $\nu \geq 0$, $\rho \neq 0$ correspond to the diffusion models; $\alpha = 0$, $\nu = 0$, $\rho = 0$ correspond to the interpenetrating model).

We have developed the boundary integral equation method in the Bessel potential (H_p^s) and Besov $(B_{p,q}^s)$ function spaces (cf. [18]) and studied the **basic** (on the whole boundary of the body a boundary condition of the same type is given, e.g., partial displacements, partial stresses or linear combinations of their components) and **mixed type** (the boundary of the body is devided into several disjoint parts and different type of boundary conditions are given on different submanifolds) **BVPs** for system (1) in the case of smooth domains.

This approach enables us to consider also the crack type problems for homogeneous composites and the interface (transmission) problems for peacewise homogeneous composites when the composite body under consideration contains interior cuts (or cuts on the interface) in the form of two-dimensional smooth open surfaces with smooth boundaries.

The three type of problems: statical, dynamical and steady state oscillation ones are treated separately.

With the help of the potential method the original BVPs are reduced to the corresponding elliptic pseudodifferential equations (ΨDEs) on the boundary of the body. Applying the theory of ΨDEs on closed manifolds and on manifolds with boundary in the H_p^s and $B_{p,q}^s$ spaces (see, e.g., [16,17]) we proved existence theorems for original BVPs in corresponding function spaces. We obtained representation formulas for solutions by potential type integrals and established the almost best regularity results.

In particular, for the crack type problems with apropriate boundary data

C^α—smoothness of solutions is proved with arbitrary $0 < \alpha < 1/2$.

Besides the regularity properties, the asymptotic behaviour of the solutions and their derivatives near the crack adges is also studied and asymptotic expansion formulas for solutions to the ΨDEs and the original BVPs are obtained.

On the basis of the theoretical results described above two computational methods: the boundary element method (the direct and indirect versions) and the method of regular sources are considered and justified.

References

1. Truesdell, C. and Toupin, R. The classical field theories (in Handbuch der Physik, vol. III/1, Springer, Berlin, 1960.

2. Green, A.E. and Naghdi, P.M. A dynamical theory of two interacting continua. Int. J. Eng. Sci., **3**, 2, 1965, 231-241.

3. Green, A.E. and Steel, T.R. Constitutive equations for interacting continua. Int. J. Eng. Sci., **4**, 4, 1966, 483-500.

4. Steel, T.R. Application of a theory of interacting continua. Q. J. Mech. Appl. Math., **20**, 1967, 57-72.

5. Steel, T.R. Determination of the constitutive coefficients for a mixture of two solids. Int. J. Solids and Struct., **4**, 12, 1968, 1149-1160.

6. Green, A.E. and Naghdi, P.M. On basic equations for mixtures. Q. J. Mech. Appl. Math., **22**, 1969, 427-438.

7. Lempreier, B.On the practicability of analysig waves in composites by the theory of mixtures. Lokheed Palo Auto Research Laboratory. Report N LMSC-6-78-69-21, 1969, 76 pp.

8. Rakhmatulin, Kh.A., Saatov, J.U., Fillipov, I.G. and Artikov, T.U. Waves in two-component media. Fan, Tashkent, 1974. (in Russian)

9. Tiersten, H. and Jahanmir, M. A theory of composites modelled as interpenetrating solid continua. Arch Rational Mech. Anal., **65**, 1977, 153-192.

10. Green, A.E. and Naghdi, P.M. On thermodynamics and the nature of the second law for mixtures of interacting continua. Q. J. Mech. Appl. Math., **31**, 1978, 265-293.

11. Mc Niven, H.D. and Mengi, Y.A. A mathematical model for the linear dynamic behaviour of two phase periodic materials. Int. J. Solids and Struct., **15**, 4, 1979, 171-180.

12. Mc Niven, H.D. and Mengi,Y.A. A mixture theory for elastic laminated composites. Int. J. Solids and Struct., **15**, 4, 1979, 180-302.

13. Khoroshun, L.P. and Soltanov, N.S. Thermoelasticity of two-component mixtures. Naukova Dumka, Kiev, 1984. (in Russian)

14. Rushitskii, J.J. Elements of the theory of mixtures. Naukova Dumka, Kiev, 1991. (in Russian)

15. Natroshvili, D., Djagmaidze, A. and Svanadze, M. Linear problems of the theory of elastic mixtures. Tbilisi University Press, Tbilisi, 1986. (in Russian)

16. Duduchava, R. On multidimensional singular integral operators, I, II. J. Operator Theory, **11**, 1984, 41-76, 199-214.

17. Shargorodsky, E. An L_p−analogue of the Vishik-Eskin theory. Memoirs on Differential Equations and Mahtematical Physics, **2**, 1994, 41-148.

18. Duduchava, R., Natroshvili, D. and Shargorodsky, E. Boundary value problems of the mathematical theory of cracks. Proc. I.Vekua Inst. Appl. Math., Tbilisi State Univ.,**39**, 1990, 68-83.

THE OPTIMAL SHAPE AND LAYOUT DESIGN OF 3 DIMENSIONAL SHELL USING HOMOGENIZATION METHOD

Hideomi Ohtsubo and Katsuyuki Suzuki

Deprtment of Naval Architecture and Ocean Engineering

The University of Tokyo

7-3-1 Hongo Bunkyo-ku Tokyo JAPAN

1. INTRODUCTION

The notion of structural optimization was widely discussed by structural engineers in the early 70s right after rapid development of finite element methods. However, it could not provide practical means to design structures except some cases of simple shape structure, because of the lack of flexible geometric modeling and due to the limited capability of interactive graphic display at that time. Since the structural design of machine parts generally involves their geometric representation, in other words, their shape, structural design must deal with shape optimization, as well as sizing optimization.

From early '80, the shape optimization problem was studies quite extensively, with the development of geometric represent method and automatic mesh generation. The difficulty of shape optimization problems arises from the fact that the geometry of a structure itself is the design variable, and the finite element model must be changed in the process of optimization. There are several works that combined shape optimization with automatic mesh generation. Another difficulty of shape optimization is the changing topology. Most shape optimization problems are restricted in the case that topology of the design domain does not change in an optimization process. However, often the internal holes can be introduced to reduce the weight of a structure without violating the design constraints. Currently, the changing the topology in the process of optimization is impossible. It is possible to begin from various topology, and to choose the best one based on a comparison of the values of objective function. However, it is clearly impractical to examine all possible topologies through such a procedure.

With these difficulties, the shape optimization problem remained difficult process and was not used much in the industrial design process. However, if the shape optimization problem was considered not as the moving boundary problem but as the distribution of material problem, these problem might be solved. For example, as shown in Fig. 1 (a), if the domain is divided into small regions and the design variables are taken as the thickness of each region, the regions that is not needed is removed and the final configuration is the optimal shape and layout. Also with this approach the re-generation of finite element mesh after shape has changed can be avoided. Rossaw abnd Taylor[1], Prasad and Haftka[2] took this approach but the results they obtained were far from satisfactory. The biggest difficulty they encounter is that when the finite element mesh is different, the optimal shape also changes which is strange since the optimal shape and layout should not depend on the analysis as long as the analysis is accurately carried out.

This behavior was explained by Cheng and Olhoff [3] that when the design variable is distributed variable, the final solution often does not exists in the space of finite number of uncontinuous points. That is, plate possesses the infinite number of ribs with infinitesmal size, and the optimal solution cannot be expressed in the form of usual functions. In this case, as Strang and Kohn [4] pointed out, the relaxation of solution space is necessary. In other words, the introduction of microstructure in advance is essential in this problem, and just chaanging the thickness is not fully relaxed. Here, as shown in Fig. 1 (b), the infinitesimal small microstructure is introduced and the optimal shape and layout design is considered to be the optimal distribution of the microstructure. Suzuki and Kikuchi [5] demonstrated that the introduction of 2 sizes and rotation angle of rectangular holes is sufficient as the relaxation.

(a)   (b)
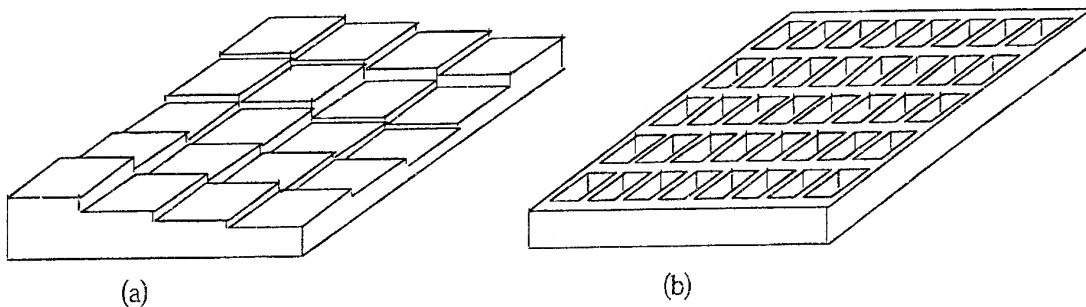
Fig. 1 Optimization with Distribution of Thickness and Distribution of Microstructure

Fig. 2 indicate the concept of the shape and layout optimization. If the hole sizes of some area are their maximum, the area is considered to be void and no material is allotted, and if the hole sizes of some area are zero, those area is considered to be material area. If the hole sizes are in between, the porous media should be allotted in those area.
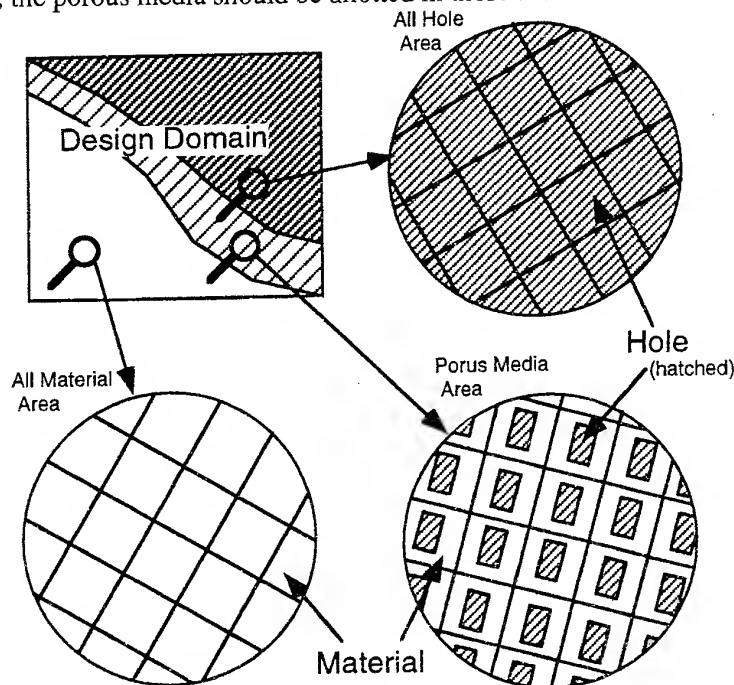
Fig. 2 TheGeneration of Shape and Topology by Microstructure

352

2. PROBLEM FORMULATION

We consider the following mathematical formulation. The mean compliance of the structure is taken as an objective function, while constraints are set on the volume of material to be used in the structure. In mathematical form, it can be written as follows.

$$\underset{\substack{Minimize \\ \text{Design variables}}}{} \quad \sum_{i=1}^{N}\int_{\Omega}\rho f_i u_i d\Omega + \sum_{i=1}^{N}\int_{\Gamma_T} t_i u_i d\Gamma$$

subjected to

Equilibrium Equatons

$$\int_{\Omega}\rho(x)d\Omega \le \Omega_s$$

As I mentioned before, thetwo sizes of the rectangular hole and the rotation angle are used as design variables. The three dimensional shell model shown in Fig. 3 is used as a microstructure. It consists of two plates with a rectangular hole in addition to a thin plate without a hole. The size and rotation angle of the hole in the upper layer and lower layer are same. Hence this layering is symmetric with respect to the middle surface and there is no coupling of bending and membrane deformations. The thickness h_0 of the middle plate (without hole) can be chosen to be either non-zero or zero. Thus, the result obtained by this microstructure can be interpreted as the optimal layout of a stiffener for reinforcement of a thin plate/shell when the thickness of minimum plate is set to be non-zero, while it can be interpreted as the optimal layout of a three-dimensional frame on a given three-dimensional (possibly curved) surface when the thickness h_0 of the middle plate is set to be zero.
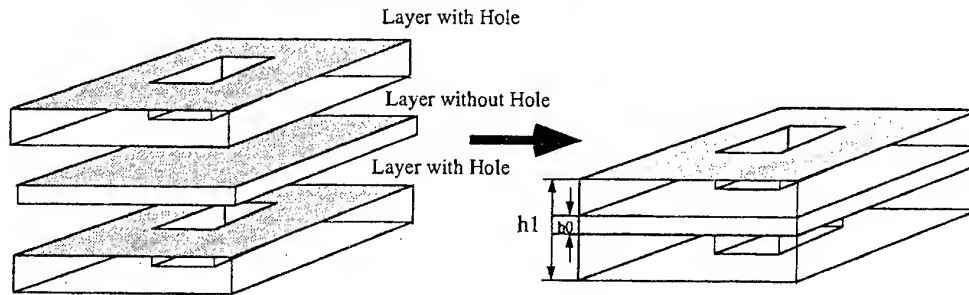
Fig. 3   Model of a Three Dimensional Microstructure for a Shell

The equivalent bending stiffness of the microstructure is computed using homogenization method. Although the sizes of the microstructure changes and the periodic conditions required by homogenization method does not totally satisfied, as the model of microstructure introduced become infinitesimally small, the rate of change of the size become zero. In general, in a plate of rapidly varying thickness, the plate theory does not hold. Here, the homogenization method based on the extension of Kohn and Vogelius [6] is used.

Generally speaking, there are two categories of optimization methods. One is mathematical programing which makes use of general methods such as the penalty function technique, the gradient projection technique or the method of feasible direction. The other is the optimality criteria method in which the condition of optimality is going to be satisfied by utilizing an intuitive approach. While in mathematical programming the updates of the design variables are

related each other , in the optimality criteria method update of each design variable can be performed independent of each other. In this sense, the optimality criteria method is much more efficient than mathematical programming. In our problem, since a large number of design variables are needed to represent the shape and topology of design domain, the optimality criteria method is the preferable choice of formulation if possible. To use optimality criteria method the following modifications of formulation are made. First we minimize potential energy with respect to displacement, and then maximize that minimized potential energy (hence displacement v satisfies the equilibrium equations) with respect to design variables with volume constraint. Note that the volume constraint does not depend on displacement. This can be written as:

$$\underset{x,\theta}{Maximize} \quad \underset{v}{Minimize} \; \Pi_\lambda(v,x,\theta)$$

subjected to

Equilibrium Equatons

$$\int_\Omega \rho(\mathbf{x})d\Omega \le \Omega_s$$

where

$$\Pi_\lambda(v,x,\theta) = \frac{1}{2}\sum_{i,j,k,l=1}^{N} \int_\Omega E_{ijkl}^{G}(x,\theta)\frac{\partial v_k}{\partial x_l}\frac{\partial v_i}{\partial x_j}d\Omega + \frac{1}{2}\sum_{i=1}^{N} \int_{\Gamma_D} \lambda(v_i - g_i)^2 d\Gamma$$

$$-\sum_{i=1}^{N} \int_\Omega f_i v_i d\Omega - \sum_{i=1}^{N} \int_{\Gamma_T} t_i v_i d\Gamma$$

Now that we have only one constraints, the optimality criteria method can be applied easily. Overall Algorithm becomes as Fig. 4. For given design variables, the equivalent stiffness of microstructure is computed using homogenization method. For the given stiffness, stress analysis is carried out using finite element method. Finally, based on the stress of each finite element, the new design variables are determined using the optimality criteria method.
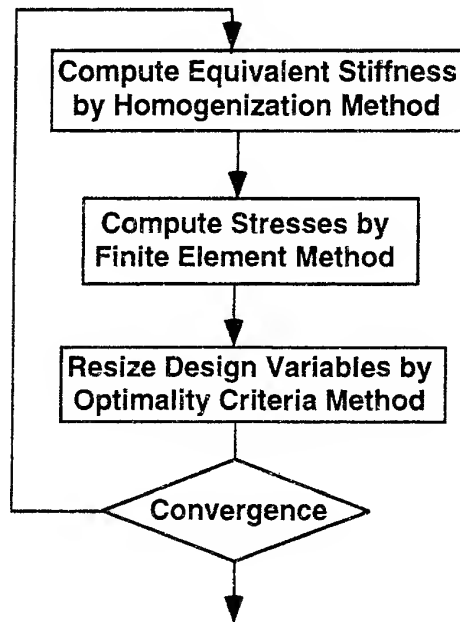
Fig. 4 Overall Algorithm of Optimization

3 OPTIMAL DESIGN OF SIMPLY SUPPORTED PLATE AND SHELL

We shall now consider a simply supported plate and a simply supported shell. The size of the projected plane of the shell is the same as that of the plate, 60 cm × 60 cm as shown in Fig. 5.

Plate, Point Load   Shell, Point Load
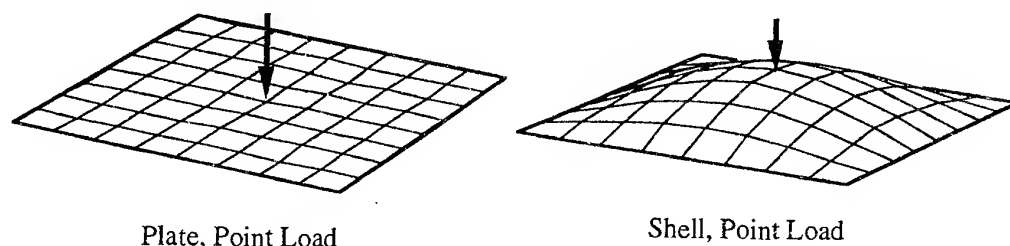
Figure 5. Examples of Plates and Shells

Using symmetry of geometry and loading conditions, one quarter of the domain need be discretized to find the optimal layout of reinforcement of a thin plate/shell characterized by the thickness $h_0 = 0.1$cm. The maximum height of stiffeners which are introduced for reinforcement is restricted to $h_1 = 1$cm. A quarter of the plate/shell, i.e. the design domain, is divided into 30x30 four-node square shell elements. Young's modulus of the solid material is assumed to be 100 GPa, while Poisson's ratio is 0.3. A point transverse force at the center on the plate/shell is applied. A curved surface $z = z_{max} sin(x/x_{max}) sin(y/y_{max})$ with $z_{max} / x_{max} = z_{max} / y_{max} = 1/12$ is assumed to define the middle surface of the shell.

The optimal distribution of stiffeners of a thin plate is obtained as shown in Fig. 6 for several volume constraints. When the volume of stiffeners (i.e., solid material added to the original thin plate) is very large, no stiffeners are assigned in the vicinity of the lines connected for the mid-points of two adjacent boundary edges of the plate (Fig. 6 (a)). A square plate rotated 45 degree is formed as a part of the stiffeners. If the thickness of the middle thin plate is assumed to be zero, i.e., $h_0 = 0$, the optimal layout for a plate structure must yield line hinges along these four 45 degree inclined lines.

These hinge lines does not imply discontinuity of the transverse displacement along these hinge lines. Rather, only the slope is discontinuous, which is still admissible in the variational formulation of an elastic plate defined in the Sobolev space $H^2(\Omega)$. The slope, i.e., the normal derivative of the transverse deflection w along a finite number of curves in the plate can be discontinuous. In this sense, the optimal reinforcement or layout pushes the transverse deflection w to the limit of the admissible space, in other words, w is just in $H^2(\Omega)$ but not in $H^{2+\delta}(\Omega)$ for $\delta > 0$. This may further imply that a careful consideration of convergence of the finite element approximations is required when the representative mesh size goes to zero. It should be possible to establish strong convergence of the finite element approximations to the optimal solution, but it may be impossible to establish an explicit rate of convergence, since regularity of the transverse deflection w cannot be expected in the optimum design.

To explain the hinge line, let us introduce a result of limit line analysis in plasticity where hinge lines also appear, see Fig. 7. It can be easily understood that the hinge lines in layout optimization are orthogonal to the hinge lines of limit analysis. This seems a natural consequence.

When limit lines appear, displacement becomes infinite in linear theory, while the objective function here is to minimize the mean compliance which yields the minimum displacement for a specified load. To avoid plastic hinges in limit analysis, hinges in an elastic plate should be "opposite", i.e. orthogonal to them.

When the volume of solid material for reinforcement or layout is relatively small, we can obtain a rather thick plus shaped stiffener at the center and thin stiffeners along the diagonals of the original plate model. Again there are two hinges in each thin diagonal stiffener at the quarter points. This result is compatible to the clamped beam optimization problem in previous section. Despite of a simply supported plate, if two diagonal lines are considered as beams, they would be clamped since rotations are restricted in both edge lines. By reducing the volume of solid material for reinforcement or layout, the optimal shape of stiffeners or plates can be clearly identified. Note that the black portion in the figures indicates that no holes are generated in stiffeners or plates whose height is fixed to be h_1-h_0. Another interesting observation is that solid stiffeners or plates are generated in most of the domain. There is very little perforation in the optimal design, although it is allowed. In other words, fine microstructure by perforation may not be the optimum as far as the present result is concerned.
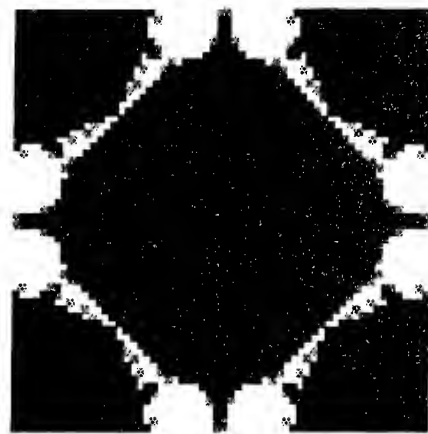
(a) volume 720/900
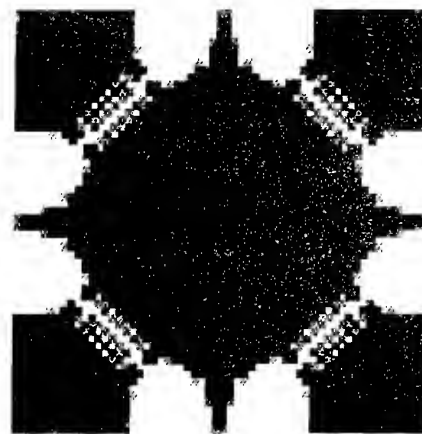
(b) volume 630/900
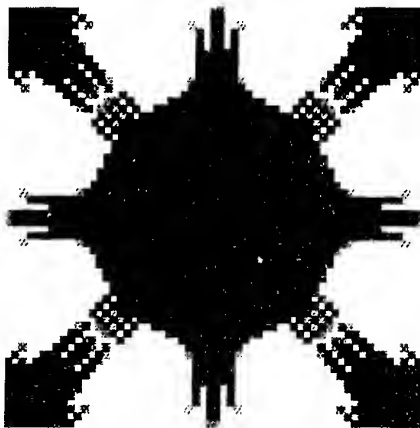
(c) volume 450/900

(d) volume 270/900

Figure 6 Optimal Layout of a Plate with Point Load
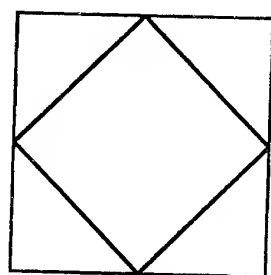
Hinge lines of optimal
solution
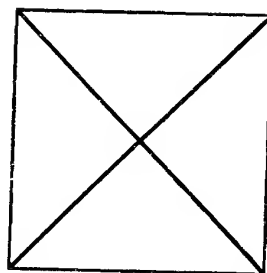
Limit lines of simply
supported shell

(a)

(b)

Figure 7 Hinges and Limit Lines of Optimization and Limit Analysis

The results for a shell are very different from those of a plate as expected from the fact that the optimal layout of an arch is dramatically different from the one of a beam shown in the previous section. Figure 8 shows the optimal distribution of stiffeners or layout of a shell for the same point transverse load applied at the center top of a shell surface. A ring shape reinforcement/layout is formed that is never generated for a plate. Inner plus shape center stiffeners for a plate disappear for a shell. Rather thick stiffeners are assigned along the diagonals. This is again very different from the plate case. Hinges appear on the diagonal stiffeners, but different from those for a plate. Another difference is that scattered reinforcement is observed inside a ring stiffener when the volume of solid material for stiffeners is reduced. This indicates the possibility of microstructure with perforation. For a plate, most stiffeners are solid. Very different layouts are obtained for a plate and for a shell. This difference may be explained by the fact that a shell is a combination of a plate and a membrane. Quite a large portion of applied forces is supported by the membrane rather than the plate in a shell structure. If a pure flat plate is considered, all loads must be supported by this plate. The mechanics for a shell being quite different from that for a plate implies different optimal layouts.
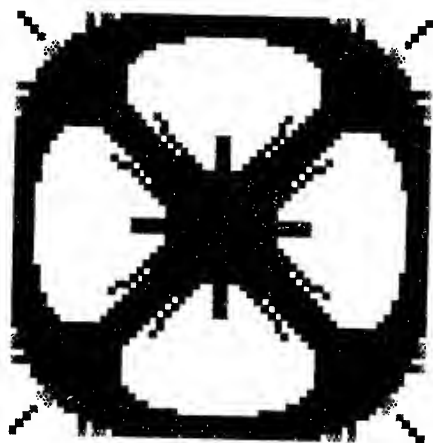
(a) volume 450/900
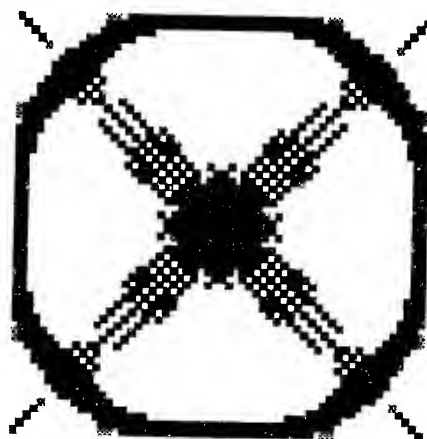
(b) volume 270/900

Figure 8 Shell with Point Load at the Center

357

4. CONCLUSION

The generalized shape and layout technique using homogenization method which has capabilities of performing not only the shape optimization but also the topology optimization was extended to the plate and 3 dimensional shell. The generation of hinge lines that are transverse to the hinge lines appears in limit analysis was observed.

There are several advantages and disadvantages in this method compared with the traditional shape optimization technique. One of biggest advantages are capability of handling topology as well as shape. This is what very few optimization techniques could do. Also the re-generation of the finite element model such as re-meshing is not necessary in this approach, which is often required in usual shape optimization Another advantage is its stable convergence. Since only sizing optimization (the sizes of microscopic holes) is performed, nonlinearity of the compliance and constraint with respect to the design variables is relatively small compared to the case in which location of boundary or nodal points are the design variables, convergence to final solution is very stable.

There are also several disadvantages in this optimization technique. One of biggest disadvantages can be computational time. Since the design domain need to be divided into relatively small areas, even compared with the mesh required in the usual finite element analysis, the computational time for just one analysis is relatively large. Moreover, there are as many design variables as that of the number of element times 3. This is huge number of design variables compared to traditional optimization. Second disadvantage is the incapability to handle other constraints, such as displacement constraint or constraints on sizes of local stress. Sometimes the manufacturability or eigenvalues have importances in the mechanical design. Also the mean compliance is sometimes less convenient as objective function in the engineering practice.

BIBLIOGRAPHY

[1] Rossow, M.P. and Taylor, J.E., A Finite Element Method for the Optimal Design of Variable Thickness Sheets, AIAA Journal Vol. 11 pp1566-1569, 1973

[2] Prasad, B. and Haftka, R.T., Optimal Structural Design with Plate Finite Elements, J. Struct. Div. ASCE 105, pp2367-2382, 1979

[3] Cheng, K.T. and Olhoff, N. An Investigation Concerning Optimal Design of Solid Elastic Plates. Int. J. Solids and Structures 17, pp 305-323, 1981

[4] Kohn, R. and Strang, G. Optimal Design and Relaxation of Variational Problems, Parts I, II, and III. Communications on Pure and Applied Mathematics, XXXIX, 113-137, 139-182, 353-378, 1986

[5] Suzuki, K., and Kikuchi, N., "Shape and Topology Optimization Using the Homogenization Method" , Computer Methods in Applied Mechanics and Engineering 93, pp 291-318, 1991

[6] Kohn, R.V.and Vogelius, M. [1] A New Model for Thin Plates with Rapidly Varying Thickness. Int. J. Solids Structures Vol 20 No 4 pp 333-350, 1984.

THE EFFECTS OF STRAIN RATE ON THE FAILURE ENERGY OF FIBRE REINFORCED COMPOSITES

O. Izeji Okoli[1] and G.F. Smith[2]

[1,2] Warwick Manufacturing Group, University of Warwick, Coventry CV4 7AL, UK ·

INTRODUCTION

Fibre reinforced composites (FRC) are still regarded as relatively new materials within the mechanical engineering field and often lack the detailed material property data associated with metals. In particular, the use of composites in safety critical applications, such as an automotive chassis cross member leads to uneasiness since the mechanical response in crash applications is not well understood. Nevertheless, since the sixties, composite materials have been a major factor in weight reduction of structural components in the aerospace and automotive industries [1].

Impact performance can in some way be measured by the energy absorbed or expended to failure of a material. Hence, establishing the rate effect on energy absorbtion is of paramount importance when designing for impact.

The relationship between energy absorption and strain rate has been reported in a number of papers [2, 3, 4, 5, 6]. The work of Kawata et al [2], reported an increase in energy with the logarithm of strain rate. It was however, not shown if this increase is linear, due to limited data. In addition, they ignored the problem of inertial response which greatly affects high speed data.

In crush tests of FRC tubes, it was reported [3, 4, 5, 6], that energy increases linearly with the logarithm of strain rate. The magnitude of the increase being less for graphite reinforced composites than for glass reinforced composite tubes.

The utilisation of FRC materials in crash applications, necessitates high speed testing of these materials. However, it has been shown elsewhere [7], that inertial response of test systems obscure data obtained at high strain rates causing inaccuracies in the analysis. It is therefore imperative to develop a technique to obtain high speed data which overcomes the problems attributed to the inertial response.

In the present study, tensile, shear and 3-point bend tests were conducted on a glass/epoxy laminate with woven reinforcement at increasing rates of strain to ascertain the relationship between energy to failure and strain rate.

EXPERIMENTAL WORK

The materials tested were 3mm thick woven glass/epoxy Tufnol 10G/40[a] composite laminates. The composite had a fibre weight fraction of 70% with 18 layers of glass. The apparatus and procedure used to obtain the tensile and shear properties have been described in a previous paper [7].

3 - Point Bend Test

3-Point bend tests were performed using 3 mm thick Tufnol 10G/40 laminated composite plates cut 80 x 15 mm. The tests were conducted at cross-head rates of 1, 10, 100, 200, 300, 400, and 500 mm/min on an Instron 4500 materials testing machine.

Instrumented Impact Test

Instrumented impact tests were performed using an ICI Instrumented impact tester to measure the impact flexural properties of 3mm thick Tufnol grade 10G/40 glass/epoxy laminates, cut 80mm by 15mm. Tests were carried out at 2 and 4m/s.

RESULTS AND DISCUSSION

Effects of Strain Rate on Energy Absorption

The energy to failure of the woven (Tufnol) laminates obtained at different strain rates is presented in Table 1. Figure 1 shows the variation of expended energy with the log of strain rate. The relationship is linear, with considerable scatter in the data. This linear tendency was also reported by Thornton et al [5]. Expended energy was found to increase by 17% per decade increase in the log of strain rate. The tendency for energy to increase as the strain rate is increased, can be attributed to the failure modes of the composite laminates since at a higher test speed, matrix yielding increases, that is, a greater part is played by the matrix in the fracture process thus, more energy is expended during fracture.

The shear energy to yield of the woven (Tufnol) laminates obtained at different strain rates is presented in Table 2, whilst Figure 2 shows the variation of shear energy to yield with the log of strain rate. The relationship has a linear tendency, with considerable scatter in the data. Shear energy was found to increase by 5.9% per decade increase in the log of strain rate. For the same reasons as before with failure in this laminate, an increase in strain rate brought about greater yielding of matrix. This results in bunch fibre pull-out, which in turn increases shear energy to failure.

---

[a]Tufnol Birmingham, Birmingham B42 2TB, U.K.

The flexural energy to yield of the woven (Tufnol) laminates obtained at different strain rates was presented in Table 3 and the variation of flexural energy to yield with the log of strain rate in Figure 3. The relationship has a linear tendency, with some scatter in the data. Flexural energy was found to increase by 8.5% per decade increase in the log of strain rate.

Since the current work has been investigating the effects of strain rate on energy absorption, it was deemed invaluable to try to verify it by extrapolating the flexural energy released in the low speed 3-point bend tests. In this way, the flexural energy could be estimated for a high speed 3-point bend test.

A summary of the material property data obtained from impact 3-point bend tests conducted at 2 and 4 m/s are presented in Table 4. However, on extrapolation to the log of the strain rate (28.8 /s) corresponding to an impact velocity of 4 m/s the estimated energy was found to be 2.813 J, compared with a value of 4.38 J, obtained from actual tests at 4 m/s. Thus, the extrapolated Figure was 64.22% of the actual value. That is, a factor of 1.557 is needed to raise the extrapolated value to the actual value. Extrapolating to the log of the strain rate (14.4 /s) corresponding to an impact velocity of 2 m/s, resulted in an estimated energy of 2.758 J. When compared with a value of 4.03 J, obtained from actual tests at 2 m/s, the extrapolated Figure was 68.44% of the actual value. That is, a similar factor of 1.461 is needed to raise the extrapolated value to the actual value. The foregoing suggests that if a factor of 1.5 is used on the extrapolated values, an agreeable estimate of the actual test energy can be obtained.

CONCLUSION

The effects of strain rate on expended energy were studied for woven glass (Tufnol) laminate. This laminate saw an increase in tensile, shear and flexural energy of 17%, 5.9% and 8.5% respectively, per decade increase in log of strain rate.

It was found that by multiplying the flexural energy obtained from the extrapolation of low strain rate values by a factor of 1.5, an approximation of the high speed test values were obtained. This implies that energy absorbed under impact in structural woven glass laminates may be estimated by the design engineer using such a factor.

REFERENCES

1.   Torres, M., "Development of Composite Material Helicopter Structures." *Proc. 37th Annual National Forum of the American Helicopter Society*, pp. 421-436 (1981).

2.   Kawata, K., Hondo, A., et al, "Dynamic Behaviour Analysis of Composite Materials." *Proc. Japan - U.S conference on Composite Materials*, ed. K. Kawata and T. Akasaka (Japan Soc. for Composite Materials, Tokyo), pp. 2-

11 (1981).

3.   Thornton, P.H., "Energy Absorption in Composite Structures." *J. Composite Materials,* **13**, pp. 247-262 (1979).

4.   Thornton, P.H., Jeryan, R.A., "Crash Energy Management in Composite Automotive Structures." *Int. J. Impact Engng.* **7**, No. 2, pp. 167-180 (1988).

5.   Thornton, P.H., Harwood, J.J., Beardmore, P., "Fibre-Reinforced Plastic Composites for Energy Absorption Purposes." *Composite Science and Technology,* **24**, pp. 275-298 (1985).

6.   Thornton, P.H., "The Crush of Fibre-Reinforced Plastics." *Handbook of Ceramics and Composites: Synthesis and Properties*, N.P. Cheremisinoff (ed.), Marcel Dekker, Inc, **1**, pp. 307-337 (1990).

7.   Okoli, O.I., Smith, G.F., "Overcoming Inertial Problems in the High Strain Rate Testing of a Glass/Epoxy Composite." *Proceedings of Society of Plastics Engineers Annual Technical Conference, Advanced Polymer Composites Div.,* **2**, pp. 2998-3002 (1995).

Cross-Head Rate [mm/min]	1	5	10	50	600	6000
Energy to Failure [J]	15.76	18.12	15.13	18.92	22.09	26.71
Log of Strain Rate [/s]	-3.9739	-3.2321	-2.9622	-2.2569	-1.4407	-0.5513

Table 1   Energy to Failure of Tufnol Grade 10G/40 laminates at different Strain Rates.

Cross-Head Rate [mm/min]	0.5	1.0	5.0	10.0	50.0
Shear Energy to Yield $*10^{-3}$ [J]	9.883	10.920	11.520	9.838	12.400
Log of Strain Rate [/s]	-3.7215	-3.6529	-3.0101	-2.4685	-2.1079

Table 2   Shear Energy to Yield of Tufnol Grade 10G/40 laminates at different Strain Rates.

Cross-Head Rate [mm/min]	1	10	100	200	300	400	500
Flexural Energy to Yield [J]	1.765	2.122	2.166	2.169	2.209	2.411	2.313
Log of Strain Rate [/s]	-3.9208	-2.9208	-1.9208	-1.1698	-1.4437	-1.3188	-1.2218

Table 3 Flexural Energy to Yield of Tufnol Grade 10G/40 laminates at different Strain Rates.

Peak Load	Break Load	Gradient	Energy to Peak	Energy to Break	Velocity	Relative Stiffness
[N]	[N]	[Nmm]	[J]	[J]	[m/s]	[GPa]
1306.65	1306.65	269.15	3.95	4.03	2.38	20.768
1379.70	1347.00	247.20	4.20	4.38	3.94	19.075

Table 4 A summary of the material property data obtained from impact 3-point bend tests conducted at 2 and 4 m/s.
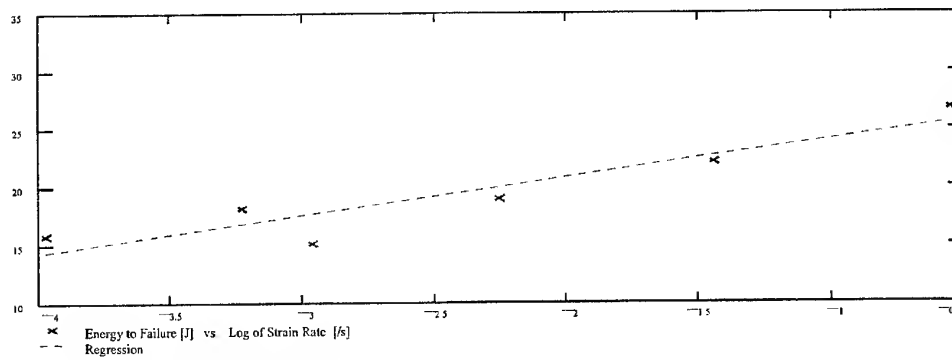
Figure 1   Energy to failure of Tufnol Grade 10G/40 laminates vs. the log of Strain Rate
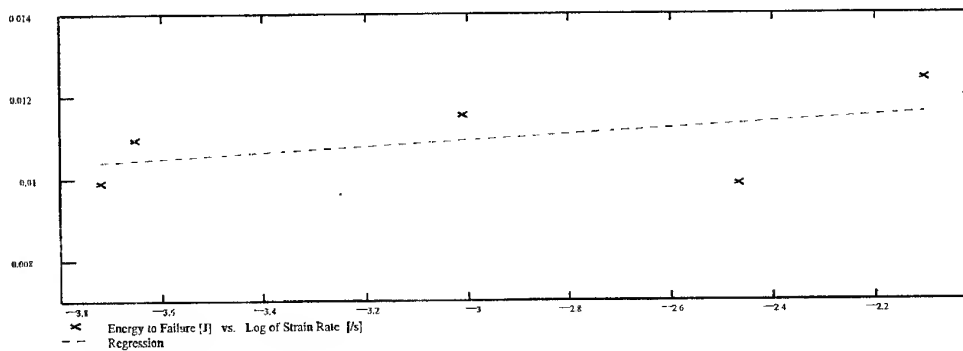
Figure 2   Shear Energy to yield of Tufnol Grade 10G/40 laminates vs. Log of Strain Rate
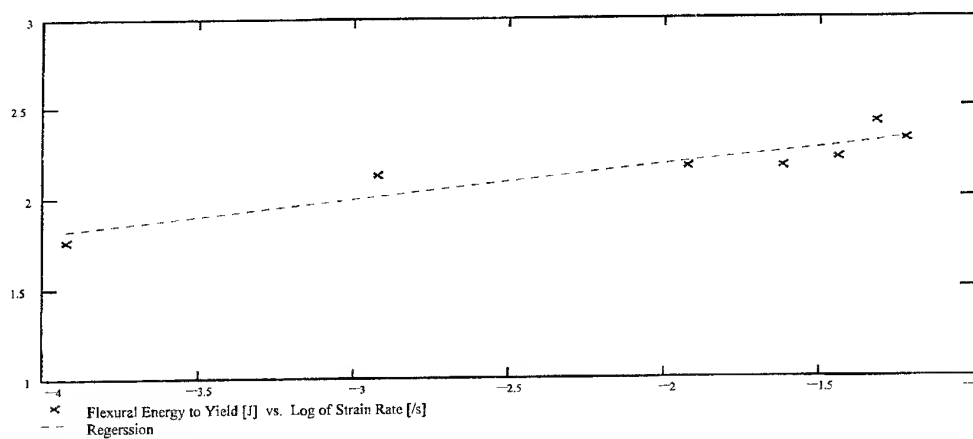
Figure 3   Flexural Energy to yield vs. Log of Strain Rate.

RESIDUAL STRESSES IN CSM/VINYL ESTER RESIN LAMINATES DUE TO POST-CURE SHRINKAGE

J F Oosthuizen[1] and M A Stone[2]

[1] Department of Mechanical Engineering, Technikon Free State,
   Private Bag X20539, Bloemfontein, 9300, South Africa
[2] Reinforced Plastics/Composites Facility, School of Mechanical Engineering,
   University of the Witwatersrand

ABSTRACT

In the design of glass reinforced plastic vessels for the chemical industry it should be recognised that the matrix can undergo significant chemical shrinkage during elevated temperature post-curing. If this shrinkage is restrained from occurring freely then residual stresses can be set up. These can quite easily exceed the levels of stress or strain allowed for by accepted design codes and are sufficient to promote environmentally assisted cracking in certain operating environments. Furthermore, in many cases the residual stresses will be significantly larger than the stresses associated with mechanical and thermal loading. This work provides some experimental results for this important type of stress. Post-cure shrinkage strain results are presented for castings of two vinyl ester resin types, flat CSM laminates and for thick walled tubes. The results for the tubes are compared to values predicted by commercial finite element software and by the use of the Rayleigh-Ritz method. Correlation between the predicted and measured values is shown to be inconsistent and possible reasons for this are explored.

INTRODUCTION

Glass reinforced plastic (GRP) is the material of choice for the manufacture of many items of chemical plant equipment. One of the major benefits of GRP is its ability to resist degradation in aggressive chemical environments. However, in order for this ability to be properly realised tensile stresses in the exposed material must be kept low to avoid possible environmentally assisted cracking. This is well recognised by codes of practice for the design of GRP equipment, see for example [1-3], which ensure specification of geometries leading to low stresses in response to mechanical loadings. However, other sources of stress may also be important, e.g. thermal, process induced. It has been shown that, when polyester and vinyl ester resins, typical of those used in process plant applications, are subject to elevated temperature post-cure after room temperature polymerisation, significant chemical shrinkage can occur [4]. Because this shrinkage occurs with the matrix already gelled, any restraint can give rise to large residual stresses. In particular, tensile surface stresses of sufficient magnitude to promote environmentally assisted cracking in many environments can be readily induced [4,5]. Although these shrinkage residual stresses are clearly important to designers of chemical process equipment, only limited experimental work appears to have been carried out to date. The aim of this work is to present experimental results for the shrinkage strains of typical materials and also for tubes of practical dimension. These results are compared to theoretical predictions made using the finite element method and the Rayleigh-Ritz method.

POST-CURE SHRINKAGE OF VINYL ESTER RESIN

Laboratory tests were carried out on CoRezyn® VE 8300 and DION 9100 vinyl ester resin castings. The castings were prepared and cured at ambient conditions for 24 and 48 hours respectively before attaching two strain gauges to the sides of each of the test pieces. The castings were then placed in an oven and heated gradually to a maximum temperature of 96°C during which the strains due to thermal expansion and chemical shrinkage and the oven temperature were recorded.

Results and discussion

The curves, *CC1* and *CC2*, shown in Figures 1 & 2, represent the strains recorded during the heating and cooling cycles. It can be seen that a maximum strain of 2970με and 1590με was attained at threshold temperatures of 72°C and 51°C for *CC1* and *CC2* respectively, where-after the test pieces underwent contractions due to the completion of the chemical curing process. The strains decreased to a constant value of 2140με at a temperature of 96°C for *CC1*, and 550με for *CC2* at a temperature of 95°C before the castings were allowed to cool.
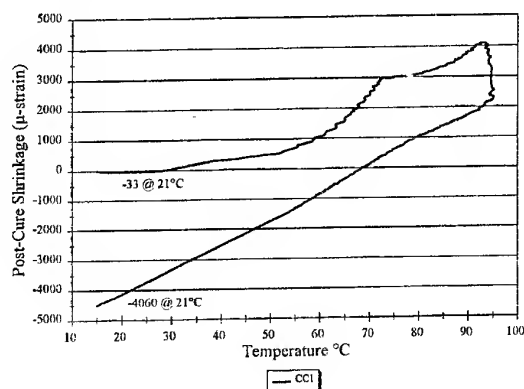
Fig. 1 Strain vs. Temperature for Clear Cast CoRezyn® VE 8300
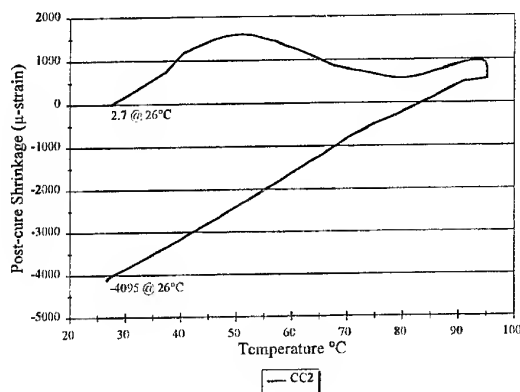
Fig. 2 Strain vs. Temperature for Clear Cast DION 9100

During the cooling period the strains decreased by magnitudes of -6652με at a temperature of 15°C for *CC1* and -4645με at a temperature of 26°C for *CC2* to obtain final shrinkage strains of -4511με and -4095με for *CC1* and *CC2* respectively. A reference temperature of 21°C was taken for *CC1* which gives a post-cure shrinkage of -4027με for CoRezyn® VE 8300. It can be seen that the two vinyl ester resins have post-cure shrinkage's in the order of -4000με. This is a clear indication that should the resin be reinforced by a material such as chopped strand mat (CSM) or woven roving mat or filaments (WR), high shear forces/stresses would be created along the fibre length of the reinforcement or high bulk stresses could be induced by restraint on free shrinkage.

POST-CURE SHRINKAGE OF CSM/VINYL ESTER TUBE

Tests were carried out on a tube manufactured from CoRezyn® VE 8300/CSM with an internal diameter of 40 mm and a wall thickness of 11 mm and a DION 9100/CSM tube with an internal diameter of 50 mm and a wall thickness of 13.5 mm and 240 mm long. During manufacturing care was taken to minimise steep temperature gradients due to exotherm. After curing strain gauges were attached to each of the tubes to measure longitudinal and hoop strains on the inner and outer surfaces and radial and hoop strains on the end of the tubes. The tubes were then placed in an oven and heated gradually to a maximum temperature of 96°C during which the strains resulting from thermal expansion and chemical shrinkage were recorded.

Results and discussion

Figures 3 and 4 show some of the strains recorded during the post-curing process. The CoRezyn® VE 8300/CSM tube expanded due to increase in temperature until approximately 63°C where-after the magnitude of the chemical shrinkage was greater than the thermal expansion. The tube was maintained at 96°C for 2 hours and then cooled to room temperature of 15°C. The shrinkage strains measured at reference temperatures of 21°C for the CoRezyn® VE 8300/CSM tube and 26°C for the DION 9100/CSM tube are given in Table 1. The shrinkage strains of the CoRezyn® VE 8300/CSM tube are in general of equal magnitude, except the radial shrinkage which is approximately of the same magnitude

366

as that of the resin casting. This could be expected since the tube is matrix dominated in the radial direction.

The DION 9100/CSM tube expanded as a result of the increase in temperature until approximately 50°C at which post-cure shrinkage initiated. The tube was maintained at 95°C for 2½ hours and then cooled to room temperature of 26°C. The results show that the hoop shrinkage strain of the inner surface is 21.8% greater than on the outer surface and the longitudinal shrinkage strain on the inner surface is 27.3% greater than on the outer surface, the reason being that a surface tissue is used as an initial layer during construction resulting in the inner surface having a higher resin content.
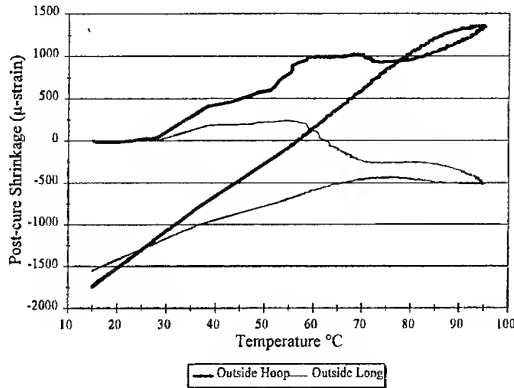
Fig. 3 Longitudinal & Hoop Strains vs. Temperature for CoRezyn® VE 8300/CSM tube on outside surface
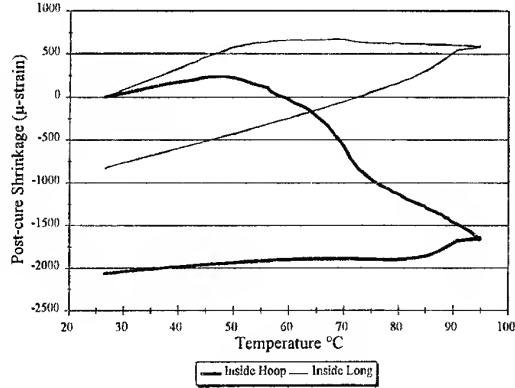
Fig. 4 Longitudinal & Hoop Strains vs. Temperature for DION 9100/CSM tube on inside surface

The diameter to wall thickness ratio of both tubes are approximately the same, i.e. 3.63 for the CoRezyn® VE 8300/CSM tube and 3.7 for the DION 9100/CSM tube, therefore the results are comparable. However, the only strains that are similar in magnitude, for the tests presented in this paper, are the values for the hoop strains on the outside surfaces of the two pipes.

Test Piece	Gauge Position & Direction	Strain Measured x 10^{-6}
CoRezyn® VE 8300/CSM tube @ 21°C	Outside Longitudinal (ε_{oy})	-1393
	Outside Hoop (ε_{oz})	-1473
	Inside Longitudinal (ε_{iy})	-1708
	Inside Hoop (ε_{iz})	-541
	Side Radial (ε_{sx})	-4574
	Side Hoop (ε_{sz})	-1408
DION 9100/CSM tube @ 26 °C	Outside Longitudinal (ε_{oy})	-653
	Outside Hoop (ε_{oz})	-1695
	Inside Longitudinal (ε_{iy})	-831
	Inside Hoop (ε_{iz})	-2065

Table 1. Shrinkage Strains of the CoRezyn® VE 8300/CSM and DION 9100/CSM tubes

POST-CURE SHRINKAGE OF VINYL ESTER/CSM PLATE

A DION 9100/CSM plate of 5.7 mm thick was fabricated under the same conditions as the DION 9100/CSM tube. Strain gauges were attached to the smooth resin rich (inner) surface and the rough (outer) surface to measure the post-cure shrinkage strains. The plate was post-cured at a temperature of 95°C for 2½ hours and then cooled to room temperature of 26°C.

367
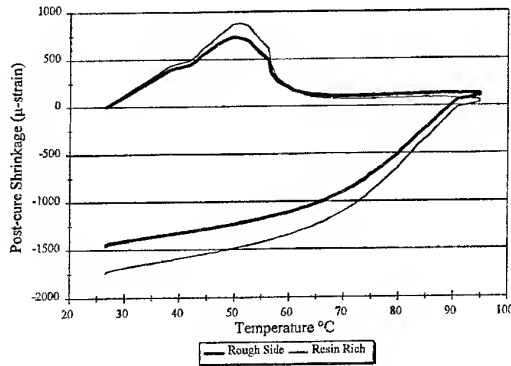
Fig. 5 Post-cure shrinkage Strains vs.
Temperature for DION 9100/CSM plate

Gauge Position	Strain Measured x 10^{-6}
"Inner" resin rich surface	-1730
"Outer" surface	-1445

Table 2. Shrinkage Strains of the DION 9100/CSM plate

Results and discussion

Figure 5 shows the strains recorded during the post-curing process. The plate expanded due to the increase in temperature until approximately 50°C where-after post-cure shrinkage initiated. The results, given in Table 2, indicate that the post-cure shrinkage strains obtained for the two surfaces differ slightly in magnitude, i.e. the "inner" surface shrinkage is marginally greater than the "outer" surface. This could be as a result of the "inner" surface being richer in resin (a surface tissue was used) and also because of finite length effects.

COMPARISON OF PREDICTED AND EXPERIMENTAL RESULTS

Results for the two tubes were predicted by finite element analysis (using Algor FEM software with axisymmetric orthotropic elements) and by the Rayleigh-Ritz method (as described in [5]). The material elastic properties were taken from [6] and the shrinkages determined according to the methods laid out in [5]. The relevant properties, Young's Modulus (E), Poisson's ratio (v) and the free post-cure shrinkage (s), follow:

Material property	DION 9100/CSM laminate	CoRezyn® VE 8300/CSM laminate
E_a	10780 MPa	10780 MPa
E_t	10780 MPa	10780 MPa
E_r	6028 MPa	6028 MPa
v_{at}	0.315	0.315
v_{ar}	0.34	0.34
v_{tr}	0.34	0.34
$s_a = s_t$	1529 µε	1505 µε
s_r	4091 µε	4027 µε

Table 3. Material properties of CoRezyn® VE 8300/CSM and DION 9100/CSM laminates

where subscripts a, r and t indicate the axial, radial and tangential directions respectively. Table 4 shows the experimental and predicted results.

Correlation between the FEM and Rayleigh-Ritz results is seen to be good, with the differences arising from the fact that the Rayleigh-Ritz method does not take finite length effects into account.

For the CoRezyn® VE 8300/CSM tube average value of experimental longitudinal strain, i.e. -1550 µε, compares favourably with both the FEM and Rayleigh-Ritz results. Both methods are seen to

368

overestimate the measured hoop strains at the inside and outside walls of the tube. This could possibly suggest alleviation of hoop strain by non-linear/time dependent material behaviour. Nevertheless, the correlation can be considered reasonable given the many variables over which one has limited control during manufacture. For the second tube, the FEM and Rayleigh-Ritz methods again predict similar strain values.

Test Piece	Strain location	Experimental $\times 10^{-6}$	FEM $\times 10^{-6}$	R-R method $\times 10^{-6}$
CoRezyn® VE 8300/CSM tube	Outside Longitudinal (ε_{oy})	-1393	-1489	-1505
	Outside Hoop (ε_{oz})	-1473	-1948	-1972
	Inside Longitudinal (ε_{iy})	-1708	-1533	-1505
	Inside Hoop (ε_{iz})	-541	-843	-881
DION 9100/CSM tube	Outside Longitudinal (ε_{oy})	-653	-1523	-1529
	Outside Hoop (ε_{oz})	-1695	-1980	-1998
	Inside Longitudinal (ε_{iy})	-831	-1523	-1529
	Inside Hoop (ε_{iz})	-2065	-880	-906

Table 4. Comparison of experimental and predicted results

However, correlation with the experimental values is poor. While the measured values cannot be immediately discarded, it would appear that the experimental data may not be representative. In particular, the average longitudinal strain, i.e. 742 $\mu\varepsilon$, is less than half of the shrinkage strain measured on the flat plate. This could suggest that some strain alleviation took place but then one would expect much smaller hoop strains as well. It is therefore recommended that the results for the second experiment not be taken as representative at this stage. It could be, however, that they indicate behaviour not currently understood theoretically and from this point of view they must be considered of some value.

The poor correlation of the results for the DION 9100/CSM tube suggests that further experiments need to be carried out. Only once more experimental data exists will one be able to sensibly judge the applicability of the theory for the purpose of design. At present one can reasonably suggest that any theoretical predictions aimed at assessing the real stresses in a practical structure should be backed up by experiment.

CONCLUSION

This work has allowed a number of factors which may effect they extent of shrinkage occurring during and elevated temperature post-cure. These include
- time required to manufacture the component,
- time interval between the lay-up of individual layers,
- variation in ambient conditions at which the components are manufactured, i.e. temperature and humidity,
- variations in glass mat thickness of individual layers due to the manufacturing process of the glass mat, specifically of the chopped strand mat,
- temperature gradients, resulting from the exothermic reaction, attained during the manufacturing process, and
- the time interval between the completion of the component and the attachment of the strain gauges and obtaining the first strain reading.

The shrinkage results show that reasonably large strains can readily be induced during post-curing. Restraint on this shrinkage can induce appreciable stresses. The comparison of the theoretical predictions with experiment was reasonable for the CoRezyn® VE 8300/CSM tube but poor for the DION 9100/CSM tube. Given that there are many important process variables that are difficult to control in practice, it is recommended that more experiments be undertaken to properly assess the theory. Only once such experiments have been undertaken can the limitations of the theory be assessed and reliable design approaches recommended.

369

REFERENCES

[1]   Specification for Design and Construction of Vessels and Tanks in Reinforced Plastics, BS 4994-1987, British Standards Institution, 1987.

[2]   Reinforced Thermoset Plastic Corrosion Resistant Equipment, ASME/ ANSI RTP-1-1989, The American Society of Mechanical Engineers, 1989.

[3]   Canadian Standard for FRP Corrosion Resistant Equipment, CGSB41G22, 1990.

[4]   Stone M.A., Schwartz I.F. and Chandler H.D., "Residual stresses arising from partial in-service post-cure of GRP structures." *Composites,* Vol. 25, pp 177-181 (1994).

[5]   Stone M.A., Schwartz I.F. and Chandler H.D., "Residual stresses associated with post-cure shrinkage in GRP tubes.", submitted for publication to Composites Science and Technology, 1995.

[6]   Kitching R, Tan A L and Abu-Mansour T M N, "The Influence of Through Thickness Properties on Glass Reinforced Plastic Laminated Structures", *Composite Structures* 2, pp 105-151 (1984).

OPTIMAL DESIGN OF AND WITH COMPOSITES

PAULI PEDERSEN

Department of Solid Mechanics
Technical University of Denmark, 2800 Lyngby, Denmark

INTRODUCTION

In the science of composites the primary problems of manufacturing and of strength estimation continue to be of major importance. From an early stage the natural wish to do things better and at the extreme to optimize these materials and their use has also created interest among researchers with a primary interest in optimal design.

The intention of this short presentation is to give a picture of the work on material optimization performed at the Technical University of Denmark and initiated about 10 years ago. Starting out with laminate design for optimal stiffness the research is now more in the direction of general material design with an emphasis on parametrization, on non−linear influences and on micromechanical modelling and manufacturing.

Effective analysis and analytical sensitivity analysis give a good background for the performed optimizations. We shall therefore firstly report some of the essential tools.

ANALYSIS OF NON−LINEAR, ANISOTROPIC ELASTICITY

For anisotropic elasticity, rotational transformations are of vital importance and the presentation will be based on contracted notations for stresses, strains, modulus etc. that transforms by orthonormal matrices. As these simple transformations are not well known we shall here give the results, and for a detailed discussion refer to Pedersen (1995). Orthonormal transformations of stresses and strains are obtained by the definitions

$$\{\sigma\}^T := \left\{\sigma_{11},\ \sigma_{22},\ \sqrt{2}\,\sigma_{12}\right\}\ ,\quad \{\epsilon\}^T := \left\{\epsilon_{11},\ \epsilon_{22},\ \sqrt{2}\,\epsilon_{12}\right\} \tag{1}$$

and the orthogonal matrix [T] that transforms second order tensors between two Cartesian coordinate systems is

$$[T] := \frac{1}{2}\begin{bmatrix} 1+c_2\ ,\ 1-c_2\ ,\ \sqrt{2}\,s_2 \\ 1-c_2\ ,\ 1+c_2\ ,\ -\sqrt{2}\,s_2 \\ -\sqrt{2}\,s_2\ ,\ \sqrt{2}\,s_2\ ,\ 2c_2 \end{bmatrix}\ ,\quad \begin{array}{l} c_2 := \cos(2\gamma)\ ,\ s_2 := \sin(2\gamma) \\ c_4 := \cos(4\gamma)\ ,\ s_4 := \sin(2\gamma) \end{array} \tag{2}$$

The tensor description of the 2D−constitutive behaviour is given by $\sigma_{ij} = C_{ijk\ell}\epsilon_{k\ell} = C\alpha_{ijk\ell}\epsilon_{k\ell}$ or in matrix notation by

$$\{\sigma\} = C\begin{bmatrix} \alpha_{1111} & , & \alpha_{1122} & , & \sqrt{2}\,\alpha_{1112} \\ \alpha_{1122} & , & \alpha_{2222} & , & \sqrt{2}\,\alpha_{2212} \\ \sqrt{2}\,\alpha_{1112} & , & \sqrt{2}\,\alpha_{2212} & , & 2\alpha_{1212} \end{bmatrix}\{\epsilon\} = C[\alpha]\{\epsilon\} \tag{3}$$

Note, that matrix $[\alpha]$ has an invariant trace, which is not the case in traditional matrix formulations. By also representing the $[\alpha]$ matrix in vector form with $\sqrt{2}$ factors for the off−diagonal elements.

$$\{\alpha\}^T := \left\{\alpha_{1111}, \alpha_{2222}, 2\alpha_{1212}, \sqrt{2}\,\alpha_{1122}, 2\alpha_{1112}, 2\alpha_{2212}\right\} \tag{4}$$

we can write the induced transformation of the constitutive relations simply by

$$\{\alpha\}_y = [R]\{\alpha\}_x , \quad \{\alpha\}_x = [R]^T\{\alpha\}_y$$

$$[R] = \frac{1}{8}\cdot\begin{bmatrix} 3 + 4c_2 + c_4 & , & 3 - 4c_2 + c_4 & , & 2 - 2c_4 & , & \sqrt{2} - \sqrt{2}c_4 & , & 4s_2 + 2s_4 & , & 4s_2 - 2s_4 \\ 3 - 4c_2 + c_4 & , & 3 + 4c_2 + c_4 & , & 2 - 2c_4 & , & \sqrt{2} - \sqrt{2}c_4 & , & -4s_2 + 2s_4 & , & -4s_2 - 2s_4 \\ 2 - 2c_4 & , & 2 - 2c_4 & , & 4 + 4c_4 & , & -2\sqrt{2} + 2\sqrt{2}c_4 & , & -4s_4 & , & 4s_4 \\ \sqrt{2} - \sqrt{2}c_4 & , & \sqrt{2} - \sqrt{2}c_4 & , & -\sqrt{2} + 2\sqrt{2}c_4 & , & 6 + 2c_4 & , & -2\sqrt{2}s_4 & , & 2\sqrt{2}s_4 \\ -4s_2 - 2s_4 & , & 4s_2 - 2s_4 & , & 4s_4 & , & 2\sqrt{2}s_4 & , & 4c_2 + 4c_4 & , & 4c_2 - 4c_4 \\ -4s_2 + 2s_4 & , & 4s_2 + 2s_4 & , & -4s_4 & , & -2\sqrt{2}s_4 & , & 4c_2 - 4c_4 & , & 4c_2 + 4c_4 \end{bmatrix}$$

$$\tag{5}$$

For two dimensional, orthotropic materials we can, in terms of the engineering constants E_L, E_T, v_{LT} and G_{LT}, write the modulus matrix $[C_0]$ and the compliance matrix $[C_0]^{-1}$ as

$$[C_0] = \frac{E_L}{\alpha_0}\begin{bmatrix} 1 & ; & \alpha_4 - \alpha_3 & ; & 0 \\ \alpha_4 - \alpha_3 & ; & 1 - 2\alpha_2 & ; & 0 \\ 0 & ; & 0 & ; & 1 - \alpha_2 - 3\alpha_3 - \alpha_4 \end{bmatrix}$$

$$\alpha_0 := 1 - v_{LT}^2 E_T/E_L$$

$$\alpha_2 := \tfrac{1}{2}(1 - E_T/E_L)$$

$$\alpha_3 := \tfrac{1}{8}(1 + (1 - 2v_{LT})E_T/E_L - 4\alpha_0 G_{LT}/E_L)$$

$$\alpha_4 := \tfrac{1}{8}(1 + (1 + 6v_{LT})E_T/E_L - 4\alpha_0 G_{LT}/E_L)$$

$$\tag{6}$$

$$[C_0]^{-1} = \frac{1}{E_L}\begin{bmatrix} 1 & ; & \beta_4 - \beta_3 & ; & 0 \\ \beta_4 - \beta_3 & ; & 1 - 2\beta_2 & ; & 0 \\ 0 & ; & 0 & ; & 1 - \beta_2 - 3\beta_3 - \beta_4 \end{bmatrix}$$

$$\beta_2 := \tfrac{1}{2}(1 - E_L/E_T)$$

$$\beta_3 := \tfrac{1}{8}(1 + E_L/E_T - E_L/G_{LT} + 2v_{LT})$$

$$\beta_4 := \tfrac{1}{8}(1 + E_L/E_T - E_L/G_{LT} - 6v_{LT})$$

372

For material optimization the following classification is important

A material has low shear stiffness (defined as a material with $\alpha_3 > 0$) as well as high shear compliance $(\beta_3 < 0)$ for

$$G_{LT} < \frac{E_L E_T}{E_L + (1 + 2\nu_{LT})E_T} \tag{7a}$$

Low shear stiffness $(\alpha_3 > 0)$ and low shear compliance $(\beta_3 > 0)$ for

$$\frac{E_L E_T}{E_L + (1 + 2\nu_{LT})E_T} < G_{LT} < \frac{E_L(E_L + E_T(1 - 2\nu_{LT}))}{4(E_L - \nu_{LT}^2 E_T)} \tag{7b}$$

while, lastly, high shear stiffness $(\alpha_3 < 0)$ and low shear compliance $(\beta_3 > 0)$ is the case for

$$\frac{E_L(E_L + E_T(1 - 2\nu_{LT}))}{4(E_L - \nu_{LT}^2 E_T)} < G_{LT} \tag{7c}$$

The detailed analysis that gives the characterizations (7) can be found in Cheng & Pedersen (1996).

In the 1D modelling of a power law for non−linear elasticity we have $\sigma = E\epsilon^p$. Using the 2D and 3D modelling with the energy based definition of the effective strain as

$$\{\sigma\} = E\epsilon_e^{p-1}[\alpha]\{\epsilon\} \quad ; \quad \epsilon_e^2 := \{\epsilon\}^T[\alpha]\{\epsilon\} \rightarrow 2\epsilon_e d\epsilon_e = 2\{\epsilon\}^T[\alpha]\{d\epsilon\} \tag{8}$$

we obtain an energy density as for the 1D−case. In relation to our optimization studies and sensitivity analysis, the main result proven for 1D−, 2D− and 3D−problems is the relation

$$u^C = pu \tag{9}$$

This is a not too well known result, although commented already in Hill (1956). In words it says: the ratio between stress energy density u^C (complementary) and strain energy density u is the power p and thus independent of the actual energy density level. This holds for anisotropic as well as for isotropic cases.

LOCALIZED DETERMINATION OF SENSITIVITY RESULTS

Sensitivity analysis has a strong relation to research on optimal design but is in reality of much wider importance and applicability. Often the results are derived for specific models, and the generality is lost or at least not visible. When the quantity for which we

seek the sensitivity is related to a global energy quantity, we have results that can be calculated locally. These results are without reference to a specific model and are thus valid for one–, two– and three–dimensional models, for analytical calculations and for numerical models and are valid independent of the numerical method chosen, say finite difference, finite element, or more global Galerkin approaches. We shall concentrate on results for sensitivities of the strain energy U. For linear elasticity and design independent loads the result from Wasiutynski (1960) is

$$\frac{dU}{dh} = \left(\frac{\partial U}{\partial h}\right)_{\text{fixed strains}} + \frac{\partial U}{\partial \epsilon}\frac{\partial \epsilon}{\partial h} = -\left(\frac{\partial U}{\partial h}\right)_{\text{fixed strains}} \qquad (10)$$

where h is any design parameter and ϵ symbolized the whole strain field. With the result (9) we are able to extend the result (10) to cover also non–linear power–law elasticity and get

$$\frac{dU}{dh} = -\frac{1}{p}\left(\frac{\partial U}{\partial h}\right)_{\text{fixed strains}} \qquad (11)$$

If a design is divided into domains, i.e. $U = \Sigma\ U_j$, then (11) gives the localized determination of the sensitivity with a local design parameter h_j

$$\frac{dU}{dh} = -\frac{1}{p}\left(\frac{\partial U}{\partial h}\right)_{\text{fixed strains}} = -\frac{1}{p}\left(\frac{\partial U_j}{\partial h_j}\right)_{\text{fixed strains}} \qquad (12)$$

It is important to note that the local physical change in strain energy dU_j/dh_j is not easily determined.

OPTIMAL MATERIAL ORIENTATION

If our general design parameter h is taken to be the material orientation θ_j in the domain j then, with power–law elasticity and dead loads we have directly from (12)

$$dU/d\theta_j = -\frac{1}{p}V_j\left(\partial\bar{u}_j/\partial\theta_j\right)_{\text{fixed strains}} \qquad (13)$$

where $\bar{u}_j$ is the mean strain energy density in domain j with volume V_j. For a pointwize version of (13) $\bar{u}_j$ will directly be the strain energy density. For coupled plate/disc problems using traditional symbols from laminate analysis, the energy density per plate area $u_j t_j$ is for linear elasticity $(p = 1)$ given by

$$u_j t_j = \frac{1}{2}\left\{\epsilon^0\right\}^T[A]\left\{\epsilon^0\right\} + \left\{\epsilon^0\right\}^T[B]\{\kappa\} + \frac{1}{2}\{\kappa\}^T[D]\{\kappa\} \qquad (14)$$

with t_j denoting plate thickness, $\{\epsilon^0\}$, $[A]$ mid−surface strains and extensional stiffnesses; and $\{\kappa\}, [D], [B]$ curvatures, bending stiffnesses and coupling stiffnesses. Applying the result (13) we get

$$\frac{dU}{d\theta_j} = -a_j\left[\frac{1}{2}\{\epsilon^0\}^T\left[\frac{\partial A}{\partial\theta_j}\right]\{\epsilon^0\} + \{\epsilon^0\}^T\left[\frac{\partial B}{\partial\theta_j}\right]\{\kappa\} + \frac{1}{2}\{\kappa\}^T\left[\frac{\partial D}{\partial\theta_j}\right]\{\kappa\}\right] \quad (15)$$

with a_j being the domain area. Even for the fully coupled problems this result can be written

$$\frac{dU}{d\theta_j} = U_1\sin 2\theta_j + U_2\cos 2\theta_j + U_3\sin 4\theta_j + U_4\cos 4\theta_j \quad (16)$$

This follows from the fact that all the matrices $[A]$, $[B]$, and $[D]$ originate from the constitutive matrix $[C]$, which, as seen from (5), contains only the trigonometric functions included in eq. (16).

Before treating the specific and simplified problems it should be appreciated that, according to (16) we, in the general case, can find at most four different solutions to $dU/d\theta_j = 0$. This follows from rewriting $dU/d\theta_j$ as a fourth order polynomial. For orthotropic materials and models where only the cosine terms are involved, analytical solutions to $dU/d\theta_j = 0$ are obtainable. Such analytical results for simply supported plates in bending can be found in Bert (1977) and in Pedersen (1987). For the membrane problem, alignment of principal strain− , principal stress− and principal material directions is one of the main results. For discussions see Pedersen & Bendsøe (1995) and Cheng & Pedersen (1996).

In a recent paper by Hammer, Bendsøe, Lipton and Pedersen (1996) we have shown the advantage of parametrization by the so−called lamination parameters. These express the relation between the material parameters for the laminate and the laminate lay−up and are given as moments of the trigonometric functions that appear in the rotation formulas for stiffness matrices. These relations are given in a form suitable for optimization studies. The conditions for the laminate itself to be orthotropic can be stated directly in terms of the lamination parameters.

On a more or less heuristic basis, designs for optimal strength have commonly been taken to be designs where principal stress direction is aligned with material orthotropy direction. With a non−symmetric strength criterion like the Tsai−Wu criterion, such solutions can not be the optimal ones, because optimal stiffness design will be different from optimal strength design. The strength problem is a local problem and therefore

simple results from sensitivity analysis like (15) can not be expected. To solve the optimal design problem in a proper way, we have to use mathematical programming. The optimization problem formulated in words is: maximize a common load factor, subject to given strength constraints. Multiple layers, multiple loads, and multiple strength constraints are included in the formulation. Analytical sensitivity analysis, as shown in Hammer (1994), can still be carried through and the main difficulty is related to the existence of a large number of local optima. In a way this is to be expected. Different solutions to this problem includes strategies for choosing the initial design before mathematical programming is applied. A valuable alternative is to describe the design with global design parameter (orthogonal functions). This new approach is described in Pedersen & Hammer (1994).

OPTIMAL THICKNESS/DENSITY DISTRIBUTION

The sizing problem of optimal design for a thickness or density distribution has a long history, and for the most simple formulations the optimality criteria methods play a dominating role. We shall concentrate the present description on the material non—linear elastic problems. For the unconstrained optimization problem of orientational design, the necessary optimality criterion is zero gradients. For optimization problems with only a single constraint, an equally simple optimality criterion is given by constant ratio of the gradients. As an example, the optimality criterion is

$$\frac{\partial U}{\partial t_j} = A\frac{\partial V}{\partial t_j} \quad \text{for all} \quad j \tag{17}$$

if we want to minimize elastic energy U for given volume V. The thickness/density design parameter is denoted t_j for the domain j, and A is a constant. From this we get directly the well—known and intuitive criterion of constant energy density, equal to the mean energy density $\bar{u}$ (Wasiutynski (1960))

$$\bar{u}_j = \bar{u} \quad \text{for all} \quad j \tag{18}$$

We shall immediately see that the sensitivity result (12) will again result in the optimality criterion (18). From (12) follows (with t_j as design parameter):

$$\frac{\partial U}{\partial t_j} = -\frac{1}{p}\left(\frac{\partial U}{\partial t_j}\right)_{\text{fixed strain}} = -\frac{1}{p}\left(\frac{\partial U_j}{\partial t_j}\right)_{\text{fixed strain}} = -\frac{\bar{u}_j}{p}\left(\frac{\partial V_j}{\partial t_j}\right) \tag{19}$$

With uniform energy density (18), we get uniform effective strain, and then by (6) the same constitutive secant matrix in all domains (all points). Thus the optimal thickness

distribution is independent of the power p of the constitutive matrix. To state it in other terms: the optimal structure is equally loaded (in terms of strain energy density) at all points. We thus "bridge" the classical solutions of linear elasticity by Wasiutynski (1960) and of ideal plasticity by Prager and Shield (1967).

DETAILED MATERIAL DESIGN

The orientational design and the thickness design in fact show how to use given materials. From these studies extends a natural wish to design the material itself. A very up to date account for this active research area is given in the monograph by Bendsøe (1995). Here we shall discuss only the full parameter model (Bendsøe *et al.* 1994). Finally, we shall mention the solution of inverse homogenization problems, as in the papers by Sigmund (1994 and 1995).

We make use of a frame–independent description of cost and choose the trace $\left(\alpha_{1111} + \alpha_{2222} + 2\alpha_{1212}\right)C$ of the constitutive matrix. The strain energy density in the frame of the principal strains ϵ_I and ϵ_{II} is

$$u = \frac{1}{2}\left(\alpha_{1111}\epsilon_I^2 + \alpha_{2222}\epsilon_{II}^2 + 2\alpha_{1122}\epsilon_I\epsilon_{II}\right)C \tag{20}$$

This function does not depend on the value of α_{1212}, and as this non–negative parameter enters in the cost function, we can conclude that the parameter should have value zero. Moreover, it then follows that $\alpha_{1212} = \alpha_{1112} = \alpha_{2212} = 0$ because the constitutive matrix must be positive semi–definite. The parameter α_{1122} in (20) have no influence on the trace, so to maximize the strain energy density this parameter should be chosen as numerically large as possible and with the same sign as $\left(\epsilon_I\epsilon_{II}\right)$. Also this limit follows from the semi–definite restriction and we have

$$u = \frac{1}{2}\left(\alpha_{1111}\epsilon_I^2 + \alpha_{2222}\epsilon_{II}^2 + 2\sqrt{\alpha_{1111}\alpha_{2222}}\,|\epsilon_I\epsilon_{II}|\right)C = \frac{1}{2}\left(\sqrt{\alpha_{1111}}\,|\epsilon_I| + \sqrt{\alpha_{2222}}\,|\epsilon_{II}|\right)^2 C \tag{21}$$

The problem is reduced to that of finding the vector $\left(\sqrt{\alpha_{1111}}\,,\,\sqrt{\alpha_{2222}}\right)$ which maximizes u for given $\rho = \alpha_{1111} + \alpha_{2222}$, i.e. the problem of finding a positive vector of length $\sqrt{\rho}$ for which the inner product with the vector $\left(|\epsilon_I|\,,\,|\epsilon_{II}|\right)$ is maximal. The solution is unique and is the obvious one, namely

$$\alpha_{1111} = \rho\frac{\epsilon_I^2}{\epsilon_I^2 + \epsilon_{II}^2}\,,\,\alpha_{2222} = \rho\frac{\epsilon_{II}^2}{\epsilon_I^2 + \epsilon_{II}^2}\,,\,\alpha_{1122} = \rho\frac{\epsilon_I\epsilon_{II}}{\epsilon_I^2 + \epsilon_{II}^2} \tag{22}$$

377

The first reaction to this simple result is the immediate question about the existence of such a material. In fact this question goes beyond the present optimization and are similar to questions like: Can we find a material with negative Poisson's ratio? or generally: Can we find a material corresponding to a given constitutive matrix? The answers to all these questions are yes and the corresponding problem is here termed the inverse homogenization problem or the material identification problem. Sigmund (1994,1995) addresses this problem numerically in order to achieve any properties, while Milton and Cherkaev (1995) through analytical studies and construction of extreme material provides a theoretical basis for this affirmative answer. Like with most identification problems we can not expect a unique solution, but in fact this is an advantage because then it is possible to put priorities and/or penalties.

REFERENCES

Bendsøe, M.P. "Methods for the optimization of structural topology, shape and material". Springer Verlag, Berlin, 271p. (1995).

Bendsøe, M.P., Guedes, J.M., Haber, R.B., Pedersen, P. and Taylor, J.E. "An analytical model to predict optimal material properties in the context of optimal structural design". *J. Appl. Mech.* **61**, pp. 930–937 (1994).

Bert, C.W. "Optimal design of a composite–material plate to maximize its fundamental frequency". *J. Sound and Vibration* **50**, pp. 229–239 (1977).

Cheng, G. and Pedersen, P. "Sufficiency conditions for optimal design based on extremum principles of mechanics". *J. of the Mech. & Phys. of Solids* (to appear) (1996).

Hammer, V.B. "Strength optimization by fibre orientation". Solid Mechanics, Techn. Univ. of Denmark (in Danish) (1994).

Hammer, V.B., Bendsøe, M.P., Lipton, R. and Pedersen, P. "Parametrization in laminate design for optimal compliance". *Solids & Structures* (to appear) (1996).

Hill, R. "New Horizons ...". *J. of the Mech. & Phys. of Solids* **5**, pp. 66 (1956).

Milton, G.W. and Cherkaev, A.V. "Which elasticity tensors are realizable". *J. of Engineering Materials and Technology* **117**, pp. 483–493 (1995).

Pedersen, P. "On sensitivity analysis and optimal design of specially orthotropic laminates". *Eng. Opt.* **11**, pp. 305–316 (1987).

Pedersen, P. "Simple transformations by proper contracted forms – can we change the usual practice?". *Comm. in Num. Meth. in Eng.* **11**, pp. 821–829 (1995).

Pedersen, P. and Bendsøe, M.P. "On strain–stress fields resulting from optimal orientation". Proc. WCSMO–1, Goslar, Germany, Elsevier, pp. 243–249 (1996).

Pedersen, P. and Hammer, V.B. "On global design description for orientational strength optimization". Proc. ASME 'Advances in Design Optimization', DE–Vol. 69–2, pp. 221–224 (1994).

Prager, W. and Shield, R.T. "A general theory of optimal plastic design". *J. Appl. Mech.* **34**, pp. 184–186 (1967).

Sigmund, O. "Materials with prescribed constitutive parameters: An inverse homogenization problem". *Int. J. Solids Structures* **31**(17), pp. 2313–2329 (1994).

Sigmund, O. "Tayloring materials with prescribed elastic properties". *Mechanics of Materials* **20**(4), pp. 304–368 (1995).

Wasiutynski, Z. "On the congruency of the forming according to the minimum potential energy with that according to equal strength". *Bull. de L'Academie Polonaise des Sciences*, Serie des sciences technique, VIII, **6**, pp. 259–268 (1960).

TETRAGONAL ZIRCONIA - TUNGSTEN CARBIDE COMPOSITES MANUFACTURING, MICROSTRUCTURE AND PROPERTIES

Z. Pędzich[1], K. Haberko[1], M. Faryna[2]

[1] Department of Special Ceramics, University of Mining and Metallurgy, al. Mickiewicza 30, 30-059 Cracow, Poland
[2] Regional Laboratory for Physico-chemical Analyses and Structural Research, Jagiallonian University, Poland

INTRODUCTION

Tetragonal zirconia polycrystals (TZP) show excellent mechanical properties. But relatively low hardness of these materials limits their application. Hardness, wear resistance and fracture toughness of these materials can be effectively improved by incorporation into the TZP matrix hard carbide inclusions. Earlier investigations show that the silicon carbide whiskers [1], platelets [2] and isometric particle [3] additives lead to the better properties of the bodies. But densification of such materials under the pressure-less conditions was not sufficiently high. So, hot uniaxial or isostatic pressing had to be applied.

The aim of the present work was to prepare dense tungsten carbide particulate - TZP matrix composites by the pressure-less sintering. The nanometric Y-TZP powder had to be utilised. The powder of high sintering activity was manufactured by the coprecipitation - calcination technique [5]. It was demonstrated in our previous works [6, 7] that the Y-TZPs placed in a carbon bed and sintered in the argon atmosphere did not loose their good properties. Thermodynamic calculations [8] allowed us to state that under the potentially necessary sintering conditions reaction between ZrO_2 and WC could not result in the formation of any of the tungsten oxides. But the reaction (1)

$$ZrO_2 + 6WC = ZrC + 3W_2C + 2CO \qquad (1)$$
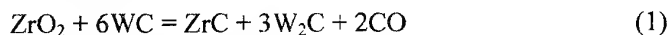
could proceed towards the right hand side provided the CO partial pressure would be lower than 0.95 atm at 1400°C and 5.20 atm at 1500°C. Another potential reaction considered was between zirconia and the carbon bed (2):

$$ZrO_2 + 3C = ZrC + 2CO \qquad (2)$$

In this case the maximum CO partial pressures below which formation of ZrC was expected to occur were 0.054 and 0.20 at 1400°C and 1500°C, respectively.

EXPERIMENTAL

As a matrix material the 2.8 mole % Y_2O_3 - 97.2 mole % ZrO_2 solid solution (2.8Y-TZP) was selected. The two tungsten carbide powders of different grain sizes were applied. Characteristics of all powders utilised in the present work are given in Table1.

Homogenisation of the oxide an carbide powders was performed by one hour attrition milling in ethyl alcohol using 2 mm Y-TZP balls as a grinding media. Carbide additives ranged from 10 to 30 vol. %. Dry powders with no lubricating additives were uniaxially pressed under 50 MPa and isostatically repressed under 350 MPa. By this procedure cylindrical samples of 23 mm diameter and 10 mm thickness and bars of 4×3 mm cross section and 45 mm length (after sintering) were prepared. The samples were placed in a carbon bed and sintered in the argon atmosphere at 1400 and 1500°C with the two hour soaking at each temperature. Sintering was performed in a furnace equipped with the tungsten heating elements.

Table 1. Characteristics of the starting powders.

Material	Phase Compositon	S [m²/g]	D$_{BET}$ [nm]	D$_{111}$ [nm]
2,8Y-ZrO$_2$	91 % tetragonal phase [9] 9 % monoclinic phase	51,9	19,1 ±0,2	18,4 ±0,2
WC-1	WC, traces W$_2$C and W, ~ 6 % C	0.23	1600 ±600	-
WC-2	WC, traces W$_2$C and W, ~ 6 % C	2,94	130 ±50	-

S - specific surface area measured by the BET method (Carlo Erba Sorpty 1750), $D_{BET}=6/S\bullet\rho$, where ρ is the physical powder density, D$_{111}$ - crystallite size determining by the X-ray line broadening

On the basis of the green sample sizes and weights relative densities of the green samples could be determined, assuming physical density of 2.8Y-TZP and WC 6.1 and 15.7 g/cm³, respectively as well as their proportion in a mixture,. The same physical densities were applied to measure by hydrostatic weighing densification of the sintered materials.

Standard X-ray diffraction was useful to find the phase composition of the near surface layers of a sample. Removal by polishing of about 100 mm thickness of a sample allowed us to study the phase composition of the bulk material.

Transverse and longitudinal ultrasonic wave propagation velocities were useful in the elastic modulus, modulus of rigidity and Poisson number determination. Vickers indentation was helpful in the hardness (1.96 N load) and fracture toughness (K$_{Ic}$, 98.1 N load) determination. In the latter case the Palmqvist crack model and the Niihara [11] equation were used. In some cases fracture toughness could be found by the single-edge notched beam where pre-notch of 1mm depth has been introduced using a 0,025 mm diamond saw. The support span was of 40 mm and the traverse shifting rate of 1 mm/min. Results were calculated according to ASTM E 399-1983 [12]. Four-point loading method was used to determine bending strength of the materials. Span of 20/40 mm was applied. Polished surfaces were thermally etched at 1350°C to reveal microstructure of the samples. Grain sizes and grain size distributions were found by the Saltykov method [13].

Wear resistance was tested according to the ASTM G 6585 method [14]. As an abrasive material SiC powder of 0.4 - 0.5 mm grain sizes introduced between a rubber wheel of 50 mm diameter and 15 mm width and the tested sample was applied. The wheel load was of 44 N. Volume of the removed material resulting from the 5000 revolutions of the wheel was taken as a measure of the material wear susceptibility. For the comparison purposes some other materials were tested by this method.

RESULTS

It was found that the green relative density of the compacts is the higher the higher is WC content in a mixture. It changes from 55% to 61% for the pure matrix powder and the composite powder of 30 vol.% WC additive, respectively. Higher densification reach the systems with the coarser carbide additive.

Fig.1 demonstrates that carbide inclusions hinder densification of the composites. The effect is the stronger the higher is concentration of the inclusions and the smaller is their grain size. This phenomenon agrees with the generally observed role played by the inert inclusions [3,15,16]. Nevertheless densifications obtained in this work at WC concentrations up to 20 vol.% are reasonably good.
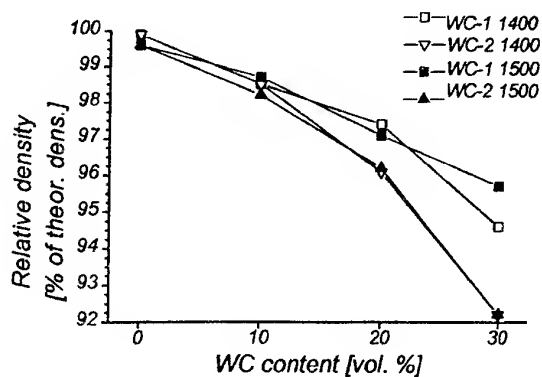
Fig. 1. Relative density vs. WC content
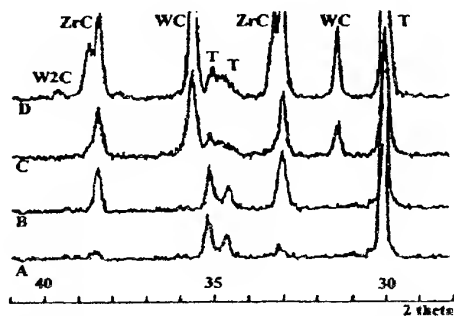
Fig. 2. X ray diffraction pattern of the pol-ished samples (~100 μm). A, B denote the TZP matrix, C, D composites TZP - 20% WC sintered at 1400 and 1500°C, respec-tivelly
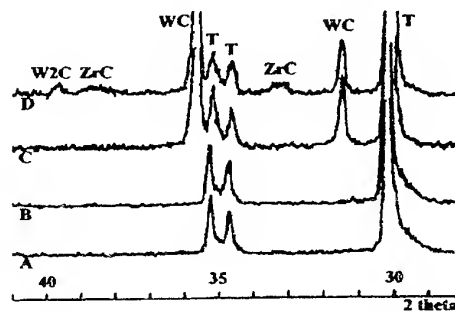
Fig. 3. X ray diffraction pattern of the *as recived* sample surfaces. The plot descrip-tion same as in Fig. 2.

Fig. 2 shows X-ray patterns of the pure matrix and composite with 20 vol.% WC-1 additive. The near surface layer was in this case removed. In the matrix only tetragonal phase is ob-served. But the composite material sintered at higher temperature reveals phases not introduced into the starting material; these are ZrC and W_2C. They undoubtedly result from the reaction (1). As it is demonstrated by the formation of ZrC at 1400°C (Fig.3) reaction (2) takes place at the sample surface being in the direct contact with the carbon bed. It indicates that CO partial pressure at 1400°C is lower than 0.054 atm. Under such conditions reaction (1) should also proceed at 1400°C. This is not the case plausibly because of the kinetic effect.

Hardness of the composites is higher than that of the pure matrix material (Table 2). Higher of the two applied temperatures and finer WC inclusions give better results. Most probably composites sintered at 1500°C are better densified although it does not come clearly from the plots in Fig.1. But we must realise that assessment of the sintered sample densification does not take into account the change of their true density due to some deoxidation of the sys-tems on the oxygen free heat treatment [7, 17,18]. Higher hardness of the samples with the finer inclusions can probably be attributed to their better consolidation with the matrix due to the reaction (1). This should be more advanced in case of the finer material. Presumably because of this strong link formation no decrease of the material strength (Fig.4) and fracture toughness occur (Table 2.). In a similar system SiC - TZP as high as 40% decrease of strength was ob-served [3].

Table 2. Machanical properties of the matrix and composites.

Material/ Sintering temperature	Young Modulus E, [GPa]	Modulus of Rigidigity G, [GPa]	Poisson Ratio ν	Vickers Hardness HV, [GPa]	Fracture Tougheness Indentation Method K_{Icl}, [MPam$^{0.5}$]	Fracture Tougheness Notched Beam Method K_{IcN}, [MPam$^{0.5}$]
osnowa 1400	217,4 ±1,7	83,2 ±0,3	0,307 ±0,002	14,7 ±0,5	6,8 ±0,6	-
1500	220,5 ±1,7	84,7 ±0,3	0,301 ±0,002	14,4 ±0,5	6,8 ±0,2	6,1 ±0,5
10WC-1 1400	232,6 ±2,1	89,8 ±0,3	0,295 ±0,002	14,2 ±1,3	6,1 ±0,2	-
1500	238,3 ±3,1	92,2 ±0,2	0,293 ±0,002	14,5 ±1,5	8,3 ±0,4	6,4 ±0,2
20WC-1 1400	255,0 ±2,5	99,6 ±0,2	0,280 ±0,002	13,0 ±0,5	7,3 ±0,7	-
1500	258,9 ±3,2	101,3 ±0,4	0,275 ±0,003	14,8 ±1,6	8,6 ±0,3	6,4 ±0,4
30WC-1 1400	263,4 ±1,8	104,2 ±0,2	0,264 ±0,002	11,8 ±0,8	8,6 ±1,1	-
1500	273,6 ±3,6	111,0 ±0,3	0,263 ±0.003	12,3 ±0,6	6,7 ±0,7	7,2 ±0,7
10WC-2 1400	238,7 ±2,5	92,2 ±0,5	0,295 ±0.003	16,8 ±1,8	6,2 ± 0,8	-
1500	240,4 ±2,4	93,1 ±0,2	0,292 ±0.002	17,0 ±1,1	6,7 ±0,8	7,8 ±0,5
20WC-2 1400	253,8 ±1,8	99,1 ±0,2	0,280 ±0,002	14,7 ±0,6	8,1 ±0,8	-
1500	258,6 ±2,9	100,5 ±0,4	0,279 ±0,003	16,8 ±0,7	7,3 ±1,5	7,4 ±0,4
30WC-2 1400	254,1 ±1,5	100,7 ±0,2	0,261 ±0,001	14,2 ±0,6	9,4 ±0,4	-
1500	259,7 ±4,5	102,8 ±0,3	0,264 ±0,004	16,7 ±1.1	7,5 ±0,5	7,7 ±0,4

± denotes the 95 % confidence interval.
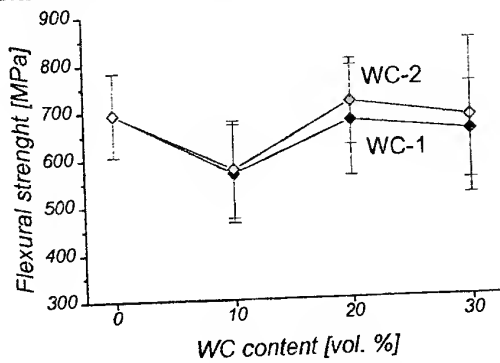
Fig. 4. Flexural strenght vs. WC content. Samples sintered at 1500°C.

The WC inclusions due to their lower coefficient of thermal expansion ($\alpha_{WC} = 5.2 \times 10^{-6}$ K^{-1}) than the TZP matrix ($\alpha_{TZP} = 11.0 \times 10^{-6}$ K^{-1}) lead to the creation of tensile stresses in the matrix during cooling of the sintered material. Their value assessed on the basis of the Taya et al. relation [19] is demonstrated in Table 3. The decisive influence on these stresses shows volume fraction of the inclusions. Much weaker is the effect of sintering temperature. Generally tensile stresses in the composite matrix should lead to the decreased fracture toughness of the whole system. But in case of the materials under study quite reverse tendency occurs. It suggest that mechanisms hindering crack propagation should operate. Crack deflection is obvious from the micrographs in Fig.5. But according to Faber and Evans [20] the K_{Ic} increase of 15% in a composite containing 20 vol.% inclusion should be expected. It does not explain the observed fracture toughness increase. Most probably some other mechanisms are active. Among them crack branching and bridging should be considered. It cannot be excluded that the above mentioned tensile stresses in the TZP matrix influence the transformation zone around the crack advancing through the material contributing in the toughening of the system. This is a well known reason of high fracture toughness of the TZPs.

Tablea 3. Thermal residual stresses in the 2,8Y-TZP matrix.

Material / Sintering temperature	1400°C	1500°C
TZP + 10% WC	180 MPa	195 MPa
TZP + 20% WC	355 MPa	380 MPa
TZP + 30% WC	520 MPa	560 MPa
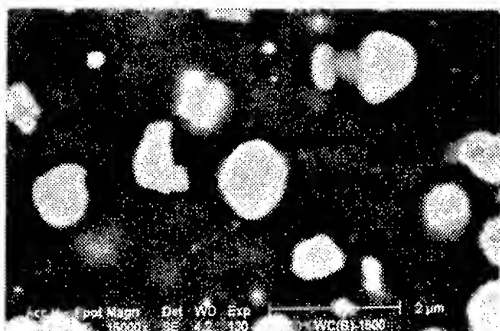
Fig. 5. Crack deflection in the TZP - 20% WC-1 composite.
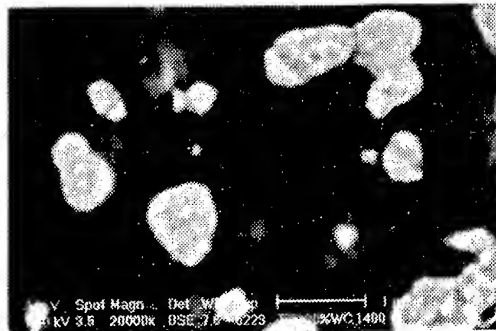
Fig. 6. Microstructure of the TZP - 20% WC-1 composite sintered at 1400°C.

The composite microstructure show that pores concentrate in the vicinity of the carbide agglomerates (Fig.6). The carbide inclusions hinder grain growth of the matrix. Mean TZP grain size in the pure matrixes sintered at 1400 and 1500°C is 0,56 ±0.11 mm and 0.82 ±0.26 mm (± is one standard deviation). Whereas in case of the composite with 20 vol.% WC-1 inclusion, prepared under the same conditions it is 0,53 ±0.10 mm and 0.66 ±0.19 mm respectivelly.
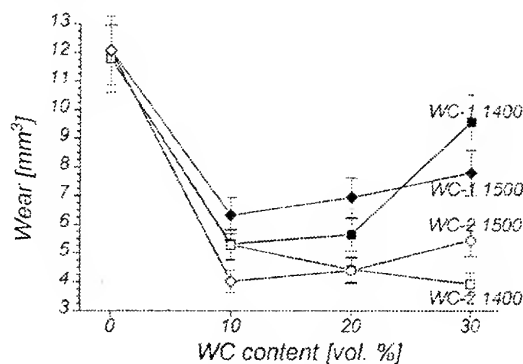
Fig. 7. Wear vs. WC content.
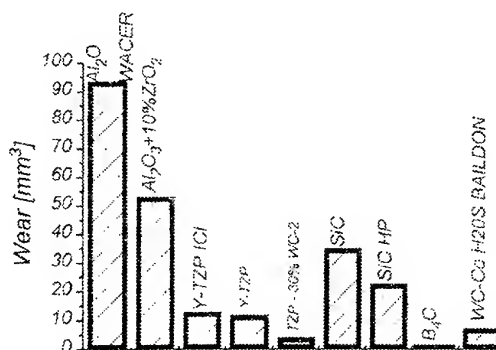
Fig. 8. Comparision of the wear for indicated ceramic materials.

Results of the wear tests are shown in Fig.7. It appears quite clear that the carbide additives increase wear resistance of the material. Carbide inclusions of smaller grain sizes improve wear resistance to a greater extent than the coarse ones. SEM micrographs of the worn surface indicate that the carbide inclusions stop ploughing traces formed by the SiC grains during the wear test. Destruction of the material proceeds by pulling out the carbide inclusions from the matrix. Because of the strong link between the carbide inclusions and the matrix this is an energy consuming process. This seems to be a plausible explanation of the better wear resistance of the composites containing smaller WC grain size inclusions.

Comparison of the wear susceptibility of different materials (Fig.8) indicates that only B_4C among the materials usually recognised as a wear resistant shows better properties than the WC-TZP composites. But we should remember that highly densified B_4C has to be hot pressed or sintered at temperatures approaching 2000°C, whereas the TZP based composites densify well at 1500°C

CONCLUSIONS

Thanks to the high sintering ability of the 2.8Y-TZP powders we were able to obtain dense composites with WC inclusions by simple pressureless sintering technique at temperatures not higher than 1500°C.

During sintering reaction at the interface WC/ZrO$_2$ and ZrO$_2$/C (carbon bed) takes place. It results in the W$_2$C and ZrC formation inside the material and ZrC formation on its surface.

Young modulus and modulus of rigidity, hardness and fracture toughness of the composites are increased by incorporation WC inclusions into the TZP matrix. Simultaneously wear resistance is increased up to three times.

REFERENCES

1. N. Claussen, K. L. Weisskopf, M. Ruhle, *J. Am. Ceram. Soc.*, **68** 288 (1986)
2. M. Poorteman, P. Descamps, F. Cambier, J. Leriche, B. Thierry, *J. Europ. Ceram. Soc.*, **12** 103 (1993)
3. Zh. Dingh, R. Oberacker, F. Thummler, *J. Europ. Ceram. Soc.*, **12** 377 (1993)
4. Zh. Dingh, R. Oberacker, H. Frei, F. Thummler, *J. Europ. Ceram. Soc.*, **10** 255 (1992)
5. Z. Pędzich, K. Haberko, *Ceramics International*, **20** [2] 85-89 (1994)
6. K. Haberko, W. Pyda, J. Piekarczyk, M. M. Bućko, *J. Am. Ceram. Soc.*, **75** [5] 1272 (1992)
7. K. Haberko, Z. Pędzich, J. Piekarczyk, M. M. Bućko, W. Suchanek, Third Euro-Ceramics, vol. 3, *Engineering Ceramics*, P. Duran, J. F. Fernandez (Ed.), Faenza Editrice Iberica S. L., Madryt 629 (1993)
8. K. Haberko, Z. Pędzich, G. Róg, M. M. Bućko, M. Faryna, *Europ. J. Solid State Inorg. Chem.*, **32** 593-601 (1995)
9. D. L. Porter, A. H. Heuer, *J. Am. Ceram. Soc.*, **62** 298 (1979)
10. Piekarczyk, H. W. Hennike, R. Pampuch, *Ceramic Forum International, (Ber. Dtsch. Keram. Ges.)*, **59** [4] 227-232 (1982)
11. A. Niihara, *J. Mater. Sci. Lett.*, **2** 221 (1983)
12. Norma ASTM E 399-1983, Test Method for Plane-Strain Fracture Toughness of Metallic Materials
13. S. A. Sałtykow, *Stereological Metallurgy*, Ed. Metallurgia, 3rd edition, Moscow, 1970
14. ASTM Standard G 6585, Dry Sand Test
15. Weiser, L. C. De Jonghe, 71 [3] C12-C127 (1988)
16. W. Scherer, *J. Am. Ceram. Soc.*, **70** [10] 719-725 (1987)
17. Cheng, D. P. Thompson, British Ceramics Proceedings no. 49, "Special Ceramics 9", April 1992
18. Kountouros, G. Petzow, *Science and technology of Zirconia V*, S. P. S. Badwall, M. J. Bannister, R. H. Hannink (Ed.), Technomic Publishing Co. Inc. 1993 p.30
19. Taya, S. Hayashi, A. S. Kobayashi, H. S. Yoon, *J. Am. Ceram. Soc.*, **73** 1382 (1990)
20. K. T. Faber, A. G. Evans, *Acta Metall.*, **31** 565 (1983)

THE ELASTIC MODULI OF EPOXY MATRIX AT LOW TEMPERATURE

I.Perepechko, V.Danilov and V.Nizhegorodov

Department of Physics Moscow State Academy of the Automobile and Tractor Engineering, B.Semenovskaja Street 38, Moscow, Russia.

INTRODUCTION

In recent years has been the ever increasing interest to viscoelastic and acoustic properties of polymeric materials [1] at low temperatures including the liquid - helium temperature [2]. It bears a relation to the polymeric matrices, including the epoxide resins. Nevertheless, only a small number of investigations devoted to the studying of the acoustic properties of epoxide resins by T→0 K are available. It is less studied the frequency dependence (dispersion) of the elastic waves velocity in cured epoxide at T < T_g. This has attitude to the dispersion of the elastic waves velocity in polymeric matrices at low temperatures. It can be expected that at T→0 K when in polymers are largely "freezing" the relaxation processes, the dispersion of the elastic waves velocity become apparent more distinctly.

The goal of our work is the study of the acoustic and viscoelastic properties of the cured epoxide matrix in the temperature interval from 4.2 K to 293 K on some frequencies from 1 Hz to $5*10^6$.

EXPERIMENTAL

In connection with that were measured the velocities of longitudinal and shear ultrasonic waves on frequency 5 MHz in temperature interval 4.2 - 293 K in epoxide resin on the basis of bisphenol - A (ED - 20). The investigated epoxide resin has contented 20,79 % epoxy groups and was cured by the meta-phenylene diamine. It were investigated the analogous resins cured by the maleic anhydride. From the results of the measurements of velocities of longitudinal and shear ultrasonic waves were calculated the dynamic elastic moduli: Young's modulus E', shear modulus G' and bulk modulus K'_s.

At the same time were carried measurements E' and velocity of longitudinal elastic waves in rod c_{11}. For these measurements was used the method of forced resonance oscillations sample clamped at one end. The experimental apparatus allowed to measure E' and c_{11} in interval of temperatures from 4.2 - 540 K on the frequencies 250 - 200 Hz.

For measurement of dynamic shear modulus G' and low-frequency velocity of shear waves c_{lt} was used the automatic inverted torsion pendulum [3]. In this case G' and c_{lt} were measured in interval of temperatures 77...540 K on the frequency ~2 Hz.

The inaccuracies of the determination of longitudinal and shear waves velocities was 1%. For compare the results obtained on the ultrasonic frequency (f_2=5 MHz) with the low frequencies measurements c_{ll} (f_1=250 Hz) we calculated c_{2l}. In this case we used the value E' obtained from the ultrasonic measurements. The values c_{2l} obtained by this were compared with c_{ll}. This problem not there is for the shear waves. The results of measurements on the ultrasonic frequencies c_{at} can compare with the values c_{at} obtained on the infrasonic frequencies.

RESULTS AND DISCUSSION

The results of the investigation of longitudinal and shear waves velocities is showed on the fig.1. The analysis of these results shows that by decreasing of the temperature from 293 to 4,2 K the sound velocity c_{2l} and c_{2ll} increases continuously and only near 180 K is observed the break on the graph, c_{2l}=f(T). Above and below of T_{tr}=180 K the longitudinal waves velocity depends linearly on the temperature and good agrees with curve calculated on the well - known formula [3]. On the plot c_{2t}=f(T) this break is obtained by more low (140 K) temperature. The temperature of this Ttr shifts towards higher temperatures with increasing frequency, this being indicative of the relaxation nature of the process. It was showed that the given transition is associated with the unfreezing of the classical rotation of CH_3 groups.
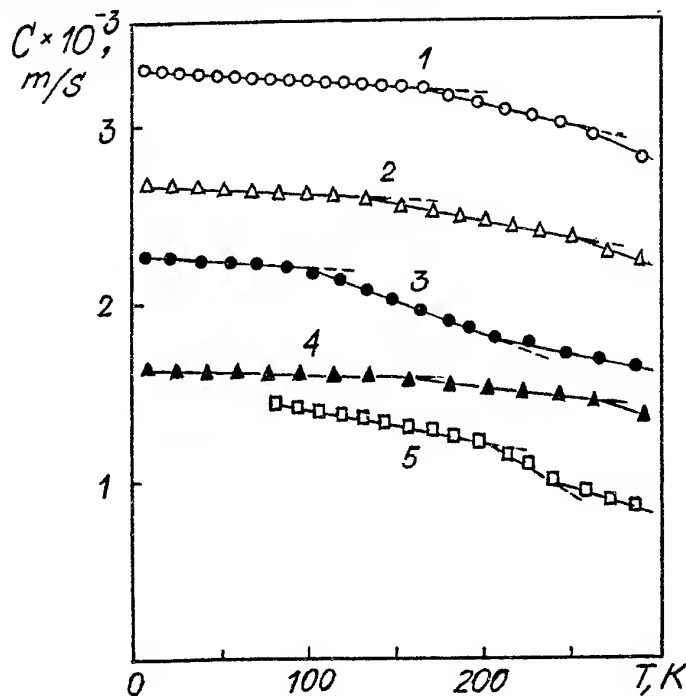
Fig.1. The plots of elastic waves velocity vs. temperature in epoxide resin ED-20:
1-c_l, (f_2=5 MHz); 2-c_{2ll}, (f_{2l}=5 MHz); 3-c_{1ll}, (f_{1l}=250 Hz); 4-c_{2t}, (f_{2t}=5 MHz); 5-c_{lt}, (f_{lt}=2,3 Hz).

The distinguish feature of all dependencies $c_i=f(T)$ in epoxide resin are:
1) the increase of longitudinal waves velocity by T - 4.2 K;
2) the constant magnitude of the dispersion of sound velocity in temperature interval from 100 to 4.2 K.

It is supposed that these both factors indicate that in ED-20 up to 4.2 K last the relaxation process which is not thermal-activation.

Meanwhile for relaxation processes of the thermal-activation type the dispersion must change with the temperature changes. The dispersion can be the valuable instrument for the study of the viscoelastic relaxation.

As the basic parameter for the study of the dispersion use the value $\Delta c/c_0$ where $\Delta c = c_\infty - c_0$. Here c_∞ is the sound velocity corresponding to the case when the frequency $\omega \to \infty$, c_0 conforms to the measurements on lowest frequencies when $\omega \to 0$. By the investigation of polymers c_0 and c_∞ as rule are not known. One would think one can carry the measurements of sound velocity c_1 and c_2 on two arbitrary frequencies f_1 and f_2. The frequencies f_1 and f_2 which distinguish in a few orders, and the magnitude $\Delta c/C_0$, where $\Delta c = c_2 - c_1$ one can consider as the quantitative measure of the dispersion. But it is not correct since in this case not take into account the changes of frequency of the sonic oscillation.

We account that the quantitative measure of the sound velocity dispersion can be the parameter

$$\alpha = \frac{\Delta c * 100\%}{c_1 * \lg(f_2 / f_1)} \tag{1}$$

Here $\Delta c = c_2 - c_1$ and the sound velocity c_2 and c_1 correspond to the frequencies f_2 and f_1. The parameter α has a simple physical sense, he shows the magnitude of the dispersion by changes of frequency in 10 time. The results of the calculations of parameter α for the case of longitudinal waves in rod (c_1, c_{1l}, c_{2l}, f_1 and f_2) and shear waves αt are shown on fig.2.
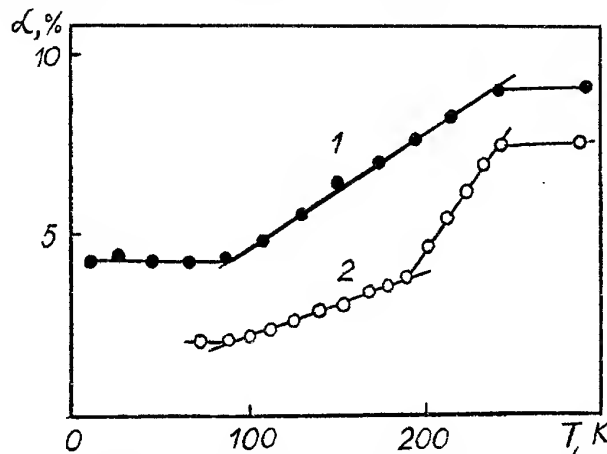
Fig.2. The plots of velocity dispersion of longitudinal α_l and shear α_t waves vs. temperature:
1-α_l=f(T), 2-α_t=f(T).

The analysis of the results represented on fig.2 has shown that the dispersion of velocity of longitudinal waves in rod for ED-20 from 4,2 to 100 K is constant (α_l=4,2%), above 100 K α_l increase linearly up to 240 K, and by more higher temperatures (from 240 to 293 K) weakly increases and mounts to α_l=9.1% at 293 K. Thus on relaxation processes dues the motion of the methyl groups falls on the increasing α_l approximately in 2 time. The results of the studing the dispersion of velocity of shear waves α_t are found not less interesting. Until T=100 K α_t in ED - 20 is constant (α_t=2%) and in interval from 100 K to 200 K increase linearly to α_t=4.7%. By the subsequent increasing of temperature the parameter α_t increases linearly with temperature and by T>240 K increases weakly and mounts to α_t=7.4% at 293 K. Thus by the change of the temperature from 100 K to 293 K the dispersion of the velocity of shear waves increase in 3.7 time. If every break on the graph α=f(T) consider as the temperature transition on the plots α_l=f(T) there are 2 such transitions: the first transition at 100 K can consider as initial temperature by which begin the relaxation process, the second transition at 240 K as the temperature of termination. On the plot α_t=f(T) in interval 100...200 K there are two relaxation processes. One of them takes place in interval from 100 to 200 K. From that we conclude that α_t=f(T) has the greater sensitivity by the investigation of relaxation processes than α_l.

It is known that the dynamic module depend on the frequency [1]. The results of our measurements of the dynamic Young's moduli E' carried on the frequencies f_1=2.5*10^2 Hz and f_2=5*10^6 Hz and of the dynamic shear moduli on the frequencies f_1=2.3 Hz and f_2=5*10^6 Hz represented on the fig.3.
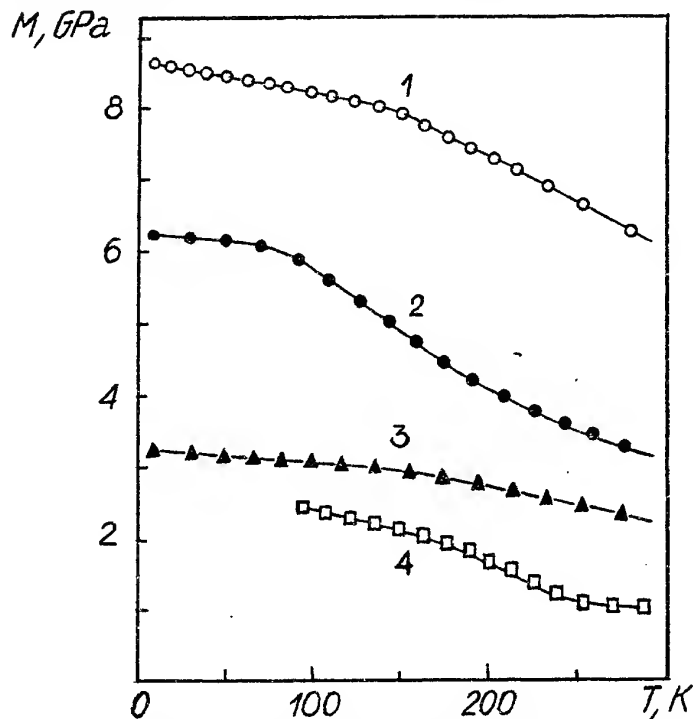
Fig.3. The plots of dynamic modulus vs. temperature:
1-E'$_2$, (f$_2$=5 MHz); 2-E'$_1$, (f$_1$=250 Hz); 3-G'$_2$, (f$_2$=5 MHz); 4-G'$_1$, (f$_1$=2,3 Hz).

By analogy with the formula (1) one can introduce the parameter for dispersion of dynamic moduli

$$\beta = \frac{\Delta M * 100\%}{M_1 * \lg(\frac{f_2}{f_1})} \qquad (2)$$

Here M is every of the dynamic moduli (M can be equal E', G' etc.), $\Delta M = M_2 - M_1$, M_2 and M_1 are moduli measured on the frequencies f_2 and f_1.

The results of the calculations of values β_l and β_t are represented on the fig.4. An analysis of the results represented in fig.3 has shown that for all temperatures β_l is greater than β_t. In interval from 4.2 to 80 K β_l is constant and is equal 8.8% that is approximately in 2 time higher than α_l. In interval from 80 K o 240 K β_l increases linearly with the temperature and above 240 K increases weakly and mounts to $\beta_l = 21.6\%$ at 293 K. The dependencies $\beta_l = f(T)$ and $\beta_t = f(T)$ repeat qualitatively the temperature dependencies α_l and α_t.
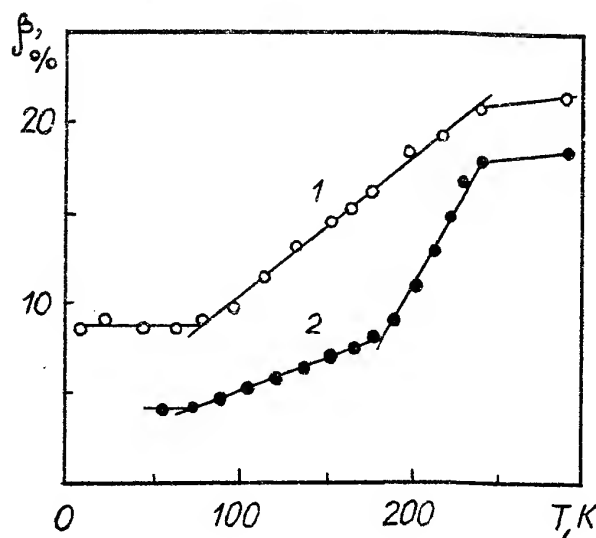
Fig.4. The plots of dynamic modulus dispersion vs. temperature: 1-$\beta_l = f(T)$, 2-$\beta_t = f(T)$

REFERENCES

[1] Perepechko, I.I. "Acoustic Methods of Investigating Polymers", Moscow, Mir (1975).
[2] Perepechko, I.I. "Low-Temperature Properties of Polymers", Moscow, Mir (1980).

389

[3] Perepechko, I.I. "Acoustical spectroscopy of polymeric matrices", Proc. 10 Int. Conf. Compos. Mat. Whistler, B.C. Canada, **5**, pp. 445-451.

390

STATIC STRENGTH AND FATIGUE LIFE OF MULTIPLE-ROW BOLTED JOINTS IN CARBON/EPOXY LAMINATES

Erik Persson and Ingvar Eriksson
Department of Lightweight Structures, Royal Institute of Technology (KTH),
100 44 Stockholm, Sweden

INTRODUCTION

Optimal design of bolted joints in advanced composite structures is an important means of reducing weight, and increasing strength and/or fatigue life. A design method is divided into a number of distinct phases. First, the load and stress distribution in the joint must be determined; second, models for strength prediction have to be used; third, a model has to be derived to predict fatigue life accurately. Fatigue life prediction models in practice today are based on empirical, strength degradation, stiffness degradation, and actual damage state theories [1].

Experimental work on fatigue life of bolted composite laminates has been carried out by, for example, Ramkumar and Tossavainen [2], Crews [3] and Kam [4]. Static and fatigue testing of unnotched, notched, single bolted, and multiple bolted (two bolts in the load direction) laminates was carried out by e.g. Schutz, Gerharz, and Alschweig [5]. The results showed that when the hole elongation during fatigue loading exceeded 1-2% of the bolt diameter, the growth of elongations increased dramatically [2]. Furthermore, high bolt clamp-up force compared with low clamp-up force resulted in higher static strength and longer fatigue life of the joints [2, 3]. When interference fit bolts were used, the change in hole elongations occurred abruptly, whereas use of clearance fit bolts resulted in a steady growth of hole elongation [4]. It was also shown that composite laminates containing high-strength (HT) fibres yielded higher static strength compared with laminates having the same lay-up sequence, but containing high modulus (HM) fibres. However, the difference in strength decreased at a high number of cycles [5].

In a recent research program Persson et al. [6] investigated the effect of hole machining defects on static strength and fatigue life of carbon/epoxy laminates subjected to compressive- and pin-loading. In the same program they also studied defect propagation around holes in the laminates during cyclic pin-loading [7]. The results from these investigations showed that absence of intrinsic defects around holes in composite laminates resulted in higher strength and longer fatigue life compared with laminates containing hole machining defects such as matrix cracks and delaminations.

For a deeper understanding of the parameters affecting static strength and fatigue life of bolted composite laminates it is of interest to test more structure-like bolted joints, i.e. multiple-row bolted specimens.

This paper presents some initial results from a comprehensive test programme to determine the influence of significant parameters on strength and fatigue life of multiple-row bolted joints. In particular, the effect of hole machining defects on fatigue life is investigated. Other objectives are to determine the static strength and by-pass loading condition in the joint. Test results from two types of multiple-row joints are presented.

EXPERIMENTAL PROGRAM

The parameters affecting the strength and fatigue life can be listed in five categories: material, machining, joining, design, and environmental. To prevent the test program growing out of proportion, the most important parameters were selected and a reduced multi-factorial test plan was defined. The parameters in the basic program are:

Material parameter: Two types of prepreg material systems are included: one system containing a high-strength (HT) fibre, and one containing an intermediate modulus (IM) fibre.

<u>Machining parameters</u>: The extent of initial hole machining damage is varied by machining the holes using on the one hand the recently proposed KTH-method[1] ,which gives no detectable damage, and on the other hand a traditional drilling method using an ordinary cemented carbide drill, which causes substantial machining defects.

<u>Joining parameter</u>: Flush-head and protruding head bolts are included as well as high and low bolt torque.

<u>Design parameters</u>: These are lay-up sequence, laminate thickness, width to bolt diameter ratio (w/d), and edge distance to bolt diameter ratio (e/d). In this paper only lay-up sequence is included.

<u>Environmental parameter</u>: Two conditions are tested: room temperature and dry laminates (RTD), and elevated temperature and moisture-conditioned laminates (HTW).

During the course of the investigation sixteen different types of specimens will be made and in each test group three of the specimens will be subjected to static loading and seven subjected to fatigue loading at five different load levels. In this report data and results from two groups are presented.

SPECIMEN PREPARATION

Laminates with a thickness of 3.12 mm were fabricated from the HTA7/6376 prepreg system available from Ciba-Geigy with high tensile modulus fibres (HT). Both quasi-isotropic and highly orthotropic laminates were made. The 0°-laminae were aligned with the load direction (Figure 1).

Specimens were cut with diamond grain coated tools. The holes in upper and lower plates were machined in the same operation (co-drilled). The diameter of the holes was 6 mm (6.000-6.048 mm, ISO tolerance H10). The test specimens were then joined with 6 mm (5.990-5.978 mm, ISO tolerance f7) flush-head or protruding head bolts. The bolts were torqued to 6 or 8 Nm depending on specimen configuration. Figure 1 shows the specimen type containing flush-head bolts (called specimen A-n; n=1,...,10 denotes the individual specimen). The member plates with countersunk and cylindrical holes are referred to as upper and lower plate, respectively.
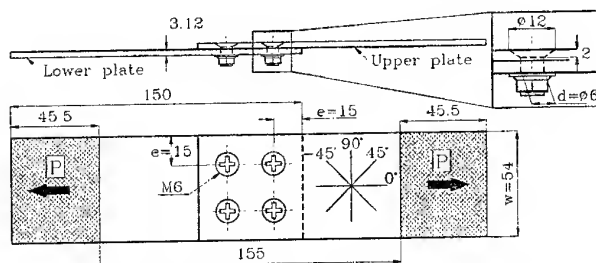
Figure 1. Specimen type A with flush-head bolts

The specimens containing protruding head bolts (called specimen B-n; n=1,...,10 denotes the individual specimen) were the same shape as the A type specimen (except that the holes were not countersunk). The specimens were made according to the MIL-STD-1312-21 standard, but the specimen width to bolt diameter ratio (w/d) was 4.5 and edge distance to bolt diameter ratio (e/d) was 2.5.

Traditional hole drilling was carried out with a cemented carbide flute drill according to aircraft industry standards. The exit side of the laminate was supported with a piece of wood to minimise delaminations as the drill punched through the laminate. The rotation speed of the drill was 3000 rpm and the drill was fed through the laminates by hand.
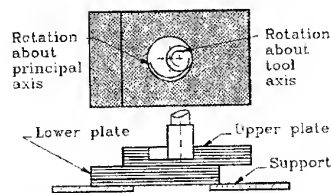
Figure 2. Hole machining using the KTH-method.

The KTH-method, [6, 7] was used to machine defect-free or nearly defect-free holes. The hole in the laminate is machined both axially and radially by rotating the cutting tool about its own axis as well as eccentrically about a principal axis as the tool moves through the laminate (Figure 2).

This method reduces the axial forces by means of a moving tool centre. Thus, the risk of delamination is reduced. Hole machining was carried out in a lathe. Support was only applied on the exit side of the laminate outside a distance of 5 mm from the hole edge. An air driven machine was mounted in the tool holder and the specimen attached to a fixture in the chuck of the lathe. The rotation speeds of the tool, a diamond-coated mandrel, and spindle were 25 000 rpm and 125 rpm, respectively.

---

[1] Described under SPECIMEN PREPARATION below.

The configurations of specimen types A and B are presented in Table 1.

Table 1. Specimen configurations

Specimen type	Lay-up sequence	Hole machining method	Bolt	Bolt torque (Nm)
A	Quasi-isotropic, $[(\pm 45/0/90)_3]_{s}24^2$	KTH-method	Flush-head	6
B	Highly orthotropic, $[(\pm 45/0_4/90/\pm 45/0_3)]_{s}24$	Traditional drilling	Protruding head	8

NON-DESTRUCTIVE EVALUATION

To determine the extent of hole machining defects, two specimens in each group were studied prior to testing using X-ray radiography. A film placed on the opposite side of the specimen (upper and lower plates were placed separately on the film) in relation to the X-ray source recorded the attenuation through the thickness of the specimen. To enhance the contrast between damaged and undamaged material, a penetrant [mixture of isopropanol (10 ml), water (10 ml), zinc iodide (60 g), and detergent (1 ml)] was applied to the hole edges.

TESTING

Static tests were carried out in a universal testing machine (INSTRON 4505) and in a servo hydraulic testing machine (Schenk). A tensile load was applied to the specimens at a constant speed of 1 mm/min. Five 5 mm gauge length strain gauges were placed between the bolt rows on the outer surface and two 2 mm gauge length strain gauges on the edges (see Figure 3) on two specimens in each group to determine the by-pass loads. Three specimens were tested in each group.
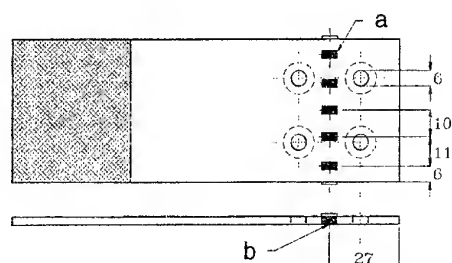
Figure 3. Locations of 5 mm (a) and 2 mm (b) gauge length strain gauges for measuring by-pass loads on the countersunk member.

The fatigue tests were carried out in the Schenk machine with a sinusoidal load, with constant amplitude at a frequency of 3 Hz. The skin in aircraft wing structures is subjected to tensile and compressive loading due to bending of the wing. Therefore, a ratio between the minimum and maximum loads (R) of minus one was chosen. The tests were conducted at room temperature with dry laminates (RTD). Seven specimens in each groups were tested at five different loads between 35% and 55% of ultimate failure load. To prevent out-of-plane deflections and to minimise secondary bending, a lateral support was applied at the gauge length of the specimens.

Specimen deflections in the load direction were determined by measuring the location of the hydraulic cylinder at maximum and minimum load. A PC sampled the deflections every ten, twenty, or thirty seconds. Testing was stopped when deflections at maximum and minimum load deviated more than 0.3 mm from deflections registered immediately after loading was applied. Allowing less deviation would lead to unnecessary stops, whereas allowing more would lead to severe crushing of the hole edge, but not to significantly longer fatigue life.

EXPERIMENTAL RESULTS

X-ray radiographs were taken of two specimens in each group. In Figure 4, the extent of hole machining defects is shown for specimens A-7 and B-7. Around the holes in specimen A-7 containing holes machined using the KTH-method no detectable defects were found. The countersunk areas around the holes in the upper plate (Figure 4a) did not attenuate the X-rays as much as the full thickness of the laminate, i.e., the circular white areas are larger than the white areas in the other plates. On the lower plate, delaminations (the dark areas) were present around

---

2 s24 defines a symmetric laminate with a total of 24 layers.

the holes at the exit side of the laminate in specimen B-7 with holes machined using the traditional drilling method. On the upper plate, no or small defects were detected.
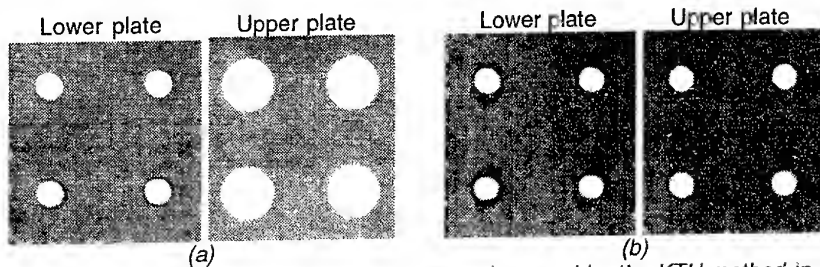
Figure 4. Extent of hole machining defects (the dark areas) caused by the KTH-method in specimen A-7 (a) and by a cemented carbide drill in specimen B-7 (b).

In Figure 5, the maximum gross section stresses (σ_{gross}) are plotted for the A and B type specimens as a function of number of cycles.
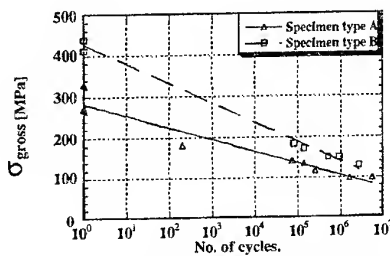
Figure 5. S-N curve for A and B specimens.

The static strength was much higher for B specimens compared with A specimens, but it can be observed that during cyclic loading the difference in gross section stress between the specimen types decreases with longer fatigue lives.

During fatigue testing, a PC sampled maximum and minimum deflection (δ) (i.e. the location of the hydraulic cylinder at maximum and minimum load) every ten, twenty, or thirty second intervals depending on the expected specimen fatigue life. A stop criterion was chosen which considered failure to have taken place when the maximum and minimum deflection exceeded ±0.3 mm from the value registered immediately after cyclic loading was applied.

Figure 6 shows maximum and minimum deflections (δ) as a function of number of cycles for specimens A-8 (a) and B-4 (b). The specimens were subjected to cyclic loading with an amplitude of 22.7 kN and 25.4 kN, respectively. In the beginning of loading, deflections of approximately ±0.60 mm were observed for both specimens A-8 and B-4. Only small changes in deflections (less than 0.05 mm) were registered until a certain fatigue limit was reached, after which the changes accelerated dramatically. Failure was considered to have occurred when the deflection exceeded approximately ±0.9 mm for both specimens. This happened after 142 400 cycles for specimen A-8 and after 514 700 cycles for specimen B-4. The change in deflection from the stable phase to failure occurred over a smaller part of the total fatigue life for B specimens compared with A specimens. After testing, permanent hole elongations of approximately 0.1-0.2 mm were measured in all specimens.
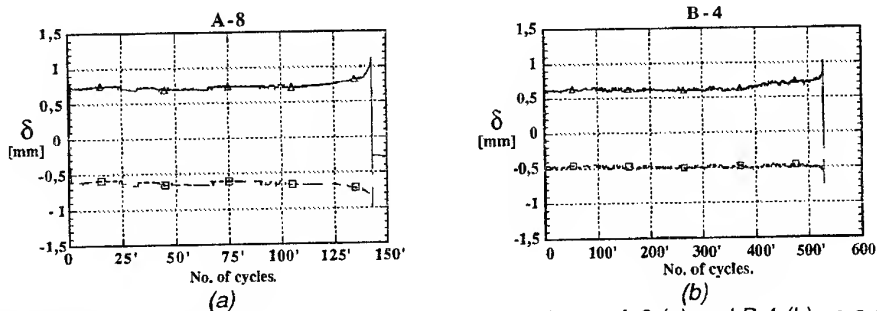
Figure 6. Deflections at minimum and maximum load in specimens A-8 (a) and B-4 (b) as a function of fatigue cycles.

To determine the by-pass strains, strain gauges were mounted between the bolt rows on two of the specimens in each group subjected to static loading. First, the bolts were only finger tightened

and the specimens were subjected to loading up to approximately 30% of ultimate failure load (load case I), then subsequently unloaded. After that, the bolt were torque tightened and the specimens were then loaded to their ultimate failure load (load case II). The by-pass strains were measured at seven locations along the specimen width. Average by-pass loads were calculated with the extensional stiffness matrix by using the average by-pass strain. In Figure 7, the loads and strains are shown schematically.

The by-pass load in the countersunk member of specimen A-2 was approximately 50 % of the applied load until it reached approximately 30 kN. From 30 kN to maximum applied load, the by-pass load increased to approximately 60 %. The by-pass load was slightly less than 50 % for specimen B-3 during the entire load cycle.
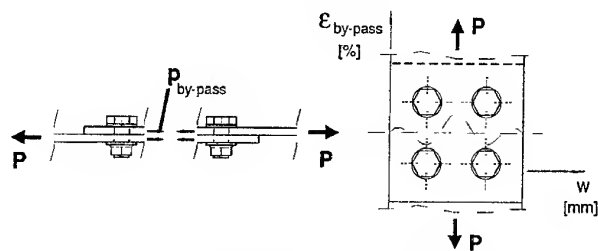
Figure 7. Schematic lay-out of applied load (P), by-pass load (P$_{by-pass}$) and variation of by-pass strain ($\varepsilon_{by-pass}$) in a test specimen.

By-pass strain ($\varepsilon_{by-pass}$) variations along the width (w) are plotted in Figure 8 for specimen A-2 for load case I (a) and II (b) at different applied loads (P). For comparison, the by-pass strain variation is plotted for case II at 15 kN applied load in Figure 8a. The curve fits were generated with a cubic spline function. By-pass strain reached minima at w equal to 15 and 39 mm (i.e. the same locations along the width where the bolts were situated) in case I.

In case II, the strain minimum was present in the middle of the specimen width (w=27 mm). As the load increased, the strain increased in the middle and minima were instead present at w equal to 15 and 39 mm. The difference between minima and maxima was small at low loads, but at higher loads it increased.
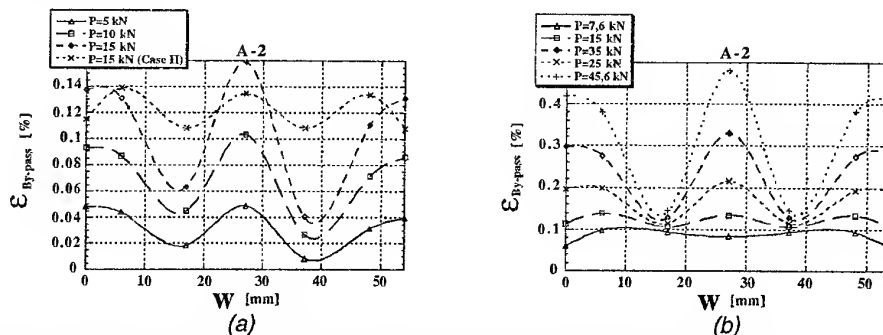
Figure 8. By-pass strains for specimen A-2 in case I at 5, 10, and 15 kN applied loads and case II at 15 kN applied load (a), and in case II at applied loads from 7.5 to 45.6 kN (b).

In the B-3 specimen strain minima were also present at w equal to 15 and 39 mm for load case I. At low loads in load case II, strain minimum was present in the middle of the specimen width (w=27 mm) and maxima at w equal to 15 and 39 mm.

SUMMARY AND CONCLUSIONS

Results from the non-destructive evaluation showed that even though the exit side of the lower plate in the B type specimen was supported at the holes, the conventional drilling technique caused delaminations around the holes. No delaminations were detected in the A type specimen with holes machined with the KTH-method (where no support was applied at the locations of the holes). Possibly the delaminations were caused by high axial force from the drill punching through the laminate.

As would be expected, the static strength was much higher for B specimens compared with A specimens. The B specimens consisted of a highly orthotropic laminate containing protruding head bolts, whereas the A specimens were made of a quasi-isotropic laminate containing flush-head bolts. However, it was observed that the difference in peak gross section stress between the

specimen types decreased with longer fatigue lives. Similar observations have been made by Ramkumar and Tossavainen [2].

Deflections for B specimens immediately before failure changed faster compared with A specimens; otherwise the deflections behaved similarly during the stable phase for all specimens. This indicates that there may have been some growth of damage which did not affect the overall structural response of the specimen until the damage reached a critical extent. The hole elongations observed in the specimens after testing indicated bearing failure.

The increase of the by-pass load observed in the countersunk (upper) plate of the A type specimen was possibly due to uneven load distribution in the joint. This may have been caused by severe crushing of the hole edges in the row of bolts subjected to both bearing and by-pass loads.

At low loads and when torqued bolts were used, the strain variation showed a minimum in the middle of the specimen width and maxima at the same locations along the width where bolts were present. At high loads when torqued bolts were used and during the entire load cycle when finger tightened bolts were used, strain minima were present at the same locations along the width where the bolts were situated.

The maxima found at the same locations along the width where the bolts were situated was possibly caused by the load being carried between the laminates by friction as well as shear in the bolts. The locations of highest friction were possibly close to the circumference of the bolts where the highest clamping force was present.

ACKNOWLEDGMENTS

REFERENCES

[1]   Sendeckyj, G. P. "Life prediction for resin-matrix composite materials" In *Fatigue of composite materials*, K.L. Reifsnider Ed., Elsevier Science Publishers B. V., pp. 431-483 (1991).

[2]   Ramkumar, R. L., Tossavainen, E. W. "Strength and Lifetime of Bolted Laminates", *Fatigue in Mechanically Fastened Composite and Metallic Joints, ASTM STP 927*, John M. Potter. Ed.. American Society for Testing and Materials, Philadelphia , pp. 251-273 (1986).

[3]   Crews, J. H. "Bolt-Bearing Fatigue of a Graphite-Epoxy Laminate", *Joining of Composite Materials*, ASTM STP-749, T. Kedward, ed., American Society for Testing and Materials, pp. 131-144 (1981).

[4]   Kam, C. Y. "Bolt Hole Growth in Graphite-Epoxy Laminates for Clearance and Interference Fits When Subjected to Fatigue Loads", *Fatigue of Fibrous Composite Materials*, ASTM STP 723, American Society for Testing and Materials, pp. 21-30.

[5]   Schutz, D., Gerharz, J. J., Alschweig, E. "Fatigue Properties of Unnotched, Notched, and Jointed Specimens of a Graphite/Epoxy Composite", *Fatigue of Fibrous Composite Materials*, ASTM STP 723, American Society for Testing and Materials, pp. 31-47.

[6]   Persson, E., Eriksson, I., Zackrisson, L. "The Effect of Hole Machining Defects on Strength and Fatigue Life of Composite Laminates", submitted for publication in *Composites Part A: Applied Science and Manufacturing*.

[7]   Persson, E., Hammersberg, P., Eriksson, I. "Propagation of Hole Machining Defects in Pin-loaded Composite Laminates", submitted for publication in *Journal of Composite Materials*.

DAMAGE TOLERANCE OF FRP TOP-HAT STIFFENERS

H. J. PHILLIPS, C. E. MOSS and R. A. SHENOI

Department of Ship Science, University of Southampton
Southampton, SO17 1BJ, UK

ABSTRACT

This paper examines the strength and tolerance to propagation of delamination-induced cracks in top-hat stiffened FRP panels. Both strength and fracture resistance are assessed using finite element modelling. The aim of the strength analysis is to identify the zones likely to see delamination damage under different loading conditions. The fracture mechanics aspect focuses on the likely damage zones. The paper presents strain energy release rate levels for a variety of parameters likely to influence the propagation of such cracks.

INTRODUCTION

The twin characteristics of FRP materials are high specific strength and low specific stiffness. The latter feature implies the need to stiffen large unsupported plate panels by some suitable stiffeners; in the main these have been of a top-hat configuration. Much work has been carried out with regard to the static/dynamic/buckling responses of these stiffened panels. One area of weakness is the ability to predict the safe tolerance levels associated with the most common defect, namely delamination within the top-hat and at the panel-stiffener intersection (1). The structure is prone to high interlaminar stresses in such a location; these are exacerbated by the presence of a delamination. A further need, from a safe operations viewpoint, is an ability to predict the potential for growth of this delamination (2). The objective of this paper is to assess the delamination growth in a top-hat stiffener, see Figure 1, by evaluating strain energy release rates. Critical G values will be computed using finite element analyses for a variety of top-hats with varying load conditions and delamination configurations.

FRACTURE MECHANICS CONCEPTS

The condition for a delamination induced crack to propagate can be explained in terms of the strain energy release rate, G, whose general form is (3):

$$G = \frac{1}{B} \frac{dU}{da} \qquad (1)$$

where U is the strain energy stored in the body, B is the material thickness and a is the crack length dimension. It can be shown that for plane strain, the above can be written as:

$$G = \frac{\pi(1-v^2)}{E} \sigma^2 a \qquad (2)$$

where E is the Young's modulus of the material, σ is the field stress and v is the Poisson's ratio.

Using the relationship:

$$K_I = \sigma\sqrt{\pi a} \qquad\qquad (3)$$

with K_I being the stress intensity factor, or SIF, for the opening mode, and substituting it in eqn. (2), the strain energy release rate for the corresponding mode is:

$$G_I = \frac{K_I^2}{E}(1-v^2) \qquad\qquad (4)$$

A similar expression is valid for the pure shearing mode II. For the tearing mode III, the strain energy release rate is given by:

$$G_{III} = (1+v)\frac{K_{III}^2}{E} \qquad\qquad (5)$$

Very often, especially in the case of laminated FRP materials it is not possible to ascribe one single mode. Rather the failure is a result of mixed mode consequences. The strain energy release rate in such a case, is:

$$G = (K_I^2 + K_{II}^2)\frac{(\kappa+1)(1+v)}{8E} + K_{III}^2\frac{(1+v)}{2E} \qquad\qquad (6)$$

where:

$$\kappa = 3 - 4v \qquad\qquad (7)$$

If the values of G are known and found to be less than critical values for the material then it is likely that the crack will not extend under the given load and boundary conditions and hence the defect associated with the crack or delamination can be safely tolerated.

STRENGTH ANALYSIS: POTENTIAL DAMAGE SITES

The first task in assessing crack damage tolerance is to identify the potential zones of weakness. This is best achieved through a detailed finite element analysis (FEA) of a typical stiffener. The FEA model was generated using the ANSYS package (4). The model was a two-dimensional one, and used quadrilateral elements having extra displacement shapes to improve bending performance. The critical part of the stiffener, i.e the overlaminate, was constructed of 12 elements through the thickness with one element representing a layer of woven roving material. The flange, being of lesser interest, was constructed as a single element through the thickness. The material properties used in the modelling are given in Table 1.

Validation of the FEA model was achieved by comparing its load-deflection characteristics against those generated through laboratory testing of physical specimens (5). Three loading configurations were chosen: (a) Three-point bend; (b) reverse bend; (c) pull-off. These are shown schematically in Figure 2. The load-deflection plot pertaining to the three-point bend

398

situation for the FEA and physical model, for example, is shown in Figure 3. It can be noticed that there is fairly close agreement between the experimental and FEA results.

Having validated the FEA models, stress distributions in the overlaminate (through-thickness and in-plane), flange (through-thickness and in-plane) and fillet (principal) were investigated. The regions where the maximum stresses occurred were noted in each case in order to yield a table of damage sites. The results are summarised in Table 2. For each loading configuration, the stress distributions at two load levels were investigated. The first load corresponds to delaminations in the curved part of the overlaminate for the three-point bending, fillet cracking for the reverse bend and cracks at the flange/fillet interface for the pull-off. The second load level corresponds to the failure load of the top-hat.

From the diagrams in Table 2 it can be noted that the critical regions where delaminations are most likely to occur, are in the curved region of the overlaminate and in the flange.

FRACTURE MECHANICS STUDIES

Having identified the potential damage sites, a finite element fracture analysis was undertaken so as to carry out a sensitivity study on the effect of (i) crack depth and (ii) crack length on the strain energy release rate, G. These were intended to represent possible delaminations in the overlaminate of the top-hat. The FEA model used for the strength analysis was modified for the fracture studies in the area of the intended cracks. Elements in the crack region were six-noded triangular elements with midside nodes and quadratic displacement shapes, so as to be able to cope with stress singularities at the crack tip. Gap elements with a very high compressive stiffness and zero tensile stiffness were placed between the two crack faces to prevent cross-over. The modelling assumed plane strain conditions. A typical plot of the crack tip region used in the finite element modelling is shown in Figure 4. Values for G were yielded in each case and then compared with a critical value, G_c of 0.54 N/mm. If the calculated value of G is greater than G_c then the crack can be assumed to propagate under the given load conditions.

The parameters varied in the sensitivity study, crack depth and length, are shown schematically in Figure 5. In the case of the depth variation, the 8 mm crack is horizontal and its depth varies from 2 mm to 8 mm below the outer surface. The total overlaminate thickness is 12 mm. In the case of the length variation, each crack is 6 mm deep and the location of the crack tip furthest away from the fillet is kept constant. i.e the length is increased around the radius of the overlaminate.

Results under three-point bend and pull-off loads of 10 kN are shown in Figure 6. This load represents inception of a knee in the experimental load-deflection plot in the three-point bend condition, which could potentially have indicated a delamination.

DISCUSSION

The results of the finite element strength analysis give reasonable correlation with the experimental behaviour. The models predicted the regions which were subjected to the highest stresses and hence which parts of the top-hat stiffeners are likely to fail under a given set of boundary conditions. The results from the modelling of the three-point bending tests was

particularly encouraging since it not only predicted the regions under the highest levels of stress but also gave comparable actual values. For example, the top-hat ultimately failed in the flange at a load of 16.5 kN (second row in Table 2). The assumed in-plane failure stress of the flange plate material is 210 MPa and the stress predicted by the finite element modelling is 208 MPa.

In the case of the crack depth variation for the three-point bending model, it can be noted that all the values of G are well below the critical value, thus implying that none of these cracks are likely to propagate under the assumed loading conditions. The gradual increase in G as a depth of 4 mm is approached and then a gradual decrease indicates that cracks at depths of about 4 mm are more likely to propagate. It must be pointed out however, that the values of G near the surface may in fact be influenced by the fact that the element mesh becomes more coarse near the surface as the crack becomes shallower. This feature needs further investigation. In the case of the crack length variation a definite trend is achieved. Assuming that G_{cr} is 0.54 N/mm, it can be shown that cracks over a length of about 37 mm are likely to propagate. Similar trends are obtained for the pull-off model except that critical crack length is about 30 mm.

CLOSURE

The purpose of this paper has been to highlight the strength and fracture performance of top-hat stiffeners. The work presented here has identified the curved part of the overlaminate as a potential damage site for the inception of delamination cracks. A new approach for assessing damage tolerance using a strain energy release rate criterion has been presented. This has been successfully applied in context of a typical top-hat stiffener. Finally, the results of a sensitivity study, examining the influence of changing crack length and depth, are presented.

REFERENCES

[1]   Gable, C. W. "The Effects of Defects in Glass-Reinforced Plastic (GRP)", Marine Technology, 28(2), pp 91-98, (1991).

[2]   Shenoi, R. A. & Hawkins, G. L. "An Investigation into the Performance Characteristics of a Top-Hat Stiffener to Shell Plating Joint", Composite Structures, 30(1), pp 109-121, (1995).

[3]   Parker, A. P. "The Mechanics of Fracture and Fatigue", E&F Spon Ltd., London, (1981).

[4]   ANSYS Fracture Mechanics Users Manual, Swanson Analysis Systems, Inc., Houston, PA. (1989).

[5]   Elliot, D. M. "Mechanical Testing of Composite Joints - Interim Report." DRA Report, April 1994. [Restricted].

Material	E_x	E_y	G_{xy}	υ_{xy}
	MPa	MPa	MPa	
Woven Roving /Polyester	13060	7770	-	0.25
Fillet Resin	1500	1500	-	0.25
Foam Former (non-structural)	0.001	0.001	0.001	-

Table 1.   Material Properties used in Finite Element Modelling

Test	Load (KN)	Fillet Value	Fillet Location	Overlaminate Inplane Value	Overlaminate Inplane Location	Overlaminate Through thickness Value	Overlaminate Through thickness Location	Flange Inplane Value	Flange Inplane Location	Flange Through thickness Value	Flange Through thickness Location
Three point bend	13.5	14.81		55.08		75.95		170.52		5.03	
Three point bend	16.5	18.09		67.33		92.83		208.42		6.15	
Reverse bend	5.0	5.91		41.53		25.43		32.83		0.75	
Reverse bend	14.0	16.55		116.27		71.20		91.92		2.11	
Pull off	5.5	6.41		46.96		37.34		35.49		2.29	
Pull off	7.0	8.16		59.77		47.52		45.18		2.51	

Table 2.   Table of Damage Sites
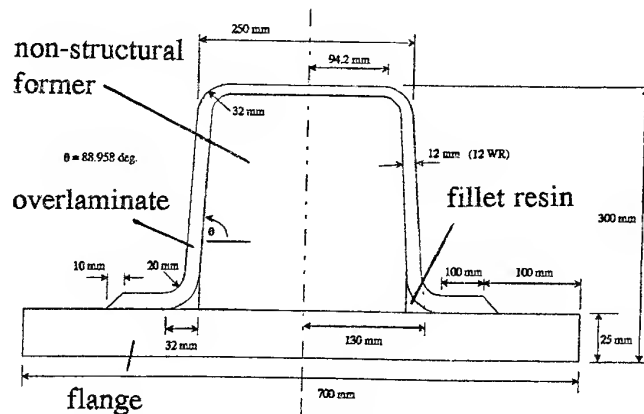
Figure 1.   Schematic of the Top-Hat Stiffener

(a)   Three-Point Bend   (b)   Reverse Bend   (c)   Pull-Off
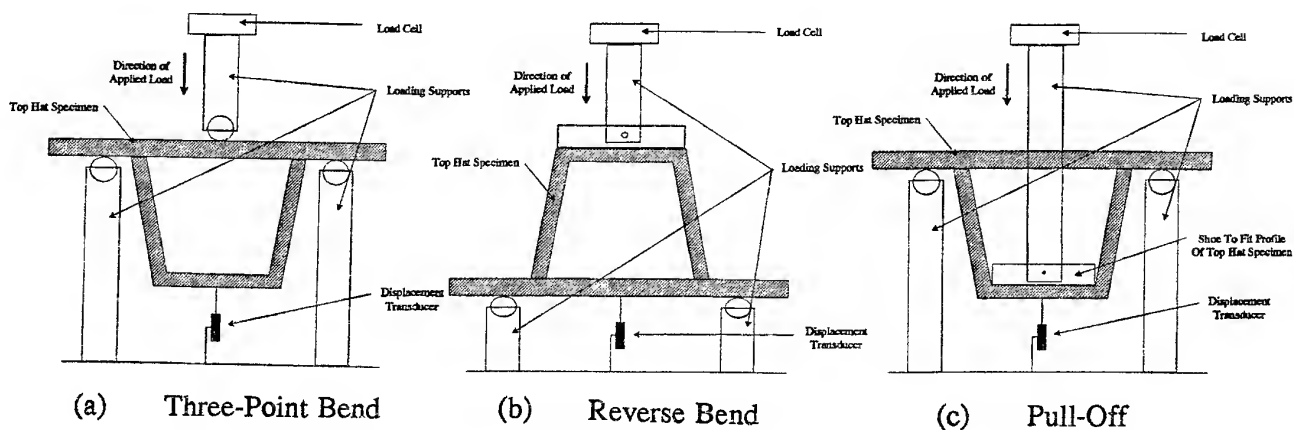
Figure 2.   Test Loading Configurations
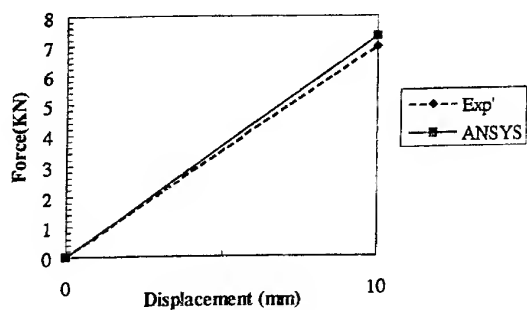
Figure 3.   Load Deflection Plot for
             Three-Point Bend
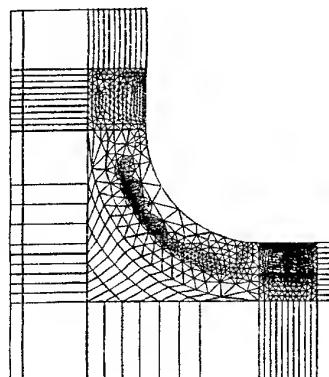
Figure 4.   FE Model for Crack Problem
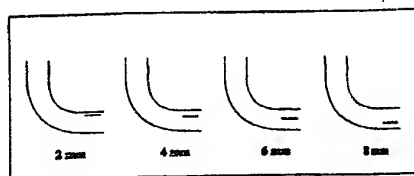
(a)   Crack Depth
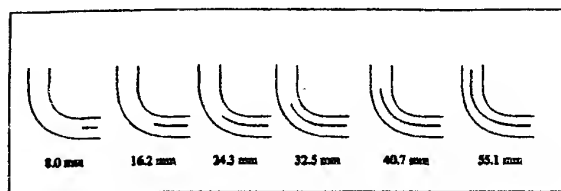
(b)   Crack Length

Figure 5.   Parameters Varied in Sensitivity Study
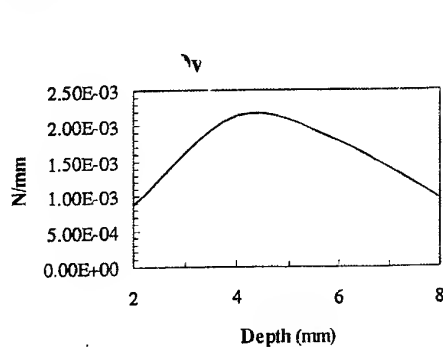
(a)   Results for Three-Point Bend
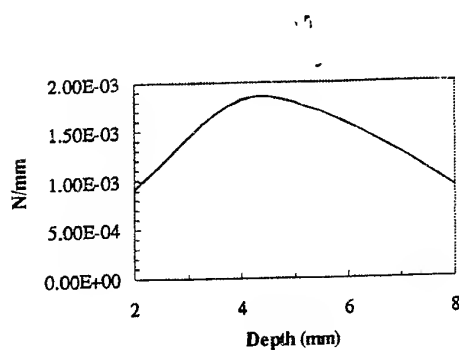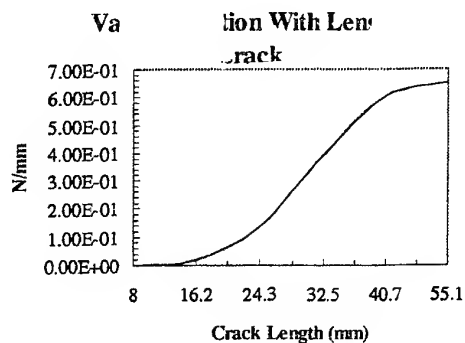
(b)   Results for Pull-Off
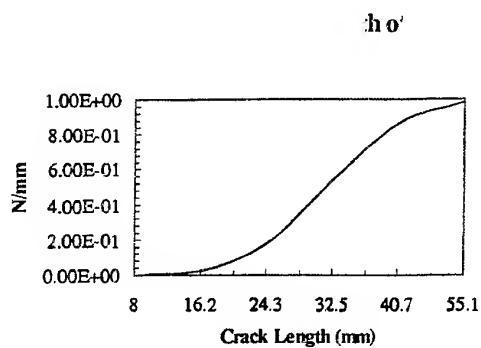
Figure 6.   Typical Variations in G

DYNAMIC THERMOELASTICITY OF LAMINATED COMPOSITE SHALLOW SHELLS AND PLATES

V. G. PISKUNOV and O. N. DEMTCHOUK

Department of Strength of Materials and Structural Mechanics, Ukrainian Transport University,
Suvorova Street No. 1, Kiev 252010, Ukraine

INTRODUCTION

Design of the composite laminated shallow shells and plates in the frames of uncoupled dynamic thermoelasticity is considered. This problem requires special study because of the additional effects of the transverse shear and temperature deformations have to be taken into account for its design. This paper considers two-dimensional solution of dynamic thermoelasticity problem for cross-ply laminated rectangular shallow shells and plates. The high-order refined theories [1] are applied both the heat conduction and elasticity problem. These theories are taken by the iterative principle for the construction of two-dimensional models of physics-mechanical processes [2].

PROBLEM STATEMENT

A laminated shell of constant thickness and constituted by n homogeneous orthotropic layers is considered. The shell is referred to an orthogonal curvilinear coordinate system (Fig. 1). The curves x_1,

Fig. 1. Geometry of laminated shell

x_2 are lines of principal curvature on the reference surface $x_1 O x_2$ and the coordinate $x_3 = z$ is defined along the normal to the reference surface what may be positioned arbitrarily through the thickness of the shell. It is assumed that coefficients of the first quadratic form of surface are close to unity $(A_i = 1)$ and the main curvatures are constant $(k_i = const)$. The total thickness of the shell is small in comparison to the radii of the curvatures $(1 + k_i z \approx 1)$. The indexes $i, j = 1, 2$ refer to the coordinate directions. A subscript after a comma denotes partial differentiation with respect to the variable following the comma. The points over the function denote differentiation at the time. A superscript is expressed in brackets to distinguish it from an exponent.

We assume that laminated shell is heated from the lower and upper surfaces by surrounding media with relative heat transfer coefficients α^- and α^+ or by the heat fluxes q^- and q^+. The temperatures of the surrounding media on the lower and upper surfaces are denoted T_∞^- and T_∞^+, respectively.

The dynamic theory of linear thermoelasticity is adopted in present study. The coupling between the heat conduction problem and the elasticity problem is neglected. In this case, general thermal-stress problem separates into two different problems: the heat conduc-tion problem and the elasticity problem for a shell under prescribed temperature field.

403

For reduce the non-stationary three-dimensional heat conduction problem to two-dimen-sional problem we are using the following assumption on the variation of the temperature in the k th layer of the shell [1]:

$$T^{(k)} = \sum_{m=0}^{M} \left(d_{1m}^{(k)} t_m + d_{2m}^{(k)} q_m \right)$$

(1)

where $T^{(k)} = T^{(k)}(x_j, z, \tau)$ is the temperature change at the time moment τ; $d_{1m}^{(k)}(z)$ and $d_{2m}^{(k)}(z)$ are the assigned functions of the temperature distribution through the laminate thickness, what satisfy to the ideal heat contact conditions on the surfaces of contact between the layers. Functions $t_m(x_j, \tau)$, $q_m(x_j, \tau)$ describe the temperature and the heat flux at the level of the reference surface $(m = 0)$, and the alteration speed of these characteristics $(m = 1...M)$. The maximal order of polynomials $d_{im}^{(k)}(z)$ depends on the number of items in the expansion (1) and equal $2M - 1$.

The system of heat conduction equations is received from a variational principle with using eqn (1) and is presented as following matrix form:

$$\mathbf{H T} + \mathbf{C} \dot{\mathbf{T}} = \mathbf{q}$$

(2)

where $\mathbf{T}$ is vector of unknown functions:

$$\mathbf{T} = \left\{ \{t_0, q_0\} ... \{t_M, q_M\} \right\}^T ;$$

(3)

$\mathbf{q}$ is the heat load vector:

$$\mathbf{q} = \left\{ \left\{ d_{1m}^{(1)}(a_0) f^- + d_{1m}^{(n)}(a_n) f^+, d_{2m}^{(1)}(a_0) f^- + d_{2m}^{(n)}(a_n) f^+ \right\} \right\}^T, \quad f^{\pm} = \alpha^{\pm} T^{\pm} + q^{\pm}.$$

(4)

Matrixes of differential operators have the following block form:

$$\mathbf{H} = \left[\mathbf{H}_{ps} \right]; \quad \mathbf{C} = \left[\mathbf{C}_{ps} \right] \quad (p, s = 0...M)$$

(5)

where elements of matrixes $\mathbf{H}_{ps}$ and $\mathbf{C}_{ps}$ are defined as

$$h_{ij}^{(ps)} = -P_{11}^{(ipjs)}(...)_{,11} - P_{22}^{(ipjs)}(...)_{,22} + P_{33}^{(ipjs)}(...) + \alpha^- d_{ip}^{(1)}(a_0) d_{js}^{(1)}(a_0)(...) +$$

$$+ \alpha^+ d_{ip}^{(n)}(a_n) d_{js}^{(n)}(a_n)(...); \quad c_{ij}^{(ps)} = C^{(ipjs)}(...) \quad (p, s, m = 0...M).$$

(6)

The eqn (6) include the integral characteristics of laminated shell that take into account the heat conduction and the heat inertia

$$P_{rr}^{(ipjs)} = \int_{a_0}^{a_n} \lambda_{rr}^{(k)} d_{ip}^{(k)} d_{js}^{(k)} dz; \quad P_{33}^{(ipjs)} = \int_{a_0}^{a_n} \lambda_{33}^{(k)} d_{ip,3}^{(k)} d_{js,3}^{(k)} dz;$$

$$C^{(ipjs)} = \int_{a_0}^{a_n} c_v^{(k)} d_{ip}^{(k)} d_{js}^{(k)} dz \quad (r = 1,2).$$

(7)

Here $\lambda_{rr}^{(k)}$, $\lambda_{33}^{(k)}$ and $c_v^{(k)}$ arc the thermal conductivity and the specific heat of the k th layer. The overall order of the system (2) is not depended on the number of layers and is equal to $4M + 4$.

For solution of the elasticity problem for laminated shell under prescribed temperature field has been applied high-order refined theory [1], which take into account the transverse shear deformations and temperature deformations in the lateral direction. The transverse normal stresses $\sigma_{33}^{(k)}$ are neglected. The distribution of transverse shear stresses as the temperature distribution taken by the iterational approach [2] and can be written as

$$\sigma_{i3}^{(k)} = \sum_{r=1}^{R} f_{ir}^{(k)} \chi_{ir} + \sigma_{i3T}^{(k)}. \tag{8}$$

Functions of reference surface $\chi_{ir}(x_j, \tau)$ describe transverse shear deformations in orthogonal directions x_j. Components $\sigma_{i3T}^{(k)}(x_j, z, \tau)$ take into account the influence of the temperature field. Functions $f_{ir}^{(k)}(z)$ are the through the thickness distribution functions and are obtained by the recursive formulas [1]. Shear stresses (8) are satisfied of the perfectly bounded conditions at the surfaces of contact between the layers and are vanished at the lower and upper surfaces.

Temperature deformations in the lateral direction are presented as

$$e_{33}^{(k)} = \alpha_{33}^{(k)} T^{(k)} = \alpha_{33}^{(k)} \sum_{m=0}^{M} \left(d_{1m}^{(k)} t_m + d_{2m}^{(k)} q_m \right) \tag{9}$$

where $\alpha_{33}^{(k)}$ is the coefficient of thermal expansion for k th layer of shell. The transverse shear deformations are obtained from constitutive law.

The displacement field of the refined theory may be expressed in the following form:

$$u_i^{(k)} = v_i - w_{,i} - \sum_{r=1}^{R} \psi_{ir}^{(k)} \chi_{ir} + u_{iT}^{(k)}; \qquad u_3^{(k)} = w + u_{3T}^{(k)} \tag{10}$$

where $u_i^{(k)}(x_j, z, \tau)$, $u_3^{(k)}(x_j, z, \tau)$ are displacements on the k th layer of shell; $v_i(x_j, \tau)$, $w(x_j, \tau)$ are the displacements of the reference surface;

$$u_{i3T}^{(k)}(x_j, z, \tau) = \int_0^z \left(\sigma_{i3T}^{(k)} / G_{i3}^{(k)} - u_{3T,i}^{(k)} \right) dz; \qquad u_{3T}^{(k)}(x_j, z, \tau) = \int_0^z \alpha_{33}^{(k)} T^{(k)} dz. \tag{11}$$

The tangential strains $e_{ij}^{(k)}$ are obtained from Cauchy's equations; the tangential stresses $\sigma_{ij}^{(k)}$ are taken from constitutive law. Using Hamilton's variational principle, the motion equations for displacement field (10) are derived as

$$N_{ij,j} = U_j; \qquad M_{ij,ij} - k_i N_{is} = U_{is,i} + U_{3i};$$
$$N_{ij,j}^{(sr)} + Q_{i3}^{(sr)} = U_i^{(sr)} \qquad (r = 1...R; \ s = i) \tag{12}$$

where summation is assumed over subscripts $i, j = 1,2$. In eqn (12) we use the internal forces and moments

$$\left(N_{ij}, M_{ij}, N_{ij}^{(ir)} \right) = \int_{a_0}^{a_n} \sigma_{ij}^{(k)} \left(1, z, \psi_{ir}^{(k)} \right) dz; \qquad Q_{i3}^{(ir)} = \int_{a_0}^{a_n} \sigma_{i3}^{(k)} F_{ir}^{(k)} dz \tag{13}$$

405

and forces of inertia

$$\left(U_i, U_{ii}, U_i^{(ir)}\right) = \int_{a_0}^{a_n} \rho^{(k)} \ddot{u}_i^{(k)}\left(1, z, \psi_{ir}^{(k)}\right) dz; \quad U_3 = \int_{a_0}^{a_n} \rho^{(k)} \ddot{u}_3^{(k)} dz \qquad (14)$$

where $\rho^{(k)}$ is material density of k th layer. Then the system (12) is expressed in terms of displacements. The overall order of this system is not depended on the number of layers and is equal to $8 + 4R$, where R is number of shear functions in expansion (8).

ANALYTICAL SOLUTION AND SOME RESULTS

The analytical solution for cross-ply rectangular simply supported shallow shells and plates is considered. The boundary conditions on the all edges of shell are the following:

$$at \ x_1 = 0, a: \ T = u_1 = u_3 = \sigma_{11} = 0; \quad at \ x_2 = 0, b: \ T = u_2 = u_3 = \sigma_{22} = 0 \qquad (15)$$

where a, b are the lengths of shell sides on the reference surface. The initial conditions for temperature and displacements are assumed to zero. The heat fluxes and the tempe-ratures of the surrounding media on the lower and upper surfaces are the following:

$$\left(q^\pm, T_\infty^\pm\right) = \left(\bar{q}^\pm(\tau), \overline{T}_\infty^\pm(\tau)\right) \sin \beta x_1 \sin \gamma x_2 \qquad (16)$$

where $\bar{q}^\pm(\tau), \overline{T}_\infty^\pm(\tau)$ are the assigned functions of time; $\beta = \pi/a$, $\gamma = \pi/b$. The relative heat transfer coefficients α^- and α^+ are constant. The boundary conditions (15) will be satisfied if the temperature and displacements represent as

$$\left\{ \begin{array}{c} t_m \\ q_m \end{array} \right\} = \left\{ \begin{array}{c} \bar{t}_m(\tau) \\ \bar{q}_m(\tau) \end{array} \right\} \sin \beta x_1 \sin \gamma x_2; \quad \left\{ \begin{array}{c} v_1 \\ v_2 \\ w \\ \chi_{1r} \\ \chi_{2r} \end{array} \right\} = \left\{ \begin{array}{c} V_1(\tau) \cos \beta x_1 \sin \gamma x_2 \\ V_2(\tau) \sin \beta x_1 \cos \gamma x_2 \\ W(\tau) \sin \beta x_1 \sin \gamma x_2 \\ X_{1r}(\tau) \cos \beta x_1 \sin \gamma x_2 \\ X_{2r}(\tau) \sin \beta x_1 \cos \gamma x_2 \end{array} \right\}. \qquad (17)$$

Using eqns (16) and (17), the heat conduction equations and motion equations can be written as

$$\mathbf{H T} + \mathbf{C} \dot{\mathbf{T}} = \mathbf{q}; \quad \mathbf{SV} + \mathbf{M} \ddot{\mathbf{V}} = \mathbf{F} \qquad (18)$$

where $\mathbf{T}$ is vector of unknown temperature functions

$$\mathbf{T} = \left\{\left\{\bar{t}_m(\tau), \bar{q}_m(\tau)\right\}\right\}^T \quad (m = 0..M); \qquad (19)$$

is vector of unknown displacement functions

$$\mathbf{V} = \left\{V_i(\tau), W(\tau), \left\{X_{1r}(\tau), X_{2r}(\tau)\right\}\right\}^T \quad (r = 1...R); \qquad (20)$$

$\mathbf{q}, \mathbf{F}$ are the heat load vector and temperature load vector respectively. All matrixes in eqn (18) are the positive definite matrixes and, consequently, all eigenvalues and eigenvectors of these matrixes are the real.

406

The solutions of system (18) are presented in form [3]

$$T = \sum_{s=0}^{2M} \mathbf{a}_s y_s(\tau); \quad V = \sum_{p=1}^{3+2R} \mathbf{b}_p z_p(\tau) \tag{21}$$

where the eigenvectors $\mathbf{a}_s, \mathbf{b}_p$ are obtained from the eigenvalue problems $(\mathbf{H} + \lambda \mathbf{C}) \mathbf{a} = 0$ and $(\mathbf{S} - \omega^2 \mathbf{M}) \mathbf{b} = 0$. The unknown functions $y_s(\tau), z_p(\tau)$ are defined from equations

$$\dot{y}_s - \lambda_s y_s = \mathbf{a}_s^T \mathbf{q}; \quad \ddot{z}_p + \omega_p^2 z_p = \mathbf{b}_p^T \mathbf{F} \tag{22}$$

which to allow the analytical solution.

As numerical example the dynamic thermoelastic response of cross-ply square plates. The upper surface is heated by surrounding media with relative heat transfer coefficient α^+ and temperature $\overline{T}_\infty^+(\tau) = const$. The lower surface has heat isolation. Let the fiber-reinforced composite with thermoelastic properties

$$E_L = 25E_T; \ G_{LT} = 0.5E_T; \ G_{TT} = 0.2E_T; \ v_{LT} = v_{TT} = 0.25; \ E_T = 6900\,MPa;$$

$$\lambda_L = 15\lambda_T; \ \lambda_T = 1\,W/\,(^\circ K \cdot m); \ c_v = 1.595 \cdot 10^6 J\,/\,(^\circ K \cdot m^3); \ \rho = 1450\,kg\,/\,m^3;$$

$$\alpha_L = -2 \times 10^{-6}\,/^\circ\,K; \ \alpha_T = 50 \times 10^{-6}\,/^\circ\,K$$

where subscripts L and refer to the fiber direction and transverse direction.
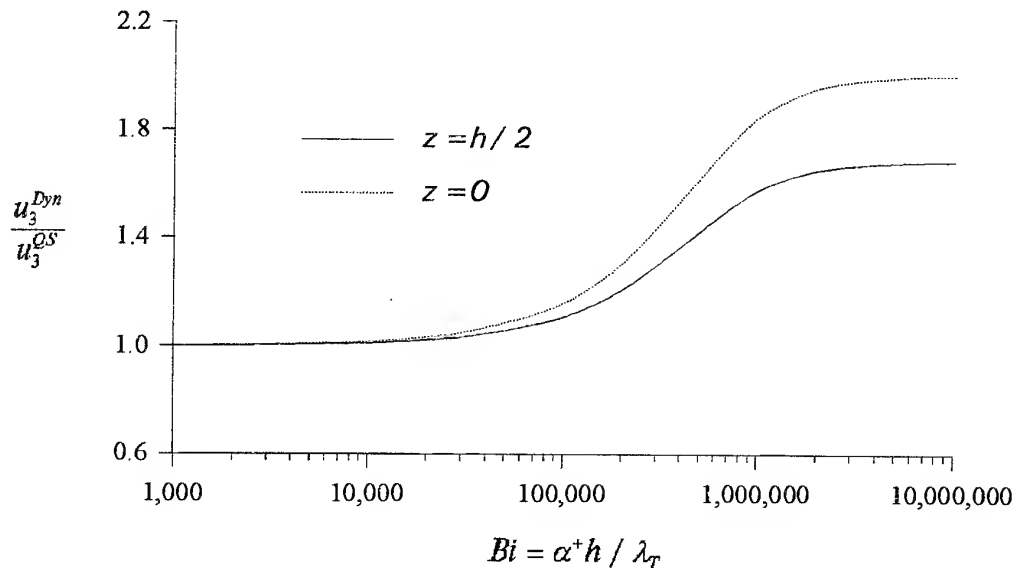
Fig. 2. Comparison the dynamic and quasi-static maximal normal deflections in three-layered $0°/\ 90°/\ 0°]$ square plate $(a\ /\ h = 10)$ with $h_k = (0.25; 0.50; 0.25)\,h$.

For the solution of the heat conduction problem the model with $M = 4$ in eqn (1) is used. For the solution elasticity problem the model with $R = 1$ in eqn (8) is applied. The ratio of the maximal dynamic and quasi-static normal deflections depends from criteria $Bi = \alpha^+ h\,/\,\lambda_T$ (Fig. 2). For $Bi \leq 10^4$ the calculation can be produced by the quasi-static theory. The deflection-ratio achieves of maximal values for $Bi\ f\ 10^6$.

407

CONCLUSIONS

Thus, the dynamic high-order refined theory is constructed for laminated shallow shells and plates The numerical results show the values of criteria Bi for which the dynamic effects must be taken into account.

REFERENCES

[1] Demtchouk, O. N. 'Comparison of approximate refined and exact three-dimensional thermoelasticity solutions for laminated anisotropic plates." *Mechanics of Composite Materials* **31**, No. 2, pp. 216-226 (1995).

[2] Piskunov, V. G. 'Problem of the construction of models of physics-mechanical processes in laminated structure systems." *Mechanics of Heterogeneous Structures* **1**, pp. 211-212 (1987).

[3] Demtchouk, O. N., Starodub, R. A. 'Determination of unsteady-state temperature fields in multilayered orthotropic plates." *Journal of Engineering Physics and Thermophysics* **63**, No. 4, pp. 1050-1055 (1192).

GROWTH LAW FOR THE COMPOSITES *IN SITU* OF REGULAR STRUCTURE

K. Rabczak[1], B. Billia[2] and W. Wołczyński[3]

[1]Foundry Research Institute
Zakopiańska 73, Kraków 30 418, Poland
[2]MATOP-Laboratory, University of Aix-Marseille, France
[3]Institute of Metallurgy and Materials Science,
Polish Academy of Sciences, Poland

INTRODUCTION

The technologist can control independently both growth rate v, and temperature gradient G during composite *in situ* production. However, it has been used to consider that only growth rate influences the λ- spacing for a given alloy. Jackson & Hunt [1] have shown that the stable growth occurs at or near the minimum undercooling for a given growth rate of composite. Lesoult & Turpin [2], next Bolze, Puls & Kirkaldy [3] have attempted to replace this intuitive condition by the substantiated criterion of the minimum entropy production. They were able to suggest the growth laws in which the λ - spacing was decided by the growth rate v only. However, some results of λ- parameter measurement prove that above distance varies with experiment for a given growth rate. So, it seems obvious that λ- spacing depends not only on growth rate, but also on another parameter. A hypothesis is postulated that temperature gradient is a second parameter which matters

Moreover, the above hypothesis is substantiated theoretically. It may be proved using a paraboloid of the entropy production derived for two thermodynamic forces appearing in the process under investigation. Thus, it seems necessary to produce a new growth law in which interlamellar spacing λ, is decided by both growth rate and temperature gradient.

PROBLEM STATEMENT

The entropy production is expressed by means of two thermodynamic forces: (X_C, X_T) from thermodynamic viepoint. A suggested growth law is to be an equation comprising all three technological parameters (λ, v, G), for a given set of material parameters. So, the transformation of entropy production from thermodynamic system to technological one is required. The following assumption is to be fulfilled for above transformation:

$$\min P(X_C, X_T) \rightarrow \min P(\lambda, v) \tag{1}$$

The assumed transformation may be shown schematically by means of paraboloid of the entropy production (Fig. 1).
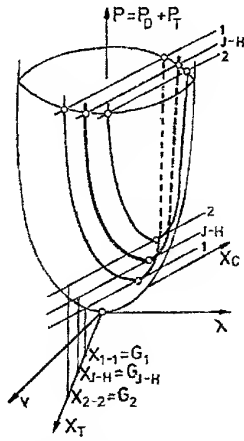
Fig.1
Trajectory of local minima of the entropy production traced for the different forces $X_T = G$. It may be concluded that spacing λ is decided by temperature gradient, G. Jackson & Hunt's theory is also placed on the paraboloid for the virtual temperature gradient so the approach is related to one parabola only, which corresponds to one minimum determined for the X_{JH}- plane.

Entropy production per unit time is given as a volume integral:

$$P = \int_V \sigma \cdot dV \tag{2}$$

where entropy production per unit time and volume σ is expressed as follows:

$$\sigma = \sum_i J_i X_i \geq 0 \tag{3}$$

However, in the first approximation the contribution to entropy production, σ_D due to mass transfer is considered only. The heat transfer will be taken into account in a second approximation, since its contribution to entropy production is smaller. The s/l interface is assumed to be isothermal one for regular structure formation and in this case:

$$\sigma_D = \{DN_i/[(1 - N_i)R_g T^2 \varepsilon]\} \, |grad.\bar{\mu}_i|^2 \tag{4}$$

$$\varepsilon = 1 + \partial \ln \gamma_i / \partial \ln N_i$$

$$grad.\bar{\mu}_i = (R_g T \varepsilon / N_i) grad.N_i \tag{5}$$

Combining (2) and (4)-(5) the entropy production per unit time P_D due to mass transfer may be calculated as follows:

$$P_D = \{R_g \varepsilon/[N_i(1 - N_i)]\} \int_0^{0.5\cdot\lambda} \int_{g(x)}^{\delta_D} D\, |grad.N_i|^2 \cdot dz\,dx \tag{6}$$

After some rearrangements the integral (6) is to be split into two parts adequately to the dimensions of half the widths of lamellae differentiated in composite *in situ* structure:

$$P_D = \int_0^{S_\alpha} \int_{g(x)}^{\delta_D} D[(\partial N/\partial x)^2 + (\partial N/\partial z)^2] \cdot dz\,dx + \int_{S_\alpha}^{0.5\cdot\lambda} \int_{g(x)}^{\delta_D} D[(\partial N/\partial x)^2 + (\partial N/\partial z)^2] \cdot dz\,dx \tag{7}$$

The analysis of concentration field in the liquid allows to introduce some parameters of a deviation from the thermodynamic equilibrium into integral (7), taking into account the existence of transition layer defined by Wołczyński [4], additionally.

410

Such an analysis is given by the following set of equation:

$$N^L = N_E^L \pm \delta N^L \qquad N^\alpha = N_E^\alpha + \delta N^\alpha \qquad N^\beta = N_E^\beta - \delta N^\beta \tag{8}$$

Introducing (8) into (7) and taking into account some parameters of concentration field:

$$P_D = v(N_E^L - N_E^\alpha) \int_0^{S_\alpha} \delta N^L \cdot dx + v(N_E^\beta - N_E^L) \int_{S_\alpha}^{0.5\cdot\lambda} \delta N^L \cdot dx + v \int_0^{S_\alpha} (\delta N^L)^2 \cdot dx$$

$$+ v \int_{S_\alpha}^{0.5\cdot\lambda} (\delta N^L)^2 \cdot dx - v \int_0^{S_\alpha} \delta N^L \delta N^\alpha \cdot dx - v \int_{S_\alpha}^{0.5\cdot\lambda} \delta N^L \delta N^\beta \cdot dx \tag{9}$$

Equation (9) shows the solution to integral (2), over the variable z, due to mass transfer.

The - $\delta N^\alpha, \delta N^\beta$ unknowns are developed by Lesoult & Turpin [2] using capillarity parameters associated with the s/l interface. Thus, equation (9) transforms to:

$$P_D = v(N_E^L - N_E^\alpha) \int_0^{S_\alpha} \delta N^L \cdot dx + v(N_E^\beta - N_E^L) \int_{S_\alpha}^{0.5\cdot\lambda} \delta N^L \cdot dx$$

$$+ v(1 - k_\alpha) \int_0^{S_\alpha} (\delta N^L)^2 \cdot dx + v(1 - k_\beta) \int_{S_\alpha}^{0.5\cdot\lambda} (\delta N^L)^2 \cdot dx$$

$$- v \int_0^{S_\alpha} \sigma_\alpha^L K_\alpha(r_\alpha)^{-1} \delta N^L \cdot dx - v \int_{S_\alpha}^{0.5\cdot\lambda} \sigma_\beta^L K_\beta(r_\beta)^{-1} \delta N^L \cdot dx \tag{10}$$

The equation (10) takes into account:
- the existence of real shape of the s/l interface considering its curvature: $1/r_S, (S = \alpha, \beta)$,
- some parameters of concentration field defined for planar interface, without curvature. The above contradiction may be deleted by introduction of the $g_S, (S = \alpha, \beta)$ - coefficient of an interplay between curvature of the real interface and *ideal* concentration field.

$$\delta N^L(x) \cdot dx = \delta N^0(x) \cdot dx + g_S(x) \cdot [r_S(x)]^{-1} \cdot dx \tag{11}$$

For an average curvature of the s/l interface the coefficient of interplay may be simplified.

$$1/\bar{r}_S = 2[(V_\alpha + V_\beta)/(V_S\lambda)] \sin \theta_S^L \tag{12}$$

$$g_S = \bar{r}_S(\delta N^L - \delta N^0) \tag{13}$$

Additionally, the geometry of oriented regular structure allows to define the widths of lamellae in function of volume fraction of composite *in situ* phases: $V_S, \quad (S = \alpha, \beta)$

$$S_S = 0.5\lambda V_S/(V_\alpha + V_\beta) \tag{14}$$

The equations (12)-(14) are used to solve the integral (10) over the variable x due to mass transfer in the liquid. Finally:

411

$$P_D = 0.5(R^*/D)N_0(2N_E^L - N_E^\alpha - N_E^\beta) \cdot v^2\lambda^2$$

$$+[(N_E^L - N_E^\alpha)g_\alpha\sin\theta_\alpha^L + (N_E^\beta - N_E^L)g_\beta\sin\theta_\beta^L] \cdot v$$

$$+0.5R_0^*(N_0/D)^2(1-k) \cdot v^3\lambda^3$$

$$+2(V_\alpha + V_\beta)[(1-k_\alpha)((g_\alpha)^2/V_\alpha)\sin^2\theta_\alpha^L + (1-k_\beta)((g_\beta)^2/V_\beta)\sin^2\theta_\beta^L] \cdot v/\lambda$$

$$+2(V_\alpha + V_\beta)[-\sigma_\alpha^L K_\alpha(g_\alpha/V_\alpha)\sin^2\theta_\alpha^L - \sigma_\beta^L K_\beta(g_\beta/V_\beta)\sin^2\theta_\beta^L] \cdot v/\lambda$$

$$+2(V_\alpha + V_\beta)R^*(N_0/D)[(1-k_\alpha)(g_\alpha/V_\alpha)\sin\theta_\alpha^L - (1-k_\beta)(g_\beta/V_\beta)\sin\theta_\beta^L] \cdot v^2\lambda$$

$$+(V_\alpha + V_\beta)R^*(N_0/D)[-\sigma_\alpha^L(K_\alpha/V_\alpha)\sin\theta_\alpha^L + \sigma_\beta^L(K_\beta/V_\beta)\sin\theta_\beta^L] \cdot v^2\lambda \qquad (15)$$

The coefficients $W_n, (n = 1, .., 7)$ are defined to simplify the obtained solution (15). Thus,

$$P_D = W_1 \cdot \lambda^2v^2 + W_2 \cdot v + W_3 \cdot \lambda^3v^3 + (W_4 + W_5) \cdot \lambda^{-1}v + (W_6 + W_7) \cdot \lambda v^2 \quad (16)$$

An optimum condition for regular structure growth is fulfilled when: $\partial P_D/\partial\lambda = 0$. Then,

$$3W_3 \cdot (\lambda^2v)^2 + 2W_1 \cdot \lambda^3v + (W_6 + W_7) \cdot \lambda^2v = W_4 + W_5 \qquad (17)$$

The growth law (17) describes formation of regular structure of composites *in situ*. Till now, however it does not show the influence of temperature gradient on the λ - spacing. It may be revealed during calcualtion of the δN^L - parameter in equation (13)

$$\delta N^L = \partial N^L/\partial T \cdot \partial T/\partial x \cdot \delta x \qquad (18)$$

The $\partial T/\partial N^L$ - parameter is the slope of liquidus line at a point of eutectic transformation and is denoted as $m_S, (S = \alpha, \beta)$. The interplay between interface curvature $1/r_S$, and concentration field is developed on the whole diffusion zone δ_D, $\delta_D = \sum_i \delta z_i$.

$$g_S = 0.5\lambda(V_S/[\delta_D(V_\alpha + V_\beta)\sin\theta_S^L])\sum_i((G_x^S/m_S)S_S - \delta N_i^{0S}) \cdot \delta z_i \qquad (19)$$

The equation (19) comprises different terms: first - associated with interface curvature, second - associated with temperature gradient $\partial T/\partial x = G_x$, (heat transfer), third - associated with concentration field (δN^0), (mass transfer). So, it has been proved that temperature gradient G_x influences on interface curvature formation and on λ - spacing.

The use of criterion of minimum entropy production in the current description allows to take into account the both transport phenomena, whereas Jackson & Hunt's theory [1], applying condition of minimum undercooling of interface considers mass transfer, only. Therefore, the current model shows the influence of both control parameters (v, G), on interlamellar spacing selection, while Jackson & Hunt's theory [1], is able to reveal the influence of growth rate v. It may be concluded that current model should be reducible to Jackson & Hunt's theory [1].

So, it is sufficient to eliminate influence of temperature gradient on structure formation in order to carry out the reduction, $(\delta N^L = \delta N^0)$. In this case equation (13) reduces to:

$$\lambda^2 v = -W_7/W_3 = const._{RBW} \tag{20}$$

and under certain simplifications, is identical to growth law given by Jackson & Hunt [1]:

$$\lambda^2 v = a^L/Q^L = const._{JH} \tag{21}$$

However, some calculations by means of the growth law (17) are possible when the temperature gradient G_x is known. So, the present growth law (17) requires to determine the temperature field within the aggregate of two eutectic lamellae. The coupling of the macro - model for the whole system (according to the heat transfer model described in [5]) and the micro - model (temperature micro - field and solidification kinetics with the special interregional boundary conditions) for the s/l interface surroundings, simplifies the numerical solution. Approximation of interrelation both the thermal and the diffusion models (under some additional assumptions) with determined λ - interlamellar spacing and (v - growth rate, G - temperature gradient) relationships allows to extend experimental verification of these models.

D	-	diffusion coefficient,
g_S	-	coefficients of interplay between interface curvature and concentration field for composites *in situ* of regular structure ($S = \alpha, \beta$),
G	-	temperature gradient, ($G = G_x, G_z$),
J_i	-	fluxes of the irreversible processes,
k_S	-	distribution coefficient, ($S = \alpha, \beta$),
K_S	-	thermodynamic coefficients involved with eutectic transformation,($S = \alpha, \beta$), defined by Lesoult & Turpin [2],
m_S	-	slope of the liquidus line, ($S = \alpha, \beta$),
N_i	-	concentration of the i - component in a given solution,
N^L	-	the solute concentration at the real interface,
N_E^L	-	the solute concentration in the liquid for eutectic point,
N^α	-	the solute concentration at solidus line of the α - solid solution,
N^β	-	the solute concentration at solidus line of the β - solid solution,
N_E^α	-	the solute concentration in the α - solid solution at eutectic temperature,
N_E^β	-	the solute concentration in the β - solid solution at eutectic temperature,
P_D	-	entropy production per unit time due to mass transfer,
r_S	-	radius of the local curvature, ($S = \alpha, \beta$),
R_g	-	thermodynamic constant,
R^*	-	structure periodicity parameter defined by Jackson & Hunt [1],
R_0^* -	-	structure periodicity parameter defined by Lesoult & Turpin [2],
S_S	-	half the width of the S - phase lamella in regular structure, ($S = \alpha, \beta$),
T	-	temperature,
T_E	-	eutectic temperature,
v	-	growth rate,
V	-	integration volume, (macroscopic point),

V_S	-	volume fraction of a given solid solution, $(S = \alpha, \beta)$,
X_i	-	forces of the irreversible processes,
$\delta...$	-	variation of parameters due to deviation from thermodynamic equilibrium,
δ_D	-	length of diffusion zone,
δN^0	-	variation of the solute concentration at the s/l interface assumed to be plane,
γ_i	-	activity coefficient of the i - component in a given solid solution,
θ_S^L	-	angle between interface and horizontal at triple point of interface, $(S = \alpha, \beta)$,
λ	-	interlamellar spacing within regular structure,
$\bar{\mu}_i$	-	chemical potential of the i - component in a given solution,
σ	-	entropy production per unit time and volume,
σ_D	-	entropy production per unit time and volume due to mass transfer,
σ_S^L	-	specific free energy at the triple point of the s/l interface, $(S = \alpha, \beta)$.

CONCLUSIONS

Thermodynamic consideration of the whole process under investigation which has taken into account both transport phenomena in system allowed to present the general outline of regular structure formation in composites *in situ* contrary to Jackson & Hunt's theory that considers thermodynamics of the s/l interface behaviour and the mass transfer only. Therefore, the reduction of current description to that given by Jackson & Hunt's theory was possible. It is also possible to calculate temperature gradient for which growth law (20), formulated by Jackson & Hunt [1] is valid and for which it may be placed on the paraboloid of entropy production, (as shown schematically in Figure 1).

The obtained growth law (17), (accompanied by definition (19)) has allowed to analyse influence of both control parameters v and G_x on interlamellar spacing λ selection for a given set of material parameters. The significant influence of growth rate v is shown by growth law (17) and secondary of temperature gradient G_x by definition (19). It says: *"at a given temperature gradient represented by its component $G_x = \partial T/\partial x$ and at a given solidification rate v eutectic transformation occurs in stationary state, in such a way that selected interlamellar spacing λ within regular structure of composite is associated with minimum entropy production for the process under investigation".*

REFERENCES

[1] Jackson, K.A., Hunt, J.D. "Lamellar and Rod Eutectic Growth." *Transactions of the Metallurgical Society of AIME* **236**, pp. 1129-1142 (1966).

[2] Lesoult, G.,Turpin, M."Etude theorique sur la croissance des eutectiques lamellaires." *Memoires Scientifiques Revue de Metallurgie* **66**, pp. 619-631 (1969).

[3] Bolze, G., Puls, M.P., Kirkaldy, J.S. "Contribution to the Theory of Eutectoid and Eutectic Transformations." *Acta Metallurgica* **20**, pp. 73-85 (1972).

[4] Wołczyński, W. "Contribution to Transition Layer Determination for Oriented Eutectic Growth." *Crystal Research and Technology* **25**, pp.1433-1437 (1990).

[5] Domański, R., Fiszdon, J.K., Styczek, A. "A Theoretical Model of a Crystallization Process" *ASME 102nd Winter Annual Meeting, Washington 1981, Conf. Proc.* pp.12-16 (1981).

THERMOELASTIC AND PHOTOELASTIC ANALYSES TO CHARACTERISE STRESSES IN FRP CONNECTIONS

P.J.C.L. READ[1], J. DULIEU-SMITH[2] and R.A. SHENOI[1]

[1] Department of Ship Science, University of Southampton, UK
[2] Department of Mechanical Engineering, University of Liverpool, UK

ABSTRACT

A key area of potential weakness in FRP structures is the connection between two panels. This paper deals with a tee connection which is typically found in large structures such as ship hulls. The aim of the paper is to outline two approaches, namely thermoelastic and photoelastic analyses, to experimentally determine stresses in such connections and to indicate how results obtained can be used to infer load transfer and failure mechanisms.

INTRODUCTION

A major element in the design of FRP structures is the correct choice of details vis-a-vis connections between two panels. The problem is compounded when the load transfer is to be effected in an out-of-plane manner, i.e. through tee connections. Current practice is to adopt secondary bonding or laminating to achieve the connection. The principal area of concern is the mechanism of load transfer between the two orthogonal members through the overlaminate connecting them. All previous work [1] has relied on finite element analyses (FEA) to predict such behaviour. The FEA models have generally been benchmarked by matching overall load-deflection behaviour with test results. The experiments themselves have had minimal instrumentation. The main responses of interest, namely in-plane and through-thickness strains in the overlaminate, have proved difficult to assess using traditional strain gauge techniques. The aim of this paper is to introduce the novel use of thermoelastic [2] and photoelastic [3] techniques for measuring stresses and strains in the overlaminate forming the tee connection.

EXPERIMENTAL TECHNIQUES

Thermoelastic stress analysis (TSA) is based on the measurement of the small temperature change that is induced in a material subjected to elastic cyclic loading. The standard equipment for TSA is the SPATE (Stress Pattern Analysis by Thermal Emissions) System [2]. The measurement of the small temperature change is permitted by the use of a highly sensitive infra-red detector incorporated in the SPATE system. In an isotropic material the temperature change is simply related to the sum of the principal stress changes on the surface of a material. In an orthotropic material the thermoelastic theory is modified so that the temperature change is also related to the coefficients of thermal expansion of the material. It is readily shown that the voltage signal from the detector is related to the stresses by the following equation

$$\sigma_1 + \alpha \dot{\sigma}_2 = A'S$$

(1)

Where σ_1 and σ_2 are the changes in the stresses in the principal material directions, $\alpha = \alpha_2/\alpha_1$ (where α_1 and α_2 are the coefficients of thermal expansion in the principal material directions), A' is a calibration constant and S is the voltage signal from the SPATE detector.

The photoelastic work described in this paper uses a reflection polariscope. For this approach a thin birefringent coating is bonded to the surface of a component to be analysed. The interface between the coating and the component is made reflective by including reflective particles in the adhesive that bonds the coating to the surface. When the component is loaded the strains in the component are fully transferred to the coating. It is assumed that the coating is sufficiently thin so that the stress in the direction normal to the surface of the coating is zero and it follows that for a material [3].

$$\varepsilon_1 - \varepsilon_2 = Nf \qquad\qquad (2)$$

where ε_1 and ε_2 are the principal strains in the component, N is the fringe order and f is the coating material fringe value.

Prior to the work described in this paper, the experimental data available on the mechanical behaviour of the tee joint [4] provided only the magnitude of the failure load and the positions of delaminations. Both TSA and photoelasticity provide full-field information so that the load path through the tee joint and the resulting stress/strain distribution can be clearly observed. Both techniques are high resolution and are particularly attractive for analysis of composite materials.

TEST PROGRAMME AND RESULTS

The Programme

A typical tee joint construction is shown in figure 1. The tee joint construction used in the experimental work comprised a 560mm flange and a 260mm web. The flange and web were constructed from 17 plies of woven roving (WR) set in Scott Bader Crystic 489 Polyester resin. Connection was achieved with pure resin, which was injected between the plates on both sides of the web to form a fillet of nominally 50mm radius. The fillet was then overlaminated to form boundary angles. The fillet was constructed of Crestomer 1152 Urethane Acrylate resin. The boundary angles had 12 plies and their lay-up from the inside was 2 x 600g Chopped Strand Mat (CSM), 1 x 780g WR, 2 x CSM, 1 x WR, 2 x CSM, 1 x WR, 1 x CSM, 2 x WR, in a Crestomer 1200 resin, which is a 50-50 mix of polyester and urethane acrylate resins. On curing 100mm wide sections were cut providing a convenient form for testing.

The tests involved a 45° 'pull-off' load being applyed to the tee joint by fully clamping the flange close to the fillet on both sides of the web and then applying a load near to the top of the web.

Thermoelastic Analysis

The tee joint was subjected to a load level of 1.7 ± 0.7 kN and a frequency of 8Hz. The thermoelastic analysis was performed using a SPATE 9000 system with the detector tilted at an angle of 10° and set at a working distance of 380mm from the test specimen. The signal was calibrated by deriving A' (see Equation (1)) using techniques that are described in detail in reference [5].

SPATE readings were taken from both sides of the tee joint which produced practically identical readings. A SPATE line plot through the thickness of the tee joint close to the root of the radius of the fillet is shown in figure 2. It should be noted that the value of A' used to produce these

results was valid for the boundary angle material only, therefore only qualitative indications of the stress distributions can be obtained from the fillet and web. Figure 2 shows that the signal varies from 5.5 MPa to -4 MPa. The nominally constant level of 5.5 MPa in the first 15 mm of the line plot are readings from the boundary angle material. At approximately 15 mm the signal drops to virtually zero; this is the fillet material. At between 22 mm and 45 mm the scan passes through the web material and at 45 mm the material changes back to that of the boundary angle. An interesting feature is the "spike" at 51 mm; a void was located in the tee joint at this point.

Photoelastic Analysis

To produce comparable results to that of the SPATE scan, the photoelastic analysis was performed at a load of 1.4 kN, i.e. equivalent to the load range used for the thermoelastic analysis. The photoelastic coating employed, had a thickness of 0.5mm and a fringe value of 3790 µm/m per fringe and it was bonded to the tee specimen using a reflective epoxy adhesive. The analysis was performed using a reflection polariscope; fractional fringe orders were obtained by using a null-balance compensator.

A full field picture of the strain distribution within the tee joint at a load of 5 kN, is shown in figure 3. This is a photograph of the fringe patterns given by the photoelastic coating. The relatively high strains in the fillet material are immediately evident. The strain distribution in the overlaminate is difficult to visualize and must be measured.

Photoelastic measurements were made at regular intervals along approximately the same line chosen for the SPATE readings. The results of these measurements are given in figure 4 in the same format as figure 2. Initially on the tension side of the joint there is peak strain of 840 µstrain, at about 4 mm the strain difference becomes negative at around -400 µstrain until at 11mm a peak strain difference occurs of 770 µstrain. This is at the interface between the overlaminate and fillet. the strain is then seen to drop away almost linearly until at 23mm the web is encountered. The strain difference increases across the web again almost linearly until 40mm. At 45 mm there is a large peak in strain difference within the fillet material of 1540 µstrain this then drops away when at 50mm the interface between the fillet and overlaminate is encountered again. The strain difference then levels out at about 630 µstrain until near the edge of the overlaminate where the strain difference drops to 200 µstrain.

A better comparison of the TSA and photoelastic analysis may be achieved by taking thermoelastic readings from the photoelastic coating. Some preliminary work has been carried out and is very encouraging. A SPATE line plot along an identical line to that in figure 2 is shown in figure 5; the applied load was identical to the above TSA work. For comparative purposes the coated joint was calibrated using the same values used for the uncoated joint. This means that the values provided by figure 5 are not quantitative; calibration of the coated boundary angle material is currently underway and will be presented elsewhere. However it can be seen that the form of figure 5 is practically identical to figure 2, except that figure 2 is less noisy than figure 5. The large spike at the beginning of the plot is caused by the edge of the coating. Also the spike caused by the void does not appear in figure 5, although there is a slight indication of it at 49 mm into the plot.

DISCUSSION

There are three key points that emerge from this preliminary study. Firstly, one of the main purposes of the experimental stress measurements was to be able to benchmark the finite element

417

analysis (FEA) procedure adopted in the wider study of joint behaviour [4]. Figures 6(a) and 6(b) show line plots of the stress and strain terms as indicated in equations (1) and (2) with the stress and strain values obtained from the FEA model. When compared with the test results as shown in figures 2 and 4, the indications are that the FEA results are reasonably accurate.

Secondly, the significance of the stress contours is that they confirm load transfer being achieved primarily through the in-plane stress path in the overlaminate. The other major response concerns the through-thickness strain, which has been shown to be very high. This is consistent with previously observed trends of final failure occurring through delaminations [4].

The third feature concerns a fundamental assumption made in the thermoelastic analysis [5], namely that the principal directions of the material in the overlaminate correspond with the ply orientation around the curved region of the joint and through-thickness direction respectively. Figure 7 presents the results of the actual measured orientation of the principal strain directions taken from the photoelastic analysis. This seems to validate the above-mentioned assumption.

CONCLUDING REMARKS

The main object of the paper has been to highlight the importance of load transfer mechanisms in out-of-plane directions through laminated tee connections. An outline has been presented of the two potentially applicable techniques for identifying stress and strain fields using thermoelastic and photoelastic analyses. Both techniques have been applied to a typical single-skin laminated tee joint.The work outlined here has achieved what has hitherto eluded researchers, namely full-field stress and strain measurements. Current work is directed mainly towards achieving stress and strain separation in the principal directions and will be reported in a separate forum.

REFERENCES

[1] Pei Junhou and Shenoi, R.A., "Examination of key aspects defining the performance characteristics of out-of-plane joints in FRP marine structures", Composites, Part A, 27(A), pp89-103, (1996).

[2] Harwood,N. And Cummings,W.M., "Thermoelastic Stress Analysis", IOP Publishing Ltd., Bristol, (1991).

[3] Durelli, A.J. and Riley, W.F., "Introduction to Photomechanics", Prentice Hall Inc., New Jersey, (1965).

[4] Shenoi, R.A., Read, P.J.C.L. and Hawkins, G.L. "Fatigue Failure Mechanisms in Fibre-Reinforced Plastic Laminated Tee Joints" Int. J. Fatigue, 17(6), pp 415-426, (1995).

[5] Dulieu-Smith, J.M., Shenoi, R.A., Read, P.J.C.L., Quinn, S. and Moy, S.S.J., "Thermoelastic stress analysis of a GRP tee joint", submitted to J. App. Composite Materials.
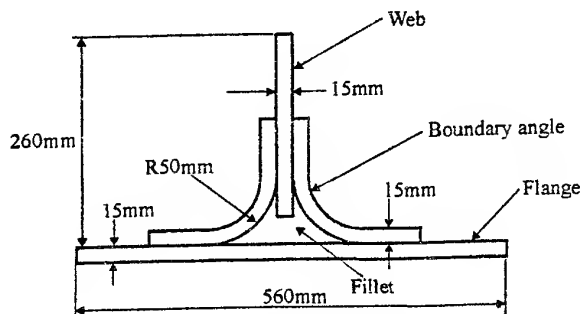
Figure 1. Tee Joint Construction
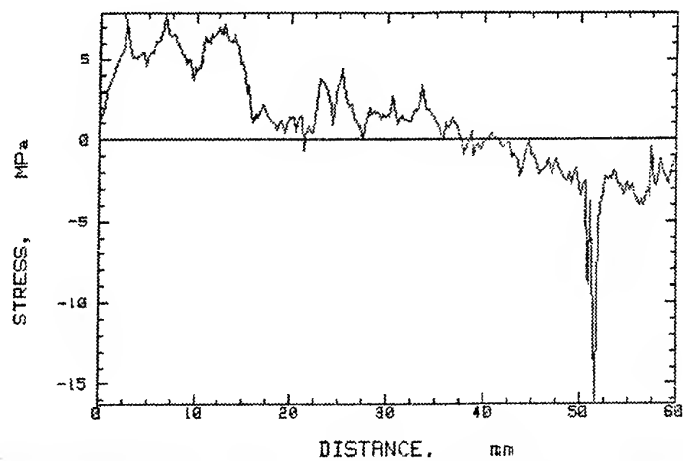
Figure 2. SPATE Line Plot without Photoelastic Coating
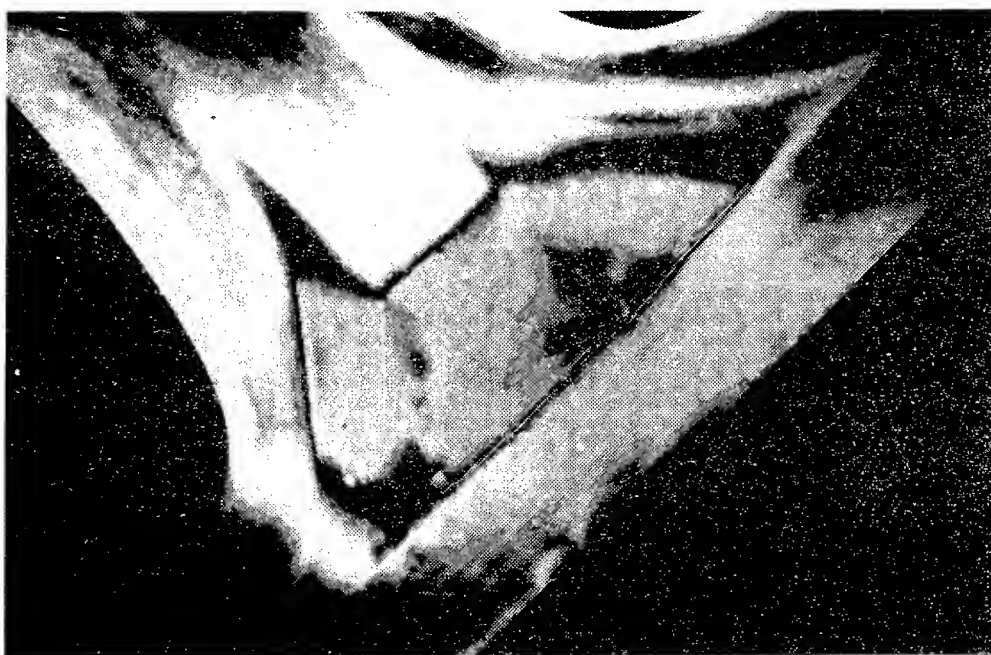
Figure 3. Photoelastic Fringe Pattern
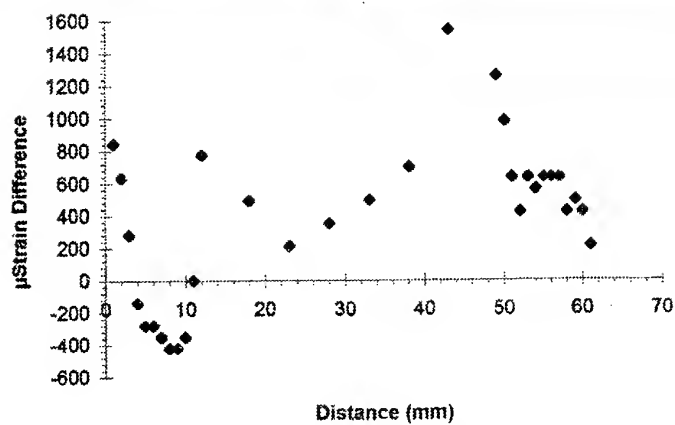
Figure 4. Photoelastic Analysis Line Plot

419

Figure 6(a). FEA Stress Line Plot

Figure 7. Principal Strain Orientation

Figure 5. SPATE Line Plot with Photoelastic Coating

Figure 6(b). FEA Strain Line Plot

REFINED THEORIES AND COMPUTATIONAL PROCEDURES FOR THE MODELLING OF SMART COMPOSITE STRUCTURES

J. N. Reddy

Oscar S. Wyatt Chair in Engineering

Department of Mechanical Engineering
Texas A & M University
College Station, Texas 77843-3123

ABSTRACT

The equivalent single–layer theories, layerwise theories, and multiple model methods used to analyze laminated composite plates are reviewed, and a simplified third–order theory to analyze laminated composite plates with piezoelectric laminae is presented. A layerwise expansion for electric field is used. A variable kinematic computational methodology is also described and illustrated through a numerical example.

INTRODUCTION

The analyses of composite plates in the past have been based on one of the following approaches:

(1) Equivalent single–layer theories (2D)

(2) Layerwise theories (3D)

(3) Multiple model approaches (2D and 3D)

The equivalent single–layer (ESL) theories are derived from the 3–D elasticity theory by assuming the form of the displacement field or the stress field through the thickness of the laminate. These assumptions allow the reduction of a 3–D problem to a 2–D problem. In the three–dimensional elasticity theory or in a layerwise theory, each layer is modeled as a 3–D solid. In a multiple model approach, a combination of single–layer and three–dimensional elasticity theories is used to achieve the level of accuracy needed in different regions of the same problem (*i.e.*, global–local analyses).

AN OVERVIEW OF LAMINATE THEORIES

Equivalent Single–Layer Theories

The equivalent single–layer laminate theories are those in which a heterogeneous laminated plate is treated as a statically equivalent, single layer having a (possibly) complex constitutive behavior, reducing the 3–D continuum problem to a 2–D problem. The ESL theories are developed by assuming the form of the displacement field or stress field as a linear combination of unknown functions and the thickness coordinate. The governing equations are determined using the principle of virtual displacements. Since all functions are explicit in the thickness coordinate, the integration over plate thickness is carried out explicitly, reducing the problem to a two–dimensional one.

The simplest ESL laminate theory is the *classical laminated plate theory* (CLPT), which is an extension of the Kirchhoff (classical) plate theory to laminated composite plates. The theory is based on the assumptions that straight lines normal to the xy–plane before deformation remain straight and normal to the midsurface after deformation. The Kirchhoff assumption amounts to neglecting both transverse shear and transverse normal effects. The next theory in the hierarchy of ESL laminate theories is the *first order shear*

deformation theory (FSDT), which extends the kinematics of the CLPT by including a gross transverse shear deformation in its kinematic assumptions, *i.e.*, the transverse shear strain is assumed to be constant with respect to the thickness coordinate. Inclusion of this rudimentary form of shear deformation allows the normality restriction of the classical laminate theory to be relaxed. The first order shear deformation theory requires shear correction factors, which are difficult to determine for arbitrarily laminated composite plate structures. The shear correction factors depend not only on the lamination and geometric parameters but also on the loading and boundary conditions. Second and higher order ESL laminated plate theories use higher–order polynomials in the expansion of the displacement components through the thickness of the laminate. The *third-order laminate theory of Reddy* [1] accommodates quadratic variation of transverse shear strains (and hence stresses) and vanishing of transverse shear stresses on the top and bottom of a general laminate composed of monoclinic layers. Thus no shear correction factors are required in the third–order theory.

In addition to their inherent simplicity and low computational cost, the ESL models often provide sufficiently accurate description of global response for thin to moderately thick laminates, *e.g.*, gross deflections, critical buckling loads, fundamental vibration frequencies and associated mode shapes. However, the ESL models have several serious limitations that prevent them from being used to solve the whole spectrum of composite laminate problems. First, the accuracy of the global response predicted by the ESL models deteriorates as the laminate becomes thicker. Second, the ESL models are often incapable of accurately describing the state of stress and strain at the ply level near geometric and material discontinuities or near regions of intense loading—the areas where accurate stresses are needed most.

Layerwise Theories

In all equivalent–single layer laminate theories based on assumed displacement fields, the interlaminar strains are continuous. Hence, the interlaminar stresses are discontinuous at dissimilar–material layer interfaces. For thin laminates, the interlaminar stress discontinuity can be negligible. However, for thick laminates, the ESL theories can give erroneous results for all stresses, requiring use of layerwise theories.

In contrast to the ESL theories, the layerwise theories are developed by assuming that the displacement field exhibits only C^0–continuity through the laminate thickness [2,3]. Thus the interlaminar starins may be discontinuous thereby allowing for the possibility of continuous interlaminar stresses. Layerwise displacement fields provide a much more kinematically correct representation of the moderate to severe cross sectional warping associated with the deformation of thick laminates.

Multiple Model Methods

The term 'multiple model analysis' is used here to denote any analysis method that uses different mathematical models and/or distinctly different levels of discretization for different subregions of the computational domain. The phrase 'global–local analysis' refers to a special case of the more general 'multiple model analysis'; the former term is typically used when there exists a particular subregion of interest that occupies a small portion of the computational domain.

To accurately capture the localized 3-D stress fields in practical laminated composite structures, it is usually necessary to resort to a simultaneous multiple model approach in which different subregions of the problem domain are modeled using appropriate kinematic structural theories. The objective of a simultaneous multiple model analysis is to

match the most appropriate structural theory with each subregion based on the physical characteristics, applied loading, expected behavior, and level of solution accuracy desired within each subregion. Thus solution economy is maximized without sacrificing solution accuracy.

To overcome the difficulties encountered in the conventional global–local analysis of practical composite laminates, a hierarchical finite element model was developed by the author and his colleagues [4–6]. The displacement field hierarchy included in the model contains both conventional equivalent single–layer and full layerwise expansions. The hierarchical nature of the model permits the computational domain to be divided into different subregions that are incompatible with respect to mathematical model type and level of finite element mesh discretization. The hierarchical model is a convenient vehicle for the analysis of composite laminates using simultaneous multiple models, and completely overcomes the difficulties associated with enforcing displacement continuity along boundaries separating incompatible subregions. In addition, the hierarchical model provides a convenient means to add progressively higher–order effects to existing models as deemed necessary by previous solutions.

A SIMPLIFIED THIRD–ORDER THEORY
FOR LAMINATES WITH PIEZOELECTRIC LAMINAE

Introduction

The study of embedded or surface mounted piezoelectric materials (*e.g.*, conventional ferroelectric polycrystals in the form of ceramics, natural crystals, and polyvinylidene (PVDF)) in the active control of structures has received considerable attention in recent years [7,8]. A laminated structure with piezoelectric laminae receives actuation through an applied electric field, and the piezoelectric laminae send electric signals that are used to measure the motion or deformation of the laminate. In these problems, the electric field that is applied to actuate a structure provides an additional body force, which couples the mechanical problem to the electrostatic problem. This coupling is similar to a temperature field inducing a body force that couples the mechanical problem to the thermal problem.

In the present study, the simplified Reddy third–order theory [1,9] is developed to study the extensional and flexural motions of plates laminated of orthotropic layers and piezoelectric laminae (see Reddy and Mitchell [8]). A layerwise expansion is used for the electric field. In addition, the formulation includes geometric nonlinearity through the von Kármán strains.

Electroelasticity

Electroelasticity deals with the phenomena caused by interactions between electric and mechanical fields. The *piezoelectric effect* is a linear phenomenon of electroelasticity, and it is concerned with the effect of the electric field and polarization on the deformation. The effect is described by the *polarization vector* **P**, which represents the electric moment per unit volume or polarization charge per unit area. The relation between the stress tensor σ and polarization vector **P** is known as the direct effect, and the converse effect relates the electric field vector **E** to the linear strain tensor ε:

$$\mathbf{P} = \mathbf{d} : \sigma \ \text{ or } \ P_i = d_{ijk}\sigma_{jk} \quad \text{and} \quad \varepsilon = \mathbf{E} \cdot \mathbf{d} \ \text{ or } \ \varepsilon_{ij} = d_{kij}E_k \tag{1}$$

where **d** is the third–order tensor of piezoelectric moduli, and d_{ijk} and σ_{jk} denote the rectangular Cartesian components.

423

The coupling between the mechanical, thermal, and electrical fields can be established using thermodynamics principles and Maxwell's relations. Analogous to the strain energy density function U_0 for elasticity and the free–energy density function Ψ_0 for thermoelasticity, we assume the existence of a density function Φ_0, called the electric *Gibb's function* or *enthalpy function*, such that

$$\sigma_{ij} = \frac{\partial \Phi_0}{\partial \varepsilon_{ij}} = C_{ijk\ell}\, \varepsilon_{k\ell} - e_{kij}E_k - \beta_{ij}\theta \tag{2a}$$

$$D_k = -\frac{\partial \Phi_0}{\partial E_k} = e_{kij}\, \varepsilon_{ij} + \epsilon_{k\ell}E_\ell \tag{2b}$$

where $C_{ijk\ell}$ are the elastic moduli, e_{ijk} are the piezoelectric moduli, ϵ_{ij} are the dielectric constants, β_{ij} are the temperature expansion coefficients, c_v is the specific heat per unit mass, and θ is the nondimensionalized temperature. Equations (2a,b) provide linear constitutive relations for the problem at hand.

In the following derivations, we account for thermal and piezoelectric effects only with the understanding that the material properties are independent of temperature and electricity, and that the temperature T is a known function of position (hence, its variation is zero: $\delta T = 0$). Thus temperature enters the formulation as a known function through constitutive equations (2a,b). However, since we are primarily interested in developing the coupled equations of piezoelectricity, the electric field $\mathbf{E}$ will be treated as a dependent variable (*i.e.*, variable subject to variation). It can be shown that for electrostatics, the electricfield $\mathbf{E}$ is derivable from a scalar potential function ψ

$$\mathbf{E} = -\nabla\psi \tag{3}$$

Approximation of Electric Field Potential

In the interest of representing the electric potential more accurately, we model it using the layerwise approximation

$$\psi(x,y,z,t) = \sum_{J=1}^{M} \psi_J(x,y,t)\Phi^J(z) \tag{4}$$

where $\psi_J(x,y,t)$ denote the nodal values of ψ, M is the number of nodes through thickness, and Φ^J are the *global* Lagrange interpolation functions for the discretization of ψ through thickness. This is equivalent to modeling through–the–thickness variation of $\psi(x,y,z,t)$ with one–dimensional finite elements. Non–piezoelectric lamina can be modelled by simply setting the piezoelectric constants to zero and retaining the dielectric permittivity constants if neccessary. In this way it is possible to model arbitrary applied potential loading conditions as well as more than one material type, including piezoelectric.

Simplified Third–Order Plate Theory

The displacement field of the third–order theory of Reddy [1,9] is given by

$$u(x,y,z,t) = u_0(x,y,t) + z\phi_x(x,y,t) - c_1 z^3\left(\phi_x + \frac{\partial w_0}{\partial x}\right)$$
$$v(x,y,z,t) = v_0(x,y,t) + z\phi_y(x,y,t) - c_1 z^3\left(\phi_y + \frac{\partial w_0}{\partial y}\right)$$
$$w(x,y,z,t) = w_0(x,y,t) \tag{5}$$

where $c_1 = 4/(3h^3)$. The equations of motion associated with the displacement filed (5) and electric field (4) are obtained using the virtual work statement

$$0 = \int_0^T \left(\delta\Phi + \delta V - \delta K \right) dt \tag{6}$$

where $\delta\Phi$ is the virtual Gibb's energy (the volume integral of $\delta\Phi_0$), δV is the virtual work done by applied forces and possibly charge, and δK is the virtual kinetic energy. The equations of motion of the *simplified theory* (see [10]) are given by

$$\frac{\partial N_{xx}}{\partial x} + \frac{\partial N_{xy}}{\partial y} = I_0 \ddot{u}_0 + J_1 \ddot{\phi}_x \ , \quad \frac{\partial N_{xy}}{\partial x} + \frac{\partial N_{yy}}{\partial y} = I_0 \ddot{v}_0 + J_1 \ddot{\phi}_y$$

$$\frac{\partial \bar{M}_{xx}}{\partial x} + \frac{\partial \bar{M}_{xy}}{\partial y} - \bar{Q}_x = J_1 \ddot{u}_0 + K_2 \ddot{\phi}_x \ , \quad \frac{\partial \bar{M}_{xy}}{\partial x} + \frac{\partial \bar{M}_{yy}}{\partial y} - \bar{Q}_y = J_1 \ddot{v}_0 + K_2 \ddot{\phi}_y$$

$$\frac{\partial \bar{Q}_x}{\partial x} + \frac{\partial \bar{Q}_y}{\partial y} + \mathcal{N}(w_0) + q = I_0 \ddot{w}_0 \ , \quad \frac{\partial P_x^I}{\partial x} + \frac{\partial P_y^I}{\partial y} - P_z^I = p^I \tag{7}$$

where (N, Q, M) are the usual force and moments resultants, (P_{xx}, P_{yy}, P_{xy}) and (R_x, R_y) denote the higher–order stress resultants

$$\left\{ \begin{array}{c} P_{xx} \\ P_{yy} \\ P_{xy} \end{array} \right\} = \int_{-h/2}^{h/2} \left\{ \begin{array}{c} \sigma_{xx} \\ \sigma_{yy} \\ \sigma_{xy} \end{array} \right\} z^3 dz \ , \quad \left\{ \begin{array}{c} R_x \\ R_y \end{array} \right\} = \int_{-h/2}^{h/2} \left\{ \begin{array}{c} \sigma_{yz} \\ \sigma_{xz} \end{array} \right\} z^2 dz \tag{8a}$$

$$\left\{ \begin{array}{c} P_x^I \\ P_y^I \end{array} \right\} = \int_{-h/2}^{h/2} \left\{ \begin{array}{c} D_x \\ D_y \end{array} \right\} \Phi^I dz \ , \quad P_z^I = \int_{-h/2}^{h/2} D_z \frac{d\Phi^I}{dz} dz \ , \quad I_i = \int_{-h/2}^{h/2} \rho(z)^i dz \tag{8b}$$

$$\mathcal{N}(w_0) = \frac{\partial}{\partial x}\left(N_{xx}\frac{\partial w_0}{\partial x} + N_{xy}\frac{\partial w_0}{\partial y} \right) + \frac{\partial}{\partial y}\left(N_{xy}\frac{\partial w_0}{\partial x} + N_{yy}\frac{\partial w_0}{\partial y} \right) \tag{8c}$$

$$\bar{M}_{\alpha\beta} = M_{\alpha\beta} - c_1 P_{\alpha\beta}, \quad \bar{Q}_\alpha = Q_\alpha - c_2 R_\alpha \tag{9a}$$

$$J_i = I_i - c_1 I_{i+2} \ , \quad K_2 = I_2 - 2c_1 I_4 + c_1^2 I_6 \ , \quad c_1 = \frac{4}{3h^2} \ , \quad c_2 = 3c_1 \tag{9b}$$

and q is the distributed transverse load, p^I is the charge at I–th node.

It is easy to verify that the transverse shear strains γ_{xz} and γ_{yz} are zero at the upper and lower surfaces of the plate, and that they vary quadratically through the thickness. Although this particular approximation was developed for laminate plates without piezo-electric lamina, it also serves well when piezoelectric lamina are present since contributions to the shear stress on the major surfaces due to piezoelectric lamina are derived from the gradient of the potential function. Note that only the tangential component of the electric field is required to be continuous across boundaries having material discontinuities. A plate having piezoelectric laminae on its outer surfaces covered with a thin electrode will not have any component of inplane electric field on these surfaces because the electric field is zero inside the conductor. Further, since transverse shear stresses due to piezoelectric effects result from components of the inplane electric field (this depends upon the partic-ular form of the constitutive relations), it follows that shear stresses on the free surfaces are only due to mechanical effects.

The stress resultants can be expressed in terms of the strains (see Reddy [9]) using the lamina constitutive equations (2a,b). For example, we have

$$
\left\{ \begin{array}{c} N_{xx} \\ N_{yy} \\ N_{xy} \end{array} \right\} = \begin{bmatrix} A_{11} & A_{12} & A_{16} \\ A_{12} & A_{22} & A_{26} \\ A_{16} & A_{26} & A_{66} \end{bmatrix} \left\{ \begin{array}{c} \varepsilon_{xx}^{(0)} \\ \varepsilon_{yy}^{(0)} \\ \gamma_{xy}^{(0)} \end{array} \right\} + \begin{bmatrix} B_{11} & B_{12} & B_{16} \\ B_{12} & B_{22} & B_{26} \\ B_{16} & B_{26} & B_{66} \end{bmatrix} \left\{ \begin{array}{c} \varepsilon_{xx}^{(1)} \\ \varepsilon_{yy}^{(1)} \\ \gamma_{xy}^{(1)} \end{array} \right\}
$$

$$
+ \begin{bmatrix} E_{11} & E_{12} & E_{16} \\ E_{12} & E_{22} & E_{26} \\ E_{16} & E_{26} & E_{66} \end{bmatrix} \left\{ \begin{array}{c} \varepsilon_{xx}^{(3)} \\ \varepsilon_{yy}^{(3)} \\ \gamma_{xy}^{(3)} \end{array} \right\} + \sum_{I=1}^{M} \left\{ \begin{array}{c} B_{31}^{I} \\ B_{32}^{I} \\ B_{36}^{I} \end{array} \right\} \psi_I - \left\{ \begin{array}{c} N_{xx}^{T} \\ N_{yy}^{T} \\ N_{xy}^{T} \end{array} \right\} \qquad (10a)
$$

$$
\left\{ \begin{array}{c} P_x^I \\ P_y^I \end{array} \right\} = \begin{bmatrix} A_{14}^{I} & A_{15}^{I} \\ A_{24}^{I} & A_{25}^{I} \end{bmatrix} \left\{ \begin{array}{c} \gamma_{yz}^{(0)} \\ \gamma_{xz}^{(0)} \end{array} \right\} + \begin{bmatrix} \hat{A}_{14}^{I} & \hat{A}_{24}^{I} \\ \hat{A}_{15}^{I} & \hat{A}_{25}^{I} \end{bmatrix} \left\{ \begin{array}{c} \gamma_{yz}^{(2)} \\ \gamma_{xz}^{(2)} \end{array} \right\} - \sum_{J=1}^{M} \begin{bmatrix} E_{xx}^{IJ} & E_{xy}^{IJ} \\ E_{xy}^{IJ} & E_{yy}^{IJ} \end{bmatrix} \left\{ \begin{array}{c} \frac{\partial \psi_J}{\partial x} \\ \frac{\partial \psi_J}{\partial y} \end{array} \right\} \qquad (10b)
$$

where $\{N^T\}$ denote thermal force resultants, and various laminate stiffnesses are defined as follows

$$
(A_{ij}, B_{ij}, E_{ij}) = \int_{-h/2}^{h/2} \bar{Q}_{ij} \left(1, z, z^3\right) dz \ , \quad (A_{ij}^{I}, \hat{A}_{ij}^{I}) = \int_{-h/2}^{h/2} \bar{e}_{ij} \Phi^I (1, z^2) \, dz \qquad (11a)
$$

$$
B_{ij}^{I} = \int_{-h/2}^{h/2} \bar{e}_{ij} \frac{d\Phi^I}{dz} \, dz \ , \quad (E_{xx}^{IJ}, E_{yy}^{IJ}, E_{xy}^{IJ}) = \int_{-h/2}^{h/2} (\epsilon_{xx}, \epsilon_{yy}, \epsilon_{xy}) \, \Phi^I \Phi^J \, dz \qquad (11b)
$$

VARIABLE KINEMATIC MODELS

Introduction

The ESL models and layerwise models each have their own advantages and disadvantages in terms of solution accuracy, solution economy, and ease of implementation. Used alone, neither of these models is suitable for general laminate analysis; each is restricted to a limited portion of the composite laminate modeling spectrum. However, by combining the two types of models in a multiple model analysis or global–local analysis, a very wide variety of laminate problems can be solved with maximum accuracy and minimal cost.

All multiple model methods represent an attempt to distribute limited computational resources in an optimal manner to achieve maximum solution accuracy with minimal solution cost, subject to certain problem specific constraints. This task often requires the joining of incompatible finite element meshes and/or incompatible mathematical models. Note that for the case of joining incompatible mathematical models, the numerical methods used to implement each of the mathematical models may be the same or different; often the finite element method is used to implement each of the models. The traditional difficulty with multiple model analyses is the maintenance of displacement continuity and force equilibrium along boundaries separating incompatible subregions.

Multiple Assumed Displacement Field

The hierarchical, variable kinematic finite element is developed using a multiple assumed displacement field approach, *i.e.*, by superimposing two or more different types of

426

assumed displacement fields in the same finite element domain. In general, the multiple assumed displacement field can be expressed as [4–6]

$$u_i(x,y,z) = u_i^{ESL}(x,y,z) + u_i^{LWT}(x,y,z) \qquad (12)$$

where i=1,2,3, and $u_1 = u, u_2 = v$, and $u_3 = w$ are the displacement components in the x, y, and z directions, respectively. The underlying foundation of the displacement field is provided by u_i^{ESL}, which represents the assumed displacement field for any desired 'equivalent single–layer' theory. The second term u_i^{LWT} represents the assumed displacement field for any desired full layerwise theory of the form in Eq. (3). The layerwise displacement field is included as an optional, incremental enhancement to the basic ESL displacement field, so that the element can have full 3–D modeling capability when needed. Depending on the desired level of accuracy, the element may use none, part, or all of the layerwise field to create a series of different elements having a wide range of kinematic complexity. Displacement continuity is maintained between these different types of elements by simply enforcing homogeneous essential boundary conditions on the incremental layerwise variables, thus eliminating the need for multi–point constraints, penalty function methods or special transition elements. It should be noted that a conventional 3–D finite element displacement field could be used instead of the full layerwise field in equation (12); however, the 2–D data structure of the full layerwise finite elements permits much easier coupling with the 2–D ESL field.

Surface–Bonded Piezoelectric Actuator

To illustrate the effectiveness of the VKFE model (with mesh superposition) in resolving local effects, we consider an unconstrained square aluminum plate with a surface bonded piezoelectric actuator. While this is a relatively simple example of a plate/actuator system, it is sufficiently complex to allow illustration of the capabilities of the VKFE model. The objective of the analysis is to determine the transverse stresses in the thin adhesive layer near the free edge of the piezoelectric actuator, and to determine the location along the edge of the actuator where the free edge stresses in the adhesive layer attain maximum value. The isotropic material properties of the aluminum, adhesive and piezoelectric are listed below.

$$
\begin{aligned}
\text{Aluminum:} \quad & E = 10^7 \text{ psi}, \ G = 0.4 \times 10^7 \text{psi}, \ \nu = 0.25 \\
\text{Adhesive:} \quad & E = 10^6 \text{ psi}, \ G = 0.357 \times 10^6 \text{psi}, \ \nu = 0.4 \\
\text{Piezoelectric:} \quad & E = 10^7 \text{psi}, \ G = 0.4 \times 10^7 \text{psi}, \ \nu = 0.25
\end{aligned}
\qquad (15)
$$

The composite plate is loaded by inducing an inplane strain field in the piezoelectric actuator ($\varepsilon_{xx} = \varepsilon_{yy} = -0.001$). Due to the symmetry of the problem, the quadrant consisting of a square region ($0 < x/a < 1$, $0 < y/a < 1$, $0 < z/h < 1.21$) is selected as the computational domain. The displacement boundary conditions for the quadrant are: $u_0(0, y, z) = 0, v_0(x, 0, z) = 0$, and $w_0(0, 0, 0) = 0$.

Figure 1a shows a coarse 8×8 global mesh of eight–node quadrilateral FSDT elements used to capture the macro–behavior of the plate/actuator system. Due to the symmetry of the problem it suffices to determine the interlaminar stresses in the adhesive layer along either one of the two free edges of the actuator. In this case the stresses will be determined along line AB shown in Figure 1a. While the global mesh of FSDT elements shown in Figure 1a is capable of accurately determining the overall deformed shape of the laminate,

the FSDT elements completely fail to capture any of the local effects near the free edges of the actuator. To capture these local effects along line AB, a series of full layerwise (LWT2) overlay meshes are constructed and superimposed on the 8 × 8 global FSDT mesh. By assimilating the results of the various global–local analyses, a composite picture of the interlaminar stresses in the adhesive layer are determined along line AB.

The LWT2 elements in the overlay mesh are eight–node quadrilaterals. The discretization through the laminate thickness consists of five linear layers through the aluminum, three linear layers through the adhesive, and three linear layers through the piezoelectric. The thicknesses of the eleven linear layers are, from bottom to top: aluminum $(h/4, h/4, h/4, 0.24h, 0.01h)$, adhesive $(0.01h/3, 0.01h/3, 0.01h/3)$, piezoelectric $(.01h, .09h, 0.1h)$.

Figure 1a also shows the first composite mesh (denoted composite mesh 1) formed by superimposing a 3 × 9 overlay mesh of LWT2 elements on global FSDT elements 25 and 33. The overlay mesh contains 3 equal length elements in the x–direction and contains 9 elements of varying length in the y–direction. The lengths of the overlay elements in the y–direction are, from $y = 0.3h$ to $y = 0.5h$: $0.05h$, $0.025h$, $0.02h$, $0.004h$, $0.00067h$, $0.00033h$, $0.005h$, $0.02h$, and $0.075h$. Global FSDT element 25 is overlaid by 18 of the LWT2 elements in the overlay mesh while global FSDT element 33 is overlaid by 9 of the LWT2 elements in the overlay mesh.

Figure 1b shows a composite picture of the interlaminar stresses in the adhesive layer along line AB. The results were obtained using the overlay mesh on different parts of line AB. Figure 1b shows the variation of σ_{zz} and σ_{xz} along line AB for transverse coordinates $z = 1.002h$, $1.005h$, $1.008h$. Notice that the transverse normal stress remains relatively constant with respect to x over most of line AB. As the free corner is approached (at $x = 0.4a$) the transverse normal stress increases dramatically. The highest transverse normal stress occurs at the intersection of the adhesive/aluminum interface and the free corner, thus this point is the most likely location for debonding to initiate. The transverse shear stress remains insignificant over much of the free edge AB, it increases dramatically as the point $x = 0.4a$ is approached.
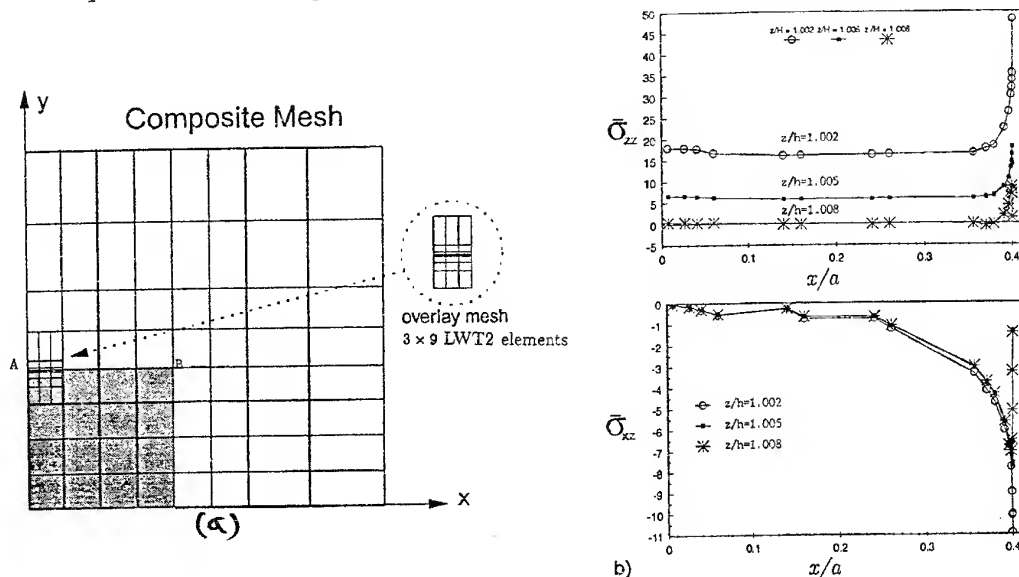
Figure 1. (a) Composite mesh (mesh 1) of FSDT and LWT2 elements in a quadrant of the plate. (b) Variation of interlaminar stresses along the plate–actuator interface.

CLOSURE

A simplified higher-order plate model is developed for the analysis of laminated plates with piezoelectric laminae. The kinematics of deformation are based on the Reddy third-order plate theory and the electric potential is represented using a layerwise (3-D) expansion that allows discrete actuation and sensing. No numerical results are presented here.

A variable kinematic computational model that contains both the ELS and layerwise displacement fields is described for global-local analyses. The global-local transition is accomplished by setting the layerwise variables to zero at the interface of the two regions, and thus avoid the use of special transition elements. The accuracy of the approach is illustrated by considering an unconstrained aluminum plate with a surface mounted actuator. For accurately resolving localized 3-D stress fields, the local regions must discretized with full layerwise elements. Further, the elements should contain at least three linear layers or two quadratic layers per distinct material ply if reasonably accurate 3-D stresses are desired. For laminates with a large number of distinct material plies, it may be necessary to resort to ply grouping in order to conserve enough computational resources to achieve this recommended level of discretization within a small select group of adjacent plies.

REFERENCES

1. Reddy, J. N., "A Simple Higher-Order Theory for Laminated Composite Plates," *Journal of Applied Mechanics,* **51**, 745-752 (1984).

2. Reddy, J. N., "A Generalization of Two-Dimensional Theories of Laminated Composite Plates," *Communications in Applied Numerical Methods,* **3**, 173-180 (1987).

3. Robbins, D. H., Jr., and Reddy, J. N., "Modeling of Thick Composites Using a Layerwise Laminate Theory," *International Journal for Numerical Methods In Engineering,* **36**, 655-677 (1993).

4. Reddy, J. N., and Robbins, D. H., "Analysis of Composite Laminates Using Variable Kinematic Finite Elements," *RBCM-Journal of the Brazilian Society of Mechanical Sciences,* **14**(4), 299-326 (1992).

5. Reddy, J. N., and Robbins, D. H., Jr., "A Simultaneous Multiple Model Approach for the Analysis of Composite Laminates," *Journal of the Aeronautical Society of India,* **45**, 157-177 (1993).

6. Robbins, D. H., Jr., and Reddy, J. N., "Variable Kinematic Modeling of Laminated Composite Plates," *International Journal for Numerical Methods in Engineering,* in press.

7. Mitchell, J. A. and Reddy, J. N., "A Refined Hybrid Plate Theory for Composite Laminates with Piezoelectric Laminae," *Journal of Solids and Structures,* **32**(16), 2345-2367 (1995).

8. Reddy, J. N. and Mitchell, J. A., "Refined Nonlinear Theories of Laminated Composite Structures with Piezoelectric Laminae," *Sadhana* (Journal of the Indian Academy of Sciences), **20**, Parts 2-4, 721-747 (1995).

9. Reddy, J. N., *Theory and Analysis of Laminated Composite Plates and Shells,* to appear.

PROPERTIES OF POLYMER COMPOSITES TREATED BY STRONG MAGNETIC FIELD

J. Rodins
Institute of Polymer Mechanics
Latvian Academy of Sciences
23 Aizkraukles Street, Riga, LV 1006, Latvia

INTRODUCTION

In the present report the results of studies of the effect of static magnetic fields (SMF), i. e. magnetic fields with a constant strength in time, on traditional polymeric composite materials during their formation are analysed. Special attention is focused on the properties of thermosetting polymers, such as epoxy resin, which is most popular matrix for composites.

The report reveals the current understanding of the mechanism of interaction of SMF with a polymer on different levels of its structural organization begining with the molecular and ending with the macrostructure of the polymer composite. The main reason of magnetic effects in polymers is the orientation of macromolecules by SMF.

ACTION OF SMF ON POLYMER MOLECULES

On the basis of earlier studies [1] the behavior of polymer molecules in homogeneous SMF can be described in the simplest case in terms of a model of rigid asymmetrically shaped, noninteracting particles, which possess anisotropy of magnetic susceptibility $\Delta\chi$, and present in a low viscosity medium. In the simplest case $\Delta\chi$ is the difference in magnetic susceptibilities in the directions parallel and perpendicular to the molecular axis.

In the case of nonaromatic molecules, in which delocalized currents are impossible, the susceptibility of the macromolecule along its axis is determined by Pascal's additive scheme [2]:

$$\chi_3 = \Sigma\chi_i + \lambda,$$

where χ_i is the susceptibility of the individual chemical bond, λ is the correction factor, a function of the structure of the molecule. Aromatic molecules are characterized by elevated diamagnetic susceptibility caused by the presence of so called ring current [3]. In the general case the magnetic susceptibility of macromolecules is described by a tensor in two dimensions.

According to [1] such particle in SMF acquires a mechanical moment

$$M = \frac{\Delta \chi}{2 \mu_0} B^2 V \sin \alpha,$$

where B is field induction; V – volume of the particle; and α – angle between the vector $\mathbf{B}$ and the direction with maximum χ. The moment M brings the particles into rotation with a nonuniform distribution of the longitudinal axes of the particles at angles of orientation α, which is characterized by the distribution function $\rho (\alpha) = dN/d\alpha$, where dN is the number of particles, the longitudinal axes of which lie in the angular interval of α to $\alpha + d\alpha$. According to [1]

$$\rho = \rho_0 \left[1 - \frac{\beta}{\sigma} (1 - e^{F\sigma t}) \cos \alpha \right],$$

where $\sigma = 1 - \beta(\cos 2\alpha / \cos \alpha)$, F – coefficient of rotational diffusion, t – time, $\beta = \Delta \chi B^2 / 2 \mu_0 kT$ characterises the ratio of the magnetic and thermal energies.

According to [4] the distribution function ρ can be related to the dichroic ratio R in the infrared spectrum, characterizing the degree of orientation of the polymer,

$$R = \frac{\sin^2 \theta + S}{2 \cos^2 \theta + S},$$

where Θ is the angle between the transition moment of vibrations and the axes of the molecular segment, S is an orientation parameter which is only dependent on the type of ρ and determined from the expressions

$$S = \frac{L}{Z - 3/2L}; \quad Z = \int_0^{\pi/2} \rho \, d\alpha; \quad L = \int_0^{\pi/2} \sin^2 \alpha \, d\alpha$$

Fig. 1 shows the curve of the dependence of R on the time of action of SMF t, and on the aftereffect time τ, plotted from calculations, as well as from experimental points. For the experiment we used epoxy resin ED–20, which was poured between two polyfluoroethylene films, fixed in nonmagnetic holder. After the magnetic action, whose maximal time was 20 min at field strength H = 5000 Oe, the holder with resin was placed in the measuring channel of a UR–20 spectrometer, where by means of a polarizer the absorption spectra were recorded at two positions – when the electric light vector is parallel and perpendicular to **H**. The value of dichroic ratio R was determined using the optical densities of the absorption band with maximum at 2870 cm^{-1}, characterizing the symmeyrical streching vibrations of the CH_2 groups [5]. The mean error in determination of R did not exceed 1,5% [6]. Thus epoxy resin behaves like a liquid crystalline system with respect to a magnetic effect.

In the process of curing in mixture with amine curing agent the orientational order created under the effect of SMF causes an increase in the number of hydrogen bonds between molecules of the oligomer, resulting in the formation of intermolecular

432
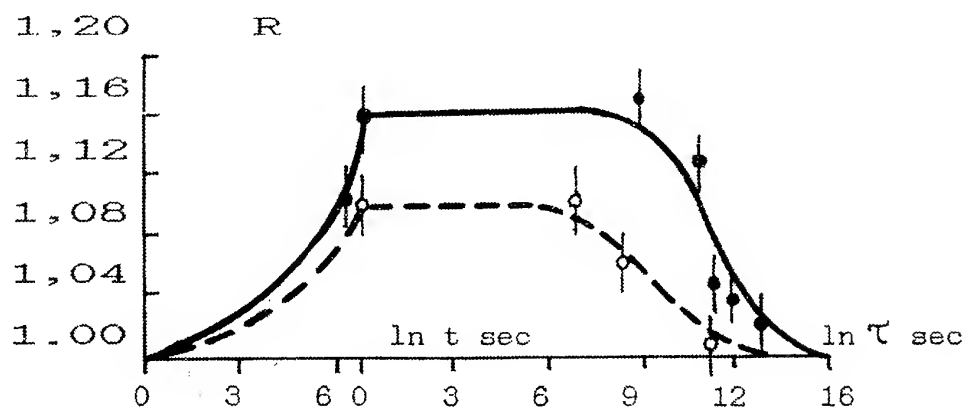
Figure 1. Dependence of dichroic ratio R on the time of action of the magnetic field t and the time of aftereffect τ for two cases: $t_{1max} = 10$ min (– – –), $t_{2max} = 20$ min (——); solid line – theoretical curve, dots – experiment.
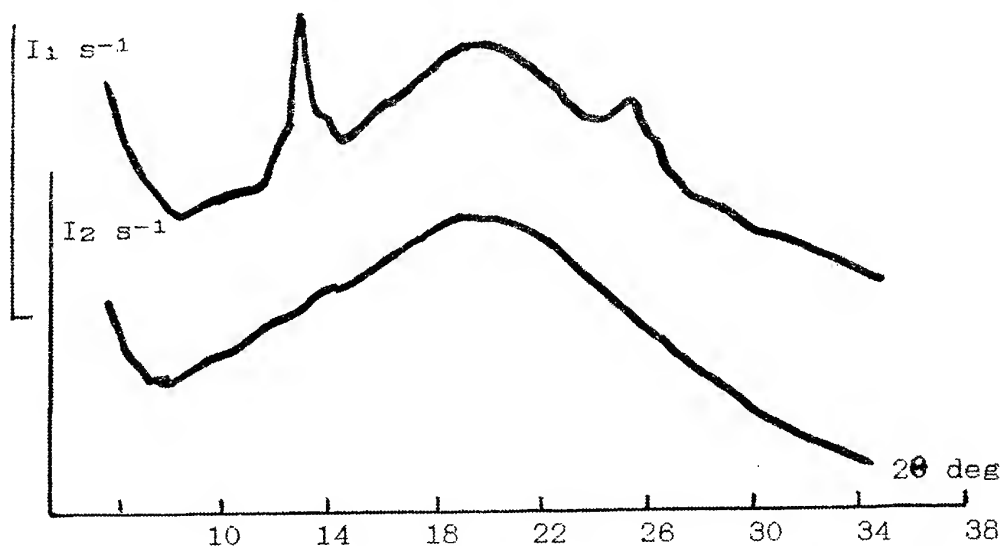
Figure 2. X–ray patterns of epoxy samples: 1 – the sample treated in SMF; 2 – the control sample.
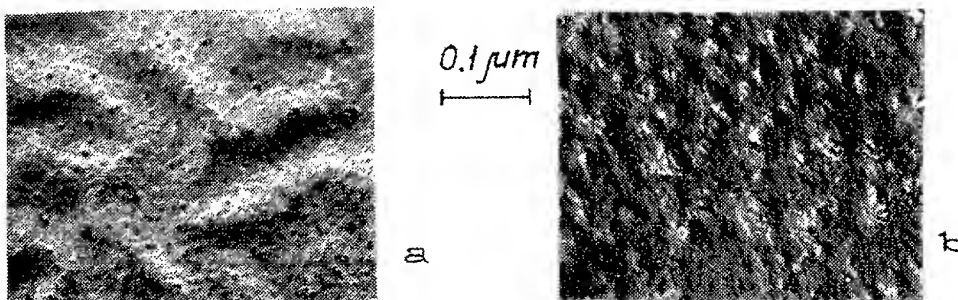
Figure 3. Electron photo micrographs of the fracture surface of an epoxy resin obtained by replica method: a – original structure, b – after magnetic treatment.

complexes with chemical **C–O–C** bonds [7]. Theese bonds together with crosslinking throw the aminogroup participate in the formation of epoxy network strengthening it.

MOLECULAR ORDER OF EPOXY RESIN IN SMF

In *Fig. 2* the distribution of X–ray diffraction intensity on the hardened epoxy specimens, studied on a URS–501 diffractometer with the use of the transmission photography method, is shown. As a result of hardening in mixture with amines the totally disordered spacial net tied by chemical bonds has been created. As can be seen from *Fig. 2* the X–ray diffraction pattern taken of specimen polymerized under standart conditions has the typical amorphous halo without indications of the reflections which would provide evidence of the presence of longe–range order. On the X–ray pattern taken from the specimens cured under the action of SMF of strength 8 kOe two maxima at reflection angles of 2 Θ, equal to 12°40' and 25°20' are observed (one is strong enough, the image of the second is blured). A net elements (atomic groups) responsible for the reflections can be identified in this complicated system using the results of IR spectrometry [7]. The period of ordering correlates with the length of epoxy net elements calculated at the base of IR spectroscopic studies.

In *Fig. 3* electron photomicrographs of the carbon replicas from the cleavage face of the epoxy compound are shown. As seen on the original sample, the supramolecular structure of the epoxy resin is globular in nature. As a result of the action of the magnetic field the size of the supramolecular formations is considerably increased. These formations have a form of oriented crystallites, embedded in a matrix of low molecular mass.

MECHANICAL PROPERTIES OF POLYMER COMPOSITES PROCESSED IN SMF

Thus the effect of SMF on the process of curing of epoxy binder has the signs of the liquid crystalline nature. This made it possible to use magnetic methods for strengthening thick–walled structures made of reinforced polymers [8]. A direct current passed throw a flat conductor (aluminium foil, carbon–fiber–reinforced tape) was employed as a source of inhomogeneous SMF. The intensity of the SMF drops off sharply with increasing distance from the surface of the conductor, but it high enough to cause structural changes in the material contact zone up to 2 mm from the conductor [9].

The binder EDT–10 was treated magnetically as it hardened by passing a direct current from a VSA–5 rectifier through a sheet of aluminum foil 0,01 mm thick whith the dimensions 200 × 300 mm², which the teflon form where the resin was poured was lined with. For a different contact subconnection and different foil layout, the direction of the magnetomotive force (MMF), which coincides with the direction of the current, was set at angles of 0, 45, and 90° to the longitudinal axis of the specimens. Both the specimens treated with the SMF and control specimens were hardened in a thermostat simultaneously in accordsance with the same temperature–time regime.
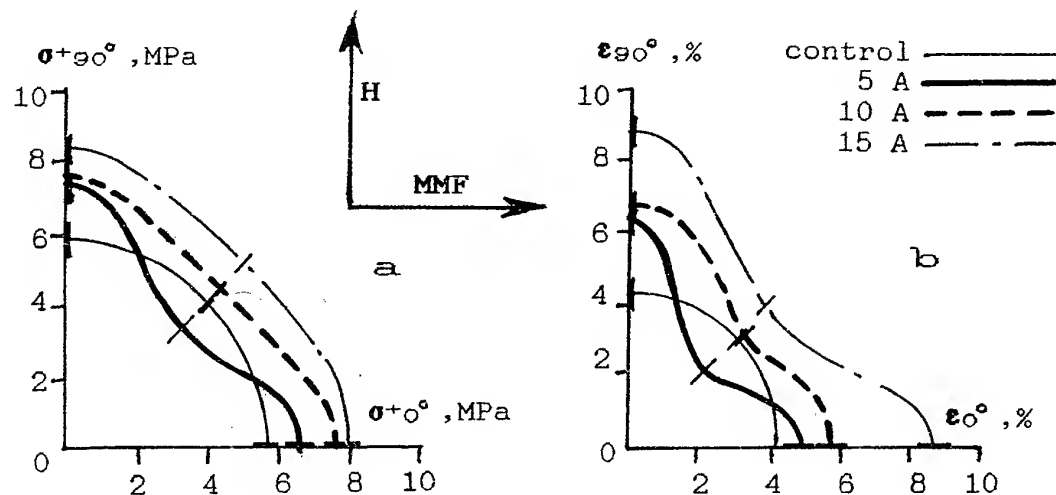
Figure 5. Clock diagrams of the tensile strength σ_+ (a) and maximum strain ε (b) for the control specimens of epoxy binder EDT-10 and specimens, subjected to treatment in inhomogeneous SMF with magnetomotive forces (MMF) of 5, 10, and 15 A and tested in directions of 0, 45 and 90° with respect to the MMF vector.

In *Fig.5* the clock diagrams of the tensile strength σ_+ and maximum strain ε are presented for the control specimens of epoxy binder EDT-10 and specimens, subjected to treatment in inhomogeneous SMF with magnetomotive forces (MMF) of 5, 10, and 15 A and tested in directions of 0, 45 and 90° with respect to the MMF vector. Analyzing the curves it can be stated that a significant increase in strength and limiting strain is observed for magnetically treated specimens. The elastic modulus in all three directions does not differ from that of the control specimens within the limits of spread; this suggests an increase in resin plasticity. Thus SMF forms an ordered net within the amorphous matrix (this is confirmed by X-ray structural investigations), which contributes to an increase in the strength and deformation in the directions of 0 and 90°. On applying a load, this net is warped and the strength characteristics are reduced in the 45° direction.

From a thecnological point of view, the use of inhomogeneous SMF created with a direct electrical current passed along a conducting armature or along the conducting surface of a press mold is especially promising as the strength properties of articles made of composites in the most dangerous construction sites can be increased. As an example can be mentioned the magnetic treatment of organoplastical tubes, containing layers of a composite electrically conducting filament (ECF), and produced by the wet winding process [10]. The organic fibers were impregnated with epoxy binder, wound on a bobbin, and cured in a temperature chamber. In cross section theese organoplastic products are strustured as follows: one layer of ECF, three layers of organic fibres, one layer of ECF. A direct current was passed through the ECF during the curing process. As a result strength measurements performed on rings during tensile tests reveal that magnetic treatment has increase their strength by 44,5%, and modulus of elasticity

by 13%. It is to be noted that magnetic treatment also causes the mechanical properties to become more uniform, as indicated by the sharply decreasing spread of data on magnetically treated specimens. As a result of magnetic treatment the coefficient of variance has decreased from 23 to 9% in the case of strength and from 10 to 4% in the case of modulus of elasticity.

CONCLUSIONS

1. A static magnetic field exerts a substantial influence on the strength characteristics of polymer composite materials based on epoxy binders.
2. The changes in the properties of polymer composite materials under the action of magnetic field are due to changes in the structure and properties of of the epoxy binder, particularly due to its structure becoming more regular.

REFERENCES

[1] Rodin, Yu.P., Molchanov, Yu.M. "Behaviour of atactic polystyrene macromolecules in a uniform static magnetic field" *Mechanics of Composite Materials* (New York) **4**, p.p. 463–469 (1982).
[2] Dorfman, Ya.G. *Diamagnetism and the chemical bond* [in Russian], Moscow (1961).
[3] Maret, G., Drasfeld, K. "Biomolecules and polymers in strong static magnetic fields" in *Strong and Ultrastrong Magnetic Fields and Their Use* [in Russian], Moscow, p.p.180–262 (1988).
[4] Zbinden, R. *IR Spectroscopy of High Polymers* [in Russian], Moscow (1966).
[5] Sidyakin, P.V. "IR spectroscopic study of curing of epoxides with amines" *Vysokomolek. Soedin.*[in Russian] A14 **5**, p.p. 979–988 (1972).
[6] Rodin, Yu.P., Molchanov, Yu.M. "Orientation of epoxy oligomer molecules in a homogeneous static magnetic field" *Mechanics of Composite Materials* (New York) **6**, p.p. 1056–1059 (1982).
[7] Rodin, Yu.P., Molchanov, Yu.M. "Effect of conformational changes caused by a homogeneous static magnetic field on curing of epoxy resin" *Mechanics of Composite Materials* (New York) **3**, p.p. 380–384, (1988).
[8] Rodin, Yu.P., Molchanov, Yu.M., Kharitonova, N.V. "Anisotropy of strength properties of plastics and their components treated in a magnetic field" *Mechanics of Composite Materials* (New York) **3**, p.p. 367–372 (1984).
[9] Rodin, Yu.P., Molchanov, Yu.M. "Special arrangement of the grid elements of EDT–10 compound in a layer bordering a conducting surface – source of a nonuniform permanent magnetic field" *Mechanics of Composite Materials* (New York) **5**, p.p. 566–571 (1990).
[10] Rodin, Yu.P., Molchanov, Yu.M., Kisis, E.R. "Properties of polymer composite materials formed under the action of a nonuniform constant magnetic field" *Mechanics of Composite Materials* (New York) **5**, p.p. 586–589 (1981).

The Development and Application of Lightweight Structural Composite Materials.

Peter J Rowberry MSc. (Eng.)
Warwick Manufacturing Group
University of Warwick
Coventry. U.K.

Abstract:

Polymeric composite materials have, in many industrial and commercial application, demonstrated their many desirable properties over other materials. However, in the high volume automotive polymeric composite materials have not had the success that many considered they should. With future vehicle needing to be designed to overcome weight problem, then the application of polymeric composites again can be considered. This paper discuss the development and application of a special type of lightweight composite materials and their potential in the vehicle of the future.

Introduction

In the majority of polymeric based composites a reinforcing fillers is incorporated within a resin matrix to achieve desirable properties for a specific component design and application.

In polymeric composite materials the fillers that are commonly used are reinforcing materials of glass, carbon or aramid, which when used in a specific form, such as fibres, tow, sheets or mattings, impart very special properties of strength and stiffness.

However, the fillers used in lightweight composites are very unique, being based on hollow spheres of glass, ceramic or plastic composition. Using hollow spherical fillers imparts a range of very diverse properties to the plastic into which they are incorporated, hence producing a unique cellular material.

Lightweight composites are based on a form cellular plastic materials in which the apparent density is decreased substantially by the presence of numerous cells disposed throughout its mass.

The lightweight composite materials are classified as tertiary systems, they have a closed-cell systems and differ from conventional foams because the hollow microspheres and the polymer are usually made from different materials and the cells are totally independent.

Lightweight composite materials, also known in some application as syntactic foams, have been used for more than 25 years, the increase in their application in industrial and consumer products has taken place over the last four years (Ref: 1).

437

The main reason for this increase in applications, has been the transfer of advanced technologies, chiefly from the aerospace and automotive industry and a need to reduce the weight of components and structures.

Warwick Manufacturing Group, part of the Engineering faculty in the University of Warwick, has been researching into Lightweight Materials for a number of years, and over the last two years has been developing commercial applications for these materials in the automotive industry. With specific application areas for Impact Absorbing Materials, Crash Protection Structures and Progressive Failure Mechanisms.

1. Lightweight Composite Materials (Ref: 1 & 2)

Lightweight composites have better strength-to-weight ratios than conventional foamed plastics, absorb water poorly and can withstand considerable hydrostatic pressures. Using a hollow and spherical filler results in a final material that is lighter and has lower residual stress than one containing a compact filler, such as glass fibres. The microspheres can be successfully used as fillers in thermoplastics and thermosets to form the light-weight-composites. These materials have high the compressive strength, improved flexural and shear moduli, reduced shrinkage, low thermal expansion coefficient, low thermal conductivity and acoustical attenuation.

2. Lightweight Fillers

Lightweight fillers are based on spherical particles which provide unique properties to plastics when used as filler. Spherical fillers have a minimum surface to volume ratio when compared with other non-spherical fillers, e.g., flakes, platelets, granules, fibres, whiskers, and irregular shaped powders. This characteristic brings many advantages as follows:

* Low surface area to volume ratio which means low resin absorption. This allows for high loading of spherical particles with little effect on viscosity.

* Regularity of shape gives ease of wetting and uniform stress distribution with predictable physical properties.

* Spherical fillers aid in the dispersion and re-orientation of other fillers, e.g., fibres, into resin so that more uniform properties of composite in all directions.

Spherical fillers which are less than 500µm in diameter are called microspheres whereas, when the sizes are between 1-100mm they are classified as macrospheres.

Microspheres and macrospheres are either solid or hollow. The solid types are most commonly used as reinforcement in plastics and are made of glass or ceramic. Sphere manufactured from carbon, graphite and zinc are employed in special applications such as electromagnetic radiation shielding.

Hollow microspheres are made of glass, ceramic, carbon or resins and are used to achieve specific, special, properties from a composite material.

Macrospheres are used with the microspheres to form high packing systems due to wide range of particle size distribution.

2.1 Property Modification

Whichever type of hollow spheres are used in a polymeric matrix, their main advantages are spherical, non-cohesive, strong, intact, moisture and chemically resistant, and hydrolytically stable. However, there are many types of hollow spheres available and with their own properties. The most important factors determining the mechanical properties of a syntactic foam is the distribution of its microspheres with respect to size, shape, and strength, the best properties being attained if these distributions are homogeneous.

Glass spheres are used to improve:

*   Tensile strength

*   Flexural modulus

*   Hardness

*   Abrasion resistance

*   Compressive strength

*   Heat deflection temperature

*   Water resistance

*   Corrosion resistance

*   Flame retardance

*   Improved dispersion of other ingredients

*   Electrical properties

*   Fracture toughness

Effect of hollow microspheres on the properties and fabrication of various composites.

	Injection Moulding	Cellular Plastics	Reaction Injection Moulding	Resin Casting	Rotational Casting	Compression Moulding	Hand Lay-up	Spray-up	Filament Winding	Pultrusion
Processing/Viscosity	=	=	=	+	+	−	+	+	+	+
Cycle Time	−	=	−	=	=	=	=	=	=	=
Modulus	+	+	+	+	+	−	+	+	−	−
Strength	−	±	−	−	−	−	−	−	−	−
Impact Strength	−	±	±	−	−	±	−	−	−	−
Modulus vs Temperature	+	+	+	+	+	=	=	=	=	=
Strength vs Temperature	=	+	=	+	=	=	=	=	=	=
Shrinkage	−	−	−	−	−	−	−	−	−	−
Coefficient of Thermal Expansion	−	−	−	−	−	−	−	−	−	−
Thermal Conductivity	−	−	−	−	−	−	−	−	−	−
Cost (Part)	−	±	−	−	−	−	−	−	−	−

Note : + increase in value
     − decrease in value
     = little or no change
     ± increase or decrease depending on specific matrix

2.2 Lightweight Filler Materials

Lightweight fillers can be formed from a wide range of materials, each of which when combined to form the composite materials provide specific properties and hence application areas.

However, in many instances it is possible, and often done, to combine these fillers into a multi-functional composite structural material. The main fillers used are:

2.2.1 Glass Microspheres

Glass microspheres have been used as fillers in plastics for over 20 years. They have the appearance of a very fine flowing white powder and have been used extensively as fillers for plastics because of their low prices and can be used as property modifiers.

High-strength glass microspheres are available having an isostatic crush resistance of 70 Mpa. This opens the way for glass microsphere applications in many injection-moulded thermoplastics.

2.2.2 Polymeric Microspheres

The polymeric microspheres have been used in syntactic foam nearly twenty years. The microspheres filled in polymer composites provide the advantages of greatly reduced weight, improved stiffness, improved nailability and screwability, improved impact strength, buoyancy and reduced cost for the composites materials. These syntactic foams therefore are utilised in application such as polyester synthetic wood casting, reinforced thermoformed acrylic structures and sandwich panel constructions.

2.2.3 Ceramic Microsphere

Ceramic microspheres are very cheap, strong and stable at high temperature, therefore, they have been used as fillers in plastics, e.g. polyester for lowering the material cost and reducing the mass of final product.

2.2.4 Metallic Coated Microspheres

Metallic coated microspheres usually glass spheres, are coated with a layer of conductive metal. The increasing importance of EMI/RFI shielding for electronic components or products gives the ways of development of metallic coated microspheres. One way is to apply EMI/RFI coating, a formulated metallic coated microspheres solvent mixture, to an inner surface of business machine housing or avionics cabinet by spraying. Another is to use these microspheres as conductive fillers in composites, called conductive syntactic foams, compounds, adhesive and gaskets for EMI shielding. Several metallic coated microspheres are available in present industries. These microspheres are not limited to EMI shielding, they are also on other applications, e.g., decoration, coatings for structural parts, body fillers, and etc.

2.2.5 Macrospheres

General speaking, hollow macrospheres have densities of 200-500 kg/m^3 and are larger than 1mm and they are usually Polymeric. By using macrospheres and microspheres together the apparent density of a syntactic foam can be reduced, however its specific strength is also less than that of a foam made only with microspheres.

2.3 Properties of Binder

Lightweight Composite materials are basically formed by mixing the spherical fillers, e.g. microspheres and/or macrospheres, and a resins binder. The binder must has a low viscosity, easily controlled gelation time, has a small exothermal effect during curing, small curing shrinkage, and good adhesions to the filler.

It must be compatible with modifiers and fillers such as diluents, plasticizers, dyes, and antipyrogenes. When the mixture leaves the mixer, its viscosity must be low enough for the mould to be filled rapidly, although once there, the viscosity should rise rapidly to prevent the mixture from becoming laminated. In addition, the binder must be able to withstand the heat applied during the mixing to produce a homogeneous mixture.

2.4 Properties of Hollow Microspheres

The property and density of the mixture depends on the binder/filler ratio but also on the microspheres themselves, their size, sphericity, polydispersity, apparent and bulk density, the thickness and uniformity of their shells. Thus at a given binder/filler ratio, the fluidity of a mixture depends on the size of the microspheres and the apparent density depends on their bulk density. As the bulk density of the microspheres increases (the filler particles become larger), the final strength of the material decrease.

Since the binder's viscosity helps the microspheres to move with respect to each other, therefore, smaller microspheres having higher surface area per mass will have higher fluidity during mixing and moulding.

2.5 Binder-and-Filler Fraction

The fluidity of an initial mixture depends on the binder:filler weight ratio, all other parameters (binder viscosity, microsphere type, shape, size, density, and mixing condition) being equal. If the microsphere concentration exceeds a certain threshold value, called the space factor, the mixture loses its fluidity and turns from a casting composition to a press-moulding composition.

2.5.1 Three-Phase Packing (Ref: 1)

The voids are usually an incidental part of the composite, as it is not easily to avoid their formation. Nevertheless, voids are often introduced intentionally to reduce the density below the minimum possible in a close-packed two-phase structure. In such three-phase systems the resin matrix is mainly a binding material, holding the structure of the microspheres together. In a three phase systems, the relative proportions (volume fractions) of microspheres, resin matrix, and dispersed air determine the density of a syntactic foam.

The following figure represents the structures for lightweight composites, in which the microspheres are dispersed randomly (a) and uniformly in close packing (b). In both structures, the two phases fill completely fills the whole volume (no dispersed air voids) and the density of the product is thus calculated from the relative proportions of the two. Measured density values often differ from the calculated ones, due to the existence of some isolated or interconnected, irregularly shaped voids as shown in figure (c).

2.5.2 Microsphere Space Factor

As mentioned before, if the microsphere concentration exceeds a certain threshold value, called the space factor (K_s), the mixture loses its fluidity and turns from a casting composition to a press-moulding composition.

Each type of microspheres has its own binder/filler ratio at which this transition occurs, making the boundary between castable and mouldable compositions.
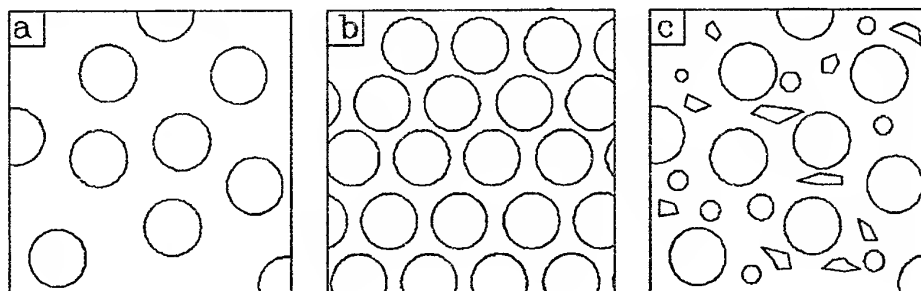
Figure (a-c). Graphic representation of Lightweight Composite Material Structures:

a Random dispersion of spheres, two-phase composite;

b Hexagonal closed-packed structure of uniform-sized spheres, two-phase composite;

c Three-phase composite containing packed microspheres, dispersed voids, and binding resin.

The space factor is given by the volume the microspheres occupy when packed the closet, i.e.

$$K_s = \vartheta_{sph}/\vartheta_o \qquad (1)$$

Where :

ϑ_{sph} is the true volume fraction of the spheres,

ϑ_o is the closest packed volume fraction of the spheres.

443

The apparent density γ_t, can be calculated:

$$\gamma_t = \gamma_{sph}(1 - \vartheta_b) + \gamma_b \vartheta_b \qquad (2)$$

Where:

ϑ_b is the binder volume fraction,

γ_b is the binder density kg/m^3, and

γ_{sph} is the apparent density of the microspheres in kg/m^3.

To obtain a lightweight composite with the lowest apparent density and approach the maximum specific strength, there are several ways are recommended.

* Mix, cast or mould under vacuum
* Moulding at pressure, e.g. mould vibration, high moulding pressure, etc.
* Using microspheres with a large value of K_s
* Using macrospheres and microspheres together as filler

3.0 Properties of Lightweight Composite Materials

Lightweight composite materials which offer many characteristics including high compressive strength, water resistant, low thermal conductivity, variable electrical conductivity, good dielectric properties, chemical stable and the most important feature of low density.

The properties of lightweight composites are influenced by several factors including the types of microspheres and resin systems used, binder/filler ratio, the process and hardening conditions, and physicochemical process at the binder/filler interface.

3.1 Strength Properties

Lightweight composite materials appear to have the highest specific strength strengths of all known plastic materials. In terms of solid resins, as well as foams. Hollow microspheres significantly improve compressive, flexural and shear moduli. Compressive and shear strength are increased as well. When compared to other fillers and fibrous reinforcements, microspheres' modification to matrix materials tends to be more isotropic and predictable. This results in more even stress distribution when under load. Spherical particles also tend to introduce less stress concentration than fibres and irregular shaped fillers. As a result, impact and fatigue strength are improved as well.

3.1.1 Strengthening Effects

Adding microspheres into polymeric resin may strengthen or weaken the resultant composite. The absolute values of the strength and elastic parameters of an lightweight composites are lower than those of the monolithic plastic. In addition, supposing a lightweight composite system with 60% glass microspheres (bulk density of 300 kg/m^3) consists of 40 vol% polymer, 53% air, and 7% glass, a reduction of the polymer content by 60% reduces; the strength only by 55%. This effect is termed strengthening effect of the microspheres. This strengthening effect is even more prominent if the binder is weak, its modulus is low.

Two factors governing the strength and elasticity of a lightweight composite are the residual internal stresses in its bulk and the adhesion strength between the binder and the filler. Accordingly, an obvious way of improving these parameters is to use strong binders and to strengthen the microspheres. Simply rejecting defective spheres can increase a lightweight composites strength by 15-20%.

3.1.2 Binder-Filler Interface Problem

The properties of lightweight composites are not only influenced by the properties of the system's components, but also by actions at the binder-filler interface. This is where dressing additives are most likely to have their effect.

The coefficient of thermal expansion of a polymer is an order of magnitude higher than that of glass, and as a result the glass filler will be squeezed into the polymer matrix during cooling of the composite. Any interaction between binder and filler will depend on the pressure and friction between them. The effect of water is due to its lubricating effect at the polymer-glass interface, reducing the friction.

4.0 Processing Technologies
(Ref: 3)

4.1 Casting

To fill a mould with an appropriate amount of spheres and pour over it a pre-measured amount of the catalysed resin solution. The solution penetrates into the intersphere voids due to gravity, capillary forces and sometimes with the aid of vacuum or positive pressure. Final curing is performed after solvent removal. In another method a measured amount of spheres is introduced into a dilute resin solution. After removal of most of the solvent the system has a consistency of wet sea-sand. This "wet-sand" is then filled, manually, into a mould. The final steps are again removing of the solvent and curing. It is important to note that mould release agents are applied on moulds between castings.

4.2 Compression Moulding

A resin either available in powder or solution can be moulded by direct compressive moulding or transfer moulding.

Compound form :- Microspheres can be mixed into a resin paste, which is impregnated with chopped glass fibre, using special machinery to form sheet moulding compounds or can be formulated by mixing microspheres to form bulk moulding compounds. They are made the same way as standard SMC or BMC.

The principal difference is use of vinyl ester resin or polyester. These compounds can be further processed by compression moulding to form SMC or BMC parts.

4.3 Hand lay up

This method is direct mixing of the glass spheres and the liquid resin to form a viscous paste, which can be hand laid in a mould and cured there. It is important that the viscosity of the intermediate mixture be as low as possible to prevent trapped air-bubbles in the final product if a two-phase system is required.

4.4 Injection Moulding

Flow characteristics are even more critical for injection of thermoplastic resin. To achieve any kind of flow at all, the resins are heated to beyond melt viscosity and then forced into moulds at high pressures under extremely high shear condition.

Not all hollow microspheres have the mechanical properties to withstand such processing conditions except the newer and stronger glass and ceramic hollow microspheres, they are stronger than the other microspheres, can now be used in moulding compounds and low pressure injection moulding resins.

The operations of injection moulding for syntactic materials are similar to the conventional injection methods. Pre-compounding of glass bubbles with resin is also necessary before moulding operation. However, the bubble should be added at the downstream part of compounding extruder.

5.0 Reinforced Syntactic Foams

Lightweight reinforced composites are a new application of microspheres. In many fibreglass reinforced plastics applications where stiffness is important, parts are a control laminate consisting of alternating layer of glass fibre.

6.0 Applications (Ref: 4)

The technology development of lightweight composite materials during the past four years has significantly advanced the state-of-the-art and continues to broaden the application possibilities by expanding the available range of properties.

The high strength-to-weight ratio, low water absorption, resistance to hydrostatic pressure, thermal and electrical insulation properties and acoustic characteristics of this unique material are increasing the areas of application where lightweight composites should be considered.

6.1 Current Research (Ref: 5)

A current series of research projects involved with applications for lightweight composite materials is taking place within the Warwick Manufacturing Group's International Manufacturing Centre.

The research, supported by international collaborators, aims at developing a series of impact absorbing and crash energy management systems for future vehicle designs. Such as:

6.1.1 Energy Management Composites Systems

Energy management systems for future space frame vehicles will need to be designed such they form integral components within the bulk heads and within the body components.

Such systems will need to be based on the combination of several discrete energy management systems, including: impact absorbing systems; progressive failure mechanisms and energy management systems. The combination of these systems will be integrated throughout the vehicle structure to maximise the protection needed for predicted impact energies.

The impact strength of a material is referred to its ability to withstand the application of a sudden impact load without failure or with very little failure. The fundamental mechanism of impact failure must be understood in order to analyse and determine the impact damage of plastic materials. There are two basic types of impact failure which are: brittle failure and ductile failure.

6.1.2 Composite Energy Absorbing Structures (Ref: 6)

Plastic foam materials are good energy absorbing materials and are used in applications which require shock and vibration damping. They can undergo large compressive deformations and absorb significant amounts of energy during a deformation cycle.

6.2 Failure Mechanics

With plastic materials there are four classes of impact failure behaviour, these are:-

- Brittle fracture. The specimen breaks completely into two or more pieces or it may crack extensively. There is no sign of yielding or only a little indication of yielding.

- Ductile fracture. the specimen will initially yield and will then crack.

Fracture mechanics are concerned with the stresses and strains in the region around the tip of the crack and the two important basic physical properties of the impact failure are those of crack initiation and crack propagation.

6.2.1 Impact Absorbing Materials

The initial research involved developing a material which would be suitable has an impact absorbing system.

This was achieved by incorporating hollow spheres into a polymeric resin system. Experimental analysis, for different volume loading of the filler, were evaluated using a falling weight impact measurement procedure.

An analysis of the impact measurements demonstrated that the impact absorbing material developed had undergone a ductile failure, with the development of micro-cracks present within the resin matrix. However, most the hollow spheres where still intact.

The impact absorbing system was therefore capable of performing in several distinct application areas.

Unfilled resins have very low resistance to crack propagation. When a particulate filler is added to the relatively brittle resins the particles inhibit the crack growth and increase the fracture energy dramatically. A crack in the filled resin is pinned by a row of particles.

Due to the pinning of the cracks and the inhibiting of its propagation by the particles, the toughness of the resin system is increased significantly. The degree of toughness depends on the volume fraction and particle size of the filler.

The mechanism of crack pinning can be explained as:

- Initially the crack front is interacting with the particle
- The crack is pinned by these particles
- Due to this pinning effect the crack bows out, this has also led to the increase in crack length and forming of new fracture surfaces.

6.2.2 Progressive Failure Mechanism

A progressive failure mechanism was developed by extruding a cellular tube structure from a thermoplastic polyester resin containing various loading of hollow spheres. The range and type of hollow spheres used dictated the failure mechanism of the system.

In instances where the failure mechanism was to occur at varying rates the structure of the cellular tube was modified or special inserts where incorporated.

Where the progressive failure mechanism is embedded within the energy management system, the failure mechanism has been developed such that maximum energy is transmitted throughout the system.

The impact absorbing system was therefore capable of performing in several distinct application areas.

6.2.3 Crash Energy Management Systems

The initial research involved developing a material which would be suitable for an energy management system.

This was achieved by incorporating hollow spheres of diameters microns into an resin system; and curing the systems with a flexible catalyst. Experimental analysis with different high volume loading were evaluated using the falling weight impact measurement procedure.

An analysis of the impact measurements demonstrated that the energy management material developed had undergone a failure mechanism in which the resin is used as a binder through which the energy is passed directly to the hollow spheres.

The loading of the hollow spheres is such that the inter-spatial distances are minimal and under high energy transmissions there is a tendency for the spheres to collide.

REFERENCES

(1) Puterman M. & Narkis M. J. Journal of Cellular Plastics - Syntactic Foams 1. Preparation, Structure and Properties, 16 No. 4 225, 1980.

(2) Shutov, F. A., Advanced Polymer Science - Syntactic Foams. No. 67, 1986

(3) Shutov F.A. & Chaikin I.I., Annual Conference. LISI, Leningrad USSR. 1983

(4) Passenger Safety and Impact Management. Research Project. Warwick Manufacturing Group, University of Warwick, 1995

(5) Rowberry P.J. Impact Absorption and Energy Management Strategy. Warwick Manufacturing Group. 1993

(6) Rowberry P.J. Impact Management and Passenger Safety. Autotech 95. Birmingham. 7-9 November 1995

MECHANICAL DAMAGE ON WOVEN TEXTILE COMPOSITE INTERPHASE

S.H. Saidpour and M. Sezen
School of Design, Engineering and Computing,
Bournemouth University,
Studland House, 12 Christchurch Road,
Bournemouth BH1 3NA, United Kingdom
(Email: hsaidpou@bmth.ac.uk)

ABSTRACT

This paper assesses the effect of glass fibre surface treatments on the tensile and flexural damage of woven textile reinforced epoxy composites. The two competing surface treatments studied include TD22, a newly developed matrix oriented size, and the widely used Z6040 silane coupling agent. The TD22 size system showed improvements in mechanical performance compared to Z6040 silane finish which has produced a brittle composite with lower strength. The Acoustic Emission (AE) analysis supports the fracture analysis as the number of ringdown counts from the sized material is smaller than the counts produced by the Z6040 finished material, thus indicates that more damage can be tolerated by the TD22 sized composite. The AE data that correlated with mechanical test results shows the onset of the AE activity corresponds to the knee-point of the stress-to-strain curve in woven composites.

INTRODUCTION

Woven textile structural composites are rigid materials designed for structural or load bearing applications, and provide more balanced properties in the fabric plane than unidirectional laminates. Aerospace ,aeronautics, sports goods, and automotive industries use more and more of textile composites as their competitiveness increases with regard to the ratios of performance/weight/cost. The use of the textile architectures in composites however requires an increase in their compatibility with the matrix resin. In a polymer matrix composite, the stress acting on the matrix is transmitted to fibres across the interface, so that the ability to transmit stress depends on the mechanical properties of the matrix, the load bearing ability of the fibres and the strength of the fibre/matrix adhesion. Therefore, the interphase region between the fibre and matrix plays a major role in the mechanical properties of composite materials. Chemical surface treatments over the years have been developed in order to improve the properties of the interphase. In most cases, the strong adhesion is required to give product the best response to mechanical behaviour, but a weaker elastic adhesion is sometimes needed to improve the damage tolerance.

In their studies, Drzal et al concentrated on the action of a silane coupling agent-containing sizing system, and showed that the interaction of the size with the matrix produces a material with a higher modulus, a greater tensile strength, but a lower toughness[1]. They also proved that changes in interfacial strength due to the effect of sizing[2].

It is often that a composite fail gradually, with a great deal of interfacial debonding; an excessively high bond strength will lead to a catastrophic brittle fracture of fibres and matrix simultaneously. Thus inferences concerning the strength at interphase can be drawn from the longitudinal tensile strength that was shown to be sensitive to degradation of the fibre itself that is affected by the glass fibre size[3]. A strong correlation between tensile strength and surface treatment level has been reported and suggested that the fabric structure and fibre orientation should be taken into account in order to determine the interfacial effect on the mechanical properties of woven composites, such as the weave style and loading directions (warp/weft)[4].

Flexural tests are widely used for quality control and comparative purposes. A flexural load simultaneously imposes flexural tensile, flexural compressive, and shear stresses on different locations within a structure. Shih and Ebert[5] pointed out that the flexural compressive and shear strengths of composites were affected in the same sense as the interfacial strength. However the interpretation of the data from flexural test is complicated, proper conclusions can be drawn if the constituents of the material are well known and the failure criteria is determined.

Acoustic emission have been used as a non-destructive technique to assess the strength or the integrity of composite materials and to determine the location of growing discontinuities. This potential exists because observations indicate that many fibre reinforced composites fail as a result of discontinuities generated by progressive damage that occurs during loading[6]. Caldwell et al[7] studied glass reinforced epoxy composites and used AE to rank the composites' resistance to damage during several standard mechanical tests. Narisawa and Oba[8] obtained experimental conformation of a one-to-one correlation between an acoustic event and an individual occurrence of damage. By simply counting the acoustic events, they were able to estimate the critical lengths of the fibres thus calculate the interfacial strength. Drzal[9] used thermoacoustic method which relies on laser heating of a high volume fraction composite to induce interfacial failure which can be detected by acoustic measurement method and samples with weaker interphases yield stronger AE signals than those with a strong interfacial bonding. Some researchers[10] concentrated on wave speed and its relation to the elastic properties of woven glass fibre reinforced plastics since the velocity of propagation of an acoustic wave is a function of the elastic moduli relevant to the direction and mode of propagation.

A well-known phenomena of woven textile composites is the "knee-point" in a stress-strain behaviour. The knee-point appears on a stress-to-strain curve as a result of microfracture that is initiated by transverse fibres, inducing matrix cracking and local softening in the material during tensile loading. The elastic stiffness and knee-stress in satin weave composites are higher than those in plain weave composites. The presence of bridging regions, that surround the interlaced regions, are responsible for the higher stiffness and knee-stress in satin weave composites[11]. The effect of surface treatments can be measured from microstructure analysis that the initial microfracture stress and strain can be increased or decreased by variations in silane concentration levels[12]. We carried out the acoustic emission monitoring for the appearance of the knee-point during destructive testing of composites treated with TD22 size and Z6040 silane coupling agent. The method of AE used was the "ringdown count" that each stress wave reaches the transducer as collection of complex waves. If the signal is amplified and fed to a counter that identifies all positive crossings of a given threshold the number of counts recorded will be much higher than the absolute number of microfailure events that have occurred[13]. This greatly enhances the successful studies of failure mechanisms in composites. The combined study of AE and knee phenomenon allowed us to establish patterns of emission behaviour for various types of failure criteria, such as matrix cracking, debonding and fibre breakage.

EXPERIMENTAL DETAILS

The reinforcement used included two kinds of 8-shaft satin weave E-glass fabrics, supplied by CS-Interglas. Fabric style 7581 was woven from a 9 micron diameter glass fibre yarn which was treated with TD22 size, produced by Vetrotex. The style 7781 was woven from a 6 micron diameter yarn that was coated with a textile size which was removed by heat-cleaning after weaving, then the Z6040 finish is applied onto the fabric. The resin system used was bisphenol A-based Fibredux 913 epoxy film produced by Ciba Composites.

A resin film layer was stuck to each side of a glass layer by heat in order to achieve 50% fibre content by volume. The plies of the prepreg was placed on top of each other for the required thickness and the prepreg was moulded in a hydraulic press for 2 hours at 125 °C. Tensile tests were performed according to ISO 3268[14], wit crosshead speed of 2 mm/min. Flexural tests were carried out according to BS 2782[15] using a 3-point bending rig at a rate of 10 mm/min. Acoustic Emission (AE) was also monitored during both tensile and flexural tests using Marandi 1004 analysis equipment.

RESULTS AND DISCUSSION

The Ultimate Tensile Strength (UTS) and Ultimate Flexural Strength (UFS) values are presented in Table 1. The results show that composites with TD22 size have superior mechanical properties, with 10% higher UTS, than those of the Z6040 finished composites.

Tensile Failure

Tensile test specimens of TD22 sized composites failed with a propagation of the crack running across the test piece diagonally following the weave pattern as shown in picture (Pic.1). The Z6040 finished material has failed across the middle with a lower failure strain. The failed sections can be seen in Pic.2. For TD22 sized specimens, fibres parallel to the loading direction (along warp) have broken at points where they cross over the weft yarns. This indicates that the transverse (weft) fibres were controlling the debonding process by holding the longitudinal warp fibres. The interphase in the Z6040 finished material appeared to be stronger, and the delamination was initiated by longitudinal warp yarns as they started to break. Once these cracks exceeded the critical stress, the specimen failed catastrophically. Comparisons of tensile results with acoustic emission counts confirm the variations in failure modes between the two composites, as seen in Fig.1 and Fig.2.

Gradual failure of the TD22 sized specimens produced a fairly linear AE curve which indicates a good stress transfer and a well-balanced interphase. The non-linearity of the AE curve for the Z6040 finished material illustrated a higher delamination. The higher the strength of interphase the higher the number of counts produced as seen in the case of Z6040 finished specimens. In both graphs in Fig.1 and Fig.2, the onset of the AE curves correspond to the knee-point on the stress-to-strain curve. The knee-point has been identified at the point of first microfracture stress in a stress-to-strain curve for tensile loading of woven composites. The results of AE analysis are shown in Table 2.

The initiation of fracture in transverse fibres is the cause of the knee-point that it limits the elastic region in tensile loading[16]. Therefore, the position of the knee-point for each composite reflects the level of adhesion in the fabric/matrix interphase. We observed that the knee-point for Z6040 finished material is higher due to the effect of strong interphase. The toughness of the composite is reduced that the elastic strain energy is released quickly, after the knee-point, rather than being absorbed as it

453

was the case for TD22 sized composite which has got lower knee-point but higher tensile strength and strain.

Coating	UTS (MPa)	UFS (MPa)
TD22	500	655
Z6040	450	640

Table 1. Mechanical test results for specimens tested in warp direction

FABRIC COATING	TENSILE TEST			FLEXURAL TEST		
	Knee-stress (MPa)	Knee-strain (%)	Total Ringdown Counts	AE Onset Stress (MPa)	AE Onset Strain (%)	Total Ringdown Counts
TD22	150	0.75	1,500,000	190	1.1	50,000
Z6040	200	0.95	2,500,000	265	1.5	82,000

Table 2. Acoustic emission analysis results from mechanical testing of the composites

Flexural Failure

The load-deflection curves for flexural tests indicate a linear load distribution for both materials up to the maximum load shown in graphs in Fig.3 and Fig.4. During flexural testing of TD22 sized specimens the matrix cracking propagated along the top surface of the specimen which caused a compressive damage that is shown in Pic.3, unlike the Z6040 finished composite in Pic.4. The lack of penetration of the failure through-to-thickness indicates that release of the strain energy was being absorbed by transverse fibres on the top surface rather than by matrix cracks into the specimen.

This is also evident in the AE results showing less number of ringdown counts as the energy absorbed by the interphase is less. As expected, Z6040 composite which has a brittle interphase produced more AE ringdown counts, seeTable 2. The onset of the AE activity appeared again earlier for the TD22 composite similar to tensile loading. However, the increased flexural toughness of the material by TD22 size improved the load-carrying capability of the composite. The failure in the Z6040 finished specimens was however propagated through-to-thickness which is supported by the non-linearity of the AE plot. Regions of tensile failure (fibre pull-out) and compressive failure (crushing) appeared on both sides of the Z6040 specimens, the dominant failure mode tended to change from flexural compressive to tensile fibre pull-out when the strength of the interphase decreased.

CONCLUSION

The matrix oriented size, TD22, actually enhances the mechanical strength of woven textile composites with better controlled interphase compared to the conventional Z6040 silane coupling agent. The knee-point in tensile loading of woven textile composites also corresponds to the onset of the Acoustic Emission activity. It is also observed that the elastic stiffness and knee-stress in Z6040 finished composites are higher than those treated with TD22 size due to the presence of the stronger interphase. However, the composite with TD22 can absorb more strain energy with increased toughness of the material.

References

[1] E.K Drown., H Moussawi., L.T. Drzal., "Glass fibre 'sizings' and their role in fibre-matrix adhesion", J. Adhesion Sci. Tech., Vol. 5, No. 10, pg. 865-881, (VSP 1991)

[2] E.K Drown., H Moussawi., L.T. Drzal, "The glass fibre sizing interphase and its effects on adhesion and composite properties", 6th Technical Conf., American Society for Composites N.Y. 7-9 Oct. (1991)

[3] D. L. Caldwell, "Interfacial analysis", Composites Encyclopaedia ed. S. M. Lee, Vol. 2, (VCH Publications 1992)

[4] H. Ichihashi, H. Hamada, N. Ikuta, Z. Maekawa, "Effect of silane coupling Treatment on Microfracture in plastic reinforced with plain woven glass fabric", Journal- Society of Fibre Sci., Vol. 49, No. 4, pg. 169-175, (Japan April 1993)

[5] G.C. Shih, L.J. Ebert, J. Materials Science, No. 21, pg. 3957, (1986)

[6] C. Zwebwen , 'A Bounding approach to the strength of composite materials', Engineering and Fracture Mechanics, Vol. 4, No 1, (1972)

[7] D.L. Caldwell, D. L. Steele, L.T. Guth, J. Reinf. Plast. Composites, No. 6 pg. 193, (1987)

[8] I. Narisawa , H. Oba , J. Materials Science, No. 7 pg. 1113, (1972)

[9] P. Herrera-Franco et al, "Contemporary methods for the measurement of fibre-matrix interfacial shear strength", 4th Annual Conf., session 14-B, Composites Institute, The society of plastics industry, Feb. 18-21 (1991)

[10] E.O. Ibitolu, J. Summerscales , "Acoustic emission source location in bidirectionally reinforced composites Part 2", TEQ '87 Conf. pg. 128-133, (Butterworths 1987)

[11] T. Ishikawa, T.Chou, "Analysis and Modelling of Two Dimensional Fabric Composites", Textile Structural Composites, chapter 7, pg. 209 (1989)

[12] H. Ichihashi, H. Hamada, N. Ikuta, Z. Maekawa, "Effect of silane coupling Treatment on Microfracture in plastic reinforced with plain woven glass fabric", Journal- Society of Fibre Sci., Vol. 49, No. 4, pg. 169-175, (Japan April 1993)

[13] B. Harris, M.G . Phillips, 'Non-Destructive evaluation of the quality and integrity of reinforced plastics' in Developments in GRP Technology-1 (ed. Harris B.), p. 224, (Applied Science Publisher 1985)

[14] ISO 3268, Plastics-Glass reinforced materials-Determination of tensile properties (1978)

[15] BS 2782, Part 10 Glass Reinforced Plastics, Method 1005, 'Determination of flexural properties. Three point method' 1977

[16] S. Kadamoto, "A determination method of interfacial material constants of glass/epoxy Composites (I)", Poster Booklet, Kyoto Institute of Technology, Polymer Mechanics Lab., pg. 37 (Japan 1995)
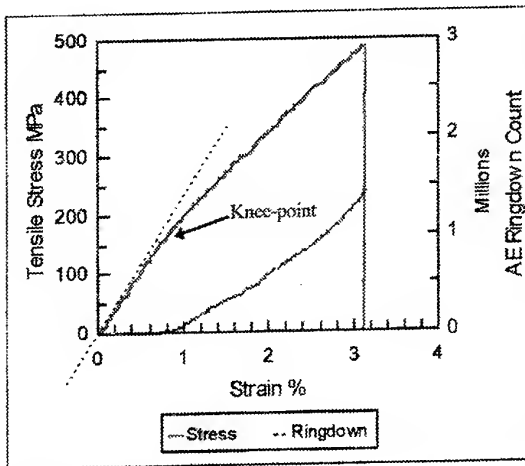
Fig.1. Tensile Stress &AE against Strain for TD22 composite
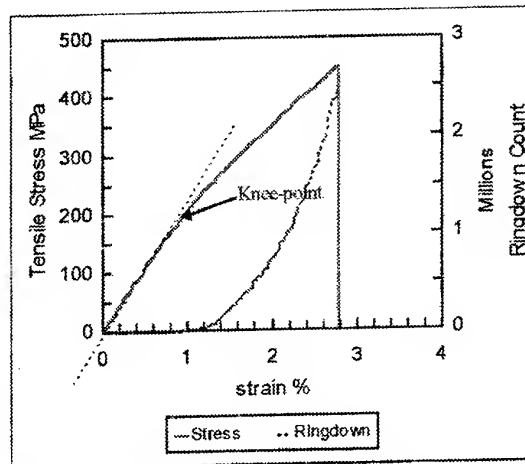
Fig.2. Tensile Stress &AE against Strain for Z6040 composite
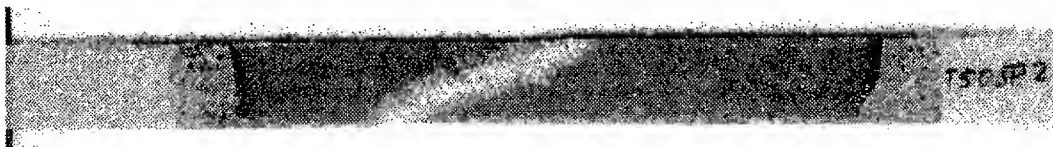
Pic.1. Failed section of tensile specimen from TD22 sized composite

Pic.2. Failed section of tensile specimen with Z6040 finish
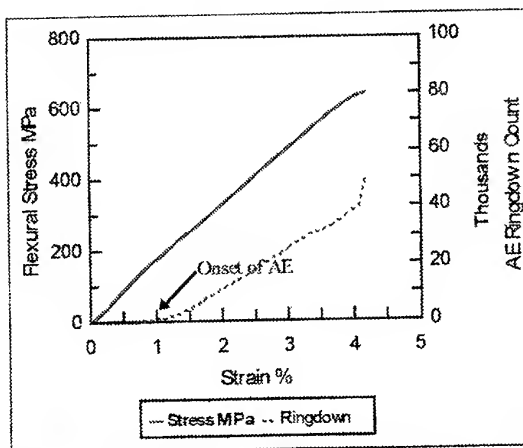
Fig.3. Flexural Stress and AE against Strain for TD22 Composite
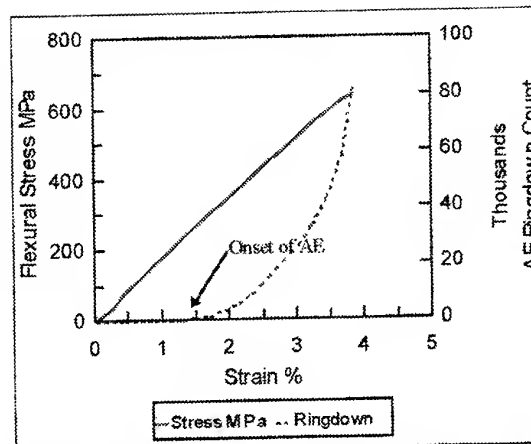
Fig.4. Flexural Stress and AE against Strain for Z6040 composite
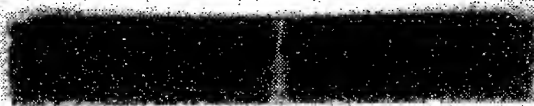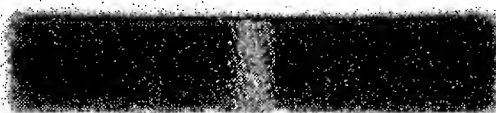
Pic.3. Broken flexural specimen of TD22 composite   Pic.4. Broken flexural specimen of Z6040 composite
Both pieces are viewed from loading surface, showing the compressive damage.

456

ANISOTROPIC ELASTO-PLASTIC AND STICK-SLIP EFFECTIVE BEHAVIOUR OF PERIODIC COMPOSITE MATERIALS

B.A. Schrefler*, U. Galvanetto* and M. Lefik[1]

*Istituto di Scienza e Tecnica delle Costruzioni,
Via Marzolo 9, 35131 Padova, Italy

[1]Department of Mechanics of Materials,
Technical University of Lodz, Poland

1. INTRODUCTION

Homogenization techniques have been extensively applied to the study of linear composite materials with periodic structure [1, 2, 3]. The structure of such materials can be thought of as repetition of an element called cell of periodicity and the main idea of the homogenization theory is the hypothesis that the geometric periodic structure induces similar periodic perturbations on the stress and strain fields. These can then be considered as superposition of two principal contributions: an averaged contribution and a periodic fluctuating contribution with zero mean value. In such a heterogeneous medium two scales are distinguished: a macroscopic scale, in which the heterogeneities are small, and a microscopic scale which is the scale of the heterogeneities, that is, of the cell of periodicity. Further we distinguish *macroscopic* quantities, which are applied in a homogeneous equivalent medium, and *microscopic* quantities, which are the real quantities in the heterogeneous medium. In the following capital letters indicate *macroscopic* quantities and small letters indicate *microscopic* quantities, for example: Σ and E are respectively the macroscopic (or global) stress tensor and the relevant strain tensor while σ and e indicate the microscopic (or local) stress and strain tensors. Arguments typical of the asymptotic analysis show that macroscopic stresses and macroscopic strains are the averages of the corresponding local quantities:

$$\Sigma_{ij} = \frac{1}{|V|} \int_V \sigma_{ij} dV, \quad E_{ij} = \frac{1}{|V|} \int_V e_{ij} dV \tag{1}$$

where V is the volume of the cell of periodicity. Homogenization is a method that allows the definition of a constitutive relation between Σ and E following eq. (1) and the constitutive relations of the components.
The main problem addressed in the present paper is the extension of homogenization techniques to nonlinear material components, in particular to elasto-plastic components or to composites in which bonding between

different constituents is not perfect and some slip phenomena can occur. Several problems arise as soon as the usual hypotheses of linear, isotropic and symmetric material behaviour are abandoned: non symmetric behaviour in tension and in compression has to be considered for non-perfect bonding, anisotropic yield criteria for elasto-plastic components and slip criteria for non-perfect bonding between components are necessary, moreover anisotropic hardening laws seem to be required in order to describe in a realistic way the elasto-plastic behaviour.

Two main ideas are proposed to introduce a homogenised nonlinear description of composite materials: the introduction of 'classical' global yield criteria and a fully numerical characterisation of the nonlinear global constitutive behaviour.

2. CLASSICAL GLOBAL YIELD CRITERIA
2.1) Hill anisotropic yield criterion
We assume that for each constituent of the composite the stress field is constrained as follows:

$$\sigma(y) \in P(y) \tag{2}$$

where $P(y)$ is a domain in the six-dimensional space of stresses (or in 3D space of principal stresses). $P(y)$ depends on the material, thus on the position y in the cell of periodicity. This surface is given for each component of the composite. For metallic materials it is usual to restrict the discussion to the following form of $P(y)$:

$$P(y) = \left\{ \sigma \middle| \sqrt{\frac{3}{2} s_{ij} s_{ij}} \leq \sigma^0(y) \right\} \tag{3}$$

where s denotes deviatoric part of the stress tensor.
We assume that there exists a region P^{eff} in the stress space, such that mean stresses obey the following constraints [4]:

$$\Sigma \in P^{eff} \tag{4}$$

The boundary of this region will be called "effective yield surface". Properties of such a surface are discussed in [4]. According to [4] it is also possible to deduce a qualitative form of an effective yield surface. According to the global yield criteria, and following Hill [5], in this approach, we assume the form of this effective yield surface. Having in mind the results of numerical elasto-plastic tests, which will be shown in the next paragraph, we realise that the composite material in macro-scale exhibits plastic anisotropy. Such a plastic anisotropy can be described using Hill's anisotropic yield criterion. Hill's yield surface in the space of stresses can be expressed by the following equation [5]:

$$2f(\tilde{\sigma}_{ij}) \equiv F(\tilde{\sigma}_{22} - \tilde{\sigma}_{33})^2 + G(\tilde{\sigma}_{33} - \tilde{\sigma}_{11})^2 + H(\tilde{\sigma}_{11} - \tilde{\sigma}_{22})^2 + \\ 2L\tau_{23}^2 + 2M\tau_{13}^2 + 2N\tau_{12}^2 \tag{5}$$

The admissible region in the space of stresses is:

$$\mathbf{P} = \left\{ \sigma \mid \sqrt{f} \leq \sigma^0 \right\} \tag{6}$$

In the above σ^0 is a reference yield stress.

Six constant F, G, H, L, M, N can be identified from unidirectional experimental tests, for details see [5]. Equations (7, 8) are quoted after [6]:

$$F = \frac{\sigma_0^2}{2}\left(\frac{1}{\ddot{\sigma}_{22}^2} + \frac{1}{\ddot{\sigma}_{33}^2} - \frac{1}{\ddot{\sigma}_{11}^2}\right) \quad G = \frac{\sigma_0^2}{2}\left(\frac{1}{\ddot{\sigma}_{33}^2} + \frac{1}{\ddot{\sigma}_{11}^2} - \frac{1}{\ddot{\sigma}_{22}^2}\right) \quad H = \frac{\sigma_0^2}{2}\left(\frac{1}{\ddot{\sigma}_{11}^2} + \frac{1}{\ddot{\sigma}_{22}^2} - \frac{1}{\ddot{\sigma}_{33}^2}\right) \tag{7}$$

$$L = \frac{\sigma_0^2}{2}\frac{1}{\ddot{\sigma}_{23}^2} \qquad M = \frac{\sigma_0^2}{2}\frac{1}{\ddot{\sigma}_{13}^2} \qquad N = \frac{\sigma_0^2}{2}\frac{1}{\ddot{\sigma}_{12}^2} \tag{8}$$

In case of composite materials all $\ddot{\sigma}_{ij}$ are assumed to be global quantities and they can be deduced from graphs of mean strain versus mean stress.

We note that the hardening rule for this model can be also, in principle, deduced from these graphs. A similar scheme was already adopted by Swan and Cakmak [7] in their applications to masonry structures.

2.2) Hoffman anisotropic non symmetric yield criterion

The previous Hill yield criterion assumes that there is no difference between tensile and compressive yield strength. Such an assumption cannot be accepted in the case of non-perfect bonding because, in general, the compressive strength is higher than the tensile one. Hoffman modified Hill's criterion by introducing terms which are linear in the stress [8]. Such a criterion was utilised by Schellekens and de Borst [9] who, with use of a yield function $\Phi(\sigma)$ rewrote Hoffman criterion as follows:

$$\Phi(\sigma) = \alpha_{23}(\sigma_{22} - \sigma_{33})^2 + \alpha_{31}(\sigma_{33} - \sigma_{11})^2 + \alpha_{12}(\sigma_{11} - \sigma_{22})^2 + \alpha_{11}\sigma_{11} + \alpha_{22}\sigma_{22} +$$
$$+ \alpha_{33}\sigma_{33} + 3\alpha_{44}\sigma_{23}^2 + 3\alpha_{55}\sigma_{31}^2 + 3\alpha_{66}\sigma_{12}^2 - \overline{\sigma}^2 = 0 \tag{9}$$

The material parameters α_{ij} are determined by:

$$\alpha_{12} = \frac{\overline{\sigma}^2}{2}\left(\frac{1}{\overline{\sigma}_{11}^*\overline{\sigma}_{11}} + \frac{1}{\overline{\sigma}_{22}^*\overline{\sigma}_{22}} - \frac{1}{\overline{\sigma}_{33}^*\overline{\sigma}_{33}}\right) \quad \alpha_{13} = \frac{\overline{\sigma}^2}{2}\left(\frac{1}{\overline{\sigma}_{11}^*\overline{\sigma}_{11}} - \frac{1}{\overline{\sigma}_{22}^*\overline{\sigma}_{22}} + \frac{1}{\overline{\sigma}_{33}^*\overline{\sigma}_{33}}\right)$$

$$\alpha_{23} = \frac{\overline{\sigma}^2}{2}\left(-\frac{1}{\overline{\sigma}_{11}^*\overline{\sigma}_{11}} + \frac{1}{\overline{\sigma}_{22}^*\overline{\sigma}_{22}} + \frac{1}{\overline{\sigma}_{33}^*\overline{\sigma}_{33}}\right) \quad \alpha_{11} = \overline{\sigma}^2\left(\frac{\overline{\sigma}_{11}^* - \overline{\sigma}_{11}}{\overline{\sigma}_{11}^*\overline{\sigma}_{11}}\right)$$

$$\alpha_{22} = \overline{\sigma}^2\left(\frac{\overline{\sigma}_{22}^* - \overline{\sigma}_{22}}{\overline{\sigma}_{22}^*\overline{\sigma}_{22}}\right)$$

$$\alpha_{33} = \overline{\sigma}^2\left(\frac{\overline{\sigma}_{33}^* - \overline{\sigma}_{33}}{\overline{\sigma}_{33}^*\overline{\sigma}_{33}}\right) \quad \alpha_{44} = \frac{\overline{\sigma}^2}{3\overline{\sigma}_{12}^2} \quad \alpha_{55} = \frac{\overline{\sigma}^2}{3\overline{\sigma}_{13}^2} \quad \alpha_{66} = \frac{\overline{\sigma}^2}{3\overline{\sigma}_{23}^2} \tag{10}$$

where $\overline{\sigma}$ is a normalised yield stress, $\overline{\sigma}_{ii}^*$ and $\overline{\sigma}_{ii}$ the compressive and tensile yield stresses, and $\overline{\sigma}_{ij}$ the shear yield stresses, all these quantities, in case of composite materials, are global.

2.3) Discussion

The application of Hill or Hoffman criteria require the determination of the global yield stresses, six for Hill criterion, nine for the Hoffman one. These

stresses can be determined computationally with numerical tests which substitute much more expensive laboratory tests. Once the constants of the models have been determined the composite structure is substituted by a homogeneous one with the predetermined elasto-plastic behaviour. The method seems to be elegant but several questions arise:

a) the shape of the elastic frontier strongly depends on geometry and material composition of the unit cell, that means that for each different cell of periodicity it is necessary to 'guess' such a shape.

b) Once the elastic frontier has been reached the hardening behaviour is quite complex, as will be shown below in an example; similar hardening behaviour is not well known and represents a further difficulty in the line of the present approach.

This method is especially attractive because of the small numbers of numerical, or physical, experiments needed in order to fully characterise the elasto-plastic behaviour of the unit-cell and therefore of the whole composite structure. In the plane stress case a one-parameter biaxial kinematic loading or a pure shear loading is imposed to the unit cell, as will be clearer in the next section. We consider hence the following form of the incremental kinematic loading in the necessary numerical tests:

$$u_i = E_{ij} y_j \tag{11}$$

To be consistent with the interpretation of $\overline{\sigma}_{ij}$ in equations (10) we choose the global strains E_{ij} giving global uniaxial stress responses (even if local values may differ).

3. FULLY NUMERICAL APPROACH

According to eq. (11) a cell of periodicity is now subjected to a large numbers of different numerical tests so as to describe many cases of different displacement histories. In figure (1) an example of cell of periodicity is shown. Adopting the unit-cell approach [10] a single cell of periodicity is subjected to the following boundary conditions:

$$u_1 = 0 \quad at \quad x_1 = 0$$
$$u_2 = 0 \quad at \quad x_2 = 0$$
$$u_1 = U_1 \quad at \quad x_1 = l_1$$
$$u_2 = U_2 \quad at \quad x_2 = l_2$$

Figure 1
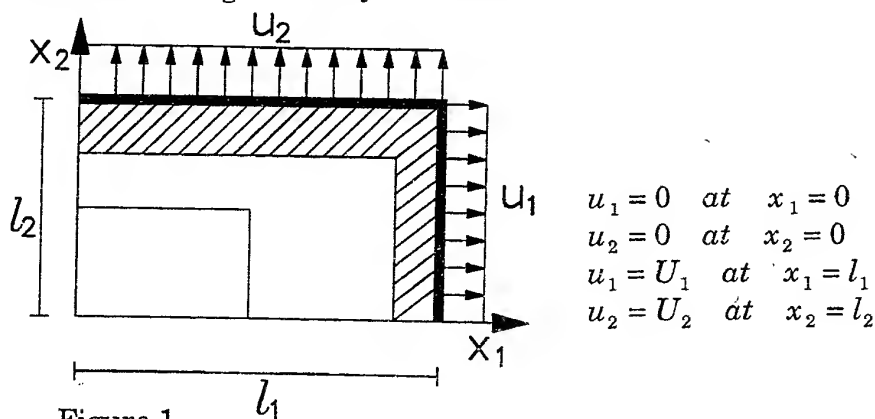
where U_1 and U_2 are prescribed displacements, the ratio U_1/U_2 is fixed for each experiment. In the case of our specific example the 2-D unit-cell is

460

composed of steel, epoxy and void. The first two are isotropic, symmetric, elastic perfectly-plastic materials with Von Mises plasticity. Computations are realised under plane stress hypothesis, perfect bonding is assumed but a completely analogous approach is possible if slip phenomena are allowed. The general purpose code ABAQUS is utilised in the computations: to the representative unit-cell a displacement history is imposed in which the ratio U_1/U_2 is constant, the sides of the cell are maintained straight during the load history because, as usual in such conditions, the unit cell is thought to be in an infinite periodic medium among cells which undergo the same displacement history. For each step of the displacement history the averaged stresses are computed according to eq. (1), therefore in this manner it is possible to draw the curves Σ_{ij} vs U_i and Σ_{ij} vs Σ_{kl} which illustrate the behaviour of the material. This is done using our post processor which elaborates output data from ABAQUS and prepares the numerical description of the constitutive law. Figure (2) shows the elastic (dots) and the plastic domain for the cell of figure (1). It is interesting to observe that the elastic domain is almost isotropic, whereas the plastic domain is clearly anisotropic and much wider than the elastic one. Consequently a good approximation would be obtained with a global isotropic yield criterion but an anisotropic hardening law should be taken into account. Moreover it is interesting to note that the form of the yield surface obtained here does not match the von Mises yield surface (assumed for the components) nor the Hill and Hoffman yield surfaces. We highlight the fact that the effective constitutive law is still associative as is shown by the numerical experiments; the arrows of figure (2) show the directions and the values of the plastic strain increments on the yield surface.

From a different point of view the Σ_{ij} vs Σ_{kl} and Σ_{ij} vs E_{kl} curves could also be used with some interpolation technique to macroscopically describe the relation between Σ and E. In this way every 'imaginative' effort would be avoided and a very general method could be determined which can be applied to any prismatic cell of periodicity. The drawbacks of this method are the very high number of numerical tests necessary to have a reasonably good description of the constitutive behaviour and the fact that, at the moment, only monotonic displacement histories have been considered.

CONCLUSIONS
Two main ideas are presented in the paper to carry out nonlinear homogenised computations of periodic composite materials:
a) calibration of classical anisotropic yield criteria for global quantities;
b) fully numerical description of the global behaviour.
Advantages and drawbacks of the two methods are pointed out.
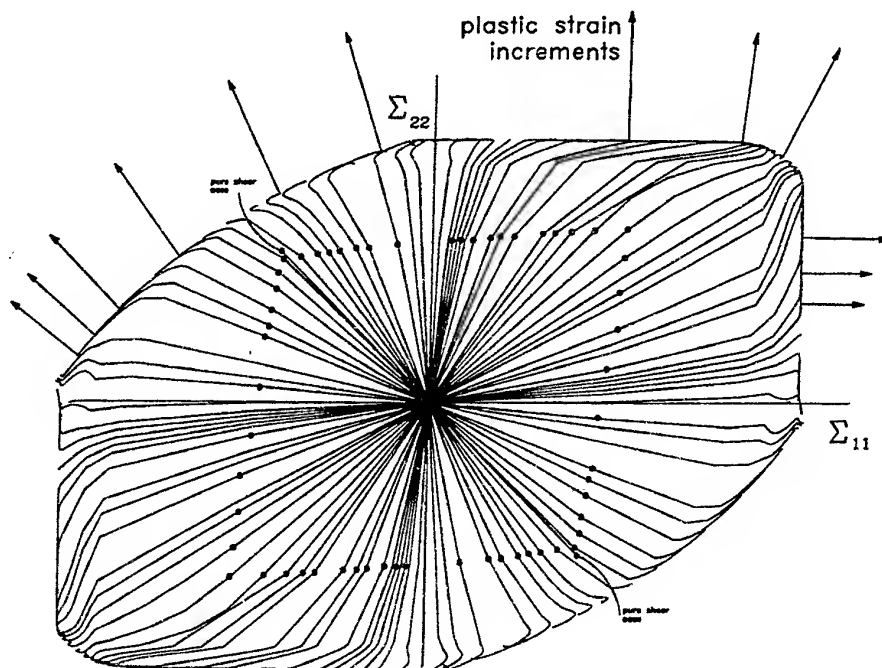
Figure 2

REFERENCES

1) Sanchez-Palencia E., *Non-homogeneous media and vibration theory*, Springer Verlag, Berlin, 1980.

2) Lefik M., Schrefler B.A., 'Homogeniszed material coefficients for 3D elastic analysis of superconducting coils', in P. Ladeveze and O. C. Zienkiewicz (Editors) *New Advances in Computational Structural Mechanics*, Elsevier Science Publishers B.V. 1992.

3) Lefik M., Schrefler B.A., 'Application of the homogenisation method to the analysis of superconducting coils', *Fusion Engng. Des.*, **24**, pp. 231-255, 1994.

4) Suquet P.M., 'Elements of homogenisation for inelastic solid mechanics', in *Lecture Notes in Physics 272*, Homogenisation techniques for composite media, Springer Verlag, Berlin, 1985.

5) Hill R., 'A theory of yielding and plastic flow of anisotropic materials', *Proc. Roy. Soc.* **A193**, pp. 281-297, 1947.

6) ABAQUS Users Manual, Hibbitt, Karlsson & Sorensen Inc., Version 5.4, 1994.

7) Swan C.C., Cakmak A.S., Techniques for stress and stain controlled homogenisation of inelastic periodic composites, *Comp. Meth. Appl. Mech. Engrg.*, **117**, pp. 249-267, 1994.

8) Hoffman O., 'The brittle strength of ortotropic materials', *Journal Comp. Mat.*, **1**, pp. 200-206, 1967.

9) Schellekens J.C.J., De Borst R., 'The use of the Hoffman yield criterion in finite element analysis of anisotropic composites', in *Composite Materials Design and Analysis*, deWilde W.P. & Blain W.R. editors, Springer Verlag, 1990.

10) Tvergaard V., 'Analysis of tensile properties for a whisker-reinforced metal-matrix composite', *Acta metall. mater.*, **38**, pp. 185-194, 1990.

MODELLING OF THE EFFECT OF THERMOFORMING ON THE MECHANICAL PROPERTIES OF DISCONTINUOUS ALIGNED FIBER COMPOSITES

J. Schuster and K. Friedrich

Institute for Composite Materials Ltd., University of Kaiserslautern,

Schroedingerstraße 58, 67663 Kaiserslautern, Germany

ABSTRACT

Specimens made of uni- and bidirectional **Discontinuous Aligned Fiber** (DAF) composite materials were elongated to different states of deformation by thermoforming. Tensile tests were performed using pre-stretched specimens. Thermoforming behavior was modelled using the Herschel-Bulkley model. The effect of fiber orientation during thermoforming was described by applying the Jeffrey-Equation. A combination of both the Herschel-Bulkley-Model and the Jeffrey-Equation enabled, under consideration of thermal stresses, the determination of the ultimate tensile strength of thermoformed uni- and bidirectional DAF-materials. These results were in good agreement with those of the experimental tensile tests.

Keywords: composites, nondestructive testing, ultrasonics, discontinuous aligned fiber composites, fatigue, specimen type, thermoforming, Herschel-Bulkley-Model

INTRODUCTION

Over the last decade, a large number of rapid and cost effective manufacturing methods have been developed suitable for processing of continuous fiber reinforced thermoplastic materials [1]. Utilizing related processes known from thermosetting composites and neat thermoplastic materials and adopting sheet forming teehniques typical to those used with metallic materials fabrication techniques such as thermoforming were developed [2, 3]. In comparison with traditional processing of thermosetting composites into complex geometries, thermoforming of advanced continuous fiber reinforced thermoplastic composite sheets offers several advantages such as in-situ consolidation, and faster processing cycles. However, some important processing issues have to be resolved before this can become a viable economical process. E.g. when transferring a flat continuous fiber reinforced laminate into a 3-D shaped component, a number of different deformation mechanisms have to be taken into account [3, 4]. Unlike isotropic metallic sheets, continuous fiber reinforced thermoplastics are inextensible in the fiber direction. For these material systems, the dominant mode of the deformation parallel to the fiber direction during forming is thus shearing within the individual plies and between them, i.e. intra- and interply shear [3]. Besides these two mechanisms, three others (fiber rotation, resin percolation, and transverse fiber flow) are also active with less importance. These slipping processes depend strongly on the laminate lay-up, the fiber/matrix combination used, and the processing conditions such as pressure, temperature, and forming speed; all of them have a great influence on the final part quality .

In order to avoid buckling problems whilst retaining acceptable processing times, a Discontinuous Aligned Fiber (DAF) composite material which provides a "drawable" feature was recently developed by DuPont to overcome the thermoforming limitations encountered with continuous fiber systems [6]. DAF consists of aligned carbon fibers, having an average length of L = 5 cm, in a thermoplastic PEKK-matrix, with a fiber volume fraction of ϕ_F=58%. Due to the fiber discontinuity, a sixth deformation mechanism, the longitudinal fiber slip, is allowed. Concerns about the strength and stiffness properties of undeformed DAF-material can be neglected due to the high degree of efficiency of 0.95 based on high fiber length and their nearly perfect alignment.

Models describing intra- and interply slip have recently been developed and integated into FEM-codes [7]. In order to extend such codes for DAF-material, a model for the longitudinal fiber slip needed to be developed. Although quite a few publications are available on processing, rheology and morphology aspects of DAF, none of them derives a model capable to predict stresses in the material during thermoforming. This paper describes the principal factors dominating deformation load requirements in the processing stage. These factors will be taken into account in a model that will be shown capable to accurately describing the load/deformation behavior of DAF during one dimensional thermoforming .

MATERIAL AND THERMOFORMING PROCEDURE

The material used in this study was a discontinuous but highly collimated carbon fiber polyetherketoneketone (CF/PEKK) system described above. Platens with a thickness of approximately 2 mm and lay-up sequence of $[0°]_{16}$ and $[(90, 0)_7 90]$ were cut into specimens with a width of 27 mm and a length of 400 mm. In order to generate the desired states of deformation in the specimens prior to the tensile tests, they were subjected to a thermoforming procedure. The forming process of the DAF-samples was realized by employing a particular stretch-forming technique. The stretch-forming was carried out using a setup consisting of a tensile testing machine providing the tensile force F and a laboratory hot press integrated into the testing machine (Fig. 1).
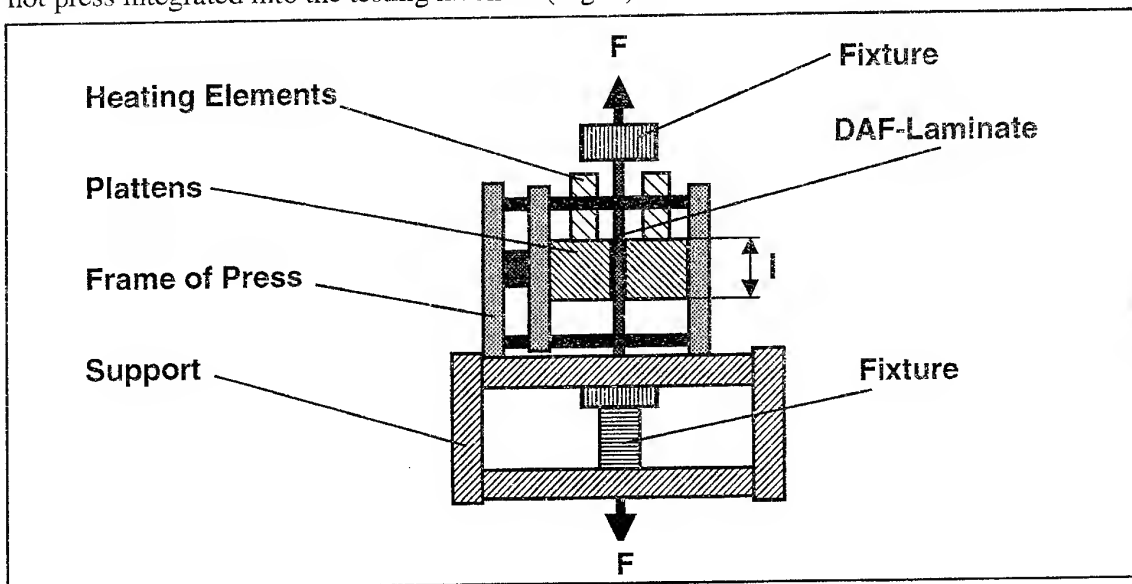
Fig. 1: Device for thermoforming

The use of a press tool was necessary in order to apply a sufficiently high pressure (13.6 MPa). This press tool, width 28 mm and length of l = 160 mm, was placed between the heated plates. Before thermoforming, the heating plates had to be coated with a thin film of a release agent and covered with a sheet of polyimide foil in order to ensure easy demolding. It was aimed to generate elongations of 3%, 6%, 9%, and 12% of the 160 mm specimen length. The temperature-pressure course of the deformation process was as following: after preheating the sample up to 390 °C, it was deformed without external pressure. Once the desired elongation was reached, a consolidation pressure of 13.6 MPa was applied and the sample was cooled down. It was then removed after the temperature had dropped below crystallization temperature of the PEKK-matrix (255 °C). Although the consolidation pressure was as high as 13.6 MPa, the 12%-deformed unidirectional samples could not be fully consolidated due to local necking effects. During thermoforming, the pulling force and the elongation due to cross-head movement were recorded by a plotter. Evaluations of the plotted outputs (Fig. 2) indicated thixiotropic behavior in terms of a beginning shear flow. It was noticed in previous experiments that the maximum tensile stress increased with the

speed of deformation (cross-head speed). Thus, a low cross-head speed of 1 mm/min was chosen for this investigation.
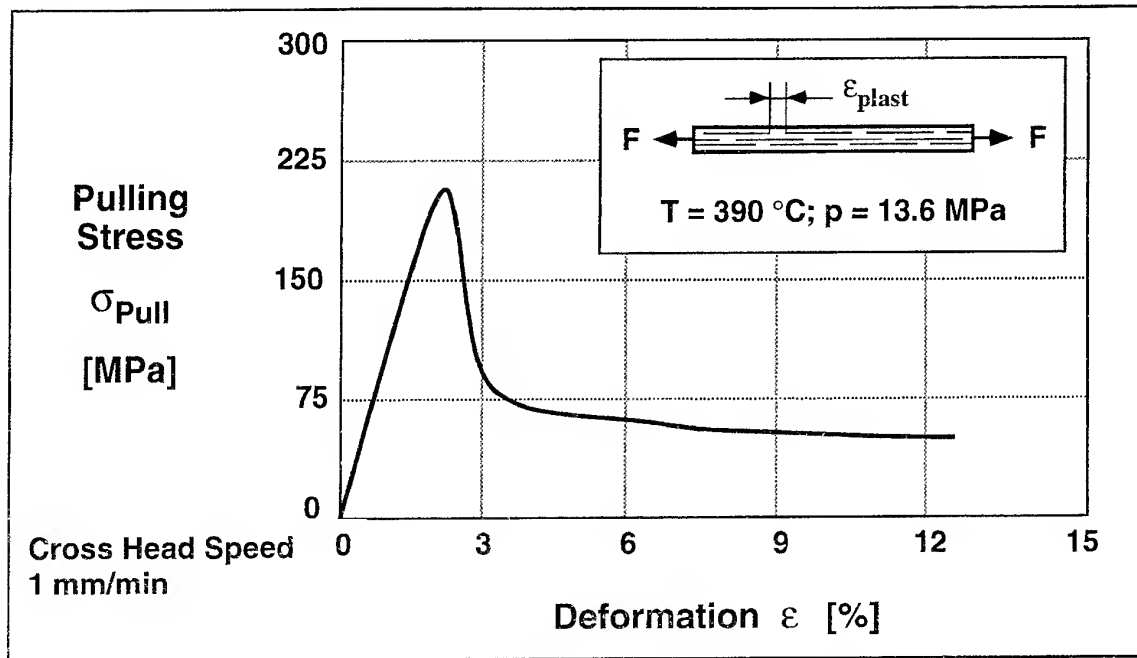
Fig. 2:Stress-deformation-curve during thermoforming of bidirectional DAF

TENSILE TESTS

The tensile tests on the unidirectional and bidirectional samples were performed according to ASTM 3039 employing a Zwick 1485 universal tensile testing machine. Fig. 3 depicts that the state of pre-deformation has an obvious influence on the tensile strength of uni- and bidirectional laminated DAF-samples. In the case of the unidirectional samples, the 3%-elongated specimens possess the highest strength.
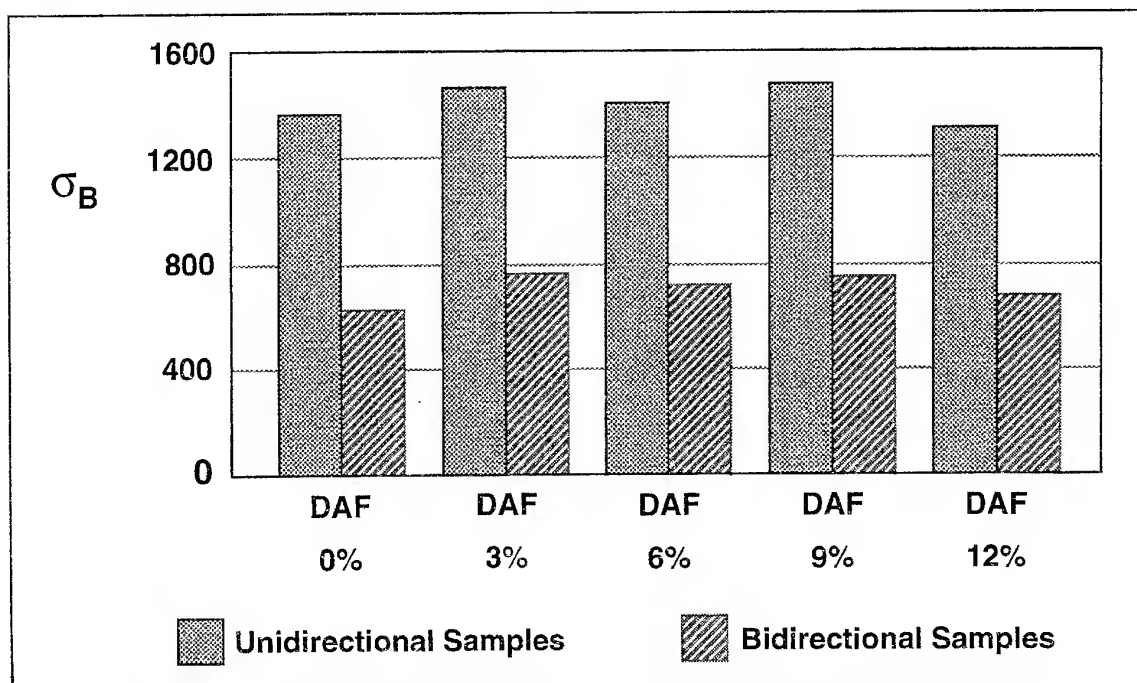
Fig. 3: Tensile strength of thermoformed uni- and bidirectional DAF-samples

465

This can be explained by the initial straightening of the approximately 95% aligned fibers in the original DAF-sheet, which up to a certain strain value causes stiffening and higher loading efficiency. In addition, residual compressive stresses were induced in the DAF-material during stretch-forming by clamping it in fixtures until its removal from the forming device. Thus, the sample was still under tensile loading which turned into a compressive inner stress state after releasing the clamps so that an elastic redeformation could occur. The drop in the tensile properties of the 12%-deformed unidirectional samples is due to the insufficiently consolidated sections. Similar effects can be noticed for bidirectional samples. However, the influence of these effects on the tensile properties was lower because only the 0°-fibers were significantly affected during the stretch-forming procedure [8].

MODELLING

In general, the ultimate tensile strength σ_B as a function of the deformation ε can be calculated by considering changes in fiber orientation ($\sigma_{B\eta}$) and by taking into account the residual compressive stresses σ_{Com}:

$$\sigma_B(\varepsilon) = \sigma_{Com} + \sigma_{B\eta} \tag{1}$$

with the modified rule of mixture for long fibers:

$$\sigma_{B\eta} = \sigma_F \phi_F \eta_F + \sigma_M (1 - \phi_F) \tag{2}$$

where η_F represents the fiber orientation, ϕ_F the fiber volume fraction, and σ_F as well as σ_M the tensile strength of the fibers and the matrix, respectively. Therefore, the modelling of the mechanical properties is divided into two parts: (1) Modelling of the thermoforming behavior and thus the residual compressive stress; (2) Modelling of the improvement in fiber orientation.

MODELLING OF THE COMPRESSIVE RESIDUAL STRESSES AFTER THERMO-FORMING

The residual compressive stress results from the pulling forces F_{pull}, frozen in the material during thermoforming. Thus, at a deformation of 3% the residual compressive stress is higher than for 9% (Fig.2). Assuming that σ_{com} equals to σ_{pull}, a model for the stretch-forming process can be applied to describe σ_{com} via an expression for σ_{pull}. This model is introduced for unidirectional material because bidirectional laminates can be converted into unidirectional structures when neglecting fiber directions perpendicular to the direction of deformation. This procedure is valid due to the 10^5 to 10^8 lower mechanical properties of transverse laminae in comparison to longitudinal laminae in the molten state. In order to describe the visco-plastic behavior of unidirectional DAF, a mechanical-rheological model has to be applied fulfilling two requirements: 1) a description of the increasing pulling stress until a maximum is reached and 2) a description of the following stress relaxation. One model being excellently suitable for this task is the Herschel-Bulkley-Model [5,7]. It consists of the well-known Maxwell-Model combined with the ideal plastic Saint Venant Element situated parallel to the damping element. For stresses lower than a certain limit, the SaintVenant Element acts as a mechanical friction related blockade of the damper with the strength σ_{Ad} leading to an exclusive loading of the spring. Thus, the following expression for σ_{Com} can be derived

$$\sigma_{Com} = \left(\sigma_{Ad} - \eta\frac{v}{l}\right)e^{-\frac{Et}{\eta}} + \eta\frac{v}{l} \tag{3}$$

where v/l (v = cross head speed, l = tool length) equals to the strain rate ε. The viscosity η can either be obtained experimentally by evaluating the stress-deformation curve for $\sigma(t \to \infty)$ or via a theoretical approach. In the first case, a $\sigma(t \to \infty)$ of 48 MPa leads to a viscosity of $4.6 \cdot 10^{11}$ Pa s. A theoretical solution was developed by Coffin and Pipes [9]:

$$\eta = \eta_{11} = \frac{\eta_0 A_T (1-\mu) \phi_F}{2\mu} \left(\frac{L}{D}\right)^2 \left[1 + \frac{A_T^2 (1-\mu)^2}{4\mu^2} \left(\frac{L}{D}\right)^2 (\lambda \dot{\varepsilon})^2\right]^{\left(\frac{n-1}{2}\right)} \tag{4}$$

where ϕ_F is the fiber volume fraction, L the length, D the diameter of the fiber, λ determines the onset of nonlinearity, and A_T the temperature shift factor. The factor μ is defined as

$$\mu = 1 - \sqrt{\frac{\phi_F 4}{\pi}} \tag{5}$$

The power law exponent, n, determines the degree of nonlinerarity. The value of $n = 1$ corresponds to a Newtonian fluid, and as the exponent decreases the fluid exhibits increased shear thinning. The effective viscosity η_{11} of the medium (molten DAF in fiber direction) can be calculated by Equation 4. The L/D-ratio for the material used is about 10^4 leading to an effective viscosity of $1.63 \cdot 10^{11}$ Pas.

MODELLING OF THE IMPROVEMENT IN FIBER ORIENTATION

A model for determining the angle of fiber orientation θ immersed in a flowing viscous fluid is based on the Jeffrey-equation [10]:

$$\dot{\theta} = -\sin\theta\cos\theta\frac{\partial v_x}{\partial x} - \sin^2\theta\frac{\partial v_x}{\partial y} + \cos^2\theta\frac{\partial v_y}{\partial x} + \sin\theta\cos\theta\frac{\partial v_y}{\partial y} \tag{6}$$

The flowing velocity v is identical to the crosshead speed mentioned before. For a one-dimensional flow in x-direction Eqn. 6 reduces to

$$\dot{\theta} = -K_i \sin\theta\cos\theta\frac{\partial v}{\partial x} = -K_i \frac{\partial v}{\partial x}\frac{1}{2}\sin 2\theta \tag{7}$$

where the fiber interactions have been considered by an interaction factor K_i. Integrating Equation 7 along the tool length l leads to

$$\dot{\theta} = -\frac{1}{2} K_i \frac{v}{l} \sin 2\theta \tag{8}$$

The solution of this differential equation comes down to

$$\theta = \arctan\left(C\, e^{-K_i \frac{v}{l} t}\right) = \arctan\left(C\, e^{-K_i \varepsilon}\right) \tag{9}$$

The parameters C and K_i were determined for 0°- and 90°-fibers by using boundary conditions measured in a scanning electron microscope:

(1a)	$\theta\,(\varepsilon = 0\,\%) = 7°$	0°-fibers
(2a)	$\theta\,(\varepsilon = 3\,\%) = 3.63°$	0°-fibers
(1b)	$\theta\,(\varepsilon = 0\,\%) = 83°$	90°-fibers
(2b)	$\theta\,(\varepsilon = 3\,\%) = 71°$	90°-fibers

Therefore, the equations to describe fiber orientation during stretch-forming of DAF are

$$\theta = \arctan\left(0.122\ e^{-21.84\,\varepsilon}\right) \qquad 0°\text{-fibers} \qquad (10)$$

$$\theta = \arctan\left(8.144\ e^{-34.37\,\varepsilon}\right) \qquad 90°\text{-fibers} \qquad (11)$$

$$\eta_F = \cos^2\theta \qquad (12)$$

Now, the ultimate tensile strength σ_B can be calculated according to Equation 1 and 2.

COMPARISON OF EXPERIMENTAL AND MODELLING DATA

The outcome of modelling the ultimate tensile strength of thermoformed DAF is depicted in Fig. 4 collectively with the experimental data (see also Fig. 3). It is obvious that the model introduced fits the measured data with a high precision.
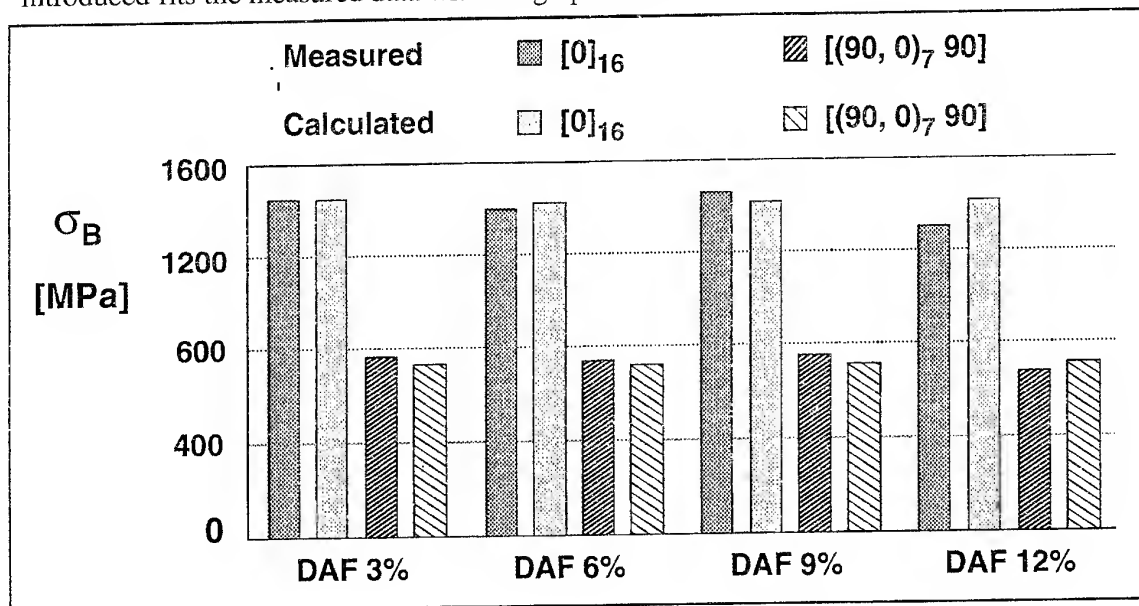
Fig. 4: Comparison of experimental and model results of the ultimate tensile stress

CONCLUSIONS

It is possible to describe the thermoforming behavior of discontinuous aligned fiber composites by using the Herschel-Bulkley-Model. It allows under consideration of thermal stresses introduced to the material during cooling, the determination of internal residual stresses. Besides fiber orientation in deformation direction, the residual stresses are a major factor to increase the ultimate tensile strength, which can be approximated by a combination of the Herschel-Bulkley-Model and a modified expression of the Jeffrey-Equation.

ACKNOWELEDGEMENTS

REFERENCES

1 Cogswell, F.N. ´Thermoplastic Aromatic Polymer Composites´ Butterworth-Heinemann Ltd, Oxford (1992)

2 Månson, J.-A.E. ´Processing of Thermoplastic-Based Advanced Composites´ in: Advanced Thermoplastic Composites: Characterization and Processing (Eds.: Kausch, H.-H. and Legras, R.), Carl Hanser Verlag, Munich, Vienna, New York, Barcelona (1993)

3 Friedrich, K., Hou, M. and Krebs, J. ´Stamp Forming of Continuous Fibre/Thermoplastic Composite Sheets´ in: Composite Materials, Vol. 12, Thermoplastic Sheet Forming, (Ed.: Bhattacharyya, D.) Elsevier Science Publisher, Amsterdam (to be published)

4 Okine, R.K.: ´Analysis of forming parts from advanced thermoplastic composite sheet materials´, SAMPE Journal 25 3 (1989) 9 - 19Amsterdam (1991)

5 Scherer, R. and Friedrich, K. ´Inter- and Intraply-Slip Processes during Thermoforming of PP/CF-Laminates´ Composites Manufacturing 2 2 (1991) 92 - 96

6 Chang, I.Y. and Pratte, J.F. ´LDF™ Thermoplastic Composites Technology´ Journal of Thermoplastic Composite Materials 4 3 (1991) 227 - 252

7 Scherer, R., Zahlan, N. and Friedrich, K. ´Modelling the Interply-Slip Process during Thermoforming of Thermoplastic Composites Using Finite Element Analysis´ in: Composite Materials - Design and Analysis (Eds.: W.P. de Wilde and W.R. Blain) Computational Mechanics Publications, Southampton (1990) 39 - 52

8 Schuster, J. and Friedrich, K. ´The Fatigue Behaviour of Thermoformed Discontinuous Aligned Fiber Composites´ Proceedings "The Tenth International Conference on Composite Materials", Whistler, Kanada (1995) I-593 - I-600

9 Coffin, D.W. and Pipes, R.B. ´Anisotropic Viscosities of an Oriented Fiber Assembly with Temperature and Strain Rate Dependence´ Proceedings " International Conference on Composite Materials VIII", Hawaii, USA (Eds.: Springer, G.S. and Tsai, S.W.), Stanford, CA (1991) 10-I-1 - 10-I-9

EFFECTS OF JOINT GEOMETRY ON THE FLEXURAL BEHAVIOR OF GLASS REINFORCED PLASTICS

A.C. Seibi, S. K. Al Oraimi, S. M. Al Alawi

Sultan Qaboos University
College of Engineering
P.O. Box 33, Al-Khod 123
Sultanate of Oman

ABSTRACT

This paper describes the flexural behavior of bolted joints of glassfiber reinforced plastics. The experimental programme involved the conduct of three point bending tests as well as bending tests of mechanically fastened joints under static loads. Variation of the joint geometry (the bending span, L, edge distance to bolt geometry (e/d), and width to diameter (w/d) ratio) affects the GRP strength and stiffness significantly. Associated failure modes taking place in GRP bolted joints under bending are also identified. A finite element stress analysis of bolted joints under bending was performed to understand the nature of the various types of failure modes and identify the associated causes. Using the maximum tensile stress theory criterion, the finite element results of such joints predicted accurately the potential causes and locations at which failure takes place.

INTRODUCTION

Composite structures made of several connected parts by means of rivets, inserts, bolts, etc., introduce particular problems to engineers when subjected to complex loading conditions where high stress concentrations near the joints may lead to unexpected failure. In order to avoid such incident from occuring, proper design procedures and stress analysis of such joints must be studied thoroughly.

Recently, GRP materials are being favoured over conventional materials to construct high strength light weight structures. Although GRP materials offer desirable characteristics, the presence of joints may raise important questions that must be answered. Though, a lot of research has been performed to examine the strength behavior of bolted joints under uniaxial tension [1-6] and reported the effects of joints geometry on the tensile strength and stiffness of GRP materials, none of these considered their flexural behavior.

The present paper, therefore, describes the effects of joint geometry on the flexural behaviour of GRP and includes the finite element stress analysis of such joints to identify failure locations along the specimen and their potential causes based on the maximum tensile stress theory.

EXPERIMENTAL PROGRAMME

Hand lay-up technique was used to fabricate flat plates of 300x300x3 mm consisting of four layers of 50% weight fraction of random glass fibers mixed with polyester. The plates were then sandwitched between two wooden smooth plates to remove any trapped air and ensure a uniform distribution of polyester within the random fiber layers. Once the cured plate was obtained, standard tensile specimens and three point bend specimens with various lengths, widths, and

pitches were cut. Holes of 8 mm diameter were drilled near the ends of the bend specimens. Figure 1 shows the geometry of a typical specimen where L, e, and w are changed in the experiment. Also shown is the bending fixture where the specimen is hand tightened at both ends to the supports by means of steel bolts. The values span, L, the joint ratio w/d (specimen width/hole diameter), and e/d (center hole to edge distance/hole diameter) are changed from 70 to 160 mm, 1.5 to 2.25, and 0.75 to 1.5, respectively. Bolted joint flexural tests were then conducted using a Lloyd M30K testing machine at a rate of 2 mm/ min. An X-Y plotter was used to plot the resulting load-deflection curves for different specimens configurations.

a) Specimen Configuration   b) Testing Arrangements
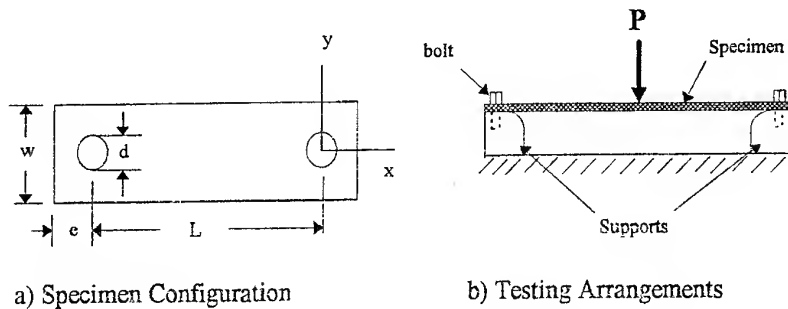
Fig. 1. Bending Test of Fastened GRP Specimens

FINITE ELEMENT MODELING

A three-dimensional brick element is used to model the composite laminate, support, and bolt as shown in Figure 2. The bolt is represented by the half circle in the model and the composite laminate with altered dimensions of w, e, and L consists of two laminae with same material properties. Because of symmetry, only one fourth of the section of the laminate is considered. The Cartesian coordinates (x,y,z) represent x, y, and z-coordinates for the bend specimen configuration. The bolt has a radius of 4 mm and the composite laminate is 3 mm thick.
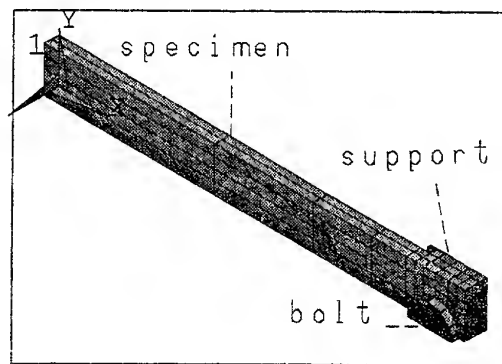
Fig. 2. 3-D Finite Element Model of Fastened GRP Specimen

In this study, it is intended to identify the failure causes and loacations of the various failure modes observed experimentally by estimating the stress distribution near the joints of different specimen configurations under bending. In the finite element model, the specimens, which are

made from randomly distributed glassfibers in plastic matrix materials, are assumed to behave isotropically. The bolt and support are modeled by brick elements with material constatnts of steel. The boundary conditions require a zero displacement in the x and y directions which represent the lines of symmetry for all the nodes lying on the x-z and y-z planes. Only vertical motion along the z-axis for all the nodes lying along the lines of symmetry is allowed. However, the rest of the nodes in the model are allowed to move freely in all directions. Since the finite element model represents one fourth of the model, the applied load is taken as one fourth of the peak failure load taken from the load-deflection curves obtained experimentally. Concentrated forces are used at the nodes lying on the surface of the specimen's mid-span in the negative z-direction. The nodal forces are obtained by obtaining the applied force per unit width. Mesh refinement was performed before starting data generation of the resulting stresses near the joints. Examination of the stress distribution near the joints assist in predicting the location of impending failure based on the maximum tensile stress theory.

RESULTS AND DISCUSSION

Bending tests of more than 130 fastened specimens were conducted to study the effects of joints geometry. A typical load displaccment curve obtained from the bolted joint flexural testing is shown in Figurc 3. The general behavior of the load-deflection curves becomes linear after a slight movement of the testing machine cross-head representing 1/10 (1 mm) of the total deflection of the tested specimen with no load being generatcd. All tested specimens exhibit a sharp drop in load before complete failure indicating a First Ply Failure (FPF) taking place at the middle of the specimens where the bending moment is maximum. This drop was followed by an increase in stiffness up to failure which generally takes place at the joint in the form of bearing, tensile, or combined failure modes. The increase in stiffness after the FPF occurs is the result of load transfer to the joints where their bearing capacity increases.

The load corresponding to the initial reduction in load is defined as the first ply failure (FPF) load; however, the failure load is defined as the maximum load (see Fig. 3). In general, four different failure modes were observed during testing which consist of 1) bending mode (mode 1) corresponding to FPF where failure takes place at the center of the specimen, 2) net tension (mode 2) where failure takes place at thc sides of the joint, 3) bearing failure (mode 3) where damage initiates near the joint and continues to develop up to the failure of the joint, and 4) mixed modes where failure takes place in the form of a combination of either modcs 1&2 or modes 1&3.
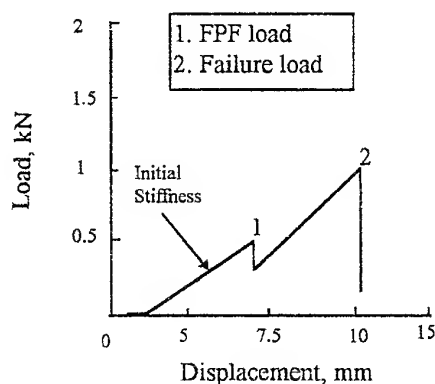
Fig. 3. Load vs. displacement for a typical joint

The effects of joint geometry on the failure loads and initial stiffnesses with respect to the various bending spans can seen in Figures 4 and 5. These figures show the variation of the failure load and initial stiffness as functions of the width to hole diameter ratio, w/d, and pitch to diameter ratio, e/d, for the extreme bending spans of 70 and 160 mm. It can be seen that, in general, as w/d or e/d increases the failure load and initial stiffness increase implying that appropriate design parameters must be taken into consideration to avoid abrupt failure.

L =70 mm   L = 160 mm
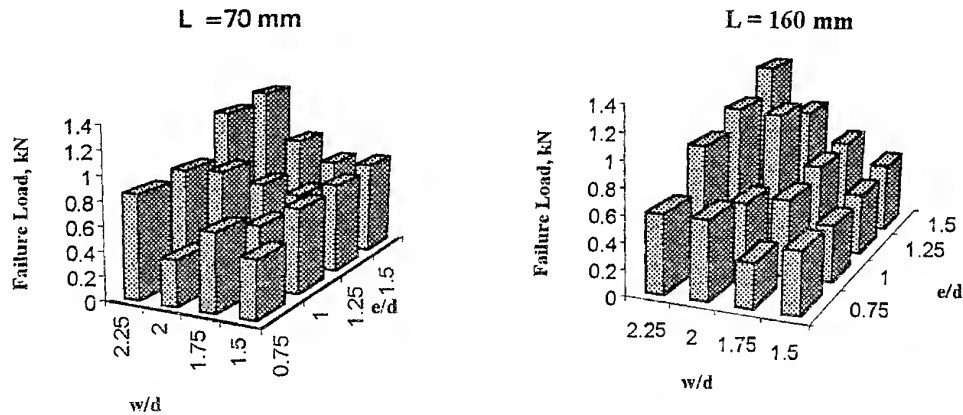
Fig. 4. Effects of Joint Gemetery on Failure Load of Fastened GRP Under Bending

L = 70 mm   L = 160 mm
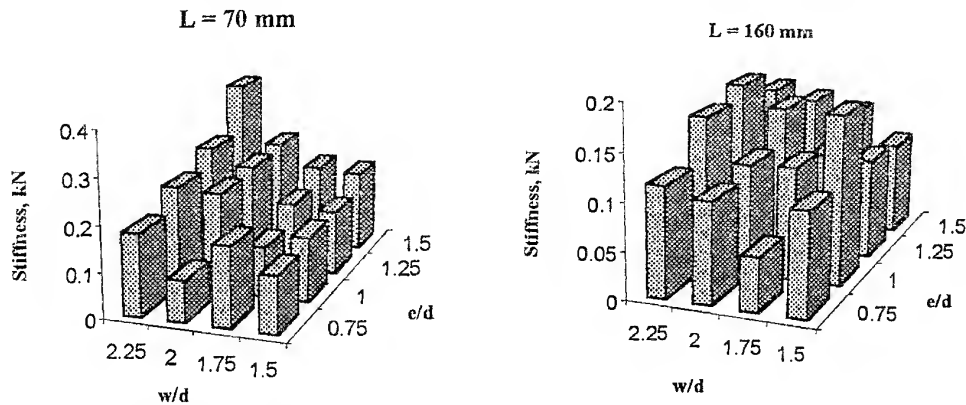
Fig. 5. Effects of Joint Gemetery on Initial Stiffness of Fastened GRP Under Bending

The experimental results were complemented by finite element modeling of fastened GRP samples under bending. Stress analysis of joints was carried out using ANSYS finite element program and three dimensional brick elements. Stress distribution at the center of the bent specimen and near the joint along the radial direction in the x- and y-axes were examined to determine the expected type of failure and its location based on the maximum tensile stress theory.

It is believed that the driving stresses that cause failure at the joint sides and ends are the axial, σ_x, and lateral, σ_y, stresses, respectively. This hypothesis was based on the criterion that failure takes place at higher normal stresses to the crack surface. In order to predict the location at

which failure takes place, both axial and lateral stress distributions along the horizontal (x-axis) and vertical (y-axis) direction near the joint as shown in Fig. 1 are studied. For instance, if the axial stress (σ_x) along the vertical direction is higher than the lateral stress on the vertical direction (σ_y), failure is expected to occur along the y-axis (net tension mode), and if σ_y along the horizontal direction is greater than σ_x along the vertical direction, a bearing failure takes place. Figs. 6 and 7 show the maximum axial and lateral stresses for various ratios of e/d and w/d, respectively. In figure 6, it can be seen that the axial stress, σ_x, is slightly affected by the ratio of e/d; howerver, the lateral stress, σ_y, decreaes as e/d increases. While it is noticeable that there is no change of the lateral stress with respect to the ratio of w/d, the axial stress decreases significantly for an increase in w/d (see Fig. 7). Comparison between both stresses along both directions will clearly specify the location at which there is a high tendency of initial failure. For instance, Fig. 6 shows that the aixal stress is higher at a ratio of e/d = 0.75 implying that failure will take place at the end of the specimen representing a bearing failure. However, failure takes place at the side of the specimen (net tension failure) since the axial stress is higher than the lateral stress for higher ratios of e/d. On the other hand, Fig. 7 shows that the axial stress at w/d ratios of 1.5, 1.75 is higher than the lateral stress implying that specimens with this geometric configuration fail from the sides (net tension mode); however, beyond these two ratios, specimens fail from the ends (bearing failure mode) since the lateral stress is higher than the axial stress. In addition, finite element results for other geometric configurations revealed that the maximum bending stress at mid span is higher than the first ply failure stress indicating that a FPF takes place at the center of the bent specimen. These results are not included are not included in this paper because of the limited allowed space. A detailed finite element stress analysis of such joints is under investigation in order to understand the inter-relationship between the failure modes and stress distribution around the joint. Future work will involve the development of a charactristic curve using finite element results from which failure modes and locations can be identified.
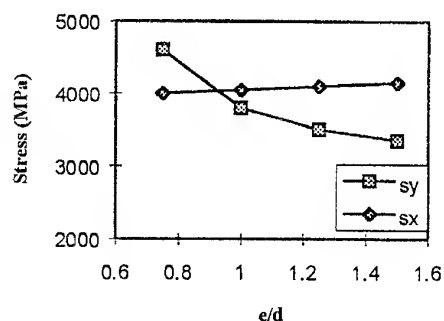
Fig. 6. Effect of e/d on Type of Failure Modes.   Fig. 7. Effect of e/d on Type of Failure Modes.
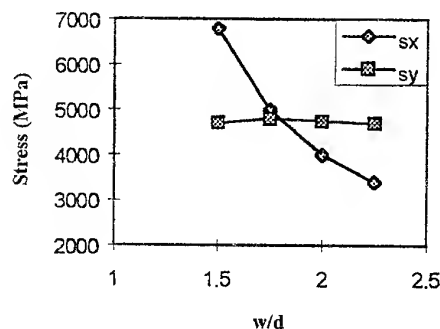
Typical failure modes obtained experimentally and numerically for a particular span (L = 100 mm) with various joint geometries is shown in Table 1. Other parameters such as first ply failure load, failure load, initial stiffness, and failure modes for the other spans are not included because of the limited space. It can be seen that the failure modes predicted by finite element method are similar to the ones obtained experimentally.

Table 1. Failure Modes of Fastened GRP Materials Under Bending for L = 100 mm

Specimen No.	w/d	e/d	Experimental	Numerical
1	1.5	0.75	bearing	Bearing
2	1.5	1	Net tension & bending	Net tension
3	1.5	1.25	Net tension	Net tension
4	1.5	1.5	Net tension	Net tension
5	1.75	0.75	Bending	Bending
6	1.75	1	Net tension	Net tension
7	1.75	1.25	Bending & net tension	Bending & net tension
8	1.75	1.5	Net tension	Net tension
9	2	0.75	Net tension	Net tension
10	2	1	Bending	Bending & net tension
11	2	1.25	Bending & net tension	Bending & net tension
12	2	1.5	Bending & net tension	Bending & net tension
13	2.25	0.75	Bearing	Bearing
14	2.25	1	Bending	Bending
15	2.25	1.25	Bending	Bending
16	2.25	1.5	Bending	Bending

CONCLUSIONS

An Experimental investigation and finite element stress analysis of fastened GRP materials under bending were performed. It was observed that, in general, the failure load and initial stiffness of the material increase as w/d and e/d ratios increase. The effect of changing the bending span was seen in terms of stiffness and failure load reduction as it increases from 70 to 160 mm. Four failure modes representing net tension, bearing, bending, and combined modes were observed. In addition, it can be concluded that finite element analysis proved to be a reliable tool in studying the stress distribution and predicting potential failure locations.

REFERENCES

[1] Alfred R. "On the Design of Prestressed and Non-prestressed Bolted Joints in Glass Fiber Reinforced UP-Laminates." Composite Structures, 4, Vol. 1, pp. 59-73 (1987).

[2] Hamada, H., Maekawa, Z., and Horino, T. "Study on Static and Long-Term Strength of Mechanically Fastened GFRP and CFRP." Composite Structures, 4, Vol. 1, pp. 74-85 (1987).

[3] Hao, S. V., Di Maria, A., and Feldman D. "Inserts for Fastening Sheet Molding Compounds." Composite Structures, 4, Vol. 1, pp. 86-99 (1987).

[4] Smith, P. A., Pascoe, K. J. "Fatigue of Bolted Joints in (0/90) CFRP Laminates." Composite Science and Technology, 29, pp. 45-69 (1988).

[5] Cooper, C. and Turvey, G. J. "Effects of Joint Geometry and Bolt Torque on the Structural Performance of Single Bolt Tension Joints in Pultruded GRP Sheet Material." Composite Structures, 32, pp. 217-226 (1995).

[6] Ramakrishna, S., Hamada, H., and Nishiwaki, M. "Bolted Joints of Pultruded Sandwich Composite Laminates." Composite Structures, 32, pp. 227-235 (1995).

MATERIAL STIFFNESS OPTIMIZATION FOR A COMPOSITE HIP PROSTHESIS

J. A. O. Simões[1], C. A. C. António[2], A. T. Marques[2]

[1] Departamento de Engenharia Mecânica da Universidade de Aveiro, Aveiro, Portugal

[2] Departamento de Engenharia Mecânica e Gestão Industrial da Universidade do Porto, Porto, Portugal

INTRODUCTION

Many different types of prosthesis and fixation techniques have been introduced in orthopaedics in these last years. To develop a new hip prosthesis one must overcome some existing incompatible design conflicts. One of these is due to the stress shielding effect and relative micromotions at the interface of the femur-prosthesis construction, and in this case, the design conflict is between stiffness and flexibility of the prosthesis stem[1]. A flexible stem provokes less stress shielding in the bone, but higher interface stresses on the proximal side. With a relative stiff stem, low proximal interface stresses occur, but massive bone resorption can occur due to the high stress shielding effect with these kind of stems. Concerning the stress shielding effect, and since the geometry of a press-fit prosthesis cannot be much modified, only a relevant design variable exists: the material stiffness. In this study, a possible scheme to optimize the Young's modulus of a press-fit hip prosthesis was developed aiming a sensible compromise of the design conflict. The optimization was performed minimizing the difference of the strain energy distribution of an intact femur and the implanted one. The constraint functions are obtained by limiting the interface stresses to the strength of cancellous bone, since this bone is the weak link of the femur-prosthesis bond. The constrained optimization problem is transformed into a sequence of unconstrained problems and the sequential unconstrained minimization technique(SUMT) is used. The minimization is performed by a conjugate gradient algorithm and the sensitivities are obtained by a discrete formulation(Finite Element Method) of the adjoint variable method. A two dimensional model of a implanted femur was used to simulate the optimization procedure.

The optimization method was also developed aiming the manufacture of a demonstrator prototype of the prosthesis. The prototype will be manufactured with an epoxy impregnated carbon fibre knitted fabric structure around a metal core by resin transfer moulding. The optimized stiffness(Young's modulus x moment of inertia - EI) of the prototype is obtained by equalling the optimized numerical stiffness to the prosthesis stiffness composed of a metal core and a composite structure. The variable Young's modulus throughout the prosthesis stem is obtained by changing the type of the knitted fabric and/or volume fibre fraction of the composite structure (optimizing through the elastic modulus - E). Changing the composite structure thickness (optimizing through the geometry of the metal core and composite structure - I) is another possibility.

FORMULATION OF THE OPTIMIZATION PROBLEM

The formulation of the optimization problem was implemented so that the *pseudo-optimized* press-fit hip prosthesis design will provoke an accepted stress shielding level, since avoiding it is totally impossible. Several theories exist on bone remodelling, and

some speculate it is stimulated by changes in strain energy density[2]. As a measure for the local bone load one can use then the strain energy density to assess the potential resorption[3], which can also be related to the stress shielding effect. The stress shielding can then be based on a direct comparison between the Strain Energy Distribution (SED) per unit of bone volume of an intact femur and the implanted one[3]. The objective function can be so that

$$\Phi(\Pi) = \left(U_b(\Pi) - U_b^* \right)^2 \tag{1}$$

where U_b^* is the product of the SED of the intact femur by the amount of stress shielding imposed, and

$$U_b(\Pi) = \frac{1}{2} \int_{V_b} \sigma \, \varepsilon \, dV_b \tag{2}$$

where U_b is the strain energy of the implanted femur bone, σ and ε are the stress and strain vectors respectively and V_b is the femur bone volume. The design variables, vector Π, are the elastic modulus of the macroelements defined on the prosthesis. The constraint functions are obtained by limiting the stresses at the interface of the femur-prosthesis construction to the strength of the cancellous bone. Here, we consider the Tsai-Wu criteria[4] which is an interactive quadratic failure criteria, and can be written as

$$f(\Pi) = \frac{1}{S_t \, S_c} \sigma_1^2 + \frac{1}{S_t \, S_c} \sigma_2^2 + \frac{1}{S_s^2} \tau^2 - \frac{1}{S_t \, S_c} \sigma_1 \sigma_2 + \left(\frac{1}{S_t} - \frac{1}{S_c} \right) \sigma_1 + \left(\frac{1}{S_t} - \frac{1}{S_c} \right) \sigma_2 = 1 \tag{3}$$

where σ_1, σ_2 and τ are the components of the stress vector, S_c, S_t and S_s are the tensile, compression and shear strength parameters. Using this failure criteria, the constraints can be written as $g_k = f(\Pi) - 1 \leq 0$ with $k=1,...,N_{str}$. The N_{str} constraints are measured at the interface bone-prosthesis and only the most critical constraint is considered active and updated along the optimization process, so $\bar{g} = MAX(g_k, \, k=1,...,N_{str})$. This set active strategy is coherent due to the stress concentration seen at the distal and proximal zones at the interface and are relevant to the bond failure. The optimization problem was then performed by the constrained minimization of the objective function established in equation (1) as

$$\left\{ \begin{array}{l} Minimize \ \Phi(\Pi) \\ Subjected \ to: \ \bar{g} \leq 0 \\ and \ \pi^l \leq \pi_i \leq \pi^u \end{array} \right. \tag{4}$$

The optimization technique applied to obtain the solution of the problem was done by a combination of the sensitivity analysis with the mathematical programming.

SENSITIVITY ANALYSIS

To obtain the optimal design it is necessary to perform the sensitivity analysis of the objective and constraint functions. The derivative of the objective function is

$$\frac{d\Phi(\Pi)}{d\pi_i} = 2 \left(U_b(\Pi) - U_b^* \right) \frac{dU_b(\Pi)}{d\pi_i} \tag{5}$$

Using the adjoint variable method, the strain energy sensitivity is obtained by the following equation

$$\frac{dU_b}{d\pi_i} = - \sum_{n \in L_p} \left[(\phi^\Phi)^T \cdot \frac{\partial K}{\partial \pi_i} \cdot u \right]_n \tag{6}$$

where L_p is the set of prosthesis elements that depend explicitly on the variable π_i, u is the actual displacement vector and ϕ^Φ is the adjoint displacement vector obtained from the following adjoint system of equations

$$K \cdot \phi^\Phi = \frac{\partial U_b}{\partial u} \tag{7}$$

The sensitivity of the most critical constraint function is obtained in a similar manner by

$$\frac{d\bar{g}}{d\pi_i} = - \sum_{n \in L_p} [(\phi^{\bar{g}})^T \cdot \frac{\partial K}{\partial \pi_i} \cdot u]_n \tag{8}$$

regarding the following adjoint system

$$K \cdot \phi^{\bar{g}} = \frac{\partial \bar{g}}{\partial u} \tag{9}$$

In both cases the partial derivatives are obtained in an analytical form using a displacement formulation of the finite element method.

OPTIMIZATION METHOD

The constrained optimization problem is transformed into a sequence of unconstrained problems and using the sequential unconstrained minimization technique (SUMT). Considering the augmented Lagrangean of the problem proposed by Rockafellar[5]

$$L(\pi, \bar{\lambda}, \bar{r}) = \begin{cases} \Phi(\Pi) + \bar{\lambda}\bar{g} + \frac{1}{2}\bar{r}\bar{g}^2 & , \quad \bar{g} + \frac{\bar{\lambda}}{r} \geq 0 \\ \Phi(\Pi) + \frac{1}{2}\frac{\bar{\lambda}^2}{\bar{r}} & , \quad \bar{g} + \frac{\bar{\lambda}}{r} < 0 \end{cases} \tag{10}$$

the dual problem is an unconstrained minimization of the functional $L(\Pi, \bar{\lambda}, \bar{r})$. The minimization is performed by a conjugate gradient algorithm with continuous update of the multiplier $\bar{\lambda}$ and penalty parameter $\bar{r}$. The formulae of multiplier updating is obtained by the minimization of $\| \nabla L(\Pi, \bar{\lambda}, \bar{r}) \|^2$ and resulting into the projection of the objective function on the most critical constraint space[5][6]. The penalty parameter is calculated as a ratio between the previous function and the square of the variation in the most critical constraint[6]. The augmented Lagrangean of the problem in equation (10) is minimized using the conjugate gradient method. It is essentially based on finding the direction such that, besides considering the highest slope direction, the search includes the information about the vector representing the previous search direction. The new search direction is chosen to reduce the number of iteration steps. The Kuhn-Tucker conditions to the dual problem are verified at the optimal solution.

RESULTS AND DISCUSSION

A two dimensional finite element model of a implanted femur with a similar Freeman's hip prosthesis design was generated. In figure 1 it is shown the finite element mesh (239 elements and 1061 nodes) of the femur-prosthesis construction and the chosen macroelements. A nine node plate finite element, based on the Mindlin theory, with a thickness of 10mm was used in the simulation. A 2320N hip force (Fh) and 700N abductor force (Fab) was applied as shown in figure 1, which satisfies the constraint that the bone is sufficiently loaded.

The cortical and cancellous bone were simulated with 20GPa and 1GPa elastic modulus respectively. A 0.33 coefficient of Poisson was used. The interface strength is assumed to be determined by the bone adjacent to the interface, according to[3] as $S_t=37MPa$, $S_c=89MPa$ and $S_s=53MPa$. A lower limit bound of 1GPa for the optimized Young's modulus was imposed. The starting design solution uses a titanium (E=100GPa) prosthesis. The total strain energy obtained within the intact femur was of 303Nmm. In figure 2 it is shown the optimized Young's modulus obtained for different normalized amount of stress shielding, this as (Uint-U*)/Uint, where Uint is the total strain energy of the intact bone.
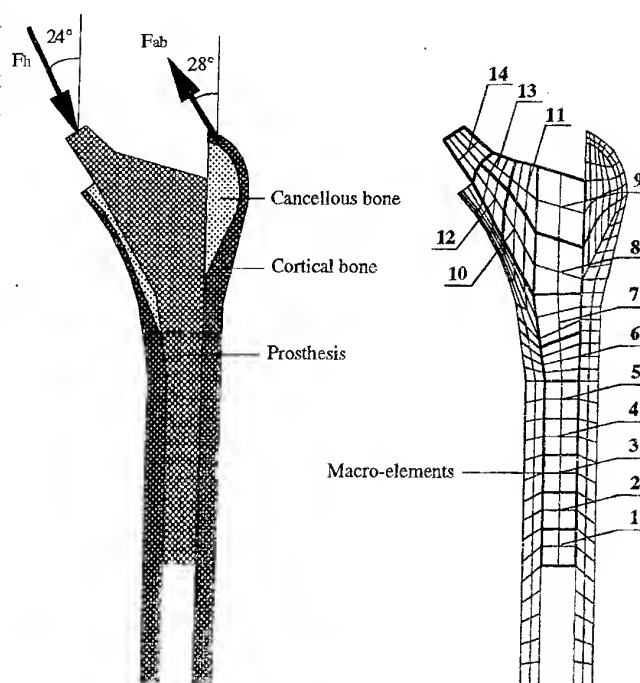
Figure 1 - The 2D femur-prosthesis construction model.

It is observed that for U=170Nmm, the constraint value is kept constant (-0.305). It looks impossible to lower the normalized amount of stress shielding beyond 13,5%, once we noticed that the total strain energy becomes constant and simultaneously it is observed a locking effect in macroelement 12. The results obtained show that the Young's modulus at the distal part of the prosthesis is very low (identical to the Young's modulus of the cancellous bone), and very stiff in the proximal part. This suggests that the stem must be short and relatively stiff compared to the surrounding bone. We observed that the proximal-medial side of the prosthesis must be more stiffer than the proximal-lateral side.
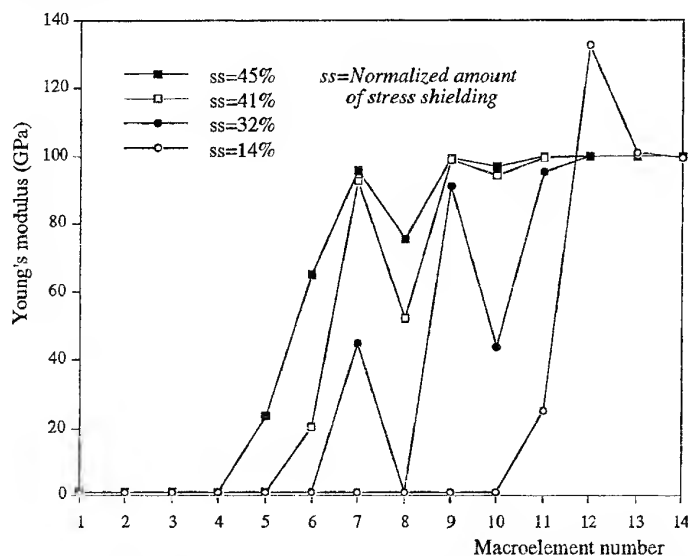
Figure 2 - Optimized Young's modulus in each macroelement for different values of the normalized amount of stress shielding.

The iterative history for the total bone strain energy and most critical constraint of the optimization process is shown in figure 3.
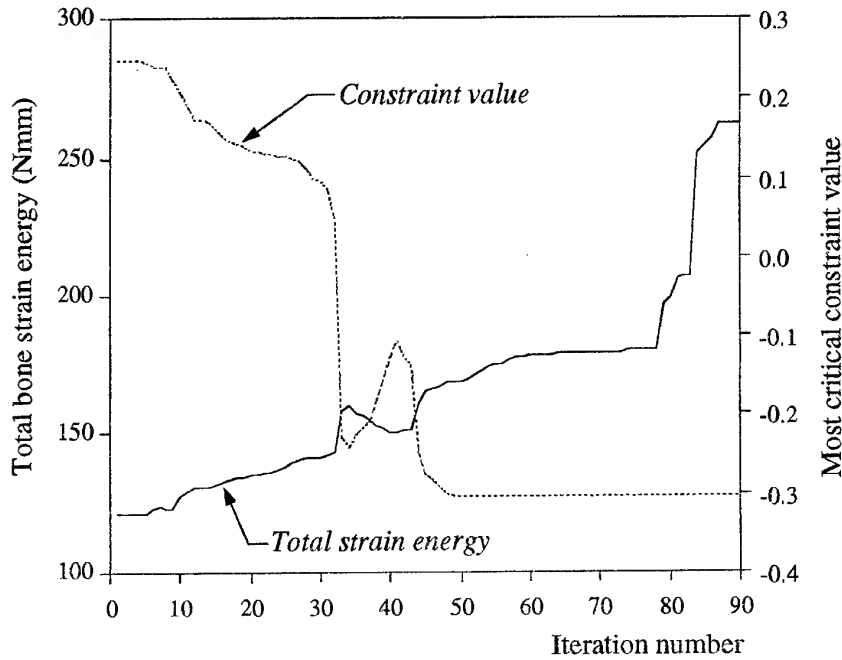
Figure 3 - Convergence of the optimization process.

THE MATHEMATICAL PROCEDURE TO OBTAIN THE PROSTHESIS WITH OPTIMIZED VARIABLE MODULUS

A mathematical procedure was developed to manufacture the optimized variable modulus prosthesis. The procedure is based on the equivalence of the flexural stiffness of the numerical optimized modulus prosthesis to the same composed by a metal core and composite structure. Therefore we obtain

$$(EI)_{opt} = (EI)_{mc} + (EI)_{cs} \tag{11}$$

where $(EI)_{opt}$ is the optimized flexural stiffness, $(EI)_{mc}$ the flexural stiffness of the metal core, and $(EI)_{cs}$ the flexural stiffness of the composite structure. The geometry of the prototypes to be manufactured is based on the Freeman's hip prosthesis design. The geometry of this prosthesis is composed by a rectangular proximal section and a circular cross section at the middle-distal portion of the prosthesis. Developing equation (11), the Young's modulus of the composite structure, as a function of its thickness, for these sections is as follows

Circular section
$$t = \frac{d}{2}\left[1 - \left(\frac{E_{opt} - E_{cs}}{E_{mc} - E_{cs}}\right)^{0.25}\right] \tag{12}$$

Rectangular section
$$(a - 2t)(b - 2t)^3 = \frac{E_{opt} - E_{cs}}{E_{mc} - E_{cs}} ab^3 \tag{13}$$

where d is the outside diameter of the circular section, a and b the side dimensions of the rectangular section, and t the thickness of the composite structure. To obtain the

481

optimized composite structure, one can either maintain its thickness constant, varying the elastic modulus, or maintain the elastic modulus constant varying the thickness. This last possibility seems more feasibility concerning the prototype fabrication. The combination of these two possibilities can also be done.

CONCLUSIONS

The optimization procedure implemented and results obtained show that the stem of the prosthesis must be relatively flexible distally and stiff proximally. This fact leads us to the conclusion that relatively short stiff stems (or bigger ones, but flexible at its distal part) can probably perform better than the traditional normal sized ones. The optimized variable modulus prosthesis obtained produces a favourable stress load transfer mechanism, including low proximal medial and distal lateral stress concentrations and minimal stress shielding over the distal two-thirds of the stem. It seems advantageous to use a hybrid modulus press-fit proximal femoral prostheses in comparison to conventional ones.

It should be evidenced that the attempt made in this study to optimize the Young's modulus of a press-fit hip prosthesis is limited in several ways. With a three dimensional finite element, and an adequate finer local FE mesh density, a better approximation would be obtained of the real simulated problem, and therefore better results can be obtained. The choice of the macroelements also influence the final result. Another aspect which deserves special attention is the clinical effect of the bone density changes. The adaptive bone remodelling may well reduce the probability of interface failure, rather than increase it, and was not included in the optimization procedure. The load case applied can be questionable. In the study done by [3], it was used a cycle of three load cases representing the probable daily loading activities. We applied a single load case, and did not take in account the influence of out-of-plane loading, although it seems that these loads do not change significantly the optimized Young's modulus distribution[3]. An important limitation of the model has to do with the bonding conditions at the interface, since we assumed a fully bonded cementless prosthesis, and this is a restrictive assumption.

In future developments, the referred limitations of the optimization model will be taken in account. With this study, one can assess the probable benefits of the optimization of non-homogeneous elastic modulus for cementless hip prosthesis. Nevertheless, the optimization carried here, or any other, depend strongly on the design objectives.

REFERENCES

[1] Huiskes, R. "Failed innovation in total hip replacement: Diagnosis and proposals for a cure", Acta Orthop. Scand., **64(6)**, pp. 699-716 (1993).
[2] Carter, D. R., Fyrie, D. P., Whalen, R. T. "Trabecular bone density and loading history: Regulation of connective tissue biology by mechanical energy", *J. Biomech.*, **14**, pp. 461-470 (1987).
[3] Kuiper, J. H. "Numerical optimization of artificial hip joint designs", PhD Thesis, Katholieke Universiteit Nijmegen, The Netherlands (1988).
[4] Tsai, S. W. "Composites Design", Think Composites, Dayton, USA (1987).
[5] Arora, J. S., Chahande, A. I., Paeng, J. K. "Multiplier methods for engineering optimization", *International Journal for Numerical Methods in Engineering*, **32**, pp. 1485-1525 (1991).
[6] Antonio, C. A. C. "Optimização de estruturas em materiais compósitos de matriz polimérica", PhD Thesis, Faculty of Engineering, University of Porto (1995). Translated as: Optimization of polymeric composite material structures.

OPTIMISATION OF THE HEAT TREATMENTS FOR IMPROVING THE MECHANICAL PROPERTIES OF C - PEEK COMPOSITES

T. SINMAZÇELİK [1], A.A. ARICI [1], H. PEKEY [1]
and
V. GÜNAY[2,3]

[1] Mechanical Engineering Dept., Kocaeli University, Anıtpark Yanı, İzmit / TURKEY
[2] Metallurgical Engineering Dept., İstanbul Technical University, İstanbul / TURKEY
[3] TÜBİTAK - MRC, Materials Dept., P.O. Box 21, Gebze / TURKEY

INTRODUCTION

In recent years there has been a remarkable growth in the large - scale industrial application of fiber reinforced polymer matrix composites. Because of their superior specific strength and stiffness properties, these are excellent materials for a variety of structural applications as in aerospace, automotive and chemical industries.

PEEK is a high performance, semicrystalline thermoplastic. It' s relatively stiff backbone gives excellent high - temperature stability. It has a high glass transition temperature and high melting point and a high continuous service temperature with the advantages of easy process ability by injection molding and other techniques common to thermoplastic polymers [1,2,3].

The mechanical properties of thermoplastic matrix composites depend significantly on the microstructure parameters, such as the degree and type of crystals. The size of the spherulites are controlled by controlling the heat - treatment during the manufacturing of the composites (4-6) and by the microstructure of the fibre, which determines the ability to develop a transcrystalline layer (7) There are several indications that slow - cooled or annealed materials, which have a fully developed crystalline structure, exhibit better mechanical properties (8). Likewise the presence of transcrystallinity was shown to influence the mechanical performance through its effect on fibre / matrix bonding and on the stress transfer mechanism (9,10)

It is possible to control the microstructure, especially the crystallinity of a part fabricated from PEEK by using suitable heating and cooling cycles. It is already well known that there is an important relationship between crystallinity and mechanical properties. For example both the tensile strength of PEEK increase with an increase in crystallinity. The level of crystallinity also effects the resistance to hostile environments, moreover achieving a desired level of mechanical response above the glass transition temperature is also influenced by the level of crystallinity. Of course, not only does the degree of crystallinity effect the

mechanical properties but the detailed morphology of the crystalline phase will also be important [11]

The role of the fibre / matrix interphase in composite materials is currently the focus of an increasing number of studies. An interphase (interlayer) is a third, relatively thick, intermediary phase present between the constituents. Its elastic and mechanical properties are specifically designed to produce a certain effect on the overall performance of the composite material.

For example a gradient modulus interphase approach has been proposed to promote the mechanical properties and the fatigue life by reducing the modulus mismatch of fibres and the matrix . while a soft, elastic interphase has been advocated for high fracture toughness, and for reduced stress concentrations in the matrix around the fibres .

A number of theoretical models link the properties of the interphase and its relative thickness to the performance of the composite material. This can be exemplified by studies of the mesaphase, a region with variable properties between the fibre and the matrix. The advantages of intentional addition of an interphase, with its wide spectrum of design parameters, emerge clearly compared with a fibre / matrix interface. The latter which is formed spontaneously when a composite material is prepared has a single design parameter, namely, the fibre / matrix bond strength. [12]

MATERIALS

In this study, cross -ply carbon fiber reinforced PEEK composites (C - PEEK) were produced according to manufacturer (ICI, UK) suggestions from prepregs by using hot pressing technique and the details were given elsewhere [13]. Composites were produced at 380 ° C these samples (as received) have around 19 % crystallinity.

TESTING PROCEDURE

Fracture Toughness of the specimens are investigated with a Charpy - V tester. The dimensions of samples are 2.1 × 12 × 60 mm.

In this study mainly 3 different heat treatments applied to the samples. Table 1 shows the heat - treatments applied at various temperature for different times.

It is known that heat treatments should be applied higher than glass transition temperatures. In this study it is aimed to investigate the microstructure and mechanical property changes of the C - PEEK composites by applying heat - treatment to the as received and quenched samples at various temperatures for various times.

Table 1 Various heat - treatments which were applied to C - PEEK composites
Slow Heating rate   :10 ° C / min, Slow Cooling rate   :10 ° C / min

Isothermal Crytallization (IC)	Annealing (A + A)	Quenching + Annealing (Q + A)
As Received sample Slow Heating (SH) 380 °C (6 min) Slow Cooling (SC) 310 °C (40 min) IC Slow Cooling.	As Received sample Slow heating (SH) 310 °C (30 min) Slow cooling (SC)	Quenched sample Slow heating (SH) 310 °C (30 min) Slow cooling (SC)
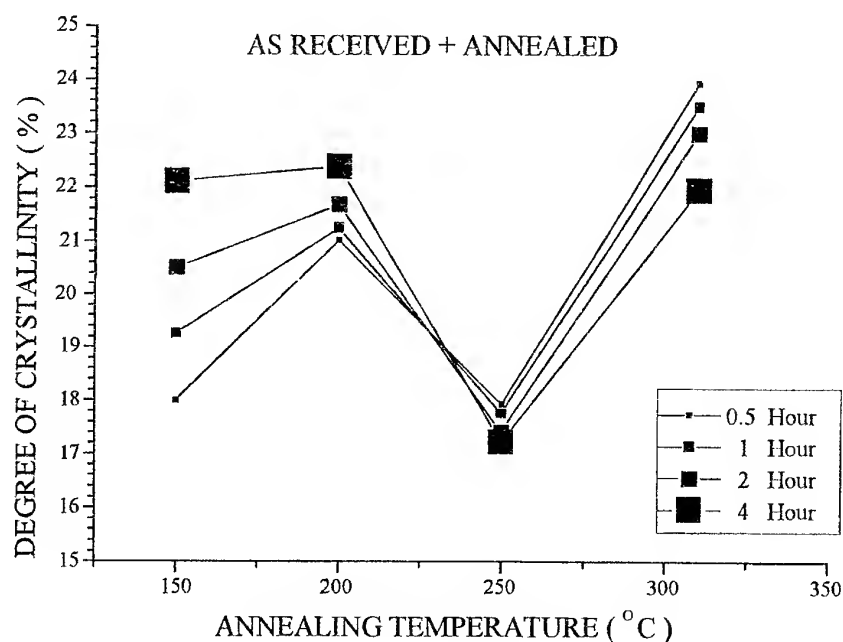
Fig 1

As seen from Fig 1 especially at low annealing temperatures crystallinity is increased with increasing annealing time. It is understood that both crystal growth and perfection process were in operation. This process occurred at 150 °C. An increase in crystallinity was observed at 200 °C. There was a decreases in crystallinity for all heat-treatments times at 250 ° C and the decrease was longer with increasing heat - treatment time. At 310 ° C, there was an increase in crystallinity and these increases were higher for shorter heat -treatment times. These results were exactly opposites to the results at 200 ° C.

Briefly experimental results indicate that with an increase in annealing time at 150 °C both the crystal growth and perfection processes were in operation. Initial annealing caused rapid crystal growth. However further annealing caused a reduction in the measured crystallinity probably associated with matrix degradation.

Fig 2 shows the crystallinity levels as a results of WAXD studies of quenched and annealed samples. After quenching in ice water, PEEK matrix become completely amorphous. This is different in as received samples because they usually have 19 % crystallinity after processing. In quenched samples there is homogenous matrix which causes homogenous crystal growth. There is linear increase in crystallinity with increasing annealing temperature and time. Crystal perfection mechanism is continue without causing matrix degradation at higher annealing times.
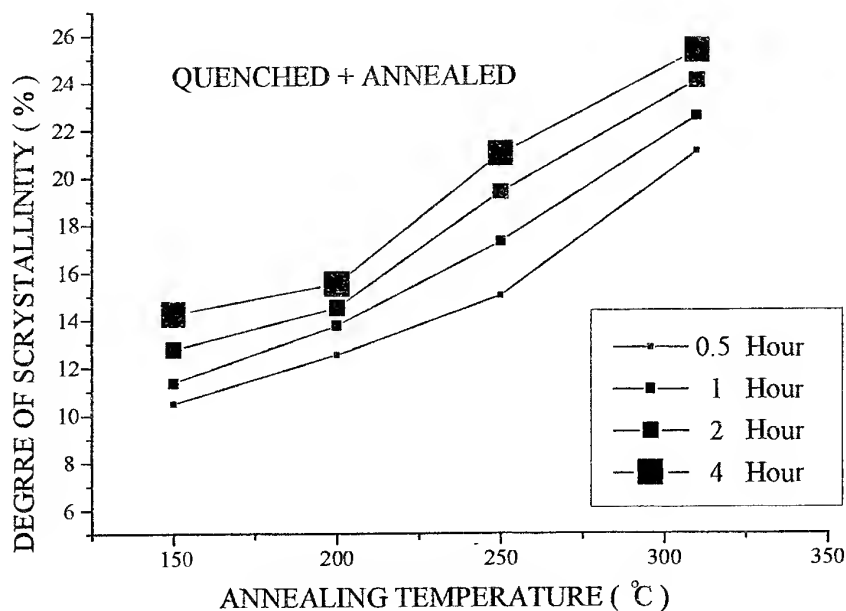
Fig 2

Fig 3 represents the level crystallinity as a results of WAXD studies of isothermally crystallised samples. As seen in Fig 3 that, the degree of crystallinity didn' t show a large variation which increasing in temperature. Figure 4 gives the Charpy - V test results of IC (Isothermally Crystallized), Q + A (Quenched + Annealed) and A + A (As received and Annealed) samples.
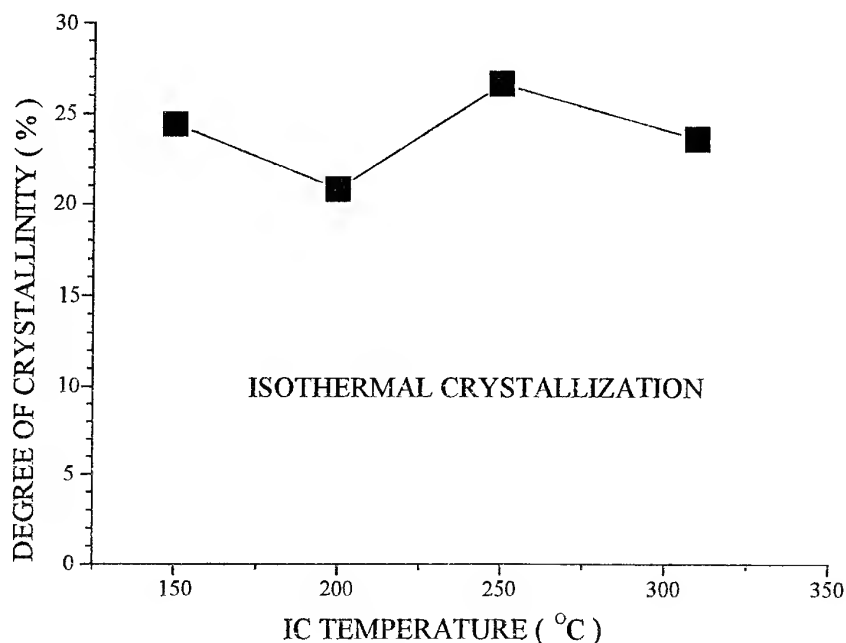
Fig 3

It is seen from Fig 4 that the highest fracture toughness values were in IC samples. Although there was not much increase in the degree of crystallinity in these samples (see Fig 3) with increasing heat - treatment temperature, there was increases in fracture toughness with increasing heat - treatment temperatures. It is nearly the same for A + A samples. It is clearly seen from these results that, however the degree of crystalinity being equal, the type of the crystals still play a significant role in fracture toughnesses. The more organized crystals formed by IC treatments results in better static and fatigue performances compared to these results from the annealing crystallization.

In Q + A samples, there is very residual stresses formed during quenching and these strongly affect the fracture toughness of the samples. Increase in annealing temperature, relieves these stresses and in turn, the fracture toughness values increased.

At 310 ° C, fracture toughness values of all the samples were very close to each other. At these temperature, all samples show nearly same crystallinity and although not given in this paper, the same crystal form and microstructure these similarity in samples result with similar fracture toughness values. In fracture toughness, Q + A sampies showed the largest changes with increasing annealing temperatures being around 54 (Kp. cm / cm ^{2}) at 150 ° C and around 100 (Kp. cm / cm ^{2}) at 310 ° C for 30 minutes.
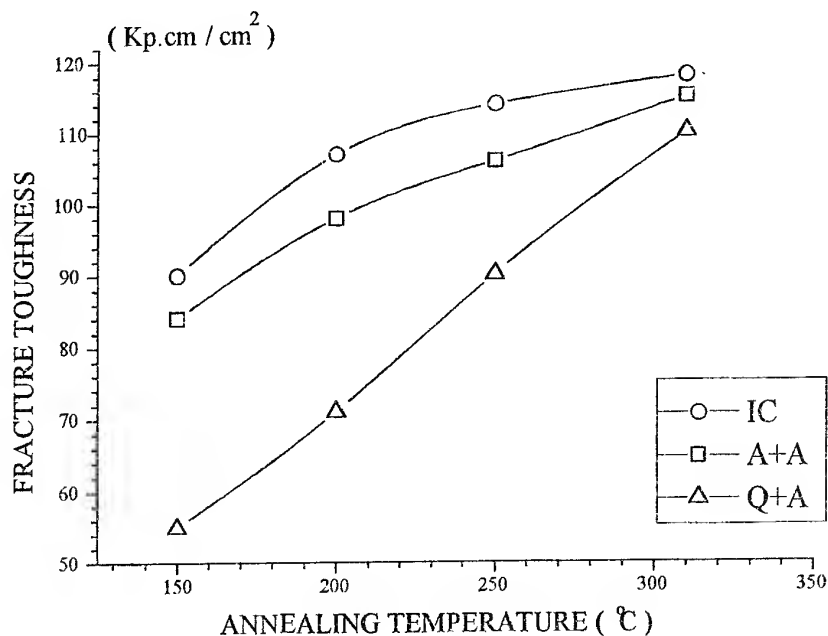
Fig 4

CONCLUSIONS

Thermal treatment can cause significant crystal morphology changes which, in turn, affect the mechanical properties of C - PEEK composites. At lower temperatures post annealing cause both crystal growth and perfection processes were in operation. Post annealing at higher temperature caused rapid crystal growth. Further annealing caused a reduction in the measured crystallinity probably associated with matrix degradation but an increase in the perfection of the remaining crystal structure.

REFERENCES

[1] D.J.Blundell and B.N.Osborn, *Polymer*, 25 (1983) pp. 953-958

[2] D.P.Jones, D.C. Leach and D.R.Moore, *Polymer*, 26 (1985) pp.1385 - 1393.

[3] LNP-Plastics: Lubricomp, *LNP- Bulletin* pp.254-988,1988

[4] Curtis, P.T., Davies, P., Partridge,I.K. / Sainty,J. P., Elsevier App. Sci. Publ., Barking, 1987, p.4.401

[5] Mijovic, J. / Gsell, T.C., *SAMPE Q.*, 21 (2) 1990 pp 42.

[6] Olley, R.H., Bassett, D.C. & Blundell, D.J., *Polymer*, 27 (1986) pp 344

[7] Hartness, J. T., *SAMPE J.*, 20 (1986) pp 26

[8] Manson, J. E., Schneider, T. L. & Seferis, J. C., *Polym. Composites*, 11 (1990) pp 114

[9] Saiello, S., Kenny, J. & Nicholais, L., *J. Mater. Sci.*, 25 (1990) pp 3493

[10] Incardona, S., Migliarcsi, C., Wagner, & Marom, G., *Composites Sci. Technol.*, 47 (1993) pp 43

[11] Folkes, M.J., Kalay, G., & Ankara, A., *Composites Science and Technology* 46 (1993) pp 77 - 83

[12] Incardona, Silva et al., *Composites Science and Technolgy* 47 (1993) 43 - 50

[13] Bakan, İ.H, Uzunali, A, Günay, V., *6 th Denizli Materials Symposium, pp 513 - 520, 1995 (In Turkish)*

VISCO-DAMAGE IN SWIRL-MAT FIBERGLASS COMPOSITES

L. V. Smith and Y. J. Weitsman

Mechanical and Aerospace Engineering and Engineering Science
University of Tennessee
307 Perkins Hall
Knoxville, Tennessee, USA

ABSTRACT

The creep/recovery response of randomly oriented fiberglass composites, suitable for automotive scale production, has been examined under ambient conditions. Below approximately 20% of the material ultimate strength strain behavior could be modeled using linear viscoelasticity. Above 20% UTS non-linearity, associated with the accumulation of damage, was observed through an increase in compliance and the formation of non-recoverable strains upon load removal. NDE investigations indicate damage to be in the form of multitudes of micro-cracks, forming primarily within fiber bundles, on which compliance is obviously dependent. Permanent strains are believed to be associated with incomplete closure of rough crack surfaces due to the random fiber orientations. A one-dimensional model based on the above phenomena and incorporating elements of viscoelasticity, continuum damage, plasticity and viscoplasticity is presented. The model forms a rational means of understanding damage growth and its effects on material behavior.

INTRODUCTION

Swirl-mat composites consist of continuous fiber strands laid out in circular patterns and combined to form a "dry" mat as shown in Fig. 1. The mat is injected with a polymeric resin that binds the strands within the mat. Each strand contains several hundred individual fibers.

A major advantage of swirl-mat composites is that they are easily adapted to take a variety of shapes and can be manufactured rapidly and at relatively low cost by introducing the resin through a structural reaction injection molding (SRIM) process. These advantages render swirl-mat composites as attractive materials in cost sensitive applications, such as the automotive industry.

This article is concerned with the room temperature creep response of glass fiber / urethane matrix swirl-mat composites. It presents experimental data with some microscopic observations and proposes a constitutive model to represent the data.

EXPERIMENTAL

The experimental data to be reported herein consist mainly of records of creep and recovery strains in tensile coupons of dimensions 1"x1/8"x8" caused by the abrupt application and removal of constant loads as sketched in Fig. 2.

Accordingly, the applied stresses were all of the form

$$\sigma(t) = \sigma_o\left[H(t) - H(t - t_o)\right].$$ (1)

In the test program σ_o was varied between 10% and 70% of the material ultimate tensile strength (UTS=20 ksi) and the time under stress, t_o, ranged from 1 to 10,000 minutes.

Due to the pronounced scatter caused by the randomness of the material and the non-uniformity in processing, the creep data for each coupon were scaled by its "instantaneous" compliance. In this manner, major portions (though by no means all) of the scatter were eliminated and consistent trends came to light.

It was noted that up to a threshold stress level, $\hat{\sigma}$, of approximately 20% UTS, the creep strains varied linearly with stress, with complete strain recovery upon load removal. That complete recovery was reached at times $t \approx 4t_o$ (t_o depicted in Fig. 2). Furthermore, (for $\sigma < \hat{\sigma}$) it was possible to employ linear viscoelasticity and express the creep and recovery data by a power-law form, namely

$$\varepsilon(t) = \begin{cases} \left(D_o + D_1 t^n\right)\sigma_o & 0 < t < t_o \\ D_1\left[t^n - (t - t_o)^n\right]\sigma_o & t > t_o \end{cases} \qquad \sigma_o \leq \hat{\sigma}.$$ (2)

For $\sigma_o > \hat{\sigma}$ strain-stress linearity no longer held, with strains increasing disproportionately with σ_o. In addition, strains did not completely recover upon load removal, leaving a permanent strain, ε_p, as $t \to \infty$.

The major cause for non-linearity and permanent residual deformation was traced to debonds between individual fibers within the fiber strands (primarily those oriented normal to the loading direction) as well as to separations between the strands and surrounding matrix. This conclusion was verified by microscopic observations that used a variety of NDE techniques including confocal laser scan microscopy, thermal emission ("SPATE"), acoustic emission, ultrasonic investigations and direct optical microscopy. Typical observations are shown in Figs. 3 through 5. These, as well as other figures, demonstrate the presence of damage in the form of multitudes of micro-cracks focused at the above mentioned sites. These figures also suggest that the permanent strain, ε_p, is attributable to the roughness between opposite faces of micro-cracks, which prevent their smooth closure upon load removal.

The effect of the foregoing damage on the stress-strain response for $\sigma_o > \hat{\sigma}$ can be quantified by comparing compliances during the application of load and upon its removal. Since in reality it is impossible to apply a step load, as implied by Eq. (1), load was introduced and removed at a constant rate (100 lbs/sec) which required appropriate corrections in determining the compliance values. (Typically lowering them by 16%.) Furthermore, the "loading compliance" corresponds to data collected where $\sigma(t) < \hat{\sigma}$ while, following customary procedure, the "unloading compliance" is associated with $0.85\sigma_o > \sigma(t) > 0.15\sigma_o$. Typical measurements of normalized compliance (D_u/D_o) variations with σ_o are shown in Fig. 6. Note that for load durations $t_o < 10,000$ min. it

was impossible to discern a dependence of D_u/D_o on t_o. This does not exclude such dependence for longer time spans and appears consistent with the well documented fact that such temporal effects become pronounced only as t_o approaches the failure time, t_f.

At stress levels $\sigma_o > \hat{\sigma}$ the recorded creep compliance $D(t)=\varepsilon(t)/\sigma_o$ increased non-linearly with σ_o in direct proportion to D_u/D_o. Furthermore, the non-recoverable, permanent strain ε_p, which depended on both σ_o and t_o ($\sigma_o > \hat{\sigma}$), increased in direct proportion to $D(t_o)=\varepsilon(t_o)/\sigma_o$. These observations are illustrated schematically in Fig. 7 for the time-dependent response under $\sigma = \sigma_o H(t)$, ($\sigma_o > \hat{\sigma}$).

A MECHANICS MODEL

A mechanics model for the aforementioned behavior of swirl-mat composites was constructed employing fundamental principles of irreversible thermodynamics and concepts of viscoelasticity, continuum damage mechanics, plasticity and viscoplasticity theories. The details are omitted herein, with attention confined to the one-dimensional circumstance. Accordingly, let S denote damage, then -in general- $S=S(\sigma,t)$. However for $t \ll t_f$, $S \approx S(\sigma)$. Consequently, the scaling of the creep compliance is given by

$$D_u(S)/D_o = g(\sigma) \quad g = \begin{cases} 1 & \sigma_o < \hat{\sigma} \\ g(\sigma) & \sigma_o > \hat{\sigma} \end{cases}. \tag{3}$$

Thus,

$$D(t) = g(\sigma)D_L(t). \tag{4}$$

In Eq. (4) $D_L(t)$ denotes the linear compliance of the power law form given in (2). Similarly,

$$\varepsilon_p(t) = K_p[g(\sigma)-1]D_L(t). \tag{5}$$

Obviously, since $D_L(t)=D_{oL}+D_{1L}t^n$, ε_p will have both instantaneous and time-dependent components. This will require the utilization of both plasticity and viscoplasticity in the modeling of ε_p. For sufficiently long loading durations, the evolution of S becomes noticeably time-dependent and $S(\sigma,t)$ is to be determined by integration of $\dot{S}$, resulting in interaction between creep and damage growth. This will be discussed elsewhere.

In the present case we have $D_{oL}=7\times10^{-7}$ psi^{-1}, $D_{1L}=1.4\times10^{-7}$, n=0.08, $g(\sigma)= 1+0.023(\sigma - \hat{\sigma})H(\sigma - \hat{\sigma})$, $K_p= 3100$ Msi, $\hat{\sigma}=4.5$ ksi, and t is in minutes

CONCLUDING REMARKS

Swirl mat composite materials exhibit time-dependent response in both linear and non-linear ranges, where creep is inherently associated with the molecular motions within the polymeric phases. Non-linearity appears to stem from damage due to micro-cracking within the fiber bundles as well as debondings at fiber/matrix interfaces. Non-recoverable strains upon unloading are most likely associated with roughness within the surfaces of the micro-cracks, which prevents their perfect closure. The combination of the above

491

phenomena require the incorporation of concepts of viscoelasticity, continuum damage, plasticity and viscoplasticity within the constitutive model. However, there is no reason to assume incompressibility when employing plasticity concepts in the present case.

ACKNOWLEDGMENTS
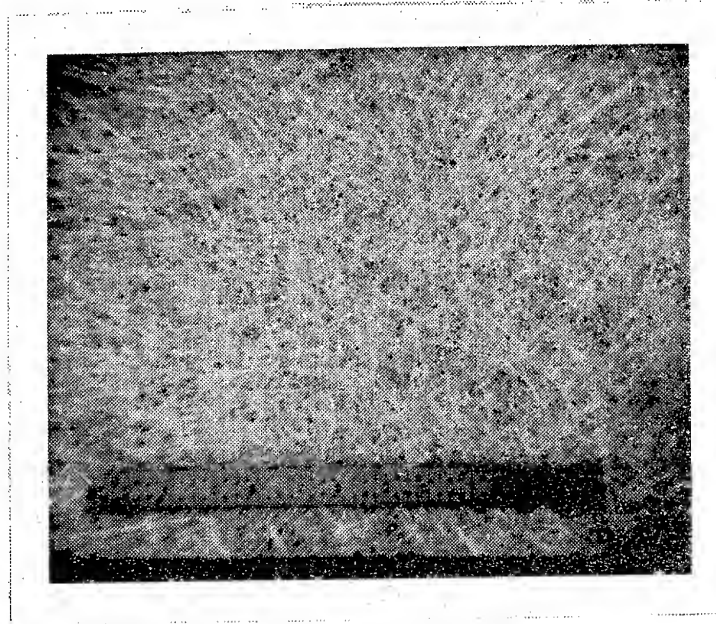
Fig. 1 Photograph of swirl mat preform.
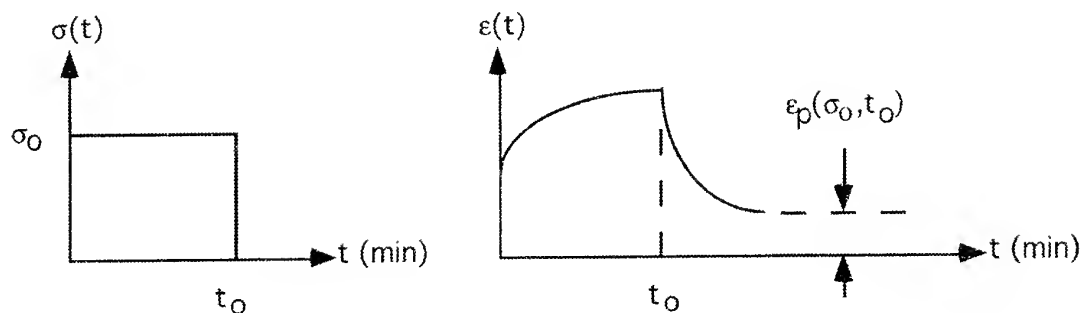
Fig. 2 Left: stress vs. time for a standard creep and recovery test. Right: cartoon of time dependent strain response from a creep and recovery test.
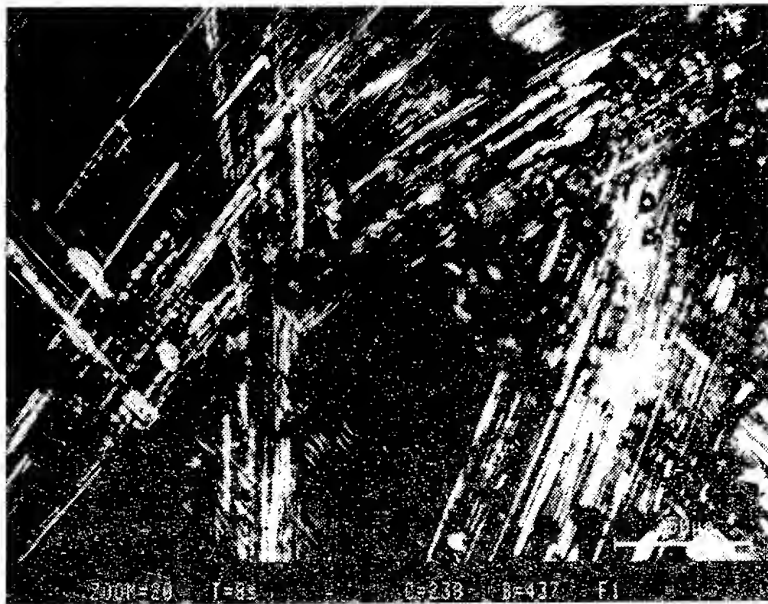
Fig. 3 Damage resulting from a 10k minute 12 ksi creep test. Image taken using a confocal laser scan microscope.

Fig. 4 Crack in a fiber bundle from a ramp load. Image taken using an optical microscope and light transmitted through the specimen.
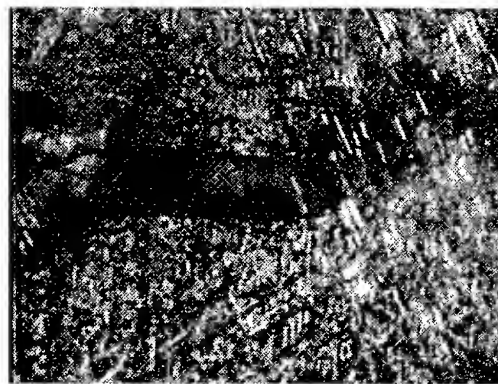
Fig. 5 Surface crack from edge notch coupon, after load removal. (Note non closing crack faces.)
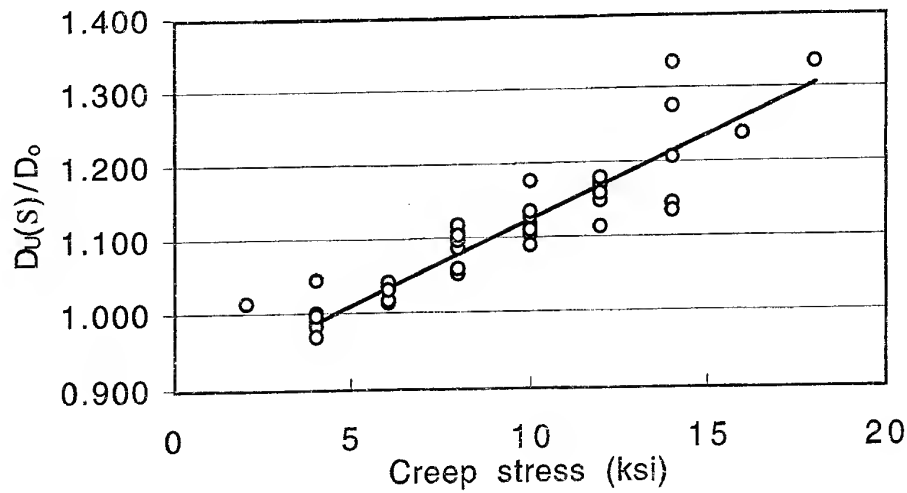
Fig. 6 Normalized compliance vs. applied creep stress, σ_o, from which $g(\sigma)$ and $\hat{\sigma}$ were obtained.
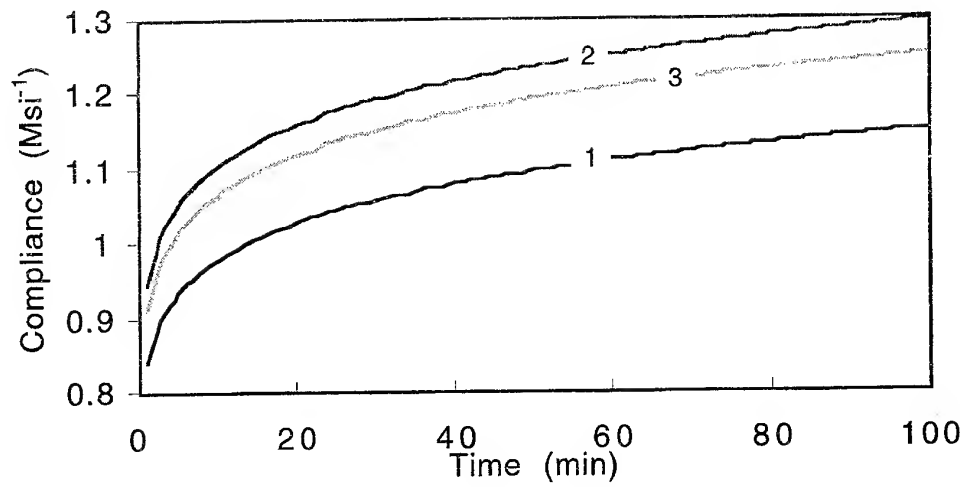
Fig. 7 Examples of time dependent compliance. "1" linear compliance, $D_L(t)$ (from Eq. (2)). "2" total compliance (including non-linear term $g(\sigma)$), $D_T(t)=g(\sigma)D_L(t)$. "3" Recoverable component, $D_T(t)-\varepsilon_p/\sigma_o$.

EFFECTS OF CARBON FIBERS ON WEAR BEHAVIOR OF Al/Al$_2$O$_3$/C HYBRID METAL MATRIX COMPOSITES

J.I.Song[1], T.Lim[2] and K.S.Han[3]

[1] Intelligent Machine Research Team, RIST, Korea
[2] Research Team 4, Hyundai Motor Co., Korea
[3] Dept. of Mechanical Engineering, POSTECH, Korea

INTRODUCTION

For engineering applications, carbon fiber reinforced MMCs which have both high mechanical properties and good wear resistance are required. Up to now, the reinforcements with one kind of fiber have been the major subject of research and development, while reinforcement with the hybrid fibers, especially, alumina based carbon hybrid metal matrix composites, has not been widely investigated[1-5]. The tribological wear behavior of one such composite, aluminum/graphite has been the subject of numerous investigations[6-10]. The purpose of this study is to investigate effects of carbon fibers on wear behavior of Al/Al$_2$O$_3$/C hybrid metal matrix composites fabricated by squeeze infiltration method. Wear tests were carried out under various sliding speed conditions to identify wear behavior clearly. Wear mechanism of MMCs is suggested by the examinations of worn surfaces.

EXPERIMENTAL

For the fabrication of Al/Al$_2$O$_3$/C hybrid composites, an AC2B aluminum alloy (JIS Type AC2B) was used as a matrix. AC2B alloys are Al-6Si-3Cu cast aluminum alloy with good casting properties and a broad limit for impurities[11]. Specifications of alumina and carbon fibers used are listed in Table 1[12,13]. Dry wear tests were carried out using the spindle type wear tester from Riken - Ogoshi Co., at room temperature. Specimens with dimensions of 50 x 20 x 6 (mm) were machined perpendicular to the direction of the applied pressure. Cast ingots for wear test were treated by T6 heat treatment. Wear tests were performed under the followings conditions; final load ; 12.6 kg$_f$, sliding distance ; 400 m, various sliding speeds ; 0.51 m/sec, 1.14 m/sec, 1.97 m/sec and 3.62 m/sec, respectively. Wear surfaces were also examined by scanning electron microscope(SEM).

Table 1 Specifications of alumina and carbon fibers

Material	Density (g/cm^3)	Diameter (μm)	Length (μm)	Aspect ratio (l/d)	T.S (GPa)	E (GPa)
Al$_2$O$_3$	3.3	4	150	38	2.0	310
Carbon	1.9	16	144	9	1.8	276

RESULTS AND DISCUSSION

Al/Al$_2$O$_3$ and Al/Al$_2$O$_3$/C hybrid composites with the same volume fraction of 20% were successfully fabricated by the squeeze casting method. Typical microstructures of Al/Al$_2$O$_3$ and Al/Al$_2$O$_3$/C composites are represented in Fig.1. To verify the distribution of reinforcements, microstructures of Al/Al$_2$O$_3$ and Al/Al$_2$O$_3$/C composites were observed through the optical microscope. The reinforcements shows uniform distributions and good bondings.
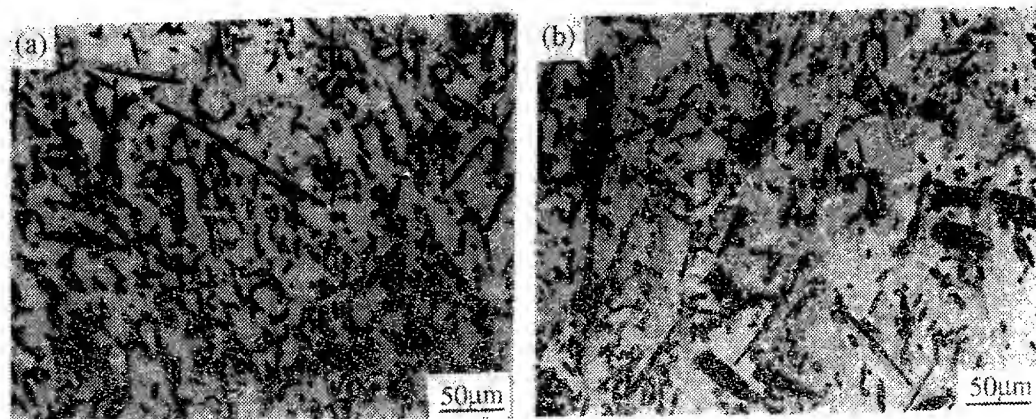
Fig. 1 Typical microstructures of (a) Al/Al$_2$O$_3$ and (b) Al/Al$_2$O$_3$/C composites

Wear Behavior

Fig. 2 shows the effects of sliding speeds on weight losses of AC2B Al alloy, Al/Al$_2$O$_3$ and Al/Al$_2$O$_3$/C hybrid composites. On the whole, above the sliding speed of 1.14 m/sec, the wear resistance of MMCs improved remarkably. This is due to reinforcements which can endure the friction force generated on the wear surface. Friction force plays an important role in wear behavior, especially in abrasive wear. Generally, the higher the friction force generated, the worse the wear resistance.

In Al matrix alloy, weight losses of AC2B Al alloy increased continuously up to 1.97m/sec. But, above the sliding speed of 1.97 m/sec, the wear loss of AC2B Al alloy increased abruptly. That is, wear behavior of AC2B Al alloy changed along with the sliding speed. Wear mechanisms are strongly dependent upon the sliding speed. Major wear mechanisms of AC2B Al alloy are abrasive and adhesive wear at sliding speeds up to 1.14 m/sec, therefore, an AC2B Al alloy is worn by the force of friction generated on the wear surface. Above the sliding speed, 1.14 m/sec, the major wear mechanism is shifted to melt wear because of the rise of the temperature on the localized wear surface. Consequently, an AC2B Al alloy starts to be worn out abruptly.

In discontinuous MMCs, however, in all speed ranges the wear resistance of Al/Al$_2$O$_3$/C composites is better than that of AC2B Al alloy, except at the sliding speed of 0.51

m/sec. Weight losses of MMCs are greater than that of the unreinforced matrix alloy at the low sliding speed, 0.51 m/sec, because reinforcements abrade the matrix by the high friction force and this abrasion deteriorates the wear resistance of Al/Al_2O_3 and $Al/Al_2O_3/C$ composites. In other words, at low sliding speed the frictional forces are large enough to fracture and pull out the reinforcements from the matrix, and these particles abrade the wear surface of composite materials. As the sliding speed increases, the friction force becomes weakened due to the reduction of the friction coefficient, and reinforcements can resist the weak friction force. In consequence, weight loss decreases until the melt wear becomes the major mechanism for wear due to the rise of temperature on the specimen. At the high sliding speeds, 3.62 m/sec, the wear resistance gets worse and weight loss starts to increase, due to the melt wear of the matrix alloy by the ascent of temperature. But the high thermal stability of MMCs due to the addition of reinforcements allows only slight deterioration of the wear resistance, compared with the Al matrix alloy.

To evaluate the effects of volume fractions on carbon reinforcements, the graph of dimensionless wear loss of $Al/Al_2O_3/C$ composites with respect to Al matrix alloy is indicated in Fig.3. In all speed range, the wear resistance of $Al/Al_2O_3/C$ composites is better than that of Al/Al_2O_3 composites. The effects of amounts of carbon fibers having volume fraction of 2% can be ignored until the sliding speed is 0.51 m/sec. Specifically, at the intermediate sliding speed of range 1.14m/sec to 1.97m/sec, the wear resistance of $Al/Al_2O_3/C$ composites containing 8 vol.% carbon fiber is found to be better than that of the rest of carbon hybrid composite. With increasing sliding speed, however, weight losses of $Al/Al_2O_3/C$ hybrid composites having nothing to do with the amount of carbon fiber converge within one point. That is, at the higher sliding speeds there is little variation in weight loss of hybrid composites. This means that at slow sliding speeds the composition of the hybrid composites (i.e. amount of reinforcements) are important and can not be ignored, but at high sliding speeds the amount of carbon volume fraction has little effect on wear resistance.
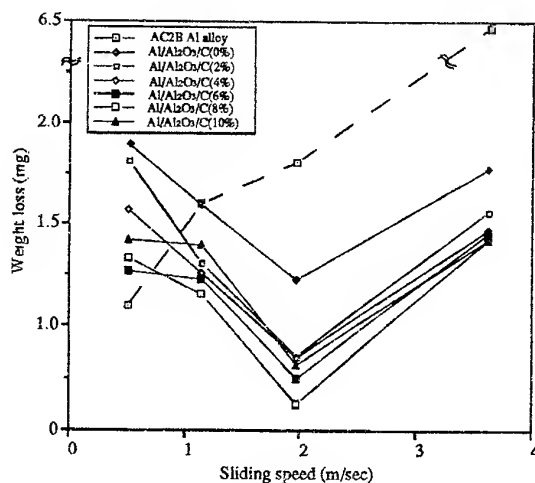

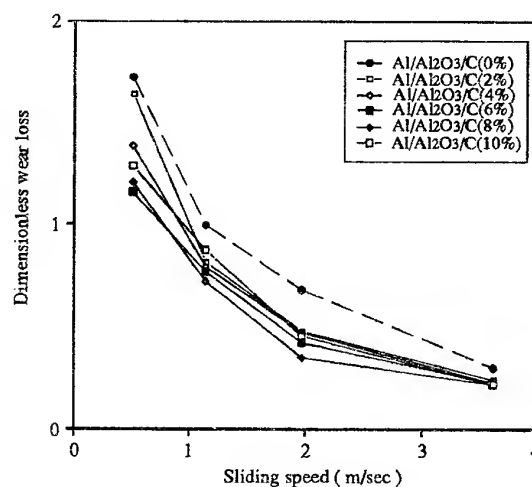Fig. 2 Effect of sliding speeds on wear behavior of hybrid composites

Fig. 3 Dimensionless wear loss of $Al/Al_2O_3/C$ composites with respect to Al alloy

497

Wear Surface Analysis

The above wear behavior can be explained based on microstructure analysis as follows. Wear surfaces of both AC2B Al alloy and Al/Al$_2$O$_3$/C composites containing 8 vol.% carbon fiber were examined by SEM. Overall wear surfaces of both materials show a similar trend except at the sliding speed of 1.97 m/sec. At low sliding speed, 0.51 m/sec, we found evidence of abrasive wear in ploughing or grooving. That is, the shapes of stripes on the wear surface seem to progressively increases because of abrasive action between the wear specimen and counter material which might be due to the high friction force applied on the wear surface. Compared with both Al matrix and composites, surfaces damages in Al/Al$_2$O$_3$/C composites are more severe than those of AC2B Al alloy. That is, at the low sliding speed, the AC2B Al alloy formed grooves by the shearing action of the friction force generated on the wear surface. However, the wear surface of Al/Al$_2$O$_3$/C composites exhibited a number of deep wear grooves. It can be considered that at low sliding speed the frictional forces of MMCs are large enough to fracture and pull out the reinforcements from the matrix, and these particles abrade the wear surface of composite materials.

At the intermediate sliding speed, 1.97 m/sec, the damaged section on the wear surface of AC2B Al alloy is shown in Fig. 4 (a). Wear debris and distorted surfaces in AC2B Al alloy are more distinguished than in Al/Al$_2$O$_3$/C composites. From the wear surface, it can be regarded that wear debris and a distorted surface play an important role in wear behavior, i.e., wear progresses by their formation and growth. The formation and growth of the distorted section are illustrated in (A) and (B) by an arrow, respectively. The distorted section and debris are formed at the locally fractured area of the matrix alloy. This localized fracture is caused by highly localized friction forces which come from the non-uniform surface of the counter material and defected areas of the wear surface. The growth of the damaged section is advanced by the fracture of the wear surface. Wear surfaces of AC2B Al alloy show that abrasive and adhesive wear is the dominant wear mechanism at intermediate sliding speeds. By contrast, the wear surface of Al/Al$_2$O$_3$/C composites is completely different from that of AC2B Al alloy. That is, the wear surface of Al/Al$_2$O$_3$/C composites shows virtually no damaged region. In Al/Al$_2$O$_3$/C composites, abrasion of reinforcements and the matrix is seldom observed due to the remarkable reduction of friction forces applied to the wear surface. Fig.4(b) illustrates an alumina fiber being pulled-out (see arrow) and being struck on the wear surface. Visible lack of damage is due to the presence of lubrication film formed by the addition of carbon fibers on the wear surface of hybrid composites. Consequently, this result gives rise to the improvement of wear resistance.

As the sliding speed increases, adhesive and slip phenomena also appear at the high sliding speed, 3.96 m/sec. Here, adhesive wear can be detected by removed materials and slip phenomenon can also be found in the wave patterns of materials. The removal of the material seems to be accelerated by fractures of short alumina fibers and the matrix which might be due to the high friction force applied on the wear surface. Localized melted areas owing to the ascent of temperature are observed in both AC2B Al alloy and Al/Al$_2$O$_3$/C composites. Wear of AC2B Al alloy seems to start by localized melting of the surface and to proceed by delaminations from the large plastic deformation of the matrix. Some wave patterns which might be related to melt and slip, indicated by an

arrow, are often seen. These figures illustrate that the major wear mechanisms at high sliding speeds are melt and slip wear of the matrix due to the rise of temperature, and less severe damage on the wear surface is seen compared with unreinforced matrix alloy.
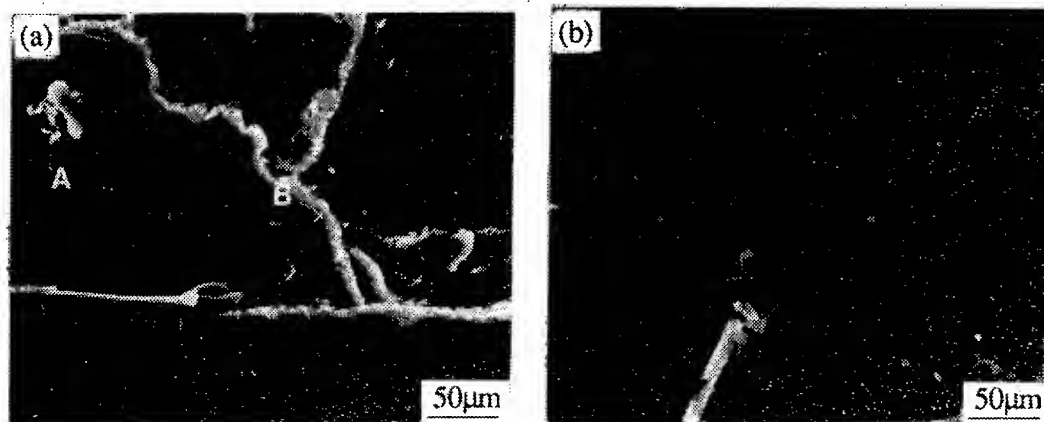
Fig. 4 Wear surfaces of (a) Al matrix and (b) Al/Al$_2$O$_3$/C composites

Fig.5(a) shows SEM micrograph of Al/Al$_2$O$_3$-12vol.%/C-8vol.% composite at the sliding speed of 1.97 m/sec. Fig.5(b) shows the distribution of carbon detected from the wear surface through electron probe micro analysis (EPMA). The presence of carbon film on the wear surface of Al/Al$_2$O$_3$-12vol.%/C-8vol.% composite was resolved by a carbon X-ray dot map. The dot-map shows a higher concentration of the carbon near the grooved section and debris of Al/Al$_2$O$_3$-12vol.%/C-8vol.% composite on the wear surface. In particular, the presence of carbon is concentrated on the debris separated from the wear surface, as shown by an arrow. Consequently, this presence of lubrication film which is formed by the addition of carbon fibers improves the wear resistance of carbon hybrid composite.
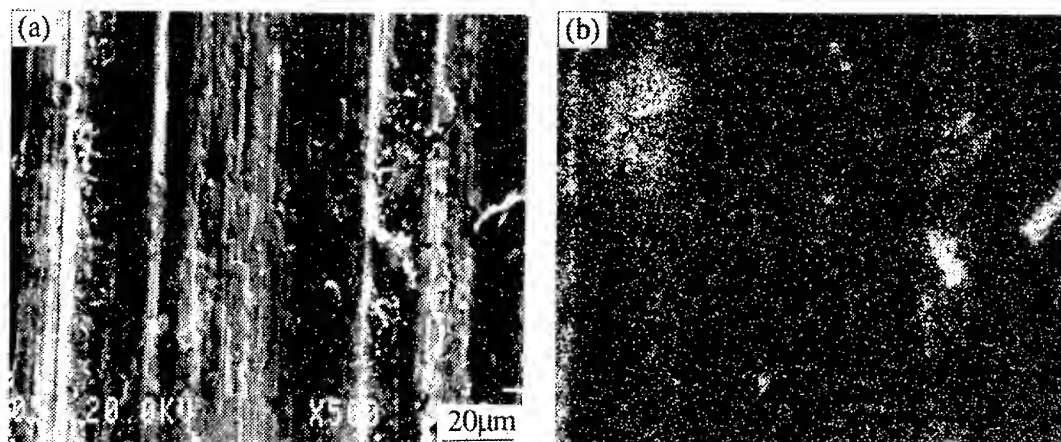
Fig. 5 Micrographs of Al/Al$_2$O$_3$/C composites at sliding speed of 1.97 m/sec
: a) wear surface and b) carbon distribution by EMPA

499

CONCLUSIONS

Effects of carbon fibers on wear behavior in Al/Al$_2$O$_3$/C hybrid composites fabricated by a squeeze infiltration method was studied. The wear resistance of Al/Al$_2$O$_3$/C composites was remarkably improved over Al/Al$_2$O$_3$ composites by adding carbon fibers to Al/Al$_2$O$_3$/C composites. At the intermediate sliding speed of 1.14m/sec to 1.97m/sec, the wear resistance of Al/Al$_2$O$_3$/C composites containing 8 vol.% carbon fiber was found to be better than that of the rest of carbon hybrid composite, but amounts of carbon volume fraction were of little effect on wear resistance at high sliding speed of 3.62m/sec.

From fractographic studies, At intermediate sliding speeds damaged sections in wear surfaces of hybrid composites were seldom observed. The solid lubrication film formed as a result of adding carbon fibers improved the wear resistance of carbon hybrid composites because this film reduced the high friction force between MMCs and counter material. At high sliding speed, localized melt and slip and large plastic deformations due to the high frictional heat are the dominant factors contributing to the removal of MMCs.

ACKNOWLEDGMENT

REFERENCES

[1] Amateau, M.F. " Progress in the Development of Graphite - Aluminum Composites Using Liquid Infiltration Technology", *J. Comp. Mat.* 10, pp. 279 - 296(1976)

[2] Das, S. and Prasad, S. V. " Microstructure and Wear of Cast (Al- Si Alloy) - Graphite Composites", *Wear* 133 , pp.173 - 187(1989)

[3] Towata, S., Yamada, S., and Ohwaki, S. "Strength and Interfacial Reaction of High Modulus Carbon Fiber Reinforced Aluminum Matrix", *Transactions of the Japan Institute of Methods* 26(8), pp. 563 - 570(1985)

[4] Das, S. , Prasad, S. V. and Rohatgi, P.K. "Modification and Refinement of Silicon in Cast Al-Si-Graphite Particle Composites", *Proceeding of International Symposium on Advances Cast Reinforced Metal Composites*, pp. 243 - 248(1988)

[5] Liu, X.C. and Bathias, C. "Defects in Squeeze-Cast Al$_2$O$_3$/Al Alloy Composites and Their Effects on Mechanical Properties," *Composites Science and Technology*, 46, pp. 245-252(1993)

[6] Lee, C.S., Kim, Y.H., Han, K.S. and Lim, T. "Wear Behavior of Aluminium Matrix Composite Materials", J. of Materials Science, 27, pp. 793 - 800(1992)

[7] Prasad, S. V. and Mecklenburg, K.R., " Friction Behavior of Ceramic fiber - Reinforced Aluminum Metal-Matrix Composites against a 440C steel counterface", *Wear*, 162-164 , pp. 47 - 56(1993)

[8] Prasad, S. V. and McConnell, B. D. " Tribology of Aluminum Metal-Matrix

Composites: Lubrication by Graphite" , *Wear* 149, pp. 241 - 253(1991)

[9] Das, S. , Prasad, S. V. and Ramachandran, T.R. " Tribology of Al - Si alloy Composites : Triboinduced Graphite Films and the Silicon Morphology", *Materials Science and Engineering* A138 , pp.123 - 132(1993)

[10] Rohatgi, P.K., Dahotre, N.B., Liu,Y. and Barr,T.L. "Tribological Behavior of Alloy Graphite and Al Alloy Microcrystalline Carbon Particle Composites", *Proceeding of International Symposium on Advances Cast Reinforced Metal Composites*, pp. 367 - 373(1988)

[11] Data Sheet from Japanese Industrial Standards (JIS) H 5303

[12] Data Sheet from ICI Co.

[13] Data Sheet from Kureha Co.

X-RAY DIFFRACTION INVESTIGATIONS OF TRANSCRYSTALLINITY IN POLYETHYLENE AND NYLON MATRIX COMPOSITES

by

Theodor Stern, Nava Klein and Gad Marom

Casali Institute of Applied Chemistry
The Hebrew University of Jerusalem
91904 Jerusalem, Israel

INTRODUCTION

Many semicrystalline thermoplastic composites exhibit transcrystalline layers due to the fact that the surfaces of the reinforcing fibres provide ample nucleation sites which enhance the rates of nucleation and crystallization of the matrix. As a result, a thick and uniform transcrystalline layer grows directly on the fibre surface in those composites. The existence of the transcrystalline layer influences the fibre dominated longitudinal properties of the composite material to an extent which cannot be accounted for by a simple 'rule-of-mixtures'. The suggested explanation, based on a series of studies aiming to link the mechanical performance to the microstructure, attributes the effect of the transcrystalline layer to a preferred crystallite orientation relative to the fibre, thereby conferring to the matrix in the fibre direction higher rigidity and reduced thermal expansion, which in turn lower the residual thermal stresses [1-5].

The properties of the transcrystalline layer, when compared with those of the matrix, reflect a higher degree of order, which would result from a more compact crystal packing and possibly from a preferred crystalline alignment. The crystalline alignment may be characterized by a particular distribution in orientation of the c-axes of the crystallites. On the molecular level, since the c-axis is parallel to the chain axis of the polymer, the physical and mechanical properties in this direction reflect the covalent nature of the polymer chain, while the properties in the perpendicular directions, along the a- and b-axes, reflect weaker intermolecular interactions (van-der-Waals and hydrogen-bonding). For both reasons, it is expected that the orientation distribution of the polymer chains in the transcrystalline layer will

503

determine the nature and extent of its effect on the properties of the composite material.

The objectives of this study were to determine the crystalline structure and its orientation relative to the fibre axis in transcrystalline layers of different composite materials. For this, x-ray diffraction analyses of isolated transcrystalline layers and of microcomposites of nylon 66 and high density polyethylene matrix composites were performed.

EXPERIMENTAL

X-ray diffraction measurements were performed on microcomposites and transcrystalline strips whose preparation techniques are described elsewhere [6,7]. X-ray diffraction patterns were obtained on imaging plates (Fuji) using a Searle camera equipped with Franks optics affixed to an Elliott GX6 rotating anode generator operating at 1.2 kW and producing Cu radiation with a 200 μm focus. The strip and microcomposite specimens were positioned vertically and the x-ray beam was directed at right angles to the plane of the film. Typical exposure times were on the order of 1 hour. The imaging plates were scanned with a He-Ne laser (Spectra Physics) in conjunction with a home made reader based on an Optronics (Chemsford, Mass.) densitometer and interfaced to an Apollo DS3500 workstation (Hewlett Packard). Images were also processed on a Power Macintosh personal computer using the public domain NIH Image program (written by Wayne Rasband at the U.S. National Institutes of Health and available from the Internet by anonymous ftp from zippy.nimh.nih.gov).

RESULTS AND DISCUSSION

An example of the transcrystallinity grown and analyzed in microcomposites is shown in Figure 1. The study pertains to the microstructural organization of transcrystalline layers of three origins, namely, nylon 66 layers grown on aramid and pitch based carbon fibres and polyethylene layers grown on polyethylene fibres.
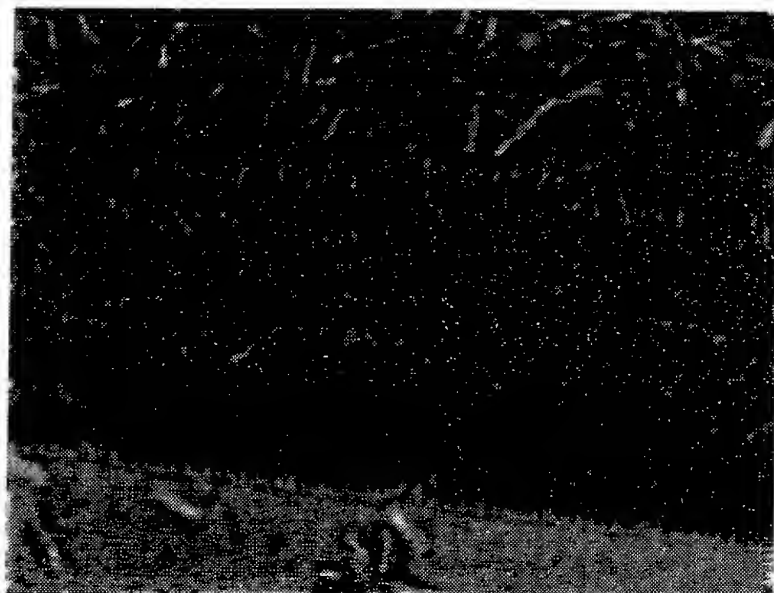
Fig. 1 Transcrystallinity in polyethylene fibre reinforced polyethylene microcomposites

The experimental data are given in detail elsewhere [6,7] and will not be repeated here. In general, however, each data set expresses some preferential alignment of the crystallites in the transcrystalline layer formed in the presence of the fibre, in contrast to the lack of such alignment in the bulk matrix. The preferential alignment is manifested by a dominant orientation of the c-axis of the polymer chain which is determined by a weighted average of the orientation distribution.

For example, the x-ray diffraction pattern of a nylon 66 film [6] is dominated by two rings of uniform intensity (the inner ring which represents the diffraction from the (100) planes and the outer ring which represents the combined diffraction from the (010+110) planes), pointing to a crystalline microstructure which lacks any preferential alignment of the crystallites. In contrast, in the presence of transcrystallinity the x-ray diffraction pattern of a microcomposite sample of carbon fibre-reinforced nylon 66 exhibits two broad arcs centered on the equator and associated with the (100) reflection of nylon 66 and two additional arcs appear on the meridian at the position of the (010+110) doublet. These arcs (in contrast to the uniform circles) are an indication that the addition of carbon fibres results in some preferential alignment of the nylon crystallites, in contrast to the lack of such alignment in the bulk matrix.

The actual results in terms of the orientation with respect to the fibre axis of the c-axis of the polymer chain in the transcrystalline layer, in all the cases studied here, show that the weighted average orientation is not parallel to the fibre axis. Clearly for the carbon fibre-reinforced nylon, and most probably for the aramid fibre-reinforced nylon, the polymer chain in the transcrystalline layer is aligned mostly at right angle to the fibre [6]. In the polyethylene - polyethylene composite a geometrical model of the microcomposite is proposed, which predicts satisfactorily the spatial distribution of the orientation, whereby the crystallites in the transcrystalline layer are oriented such that the a-axis is inclined about 39° to the fibre axis, the b-axis is directed radially outwards from the fibre surface and the direction of the c-axis is determined consequently [7].

Those results do not support the hypothesis [8], based on the expectation of epitaxial crystallization, that the c-axes of the crystallites are oriented parallel to the fibre axis throughout the thickness of the tc layer. In fact, the experimental results are compatible with the reported observations [9] that only the first laminae which nucleate on the fibre surface are oriented parallel to the fibre due to epitaxial crystallization, while most of the grown crystallite is oriented differently. It is therefore concluded that at the nucleation and initial growth stages the first laminae, at the fibre surface, are oriented in such a way that the a-, b- and c-axes of the constituent crystallites are aligned in the radial, tangential and axial directions, respectively, and in the crystal growth stage that follows, a typical sheaf structure is formed leading gradually to spherulite formation as in bulk crystallization. In the polyethylene it is proposed that the lamellar crystallites twist as the crystal grows in length, such that the b-axis is directed radially from the fibre surface while the a- and c-axes rotate in a plan which is approximately normal to the growth direction.

According to the above model, the concentration of the first laminae which nucleate on the fibre surface will be too small to be identified in the x-ray diffraction pattern. That pattern is dominated by a weighted average orientation, namely, by a maximum material volume of specific orientation. The weighted average orientation is determined by geometrical factors such as the fibre volume fraction and the density of nucleation sites on the fibre surface. These factors limit the transcrystalline growth which

determines both the orientation and the associated volume of crystalline material.

CONCLUSIONS

X-ray diffraction analysis performed on three types of transcrystalline layers in microcomposites reveals preferential orientation of the polymer chain with respect to the fibre axis. In contrast to the expectation, most of the crystallites are unparallel to the fibre axis, so that their c-axes (the direction of the polymer chain) are inclined at specific angles relative to the fibre axis. The specific orientation in each case is a consequence of the crystal growth mechanism, which results in an orientation distribution, and of geometrical factors, such as the distance between the fibres and the appearance of bulk crystallinity in the matrix, which limit the size of the transcrystalline layer and which thereby determine the weighted average orientation.

REFERENCES

[1]   Teishev, A. and Marom, G. "The effect of transcrystallinity on the transverse mechanical properties of single polymer polyethylene composites" *J. Appl. Polym. Sci.* **56**, pp. 959-966 (1995).

[2]   Klein, N., Selivansky, D. and Marom, G. "The effects of a nucleating agent and of fibers on the crystallization of nylon 66 matrices" *Polymer Composites* **16**, pp. 189-198 (1995).

[3]   Klein, N., Pegoretti, A., Migliaresi C. and Marom, G. "Determining the role of interfacial transcrystallinity in composite materials by dynamic mechanical thermal analysis" *Composites* **26**, pp. 707-712 (1995).

[4]   Wood, J.R., Wagner, H.D. and Marom, G. "Transcrystallinity in polycarbonate-carbon fibre microcomposites: The key to the mechanical role of the interphase" *J. Mater. Sci. Lett.* **14**, pp. 1613-1615 (1995).

[5]   Klein, N. and Marom, G. "Thermal expansion of transcrystalline strips" *Advanced Composites Letters* **4**, pp. 9-11 (1995).

[6]   Klein, N., Wachtel, E. and Marom, G. "The microstructure of nylon 66 transcrystalline layers in carbon and aramid fibre reinforced composites" *Polymer* submitted for publication.

[7]   Stern, T., Wachtel, E. and Marom, G. "Origin, morphology and crystallography of transcrystallinity in polyethylene-based single-polymer composites" *Composites* submitted for publication

[8]   Chen, E. J.-H. and Hsiao, S.J. "The effect of transcrystalline interphase in advanced polymer composites"*Poly.Eng. Sci.* **32**, pp. 280-286 (1992).

[9]   Wang, W., Qi, Z. and Jeronimidis, G. "Studies on interface and crystal texture of poly(ether-ether-ketone) carbon fibre composite" *J. Mater. Sci.* **26**, pp. 5915-5920 (1991).

ANALYSIS OF THE IN-PLANE PROPERTIES OF HYBRID GLASS/CARBON WOVEN FABRIC COMPOSITES

R.W. Stewart, V.E. Verijenko and S. Adali

Department of Mechanical Engineering, University of Natal, Durban, South Africa

INTRODUCTION

Woven fabric composites are of interest in various branches of engineering for several reasons. They are commonly used in industry to manufacture composite components due to their ease of use. They provide better resistance to impact than unidirectional composites and display behaviour that is closer to fully isotropic. Although the plain weave studied here is the simplest form of a woven fabric structure and does not have the isotropy displayed by more complex tri-axial weave patterns [1], [2], the theory presented here can be extended to model these more complex patterns.

Carbon fibre composites are known to have a high stiffness to weight ratio [3]. They do, however, have little resistance to impact and are expensive. Glass fibre composites are cheaper, although not as stiff or light-weight. In the study presented here, a satin weave consisting of glass fibres running in the warp direction and carbon fibres running in the fill direction is considered. This case is chosen because it allows the differences in application of pure carbon or glass weaves to be illustrated. The benefits of a hybrid weave can then also be highlighted.
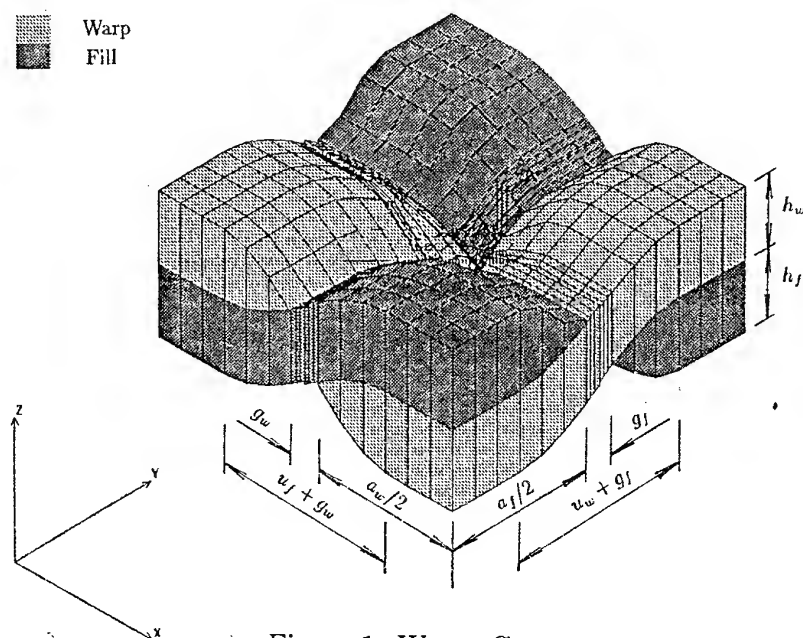
Figure 1. Weave Geometry

THEORY

The geometry relating to the weave shown in Figure 1 is as defined in [4]. The functions $hy_1(y)$, $hy_2(y)$, $hx_1(x,y)$, $hx_2(x,y)$, $hx_3(x,y)$ are for the purposes of this investigation only considered in the range of $a_0 \to a_3$ and $b_0 \to b_3$. The overall properties of the weave can then be established with the knowledge that the in-plane properties are symmetrical about a_3 and b_3. The relevant functions are then:

$$hy_1(y) \;=\; \left| \begin{array}{ll} h_t/2 - h_f & \ldots b_0 \le y \le b_1 \\ \left\{1 + sin[(y - b_3) \times \frac{\pi}{u_w + g_f}]\right\} h_f/2 + h_t/2 & \\ -h_f & \ldots b_1 \le y \le b_3 \end{array} \right. \tag{1}$$

$$hy_2(y) \;=\; \left| \begin{array}{ll} h_t/2 & \ldots b_0 \le y \le b_1 \\ (h_t/2 - hy_1(b_2))cos((y - b_1)\frac{\pi}{u_w}) + hy_1(b_2) & \ldots b_1 \le y \le b_2 \end{array} \right. \tag{2}$$

$$hx_1(x,y) \;=\; \left| \begin{array}{ll} hy_1(y) & \ldots a_0 \le x \le a_1 \\ \left\{1 - sin[(x - a_3)\frac{\pi}{u_f + g_w}]\right\}[\frac{hy_2(y)+hy_1(y)}{2}] & \\ -hy_1(y) & \ldots a_1 \le x \le a_3 \end{array} \right. \tag{3}$$

$$hx_2(x,y) \;=\; \left| \begin{array}{ll} hy_1(y) - h_w & \ldots a_0 \le x \le a_1 \\ [h_w - hy_1(y) - hx_1(a_4,y)]cos((x - a_5)\frac{\pi}{u_f}) & \\ -hx_1(a_4,y) & \ldots a_1 \le x \le a_3 \end{array} \right. \tag{4}$$

$$hx_3(x,y) \;=\; hx_1(x,y) + hy_2(y) - hy_1(y) \tag{5}$$

$$\theta_w(y) \;=\; tan^{-1}\left\{h_f/2\frac{\pi}{u_w + g_f}cos((y - b_3)\frac{\pi}{u_w + g_f})\right\} \tag{6}$$

$$\theta_f(y) \;=\; tan^{-1}\left\{\frac{hy_2(y) - h_w + hy_1(y)}{2}\frac{\pi}{u_f + g_w} \times cos[(x - a_3)\frac{\pi}{u_f + g_w}]\right\} \tag{7}$$

From [4], in the region $a_0 \le x \le a_3$, $b_0 \le y \le b_3$, the following relationship holds true:

$$[N_i] = [A_{ij}(x,y)]\left[\epsilon_j^0\right] \tag{8}$$

where N_i is the membrane stress resultant, ϵ_j^0 is the strain of the laminate mid-plane and $A_{ij}(x,y)$ is the stiffness of the laminate.

The various parameters required thus far can be determined from [5].

$$\frac{1}{E_x^F} \;=\; \frac{cos\theta_F(x,y)^4}{E_L} + \frac{sin\,\theta_F(x,y)^4}{E_T}$$
$$+[cos\theta_F(x,y)^2 sin\theta_F(x,y)^2]\left(\frac{1}{G_{LT}} - \frac{2\nu_{LT}}{E_L}\right) \tag{9}$$

$$E_y^F \;=\; E_T \tag{10}$$

$$\nu_{yx}^F \;=\; \nu_{TL}cos\theta_F(x,y)^2 + \nu_{TT}sin\theta_F(x,y)^2 \tag{11}$$

510

$$\frac{1}{G_{xy}^F} = \left\{ \frac{sin\theta_F(x,y)^2}{G_{TT}} + \frac{cos\theta_F(x,y)^2}{G_{LT}} \right\} \tag{12}$$

$$\frac{1}{E_y^W} = \frac{cos\theta_W(y)^4}{E_L} + \frac{sin\,\theta_W(y)^4}{E_T}$$

$$+[cos\theta_W(y)^2 sin\theta_W(y)^2]\left(\frac{1}{G_{LT}} - \frac{2\nu_{LT}}{E_L} \right) \tag{13}$$

$$E_x^W = E_T \tag{14}$$

$$\nu_{yx}^W = \nu_{TL}cos\theta_W(y)^2 + \nu_{TT}sin\theta_W(y)^2 \tag{15}$$

$$\frac{1}{G_{xy}^W} = \left\{ \frac{sin\theta_W(y)^2}{G_{TT}} + \frac{cos\theta_W(y)^2}{G_{LT}} \right\} \tag{16}$$

From Figure 1, it can be seen that A_{ij} can be rewritten in the following form for the region $a_0 \le x \le a_3,\ b_0 \le y \le b_3$:

$$A_{ij} = \int_{-h/2}^{hx_3(x,y)} Q_{ij}^M dz + \int_{hx_3(x,y)}^{hx_1(x,y)} Q_{ij}^F dz$$

$$+ \int_{hx_1(x,y)}^{hx_2(x,y)} Q_{ij}^W dz + \int_{hx_2}^{h/2} Q_{ij}^M dz \tag{17}$$

$$= Q_{ij}^M[hx_3(x,y) + h - hx_2(x,y)]$$

$$+ Q_{ij}^W(x,y)[hx_2(x,y) - hx_1(x,y)]$$

$$+ Q_{ij}^F[hx_1(x,y) - hx_3(x,y)] \tag{18}$$

Of the various schemes presented in [4], the one which gave predictions of material values consistent with experimental results in most cases was the parallel-series scheme. The scheme involves firstly the averaging of material properties through each of the infinitesimal pieces which are in parallel with each other with respect to the loading direction. This means averaging each section in the y-direction first if the loading direction is the x-direction. Next each of the sections is averaged in the x-direction. These sections are in series with each other with respect to the loading direction. The scheme can be summarised in the following formulae:

$$\overline{A}_{ij}^p(x) = \frac{1}{a_f + g_f} \int_0^{a_f+g_f} A_{ij}(x,y)dy \tag{19}$$

$$\overline{a}_{ij}^{ps} = \frac{1}{a_w + g_w} \int_0^{a_w+g_w} \overline{a}_{ij}^p(x)dx \tag{20}$$

Where the compliance matrix a is the inverse of the stiffness matrix A. The various in-plane material parameters are then found from:

$$E_x = \frac{1}{\overline{a}_{11}h} \ ; \quad G_{xy} = \frac{1}{\overline{a}_{66}h} \ ; \quad \nu_{xy} = \frac{\overline{a}_{12}}{\overline{a}_{11}} \tag{21}$$

MODEL DETAILS

Material properties for carbon, glass and the matrix are assumed to be as in Table 1

Input parameters for the model were as follows:

$$u/a = 0.6 \; ; \; g/a = 0.01 \; ; \; V_f = 0.6 \; ; \; h_f = h_w = h/2$$

With these parameters fixed, h/a can be varied without influencing the overall fibre volume content. This was kept at a constant value of $V_{overall} = 0.47$. This was useful in determining the effect of the thickness alone on the various material parameters.

E_y was found by swapping the material properties for glass and carbon in the model, thereby effectively changing the loading angle by $90°$.

The off-axis material properties should ideally be determined by first finding the manner in which the forces are distributed amongst the various fibres under a given load. This has been done previously [2] for weaves of very simple geometry. However, this technique is more suited to a finite element analysis of a unit cell of the weave structure. In practice such an analysis was too time-consuming for a practical determination of material properties for each thickness and load direction. It may prove useful, however, for comparison purposes.

Instead, standard transformations [6] were used to obtain the equivalent material parameters for other loading directions. These transformation equations have been used extensively in other texts, too numerous to mention, and the results appear to be quite adequate.

RESULTS AND DISCUSSION

It can be seen from Figures 2 to 4 that the various stiffness parameters E_x, E_y and G_{xy} generally increase as the thickness of the laminate (h/a) is reduced. It will be noted that this effect is most pronounced in E_x when $\theta = 0°$ and in E_y when $\theta = 90°$. These directions conform to the case when the loading direction is parallel to the carbon fibre reinforcement. It will be seen from the case when the loading direction is parallel to the glass reinforcement that the thickness does not affect the stiffness to the same extent. The carbon reinforcement has a higher stiffness for any given

Table 1: Constituent Material Properties

	Carbon	Glass	Matrix
E_L	$230\,GPa$	$72\,GPa$	$3.5\,GPa$
E_T	$40\,GPa$	$72\,GPa$	$3.5\,GPa$
G_{LT}	$14.3\,GPa$	$27.7\,GPa$	$1.3\,GPa$
ν_{lt}	0.26	0.3	0.35

thickness ratio, but is far more critical in achieving the maximum values. Several deductions are possible from this. Firstly, carbon fibre woven fabric reinforcement should only be used in thin layers to achieve maximum stiffness. This would suggest that the stiffness achieved from say a pre-impregnated layup would be superior to that of a hand layup of identical fibre volume content. On the other hand, there would be little advantage in using a pre-impregnated layup for a glass structure.

As the loading angle is varied for each of the three cases, it is seen that the stiffness parameters E_x and E_y generally decrease to a minimum at 45°. There is very little change in these parameters as the thickness is varied while holding the loading angle at around 45°. However, the modulus G_{xy} has a great variation as the thickness is varied while the loading angle is 45°. The peak rigidity is achieved when the thickness is a minimum. This effect is undoubtedly due to the influence of the carbon fibres, since there is little influence from the glass fibres. It can be seen that G_{xy} does not vary much with a change in thickness if the loading angle is 0° or 90°. This phenomenon can be closely tied to a similar behaviour of E_x and E_y at a load angle of 45°. Glass fibres have a higher rigidity than carbon fibres, which gives the composite a slightly higher stiffness (E_x, E_y) at a load angle of 45° than a pure carbon weave.

The Poisson Ratio is very small at load angles of around 0° and increases to over 0.5 for a load angle of 45°. This behaviour is consistent with a physical interpretation of the deformation of the weave structure. If the weave is loaded parallel to one of the fibre directions, the perpendicular strain will be resisted by the perpendicular fibre. Thus the Poisson Ratio must be small. However, if the fibres are loaded at a load angle of 45°, there is almost as much perpendicular deformation as parallel deformation and the Poisson Ratio is thus high.

CONCLUSIONS

The hybrid weave benefits from the best properties of carbon and glass in much the same way as a regular composite benefits from fibre reinforcement. Carbon provides improved stiffness but is sensitive to thickness, where the glass is not. Glass also has higher modulus of rigidity which improves the off-axis performance of the weave. The Poisson ratio is high at an off-axis load due to the inherent nature of the satin weave.

REFERENCES

[1] Fujita A, Hamada H, Maekawa Z, "Tensile Properties of Carbon Fibre Triaxial Woven fabric Composites." *Journal of Composite Materials* **27**, No. 15 (1993).

[2] R.W. Stewart, V.E. Verijenko, S. Adali, "Application of the Finite Element Method to Calculation of Strength for Woven Fabric Composites." *Finite Element Methods in South Africa 95* (1995).

[3] Applications Guide for Kevlar and Nomex. *Du Pont*, pp 4.1-4.17

[4] Naik, N.K. "Woven Fabric Composites." *Technomic*, pp 5-81 (1994).

[5] Leknitskii, S.G. "Theory of Elasticity of an Anisotropic Body." *MIR Publishers*, (1981)

[6] Jones, R.M. "Mechanics of Composite Materials." *McGraw-Hill* (1975).
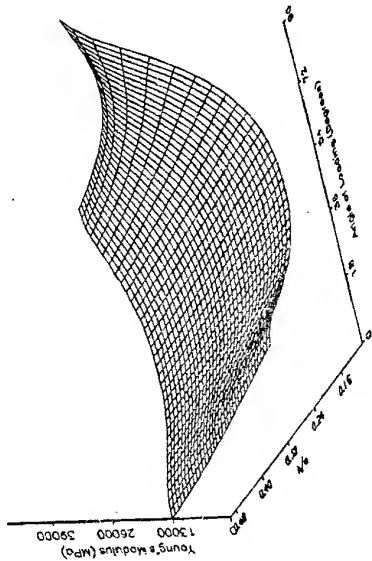
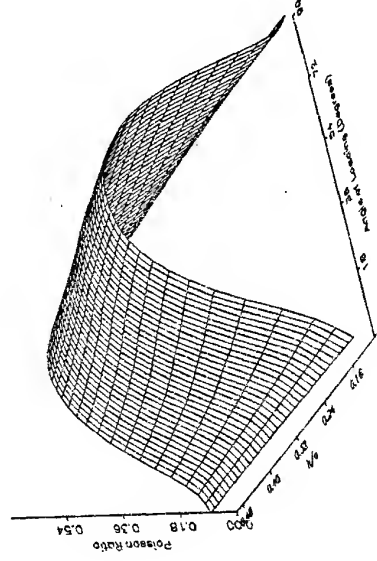Figure 3. Y-Direction Young's Modulus

Figure 5. Poisson Ratio

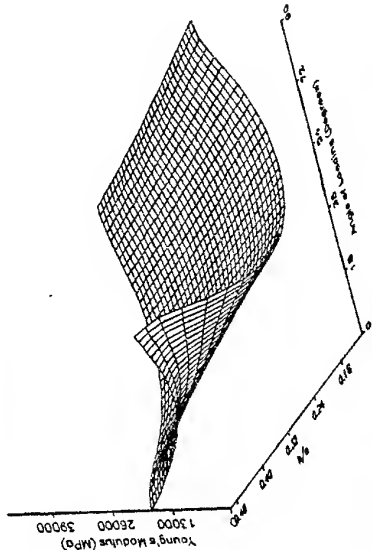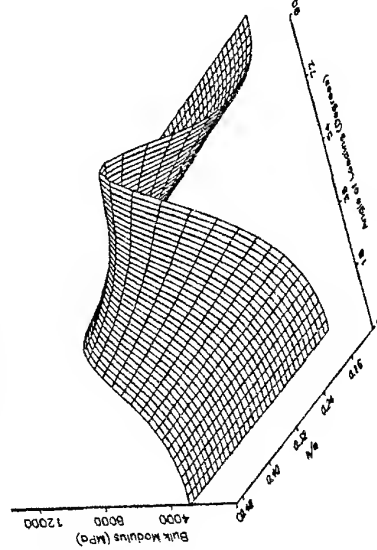Figure 2. X-Direction Young's Modulus

Figure 4. Bulk Modulus

514

TRANSIENT THERMAL STRESSES IN ORTHOTROPIC GRP TUBES

M.A. STONE

Reinforced Plastics/Composites Facility, School of Mechanical Engineering
University of the Witwatersrand, P.O. WITS, 2050, South Africa

INTRODUCTION

Glass reinforced plastics (GRPs) are extensively used for the manufacture piping designed to convey chemically aggressive fluids. In many process plant applications the fluid temperature varies as different processes are carried out. Thus it is to be expected that thermal stresses will exist and will change with time. GRPs have very low thermal diffusivity by comparison to most metals. Hence, in the case of GRP piping, relatively large temperature differences can be expected between the inner and outer walls even at thermal equilibrium. The time taken to reach equilibrium will also be greater in GRP pipes. Moreover, the coefficients of thermal expansion of GRPs are typically larger than those of metals. Hence thermal stresses are an important consideration for GRP pipes intended for process plant applications. Some studies dealing with equilibrium thermal stresses in GRP process plant equipment have been published (see for examples [1]). Transient thermal stresses (which are generally more significant than those at equilibrium) have been considered for materials and constructions typical of aerospace applications [2], but there would appear to be limited studies focussing on process plant materials and operating conditions. The objective of this work is twofold; firstly, to develop an efficient method for the numerical approximation of transient thermal stresses in GRP tubes and secondly, to present some results for cases relevant to practical application.

SOLUTION OF THE CONDUCTION EQUATION

The primary objective of this work is to predict thermal stresses but in order to achieve this the temperature distribution must first be established, i.e. the conduction equation must be solved. This work uses the spectral method, implemented using the operational-Tau approach, to solve the conduction equation. The operational-Tau approach makes for straightforward implementation of this very powerful and accurate method. It has been extensively applied to fluid flow problems for which it has been comprehensively documented. Space does not permit a detailed discussion of the method and its implementation here but there is much information available elsewhere, e.g. [3], [4].

The differential equation for heat conduction in thick wall tubes is

$$\rho c r \frac{\partial T}{\partial t} = \frac{\partial}{\partial r}\left(k r \frac{\partial T}{\partial r}\right) \tag{1}$$

where ρ is density, c is heat capacity, r is radial position, T is temperature and k is thermal conductivity. Spectral solutions rely on the problem being specified over a particular domain on which the basis functions are orthogonal. Here we choose to work on $(-1,+1)$ hence it is useful to write the problem in terms of the transformed co-ordinates $\bar{r}$ where $\bar{r} = h r/2 + r_m$, with h being the tube wall thickness and r_m being the mean radius. The temperature at position $\bar{r}$ can be approximated by the simple polynomial series $\bar{\mathbf{r}}\,\mathbf{T}$ where $\bar{\mathbf{r}} = [\bar{r}^0 \ \ \bar{r}^1 \ \ \bar{r}^2 \ \ ... \ \ \bar{r}^N]$. This can be written in terms of an orthogonal polynomial basis $\mathbf{v}$ as $T = \mathbf{v}\hat{\mathbf{T}}$ where

$$\mathbf{v} = \bar{\mathbf{r}}\,\mathbf{P} \quad \text{and} \quad \hat{\mathbf{T}} = \mathbf{P}^{-1}\mathbf{T} \tag{2}$$

with $\mathbf{P}$ describing the polynomial construction. The Legendre polynomials are used in the present study but, in principle, any polynomial set orthogonal on $(-1,+1)$ could be chosen.

The standard operator matrices, μ for multiplication by r and η for differentiation with respect

515

to r are given by

$$\mu = \begin{bmatrix} 0 \\ & 1 \\ & & 1 \\ & & & 1 \\ & & & & \ddots \end{bmatrix} \quad \text{and} \quad \eta = \begin{bmatrix} 0 & 1 \\ & & 2 \\ & & & 3 \\ & & & & \ddots \end{bmatrix} \tag{3}$$

In order to arrive at equations in terms of $\bar{r}$ one uses $\bar{\mu} = h/2\,\mu + r_m I$ for multiplication by r and $\bar{\eta} = 2/h\,\eta$ for differentiation with respect to r. To write equations in terms of the transformed basis v the matrices $\hat{\eta} = P^{-1}\bar{\eta}P$ and $\hat{\eta} = P^{-1}\bar{\mu}P$ are used. Following the standard operational-Tau approach, writing the differential equation (where the material properties are assumed to be assumed to be independent of r and T) in terms of v one obtains

$$\rho c\, v\hat{\mu}\hat{T}' = k\, v\, \hat{\eta}\hat{\mu}\hat{\eta}\hat{T} \quad \Rightarrow \quad \hat{T}' = \alpha\hat{\mu}^{-1}\hat{\eta}\hat{\mu}\hat{\eta}\hat{T} \quad \Rightarrow \quad \hat{T}' = \alpha A\hat{T} \tag{4}$$

where $\alpha = k/\rho/c$ and $A = \hat{\mu}^{-1}\hat{\eta}\hat{\mu}\hat{\eta}$. This equation cannot be solved uniquely before the boundary conditions have been introduced. Considering convective heat transfer at the inner and outer walls, the boundary conditions can be expressed as

$$k\frac{\partial T_{r=r_i}}{\partial r} = h_i(T_{r=r_i} - T_f) \quad \text{and} \quad k\frac{\partial T_{r=r_o}}{\partial r} = h_o(T_a - T_{r=r_o}) \tag{5}$$

Where h_i and h_o are the coefficients of convection for the inner and outer surfaces of the tube and T_f and T_a the internal fluid and external air temperatures respectively. Defining v_i and v_o as v evaluated at $r = r_i$ and $r = r_o$ respectively, the boundary conditions can be expressed in operator notation as

$$\begin{bmatrix} v_i(-k\hat{\eta} + h_i I) \\ v_o(k\hat{\eta} + h_o I) \end{bmatrix}\hat{T} = \begin{bmatrix} h_i T_f \\ h_o T_a \end{bmatrix} \tag{6}$$

Now letting

$$\hat{T} = \begin{bmatrix} \hat{T}_a \\ \hat{T}_b \end{bmatrix} \tag{7}$$

where $\hat{T}_b$ consists of the last two elements of $\hat{T}$, Eqn (6) can be written as

$$a\hat{T}_a + b\hat{T}_b = c \quad \text{or} \quad \hat{T}_b = b^{-1}(c - a\hat{T}_a) \tag{8}$$

Discarding the last two rows of Eqn (4) one is left with

$$\hat{T}'_a = A_a\hat{T}_a + A_b\hat{T}_b = \left[A_a - A_b b^{-1}a\right]\hat{T}_a + A_b b^{-1}c \tag{9}$$

which is a set of ordinary differential equations in terms of the elements of $\hat{T}_a$. Solutions are readily obtained by a range of available techniques, e.g. Runge-Kutta. Having solved for $\hat{T}_a$, $\hat{T}_b$ is given by Eqn (8) and the temperature distribution by $T = v\hat{T}$.

SOLUTION OF THE THERMOELASTIC EQUILIBRIUM EQUATION

The equilibrium equation, written in terms of stresses, is

$$r\sigma_{r,r} + \sigma_r - \sigma_\theta = 0 \tag{10}$$

where θ refers to the tangential (hoop) direction. In the case of long orthotropic tubes whose temperature does not vary around the circumference, the stress-strain relationship reduces to

$$\begin{bmatrix} \sigma_x \\ \sigma_\theta \\ \sigma_r \end{bmatrix} = C \begin{bmatrix} u_{,x} - \alpha_x T \\ w/r - \alpha_\theta T \\ w_{,r} - \alpha_r T \end{bmatrix} \tag{11}$$

516

where x refers to the axial direction, u is axial displacement, w is radial displacement, α refers to coefficient of thermal expansion, T is the temperature change from the stress free temperature and C is the elastic stiffness matrix. The differential equation can therefore be written in terms of the displacements as

$$rC_{13}(u_{,xr} - \alpha_x T_{,r}) + rC_{23}\left(\frac{\partial}{\partial r}\left(\frac{w}{r}\right) - \alpha_\theta T_{,r}\right) + rC_{33}(w_{,rr} - \alpha_r T_{,r})$$

$$+C_{13}(u_{,x} - \alpha_x T) + C_{23}\left(\frac{w}{r} - \alpha_\theta T\right) + C_{33}(w_{,r} - \alpha_r T)$$

$$+C_{12}(\alpha_x T - u_{,x}) + C_{22}\left(\alpha_\theta T - \frac{w}{r}\right) + C_{23}(\alpha_r T - w_{,r}) = 0 \qquad (12)$$

Given that the tube is relatively long, i.e. there is no local bending of the wall, $u_{,xr} = 0$. Performing the differentiation appearing in the second term and multiplying throughout by r the above becomes

$$C_{33}(r^2 w_{,rr} + r w_{,r}) - C_{22}w - r^2\left(C_{13}\alpha_x + C_{23}\alpha_\theta + C_{33}\alpha_r\right)T_{,r} + r(C_{13} - C_{12})u_{,x}$$
$$+r\left[(C_{12} - C_{13})\alpha_x + (C_{22} - C_{23})\alpha_\theta + (C_{23} - C_{33})\alpha_r\right]T = 0 \qquad (13)$$

Letting $w = \mathbf{v}\hat{\mathbf{W}}$, $u_{,x} = \mathbf{v}\hat{\mathbf{U}}$ and knowing $T = \mathbf{v}\hat{\mathbf{T}}$ the differential equation can be written in operator form as

$$\mathbf{v}\left\{\left[\left(\hat{\mu}^2\hat{\eta}^2 + \hat{\mu}\hat{\eta}\right)C_{33} - IC_{22}\right]\hat{\mathbf{W}} + \hat{\mu}(C_{13} - C_{12})\hat{\mathbf{U}} + \left[-\hat{\mu}^2\hat{\eta}\left(C_{13}\alpha_x + C_{23}\alpha_\theta + C_{33}\alpha_r\right)\right.\right.$$
$$\left.\left.+\hat{\mu}\left((C_{12} - C_{13})\alpha_x + (C_{22} - C_{23})\alpha_\theta + (C_{23} - C_{33})\alpha_r\right)\right]\right\}\hat{\mathbf{T}} = 0 \qquad (14)$$

Eqn (14) can be written as

$$\mathcal{A}\hat{\mathbf{W}} + \mathcal{B}\hat{\mathbf{U}} + \mathcal{C}\hat{\mathbf{T}} = \mathbf{0} \qquad (15)$$

The boundary conditions are that the radial stresses are zero at both of the wall surfaces, i.e. $\sigma_r = 0$ at $r = r_i$, r_o. This can be expressed as

$$C_{13}r(u_{,x} - \alpha_x T) + C_{23}(w - r\alpha_\theta T) + C_{33}r(w_{,r} - \alpha_r T) = 0 \quad \text{at} \quad r = r_i, \ r_o \qquad (16)$$

or, in operator notation, as

$$\begin{bmatrix} \mathbf{v}_i \\ \mathbf{v}_o \end{bmatrix}\left[(C_{23}I + C_{33}\hat{\mu}\hat{\eta})\hat{\mathbf{W}} + C_{13}\hat{\mu}\hat{\mathbf{U}} - \hat{\mu}(C_{13}\alpha_x + C_{23}\alpha_\theta + C_{33}\alpha_r)\hat{\mathbf{T}}\right] = \mathbf{0} \qquad (17)$$

It is convenient to write the above in the same form as Eqn (15), i.e.

$$a\hat{\mathbf{W}} + b\hat{\mathbf{U}} + c\hat{\mathbf{T}} = \mathbf{0} \qquad (18)$$

A further condition is that the net axial force must be zero, i.e.

$$\int_{r_i}^{r_o} r\sigma_x \, dr = 0 \quad \Rightarrow \quad \int_{r_i}^{r_o} C_{11}r(u_{,x} - \alpha_x T) + C_{12}(w - r\alpha_\theta T) + C_{13}r(w_{,r} - \alpha_r T) \, dr = 0 \qquad (19)$$

or, expressed in operator notation

$$\int_{-1}^{1} \mathbf{v} \, d\bar{r}\left[C_{11}\hat{\mu}\hat{\mathbf{U}} + (C_{12}I + C_{13}\hat{\mu}\hat{\eta})\hat{\mathbf{W}} - \hat{\mu}\left(C_{11}\alpha_x + C_{12}\alpha_\theta + C_{13}\alpha_r\right)\hat{\mathbf{T}}\right]$$

$$= \phi\left[C_{11}\hat{\mu}\hat{\mathbf{U}} + (C_{12}I + C_{13}\hat{\mu}\hat{\eta})\hat{\mathbf{W}} - \hat{\mu}\left(C_{11}\alpha_x + C_{12}\alpha_\theta + C_{13}\alpha_r\right)\hat{\mathbf{T}}\right] = \mathbf{0} \qquad (20)$$

where ϕ is the matrix for integration, i.e. $\phi = 2 \begin{bmatrix} 1 & 0 & \frac{1}{3} & 0 & \frac{1}{5} & \cdots \end{bmatrix} P$. Since one knows that $\hat{U}_0$ is the only non-zero entry in $\hat{U}$ one can write $\hat{U}$ as a function of $\hat{W}$ and $\hat{T}$, i.e. $\hat{U} = u_w \hat{W} + u_t \hat{T}$. Substituting this into Eqns (15) and (18) one obtains

$$[\mathcal{A} + \mathcal{B} u_w] \hat{W} = -[\mathcal{C} + \mathcal{B} u_t] \hat{T} \tag{21}$$

$$[a + b u_w] \hat{W} = -[c + b u_t] \hat{T} \tag{22}$$

Following the operational procedure the last two rows of Eqn (21) are replaced by Eqn (22) to yield $\hat{\mathcal{A}} \hat{W} = \hat{\mathcal{C}} \hat{T}$ which can be solved directly for $\hat{W}$.

The preceeding description of the method applies to tubes in which the material remains the same throughout the wall thickness. Application to tubes consisting of segments of different material follows along similar lines, with a set of equations being written for each segment. Solutions are obtained after enforcing thermal, geometric and radial stress compatibly at interfaces.

RESULTS

Significant transient thermal stresses are induced under conditions of "thermal shock" where the material is either suddenly heated or suddenly cooled. In process applications these conditions occur when a pipe at ambient temperature is rapidly filled with hot liquor which is then conveyed for a long period before cool (ambient temperature) liquor is suddenly introduced and conveyed for a further long period. Results are presented herein for the above situation where the tube is taken to be stress free at the ambient temperature and the hot liquor is taken to be 80°C above ambient. This operating condition is close to the worst case that the process designer might allow for when using currently available GRP materials (for which operation above 100°C is seldom recommended in corrosive environments). Two different tube reinforcement constructions are considered, namely tubes made entirely from E-glass chopped strand mat (CSM) and and tubes made using a thin CSM chemical barrier overlaid with E-glass filament wound (FW) layers at angles $+$ and $-\theta$ to the tube axis.

The properties used for the materials are shown in Table 1. Note that for the filament windings the properties shown are for the unidirectional $\theta = 0°$ case and this data is used in calculating properties for laminates for which $\theta \neq 0°$. The convection coefficients for the inside and outside

Table 1: Properties used for CSM and FW materials

	E_x GPa	E_θ GPa	E_r GPa	$\nu_{x\theta}$	ν_{xr}	ν_{tr}	α_x $\mu\epsilon$/K	α_θ $\mu\epsilon$/K	α_r $\mu\epsilon$/K	k W/m/K	c J/kg/K	ρ kg/m³
CSM	10.78	10.78	6.03	0.32	0.34	0.34	30	30	60	0.32	2000	1500
FW	27.5	8.08	8.08	0.30	0.41	0.30	15	50	50	0.38	1800	1670

walls are taken as 2000 (in the range of what can be expected for water) and 50 W/m²/K (in the range of what can be expected for unforced air) respectively. Fig. 1 shows the levels of hoop stress at the inner wall that can be expected for CSM tubes having $r_i = 50$ mm and three different ratios of inner radius to wall thickness. The stresses are plotted against normalised time $\bar{t} = h^2 \sqrt{r_i/(4h)} / \alpha$, this time base being chosen to allow thermal equilibrium to be attained for all three tubes. The nature of the behaviour is the similar for the three tube geometries. As the hot fluid is introduced at the start of the cylce the stresses very rapidly become compressive, with the heated portion of the laminate being restrained by the cooler regions away from the inner wall which take longer to heat up. The maximum compressive stress attained is observed to be a function of wall thickness. Note that this is only the case where heating of the inner wall occurs over a finite time. When heating is intantaneous, i.e. the convective coefficient is infinite, then the peak compressive stress is the same for all geometries. As the average temperature of

the wall increases so the inner wall compressive stresses decay toward their thermal equilibrium values. The equilibrium value for the thin walled tube is observed to be much less than for the thick walled tube, this being a consequence of the bigger difference between inner wall and average laminate temperatures for the thick walled tube and the fact that differences in hoop and radial coefficients of thermal expansion play a bigger role as the ratio of wall thickness to radius increases. The equilibrium stress levels for the thicker laminate are observed to be of the order of the stress allowables defined by design codes, e.g. BS6464. This need not, however, be of concern since the stresses are compressive and hence are unlikely to be deterimental in a corrosive environment. The fluid at ambient temperature is introduced at $\tilde{t} = 1$ and the stresses
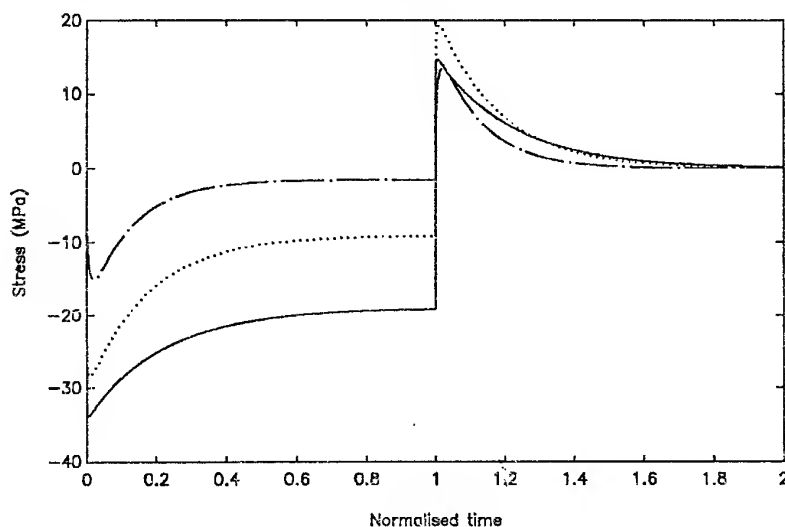
Figure 1: Inner wall stresses for CSM tubes ——$h/r_i = 0.5$ $\cdots h/r_i = 0.1$ $-\cdot-h/r_i = 0.01$

are observed to swing rapidly from compressive to tensile. The peak tensile stress is seen to be a function of geometry, however, the fact that the thinnest tube experiences the highest stress might be unexpected since the average temperature of this tube is highest at equilibrium. The behaviour observed is explained by the fact that it takes a finite time for the inner wall to reach ambient temperature. During this time the average temperature of the thin walled tube decays much faster than that of the thicker tubes, hence the peak stress attained is smaller. Note that in cases where inner wall cooling is instantaneous the highest stresses would occur in the thin walled tube.

The tensile stresses attained are, for all three geometries, observed to be large proportions of the stresses allowed for by codes of practice. Shock cooling probably represents the most severe load case for many installations and can, if repeated, lead to rapid material degradation in aggressive environments. It should therefore be considered in the design of pipework but the greatest benefits can probably be obtained through process design which avoids rapid cooling cycles.

Figs. 2 (a) and (b) show the inner wall axial and hoop stresses respectively for a tubes made with a CSM chemcial barrier overwound with layers at $+/-30°$, at $+/-45°$ and at $+/-55°$. The tubes have $r_i=50$ mm, $h_{CSM}=2$ mm, $h_{FW}=8$ mm and are subject to a similar thermal cycle to that considered for the CSM tubes. The fibre winding orientation is observed to have little effect on the peak compressive stress values which are similar for the axial and hoop directions. There is, however, stong dependence of the equilibrium stress state on θ, this being a consequence of the variation in CTE of the FW layers. The peak tensile stresses, which occur just after introduction of the cool liquor at $t = 15$ min, are also observed to be strongly dependent on θ. In practice $\theta = 55°$ is commonly used since this gives a ratio of 2 to 1 in hoop to axial strength which

matches the stress state for internal pressurisation. This construction is observed, however, to give rise to high axial stresses upon rapid internal cooling. Given that one would be unlikely to design for mechanical stresses (e.g. arising from pressure) of much more than 15 MPa in chemically demanding applications, the wisdom of choosing laminate constructions on the basis of the stress state associated with mechanical loadings alone must be questioned. It is likely that fibre orientations different from the commonly specified 55° would offer better life in applications involving thermal shock. Determining the best construction would, however, require real understanding of the mechanism of degradation by thermal stress. The ability to predict macro-level stresses is not sufficient in this regard and one would need to consider the rather more complicated micro-level stress states.
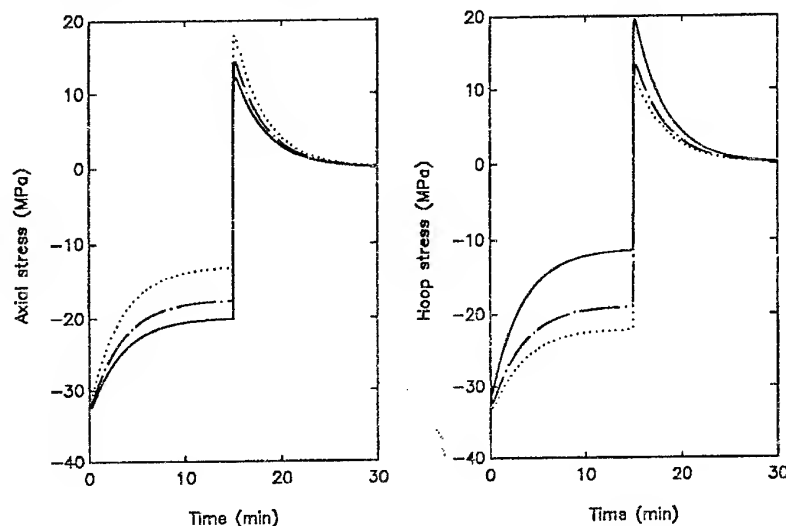
Figure 2: (a) Variation in axial stress   (b) Variation in hoop stress

$$—\theta = 30° \quad -\cdot-\theta = 45° \quad \cdots\theta = 55°$$

CONCLUSION

The spectral method, implemented using the operational-Tau approach, has been applied to obtain solutions to the heat conduction and thermoelastic equilibrium equations for thick walled orthotropic tubes. Development of the method has been outlined and its application is observed to be simple and efficient relative to other approaches. The method has been used to obtain solutions for stresses in GRP tubes subject to rapid internal heating and cooling. The geometry and laminate construction both play a major role in determining the peak thermal stresses encountered. The severest stresses are observed to occur just after rapid cooling of the interior of a tube and can easily exceed typical design allowables. These stresses can be reduced by changing geometry and laminate construction but are most effectively reduced by designing process operations to avoid rapid cooling.

REFERENCES

[1] Hoa S.V., *Analysis for design of fiber reinforced plastic vessels and pipings*, Technomic, Pennsylvania, 1991.

[2] Kardomateas G.A., 'Transient thermal stresses in cylindrically orthotropic composite tubes', *Journal of Applied Mechanics*, Vol. 56, 1989, pp 411-417.

[3] Ortiz E.L. and Samara H., 'An operational approach to the Tau method for the numerical solution of non-linear differential equations', *Computing*, Vol 27, 1981, pp 15-25.

[4] Abbot A.H., 'The transition to turbulence in strongly accelerated pipe flows', PhD Thesis, School of Mechanical Engineering, University of the Witwatersrand, 1995.

AN ASYMPTOTIC VARIATIONAL APPROACH FOR STRESS ANALYSIS OF MULTILAYERED COMPOSITE PLATES

J. Q. TARN

Department of Civil Engineering, National Cheng Kung University,
Tainan, Taiwan 70101, R.O.C.

INTRODUCTION

In several recent papers [1–4] an asymptotic theory has been developed for elasto-static and dynamic analyses of laminated plates. Three-dimensional solutions for the problems can be determined by solving equations of the classical laminated plate theory (CLT) in a systematic and hierarchic way. There is no need to consider the laminated system layer by layer nor to treat the interfacial continuity conditions in particular. While the theory is at the same level of simplicity as CLT, the CLT equations are three simultaneous partial differential equations that are very difficult to solve in general. To facilitate practical applications, it is essential to develop an associated numerical scheme capable of versatile computation. On the basis of asymptotic variational formulation, an effective and efficient computational model for interlaminar stress analysis of multilayered anisotropic plates is presented herein.

ASYMPTOTIC VARIATIONAL FORMULATION

The problem of an anisotropic heterogeneous plate of uniform thickness $2h$, having at each point one plane of elastic symmetry parallel to the middle plane, subjected to transverse loads on the lateral surfaces $x_3 = \pm h$ is considered. The formulation begins with the Hellinger–Reissner principle [5] in which the displacements and transverse stresses are taken to be the functions subject to variation. After performing the variation, integrating by parts the terms associated with $\delta u_{1,3}$, $\delta u_{2,3}$ and $\delta u_{3,3}$, then using the lateral boundary conditions, the following H–R variational functional for the problem results.

$$\delta\Pi_R = \int_{-h}^{h} \int_{\Omega} \{(L_{14}u_1 + L_{24}u_2 + c_{13}c_{33}^{-1}\sigma_{33})\delta u_{1,1} + (L_{15}u_1 + L_{25}u_2 + c_{23}c_{33}^{-1}\sigma_{33})\delta u_{2,2}$$

$$+ (L_{16}u_1 + L_{26}u_2 + c_{36}c_{33}^{-1}\sigma_{33})(\delta u_{2,1} + \delta u_{1,2}) - \sigma_{33,3}\delta u_3 + \sigma_{13}\delta u_{3,1} + \sigma_{23}\delta u_{3,2} - \sigma_{13,3}\delta u_1$$

$$- \sigma_{23,3}\delta u_2 + u_{3,3}\delta\sigma_{33} + (u_{2,3} + u_{3,2})\delta\sigma_{23} + (u_{1,3} + u_{3,1})\delta\sigma_{13} + (L_{13}u_1 + L_{23}u_2 - c_{33}^{-1}\sigma_{33})\delta\sigma_{33}$$

$$- (s_{44}\sigma_{23} + s_{45}\sigma_{13})\delta\sigma_{23} - (s_{45}\sigma_{23} + s_{55}\sigma_{13})\delta\sigma_{13}\} dx_1 dx_2 dx_3 - \int_{-h}^{h}\int_{\Gamma_\sigma} \overline{T}_i \delta u_i d\Gamma\, dx_3 = 0, \qquad (1)$$

where the subsidiary condition is the displacement boundary condition; Ω denotes the x_1-x_2 plane domain, Γ_σ the portions of the edge boundary where the traction $\overline{T_i}$ is prescribed. The differential operators L_{ij} and notations used hereafter follow the same definitions as in previous work [1–3].

To bring in a perturbation parameter in the formulation, the field variables are scaled as

$$
\begin{array}{lll}
x = x_1/l, & y = x_2/l, & z = x_3/h, \\
u = u_1/h, & v = u_2/h, & w = u_3/l, \\
\sigma_x = \sigma_{11}/\varepsilon Q, & \sigma_y = \sigma_{22}/\varepsilon Q, & \sigma_{xy} = \sigma_{12}/\varepsilon Q, \\
\sigma_{xz} = \sigma_{13}/\varepsilon^2 Q, & \sigma_{yz} = \sigma_{23}/\varepsilon^2 Q, & \sigma_z = \sigma_{33}/\varepsilon^3 Q,
\end{array}
\tag{2}
$$

where $\varepsilon = h/l < 1$ is a small parameter characteristic to the problem, l denotes a typical in-plane dimension of the plate, $-1 \le z \le 1$, Q is a reference elastic modulus.

Upon nondimensionalization, equation (1) can be made dimensionless in the form

$$
\delta\Pi_R = c_{33} h^3 \Big\{ \int_{-1}^{1} \int_{\Omega} \{ (\mathbf{L}_1 \mathbf{u})^T + \varepsilon^2 \sigma_z \mathbf{L}_2^T)(\mathbf{D}_1 \delta \mathbf{u}) - \sigma_{S,z}^T \delta \mathbf{u} + \sigma_S^T (\mathbf{D}\delta w) - \sigma_{z,z} \delta w
$$
$$
+ [w_{,z} + \varepsilon^2 \mathbf{L}_2^T (\mathbf{D}_1 \mathbf{u}) - \varepsilon^4 \tilde{c}_{33}^{-1} \sigma_z] \delta \sigma_z + (\mathbf{u}_{,z}^T + \mathbf{D}^T w - \varepsilon^2 \sigma_S^T S) \delta \sigma_S \} d\tilde{\Omega} dz
$$
$$
- \int_{-1}^{1} \int_{\Gamma_\sigma} (\overline{\mathbf{P}}^T \delta \mathbf{u} + \overline{p}_3 \delta w) d\tilde{\Gamma} dz \Big\} = 0.
\tag{3}
$$

The variational functional (3) contains only terms of even power of ε, in which the highest derivative of the field variables is the first; it represents a weak form for the problem. Application of the perturbation procedure by expanding the displacement and stress components in powers of ε^2 and collecting terms of equal power of ε, it can be decomposed into a sequence of functionals as follows:

$$
\delta\Pi_R = c_{33} h^3 (\delta\Pi_{(0)} + \varepsilon^2 \delta\Pi_{(1)} + \varepsilon^4 \delta\Pi_{(2)} + \ldots) = 0,
\tag{4}
$$

with

$$
\delta\Pi_{(0)} = \int_{-1}^{1} \int_{\Omega} [(\mathbf{L}_1 \mathbf{u}_{(0)})^T (\mathbf{D}_1 \delta \mathbf{u}) - \sigma_{S(0),z}^T \delta \mathbf{u}_0 + \sigma_{S(0)}^T (\mathbf{D}\delta w) - \sigma_{z(0),z} \delta w + w_{(0),z} \delta \sigma_z
$$
$$
+ (\mathbf{u}_{(0),z}^T + \mathbf{D}^T w_{(0)}) \delta \sigma_S] d\tilde{\Omega} dz - \int_{-1}^{1} \int_{\Gamma_\sigma} (\overline{\mathbf{P}}^T \delta \mathbf{u} + \overline{p}_3 \delta w) d\tilde{\Gamma} dz = 0,
\tag{5}
$$

$$
\delta\Pi_{(k)} = \int_{-1}^{1} \int_{\Omega} \Big\{ [(\mathbf{L}_1 \mathbf{u}_{(k)})^T + \sigma_{z(k-1)} \mathbf{L}_2^T](\mathbf{D}_1 \delta \mathbf{u}) - \sigma_{S(k),z}^T \delta \mathbf{u} + \sigma_{S(0)}^T (\mathbf{D}\delta w)
$$
$$
- \sigma_{z(k),z} \delta w + [w_{(k),z} + \mathbf{L}_2^T \mathbf{D}_1 \mathbf{u}_{(k-1)} - (h/l)^2 \tilde{c}_{33}^{-1} \sigma_{z(k-1)}] \delta \sigma_z
$$
$$
+ [\mathbf{u}_{(k),z}^T + \mathbf{D}^T w_{(k)} - \sigma_{S(k-1)}^T S] \delta \sigma_S \Big\} d\tilde{\Omega} dz \quad (k = 1, 2, \cdots).
\tag{6}
$$

Equation (4) is in effect an asymptotic expression of (3). An adaptive computational model can be constructed based on (5) and (6) in conjunction with the finite element method. The solution derived from the leading-order functional represents the first-order approximation. Treatment of the higher-order functionals yields corrections to the approximation in a systematic and hierarchic manner.

ASYMPTOTIC FINITE ELEMENTS

The x-y plane of the domain is represented by a finite element mesh and variations of the field variables in an element are expressed in terms of the generalized nodal DOF by

$$\mathbf{u}_{(0)}(x, y, z) = \mathbf{N}_u \mathbf{u}_{(0)}^e(z), \tag{7}$$

$$w_{(0)}(x, y, z) = \mathbf{N}_w \mathbf{w}_{(0)}^e(z), \tag{8}$$

$$\sigma_{S(0)}(x, y, z) = \mathbf{N}_S \sigma_{S(0)}^e(z), \tag{9}$$

$$\sigma_{z(0)}(x, y, z) = \mathbf{N}_z \sigma_{z(0)}^e(z), \tag{10}$$

where $\mathbf{N}_u$, $\mathbf{N}_w$, $\mathbf{N}_S$, $\mathbf{N}_z$ denote interpolation functions of x and y; the generalized nodal DOF $\mathbf{u}_{(0)}^e = [u_{(0)}^e \ v_{(0)}^e]^T$, $\mathbf{w}_{(0)}^e$, $\sigma_{S(0)}^e = [\sigma_{xz(0)}^e \ \sigma_{yz(0)}^e]^T$ and $\sigma_{z(0)}^e$ are functions of z. The through-thickness variations of the generalized nodal DOF can be derived analytically through successive integration. The transverse stress DOF are condensed along the way in the element level; only the displacement DOF enter the system equation at each level.

Substitution of (7)–(10) in $\delta\Pi_{(0)}$ gives

$$\delta\Pi_{(0)} = \int_{-1}^{1} \{[(\mathbf{u}_{(0)}^e)^T \Psi - (\sigma_{S(0),z}^e)^T \Phi_1 - \mathbf{P}^T]\delta\mathbf{u}_0^e$$

$$+ [(\sigma_{S(0)}^e)^T \Phi_2 - (\sigma_{z(0),z}^e)^T \Phi_3 - \mathbf{P}_w^T]\delta\mathbf{w}_0^e + (\mathbf{w}_{(0),z}^e)^T \Phi_3^T \delta\sigma_{z(0)}^e$$

$$+ [(\mathbf{u}_{(0),z}^e)^T \Phi_1^T + (\mathbf{w}_0^e)^T \Phi_2^T]\delta\sigma_{S(0)}^e\}dz, \tag{11}$$

where
$$\Psi = \Psi^T = \int_{\Omega_e} (\mathbf{L}_1 \mathbf{N}_u)^T (\mathbf{D}_1 \mathbf{N}_u)dxdy, \qquad \Phi_1 = \int_{\Omega_e} \mathbf{N}_S^T \mathbf{N}_u dxdy,$$

$$\Phi_2 = \int_{\Omega_e} \mathbf{N}_S^T (\mathbf{DN}_w)dxdy, \quad \Phi_3 = \int_{\Omega_e} \mathbf{N}_z^T \mathbf{N}_w dxdy, \quad \mathbf{P} = \int_{\Gamma_\sigma^e} \mathbf{N}_u^T \bar{\mathbf{P}} d\tilde{\Gamma}, \quad \mathbf{P}_w = \int_{\Gamma_\sigma^e} \mathbf{N}_w^T \bar{P}_3 d\tilde{\Gamma},$$

Ω_e denotes the element area; $\mathbf{P}$ and $\mathbf{P}_w$ appear only at the element boundaries associated with the edge boundary on which the traction is prescribed. Although it is not necessary to do so, the matrices Φ_1, Φ_3 can be made equal and symmetric if the same shape functions are used for interpolation in (7)–(10).

523

At the element level, the condition $\delta\Pi_{(0)} = 0$ leads to

$\delta\sigma_z^e$:
$$\frac{d}{dz}\mathbf{w}_{(0)}^e = \mathbf{0}, \tag{12}$$

$\delta\sigma_S^e$:
$$\frac{d}{dz}\mathbf{u}_{(0)}^e + \Phi_1^{-1}\Phi_2\mathbf{w}_{(0)}^e = \mathbf{0}, \tag{13}$$

$\delta\mathbf{u}^e$:
$$\Psi\mathbf{u}_{(0)}^e - \Phi_1^T\frac{d}{dz}\sigma_{S(0)}^e - \mathbf{P} = \mathbf{0}, \tag{14}$$

$\delta\mathbf{w}^e$:
$$\Phi_2^T\sigma_{S(0)}^e - \Phi_3^T\frac{d}{dz}\sigma_{z(0)}^e - \mathbf{P}_w = \mathbf{0}. \tag{15}$$

Equations (12)–(15) can be integrated with respect to z in succession to give

$$\mathbf{w}_{(0)}^e(z) = \mathbf{w}_0^e, \tag{16}$$

$$\mathbf{u}_{(0)}^e(z) = \mathbf{u}_0^e - z\Phi_1^{-1}\Phi_2\mathbf{w}_0^e, \tag{17}$$

$$\sigma_{S(0)}^e(z) = (\Phi_1^T)^{-1}\int_{-1}^{z}[\Psi(\mathbf{u}_0^e - \Phi_1^{-1}\Phi_2\mathbf{w}_0^e) - \mathbf{P}]d\eta, \tag{18}$$

$$\sigma_{z(0)}^e(z) = (\Phi_3^T)^{-1}\Big\{ \Phi_2^T(\Phi_1^T)^{-1}\int_{-1}^{z}(z-\eta)[\Psi(\mathbf{u}_0^e - \eta\Phi_1^{-1}\Phi_2\mathbf{w}_0^e) - \mathbf{P}]d\eta$$

$$-\int_{-1}^{z}\mathbf{P}_w d\eta \Big\} - \tilde{\mathbf{q}}_e^-, \tag{19}$$

where $\mathbf{w}_0^e, \mathbf{u}_0^e$ are the integration constants representing the leading-order approximation to the midplane displacement DOF; $\tilde{\mathbf{q}}_e^-$ denotes the equivalent nodal value of the lateral load acting on the top surface of the plate.

With (18) and (19) the associated lateral boundary conditions are satisfied exactly by letting

$$\int_{-1}^{1}\Psi(\mathbf{u}_0^e - \eta\Phi_1^{-1}\Phi_2\mathbf{w}_0^e)d\eta = \int_{-1}^{1}\mathbf{P}d\eta, \tag{20}$$

$$\Phi_2^T(\Phi_1^T)^{-1}\int_{-1}^{1}(1-\eta)[\Psi(\mathbf{u}_0^e - \eta\Phi_1^{-1}\Phi_2\mathbf{w}_0^e) - \mathbf{P}]d\eta$$

$$= \int_{-1}^{1}\mathbf{P}_w d\eta + \Phi_3^T(\tilde{\mathbf{q}}_e^- + \tilde{\mathbf{q}}_e^+). \tag{21}$$

After simplification of (21) using (20), these equations can be written in a matrix form:

$$\begin{bmatrix} \mathbf{K}_{uu} & \mathbf{K}_{uw} \\ \mathbf{K}_{wu} & \mathbf{K}_{ww} \end{bmatrix}\begin{Bmatrix} \mathbf{u}_0^e \\ \mathbf{w}_0^e \end{Bmatrix} = \begin{Bmatrix} \mathbf{F}_{u0} \\ \mathbf{F}_{w0} \end{Bmatrix}, \tag{22}$$

where $\qquad \mathbf{K}_{uu} = \int_{-1}^{1} \mathbf{\Psi} \, dz, \qquad \mathbf{K}_{uw} = \mathbf{K}_{wu}^{T} = -(\int_{-1}^{1} z \mathbf{\Psi} \, dz)(\Phi_{1})^{-1} \Phi_{2},$

$$\mathbf{K}_{ww} = \Phi_{2}^{T}(\Phi_{1}^{T})^{-1}(\int_{-1}^{1} z^{2} \mathbf{\Psi} \, dz)\Phi_{1}^{-1}\Phi_{2}, \qquad \mathbf{F}_{u0} = \int_{-1}^{1} \mathbf{P} \, dz, \qquad \mathbf{F}_{w0} = \Phi_{3}^{T}(\tilde{\mathbf{q}}_{e}^{-} + \tilde{\mathbf{q}}_{e}^{+}) + \int_{-1}^{1} \mathbf{P}_{w} \, dz.$$

Equation (22) consists of $3n$ equations for $3n$ unknown DOF of an element with n nodes, in which the stiffness matrix is symmetric. After assembling the element matrices into system equations, the unknown DOF at the interior nodes and at the boundary nodes on Γ_{σ} can be computed, whereas at the nodes on the boundary where the displacements are prescribed the corresponding components in the generalized force vectors can be computed. Afterwards, the leading-order approximation to the displacements and stresses are determined by back substitution of the nodal DOF in (16)–(19) and (7)–(10).

The leading-order approximation can be improved by treating the higher-order variational functionals in the same way. The corrections to the displacements and transverse stresses are interpolated and substituted in (6). Successive integration of the equations derived from the stationary condition $\delta \Pi_{(k)} = 0$ yields the results in the form

$$\mathbf{W}_{(k)}^{e}(z) = \mathbf{W}_{k}^{e} + \mathbf{G}_{k}(z), \tag{23}$$

$$\mathbf{u}_{(k)}^{e}(z) = \mathbf{u}_{k}^{e} - z\Phi_{1}^{-1}\Phi_{2}\mathbf{W}_{k}^{e} + \mathbf{H}_{k}(z), \tag{24}$$

$$\sigma_{S(k)}^{e}(z) = (\Phi_{1}^{T})^{-1}\int_{-1}^{z}[\mathbf{\Psi}(\mathbf{u}_{k}^{e} - z\Phi_{1}^{-1}\Phi_{2}\mathbf{W}_{k}^{e}) + \mathbf{I}_{k}]d\eta, \tag{25}$$

$$\sigma_{z(k)}^{e}(z) = (\Phi_{3}^{T})^{-1}\Phi_{2}^{T}(\Phi_{1}^{T})^{-1}\int_{-1}^{z}(z-\eta)[\mathbf{\Psi}(\mathbf{u}_{k}^{e} - z\Phi_{1}^{-1}\Phi_{2}\mathbf{W}_{k}^{e}) + \mathbf{I}_{k}]d\eta, \tag{26}$$

where the functions $\mathbf{G}_{k}$, $\mathbf{H}_{k}$ and $\mathbf{I}_{k}$ are completely defined by the lower-order solutions.

Imposition of the associated lateral boundary conditions on (25) and (26) leads to

$$\begin{bmatrix} \mathbf{K}_{uu} & \mathbf{K}_{uw} \\ \mathbf{K}_{wu} & \mathbf{K}_{ww} \end{bmatrix} \begin{Bmatrix} \mathbf{u}_{k}^{e} \\ \mathbf{w}_{k}^{e} \end{Bmatrix} = \begin{Bmatrix} \mathbf{F}_{uk} \\ \mathbf{F}_{wk} \end{Bmatrix}. \tag{27}$$

At the higher levels, the stiffness matrix remains the same as that at the leading order, only the generalized force vector needs to be computed using the lower-order solutions.

Solution to the system equations at each asymptotic level must be supplemented with edge conditions. It can be shown that the exact edge boundary conditions require specifying tractions or displacements along the edges. Nevertheless, the interior solution can be determined by neglecting the boundary layer effect and using statically equivalent edge conditions instead.

CONCLUSIONS

An adaptive computational model for stress analysis of multilayered composite plates is developed on the basis of asymptotic variational formulation. The model is 3D in effect, yet it requires only 2D discretization on the plane form of the plate. Interpolating in the thickness direction is unnecessary. The through-thickness effects are accounted for in a consistent and hierarchical way. Reformulation of the stiffness matrix at higher levels is not required; the one generated at the leading order is always used in the multi-level computations. Numerical comparisons with benchmark solutions show that the method is effective in modeling of multilayered composite plates. Derivations and applications of the asymptotic finite element method in detail can be found in forthcoming publications [6, 7].

REFERENCES

[1] Tarn, J. Q. and Wang, Y. M. "An asymptotic theory for dynamic response of anisotropic inhomogeneous and laminated plates." *International Journal of Solids and Structures* **31**, pp. 231–246 (1994).

[2] Wang, Y. M. and Tarn, J. Q. "A three-dimensional analysis of anisotropic inhomogeneous and laminated plates." *International Journal of Solids and Structures* **31**, pp. 497–515 (1994).

[3] Tarn, J. Q. and Wang, Y. M. "Asymptotic theory for thermoelastic analysis of anisotropic inhomogeneous and laminated plates." *Journal of Thermal Stresses* **18**, pp. 35–58 (1995).

[4] Tarn, J. Q. "Elastic buckling of multilayered composite plates." *Journal of the Mechanics and Physics of Solids* (in press).

[5] Washizu, K. *Variational Methods in Elasticity and Plasticity*, third edition, Pergamon Press, Oxford, England (1982).

[6] Tarn, J. Q., Wang, Y. B. and Wang Y. M. "Three-dimensional asymptotic finite Element method for anisotropic inhomogeneous and laminated plates." *International Journal of Solids and Structures* (in press).

[7] Tarn, J. Q. "An asymptotic variational formulation for dynamic analysis of multilayered composite plates." *Computer Methods in Applied Mechanics and Engineering* (in press).

PLANE PIEZOTHERMOELASTIC RESPONSE OF A HYBRID LAMINATE - A BENCHMARK PROBLEM

Theodore R. Tauchert
Department of Engineering Mechanics
University of Kentucky, Lexington, KY 40506-0046,USA

INTRODUCTION

The concept of incorporating piezoelectric elements into structural systems as a means for altering the structure's response has received considerable attention in recent years. Investigations have demonstrated the feasibility of suppressing thermomechanically induced deformation and stress in laminates through application of an electric potential to attached or embedded piezoelectric layers. Various lamination theories, including classical [1] and refined [2-3] formulations, have been developed for analyzing the piezothermoelastic response. In the present investigation, a benchmark problem is proposed for assessing the validity of approximate plate-theory solutions for the piezothermoelastic behavior of hybrid laminates. In particular, cylindrical bending of a five-layer (piezoelectric/orthotropic,0^0/isotropic/orthotropic,90^0/piezoelectric) plate subject to specified thermal and electric-potential surface loadings is considered. A recently derived analytical solution [4] for the stationary two-dimensional response of hybrid laminates is used to obtain the "true" stress and displacement distributions for this problem. Also, a third-order displacement formulation which includes transverse normal and shear strains is developed, the results of which are compared with the corresponding piezothermoelasticity results.

PIEZOTHERMOELASTIC FORMULATION

The laminate under consideration experiences arbitrary distributions of thermal boundary conditions (prescribed temperature, heat flux or convection) on its lower and upper faces ($z = \pm t/2$), while the temperature on the ends ($y = 0,b$) remains constant. Assuming ideal thermal contact at the layer interfaces, the general solution to the stationary heat conduction equation for the temperature $\theta^{(i)}$ within a typical layer i (i = 1,...,N) can be expressed as [4]

$$\theta^{(i)} = \sum_{p=p_i}^{\infty} [A_1^{(i)} sh\frac{pz}{k^{(i)}} + A_2^{(i)} ch\frac{pz}{k^{(i)}}]\sin py \qquad (1)$$

where $p_n = n\pi/b$, $k^{(i)^2} = k_z^{(i)}/k_y^{(i)}$ is the ratio of coefficients of heat conduction in the z and y directions, respectively, and coefficients $A_j^{(i)}$ are determined from the specified thermal surface conditions.

For electric loading of the piezoelectric layers, consisting of either a large applied surface voltage or electric displacement, it is assumed that the electric field resulting from variations in stress or temperature (the *direct piezoelectric effect*) is insignificant compared with that produced by the electric loading. The potential at each end of the laminate is taken to be zero, whereas arbitrary distributions of electrostatic conditions are prescribed on the upper and lower surfaces of each piezoelectric layer. A solution to the uncoupled electrostatic equation for the electric potential $\phi^{(i)}$ within layer i is [4]

$$\phi^{(i)} = \sum_{p=p_1}^{\infty} [B_1^{(i)} \text{sh} \frac{pz}{h^{(i)}} + B_2^{(i)} \text{ch} \frac{pz}{h^{(i)}}] \sin py \qquad (2)$$

where $h^{(i)^2} = \eta_z^{(i)}/\eta_y^{(i)}$ is the ratio of permittivities in the z and y directions, and $B_j^{(i)}$ are determined from the prescribed electrostatic conditions.

For an assumed state of plane strain perpendicular to the x-axis, the stress components $\sigma_{jk}^{(i)}$ in layer i are related to the displacements $v^{(i)}$ and $w^{(i)}$, the temperature $\theta^{(i)}$, and the electric potential $\phi^{(i)}$, by

$$\sigma_{xx}^{(i)} = c_{12}^{(i)} v_{,y}^{(i)} + c_{13}^{(i)} w_{,z}^{(i)} - \beta_1^{(i)} \theta^{(i)} + e_{31}^{(i)} \phi_{,z}^{(i)}$$
$$\sigma_{yy}^{(i)} = c_{22}^{(i)} v_{,y}^{(i)} + c_{23}^{(i)} w_{,z}^{(i)} - \beta_2^{(i)} \theta^{(i)} + e_{32}^{(i)} \phi_{,z}^{(i)} \qquad (3)$$
$$\sigma_{zz}^{(i)} = c_{23}^{(i)} v_{,y}^{(i)} + c_{33}^{(i)} w_{,z}^{(i)} - \beta_3^{(i)} \theta^{(i)} + e_{33}^{(i)} \phi_{,z}^{(i)}$$
$$\sigma_{yz}^{(i)} = c_{44}^{(i)} (v_{,z}^{(i)} + w_{,y}^{(i)}) + e_{24}^{(i)} \phi_{,y}^{(i)}$$

where $c_{jk}^{(i)}$ are orthotropic elastic stiffness coefficients, $\beta_j^{(i)}$ are stress-temperature coefficients, and $e_{jk}^{(i)}$ are piezoelectric coefficients.

In the case of layers having isotropic elastic properties and orthorhombic (class mm2) piezoelectric properties, the solutions for the displacements have the general form [4]*

$$v^{(i)} = \sum_{p=p_1}^{\infty} \{K_{11}^{(i)} \text{sh} pz + K_{12}^{(i)} \text{ch} pz + K_{21}^{(i)} [pz \text{sh} pz + c^{(i)} \text{ch} pz] + K_{22}^{(i)} [pz \text{ch} pz + c^{(i)} \text{sh} pz]$$

$$+ \frac{d^{(i)}}{p^2} [-A_1^{(i)} \text{sh} pz - A_2^{(i)} \text{ch} pz] + \frac{\Delta_1^{(i)}}{p\Delta^{(i)}} [B_1^{(i)} \text{ch} \frac{pz}{h^{(i)}} + B_2^{(i)} \text{sh} \frac{pz}{h^{(i)}}]\} p \cos py \quad (4)$$

---

* Equation (4) for the displacements is valid providing $h^{(i)} \neq 1$; results for the case $h^{(i)} = 1$ are given in Ref. [4].

$$w^{(i)} = \sum_{p=p_1}^{\infty} \{K_{11}^{(i)} \operatorname{ch} pz + K_{12}^{(i)} \operatorname{sh} pz + K_{21}^{(i)} pz \operatorname{ch} pz + K_{22}^{(i)} pz \operatorname{sh} pz$$

$$+ \frac{d^{(i)}}{p^2}[A_1^{(i)} \operatorname{ch} pz + A_2^{(i)} \operatorname{sh} pz] + \frac{\Delta_2^{(i)}}{p\Delta^{(i)}}[B_1^{(i)} \operatorname{sh} \frac{pz}{h^{(i)}} + B_2^{(i)} \operatorname{ch} \frac{pz}{h^{(i)}}]\} p \sin py \quad (4)$$

whereas for layers having orthotropic elastic properties the displacements are expressible as [4]

$$v^{(i)} = \sum_{p=p_1}^{\infty} \{K_{11}^{(i)} \operatorname{sh} \frac{pz}{\gamma_1^{(i)}} + K_{12}^{(i)} \operatorname{ch} \frac{pz}{\gamma_1^{(i)}} + K_{21}^{(i)} \operatorname{sh} \frac{pz}{\gamma_2^{(i)}} + K_{22}^{(i)} \operatorname{ch} \frac{pz}{\gamma_2^{(i)}}$$

$$+ \frac{\kappa^{(i)}}{p^2}[A_1^{(i)} \operatorname{sh} \frac{pz}{k^{(i)}} + A_2^{(i)} \operatorname{ch} \frac{pz}{k^{(i)}}] + \frac{\Delta_1^{(i)}}{p\Delta^{(i)}}[B_1^{(i)} \operatorname{ch} \frac{pz}{h^{(i)}} + B_2^{(i)} \operatorname{sh} \frac{pz}{h^{(i)}}]\} p \cos py$$

$$(5)$$

$$w^{(i)} = \sum_{p=p_1}^{\infty} \{\frac{\lambda_1^{(i)}}{\gamma_1^{(i)}}[K_{11}^{(i)} \operatorname{ch} \frac{pz}{\gamma_1^{(i)}} + K_{12}^{(i)} \operatorname{sh} \frac{pz}{\gamma_1^{(i)}}] + \frac{\lambda_2^{(i)}}{\gamma_2^{(i)}}[K_{21}^{(i)} \operatorname{ch} \frac{pz}{\gamma_2^{(i)}} + K_{22}^{(i)} \operatorname{sh} \frac{pz}{\gamma_2^{(i)}}]$$

$$+ \frac{\mu^{(i)}\kappa^{(i)}}{k^{(i)}p^2}[A_1^{(i)} \operatorname{ch} \frac{pz}{k^{(i)}} + A_2^{(i)} \operatorname{sh} \frac{pz}{k^{(i)}}] + \frac{\Delta_2^{(i)}}{p\Delta^{(i)}}[B_1^{(i)} \operatorname{sh} \frac{pz}{h^{(i)}} + B_2^{(i)} \operatorname{ch} \frac{pz}{h^{(i)}}]\} p \sin py$$

in which $K_{jk}^{(i)}$ are arbitrary integration constants to be determined from the traction or displacement boundary conditions; all other coefficients are functions of the piezothermoelastic material properties, as defined in [4].

HIGH-ORDER PLATE FORMULATION

Next consider a plate formulation in which both the in-plane (v) and out-of-plane (w) displacement components are assumed to have cubic variations through the thickness of the laminate. Expressions for the displacements, which satisfy identically the condition of zero transverse shear stress on the top and bottom plate surfaces, are (see [3])

$$v = v^0 + z\psi_y + z^2[-\frac{1}{2}\psi_{z,y} - \frac{t^2}{8}\phi_{z,y}] + z^3[-\frac{4}{3t^2}(\psi_y + w_{,y}^0 + \frac{t^2}{4}\xi_{z,y})]$$

$$(6)$$

$$w = w^0 + z\psi_z + z^2\xi_z + z^3\phi_z$$

in which v^0 and w^0 represent mid-plane displacements, while ψ_y, ψ_z, ξ_z and ϕ_z are additional deformation variables to be determined.

Stress resultants are introduced, defined by

$$\begin{Bmatrix} N_y, M_y, S_y, P_y \\ N_z, M_z, S_z, P_z \\ Q_y, V_y, R_y, W_y \end{Bmatrix} = \sum_{i=1}^{N} \int_{z_{i-1}}^{z_i} \begin{Bmatrix} \sigma_{yy} \\ \sigma_{zz} \\ \sigma_{yz} \end{Bmatrix}_i (1, z, z^2, z^3) dz \qquad (7)$$

Equations of equilibrium governing these stress resultants, obtained using the principle of virtual displacements, are

$$N_{y,y} = 0$$

$$Q_{y,y} - \frac{4}{t^2} R_{y,y} + \frac{4}{3t^2} P_{y,yy} = 0$$

$$M_{y,y} - Q_y + \frac{4}{t^2} R_y - \frac{4}{3t^2} P_{y,y} = 0 \qquad (8)$$

$$S_{y,yy} - 2N_z = 0$$

$$P_{y,yy} - 6M_z = 0$$

$$\frac{t^2}{8} S_{y,yy} - 3S_z - \frac{t^2}{4} V_{y,y} + W_{y,y} = 0$$

Substitution of eqs. (3) and (6) into (7), with the results inserted into (8), yields the deformation equations of equilibrium. A solution to these equations, for the case of a simply supported laminate ($w^0 = \psi_z = \xi_z = \phi_z = N_y = M_y = S_y = P_y = 0$), can be found by expressing all loads (i.e., the thermal and electric stress resultants) in Fourier series form, taking

$$(v^0, \psi_y) = \sum_{n=0}^{\infty} (A_n, B_n) \cos\beta_n y$$

$$(w^0, \psi_z, \xi_z, \phi_z) = \sum_{n=1}^{\infty} (C_n, D_n, E_n, F_n) \sin\beta_n y \qquad (9)$$

where $\beta_n = n\pi/b$, and then solving the resulting algebraic equations for $A_n, \ldots, F_n$.

BENCHMARK PROBLEM RESULTS

As a benchmark problem, cylindrical bending of a five-layer plate subject to prescribed thermal and electric-potential surface loadings is considered. The laminate consists of an isotropic middle layer, two adjacent orthotropic layers (0^0 and 90^0 ply angles), and piezoelectric outer layers (see Fig. 1).Material properties of these layers are listed in Table 1.

Table 1. Material properties (k_o, E_o, v_o=0.25, α_o, η_o and d_o denote arbitrary reference values of thermal conductivity, Young's modulus, Poisson's ratio, thermal expansion, permittivity and piezoelectric coefficient, respectively).

Isotropic	$k = k_o$, $E = E_o$, $v = v_o$, $\alpha = \alpha_o$
Orthotropic	$k_1 = 100k_o$, $k_2 = k_3 = k_o$
	$E_1 = 90E_o$, $E_2 = E_3 = 5E_o$
	$G_{12} = G_{13} = 4E_o$, $G_{23} = 1.5E_o$
	$v_{12} = v_{13} = v_{23} = v_o$
	$\alpha_1 = 0.0002\alpha_o$, $\alpha_2 = \alpha_3 = 0.2\alpha_o$
Piezoelectric	$k = k_o$, $E = E_o$, $v = v_o$, $\alpha = \alpha_o$
	$\eta_1 = \eta_2 = \eta_o$, $\eta_3 = 10\eta_o$
	$d_{31} = d_{32} = d_{24} = d_o$, $d_{33} = 1.4d_o$

Fig.1. Laminate configuration.

For a first example, a laminate having a length-to-thickness ratio $b/t = 5$ is subject to a temperature rise $\theta = \theta_o \sin(\pi y / b)$ on the surface $z = -t/2$, while $\theta = 0$ on $z = t/2$. Distributions of the nondimensionalized displacement $w^* = wt / \alpha_o \theta_o b^2$ and bending stress $\sigma_{yy}^* = \sigma_{yy} / \alpha_o E_o \theta_o$ at y=b/2, based on both the thermoelasticity and high-order formulations, are shown in Fig. 2 and 3. Also shown in these figures are results obtained using classical (Kirchhoff) bending theory. From Fig.2 it is seen that the high-order theory, which accounts for transverse normal as well as transverse shear deformation, gives a more accurate prediction of the maximum transverse deflection than does the classical theory. Both plate theories give reasonably accurate results for the bending stress distributions for the particular laminate considered, as shown in Fig. 3.

As a second example, the laminate is exposed to a potential difference $\phi = \phi_o \sin(\pi y / b)$ across each of the piezoelectric layers. Calculated induced nondimensionalized displacement $w^* = wt^2 / d_o \phi_o b^2$ and stress $\sigma_{yy}^* = \sigma_{yy} t / E_o d_o \phi_o$ distributions are shown in Figs. 4 and 5. As in the case of thermal loading, the high-order theory predicts a variation in the displacement w which is in reasonable agreement with the piezothermoelasticity solution. The electrically-induced bending stress distribution obtained by either the classical or high-order theory is seen to provide a close approximation to the exact solution, even for the relatively thick plate considered here.

References

[1] Tauchert, T.R.,"Piezothermoelastic behavior of a laminated plate",*Journal of Thermal Stresses* **15**, pp. 25-37 (1992).

[2] Jonnalagadda, K.D., Blandford, G.E. and Tauchert, T.R., "Piezothermoelastic composite plate analysis using a first-order shear deformation theory", *Computers and Structures* **51**, pp. 79-89 (1994).

[3] Jonnalagadda, K.D., Tauchert, T.R. and Blandford, G.E., "High-order displacement formulation for a piezothermoelastic laminate", *Mechanics of Electromagnetic Materials and Structures*, ASME, AMD-161/MD42, pp.145-156 (1993).

[4] Tauchert, T.R., "Cylindrical bending of hybrid laminates under thermo-electro-mechanical loading", *Journal of Thermal Stresses* (forthcoming).

Fig.2. Transverse deflection due
to thermal loading.

Fig. 3.Bending stress due
to thermal loading.

Fig.4. Transverse deflection due
to electric loading.

Fig. 5.Bending stress due
to electric loading.

HYPERVELOCITY IMPACT DAMAGE
TO COMPOSITE STRUCTURES

R. C. TENNYSON and G. SHORTLIFFE

University of Toronto Institute for Aerospace Studies
4925 Dufferin Street, North York, Ontario, Canada, M3H 5T6

INTRODUCTION

Spacecraft in low Earth orbit (LEO) are vulnerable to impact damage resulting from collisions with micrometeoroids and orb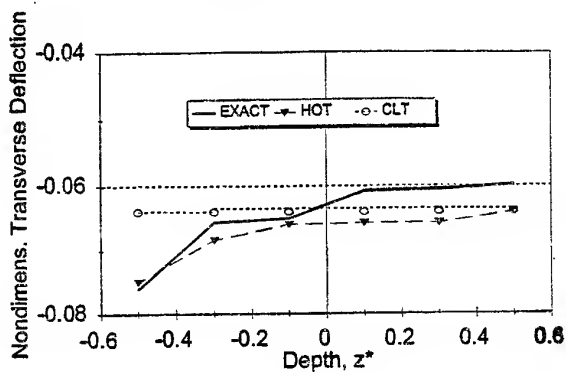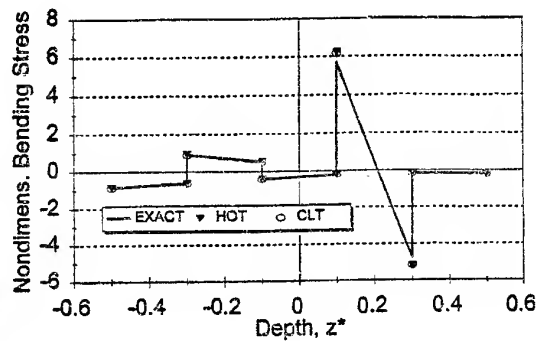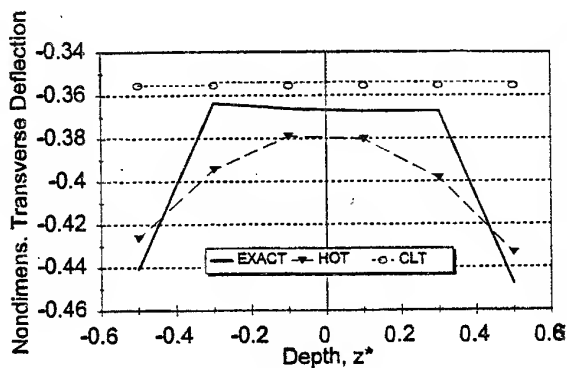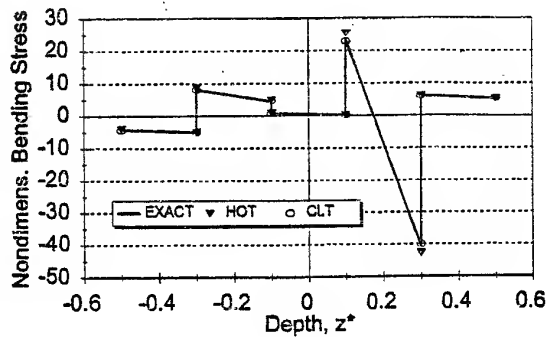ital debris (M/OD). Micrometeoroids originate naturally from planetary or asteroidal collisions and cometary ejecta. Although there is no particular direction in which micrometeoroids approach the Earth, spacecraft experience a bias in the direction of travel. Artificial space debris consists of everything from spent satellites and rockets to aluminum oxide fuel particles, paint chips, and fragmentation objects arising from collisions of these bodies in orbit.

Although micrometeoroids have been a design issue since the 1960's, concern about the growing amount of orbital debris did not receive serious attention until the mid-1980's. The problem has grown to such an extent that the probability of impact by space debris exceeds that due to micrometeoroids. There is currently an astounding 2.5×10^6 kg of debris in LEO. Since first entering space in 1957, almost 20,000 objects have been launched with approximately 7,000 still in orbit.

Polymer matrix composites are used extensively in spacecraft structures and components, such as antenna struts and panels. These materials provide significant advantages over metals because of their high specific stiffness and strength, and low coefficients of thermal expansion. On the other hand, they also pose serious problems in the space environment such as outgassing in vacuum, erosion due to atomic oxygen, and degradation from ultra-violet radiation. Protective measures have been developed such as coatings and improved resin formulations. However, the problem of surface and structural damage due to M/OD impacts has not been resolved. Not only can M/OD cause local fracture and delamination of composites, but degradation of protective coatings can occur and can open sites for erosion of the substrate.

Very few studies have been conducted on M/OD hypervelocity impact damage to polymer matrix ·composites. Some of the earlier work on graphite/epoxy plates includes that done by Yew et al [1] (identified in graphs as "Austin" data) at the NASA Johnson Space Center in 1986 using two of their light gas guns to achieve hypervelocity impact conditions. A wide range of plate thicknesses was investigated using quasi-isotropic lay-ups.

A more detailed series of tests was reported by Christiansen in 1988 [2] (identified in graphs as "Eagle" data) in which both low and high modulus graphite/epoxy plates and tubes were studied. Again, various target thicknesses were used and different impact angles were employed. It was observed that fiber modulus has a greater effect than lay-up. Christiansen developed two impact damage models based on this data for energies above and below 150J. Lower energy impact data on both graphite/epoxy and PEEK plates were reported in [3] (identified as "Auburn" data) but the range of test parameters was very restricted.

PROBLEM STATEMENT

In the development of the Canadian Space Station Remote Manipulator System, it was decided to employ a graphite/PEEK material to construct the robot arm tube structures. This was done to meet weight and stiffness criteria. Thus, the wall thickness and laminate configuration are such as to provide maximum

specific stiffness while achieving as low a coefficient of thermal expansion as possible. Although strength is an important consideration as well, no M/OD impact test data was available for this material system and laminate structure. Thus, a series of tests on PEEK/IM7 laminates of varying thickness and lay-ups were conducted at the NASA Johnson Space Center ("JSC" data), the Southwest Research Institute ("SwRI" data), and the NASA Marshall Space Flight Center ("MSFC" data) using their 2-stage light gas guns. A summary of the tests conducted is presented in Table 1.

One notable feature of these tests is the use of a second plate (secondary target) located about 33 cm (13 in) behind the primary impact plate (primary target) to simulate the opposite wall of the cylinder structure. The purpose was to determine the ejecta damage emanating from the first wall impact and assess the extent of rear wall penetration and overall structural degradation (i.e., loss in stiffness and strength). All tests were conducted with aluminum impactor spheres of varying diameter and at different velocities. Energies ranging from 2 to 2000 J were investigated. In the following graphs, results from other test programs are also included for comparison purposes.

Shot Id	Configuraton	Primary Target		Secondary Target		Projectile		
		Thickness [mm]	Layup	Thickness [mm]	Layup	Diameter [mm]	Velocity [km/s]	Energy [J]
JSC #1	PEEK & Al proj. (0 deg.)	2.7	(+/-43)s	0.5	(0,90)s	1.5	6.05	90.6
JSC #2	PEEK & Al proj. (0 deg.)	2.0	(0,+/-45,90)s	1.9	(0,+/-45,90)s	2	6.75	267.2
JSC #3	PEEK & Al proj. (0 deg.)	1.8	(0,+/-45,90)s	2.0	(0,+/-45,90)s	3	6	712.5
JSC #4	PEEK & Al proj. (0 deg.)	0.5	(0,90)s	0.5	(0,90)s	1.5	7	121.2
JSC #5	PEEK & Al proj. (0 deg.)	2.9	(0,+/-45,90)s	2.9	(0,+/-45,90)s	2.5	6.98	558.0
JSC #6	PEEK & Al proj. (0 deg.)	2.7	(+/-43)s	2.0	(0,+/-45,90)s	2	7.2	304.0
JSC #7	PEEK & Al proj. (0 deg.)	2.7	(+/-43)s	1.9	(0,+/-45,90)s	2.5	6.85	537.4
JSC #8	PEEK & Al proj. (0 deg.)	2.9	(0,+/-45,90)s	1.9	(0,+/-45,90)s	2.5	6.21	441.7
JSC #9	PEEK & Al proj. (0 deg.)	1.0	(0,+/-45,90)s	0.9	(0,+/-45,90)s	2	5	146.6
SwRI #1	PEEK & Al proj. (0 deg.)	0.5	(0,90)s	0.5	(0,90)s	1	6.82	20.9
SwRI #2	PEEK & Al proj. (0 deg.)	0.9	(0,+/-45,90)s	1.0	(0,+/-45,90)s	1	7.27	23.8
SwRI #3	PEEK & Al proj. (0 deg.)	2.9	(0,+/-45,90)s	2.9	(0,+/-45,90)s	1	7.18	23.2
SwRI #4	PEEK & Al proj. (0 deg.)	0.4	(0,90)s	0.5	(0,90)s	0.4	6.26	2.0
SwRI #5	PEEK & Al proj. (0 deg.)	1.9	(0,+/-45,90)s	1.9	(0,+/-45,90)s	1	7.18	25.8
SwRI #6	PEEK & Al proj. (0 deg.)	1.9	(0,+/-45,90)s	1.9	(0,+/-45,90)s	0.4	7.3	2.7
SwRI #7	PEEK & Al proj. (0 deg.)	1.0	(0,+/-45,90)s	1.0	(0,+/-45,90)s	0.4	7.07	2.5
MSFC #1	PEEK & Al proj. (0 deg.)	0.9	(0,+/-45,90)s	0.9	(0,+/-45,90)s	4.0	6.57	1978

TABLE 1. HVI Shot Matrix Performed on Graphite/PEEK Composite.

TEST RESULTS

A typical front face impact site on one of the graphite/PEEK laminates is shown in Figure 1. The hole (i.e., crater) in the laminate defines a complete penetration while the surrounding surface damage is limited to several plies, the extent of which was determined by C-scan techniques. To quantify crater and entry damage for comparison, an equivalent circle diameter was calculated having an enclosed area equal to the measured crater or surface damage area, respectively.

Figure 2 presents a plot of the crater diameter as a function of an energy parameter $[Et/D_p]^{1/3}$, which was first defined by Christiansen [2] for use with composites. As noted above, other test results for graphite/epoxy and graphite/PEEK laminates are included in Figure 2 based on similar hypervelocity impact
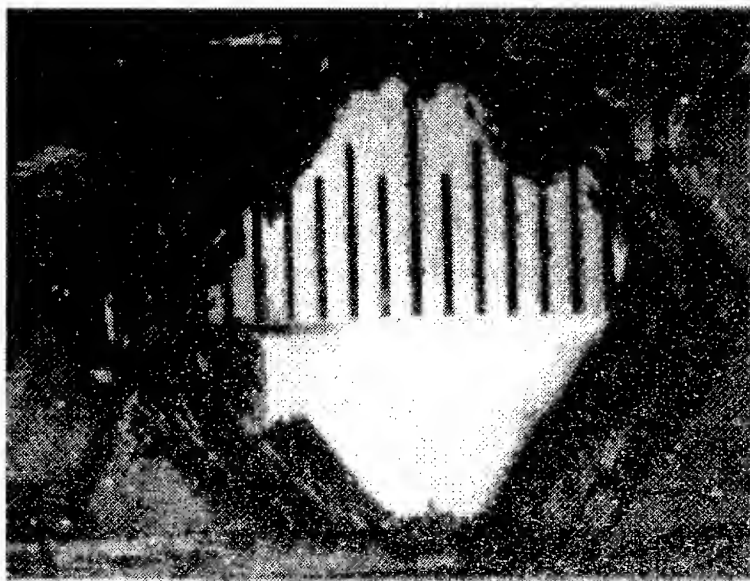
FIGURE 1

UTIAS HVI Program
Crater Diameter vs. $\sqrt[3]{E\frac{t}{D_p}}$

▽ Auburn GRE (SiC)	▼ Auburn PEEK (SiC)	■ JSC PEEK (Al)
● SwRI PEEK (Al)	○ USAF #1 PEEK (Al/Nylon)	□ Austin GRE (Al)
▲ Eagle GRE (Low E & Al)	△ MSFC PEEK (Al)	—— Regression

$$D_{crater} = .89 \sqrt[3]{E\frac{t}{D_p}}$$

$$\sqrt[3]{E\frac{t}{D_p}} \quad [\sqrt[3]{J}]$$
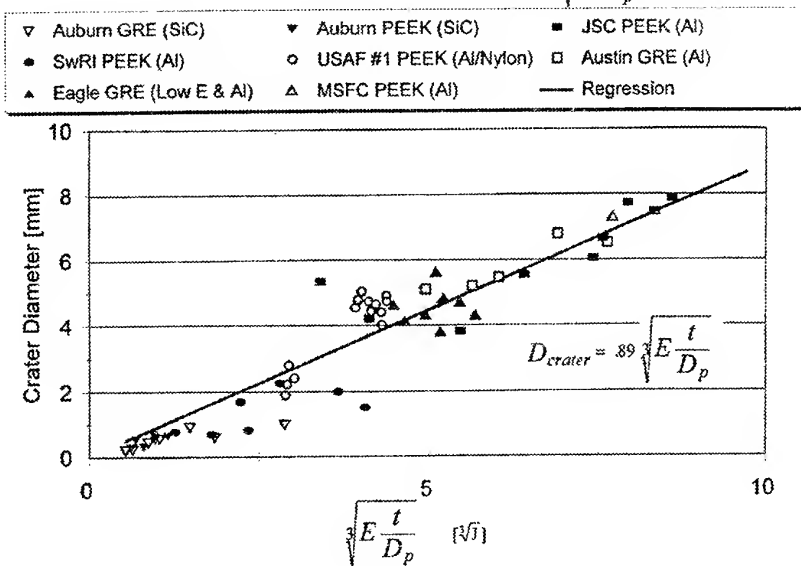
FIGURE 2

tests using different projectile materials as well. The parameters are: E = energy of projectile (J); t = laminate thickness (mm); D_p = projectile diameter (mm). The legend details the source of the data, the target material, and the projectile material, respectively.

A regression curve, forced to pass through zero, is shown based only on the PEEK data presented. It is evident that a good correlation exists for the range of energy parameters studied despite the different laminate lay-ups investigated. Although there is some variance with the graphite/epoxy data and the nylon cylinder impactor results (identified in graphs as "USAF" data), it is clear that this curve can be used to provide an estimate of crater damage for the wide range of parameters investigated.

Entry damage as defined by the equivalent diameter method is plotted in Figure 3 as a function of the same energy parameter. Included in this plot is the regression curve based on C-scan measurements of the sub-surface damage zones. It can be seen that even though the delamination lies below the surface, the enhanced area is only about 20%

UTIAS HVI Program
Entry Damage Diameter vs. $\sqrt[3]{E\dfrac{t}{D_p}}$
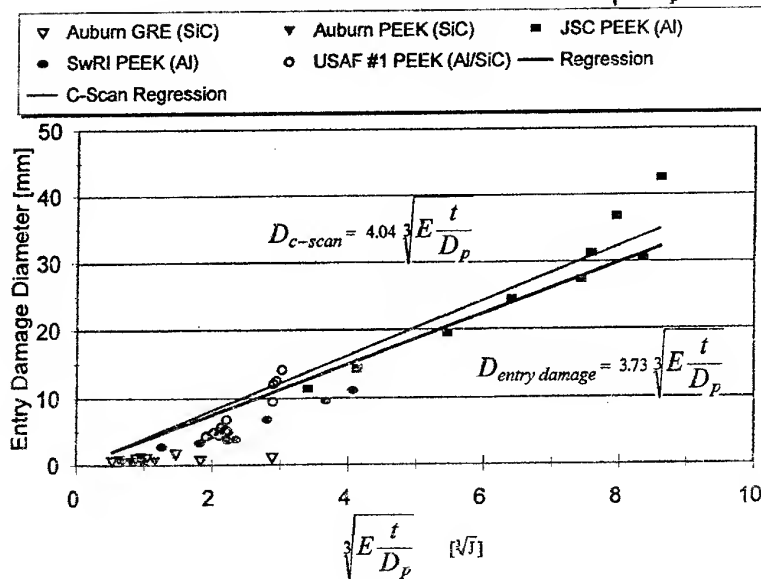
FIGURE 3

UTIAS HVI Program
Spall Damage Diameter vs. $\sqrt[3]{E\dfrac{t}{D_p}}$

FIGURE 4

greater than the surface area.

From a design point of view, the entry damage area can be estimated from measuring the crater area, based on the equivalent diameter method, using the formula: Entry Area = 20 × Crater Area.

Rear face spallation damage on the primary impact plate was also measured, the results of which are plotted in Figure 4. The regression analysis indicates that the damage area is comparable to that observed on the front face for a given energy parameter.

A plot of the crater diameter as a function of the projectile diameter is shown in Figure 5. The regression curve was constructed only through the PEEK data, excluding the nylon cylinder results. There appears to be no energy dependence for the range of parameters studied. Interestingly, one can see that the nylon results correlate with the curve quite well, although the sub-millimeter SiC particle impact data do not agree at all. Generally one can assume that for hypervelocity impacts for particles greater than 1 mm in diameter, the crater hole size produced will be about 2.7 × the projectile diameter. Below this threshold, it would appear that the hole diameter can be taken as equal to the particle diameter.

UTIAS HVI Program
Crater vs. Projectile Diameter

Legend:
▽ Auburn GRE (SiC) ▼ Auburn PEEK (SiC) ■ JSC PEEK (Al)
● SwRI PEEK (Al) ○ USAF #1 PEEK (Al/Nylon) □ Austin GRE (Al)
▲ Eagle GRE (Low E & Al) —— Regression

$$D_c = 2.67\, D_p$$
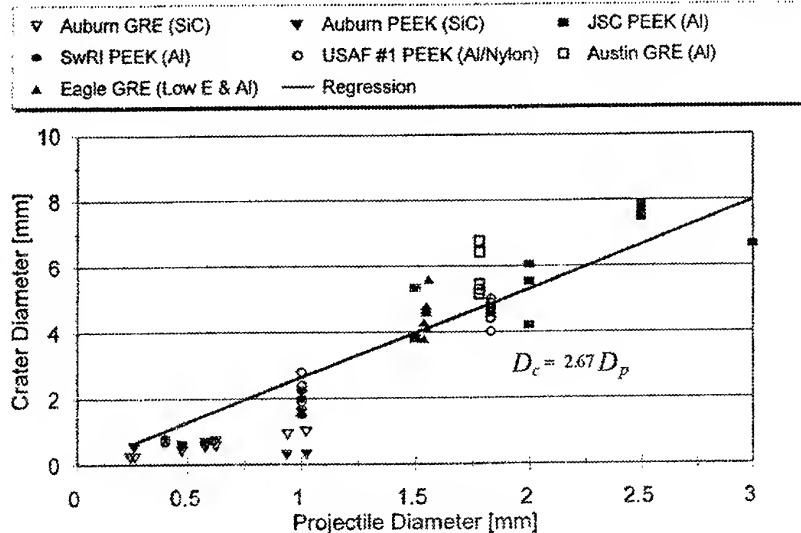
FIGURE 5

UTIAS HVI Program
Debris Cone Angle vs. $\sqrt[3]{E\,\dfrac{t}{D_p}}$

Legend:
■ JSC PEEK (Al) ● SwRI PEEK (Al) —— Regression

Cone angle = 11.6°

x-axis: $\sqrt[3]{E\,\dfrac{t}{D_p}}$ [√J]
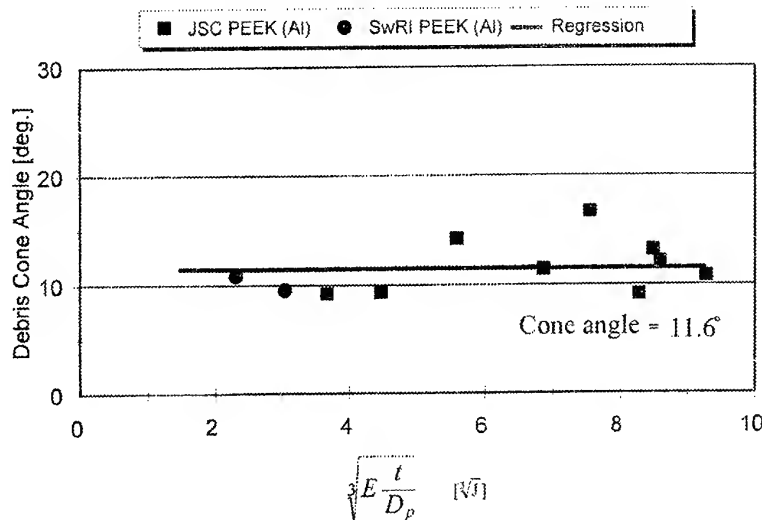
FIGURE 6

Considerable effort was made to investigate the debris plume size and corresponding damage to the rear wall. For tube structures, this of course represents the interior of the back wall opposing the impact damage site. The debris plume is composed of impactor fracture particles and delaminated spallation particles. Based on detailed mapping of the debris impact sites, the primary debris plume cone angle was measured. These results are plotted in Figure 6 and demonstrate a consistent angle of about 11.6°.

Thus, knowing the cylinder diameter or separation distance between the front and rear faces of the structure, one can readily calculate the damage zone diameter due to impact ejecta for these composite materials. This information is critical in assessing the structural damage due to local fracture and penetration of the composite and the resulting loss in stiffness.

For example, using the separation distance for these tests, a plot of the 87 craters observed on the rear face showed the pattern 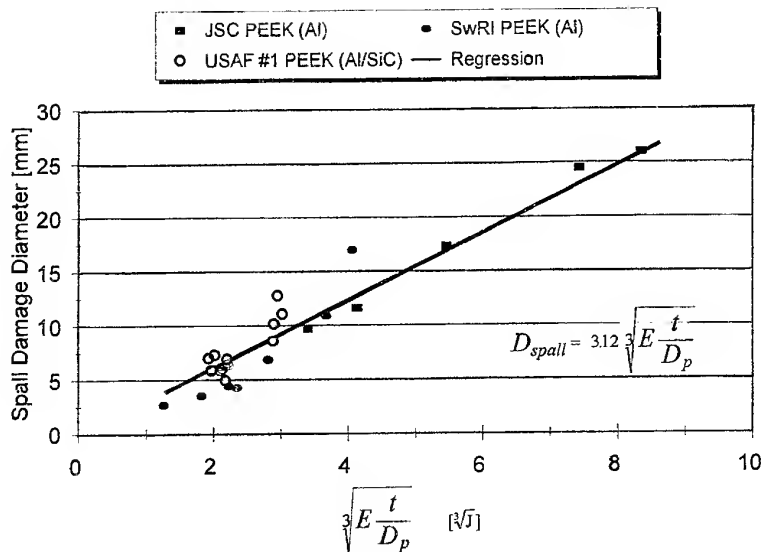illustrated in Figure 7. The radius of influence was measured at about 60 mm and if one assumes this is equivalent to a 60 mm cutout, then a substantial reduction in strength and stiffness would result for a 330 mm diameter cylinder. Although the pattern is composed of 87 distinct holes (most of them represent through - thickness penetrations), one would assume that cracks would eventually

emanate from these holes and link up to form a cutout. This is quite probable in the space environment where thermal cycling is occurring every orbit.

UTIAS HVI Program
JSC #9 Secondary Debris Impact Sites

Cone angle = 11.6° $r_{influence} \approx 60\,mm$
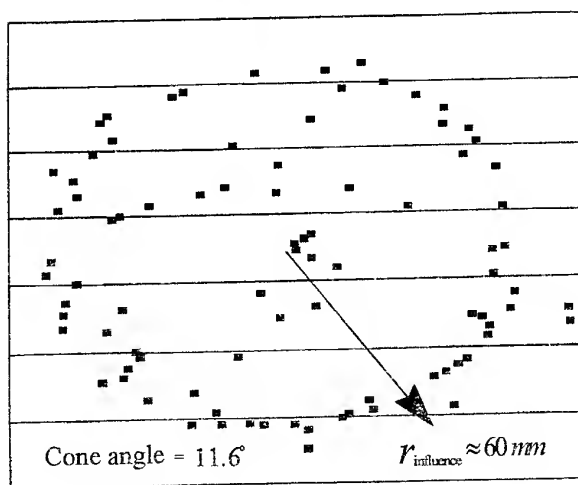
87 distinct craters catalogued

FIGURE 7

CONCLUSIONS

The following conclusions relate specifically to graphite/PEEK laminates, although evidence showing good correlations with graphite/epoxy materials was also exhibited.

Impact damage was found to correlate with the energy parameter described by Christiansen [2]. In general, one can assume that the entry damage (i.e., equivalent circular diameter) can be equal to about 12 times the projectile diameter for particles greater than 1 mm in size. This damage zone extends in the form of delamination through the top layers of the laminate, and is of comparable size on the back face as spallation damage. It would appear that these results are independent of laminate configuration .

The primary debris plume produced by hypervelocity impact is characterized by a cone angle of approximately 11.6°. The ejecta thus formed can impact rear wall laminates with sufficient energy to penetrate the structure and produce the equivalent of a large diameter cutout. This can lead to significant reductions in structural stiffness and strength. Even if penetration does not occur, subsequent cracking of the laminate is possible.

REFERENCES

[1]   Yew, C. H.,Yang, C. Y., and Crews, J., "A Phenomenological Study of the Effect of Hypervelocity Impacts on Graphite-Epoxy Plates", Engineering Mechanics, University of Texas at Austin and NASA JSC, 1986.

[2]   Christiansen, E. L.,"Investigation of Hypervelocity Impact Damage to Space Station Truss Tubes", Journal of Impact Engineering, Vol. 10, 1990

[3]   Tennyson, R. C., "Debris and Micrometeoroid Impact Damage on Spacecraft Materials and Structures", Final Report, Canadian Space Agency, Contract No. 9F011-3-1372/01-XSD, March 1994.

ACKNOWLEDGEMENTS

LOAD INTRODUCTION ASPECTS
IN SANDWICH PANELS WITH HARD POINTS

O. T. THOMSEN

Institute of Mechanical Engineering, Aalborg University
Pontoppidanstræde 101, DK-9220 Aalborg East, Denmark

ABSTRACT

A higher-order sandwich plate theory is introduced. The theory includes separate descriptions of the face-plates and the core material, and general specification of loads and boundary conditions. The theory has been adapted especially for the purpose of studying sandwich panels hard points in the form of 'through-the-thickness' inserts, and the resulting sets of partial differential equations are solved numerically using a direct integration scheme. An example of non-axisymmetric loading is analysed, and a few guidelines for design are given.

INTRODUCTION

Structural sandwich elements with metal or FRP face-plates and polymeric foam, Nomex or aluminium honeycomb cores are used extensively for lightweight spacecraft, aircraft and marine structures. The introduction of loads into such structural elements is often accomplished using inserts, which may be of the through-the-thickness, fully potted or partially potted types as illustrated in Fig. 1.
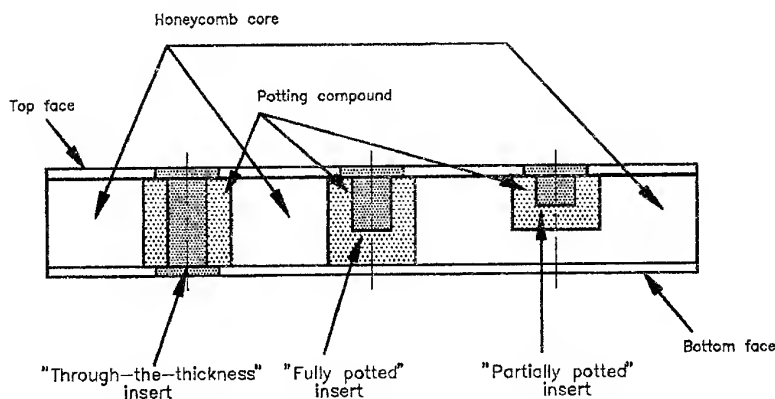
Figure 1. Insert types typically used for sandwich panels.

For all insert types, the ideal load transfer mechanism is disturbed in the regions close to the inserts, where severe local bending effects are present. This results in severe local stress concentrations in the face-plates, in the core material and in the interfaces between the face-plates and the core. This can lead to a premature failure, as sandwich panels with transversely flexible cores are susceptible to failure due to local stress concentrations. The local bending effects causing such structural failures cannot be accounted for using classical 'antiplane' sandwich plate theories summed up in Plantema [1], Allen [2], as such theories do not include the transverse flexibility of the core material. The importance of including the transverse flexibility of the core when addressing load introduction problems, support problems, and problems involving material and geometric discontinuities in sandwich beams was pointed out by Frostig and Baruch [3], Frostig [4] and Frostig and Shenhar [5]. This was done by

539

formulating a high-order sandwich beam theory, which includes separate description of each face and separate description of the core material. The core material is modelled as a special type of transversely isotropic solid where only the out-of-plane stiffness is accounted for.

The present paper addresses the problem of analysis of sandwich plates with inserts of the 'through-the-thickness' type (see Fig. 1). The problem is formulated by adapting and extending the principles behind the sandwich theory developed for sandwich beams in refs. [3]-[5] to circular sandwich plates. Full details about the mathematical formulation can be found in Thomsen [6] for sandwich plates with 'through-the-thickness' inserts, and in Thomsen [7] for sandwich plates with 'fully potted' inserts.

FORMULATION

In the modelling of the insert/sandwich plate system it is assumed that the interaction between adjacent inserts, as well as the interaction between the considered insert and the plate boundaries or other sources of local disturbances, can be ignored. Fig. 2 defines the constituent parts, the geometry as well as the possible external load cases. The sharp separation between the potting and the core (honeycomb) indicated in Fig. 2 is a strong idealisation, as the potting/honeycomb intersection is not defined precisely in a geometrical sense.

Figure 2. Definition of model of sandwich plate with 'through-the-thickness' insert.
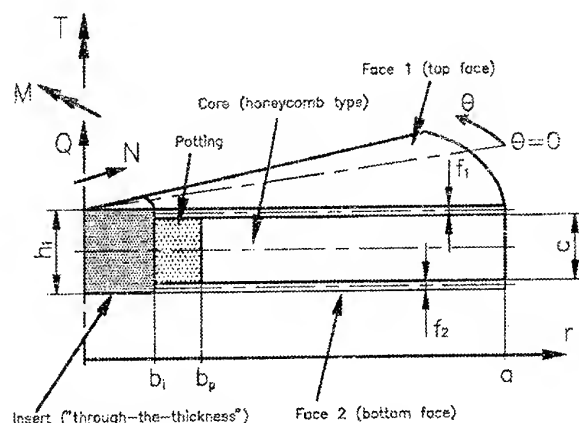
Due the limited space available, the details of the derivations cannot be given here, and instead reference is given to Thomsen [6]. The principles behind the modelling, however, are described briefly in the following. As suggested by Frostig et al. [3]-[5], the core material is described as a special type of transversely isotropic solid where only the 'through-the-thickness' stiffness is accounted for. Setting up the equilibrium conditions, and using the kinematic and constitutive relations for the core yields a set of equations describing the complete core stress and displacement fields in terms of the transverse core coordinate z_c (z_c is measured from the core middle surface) [6], [7]

$$\tau_{rz}(r,\theta,z_c) = \tau_{rz}(r,\theta), \quad \tau_{\theta z}(r,\theta,z_c) = \tau_{\theta z}(r,\theta)$$

$$\sigma_c(r,\theta,z_c) = \frac{E_c}{c}\{w^1 - w^2\} - \left\{\tau_{rz,r} + \frac{1}{r}\tau_{rz} + \frac{1}{r}\tau_{\theta z,\theta}\right\}z_c$$

$$w_c(r,\theta,z_c) = w^1 + \frac{\{w^1 - w^2\}}{c}\left\{z_c - \frac{c}{2}\right\} - \frac{1}{2E_c}\left\{\tau_{rz,r} + \frac{1}{r}\tau_{rz} + \frac{1}{r}\tau_{\theta z,\theta}\right\}\left\{z_c^2 - \frac{c^2}{4}\right\} \qquad (1a\text{-}e)$$

$$u_c(r,\theta,z_c) = u_{0r}^1 + \frac{w_{,r}^1}{2}\left\{t_1 - \frac{z_c^2}{c} - z_c + \frac{3c}{4}\right\} + \frac{w_{,r}^2}{2}\left\{\frac{z_c^2}{c} - z_c + \frac{c}{4}\right\} + \frac{\tau_{rz}}{G_c}\left\{z_c - \frac{c}{2}\right\}$$

$$+ \frac{1}{2E_c}\left\{\tau_{rz,rr} + \frac{1}{r}\tau_{rz,r} - \frac{1}{r^2}\tau_{rz} + \frac{1}{r}\tau_{\theta z,\theta r} - \frac{1}{r^2}\tau_{\theta z,\theta}\right\}\left\{\frac{z_c^3}{c} - \frac{c^2 z_c}{4} + \frac{c^3}{12}\right\}$$

540

$$v_c(r,\theta,z_c) = u_{o\theta}^1 + \frac{w_{,\theta}^1}{2r}\left\{t_1 - \frac{z_c^2}{c} - z_c + \frac{3c}{4}\right\} + \frac{w_{,\theta}^2}{2r}\left\{\frac{z_c^2}{c} - z_c + \frac{c}{4}\right\} + \frac{\tau_{\theta z}}{G_c}\left\{z_c - \frac{c}{2}\right\}$$

$$+ \frac{1}{r2E_c}\left\{\tau_{rz,r\theta} + \frac{1}{r}\tau_{rz,\theta} + \frac{1}{r}\tau_{\theta z,\theta\theta}\right\}\left\{\frac{z_c^3}{c} - \frac{c^2 z_c}{4} + \frac{c^3}{12}\right\}$$

(1f)

In Eqs. (1) E_c, G_c are the core elastic constants, σ_c is the core transverse normal stress, τ_{rz} and $\tau_{\theta z}$ are the core shear stresses, u_c, v_c and w_c are the radial, circumferential and transverse displacement components, $u_{o}^{\,i}$, $u_{o\theta}^{\,i}$ and w^i ($i=1,2$) are the radial, circumferential and transverse displacement components of the top and bottom faces, and r, θ are the radial and circumferential coordinates. Differentiation with respect to a spatial coordinate is denoted by subscript comma.

From Eqs. (1) it is noticed that τ_{rz} and $\tau_{\theta z}$ are constant, that σ_c varies linearly, that w_c varies quadratically and finally that u_c and v_c varies cubically over the thickness of the core. The core material is coupled with the faces by requiring continuity of the displacement and stress fields across the core/face interfaces.

The faces are modelled using classical Kirchhoff theory, where the faces are treated as homogeneous, isotropic and linear elastic. Obviously, this is a simplifying assumption as the faces are made as FRP-laminates in many applications, but the approximation adopted is quite reasonable in reality. This is due to the fact, that strongly orthotropic face-laminates are hardly ever used around inserts or other areas of load introduction. Instead, if the global sandwich structure is made with strongly orthotropic face-laminates, the zones around the inserts will be reinforced locally such that the resulting laminates appear as nearly quasi isotropic.

Formulating the equilibrium, kinematic and constitutive equations for the top and bottom faces and combining those with the 'core equations' (1) and the continuity requirements yields the governing set of partial differential equations. In the formulation, the order of the set of governing equations is 24, and consequently the governing equations can be reduced to 24 first order partial differential equations with 24 unknowns. If the 24 unknowns, henceforth called the fundamental variables, are those quantities that appear in the natural boundary conditions at an edge r=constant, then the boundary value problem can be stated completely in terms of these variables. In the present case, the 24×1 matrix of fundamental variables can be written as

$$\{y(r,\theta)\} = \left\{u_{o}^1, u_{o\theta}^1, w^1, \beta_r^1, \beta_\theta^1, N_r^1, N_{r\theta}^1, M_r^1, M_{r\theta}^1, Q_r^1,\right.$$
$$\left. \tau_{rz}, q_r, \tau_{\theta z}, q_\theta, u_{o}^2, u_{o\theta}^2, w^2, \beta_r^2, \beta_\theta^2, N_r^2, N_{r\theta}^2, M_r^2, M_{r\theta}^2, Q_r^2\right\}$$

(2)

where β_r^i, β_θ^i are the midsurface rotations, N_r^i, $N_{r\theta}^i$ are the face in-plane stress resultants, M_r^i, $M_{r\theta}^i$ are the face moment resultants, and Q_r^i are the face radial transverse shear stress resultants ($i=1,2$). In Eq. (2) two new 'core variables' q_r, q_θ have been introduced

$$q_r(r,\theta) = \tau_{rz,r}, \quad q_\theta(r,\theta) = \tau_{\theta z,r}$$

(3)

Adopting the matrix of fundamental variables $\{y(r,\theta)\}$, the governing equations can be reduced to the form

$$\{y(r,\theta)\}_{,r} = \Psi\left(r,\theta,\{y\},\{y\}_{,\theta},\{y\}_{,\theta\theta},\ldots\right)$$

(4)

where Ψ denotes 24 linear functions in $\{y(r,\theta)\}$ and its derivatives with respect to θ. The dependency of the θ-coordinate is eliminated by Fourier-series expansion of the fundamental variables thus reducing the problem to a set of 24 first order ordinary differential equations.

The statement of the boundary conditions is based on the following assumptions (see Fig.2)

- $r=b$: The 'through-the-thickness' insert is considered as an infinitely rigid body to which, the sandwich faces and the potting material are rigidly connected.

541

- $r=a$: It is assumed that the face-plate and honeycomb core midsurfaces are simply supported.

The resulting boundary value problem is solved numerically using the 'multisegment method of integration'. The method is based on a transformation of the boundary value problem into a series of interconnected initial value problems. The insert/sandwich plate configuration is divided into a finite number of segments, and the solution within each segment is derived by direct integration. Continuity of the solution vectors across the separation points between the segments, as well as fulfilment of the boundary conditions is ensured by formulating and solving a set of linear algebraic equations. The implementation of the numerical solution scheme was accomplished using a UNIX-version of MATLAB®, version 4.1, installed on a HP9000/700 workstation. Reference is made to [6], [7] for detailed information about the numerical solution scheme.

EXAMPLE

To demonstrate the capabilities of the developed higher-order sandwich plate theory, an example of a circular sandwich plate with a 'through-the-thickness' insert is given. It is assumed, that the insert is subjected to an external bending moment M (non-axisymmetric load case), and that the sandwich plate is characterised by having identical faces. M is imposed by rotating the 'though-the-thickness' insert as a rigid body about the core midsurface. The external bending moment load case is highly realistic even though it is generally recommended to avoid this load type through proper design (using groups of inserts instead of just one insert). The geometry, material and external load data are (see Fig. 2)

Geometry:	$b_i=10$ mm, $b_p=30$ mm, $a=150$ mm, $c=10$ mm, $f_1=f_2=1$ mm.
Top face:	Quasi-isotropic FRP-laminate with properties $E_{fl}=40$ GPa, $v_{fl}=0.3$.
Bottom face:	As top face, i.e. $E_{fl}=E_{fl}$, $v_{fl}=v_{fl}$.
Potting compound:	Bulk epoxy, $E_p=2.5$ GPa, $G_p=0.93$ GPa.
Honeycomb core:	Hexcel honeycomb $3/16"$-5056-$0.0007"$, $E_h=310$ MPa, $G_h\approx(G_w+G_L)/2=138$ MPa.
External load:	$M=25$ Nm (non-axisymmetric load).

For further examples involving other types of external loading (Q, T and N load cases, see Fig. 2) reference is made to [6]. Examples involving 'fully potted' inserts (see Fig. 1) can be found in [7].

Fig. 3 shows w^1, w^2 and $w_c(midsurface)=w_c(z_c=0)$ along $\theta=0$ (varies as $cos(\theta)$, see Fig. 2). The lateral deflections w^1 and w^2 of the two face-plates, as well as the lateral deflection of the core midsurface $w_c(z_c=0)$, are slightly different from each other (except at $r=b_i=10$ mm and $r=a=150$ mm due to the imposed boundary conditions). A characteristic feature of the results shown in Fig. 3 is the abrupt change of 'slope', which is seen around $r=b_p=30$ mm, i.e. at the potting/honeycomb intersection. The reason for this abrupt change of 'slope' is the significant change of core stiffness at this location.

Fig. 4 shows a surface plot of the deflectional response of the top face-plate of the insert/sandwich plate system. The deformed face-plate is symmetric about $\theta=0$ ($\theta=0$ is coincident with the x-axis in Fig. 4), and therefore only one half of the deformed face-plate is shown. The central part of the deformed top face-plate, extending from $(x,y)=(0,0)$ to $r=(x^2+y^2)=b_i=10$ mm in all directions corresponds to the rigid 'through-the-thickness' insert.

Fig. 5 shows the distribution of stresses in the core material (potting and honeycomb). Four stress components are shown; σ_c^{top}, σ_c^{bottom} and τ_{rz}, which are given along $\theta=0$ (they vary as $cos(\theta)$), and $\tau_{\theta z}$, which is given along $\theta=\pi/2$ (varies as $sin(\theta)$). It is seen, that significant peaks of the transverse normal stresses σ_c^{top}, σ_c^{bottom} are present close to the insert ($r=b_i$) and around the potting/honeycomb intersection ($r=b_p$). It is further seen, that σ_c^{top} and σ_c^{bottom} have opposite signs, i.e. when σ_c^{top} is tensile σ_c^{bottom} is compressive, and vice versa. It should be noted that the absolute values of σ_c^{top} and σ_c^{bottom} are not the same. The reason for this 'asymmetric' behaviour is, that the stress states in the two face-plates are not identical, thus causing an 'asymmetric' core stress distribution to appear. The presence of $\tau_{\theta z}$ is a consequence of the non-axisymmetric nature of the M load case. It is observed, that $\tau_{\theta z}$ builds up and attains its peak value approximately in the middle of the potting (at $r\approx 20$ mm). It should be noted, that σ_c^{top}, σ_c^{bottom} and τ_{rz} attain their peaks along $\theta=0$ and $\theta=\pi$, whereas $\tau_{\theta z}$ attains its peak values for $\theta=\pi/2$ and $\theta=3\pi/2$. It is therefore concluded, that the peaks of σ_c^{top}, σ_c^{bottom} and τ_{rz} do never occur at the same

locations as the peaks of $\tau_{\theta z}$. Considering the combined influence of the transverse normal and the shear stress components on the potting and honeycomb materials it should be remembered, that the mechanical properties of the two materials are very different, ESA [8]. Thus, the stiffness and strength properties of the honeycomb material are usually an order of magnitude lower than those of the potting. Recalling from Fig. 5, that the magnitude of the peak stresses in the potting and honeycomb regions are of about the same magnitude it is then seen, that a 'weak spot' of the insert/sandwich plate system is located at the position of the potting/honeycomb intersection (at $r=b_p$) as well as a short distance into the honeycomb material. This observation complies well with practical experience, as the stress concentrations encountered at the potting/honeycomb intersection (and immediately after that) often turn out to be the cause of structural failure [8] (usually transverse shear failure of honeycomb [8]).
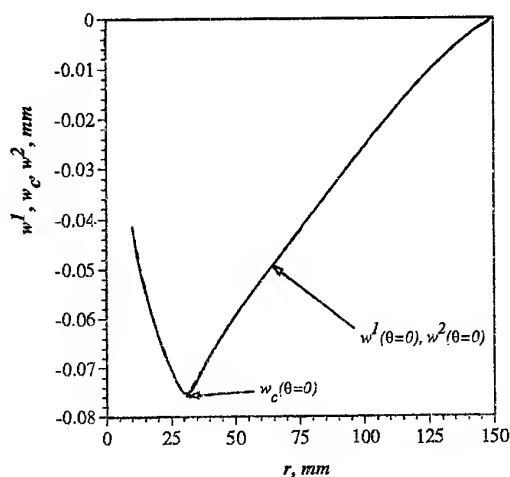
Figure 3. Lateral displacements $w^1(\theta=0)$, $w^2(\theta=0)$, $w_c(z_c=0,\theta=0)$.
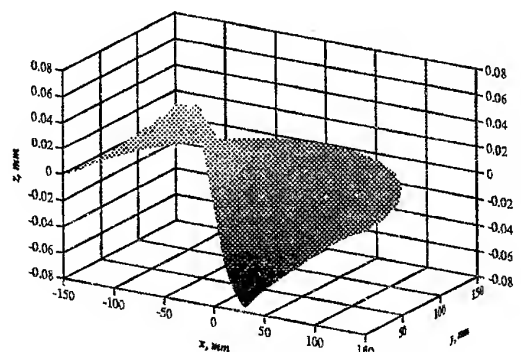
Figure 4. Surface plot of the deformed top face-plate (one half shown).
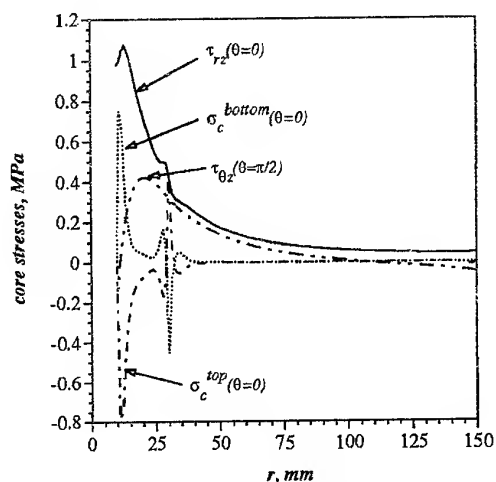
Figure 5. Core stress components $\sigma_c^{top}(\theta=0)$, $\sigma_c^{bottom}(\theta=0)$, $\tau_{rz}(\theta=0)$, $\tau_{\theta z}(\theta=\pi/2)$.
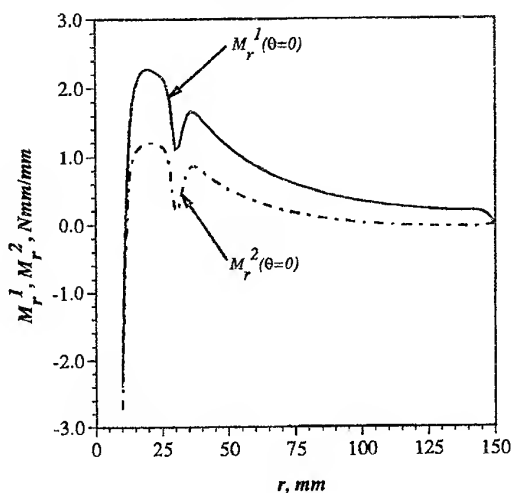
Figure 6. Radial bending moment resultants $M_r^1(\theta=0)$, $M_r^2(\theta=0)$.

Fig. 6 shows the radial bending moment resultants M_r^1, M_r^2 along $\theta=0$ (M_r^1, M_r^2 vary as $cos(\theta)$). From Fig. 6 it is seen, that the magnitudes of the bending moment resultants in the two face-plates are dissimilar. Around the potting/honeycomb intersection at $r=b_p=30$ mm a characteristic 'disturbance' of the M_r^1-distributions is seen. Comparing Figs. 5 and 6 it should be recognised, that the potting compound plays an important 'structural' role in the overall load transfer around the insert. Thus, the

presence of a potting material, which is significantly stiffer than the honeycomb core, causes a considerable relief of the peak bending (and shear) stresses in the face-plates close to the insert. In other words, the potting compound acts as an 'attractor' on the transverse loads to be transferred through the insert, thereby relieving the stress concentrations in the face-plates.

No further results will be given here, and instead reference is given to [6] and [7] for further details.

DESIGN CONSIDERATIONS AND CONCLUSIONS

Based on the results presented herein, as well as the results of extensive parametric studies [6], [7], a set of guide-lines for the design of sandwich plates with 'through-the-thickness' inserts can be specified

- If possible, the radial extension of the potting compound (b_p-b_i, see Fig. 2) should be about $0.5b_i$. This will ensure utilisation of the full shear stress transfer capability of the potting, while ensuring maximum relief of the face-sheet bending and shear stress concentrations at the same time.
- If possible, the ratio of the potting stiffness to the honeycomb stiffness E_p/E_h, should be chosen to $E_p/E_h \approx 3$-4. This will ensure a good compromise between the peak stress level in the face-sheets and in the potting and honeycomb materials.
- The external bending moment load case (results presented in this paper) should generally be avoided. This can be achieved by application of the loads through groups of inserts thus converting the bending loading to out-of-plane loads on the inserts.
- As significant stress concentrations in especially the potting and the adhesive bond lines cannot be avoided, the materials chosen for the potting and adhesive bonds should possess long elongation to failure capability.

The design guidelines listed above agrees well with the recommendations specified in for instance the ESA Insert Design Handbook [8]. However, the guidelines presented herein presents a much more detailed insight into the structural response of sandwich plates with 'through-the-thickness' inserts.

ACKNOWLEDGEMENT

REFERENCES

[1]   Plantema, F. J. 'Sandwich Construction'. John Wiley & Sons, New York, 1966.

[2]   Allen, H. G. 'Analysis and Design of Structural Sandwich Panels'. Pergamon Press, Oxford, 1969.

[3]   Frostig, Y. and Baruch, M. 'Bending of Sandwich Beams with Transversely Flexible Core', AIAA Journal **28**, pp. 523-531, 1990.

[4]   Frostig, Y. 'On Stress Concentration in the Bending of Sandwich Beams with Transversely Flexible Core'. Composite Structures **24**, pp. 161-169, 1993.

[5]   Frostig, Y. and Shenhar, Y. 'High-Order Bending of Sandwich Beams with a Transversely Flexible Core and Unsymmetrical Laminated Composite Skins'. Composites Engineering **5**, pp. 405-414, 1995.

[6]   Thomsen, O. T. 'Analysis of Sandwich Plates with Through-the-Thickness Inserts Using a Higher-Order Sandwich Plate Theory', ESA/ESTEC Report EWP-1807, 130 pages, 1994.

[7]   Thomsen, O. T., 'Analysis of Sandwich Plates with Fully Potted Inserts Using a Higher-Order Sandwich Plate Theory', ESA/ESTEC Report EWP-1827, 78 pages, 1995.

[8]   'Insert Design Handbook', ESA PSS-03-1202, Issue 1, 1987.

EXPERIMENTAL VALIDATION OF FEM CURE ANALYSIS SOFTWARE

L. Tredoux[1] and J. van der Westhuizen[2]

[1] Tokyo Institute of Technology, Japan (Previously Department of Mechanical Engineering, University of Stellenbosch, SA); tredouxl@mep5.mep.titech.ac.jp.
[2] Department of Mechanical Engineering, University of Stellenbosch, Private Bag X1, Matieland, South Africa; SIAS@sunvax.sun.ac.za.

INTRODUCTION

Numerical modelling of the cure process of composite materials provides the engineer with a powerful tool for customizing cure cycles to ensure fully cured components in the shortest possible time without excessive exotherms taking place. Curing of thermoset composites is a complex process and industry relies heavily on recommended cure cycles from raw material suppliers. However, because the supplier has no knowledge of the component and tooling geometry, he can only supply guidelines. These are often unnecessarily conservative and costly and there is no guarantee that the part will be uniformly and fully cured.

The equation governing the heat transfer process in the curing composite material is well established. For the two-dimensional case, and with the coordinate axes aligned with the principle material axes, it has the form

$$\frac{\partial}{\partial x}\left[K_x \frac{\partial T}{\partial x}\right] + \frac{\partial}{\partial z}\left[K_z \frac{\partial T}{\partial z}\right] + \rho H_R \frac{d\alpha}{dt} = \rho c \frac{\partial T}{\partial t}. \tag{1}$$

In this equation T denotes the absolute temperature, K_x and K_z are the orthotropic heat transfer coefficients for the composite, ρ is the composite density and H_R is the *heat of reaction*. The extent of the chemical cure reaction, or *degree of cure*, is denoted by α and varies from 0 (uncured) to 1 (fully cured). The rate at which the cure reaction is taking place, also referred to as the *cure rate*, is expressed through $d\alpha/dt$.

This paper summarizes the results of an experimental validation project for the software code CURE. Program CURE is a specially tailored version of the code FCURE that was originally developed by the composite materials group at the University of Stellenbosch [1]. It is a two-dimensional finite element program that solves the partial differential equation (1) and calculates the temperature and the degree of cure distribution in a composite as a function of time. CURE is written in FORTRAN and runs on a PC in a WINDOWS environment. The program makes provision for temperature, heat flux and convection boundary conditions. The code is structured in such a way that material properties are assigned on an element-by-element basis. This makes it easy to model laminates and tooling with different material properties.

All experimental work was conducted at the composites facilities of AEROTEK, CSIR (Council for Scientific and Industrial Research), Pretoria, South Africa.

EXPERIMENTAL PROCEDURE

Hexcel F155 UD glass prepreg and Fibertek FT102 UD carbon prepreg laminates were manufactured with thermocouples imbedded in them and cured in an autoclave. Thermocouple temperatures were recorded and compared with the simulation values of program CURE for validation purposes.

The laminates were 100 mm square and three thicknesses were evaluated, namely 3.5 mm, 10 mm and 20 mm. The autoclave pressure was 6 bar for all experiments and the vacuum port was vented to atmosphere when the applied pressure reached 100 kPa. A typical experimental lay-up is shown schematically in *Figure 1*.
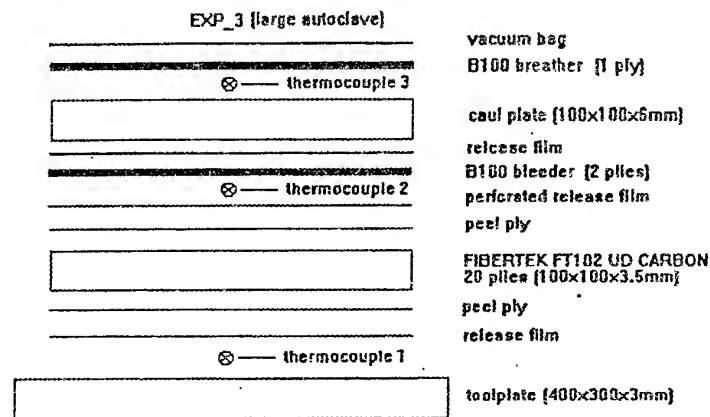
Figure 1   A typical experimental assembly

VALIDATION SIMULATIONS

One- and two-dimensional finite element models were generated to simulate the experiments. The methodology is straight-forward, except for the cure related input data that is discussed in the rest of this section.

In general the input data for program CURE consists of the following:
- tooling and lay-up geometry,
- the toolplate density, heat conduction coefficient and specific heat capacity,
- the breather cloth density, heat conduction coefficient and specific heat capacity,
- the resin/fibre mix density, heat conduction coefficient and specific heat capacity,
- the relationship between cure rate, degree of cure and temperature of the resin/fibre mix,
- the total heat of reaction of the resin/fibre mix,
- the convection heat transfer coefficient between the lay-up and the autoclave air.

The cure-related part of the input data was generated as follows:-

Tooling Properties:
> The bleeder, breather, toolplate and caulplate were included in the analysis. The thermal properties of these were readily obtained from suppliers. Peel ply and release film are both very thin and their effect on the heat transfer process was neglected.

Resin/fibre mix Properties:
> The density, heat conduction coefficient and the heat capacity were assumed to be independent of temperature and degree of cure. Values for these properties were readily obtained from the suppliers and the literature [2] through [5]. The heat of reaction, as well as the relationship between cure rate, degree of cure and temperature were determined experimentally using a Polymer Laboratories DSC machine. Refer to references [6] through [11] for the proper methodology and procedures. (The results were incorporated in program CURE as a numerical matrix.)

Convection Coefficient:
> The convection coefficient was estimated by making a dummy lay-up with a 6 mm aluminium plate and then "curing" the lay-up in the autoclave. The convection coefficient was quantified by matching the predicted aluminium plate temperature for different (guessed) convection coefficients with the actual measured plate temperature.

RESULTS AND DISCUSSION

FT102 20 ply 3.5 mm laminate: The results are reasonably accurate as shown in *Graph 1*. No noticeable exotherm is present due to the relatively thin laminate.

FT102 60 ply 10 mm laminate: The peak temperature and the time at which it occurs are very accurately predicted as demonstrated with *Graph 2* and *Graph 3*. The initial heat-up phase shows less agreement. During the remainder of the cycle the predicted laminate temperature is on average 3 °C too high with the modelling results becoming more accurate as the cure cycle progresses. Noticeable two dimensional effects were found when comparing the 1D and 2D fem simulation results. The 1D model was less accurate with a lower (and delayed) predicted peak temperature.

FT102 120 ply 20 mm laminate: The value of the peak temperature and the time at which it occurs is fairly accurately predicted, especially at the centre of the laminate. The initial heat-up phase is again underestimated by the model, especially at the top of the laminate.

Hexcel F155 20 ply 3.5 mm laminate: The results are similar to that of the FT102 experiment, but with slightly worse correlation between experimental and predicted values.

Dynamic scans were performed on samples of the laminates cured in the experiments. No residual heat of reaction was observed indicating a complete cure in all cases.

CONCLUSIONS

The experimental data agreed reasonably well with the numerical predictions and lead to the following specific conclusions:

- The estimates for composite thermal properties that are available in the literature are accurate enough for practical cure modelling.
- An average value for the heat convection coefficient can be estimated relatively easily and used successfully for autoclave cure modelling.
- Cure modelling yields accurate results (peak temperature in the centre of a 20 mm thick laminate within 5%) and is therefore useful for cure process optimization.

ACKNOWLEDGEMENTS

REFERENCES

[1] Tredoux, L. and Van der Westhuizen, J., "Development of a numerical code that simulates combined heat transfer, resin flow and compaction during composites processing", *Composites Processing* 6(2), pp. 85-92 (1995).

[2] HEXCEL data sheet for F155 prepreg.

[3] Quin, F.A. (Compiler), "Design Data-Fibreglass Composites", Fibreglass Limited, England.

[4] Chamis, C.C., "Simplified composite michromechanics equations for hygral thermal and mechanical properties", *38th Annual Conference, Reinforced Plastics/Composites Institute, The Society of the Plastics Industry, Inc.*, February 7-11, 1983.

[5] Mijovic, J. and Wang, H.T., "Modeling of Processing of Composites Part II - Temperature distribution during cure", *SAMPE Journal*, March/April 1988.

[6] Barton, J.M., "The Application of Differential Scanning Calirometry (DSC) to the Study of Epoxy Resin Curing Reactions", *Advances in Polymer Science* 72, pp. 111-117 (1985).

[7] Lee, W.I., Loos, A.C. and Springer, G.S., "Heat of Reaction, Degree of Cure, and Viscosity of Reaction of Hercules 3501-6 Resin", *Journal of Composite Materials* 16, pp. 510-520 (1982).

[8] Dusi, M.R., Lee, W.I., Ciriscioli, P.R. and Springer, G.S., "Cure Kinetics and Viscosity of Fiberite 976 Resin", *Journal of Composite Materials* 21, pp. 243-261 (1987).

[9] Sichina, W.J., "Autocatalyzed Epoxy Cure Prediction using Isothermal DSC Kinetics", *Thermal Analysis Application Brief - Du Pont Number TA-93*, Du Pont Company, Delaware.

[10] Thomas, L.C., "Interpreting Unexpected Events and Transitions in DSC Results", TA Instruments Inc.

[11] Gill, P.S., "Thermal Analysis of Epoxy-Glass Prepreg Materials", *Thermal Analysis Application Brief - Du Pont*, Du Pont Company, Delaware.

GRAPHS

GRAPH 1
FT 102 UDC 3.5 mm

Legend: air, bottom (exp), top (exp), bottom (Cure), top (Cure)

GRAPH 2
FT 102 UDC 10 mm

Legend: air, centre (exp), centre (Cure)

GRAPH 3

FT 102 UDC 10 mm

Legend:
— air
◆ top (exp)
△ top (Cure)

GRAPH 4

FT 102 UDC 20 mm

Legend:
— air
◆ centre (exp)
△ centre (Cure)

550
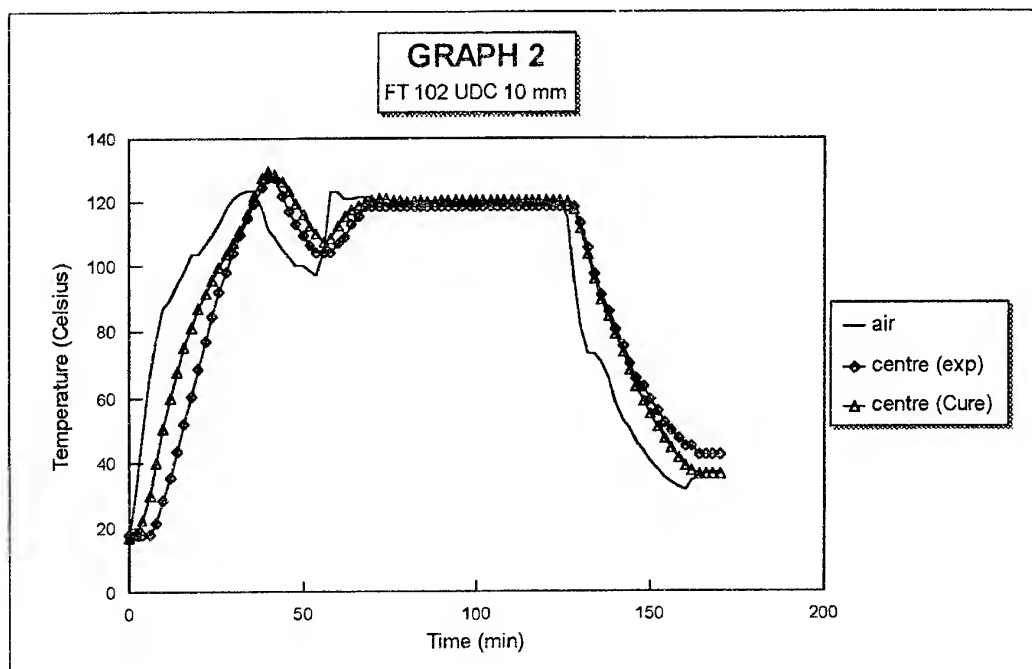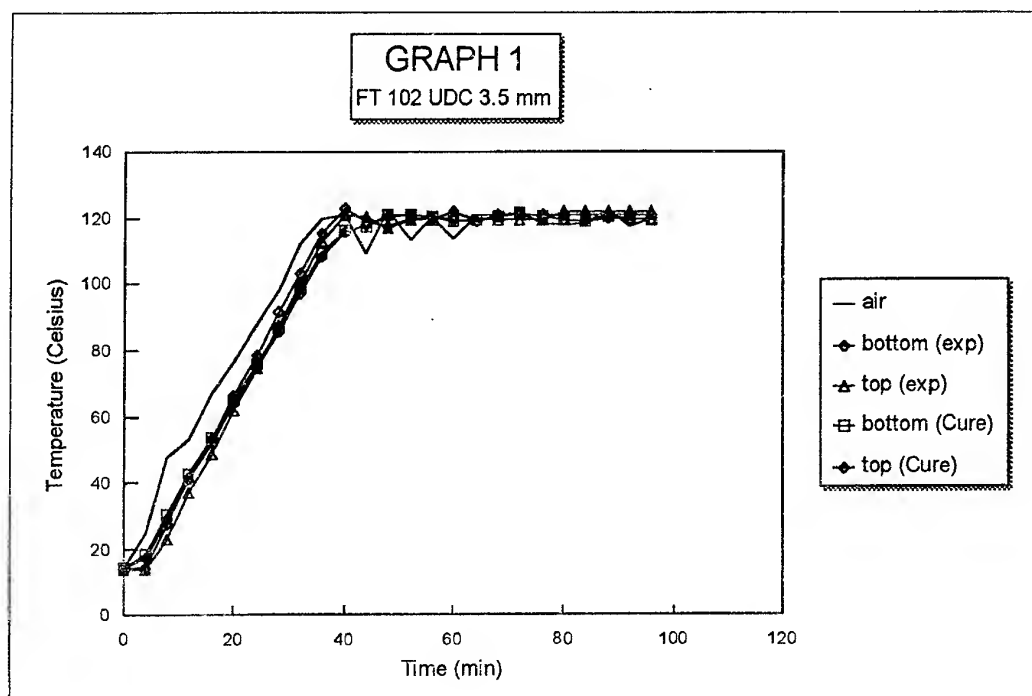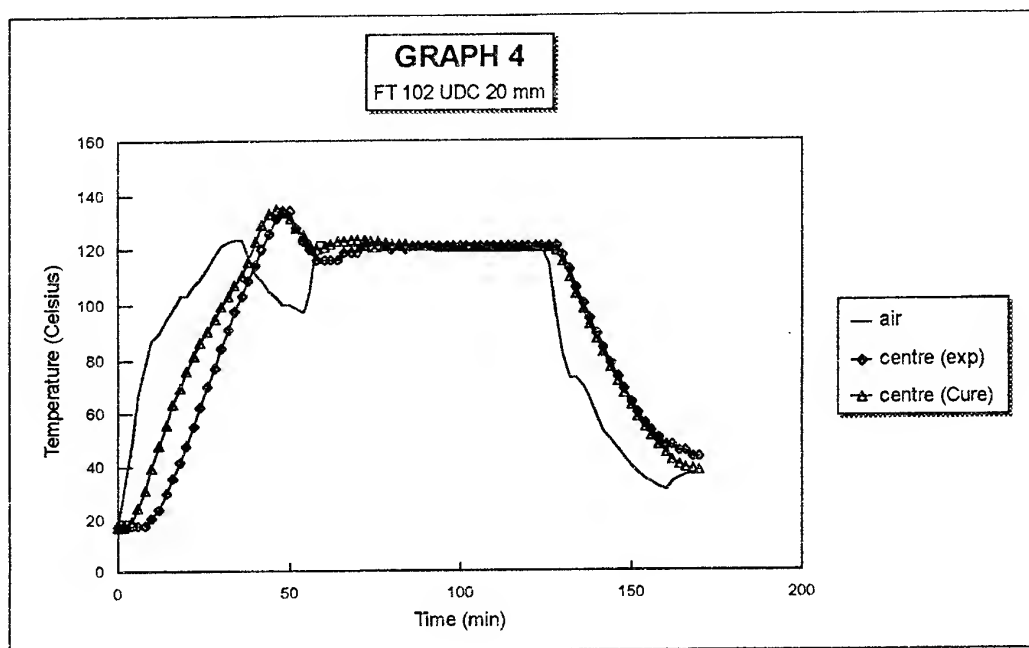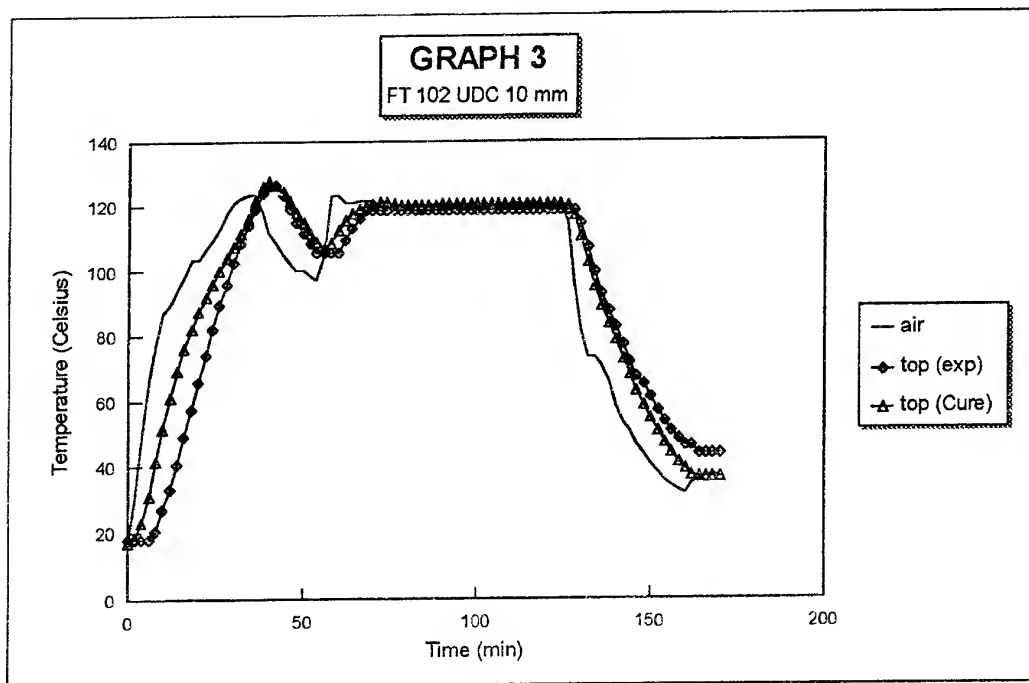
WETTABILITY OF SURFACE FLUORINATED POLYPROPYLENE FIBRES AND ITS EFFECT ON INTERFACIAL BONDING WITH CEMENTITIOUS MATRIX

L. Tu, D. Kruger
Rand Afrikaans University
PO Box 524 Auckland Park
Johannesburg 2006
Republic of South Africa

J.B. Wagener
Atomic Energy Corporation
of South Africa Limited
PO Box 582 Pretoria 0001
Republic of South Africa

ABSTRACT

The surface of high molecular weight polypropylene monofilament fibre was modified using a direct fluorination method. The fluorination treatment level was varied, and a proprietary post-treatment was applied in order to optimize the surface modification process. Contact angles of fluorinated fibres were obtained by dynamic contact angle (DCA) measurement using three liquids of known dispersion, acid and base surface free energy components. The surface free energies were then calculated according to the acid-base theory developed by Good, van Oss and Chaudhury. Surface fluorination largely increased the acid and base components of the fibres' surface free energy compared with unfluorinated polypropylene fibres. The fluorinated and unfluorinated polypropylene fibre surfaces were observed by Scanning Electronic Microscopy. It was found the surface fluorination greatly increases the roughness of the polypropylene surfaces. The interfacial shear bond strengths between the cementitious matrix and the polypropylene fibres treated under various conditions were determined by embedded fibre pull-out tests. Results showed that the fibre surface fluorination treatments increase the interfacial bond strengths. The relationships between the shear bond strength and surface free energy components were correlated.

INTRODUCTION

The interfacial bonding between the fibre and matrix has a key effect on the mechanical performance of all fibrous composites. Strong fibre/matrix interfacial bonding arises from high wetting of the fibres, mechanical interlocking and formation of strong bonds between the fibre and matrix. In order to truly understand the nature of interfacial interactions, it is necessary to separate and measure the individual physical and chemical forces leading to fibre/matrix bondings [1]. Although polypropylene (PP) fibres have been used in concrete for nearly 30 years to increase the impact resistance, plastic and drying shrinkage cracking resistance and failure strain capacity [2,3,4], the bonding between the PP fibres and cementitious matrix is widely accepted as poor because of the low wettability of PP fibres which arises from the hydrophobic surface nature of polypropylene due to its extremely low acid and base surface free energy components [5,6]. The shear bond strengths between the fibres and the cementitious matrices, which varies from 0.3 to 1.0 MPa for fibrillated PP fibres, are much lower compared with the tensile strengths of cementitious matrices which range from 3 to 4 MPa [2,3,7]. Thus, in order to exploit the reinforcing potential of PP

fibres in concrete, further improvement in interfacial bonding is needed. Various PP fibres with different profiles have been extensively developed to introduce mechanical bonding or interlocking while pure chemical surface modification of PP fibres for use in concrete has not been reported yet. The purpose of this investigation is to develop surface modified PP fibres with enhanced fibre/concrete interfacial bonding.

THEORETICAL BACKGROUND
1. DIRECT FLUORINATION OF POLYPROPYLENE

The reaction between fluorine and hydrocarbons is very rapid and exothermic, oftern leading to combustion [8]. One way to overcome this problem is to dilute the fluorine with an inert gas [8,9]. In this investigation, the polypropylene (PP) fibres were surface fluorinated using a F_2/N_2 gas mixture at room temperature. The partial fluorination causes H-atoms adjacent to F-atoms on the polymer chain to become Lewis acidic, due to the high electronegativity of fluorine.

2. THE ACID-BASE INTERACTION CONCEPT

The surface free energy γ_i of a condensed phase i can be devided into two components according to the different forces involved in molecular interactions [1], according to the equation: $\gamma_i = \gamma_i^{LW} + \gamma_i^{AB}$, where γ_i^{LW} refers to the dispersive (Lifshitz-van der Waals) interaction and γ_i^{AB} to the acid-base interaction (including hydrogen bonding).

Good et al. [6] developed the following general equation which relates the contact angle of a liquid on a solid to the surface free energy components as follows:

$$\gamma_l(1+\cos\theta)=2(\sqrt{\gamma_s^{LW}\gamma_l^{LW}}+\sqrt{\gamma_s^{\oplus}\gamma_l^{\ominus}}+\sqrt{\gamma_s^{\ominus}\gamma_l^{\oplus}})$$

$\gamma_i^{\oplus}$ and $\gamma_i^{\ominus}$ are two additional parameters related to the surface acidity and basicity respectively. If three liquids (one non-polar) with known γ_l, γ_l^{LW}, $\gamma_l^{\oplus}$ and $\gamma_l^{\ominus}$ are used for contact angle measurements, γ_s, γ_s^{LW}, $\gamma_s^{\oplus}$ and $\gamma_s^{\ominus}$ (and, from the last two, γ_s^{AB}) of the solid can be calculated [6].

EXPERIMENTAL
1. MATERIALS AND PREPARATIONS
The PP fibre used in this investigtion is a monofilament fibre having a smooth surface produced by direct extrusion of high molecular weight isotactic polypropylene, with a rectangular cross section ranging from 0.5 x 1.0 to 0.65 x 1.40 mm. It has specific gravity of 0.91, tensile strength of 120 MPa and elongation at break of 14%. The fluorinated PP fibres were prepared by conducting fluorination reactions in an aluminum reactor using a F_2/N_2 gas mixture at room temperature. To protect proprietary information exact details cannot be given, but treatments were done to different levels which are reported relative to the minimum treatment level. Fluorinated fibres were also given a proprietary post-treatment. The cementitious matrices were made from a 80% cement-20% fly ash (by

weight) mixture, natural river sand and crushed stone with a maximum size of 6 mm according to following mixing ratio: Cement : Fly ash : Water : Sand : Crushed stone = 0.8 : 0.2 : 0.42 : 1.5 : 1.5.

2. DCA CONTACT ANGLE ANALYSIS

The contact angles necessary for the calculation of surface free energy components were measured on a Cahn DCA-322 dynamic contact angle analyser, using the Wilhelmy method [10]. The liquids used were water (γ_l=72.8 mJ/m^2), ethylene glycol (γ_l= 48.2 mJ/m^2) and methylene iodide (γ_l=49.5 mJ/m^2).

3. FIBRE PULL-OUT TEST

Fibre pull-out tests were conducted by casting concrete into a custom-made dumbell shaped mould with a PP fibre embedded in the middle [5]. The embedment length was 20 mm each in two sides and double plastic sheets with a hole in the middle were used to prevent the bonding between the two parts. The specimens were released from the mould after 24 hrs and then water cured for 28 days at $23 \pm 2\,^{\circ}C$. The pull-out tests were performed on a motor driven Monsanto tensometer at an extraction rate of 10 mm/min. The shear bond strength was calculated using the following equation: τ_{bond} = P/(CL). Here P, C and L are the maximum pull-out force, perimeter of cross-section of the fibre and bonding length respectively.

RESULTS AND DISCUSSIONS

The advancing contact angles of nonpolar methylene iodide (γ^{AB}=0) and strong polar (hydrogen bonding) water (γ^{AB}=51.0 mJ/m^2) on the fluorinated and post-treated fluorinated PP fibre surfaces compared with that on unfluorinated (Treatment level = 0) PP fibres are presented in Table 1. The surface free energy components of fluorinated PP fibres with different fluorination treatment levels are shown in Table 2.

Table 1. Advancing contact angles Θ_a of nonpolar methylene iodide and strong polar water on various PP fibres surfaces with different fluorination treatment levels

Level	1	2	8	14	20	30	60	120
Water								
Unfluorinated	104.9°							
Fluorinated	95.5°	89.3°	97.3°	100°	91.4°	96.5°	87.7°	101°
Post-treated	80.5°	56.7°	95.9°	91.0°	76.4°	88.1°	72.2°	81.2°
Methylene iodide								
Unfluorinated	67.2°							
Fluorinated	78.2°	74.4°	79.6°	81.0°	75.9°	81.1°	76.1°	84.1°
Post-treated	71.7°	71.2°	73.0°	73.3°	71.8°	74.2°	74.5°	76.3°

Table 2. Surface free energy components (in mJ/m^2) of fluorinated and post-treated fluorinated (*) PP fibres with different treatment levels

Level	γ^{LW}	*	γ^{AB}	*	$\gamma^{\oplus}$	*	$\gamma^{\ominus}$	*	γ^{total}	*
0	23.8		0.35		0.16		0.19		24.2	
1	18.0	21.4	3.32	1.84	1.34	0.06	2.07	15.1	21.3	23.2
2	20.0	21.7	4.90	6.37	3.39	0.19	1.77	53.3	24.9	28.0
8	17.3	20.7	2.39	2.55	0.46	1.10	3.14	1.48	19.7	23.2
14	16.5	20.5	2.22	3.45	1.75	4.25	0.70	0.70	18.8	23.9
20	19.1	21.3	4.42	8.40	1.75	1.52	2.80	11.6	23.5	29.7
30	16.5	20.0	3.27	4.82	2.73	1.17	0.98	4.96	19.8	24.8
60	19.0	19.9	6.00	12.7	2.96	3.37	3.04	11.9	25.0	32.6
120	15.1	18.9	1.90	1.27	2.82	0.02	0.32	17.1	17.0	20.2

It can be seen from Table 1 that the wettability of the PP fibre surface by water is increased through fluorination while the wettability by non-polar liquids such as methylene iodide is reduced after fluorination. Post-treatment of fluorinated PP fibres can further benefit the wettability of PP fibres by both polar and nonpolar liquids. The increase in wettability arises from the large increase in the surface free energy components γ^{AB}, $\gamma^{\oplus}$ and $\gamma^{\ominus}$ by fluorination of PP fibres. This contributes most to the increase in wettability of PP fibres by polar liquids due to the possible stong acid-base interactions between the PP fibre surface and polar liquids. Post-treatment of fluorinated PP fibres can further improve the wettability, because in general the γ^{AB}, $\gamma^{\oplus}$ and $\gamma^{\ominus}$ values have been increased by post-treatment. The decrease of wettability in non-polar liquids is probably because incorporated F atoms reduce the dispersion component γ^{LW} of PP fibres, which was also observed by other researchers [11]. As the values of γ^{LW} are reduced more for fluorinated PP fibres than for post-treated fluorinated PP fibres, the decrease in wettability of methylene iodide is more obvious for fluorinated fibres than for post-treated fluorinated fibres. Post-treatment of fluorinated PP fibres may include the following process due to hydrolysis of weakly bond fluorine [12,13].

$$-[-CHF-CH(CH_3)-]n- \longrightarrow -[-CH=C(CH_3)-]n- + HF$$
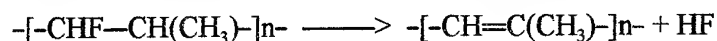
The π-bonding electrons of resulting possible C=C bonds are sufficiently exposed so as to become electron donors and therefore increase the Lewis basicity of the polymers [14]. This may be the reason why $\gamma^{\ominus}$ values are largely increased after post-treatment. The data in Table 1 and 2 exhibit scattered character. This is mainly due to the fact that direct fluorination of PP fibres results in a rough surface with strong microscopic heterogeneity, which can benefit the interfacial bonding by enhancing mechanical interlocks, see Figures 1 and 2. It can be seen that after fluorination, patches or bands with high roughness and

irregularity are created at the fibre surface which, according to Good [6], leads to different (low or high) energy component spots on PP surfaces. This kind of roughness or irregular energy patches can also affect the hysteresis of contact angles and thus the Θ_a and Θ_r measurement according to the Wentzel equation [15]. The difficulty of keeping the required constant pressure in reactor, especially for low treatment levels, may also contribute to the scattered character of the data.
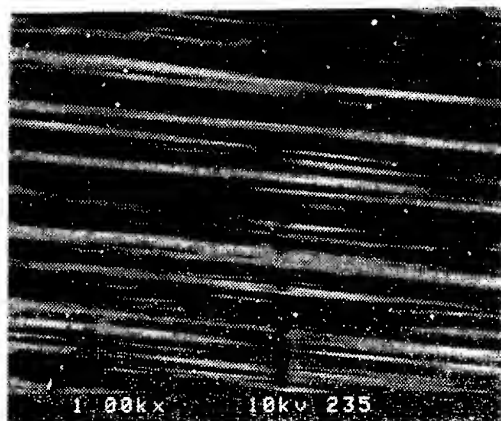
Fig 1. Microscopic surface of unfluorinated PP fibre surface (x1000)
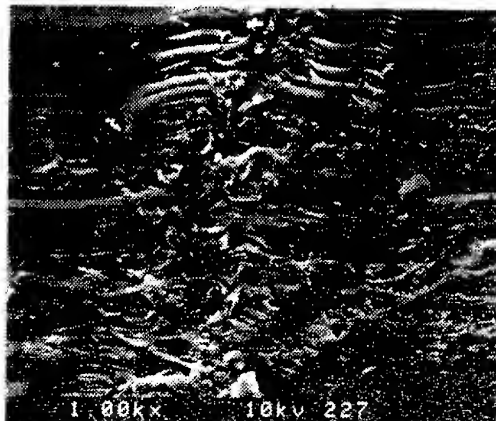
Fig.2 Microscopic surface of fluorinated (level 1) PP fibre surface (x1000)

Shear bond strengths (average of three test results) of fluorinated and post-treated fluorinated PP fibres with concrete matrix obtained by pull-out tests are shown in Table 3.

Table 3. Bond strengths of fluorinated and post-treated fluorinated PP fibres with different fluorination treatment levels compared with that of unfluorinated PP fibre (treatment level = 0)

Treatment level	Bond strength (fluorinated)	Bond strength (post-treated)
0	0.190 MPa	0.190 MPa
1	0.261 MPa	0.656 MPa
2	0.452 MPa	0.448 MPa
8	0.206 MPa	0.410 MPa
14	0.215 MPa	0.366 MPa
20	0.386 MPa	0.400 MPa
30	0.471 MPa	0.360 MPa
60	0.384 MPa	——
120	0.374 MPa	0.439 MPa

Results in Table 3 indicate that the interfacial bond strengths of fluorinated PP fibres are

obviously higher than that of unfluorinated PP fibre. As the PP fibres used in the investigation have smooth surfaces without any mechanical interlockings, the improvement in interfacial bond strength is considered as resulting from chemical bondings or interfacial interactions. Maximum shear bond strength exists for certain conditions, for example, treatment level 30 produces the highest bond strength among all fluorination treatment levels while post-treatment of treatment level 1 fluorinated PP fibre also brings out maximum bond strength. Combining the results in Table 1 and 2, it can be obviously seen that increasing of bond strengths arises from large increment of γ^{AB}, $\gamma^{\oplus}$ and $\gamma^{\ominus}$ after fluorination. Although the bond strength data also exhibit scattered character which may originate from the scattered character of surface free energies discussed above, generally higher γ^{AB}, $\gamma^{\oplus}$ and $\gamma^{\ominus}$ values lead to higher interfacial bond strengths. Post-treated fluorinated PP fibres possess higher bond strength than fluorinated PP fibres because post-treatment tremendously increase the $\gamma^{\ominus}$ and thus the γ^{AB} values of fluorinated PP fibres. Post-treatment also increases the wettability of PP fibres which benefits the interfacial bonding.

In order to understand the nature of intermolecular interactions between the fluorinated PP fibres and cementitious matrix, bond strengths of fluorinated PP fibres are correlated with surface free energy components. The PP fibre/concrete shear bond strengths are plotted versus the γ^{LW}, γ^{AB}, $\gamma^{\oplus}$, $\gamma^{\ominus}$ and γ^{total} and the correlation factors of straight lines fit are 0.055, 0.43, 0.76, 0.0099 and 0.031 respectively. Therefore, it is obvious that the molecular interactions between PP fibres and cementitious matrices are better related with $\gamma^{\oplus}$ and γ^{AB} while the correlations between the bond strengths and γ^{LW}, $\gamma^{\ominus}$ and γ^{total} can not correctly describe the molecular interactions in the PP fibre/concrete interfaces investigated in this project. This is due to the fact that fluorination largely changes the values of $\gamma^{\oplus}$ and γ^{AB} but does not greatly change the γ^{LW} and γ^{total}. The acidity of PP fibres interacts with basicity of concrete which arise from the Lewis basic group existing in cement hydration products, such as OH^- and SiO_4^{4-}, etc. The very poor correlation between the bond strength and $\gamma^{\ominus}$ probably indicates that there is no adequate acidity existing in cementitious matrix to result in an acid-base interaction. After fluorinated PP fibres are post-treated, the correlations with all the surface free energy components become poorer, with correlation factors of 0.14, 0.0078, 0.042, 0.14 and 0.011 respectively. This is because post-treatment leads to basicity dominant PP surfaces with very high $\gamma^{\ominus}$ which shield the acidity of PP surfaces. The correlations with γ^{LW}, $\gamma^{\oplus}$ of fluorinated PP fibres and $\gamma^{\ominus}$, γ^{total} of post-treated fluorinated fibres are shown in Figures 3, 4, 5 and 6, respectively.

CONCLUSIONS

1. Surface direct fluorination increases the wettability of PP (polypropylene) fibres by polar liquids such as water. Wettability is not necessarily increased as fluorination treatment level is increased.

2. γ^{AB}, $\gamma^{\oplus}$ and $\gamma^{\ominus}$ of PP fibres are increased after direct fluorination for either low or higher treatment levels while γ^{LW} and γ^{total} of PP fibres are not obviously changed by direct fluorination. The interfacial shear bond strengths between various fluorinated PP fibres with different fluorination treatment levels and cementitious matrix are enhanced compared with

unfluorinated PP fibres.

3. Interfacial bond strengths are better correlated with $\gamma^{\oplus}$ values of PP fibres while the correlations with γ^{LW} and γ^{total} are poorer. This indicates that the intermolecular interactions between the PP fibres and cementitious matrices mainly arise from the acid-base interactions due to increased Lewis acidity of fluorinated PP fibres and high Lewis basicity of cement hydration products.

4. Direct fluorination also increases the roughness of PP fibre surfaces which may affect contact angle measurement and contributes to the scattered character of surface free energy component data.

Fig. 3 Bond strengths of fluorinated PP fibres with concrete matrix vs LW component of surface free energy of the PP fibres
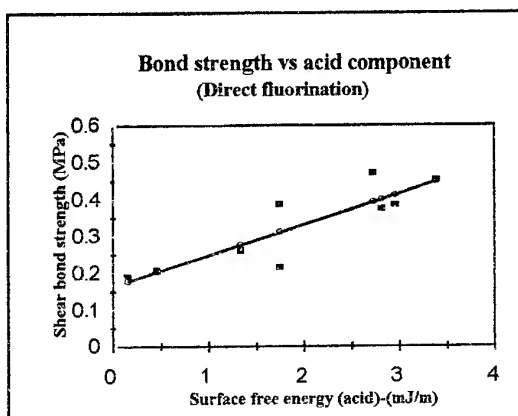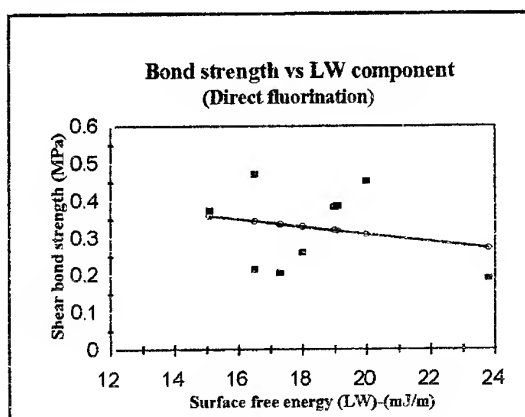
Fig.4 Bond strengths of fluorinated PP fibres with concrete matrix vs acid component of surface free energy of the PP fibres
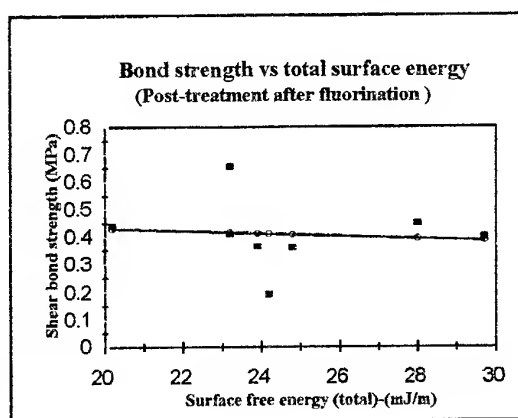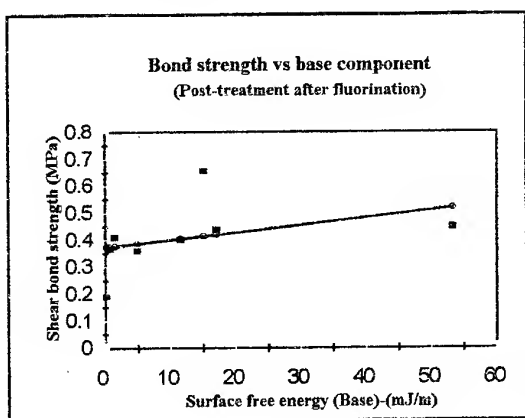
Fig. 5 Bond strengths of post-treated fibres with concrete matrix vs base component of surface free energy of the PP fibres

Fig. 6 Bond strengths of post-treated fibres with concrete matrix vs total surface free energy of the PP fibres

REFERENCES

[1]   Lee, L.H. *Fundamentals of Adhesion*, PLENUM PRESS, New York, 1991.
[2]   Bentur, A. and Mindess, S. *Fibre Reinforced Cementitious Composites*, ELSEVIER APPLIED SCIENCE, London and New York, 1990.
[3]   Hannant, D.J. *Fibre Cements and Fibre Concretes*, A Wiley-Interscience Publication, Chichester·New York·Brisbane·Toronto, 1978.
[4]   Addis, B.J. *Fulton's Concrete Technology (Seventh edition)*, Portland Cement Institute, Midrand, South Africa, 1994.
[5]   Currie, B. and Gardiner, T. "Bond between polypropylene fibres and cement matrix." *The International Journal of Cement Composites and Lightweight Concrete*, vol. 11, pp. 3-9, 1989.
[6]   Mittal, K.L. *Contact Angle, Wettability and Adhesion*, Festschrift in honor of Professor Robert J. Good, VSP BV, Utrecht, The Netherlands, 1993.
[7]   Neville, A.M. *Properties of Concrete*, PITMAN PUBLISHING LIMITED, London, 1981.
[8]   Lagow, R.J. and Margrave, J.L. Progress in Inorganic Chemistry, vol 26, pp. 161-209, 1979.
[9]   Lagow, R.J. and Margrave, J.L. "The controll reaction of hydrocarbon polymers with elemental fluorine." *Polymer Letters Edition*, vol. 12, pp. 177-184, 1974.
[10]   Chan, C.M. *Polymer Surface Modification and Characterization*, Hanser Publishers, Munich·Vienna·New York, 1994.
[11]   Hayes, L.J. "Surface energy of fluorinated surface." *Journal of Fluorine Chemistry*, vol. 8, pp. 69-88, 1976.
[12]   Dittrich, H., Andreae, B. and Wagner, R.E., Brit Patent No 1440605, 1973.
[13]   Margrave, J.L. and Lagow, R.J., US Patent No 3758450, 1973.
[14]   Jensen, W.B. *The Lewis Acid-Base Concepts An Overview*, A Wiley-Interscience Publication, 1980.
[15]   Wu, S.S and Zhang, Y.H. *Surface Chemistry*, Press of Eastern China University of Science and Technology, Shanghai, China, 1989.

INTERIOR SOLUTION FOR ANISOTROPIC STRIPS

BY POLYNOMIAL SERIES

N. TULLINI and M. SAVOIA

Istituto di Tecnica delle Costruzioni, University of Bologna,
Viale Risorgimento 2, 40136 Bologna, Italy

INTRODUCTION

Usually, the solution of two-dimensional problems for long rectangular strips is represented by double series expansions of Airy stress function in powers of axial and transverse coordinates [1, 2]. Following this way, the computation of the coefficients becomes rather involved if the degree of the polynomial load prescribed on the long sides increases. For isotropic strips, in [3] a different representation of solution is described, where the series expansion of Airy stress function is obtained in terms of polynomials of the transverse coordinate multiplying the functions which represent the top and bottom loading. In this case, the first term of the series represents the classical beam theory, and the next terms are corrections involving higher derivatives of loading function. This technique has been extended in [4, 5] to orthotropic strips. In [5] a sufficient condition for the convergence of the series expansion is also derived.

In the present paper, homogeneous anisotropic strips subject to any given continuous distribution of both normal and shear loads are considered. The interior problem is solved by means of a polynomial expansion for the Airy stress function. The polynomial functions defined in transverse direction are determined recursively and those varying along the strip length are obtained in terms of loading functions. Explicit formulas for displacement components are also given. This exact elasticity solution is finally used to derive the set of shear correction factors and to establish the range of validity of Timoshenko-like beam theories.

GOVERNING EQUATIONS

A rectangular strip of length L and height $H=2h$ is referred to a Cartesian reference frame $0x_1x_2$ where x_1 coincides with the centroidal axis and x_2 is chosen in the transverse direction. The strip is made of homogeneous anisotropic linearly elastic material, where x_1-x_2 is a plane of elastic symmetry; the strip is subject to smoothly varying tractions (for a unit width) $\mathbf{q}_t \equiv (q_{1t}, q_{2t})$ and $\mathbf{q}_b \equiv (q_{1b}, q_{2b})$ at the top and bottom faces and forces and couples $\overline{F}_1^0, \overline{F}_2^0, \overline{M}^0, \overline{F}_1^L, \overline{F}_2^L, \overline{M}^L$ at the end sections, located at $x_1 = 0, L$.

Making use of Airy stress function $F(x_1, x_2)$, the equilibrium equations with null body forces are satisfied by $\sigma_{11} = F_{,22}$, $\sigma_{22} = F_{,11}$, $\sigma_{12} = -F_{,12}$, where subscript preceded by a comma denotes partial differentiation. Introducing the dimensionless variables $x=x_1/L$, $y=x_2/h$, the compatibility equation yields the governing differential equation [6]:

$$F_{,yyyy} - 2\alpha_1 (h/L) F_{,xyyy} + \alpha_2 (h/L)^2 F_{,xxyy} - 2\alpha_3 (h/L)^3 F_{,xxxy} + \alpha_4 (h/L)^4 F_{,xxxx} = 0 \quad (1)$$

where

$$\alpha_1 = R_{16}/R_{11}, \quad \alpha_2 = (R_{66} + 2R_{12})/R_{11}, \quad \alpha_3 = R_{26}/R_{11}, \quad \alpha_4 = R_{22}/R_{11} \tag{2}$$

and R_{ij} are the usual reduced elastic coefficients. Moreover, the boundary conditions can be written in term of Airy stress function as:

$$F_{,xx}(x, \pm 1) = (\pm q_2 + p_2)L^2/2, \quad F_{,xy}(x, \pm 1) = (\mp q_1 - p_1)hL/2 \qquad \text{at } y = \pm 1 \tag{3}$$

$$\left[\left\{F_{,y}, \ F_{,x}, \ yF_{,y} - F\right\}\right]_{y=-1}^{y=1} = \left\{\overline{F}_1 h, \ -\overline{F}_2 L, \ \overline{M}\right\} \qquad \text{at } x = 0, 1 \tag{4}$$

where $q_\alpha = q_{ab} + q_{at}$, $p_\alpha = q_{ab} - q_{at}$. Eqns (1-4) can be profitably solved by considering separately the loads q_2 (case I), p_1 (II) and p_2 (III), q_1 (IV), depicted in Fig. 2.

2-D ELASTICITY INTERIOR SOLUTION

In the present section, the procedure employed in [5] to study the orthotropic strip is extended to an anisotropic strip subject to the four loading conditions. To this purpose, the stress functions is cast in the form:

$$F_C(x, y) = -\Phi_C(x) P_0^C(y) - \sum_{n=1}^{\infty} \left(\frac{h}{L}\right)^n \Phi_C^{(n)}(x) P_n^C(y) \tag{5}$$

where $(\cdot)^{(n)}$ stands for the nth derivative with respect to the axial coordinate x and index C denotes the case considered ($C = I$ to IV). Function Φ_C and polynomials P_n^C are defined in such a way the first term in eqn (5) satisfies boundary conditions (3, 4) and corresponds to the classical beam theory, whereas the summation at the right hand side of eqn (5) fulfils the field equation (1) with homogeneous boundary conditions. It is easy to verify that these requirements are verified by the following sets of functions:
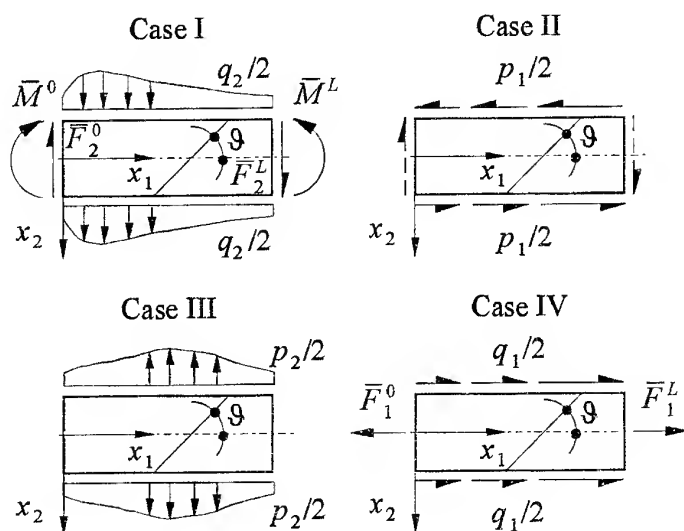

Fig. 1: Nomenclature for the four loading conditions.

$$\{\Phi_I, \Phi_{II}, \Phi_{III}, \Phi_{IV}\} = \left\{ M(x), \quad hL\int_x^1 p_1(t)dt, \quad L^2\int_x^1 (x-t)p_2(t)dt, \quad hN(x) \right\} \quad (6)$$

$$\{P_0^I, P_0^{II}, P_0^{III}, P_0^{IV}\} = \left\{ \frac{3y-y^3}{4}, \quad \frac{y-y^3}{4}, \quad \frac{1}{2}, \quad \frac{1-y^2}{4} \right\} \quad (7)$$

where $N(x)$ is the axial resultant and $M(x)$ the bending moment. Moreover, functions $P_n^C(y)$ ($n=1,...$) are polynomials which are derived from the following recursive formulas:

$$\frac{d^4 P_1^C}{dy^4} = 2\alpha_1 \frac{d^3 P_0^C}{dy^3}, \qquad \frac{d^4 P_2^C}{dy^4} = 2\alpha_1 \frac{d^3 P_1^C}{dy^3} - \alpha_2 \frac{d^2 P_0^C}{dy^2} \qquad (8a,b)$$

$$\frac{d^4 P_3^C}{dy^4} = 2\alpha_1 \frac{d^3 P_2^C}{dy^3} - \alpha_2 \frac{d^2 P_1^C}{dy^2} + 2\alpha_3 \frac{dP_0^C}{dy} \qquad (8c)$$

$$\frac{d^4 P_n^C}{dy^4} = 2\alpha_1 \frac{d^3 P_{n-1}^C}{dy^3} - \alpha_2 \frac{d^2 P_{n-2}^C}{dy^2} + 2\alpha_3 \frac{dP_{n-3}^C}{dy} - \alpha_4 P_{n-4}^C \qquad \text{for } n \geq 4 \qquad (8d)$$

subjected to the following conditions:

$$P_n^C(\pm 1) = \frac{dP_n^C(\pm 1)}{dy} = 0 \qquad \text{for } n \geq 1 \qquad (9)$$

According to eqns (8), it is easy to verify that polynomials P_n^C are independent of the elastic constants for isotropic strips ($\alpha_1 = \alpha_3 = 0$, $\alpha_2 = 2$, $\alpha_4 = 1$). Moreover, although a set of six elastic constants characterise an anisotropic strip, polynomials P_n^C depend on the four combined elastic parameters α_1, α_2, α_3, α_4 only. Moreover, making use of technique proposed for a different problem in [7], the elastic parameters can be reduced to three.

Making use of boundary conditions (9), the following solutions of the differential eqns (8a,b,c) are obtained:

$$\{P_1^I, P_1^{II}, P_1^{III}, P_1^{IV}\} = -\alpha_1(1-y^2)^2 \left\{ \frac{1}{8}, \quad \frac{1}{8}, \quad 0, \quad 0 \right\} \qquad (10)$$

$$\{P_2^I, P_2^{II}, P_2^{III}, P_2^{IV}\} = (1-y^2)^2 \left\{ \frac{y}{80}(\alpha_2 - 4\alpha_1^2), \frac{y}{80}(\alpha_2 - 4\alpha_1^2), 0, \frac{\alpha_2}{48} \right\} \qquad (11)$$

$$P_3^I = \frac{(1-y^2)^2}{240} \left[-2\alpha_1\alpha_2(2-y^2) + 4\alpha_1^3(1-y^2) + \alpha_3(13-y^2) \right]$$

$$P_3^{II} = P_3^I - \frac{(1-y^2)^2}{24}\alpha_3(3-y^2), \quad P_3^{III} = 0, \quad P_3^{IV} = \frac{y(1-y^2)^2}{120}(\alpha_1\alpha_2 - \alpha_3) \qquad (12)$$

Finally, displacement components can be derived from the stress function (5) through the integration of stress-strain relations, so obtaining:

$$u_1(x,y) = u_0(x) - \frac{h}{L}v_0'(x)y - \frac{R_{11}L}{h^2}\sum_{n=1}^{\infty}\left(\frac{h}{L}\right)^n \Phi_C^{(n-1)}(x)U_n^C(y) \qquad (13)$$

$$u_2(x,y) = v_0(x) + 2\alpha_1 u_0(x) + \frac{R_{11}L^2}{h^3}\sum_{n=2}^{\infty}\left(\frac{h}{L}\right)^n \Phi_C^{(n-2)}(x)V_n^C(y) \qquad (14)$$

where:

$$u_0'(x) = R_{11}\frac{N(x)L}{A}, \qquad v_0''(x) = -\frac{R_{11}L^2}{I}\left(M(x) + hL\int_x^1 p_1(t)\,dt\right) \qquad (15)$$

$$U_1^C = \frac{d^2 P_1^C}{dy^2} - \alpha_1\frac{dP_0^C}{dy}, \qquad V_2^C = \frac{d^3 P_2^C}{dy^3} - 2\alpha_1\frac{d^2 P_1^C}{dy^2} + \frac{R_{66}+R_{12}}{R_{11}}\frac{dP_0^C}{dy} \qquad (16)$$

$$U_n^C = \frac{d^2 P_n^C}{dy^2} - \alpha_1\frac{dP_{n-1}^C}{dy} + \frac{R_{12}}{R_{11}}P_{n-2}^C \qquad \text{for } n \geq 2 \qquad (17)$$

$$V_n^C = \frac{d^3 P_n^C}{dy^3} - 2\alpha_1\frac{d^2 P_{n-1}^C}{dy^2} + \frac{R_{66}+R_{12}}{R_{11}}\frac{dP_{n-2}^C}{dy} - \alpha_3 P_{n-3}^C \qquad \text{for } n \geq 3 \qquad (18)$$

and $A=2h$, $I=2/3h^3$ are cross-sectional area and second area moment, respectively. Equations (15) coincide with the basic equations of classical beam theory, whereas $U_n^C(y)$ and $V_n^C(y)$ represent axial and transverse warpings given by polynomial functions of higher order of y.

For an orthotropic strip in plane stress whose orthotropy axes coincide with the reference axes, the elastic parameters defined in eqns (2) reduce to $\alpha_1(0)=\alpha_3(0)=0$, $\alpha_2(0)=E_1/G_{12}-2v_{12}$ and $\alpha_4(0)=E_1/E_2$. In this case, the interior solution reduces to that obtained in [5]. In the case of a fibre-reinforced strip where the fibre direction does not coincides with the reference axes, the behavior is fully anisotropic. In this case, interesting information can be obtained by investigating the influence of fibre orientation. For instance, for a strip subject to two transverse loads $+q_2/2$ at the top and bottom faces and $\overline{M}^0 = -q_2L^2/2$, $\overline{F}^0 = q_2L$ at $x_1=0$ (case I), the Airy stress function becomes (see eqn 5):

$$F_1(x,y) = q_2 L^2\left[-\frac{(1-x)^2}{2}P_0^I(y) - \frac{h}{L}(1-x)P_1^I(y) + \left(\frac{h}{L}\right)^2 P_2^I(y)\right] \qquad (19)$$

Making use of eqns (7,10,11), the axial normal stress is derived from eqn (19) as:

$$\sigma_{11}(x,y) = \frac{qL^2}{h^2}\left[-\frac{3(1-x)^2}{4}y - \alpha_1\frac{h}{L}(1-x)\frac{1-3y^2}{2} - \left(\alpha_2 - 4\alpha_1^2\right)\left(\frac{h}{L}\right)^2\frac{3y-5y^3}{20}\right] \qquad (20)$$

The first term in eqn (20) corresponds to the classical Bernoulli solution. The second term is a parabolic variation over the strip height vanishing for a fibre 0-deg orientation (orthotropic case), since $\alpha_1(0)=0$. The third term gives a self-equilibrated stress

562

distribution over the strip height; this term depends on the combined elastic parameter $\alpha_2 - 4\alpha_1^2$, which is plotted in Fig. 2 as a function of fibres angle ϑ for some values of elastic parameters $\alpha_2(0)$ and $\alpha_4(0)$ corresponding to the 0-deg orientation. It is worth noting that small values of fiber orientation strongly influence the amplitude of this term, and a stress reversal with respect to the orthotropic case may arise.

TIMOSHENKO-LIKE BEAM THEORIES

In Timoshenko-like beam theories, two kinematic measures for displacements are usually employed. Following [8], the dimensionless averaged transverse deflection η and the mean rotation φ of the cross-section are introduced according to the following definition:

$$\eta(x) = \frac{1}{AL} \int_{-h}^{h} u_2 \, dx_2 \, , \qquad \varphi(x) = -\frac{1}{I} \int_{-h}^{h} u_1 \, x_2 \, dx_2 \tag{21}$$

Substituting eqns (13,14) in (21), the following constitutive relations are obtained:

$$\varphi = \frac{v_0'}{L} + \frac{R_{11}L}{I} \sum_{n=1}^{\infty} \left(\frac{h}{L}\right)^n a_n^C \Phi_C^{(n-1)} \, , \qquad \eta' - \varphi = \frac{R_{16}N}{A} + \sum_{n=0}^{\infty} \frac{1}{k_n^C} \frac{R_{66}\Phi_C^{(n+1)}}{AL} \tag{22}$$

where functions Φ_C are reported in eqn (6) and

$$a_n^C = \int_{-1}^{1} U_n^C(y) y \, dy \, , \qquad \frac{1}{k_n^C} = \frac{R_{11}}{R_{66}} \left(\frac{h}{L}\right)^n \left[\int_{-1}^{1} V_{n+2}^C(y) \, dy - 3 a_{n+2}^C\right] \tag{23}$$

are the first moment of higher-order displacement U_n^C and the set of shear correction factors. For instance, the first correction factor k_0, is equal to:
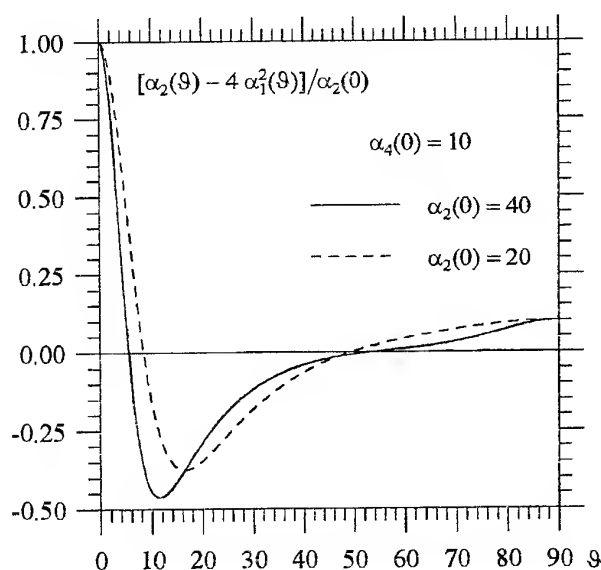

Fig. 2. Elastic parameter $(\alpha_2(\vartheta) - 4\alpha_1^2(\vartheta))/\alpha_2(0)$ versus fiber orientation ϑ.

563

$$\left\{ \frac{1}{k_0^I}, \frac{1}{k_0^{II}} \right\} = \left\{ \frac{1}{5}\left(6 + \frac{R_{12}}{R_{66}} - \frac{2R_{16}^2}{R_{11}R_{66}} \right), \frac{1}{5}\left(1 + \frac{R_{12}}{R_{66}} - \frac{2R_{16}^2}{R_{11}R_{66}} \right) \right\} \qquad (24)$$

For isotropic and orthotropic strips, it can be verified that eqn (24) gives the shear coefficients obtained in [8, 9] for constant or linear shear resultants. Eqn (22a) shows that the average shear strain η'-φ depends on the first derivatives of Φ_C (that is the shear resultant for case I, see eqn 6), as well as on all the subsequent derivatives of the same function. This summation contains higher-order shear correction factors k_n^C defined in eqn (23b) which are required for non-uniform loads. Hence, eqns (22) can be useful to establish the range of validity of Timoshenko classical theory.

FINAL REMARKS

Polynomial solutions typically refer to long strips, neglecting pointwise self-equilibrated stress distributions or displacement constraints at the end sections. Nevertheless, it is well established that Saint Venant's principle may be invoked with prudence when anisotropic materials are concerned, because the decay length of end effects is much greater than the strip height [7]. Anyway, the solution of elasticity problems can be decomposed into the interior solution, satisfying average end conditions, and the boundary solution, which re-establishes the pointwise prescriptions at the beam ends. For the solution of boundary problem, several techniques have been proposed, e.g. see [10].

REFERENCES

[1] Timoshenko, S. P., Goodier, J. N., *Theory of Elasticity*, 3rd Ed., McGraw Hill Book Co., New York (1970).
[2] Hashin, Z. "Plane anisotropic beams." *J. Appl. Mech.* **34**, pp. 257-262 (1967).
[3] Donnell, L. H., *Beams, Plates and Shells*, McGraw Hill, New York (1976).
[4] Duva, J. M., Simmonds, J. G. "Elementary, static beam theory is as accurate as you please." *J. Appl. Mech. ASME* **57**, pp. 134-137 (1990).
[5] Tullini, N., Savoia, M. "Elasticity interior solution for orthotropic strips and accuracy of beams theories." Submitted.
[6] Lekhnitskii, S. G., *Theory of Elasticity of an Anisotropic Body*, Mir Publ., Moscow (1981).
[7] Miller, K. L., Horgan, C. O. "End effects for plane deformations of elastic anisotropic semi-infinite strip." *J. Elasticity* **38**, pp. 261-316 (1995).
[8] Cowper, G. R. "The shear coefficient in Timoshenko's beam theory." *J. Appl. Mech.* **33**, pp. 335-340 (1966).
[9] Dharmarajan, S., McCutchen Jr, H. "Shear coefficients for orthotropic beams." *J. Comp. Mat.* **7**, pp. 530-535 (1973).
[10] Savoia, M., Tullini, N. "Beam theory for strongly orthotropic materials." *Int. J. Solids Struct.*, in printing (1996).

ON GENERAL CONCEPTS OF STRUCTURAL DESIGN

V.V. Vasiliev[1], Z. Gürdal[2]

[1] *Moscow State University of Aviation Technology, Russia*
[2] *Virginia Polytechnic Institute and State University, USA*

The presentation is devoted to the general problem of structural design formulated as the inverse problem of mechanics of solids.

The first basic concept that is used to study the problem is associated with the structural formulation of the optimality criterion which, being conventionally written in terms of design variables of the structure, is now expressed through the field variables, i.e., stresses, strains, displacements to provide the proper quality of the structure (e.g., minimum mass). General analysis and particular examples show that if such a criterion can be constructed, it turns out to be universal and unique and allows to solve the optimization problems not resorting to variational methods or cumbersome iterative numerical procedures.

The second basic concept is associated with the optimal three-dimensional structural space which includes the optimal structure irrespective of its particular model and can be further reduced to some real structure in the form of a truss, beam, plate or shell using additional information concerning material properties and possibilities of the technology. Optimal space is not Euclidean, its curvature is governed by the system of principal stresses whose trajectories are in correspondence with the geodesic lines of the space.

Analogies between the introduced concepts of structural design and the laws according to which the natural structure (e.g., plants) are formed in the process of evolution are discussed.

Typical formulation of the design problem includes a set of constraints and the quality criterion or the objective functions that should be maximized or minimized by the proper choice of design variables. The principal feature of the optimization problem for the load-bearing structures is associated with the fact that the design variables which determine the geometry and the properties of the structure and specify the quality criteria do not enter directly into the constraints which provide the proper strength and stiffness of the optimal structure and are usually written in terms of field variables, i.e., stresses, strains, and displacements. The first principal problem occurring in connection with this is that the field variables, as a rule, cannot be explicitly expressed through the design variables. To solve this problem, we need to attract the equations of solid mechanics which, for real structures, can be solved, only with numerical methods. This results in the necessity to construct an iterative optimization procedure which improves the structure starting from some initial set of design variables and involves the calculation of the structure stress-strain state at each step of

the iteration process in order to check strength and stiffness constraints. Thus, the inverse problem of mechanics (which are the problems of design) is reduced to a set of direct problems of analysis. Despite the wide practical application of this approach, it does not look natural because the inverse problem is usually less complicated than the direct one.

To illustrate the foregoing reasoning, consider the problem of optimization for an isotropic homogeneous plate which is loaded with normal pressure p and should have the thickness distribution $h(x, y)$ providing minimum mass for a restricted stiffness, e.g., deflection w. Equation describing this problem

$$L(w, h) = p \tag{1}$$

has the fourth order for the field variable w and the second order for the design variable h. So, the inverse problem (to determine h) is more simple than the direct problem (to determine w).

However, the traditional condition of minimum mass, i.e.

$$\min_h M(h) \tag{2}$$

does not allow to formulate the inverse problem and to use the second order equation (1) because it does no specify the deflection of the optimum plate. Thus, we have arrived at the second principal problem of the theory of optimal design which is th problem of structural formulation of the optimality criterion. This means that, in contrast to condition of minimum mass (2) which includes h, this formulation providing the same final result should include the entire plate characteristic specifying the behavior of the optimal structure, i.e. w.

To illustrate the structural formulation of the optimality criterion, consider another example. Let a laminated plate loaded in its plane with forces N_x, N_y, and N_{xy} uniformly distributed along its edges consist of k monothropic (working only in one direction) layers of fibers such that any i-th layer is characterized with its thickness h_i and the fiber orientation angle φ_i. Then equilibrium equations can be written as [1]

$$L_x = N_x - \sum_{i=1}^{k} \sigma_i h_i \cos^2 \varphi_i = 0, \qquad L_y = N_y - \sum_{i=1}^{k} \sigma_i h_i \sin^2 \varphi_i = 0,$$
$$L_{xy} = N_{xy} - \sum_{i=1}^{k} \sigma_i h_i \sin \varphi_i \cos \varphi_i = 0, \tag{3}$$

where σ_i is the stress acting in the fibers of the i-th layer. Forces N_x, N_y and N_{xy} induce the strains ε_x, ε_y and ε_{xy} which are assumed the same for all the layers and can be transformed to the layer strains $\varepsilon_1^{(i)}$, $\varepsilon_2^{(i)}$ and $\varepsilon_{12}^{(i)}$ in principal material coordinates of the layer 1, 2 (axis 1 is directed along the fibers) with the aid of the following relationships (equation for $\varepsilon_2^{(i)}$ is om tted)

$$\varepsilon_1^{(i)} = \varepsilon_x \cos^2 \varphi_i + \varepsilon_y \sin^2 \varphi_i + \varepsilon_{xy} \sin \varphi_i \cos \varphi_i$$

$$\varepsilon_{12}^{(i)} = (\varepsilon_y - \varepsilon_x) \sin 2\varphi_i + \varepsilon_{xy} \cos 2\varphi_i. \tag{4}$$

The first formula (4) allows to write the constitutive equation for the fibers of the i-th layer

$$\sigma_i = E\varepsilon_1^{(i)} = E(\varepsilon_x \cos^2 \varphi_i + \varepsilon_y \sin^2 \varphi_i + \varepsilon_{xy} \sin \varphi_i \cos \varphi_i), \tag{5}$$

where E is the modulus of elasticity, while equations for $\varepsilon_2^{(i)}$ and $\varepsilon_{12}^{(i)}$ specify transverse and shear strains which, in accordance with the assumed material model, are not accompanied by stresses. Equations (3), (4), and (5) readily yield the solution of the direct problem. Indeed, knowing design variables h_i and φ_i and substituting σ_i into equations (3) we arrive at three equations for strains ε_x, ε_y and ε_{xy}. Then the strains of all the layers can be found using equations (4) and equation (5) gives the stresses.

Consider the traditional formulation of the optimization problem. Criterion (2) can be presented in the case under study as

$$\min_{h_i, \varphi_i} h = \sum_{i=1}^{k} h_i \tag{6}$$

According to traditional approach, we should minimize thickness (6) with allowance for constraints following from equations (3) and (5). Introducing Lagrangian multipliers λ we get the following augmented functional.

$$H = \sum_{i=1}^{k} h_i + \lambda_x L_x + \lambda_y L_y + \lambda_{xy} L_{xy} + \sum_{i=1}^{k} \lambda_i (\sigma_i - E\varepsilon_1^{(i)})$$

Minimization with respect to design variables h_i and φ_i yields

$$\sigma_i (\lambda_x \cos^2 \varphi_i + \lambda_y \sin^2 \varphi_i + \lambda_{xy} \sin \varphi_i \cos \varphi_i) = 1 \tag{7}$$

$$\sigma_i h_i [(\lambda_y - \lambda_x) \sin 2\varphi_i + \lambda_{xy} \cos 2\varphi_i] = E\lambda_i [(\varepsilon_y - \varepsilon_x) \sin 2\varphi_i + \varepsilon_{xy} \cos 2\varphi_i]. \tag{8}$$

Equation (8) has the following evident solution

$$\lambda_x = E\varepsilon_x \lambda_i / (\sigma_i h_i), \qquad \lambda_y = E\varepsilon_y \lambda_i / (\sigma_i h_i), \qquad \lambda_{xy} = E\varepsilon_{xy} \lambda_i / (\sigma_i h_i),$$

from which it follows that combination $\lambda_i / (\sigma_i h_i)$ does not depend on i. Substitution of this solution into equation (7) allows to conclude that ratio λ_i / h_i also does not depend on i, so $\sigma_i =$ const, and the optimal structure corresponds to the structure of uniform strength. Comparing thus obtained result with equation (5) we can further conclude that for the optimal structure $\varepsilon_x = \varepsilon_y$ and $\varepsilon_{xy} = 0$.

In conjunction with the last equation (4) this gives $\varepsilon_{12} = 0$, so the fibers in the layers coincide with the directions of principal strains. So, the optimal laminate should satisfy the following optimality conditions

$$\sigma_i = \sigma, \qquad \varepsilon_{12}^{(i)} = 0 \qquad (i = 1, 2, 3 \ldots k) \qquad (9)$$

which are the structural formulation of criteria (6).

Now assume that the optimality criterion is given in the form of equations (9) rather than (6). Then, summing up the first two equilibrium equations (3) and taking into account (6) we get for the plate total thickness

$$h = (N_x + N_y)/\sigma. \qquad (10)$$

Eliminating σ from equations (3) we arrive at two optimality conditions in terms of the design variables, i.e.

$$\sum_{i=1}^{k} h_i (N_x \sin^2 \varphi_i - N_y \cos^2 \varphi_i) = 0, \qquad \sum_{i=1}^{k} h_i \left[(N_x + N_y) \sin \varphi_i \cos \varphi_i - N_{xy} \right] = 0. \qquad (11)$$

Thus, the problem under study has been solved as the inverse problem and no variational or iterational methods were employed. However, we should make two important remarks. First, criterion (9) formally coincides with the well known condition of uniform strength, but in fact it is condition of minimum mass (6).

Second, it seems that to derive criterion (9) is not less simple than to solve the initial optimization problem (6) using traditional variational approach. However, it should be taken into account that the structural formulation of the optimality criterion is rather universal and, being derived for a simple problem, can be further used for more complicated ones. Moreover, in terms of design variables h_i and φ_i entering criterion (6) the solution of the design problem is not unique because three equations (10) and (11) include $2k$ unknown parameters h_i and φ_i, while the stress-strain state following from equations (9) is he same for all the optimal laminates.

Thus, the first general design concept discussed here is associated with the structural formulation of the optimality criterion. By now, such formulations exist only for relatively simple structures, i.e., for truss systems, membrane elements, and structures made from perfectly plastic material. Being further developed, they will allow to change existing cumbersome numerical iterative methods of optimization for much more efficient analytical or numerical solutions of the inverse problems.

To discuss the second design concept, return to the example concerning the problem of bending of a plate with variable thickness. The problem of optimization for this plate has a well known solution which is remarkable because it is not continuous which means that the assumed model of the optimal structure is not

quite adequate. The optimal structure in the case under consideration is rather far from a homogeneous plate (the optimal plate consists of a system of infinitely thin and infinitely high ribs) and can hardly be described by equation (1).

Thus, we can suppose that with respect to the structural formulation of the optimality criterion discussed above the natural desire to formulate the optimization problem for some preliminary selected structural model can hinder the problem rather than simplify it.

So, it seems reasonable to develop the theory of structural optimization as the theory allowing to construct some optimal three-dimensional structural space and then to reduce it to a real structure which can be a one-dimensional beam, a truss system a two-dimensional shell, or a three-dimensional solid.

It can also be supposed that while the reduction of the optimal space to a real structure is performed by engineering methods with due regard to the existing level of technology, material science and etc., the optimal structural space itself is a un versal object which should be governed only by the laws of nature.

To introduce the structural space, consider homogeneous equilibrium equations

$$\nabla_i \tau^{ij} = 0, \tag{12}$$

where τ^{ij} is the stress tensor. As known [2], equations (12) are a particular case of the equations of the General Theory of Relativity (GTR) and can be identically satisfied by the following expression:

$$\kappa \tau_{ij} = \lambda g_{ij} - (R_{ij} - R g_{ij}/2). \tag{13}$$

Here κ and λ are some constants, g_{ij} is the metric tensor, R_{ij} is the Ricci curvature tensor which can be expressed in terms of the metric tensor and $R = g^{ij} R_{ij}$ is the invariant of the curvature. In GTR the prototype of equation (13) establishes the connection between the gravitation and the space curvature. Using this concept we can conclude that the stress field influences the space curvature like the gravitation field does. The Euclidean space existing outside and inside the solid before loading transforms into Riemannian space inside the solid after the loading. It should be noted that three equilibrium equations (12) include six stresses and the set of equilibrium equations is not complete. In solid mechanics, equilibrium equations are supplemented with compatibility equations which, being written in terms of stresses, include also mechanical characteristics of the material. However, compatibility equations in their classical form cannot exist in the Riemannian space (compatibility equations establish that the curvature of the space inside the deformed solid is zero, i.e. that this space is Euclidean). As known, there exists the invariant set of equilibrium equations which is complete. It corresponds to coordinate lines coinciding with the trajectories of principal stresses and includes three stresses. With these equations we do not need compatibility equations and, what is also important, do not need material characteristics

to construct the optimal structural space. It seems natural because this space should be, as was already noted, universal and cannot depend on the properties of a particular material. It should be emphasized that the real optimal structure to which the optimal space should be finally reduced must satisfy compatibility equations and certainly depends on material properties.

Consider now the properties of the optimal structural space. As is shown in [3], the three-dimensional Riemannian space can be included into the three-dimensional Euclidean space (in which the structure must exist) if the space is not uniform. The space curvature in this case demonstrates itself as some variable density of the Euclidean space which can further be treated as same characteristic governing the material concentration in the structure.

As known, in the Riemannian space there exist invariant and, in some sense, optimal trajectories which are called the geodetic lines and provide the minimum distance between two arbitrary points. Taking into account the existing experience of practical design according to which the forces in the optimal structures should be transferred along the shortest paths, we can suppose that there should exist some correspondence between the trajectories of principal stresses and the geodetic lines of the Riemannian space induced by these stresses.

In conclusion discuss some analogy between the design approach under consideration and the process of development of natural structures. As known, the structural elements of plants are developed under the action of the gravitation field and, as soon as the stress field provides the same effect that the gravitation one, the stress field should influence the plant structures. There exist a lot of evidences of such an influence in biomechanics where the structure of the plants growing under imposed restrictions are studied. Moreover, there exist the explanation of the regular geometric structure of plant elements (e.g. leaves, flower-petals and etc.) according to which their shape is governed by the geodetic lines of the space curved by some unknown yet physical or biological field [4].

References

1. Vasiliev, V.V. *Mechanics of Composite Structures*, Taylor and Francis, Washington, 1993.

2. Synge, J.L. *Relatively: The General Theory*, North-Holland Publishing Co., Amsterdam, 1960.

3. Vasiliev, V.V. *Stressed State of Solids and Some Geometric Effects*, Mechanics of Solids, Mekhanika Tverdogo Tela (Izvestia AN SSSR), 5(24): 30–34.

4. Grodzinskii, D.M. *Models of Living. Nature and Botanical Bionics*, Naukova Dumka, Kiev, 1966 (in Russian).

COMPOSITE MOULD DESIGN AND COST ESTIMATION FOR RESIN TRANSFER MOULDING

G. Veldsman, A.H. Basson, J. van der Westhuizen
Department of Mechanical Engineering, University of Stellenbosch,
Stellenbosch, South Africa

ABSTRACT

Low cost composite tooling RTM is well suited for small to medium production volumes. This paper presents cost estimation models for composite RTM moulds. The contributions of material and labour costs are accounted for. A procedure for the estimation of the required mould wall thickness is provided. The cost estimation models were formulated to require those parameters that a product designer would have available. The models are intended to be used by product designers to assess the cost effectiveness of RTM for a product and to identify (and review) expensive part features.

NOMENCLATURE

a	major axis of ellipse	(m)	
A_P	surface area of the part	(m²)	
A_T	total mould surface area	(m²)	Equation 4
A_V	additional mould area	(m²)	Equations 2,3
b	minor axis of ellipse	(m)	
b	top hat feature dimension	(mm)	Figure 1
G	mould area correction factor	(m²)	
h	top hat feature dimension	(mm)	Figure 1
K	top hat feature factor		Equations 25, 26, 27
L	top hat feature dimension	(mm)	Figure 1
M_C	clamping cost	(1995 Rand)	Equations 10,11
$M_{G,S,M,B}$	material cost of the gelcoat, the surface tissue, the main strengthening layers, and the mould backing	(1995 Rand)	Equations 7,8
M_T	material cost	(1995 Rand)	Equation 6
M_W	cost of the wax sheets	(1995 Rand)	Equation 9
P_i	the injection pressure	(kPa)	
S_p	the part perimeter	(m)	
S_{PO}	outer perimeter of the mould	(m)	Equation 5
t_c	core mat thickness	(m)	
T_G	gelcoat labour	(minutes)	Equation 13
T_L	laminating labour	(minutes)	Equation 19
T_{LD}	T_L for a dome part	(minutes)	Equation 23
T_{LP}	T_L for a flat or single curvature section	(minutes)	Equation 22
T_{LT}	T_L for a top hat or corner section	(minutes)	Equation 24
t_M	mould thickness	(m)	Equation 1
T_{MC}	mould cleaning labour	(minutes)	Equation 15
T_{ML}	total labour	(minutes)	Equation 12
t_p	part thickness	(m)	
T_S	labour for placing seals	(minutes)	Equations 16,17
T_T	mould trimming labour	(minutes)	Equation 14
T_W	wax modelling labour	(minutes)	Equation 18

T_{WD}	wax modelling labour for a dome	(minutes)	Equation 21
T_{WP}	wax modelling labour for a flat or single curved plate	(minutes)	Equation 20
α	b/a		
θ	top hat feature dimension	(°)	Figure 1

INTRODUCTION

RTM (resin transfer moulding) is a closed mould, low pressure manufacturing technique for producing fibre-reinforced composite parts. The RTM process typically entails laying previously prepared reinforcement material on one of the mould halves, closing the mould, injecting a thermoset resin in one continuous process to fill the mould cavity and impregnate the reinforcement material, and leaving it to cure. A number of papers reporting on variations of the process and their advantages and disadvantages have been published [1], [2], [3], [4]. The research reported here focused on low cost composite moulds for RTM, using polyester and epoxy resins. This type of tooling lends itself to the small production volumes often encountered in South African markets.

One of the aims of the research was to develop "early cost estimation models" for this type of RTM process. The purpose of the early cost estimation models is to provide manufacturing cost information to the product designer during the design process. This information can be used to assess the cost effectiveness of RTM for a particular product and to optimise part designs by identifying and reviewing expensive part features.

Little has been published about the manufacturing costs of parts produced with RTM. Some papers only highlight the material cost of the actual part [5], [6], [7], but do not consider the cost of the mould and its influence on the final cost of the part. In low production volumes the mould cost forms a significant part of the total product cost (typically 20% to 25%)

In this paper a set of cost estimation models for the manufacture of composite moulds are considered. The underlying assumptions, cost estimation equations and calibration procedure are described. Similar cost estimation models for RTM parts' material and production time are been given in [8]. In the formulation of the cost models, the inputs required from the user were kept to a minimum to make the cost model suitable for use by persons not intimately acquainted with RTM production techniques. Two aspects of the mould design, however, have such a large bearing on the mould costs, that they have to be considered by the user of the cost models. These aspects are the mould thickness and the method of clamping. To assist the user of the cost models, a procedure for estimating the required mould thickness is therefore presented. The cost models further make provision for two common forms of clamping. The cost models can therefore be used to evaluate the relative costs of using the two methods and thus contribute towards the selection of the appropriate one.

UNDERLYING ASSUMPTIONS

The cost estimation models are based on the following assumptions:

1) The part is small enough so that one or two persons can easily handle a mould half when opening and closing the mould.

2) The mould is built up out of the following layers: a layer of gelcoat, a layer of surface tissue, 2 layers of 200g/m² weaved glass cloth, and then backing material. The backing material consists of a number of layers chopped strand mat, a core material, and followed by more layers of chopped strand mat. The number of layers will be determined by the mould thickness.

ESTIMATING REQUIRED MOULD WALL THICKNESS

Determining the mould wall thickness by making use of advanced analysis techniques such as finite element analysis is justified when the mould itself is comparatively expensive to manufacture, e.g. all metal moulds or moulds with electroformed skin. All composite moulds considered here are used in low volume production and the cost of designing and manufaeturing the mould must therefore be kept as low as possible. A simplified analysis to estimate the required mould wall thickness would therefore be justified. The wall thickness has to be selected to sufficiently restrain the deflection of the mould due to the pressure of injection. Excessive mould deflection will cause either products with insufficient wall thickness (for vacuum injection) or excessive resin consumption (for pressure injection).

The procedure for mould wall thickness estimation described below is based on the following assumptions:

1) The procedure makes use of thin plate theory to determine the mould deflection [9].

2) The boundaries of the mould are assumed to be fully constrained.

3) An equivalent elasticity modulus of 10 GPa and a Poisson ratio of 0.26 are assumed [10].

4) A constant mould wall thickness throughout the mould is assumed.

5) The pressure gradient between the injection and venting points are ignored, and the pressure is assumed to be equal to the injection pressure.

6) The mould deflection is not to exceed 10 % of the part thickness.

The method used makes use of an elliptical plate with an equivalent aspect ratio solution. For a four sided part the distances between the midpoints of the opposite sides are used as the axes of the elliptical plate. For a three sided part the maximum of the distances between the midpoints of the sides and their respective opposite corners is taken as the major axis, while the distance between the other two midpoints is taken as the minor axes.

By making use of the above assumptions, the following expression for the required mould wall thickness can be derived:

$$t_M = 1.12 * 10^{-3} * \sqrt[3]{\frac{P_i * 10^3 * b^4}{t_p * (3 + 2 * \alpha^2 + 3 * \alpha^4)} - \frac{t_c^3}{1.12 * 10^{-3}}} \tag{1}$$

An investigation of the accuracy of this approach for moulds of various flat shapes indicated that typical errors in mould thickness are less than 15%. Mould-shape features that provide additional stiffness will reduce the mould deflection. The associated error in the estimation procedure will be offset partly by the somewhat optimistic assumption that the mould boundaries are fully restrained (point 2 above). The results of Equation (1) should therefore be considered to be the maximum wall thickness that would used.

TOTAL MOULD AREA

The total mould area is determined by the part area and the type of clamping used. Although the type of clamping is influenced by the part size, injection pressure and production rate, the selection is eventually based on cost. The cost models therefore distinguish between vacuum clamping and manually actuated toggle clamps, to provide the designer with the capability to compare the respective mould costs associated with these two commonly used methods.

The additional mould area required respectively for these methods of clamping can be estimated as follows:

$$A_V = \frac{P_i}{80} * A_P * 1.3 \qquad \text{(Vacuum clamping)} \qquad (2)$$

$$A_V = S_p * 0.1 + G \qquad \text{(Toggle clamps)} \qquad (3)$$

with G=0.04 m^2 for rectangular outlines and G=0.01 m^2 for circular outlines.

The total mould surface area is then:

$$A_T = A_P + A_V \qquad (4)$$

$$S_{PO} = 2 * \sqrt{\pi * A_V} \qquad (5)$$

MATERIAL COST ESTIMATION

A summary of the equations that comprise the composite mould material cost estimation model are given here. Details of the development of the equations are given in [8].

The material cost takes into account the direct material cost of the mould as well as the material cost involved in modelling the mould cavity with wax sheets when the mould is drawn from the master model. The material cost can be estimated as follows:

$$M_T = \left(M_{G,S,M,B} \right)_{Male} + \left(M_{G,S,M,B} \right)_{Female} + M_W + M_C \qquad (6)$$

$$M_{G,S,M,B} = \left(104.5 + 17E3 * t_M - 11E3 * t_C \right) * A_T \qquad \text{(polyester moulds)} \qquad (7)$$

$$M_{G,S,M,B} = \left(569 + 54E3 * t_M - 48E3 * t_C \right) * A_T \qquad \text{(epoxy moulds)} \qquad (8)$$

$$M_W = 112 * A_P * t_P * 10^3 \qquad (9)$$

$$M_C = 250 * S_p \qquad \text{(toggle clamps)} \qquad (10)$$

$$M_C = 0 \qquad \text{(vacuum clamping)} \qquad (11)$$

LABOUR COST ESTIMATION

A summary of the equations that comprise the composite mould labour cost estimation model are given here. Details of the developments of the equations are given in [8].

The labour cost can be calculated by dividing T_{ML} by 60 and multiplying it with an hourly rate. The total labour can be estimated by means of the following equations:

$$T_{ML} = \left(T_G + T_L + T_T + T_{MC} \right)_{Male} + T_W + T_S$$
$$+ \left(T_G + T_L + T_T + T_{MC} \right)_{Female} \qquad (12)$$

$$T_G = A_T * 30 \qquad (13)$$

$$T_T = 10 + 7.6 * S_{PO} \qquad (14)$$

$$T_{MC} = 157 * A_T \qquad (15)$$

$$T_S = T_{LT}(S_P) + T_{LT}(S_{PO}) + 2*(S_P + S_{PO}) \qquad \text{(Vacuum clamping)} \qquad (16)$$

$$T_S = T_{LT}(S_P) + 2*S_P \qquad \text{(Toggle clamps)} \qquad (17)$$

$$T_W = \Sigma(T_{WP}, T_{WD}) \qquad \text{(see next paragraph)} \qquad (18)$$

$$T_L = \Sigma(T_{LP}, T_{LD}, T_{LT}) \qquad \text{(see next paragraph)} \qquad (19)$$

Since T_W and T_L are part geometry dependent, they are calculated as the sum of the labour for the respective features that constitute the mould shape. Flat, single curvature, dome like and top hat features are provided for in Equations (20) and (21) for T_W, and Equations (22), (23) and (24) for T_L.
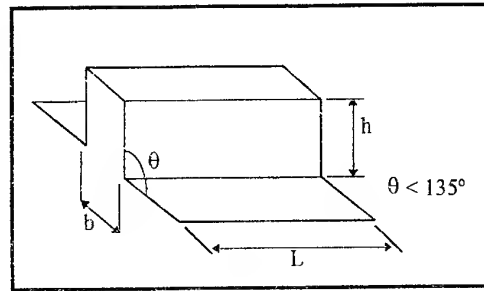

Figure 1: Top hat section

$$T_{WP} = (2.5*S_P + 9*A_P)*n_W + 120*A_P \text{ (flat, single curvature or top hat feature)} \qquad (20)$$

$$T_{WD} = 45 + (64 + 0.675*\pi*D)*n_W + 60*\pi*D \qquad \text{(dome type feature)} \qquad (21)$$

$$T_{LP} = (60*A + 12)*n \qquad \text{(flat or single curvature feature)} \qquad (22)$$

$$T_{LD} = (72*A + 38)*n \qquad \text{(dome type feature)} \qquad (23)$$

$$T_{LT} = (5 + 15*L)*n + K \qquad \text{(top hat feature, } \theta < 135°) \qquad (24)$$

$$K = 2*T_{LP}(h*L) \qquad \text{(if } h > 50 \text{ mm)} \qquad (25)$$

$$K = T_{LP}(b*L) \qquad \text{(if } b > 50 \text{ mm)} \qquad (26)$$

$$K = 2*T_{LP}(h*L) + T_{LP}(b*L) \qquad \text{(if } h > 50 \text{ mm and } b > 50 \text{ mm)} \qquad (27)$$

MODEL CALIBRATION

The cost models were developed by considering the detailed cost breakdown for a typical RTM part, as measured in the laboratory of the Group for Composite Materials of the University of Stellenbosch [8]. Although the overall format of the cost models has been formulated to be fairly generally applicable, the numerical values given above should be considered to be preliminary as they are being refined in further calibration studies.

CONCLUSION

Mould costs constitute a significant proportion of RTM products in low production volume situations. Low cost composite moulds are therefore particularly suited to this type of application. The cost estimation models for composite tooling presented here can be used by a product designer to partly assess the financial viability of RTM for a product, without having intimate knowledge of RTM production procedures. The models can also be used to identify part features that contribute significant proportions of the mould costs. These features can then be reviewed by the designer.

A procedure to estimate the required mould wall thickness was presented as part of the cost estimation model.

Similar cost estimation models for RTM parts' material and production time have been given in [8].

The calibration of the cost models is being refined.

ACKNOWLEDGMENTS

REFERENCES

[1]   Harrison, A.R., Sudol, M.A., Priestly, A., Scarborough, S.E., "A low Investment Cost Composites High Roof for the Ford Transit Van using Electroformed Shell Tooling and Resin Transfer Moulding." 4th Int. Conf. on Automated Composites, pp. 511-525, 1995.

[2]   Foley, F.M., "The flexible RTM Process", SAMPE Journal, Vol. 28 No. 6, pp. 15-24, 1992.

[3]   Stockton, J.E., "Structural Resin Transfer Moulding of High Temperature Composites", 34th Int. SAMPE Symposium, pp. 1032-1040, 1989.

[4]   Cohen, S.E., Graves, C.T., Bernardon, E,. West, H., "Experimental and Analytical Development of the FRTM Process", 38th Int. SAMPE Symposium, pp. 391-403, 1993.

[5]   Harper, A.R., "Resin Transfer Moulding Today", Source Unknown, Undated.

[6]   Scott, F.N., Heath, R.J., "RTM for Civil Aircraft Manufacture", SAMPE Journal, European Chapter, pp. 235-247, 1992.

[7]   Bonner, H.M., Teeter, D.B., "Resin Transfer Molding Applications in the Kitplane Industry", Proceedings of the 38th Int. SAMPE Symposium, pp. 488-495, 1993.

[8]   Veldsman, G., Aspects of Design for Manufacturing for RTM, M.Eng. Thesis, Dept. Mechanical Eng., Univ. of Stellenbosch, Stellenbosch, March 1996.

[9]   Roark, R.J., Young, W.C., "Formulas for Stress and Strain", 5th ed., McGraw-Hill, pp. 324-404, New York, 1975.

[10]   Hull, D., "An Introduction to Composite Materials", Cambridge University Press, Cambridge, 1990.

NUMERICAL SOLUTION OF CONTACT PROBLEMS FOR LAMINATED COMPOSITE SHELLS

V. E. VERIJENKO[1], S. G. ZHURAVLEV[2], S.ADALI[1], P. Y. TABAKOV[1]

[1]Dept. of Mechanical Engineering, University of Natal, Durban, Republic of South Africa
[2]Moscow Highway Engineering Institute, Moscow, Russia

INTRODUCTION

A method for the numerical solution of contact problems for multilayered thin–walled shells is given. The theory developed is based on the high order theory of heterogeneous shells which takes into account both transverse shear and normal compression. The numerical results are obtained using the finite element method.

We consider plates and shells with nonuniform structure through the thickness. In the general case no limitations are placed on the thicknesses, rigidity, density, number and/or sequence of the layers. The physical and mechanical characteristics of the layers may vary through the thickness and in transverse direction as a result of design requirements. For generality of the approach it is assumed that the material of each layer is anisotropic and possesses one plane of elastic symmetry. In particular, the given approach allows to consider both macrostructural (macrolayer of anisotropic material) and microstructural properties of two materials. In the former case, the composite characteristics are equalized and a macroscopic homogeneous medium is considered. In the latter case, the reinforced materials (glass, metal, graphite fabric, etc) and the binding materials (polymer, metal and other matrices) are taken as separate layers, i.e. directly for each phase of heterogeneous system.

MODELLING

Let us build a geometrically nonlinear model for laminated plates and shallow shells which is suitable for solving contact problems. Dynamic loads are applied on the outer and inner surfaces of the laminate so that

$$q^{\pm} = q_s^{\pm}(x,t), \qquad s = 1,2,3 \tag{1}$$

where q^+ and q^- are loads applied on the outer and inner surfaces, respectively, t is time, and the subscript s denotes the corresponding coordinate axes. The reference surface may be positioned arbitrary through the thickness of the shell. It may be chosen, within any layer, to coincide with the interlaminar or external surfaces as dictated by the nature of the problem under consideration. The stress conditions on the external surfaces may be written as

$$\begin{aligned}
\sigma_{s3}^{(1)} &= -q_s^{-}, && \text{for } z = a_0 \ (k = 1) \\
\sigma_{s3}^{(n)} &= q_s^{+}, && \text{for } z = a_n \ (k = n)
\end{aligned} \tag{2}$$

577

Figure 1.

Geometry of laminated shell.
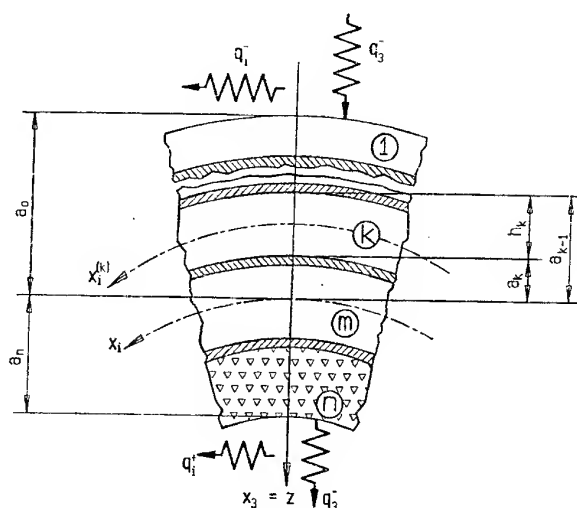
The layers are assumed to be perfectly bonded, i.e. for $z = a_{k-1}$ we have

$$\sigma_{s3}^{(k-1)} = \sigma_{s3}^{(k)}; \quad u_s^{(k-1)} = u_s^{(k)} \tag{3}$$

In the following derivation summation is assumed over "mute" indices $i, j = 1, 2$; s, $t = 1, 2, 3$; p, g, q. No summation is implied over k, r, m. A subscript after a comma denotes differentiation with respect to the variable following the comma and superscript is expressed in brackets to distinguish it from an exponent.

By analogy with [1,2,3,4] we shall introduce the following hypotheses to determine the displacements in the laminated shell

$$\{U\} = [F]\{W\} \tag{4}$$

where $\{U\} = \{U_s^{(k)}(X, t)\}^T$ is a displacement vector at an arbitrary point within the k-th layer of the shell (plate); $X = (x_i, z)$ is orthogonal system of coordinate; $\{W\} = \{\{W_s\}\}^T$ is a vector of desired functions and their derivatives and the components of which are

$$\{W_1\} = \{v_i, w, \theta_i\} \tag{5}$$

where $v_i(X, t)$, $w(X, t)$ are vectors of tangential and normal deflections, respectively, $\theta_i(X, t)$ is a slope of the reference surface which corresponds to the Timoshenko model;

$$\{W_2\} = \{\chi_1, \chi_{1,i}, \ldots, \chi_5, \chi_{5,i}\} \tag{6}$$

is a vector of additional degrees of freedom of the reference surface, related to transverse shear and normal compression arising from the Poisson's effect, and it accounts for special features of the dynamic problem;

$$\{W_3\} = \{\chi_6, \chi_{6,i}, \ldots, \chi_9, \chi_{9,i}\} \tag{7}$$

is a vector of unknown functions of transverse shear and normal compression arising from the direct influence of the full load vector applied on the external surfaces of the shell (see Fig 1.);

$$[F] = [[F_s^{(k)}]] \tag{8}$$

578

is a 3×32 matrix of distribution functions through the thickness of the shell. The structure of submatrix is illustrated by writing it explicitly, viz. $[F_3^{(k)}]$

$$[F_3^{(k)}] = \begin{bmatrix} 0 & \psi_{61}^{(1)} & \psi_{62}^{(1)} & 0 & \psi_{71}^{(1)} & \psi_{72}^{(1)} & 0 & \psi_8 & 0 & 0 & \psi_9 & 0 \\ 0 & \psi_{61}^{(2)} & \psi_{62}^{(2)} & 0 & \psi_{71}^{(2)} & \psi_{72}^{(2)} & 0 & 0 & \psi_8 & 0 & 0 & \psi_9 \\ -\varphi_6 & 0 & 0 & -\varphi_7 & 0 & 0 & -\varphi_8 & 0 & 0 & -\varphi_9 & 0 & 0 \end{bmatrix} \quad (9)$$

The entire matrix $[F]$ is not shown here because of its size.

The distribution functions $\varphi(z)$ and $\psi(z)$ in the matrix $[F]$ satisfy boundary conditions (3) and also conditions on the reference surface, i.e. when $z = 0$ $k = m$ the normal and tangential displacements are equal to the displacements of the reference surface:

$$u_3^{(m)}(x, 0, t) = w(x, t); \quad u_i^{(m)} = v_i(x, t) \quad (10)$$

Their form is determined after solving the problem in the first approximation on the basis of the classical shell theory in a similar way to those given in [1,2,3] for the transversely orthotropic materials.

The Cauchy relations and hypotheses (4) allow to obtain the components of the tensor of deformations, which in a matrix form take the following form

$$\{e\} = [\Psi]\{\Theta\} \quad (11)$$

Here $\{e\} = \{e_{11}^{(k)}, e_{22}^{(k)}, e_{33}^{(k)}, 2e_{23}^{(k)}, 2e_{13}^{(k)}, 2e_{12}^{(k)}\}^T$ is the vector of deformations for the k-th layer of the shell; $\{\Theta\} = \{\{\theta_s\}\}^T$ is the vector of deformations for the reference surface, in which the first group of deformations

$$\{\theta_1\} = \{\epsilon_{11}, 2\epsilon_{12}, \epsilon_{22}, \gamma_2, \gamma_1, \theta_{1,i}, \theta_{2,i}\} \quad (12)$$

corresponds to the Timoshenko model as in the displacement vector (4). The second group

$$\{\theta_2\} = \{\chi_1, \kappa_{11}^{(1)}, \kappa_{12}^{(1)}, \kappa_{22}^{(1)}, \ldots, \chi_5, \chi_{5,1}, \chi_{5,2}, \kappa_{11}^{(5)}, \kappa_{12}^{(5)}, \kappa_{22}^{(5)}\} \quad (13)$$

takes into account transverse shear and normal compression arising from the Poisson's effect and acceleration. The third group

$$\{\theta_3\} = \{\chi_6, \chi_{6,1}, \chi_{6,2}, \kappa_{11}^{(6)}, \kappa_{12}^{(6)}, \kappa_{22}^{(6)}, \ldots, \chi_9, \kappa_{11}^{(9)}, \kappa_{12}^{(9)}, \kappa_{22}^{(9)}\} \quad (14)$$

is a result of taking into account the transverse shear and normal compression arising from the direct influence of the external load. In (12)–(14) the following relations are used

$$\begin{aligned} 2\epsilon_{i,j} &= v_{i,j} + vj, i + 2k_{ij}w + w_{,i}w_{,j}; \quad \gamma_i = w_{,i} + \theta_i \\ \kappa_{ij}^{(p)} &= \chi_{p,ij}, \quad (p = 1, \ldots, 9) \end{aligned} \quad (15)$$

$[\Psi] = [[\psi_s^{(k)}]]$ is a 6×55 matrix of the distribution functions of deformation through the shell thickness and its structure is similar to (9).

579

The components of the stress tensor can be computed using the Hooke's law in the form of the stresses and also expression (11) for the deformation vector. Then

$$\{\sigma\} = [C][\Psi]\{\Theta\} \tag{16}$$

where $\{\sigma_{11}^{(k)}, \sigma_{22}^{(k)}, \sigma_{33}^{(k)}, \sigma_{23}^{(k)}, \sigma_{13}^{(k)}, \sigma_{12}^{(k)}\}^T$ is a stress vector. $[C]$ is the stiffness matrix for the k-th layer of the shell, which is made of anisotropic material and possesses one plane of elastic symmetry.

The relations obtained determine all components of the displacement (4), strain (11) and stress (16) vectors at an arbitrary point for the k-th layer of the piecewise heterogeneous anisotropic shell. They provide a physical and geometrical model of the stress–strain state including geometrically nonlinearity.

The following relations contribute to the model: — the system of independent unknown functions for the reference surface X and time t — $v_i, w, \theta_i, \chi_p, (p = 1, \ldots, 9)$; — given functions of the normal z which show the change of the corresponding vector components of displacements, deformations and stresses through the layer thickness. The normal functions are chosen in such a way to satisfy the interface conditions (3) and also conditions on the reference surface (10). In doing so, the layers of different thicknesses and rigidity are described equally, and both constant and variable physical and mechanical characteristics through the thickness are taken into account. Thereby, the universality of the model with respect to the shell structure through the thickness is assured.

The distinguishing feature of the model from the one given in [2] is that the new functions $\chi_p, (p = 6, \ldots, 9)$ are introduced which allow transverse shear and normal compression arising from the direct influence of external load to be taken into account. This is especially important when the shell is subject to a local load and also for the solution of contact problems.

The equations of motion and the boundary conditions may be determined using the Hamilton–Ostrogradsky variational principle.

The nonlinear differential equations for the functions $v_i, w, \chi_p, (p = 1, \ldots, 9)$

$$
\begin{aligned}
&N_{ij,j} - K_i + p_i = 0 \\
&Q_{i,i} - k_{ij}N_{ij} + (N_{ij}w_{,i})_{,j} - K_3 + p_3 = 0 \\
&Q_i - M_{ij,j} + K_{im}^{(m)} + p_i^{(m)} = 0 \\
&M_{ijs,ij} - Q_{3s} - K_{3s} - K_{iis,m} + p_3^{(s)} = 0 \\
&M_{ijt,ij} + Q_{it,i} - Q_{3t} - K_{3t} - K_{iit,m} + p_3^{(t)} = 0 \\
&(m = i, j = 1, 2; \quad s = 1, 2, 8, 9; \quad t = 3, \ldots, 7)
\end{aligned}
\tag{17}
$$

and the consistent boundary conditions, for example, uniform ones on the contour

$x_2 = const,$

$$N_{11}\delta v_1 = 0; \quad N_{12}\delta v_2 = 0; \quad (N_{11}w_{,1} + N_{12}w_{,2} - Q_1)\delta w = 0$$
$$M_{11}^{(1)}\delta\theta_1 = 0; \quad M_{12}^{(2)}\delta\theta_2 = 0; \quad M_{12p}\delta\chi_{5,1} = 0$$
$$[M_{11s,1} + 2M_{12s,2} - K_{11s} + q_1^{(s)}]\delta\chi_s = 0 \tag{18}$$
$$[M_{11t,1} + M_{12t,2} + Q_{1t} - K_{11t} + q_1^{(t)}]\delta\chi_t = 0$$
$$(s = 1,2,8,9; \quad t = 3,\ldots,7; p = 1,\ldots,9)$$

are given for internal linear forces (integral stress characteristics) and distributed inertia forces (generalized linear inertia forces). They have the following form

$$\{M\} = \int_h \{\sigma\}^T[\Psi]dz; \quad \{K\} = \int_h \{U\}^T[\rho][F]dz \tag{19}$$

where

$$[\rho] = \begin{bmatrix} \rho_1^{(k)} & 0 & 0 \\ 0 & \rho_2^{(k)} & 0 \\ 0 & 0 & \rho_3^{(k)} \end{bmatrix}$$

is a density matrix for the k-th layer. Using the expression (16) for stresses in (19), the generalized and inertia forces can be expressed through the deformations of the coordinate surface as follows

$$\{M\}^T = [D]\{\theta\}; \quad \{K\}^T = [D_\rho]\{W\} \tag{20}$$

where

$$[D] = \int_h [\psi]^T[C][\psi]dz; \quad [D_\rho] = \int_h [F]^T[\rho][F]dz$$

static and dynamic characteristics of the layer material. Now the system of equations of motion (17) of the shell can be represented in the following matrix form

$$[L][D]\{\theta\} + [J][D_\rho]\{W\} + \{P\} = 0 \tag{21}$$

Here $\{P\}$ is generalized load vector; $[L]$ diagonal "static" and "inertial" matrices of the differential operators.

The order of the system of equations (21) is equal to 46. There are 23 boundary conditions (18) to be satisfied for each end of the shell. Thus, equations (21) are the equations of the motion governing the anisotropic multilayered shell expressed in the form of displacements. On the basis of the general nonclassical model and method of finite elements, similar to [2], the discreet continuum scheme of the finite element method is derived and implemented. The principle equations of the FEM are in accordance with the system of differential equations (21), viz.

$$[K_{gs}]\{V\} + [M_{gs}]\{V\} = \{R\} \tag{22}$$

where $[K_{gs}]$ and $[M_{gs}]$ $(g,s = 0,\ldots,10)$ are stiffness and mass matrices, related to the vector of node displacements $\{V\}_m = \{V_{1m}, V_{2m}, W_m, \theta_{1m}, \theta_{2m}, \gamma_m, W_{pm}, \theta_{1pm}, \theta_{2pm}, \gamma_{pm}\}^T$, $(p = 1,\ldots,9)$; $\{R\}$ is a vector of the nodal forces.

581

Block matrices correspond to the following conditions when $g = s$: plane stress condition ($g = 0$); pure shear (Timoshenko model) ($g = 1$); shear and compression ($g = 2, \ldots, 10$), and also to the mutual influence of these conditions ($g = s$).

More detailed information concerning the implementation of the higher order theory based on FEM can be found in [2].

As a rule, when solving contact problems using the finite element method, distribution of the transverse normal stresses in the area of contact over the FE domain or its part is assumed in the form of uniformly distributed load or load considered as the acting nodal integral forces. This, on the one hand, makes the FE mesh dense in the area of reactive concentrated pressures and leads to distortion of the influence matrix, and, on the other hand (in case of nodal forces), does not allow to determine the character of the distribution of contact stresses.

The method proposed her is free from these shortcomings. The reactive forces over FE domain are distributed using a truncated pyramid law. Thus, the entire diagram of contact stresses will be a piecelinear function, continuous within the bounds of each FE.

In order to achieve the largest area of contact, the matrix of influence $[V]$ of the unit intensity of the reactive forces at the FE node is built. For this purpose, distributed load must be considered only at the nodal points. This transformation may be implemented using relations derived from the form functions of the finite element. The influence matrix derived allows to solve problems of the contact interaction for the shell structures both with rigid and elastic layers.

As an example we consider the problem of cylindrical bending of a plate with a rigid parabolic punch. Initial position of the contact surface of the punch is described using function $z = f(x_1)$. After applying vertical load to the punch it takes the form of $z_1 = f(x_1) + \Delta$. As this takes place, reactive pressure and displacement of the plate forced by the pressure must satisfy the matrix equations of equilibrium

$$[V]\{R\} = \{Z\} + \delta\{E\} \tag{23}$$

where $\{R\}$ is intensity vector of the reactive pressures at the FE nodes; $\{Z\}$ is a discrete analogue of the contact surface equation of the punch before applying external load P; $\delta\{E\}$ is displacement of the punch as a rigid body; δ is an unknown parameter; $\{E\}$ is a unit vector (column). In order to determine parameter δ, the equilibrium condition between load P applied to the punch, and contact pressure under it is given as

$$\sum_{i=1}^{n} R_i \frac{l_{i-1} + l_i}{2} = P \tag{24}$$

where l_i are FE dimensions in the area of contact.

Simulteneous solution of equations (23) and (24) allows to determine contact stresses at the FE nodes allowing for the links between the plate and the punch. Then all FE nodes with negative reactive pressure are taken to the "passive" state, i.e.

corresponding links and rows of the influence matrix $[V]$ are exluded by assigning zero values to them. Using renewed matrix $[V]$ as the base, the corrected contact stresses may be determined. The proces with truncated influence matrix mentioned above repeats as long as the following inequality takes place for each FE node, i.e.

$$\{R\} \geq 0 \tag{25}$$

In addition, an inequality of "impermeability" for the passive nodes must be checked

$$\{W\} - \{Z\} - \delta\{E\} \geq 0 \tag{26}$$

where $\{W\}$ is discrete analogue of the displacement function for the shell structure in the area of lagest possible contact.
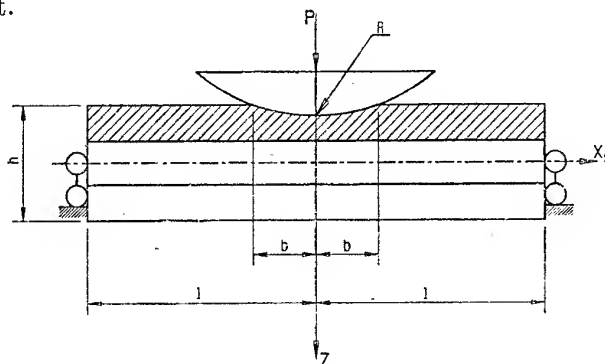

Figure 2.

Contact surface between the punch and the laminate.

The nodes, for which inequality (26) do not apply are considered as "active", that is the influence matrix $[V]$ is supplemented with corresponding rows and columns. The iterative process is terminated when inequalities (25) and (26) are satisfied simultaneously.

Thus, the proposed method allows to solve contact problems in terms of the one-sided links between contact bodies.

NUMERICAL RESULTS

Table 1 shows numerical convergence of the method depending on number of finite elements in the region of the maximum possible area of contact for the cylindrical bending of simply supported thick isotropic plate under the influence of the cylindrical punch subject to load P. The results given in the Table 1 are for the plate with a relative thickness parameter $2l/h = 2$, and Poisson's coefficient is $\nu = 0.3$. The dimension of the contact area is $\beta = b/l = 0.172$ (see Fig. 2). As seen from the table, the reactive pressure q^* and displacement w at the central point are already in good agreement with analytical solution [6] when only 14 FE are used.

Table 1.

Number of FE	q^*	w	P^*
7	0.762	74.3	20
14	0.759	74.0	20
28	0.757	73.8	20
Analitical solution	0.757	73.8	20

Figure 3 shows diagrams of the contact pressures $g^* = 2qb/P$ depending on width of the contact area $\beta = b/l$ and relative thickness $2l/h$. As seen from the figure, the contact stresses, determined using the shear model, as in [2], monotonically increase approaching the edge of the contact area. It should be stressed that the results obtained using the proposed method are in good agreement with the exact solution given in [6].
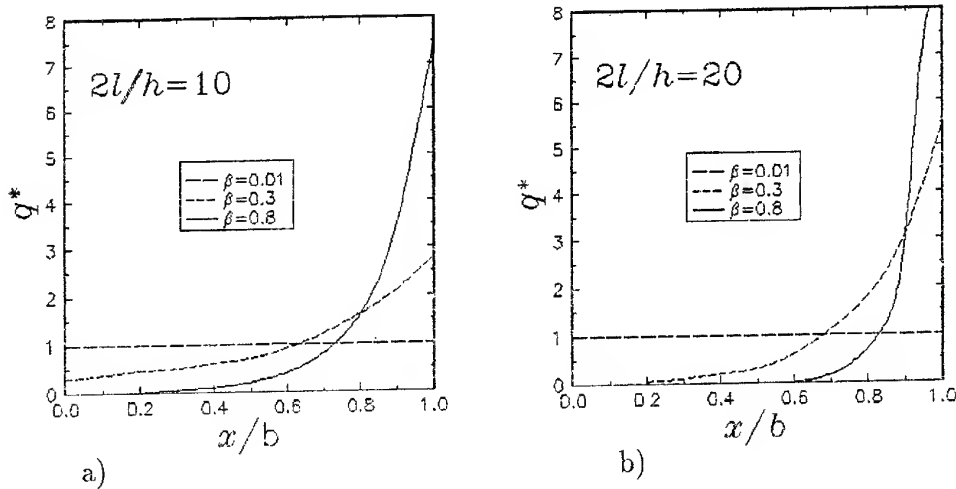

Figure 3. Contact pressure versus the distance (a) $2l/h = 10$, (b) $2l/h = 20$.

REFERENCES

1. V. G. Piskunov, V. E. Verijenko, S. Adali and P. Y. Tabakov, Transverse shear and normal deformation higher–order theory for the solution of dynamic problems of laminated plates and shells. *International Journal of Solids and Structures*, Vol. 31, 1994, pp. 3345–3374.

2. V. G. Piskunov, V. E. Verijenko and V. K. Prisyazhnyouk, *Calculation of heterogeneous shells and plates using the finite element method*. VEISHA SHKOLA, Kiev, (1987).

3. V. K. Prisyazhnyouk and V. G. Piskunov, A model of shallow shells and plates made of layered composite Materials for the Solution of Static, Dynamic and Contact Problems. *Mech. of Comp. Materials*, No. 6, pp. 1014–1021, (1987).

4. V. K. Prisyazhnyouk and I. B. Zajvelev, On the solution of the plane problem of elasticity problem for multilayered orthotropic composite. *Mech. of Comp. Materials*, No. 2, pp. 206–214, (1991).

5. S. E. Umanskij and I. K. Devidson, Solution of contact problems of the theory of elasticity and plasticity. *Strength of Materials*, No. 1, pp. 87–92, (1982).

6. L. M. Keer and M. A. G. Silva, Bending of a cantilever beam brought gradually into contact with a cylindrical supporting surface. *Int. J. Mech. Science*, No. 12, pp. 751–760, (1970).

HIGH STRAIN RATE TESTS ON FIBRE METAL LAMINATES

A. VLOT

Faculty of Aerospace Engineering, Delft University of Technology, Kluyverweg 1,
2629 HS Delft, The Netherlands

INTRODUCTION

Fibre Metal Laminates (FMLs) are a new family of laminates built up from 0.2 to 0.3 mm thin aluminium alloy sheets bonded into one laminate by intermediate 0.1 to 0.2 mm thin fibre/epoxy layers. The laminates are developed at Delft University of Technology, primarily for aircraft structures. The variant with aramid fibres is called 'ARALL', while a new generation of laminates called 'GLARE' incorporates S2-glass fibres. FMLs have a high fatigue resistance due to intact fibres in the wake of the crack which restrain crack opening. The material combines the formability and machinability of aluminium alloys and the high specific strength of composite materials. ARALL-3 is currently in production for the C-17 aft cargo door and GLARE-3 is selected for the Boeing 777 impact resistant bulk cargo floor.

GLARE material has an excellent impact resistance compared to carbon reinforced composites and even performs better than monolithic aluminium at high impact velocities (100 m/s) [1,2,3]. A part of the good impact resistance is attributed to the strain rate dependent behaviour of the glass fibres. Several authors found an effect of the strain rate on the longitudinal tensile strength of glass/epoxy [4,5,6]. Results of high strain rate tensile and fracture tests on GLARE and monolithic aluminium are discussed here in order to shed more light on the dynamic behaviour of GLARE.

TENSILE TESTS

The tested materials are divided in two typical high strength crack stopper materials (GLARE-1 and 7075-T6) and two typical fatigue resistant fuselage skin materials (GLARE-3 and 2024-T3):

- GLARE-1, in a 3/2 lay-up: three 0.3 mm thin layers of 7475-T76 and two layers of unidirectional S2-glass/epoxy prepreg. The total thickness is 1.44 mm, in the following lay-up: [7475/0°/0°/7475/0°/0°/7475]
- Aluminium 7075-T6 (bare), thickness of 1.62 mm.
- GLARE-3, in a 2/1 lay-up: two 0.2 mm thin 2024-T3 layers bonded by two cross-plied S2-glass/epoxy layers. The total thickness is 0.69 mm, with the following lay-up: [2024/0°/90°/2024]
- Aluminium 2024-T3 (bare), thickness 0.64 mm.

Unnotched, blunt notched (K_t = 1.86 for isotropic material) and sharp notched specimens were tested. The sharp notches were made by a saw cut. The specimen

585

width was 20 mm. All materials were tested at three loading rates: 2 mm/min (quasi-static), 1 m/s and 20 m/s. The quasi-statie tests were performed with a 10 kN MTS servo-hydraulic test machine, while the higher loading rates were achieved with a 10 kN Schenk hydro-pulse test machine. The cross-head speeds were constant during the tensile test. Three tests were done for each material and loading rate to obtain reliable results.

The ultimate stress and strain to failure as a function of the strain rate is plotted in Figure 1. As can be seen here, 7075-T6 shows a small decrease of the strength, while the strength of GLARE-1 increases by 16% at a strain rate of 110 s^{-1}. A lot of delamination is visible in the GLARE specimens after the tests. There was no difference in the fracture appearance of the static and high strain rate specimens.

The average test results for the unnotched and notched skin materials are given in figure 2. GLARE-3 shows an increase in strength of 11, 21, and 24%, for no notch, a blunt notch and a sharp notch respectively; while 2024-T3 shows a decrease of 11 and 16% for the blunt and sharp notch respectively. Apparently the strain rate effect is stronger for the sharper notches due to fact that the strain rate at the root of the notch is raised by the stress concentration. The unnotched GLARE specimens show a different fracture behaviour at high strain rates. The specimens fractures at two locations with more delamination and buckling due release of elastic energy of the specimen than under static loading.

RESIDUAL STRENGTH

The dynamic fracture of GLARE and 7075-T6 has been investigated on long sheet specimens with two adjacent cracks (Figure 3). When a load is applied to the specimen, the two cracks in the specimen will link-up and a single crack is formed. A sudden rise of the stress intensity at the ends of this single crack will be caused by this linking. This increase of the stress intensity can initiate a dynamic fracture of the specimen. When the ligament between the cracks is too long, both cracks behave almost independently. In that case, a crack will initiate from both sides of each crack instead of a link-up prior to final failure. The specimens were 160 mm wide and 1000 mm long. The specimen was long in order to store enough elastic energy for the rapid failure. The two collinear cracks were made by sawing slots with a fine jeweller's saw. Aluminium 7075-T6 (bare) with a thickness of 1.59 mm and GLARE-1 with a thickness of 1.43 mm, consisting of 0.3 mm 7475-T76 and 0.1 mm S2-glass/epoxy layers were tested. The GLARE material had the following lay-up: [7475/0°/0°/7475/0°/0°/7475].

Specimens with six different crack lengths were tested for both materials. The total length of the two cracks plus the width of the ligament between the two cracks was kept constant (60 mm, see Figure 3). This means for the longest crack length of a=30 mm, the length of the ligament was 0 (one single crack length $2a$=60 mm). The

ligament length was increased up to 12 mm (a=24 mm).

The Crack Opening Displacement (COD) is measured with an optical device. The load on the specimen and the COD of the collinear cracked specimens were recorded with a sample frequency of 15 kHz and stored on a disk. The load, COD, and strain of the crack stopper specimens were sampled with 10 kHz. The specimens were mounted in a 1000 kN MTS testing machine and fastly loaded with a square-step load from 0 to 200 kN, except the collinear crack specimens with one single crack (a = 30 mm) and the crack stopper specimens with a crack over the full width. These specimens were loaded quasi-statically up to failure. The COD was measured for the collinear crack specimens at a position of 5 mm from the crack tip, which is 25 mm from the centre of the specimen. A (virtual) COD at the centre of the specimen was calculated from this measured COD_{25}, assuming an elliptical crack opening:

$$COD = COD_x \frac{a_{full}}{\sqrt{(a_{full}^2 - x^2)}} = 1.8091 \ COD_{25}$$

where x=25 mm and a_{full} = 30 mm.

Typical dynamic curves are shown in Figure 4 for GLARE-1 for a = 26 mm. The link-up of the two cracks can be seen in the COD-plot as a small rise prior to final failure of the specimen. The link-up point can not be accurately determined for the 7075-T6 specimen at a = 28 mm. For the crack lengths smaller than 26 mm no link-up is found prior to final failure. For these crack lengths the interaction between the two cracks is too small. The gross stress as function of the crack length a is plotted in Figure 5. The ultimate gross stress for 7075-T6 shows a slight decrease for a decreasing crack length from a=30 mm, before a rise to the link-up boundary. GLARE-1 exhibits a small increase of the strength, starting from a=30 mm. The gross ultimate stress for 7075-T6 drops from 204.2 to 193.5 MPa (a reduction of 5.2%), whereas the gross stress of GLARE 1 rises from 329.5 to 361.9 MPa (an increase of 9.8%). No difference was found between the fracture surfaces at static and dynamic loading.

CONCLUSIONS

1. Tensile tests on unnotched specimens revealed a small decrease of the ultimate stress of the aluminium alloy 7075-T6 (6%) and an increase for GLARE-1 Fibre Metal Laminates (16%) at loading rates of 100 s^{-1}.
2. Tensile test on notched specimens showed that the strain rate sensitivity increases for sharper notches. An increase of the ultimate stress of 11, 21 and 24% was determined for GLARE-3 Fibre Metal Laminates without a notch, with a blunt notch and with a sharp notch respectively. Al 2024-T3 shows a *decrease* of 11 and 16% for blunt and sharp notches respectively.

587

3. Residual strength tests carried out under dynamic conditions revealed a slightly smaller ultimate gross stress for the aluminium 7075-T6 alloy (5%) and a 10% higher residual strength for the GLARE-1 Fibre Metal Laminate.

ACKNOWLEDGEMENT

REFERENCES

[1]   Vlot, A. "Impact Properties of Fibre Metal Laminates", *Composites Engineering* **3**, pp.911-927 (1993).

[2]   Vlot, A. *Low-velocity Impact Loading on Fibre Reinforced Aluminium Laminates (ARALL) and Other Aircraft Sheet Materials*, dissertation Delft University of Technology, (1991).

[3]   Vlot, A., "Impact loading on fibre metal laminates", *Int.J. Impact Engng.* **18**, pp.291-308 (1996).

[4]   Chiao, T.T, Moore, R.L. "Strain Rate Effect on the Ultimate Tensile Stress of Fiber Epoxy Strands", in: C.J. Hilado (ed.), *Carbon Reinforced Epoxy Systems*, Technomic USA, pp.1-4 (1974).

[5]   Daniel, I.M., Liber, T. *Strain Rate Effects on Mechanical Properties of Fiber Composites*, NASA CR-135087 (1976).

[6]   Harding, J., Welsh, J. "A Tensile Testing Technique for Fibre-reinforced Composites at Impact Rates of Strain", *J. Materials Science* **18**, pp.1810-1826 (1983).
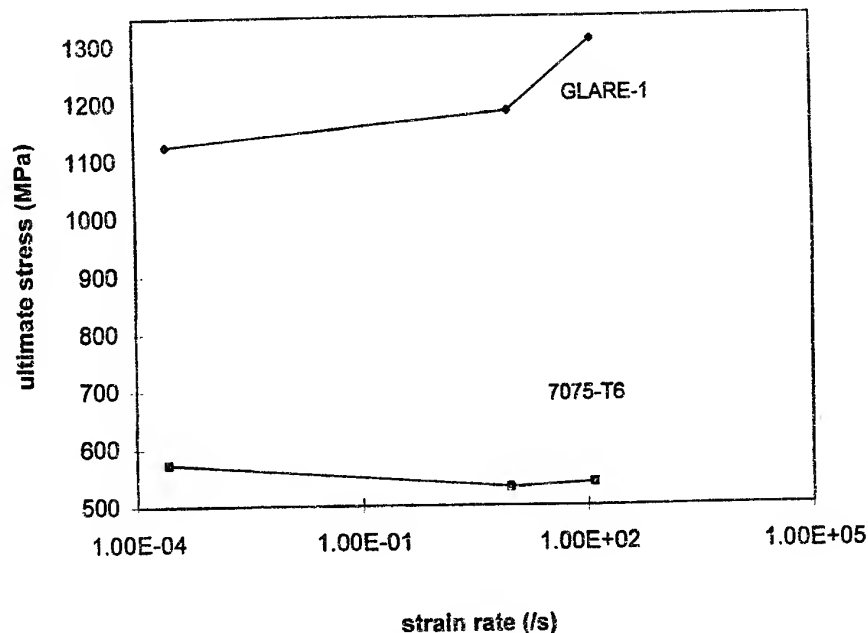
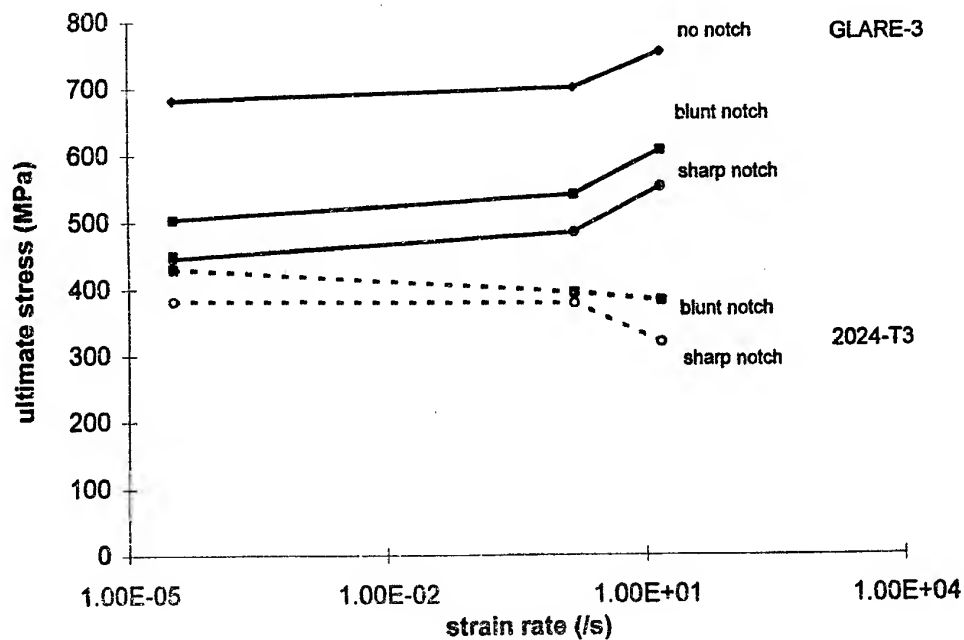Figure 1. Measured ultimate stress as function of the strain rate.

Figure 2. Measured ultimate stress for the notched and unnotched specimens.
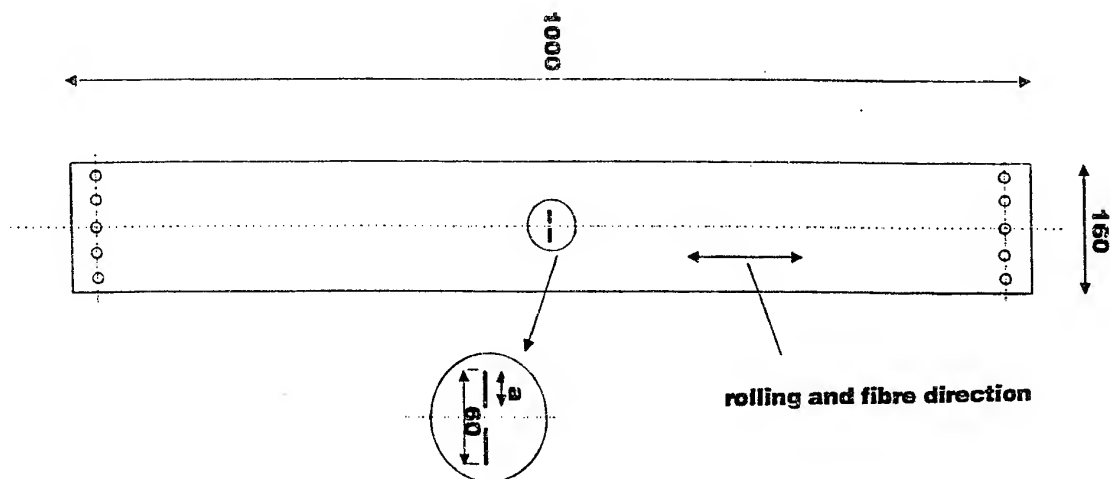

Figure 3. Collinear crack specimen to measure residual strength at a high loading rate.
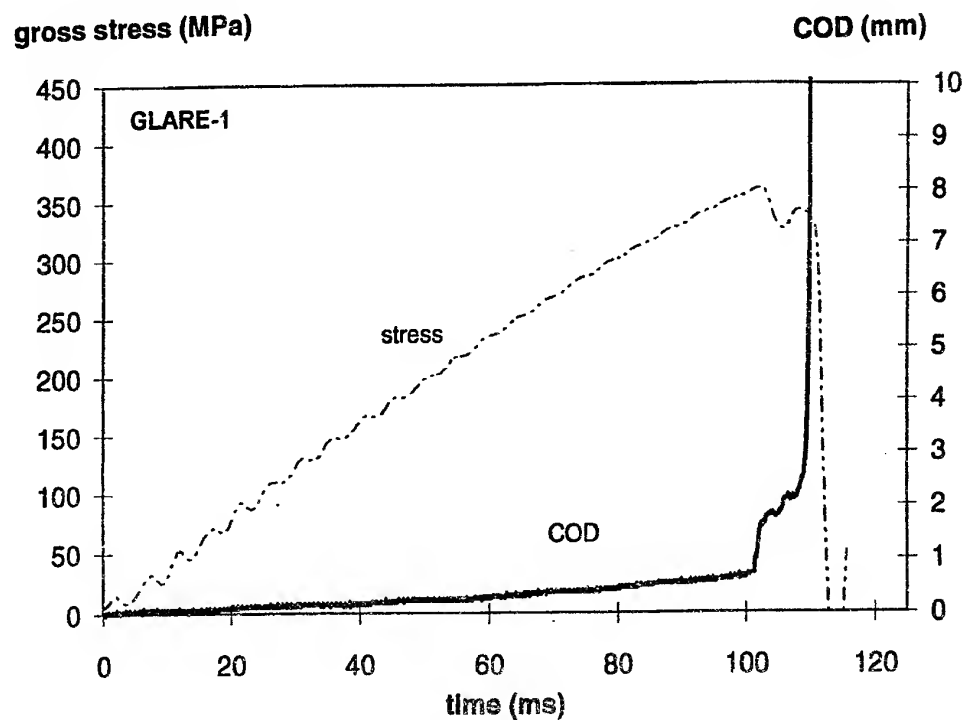
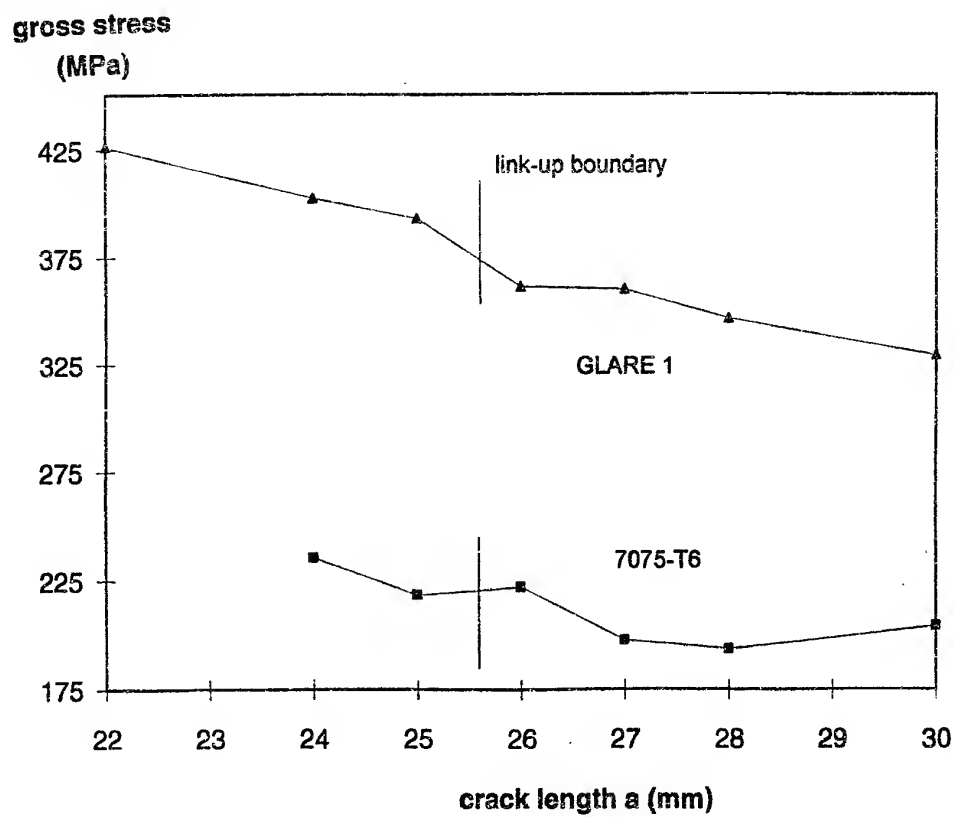Figure 5. Typical gross stress and crack opening measurements ($a = 26$ mm).

Figure 5. Ultimate gross stress versus the crack length a in the collinear crack specimen.

590

NUMERICAL ASPECTS OF THE DELAMINATION ANALYSIS IN COMPOSITE SHELL STRUCTURES

W. Wagner and F. Gruttmann

Institut für Baustatik, Universität Karlsruhe, Kaiserstraße 12,
D–76131 Karlsruhe, Germany

INTRODUCTION

In this paper a numerical model for the nonlinear analysis of laminated shells is presented. The developed isoparametric layered shell element is based on a multi–director formulation. Piecewise polynomial functions are used to interpolate the displacement field through the thickness. Thus the element is able to predict the complete stress state. Within a nonlinear static analysis onset of delamination is described by exploiting a stress based fracture criterion between adjacent layers. Additional nodal variables are introduced to describe the vector of crack opening displacements. Crack propagation and the final delamination zone for a prescribed load level is achieved by fulfilment of the weak form of equilibrium and of the fracture criterion.

Several layered finite shell elements based on multi–director formulations have been published in the literature, e.g. [1] – [6]. The delamination problem has been investigated numerically e.g. in [7], [8].

VARIATIONAL FORMULATION

The considered shell consists of n **physical** layers of thickness h^j. Within our formulation the laminate can be described with N **numerical** layers with thickness h^i. Thus each physical layer can be subdivided into several sublayers or vice versa several layers can be summarized to an equivalent numerical layer.

The initial geometry is described by an arbitrary reference surface and a normal vector as in standard shell theories. Thus the position vector $\mathbf{X}_0$ of the reference surface Ω is labeled with convective coordinates Θ^α. An orthonormal basis system $\mathbf{t}_k(\Theta^\alpha)$ is attached to this surface where $\mathbf{t}_3$ is the normal vector and Θ^3 the coordinate in thickness direction ($h_u \leq \Theta^3 \leq h_o$). The transformations between the different base systems is achieved using a proper orthogonal tensor $\mathbf{R}_0$

$$\mathbf{t}_k(\Theta^\alpha) = \mathbf{R}_0(\Theta^\alpha)\,\mathbf{e}_k\,. \tag{1}$$

Introducing a displacement field $\mathbf{u}(\Theta^i)$ the position vectors of the reference and the current configuration are given by

$$
\begin{aligned}
\mathbf{X}(\Theta^\alpha, \Theta^3) &= \mathbf{X}_0(\Theta^\alpha) + \Theta^3\,\mathbf{t}_3(\Theta^\alpha) \\
\mathbf{x}(\Theta^\alpha, \Theta^3) &= \mathbf{X}(\Theta^\alpha, \Theta^3) + \mathbf{u}(\Theta^\alpha, \Theta^3)\,.
\end{aligned}
\tag{2}
$$

For the displacement field $\mathbf{u}(\Theta^i)$ in shell space we assume a multiplicative decomposition with independent functions for the shape in thickness direction and functions defined on the reference surface of the shell. The displacement vector of the numerical layer i is interpolated through the thickness by, see ref. [1]

$$
\begin{aligned}
\mathbf{u}(\Theta^\alpha, \Theta^3) &= \sum_{l=1}^{m} \phi_l^i(\Theta^3)\, \bar{\mathbf{u}}_l^i(\Theta^\alpha) = \mathbf{\Phi}^i(\Theta^3)\, \bar{\mathbf{u}}^i(\Theta^\alpha) \\
\bar{\mathbf{u}}^i(\Theta^\alpha) &= [\bar{\mathbf{u}}_1^i, \bar{\mathbf{u}}_2^i, \quad \dots \quad, \bar{\mathbf{u}}_m^i]^T \quad (2 \le m \le 4)\,.
\end{aligned}
\tag{3}
$$

The shape functions are arranged in a matrix

$$
\mathbf{\Phi}^i = [\phi_1^i \mathbf{1}, \phi_2^i \mathbf{1}, \quad \dots \quad, \phi_m^i \mathbf{1}]
\tag{4}
$$

with hierarchical functions ϕ_l^i up to third order.

Thus (3) allows warping of cross sections and changes of thickness.

The covariant base vectors of the reference configuration are introduced as $\mathbf{G}_i = \partial\mathbf{X}/\partial\Theta^i$ whereas the dual base vectors $\mathbf{G}^i$ are defined by $\mathbf{G}_i \cdot \mathbf{G}^j = \delta_i^{\ j}$. Accordingly, one obtains the convected base vectors $\mathbf{g}_i$ and $\mathbf{g}^j$ of the current configuration.

Top and bottom surface of the shell are loaded with loads $\hat{\mathbf{p}} = \hat{p}^k\, \mathbf{e}_k$, whereas body forces are neglected for simplicity. The principle of virtual work in a material description reads

$$
\mathbf{g}(\mathbf{u}, \delta\mathbf{u}) = \int\limits_{(\Omega)} \Big[\int\limits_{(\Theta^3)} S^{kl}\, \delta E_{kl}\, J d\Theta^3 \Big]\, d\Theta^2 d\Theta^1 - \int\limits_{(\Omega_\sigma)} \hat{p}^k\, \delta u_k\, d\Omega_\sigma = 0\,.
\tag{5}
$$

with $J = (\mathbf{X}_{,1} \times \mathbf{X}_{,2}) \cdot \mathbf{X}_{,3}$. Note that integration in (5) has to be performed considering the different material parameters and fibre angles through the thickness. The covariant components of the Green–Lagrangian strain tensor $\mathbf{E} = E_{kl}\, \mathbf{G}^k \otimes \mathbf{G}^l$ and the associated variation are obtained by partial differentiation of the position vectors with respect to convective coordinates Θ^i

$$
\begin{aligned}
E_{kl} &= \tfrac{1}{2}(\mathbf{x}_{,k} \cdot \mathbf{x}_{,l} - \mathbf{X}_{,k} \cdot \mathbf{X}_{,l}) \\
\delta E_{kl} &= \tfrac{1}{2}(\delta\mathbf{x}_{,k} \cdot \mathbf{x}_{,l} + \delta\mathbf{x}_{,l} \cdot \mathbf{x}_{,k})\,.
\end{aligned}
\tag{6}
$$

The work conjugate stresses S^{kl} are the contravariant components of the Second Piola–Kirchhoff stress tensor $\mathbf{S} = S^{kl}\mathbf{G}_k \otimes \mathbf{G}_l$. Each ply is considered as a homogeneous orthotropic medium, where the axes of orthotropy coincide with the material principal axes. Hence the stresses of the physical layer j are given by the material law

$$
S^{kl} = C^{klmn}\, E_{mn}\,.
\tag{7}
$$

The constitutive parameters C^{klmn} are functions of material values $E_1, E_2, \nu, G_{12}, G_{23}$ of layer j and of the fibre angle φ^j. Here, the fibre angle is defined as angle between fibre direction and basis vector $\mathbf{t}_1$. We restrict ourselves to small strains, thus transformations between different stress tensors are neglected and material parameters of the linear theory can be used. The components expressed in matrix notation

592

refer to an orthonormal coordinate system which is a local fibre oriented basis. The material matrix has to be transformed to a global fibre independent basis system, for more details see e.g. [4].

ASSOCIATED FINITE ELEMENT FORMULATION

Next we introduce an associated 4–node isoparametric shell element based on a displacement formulation. Within an element Ω_e, the position vector $\mathbf{X}$ of the reference configuration is interpolated by

$$\mathbf{X} = \sum_{K=1}^{4} N_K(\xi, \eta) \mathbf{X}_K,$$

$$\mathbf{X}_K = \mathbf{X}_{0K} + \Theta^3 \mathbf{t}_{3K}.$$

$$(8)$$

The functions $N_K(\xi, \eta)$ are the standard bilinear element shape functions. The normal vectors $\mathbf{t}_{3K}$ are computed within the mesh generation and have to be unique at the nodes.

An orthonormal basis system is introduced at the integration points. Thus, no further transformations of the material law are necessary.

The displacement vector $\mathbf{u} = u^l \mathbf{e}_l$ is approximated using (3)

$$\mathbf{u} = \sum_{K=1}^{4} N_K(\xi, \eta) \mathbf{\Phi}^i \mathbf{v}_K.$$

$$(9)$$

Here the nodal displacement vector $\mathbf{v}_K$ consists of $ndf = 3(N+1) + 3N(m-2)$ unknowns.

To avoid shear locking the transverse shear strains $\boldsymbol{\gamma} = E_{\xi 3} \mathbf{G}_1 + E_{\eta 3} \mathbf{G}_2$ are independently interpolated

$$2E_{\xi 3} = \tfrac{1}{2}[(1-\eta)\gamma_B + (1+\eta)\gamma_D]$$

$$2E_{\eta 3} = \tfrac{1}{2}[(1-\xi)\gamma_A + (1+\xi)\gamma_C].$$

$$(10)$$

The shear strains γ_M at the midside nodes $M = A, B, C, D$ of the four–node element are derived from $(6)_1$ for layer coordinates Θ^3.

The approximation of the virtual Green–Lagrangeian strains δE_{kl} $(6)_2$ are obtained from

$$\delta \mathbf{E} = \sum_{K=1}^{4} \mathbf{B}_K(\xi, \eta) \, \delta \mathbf{v}_K.$$

$$(11)$$

where matrix $\mathbf{B}_K$ is specified in detail in ref. [4].

Inserting the preliminary interpolations into the virtual work expression (5) the contribution g^e of element e leads to

$$g^e(\mathbf{v}, \delta\mathbf{v}) = \sum_{K=1}^{4} \delta\mathbf{v}_K^T \int_{(\Omega_e)} \left[\sum_{j=1}^{n} \int_{(\Theta^3)} \mathbf{B}_K^T \mathbf{S} \, J \, \frac{h^j}{2} \, d\zeta^j \right] d\Omega_e - \sum_{l=1}^{2} \int_{(\Omega_{e\sigma})} N_K \hat{\mathbf{p}}_l \bar{J}_l \, d\Omega_{e\sigma}. \quad (12)$$

593

Here $\bar{J}_l$ denotes the surface element of the top and bottom surface $\Omega_{e\sigma}$ with applied loads $\hat{\mathbf{p}}_l$. The stress vector $\mathbf{S} = [\ S^{11}, S^{22}, S^{33}, S^{12}, S^{13}, S^{23}\ ]^T$ is obtained via the constitutive relation.

The finite element formulation of the presented multi–director formulation yields stresses at the integration points in thickness directions. However, for various stress based fracture criteria the interlaminar stresses $\boldsymbol{\sigma} = [S^{13}, S^{23}, S^{33}]^T$ have to be known. This can be achieved by a simple projection method. Application of a least square method yields a C_0-continuous shape of the stress components across the layer boundaries.

The fracture criterion of Hashin [9] is quadratic in terms of the interlaminar stresses

$$F(\boldsymbol{\sigma}) = \frac{(S^{13})^2 + (S^{23})^2}{R_0^2} + \frac{(S^{33})^2}{Z_0^2} - 1\,. \tag{13}$$

Here, Z_0 is the lamina strength in thickness direction under tension and R_0 is the shear strength. The crack criterion considers the general case of mixed mode stresses. Exploitation of the fracture criterion yields the condition for bonding or delamination. In case of delamination we introduce three additional nodal variables to describe the crack opening displacements. Assuming static loading the final delamination zone within a prescribed load level is obtained by fulfilment of the weak form of equilibrium and of the fracture criterion.

The solution of the nonlinear algebraic equation (12) is iteratively computed by Newton's method. The residual vectors and tangent matrices are integrated using Gauss quadrature with 2×2 integration within the shell surface. For each layer the numerical integration through the thickness depends on the chosen polynomial degree, e.g. two integration points for linear and three and four for quadratic and cubic interpolation, respectively.

NUMERICAL EXAMPLE: DELAMINATION ANALYSIS OF A CYLINDRICAL PANEL

Fig. 1 presents a cylindrical panel subjected to a single load at the center. The boundary conditions are: simply supported along the straight edges and free boundary along the curved edges. The laminate consists of three layers with thickness $h^j = 4.23\ mm$ for each layer and $[90°/0°/90°]$ stacking sequence, where $0°$ refers to the circumferential direction of the cylinder.

Due to symmetry one quarter of the system is discretized with 625 4–node elements. The mesh is refined along the free boundary and along the straight boundary to catch the edge effects. Each layer is subdivided into two sublayers. The calculation is carried out displacement controlled. For a prescribed deflection $w = 3\ mm$ at the center of the shell the weak form of equilibrium is computed iteratively. The results are depicted in Fig. 1. A plot of the shear stresses S^{13} in numerical layer 4 and along line $1 - 2$ shows the typical edge effect at the free boundary. The interlaminar stress components enter into the fracture criterion according to eq. (13). Then the delamination zone, plotted in Fig. 1.d, is obtained by exploitation of the fracture criterion.
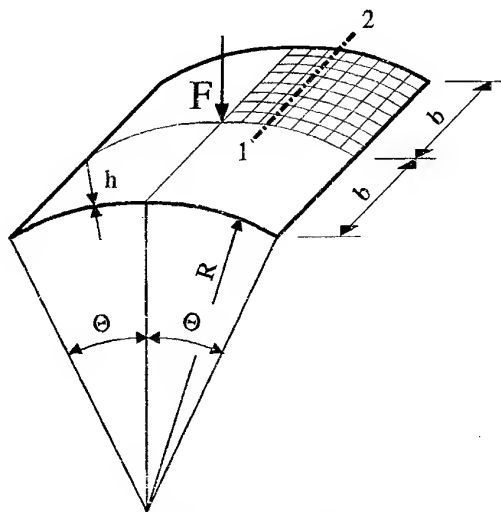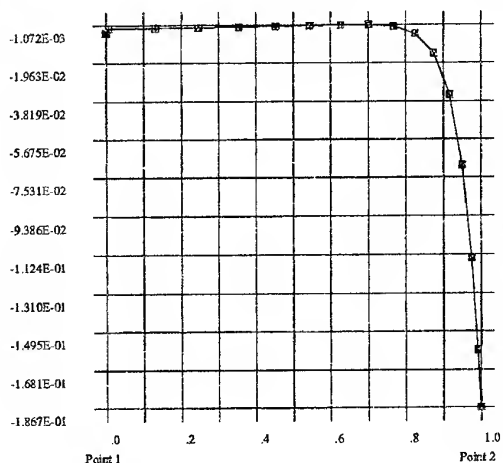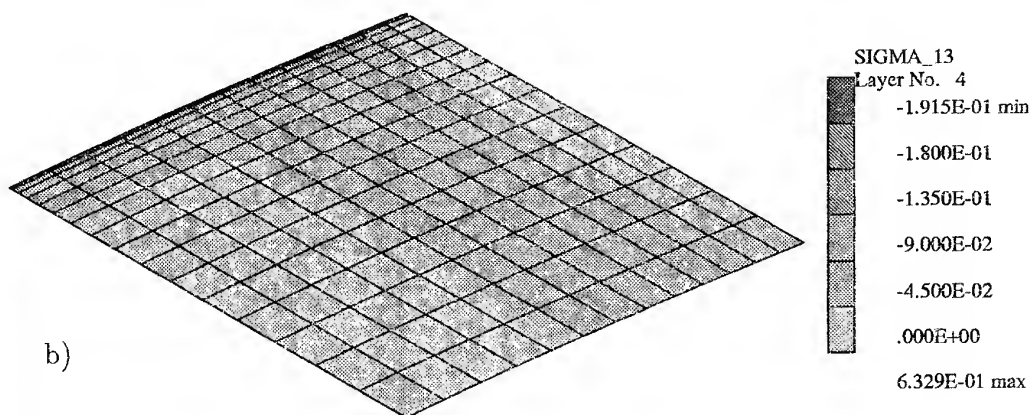
Figure 1: Hinged cylindrical panel, a) System with geometrical and material data, b) Cutout of the shear stresses S^{13}, c) Shape of the shear stresses along line 1–2, d) Plot of the damaged zones with delaminations

CONCLUSIONS

The paper presents a layered quadrilateral finite element based on a multi–director theory. The displacement field is interpolated through the thickness using hierarchical shape functions. Thus warping of the cross sections and change of thickness is included. T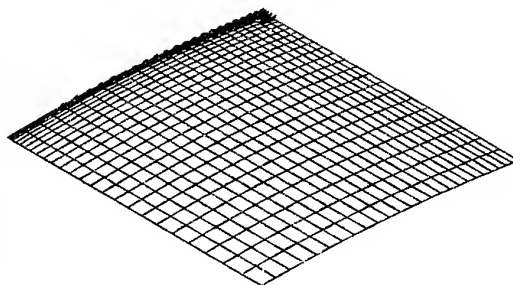he complete stress state can be described. The element is free of shear locking in thin shell applications. Onset of delamination is described using a stress based fracture criterion. Bonding and independent deformation of the sublaminates are computed within the iteration process of the nonlinear finite element equations.

REFERENCES

[1] Robbins, D. H., Reddy, J. N. "Modeling of thick composites using a layer–wise laminate theory." *International Journal for Numerical Methods in Engineering* **36**, pp. 655–677 (1993).

[2] Dorninger, K., Rammerstorfer F. "A layered composite shell element for elastic and thermoelastic stress and stability analysis at large deformations." *International Journal for Numerical Methods in Engineering* **30**, pp. 833–858 (1990).

[3] Başar, Y., Ding, Y., Schultz, R. "Refined shear–deformation models for composite laminates with finite rotations." *International Journal of Solids & Structures* **30**, pp. 2611–2638 (1993).

[4] Gruttmann, F., Wagner, W. "On the numerical analysis of local effects in composite structures." *Composite Structures* **29**, pp. 1–12 (1994).

[5] Gruttmann F., Wagner W. "Coupling of 2d– and 3d–composite shell elements in linear and nonlinear applications, *Computer Methods in Applied Mechanics and Engineering*, accepted for publication, (1996).

[6] Braun, M., Bischoff, M., Ramm, E. "Nonlinear shell formulations for complete three–dimensional constitutive laws." *Computational Mechanics* **15**, pp. 1–18 (1994).

[7] Schellekens, J. C. J., De Borst, R. "A finite element approach for the analysis of mode–I free edge delamination in composites." *International Journal of Solids & Structures* bf 30, pp. 1239–1253 (1993).

[8] Rinderknecht, S., Kröplin, B. "Delamination growth simulation with a moving mesh technique." In: B.H.V. Topping und M.Papadrakakis, editors, *Advances in non–linear finite element methods*, pp. 187–197 (1994).

[9] Hashin, Z. "Failure criteria for unidirectional composites." *Journal for Applied Mechanics* **47**, pp. 329–334 (1980).

OPTIMISATION OF SYMMETRIC LAMINATES WITH INTERNAL LINE SUPPORTS FOR MAXIMUM BUCKLING LOAD

M. Walker and B. K. Bullock

Center for Engineering Research, Technikon Natal, South Africa

INTRODUCTION

An important failure mode for laminated composite plates is buckling under in-plane compressive loading. The load carrying capacity of such plates can be improved by the use of internal line supports [1], and also by using the ply angle as a design variable, and determining these optimally.

One phenomenon associated with symmetric angle-ply configurations is the occurrence of bending-twisting coupling which may cause significantly different results as compared to cases in which this coupling is exactly zero [2]. This effect becomes even more pronounced for laminates with few layers. Due to this coupling, closed-form solutions cannot be obtained for any of the boundary conditions and this situation led to the neglecting of bending-twisting coupling in several studies involving the optimisation of symmetric laminates under buckling loads [3 - 5]. The present study adopts a numerical approach to include the effect of bending-twisting coupling and to obtain the optimal design solutions for a variety of internal line support types and boundary conditions.

Optimisation of composite plates with respect to ply angles to maximise the critical buckling load is necessary to realise the full potential of fiber-reinforced materials. Results obtained using different approaches can be found in the literature, but there is little reported on the optimal design of laminates with bending-twisting accounted for [6], with internal line supports and different boundary conditions. The finite element formulation which is used in the present study is based on Mindlin type theory for laminated composite plates and shells. Numerical results are given for various combinations of boundary conditions and internal line support types, and these are compared to optimally designed plates without such supports.

BUCKLING OF SYMMETRIC LAMINATES

Consider a symmetrically laminated rectangular plate of length a, width b and thickness h which consists of n orthotropic layers with fiber angles θ_k, $k = 1, 2, ..., K$. The plate is defined in the Cartesian coordinates x, y and z with axes x and y lying on the middle surface of the plate. The plate is subjected to biaxial compressive forces N_x and N_y in the x and y directions, respectively. Plates with these characteristics are commonly known as symmetric angle-ply laminates.

In the present study, a first-order shear deformable theory is employed to analyse

the problem and the following displacement field is assumed

$$
\begin{aligned}
u &= u_0(x,y) + z\psi_x(x,y) \\
v &= v_0(x,y) + z\psi_y(x,y) \\
w &= w(x,y)
\end{aligned}
\tag{1}
$$

where u_o, v_o and w_o are the displacements of the reference surface in the x, y and z direction, respectively, and ψ_x, ψ_y are the rotations of the transverse normal about the x and y axes.

The in-plane strain components can be written as a sum of the extensional and flexural parts and they are given as

$$
\{\epsilon\} = \{\epsilon_p\} + z\{\epsilon_f\}
\tag{2}
$$

where

$$
\{\epsilon\}^T = (\epsilon_x, \epsilon_y, \epsilon_{xy})
$$

and

$$
\{\epsilon_p\} = \begin{pmatrix} u_{o,x} \\ v_{o,y} \\ u_{o,y} + v_{o,x} \end{pmatrix}, \quad \{\epsilon_f\} = \begin{pmatrix} \psi_x \\ \psi_y \\ \psi_x + \psi_y \end{pmatrix}
\tag{3}
$$

Here, a subscript after the comma denotes differentiation with respect to the variable following the comma.

The transverse shear strains are obtained from

$$
\{\gamma\} = \begin{pmatrix} \gamma_{xz} \\ \gamma_{yz} \end{pmatrix} = \begin{pmatrix} w_{o,x} + \psi_x \\ w_{o,y} + \psi_y \end{pmatrix}
\tag{4}
$$

The equations for in-plane stresses of the k-th layer under a plane stress state may be written as

$$
\begin{pmatrix} \sigma_x \\ \sigma_y \\ \sigma_{xy} \end{pmatrix}_{(k)} = \begin{pmatrix} \bar{Q}_{11} & \bar{Q}_{12} & \bar{Q}_{16} \\ \bar{Q}_{12} & \bar{Q}_{22} & \bar{Q}_{26} \\ \bar{Q}_{16} & \bar{Q}_{26} & \bar{Q}_{66} \end{pmatrix}_{(k)} \begin{pmatrix} \epsilon_x \\ \epsilon_y \\ \epsilon_{xy} \end{pmatrix} = [\bar{Q}]_{(k)}\{\epsilon\}
\tag{5}
$$

and similarly for the transverse shear stresses as

$$
\begin{pmatrix} \tau_{yz} \\ \tau_{xz} \end{pmatrix}_{(k)} = \alpha \begin{pmatrix} \bar{Q}_{44} & \bar{Q}_{45} \\ \bar{Q}_{45} & \bar{Q}_{55} \end{pmatrix}_{(k)} \begin{pmatrix} \gamma_{yz} \\ \gamma_{xz} \end{pmatrix} = \alpha[C]_{(k)}\{\gamma\}
\tag{6}
$$

where α is a shear correction factor [7], and $\bar{Q}_{ij}$ are the transformed stiffnesses. Equations (5) and (6) may be written in compact form as

$$
\boldsymbol{\sigma}_k = \bar{Q}_k \boldsymbol{\epsilon}
\tag{7}
$$

where $\bar{Q}_k$ refers to the full matrix with elements $(\bar{Q}_{ij})_{k,}$, and $\boldsymbol{\sigma}_k$ and $\boldsymbol{\epsilon}$ represent in-plane and transverse stresses and strains, respectively. The resulting shear forces

and moments acting on the plate are obtained by integrating the stresses through the laminate thickness, viz.

$$\{V\}^T = (V_x, V_y) = \int_{-h/2}^{h/2} (\tau_{xz}, \tau_{yz}) dz$$

$$\{M\}^T = (M_x, M_y, M_{xy}) = \int_{-h/2}^{h/2} (\sigma_x, \sigma_y, \sigma_{xy}) z dz \tag{8}$$

The relations between V and M, and the strains are given by

$$\{V\} = [S]\{\gamma\}, \ \{M\} = [D]\{\epsilon_f\} \tag{9}$$

where the stiffness matrices $[S]$ and $[D]$ are computed from

$$[S] = \alpha \sum_{k=1}^{K} \int_{h_{k-1}}^{h_k} [C]_{(k)} dz$$

$$[D] = \sum_{k=1}^{K} \int_{h_{k-1}}^{h_k} [\bar{Q}]_{(k)} z^2 dz \tag{10}$$

From the condition that the potential energy of the plate is stationary at equilibrium, and neglecting the pre-buckling effects, the equations governing the biaxial buckling of the shear deformable laminate are obtained as

$$M_{x,xx} + 2M_{xy,xy} + M_{y,yy} + N_x w_{,xx} + N_y w_{,yy} = 0$$

$$M_{x,x} + M_{xy,y} - V_x = 0 \tag{11}$$

$$M_{y,y} + M_{xy,x} - V_y = 0$$

where N_x and N_y are the pre-buckling stress components. As no simplifications are assumed on the elements of the $[D]$ matrix, equations (11) include the bending-twisting coupling as exhibited by virtue of $D_{16} \neq 0$, $D_{26} \neq 0$.

FINITE ELEMENT FORMULATION

We now consider the finite element formulation of the problem. Let the region S of the plate be divided into n sub-regions S_r $(S_r \in S; r = 1, 2, ..., n)$ such that

$$\Pi(u) = \sum_{r=1}^{n} \Pi^{S_r}(u) \tag{12}$$

where Π and Π^{S_r} are potential energies of the plate and the element, respectively, and u is the displacement vector. Using the same shape functions associated with node i $(i = 1, 2, ..., n)$, $S_i(x, y)$, for interpolating the variables in each element, we can write

$$u = \sum_{i=1}^{n} S_i(x, y) u_i \tag{13}$$

599

where u_i is the value of the displacement vector corresponding to node i, and is given by

$$u = \{u_o^{(i)}, v_o^{(i)}, w_o^{(i)}, \psi_x^{(i)}, \psi_y^{(i)}\}^T \tag{14}$$

The static buckling problem reduces to a generalised eigenvalue problem of the conventional form, viz.

$$([K] + \lambda[K_G])\{u\} = 0 \tag{15}$$

where $[K]$ is the stiffness matrix and $[K_G]$ is the initial stress matrix. The lowest eigenvalue of the homogeneous system (15) yields the buckling load.

OPTIMAL DESIGN PROBLEM

The objective of the design problem is to maximise the buckling loads N_x and N_y for a given thickness h by optimally determining the fiber orientations given by $\theta_k = (-1)^{k+1}\theta$ for $k \leq K/2$ and $\theta_k = (-1)^k\theta$ for $k \geq K/2 + 1$. Let $N_x = N$ and $N_y = \lambda N$ where $0 \leq \lambda \leq 1$ is the proportionality constant. The buckling load $N(\theta)$ is given by

$$N(\theta) = \min_{m,n} [N_{mn}(m, n, \theta)] \tag{16}$$

where N_{mn} is the buckling load corresponding to the half-wave numbers m and n in the x and y directions, respectively. The design objective is to maximise $N(\theta)$ with respect to θ, viz.

$$N_{\max} \triangleq \max_\theta [N(\theta)], \ 0^o \leq \theta \leq 90^o \tag{17}$$

where $N(\theta)$ is determined from the finite element solution of the eigenvalue problem given by equation (16). The optimisation procedure involves the stages of evaluating the buckling load $N(\theta)$ for a given θ and improving the fiber orientation to maximise N. Thus, the computational solution consists of successive stages of analysis and optimisation until a convergence is obtained and the optimal angle θ_{opt} is determined within a specified accuracy. In the optimisation stage, the *Golden Section* method is employed.

NUMERICAL RESULTS AND DISCUSSION

Numerical results are given for a typical T300/5208 graphite/epoxy material with $E_1 = 181$ GPa, $E_2 = 10.3$ GPa, $G_{12} = 7.17$ GPa and $\nu_{12} = 0.28$. The symmetric plate is constructed of four equal thickness layers with $\theta_1 = -\theta_2 = -\theta_3 = \theta_4 = \theta$ and the thickness ratio is specified as $h/b = 0.01$, while $N_y/N_x = 1$. Different combinations of free (F), simply supported (S) and clamped (C) boundary conditions are implemented at the four edges of the plate. In particular, five different combinations are studied, namely, (F,S,F,S), (F,S,C,S), (S,S,S,S), (C,S,C,S) and (C,C,C,C), where the first letter refers to the first plate edge (which lays in the x-axis), and the others follow in the anti-clockwise direction.

The plates also have one of three internal simple-support types implemented, and these are referred to as case 1, 2 and 3. Case 1 consists of a simple point-support at

the center of the plate, case 2 is a line support extending from the middle of second plate side to the center, and case 3 is a line support extending from the middle of the second side to the middle of the opposite side.

The results presented in this section are obtained for rectangular plates with aspect ratios varying between 0.5 and 2. The non-dimensionalised buckling parameter N_b is defined as

$$N_b = \frac{N b^2}{h^3 E_o} \tag{18}$$

where N is the critical buckling load, and E_o is a reference value having the dimension of Young's modulus and is taken as $E_o = 1$GPa.

Table 1 compares the optimal fibre angle and maximum buckling load of plates with type 1 internal supports to those with no internal supporting, ranging in size from $a/b = 0.5$ to $a/b = 2.0$, for all five boundary cases. Here, the loading is biaxial. As expected the (C,C,C,C) boundary case gives the highest buckling loads. With all five boundary cases the maximum buckling load decreases as the aspect ratio increases, while the fibre angle follows no trend except in the case of (S,S,S,S), with internal support type 1, where θ increases with increasing a/b. Once again, it is clear that internal supports help increase an optimally designed plate's maximum buckling load.

Table 2 gives a comparison of the effect on the buckling load of the three internal support types for plates with $\lambda = 1$. Here the plates are either simply supported or clamped. N_b decreases with an increase in the aspect ratio while no trend is discernible for the optimal fibre angle, except, as was noted above, in the case of (S,S,S,S) and internal support type 1. As more internal supports are added so the maximum buckling loads increase, and therefore internal support type 3 gives significantly larger buckling loads.

CONCLUSION

A finite element solution for the optimal design of laminated composite plates with internal line supports for maximum buckling load was presented. This formulation is based on Mindlin-type laminated plate theory. The numerical approach employed in the present study is necessitated by the fact that the inclusion of the bending-twisting coupling effect and the consideration of various combinations of free, clamped and simply supported boundary conditions rule out an analytical approach.

As expected the maximum buckling load increases as the number of internal supports increase. Also, as the aspect ratio increases so the plate becomes more unstable and the maximum buckling load decreases.

REFERENCES

1. S. Abrate, *Int. J. Solids Structures*, Stability and optimal design of laminated plates with internal supports, **32**, pp. 1331 - 1347 (1995).

2. R. M. Jones, *Mechanics of Composite Materials*, Chap. 4, 166, McGraw Hill (1975).

3. T. L. C. Chen & C. W. Bert, Design of composite material plates for maximum uniaxial compressive buckling load. *Proceedings of Oklahoma Academy of Science* **56**, 104 - 107 (1976).

4. Y. Hirano, Optimal design of laminated plates under axial compression. *AIAA Journal* **17** (9), 1017 - 1019 (1979).

5. S. P. Joshi & N. G. R. Iyengar, Optimal design of laminated composite plates under axial compression. *Transactions of the Canadian Society of Mechanical Engineers* **9**, 45 - 50 (1985).

6. M. Walker, S. Adali & V. Verijenko, Optimisation of symmetrically laminates for maximum buckling load including the effects of bending-twisting coupling, *Computers & Structures*, **58**, pp. 313 - 319, (1995).

7. J. N. Reddy, *Energy and Variational Methods in Applied Mechanics*, John Wiley & Sons, New York, (1984).

	TYPE 1				TYPE 2			
	(S,S,S,S)		(C,C,C,C)		(S,S,S,S)		(C,C,C,C)	
a/b	N_b	θ_{opt}	N_b	θ_{opt}	N_b	θ_{opt}	N_b	θ_{opt}
0.5	430.0	39.6°	955.9	31.5°	481.4	44.1°	1043.5	31.5°
0.6	346.6	43.9°	677.9	29.5°	406.8	49.6°	740.0	30.3°
0.7	290.8	44.9°	514.1	45.3°	354.9	50.6°	627.8	55.1°
0.8	251.1	45.0°	443.0	46.2°	315.0	50.0°	562.4	52.7°
0.9	221.2	45.0°	391.1	45.8°	282.3	49.1°	505.9	50.6°
1.0	198.9	45.0°	350.6	45.0°	255.3	48.1°	457.7	48.9°
1.2	166.6	45.0°	292.7	44.1°	214.6	47.0°	385.4	46.8°
1.4	144.3	45.3°	252.2	45.3°	183.7	45.8°	327.4	44.9°
1.6	128.0	46.2°	236.6	60.5°	159.9	45.0°	283.7	44.9°
1.8	115.9	48.0°	235.3	60.4°	141.2	45.0°	265.9	63.9°
2.0	107.0	50.8°	233.1	59.2°	126.5	46.0°	262.5	61.5°

	TYPE 3			
	(S,S,S,S)		(C,C,C,C)	
a/b	N_b	θ_{opt}	N_b	θ_{opt}
0.5	524.8	46.9°	1082.6	30.3°
0.6	454.9	52.4°	770.2	42.7°
0.7	418.0	60.5°	703.0	64.6°
0.8	415.9	68.5°	692.7	63.5°
0.9	413.9	67.0°	679.3	61.1°
1.0	410.3	65.8°	664.1	59.2°
1.2	401.2	64.2°	646.8	62.7°
1.4	397.4	66.8°	636.4	59.6°
1.6	394.9	65.1°	630.4	62.3°
1.8	391.8	64.9°	625.2	60.5°
2.0	391.0	66.1°	622.6	61.8°

Table 2. Effect of internal support type on maximum buckling load and optimal fibre angle for $\lambda=1$

| | (S,S,S,S) | | | | (F,S,F,S) | | | |
| | No support | | Type 1 | | No support | | Type 1 | |
a/b	N_b	θ_{opt}	N_b	θ_{opt}	N_b	θ_{opt}	N_b	θ_{opt}
0.50	405.9	25.0°	430.0	39.6°	252.0	25.0°	252.6	25.0°
0.75	184.7	20.2°	270.0	45.0°	113.1	24.1°	113.3	23.1°
1.00	121.5	45.0°	198.9	45.0°	62.5	20.7°	62.5	20.7°
1.25	103.2	61.8°	160.3	45.0°	38.9	31.0°	38.9	31.0°
1.50	103.5	68.2°	135.5	45.8°	27.1	30.3°	27.5	36.2°
1.75	102.4	66.3°	118.6	47.4°	19.9	29.8°	20.6	37.7°
2.00	101.1	65.1°	107.0	50.8°	15.3	29.5°	16.1	38.1°

| | (F,S,C,S) | | | | (C,S,C,S) | | | |
| | No support | | Type 1 | | No support | | Type 1 | |
a/b	N_b	θ_{opt}	N_b	θ_{opt}	N_b	θ_{opt}	N_b	θ_{opt}
0.50	252.3	25.0°	252.7	24.8°	415.3	23.1°	510.1	47.0°
0.75	113.3	24.8°	113.5	23.8°	250.7	63.7°	351.1	44.1°
1.00	63.9	41.1°	65.4	37.9°	244.0	56.3°	264.8	43.1°
1.25	41.1	24.4°	48.8	47.7°	230.0	63.9°	229.6	64.6°
1.50	29.8	54.2°	40.2	52.0°	231.5	58.7°	235.8	62.5°
1.75	28.2	72.0°	35.1	55.8°	225.5	55.6°	234.1	59.2°
2.00	28.2	73.9°	32.0	58.9°	225.6	60.1°	229.1	57.0°

| | (C,C,C,C) | | | |
| | No support | | Type 1 | |
a/b	N_b	θ_{opt}	N_b	θ_{opt}
0.50	942.1	34.6°	955.9	31.5°
0.75	450.7	34.3°	478.2	46.8°
1.00	265.2	63.0°	350.6	45.0°
1.25	254.5	57.7°	281.2	44.1°
1.50	238.6	53.9°	239.0	52.0°
1.75	235.4	59.6°	235.6	60.5°
2.00	230.2	56.8°	233.1	59.2°

Table 1. Comparison of the effect of the boundry conditions on maximum buckling load and optimal fibre angle for plates with type 1 internal support and no internal supports, where λ=1.

604

MINIMUM DEFLECTION AND WEIGHT DESIGN OF LAMINATED COMPOSITE PLATES

MARK WALKER and TALMON REISS

Center for Engineering Research, Technikon Natal, Durban, South Africa

ABSTRACT

The minimum deflection and weight designs of laminated composite plates are given. The finite element method using Mindlin plate theory is used in conjunction with optimisation routines in order to obtain the optimal designs. Various boundary conditions are considered and results are given for varying aspect ratios and for different loading types. Comparative results are presented for minimum weight priority design as an alternative to minimum deflection/minimum weight priority design to investigate the effect of priority on the deflection and weight.

INTRODUCTION

An advantage of composite materials over conventional ones is the possibility of tailoring their properties to the specific requirements of a given application. The tailoring can be achieved by optimising the material properties with regard to design objectives. In the case of fibre composites, one of the most effective design parameters is the fibre orientation which can be used as an optimising variable.

The optimal design of laminated plates for minimum deflection and weight has been investigated by several authors [1–6]. This study considers the optimal design of symmetrically laminated plates for minimum deflection and minimum weight. In the first design problem, the ply angle is taken as the optimising variable for the minimum deflection design and the minimum weight is then obtained using the Tsai-Wu failure criterion with the optimising variable then becoming the plate thickness. Results are presented for different loadings both symmetrical and unsymmetrical, and various combinations of clamped, simply supported and free boundary conditions are considered. The effect of aspect ratio on the minimum deflection and weight, and optimal ply angle, is investigated. In the second design problem, only the minimum weight is taken as the design objective, and the fibre orientation and the laminate thickness are determined to achieve a minimum weight design. Comparative results are given to assess the effect of design priority on the deflection and weight.

BASIC EQUATIONS

Consider a symmetrically laminated rectangular plate of length a, width b and

thickness H under a transverse bending load $q(x,y)$. The plate is located in the x, y, z plane and constructed of an arbitrary number K of orthotropic layers of equal thickness h_k and fibre orientation θ_k where $k = 1, 2, ..., K$. The displacement of a point (x^0, y^0, z^0) on the reference surface is denoted by (u^0, v^0, w^0)

The governing equation for the deflection w in the z direction under a transverse load q is given by [8]:

$$D_{11}w_{,xxxx} + 4D_{16}w_{,xxxy} + 2(D_{12} + 2D_{66})w_{,xxyy} + 4D_{26}w_{,xyyy} \\ + D_{22}w_{,yyyy} = q \tag{1}$$

where variables after the comma denote differentiation with respect to that variable, and

$$D_{ij} = \int_{-h/2}^{h/2} \bar{Q}_{ij}^{(k)} z^2 \, dz \tag{2}$$

are the bending stiffnesses and $\bar{Q}_{ij}^{(k)}$ are components of the transformed reduced stiffness matrix for the $k - th$ layer.

FINITE ELEMENT FORMULATION

We now consider the finite element formulation of the problem [9]. Let the region S of the plate be divided into n sub-regions S_r ($S_r \in S; r = 1, 2, ..., n$) such that

$$\Pi(u) = \sum_{r=1}^{n} \Pi^{S_r}(u) \tag{3}$$

where Π and Π^{S_r} are potential energies of the plate and the element, respectively, and u is the displacement vector. Using the same shape functions associated with node j ($j = 1, 2, ..., n$), $S_j(x,y)$, for interpolating the variables in each element, we can write

$$u = \sum_{j=1}^{n} S_j(x,y) u_j \tag{4}$$

where u_j is the value of the displacement vector corresponding to node j, and is given by

$$u = \{u^{(j)}, v^{(j)}, w^{(j)}, \phi_1^{(j)}, \phi_2^{(j)}\}^T \tag{5}$$

The displacements $\{u, v, w, \phi_1, \phi_2\}$ are approximated as

$$u = \sum_{j=1}^{n} u_j \psi_j(x,y) \ , \ v = \sum_{j=1}^{n} v_j \psi_j(x,y) \ , \ w = \sum_{j=1}^{n} w_j \psi_j(x,y)$$

$$\phi_1 = \sum_{j=1}^{n} S_j^1 \psi_j(x,y) \ , \ \phi_2 = \sum_{j=1}^{n} S_j^2 \psi_j(x,y) \tag{6}$$

where ψ_j are Lagrange family of interpolation functions. From the equilibrium equations of the first order theory, and equations (6), we obtain the finite element model of the first-order theory,

$$\sum_{\beta=1}^{5} \sum_{j=1}^{n} K_{ij}^{\alpha\beta} \Delta_j^{\beta} - F_i^{\alpha} = 0 \ , \ (\alpha = 1, 2, ..., 5) \tag{7}$$

606

or

$$[K]\{\Delta\} - \{F\} = \{0\} \qquad (8)$$

where K and F are the stiffness and force coefficients respectively, and the variable Δ denotes the nodal values of w and its derivatives.

DESIGN PROBLEMS

A. Minimum deflection and weight design

The objective of the first design problem is to minimise the maximum deflection $w_{max}(x, y)$ and then the weight W of the laminated plate. The minimum deflection is achieved by optimally determining the fibre orientations, given by $\theta_k = (-1)^{k+1}\theta$ for $k \leq K/2$ and $\theta_k = (-1)^k\theta$ for $k \geq K/2 + 1$. The first part of the design problem may thus be stated as:

$$w_{min} \stackrel{\Delta}{=} \min_{\theta} [w_{max}(\theta)], \quad 0° \leq \theta \leq 90° \qquad (9)$$

where

$$w_{max}(\theta) = \max_{x,y} w(x, y; \theta) \qquad (10)$$

The second part of the design problem involves minimising the laminate thickness H subject to a failure criterion. In this study, the Tsai-Wu failure criterion [10] is used which stipulates that the condition for non-failure for any particular ply is

$$\begin{aligned} F(\theta) &= F_{11}\sigma_1^{(k)}\sigma_1^{(k)} + F_{22}\sigma_2^{(k)}\sigma_2^{(k)} + F_{66}\tau_{12}^{(k)}\tau_{12}^{(k)} \\ &\quad + 2F_{12}\sigma_1^{(k)}\sigma_2^{(k)} + F_1\sigma_1^{(k)} + F_2\sigma_2^{(k)} \leq 1 \end{aligned} \qquad (11)$$

where the strength parameters F_{11}, F_{22}, F_{66}, F_{12}, F_1 and F_2 are given by

$$F_{11} = 1/(X_t X_c) ; \quad F_{22} = 1/(Y_t Y_c) ; \quad F_{66} = 1/G^2$$

$$F_1 = 1/X_t - 1/X_c ; \quad F_2 = 1/Y_t - 1/Y_c ; F_{12} = -\frac{1}{2}\sqrt{F_{11}F_{22}} \qquad (12)$$

and X_t, X_c, Y_t, Y_c are the tensile and compressive strengths of the composite material in the fibre and transverse directions, and G is the in-plane shear strength.

The second part of the problem may thus be stated as

$$W_{min} = \min_{H} W(\theta_{opt}) \qquad (13)$$

subject to constraint (11), which is evaluated for all plies.

The maximum deflection w_{max} is determined from the finite element solution of the problem given by (8). The first optimisation procedure involves the stages of determining the maximum deflection $w_{max}(x, y)$ for a given θ and improving the fibre orientation to minimise w_{max}. The second optimisation stage involves evaluating $F(\theta)$

using eqn. (11) for a given H and improving the laminate thickness to minimise the weight. This step may be described explicitly as

$$\min_{H} \ |F(\theta_{opt}) - 1| \qquad (14)$$

in order to minimise thickness. Thus the computational solution consists of successive stages of analysis and optimisation until a convergence is obtained and the optimal angle θ_{opt} and then H_{min} is determined within a specified accuracy. In both optimisation stages, the *Golden Section* method is employed firstly to determine θ_{opt} and then H_{min}.

B. Minimum weight design

In the second design problem, the objective is to minimise the weight only. The problem can be stated as

$$W_{min} = \min_{\theta} W(H_{min}) \qquad (15)$$

In this case the minimum thickness H_{min} of the plate is evaluated using eqn. (11) at each value of θ until θ_{opt} is obtained. As before, H_{min} for each value of θ, and θ_{opt} are determined using the *Golden Section* method. Finally the maximum deflection $w_{max}(x, y)$ corresponding to H_{min} and θ_{opt} is obtained to compare the results with those of the first design problem.

NUMERICAL RESULTS

The structures considered in this study are four-layered symmetrically laminated plates. The material properties used for the analysis of these shells is T300/5208 graphite epoxy for which $E_1 = 181 \ GPa$, $E_2 = 10.34 \ GPa$, $E_{12} = 7.17 \ GPa$ and $\nu_1 = 0.28$. The strength values used in the Tsai-Wu failure criterion are $X_t = 1500 \ MPa$, $X_c = 1500 \ MPa$, $Y_t = 40 \ MPa$, $Y_c = 68 \ MPa$ and $S = 246 \ MPa$. The values for the material properties are taken from reference [11].

For the first study, where minimum deflection/minimum weight is the design priority (design problem 1), two loading conditions are considered. The first is a uniform pressure over the whole surface of the plate of magnitude $q = 100 KPa$.

Four different boundary conditions are implemented along the four plate edges (numbered 1 to 4 in Figure 1). These are (S,S,S,S), (C,S,C,S), (C,C,C,C) and (C,S,F,S) with S representing simply supported, C clamped and F free, while the order refers to edges 1 - 4, respectively. Rotations around the x and y axes are denoted by r_x and r_y, respectively. These conditions may be explicitly described as follows:

(S,S,S,S): $w = r_x = 0$ at $x = 0$, a and $w = r_y = 0$ at $y = 0$, b.
(C,C,C,C): $w = r_x = r_y = 0$ at $x = 0$, a and $w = r_x = r_y = 0$ at $y = 0$, b.
(C,S,C,S): $w = r_x = r_y = 0$ at $x = 0$, a and $r_y = 0$ at $y = 0$, b.
(C,S,F,S): $w = r_x = r_y = 0$ at $x = 0$ and $w = r_y = 0$ at $y = 0$, b.

For the results where the priority is the minimum weight (design problem 2), only two cases of boundary conditions, viz. (S,S,S,S) and (C,C,C,C) are studied for comparative purposes.

The accuracy for the optimal fibre angle, θ_{opt}, is 0.1° and that for the minimum laminate thickness, H_{min}, is $0.1\,mm$.

A. Minimum deflection/minimum weight design
A.1 Uniform load

Figure 2 shows the curves of minimum deflection plotted against the aspect ratio. At low aspect ratios $(a/b \leq 1.2)$, w_{max} is not monotonic. However at higher values of the aspect ratio, w_{max} tends to increase for all the boundary conditions. The minimum thicknesses corresponding to the deflections shown in Figure 2 are shown in Figure 3. For all boundary conditions, H_{min} generally increases with increasing aspect ratio. The optimal fibre angles corresponding to w_{max} are shown in Figure 4. At higher aspect ratios, θ_{opt} for (S,S,S,S), (C,C,C,C) and (C,S,F,S) all tend to 90° while for (C,S,C,S) the optimal fibre angles are found at 0°.

B. Minimum weight design
The results for the minimum weight design under the uniform pressure loading condition are given in Tables 1 and 2, together with the equivalent results for the first design problem. For the case (S,S,S,S) the second design problem leads to a decrease in the thickness of around 10% for all aspect ratios with an increase in the deflection of approximately the same magnitude. In the case of clamped plates (C,C,C,C), minimising the weight only results in an increase in the deflection of about 170% for an aspect ratio of $a/b = 0.5$ reducing to an increase of about 25% for $a/b = 2.0$.

CONCLUSIONS

The minimum deflection/minimum weight designs of symmetrically laminated plates are given as well as designs for minimum weight only. Plates of various aspect ratios and with different boundary conditions are studied. Two loading conditions are considered. In the case of the minimum deflection design it is found that for an increasing aspect ratio the minimum deflection does not always increase monotonically. At higher aspect ratios however, for both the loading conditions, the deflection generally does increase with increasing plate size.

The second design problem which involves the minimisation of the weight only shows that an entirely different optimal design may result as compared to the first design problem especially for certain boundary conditions as a result of taking the weight as the only design objective. It is shown that the boundary conditions have a substantial effect on the optimal fibre orientation of a plate as well as on its weight.

This type of study is important since the non–standard loading and boundary conditions considered lead to unpredictable trends in both the minimum deflection and weight.

REFERENCES

[1] Jiang, Y., and Chiang, Y.-C., "Optimum design of fibre reinforced (composite) materials," *Proceedings of the 4th Intl. Conf. on Mechanical Behaviour of Materials - IV*

ed. J. Carlson and N. G. Ohlson, Stockholm, Sweden, Vol. 1, 1983, pp. 439 - 441.

[2] Johnson, A. F., and Sims, G. D., "Simplified design procedures for composite plates under flexural loading," *Composite Structures 2*, ed. I. H. Marshall. Applied Science Publishers, London, 1983, pp. 302 - 325.

[3] Adali, S., Richter, A., and Verijenko, V. E., "Minimum weight design of symmetric angle-ply laminates under multiiple uncertain loads," *Structural Optimisation*, Vol. 9, 1995, pp. 89 - 95.

[4] Tauchert, T. R., and Adibhatla, A., "Design of laminated plates for maximum stiffness," *Journal of Composite Materials*, Vol. 18, 1984, pp. 58 - 69.

[5][Kam, T. Y., and Chang, R. R., "Optimum layup of thick laminated composite plates for maximum stiffness," *Engineering Optimization*, Vol. 19, 1992, pp. 237 - 249.

[6] Adali, S., Summers, E.B., and Verijenko, V. E., "Minimum Weight and Deflection Design of Thick Sandwiich Laminates via Sumbolic Computation," *Composite Structures*, Vol. 29, 1994, pp. 145 - 160.

[7] Gibson, R. F., *Principles of Composite Material Mechanics*, McGraw Hill, New York, 1994.

[8] Ochoa, O. O, and Reddy, J. N., *Finite Element Analysis of Composite Laminates*, Solid Mechanics and its Applications, Kluwer Academic Publishers, Dordrecht, 1992.

[9] Tsai, S. W., and Wu, E. M., "A general theory of strength for anisotropic materials," *Journal of Composite Materials*, Vol. 5, 1971, pp. 58 - 80.

[10] Tsai, S. W., *Composites Design*, 3rd edition, Think Composites, Dayton, Ohio, 1987.
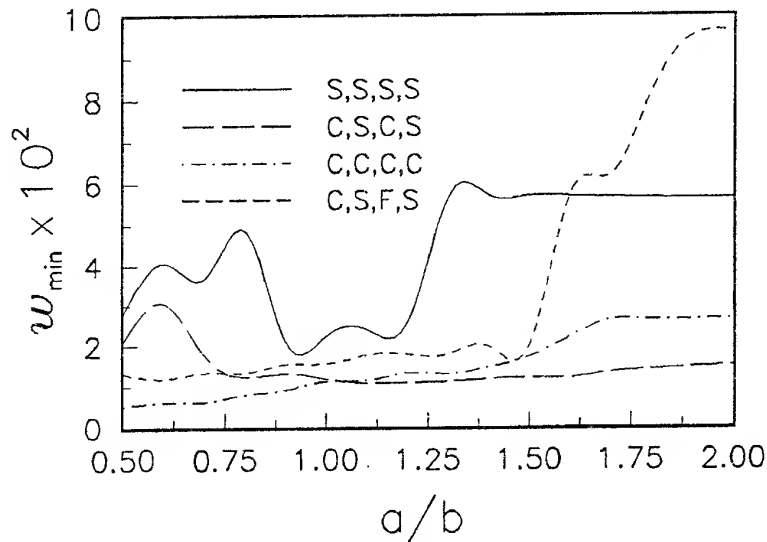
Figure 1. w_{max} versus a/b with $F(\theta) = 1$ (uniformly distributed load)
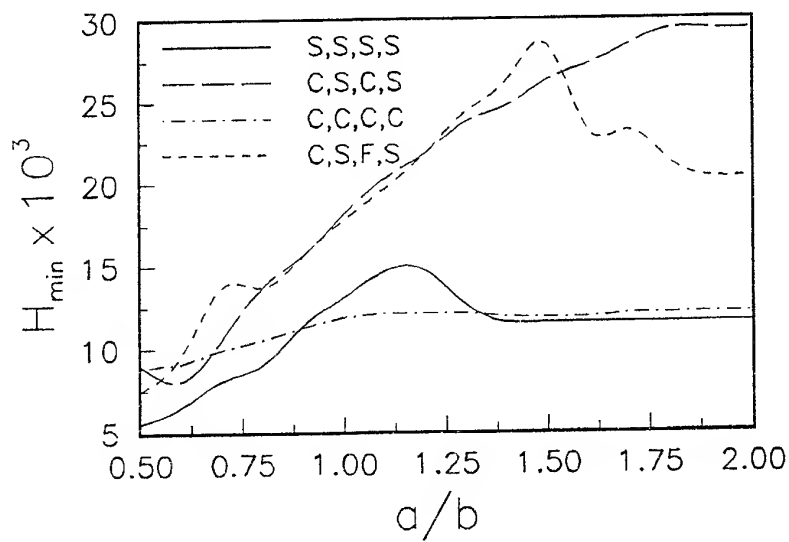
Figure 2. H_{min} versus a/b (uniformly distributed load)
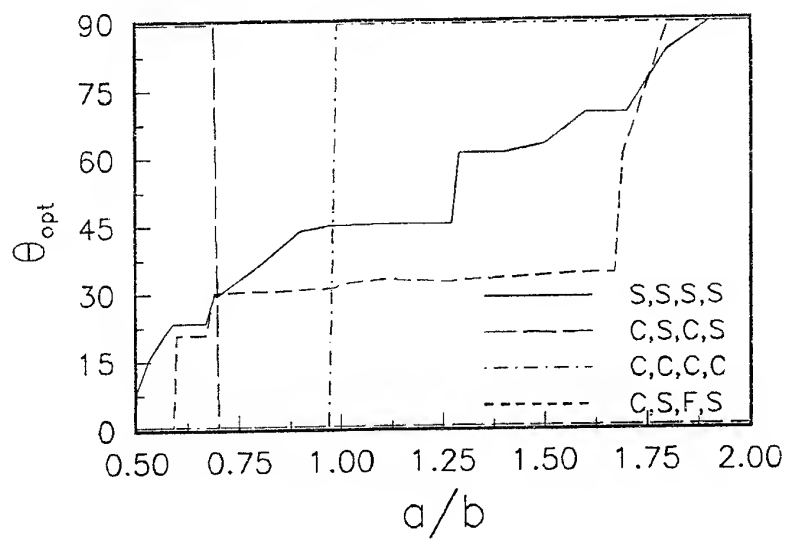
Figure 3. θ_{opt} versus a/b (uniformly distributed load)

DESIGN PROBLEM 1			DESIGN PROBLEM 2		
a/b	w_{min} $* 10^{-2}$	H_{min} $* 10^{-3}$	θ_{opt}	w_{min} $* 10e^{-2}$	H_{min} $* 10^{-3}$	θ_{opt}
0.50	3.03	5.09	10.4∘	2.79	5.52	0.0∘
0.75	4.57	8.04	0.0∘	4.21	8.52	0.0∘
1.00	5.09	11.69	90.0∘	2.25	13.09	43.4∘
1.25	5.38	11.68	90.0∘	3.11	13.02	61.1∘
1.50	5.89	10.68	90.0∘	5.70	11.54	90.0∘
1.75	6.09	10.29	90.0∘	5.66	11.54	90.0∘
2.00	6.06	10.29	90.0∘	5.64	11.54	90.0∘

Table 1.   Effect of design priority on the maximum deflection and minimum weight for simply supported laminates

DESIGN PROBLEM 1			DESIGN PROBLEM 2		
a/b	w_{min} $* 10^{-2}$	H_{min} $* 10^{-3}$	θ_{opt}	w_{min} $* 10^{-2}$	H_{min} $* 10^{-3}$	θ_{opt}
0.50	2.28	4.51	37.2∘	0.52	8.85	0.0∘
0.75	2.75	7.25	41.3∘	0.71	10.21	0.0∘
1.00	3.09	9.19	47.5∘	1.12	11.86	90.0∘
1.25	2.35	9.99	62.2∘	1.31	12.10	90.0∘
1.50	3.50	9.58	54.2∘	1.72	11.85	90.0∘
1.75	3.21	9.58	57.9∘	2.64	12.04	90.0∘
2.00	3.33	9.71	60.1∘	2.66	12.11	90.0∘

Table 2.   Effect of design priority on the maximum deflection and minimum weight for clamped laminates

THERMODYNAMIC BEHAVIOUR OF THE SYSTEM DURING COMPOSITES *IN SITU* FORMATION

W. WOŁCZYŃSKI

Institute of Metallurgy and Materials Science, Polish Academy of Sciences,
Reymonta 25, Kraków 30 059, Poland

INTRODUCTION

The technology of composites *in situ* leads to formation of different structure
in some alloys. Three typical structures may be however differentiated among
composites morphologies. There are: irregular eutectic structures, regular
eutectic structures and cellular structures. The formations of the three above
structures are different from thermodynamic viewpoint though composite
growth occurs under some conditions imposed by the method of directional
solidification. The method of solidification requires both an imposed constant
temperature gradient G, at the s/l interface and a constant growth rate v, for
the formation of composite *in situ* structure. So, a stationary state is ensured
during process under investigation.

Two fundamental phenomena occur during structure formation of composite:
mass and heat transfer in stationary state. So, thermodynamics of irreversible
processes (Prigogine [1], Glansdorff & Prigogine [2]) is the suitable theory
to worked out some approaches to a composite *in situ* growth.

The formation of regular eutectic structure occuring in stationary state may
be treated as governed by the criterion of minimum entropy production which
allowes to formulate an adequate growth law for the λ - spacing predictions.
The composite growth is more complicated in the case of irregular structure
formation. Two structural parameters are to be differentiated: interlamellar
spacing λ_i of regular structure growing in the stationary state and distance λ_s^i
of structure growing in the extreme instability of *non-faceted* phase interface.
So, the λ_i - spacing is related to the criterion of minimum entropy production
and the λ_s^i - distance may be identified with wavelength of marginal stability.
The $\tilde{\lambda}$ - intercellular distance is characteristic for cellular composite *in situ*. It
may be treated as the wavelength of the s/l interface perturbation. For that
reason a proper description of the s/l interface is to be worked out. Such a
description is involved with instability/stability neutral curve worked out by
Sekerka [3]. Thus, integration of the instability/stability diagram developed
by Billia, Jamgotchian & Trivedi [4] and the current description may be done.
It will allow to place the growth law worked out for cellular growth, within
neutral curve, assuming on the other side, that the $\tilde{\lambda}$ - parameter may be
selected with the use of the criterion of minimum entropy production.

PROBLEM STATEMENT

The regular structure formation of composites *in situ* is described by growth law formulated using the criterion of minimum entropy production:

$$3 W_3 (\lambda^2 v)^2 + 2 W_1 \lambda^3 v + (W_6 + W_7) \lambda^2 v = W_4 + W_5 \tag{1}$$

The formation of regular structure occurs in stationary state, therefore the s/l interface is stable against some perturbations. However, the deviation from equilibrium state is changed due to the imposed conditions of solidification. The deviation becomes greater with increasing temperature gradient, which is the thermodynamic force of investigated processes. Each of the processes for a sequence of thermodynamic forces may be located on the trajectory, which is drawn on paraboloid of entropy production shown in Fig.1. The mentioned trajectory joined some minima obtained by cutting a paraboloid.
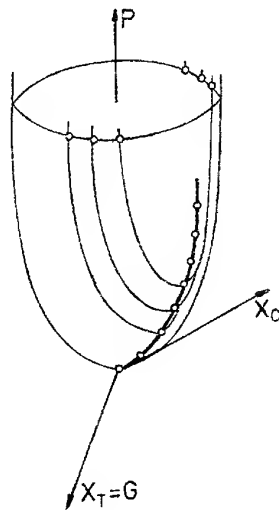
Fig. 1
Trajectory of the local minima determined for differentiated temperature gradients, at which regular structure of the composites *in situ* may be formed.
X_C - is the thermodynamic force associated with mass transfer and
X_T - is the thermodynamic force associated with heat transfer in the system, X_T is equal to temperature gradient G, measured at the s/l interface,
P - is the entropy production per unit time.

The growth law for a prediction of the average interlamellar spacing $\bar{\lambda}$ in the case of irregular structure formation, is as follows:

$$\bar{\lambda} = 0.5 \lambda_i + S_\beta^i + 0.5 \lambda_s^i \tag{2}$$

The hypothesis of the existence of two thermodynamic states has been used in order to formulate the above growth law. Thus, the λ_i - spacing is formed in a stationary state, whereas λ_s^i - distance is associated with a rotation around stationary state, (Fig.2). Therefore, λ_i - parameter may be predicted using the additional growth law (3), determined by means of the criterion of minimum entropy production, whereas λ_s^i - distance, (equation (4)) is defined applying the criterion of marginal stability.

$$3 W_3^i \cdot ((\lambda_i)^2 v)^2 + 2 W_1^i \cdot (\lambda_i)^3 v + (W_6^i + W_7^i) \cdot (\lambda_i)^2 v = W_4^i + W_5^i \tag{3}$$

$$\lambda_s^i = 2 \pi (\Gamma_\alpha / (|m_\alpha| G_C - G))^{0.5} \tag{4}$$

614

The growth law (2) incorporates additionally, the intermediate lamella of the *faceted* phase. It is defined in function of both spacings λ_i and λ_s^j: $S_\beta^j(\lambda_i, \lambda_s^j)$. Some morphologies existing between differentiated structures are treated as being under oscillation between two extreme thermodynamic states, (Fig.2).
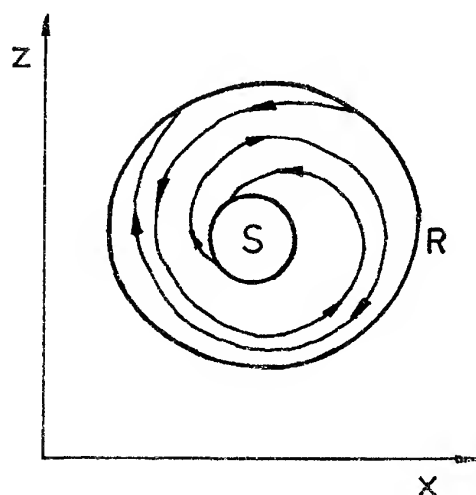

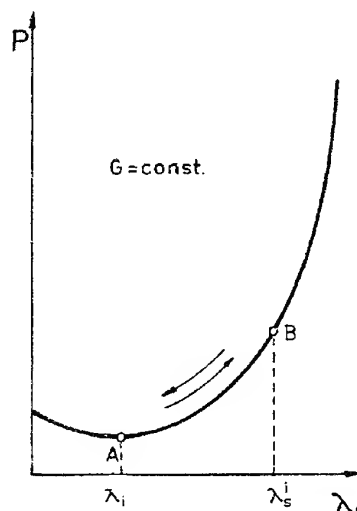Fig.2 Scheme of a system oscillation between stationary state, S and rotary state, R for $v, G = const.$

Fig.3 Definition of an *operating range, the operating points*: A-attractor point, B-bifurcation point.

From thermodynamic viewpoint some regions of the system are in stationary state while others in state of rotation. Stationary state changes continually its localization. So, some respective regions oscillate from rotation (marginal stability) to stationary state. This is the fundamental assumption in current analysis. It corresponds to so-called *operating range* (Fig.3), but contrary to Magnin-Kurz's theory [5] thermodynamic justification is found for present hypothesis. The *operating range* developed in Magnin-Kurz's theory [5] is characteristic for the geometry of perturbed interface of *faceted* phase. However, some observations of irregular eutectic interface (Major-Rutter [6]) do not confirm the perturbation of an interface of the *faceted* phase. It appears at the s/l interface of *non-faceted* phase. In the current theory above imperfection has been eliminated and the *operating range* is determined by the attractor (defined by the criterion of minimum entropy production) and the bifurcation point (defined by the wavelength of marginal stability).

The transformation of irregular structure into regular one is possible while increasing the temperature gradient or decreasing growth rate. A considered transformation is schematically sketched in Fig.5, where both paraboloid of entropy production for regular growth, (R) and irregular one, (I) are drawn. From the thermodynamic viewpoint an analysed process displaces from the I-paraboloid to the R-paraboloid at the same plane determined for a given temperature gradient, G. Mentioned displacements decrease with increasing gradient, $G = X_T$, (the transition between trajectories in Fig.5).

For that reason larger regions of irregular structure transform into regular ones. The interaction between unstable interface of *non-faceted* phase and stable interface of regular region, (through the intermediate lamellae), also vanishes. So, it is suggested that critical gradient G_K exists, at which whole irregular eutectic structure is transformed into regular one, (Fig.4).

The structure of Al-Si eutectic composite shown in Fig.4 has been obtained as a result of transformation at a very small growth rate. Structurally, the performed transformation is identical with transformation at the sufficiently large temperature gradient. Generally, the G/v - ratio is crucial for the above transformation, which may be performed in two ways, either by decrease of growth rate or by increase of temperature gradient.
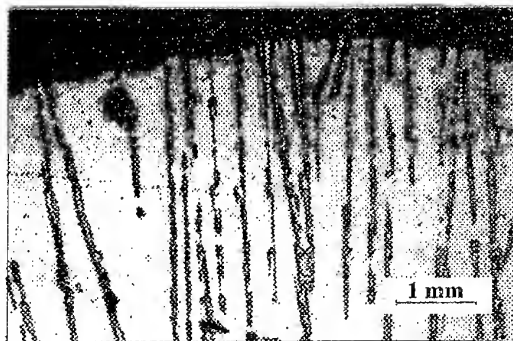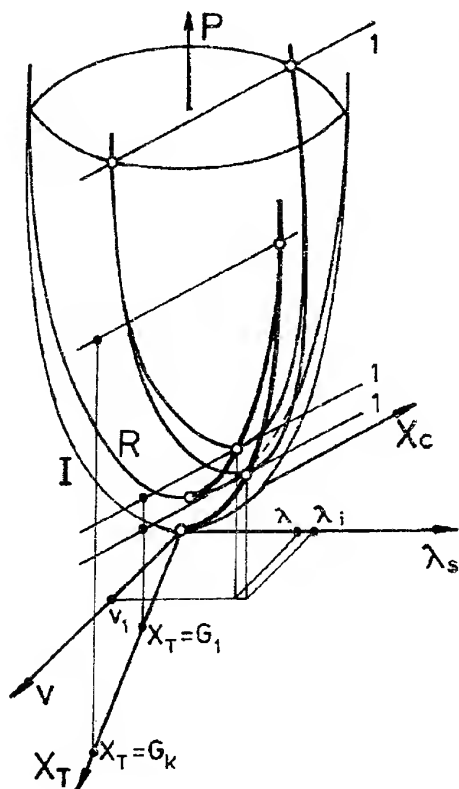
Fig.4
Regular structure and s/l interface as the result of the irregular structure transformation, [6].

Fig.5
Trajectories of local minima on I-paraboloid for an irregular growth and on R-paraboloid for a regular growth, between which the transitions are possible, (*bold lines*).

The annihilation of interface instability of *non-faceted* phase is a result of an irregular structure transformation into the regular one. The whole irregular eutectic structure may be transformed, as shown in Fig.4. In this case, the average spacing $\bar{\lambda}$, (in equation (2)) becomes identical with the λ - parameter known in regular structure description (1) and the growth law (3) becomes identical to (1), while λ_s^i - spacing, (equation (4)), reduces to $2S_\alpha$ - distance.

The formation of cellular structure may not only be treated as wave character phenomenon (as shown by Mullins & Sekerka [7]) but as an interplay among different waves appearing at the s/l interface of a growing composite *in situ*.

So, interface shape may be described by at least two factors: a first associated with fundamental ondulation of cellular pattern and the second involved with some details of cellular shape. The fundamental undulation of the cellular pattern described by the $C_U(x;v)$- function, (in the case of 1D observation of cells), comprises not only the $A_U(v)$- amplitude and the $\tilde{\lambda}(v)$- wavelength, but primordial shape of cells as well. It is defined for $G = const.$, as follows:

$$C_U(x;v) = A_U(v)\frac{(1+Q_U(v))\,\sin^2(\pi x/\tilde{\lambda}(v))}{1+Q_U(v)\,\sin^2(\pi x/\tilde{\lambda}(v))} \qquad (5)$$

The 1D observations made in function of growth rate v show that three types of cellular pattern may be differentiated: finite cells, deep cells and gothic cells, [4], [8]. The calculations of cells shape adequate to 1D observation proved that the equation (5) is not able to reproduce all the details of cell geometry. Thus, the equation (5) is modified by the addition of respective terms, $S_I(x;v)$, which also have wave character. So, cellular shape is given:
a) for finite cells observed just after the v_c - threshold, by equation:

$$C_F(x;v) = C_U(x;v) - A_F(v)\frac{(1+Q_F(v))\,\sin^2(\pi x/\tilde{\lambda}(v))}{1+Q_F(v)\,\sin^2(\pi x/\tilde{\lambda}(v))} \qquad (6)$$

b) for deep cells second term $S_E(x;v)$ tends to zero, so $C_E(x;v) = C_U(x;v)$, and the deep cells may be treated as geometrically *ideal* cells,
c) for gothic cells observed in predendritic region, by equation:

$$C_G(x;v) = C_U(x;v) + A_G(v)\frac{(1+Q_G(v))\,\sin^2(\pi x/\tilde{\lambda}(v))}{1+Q_G(v)\,\sin^2(\pi x/\tilde{\lambda}(v))} \qquad (7)$$

due to modular design of the method for cellular array description.
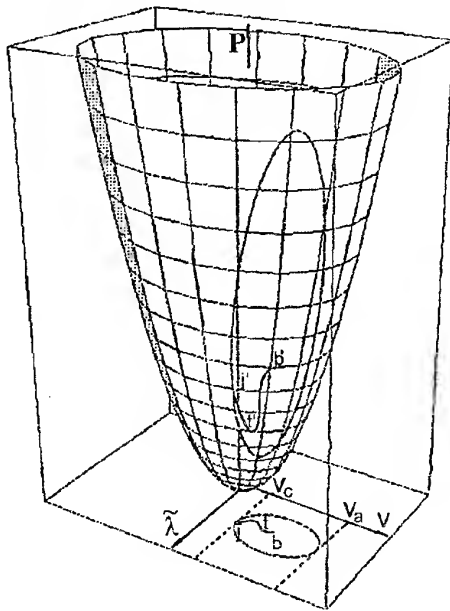
Fig.6
Integration of thermodynamic description made for a cellular growth with stability/instability microstructural diagram. The virtual growth law determined for nonplanar structure formation is given by a "j-t-b"-curve, which has been worked out by Jamgotchian, Trivedi & Billia [9], experimentally.

617

The presented formal description of cellular pattern shape (5)-(7) should be replaced by physical expressions. Thus, both theory for amplitude $A(v)$, and for wavelength $\tilde{\lambda}(v)$ are to be applied using thermodynamic consideration. Finally, microstructural stability/instability diagram and a growth law for the $\tilde{\lambda}$ - parameter selection, obtained using the theorem of minimum entropy production could be integrated as sketched schematically in Fig.6.

G_C - concentration gradient,

m_α - slope of the liquidus line at the α - phase,

S_α half the width of the α - phase lamella, within regular structure,

Γ_α - capillarity parameter of the α - phase, (*Gibbs-Thomson* coefficient).

CONCLUSIONS

The presented thermodynamic approach to regular structure formation has general meaning, being able to prove not only influence of the growth rate v, but influence of temperature gradient G, on composite morphology as well. The current theory seems to be the first which makes attempt to apply the thermodynamics of the whole investigated process. The current approach to cellular shape makes possible to integrate thermodynamic description for cellular growth with the microstructural stability/instability diagram.

REFERENCES

[1] Prigogine, I. "Introduction a la thermodynamique des processus irreversibles." *Monographies Dunod, Paris*, 1969.

[2] Glansdorff, P., Prigogine, I. "On a General Evolution Criterion in Macroscopic Physics." *Physica* 30, pp. 351-374 (1964).

[3] Sekerka, R.F. "Stability of Planar Interface. Microstructural Stability Diagram." *Journal of Applied Physics* 36, pp. 264-276 (1965).

[4] Billia, B., Jamgotchian, H., Trivedi, R. "Cellular and Dendritic Regimes in Directional Solidification. Microstructural Stability Diagram." *Journal of Crystal Growth* 106, pp. 410-420 (1990).

[5] Magnin, P., Kurz, W. "An Analytical Model of Irregular Eutectic Growth and its Application to Fe-C."*Acta Metallurgica* 35, pp.1119-1128 (1987).

[6] Major, J.F., Rutter, J.W. "Effect of Strontium and Phosphorus on Solid/Liquid Interface of Al-Si Eutectic." *Materials Science and Technology* 5, pp. 645-656 (1989).

[7] Mullins, W.W., Sekerka, R.F. "Stability of a Planar Interface During Solidification of a Dilute Binary Alloy." *Journal of Applied Physics* 35, pp. 444-451 (1964).

[8] Caroli, B., Caroli, C., Roulet, B. "Instabilities of the Planar Solidification Fronts." *Solids Far from Equilibrium, Edition C.Godreche, Alea Saclay Collection*, pp. 206-285 (1990).

[9] Jamgotchian, H., Trivedi, R., Billia, B. "Array of Doublets: A Branch of Cellular Solutions in Directional Solidification." *Physical Review E* 47, pp. 4313-4322 (1993).

OSCILLATORY MODE OF COMPOSITES *IN SITU* FORMATION

W.WOŁCZYŃSKI[1], B.BILLIA[2] and J.KLOCH[3]

[1]Institute of Metallurgy and Materials Science, Polish Academy of Sciences,
Reymonta 25, Kraków 30 059, Poland
[2] MATOP-Laboratory, University of Aix-Marseille, France
[3]Institute of Mathematics, Polish Academy of Sciences, Poland

INTRODUCTION

The directional solidification is one of the most important technology allowing structural phenomena to be easily observed and discussed.Moreover, control of structure formation is also possible during the process of composite *in situ* formation. Eventually, it allows to control properties of a given material. The process of directional solidification can be described by means of appropriate growth law which makes possible to establish precise correlation between structure parameters and condition of solidification for a given set of material parameters. Additionally, the shape of the s/l interface may also be described using proper equation.

Two oscillatory structures have been selected among different directional morphologies: a) irregular eutectic structure for which oscillation: *regular eutectic structure - maximum wavelength of the non - faceted s/l interface perturbation* has been differentiated, and b) cellular structure for which oscillation: *doublets - regular cells* may also be observed. Adequate descriptions suggested for above morphologies formation allow to discuss both mentioned oscillations. Suitable criteria for oscillatory mode of the above structures formation allow to understand how structural parameters are changed during process under investigation. The oscillatory behaviour of mentioned structures may be discussed using the neutral *Mullins-Sekerka* curve and the *Eckhaus* stability limit. However, some morphologies illustrating oscillatory mode of cellular structure formation may be easy photographed during 1D observation of transparent material solidification. In the case of irregular eutectic growth the oscillatory behaviour of the composite morphology may be directly revealed on the cross-section of a sample.

PROBLEM STATEMENT

The irregular eutectic growth occurs with macroscopic planar interface while a single phase solid can form with macroscopic planar or a nonplanar s/l interface. So, crucial for present analysis is to consider stability/instability of the s/l interface during directional solidification. For that reason the *non-faceted* phase instability in the case of irregular eutectic structure formation and stability of planar or instability of cellular interface in the case of single phase growth are to be analysed.

The control parameters of directional solidification are: the growth rate, v, the adequate temperature gradient, G, at the s/l interface and the nominal solute concentration, C_0. Two of the mentioned variables are generally kept constant, therefore usually a variation in the microstructure as a function of the third variable that is growth rate v, are studied. The directional eutectic growth occurs at a very small rates, rather. As a rate is increased from very small to very large value an interface shape (for single phase growth) changes continually form planar to cellular, next to dendritic then back to cellular and again to planar one. The microstructural transitions (from one structure to the another) can be qualitatively sketched by means of the stability/instability diagram in the growth rate - wavelength, $(v, \tilde{\lambda})$, space due to Mullins - Sekerka [1], theory developed by Sekerka [2] as linear stability analysis. The neutral curve, that is boundary of a planar/nonplanar regimes is to be traced in above diagram, (Fig.1).
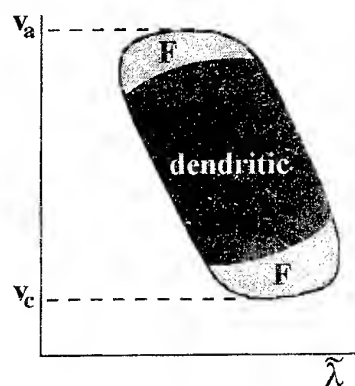
Fig.1
A microstructural stability diagram which defines the stable regimes of a planar and the different nonplanar morphologies like: dendritic, E-deep cellular, F-finite cellular, [3], v_a - absolute stability limite, v_c - threshold for the first bifurcation.

The microstructural diagram shows some regions related to well known morphologies, only. However, there are some structures revealed recently, which are not traced in the diagram. It became possible since when the *Eckhaus* stability limit had been determined, (Fig.2). *Eckhaus* limit shown in Fig.2 has been sketched for 1D periodic structure in dissipative systems. The central subband corresponds to stable structures ($D>0$), while the shaded region is adequate to unstable structures growing with the periodic interface (D vanishes) and so-called *phase diffusion coefficient D* is defined as follows:

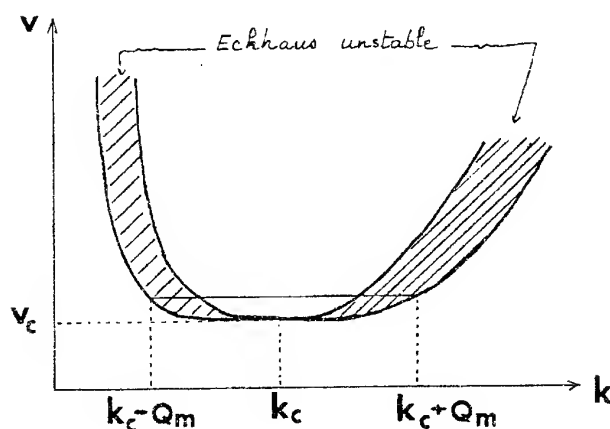$$D = 4\beta(k_c)^2[(Q_m)^2 - 3Q^2]/[(Q_m)^2 - Q^2] \tag{1}$$

Fig.2
Neutral (outside) *Mullins-Sekerka* curve and *Eckhaus* stability limit (inside), [3].
v - growth rate,
k_c - threshold wavevector,
k - wavevector of perturbation,
$Q = k - k_c$,
$Q_m = f(\beta, k_c)$,
β - interface dispersion parameter.

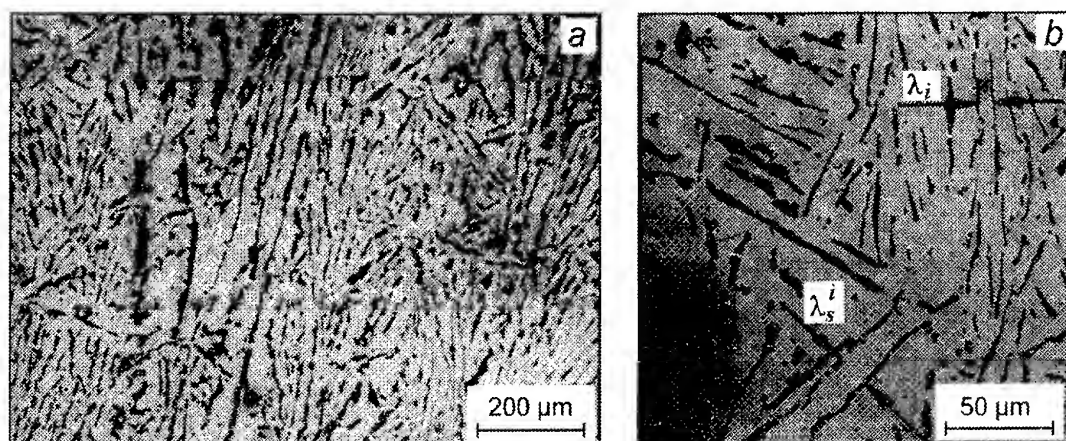Two oscillatory structures differentiated among directional morphologies are shown in Fig.3 and Fig.4.

Fig.3 Parameters λ_s^i, λ_i obtained as a result of *non-faceted* phase interface oscillation within morphology of Al-Si eutectic alloy solidified directionally,($G = 80[K/cm]$, $v = 10.4 \cdot 10^{-4}[cm/s]$), a) longitudinal, b) cross-section of the sample, (oscillatory parameters differentiated in Fig. 3b), [4].
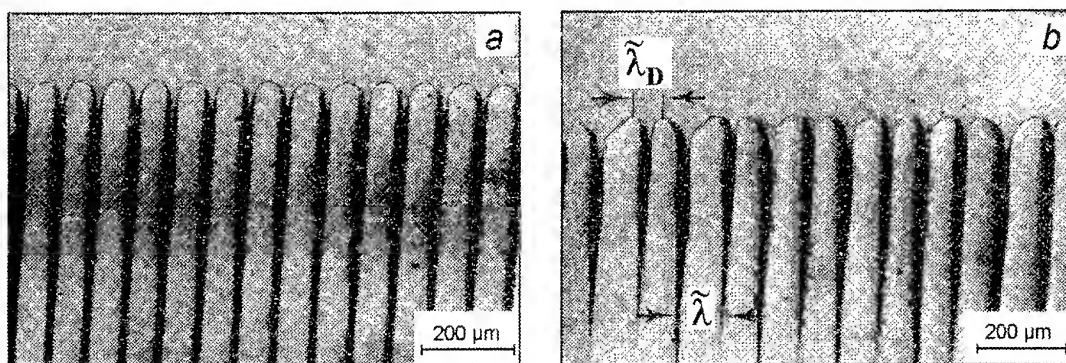

Fig.4 Cellular structure solidified directionally (1D observation): a) deep regular cellular array ($G = 62[K/cm]$, $v = 5 \cdot 10^{-4}[cm/s]$), [5], b) s/l interface of deep doublets as a result of appearance of the δv - critical fluctuation of growth rate, ($G = 65[K/cm]$, $v = 4 \cdot 10^{-4}[cm/s]$), [5].

Both above structures (Fig.3, Fig.4) may be associated with diagrams shown in Fig.1, 2. The oscillation of the irregular eutectic structure has been already discussed on the basis of the thermodynamics of irreversible processes, [6] as a result of the system oscillation between an attractor (minimum entropy production) and bifurcation point (marginal stability shown as neutral curve in Fig.2). However, oscillation of cellular array may be placed within the region in vicinity of F/E transition (as suggested in [5]), (Fig.1), but taking into account *Eckhaus* stability limit, shown in Fig.2, additionally.

According to oscillatory behaviour of irregular eutectic structure an adequate growth law has been formulated. It comprises both oscillatory parameters λ_s^i, λ_i shown in Fig.3.

$$\bar{\lambda} = 0.5\lambda_i + S_\beta^i + 0.5\lambda_s^i \tag{2}$$

$$S_\alpha^i = (2\lambda_i V_\alpha - \lambda_s^i V_\beta)/(4V_\alpha + 2V_\beta) \tag{3}$$

$$S_\beta^i = (\lambda_s^i V_\beta + \lambda_i V_\beta)/(4V_\alpha + 2V_\beta) \tag{4}$$
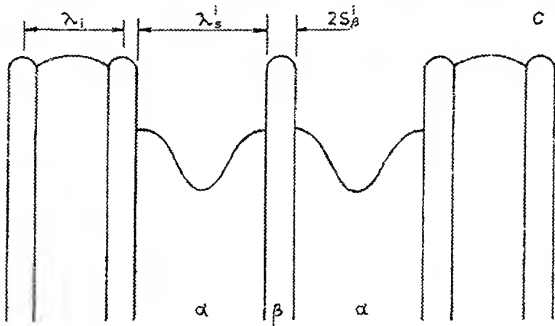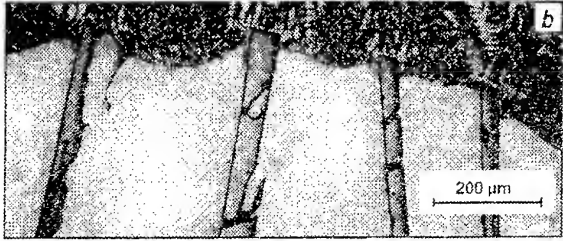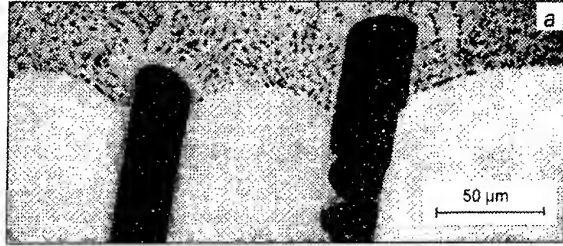
The definitions of parameters taken into account in (2), are sketched in the scheme of irregular eutectic growth (Fig.5). The λ_i - parameter can be determined with the use of growth law formulated using criterion of minimum entropy production, (a regular region of structure), [8], while λ_s^i - distance is equal to the marginal wavelength of perturbation.

Fig.5
Irregular structure of composite *in situ*:
a) interface of the Al-Si composite *in situ* formation, [7],
b) development of the instability of the *non-faceted* phase interface, due to an oscillatory mode of growth, [7],
c) scheme of the irregular morphology formation of the composite *in situ*, showing the stationary structure region, (λ_i - region), within irregular structure region, (λ_s^i - region), and a intermediate lamella of the $2S_\beta^i$ width, through which both mentioned regions effect each other.

The proper description $C_I(x,v)$ of the s/l interface shape is suggested for the regular cells formation, $(I = F, E)$. It is formulated as a sum of two terms:

$$C_I(x,v) = C_U(x,v) + S_I(x,v) \tag{5}$$

$$C_U(x,v) = A_U(v)\frac{(1+Q_U(v))\sin^2(\pi x/\tilde{\lambda}(v))}{1+Q_U(v)\sin^2(\pi x/\tilde{\lambda}(v))} \tag{6}$$

a) for finite cells observed just after the v_c - threshold, (F - region shown in Fig.1), the sum (5) is given as follows:

$$C_F(x,v) = C_U(x,v) - A_F(v)\frac{(1+Q_F(v))\sin^2(\pi x/\tilde{\lambda}(v))}{1+Q_F(v)\sin^2(\pi x/\tilde{\lambda}(v))} \tag{7}$$

622

b) for deep cells observed in the E - region, (Fig.1),

$$C_E(x, v) = C_U(x, v) + A_E(v)\frac{(1+Q_E(v))\ \sin^2(\pi x/\tilde{\lambda}(v))}{1+Q_E(v)\ \sin^2(\pi x/\tilde{\lambda}(v))} \qquad (8)$$

For doublets structure formation the third term $D_{ID}(x, v + \delta v)$, $(I = F, E)$ is to be added into equation (5). Thus,
a) for finite doublets observed before the F/E transition, shown in Fig.1,

$$C_{FD}(x, v + \delta v) = C_F(x, v) - A_{FD}(v + \delta v)\frac{(1+Q_D(v))\ \sin^2(\pi x/2\tilde{\lambda}(v))}{1+Q_D(v)\ \sin^2(\pi x/2\tilde{\lambda}(v))} \qquad (9)$$

b) for deep doublets observed after the F/E transition, shown in Fig.1,

$$C_{ED}(x, v + \delta v) = C_E(x, v) + A_{ED}(v + \delta v)\frac{(1+Q_D(v))\ \sin^2(\pi x/2\tilde{\lambda}(v))}{1+Q_D(v)\ \sin^2(\pi x/2\tilde{\lambda}(v))} \qquad (10)$$

The suitable criteria for oscillation may be formulated due to above descriptions, (2-10).
a) in the case of irregular eutectic growth:

$$2S_\alpha^i \le \lambda_s \le \lambda_s^i \qquad (11)$$

b) in the case of cellular structure growth the equation (9) or (10) may be transformed in order to determine the $\tilde{\lambda}_D$- parameter, defined in Fig.4:

$$\tilde{\lambda}_D(v + \delta v) = \tilde{\lambda}(v) \cdot f(A_U(v), A_I(v), A_{ID}(v + \delta v), Q_U(v), Q_I(v), Q_D(v)) \qquad (12)$$

and according to model assumptions an oscillatory criterion is:

$$0 \le \Delta\tilde{\lambda}(\delta v) = \frac{\tilde{\lambda}(v) - \tilde{\lambda}_D(v + \delta v)}{\tilde{\lambda}(v)} < 1 \qquad (13)$$

CONCLUSIONS

According to the oscillation criterion (11) the *non-faceted* phase within irregular eutectic structure changes its witdh between minimum value equal to $2S_\alpha^i$ and maximum value equal to λ_s^i. For minimum value of mentioned width following phenomena take place:
- irregular structure transforms in regular one, locally,
- perturbation of the s/l interface vanishes, $(\lambda_s \to 2S_\alpha^i)$,
and for maximum value of the *non-faceted* phase width:
- perturbation develops at *non-faceted* interface up to marginal wavelength, $(\lambda_s \to \lambda_s^i)$.
According to the oscillation criterion (13), doublets - regular cells oscillation is possible due to some critical fluctuation of the growth parameters, like: δv, δG. The discussed fluctuation of the growth rate δv, involves an oscillation of the $A_{ID}(v + \delta v)$ - amplitude.
- for maximum value of the $A_{ID}(v + \delta v)$ - parameter regular cells transform into doublets,
- for $A_{ID}(v) = 0$, regular cells are stable against fluctuations and doublets do not exist.

The discussed oscillations may be situated within microstructural stability diagram:
- in the case of irregular eutectic structure, an oscillation occurs between the region just below the differentiated v_c - threshold rate and neutral *Mullins-Sekerka* curve, (Fig.2),
- in the case of cellular structure, an oscillation occurs between doublets region, which is to be situated within *Eckhaus* zone and inside of neutral *Mullins-Sekerka* curve, (Fig.2).

The oscillation of the irregular eutectic structure has thermodynamic justification. It is shown that oscillation take place between an attractor (minimum entropy production) and a bifurcation point (marginal stability). The oscillation of cellular structure could also be confirmed by an appropriate calculation. However, it requires to estimate the so-called *phase diffusion coefficient D*, defined by equation (1), to verify the suggested location of doublets formation in Fig.2.

$A_I(v)$ - part of amplitude associated with some details of cellular geometry, $(I = F, E)$,
$A_U(v)$ - part of amplitude involved with fundamental undulation,
$A_{ID}(v + \delta v)$ - additional part of amplitude concerning the doublets formation, $(I = F, E)$,
$I = F, E$ - structure formation region, F-finite cells, (FC), E-deep cells, (DC), (see Fig.1),
$Q_I(v)$ - parameter responsible for cells details of geometry, $(I = F, E)$,
$Q_U(v)$ - parameter associated with fundamental undulation of the cellular s/l interface,
$Q_D(v)$ - parameter involving with doublets asymmetry,
V_S - volume fraction of the adequate eutectic phase, $(S = \alpha, \beta)$,
$\tilde{\lambda}(v)$ - wavelength of cellular undulation,
λ_s - dimension of the *non - faceted* phase interface during oscillation of eutectic structure,
$\bar{\lambda}$ - average interlamellar spacing within irregular eutectic structure.

REFERENCES

[1] Mullins, W.W., Sekerka, R.F. "Stability of a Planar Interface During Solidification of a Dilute Binary Alloy." *Journal of Applied Physics* 35, pp. 444-451 (1964).
[2] Sekerka, R.F. "Stability of Planar Interface. Microstructural Stability Diagram." *Journal of Applied Physics* 36, pp. 264-276 (1965).
[3] Billia, B., Jamgotchian, H., Trivedi, R. "Cellular and Dendritic Regimes in Directional Solidification: Microstructural Stability Diagram." *Journal of Crystal Growth* 106, pp. 410-420 (1990).
[4] Wołczyński, W., Billia, B., Rabczak, K. "Interlamellar Spacing in the Steady-State Growth of the Al-Si Eutectic Alloy." *Second International Conference on Solidification and Gravity. Miskolc-Lillafured, 1995, Conf.Proc.* pp.147-148 (1995).
[5] Jamgotchian, H., Trivedi, R., Billia, B. "Array of Doublets: A Branch of Cellular Solutions in Directional Solidification." *Physical Review E* 47, pp. 4313-4322 (1993).
[6] Wołczyński, W. "Thermodynamic Description for Irregular Eutectic Growth." *Second International Conference on Solidification and Gravity. Miskolc-Lillafured, 1995, Conf.Proc.* pp.80-81 (1995).
[7] Major, J.F., Rutter, J.W. "Effect of Strontium and Phosphorus on the s/l Interface of Al-Si Eutectic." *Materials Science and Technology* 24, pp.645-656 (1989).
[8] Wołczyński, W., Billia, B. "Influence of Control and Material Parameters on Regular (*Non-Faceted-Non-Faceted*) Eutectic Growth." *Second International Conference on Solidification and Gravity. Miskolc-Lillafured, 1995, Conf.Proc.* pp.145-146 (1995).

PROCESSING AND PROPERTIES OF PHENOXY TOUGHENED PHENOLIC RESIN COMPOSITES

Hew-Der Wu and Chen-Chi M.Ma*

Institute of Chemical Engineering,
National Tsing-Hua University
Hsinchu, Taiwan, Republic of China, 30043

ABSTRACT

A novel method has been developed to toughen phenolic resin by phenoxy resin. Phenoxy resin was dissolved in phenol to form a glutinous mixture at 110 °C. An acid catalyst was utilized to reduce the viscosity of the mixture and then blended with phenolic. The flexural and Izod notched impact strengths of the glass fiber reinforced phenoxy toughened phenolic composite were improved significantly. The wet-out of the glass fiber was also improved.

INTRODUCTION

Phenolic resin is one of the earliest synthetic resins which possesses excellent fire retardance, low smoke density and toxic emissions[1-4]. It is widely used in construction and electrical industry, etc.[3,5] However, phenolic resin is a brittle material and its application is limited. Many researches have been conducted to improve the phenolic properties[6-7].

There are two types of polymer blending processes, i.e. the melt blending and solution blending method. For the active resole type phenolic resin, it will be cured and is difficult to blend with other resins after melted. The solution method is a better method to blend the high active resole type phenolic resin with other polymer. Viscosity would play a key role for the process. In this study, a unique blending method was developed which will provide a high modifier content and lower viscosity at lower temperature. The rhology of the

Phenoxy/phenol solution, and the correlation between the mechanical properties and processing were investigated.

EXPERIMENTAL

Materials: Phenoxy resin, PKHH, was obtained from Union Carbide Co. U.S.A. and the molecular weight Mn is 23,000. Phenolic resin, PF-750 a resole type phenolic with 75 wt% solid content, was obtained from the Chung-Chen Resin Co. Hsin-Chu, Taiwan. The catalyst, p-toluene sulfonic acid (PTSA), was obtained from the Hayashi Pure Chemical Industries Ltd. Japan. Reactive solvent, phenol, was purchased from the Merck Co. The E-glass fiber roving was obtained from PPG Co. U.S.A.

Blending Process:

1. Mixtures with various Phenoxy/phenol ratios were heated at 110°C for one-half hour. Then 5 wt% of p-toluene sulfonic acid (based on the amount of phenolic resin) was added to the phenoxy/phenol solution at 110 °C for another one-half hour.

2. The p-toluene sulfonic acid(PTSA) solution and phenolic resin was stored at 80 °C. The PTSA solution and phenolic resin were mixed in a stirrer glass reactor until the mixture was cooled to ambient temperature.

Viscosity Measurements: In order to investigate the effect of the p-toluene sulfonic acid on the viscosity of the phenoxy/phenol solution and the pot life of the polyblends, the viscosity versus time was measured at 110 °C using a Brookfield viscometer, following the specification of ASTM D 2373.

Pultruded Specimen : The pultrusion machine used was described elsewhere[7]. The dimensions of the pultrusion die are 82cm $\times$ 1.27cm $\times$ 0.33cm. The pulling rate is 30 cm/min at die temperature of 180°C and 200°C. The diameter of E-glass type Glass fiber used is 13.1 μ m.

Mechanical Properties: Izod notched impact strength (ASTM-D256), tensile strength (ASTM-D638), and flexural strength (ASTM D-790) test were carried out at ambient conditions.

RESULTS AND DISCUSSION

(a) Effect of PTSA Contents on the Viscosity of Solution:

The viscosities of the phenoxy/phenol solution with various PTSA contents are shown in Table I. The physical cross-links due to entanglements will restrict the flow rate of the sticky solution. The PTSA free mixture shows a sticky solution, since the extent of the phenoxy chains in phenol solvent has a higher degree of molecular entanglements and a lower intermolecular interaction. The entanglements will be decreased and the average strength of the hydrogen-bond interaction between phenol and phenoxy was increased when the PTSA was added to the solution. It indicted that the mixture was mixed well and the motion of the phenoxy in the blend system increased. The average strength and amount of the hydrogen bond increased resulting a lower viscosity. The organic-acid catalyst will adjust viscosity of the phenoxy/phenol solution.

(b) Morphology:

The morphology of pultruded fiber reinforced phenoxy toughened phenolic resin is investigated by SEM photography as shown in Figure 1. From Figure 1(a), it is observed that the fiber bundles are distributed evenly in the pure phenolic matrices, however, the wet-out of fiber is poor. Figure 1(b), shows the wet-out of fiber reinforced phenoxy/phenolic composite is better than that shown in Figure 1(a). The polymer blend contains 18 wt% of phenoxy may have the best fiber wet-out. The hydroxyl group of phenoxy can interact with the hydroxyl group of glass fiber. There are some enhanced interfaces between the resin and the glass fiber, consequently, phenoxy will improve the bonding between glass fiber and matrix.

From Figure 1(a), the SEM photograph shows crack propagates under cleavage fracture. From Figure 1(b) it can be seen that the wave pattern becomes more seriously. It was found that the soft segment of phenoxy

627

absorbs fracture energy by yielding and the matrix was softened. Results show that the notched Izod impact strength increases with the phenoxy content.

(c) Mechanical Properties:

Table II shows the impact strength of the polymer blends based composites increased with phenoxy contents, the maximum value appears at the 12 phr phenoxy contents, Tensile strength of the polymer blends based composites are almost independent of the phenoxy contents of the phenolic matrix. In this system, the solvent (phenol) in the matrix may increase the density of crosslink, and reduce the wet-out of glass fiber, hence the polymer is brittle. As mentioned earily, the presence of the phenoxy may improve the wet-out of glass fiber. Both opposite factors cause the tensile strength is almostly independent of the phenoxy contents. The flexural strength of the polymer blends based composites increased with phenoxy contents, the maximum value appears at 12 phr phenoxy contents. The postcured composites show higher mechanical properties than those of the unpostcured, since the postcured resin reacted completely.

CONCLUSIONS

The presence of the organic-acid catalyst in phenoxy/phenol solution improves the processability of the polymer blend, which is contributed to the increasing of the interaction between phenol and the phenoxy chains.

The hydrogen group of phenoxy will interact with the glass fiber, hence, the wet-out of the glass fiber will be improved. The mechanical properties of the phenoxy toughened phenolic composite are better than those of virgin phenolic composite.

REFERENCES:

1. Y. Zaks, Jeelen Lo, D. Raucher, and E.M. Pearce, J. Appl. Polym. Sci. 27. 913~930, 1982

2. Elsevier Science Publishers Ltd. " Low-Smoke Resin Fends Fires Effectively" Reinforced Plastics, p. 36 June 1994

3. Elsevier Science Publishers Ltd. "Phenoic GRP-Where is it today?" Reinforced Plastics, p.30 June 1992

4. Elsevier Science Publishers Ltd. " Pultruding the unprocessable?" Reinforced Plastics, p.36 October 1994

5. Chen-Chi M. Ma, " Research on the Pultruded of Fiber Reinforced Phenolic Resin composite (II)" National Sci. Coun. R.O.C. Taiwan, 1994

6. A.Matsumoto, K.Hasegawa, A.Fukuda and K.Otsuki, "Study on modified phenolic resin.III.: Modification with p-Hydroxyphenylmaleimide/ Acrylic Ester copolymer" J. Appl. Polym. Sci. v.44 p.1547-1556 1992

7. H.D. Wu, C.C.M. Ma, M.S. Lee and Y.D.Wu, "Pultruded Fiber Reinforced Polyurethane Tiughened Phenolic Resin.I.: Reactivity and Morphology", Die. Angew. Makromol. Cheme. accept, 1995

ACKNOWLEDGEMENT:

Table 1 The viscosity of Blend with various ratios of Phenoxy/Phenol

The ratio of Phenoxy/Phenol*	3/15	6/15	9/15	12/15	15/15	18/15
Viscosity of the solution PTSA free (cps)*	200	1,310	8,900	30,000	120,000	320,000
Viscosity of the solution with PTSA (cps)*	40	60	180	220	300	420

* The weight of PTSA is based on 1/15 of the weight of Phenol.
* The test tempersture is at 110 °C.
* The ratios based on weight.

Table 2 The mechanical properties of the modified phenolic composite.

	Phenoxy Contents, phr	0	3	6	9	12	15	18
uncured specimen	Flexural strength, MPa	32.3	45.1	45.3	57.2	69.4	66.9	61.8
	Tensile strength, GPa	571	518	531	546	548	541	595
	notched Izod impacted strength, KJ/m	1.04	1.28	1.92	2.03	3.20	2.88	2.56
cured specimen	Flexural strength, MPa	363	547	547	667	770	812	694
	Tensile strength, GPa	693	679	697	703	706	732	660
	notched Izod impacted strength, KJ/m	1.76	2.08	2.62	2.96	4.00	3.81	3.68
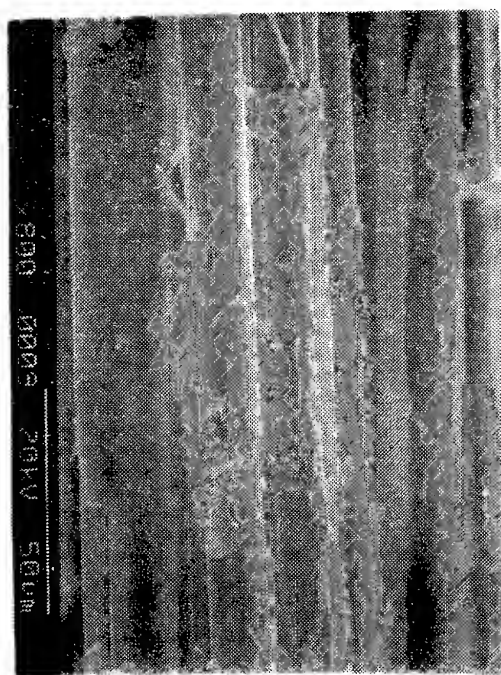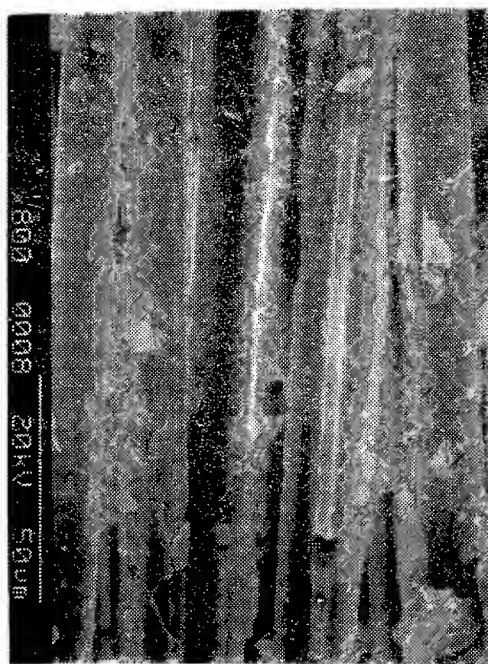
(a)   (b)

Figure 1 The SEM photograph of the morphology of pultruded fiber reinforced phenoxy toughened phenolic resin with various phenoxy contents. (a) 0. (b) 18 phr

NANOMETER-SCALE CONCEPTION OF COMPUTER MODELING OF POLYMER COMPOSITES: MICRO- AND MACROMECHANICAL PROPERTIES AND BEHAVIOR

YU. YANOVSKY and I. OBRAZTSOV

Department of Mechanics of Structured and Heterogeneous Continua,
Institute of Applied Mechanics of Russian Academy of Sciences,
Leninsky Prospect 32A, Moscow, 117334, RUSSIA

INTRODUCTION

Mathematical modeling is one way of solving technical problems encountered in the development and prediction of the properties and processing technology of polymer composite materials and of describing their properties under diverse service conditions. The construction of various models and the need to study them require a search for numerical and analytical methods for their analysis.

For describing of macromechanical properties of the polymer composites it is very important to model their micromechanical behavior, in particular properties of the matrix and interphase composite layers.

As one known for polymer composite materials physico-mathematical models provide basic information to guide design. The first estimates of the elastic and viscoelastic properties of these materials from model viewpoint were undertaken on the basis of the well known phenomenological models (Voigt, Reuss, Kerner, Takayanagi etc.). To be more predictive the phenomenological approaches and models need to be modified. A useful micromechanical framework have to be built to model. If there is no micromechanical framework it is nearly impossible to establish quantitatively the contribution of the constituents and the interface. Empirical approach alone is not adequate.

From this standpoint, a structural micromechanical model can be considered more systematic and improved in this for composites. It considers not only the properties of the filler and matrix, but also the intermediate layer appearing on the boundary of the fillers (interphase layer) and having specific properties that differ from those of the matrix.

MICROMECHANICAL APPROACHES IN MODELING OF STRUCTURE AND PROPERTIES OF COMPOSITES

We propose a multy-elements structural model which considers as the properties of the composite filler and matrix so the interphase layers. The framework of the nanoscale conception in an appropriate for computer simulation form one can write as follows.

Nanoscale-Level	Modeling of the filler surfaces, of the potentials of interaction of the heterogeneous composite separate phases and the regularities of its variation by stresses and temperature
Mezoscale-Level	Modeling of the structure, of the mechanical and relaxation properties of a polymer matrix and the interphase composite layers
Micro-Level	Modeling of a structure and mechanical properties of the periodicity and representative elements
Macro-Level	Modeling of composites media effective properties.
Theoretical and Experimental Verification of Modeling and Calculation Adequacy	Test experimental investigations and mathematical correction on the base of the general adaptive program.

Take into account the stated above the set of new approaches and computational methods for studying of strength-stress and mechanical behavior of advance polymer composites was developed.

DESCRIPTION OF POLYMER COMPOSITE MATRIX PROPERTIES

For nano- and mezoscale levels we are solving the problem of computational describing of the polymer composite matrix properties within a broad range of variation of the magnitudes and laws of deformation. In common case that problem consists in determining the time dependences of the mechanical characteristics, i.e. the material functions reflecting the viscoelastic mechanism of the behavior of these systems.

As one known the theory of viscoelasticity is based on function which completely characterizes the material, the relaxation spectrum [1]. In principle, from this one pivotal function all other material functions may be deduced. Although this seems rather straightforward in theory, in practice serious difficulties arise, to start with in obtaining a reliable and unique relaxation spectrum from experimental measurements.

The difficulties encountered are two fold. Firstly, considerable noise is superposed on the discrete values measured depending on the method, and secondly the domain of the discrete values is certainly restricted in any experiment. Further, the inverse problem of finding the relaxation spectrum, the kernel of a Fredholm equation of the first kind, from measured data is an ill-posed problem [2]. Inverting this integral equation is not an easy task because the solution to the inverse problem is not unique. It can be made unique only by introducing additional assumptions or additional a priori information. Further, in any experimental data, in addition to the inherent noise, there is embedded another set of experimental values which are not accounted for by any error estimate and distribution, called outliers. The answer to the question as to how large is this set depends on many factors. But it is certainly not negligible by any means. Lastly, we remark that if the data has been obtained in a restricted region, which it is almost always, extending the

relaxation spectrum deduced from it by whatever to a larger range, which is always necessary in practice, is a moot question by definition if the method used to obtain the spectrum in the limited range has shortcomings to begin with.

The new algorithm based on the minimax method we developed does not require a priori error estimates and the set of outliers are taken into account. The principles of method and algorithm constructing together with several hypothetical examples for testing of the reliability and exactness of the method is discussing in [3].

When speaking of the merits and shortcomings of the theoretical approaches used to description the viscoelastic behavior of polymer we must have in view that we dealt with macromolecules far from the surface. Near a surface one must consider the interaction of separate parts of a macromolecule with the surface. Here we should expect changes in the mobility of a macromolecule and the relaxation time.

DESCRIPTION OF INTERPHASE LAYERS MECHANICAL PROPERTIES

For nano- and mezoscale levels the new model approach (Collision Molecular Dynamics Method) was created and involved for calculation of the structure and specific mechanical properties of the polymer composite interphase layers. Numerical experiments modeling of molecular dynamics of the polymer chains adsorbed on the phase surface "solid"-"viscoelastic matrix" by action of the shear forces were made.

Polymer adsorption is of interest in a large number of technically important problems. The investigation of the adsorption of linear polymers at a surface has been an area of intensive activity for many years. The majority of work has been devoted to the case of adsorbed chains in quietscent systems, though the most applications in which polymer adsorption is important involve the presents of a deformation.

Experimental studies [4,5] have demonstrated that the average thickness of adsorbed polymer layers is a function of the wall shear rate.

A linear macromolecul consisted of the elastic links was used as a polymer model. Interiormolecular bulk interactions were inserted through Lennard-Jons potential. Polymer chains ends were fixed by means of elastic force on the unpenetrated for the macromolecular atoms phase surface. Chain interactions with a liquid phase by shear have been modeling through collision dynamics method. According to this method environment polymer medium has been modeling by virtual particles collising with polymer chain atoms. Virtual particles medium is characterized through the temperature, viscosity and parameters of deformation. Below we will discuss the numerical experimental results for one hundred chain links. Influence of deformation shear parameters on the polymer chain dynamics has been analising in the macromolecular geometrical characteristic terms, that is, distribution links density, efficient shear viscosity vs shear rate dependences etc.

As an example of the calculation results on the figures 1-2 one can see the effect of shear rate $\dot{\gamma}$ on deformation and orientation of the chain for two cases, the chain is terminally attached at repulsive surface, and in the second case the chain is free space one. This corresponds to an adsorbed polymer, and to a nonadsorbed polymer, which is located far from the surface.
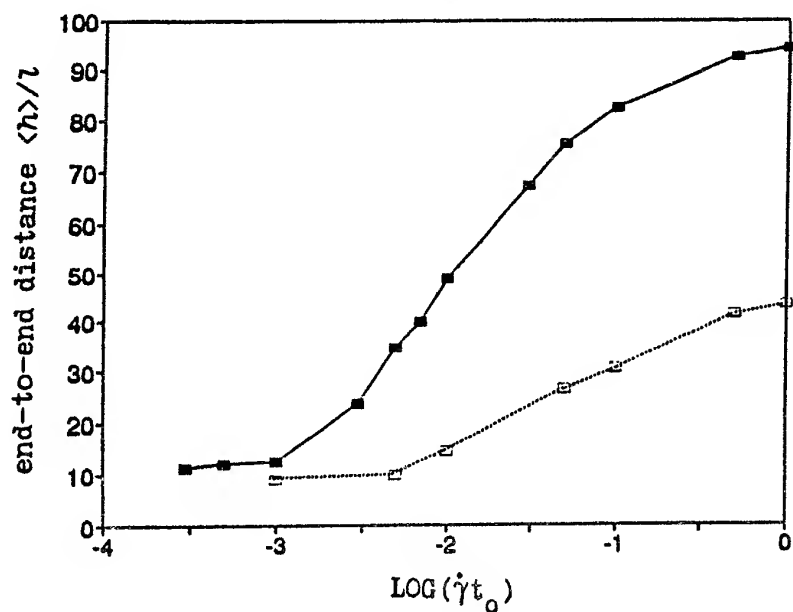
633

Fig.1. Average end-to-end distance $\langle h \rangle$ of a 101-bead chain as a function of the shear rate $\dot{\gamma}$. Comparison between the $\langle h \rangle (\dot{\gamma})$ dependence for the case of terminally anchored chain (solid line) and the $\langle h \rangle (\dot{\gamma})$ dependence for the free-spaced chain (dashed line).
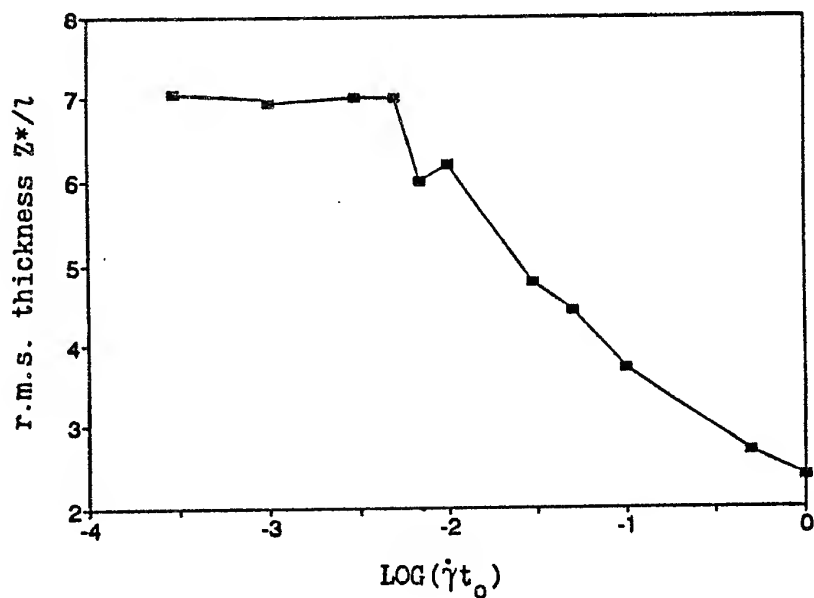

Fig.2. Average thickness of adsorbed polymer Z^* vs. shear rate $\dot{\gamma}$ for terminally anchored chain.

MODELING OF MECHANICAL PROPERTIES OF THE PERIODICITY CELLS AND REPRESENTATIVE ELEMENTS

To calculate the stressed state of the element periodicity and representative element of rubber composite media with periodical or non-periodical structure it is convenient to employ the method of finite elements. An object-oriented conception of its seems to be more perspective along this path. All algorithms, functions and methods of the object-oriented programs are constructed pursuant to the laws of mathematical abstraction (mathematical laws of objects transformation). In this approaches the vectorial and tensoral nature of displacements, strain and stresses has been used for solution of the continious media and composite materials mechanics.

An object-oriented approach was employed in the new finite-elements program complex developed for calculation of strength-stress elastic, elasto-plastic and viscoelastic behavior of polymer composites with interface layers.

As an example below the are given calculations of composite materials properties in which we used the model of elastoplastic deformation based on the Drucker-Prager strength criterion:

$$F = \alpha I_1 + \sqrt{I_2} - k = 0$$

where I_1 is the first invariant of the stress tensor, I_2 is the second invariant of the stress deviate, α and k are the strength characteristics. The choice of this criterion was due to the fact that the conditions of plastic flow of Tresk and Von Mises, and also, for conditions of plane deformations, the failure criteria of Coulomb and Mohr-Coulomb are particular cases of it.
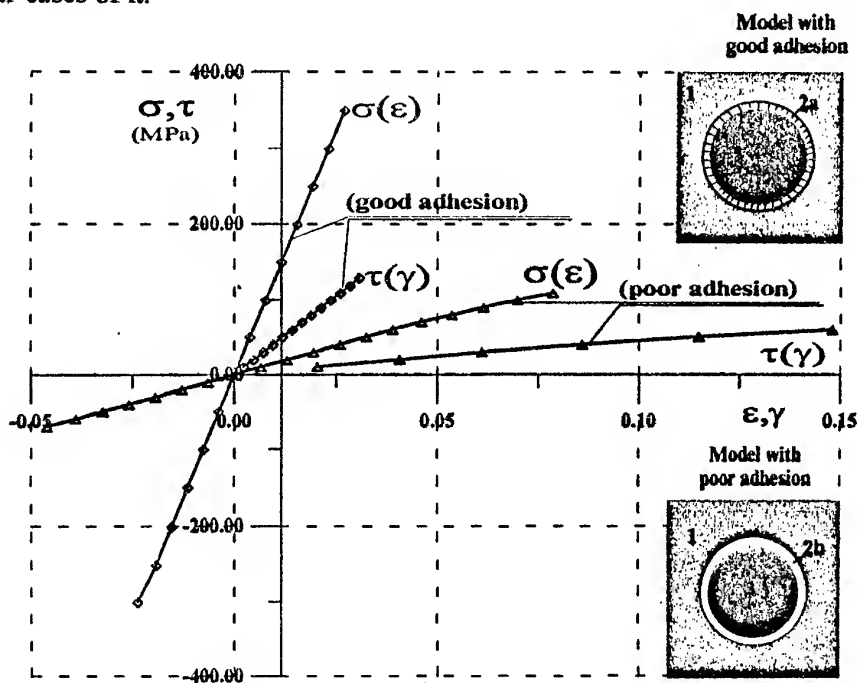
Fig.3. Influence of the Interphase Interactions on the Composite Deformation Properties by Shear $\tau(\gamma)$ and Compression-Tension $\sigma(\varepsilon)$.

Figure 3 presents the results of calculations for uniaxial compression and tension $\sigma(\varepsilon)$ and for shear $\tau(\gamma)$ under conditions of plane deformation performed with the use of the developed program complex for a periodicity cell of a particles filled polymer composite with consideration of the interphase layer. The composite material contained 60 vol.% of filler. (All calculations were made by Polywell RISC Systems Workstation.)

CONCLUSIONS

Based on the structure-mechanical model of heterogeneous medium with interphase layers the new approaches and computational methods of studying of strength-stress and mechanical behavior of advance polymer composites were developed. Program of calculation contains the stages which are modeling the composites properties at the different structure organization levels: mezoscale level, micro-level and macro-level.

REFERENCES

1. Yu.G.Yanovsky, Polymer Rheology: Theory and Practice, Chapman and Hall, London,)1993).
2. J.Hadamard, Lectures on Gauchy's Problem in Linear Partial Differential Equations, Yale University Press, (1923).
3. Yu.G.Yanovsky and Yu.A.Basistov, Polymer Testing 14, 315-328, (1995).
4. Y.Cohen, Macromolecules, 21, 494, (1988).
5. M.Bagassi, G.Chauveteau, J.Englert, M.Tirrell, Macromolecules, 22, 262, (1989).

BUCKLING/PLASTIC COLLAPSE BEHAVIOUR OF STRUCTURES COMPOSED OF STEEL PLATES HAVING SURFACE LAYER WITH ULTRA FINE GRAIN MICROSTRUCTURE

Tetsuya Yao[1], Hiroshi Yajima[1], Motomichi Yamamoto[1],
Masahiko Fujikubo[1], Yukito Hagiwara[2], Tadashi Ishikawa[2]

[1] Department of Naval Achitecture and Ocean Engineering, Faculty of Engineering,
     Hiroshima University, 1-4-1, Kagamiyama, Higashi-Hiroshima 739, Japan
[2] Oita R & D Laboratory, Nippon Steel Corporation, Nishinosu 1, Oita 870, Japan

INTRODUCTION

During the World War II, many war-time standard ships were broken into two due to the occurrence of brittle fracture. Since that time, plenty of research works have been conducted on brittle fracture, and enormous efforts were made to develop steel plate with high fracture toughness. TMCP (Thermo Mechanical Control Process) steel plate is one of the results of these efforts. TMCP steel plate has high fracture toughness, and is now widely used in ship and offshore structures.

Recently, steel plate of a new type has been developed with SUF (Surface Layer of Ultra Fine Grain Microstructure) of 1 to 3 micrometers in diameter utilising the TMCP technology. A research project was formed to examine the applicability of the new steel plate to ship and offshore structures. Series of fracture toughness tests were carried out, and the results were reported in Refs. [1] through [3]. They are briefly introduced in the following section. Through the tests, it was known that the yield stress in surface layer is increased by about 20% at maximum compared to that in the mid-thickness layer. This may result in the increase in buckling/plastic collapse strength when structures are constructed with this new steel plating.

In the present study, seires of column buckling tests are conducted using new steel plate with SUF. Elastoplastic large deflection analysis is also performed on the column specimens by FEM, and the accordance between calculated and measured results is examined. Then, the same analyses are carried out both on isolated and stiffened plates in a ship structure, and the advantage of using new steel plate is discussed from the viewpoint of ultimate strength.

CHARACTERISTICS OF SUF STEEL PLATE

Surface layer with ultra fine grain size was achieved based on the new metallurgical principle of "working the surface layers in reoccurrence process after inner-pass cooling." A typical microstructure of SUF steel plate is shown in Photo 1 [2], and the chemical compositions in Table 1 [1]. The chemical compositions are the same

through the thickness, but the ultra fine-grained surface layer has very high toughness and high yield stress. This surface layer always fractures in ductile manner at possible service temperatures of ship and offshore structures. Because of this, SUF steel plate has high crack arrestability.
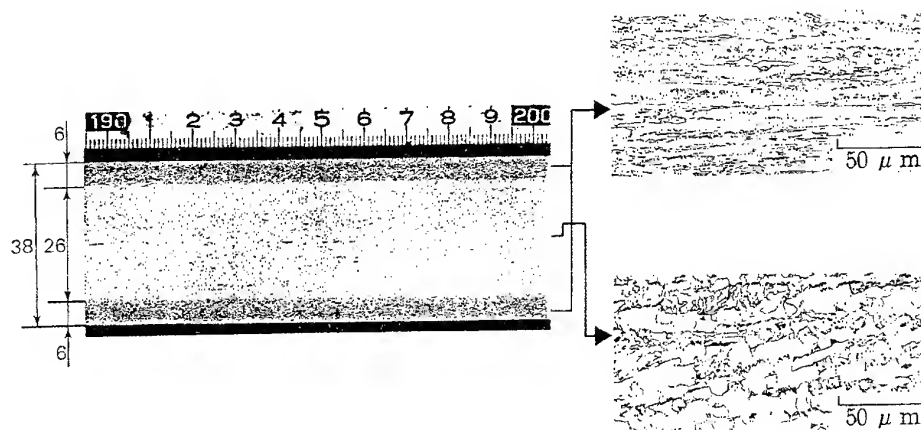

Photo 1   Macro- and micro-structures of SUF steel plate

Table 1   Chemical compositions

C	Si	Mn	P	S	Al	Ceq
0.13	0.20	1.27	0.007	0.002	0.027	0.34
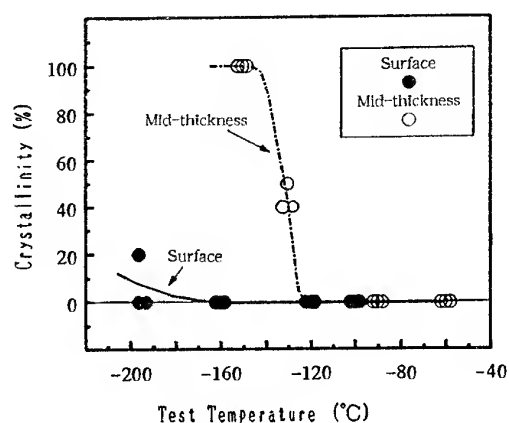
Fig. 1   Results of Charpy impact tests
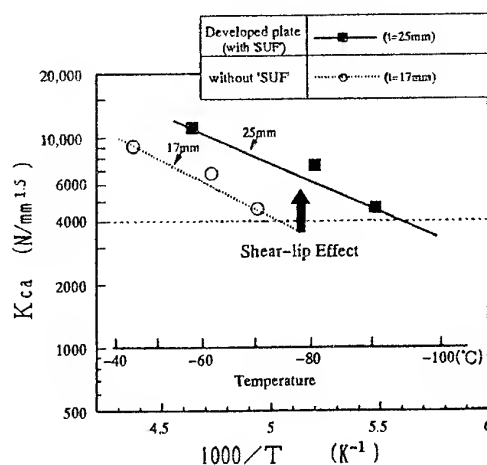
Fig. 2   Results of ESSO tests

The results of Charpy impact tests for 25 mm thickness plate using sub-sized specimens from the surface and the mid-thickness layers are compared in Fig. 1 [1]. It is known that the transition temperature from brittle to ductile is very low in SUF. Figure 2 indicates the results of ESSO tests with temperature gradient for the same SUF steel plate [1]. It is observed that high fracture toughness is attained owing to the SUF. This is called "shear-lip effect."

COLUMN BUCKLING TESTS AND CALCULATIONS

Series of buckling collapse tests were carried out on six column specimens of SUF steel plate with 25 mm thickness. The mechanical properties in the surface and the mid-thickness layers are shown in Table 2. Axial load was applied through special

Table 2   Mechanical properties of SUF steel plate

Position	Yield Stress (MPA)	Tensile Stress (MPA)	Elongation (%)
Surface	508	559	26.4
Mid-th.	389	499	31.6

ℓ = 710 mm
      500 mm
      360 mm

b = 50 mm

t = 24 mm
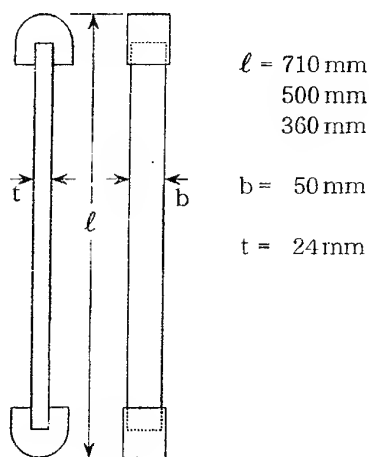
Fig. 3   Column specimen

$$\sigma_{cr} = \frac{\pi^2 E}{(\ell/k)^2}$$

$$k = \sqrt{I/A}$$
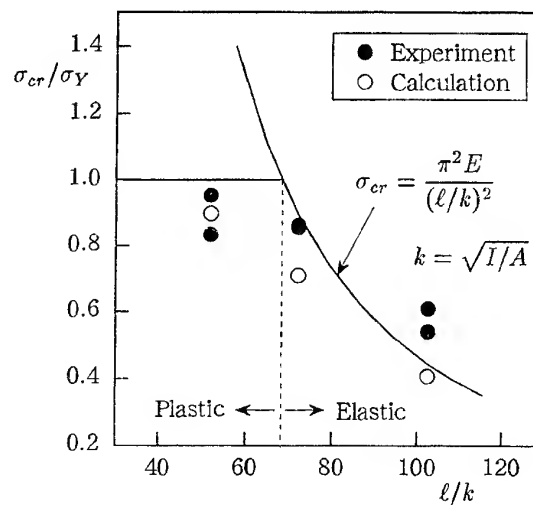
Fig. 4   Measured and calculated buckling strength
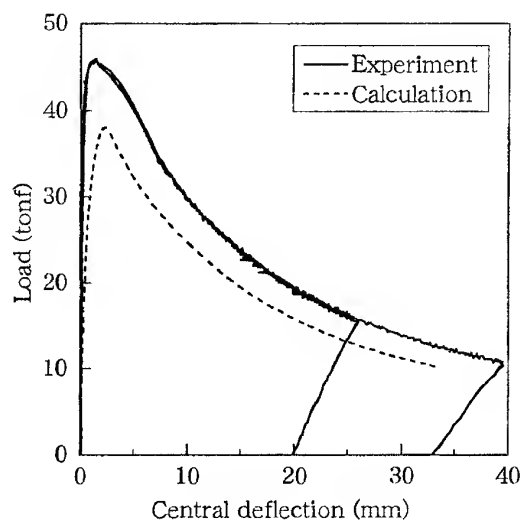
Fig. 5   Comparison between measured and calculated results

ε_{Ym}:   YIELD STRAIN IN MID-THICKNESS LAYER
ε_{Ys}:   YIELD STRAIN IN SURFACE LAYER

O: INITIAL YIELDING POINT

ε_a: AXIAL STRAIN
ε_b: BENDING STRAIN

(a)   (b)
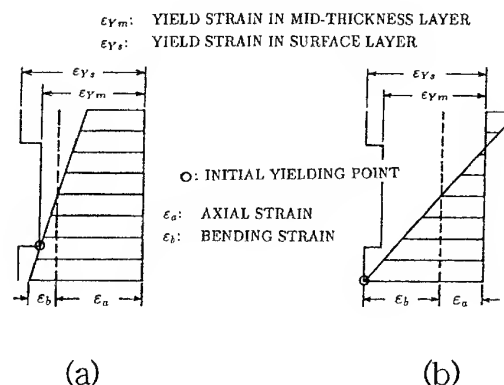
Fig. 6   Initial yielding point

caps attached to both ends as illustrated in Fig. 3. This is to obtain simply supported condition at both ends.

Measured buckling strength is plotted against the column slenderness ratio together with the calculated results in Fig. 4. For the calculation, computer code "ABAQUS" was used giving the corresponding yield stress to each layer. The measured buckling strength is a little higher than the calculated results. This is because of poor achievement of intended boundary condition of simply support. On the other hand, calculated buckling strength is reasonable compared to the theoretical Eulerian curve.

Figure 5 shows the load-deflection relationships obtained by experiment and calculation. Although the buckling strength is different between the measured and calculated curves, the buckling collapse behaviour is fundamentally well simulated by the calculation.

COLLAPSE BAHAVIOUR OF PLATE UNDER THRUST

Elastoplastic large deflection analysis was performed on square plate of 800×800 mm subjected to uniaxial thrust. The plate thickness was taken as 9.8 mm and 19.6 mm. The thickness of surface layer, t_s, with high yield stress was changed as $t_s/t = 0.0, 0.1$ and 0.2. The yield stress in SUF, σ_{Ys}, was taken as 1.2 times that of inner layer, σ_{Ym}, where $\sigma_{Ym} = 353$ MPA.

Usually, the strain distribution towards the thickness is as indicated by solid lines in Fig. 6, which are the sum of inplane and bending components. When the yield stress is not uniform through the thickness, the yielding takes place at the surface or at the boundary of different yield stress depending on the ratio of bending strain to inplane strain. This is schematically illustrated in Fig. 6.

(a) Average stress-average strain relationships

(b) Average stress-central deflection relationships
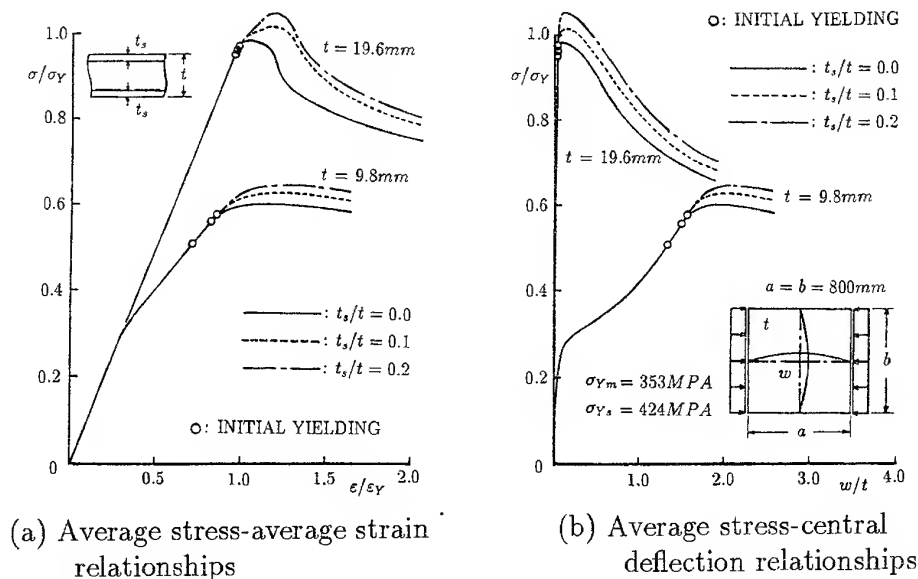
Fig. 7   Influence of SUF on collapse behaviour of plate under thrust

The calculated average stress-average strain and average stress-central deflection relationships for plate are plotted in Figs. 7 (a) and (b). For this calculation, the computer code "ULSAS" was used.

When the thickness is 9.8 mm, elastic buckling takes place at the knuckle point of stress-strain curve. $\bigcirc$ on the curves indicates the start of yielding. When $t_s/t = 0.0$, initial yielding takes place at the surface, while in other cases at the boundary of different yield stress as indicated in Fig. 6 (a). The behaviour after the yielding depends on the t_s/t ratio, and the higher ultimate strength is attained with larger value of t_s/t.

When the thickness is 19.6 mm, almost the same behaviour is observed, although the plate undergoes plastic buckling. It is known from this figure that higher ultimate strength can be expected when SUF steel plate is used than using conventional steel plate.

COLLAPSE BAHAVIOUR OF STIFFENED PLATE UNDER THRUST

When stiffeners of the same size is provided in equal spacing as deck plating of a ship's hull, a stiffened plate under thrust can be modeled by one stiffener and attached plating with breadth of one-spacing. For this model, uniaxial thrust was applied assuming longitudinal ship hull bending. The size of the analised stiffened plate and yield stresses are indicated in Fig. 8, where calculated average stress-average strain relationships are plotted. Also for this calculation, computer code "ULSAS" was used.

The solid line in Fig. 8 represents the result for stiffened plate made of SUF steel plate, and the dotted line that made of conventional steel plate of which yield stress
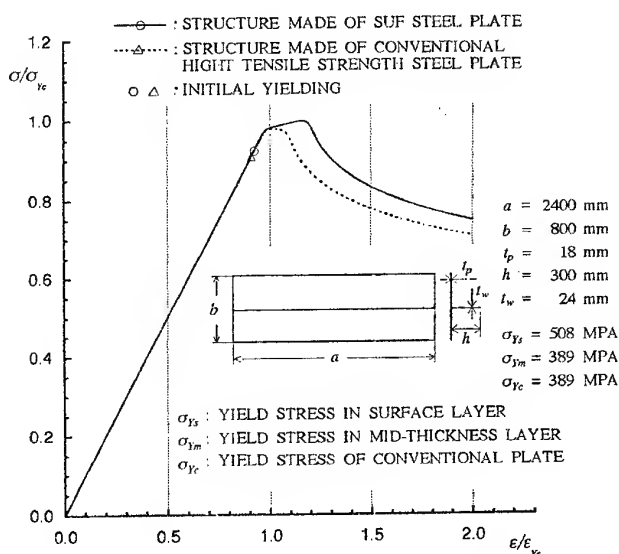
Fig. 8   Influence of SUF on collapse behaviour of stiffened plate under thrust

is equal to that of mid-thickness layer of SUF steel plate. In both cases, general yielding takes place before lateral deflection is produced. The point of strength reduction after general yielding corresponds to the start of plastic panel buckling. It is known from this figure that the strength reduction after geneal yielding is delayed by the influence of high yield stress in the fine-grained surface layer. This is the advantage of using SUF steel plate from the viewpoint of buckling/plastic collapse strength.

CONCLUSIONS

In the present paper, at first, results of fracture toughness tests in references on the newly developed steel plate with surface layer of ultra fine grain size were briefly introduced. This plate has high toughness preventing brittle fracture, as well as high yield stress in the surface layer.

Then, column bucklng tests and calculations were described, and relatively good correlations between measured and calculated results were shown.

The buckling/plastic collapse analyses were performed also on isolated and stiffened plates. The influence of high yield stress in surface layer was discussed, and the advantages of using SUF steel plate were shown. It can be concluded that higher ultimate strength and later occurrence of panel plastic buckling are attained by using SUF steel plate.

ACKNOWLEDGEMENT

REFERENCES

[1] Ishikawa, T., Nomiyama, Y., Hagiwara, I. and Aihara, S.: "Study on unstable brittle crack arrest toughness of newly developed steel with surface layers with ultra fine grain microstructure - Improvement of arrest toughness by enhanced shear-lip formation -." J. Soc. Naval Arch. of Japan **177**, pp.259-267 (1995), (in Japanese).

[2] Yajima, H., Yamamoto, M., Hagiwara, I., Ishikawa, T., Kawakami, Y., Miyamoto, T. and Miyamoto, H.: "Consideration on fracture toughness of steel plate having surface layer with ultra fine grain microstructure." J. West Japan Soc. Naval Arch. **91**, in printing (1996) (in Japanese).

[3] Ishikawa, T., Hagiwara, I., Oshita, S., Inoue, T., Hashimoto, K., Kuroiwa, T., Tada, M. and Yajima, H.: "Crack arrestability of steel plate for accidental conditions in ship hull structures (Application of high arrestability-endowed ultra fine-grain surface layer steel)," Proc. OMAE'96, in printing (1996).

BENDING BEHAVIOR OF DELAMINATED COMPOSITE PLATES WITH CONTACT EFFECTS

Meng-Kao Yeh[*] Lian-Bin Fang[+] Ming-Huei Kao[+]
Department of Power Mechanical Engineering
National Tsing Hua University
Hsinchu, 30043 Taiwan, ROC

INTRODUCTION

Composite laminates delaminate occasionally due to manufacturing defects, low energy impact or compressive loadings during their service life. This delamination problem generally results in unexpected degradation of the structure. The delamination in composite plates can be classified into types of edge [1], strip [2], elliptical [3], etc. Researchers mainly focused on finding the buckling load and fracture strength for the above-mentioned problems under uniaxial compression. Besides, Kardomateas [4] examined the snap buckling of delaminated composites under pure bending by an energy procedure and demonstrated it experimentally. Lu et al. [5] found the energy release rate for delaminated beams under transverse shear and bending by finite element method. Analysis with contact effects to avoid artificial penetration between the upper and lower sublaminate surfaces for delaminated composite is inevitable as observed by researchers [6-8]. Recently, Whitcomb [7] investigated the behavior of a postbuckled embedded delamination using geometrically-nonlinear 3-D finite element analysis with approximate contact constraints.

In this paper, we investigated laminated plate with strip-type delamination under pure bending analytically and experimentally. The size of the delaminated region and the position of the delaminated region in the thickness direction were varied to evaluate their influences on the bending behavior of the plates.

UPDATED LAGRANGIAN FORMULATION

Figure 1 shows a simply supported laminated composite plate of length L with strip-type delamination of length a. The uniform distributed forces at a distance L_e from both ends result in a state of pure bending in middle span L_a. Since large deflection cause geometric nonlinearity in the delaminated region where possible local buckling of sublaminate may occur, the equilibrium equation of the laminated plates with strip-type delamination is derived in incremental form using the updated Lagrangian formulation [9]. All variables and the equilibrium state of the laminated plate considered are updated to the current configuration. The next equilibrium state is obtained from the linearized equation of the problem derived from the principle of virtual work [9]

$$\int_V C_{ijrs} e_{rs} \delta e_{ij} dV + \int_V \tau_{ij} \delta \eta_{ij} dV = \int_{S^\beta} P_i^\beta \delta U_i dS - \int_V \tau_{ij} \delta e_{ij} dV \tag{1}$$

where C_{ijrs} and τ_{ij} are the tensor of the elastic constants and the Cauchy stress tensor

[*] Professor, the author for correspondence, Fax: 886-35-726414, e-mail: mkyeh@pme.nthu.edu.tw
[+] Graduate student

in the current configuration; e_{ij} and η_{ij} are the linear and nonlinear parts of the strain incremental tensor of the current configuration; P_i^β is the external force in the next unknown configuration β; U_i is the incremental displacement vector from the current configuration to the next unknown configuration β.

Transformation Matrix Method

The contact condition between the upper and lower sublaminates at the delaminated region was formulated using the transformation matrix method [10] with the advantage of reducing the number of system unknowns. In Figure 2, a laminated plate with a strip-type delamination deformed from the current configuration α to the next unknown configuration β. The displacement of point p on the surface of upper sublaminate A is expressed in terms of the gap displacement vector $\underline{h}$, the sticking displacement vector $\underline{U}_{p'q'}$ and the relative sliding displacement vector $\underline{U}_{q'q}$. The gap displacement vector $\underline{h}$ is the difference between position vectors of point p on the surface of upper sublaminate A and its projection p' on the surface of lower sublaminate B; the sticking displacement vector $\underline{U}_{p'q'}$ can be interpolated using the shape matrix $[N_B]$ and the nodal displacement vector $\underline{U}_B$ of the element which the point p' belongs to; the relative sliding displacement vector $\underline{U}_{q'q}$ can be obtained as the product of the tangential vector $\underline{t}$ at point p' and the magnitude of relative sliding displacement u_s of point p. The displacement vector $\underline{U}_A$ of point p on the surface of upper sublaminate A can be obtained as following

$$\underline{U}_A = \underline{U}_{pq} = \underline{U}_{pp'} + \underline{U}_{p'q'} + \underline{U}_{q'q} = \underline{h} + [N_B]\underline{U}_B + \underline{t}u_s = \underline{h} + [g]\underline{u} \qquad (2)$$

in which $[g] = [[N_B] \quad \underline{t}]$ is the transformation matrix; $\underline{u} = \{\underline{U}_B^T \quad u_s\}^T$. For the noncontact node on surface of sublaminate A, the transformation matrix $[g]$ is a unit matrix and the gap displacement $\underline{h}$ is a zero vector, i.e., $\underline{U}_A = \underline{u}$. The total relative incremental displacement between points on surfaces of sublaminates A and B is $\underline{U}_{pq} - \underline{U}_{p'q'}$ or $\underline{U}_A - \underline{U}_B$.

Finite Element Method

Four-point isoparametric element [9] was used to descretize the continuous plate system. The transformation between the local coordinate (r, s) and the global Cartesian coordinate (x, y) is obtained through a Jacobian matrix. For each nodal incremental displacement, there are two translational degrees of freedom which result in a total of eight degrees of freedom in each element.

To consider the contact condition between the surfaces of upper and lower sublaminates A and B, we rewrite Equation (1) as

$$\int_V C_{ijrs}e_{rs}\delta e_{ij}dV + \int_V \tau_{ij}\delta\eta_{ij}dV$$
$$= \int_{S^\beta} P_i^\beta\delta U_i dS - \int_V \tau_{ij}\delta e_{ij}dV + \int_{S_C^\beta} P_{Ai}^\beta\delta U_{Ai}dS + \int_{S_C^\beta} P_{Bi}^\beta\delta U_{Bi}dS \qquad (3)$$

where S^β is the surface not dealing with contact condition; P_{Ai}^β and P_{Bi}^β are the contact force on contact surfaces S_C^β of sublaminates A and B in the unknown configuration β and U_{Ai} and U_{Bi} are the corresponding incremental displacement vectors. After some manipulations, and assembling the element equations, we obtained the global system equation of laminated plate with Coulomb's friction law

$$\left[\begin{bmatrix} G \end{bmatrix}^T - \text{sign} \cdot \mu \cdot [n] \quad [I_B] \quad [I_D] \right] \cdot \begin{bmatrix} [K_A] & [0] & [0] \\ [0] & [K_B] & [0] \\ [0] & [0] & [K_D] \end{bmatrix} \cdot \begin{bmatrix} [G] \\ [I_B] \\ [I_D] \end{bmatrix} \cdot \underline{U}$$

$$= \left[\begin{bmatrix} G \end{bmatrix}^T - \text{sign} \cdot \mu \cdot [n] \quad [I_B] \quad [I_D] \right] \cdot \left(\begin{Bmatrix} \underline{P}_A^\beta - \underline{F}_A \\ \underline{P}_B^\beta - \underline{F}_B \\ \underline{P}_D^\beta - \underline{F}_D \end{Bmatrix} - \begin{bmatrix} [K_A] & [0] & [0] \\ [0] & [0] & [0] \\ [0] & [0] & [0] \end{bmatrix} \cdot \begin{Bmatrix} \underline{H} \\ 0 \\ 0 \end{Bmatrix} \right)$$

(4)

in which [G] is a global transformation matrix; 'sign' = '+1' or '-1', is the relative sliding directions; μ is friction coefficient; [n] is the matrix of global normal vectors of nodes on the contact surface of sublaminate A; $[I_B]$ and $[I_D]$ are unit matrices; $[K_A]$, $[K_B]$ and $[K_D]$ are the global stiffness matrices of the sublaminates A, B and region D without delamination; $\underline{U}$ is the global incremental displacement from the current configuration α to the next configuration β, which contains global incremental displacements of the noncontact parts of the sublaminates A and B and the global incremental relative sliding displacements; $\underline{P}_A^\beta$, $\underline{P}_B^\beta$ and $\underline{P}_D^\beta$ are the external force vectors of the sublaminates A, B and region D without delamination in the configuration β; $\underline{F}_A$, $\underline{F}_B$ and $\underline{F}_D$ are the global internal force vectors of sublaminates A, B and region D without delamination in the current configuration α; $\underline{H}$ is the global gap displacement.

For the two dimensional nonlinear finite element analysis, a plane strain condition in the width direction was adopted. The modified Newton-Raphson iteration method was used to solve the resulting nonlinear finite element equation of the delaminated plate and a load-control scheme was implemented in the incremental solution procedure. In each increment, the iteration process was performed until the contact conditions were satisfied. The contact conditions include no penetration between sublaminates A and B, no tensile stresses between upper and lower contacting surfaces and correct sliding or sticking condition of each node on the contact surfaces.

EXPERIMENT

The facilities used in the experimental procedure were a hot press, a tension/compression testing frame with a four-point bending device and a data-acquisition system operated by a microcomputer. More detailed descriptions about the experimental procedure can be found in Ref. [3].

The specimens used in the bending experiment had length 160 mm, width 20 mm and 16 layers. The measured thickness of the specimen was 1.96 ± 0.15 mm. The length of the pure bending section (L_a in Figure 1) was 80 mm with 20 mm used as the arm (L_e in Figure 1) of the couple forces at each side. Strip-type teflon pieces (0.08 ± 0.01 mm thick) were embedded in the specimens at the ply interface to simulate delamination through the width. The laminated plate in the experiment was unidirectional, $[0°]_{16}$. The material properties of the delaminated plates were obtained from tensile-testing experiment and were used in the finite element analysis for comparison. Five material constants, the longitudinal modulus E_{11}, the transverse modulus E_{22}, the shear modulus G_{12} and the Poisson's ratios v_{12} and v_{23} are needed to describe the material property of each transversely isotropic layer [11]. v_{23}

645

is assumed equal to v_{12} as conventional [1-2]. Three experiments were performed for measuring each material constant. The four material constants were measured to be $E_{11} = 161.88 \pm 0.6$ GPa, $E_{22} = 10.6 \pm 0.3$ GPa, $v_{12} = 0.313 \pm 0.06$ and $G_{12} = 5.89 \pm 0.4$ GPa.

RESULTS AND DISCUSSION

We assumed a circular arc of radius R for the deformed laminated plates under pure bending. The radius of curvature was obtained as $R = [(d)^2 + (L_a / 2)^2] / 2d$, in which d is the vertical displacement at the middle point of the laminated plate; L_a is the span of the pure bending region (see Figure 1); the curvature κ is equal to 1/R. Since the laminated plates were under pure bending, there existed no shear force between the contacting surfaces of sublaminates A and B. The friction coefficient is assumed to be $\mu = 0.2$ in this analysis.

Figure 3 shows analytical and experimental moment-curvature curves of the delaminated composite plates ($[0°]_{16}$, t/T=1/8, a=60 mm) under pure bending. In analysis, the bending moment increased linearly to about 0.404 N-m, then a bulge-up local buckling mode of the sublaminate occurred as noticed by a slight slope change from 2.087 $N \cdot m^2$ to 2.142 $N \cdot m^2$ on the moment-curvature curve. In experiment, the strain on the mid-upper surface of the upper sublaminate changed its sign as shown in Figure 3. The local buckling of the upper sublaminate also occurred for the laminated plates with longer delamination ($[0°]_{16}$, t/T=1/8, a=80 mm) and had no significant effects on the bending responses of the delaminated plates. Figure 4 shows the analytical results of delaminated composite plates ($[0°]_{16}$, t/T=3/8, a=60 mm) with and without contact analysis. The upper sublaminate penetrated into lower sublaminate in the case without contact analysis. Therefore, to make the results reasonable the contact effect should be considered in the analysis.

Figure 5 shows the analytical and experimental bending rigidities for specimens ($[0°]_{16}$, t/T=1/8, W=20 mm) with various sizes of delamination. The analytical results are almost constant and slightly larger than the experimental ones. The upper sublaminates buckled locally but had no significant influence on the bending rigidity of the delaminated plates.

For the cases with delamination located further into the center of the plate in the thickness direction (t/T=3/8), no local buckling occurred and the bending rigidity are almost constant as well. The analytical and experimental bending rigidities for specimens ($[0°]_{16}$, a=60 mm, W=20 mm) with delamination located at varied depth are shown in Figure 6. Good agreement between the analytical and experimental results can be seen. In addition, the bending rigidities for cases with $[0° / 90°]_{4S}$ and $[90° / 0°]_{4S}$ lay-up varied slightly for delamination further into the center of plate in the thickness direction due to unsymmetries above and below the delamination.

CONCLUSIONS

The following conclusions can be drawn for the delaminated composite plates under pure bending.
1. The penetration between upper and lower sublaminates can be overcome by

646

contact analysis of the delaminated composite plates under pure bending.
2. Although the local buckling occurred for delaminated composite plates with longer and thinner sublaminates, the size of delaminated region had no significant influence on the bending rigidities of the delaminated plates.
3. The unsymmetric sublaminates lay-up ($[0° / 90°]_{4S}$ and $[90° / 0°]_{4S}$) of laminated plates above and below delamination affect bending rigidity of the delaminated plates slightly as the delamination is located further into the center of plate in the thickness direction.

ACKNOWLEDGEMENT

REFERENCE

[1] Kim, K. S. and Hong, C. S., "Delamination Growth in Angle-Ply Laminated Composites," *Journal of Composite Materials*, **20**, pp. 423-439 (1986)

[2] Whitcomb, J. D., "Parametric Analytical Study of Instability-Related Delamination Growth," *Composites Science and Technology*, **25**, pp. 19-48 (1986)

[3] Yeh, M. K. and Tan, C. M., "Buckling of Elliptically Delaminated Composite Plates," *Journal of Composite Materials*, **28**, pp. 36-52 (1994)

[4] Kardomateas, G. A., "Snap Buckling of Delaminated Composites under Pure Bending," *Composites Science and Technology*, **39**, pp. 63-74 (1990)

[5] Lu, T. J., Xia, Z. C. and Hutchinson, J. W., "Delamination of Beams under Transverse Shear and Bending," *Materials Science and Engineering*, A188, pp. 103-112 (1994)

[6] Kao, M. H. and Yeh, M. K., "Delaminatied Plates under Pure Bending and Local Buckling," *Proceedings of the 18th National Conference on Theoretical and Applied Mechanics*, Hsinchu, Taiwan, ROC, **3**, pp. 89-96 (1994), (in Chinese)

[7] Whitcomb, J. D., "Analysis of a Laminate with a Postbuckled Embedded Delamination, Including Contact Effects," *Journal of Composite Materials*, **26**, pp. 1523-1535 (1992)

[8] Mukherjee, Y. X., Gulrajani, S. N., Mukherjee, S. and Netravali, A. N., "A Numerical and Experimental Study of Delaminated Layered Composites," *Journal of Composite Materials*, **28**, pp. 1009-1392 (1994)

[9] Bathe, K. J., *Finite Element Procedures in Engineering Analysis*, Prentice-Hall, New Jersey (1982)

[10] Chen, W. H. and Yeh, J. T., "Finite Element Analysis of Finite Deformation Contact Problems with Friction," *Computers & Structures*, **29**, pp. 423-436 (1988)

[11] Christensen, R. M., *Mechanics of Composite Materials*, New York: Wiley (1979)
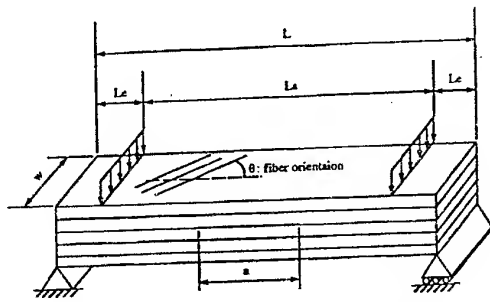
Figure 1. Composite plate with strip-type delamination under four-point bending
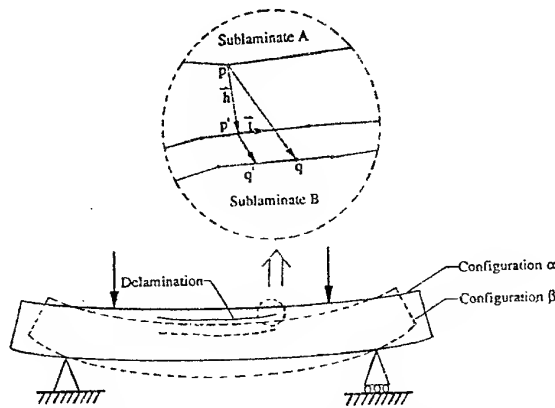

Figure 4. Analytical results for composite laminates ($[0°]_{16}$, t/T=3/8, a=60 mm) with and without contact analysis

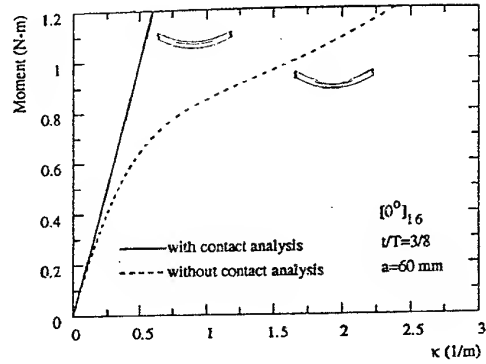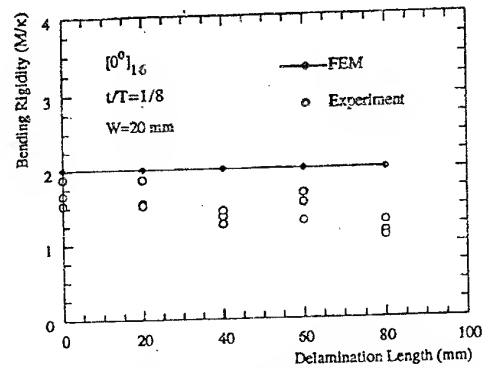**Figure 2.** Delaminated plate deformed from the current configuration α to the next unknown configuration β

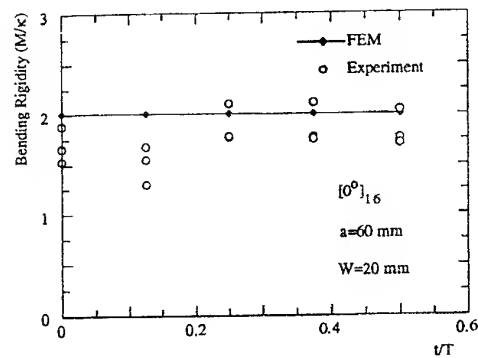**Figure 5.** Analytical and experimental results for specimens ($[0°]_{16}$, t/T=1/8, W=20 mm) with various sizes of delamination

Figure 3. Analytical and experimental moment-curvature relation and strain variation for delaminated plate specimens ($[0°]_{16}$, t/T=1/8, a=60 mm)

Figure 6. Analytical and experimental results for specimens ($[0°]_{16}$, a=60mm, W=20 mm) with delamination located at varied depths

648

ANALYTICAL AND NUMERICAL TECHNIQUES FOR BOUNDARY PROBLEMS FOR THIN UNSYMMETRIC LAMINATES

D. D. ZAKHAROV

Institute for Problems in Mechanics, Russian Academy of Sciences,
101 Vernadskogo avenue, 117526 Moscow, Russia

INTRODUCTION

We consider the internal stressed and strain state of composite laminates in the long–wave approximation, i.e., with the assumed small parameter $\epsilon = h/l \ll 1$ (h is a total semi-thickness; l is a character longitudinal scale, a wavelength). In contrast to the first theories of S. A. Ambartsumyan [1] and R. M. Christensen [2], we imply no restriction on the anisotropy type, study the dynamics, perform the asymptotic analysis and the classification. The ply numbers N is arbitrary. Due to their anisotropy and unsymmetric packing, the attention is focused on the problems of connected bending and stretching. In the range of obtained generalized model of Kirchhoff type, the methods of solving the boundary problems are suggested.

GENERAL 2D THEORY: PROPERTIES AND CLASSIFICATION

Let each j-th ply occupy a region $(\mathbf{x}, z \equiv x_3) \in \Omega \times [z_j, z_{j+1}] \subset R^3; z_{N+1,1} = z^{\pm}$ $(j = 1, \ldots, N)$. In 3D Hooke's law for the stresses $\sigma_{\alpha\beta}^j$ and deformations $\varepsilon_{\alpha\beta}^j$ the 6×6 stiffness matrix $\mathbf{G}_j$ is supposed to be complete. The interface contact is perfect, plate is initially non-deformable, and then charged on the faces by the transversal and tangential loads $\sigma^{\pm} = O(1)$, $\tau^{\pm} = O(\epsilon^{-1})$. Starting with the equations of 3D dynamic elasticity we find the asymptotic expansions of transversal and longitudinal displacements $W, \mathbf{U}$ (and stresses) into ϵ–power series

$$W_j = l\epsilon^{-m}(W_0 + \epsilon W_1 + \cdots)_j, \qquad \mathbf{U}_j = l\epsilon^{-n}(\mathbf{U}_0 + \epsilon \mathbf{U}_1 + \cdots)_j$$

$$\Sigma_j^T \equiv (\sigma_{11}, \sigma_{22}, \sigma_{33}, \sigma_{23}, \sigma_{13}, \sigma_{12})_j, \qquad \mathbf{E}_j^T \equiv (\varepsilon_{11}, \varepsilon_{22}, \varepsilon_{33}, 2\varepsilon_{23}, 2\varepsilon_{13}, 2\varepsilon_{12})_j$$

$$\Sigma_j = \mathbf{G}_j \mathbf{E}_j; \qquad \mathbf{G}_j = \|g_{rs}\|_j, \quad g_{rs}^j \neq 0 \qquad (r, s = 1, \ldots, 6).$$

At the typical timescale of process $O(\epsilon^{-1})$ the orders are $m = 3, n = 2$. The average membrane ($k = 1$), membrane-bending ($k = 2$) and bending ($k = 3$) rigidities d_{pq}^k, and main operators are introduced as follows ($1 \leftrightarrow 2$)

$$\mathbf{D}_k = \frac{1}{k}\sum_j (z_{j+1}^k - z_j^k)\boldsymbol{\Gamma}_j, \quad \boldsymbol{\Gamma}_j = \begin{bmatrix} \gamma_{11} & \gamma_{16} & \gamma_{12} \\ \cdots & \gamma_{66} & \gamma_{62} \\ \text{Symm.} & \cdots & \gamma_{22} \end{bmatrix}_j, \quad \gamma_{pq} = \frac{G_q^p}{G_0}$$

$$\chi_{11}(\boldsymbol{\Gamma}) = \mathbf{i}_1(\gamma_{11}\partial_1 + \gamma_{16}\partial_2) + \mathbf{i}_2(\gamma_{16}\partial_1 + \gamma_{12}\partial_2)$$

$$\chi_{12}(\boldsymbol{\Gamma}) = \mathbf{i}_1(\gamma_{16}\partial_1 + \gamma_{66}\partial_2) + \mathbf{i}_2(\gamma_{66}\partial_1 + \gamma_{26}\partial_2)$$

where G_0 is a minor $G\binom{345}{345}$ in the stiffness matrix, the minor G_q^p is constructed by adding of p-th line and q-th column to G_0 at the bottom and right side. For the main component of displacements (j-independent), stresses, stress resultants and couples, the following formulas and equations are obtained (δ is Kroneker delta, ρ is an average mass density):

$$l\epsilon^{-3}W_0 = w(\mathbf{x}, t), \; l\epsilon^{-2}\mathbf{U}_0 = \mathbf{u}(\mathbf{x}, t) - z\,\mathrm{grad}\,w; \quad \sigma_{\alpha\beta}^j = \chi_{\alpha\beta}(\boldsymbol{\Gamma}_j)(\mathbf{u} - z\,\mathrm{grad}\,w) \quad (1)$$

$$\begin{bmatrix} Q_{\alpha\beta} \\ M_{\alpha\beta} \end{bmatrix} = \begin{bmatrix} \mathbf{D}_1 & \mathbf{D}_2 \\ \mathbf{D}_2 & \mathbf{D}_3 \end{bmatrix} \begin{bmatrix} \epsilon_{\alpha\beta} \\ \kappa_{\alpha\beta} \end{bmatrix}, \qquad \mathbf{D} = \begin{bmatrix} \mathbf{D}_1 & \mathbf{D}_2 \\ \mathbf{D}_2 & \mathbf{D}_3 \end{bmatrix} \qquad (\alpha\beta = 11, 12, 22)$$

$$(\epsilon_{\alpha\beta}, \kappa_{\alpha\beta}) = (\varepsilon_{\alpha\beta}, \theta_{\alpha\beta})(1 + \delta_{\alpha+1}^{\beta}); \; \varepsilon_{\alpha\beta} = 1/2(\partial_\alpha u_\beta + \partial_\beta u_\alpha), \; \theta_{\alpha\beta}(w) = -\partial_{\alpha\beta}^2 w$$

$$Q_{\alpha3} = \partial_\beta M_{\alpha\beta} + z^+ \tau_\alpha^+ - z^- \tau_\alpha^-$$

$$\partial_\beta \chi_{\alpha\beta}(\mathbf{D}_1)\mathbf{u} - \partial_\beta \chi_{\alpha\beta}(\mathbf{D}_2)\operatorname{grad} w + T_\alpha = 0$$
$$\partial_{\alpha\beta}^2 \chi_{\alpha\beta}(\mathbf{D}_2)\mathbf{u} - \partial_{\alpha\beta}^2 \chi_{\alpha\beta}(\mathbf{D}_3)\operatorname{grad} w + T_3 = \rho \partial_t^2 w \tag{2}$$

$$\partial_\alpha Q_{\alpha\beta} + T_\alpha = 0, \qquad \partial_{\alpha\beta}^2 M_{\alpha\beta} + T_3 \equiv \partial_\alpha Q_{\alpha3} + T_3^* = \rho \partial_t^2 w \tag{3}$$

$$T_\alpha = \tau_\alpha^+ - \tau_\alpha^-; \quad T_3^* = \sigma^+ - \sigma^-, \; T_3 = T_3^* + \operatorname{div}(z^+ \boldsymbol{\tau}^+ - z^- \boldsymbol{\tau}^-) \quad (\alpha, \beta = 1, 2).$$

The expressions for small stresses $\sigma_{\alpha z}^j, \sigma_{zz}^j$ are presented in [3]. Notice, that in Eqs. (2),(3) only the "spoiled" bending equation is dynamic, two other ones are quasistatic. The position of coordinate plane $z = 0$ is found from the criterion of minimum connection norm between bending and stretching

$$z^- : \xi(z^-) = min \mid \partial_{\alpha\beta}^2 \chi_{\alpha\beta}^2(\mathbf{D}_2) \mid. \tag{4}$$

Let us briefly summarize the main properties of presented model:
1. Each real symmetric matrix $\mathbf{\Gamma}_j, \mathbf{D}_1, \mathbf{D}_3, \mathbf{D}$ is positively determined.
2. The symbols of operators (2), as well as of membrane operator $\partial_\beta \chi_{\alpha\beta}(\mathbf{D}_1)$ and bending operator $\partial_{\alpha\beta}^2 \chi_{\alpha\beta}(\mathbf{D}_3) \operatorname{grad}$, are of elliptic type.
3. The positive energy density and average potential energy exist and given below. The following relations of energy balance between the internal energy, work and power of facing and lateral loads, hold in statics and dynamics ($\mathbf{n}, \boldsymbol{\tau}$ are the unit vectors, normal and tangent to $\partial\Omega$)

$$(T + \Pi)^\cdot = \mathcal{W} + \int_{\partial\Omega} Q_n u_n^\cdot + Q_\tau u_\tau^\cdot + M_n \phi_n^\cdot + P_n w^\cdot \, d\tau, \qquad T \equiv \int_\Omega \rho w^{\cdot 2} \, d\Omega$$

$$\Pi = \mathcal{A} + \int_{\partial\Omega} Q_n u_n + Q_\tau u_\tau + M_n \phi_n + P_n w \, d\tau, \qquad P_n \equiv Q_{n3} + \partial_\tau M_\tau$$

$$\pi_j = \mathbf{e}^T \mathbf{\Gamma}_j \mathbf{e}, \quad \mathbf{e}^T = (\varepsilon_{11}, 2\varepsilon_{12}, \varepsilon_{22}); \qquad \Pi = \frac{1}{2} \int_\Omega Q_{\alpha\beta}\varepsilon_{\alpha\beta} + M_{\alpha\beta}\theta_{\alpha\beta} \, d\Omega.$$

4. The uniqueness of stress-strain state in the boundary problem (BP) in statics and dynamics is proved when the boundary conditions (BC) are given in the form
1) first BP $\quad u_n, u_\tau, \phi_n, w$;
2) second BP $\quad Q_n, Q_\tau, M_n, P_n$;
3) mixed combinations of BC 1) and 2);
on each of segments $S_l : \partial\Omega = \bigcup S_l$. In dynamics we add the initial conditions $w(\mathbf{x}, t = 0), w^\cdot(\mathbf{x}, t = 0)$; there is no need to add them for tangential displacements, since their equations are quasistatic.
5. Each two fields $\mathbf{V}^\mu = (u_\alpha, w)^\mu$ and $\mathbf{V} = (u_\alpha, w)$, caused by loads $\mathbf{T}^\mu = (T_\alpha, T_3^*)^\mu$ and $\mathbf{T} = (T_\alpha, T_3^*)$, and some boundary conditions in statics and stationary dynamics, satisfy the reciprocity relations ($\mathcal{A}(\mathbf{V}, \mathbf{T}^\mu)$ is a work of loads $\mathbf{T}^\mu$ on displacements $\mathbf{V}$):

$$\mathcal{A}(\mathbf{V}, \mathbf{T}^\mu) - \mathcal{A}(\mathbf{V}^\mu, \mathbf{T}) = \int_{\partial\Omega} Q_n u_n^\mu + Q_\tau u_\tau^\mu + M_n \phi_n^\mu + P_n w^\mu - Q_n^\mu u_n - \ldots \, d\tau. \tag{5}$$

650

The asymptotic accuracy of Eqs. (2) and (3) is $O(\epsilon)$. For next contributions $\mathbf{U}_1, W_1$ these equations are more complicated by virtue of transverse shear deformations, and obtained by recurrent procedure with $\mathbf{U}_0, W_0$ as perturbation terms. However, at the monoclinic anisotropy with local longitudinal plane of elastic symmetry in plies, Eqs. (1)–(5) and properties 1–5 remain in force for contributions $l\epsilon^{-3}(W_0 + \epsilon W_1)_j = w(\mathbf{x}, t)$, $l\epsilon^{-2}(\mathbf{U}_0 + \epsilon \mathbf{U}_1)_j = \mathbf{u}(\mathbf{x}, t) - z \operatorname{grad} w$. The accuracy of equations becomes $O(\epsilon^2)$ and rigidities γ_{pq}^j are simplified. For the orthotropy with principal axes x_1, x_2 the general structure of equations is the same. All the bending–stretching processes are generally connected at $\xi \neq 0$. Their separation ($\xi = 0$) is possible only in the case of symmetric ply packing, or in some particular cases [3]. When the plies are made of isotropic or transversely (towards the faces) isotropic materials, always $\xi = 0$. It means that a plane, non-deformable at bending, may exist and found from the equation $d_{11}^2(z^-) \equiv d_{22}^2 \equiv d_{12}^2 + 2d_{66}^2 = 0$; $z = 0$.

Anisotropy of laminae	Order of equations		Separation parameter ξ		Accuracy	
	Sym.	Asym.	Sym.	Asym.	Sym.	Asym.
General					$O(\epsilon)$	
Monoclinic Anisotropy, Orthotropy	4, 4	8	$= 0$	$\neq 0$	$O(\epsilon^2)$	
Usual and Transversal Isotropy	4, 4		$= 0$			

All classified cases for the different anisotropy types, and for the symmetric/unsymmetric packing are presented in the Table. The separation of equations ($\xi = 0$) is not equivalent to the BC separation, since ξ contains the variable $d_{12}^2 + 2d_{66}^2$ and each of these rigidities may be not zero. From the viewpoint of solving method such boundary problems are classified into three groups:
1) First BP can be solved as the classical one, by the same method. Besides, we must keep in mind that some stress resultants/couples may be not zero at bending/stretching.
2) Second and mixed BP are reduced to the system of separate equations but connected BC; sometimes this connection may be small. For example, the laminate of isotropic plies with different Poisson's ratios belongs to this group (rigidities in $\mathbf{D}_2$ are proportional to differences of Poisson's ratios);
3) second and mixed BP are completely separated for bending and stretching ($\mathbf{D}_2 = 0$). In the cited example, the equivalence of Poisson's ratios is sufficient for that.

Remark. As known [4], the classical Kirchhoff BC for plates have the error $O(\epsilon)$, and need corrections to obtain the accuracy $O(\epsilon^2)$. For the ordinary accuracy the BC corrections are necessary in the following situations:
1) high difference in the properties of plies, up to the appearance of new small (large) parameters, comparable with ϵ;
2) high inhomogeneous distribution of lateral forces on $\partial\Omega$.
Usual cases do not request corrections. Let us study the connected BP.

BOUNDARY INTEGRAL EQUATIONS

Using the relations (5) and Green tensor we can deduce the boundary integral equations (BIE) by familiar method. Let us represent the obtained results in statics.

On applying the loads in the form of Dirac functions in the point $\mathbf{x}_0$: $\sigma^\pm = \pm 1/2\delta_3^\mu \delta(\mathbf{y})$, $\tau_\alpha^\pm = \pm 1/2\delta_\alpha^\mu \delta(\mathbf{y})$, $\mathbf{y} = \mathbf{x} - \mathbf{x}_0$ ($\mu = 1,2,3$), for the simply connected domain with smooth boundary we obtain:

$$w^3 = 2\mathrm{Re}\Big(\sum_k c_{3k}^3 f(\zeta_k)\Big), \qquad u_\alpha^3 = 2\mathrm{Re}\Big(\sum_k c_{\alpha k}^3 f'(\zeta_k)\Big)$$

$$w^\mu = 2\mathrm{Re}\Big(\sum_k c_{3k}^\mu f'(\zeta_k)\Big), \quad u_\alpha^\mu = 2\mathrm{Re}\Big(\sum_k c_{\alpha k}^\mu f''(\zeta_k)\Big) \quad (\mu = 1,2) \qquad (6)$$

$$f(\zeta_k) = 1/2\zeta_k^2(\ln \zeta_k + \gamma - 3/2), \quad \zeta_k = s_k^\alpha y_\alpha, \ \mathbf{s}_k = (1, \lambda_k); \quad \gamma \approx 0.577215\ldots$$

$$\mathbf{i}_\beta p_{\alpha\beta k} = e^{-\zeta_k} \partial_\beta \chi_{\alpha\beta}(\mathbf{D}_1) e^{\zeta_k}, \ \mathbf{i}_\beta p_{\alpha 3 k} = e^{-\zeta_k} \partial^2_{\alpha\beta} \chi_{\alpha\beta}(\mathbf{D}_2) e^{\zeta_k},$$

$$p_{33k} = e^{-\zeta_k} \partial^2_{\alpha\beta} \chi_{\alpha\beta}(\mathbf{D}_3) \,\mathrm{grad}\, e^{\zeta_k}, \ p_{0k} = (p_{11}p_{22} - p_{12}^2)_k \qquad (7)$$

$$p_k = (p_{33}p_0 - p_{22}p_{13}^2 - p_{11}p_{23}^2 + 2p_{12}p_{23}p_{13})_k$$

$$p(\lambda_k) \equiv p_k = 0, \quad r_k = \partial_\lambda p(\lambda)\mid_{\lambda = \lambda_k}; \quad \lambda_k \in C, \ \mathrm{Im}\lambda_k > 0 \quad (k = 1,2,3,4)$$

$$b_{11k} = (p_{22}p_{33} - p_{23}^2)_k, \quad b_{12k} = (p_{13}p_{23} - p_{12}p_{33})_k, \quad b_{13k} = (p_{12}p_{23} - p_{22}p_{13})_k$$

$$b_{33k} = p_{0k} \quad (1 \leftrightarrow 2); \qquad h_{\alpha k}^\mu = b_{\alpha\beta k}\delta_\beta^\mu + ib_{\alpha 3 k}(\delta_3^\mu - iz_0 s_\beta \delta_\beta^\mu), \quad i^2 = -1$$

$$h_{3k}^\mu = b_{33}(\delta_3^\mu - iz_0 s_\beta \delta_\beta^\mu) - ib_{\alpha 3 k}\delta_\alpha^\mu; \qquad z_0 = 1/2(z^+ + z^-)$$

$$(c_{3k}^3, c_{\alpha k}^3, c_{3k}^\mu, c_{\alpha k}^\mu) = -\frac{1}{2\pi r_k}(-h_{3k}^3, ih_{\alpha k}^3, ih_{3k}^\mu, h_{\alpha k}^\mu)$$

$$v_\alpha(\mathbf{x}_0) = \sum_k \mathrm{Re}\Big(2\pi i \int_{\partial\Omega} -\frac{q_{11k}^\alpha}{\lambda_k}v_1 + q_{22k}^\alpha v_2 - \frac{t_{11k}^\alpha}{\lambda_k}\phi_1 + t_{22k}^\alpha \phi_2 \frac{d\zeta_k}{\zeta_k}\Big) +$$

$$+ \int_{\partial\Omega} u_n^\alpha Q_n + u_\tau^\alpha Q_\tau + \phi_n^\alpha M_n + w^\alpha P_n d\tau + \int_\Omega u_\beta^\alpha T_\beta + w^\alpha T_3 d\Omega,$$

$$\phi_\alpha(\mathbf{x}_0) = \sum_k \mathrm{Re}\Big(2\pi i \lambda^{\alpha - 1} \int_{\partial\Omega} \frac{q_{11k}^3}{\lambda_k}v_1 - q_{22k}^3 v_2 + \frac{t_{11k}^3}{\lambda_k}\phi_1 - t_{22k}^3 \phi_2 \frac{d\zeta_k}{\zeta_k}\Big) - \qquad (8)$$

$$- \int_{\partial\Omega} \partial_\alpha^0 \big(u_n^3 Q_n + u_\tau^3 Q_\tau + \phi_n^3 M_n + w^3 P_n\big) d\tau - \int_\Omega \partial_\alpha^0 \big(u_\beta^\alpha T_\beta + w^\alpha T_3\big) d\Omega$$

$$v_\alpha = u_\alpha + z_0 \phi_\alpha, \quad t_{\alpha\beta k}^\mu = m_{\alpha\beta k}^\mu - z_0 q_{\alpha\beta k}^\mu \quad (\mu = 1,2,3); \quad \partial_\alpha^0 = \frac{\partial}{\partial x_\alpha^0}.$$

In formulas (6)–(8) we consider the general case of simple roots λ_k of 8-th order characteristic polynomial $p(\lambda) = 0$; $\lambda_k \in C$ by virtue of ellipticity; we integrate with respect to $\mathbf{x}$; $\mathbf{x}, \mathbf{x}_0 \in \partial\Omega$. The displacements v_α are taken on the mid plane $z = z_0 \neq 0$; the numbers $q_{\alpha\beta k}^\mu$, $m_{\alpha\beta k}^\mu$ are the coefficients of $\gamma + \ln \zeta_k, \zeta_k^{-1}$, and obtained by substitution of formulas (6) into expressions for $\alpha\beta$ stress resultants and couples. The main results for connected boundary equations are:
1) besides the usual singularity ζ_k^{-1} in the expressions for forces and moments of fundamental solutions (5), new singularity ζ_k^{-2} appears in functions $Q_{\alpha 3}, P_n$;
2) despite this fact Eqs. (5) are reduced to the boundary form (8) with logarithmic and Cauchy singularities of kernels;
3) first BP is reduced to the first kind Fredholm BIE (8) with respect to desired forces and moments, with integrable kernel singularity;
4) second BP is reduced to the second kind singular BIE (8) of Cauchy type, with respect to desired longitudinal displacements and rotation angles. These BIE belongs to the quasi–Fredholm system of equations, i.e., with zero index.

652

Notice, that the first BP can be also reduced to the same kind of system. Thus, the known solving algorithms (boundary elements, special polynomials, etc.) [5] are applicable. Other BP are reduced to the combination of Eqs. (8). Similarly, the case of corner point on $\partial\Omega$ and case of multiply connected domain can be analyzed.

APPLICATION OF FUNCTIONS OF COMPLEX VARIABLES

Like the classical case [6], the method of complex potential (MCP) is applicable for solving the connected BP when $T_\alpha = 0, T_3 = 0$. In contrast to, the attempt to define new Airy function is contradictory, since the corresponding expressions for longitudinal forces are symmetric, and similar expressions for moments (and shearing forces) are antisymmetric with respect to the transposition $x_1 \leftrightarrow x_2$. When the potentials are introduced directly for displacements, we have the formal symmetry everywhere; the necessary sign alternation becomes the automatic property of characteristic numbers λ_k. But the main analogy holds: the relations between potentials ψ_k and the longitudinal displacements or deflection are differential or algebraical, respectively. We arrive at the formulas (not to sum over repeated indices):

$$w = 2Re\left(\sum_k \psi_k(\eta_k)\right), \quad u_\alpha = 2Re\left(\sum_k \frac{p_{\alpha k}}{p_{0k}}\psi_k'(\eta_k)\right) + u_\alpha^0(\mathbf{x}); \qquad \eta_\mathbf{k} = \mathbf{s}_k\mathbf{x} \quad (9)$$

$$2Re\left(\sum_k \frac{p_{\alpha k}}{p_{0k}}\psi_k'\right) = u_\alpha - u_\alpha^0, \quad 2Re\left(\sum_k s_k^\alpha \psi_k'\right) = \phi_\alpha; \qquad \mathbf{x} \in \partial\Omega \quad (10)$$

$$2Re\left(\sum_k \frac{M_{\alpha\alpha k}}{s_k^\beta}\psi_k'\right) = \int_{\tau_0}^\tau M_n dx_\beta \pm P dx_\alpha - M_{\alpha\alpha}^0 x_\beta + (M_{12}^0 \pm c)x_\alpha + c_{\alpha+2}$$

$$2Re\left(\sum_k \frac{Q_{\alpha\alpha k}}{s_k^\beta}\psi_k'\right) = \int_{\tau_0}^\tau Q_n dx_\beta \pm Q_\tau dx_\alpha - Q_{\alpha\alpha}^0 x_\beta + Q_{12}^0 x_\alpha + c_\alpha \quad (11)$$

$$P \equiv \int_{\tau_0}^\tau P_n d\tau; \quad Q_{\alpha\beta}^0, M_{\alpha\beta}^0(u_1^0, u_2^0); c, \ldots, c_4 = \text{Const}; \quad \tau_0 \overset{\frown}{\tau}(\mathbf{x}) \subset \partial\Omega$$

$$2Re\left(\sum_k \frac{q_{13k}}{s_k^2}\Delta_k''\right) = \tilde{Q}_3, \quad Re\left(\sum_k s_k^\alpha s_k^\beta \Delta_k''\right) = 0, \quad Re\left(\sum_k s_k^\alpha \frac{p_{\beta k}}{p_{0k}}\Delta_k''\right) = 0 \quad (12)$$

$$2Re\left(\sum_k \frac{Q_{\alpha\alpha k}}{s_k^\beta}\Delta_k'\right) = \pm\tilde{Q}_\alpha, \quad Re\left(\sum_k s_k^\alpha \Delta_k'\right) = 0 \qquad (\alpha\beta = 12, 21)$$

$$Re\left(\sum_k \frac{p_{\alpha k}}{p_{0k}}\Delta_k'\right) = 0, \quad 2Re\left(\sum_k \frac{M_{\alpha\alpha k}}{s_k^\beta}\Delta_k'\right) = \pm x_\alpha \tilde{Q}_3 \mp \tilde{M}_\beta \tag{13}$$

$$Re\left(\sum_k \Delta_k\right) = 0, \quad 2Re\left(\sum_k \frac{Q_{22k}}{(s_k^1)^2}(\Delta_k - \eta_k\Delta_k')\right) = \tilde{M}_3, \quad Re\left(\sum_k Q_{\alpha 3k}\Delta_k'''\right) = 0 \quad (14)$$

$$\Psi_{kl}(\eta_k) = (1/2 A_{kl}\eta_k^2 + B_{kl}\eta_k + C_{kl})\ln(\eta_k - \eta_{kl}); \qquad \eta_{kl} = \mathbf{s}_k\mathbf{x}_l, \mathbf{x}_l \in \Theta_l. \quad (15)$$

Here the numbers $p_{\alpha k}$ obtained by substitution of (9) into Eqs. (2); u_α^0 are the linear functions of $\mathbf{x}$; $Q_{\alpha\beta}, M_{\alpha\beta}, Q_{\alpha 3}$ are the coefficients of potential derivatives in the expressions for forces and moments; τ_0 is a certain fixed point; $\Delta, \Delta', \ldots$, are the jumps of potential (and its derivatives) at getting around $\partial\Omega$; $\tilde{\mathbf{Q}}, \tilde{\mathbf{M}}$ are the vectors of resultant forces and of resultant moments for the total boundary loads on $\partial\Omega$.

Equations (2) are satisfied; the first BP and second BP are reduced to Eqs. (10)

and (11), respectively. The conditions of single–value for the meaningful variables, and of correspondence to the boundary loads, acquire the form (12)–(14). For the multiply connected domain with not self–balanced load on the hole Θ_l we set the multi–value part (15) of potentials, and find out the constants A_{kl}, B_{kl}, C_{kl} from Eqs. (12)–(14).

Thus, the suggested MCP involves the means of complex analysis. For example, if the domains $\Omega_k : \Omega \to \Omega_k, \mathbf{x} \to \eta_k$ is conformally mapped onto the unit circle, the Eqs. (10) or (11) and exact Schwartz formula yield ψ_k'. In addition, bye virtue of the strong analogy, MCP permits us to use the stored solutions to classical bending and plane problems (up to copying the potential structure). The main difference consists in the double dimension.

Let us mention some canonical domains with simplest solutions to the first and second BP: semi–plane, strip, wedge (using Fourier and Mellin integral transformations); internal/external ellipse and limit cases of cut or rigid inclusion (using Faber's polynomials or Schwartz formula); plane with finite set of finite coaxial cuts/inclusions. hence, we get a set of exact solutions for the testing, and for the singularity analysis in a corner point.

CONCLUSION

The general dynamic models of connected bending–stretching of composite laminates are studied and classified by the anisotropy type and asymptotic error. The methods of integral boundary equations, and of complex potentials, are suggested for numerical–analytical solving the quasistatic boundary problems. Despite the difference in details, the familiar algorithms are valid for such double–dimensional problems.

REFERENCES

[1] Ambartsumyan, S. A. "Theory of Anisotropic Plates". Nauka, Moscow, (1967) [in Russian].

[2] Christensen, R. M. "Mechanics of Composite Materials", Wiley, New York (1979).

[3] Zakharov, D. D. "Asymptotical Integration of 3D Dynamic Equations for Thin Multilayered Anisotropic Plate". *C. R. Acad. Sci. Paris*, t. 315, Série 2, pp. 315–320 (1992).

[4] Goldenweizer, A. L., et Kolos, A. V. "On the Deducing the 2D Equations for the Theory of Thin Elastic Plates". *Appl. Math. and Mech. (PMM)*, vol. 29, No. 1, pp. 141–155 (1962) [in Russian].

[5] Banerjee, P. K., et Butterfield, R. "Boundary Element Methods in Engineering Science". Mc Graw–Hill, New York (1981).

[6] Lekhnitski, S. G. "Theory of Elasticity of an Anisotropic Elastic Body". Holden Day, San Francisco (1963).

PREDICTION OF FATIGUE LIFE FOR BOLTED JOINT IN LAMINATED COMPOSITES

K.D.Zhang   and   C.H.Shi

Aircraft Department,Northwestern Polytechnical University
Mail Box 118,Xian,Shaanxi,710072,Peoples Republic of China   .

INTRODUCTION

Static strength analysis of mechanical joint in composite laminates has been broadly studied in recent twenty five years. But the fatigue response is only researched a little and up to now there is not some successful way to predict it's fatigue life. Fatigue failure is usually developed by bearing damage, and the certain value of permanent deformation of loaded hole is often adopted as the fail examination,such as 0.04D–0.06D value,where D is the diameter of the loaded hole. On the other hand,the linear stress–strain behaviour will be almost maintained for fibre reinforced composites until failure happens. Thus the stress distribution obtained from the linear elasticity theory could be used to evaluate the damage develop as well as the fatigue life.

SOLUTION OF STRESS DISTRIBUTION

The method of complex variable stress function is developed to solve the stress distribution around the loaded hole of orthotropic plates[1,2]. The general equations are as follows:

$$\begin{cases} \sigma_x = 2Re[\mu_1^2\varphi_1'(z_1) + \mu_2^2\varphi_2'(z_2)] \\ \sigma_y = 2Re[\varphi_1'(z_1) + \varphi_2'(z_2)] \\ \tau_{xy} = -2Re[\mu_1\varphi_1'(z_1) + \mu_2\varphi_2'(z_2)] \end{cases} \tag{1}$$

The results from the analytic way possess the following features: A: On the hole circumference,equations of stresses are simplified as closed analytic form;   B: The effect of friction between the fastener and the hole edge could be considered;   C: The effect of plate width on stress distribution has been considered.

Classic laminated theory could be used to compute three in–plane on–axis stresses for per lamina based on the identity of deformation. Yamada–Sun criterion and characteristic curve concept are used to evaluate the static bearing strength. Expressions of them are as follows[3]:

$$\left(\frac{\sigma_1}{X}\right)^2 + \left(\frac{\tau_i}{S}\right)^2 = 1 \tag{2}$$

655

$$r(\theta) = 0.50D + R_t + (R_c - R_t)\cos 2\theta \qquad (3)$$

DATA OF FATIGUE TESTS OF UNIDIRECTIONAL PLATE

General speaking, the fatigue life of laminated composites could be predicted from the fatigue behaviour of longitudinal cyclic loading test of [0] plate[4]. We have done such tests and obtained the corresponding S–N curve[5].

T300 / QY8911 carbon fibre / biopolyimide, [0] specimen, R = 0.10, and f = 10Hz.

Basic properties of this material are shown as table 1, and the log–mean fatigue life for diffrent maximum cyclic load is given in table 2.

Table 1   basic properties of T300 / QY8911

E_{1t} GPa	E_{2t} GPa	G_{12} GPa	γ_{12}	X_t MPa	Y_t MPa	S MPa	v_f %
135	8.8	4.47	0.33	1548	55.5	89.9	60 ± 5

Table 2   log–mean fatigue life of longtidual [0] specimens (R = 0.10)

$\sigma_{max} / \sigma_{ut}$	0.90	0.85	0.80	0.75	0.70	0.60
$\overline{N}$	2.5×10^3	2.4×10^4	1.43×10^5	1.96×10^5	4.57×10^5	$> 10^6$

Testing results may be fitted well by semi–log formulas, it is:

$$\sigma_{max} / \sigma_{ut} = A + B\log\overline{N} \qquad (4)$$

The values of factor A and B are estimated, they are 1.195 and −0.0823, respectively.

PREDICTION OF FATIGUE LIFE FOR MECHANICAL JOINT

The following assumptions are taken for prediction of fatigue life:

A: When the permanent deformation of loaded hole along the load axis reaches the value of 0.06D,the failure happens. Suppose the fastener is rigid absolutely ,the mentioned assumption means the area denoted by the dark line in figure 1 will be damaged entirely. The edge curve of damaged region could be expressed as follows:

$$r = 0.50D + 0.06D\cos\theta \qquad (5)$$

B: Devide the damaged region into several small units,then define the certain elements from per unit according to the differ stacking angle of per ply in laminates.Stress values of edge curve middle point for every element are represented as the mean value.
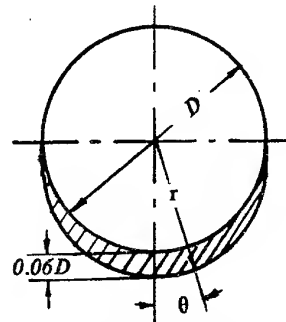
Fig.1 damage region

C: Longitudinal on—axis stress σ_1 for per element is in comparison to the static strength,it is:

$$\sigma_1 = \begin{cases} < X_t (or \quad X_c) & non-fail \\ \geqslant X_t (or \quad X_c) & fail \end{cases} \tag{6}$$

D: Reduce the modulas value of failed elements and recalculate the stress σ_1 for residual lamina elements until no—fail happens for residual plies.

E: Devide the non—failed elements into several group according to the range of σ_1 value, then calculate the cyclic number N_{11} for the first group based upon the formulas (4), reduce the modulas of the first group elements and repeat the mentioned compute procedure and obtain the number N_{12}, N_{13}....., The expression of N_{12} is as follows:

$$N_{12} = N_{11}\left(1 - \frac{N_{11}}{N_{21}}\right) \tag{7}$$

where N_{21} is the cyclic number for the second group obtained also by (4). After non—fail is examined, calculate the number for the second group and obtain the number $N_{21},N_{22},N_{23},...,$then calculate the life number of the third group,the fourth group,...,until the joint failed entirely. The total fatigue number of joint is:

$$N = \sum_{i=1}^{l} N_{1i} + \sum_{i=1}^{m} N_{2i} + \cdots\cdots \tag{8}$$

As an example, we estimated the fatigue life of mechanical joint of T300 / QY8911 $[0 / \pm 45 / 90]_s$ laminate.

Let $\Delta\theta = 10°$ from $0° < \theta < 90°$,thus there are 9 units or 36 elements in the half dark line area. Calculate the damaged elements as well as the corresponding life for $\sigma_{max} / \sigma_{ut} = 1.0,0.95,0.90,...,0.65$, respectively. Results of fatigue failure procedure and life for $[0 / +45 / 90]_s$ plate are shown in table 3.

Table 3   Fatigue failure Procedure and life for $[0 / \pm 45 / 90]_s$

$\sigma_{max} / \sigma_{ut}$ \ σ_1	1.0*	0.95	0.90	0.85	0.80	0.75	0.70	0.65	N	N_T
1.00	31**								(A≈0.87)	
0.95	19	12							5×10^3	/
0.90	18	13							7×10^3	1.2×10^4
0.85	17	1	13						2.38×10^4	4.30×10^4
0.80	17	0	1	13					1.13×10^5	1.41×10^5
0.75	16	1	0	1	13				3.15×10^5	6.02×10^5
0.70	15	1	1	0	1	13			1.344×10^6	/
0.65	13	2	1	1	0	1	13		4.41×10^6	/

* range of longitudinal stress of elements, 1.0 means $1.0\sigma_{ut} > \sigma_1$, 0.95 means $1.0\sigma_{ut} > \sigma_1 > 0.95\sigma_{ut}$.

· number means the failure elements,symbol A means the corresponding area of fail elements.

It is noted that the number of fail elements includes the first grade failure as well as the sub—failure due to stress redistribution.

Other two plates,such as [40 / 50 / 10] and [40 / 40 / 20] laminates are also calculated ,and the results are given in table 4. Number in bracket for plate 1 means 0 ° ply occupies 40% volume, ± 45 ply is 50% volume and 90 ° ply is 10% volume in the laminate.

Table 4   Fatigue life for [40 / 50 / 10] and [40 / 40 / 20] plote

σ_{max}/σ_{ut}	1.00	0.95	0.90	0.85	0.80	0.75	0.70	0.65	NUM
N	1 (A_0=0.76)	2×10^3	4×10^3	1.62×10^4	5.16×10^4	1.46×10^5	2.72×10^5	5.94×10^5	1
N	1 (A_0=0.85)	2×10^3	9.6×10^3	4.08×10^4	?	1.04×10^5	1.76×10^5	5.86×10^5	2

Figure 2 is the S—N curve for those three plates, they are basiclly to be the straight line in semi—log coordinate system which is agreement with experimental data as reported by [7].

RELATION BETWEEN THE PERMANENT DEFORMATION AND FATIGUE LIFE

During the cyclic testing the permanent deformation of loaded hole will be measured. At the beginning it's gradient is much less,then raise steadily. However,after the value reaches 0.04D,the growth rate varies faster and faster,once exceeds 0.06D deformation gredient is very steeply and failure happens. In general case,this variable tendency could be described by the following expression:

$$\delta = A_1(\sqrt{sec\gamma} - 1) \tag{9}$$

where $\delta = (2r - D)/D$, is normal permanent deformation, and

$$\gamma = \frac{\pi}{2}\frac{lgN}{lgN_0} \tag{10}$$

Suppose $N_0 = 1.20N_1$, where N_1 is the fatigue life number corresponding to the deformation value as 0.06D. The predicted results for $[0 / \pm 45 / 90]_s$ plate in the condition $\sigma_{max}/\sigma_{ut} = 0.80$ and R = 0.10 ars given in table 5, shown also in figure 4.($A_1 = 0.01108$)

Table 5   Fatigue life related to differ δ value for $[0 / \pm 45 / 90]_s$ (σ_{max}/σ_{ut}=0.80)

δ	0.01	0.02	0.03	0.04	0.05	0.06	∞
N	1.62×10^4	5.08×10^4	7.66×10^4	9.28×10^4	1.01×10^5	1.102×10^5	(1.322×10^5)

DISCUSSION

One of the key point is how to evaluate exactly the static bearing strength σ_{ut}. Yamada—Sun way is not the best because it is only the point stress criterion and can not describe the failure behaviour. But it does be accepted by engineering.

The second key problem is how to approach the damaged lamina,in othor words, how to

658

degenerate its modulas and calculate the stress redistribution of undamaged lamina? In this paper we proposed the modulas of damaged lamina will decrease 0.5—0.7 for the first failure group (according to the value of A_0) and degrade more for the sub—failure elements until the modulas is supposed to zero.

The results in this paper is obtained in the condition of $R = 0.10$. However the same approach is also suitable in cases $R > 0$, where the S—N curve of unidirectional plate or the value of factor A and B have to be selected in the condition of the same R. But the behiviour of S—N curve of [0] plate in $R < 0$ can not be used to predict the fatigue life of joint with the same R value. The season is some impact effect exists due to the gap between the fastener and the hole. This effect becomes more and more serious accompanying the growth of permanent deformation of loaded hole, it will reduce greatly the fatigue life.

CONCLUSIONS

A. The approach model and method can predict the fatigue life of mechanical joint of laminated composites in the condition of $R > 0$.

B. This method could obtain the failure develop procedure of the joint.

C. analytical results have good agreement with the limited testing data.

REFERENCES

[1] Zhang,K.D.and Ueng,C.E.S."Stresses around a pin—loaded hole in orthotropic plates with arbitrary loading direction."Composite Structures 3, pp119—143 (1985).

[2] Lekhnitskii,S.G."Anisotropic plates."(English edition—translated by S.W. Tsai and T.Cheron),London,Cordon and Breach (1968).

[3] Ueng,C.E.S.and Zhang,K.D."Strength prediction of a mechanically fastened joint in laminated composites." AIAA Journal 23, pp1832—1834 (1984).

[4] Tsai,S.W."Composites design." The third edition (1987).

[5] Guo,S.W. and Zhang, K.D. "Fatigue life prediction for typical composite laminates." (Chinese), Journal of Northwestern Polytechnical University 11, pp85—90 (1993).

[6] Herrington, P.D.and Sabbaghian,M. "Fatigue failure of composite bolted joints." Journal of Composite Materials 23, pp491—512 (1993).
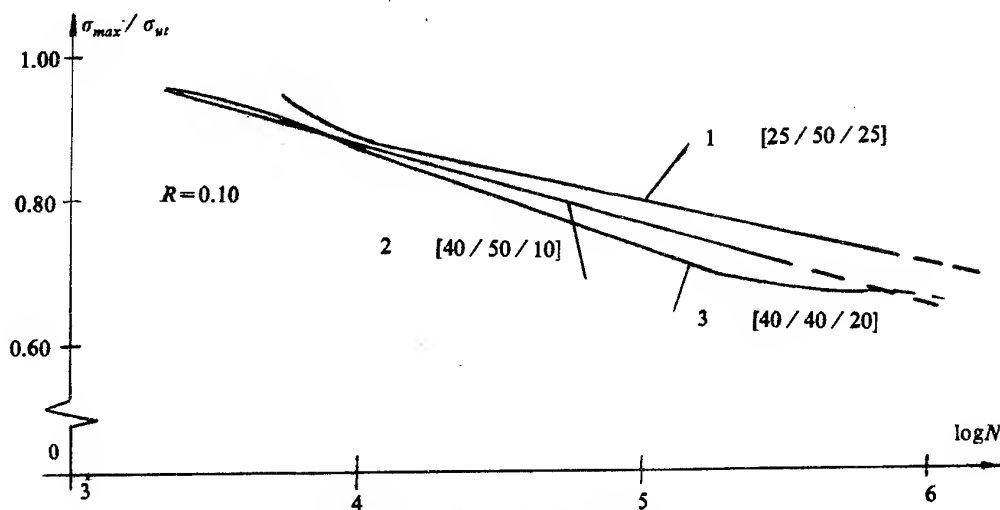
Fig.2   S–N curves of Mechanical joint (Prediction)
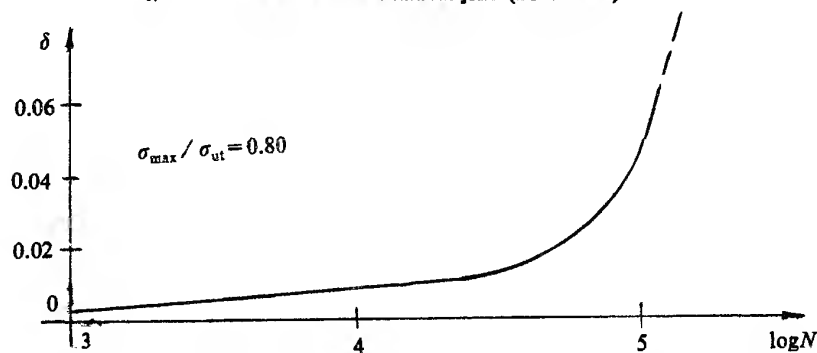
Fig.3 δ–N curve of loaded hole of $[0 / \pm 45 / 90]_s$ plate (prediction)
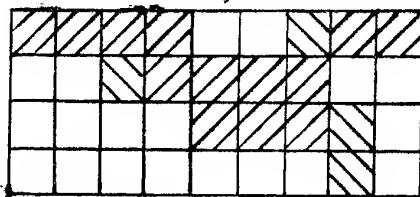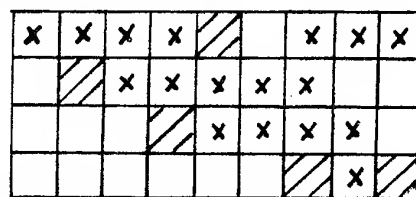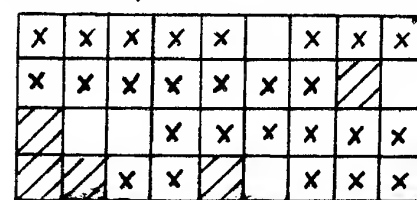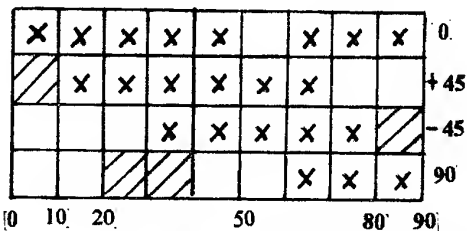
Fig.4   Failure procedure of joint of $[0 / \pm 45 / 90]_s$ plate ($\sigma_{max} / \sigma_{ut} = 0.80$)

660

DESIGN AND OPTIMIZATION OF LAMINATED COMPOSITE PANELS

Zafer Gürdal

Department of Engineering Science and Mechanics Virginia Polytechnic Institute and State University Blacksburg, VA 24061-0219

Abstract

Design of composite materials is a task which requires integration of information from a variety of fields such as micro/macro mechanics, structural mechanics, optimization, and manufacturing. The present paper addresses two of these topics in some detail, namely optimization of composites and structural concepts that are amenable to cost effective manufacturing. First part of the paper will discuss an emerging optimization tool, called Genetic Algorithms, used for laminate stacking sequence design. The presentation of the method will include a Mathematica based notebook demonstrating the key aspects of the algorithm for laminate design. The second portion of the paper will introduce a new design concept, called variable-stiffness laminates. The concept is based on latest advances in manufacturing technologies such as tow-placement machines which allow us to vary the fiber orientations continuously within a given layer. The new concept provides a wide range of design tailoring characteristics compared to traditional laminates. Solution of the in-plane and buckling problem of a rectangular laminate will be presented to demonstrate the features and benefits of the variable-stiffness laminate design.

INTRODUCTION

Design of laminated composite structures is a multilevel and multidisciplinary process which requires reliable computational models, efficient numerical schemes for the solution of those models, structural concepts and configurations that lend themselves to cost effective manufacturing, and appropriate optimization tools to obtain weight efficient structures that have maximum performance. The reliability of the computational models implies the need for accurate prediction of structural response as well as materials level response. By materials response, we mean stresses and strains at the layer level, sometimes including the interlaminar stresses and stresses at the micromechanical level. Such stresses may have important influence on local failures such as the case for compressive kinking failures. Most practical structures have discontinuities in the form of cutouts, holes, notches, ply drop-offs, and attachment joints that introduce local stress concentrations. Stress concentrations make the prediction of the structural failure a difficult task because, in addition to structural models, one needs detailed local models capable of calculating interlaminar and/or micromechanical level stresses. At the structural analysis level, on the other hand, more than often the increased appetite for weight savings results in structures that are thin and highly flexible. Such structures are generally imperfection sensitive and are prone to experiencing large out-of-plane deformations indicating the need for sophisticated nonlinear

analysis approaches that are generally computationally expensive. These aspects of composite structures make the design a difficult task.

Despite the difficulties in designing composite structures, there are various advantages of composite materials that make them desirable for many structural applications. As it is well publicized in the literature, composite materials provide substantial weight savings because of their high specific strength and specific stiffnesses. However, more important than the weight saving alone, composite materials lend themselves tailoring of the structure to meet the requirements of unique design situations, which in turn yield not only lighter structures but structures with improvement performance characteristics. Therefore, more and more designers are adopting composite materials in structural design, and utilizing the methods and tools of structural tailoring in design. One of the important tools of tailoring is mathematical programming based optimization.

Traditionally, engineers designing composite structures used classical methods of optimization for selection of the ply orientations and thicknesses treating them as continuous valued variables. Composite ply thicknesses in a laminate are fixed (typically given by manufacturer's specifications) and, therefore, laminate's total thickness is an integer multiple of the ply thickness. Also, although the engineers theoretically have considerable freedom in deciding the ply orientation angles, more than often cost of manufacturing makes it desirable to limit the selection to a fixed set of integer valued ply orientations, such as $0, \pm45, 90$-deg orientations. Once the traditional continuous variable search is performed, one can round-off the continuous design to its nearest discrete valued design. However, there are several difficulties to this approach. First of all, since one can round the design up or down to the nearest value, there are 2^N possible design configurations for an N design variable problem. For problems with up to 10 design variables the number of possible trial designs are manageable ($2^{10} = 1024$). But for problems with more design variables the number could be unmanageably large. For example for a problem with 20 design variables there are more than one million possibilities. Moreover, most of the rounded off designs may be infeasible. There is also a possibility that none of the rounded-off designs are optimal, but the best design could be a discrete combination far from the continuous optimal design. Therefore, the optimal design of a composite laminate is a combinatorial optimization problem and must be treated as such.

Genetic algorithms (GA's) have recently emerged as powerful tools for discrete valued optimization problems and, therefore, ideally suited for the design of laminated composite structures. In the following we discuss some of the features of GA's with an emphasis on their implementation for stacking sequence optimization. Following the optimization section, a new design concept based on tow-placement manufacturing technology will be introduced.

GENETIC ALGORITHMS FOR LAMINATE DESIGN

Genetic algorithms use techniques derived from biology, and rely on Darwin's principle of survival of the fittest. When a population of biological species evolves over generations, characteristics that are useful for survival tend to be passed on to future generations, because individuals carrying them get more chances to

breed. Individual characteristics in biological populations are stored in chromosomal strings. The mechanics of natural genetics are based on operations that result in structured yet randomized exchange of genetic information (i.e., useful traits) between the chromosomal strings of the reproducing parents, and consist of *crossover*, and occasional *mutation* of the chromosomal strings.

Genetic algorithms simulate the mechanics of natural genetics for artificial systems based on operations which are the counterparts of the natural ones. The reader is referred to Goldberg [1] for further discussion of the standard genetic operators and theoretical properties of genetic algorithms. Here we present a brief overview of the algorithm.

There are a few basic differences between the traditional search algorithms and the GA's. One of these differences is the number of designs used to perform the search. Traditional search algorithms typically use a single design during the search process by jumping from one design to another improved design. GA's on the other hand use a population of *NPOP* designs which simulate a biological population. This aspect of the algorithm will be contrasted with the traditional search algorithms during the presentation using computer based animation. Another aspect of the GA's is that they use a coded version of the design variables rather than the design variables themselves.

Stacking Sequence Coding

In its standard form, application of the operators of the GA, to a search problem requires the representation of design variables in terms of bit strings that are counterparts of the natural chromosomes. In specializing genetic algorithms for laminate stacking sequence design, the first departure from the classical problem formulation is in design variable coding. Since laminates are generally built from 0-, ±45-, and 90-deg plies, it is convenient to replace the binary coding with a higher alphabet. In addition, for balanced laminates we require a +45-deg ply to be paired a −45-deg ply, therefore, the coding can be simplified by using stacks of two plies each as the basic building blocks. Thus, the three possible stacks are: 0-deg coded as the integer 1, ±45-deg coded as 2, and 90-deg coded as 3. For example, the symmetric laminate $[90_2, \pm 45_2, 90_2, 0_2, \pm 45_2, 0_2]_s$ is coded as 3 2 2 3 1 2 2 1. The rightmost 1 corresponds to the stack closest to the laminate plane of symmetry.

Design of a laminate entails not only the selection of the orientations for specified thickness, but also the number of layers in the laminate to determine the optimal thickness. Thus, a mechanism which allows changing the length of the string representation of the laminate is needed. This is achieved by using, for example, zeros in the string to identify empty stacks. Naturally, a laminate cannot have void layers in its interior. Even if the initial population does not have interior voids, some of the genetic operators (such as mutation, or the permutation operator described later) can generate such voids. Interior voids are eliminated by moving the zero towards the exterior of the laminate and packing the string without disturbing the order of the other plies. This procedure is called string packing. For example, in case of a single ply coding with 0, 1, 2, 3, and 4 representing the empty ply, 0-, 45-, −45-, and 90-deg plies, respectively, following string show the coding with zeroes and its corresponding laminate stacking sequence, 1 0 4 2 0 3 ⇒ 0 0 1 4 2 3

663

$\Rightarrow$ $[0/90/45/-45]_s$ For variable thickness laminates, care must be also given to choose a long enough initial string to accommodate the optimal thickness in the event that it is larger than expected.

Genetic Operators

Basic operators used to create successive improved populations include selection, crossover, mutation, and interchange. Typically, two designs selected from a population are mated to create child design(s). In order to ensure that good designs propagate to the child populations, a higher chance to be selected as parents is given to those designs that are better than the rest of the population. Selection is a the part of the algorithm that provides better opportunity to good designs by implementing a roulette wheel which is divided into slices representing different designs. Those designs with better characteristics are given a proportionally larger slices of the wheel. When the wheel spun (simulated by using a random number generator between 0 and 1, where the circumference of the wheel is normalized to be 1), those designs that occupy larger slices of the wheel have better chance to be chosen as parent designs.

Crossover operator: Once a pair of parents are selected, the mating of the pair also involves a random process called crossover. This is achieved by generating a random integer k between 1 and $L-1$, where L is the string length. This number defines a cutoff point in each of the two strings, and separates each into two substrings. By splicing together the left part of the string of one parent with the right part of the string of the other parent a child string is generated. Consider, for example, two symmetric laminates coded in a string of length $L = 9$, and a crossover point $k = 5$

$$\text{parent 1:} \qquad 0\ 0\ 1\ 2\ 1\|3\ 1\ 1\ 1 \qquad [0/45/0/-45/0_3]_s\,,$$
$$\text{parent 2:} \qquad 0\ 0\ 0\ 0\ 1\|2\ 3\ 4\ 1 \qquad [0/45/-45/90/0]_s\,.$$

The two possible child designs are

$$\text{child 1:} \qquad 0\ 0\ 1\ 2\ 1\ 2\ 3\ 4\ 1 \qquad [0/45/0/45/-45/90/0]_s\,,$$
$$\text{child 2:} \qquad 0\ 0\ 0\ 0\ 1\ 3\ 1\ 1\ 1 \qquad [0/-45/0_3]_s\,.$$

One or both of the child designs are then selected for the next generation.

Mutation operator: Mutation is implemented by changing, at random, the value of a digit in the string with small probability, and served for the purposes of avoiding premature loss of diversity in the designs. That is inferior designs may have some good traits that can get lost in the gene pool when these designs are not selected as parents. By introducing occasional mutations, we can search/investigate different portions of the design space for valuable information.

Interchange operator: The standard crossover and mutation operators work well in searching the design space for the right combinations of ply orientations. However, these operators are less efficient for rearranging these orientations into the optimal stacking sequence. A new stochastic operator, called interchange, was developed for this purpose by Le Riche and Haftka [2]. Interchange swaps the

values of the integers between two randomly assigned points. For example,

Before interchange: 2 3 1 2 2 2 1 1 **After interchange:** 2 1 1 2 2 2 3 1

The laminate described by the first string is $[\pm45, 90_2, 0_2, \pm45_3, 0_4]_s$ and after interchange it becomes $[\pm45_4, 0_2, 90_2, 0_4]_s$. The interchange operator is appealing especially for buckling optimization problems, because it creates alternative designs with different stacking sequences without changing the in-plane properties of the laminates.

Most of the features of the GA's discussed above will be discussed using a live demonstration software during the conference presentation.

VARIABLE STIFFNESS LAMINATES

State of the art manufacturing techniques for composite laminates, such as the automated fiber/tow placement techniques, allow the fiber orientation angle of a layer to be a function of position throughout the structure (curvilinear layers). The resulting laminates have variable stiffness properties that change from one location to another without changing the thickness of the laminate. Upon loading, variable stiffness properties result in variable stress and strain distributions throughout the structure that may enhance the response of such laminates compared to the conventional straight fiber format laminates.

In-plane analysis of rectangular panels made of balanced symmetric angle-ply laminates that have $[\pm\theta]_s$ variable fiber angles along the longitudinal axis of the panel has recently been presented [3] under uniaxial compression. By using a linear fiber angle variation, closed-form solutions were determined for the in-plane stress distribution and displacements of rectangular panels with various boundary conditions under uniform applied edge displacements. Variation of the fiber orientation in one specified direction makes it possible to manufacture such panels via tow-placement machines since the fibers remain parallel to one another if they are varied in one direction only. For such panels under longitudinal compressive loads the fiber orientation angle variation might be tailored to produce transverse tensile stress field at the center of the panel where it wants to buckle so that gains in buckling load are achieved compared to straight fiber format panels. In addition, it was observed that the distribution of the internal loads can be tailored favorably to improve the buckling load of variable stiffness panels beyond the maximum buckling load that can be obtained for straight fiber format panels. More recently, manufacturing related constraints for the fabrication of variable stiffness panels were studied and two different form of stiffness variation was identified. The parallelism of the fiber paths suggested earlier proved to be in substantial error when large fiber orientation variation from one point in the panel to another takes place over a short distance. A new formulation based on true parallelism of the fibers was developed.

In the following section, first the convention for the laminate description is provided. Then, constitutive relations for a laminate with variable stiffness properties based on classical lamination theory are summarized. Results that demonstrate the benefits of the variable stiffness laminates based on two methods of fiber path generation will be presented at the conference for panels under uniaxial compressive and shear loads.

Laminate Definitions

The variable stiffness laminates studied in this paper are rectangular and obtained by varying the fiber orientation angle, θ, vary as a linear function of x' in an x'-y' coordinate system located at the center of the laminate. If θ varies linearly over a distance "a", $-a/2 \leq x' \leq a/2$, where "a" is the length of the laminate along the primary load axis x of the laminate, then the fiber angle is defined by

$$\theta(x') = \begin{cases} 2\frac{(T_o - T_1)x'}{a} + T_0 & \frac{-a}{2} \leq x' \leq 0 \\ \\ 2\frac{(T_1 - T_o)x'}{a} + T_0 & 0 < x' \leq \frac{a}{2} \end{cases} , \qquad (1)$$

where T_o is the angle at $x' = 0$ and T_1 is the angle at $x' = a/2$. It is also assume that the fiber pattern is periodic beyond the range $-a/2 \leq x' \leq a/2$.

Since there are more than one angles involved in describing a single layer, a new convention is needed for the description of a laminate. In this paper a convention is adopted to represent a single curvilinear layer by "$\langle T_o | T_1 \rangle$". Similar to the conventional representation, a $\pm$ sign in front of this unit element of a curvilinear description means that there are two layers with equal and opposite variation of the fiber orientation angle. With this description it is now possible to put together balanced symmetric laminates.

It is also possible to construct laminates by rotating the fiber orientation variation direction x' from the primary load axis x of the laminate. Therefore, a third angle, ϕ, is needed to fully describe a curvilinear layer. The modified representation of a single curvilinear layer is "$\phi\langle T_o | T_1 \rangle$". In this case the properties of the laminate may be a function of both the x and the y coordinates. One can also construct laminates with different combinations of the ϕ angle, laminates with $\pm\phi$ angles without the "$\pm$" in front of the curvilinear stack, and curvilinear laminae in combination with straight fiber layers. Several examples of variable stiffness laminates will be shown during the conference presentation.

Constitutive Relations

The analysis used for the variable stiffness laminates is based on the extension of the Classical Lamination Theory. The constitutive relations for a thin laminate are in the form

$$\begin{Bmatrix} N \\ M \end{Bmatrix} = \begin{bmatrix} A & B \\ B & D \end{bmatrix} \begin{Bmatrix} \epsilon \\ \kappa \end{Bmatrix}, \qquad (2)$$

where the vectors N and M represent the stress resultant forces and moments, and ϵ and κ denote the mid-plane strains and curvatures, respectively. For symmetric laminates the coupling matrix B is identically zero and the in-plane response is decoupled from the bending response,

$$\begin{Bmatrix} N_x \\ N_y \\ N_{xy} \end{Bmatrix} = \begin{bmatrix} A_{11} & A_{12} & A_{16} \\ A_{12} & A_{22} & A_{26} \\ A_{16} & A_{26} & A_{66} \end{bmatrix} \begin{Bmatrix} \epsilon_x \\ \epsilon_y \\ \gamma_{xy} \end{Bmatrix}, \quad \text{and} \quad \begin{Bmatrix} M_x \\ M_y \\ M_{xy} \end{Bmatrix} = \begin{bmatrix} D_{11} & D_{12} & D_{16} \\ D_{12} & D_{22} & D_{26} \\ D_{16} & D_{26} & D_{66} \end{bmatrix} \begin{Bmatrix} \kappa_x \\ \kappa_y \\ \kappa_{xy} \end{Bmatrix}. \quad (3)$$

For variable stiffness laminates the elements of the A, and D matrices are functions of the panel spatial coordinates (as opposed to being constants for the straight

fiber panels), and are calculated from the reduced transformed stiffness terms via through-the-thickness integration

$$\{A_{ij}, B_{ij}, D_{ij}\} = \int_{-h/2}^{h/2} \bar{Q}_{ij} \{1, z, z^2\} \, dz, \qquad (4)$$

where the $\bar{Q}_{ij}$ terms vary from one layer to another and are also functions of the panel coordinates. The $\bar{Q}_{ij}$ terms for the k-th layer are

$$
\begin{aligned}
\bar{Q}_{11} &= U_1 + U_2 \cos 2\theta + U_3 \cos 4\theta, & \bar{Q}_{12} &= U_4 - U_3 \cos 4\theta, \\
\bar{Q}_{22} &= U_1 - U_2 \cos 2\theta + U_3 \cos 4\theta, & \bar{Q}_{66} &= U_5 - U_3 \cos 4\theta & (5) \\
\bar{Q}_{16} &= -\frac{1}{2} U_2 \sin 2\theta - U_3 \sin 4\theta, & \bar{Q}_{26} &= -\frac{1}{2} U_2 \sin 2\theta + U_3 \sin 4\theta,
\end{aligned}
$$

where the functional form of the $\theta(x, y)$ depends on the variation of the fiber orientation angle given by Eq. 1, and the orientation of the fiber orientation variation direction for that layer from the x direction. The U's in the above equations are related to the unidirectional properties of the material. Note that the orientation of the direction of fiber orientation variation, ϕ, is accounted for via coordinate transformation from x' to x axis.

In-Plane Analysis

For straight fiber format panels the prebuckling stresses are uniformly distributed unless the panel has a discontinuity. The variable stiffness panels, on the other hand, have nonuniform distribution of in-plane displacements u and/or v, and one or more of the in-plane stress resultants are nonuniform over the panel (for example, $N_x = N_x(x, y)$ or $N_y = N_y(x, y)$). The variation of the in-plane stresses depend on the variation axis angle ϕ, the variation angles T_0 and T_1, and the in-plane boundary conditions along the unloaded panel edges. Although closed form solutions are possible for some special cases of variation axis angle and boundary conditions (see Ref. [3]), in general evaluation of the in-plane stresses requires a numerical procedure because the two in-plane equilibrium equations in terms of the u and v displacements are coupled. Details of the formulation and solution of the governing equations of the in-plane response of variable stiffness laminates that have variation of fiber orientation angle in one direction are given in Ref. [3]. In the present paper, the same numerical approach based on the elliptic differential equation solver, ELLPACK [4], used in Ref. [5] is used to solve for the in-plane displacements and stresses.

The conference presentation will demonstrate the variability of the in plane stress resultants, N_x, N_y, and N_{xy}, as a function of the fiber path variations for panels loaded by a uniform end-shortening along the edges $x = \pm a/2$, with the transverse edges, $y = \pm b/2$, free with respect to the in-plane displacements. Mechanisms that will enhance the response of the panels will be identified.

667

Buckling Analysis

Buckling analysis of variable stiffness panels was developed earlier in Ref. [5] based on Ritz method. For the panels considered here all four edges are assumed to have zero out-of-plane displacements, and the applied moment at each edge is identically zero. A series approximation for the out-of-plane displacement of the following form,

$$w(x,y) = \sum_{m=1}^{M} \sum_{n=1}^{N} A_{mn} \sin\left(\frac{m\pi x}{a}\right) \sin\left(\frac{n\pi y}{b}\right), \tag{6}$$

satisfies these boundary conditions and can be easily incorporated into the analysis. After substituting the assumed displacement into the expression for the total potential energy of the panel, application of the stability criterion yields a matrix eigenvalue problem of the form

$$[K]\{A\} - \lambda[M]\{A\} = 0, \tag{7}$$

where the elements of the stiffness matrix $[K]$ are sums of integrals in the potential energy expressions containing the D_{ij} terms, and the elements of the geometric stiffness matrix $[M]$ are sums of integrals containing the stress resultants. Note that for straight fiber panels, the D_{ij} terms and stress resultants may be moved out of the integrals since they are independent of x and y. However, for variable stiffness panels the D_{ij} and the stress resultants may be functions of x and y and must remain as part of the integrand.

Buckling response of various variable stiffness panels for different fiber path definitions and loading combinations will be shown during the conference presentation, and comparison of the results with those of straight fiber panels will be made.

REFERENCES

1. Goldberg, D.E., "Genetic Algorithms in Search, Optimization, and Machine Learning", *Addison-Wesley Publishing Co. Inc.*, Reading, MA, 1989.

2. Le Riche, R., and Haftka, R.T., "Optimization of Laminate Stacking Sequence for Buckling Load Maximization by genetic Algorithm," *AIAA Journal*, Vol. 31, No. 5, pp. 951-970, 1993.

3. Gürdal, Z., and Olmedo, R. A., "Composite Laminates with Spatially Varying Fiber Orientations: Variable Stiffness Panel Concept," *AIAA Journal*, Vol. 31, No. 4, pp. 751-758, 1993.

4. Rice, J. R., and Boisvert, R. F., "Solving Elliptic Problems Using ELLPACK", *Springer-Verlag*, New York, NY, 1984.

5. Olmedo, R. A., and Gürdal, Z., "Buckling Response of Laminates with Spatially Varying Fiber Orientations," Proceedings of the AIAA/ASME/ASCE/AHS/ASC 34th SDM Conference, April 19-21, La Jolla, CA, pp. 2261-2269, 1993.

AUTHOR INDEX